CHALMERS

16th International Symposium on Space Terahertz Technology

Conference Proceedings ISSTT 2005
May 2-4
Göteborg, Sweden

ONSALA SPACE OBSERVATORY
CHALMERS UNIVERSITY OF TECHNOLOGY

MC2
Microtechnology and Nanoscience

Proceedings of the 16th International Symposium on Space Terahertz Technology

Mattias Ingvarson, Jan Stake, Harald Merkel, Editors

Chalmers University of Technology
Department of Microtechnology and Nanoscience (MC2)
Microwave Electronics Laboratory
SE-412 96 Göteborg, Sweden
Phone: +46 (0) 31 772 1000

ISSN 1652-0769
Technical Report MC2-63

Cover

Vinga lighthouse, on the island Vinga in the archipelago of Göteborg, Sweden.
Photograph by Kjell Holmner.

The beautiful island of Vinga is known as the last outpost before the open waters of the North Sea. Vinga is only on hour and 15 minutes by boat from Göteborg. The famous Swedish poet Evert Taube grew up here, where his father was the lighthouse keeper. There are fine sites for swimming on the island and it is said that the sun almost always shines on Vinga!

SPONSORS

Chalmers Center for High-Speed Technology

Swedish Research Council

TABLE OF CONTENTS

INTRODUCTION

The sixteenth International Symposium on Space Terahertz Technology (ISSTT) was held at Chalmers, Göteborg, Sweden on May 2-4, 2005. This was the first time the ISSTT meeting was held outside the USA. More than 147 delegates from Europe, USA and Asia attended and 147 scientific papers were presented. The program was divided into 11 oral sessions with 63 papers (5 invited) and one poster session with 83 papers.

The meeting was organised by research groups at the microwave electronics laboratory, MC2, and GARD, Onsala space observatory. The latest results on terahertz technologies for space applications were presented, such as sensitive superconducting electronics (HEB/SIS), detectors, sources and systems. New applications of terahertz technology, e.g. for biotechnology, were also presented by Peter Siegel, Caltech (invited talk). Furthermore, we offered lab tours through MC2 on the Monday, a conference dinner at Älvsborgs fästning on the Tuesday, and finally a trip to Onsala space observatory after closing the scientific meeting on the Wednesday afternoon.

The geographical distribution of the paper contribution at the meeting is shown below:

	Papers	**Participants**
USA, Canada		32
Europe, Middle East		104
Asia and Pacific		11
Total:		147

The symposium was sponsored by the Swedish Research Council (VR), the IEEE Sweden Section, the Swedish Space Corporation, Ericsson AB, COMSOL AB and our exhibitors: Omnisys Instruments AB, SAAB Ericsson Space AB, and the European Southern Observatory (ESO). I would like to thank these organisations for their support. I would also like to thank everyone who helped to make the Symposium a success: the international steering committee for advice and for reviewing abstracts; the local organising committee; Eva Hellberg and Peter Jönsson for all WEB support; Monica Hansen-Torvaldsson, Catharina Forssén, and Ingrid Collin for help with registrations and payments; Chalmers president Jan-Eric Sundgren and Erik Kollberg for opening the meeting; staff at Chalmers Conference Centre; the session chairs; and everyone who attended or contributed a presentation. Also an additional thanks to Mattias Ingvarson for putting this proceedings together.

Jan Stake

The next symposium (ISSTT 2006) will be held in Paris, May 10-12, 2006.

ORGANISING STAFF

Organising committee

Jan Stake	Harald Merkel	Victor Belitsky
Therese Berg	Sergey Cherednichenko	Vessen Vasilev
Arne Øistein Olsen	Pourya Khosropanah	Arezoo Emadi
Josip Vukusic	Erik Kollberg	Eva Hellberg
Catharina Forssén	Raquel Rodriguez-Monje	Mathias Fredrixon

International steering committee

The organisers would like to thank the international steering committee for helping to review all submitted abstracts and papers:

Tom Crowe	Qing Hu	Peter Siegel
Jack East	Karl Jacobs	Edward Tong
Heribert Eisele	Teun Klapwijk	Christopher Walker
Brian Ellison	Antony Kerr	Stafford Withington
Neal Erickson	Imran Mehdi	Wolfgang Wild
Gregory Gol'tsman	Antti Räisänen	Sigfrid Yngvesson

CONFERENCE PROGRAMME

Sunday, May 1, 2005
18.00 - 21.00 Registration in Chalmers kårhus

Monday, May 2, 2005
07.00 -12.00 Registration in Chalmers kårhus
08.30 - 09.20 Session 1 : Introduction (Erik Kollberg)
09.20 - 10.30 Session 2 : Sources I (Antti Räisänen)
10.30 Coffee
11.00 - 12.30 Session 3 : SIS I (Viktor Belitsky)
12.30 Lunch
14.00 - 15.40 Session 4 : Systems I (Heribert Eisele)
15.40 Coffee
16.00 - 19.00 Session 5 : Poster Session (H. Merkel, J. Stake, J. Vukusic)
19.00 - 21.00 Lab tour, MC2

Tuesday, May 3, 2005
08.30 - 10.25 Session 6 : Sources II (Jan Stake)
10.25 Coffee
11.00 - 12.30 Session 7 : HEB I (Sigfrid Yngvesson)
12.30 Lunch
13.30 - 15.25 Session 8 : SIS II (Netty Honingh)
15.25 Coffee
15.40 -17.10 Session 9 : HEB II (Heinz-Wilhelm Huebers)
18.30 - 23.00 Boat trip and dinner at Älvsborgs fästning

Wednesday, May 4, 2005
08.30 - 09.45 Session 10 : Schottky receivers (Tony Kerr)
09.45 Coffee
10.00 - 11.45 Session 11 : Components (Alexandre Karpov)
12.15 Lunch
13.00 - 15.00 Session 12 : New detectors (Eyal Gerecht)
15.00 - 15.30 Session 13 : Closing session (Jan Stake)
16.00-19.00 Exhibit tour to Onsala Space Observatory

CONFERENCE PHOTOS 1

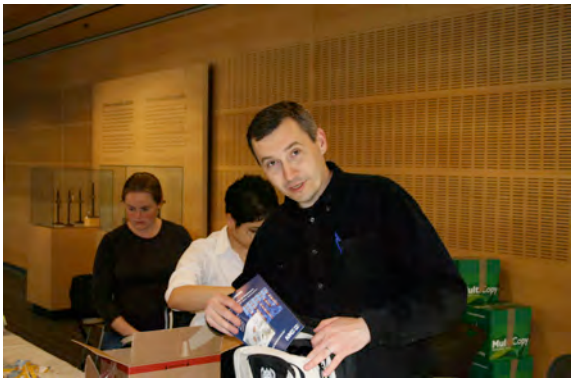

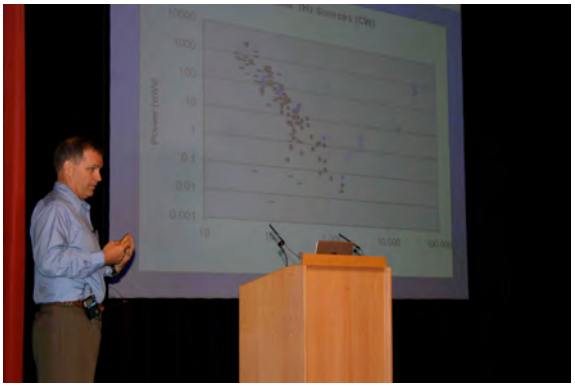

CONFERENCE PHOTOS 2

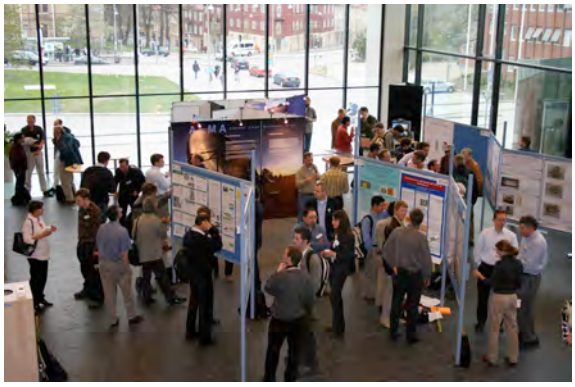

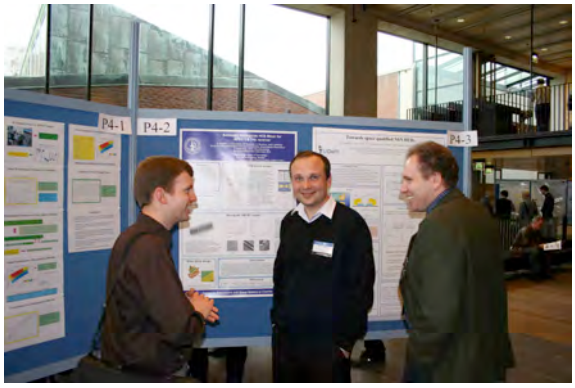

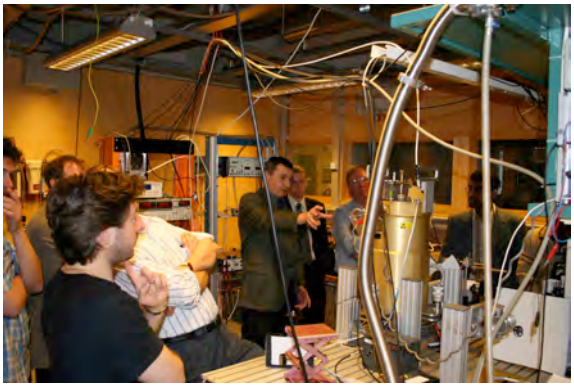

CONFERENCE PHOTOS 3

Session 1:

Introduction

Monday May 2, 8:30-9:20
Chairman: Erik Kollberg

Astronomy at sub-millimetre wavelengths.
An overview of the forthcoming projects and their scientific goals.

Roy Booth,
Onsala Space Observatory

The sub-millimetre part of the electromagnetic spectrum is one of the last to be opened up for astronomy, partly because of the Earth's atmospheric opacity and partly because of the technical difficulties of building radio astronomy receivers at these wavelengths. However, recognition of the astronomical importance of the Teraherz bands has driven the engineering effort to build space-borne submm telescopes and, after relatively simple beginnings with, for example, the 1.1m ODIN telescope project, we can look forward to the Herschel mission and the Sophia high altitude aeroplane in the next few years. We have even found high altitude sites where the atmospheric transparency is sufficiently high to allow observations at frequencies up to 1.5 THz and already the James Clerk Maxwell telescope and the Smithsonian Submillimetre Array are operational on Hawaii and the APEX telescope and the ALMA array are underway on the Andean site of Llano Chajnantor at 5 km altitude.

The scientific rewards for this effort will be spectacular. At submm wavelengths we will observe the cold, dust enshrouded regions of space where the cosmic molecules are concentrated. At submm wavelengths we will see, with more and more clarity, what is behind the dust and with that clarity will emerge a picture of protostars and early stellar evolution as well as further understanding of galaxy formation in the distant (early) Universe.

In this presentation I will review these new projects and their scientific motivation, with special reference to the APEX project, a collaboration between the Max-Planck-Institüt für Radioastronomie, Bonn, ESO and Sweden (Onsala).

Session 2:

Sources I

Monday May 2, 9:20-10:30
Chairman: Antti Räisänen

Terahertz quantum-cascade lasers

Qing Hu
Massachusetts Institute of Technology, Cambridge MA 02139

The main challenge for the space THz program is solid-state local oscillators that can meet space qualifications in terms of output power levels and power efficiencies. Semiconductor electronic devices (such as frequency multipliers) are limited by the transient time and *RC* roll-off to below 2 THz. Conventional semiconductor photonic devices (such as bipolar laser diodes) are limited to above 10 THz even using small-gap lead-salt materials. Transitions between subbands in semiconductor quantum wells were suggested as a method to generate long wavelength radiation at customizable frequencies. However, because of difficulties in achieving population inversion between narrowly separated subbands and mode confinement at long wavelengths, THz lasers based on intersubband transitions were developed only very recently. The first THz quantum cascade lasers were developed based on a chirped superlattice structure. Recently, taking a completely different approach, we have developed THz quantum-cascade lasers based on resonant-phonon-assisted depopulation and using metal-metal waveguides for mode confinement. The band diagram of the QCL structure is illustrated in Fig. 1(a). Based on the combination of these two unique features, we have developed many THz QCLs with record performance, including a maximum pulsed operating temperature at 147 K (Fig. 1(b)), a maximum cw operating temperature at 97 K (Fig. 1(c)), and the longest wavelength (~141 μm) QCL to date without the assistance of magnetic fields (Fig. 1(d)). We will present more details and perspective at the symposium.

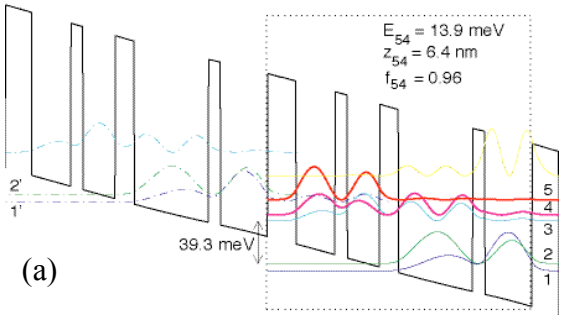

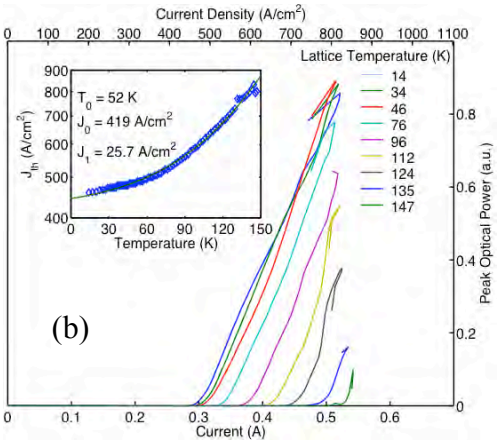

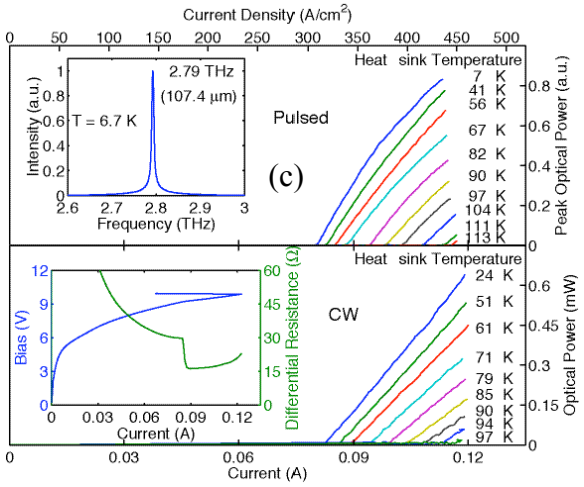

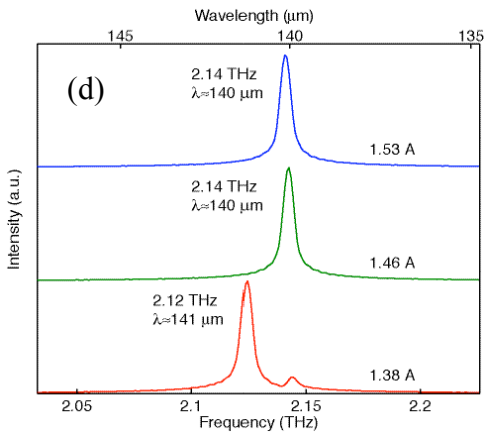

Investigation of a 2.5 THz Quantum Cascade Laser as Local Oscillator

H.-W. Hübers, S. G. Pavlov, A. D. Semenov
German Aerospace Center (DLR)
Rutherfordstr. 2, 12489 Berlin, Germany

A. Tredicucci, R. Köhler, L. Mahler
NEST-INFM and Scuola Normale Superiore
Piazza dei Cavalieri 7, 56126 Pisa, Italy

H. E. Beere, E. H. Linfield, D. A. Ritchie
Cavendish Laboratory, University of Cambridge, Madingley Road,
Cambridge CB3 0HE, United Kingdom

Heterodyne spectroscopy of molecular rotational lines and fine structure lines of atoms or ions is a powerful tool for exploring the interstellar medium as well as planetary atmospheres. The Terahertz (THz) part of the electromagnetic spectrum is especially rich in these lines. Some examples are the CII fine structure line at 1.6 THz, the OH rotational transition at 2.5 THz, and the OI fine structure line at 4.7 THz. Typically, below ~2 THz multiplied microwave sources are used as local oscillator in a heterodyne receiver. However, at higher frequencies the output power of these sources is still too low to be used as local oscillator. Recently developed THz quantum cascade lasers (QCL) are a promising alternative. The lasing mechanism is based on intersubband transitions in the conduction band of GaAs/AlGaAs heterostructures. Attractive features of a QCL, which have been demonstrated until now, are laser emission between 1.9 THz and 4.8 THz, operation temperatures up to ~140 K, high output power up to ~90 mW, single mode operation and narrow linewidth. In addition, the laser threshold can be as low as 19 mA at 4.2 K. We will report on the characterization of a 2.5 THz QCL with respect to performance parameters relevant for the use as a local oscillator. Fourier transform measurements show that the laser emission is mono-mode over a wide range of current and temperature. At high current when the laser emission is multi-mode the mode structure has been analyzed by homodyne mixing experiments and the frequency stability with respect to the operation temperature and current was investigated. The linewidth of the QCL was below 30 kHz. The beam profile of the QCL was shaped in order to match it to the antenna pattern of a quasi-optical hot electron bolometer (HEB) mixer. With this optical setup the HEB could be pumped into the normal state. Noise temperature measurements of the HEB at 2.5 THz with the QCL as local oscillator yielded the same results as with a gas laser at 2.5 THz. For these measurements the HEB was mounted in an optical cryostat while the QCL stayed in a mechanical cryocooler. In summary the QCL is a very promising candidate for a local oscillator.

A novel terahertz heterodyne receiver based on a quantum cascade laser and a superconducting bolometer

J.R. Gao, J.N. Hovenier, Z.Q. Yang, J.J.A. Baselmans, A. Baryshev, M. Hajenius, T.M. Klapwijk, A.J.L. Adam, T.O. Klaassen, B.S. Williams, S. Kumar, Q. Hu and J. L. Reno

Abstract— **We report the first demonstration of an all solid-state heterodyne receiver that can be used for high-resolution spectroscopy above 2 THz suitable for space-based observatories. The receiver uses a NbN superconducting hot electron bolometer as mixer and a quantum cascade laser operating at 2.8 THz as local oscillator. We measure a double sideband receiver noise temperature of 1400 K at 2.8 THz and 4.2 K, uncorrected for losses in the optics, and find that the free-running QCL has sufficient power stability for a practical receiver, demonstrating an unprecedented combination of sensitivity and stability. The output power of the QCL is more than adequate for use with HEB's. The complete system provides a unique solution for high-resolution THz spectroscopy for astronomy as well as Earth science in space.**

Index Terms—**heterodyne receiver, mixer, superconducting hot electron bolometer mixer, quantum cascade laser, LO source, and terahertz.**

I. Introduction

Understanding of the complex astrophysics depends critically on the ability to perform high-resolution spectroscopy in the THz frequency region. There are about 4×10^4 individual spectral lines present in the interstellar medium (ISM), only a few thousand of which have been resolved and many of these have not been identified [1,2]. Detection of the emissions from the ISM is critical to the study of the cycle of gestation, birth, evolution, and death of stars and planets [3]. The THz region also covers all of the critical spectral emissions from the key molecules involved in atmospheric chemistry both on Earth and on the planets. Some of them have been identified as crucial to our understanding and monitoring of the global ozone depletion problem [4].

Heterodyne receivers are the only receivers that can offer very high spectral resolution ($\nu/\Delta\nu > 10^6$ where ν is the frequency) combined with quantum noise limited sensitivity [5]. A heterodyne receiver mixes an astronomical signal with a local-oscillator (LO) signal in a nonlinear element (mixer) to produce a signal at an intermediate frequency (IF), which is the difference between the LO frequency and astronomical signal frequency. The IF signal, normally at several GHz, is suitable for further amplification and spectral analysis. Present day heterodyne receivers use a combination of an electronically tunable solid state LO source [6], with either a superconductor-insulator-superconductor (SIS) [7] mixer or a hot electron bolometer (HEB) mixer [8,9]. The latter type of mixer is the detector of choice for frequencies above 1.5 THz. The Heterodyne Instrument for the Far Infrared (HIFI) on the Herschel Space Observatory[10], to be launched in 2007, is the first instrument to perform heterodyne spectroscopy using such receivers from 480 GHz to 1.9 THz in space.

Future space missions require improved angular resolution, improved sensitivity and, most importantly, an increase in frequency from 2 to 6 THz [2,11,12]. The development of new receivers operating at such high frequencies is limited by the availability of suitable LO sources. The existing solid state LO's are unlikely to generate sufficient output power at such high frequencies since the power falls off rapidly with increasing frequency due to reduced multiplication efficiency [6]. Optically pumped gas lasers can operate at higher frequencies but are in general massive, bulky, power-hungry, and not tunable. Such a gas laser is used in the Earth observing system microwave limb sounder (EOS-MLS)[13] launched by NASA in 2004 and is also planned for the 4.7 THz channel in the SOFIA airborne observatory [14]. The fact that these observatories are being built despite the obvious disadvantages of the gas lasers is a clear indication of the scientific driver to extend the frequency range of present day heterodyne receivers to higher frequencies, fed by the expected wealth of knowledge and new discoveries hidden in the THz range of the spectrum. Very recently, a new type of solid-state THz source was developed based on quantum cascade laser (QCL) structures [15]. This new source holds great promise for LO applications because of its compactness and high power efficiency. Here

Manuscript received May 2, 2005. The work in NL is supported by RadioNet and ESA. The work at MIT is supported by AFOSR, NASA and the NSF. Sandia is a multi-program laboratory operated by Sandia Corporation, a Lockheed Martin Company, for the US Dept. of Energy under Contract DE-AC04-94AL85000.

J.R. Gao and M. Hajenius are with SRON National Institute for Space Research, Sorbonnelaan 2, 3584 CA, Utrecht, The Netherlands and Kavli Institute of NanoScience, Faculty of Applied Sciences, Delft University of Technology, Lorentzweg 1, 2628 CJ, Delft, The Netherlands. e-mail: j.r.gao@tnw.tudelft.nl.

J.N. Hovenier, T.M. Klapwijk, A.J.L. Adam, and T.O. Klaassen are with Kavli Institute of NanoScience, Faculty of Applied Sciences, Delft University of Technology, Lorentzweg 1, 2628 CJ, Delft, The Netherlands.

Z.Q. Yang, J.J.A. Baselmans, and A. Baryshev are with SRON National Institute for Space Research, Sorbonnelaan 2, 3584 CA, Utrecht, The Netherlands.

B.S. Williams, S. Kumar, and Q. Hu are with Department of Electrical Engineering and Computer Science and Research Laboratory of Electronics, Massachusetts Institute of Technology, Cambridge MA 02139, U.S.A.

J. L. Reno is with Sandia National Laboratories, Albuquerque, NM 87185-0601, U.S.A.

we report the first demonstration of a fully operational heterodyne system at 2.8 THz based on such a THz QCL as LO source and a hot-electron bolometer as mixing element.

The concept of a QCL was first demonstrated in the mid-infrared ($\lambda \cong 4$ μm; 75 THz) by Faist *et al* [16]. Photons are created via electronic intersubband transitions in semiconductor heterostructures that take place entirely within the conduction band. Furthermore, in a QCL the heterostructure active region consists of a stack of repeated identical quantum well modules (typically 20-200), which enables a single electron to cascade down and emit a photon in each module. Due to this cascading effect, QCLs have large quantum efficiency and high output power. The QCL frequency range is determined by the energy spacing of the subbands, which is set by the design and growth of the quantum-well structure. The precise operating frequency is determined by the waveguide cavity of the laser. While the development of a THz QCL has proven to be more challenging than for mid-infrared QCLs because of the difficulty of achieving population inversion for small subband separations and of obtaining a low-loss cavity for long wavelengths, a first THz QCL was demonstrated at 4.4 THz by Köhler *et al* [15]. To be suitable as an LO, a QCL has to meet a number of essential requirements, such as single line lasing with a high spectral purity, continuous-wave (CW) operation, adequate output power, and good stability.

The work reported here uses a QCL-device described in Ref. 17, which is based on resonant phonon scattering to selectively depopulate the lower radiation level, while maintaining a long upper level lifetime. The active region contains 176 GaAs/$Al_{0.15}Ga_{0.85}As$ quantum-well modules grown by molecular beam epitaxy (MBE), with the total thickness of 10 μm. The cavity of the QCL is a double-sided metal-metal waveguide fabricated via Cu-Cu thermocompression wafer bonding, which provides low-loss mode confinement at THz frequencies. Similar QCLs have allowed lasing at lower frequencies down to 2.1 THz [18]. Although not taken advantage of in this work, these devices lase in CW mode up to 93 K [19]. The 25-μm-wide ridge waveguide was cleaved at both ends to form a 670-μm-long Fabry-Perot cavity (shown schematically in the inset of Fig. 1). The QCL is indium soldered to a copper mount and is attached to the cold plate of a Helium vacuum dewar. The main figure shows a typical spectrum of the QCL lasing at 2.814 THz (wavelength λ_0=106.6 μm), measured using a Fourier-transform spectrometer (FTS). It is biased with a DC current of 84 mA and dissipates a power of about 1 W. When operated in CW and free-running mode, a single lasing line is observed, with a linewidth of about 1 GHz, which is limited by the resolution of the FTS. The actual linewidth is likely to be much smaller, e.g. 30 kHz (measured in msec-time scale) [20] and 65 kHz (obtained over an arbitrarily long period of time using frequency/phase locking)[21]. The maximum output power is 1 mW, measured using a Winston cone in front of the QCL to collect all the radiated power. In a practical heterodyne experiment the available power will be limited by the divergence of the beam, the window size and the distance between the QCL and the first focusing element of the optics.

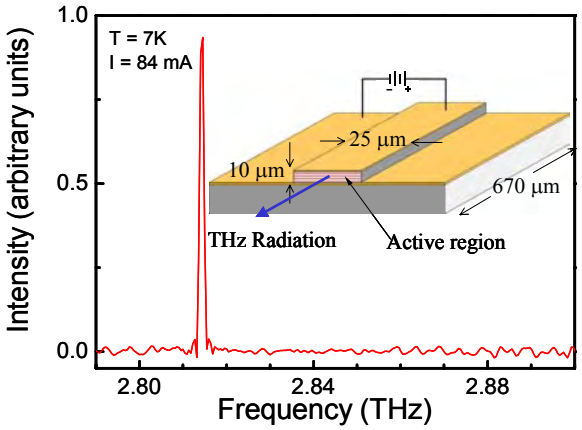

Fig. 1. Emission spectrum of the quantum cascade laser biased with a DC current I of 84 mA and operated at a temperature T around 7 K. The inset shows a schematic view of the QCL and the dimensions of the laser cavity.

In recent years phonon-cooled HEB mixers [22,23] have matured as the only sensitive mixer for the frequency range from 2 to 6 THz. It uses the response to radiation of the temperature-dependent resistance of a small NbN superconducting bridge [8]. The electrons (hot electrons) in the superconducting bridge are heated by the THz photons (predominantly by the LO signal) and the local electron temperature reaches the critical temperature of the superconductor. The mixing signal at IF is the result of the fact that the electron temperature can follow the beat-frequency of the LO signal and the signal to be detected. The sensitivity of receivers is characterized by their receiver noise temperature ($T_{N,\ rec}$) in Kelvin, which reflects the detection efficiency and the noise contributed by the mixer, and other factors such as the optics, the IF amplifier noise and the net transmission efficiency of the atmosphere. The HEB receivers have demonstrated superior sensitivity, e.g. a $T_{N,\ rec}$ of 950 K at 2.5 THz [23]. The principle of operation allows a wide frequency range, demonstrated up to 5.2 THz [22], and reaches an IF bandwidth of 6 GHz [23], reflecting the fast response of the electron temperature. Because of the small volume used, a HEB can operate with a very low LO power of 80 nW at the detector.

II. Measurement Setup

Figure 2 shows a schematic view of the experimental setup with the QCL and the HEB mounted in two separate dewars. A wideband spiral antenna coupled NbN HEB mixer is used with a superconducting bridge of 4 μm wide, 0.4 μm long, and about 4 nm thick. The normal state resistance R_N of the device, measured above the critical temperature of 9 K, is 65 Ω. Without radiation applied a critical current I_c of 320 μA is observed at 4.2 K. The radiation is coupled to the antenna using a standard quasi-optical technique: the Si chip with the

HEB is glued to the back of an elliptical, anti-reflection coated Si lens. The lens is placed in a metal mixer block, thermally anchored to the 4.2 K cold plate. When used with a gas laser at 2.5 THz a $T_{N,\,rec}$ is obtained of 1200 K [24] using identical optics and amplifiers as in the experiment with the QCL.

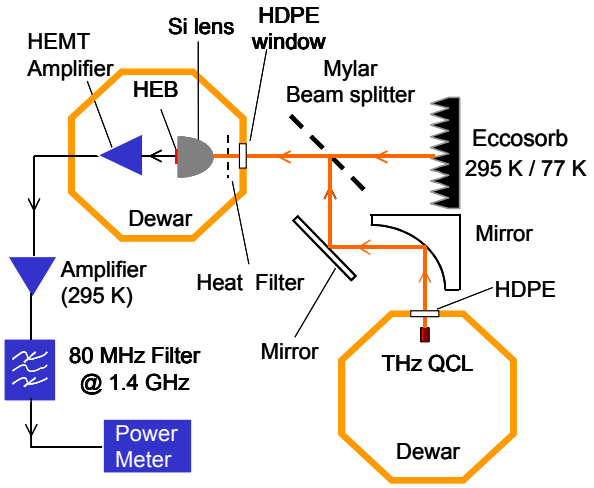

Fig. 2. Schematic view of the heterodyne measurement setup, where the mixer is a superconducting NbN hot electron bolometer (HEB) and the local oscillator is a quantum cascade laser. Both are operated in liquid-Helium vacuum dewars.

The divergent beam from the QCL passes through a high-density polyethylene (HDPE) dewar-window and is collimated with a parabolic mirror. The radiation is further guided to the HEB dewar through a flat mirror and a 6 μm thick Mylar beam splitter, which acts as a directional coupler. A blackbody source (of Eccosorb) is used as the signal, which defines a hot load at 295 K and a cold load at 77 K. The signal is combined with the QCL beam through the beam splitter. Both signals pass through the thin HDPE window and a metal mesh heat filter at 77 K of the HEB dewar. The total known loss is –16.2 dB for the QCL (to the HEB) optical path and –4.0 dB for the hot/cold load path. The IF signal, resulting from the mixing of the LO and the hot/cold load signal, is amplified using a low noise amplifier operated at 4.2 K, and is further fed to a room temperature amplifier and filtered at 1.4 GHz in a band of 80 MHz. The entire IF chain has a gain of 80 dB and a noise temperature of 4 K.

III. Results

A. Heterodyne sensitivity

The key result of this work is demonstrated in Figure 3. A set of current versus voltage (I-V) curves of the HEB is shown for various levels (270, 300, 330 nW) of the effective power of radiation absorbed at the HEB, together with the receiver noise temperature, $T_{N,\,rec}$, as a function of voltage. (The inset shows a top view of the HEB with its spiral antenna). The power level, which is estimated at the HEB by the isothermal technique [25], is varied by changing the DC bias current of the QCL. The noise temperature $T_{N,\,rec}$ is determined from the ratio of the IF output noise power for a hot and a cold load [24]. Each set of $T_{N,\,rec}$-V data shows a minimum region, indicating the optimum bias point. Best results are obtained for 300 nW LO power and 0.7 mV DC bias with $T_{N,\,rec}$ being as low as 1400 K, comparable to what was obtained with the gas laser at the lower frequency of 2.5 THz (with the same device and identical setup). The maximum power from the QCL coupled to the HEB, taking all losses into account, is estimated to be 14 μW. This is only about 1.4 % of the total output power available from the QCL, which is due to the poor optical coupling of the divergent beam. Besides, we also measured a small HEB (1 μm×0.15 μm×~4 nm) coupled with a twin slot antenna using the QCL as LO and obtained a $T_{N,\,rec}$ of 3200 K at 2.8 THz. It is interesting to note this device uses only 500 nW power at the QCL.

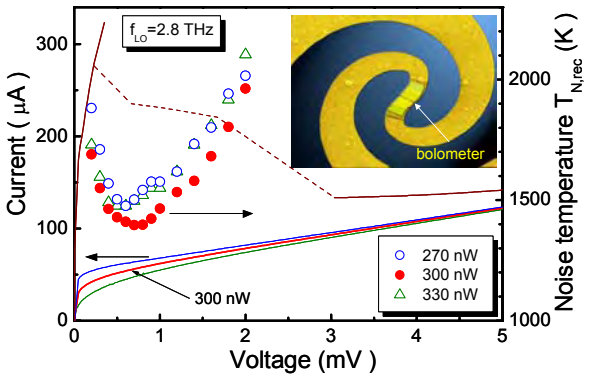

Fig. 3. Current-voltage characteristics (full lines, left axis) of a NbN hot electron bolometer (HEB) mixer without and with radiation from the QCL at 2.814 THz. The dashed line indicates an unstable bias region. The measured receiver noise temperature $T_{N,\,rec}$ (symbols, right axis) versus the bias voltage for different LO power levels at the HEB. The lowest value of $T_{N,\,rec}$ is 1400 K for 300 nW LO power and 0.7 mV DC bias. The bath temperature is 4.2 K. The inset shows a top view of the HEB with its spiral antenna.

B. The Allan Variance

We have performed two separate experiments to determine the stability of the HEB-QCL receiver, in which the HEB is operated at the point where it gives the lowest noise temperature. First, we measured the Allan Variance $\sigma^2_A(\tau)$ of the normalized IF output power, given [26] by $\sigma^2_A(\tau) \equiv \frac{1}{2}\sigma(\tau)^2$, where σ^2 is the average squared standard deviation of each number from its mean and τ is the sampling period. The noise of any receiver is a combination of three terms: white (uncorrelated) noise, 1/f electronic noise, and low frequency drift. Since, to first order, only white noise can be integrated out, there is an optimum integration time, known as the "Allan" time T_A, beyond which the signal/noise ratio no longer improves [27]. A measurement of $\sigma^2_A(\tau)$ is a powerful tool to distinguish the various noise terms in a real receiver and to evaluate its optimal integration time. The measured $\sigma^2_A(\tau)$ for the HEB-QCL receiver is plotted as a function of the sampling period in Figure. 4. As a comparison we also plot $\sigma^2_A(\tau)$ obtained using a similar HEB mixer pumped by a phase-locked solid state LO at 1.5 THz [6]. Both

measurements indicate an identical T_A of about 0.5 sec within the 80 MHz bandwidth of the IF chain. In the same figure we also include the measured $\sigma^2_A(\tau)$ when the HEB is biased at 10 mV, which shows the expected white noise behavior. This suggests that the observed "Allan" time is limited by the HEB mixer itself and not by any other sources, such as mixer bias, amplifier fluctuations etc. Secondly, we have measured the output power of the QCL as a function of time using the HEB as a direct detector. As shown in the inset of Figure 4, the averaged current of the HEB varies only 0.2 % in a period of 1000 seconds, indicating that the output power of a free-running QCL is sufficiently stable over a long time scale to maintain the HEB at its optimal operating point.

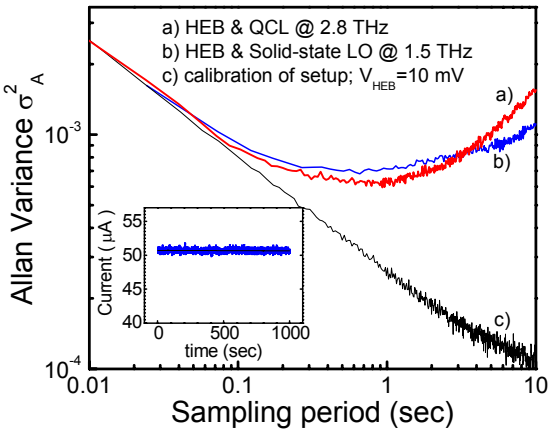

Fig. 4. Allan Variance σ^2_A of the normalized output power of the HEB as a function of the sampling period: a) for the HEB-QCL receiver at optimum operating point (red curve); b) for a similar HEB mixer at its optimum operating point using a phase-locked solid state LO operated at 1.52 THz (blue curve); c) for the receiver when the HEB is biased at 10 mV (black curve). The data is taken in a 80 MHz bandwidth around 1.4 GHz. The inset shows the current of the HEB at optimum operating point as a function of time. Its averaged value changes only 0.2 % in a period of 1000 seconds..

IV. Conclusions

In conclusion, we have demonstrated that a heterodyne receiver based on a QCL and an HEB can be operated with an excellent noise temperature of 1400 K at 2.8 THz. The free-running QCL has sufficient power stability for a practical receiver and the output power is more than adequate for use with HEB's. The key results described here have been accepted for publication [28].

The demonstrated QCL-HEB receiver can easily be extended to other frequencies in the range of 2-6 THz and with further optimization has the potential to reach (near) quantum noise limited sensitivity. It also offers the possibility of a multi-pixel array using one QCL as LO source, since the QCL output power is in principle sufficient for many HEB mixers. To achieve a wide frequency coverage and tunability one needs an array of QCL's, each with slightly different frequencies. We envision the QCL's, the HEB's and other components to be integrated together into a mechanical cryocooler at 4 K, leading to a compact, easy to use, rugged and space qualifiable all solid-state receiver system. Note that the beam pattern of a QCL was also studied [29] and a heterodyne measurement using a combination of a QCL and a HEB was also reported recently by other group [30].

Acknowledgment

We acknowledge J.W. Kooi for his advice on the Allan Variance measurement and G.N. Gol'tsman and B. Voronov for providing the NbN films. The work in NL is supported by RadioNet and ESA. The work at MIT is supported by AFOSR, NASA and the NSF. Sandia is a multi-program laboratory operated by Sandia Corporation, a Lockheed Martin Company, for the US Dept. of Energy under Contract DE-AC04-94AL85000.

References

[1] Phillips, T.G. and Keene, J., Submillimeter Astronomy, *Proceedings of the IEEE*. **80**, 1662-1678 (1992).

[2] Leisawitz, D. et al., Scientific motivation and technology requirements for the SPIRIT and SPECS far-infrared/submillimeter space interferometers," *Proceedings of the SPIE: UV, Optical and IR Space Telescopes and Instruments*. Vol. 4013, 36-46 (2000).

[3] van Dishoeck, E.F., and Tielens, A.G.G.M., Space-borne observations of the lifecycle of interstellar gas and dust, in: *The Century of Space Science, eds. J.A.M. Bleeker et al.* 2001 Kluwer Academic Publishers (Dordrecht), pp. 607-645.

[4] Waters, J.W., Froidevaux, L., Read, W.G., Manney, G.L., Elson, L.S., Flower, D.A., Jarnot, R.F., and Harwood, R.S., Stratospheric ClO and ozone from the microwave limb sounder on the upper atmosphere research satellite. *Nature (London)*. 362, 597-602 (1993).

[5] Siegel, P. H., Terahertz Technology, *IEEE Trans. Microwave Theory Tech*. **50**, 910-928 (2002).

[6] Mehdi, I., Schlecht, E., Chattopadhyay, G., and Siegel, P.H., THz local oscillator sources: performance and capabilities, *in Millimeter and Submillimeter Detectors for Astronomy, Proceedings of SPIE,* Vol. 4855, pp. 435-446, T.G. Phillips and J. Zmuidzinas, editors, 2003.

[7] Jackson, B.D., Baryshev, A.M., de Lange, G., Gao, J.R., Shitov, S.V., Iosad, N.N., and Klapwijk, T.M., Low-noise 1 THz superconductor-insulator-superconductor mixer incorporating a NbTiN/SiO_2/Al tuning circuit. *Appl. Phys. Lett*. **79**, 436-438 (2001).

[8] Gershenzon, E.M., Gol'tsman, G.N., Gogidze, I.G., Gusev, Y.P., Eliantev, A.I., Karasik, B.S., and Semenov, A.D., Millimeter and submillimeter range mixer based on electron heating of superconducting films in the resistive state, *Sov. Phys. Superconductivity*. **3**, 1582-1596 (1990).

[9] Cherednichenko, S., Khosropanah, P., Kollberg, E., Kroug, M., and Merkel, H., Terahertz superconducting hot-electron bolometer mixers, *Physica C*. 372-376, 407– 415(2002).

[10] http://sci.esa.int/science-e/www/area/index.cfm?fareaid=16

[11] Benford, D.J., and Kooi, J.W., Heterodyne receiver requirements for the single aperture far-infrared (SAFIR) observatory, *Proc. 14th Int. Symp. on Space Terahertz Technology*, 22-24 April 2003, Tucson, Arizona, USA, pp. 529-534, eds by C. Walker and J. Payne.

[12] de Graauw, Th., et al, Exploratory submm space radio-interferometric telescope (ESPRIT), in Optical, Infrared, and Millimeter Space Telescopes, ed. J.C. Mather, *Proceedings of the SPIE conference "Astronomical Telescopes and Instrumentation 2004",* Glasgow, UK, 21-25 June 2004, Vol. 5487, p. 1522-1525.

[13] http://mls.jpl.nasa.gov/index.shtml

[14] http://sofia.arc.nasa.gov/; also see Guesten, R. et al, GREAT: The German receiver for astronomy at terahertz frequencies, Airborne Telescope Systems II. Edited by R. K. Melugin, H-P. Roeser . Proceedings of the SPIE, Vol. 4857, pp. 56-61 (2003).

[15] Köhler, R., Tredicucci, A., Beltram, F., Beere, H.E., Linfield, E.H., Davies, A.G., Ritchie, D.A., Iotti, R.C., and Rossi, F., Terahertz semiconductor-heterostructure laser, *Nature* (London). **417**, 156-159 (2002).

[16] Faist, J., Capasso, F., Sivco, D.L., Sirtori, C., Hutchinson, A.L., Cho, A.Y., Quantum cascade laser, *Science*. **264**, 553-556 (1994).
[17] Hu, Q., Williams, B.S., Kumar, S., Callebaut, H., Kohen, S., and Reno, J.L, Resonant-phonon-assisted THz quantum cascade lasers with metal-metal waveguides, to be published in *Semiconductor Sci. Technol.* (2005).
[18] Williams, B.S., Kumar, S., Hu, Q., and Reno, J.L., Resonant-phonon terahertz quantum-cascade laser operating at 2.1 THz, *Electronics Letters*. 40, 431- 433 (2004)
[19] Kumar, S., Williams, B.S., Kohen, S., Hu, Q., and Reno, J.L., Continuous-wave operation of terahertz quantum-cascade lasers above liquid nitrogen temperature, *Appl. Phys. Lett*. 84, 2494-2496 (2004).
[20] Barkan, A., Tittel, F.K., Mittleman, D.M., Dengler, R., Siegel, P.H., Scalari, G., Ajili, L., Faist, J., Beere, H.E., Linfield, E.H., Davies, A.G. and Ritchie, D.A., Linewidth and tuning characteristics of terahertz quantum cascade laser, *Opt. Lett*. 29, 575-577 (2004).
[21] Betz, A.L.(private communication), Center for Astrophysics & Space Astronomy, UCB 593, University of Colorado, Boulder, CO 80309.
[22] Semenov, A.D., Hübers, H.-W., Schubert, J., Gol'tsman, G.N., Elantiev, A.I., Voronov, B.M., and Gershenzon, E.M., Design and performance of the lattice-cooled hot-electron terahertz mixer, *J. Appl. Phys*. 88, 6758-6767 (2000)
[23] Baselmans, J.J.A, Hajenius, M., Gao, J.R., Klapwijk, T.M., Korte, P.A.J. de, Voronov, B., and Gol'tsman, G.N., Doubling of sensitivity and bandwidth in phonon cooled hot electron bolometer mixers. *Appl. Phys. Lett,* 84, 1958-1960 (2004).
[24] We use the Callen-Welton definition for the double sideband receiver noise temperature, as described in: Kerr, A.R., Suggestions for revised definitions of noise quantities, including quantum effects, *IEEE Trans. Microwave Theory Tech.* 47, 325-329 (1999).
[25] Ekström, H., Karasik, B.S., Kollberg, E.L., and Yngvesson, K.S., Conversion gain and noise of niobium superconducting hot-electron mixers. *IEEE Trans on Microwave Theory and Tech*. **43**, 938-947 (1995).
[26] Allan, D.W., Statistics of atomic frequency standards, *Proceedings of the IEEE.* 54, 221-231 (1996).
[27] Kooi, J.W., Chattopadhyay, G., Thielman, M., Phillips, T.G., and Schieder, R., Noise stability of SIS receiver, *Int. J. IR and MM Waves.* 21, 689-716 (2000).
[28] J.R. Gao, J.N. Hovenier, Z.Q. Yang, J.J.A. Baselmans, A.Baryshev, M. Hajenius, T.M. Klapwijk, A.J.L Adam, T.O. Klaassen, B.S. Williams, S. Kumar, Q.Hu and J.L. Reno, "Terahertz heterodyne receiver based on a quantum cascade laser and a superconducting bolometer", Appl. Phys. Lett. **86**, 244104 (2005).
[29] A.J.L. Adam, J.N. Hovenier, I. Kasalynas, T.O. Klaassen, J.R. Gao, B.S. Williams, S. Kumar, Q. Hu, E.E. Orlova, and J. L. Reno, "Near and Far Field Beam Pattern Measurements on Quantum Cascade Lasers Operating at 2.8 THz", in these proceedings.
[30] H-W. Hübers et al, "Investigation of a 2.5 THz Quantum Cascade Laser as Local Oscillator", in these proceedings.

1.55 µm photomixer LO sources operating at cryogenic temperatures for heterodyne mm-wave receivers

J. E. J. Warner, B. Alderman, P. G. Huggard* and B. N. Ellison

Millimetre Wave Technology Group,
Rutherford Appleton Laboratory,
Didcot OX11 0QX, UK.

***Tel. +44 1235 445245, E-mail: p.g.huggard@rl.ac.uk**

Photomixing is a flexible and efficient method of providing the local oscillator input to mm-wave heterodyne receivers. Photodiode based photomixers have conventionally been characterised at room temperature, but for use with superconducting mixers for astronomy it is desirable to locate and operate them in a cryogenic environment close to the superconductor-insulator-superconductor junction. We have thus investigated the effects of cooling W-Band waveguide photomixers based upon 70 GHz bandwidth, λ = 1.55 µm, photodiodes from u^2t Photonics AG.

Operation is maintained to ambient temperatures below 30 K, and optical to mm-wave power conversion efficiency is found to increase upon cooling. In contrast to 300 K operation, the photocurrent is found to depend strongly with reverse bias, Fig. 1, although the $(\text{photocurrent})^2$ dependence of output power is maintained. Maximum detected mm-wave powers are of are order 100 µW at 85 GHz, and have been limited by the capability of the bias current supply. Temperature cycling the photomixer to 300 K was found to restore the original room temperature photoresponse.

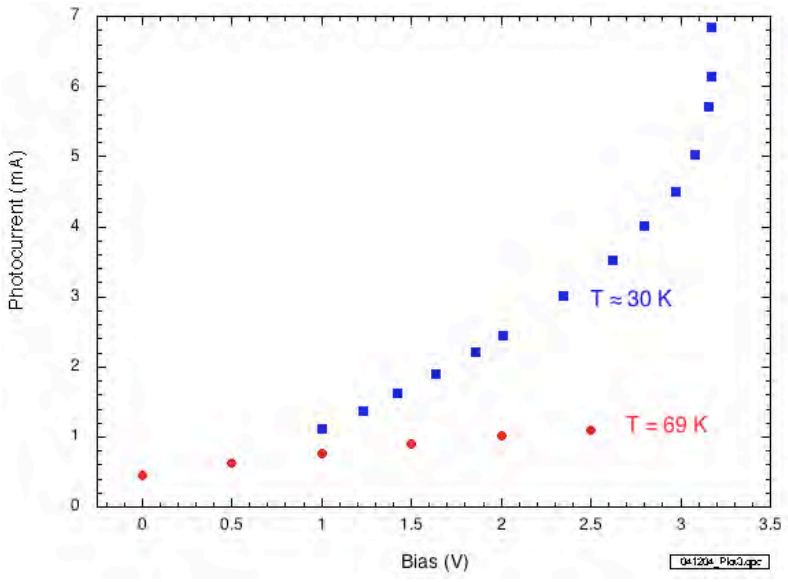

Figure 1: Mm-wave power as a function of bias for cryogenic photomixer operation.

Session 3:

SIS I

Monday May 2, 11:00-12:30
Chairman: Viktor Belitsky

Embedding the Quantum Mixer Theory into a Time Domain Field Solver

Douglas W. Henke, Poman P. M. So, Stéphane M. X. Claude, and Wolfgang J. R. Hoefer

***Abstract*—To completely account for the quantum-mechanical features of the *superconductor-insulator-superconductor* (SIS) junction, Tucker's quantum mixer theory must be used. The standard approach is to perform the computations in the frequency domain. To determine the large signal waveform resulting across the junction, a time domain formulation has also been used in the *voltage update method* (VUM). Even using this method, the nonlinear diode current (computed using the time domain equations) is related to the rest of the circuit in the Fourier domain. An iterative procedure enables the correct junction voltage to be found.**

This paper proposes a variation to the VUM such that all calculations are performed in the time domain, in a time-stepping fashion, enabling the theory to be implemented into a time domain field solver. The main advantages of performing simulations within the time domain are the ability to process arbitrary time signals applied to the nonlinear junction and to generate complete information on the mixing products over a wide frequency range. It is recognized that a noise analysis is not feasible within the time domain and would be treated separately.

***Index Terms*—Quantum mixer theory, time domain analysis, superconductor-insulator-superconductor devices**

I. Introduction: Time Domain Quantum Mixer Theory

THE time domain formulation of the quantum mixer theory has been presented in [1]-[3]. Time domain theory has already been used for certain aspects of simulation, e.g., determining the local oscillator (LO) voltage waveform established across the junction using the *voltage update method* [4],[5]. However, a full embedding of the mixer theory into a time domain 3D electromagnetic field solver has not yet been done. While the current and voltage waveforms can be modeled in the time domain, it is not feasible to predict the noise, and so this would need to be treated separately.

Abstract received February 24, 2005. This work was supported in part by the National Research Council of Canada at the Herzberg Institute of Astrophysics through research contributions under the D. C. Morton Fellowship, and by the Natural Science and Engineering Research Council of Canada (NSERC).

D. W. Henke is with the Department of Electrical and Computer Engineering, University of Victoria, Victoria, BC, V8W 3P6, Canada (e-mail: dhenke@ece.uvic.ca).

P. P. M. So is with the Department of Electrical and Computer Engineering, University of Victoria (e-mail: pso@ece.uvic.ca).

S. M. X. Claude is with the Herzberg Institute of Astrophysics, National Research Council, Victoria, BC, V9E 2E7, Canada (e-mail: Stephane.Claude@nrc.ca).

W. J. R. Hoefer is with the Department of Electrical and Computer Engineering, University of Victoria (e-mail: whoefer@ece.uvic.ca).

The following summarizes the time domain theory presented in [1]-[3]. In this first section, only the simple current-to-voltage relationship will be reviewed; no source impedance or junction capacitance is included. To provide further insight, a MATLAB [6] implementation is used to demonstrate junction currents and photon-assisted tunneling.

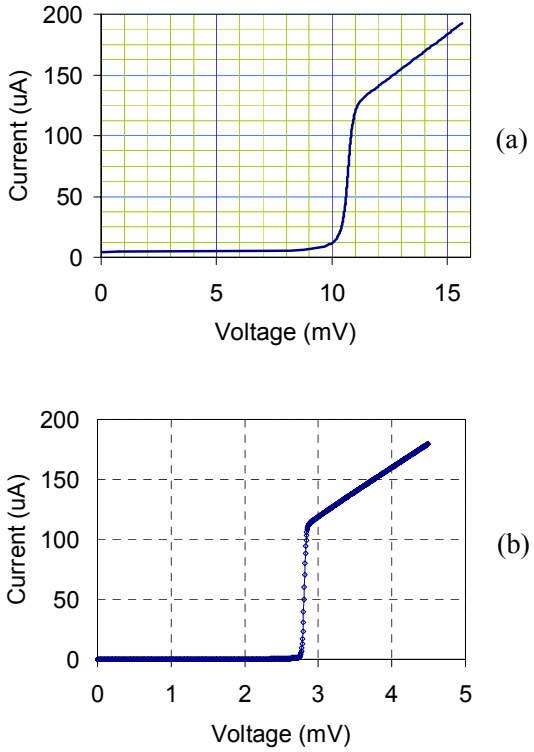

Fig. 1. Unpumped I-V curves that may be used for analysis. (a) Measured I-V curve for a series array of four Nb junctions. This is the typical response of the mixers used within the ALMA Band 3 receivers [7]. (b) I-V curve characteristic mimicking a measured response for a single Nb junction [9]. All MATLAB results contained herein are based on this fitted curve.

Recall that the unique result of the quantum mixer theory is that the unpumped curve provides sufficient information to predict the RF performance of the mixer. Fig. 1a shows a measured I-V curve for a typical mixer used in the ALMA Band 3 receivers [7],[8]. These mixers each contain four junctions arranged in a series array. For simplicity, the I-V curve characteristic used within this paper to demonstrate the time domain theory is shown in Fig. 1b and represents data that might be measured for a single niobium (Nb) junction [9].

In the time domain, the response function is defined in the following manner:

$$\bar{\chi}(t) = \frac{2}{\pi}\int_0^{\infty}\left(I_{DC}(\hbar\omega/e) - \frac{\hbar\omega}{eR_n}\right)\sin\omega t\, d\omega \qquad (1)$$

where e is the electron charge magnitude and $\hbar$ is Planck's constant scaled by 2π. The function, $I_{DC}(V)$, is the equation that describes the measured unpumped I-V curve and is assumed to be an odd function that tends toward the normal state conductance, $1/R_n$, at large bias voltages. Since $I_{DC}(V)$ is a function of voltage, it is evaluated at the corresponding photon voltages for each ω. The response function characterizes the quantum-mechanical features of the SIS junction; it is based entirely on the I-V curve and is independent of any applied voltage. The response function only needs to be calculated once and, noting the bracketed expression of (1), computation is seen to converge when $I_{DC}(V) \rightarrow V/R_n$.

Fig. 2 depicts the initial time segment of the response function that was calculated for the I-V curve data of Fig. 1b. The response function will oscillate at a frequency proportional to the *gap energy*, 2Δ. Depending on the quality of the junction, i.e., the sharper the nonlinearity of the I-V curve, the longer it will take for the response function to decay [10].

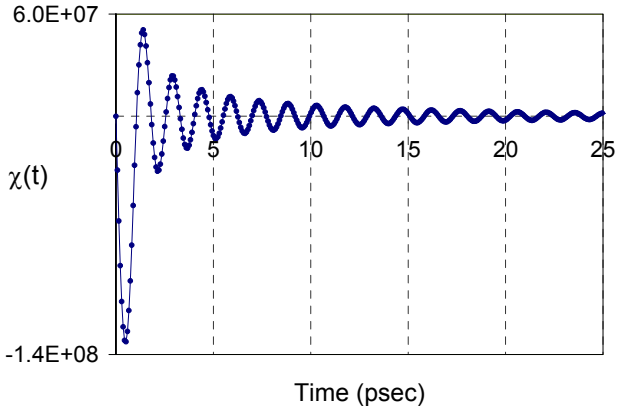

Fig. 2. The response function, χ(t), derived from the I-V curve data shown in Fig. 1b. The response function characterizes the nonlinearities and quantum-mechanical effects of the SIS junction in the time domain.

Consider the full time domain expression for the current across the junction for a given applied voltage, $V(t)$. The expected quasiparticle tunneling current is given as

$$\langle I(t)\rangle = \frac{V(t)}{R_n} + \mathrm{Im}\left(U^*(t)\int_{-\infty}^{t}\bar{\chi}(t-t')U(t')dt'\right). \qquad (2)$$

where $U(t)$ is the phase factor and is given as

$$U(t) = e^{i\phi(t)} \qquad (3)$$

and

$$\phi(t) = \frac{e}{\hbar}\int_{-\infty}^{t} V(t')dt'. \qquad (4)$$

As pointed out in [10], the expected current of (2) shows an instantaneous response (the first term) and a delayed component due to the convolution. In this way, the current depends on the past history of the applied voltage. This manifests itself in the frequency domain in the form of a quantum susceptance [3].

Even though the time domain implementation can accept an arbitrary applied voltage, in order to provide continuity with the frequency domain approach, consider the large signal voltage defined as

$$V(t) = V_{DC} + V_{LO}\cos(\omega_{LO}\, t). \qquad (5)$$

This waveform shows a DC bias voltage component combined with a local oscillator voltage signal of magnitude V_{LO}. It is assumed that $V(t)$ is the voltage that falls across the junction and, therefore, no LO source impedance has been taken into account.

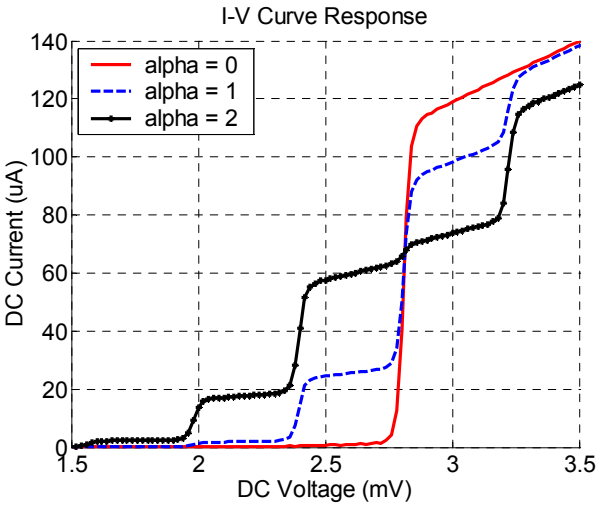

Fig. 3. Photon-assisted tunneling demonstrated with pumped I-V curves. Each curve was generated by extracting the DC component from the time domain response. No source impedance has been taken into account.

An interesting verification of the time domain equations is to demonstrate the quantum-mechanical effect of photon-assisted tunneling, as shown most clearly in the pumped I-V curve. The time-varying current was calculated at incremental DC bias voltages, from which the DC component of the current was then extracted through a Fourier transform. Fig. 3 shows the pumped curves that were computed for different pumping strengths, as defined in (9). Each step has an approximate width of 0.4 mV, which correctly corresponds to the photon voltage of the local oscillator (f_{LO} = 100 GHz).

Since, in practice, the junction is most often biased near the midpoint of the first photon step below the gap voltage, it serves well to look at the transient current for this condition. Fig. 4a shows the initial transient behavior and how, after

several local oscillator periods, the signal will reach a steady state. The next figure displays a steady state sample of this same waveform separated into the individual components of (2): the instantaneous current and the current arising from the convolution term.

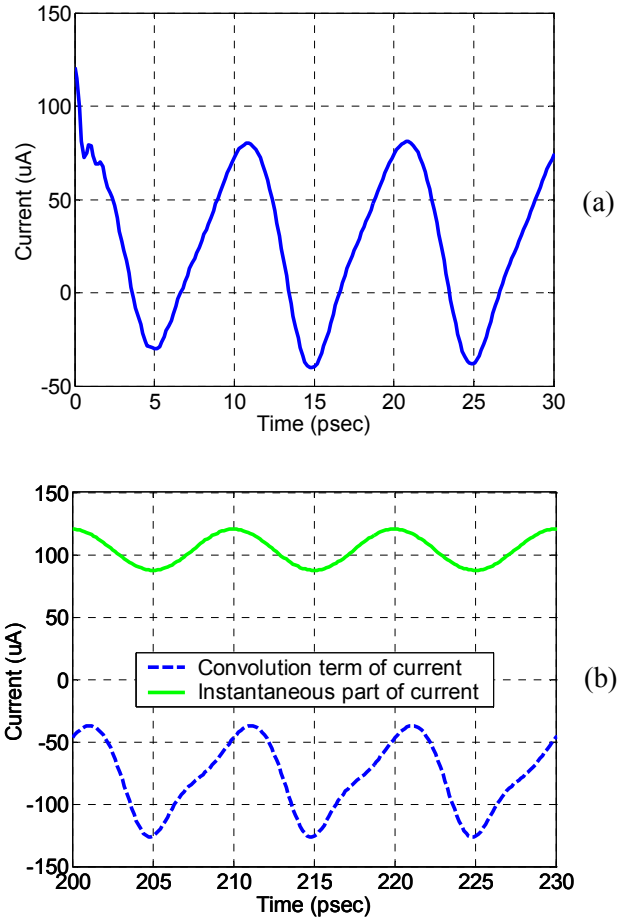

Fig. 4. (a) Transient response of the junction current when the DC bias voltage is centered on the first photon step and the LO is pumped at α = 1. (b) Comparison of the two contributions of current once it has reached a steady state.

II. Accounting for the Source Impedance

To solve for the large signal waveform across the junction within an embedding network, the time domain equations have been used in the *voltage update method* (VUM) [4],[5]. Even using this method, however, the nonlinear diode current (computed using the time domain equations) is related to the rest of the circuit in the Fourier domain. A short review of this technique is given and then a variation is presented, allowing full computation of the current in the time domain.

A. Voltage Update Method (VUM)

During the large signal analysis of the quantum mixer theory, approximations are made with respect to the LO and its harmonics. For example, when using a three-port approximation, all harmonics are considered to be shorted out, and the LO is treated as a pure sine wave. As higher-order harmonics are included, the resulting LO waveform across the mixer becomes increasingly complex. A further complication is due to the dispersive nature of the LO source impedance so that higher-order harmonics see a different impedance than the fundamental.

Fig. 5 demonstrates how the VUM allows the user to specify the source impedance, $Z_{source}(\omega)$, at each harmonic frequency. The generator voltage, V_{gen}, is represented by a DC bias and a pure sinusoidal source at the LO frequency. The dotted line divides the nonlinear and linear parts of the circuit.

The correct voltage falling across the junction is determined through an iterative process designed to match the terminal voltage of the linear network, $V^{LIN}(t)$, to the nonlinear part, $V^{NL}(t)$. The procedure starts with an initial guess on the voltage, $V^{NL}(t)$, falling across the junction and the corresponding diode current is found. Using circuit theory, the linear network voltages at the interface are found by

$$V_n^{LIN} = Z_n^e I_n^{LIN} + V_{gen,n} \tag{6}$$

where $n = 0, 1, 2, ..., N$ denotes the index of the Fourier amplitude corresponding to the n[th] harmonic of the local oscillator, and $Z_n^e = \left(Z_{source,n} \| Z_{C,n}\right)$ is the equivalent source impedance that includes the junction capacitance. The Fourier amplitudes of the current are found through transformation.

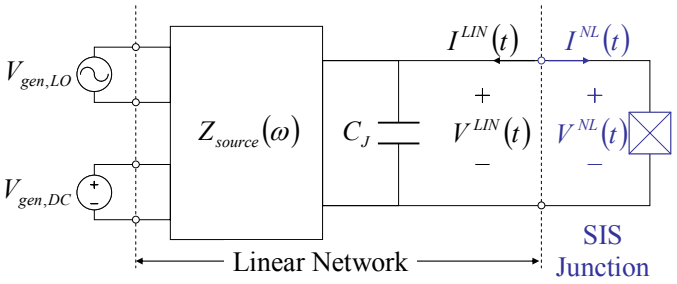

Fig. 5. Circuit describing the relation of the nonlinear diode current to the rest of the circuit in the voltage update algorithm [5]. The nonlinear current is transformed into the frequency domain and then linearly related to each harmonic of the LO.

Once the Fourier amplitudes, V_n^{LIN}, of the linear network voltages have been found, $V^{LIN}(t)$ is calculated through the inverse Fourier transform. If $V^{LIN}(t) = V^{NL}(t)$, then the junction voltage has been found. Otherwise, the voltage may be updated according to

$$V^{NL}(t) = pV^{LIN}(t) + (1-p)V^{NL}(t) \tag{7}$$

where p is a convergence parameter valid over the range of $0 < p < 1$. Convergence is better for the VUM when the terminating impedances approach a short-circuit, but may become a problem when the source impedance is high compared with the input impedance of the junction [5].

B. Variation: Time Domain Voltage Update Method (TDVUM)

Since the VUM computes the linear network voltages in the frequency domain, it is assumed that the voltage waveforms only contain harmonics of the LO and are in a steady state. If the VUM is modified so that all calculations are performed in the time domain, denoted as the *time domain voltage update method* (TDVUM) for comparison purposes, true transient behavior and arbitrary time signals can be analyzed [11]. To be compatible with time domain circuit and field solvers, the new algorithm must be able to evolve with each additional time step, yet still be accurate to the complexities of (2).

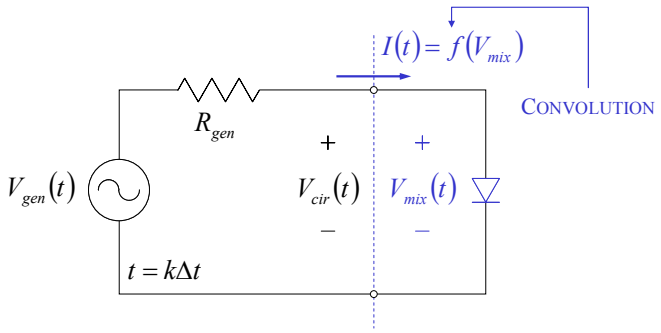

Fig. 6. Circuit describing the time domain voltage update method (TDVUM). The source impedance is represented here as a simple resistor, but may be a more complicated network. For each time step, Δt, the mixer voltage is iteratively matched to the circuit voltage at the terminal interface. However, since the quantum mixer current requires a convolution of previous voltage values, each iteration also requires a convolution. Note that V_{gen} includes the DC voltage bias.

Fig. 6 depicts a simplified circuit representation for the TDVUM such that the source impedance is given by a simple resistor. The generator voltage is assumed to include the DC bias. As with the VUM, the terminal voltages are matched through an iterative process. Given a specified generator voltage, an initial guess on the mixer voltage, V_{mix}, is made. The nonlinear diode current is calculated, and the circuit voltage is found by

$$V_{cir}(t) = V_{gen}(t) - I(t)\,R_{gen} \tag{8}$$

where $t = k\,\Delta t$ and is evaluated for the k^{th} time step. If the terminal voltages match, then the algorithm is complete, otherwise, V_{mix} is updated according to (7). However, this is not as simple as it appears, because the current, found by (2), requires a convolution operation that depends on the past history of the voltage across the junction. Therefore, not only is the convolution operation called during each time step, but also for numerous times within each iteration of that time step – creating a very demanding computational algorithm.

One simplification to the convolution procedure is that the storage of the entire voltage time sample is not required; only a time sample equal to the length of the response function, calculated by (1), is necessary. This, of course, assumes that the time sample of the response function is long enough so that it has converged (e.g., longer than what is shown in Fig. 2). Furthermore, the convolution within each k^{th} time step may be broken up into two parts: a term depending on the most recent k^{th} voltage guess and a term that makes use of the previous time samples already determined, denoted as the $k-1$ *convolution term*. By re-using this latter term during the iteration process, the computational effort is greatly diminished.

Implementing these concepts, a MATLAB algorithm was programmed in the following steps:

- *Initialize parameters* – the I-V curve parameters and time step are determined and the response function is calculated. Then for each k^{th} time step:
- *Guess initial voltage* $V_{mix} = V_{gen}$.
- *Compute current* – the phase factor and current are calculated for the initial voltage guess and the $k-1$ convolution term is stored.
- *Perform iteration and voltage update* – the circuit of Fig. 6 is solved for each new test voltage. Each voltage guess requires re-calculating the k^{th} term of the phase factor. The current is calculated for the new test voltage and the $k-1$ convolution term is re-used each time. If $V_{cir} = V_{mix}$, then the correct voltage has been found, otherwise, the new test voltage is modified by (7).

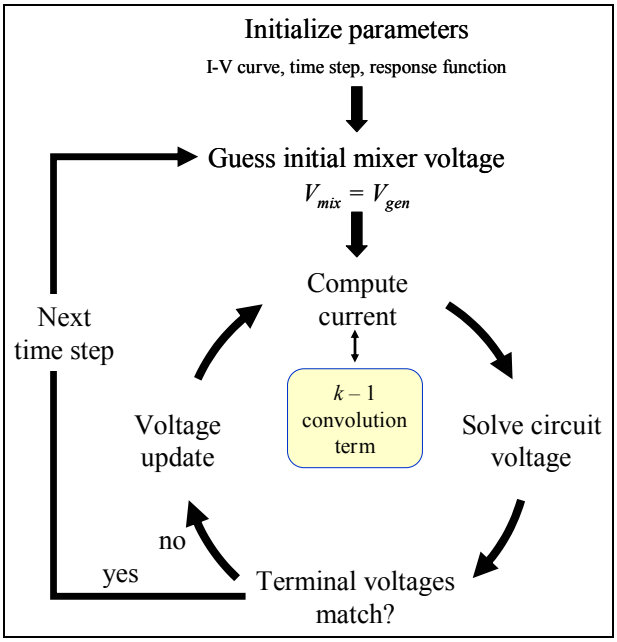

Fig. 7. Algorithm of the time domain variation of the Voltage Update Method.

As a consequence of working within the time domain, the source impedance of Fig. 6 must be implemented using real elements. The implication is that if a resistor is used, it is considered ideal and present for all frequencies including DC. In reality, mixer designs have DC bias networks, dispersive transmission line impedances and junction capacitance. More complex source networks, including DC bias elements, can be modeled, but the intention of this paper is to keep the demonstration simple.

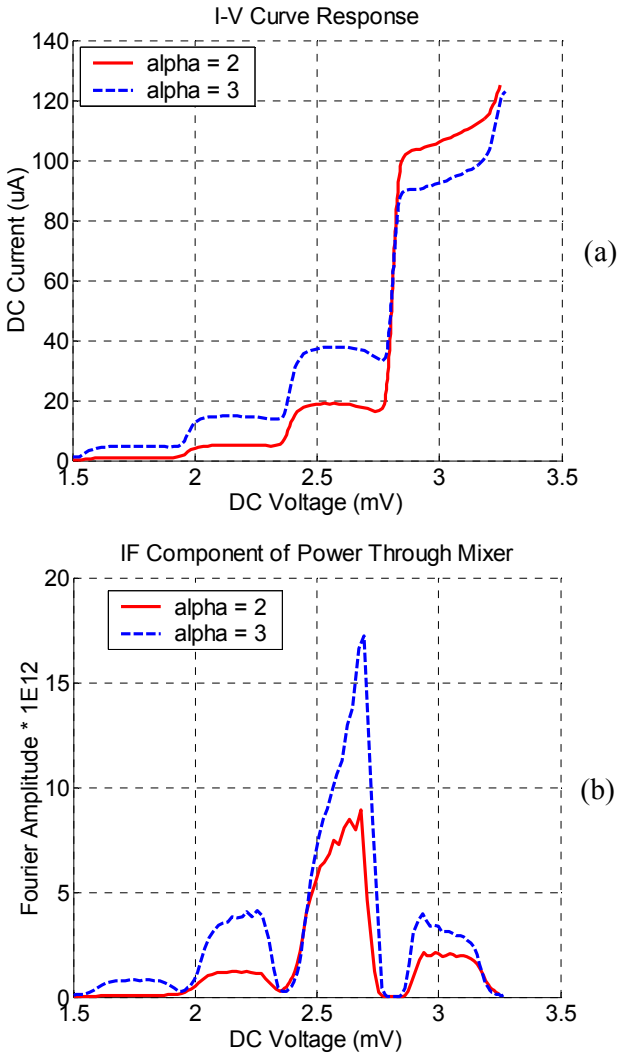

Fig. 8. (a) Pumped I-V curve response for two different source pumping strengths. The source impedance has been implemented as an ideal resistor of 10 Ω. (b) Two small signal tones, spaced at ±10 GHz from the LO and with amplitude of hf_{LO} / 20e, were combined with the LO across the junction. The Fourier amplitude of the IF component of the power through the junction was extracted and plotted with respect to the DC voltage bias.

Using the I-V curve of Fig. 1b, the optimum source resistance is found to be $R_{S,opt} \approx 10\ \Omega$ [12]. Fig. 8 demonstrates the responses for the simple source resistance shown by the circuit of Fig. 6. It is appropriate to define a *source* pumping parameter

$$\alpha_{source} = eV_{gen,AC} / \hbar\omega_{gen} \tag{9}$$

where the distinction is made from [3] in that the voltage, $V_{gen,AC}$, is the amplitude of the AC *generator* voltage, not the voltage established across the junction. By adding two small signal tones to the source, each of amplitude hf_{LO} / 20e and set at ±10 GHz from the LO, the full spectrum of mixing products are available. Fig. 8b displays the IF component of the power through the mixer and shows the familiar peaks corresponding to each photon step, with the greatest amplitude at the first photon step below the gap voltage.

III. Implementation of TDVUM into 3D EM Field Solver (MEFiSTo)

After demonstrating the algorithm of the TDVUM, the groundwork has been laid for a full embedding into a circuit solver or field solver. MEFiSTo-3D Pro [13] is a full wave 3D electromagnetic field solver that is based on the *transmission line matrix* (TLM) method [14],[15]. An interconnection between SPICE [16] circuit models and the field has already been developed in MEFiSTo by means of representing the TLM network by an equivalent Thévenin or Norton source and impedance [17]. The transmission line impedance is found through an equivalent combination of input link lines. A similar technique was used to implement the SIS quantum theory via a TLM-MATLAB connection, such that the full time domain SIS mixer algorithm was implemented within the MATLAB element containing the TDVUM scripts written to calculate the SIS junction current.

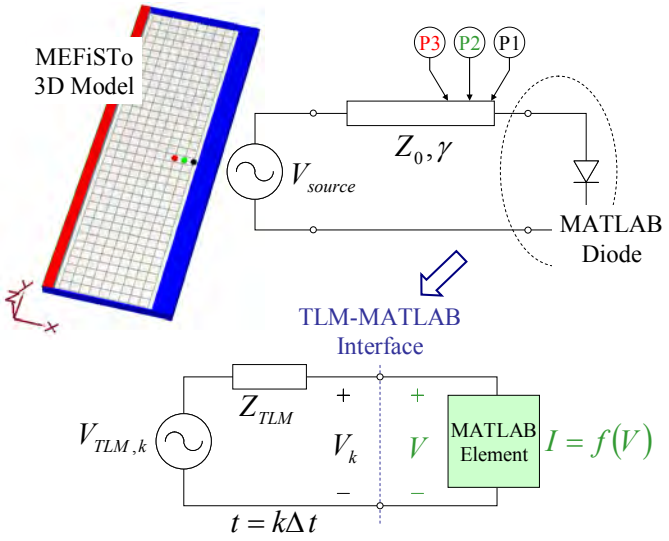

Fig. 9. MEFiSTo implementation of a parallel plate waveguide terminated with a MATLAB diode. The 3D model shows a distributed source connected to a short section of transmission line with three probes placed to monitor the voltage and current at each location. The lower figure describes the TLM-MATLAB interface where the distributed TLM mesh has been reduced to a Thévenin source and resistance .

Fig. 9 illustrates this concept whereby a short section of parallel plate waveguide is terminated by a shunt diode. The distributed field components at the TLM-MATLAB connection are reduced to a simple Thévenin source and resistance. Since the signals are within the time domain, the source impedance is real and the phase information is preserved within the signal itself. The result is that even though complex source and dispersive tuning networks surround the junction, they may be reduced at the junction terminal to the simple circuit shown in Fig. 6.

In cases where either the voltage or current tends to zero at the interface, extrapolation is necessary to obtain the true response. According to [17], the actual TLM-MATLAB connection is made halfway between the MATLAB cell boundary and the MATLAB node. Another note is that since

the time step within MEFiSTo is dependent on the mesh resolution, it is important that the mesh be discretized uniformly in all directions and that the time step is kept the same within the MATLAB code.

A great advantage of embedding the SIS model into a time domain field solver is the ability to visualize the fields, including the transient and standing waves. Fig. 10 shows the field animation along a parallel plate waveguide designed to have a characteristic impedance of 10 Ω. The transmission line is terminated by a SIS MATLAB element and excited using a DC and LO voltage generator (which may be defined independently in MEFiSTo).

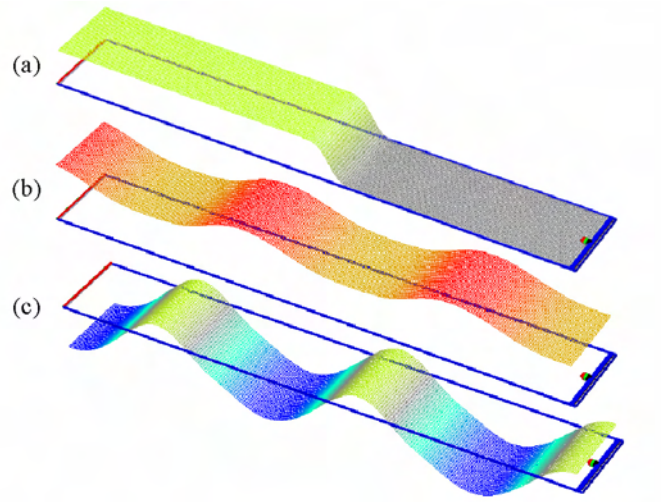

Fig. 10. MEFiSTo model of a parallel plate waveguide terminated with a SIS mixer diode. (a) Transient view capturing the DC bias voltage applied from the generator (left) toward the SIS junction (right). (b)-(c) Steady state view of the resulting voltage and current field components, respectively, due to an applied local oscillator.

IV. Conclusion and Future Work

The time domain theory of the quasiparticle tunnel junction has been reviewed and a new time-stepping algorithm, based on the voltage update method, has been demonstrated using MATLAB. The new time domain variation of the voltage update method (TDVUM), has immediate application in determining large signal voltage developed across the junction while accounting for the source impedance.

It has also been shown that the TDVUM algorithm is well suited for embedding within a time domain field solver where the fields may be reduced to a Thévenin or Norton equivalent at the junction terminals.

Future work would include implementing a 3-terminal, 2-port MATLAB element. In the above results, a 2-terminal, 1-port element was used to terminate a section of transmission line. Using the 2-port element, an output IF section can be modeled as it appears on the mixer chip. MEFiSTo already has this feature for SPICE elements. Further experimentation with complex geometries, including biasing networks, junction capacitance, and tuning elements must also be completed.

References

[1] J. R. Tucker, "Quantum limited detection in tunnel junction mixers," *IEEE J. of Quantum Electronics.,* vol. QE-19, no. 11, pp. 1234-1258, November 1979.

[2] J. R. Tucker, "The quantum response of nonlinear tunnel junctions as detectors and mixers," *Reviews of Infrared and Millimeter Waves*, New York: Plenum, vol. 1, pp. 1-46, 1983.

[3] J. R. Tucker and M. J. Feldman, "Quantum detection at millimeter wavelengths," *Rev. Mod. Phys*., vol. 57, no. 4, pp. 1055-1113, October 1985.

[4] R. G. Hicks and P. J. Khan, "Numerical analysis of nonlinear solid-state device excitation in microwave circuits," *IEEE Trans. Microwaves Theory Tech.*, vol. 30, no. 3, pp. 251-259, March 1982.

[5] R. G. Hicks, M. J. Feldman, and A. R. Kerr, "A general numerical analysis of the superconducting quasiparticle mixer," *IEEE Trans. Magn*., vol. MAG-21, no. 2, pp. 208-211, March 1985.

[6] MATLAB, The MathWorks, Inc., 3 Apple Hill Drive, Natick, MA 01760-2098, USA. Available: http://www.mathworks.com, April, 2005.

[7] S. -K. Pan, A. R. Kerr, M. W. Pospieszalski, E. F. Lauria, W. K. Crady, N. Horner, Jr., S. Srikanth, E. Bryerton, K. Saini, S. M. X. Claude, C. C. Chin, P. Dindo, G. Rodrigues, D. Derdall, J. Z. Zhang and A. W. Lichtenberger, "A fixed-tuned SIS mixer with ultra-wide-band IF and quantum-limited sensitivity for ALMA Band 3 (84-116 GHz) receivers," *15th Int. Symp. on Space Terahertz Tech*., Northampton, MA, April 2004.

[8] http://www.alma.info/ , April, 2005.

[9] A. Navarrini, "Development of DSB and SSB SIS mixers for radio astronomy in the frequency band 250-370 GHz," Ph. D. dissertation, Université Joseph Fourier, Grenoble, France, 2002.

[10] R. E. Harris, "Intrinsic response time of a Josephson tunnel junction", *Phys. Rev. B*, vol. 13, no. 9, pp. 3818-3821, May 1976.

[11] D. W. Henke, "Measurement and time domain modeling of superconductor-insulator-superconductor (SIS) mixing junctions for radioastronomy," M. A. Sc. dissertation, University of Victoria, Victoria, Canada, 2005.

[12] A. R. Kerr, S. -K. Pan, A. W. Lichtenberger, and D. M. Lea, "Progress on tunerless SIS mixers for the 200-300 GHz band," *IEEE Microwave Guided Wave Lett*., vol. 2, no. 11, pp. 454-456, November 1992.

[13] MEFiSTo-3D Pro, FAUSTUS Scientific Corporation, 1256 Beach Drive, Victoria, BC, V8S 2N3, Canada. Available: http://www.faustcorp.com, April, 2005.

[14] P, B. Johns, "The art of modeling," *IEE Trans. Electron. Power*, vol. 25, no. 8, pp. 565–569, August 1979.

[15] W. J. R. Hoefer, "The transmission-line matrix method—Theory and applications," *IEEE Trans. Microwave Theory Tec*h., vol. MTT-33, pp. 882-893, October 1985.

[16] SPICE, University of California, Berkeley, USA. Available: http://bwrc.eecs.berkeley.edu/Classes/IcBook/SPICE/, April, 2005.

[17] P. P. M. So and W. J. R. Hoefer, "A TLM-SPICE interconnection framework for coupled field and circuit analysis in the time domain," *IEEE Trans. Microwaves Theory Tech*., vol. 50, no. 12, pp. 2728-2733, December 2002.

230 GHz SSB SIS mixer for band 3 of the new generation receivers for the Plateau de Bure interferometer

D. Maier, S. Devoluy, M. Schicke, and K. F. Schuster

***Abstract*—A single sideband SIS mixer with a 4-8 GHz IF band and covering the RF frequency range of 200 to 265 GHz has been developed and characterized. This mixer will be integrated into band 3 of the new generation receivers for the Plateau de Bure interferometer. LSB noise temperatures as low as 40 K could be obtained over the whole LO frequency range. USB noise temperatures are slightly higher.**

***Index Terms*—single sideband mixer, SIS mixer**

I. Introduction

IRAM is currently developing new generation receivers for the six element Plateau de Bure interferometer. These receivers will cover the four frequency bands 83-115 GHz, 129-174 GHz, 200-265 GHz, and 275-373 GHz, each with two polarizations, single-sideband operation, and an IF band of 4 to 8 GHz. Installation is foreseen before winter 2006/2007.

This paper presents design and characterization of a single sideband SIS mixer for band 3 (initially defined from 200 to 260 GHz) using a moveable backshort for image rejection.

II. RF design

The design of this mixer is quite similar to the one designed for ALMA band 7[1]. A layout of the mixer chip is shown in Fig. 1. The mixing element is a 1μm^2 Nb-Al/AlO_x-Nb tunnel junction made by e-beam lithography [2]. This junction is embedded into a superconducting circuit consisting of the antenna, the RF choke, and the tuning structure.

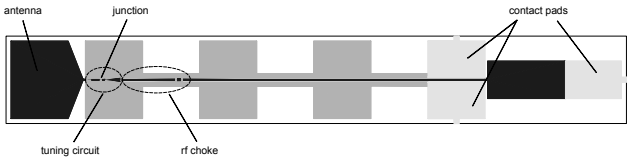

Fig. 1. Layout of the mixer chip with a size of 2.5 × 0.35 × 0.1 mm³.

D. Maier, S. Devoluy, M. Schicke, and K.F. Schuster are with the Institut de RadioAstronomie Millimétrique, 300, rue de la piscine, 38406 St. Martin d'Hères, France (phone: +33476824900; fax: +33476515938; e-mail: maier@iram.fr).

The antenna providing the full-height waveguide to suspended microstrip transition consists of a probe structure on a quartz substrate which is placed in a channel perpendicular to the waveguide axis and stretches partly into the waveguide as can be seen in Fig. 2. Behind the mixer chip a backshort can be moved inside the waveguide.

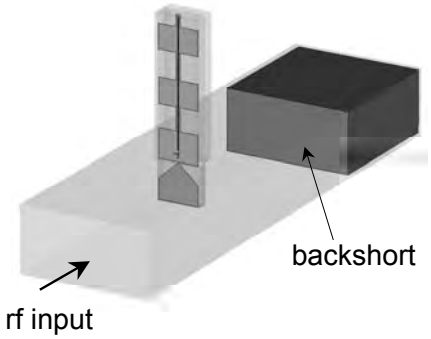

Fig. 2. Full-height waveguide to microstrip transition.

In order to evaluate the antenna impedance, simulations using CST Microwave Studio [3] were carried out for a large distance between junction and backshort. Fig. 3 shows the result of such a simulation for frequencies between 200 and 260 GHz and a distance of 30 mm between junction and backshort. The Smith chart is normalized to 60 Ω. Since the circles move around the center of the chart, antenna impedances around 60 Ω are obtained for matched backshort positions.

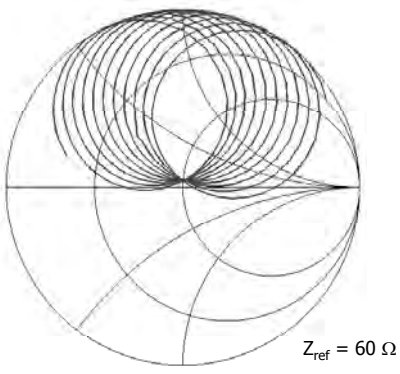

Fig. 3. Antenna impedances for frequencies between 200 and 260 GHz and a backshort distance of 30 mm. Smith chart is normalized to 60 Ω.

The superconducting tuning circuit is the same as in [1] adapted to the PdBNG band 3 frequency range using Sonnet [4] and ADS [5]. A photo of a fabricated mixer chip with a close-up of the tuning structure is shown in Fig. 4. The equivalent circuit is presented in Fig. 5.

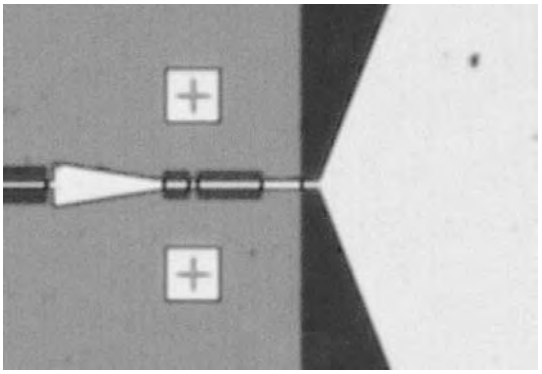

Fig. 4. Photo of the tuning circuit.

Compensation of the junction's capacitance is achieved with a parallel inductance consisting of a coplanar waveguide. A delta-stub creates the virtual ground. The delta-stub has been chosen in order to limit the parasitic capacitances and ensure a large IF bandwidth. A λ/4-transformer finally provides matching to the antenna impedance.

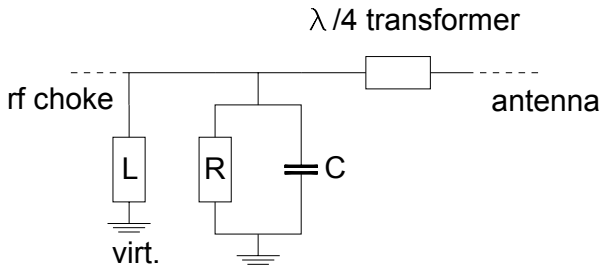

Fig. 5. Equivalent circuit of the tuning structure.

The mixer has been designed to work in USB mode for the upper end of the RF band and in LSB mode for the lower frequencies. In the middle of the band there is a choice of USB or LSB operation. For each LO frequency a backshort position can be found providing an optimum match at the USB (LSB) frequency and simultaneously presenting a reactive termination to the junction at the LSB (USB) frequency. Fig. 6 shows an example for a signal frequency of 230 GHz. The Smith chart on the left-hand side shows the embedding impedance of the junction for a backshort distance of 3.590 mm. For this backshort position the frequency band of 228 to 232 GHz is well matched whereas for frequencies between 216 and 220 GHz a reactive termination is presented to the junction. Hence, this position corresponds to observing at 230 GHz in USB mode. The Smith chart on the right-hand side in Fig. 6 shows the embedding impedance of the junction for a backshort distance of 6.085 mm. The frequency band of 228 to 232 GHz is still well matched, but now the junction sees a reactive termination for frequencies between 240 and 244 GHz. Accordingly the mixer is set to LSB operation for a signal frequency of 230 GHz.

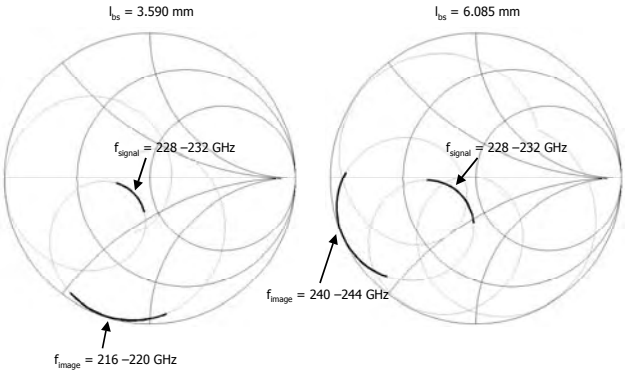

Fig. 6. Example of observing at 230 GHz. Left: Embedding impedance of the junction for a backshort distance of 3.590 mm corresponding to LSB operation at 236 GHz LO frequency. Right: Embedding impedance of the junction for a backshort distance of 6.085 mm corresponding to USB operation at 224 GHz LO frequency. Both Smith charts are normalized to the junction's RF impedance.

In order to obtain the matching of the junction over the whole RF frequency range backshort positions are determined for each LO frequency for both USB and LSB operation of the mixer and the junction's embedding impedance is calculated. The result is shown in the Smith chart in Fig. 7 for signal frequencies between 200 and 260 GHz for LSB (grey line) and USB (black line) operation.

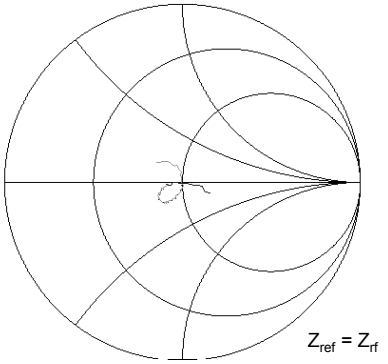

Fig. 7. Embedding impedance of the junction. Smith chart is normalized to the junction's RF impedance. LSB operation is represented by the grey line, USB operation is plotted in black.

A good match could be obtained over the whole frequency range as can also be seen by the plot in Fig. 8 representing the fraction of power coupled to the junction. For all signal frequencies more than 97% of the incident power is coupled to the junction. In the middle of the band USB and LSB operation give the same theoretical results. Hence, coupling to the junction does not depend on LSB or USB operation, but only on the signal frequency.

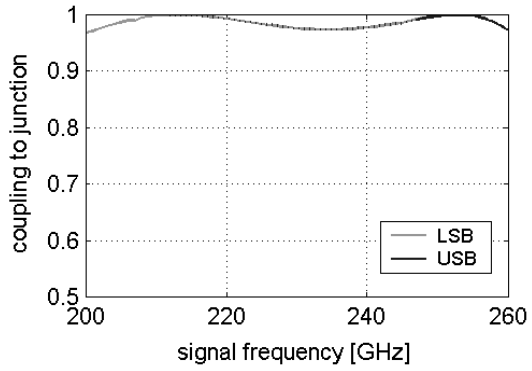

Fig. 8. Fraction of power coupled to the junction. LSB operation is represented by the grey line. The black line indicates results for USB operation.

III. Mixer Block and Magnetic Yoke Assembly

The actual mixer block consists of a front and a rear block with a waveguide going through both (see Fig. 9). A mechanism for moving the backshort inside the waveguide is fixed to the rear part. The IF circuit consisting of a 50 Ω line realized as microstrip with a Rodgers 4003 substrate is mounted into a substrate holder which is fixed on top of the mixer block. The mixer chip is contacted via bonding wires to the block and the Rodgers microstrip. A local magnetic field is applied to the junction in order to suppress Josephson currents, which are a source of mixer noise and instability. For this purpose a custom-made superconducting magnet and yoke assembly is attached to the mixer block (not shown on the photo). For mixer tests the block is mounted directly onto an LO coupler. In order to better demonstrate the RF input a feedhorn has been mounted onto the mixer block for the photo shown in Fig. 9.

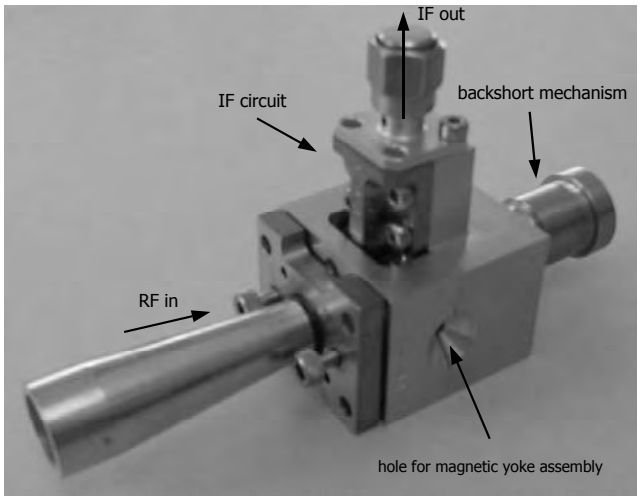

Fig. 9. Photo of the mixer block with feedhorn, backshort mechanism, and IF circuit.

IV. Noise Measurements

So far only one batch of junctions with results for normal state resistance and area close to the design values has been fabricated and three junctions have been tested as mixers. A representative result of the noise measurements is shown in Fig. 10. For LSB operation noise temperatures around 40 K could be obtained over the whole LO frequency range (grey circles). USB noise temperatures are between 40 and 70 K (black squares).

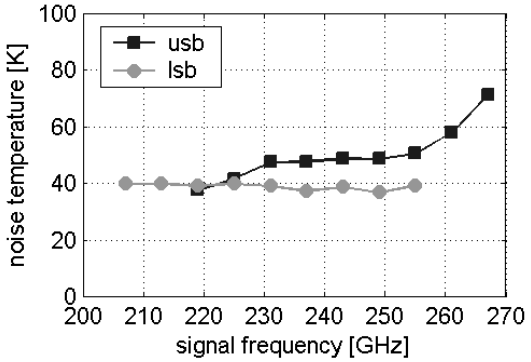

Fig. 10. SSB noise measurements of junction 11-34-02. LSB noise temperatures are represented by the grey circles. USB results are plotted with black squares.

The increase of noise for USB operation and signal frequencies above 255 GHz indicates that the junction's capacitance is higher than assumed in the design. Consequently the noise performance at the upper frequency end might be improved by employing smaller junctions.

V. Image Rejection

Since the backshort position can only be optimized for the rejection of one distinct frequency, image rejection is a critical issue of backshort mixers, especially for large IF bands. Fig. 11 shows the image rejection obtained for an LO frequency of 231 GHz with the backshort set to USB operation. Note that the backshort position was not changed during the measurement. As expected, best values are obtained in the middle of the IF band. But even at the IF band edges an image rejection of better than –10 dB could be achieved.

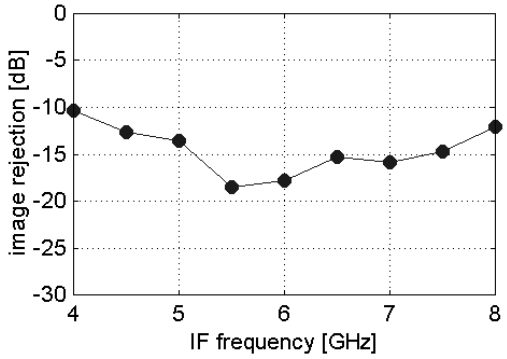

Fig. 11. Image rejection as function of the IF frequency measured for USB operation at f_{LO} = 231 GHz.

VI. Conclusions

A single sideband SIS mixer for band 3 of the new generation receivers for the Plateau de Bure interferometer has been successfully developed, fabricated and characterized. Initially designed for the RF frequency range of 200 to 260 GHz it works well up to 267 GHz, thus covering the later extended PdBNG band 3 frequency range

of 200 to 265 GHz. Because of its low static capacitance it works without IF impedance transformer over the whole IF band of 4 to 8 GHz. Noise temperatures of 40 K could be obtained for LSB operation over the whole LO frequency range. USB noise temperatures are between 40 and 70 K and might be improved by employing smaller junctions.

REFERENCES

[1] D. Maier, A. Barbier, B. Lazareff, and K.F. Schuster, "The ALMA band 7 mixer," same proceedings
[2] I. Péron, P. Pasturel, and K.F. Schuster, "Fabrication of SIS junctions for space borne submillimeter wave mixers using negative resist e-beam lithography," IEEE Trans. Applied Superconductivity, Vol. 11, pp. 377-380, March 2001
[3] CST Microwave Studio, Bad Nauheimer Str. 19, D-64289 Darmstadt, Germany
[4] Sonnet Software, 100 Elwood Davis Road, North Syracuse, NY 13212
[5] Advanced Design System, Agilent Eesof EDA

Design and Characterization of a Sideband-Separation SIS Mixer/IF Module for use on a Focal-Plane Array

Gopal Narayanan, Prachi Deshpande, Neal Erickson, Vikram Kodipelli, Ron Grosslein, and Vern Fath
Department of Astronomy, University of Massachusetts, Amherst, MA 01002.

A dual polarization 16-pixel heterodyne focal-plane array receiver is proposed to be built to operate in the 210 – 275 GHz ($\sim$ 1mm wavelength band) atmospheric window for use on the Large Millimeter Telescope (LMT). The LMT is a 50 m diameter millimeter-wavelength telescope being built in Mexico as a joint project between UMass and Instituto Nacional de Astrofisica, Optica, y Electronica (INAOE) in Mexico. Each pixel of the proposed focal-plane array receiver will feature SIS mixers operated in a novel sideband-separation mode with wideband low-noise IF amplifiers (4 – 12 GHz). In this paper, we will present design details, test results, and characterization of the components that make up the novel array mixer-block.

The array mixer-block is a highly integrated assembly (see Figure 1) that has been optimized for use and integration into a 4×4 array. The mixer-preamplifier (MPA) block consists of a input RF 90° waveguide hybrid, a dual-directional LO coupler, two SIS junctions, two hybrid IF LNAs with a IF 3dB 90° Lange coupler interspersed between the stages. Two SMA outputs from the mixer block bring out the separated upper and lower sidebands. Two magnetic coils that are used to suppress Josephson noise are also embedded in this integrated mixer-preamplifier (MPA) block. A hybrid IF LNA with a discrete JFET followed by a MMIC amplifier has been designed, fabricated and tested. The integrated implementation of the IF Lange hybrid coupler between the stages of the hybrid IF LNAs considerably eases the amplitude and phase balance requirements of components in the rest of the IF chain.

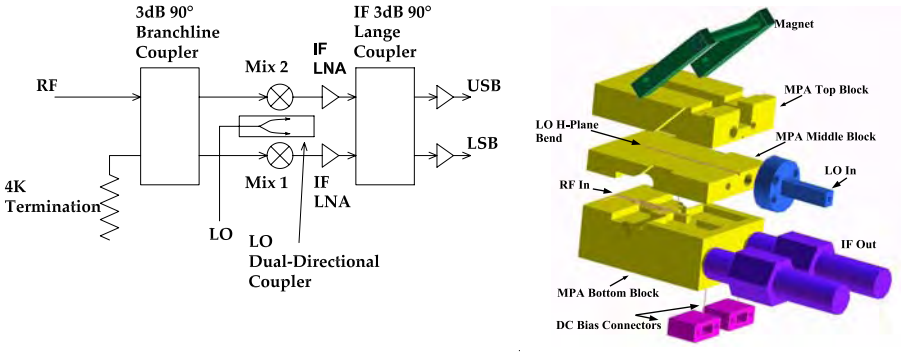

Figure 1: Array Mixer block (a) Schematic of the sideband separation mixer configuration (b) A 3-d exploded view of the Split-block construction of the array mixer-block.

Sideband Separating SIS Mixer with On-Substrate LO-Injection Circuitry

V. Vassilev, R. Monje, A. Pavolotsky, I. Lapkin, C. Risacher and V. Belitsky
Group for Advanced Receiver Development (GARD)
Onsala Space Observatory, Chalmers University of Technology

***Abstract*—We present results of the development and characterization of a second generation sideband separating (2SB) SIS mixer for 85-115 GHz band.**

In the mixer design the LO power is injected into the RF signal path through a -15 dB microstrip directional coupler which requires a matched termination. We use a "dot" termination, which is made of a resistive normal-metal film and is designed such that it occupies a minimum area on the substrate providing a good return loss over the whole LO band. The required sheet resistance of the film forming the dot is obtained by sputtering Ti in atmosphere containing N_2.

Preliminary mixer tests show minimum SSB noise temperature of 50 K and below 65 K in the band 86-115 GHz with sideband rejection around 10 dB.

***Index Terms*— SIS mixer, sideband separating mixer, double probe transition, sideband suppression ratio**

I. Introduction

The advance of two big international projects ALMA and APEX prompted the development of sideband separating (2SB) mixer technology for mm-wavelengths [1]-[7]. The motivation for using 2SB mixers for radio astronomical applications at mm-wavelengths is that the noise performance of a double-side band (DSB) heterodyne receiver is often limited by the atmospheric noise fed into the system via the image band [8]. Thus, to further increase the system sensitivity, 2SB or single sideband (SSB) operation is preferred where the image band is either filtered out reactively or dissipated on a low temperature load.

2SB mixers are based on a quadrature scheme where the RF and LO signals are divided and introduced to two identical DSB mixers. The IF components of both DSB mixers are combined in an IF hybrid where the sideband cancellation takes place. The quadrature scheme requires 90^0 phase delay for either RF or LO signals in one of the mixer channels.

A common feature of 2SB mixers is that they require power division for the RF/LO signals. On-substrate power dividers such as branch line coupler require matched terminations at the fourth port, usually a lumped resistor, which is inconvenient to produce at mm-wavelengths using thin-film technology. The same issue concerns if the LO power is coupled to the RF through microstrip coupled lines. Therefore most of the 2SB mixer designs demonstrated at mm-wavelengths avoid using microstrip couplers and instead use waveguide components to divide RF/LO power and to provide LO coupling to the RF [4], [5], [6], [7]. In this case waveguide terminations are easily realized using absorbers built in the waveguide cavity [9]. This type of designs allows two DSB mixer blocks to be pre-selected and connected to a block containing all waveguide components, but increases the overall size and mechanical complexity of the 2SB mixer unit.

In this paper we suggest a more compact design where all mixer components are placed on a single substrate containing both mixers with their tuning circuitry together with the LO injection circuitry. The design requires only two microstrip terminations, which are realized using a circular area of resistive material connected to the line – "a dot termination" [10], [11].

II. Mixer Design

A. Mixer Description

Figure 1 shows a block diagram of the suggested 2SB mixer and Figure 2 illustrates the mixer substrate coupled to the LO/RF waveguides.

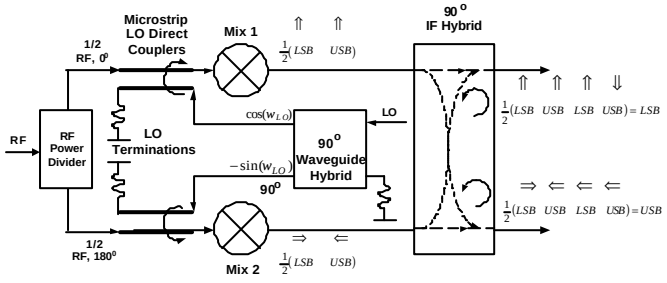

Figure 1 Block diagram of the 2SB mixer. Sideband separation is achieved by using a quadrature scheme where two identical mixer junctions are pumped by a local oscillator (LO) with 90° phase difference. To illustrate the sideband cancellation, the relative phases of the sideband signals are shown at different points of the mixer. USB and LSB stand for Upper and Lower Side Band respectively. A waveguide hybrid is used to divide the LO power with the required 90^0 phase delay and coupled to the RF through microstrip coupled lines. The RF power divider is a 3-port structure, which does not contain resistive terminations.

To divide the input RF signal and to couple it to the substrate we designed a special structure, a waveguide to

microstrip double probe transition [12]. This structure has a simple geometry and does not require any termination load; in this case the amount of microstrip terminations is minimized to two.

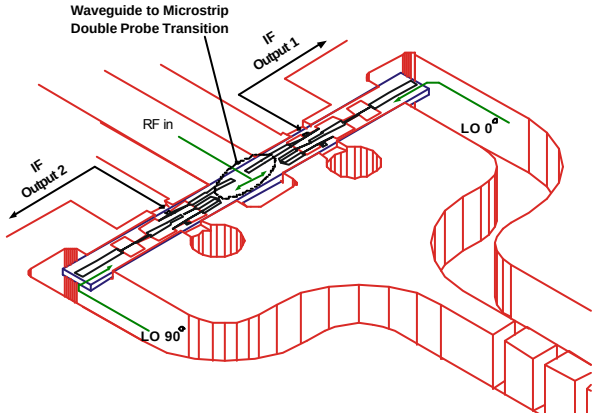

Figure 2 The mixer substrate penetrates 3 waveguides in the mixer block. The divided LO power is introduced at the ends of the substrate while the RF power is coupled to the substrate in the middle and divided between the two mixer junctions by the waveguide to microstrip double probe transition. The mixer substrate is a Z cut crystal quartz with dimensions 0.7 / 8.74 / 0.15mm (W/L/H). The substrate size is chosen such that it does not allow waveguide modes inside the substrate channel.

B. The First Generation 2SB Mixer

The divided LO power is coupled at the ends of the substrate via an E-probe and fed to the 15 dB LO-directional coupler through a microstrip circuit. The RF and LO signals are then fed to each of the mixer junctions with its tuning circuitry.

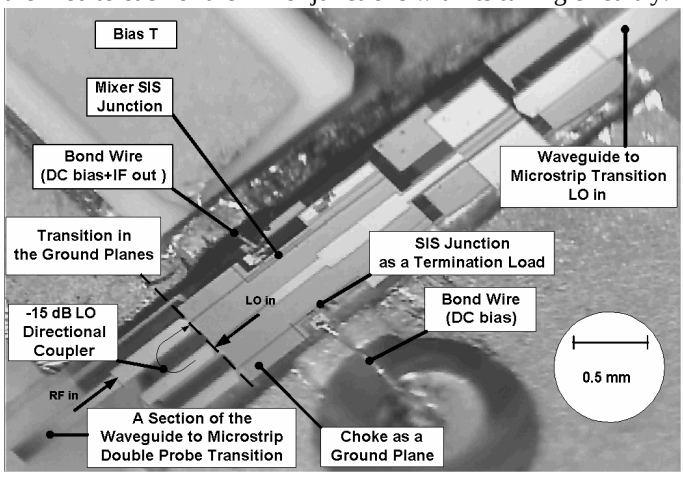

Figure 3 A closer view of the mixer components. The LO is injected to the RF line through a -15dB directional coupler. A second SIS junction and its tuning circuitry provides real impedance to terminate the rest of the LO at the idle port of the LO coupler. To avoid critically small spacing between the lines, the LO coupler uses the 0.15 mm thick crystal quartz substrate as a dielectric and substrate backside metallization as a ground plane. The choke serves as a ground plane for the rest of the circuitry.

In the first 2SB mixer generation [13], [14] the fourth ports of the directional couplers are terminated by an additional pair of SIS junctions which requires in total four SIS junctions per 2SB mixer.

C. The Second Generation 2SB Mixer

To reduce the complexity and to facilitate the mixer tuning, in the current design we use a "dot" termination which is made of a resistive normal-metal film [10], [11]. The dot is designed such that it occupies a minimum area on the substrate and provides return loss S11<-12 dB over the whole LO band [15]. The required sheet resistance of the film forming the dot is obtained by sputtering Ti in atmosphere containing N_2, resulting in a Ti/N_2 mixture.

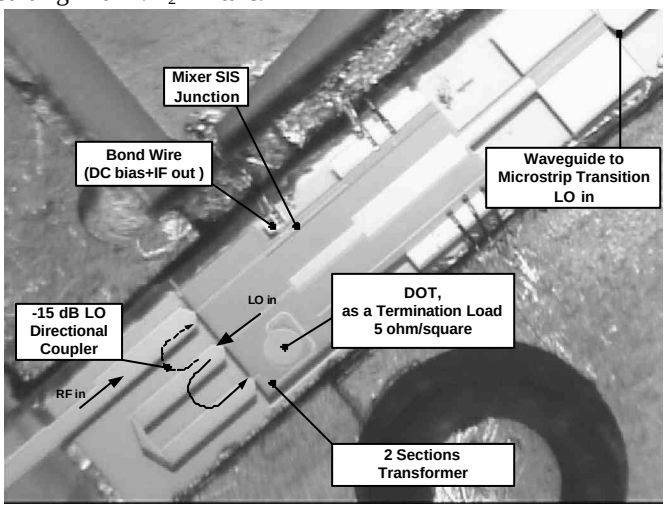

Figure 4 The LO-injection circuitry in the second 2SB mixer. The SIS-load junction is replaced by a dot termination made of Ti/N2 mixture having sheet resistance of 5 Ohm/square resulting in dot input impedance of about 5 Ohm. The dot impedance is transformed to a high impedance value of 70 Ohm required to terminate the LO directional coupler.

We find the "dot" termination particularly convenient for use in 2SB mixers at mm-wave frequencies. It has number of advantages compared to a lumped resistor load.

- It does not require connection to ground.
- Important limitation of the lump resistor termination is that in order to realize large resistor values with good accuracy one needs couple of squares long resistors, leading to increased inductance which affects the impedance of the resistor.
- The "dot" is tolerant to variation in the resistance per square resulting in only a minor change of the return-loss of the structure (dot plus transformer lines).
- The dot does not require very thin films. The required value of the sheet resistance is controlled not only by the film thickness but also by the content of N_2 atoms in the film. For example to obtain resistance of 5 Ohm/square we use a 200 nm Ti film sputtered in atmosphere containing 1% of N_2.
- Films with high sheet resistance can be fabricated using the technology suggested above. Film with resistance of 50 Ohm/square was obtained on a 40 nm thick Ti film.

III. Results

The 2SB mixer is measured with IF hybrid following the amplifiers, as shown in Figure 5.

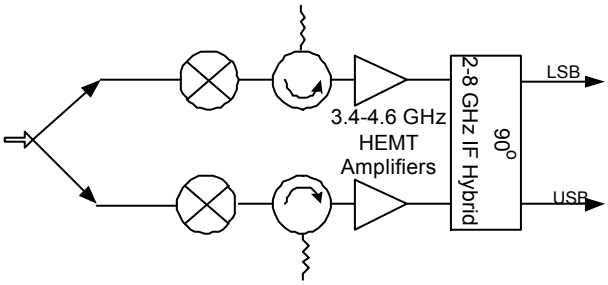

Figure 5 The configuration of the 2SB mixer used in the measurements.

The 2SB mixer is characterized at 5 LO frequencies by Y-factor and sideband-separation measurements. For each LO point a CW test signal is injected at number of frequencies at both RF sidebands and the response of the mixer is measured at the IF outputs by a spectrum analyzer. The difference between the CW amplitude at the signal and the image band is a measure for the sideband separation ratio. An example of the mixer operating in 2SB mode is illustrated in Figure 6.

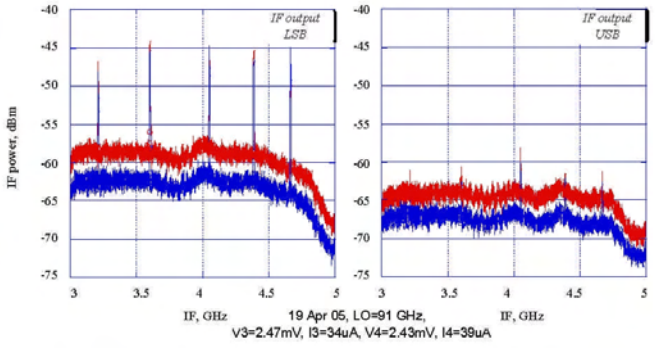

a)

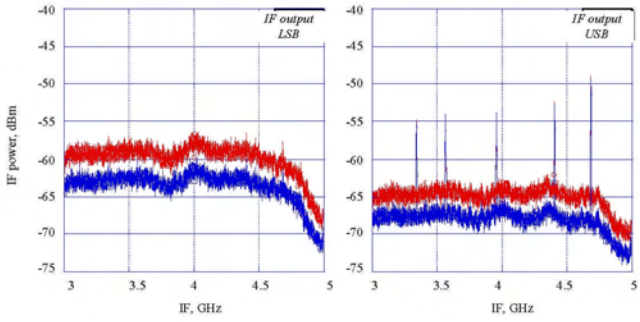

b)

Figure 6 An illustration of the sideband separation properties of the mixer for LO=91 GHz. A CW signal is applied at number of frequencies first at the LSB a) and then at the USB b), the mixer response is shown at both IF outputs.

Both sideband separation ratios are consistent along the IF band with typical value of 13 dB. The calculated SSB mixer noise, shown in Figure 7, is based on the measured Y-factor and sideband separation ratios which account for the noise contributed by the image band.

IV. Discussion

We present the design and first results on our second generation sideband separating mixer. This design differs from its predecessor in the LO-injection circuitry, where the idle ports of the microstrip directional couplers are terminated by "dots" of resistive film instead of an extra pair of SIS-junctions.

Only one mixer chip has been tested. The typical measured Y-factor is about 4.1 dB over the 3.4-4.6 GHz IF band, compared to 4.5 dB previously measured with the first mixer generation. This extra mixer noise temperature is expected since the SIS junctions' areas were measured to be 2.6 μm instead of the required 4 μm. Because of that, in order to maintain mixer stability, the mixer junctions were pumped with less LO power than the required for optimum mixer performance.

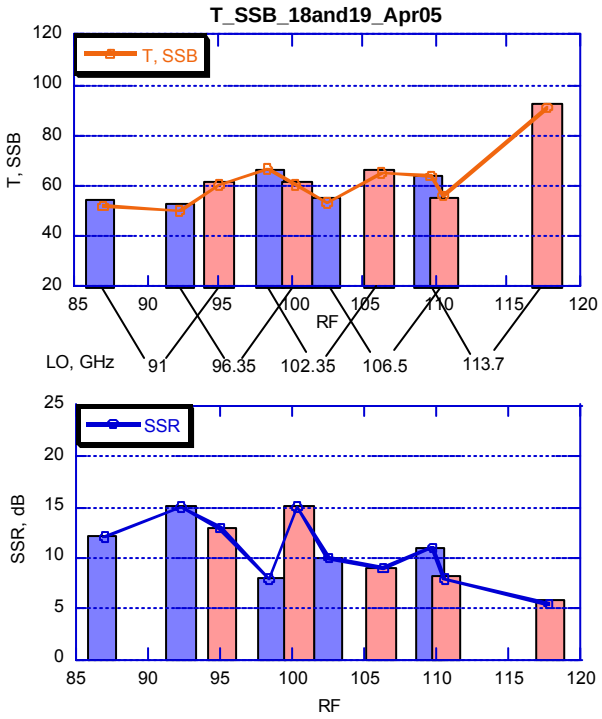

Figure 7 The calculated mixer SSB noise temperature and the measured sideband separation ratios (SSR) for 5 LO frequencies.

A second consequence of the reduced junction area is out of the IF band oscillations which were registered at 6 and 8 GHz for most of the LO frequencies. The oscillations amplitudes were comparable to the test signal peak value, which is used to measure sideband separation ratios. These oscillations were found to seriously affect the sideband rejection leading to ratios as low as 8 dB as for example at LO=102.35 GHz.

In order to achieve good sideband separation ratios when the IF amplifiers are connected between the mixers and the 90^0 IF hybrid (as shown in Figure 5) requires amplifiers with balanced phase and gains. No special care was taken to equalize the gains of the amplifiers in the measurements reported above, which additionally limits the attainable image rejection ratios. A different set of measurement was done

where the IF amplifiers are placed after the hybrid resulting in typical sideband separation ratios of about 20 dB.

The mixer design presented above is a prototype used to verify the suggested technology. Parts of this mixer will be used in future 2SB mixers developed at GARD as for example APEX band 1, 2 and 3.

ACKNOWLEDGMENT

Authors would like to acknowledge Professor R. S. Booth for his constant trust and support of our work. Thanks to Sven-Erik Ferm for his effort on fabricating the mixer block. M. Pantaleev and M. Svensson are acknowledged for their help with the SIS bias supply and support during the measurements.

This work is a part of the APEX Project, supported by the Swedish Research Council and the Wallenberg Foundation by their respective grants.

REFERENCES

[1] R. L. Akeson, J. E Carlstrom, D. P. Woody, J. Kawamura, A. R. Kerr, S. -K. Pan and K. Wan, "Development of a Sideband Separation Receiver at 100GHz", *Proc of Fourth International Symposium on Space Terahertz Technology*, pp.12-17, Los Angeles, USA, March, 1993.

[2] A. R. Kerr, S.-K. Pan and H. G. LeDuc, "An integrated sideband separating SIS mixer for 200-280 GHz", *Proc. of the Ninth Space Terahertz Technology Symposium*, pp.215-222, Pasadena, USA, March, 1998.

[3] A. R. Kerr and S.-K. Pan, "Design of Planar Image Separating and Balanced SIS Mixers," *Proc. of Seventh International Symposium on Space Terahertz Technology*,pp. 207-219, March 12-14, 1996.

[4] S. M. X. Claude, "Sideband-Separating SIS Mixer for ALMA Band 7 275-370 GHz," *Proc. 14th Int'l. Symp.on Space Terahertz Tech.*, 22-24 April 2003.

[5] S. Asayama, et al., "An Integrated Sideband-Separating SIS mixer Based on Waveguide Split Block for 100 GHz Band", *ALMA Memo 453*, http://www.alma.nrao.edu/memo/, April 2003.

[6] S. Asayama, et al., "Prelominary Tests of Waveguide Type Sideband-Separating SIS Mixer for Astronomical Observation", *ALMA Memo 481*, http://www.alma.nrao.edu/memo/, November 2003.

[7] C. C. Chin, D. Derdall, J. Sebesta, F. Jiang, P. Dindo, G. Rodrigues, D. Bond, S.-K. Pan, A. R. Kerr, E. Lauria, M. Pospieszalski, J. Zhang, T. Cecil, and A. W. Lichtenberger, "A Low Noise 100 GHz Sideband-Separating Receiver," *Int. J. Infrared and Millimeter Waves*, vol. 25, no. 4, pp. 569-600, Apr. 2004.

[8] P. R. Jewell and J. G. Magnum, "System Temperatures, Single Versus Double Sideband Operation, and Optimum Receiver Performance", *ALMA Memo 170*, http://www.alma.nrao.edu/memos/index.html.

[9] A. R. Kerr, H. Moseley, E. Wollak, W. Grammer, G. Reiland, R. Henry, K. P. Stewart, „MF-112 AND MF-116: Compact Wavguide Loads And FTS Measurements At Room Temperature And 5 K", ALMA Memo 494, http://www.alma.nrao.edu/memos/index.html.

[10] B. Oldfield, "Connector and termination construction above 50 GHz," *Applied Microwave & Wireless*, pp. 56-66, April 2001.

[11] Matthew Morgan and Sander Weinreb, "Octave-bandwidth high-directivity microstrip codirectional couplers", *IEEE MTT-S Intl. Microwave Symp. Digest*, pp. 1227-1230, Philadelphia, PA, 2003.

[12] V. Vassilev, V. Belitsky, D. Urbain, S. Kovtonyuk, "A New 3 dB Power Divider for MM-Wavelengths", *IEEE Microwave and Wireless Components Letters*, page 30-32, vol.11, January 2001.

[13] V. Vassilev, V. Belitsky, C. Risacher, I. Lapkin, A. Pavolotsky, E. Sundin, "A Sideband Separating Mixer for 85-115 GHz", *IEEE Microwave and Wireless Components Letters*, vol. 14, pp.256-258, June 2004.

[14] V. Vassilev, "Development of a Sideband Separating SIS Mixer Technology for MM-Wavelengths", *Technical report No. 465*, School of Electrical Engineering, Chalmers University of Technology, ISSN 1651-498X.

[15] R. Monje, V. Vassilev, V.Belitsky, C. Risacher, A. Pavolostsky."High Performance of Resistive Thin-Film Termination for Microstrip Lines", *Conference digest, 29th International Conference on Infrared and Millimeter Waves and 12th International Conference on Terahertz Electronics*, September 2004.

Improved design for low noise Nb SIS devices for Band 9 of ALMA (600 - 720 GHz)

C. F. J. Lodewijk, M. Kroug and T. M. Klapwijk
Kavli Institute of Nanoscience, Faculty of Applied Sciences,
Delft University of Technology,
Lorentzweg 1, 2628 CJ Delft, The Netherlands

F. P. Mena, A. M. Baryshev and W. Wild
Space Research Organisation of the Netherlands,
Kapteyn Astronomical Institute,
Landleven 12, 9747 AD Groningen, The Netherlands

***Abstract*— Superconducting-insulating-superconducting mixers incorporating a novel design were fabricated and evaluated for heterodyne detection in the frequency range of 600 to 720 GHz (ALMA Band 9). The improved design consists in tapering the corners of the RF transformer and a careful optimization of the dimensions to obtain a flat response over the full band. We demonstrate that this new design together with state-of-the-art technology lead to an improved noise temperature of T_N=100K. Since the working frequency of our devices crosses the superconducting gap frequency, we had to include the Mattis-Bardeen theory to simulate the response of this particular design. The results of the simulation are in excellent agreement with the experimental data.**

I. Introduction

Since their introduction, almost 30 years ago [1], [2], superconducting-insulating-superconducting (SIS) junctions have become the dominant mixing elements for heterodyne detection for space research in which the highest sensitivity is needed. Currently, two instruments are being developed[4], spanning the frequency range of 600 to 720 GHz. The most straightforward state-of-the-art technology uses niobium with a gap-frequency of about 700 GHz, which means that losses in the tuning structure must be taken into account in the design. Most designs [3] use some kind of lumped circuit to model the various pieces of the tuning structure. In practice they do not provide a proper prediction of the bandwidth and leave room for further improvement in noise temperature. In this article we present results obtained with SIS mixers for Band 9 of the Atacama Large Millimeter Array (ALMA), fabricated with state-of-the-art technology and which have been incorporated in a tuning structure using a new design, with 75 degree tapered edges, permitting to achieve an improvement of the noise temperature. Up to now the best noise temperature was about 150 K at 640 GHz [6]. We now report a double sideband uncorrected noise temperature of 100 K over 60% of the band, with a minimum of 93 K at 654 GHz and a slight increase towards $\sim$175K.

II. Devices

The mixers incorporate a SIS junction and a stripline that tunes out the capacitance of the junction. This structure consists of a superconducting ground plane with a thickness of 200 nm Nb, at the junction an about 7 nm thick Al layer covered with AlO_x as the tunnel barrier and a 500 nm Nb top wire. Between ground plane and top wire a 250 nm layer of SiO_2 serves as dielectric. Contact pads are made of 50 nm thick Au. A schematic cross section along the tuning stripline is shown in Fig. 1(a).

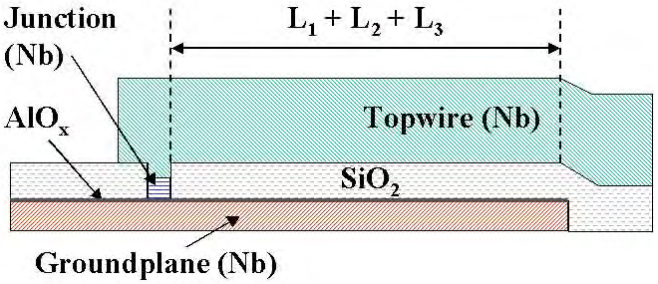

(a) Schematic cross section of SIS junction, wiring and dielectric, along the stripline. The indicated length L_1+L_2+L_3 is the total length of the stripline, L_i referring to the different sections shown in the figure on the right.

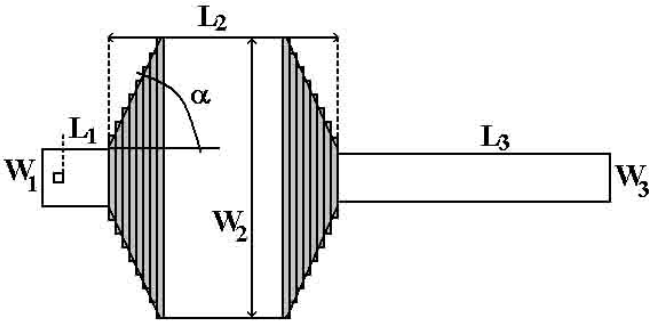

(b) Schematic picture of the tuning structure. The design has tapered edges of the middle section with an angle α of 75 degrees. The tapered part has been modeled by dividing the middle section into small segments, each characterized by an impedance and a propagation constant. The stripline is defined by the widths W_i and lengths L_i of its sections.

Fig. 1. Schematic representations of a tuning stripline.

The devices are fabricated on a quartz substrate. First, a Nb monitor layer is deposited, after which an optically defined ground plane pattern of Nb/Al/AlO_x/Nb is lifted off. Junctions

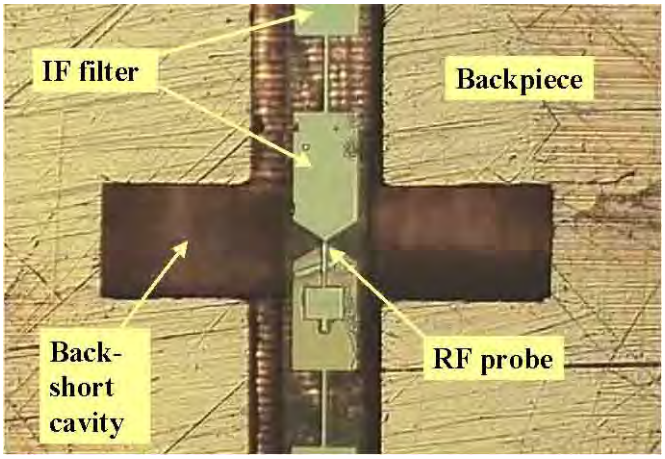

(a) Photograph of a SIS device with low-pass IF filter, mounted across the backshort cavity. The electromagnetic radiation of the waveguide is coupled into the center of the bowtie (RF probe). The stripline has a design with rectangular middle section.

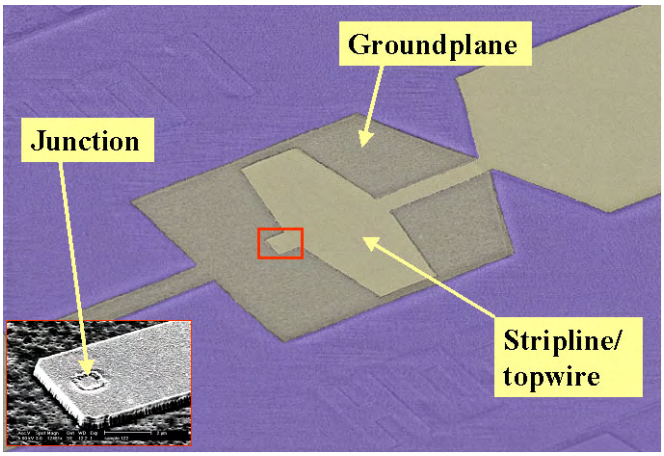

(b) Scanning electron micrograph of SIS wiring system, with the tapered tuning stripline. Inset shows SIS junction.

Fig. 2. Images of superconducting tuning structures and their surroundings.

are defined by e-beam lithography in a negative e-beam resist layer and etched out with a SF_6/O_2 reactive ion etch (RIE) using AlO_x as a stopping layer. The junction resist pattern is subsequently used as a lift off mask for a dielectric layer of SiO_2. A Nb/Au top layer is deposited and Au is etched with a wet etch in a KI/I_2 solution using an optically defined mask. Finally, using an e-beam defined top wire mask pattern, the layer of Nb is etched with a SF_6/O_2 RIE, finishing the fabrication process.

Part of the top wire is the tuning structure to tune out the capacitance of the SIS junction. In previous designs a narrow strip attached to the junction is connected to a wide section of a certain length followed again by a narrow section. Each section is described by a series and parallel impedance.

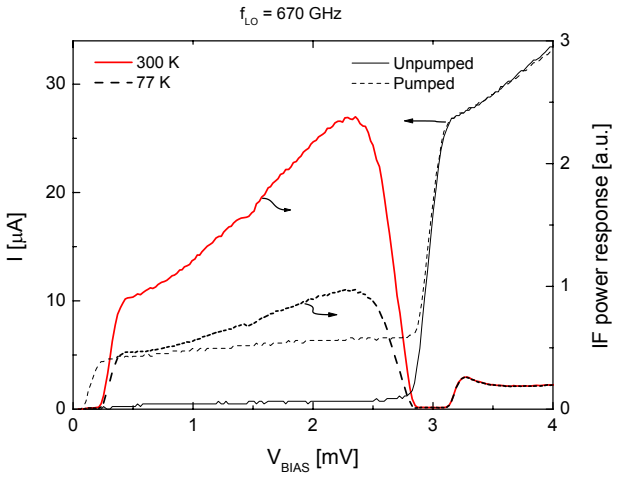

Fig. 3. I-V characteristics and IF response for the SIS mixer pumped at a frequency of 670 GHz.

As usual a periodic RF choke structure is connected to both the groundplane and the top wire to act as a low-pass filter for the intermediate frequency (IF). The complete device is mounted on a backpiece, perpendicular to a waveguide. This waveguide is connected to the feed horn of the astronomical signal. The waveguide ends in a backshort cavity. A photograph of a mixer device mounted across the backshort cavity can be found in Fig. 2(a).

Fig. 3 shows the IV characteristics in the pumped and unpumped situation. Notice that in the pumped situation the first photon assisted tunneling step covers almost the full gap ($\hbar\omega \simeq 2\Delta$).

III. Rectangular Tuning Structure

The input impedance at the RF probe point of the SIS mixer, the center point of the bowtie structure, as can be seen in Fig. 2(a), has been calculated with Microwave Studio™. The input impedance is connected to the SIS junction via the multi-section stripline. The stripline serves as a tuning structure to match the input impedance with the SIS impedance. In this paper, we focuss on improvements of this tuning structure. Its design has been modeled with the software package Mathematica™.

Since we are working close to or above the gap-frequency of the superconductor (Fig. 3), we have to use the complex conductivity, defined as $\sigma = \sigma_1 - i\sigma_2$, and derived from the microscopic theory by Mattis and Bardeen [7]. The surface impedance of a superconductor, in the local limit since we are using Nb[3], is given by

$$Z_s = \sqrt{\frac{i\omega\mu_0}{\sigma}}\coth(\sqrt{i\omega\mu_0\sigma}t) \qquad (1)$$

for a strip of thickness t at an angular frequency ω; μ_0 represents the permeability of free space. The series impedance of a part of the strip line is now the sum of the geometrical inductance and the surface impedance of the superconductor, the parallel impedance is formed by the capacitance of the

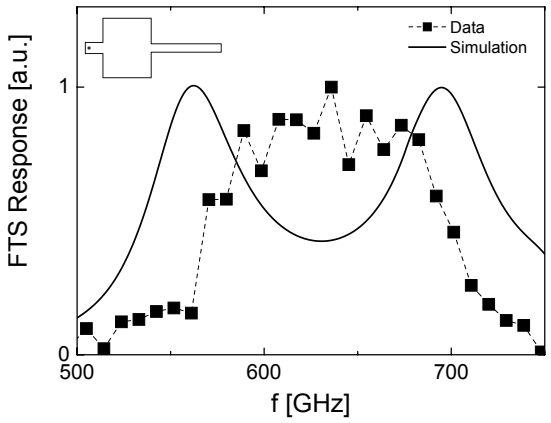

Fig. 4. Frequency response of the mixer with old stripline design: experimental data (solid squares) and simulation with design parameters (full line).

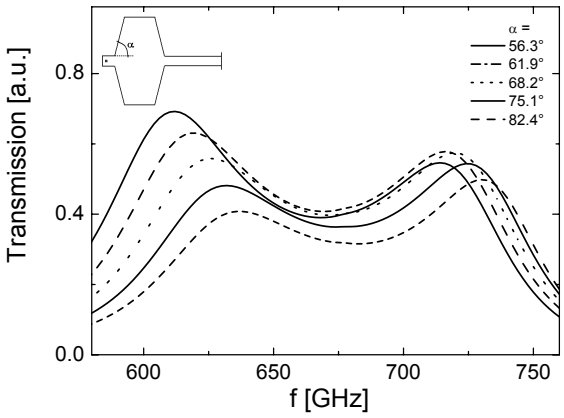

Fig. 5. Calculated transmission as a function of frequency for striplines with tapered middle section. Different lines represent different tapering angles α, while maintaining the same length L_2 (see Fig. 1(b)).

dielectric layer. Following *e.g.* Pozar [8], for each part of the strip line a propagation constant γ and a characteristic impedance Z_0 can be derived; using these two parameters a transmission (or ABCD) matrix is defined.

For the complete strip line, the transmission matrix can be calculated by matrix multiplication. For a strip line consisting of three parts, this yields $A_{tot} = A_1.A_2.A_3$, where the A_i's are the individual ABCD matrices.

The total transmission of electromagnetic radiation from the RF probe to the SIS junction is found as follows. A matrix $A_{j,i}$ is calculated for the imaginary part of the junction impedance and a matrix $A_{a,i}$ for the imaginary part of the antenna impedance [8]. From this, a final transmission matrix X is calculated: $X = A_{j,i}.A_{tot}.A_{a,i}$. Using the real part of the junction impedance, R_j, and the real part of the antenna impedance, R_a, the total transmission coefficient T reads

$$T = \frac{4R_j}{R_a \left| \frac{R_a X_{1,1} + X_{1,2} + R_j R_a X_{2,1} + R_j X_{2,2}}{R_a} \right|^2} \qquad (2)$$

where the $X_{i,j}$'s are the matrix elements of the final transmission matrix X.

We have fabricated devices with a rectangular tuning stripline. The frequency response has been determined using a home-made Fourier Transform spectrometer by measuring the changes produced by the incoming light in the bias current at a particular chosen bias voltage which is selected to be close to the gap.

For these devices, the measured FTS response was flat, but it covered mostly the lower part of the 600 - 720 GHz band. To get a better hold of what was going on, the transmission of these devices has been calculated. As can be seen in Fig. 4, experiment and calculations clearly do not match. Changing the parameters that may have varied due to fabrication uncertainties were not successful to make the correspondence better. As a result, we were unable to improve the performance of these rectangular devices, experimentally nor theoretically.

IV. Tapered tuning structure

If the middle strip is much wider than the two outer parts, the simple way of calculating the transmission matrix as described in the previous section is inaccurate, because there is expected to be a gradual change in current density. This means there are parts of the wide sections where no current flows, which will add extra capacitance.

In using normal metal striplines, extra capacitors should be added to the model to compensate for the step in width [8]. For superconducting striplines the right method of compensation is unclear. As an alternative, we introduce in the design itself a gradual change, by tapering the corners of the wide section. This has been modeled by artificially dividing the middle strip into small segments with increasing and decreasing widths, as can be seen in Fig. 1(b). The total transmission matrix is now

$$A_{tot} = A_1.A_{21}.A_{22}.(...).A_{2n}.A_3 \qquad (3)$$

where A_{2i} are the partial ABCD matrices of the n parts the middle strip was divided into.

We have calculated the transmission for striplines with different tapering angles, plotted in Fig. 5. It can be seen that for smaller tapering angles, corresponding to a smoother transition to and from the middle section, the high end cutoff frequency remains more or less the same, determined by the frequency-dependence of the surface resistance of the superconductor, but the lower side of the band shifts downwards.

It was decided to design and fabricate mixers with a 75^o tapered stripline. For a top view of such a device, a scanning electron microscope (SEM) picture is shown in Fig. 2(b). The simulation was changed accordingly and when the measured FTS data are compared with the calculated transmission, as shown in Fig. 6, it is clear that there is a much better correspondence between the two. The FTS data show a flat response and a frequency coverage beyond 700 GHz. The difference in size of the bandwidth can be attributed to uncertainties in

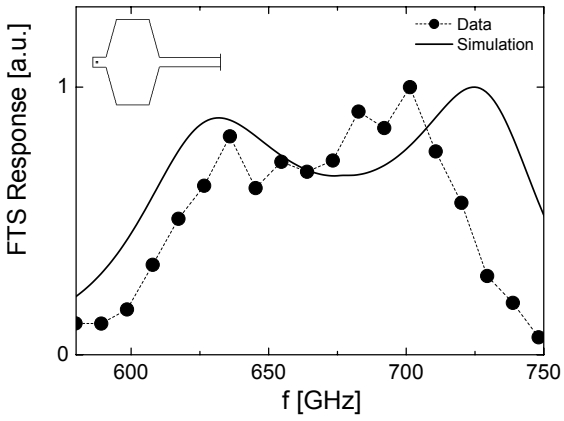

Fig. 6. Frequency response of the mixer with tapered stripline design: experimental data (solid dots) and simulation with design parameters (full line).

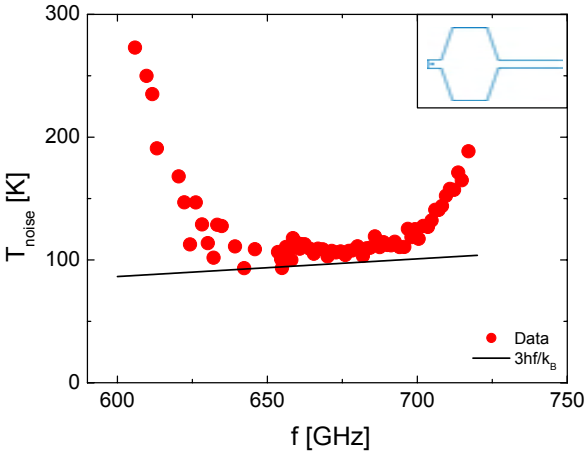

Fig. 7. Uncorrected DSB noise temperature realized with improved tuning structure. Inset shows the tuning stripline with the tapered middle section. The full line shows a noise level of $3hf/k_B$.

fabrication parameters, such as thickness of the SiO_2 and the area (i.e. capacitance) of the junction.

V. Noise Temperature

The noise temperature of the mixer, the accompanying optics and IF chain [5] has been measured using the standard Y-factor method. The hot and cold loads were kept at 295 and 77 K, respectively, and their radiation was mixed with the local oscillator (LO) signal using a 10 μm mylar beam splitter. The SIS mixer is kept in a cryostat which has a quartz window coated with an antireflection layer. As an example, in Fig. 3, we show the IV curve when the mixer is pumped with an LO frequency of 670 GHz. The same figure also shows the IF power levels at the same frequency. The resulting uncorrected DSB noise temperatures at different LO frequencies are presented in Fig. 7. The noise temperature is as low as 93 K at 654 GHz and is about 100 K for 60% of the 600 - 720 GHz band. The results presented here correspond to the mixer exhibiting the best noise temperature. However, the reproducibility between mixers is excellent, the maximum achieved noise temperature being no more than 30% higher than the one presented in Fig. 7.

VI. Conclusions and Discussion

SIS mixers with a new design have been fabricated and evaluated for heterodyne detection in the frequency range of 600 to 720 GHz (ALMA band 9). We have shown that the combination of this design with state-of-the-art technology results in the lowest noise temperature ever achieved in this frequency band. The improved design consists in tapering the corners of the RF transformer which traditionally is rectangular. As a result, the frequency response is flatter in the desired band and the noise temperature is lower, compared to previous devices.

Acknowledgements

The authors would like to thank NanoImpuls, the Dutch Research School for Astronomy (NOVA), the Dutch Organisation for Scientific Research (NWO) and the European Southern Observatory (ESO) for funding this project.

References

[1] G. J. Dolan, T. G. Phillips, and D. P. Woody, Appl. Phys. Lett. **34**, 347 (1979)
[2] P. L. Richards, T. M. Shen, R. E. Harris and F. L. Lloyd, Appl. Phys. Lett. **34**, 345 (1979)
[3] G. de Lange, J. J. Kuipers, T. M. Klapwijk, R. A. Panhuyzen, H. van de Stadt, and M. W. M. de Graauw, J. Appl. Phys. **77**, 1795 (1995).
[4] For example, two main astronomical large projects that are demanding such applications are ALMA (http://www.eso.org/projects/alma/) and its precursor CHAMP (http://www.mpifr-bonn.mpg.de/div/mm/apex/).
[5] A. Baryshev, E. Lauria, R. Hesper, T. Zijlstra, and W. Wild, ALMA memo 429.
[6] C. M. Gaidis, H. LeDuc, M. Bin, D. Miller, J. A. Stern, and J. Zmuidzinas, IEEE Transactions on Microwave Theory and Techniques **44**, 1130 (1996).
[7] D. C. Mattis and J. Bardeen, Phys. Rev. **111**, 412 (1958).
[8] D. M. Pozar, *Microwave Engineering*, John Wiley and Sons (1998).

A 700 GHz single chip balanced SIS mixer

Paul Grimes*‡§, Ghassan Yassin*§, Karl Jacobs†, Stafford Withington*
*Astrophysics Group, Cavendish Laboratory, Madingley Road, Cambridge, CB3 0HE, UK.
†KOSMA, I. Physikalisches Institut, University of Cologne, Cologne, Germany.
‡Email: pxg@astro.ox.ac.uk
§PG and GY are now with Oxford University's Radio Experimental Cosmology Group, Astrophysics, Denys Wilkinson Building, Keble Road, Oxford, OX1 3RH

***Abstract*— We present the design and simulated performance of a single chip balanced SIS mixer for the 600-720 GHz band. The mixer is based on back-to-back finline transitions, fed by a pair of Pickett-Potter horn-reflector (PPHR) antennas. As all of the signal combination is carried out on the chip in microstrip planar circuits, the split mixer block is very simple to manufacture. The simulation results predict that the performance of the balanced mixer will be significantly better than previous single-ended finline SIS mixers in this band, and that the mixer with have much lower LO power requirements than single-ended SIS mixers. We also show how the performance of the 700 GHz quadrature hybrid used can be measured by using the balanced mixer in the direct detection mode as a bolometric interferometer.**

I. Balanced SIS mixers

BALANCED mixers combine two identical single-ended mixers with a 3 dB, $90°$ or $180°$ hybrid junction in the RF signal path and a 3 dB, $180°$hybrid in the IF signal path (fig. 1). Balanced mixers offer a number of advantages over single-ended mixers[1]:

- A LO coupler or diplexer is not required in the signal path to the mixer
- The required LO power is substantially reduced over a single-ended mixer with weak LO coupling
- Sideband noise from the LO is rejected

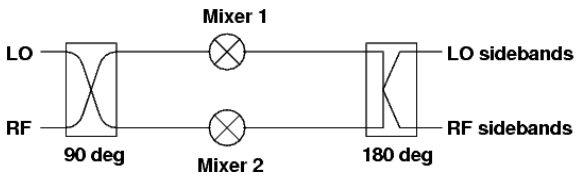

Fig. 1. Circuit diagram of a general balanced mixer using a $90°$ RF hybrid.

A number of balanced SIS receivers have been reported. In particular the CalTech Submillimeter Observatory is currently upgrading all of it's SIS receivers below the 660 GHz band to balanced SIS receivers[2], and a number of groups are investigating balanced and image separation mixers for use on ALMA[3].

Most previously reported balanced SIS receivers have implemented the RF hybrid as a waveguide branchline circuit, and used two separate SIS mixer chips. This has limited the availability of balanced SIS receivers at high frequencies due to the difficulty in machining waveguide hybrids at these frequencies. In an effort to avoid the problem of machining complicated waveguide circuits, Kerr *et al*[4], [5] have built and tested single chip balanced and image separation SIS mixers operating in the 200-300 GHz band.

The degree of LO sideband rejection in a balanced mixer depends on the accurate matching of the amplitude and phase through the two arms of the circuit. The total amplitude and phase imbalances are given by

$$\Delta A = \Delta A_{RF} + \Delta G + \Delta A_{IF} \quad (1)$$

$$\Delta\theta = 2\Delta\theta_{RF} + \Delta\theta_{IF} \quad (2)$$

where RF and IF refer to the two hybrid couplers and ΔG is the difference in the gains of the two SIS mixing elements. From (1) it can be seen that amplitude imbalance in the hybrids can be at least partially cancelled by controlling the relative gain of the two mixing elements by biasing at different points on the I-V curve. No such cancellation can be achieved in the phase imbalance. Fig. 2 shows contours of LO sideband rejection as a function of the amplitude and phase imbalances in a balanced mixer.

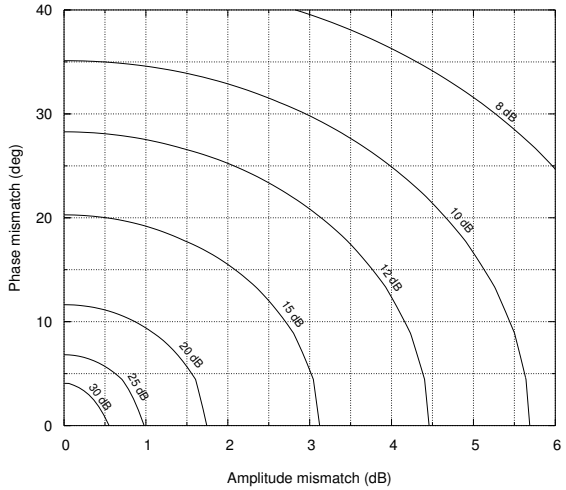

Fig. 2. Contours of LO sideband rejection as a function of amplitude and phase imbalance (after Kerr *et al*[4].).

II. The Single Chip Finline Balanced Mixer

Our single chip balanced mixer is based on the back-to-back finline layout previously used by Campbell *et al*[6] as the basis for a 350 GHz bolometric interferometer. A single split mixer block is used, incorporating Pickett-Potter horn-reflector (PPHR) antennae[7] coupled to either end of a $160 \times 320\,\mu\mathrm{m}$ waveguide. The mixer chip incorporating the finline transitions, RF circuit and SIS mixers is mounted in slots in the side of the waveguides. An external IF hybrid is mounted on the Dewar cold plate along with the cryogenic IF amplifiers.

A. Mixer block

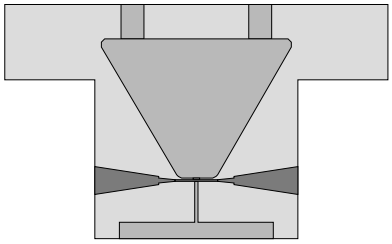

Fig. 3. One half of the mixer split block. The IF board pocket is in mid-grey and the back-to-back horns, waveguide and chip slot in dark-grey.

The mixer block (fig. 3) is machined in two halves from aluminium, and includes the PPHR, waveguide, chip mounting slots and a pocket for the IF connection board. After machining the two halves of the block are sputtered with niobium to reduce losses below the niobium gap frequency of ~ 680 GHz.

The Pickett-Potter horn-reflector antennae are identical to those used on our previous single-ended 700 GHz finline SIS mixers[7], and give a low sidelobe, 10° beam across a 15% bandwidth. The reflectors are mounted on the outside of the mixer block after the block is assembled, along with the IF SMA connectors and the superconducting electromagnet used to suppress the Josephson current in the SIS junctions.

B. Mixer chip

Working towards the centre of the chip, the mixer chip (fig. 4) is made up of finline waveguide-to-microstrip transitions at either end, bond pads to connect the bias and IF circuits, two parallel junction SIS mixers, DC/IF blocking capacitors (to prevent leakage of the IF signal from one mixer to the other, and to allow independent biasing of the mixers) and the quadrature RF hybrid at the center of the chip. Ground connections are made by bonding the pad at the top of the chip to the mixer block.

The mixer chip is being fabricated at KOSMA on a $220\,\mu\mathrm{m}$ thick quartz substrate in 6 layers (fig. 5). A $\mathrm{Nb} - \mathrm{AlO_x} - \mathrm{Nb}$ trilayer is deposited first to form the ground-plane, lower finlines and SIS junctions. The junctions are defined and the lower $200\,\mu\mathrm{m}$ thick SiO insulation layer deposited, followed by a second $225\,\mu\mathrm{m}$ SiO insulation layer. A $400\,\mu\mathrm{m}$ Nb layer forms the bond pads, mixer tuning circuits and top contacts to the SIS junctions. The ends of the microstrip input to the mixer

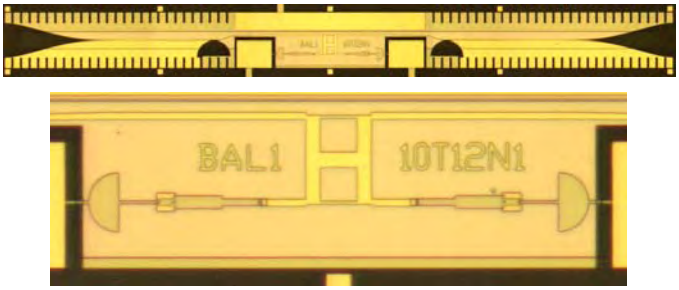

Fig. 4. *Top*, completed balanced finline mixer chip; *Bottom*, Enlarged image of circuits at the centre of the chip

tuning circuits are anodised to form $5 \times 7\,\mu\mathrm{m}$ parallel plate capacitors with a $30\,\mathrm{nm}$ thick $\mathrm{Nb_2O_5}$ dielectric. Finally the RF hybrid, top capacitor electrodes and top finlines are deposited as a $400\,\mu\mathrm{m}$ thick Nb layer, topped by a gold passivation layer. Prior to mounting in the mixer block, the mixer chip is lapped to $60\,\mu\mathrm{m}$ thickness and points are diced onto the end of the finlines.

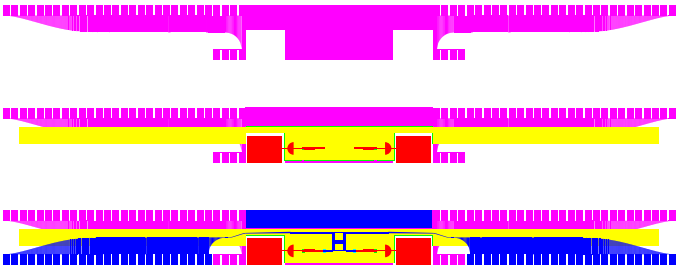

Fig. 5. Layers deposited during mixer chip fabrication. *Top*, ground-plane trilayer; *Middle*, ground-plane, insulation and junction definition layers and first wiring layer; *Bottom*, completed chip.

C. Planar circuit components

The quadrature RF hybrid is a 2-stage microstrip branchline design[1] (fig. 6) optimised in ADS and Sonnet Inc.'s *em* to provide good phase and amplitude balance across a 550-750 GHz band. The Sonnet simulations in fig. 7 include the effects of the frequency dependence of the surface impedance of Niobium across the superconducting gap, including above gap losses. Due to our choice of dielectric and wiring layer thickness, the highest impedance microstrip lines that can be reliably fabricated by UV photo-lithographic techniques are $2 - 3\mu\mathrm{m}$ wide, with characteristic impedances of $27 - 20\,\Omega$. In order to give good performance, the 2-stage branchline hybrid designs requires that the highest impedance lines have characteristic impedances approximately twice the characteristic impedance of the input lines. We therefore switched from the $20\,\Omega$ impedance input used in our previous finline mixers to a $10\,\Omega$ input impedance. The $20\,\Omega$, $3\,\mu\mathrm{m}$ wide output microstrip line from the finline design is tapered over several wavelengths to $10\,\Omega$, $7\,\mu\mathrm{m}$ wide microstrip. In this way, the use of finline tapers in transforming the waveguide mode to microstrip modes allows an essentially free choice of microstrip impedance with little impact on performance,

except for an increase losses above the gap frequency due to the extra length of transmission line used to implement the taper.

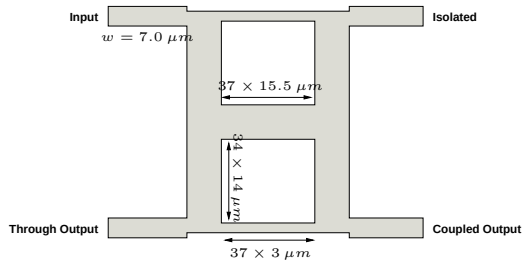

Fig. 6. Final RF quadrature hybrid design.

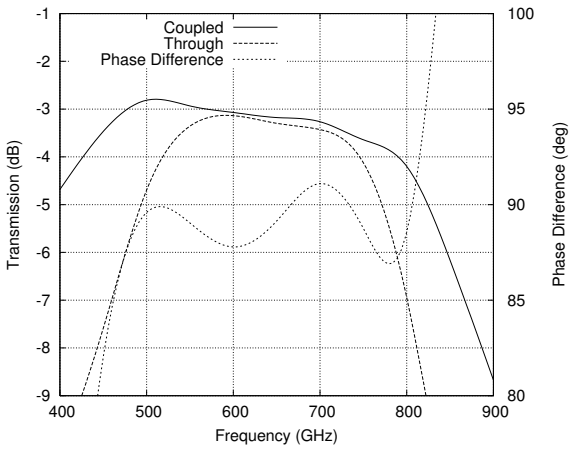

Fig. 7. Simulated transmission and phase balance of the RF hybrid.

The change from $20\,\Omega$ input to $10\,\Omega$ input has an additional advantage, in that it allows the use of larger SIS junctions in the parallel junction tuning circuit (fig. 8), improving the tolerance of the tuning response to slight inaccuracies in the area of the junctions. The impedance change also effectively increases the IF system input impedance relative to the junction impedance, which in turn increases the conversion gain of mixers. The parallel junction tuning circuit was chosen for its broadband tuning characteristics, thus reducing the risk of badly matched tuning responses for the two mixers on the mixer chip. The tuner design was extensively simulated as a single-ended mixer in SuperMix[8] using measured I-V characteristics from previous finline mixers produced at KOSMA with similar critical current densities to those required for this mixer.

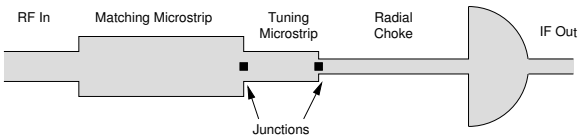

Fig. 8. Parallel junction tuning circuit.

Although balanced mixers can be operated by using a simple microstrip tee to combine the IF signals, this discards the LO sideband signal. Therefore we have decided to use a $180°$hybrid to combine the IF signals so that the down converted LO sideband signal is available for diagnostic purposes. This method also allows us to bias the mixers with identical or opposite voltages and still recover both IF signals, which may be helpful in removing the effects of trapped flux.

The IF hybrid is based on a broadband 2-stage rat-race design (fig. 9) reported by Knoechel and Mayer[9]. The design was adapted using ADS and Sonnet *em* to give good amplitude and phase matching across the 4.2-5.8 GHz bandwidth of our IF systems. The IF hybrid was fabricated on the same RT/Duroid 6010LM material used for the IF connection boards on this and previous finline mixers, and tested at room temperature on a VNA. The measured amplitude and phase balance is shown in fig. 10.

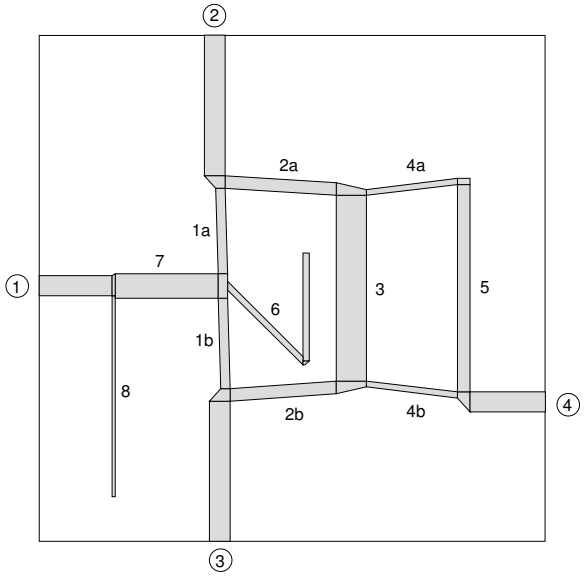

Fig. 9. IF hybrid, based on the Knoechel and Mayer design[9].

D. Optics

The layout of the back-to-back PPHR in the mixer block gives two output beams pointing in the same direction, separated by $23\,\mathrm{mm}$. To produce enough separation between the two beams, so that the LO coupling optics do not impinge on the RF signal beam, the reflector on one of the PPHR antennae is reversed and two flat mirrors added inside the cryostat to bring the LO beam to a separate window. The beam from the Gunn-doubler-tripler source is focused onto the PPHR antenna using a parabolic mirror outside the cryostat. The RF beam is coupled directly from the cryostat to the hot/cold load. The layout to be used for mixer tests is shown in fig. 11.

III. Mixer Performance

The mixer chips are currently being fabricated at KOSMA. Once these chips are completed, testing of the balanced receiver will begin by measuring the mixer performance of the receiver without the IF hybrid in place. Although the noise performance in this configuration will be poor, due to the 3 dB

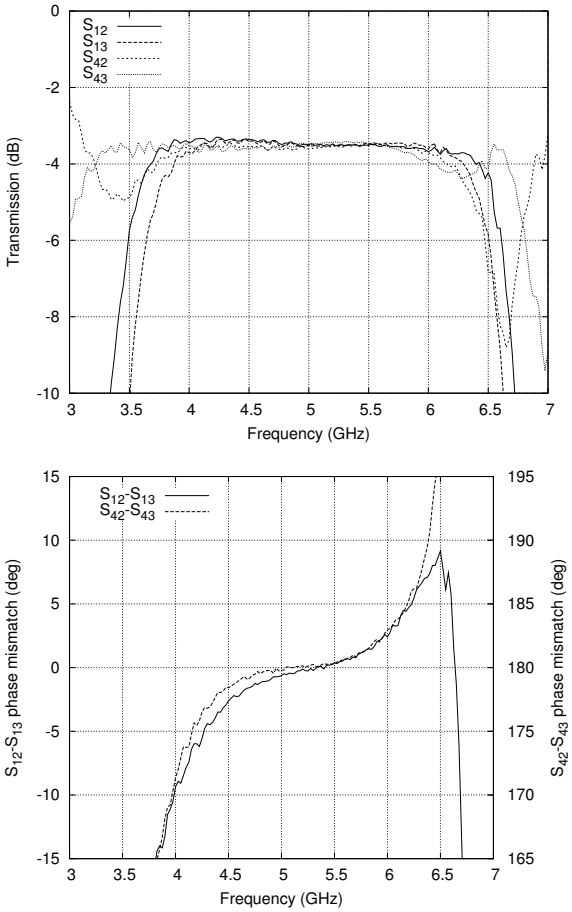

Fig. 10. Performance of the IF hybrid as measured at room temperature.

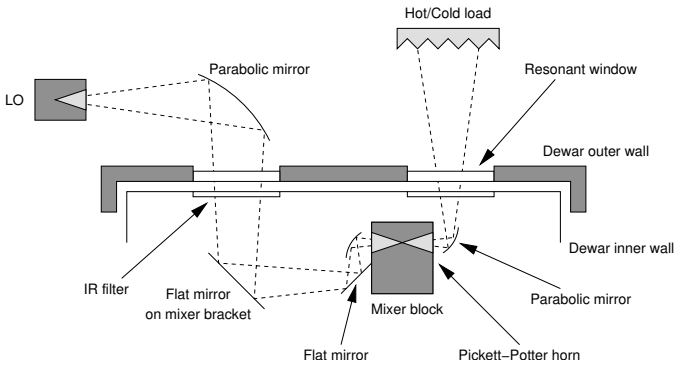

Fig. 11. Optical layout of the test receiver.

coupling to the 300 K LO sidebands, the conversion gain and LO distribution between the two mixers can be evaluated, providing a measure of the amplitude matching in the RF hybrid and between the conversion gains of the two component mixers. Adding the IF hybrid back into system will allow the performance of the full balanced receiver to be measured.

SuperMix based software has been used with Sonnet results for the two hybrids and I-V curves from previous finline mixers to predict the performance of the balanced receiver. These simulations include all components of the receiver from the output of the finline transitions to the inputs of the two IF amplifiers. The predicted mixer conversion gain, LO sideband rejection and DSB noise temperature is shown as a function of LO frequency in fig. 12. The effect of varying the bias voltage of one of the mixing elements on the conversion gains between the input sidebands and output signals is shown in fig. 13. Fig. 14 shows that the balanced performance should be maintained across the full IF bandwidth.

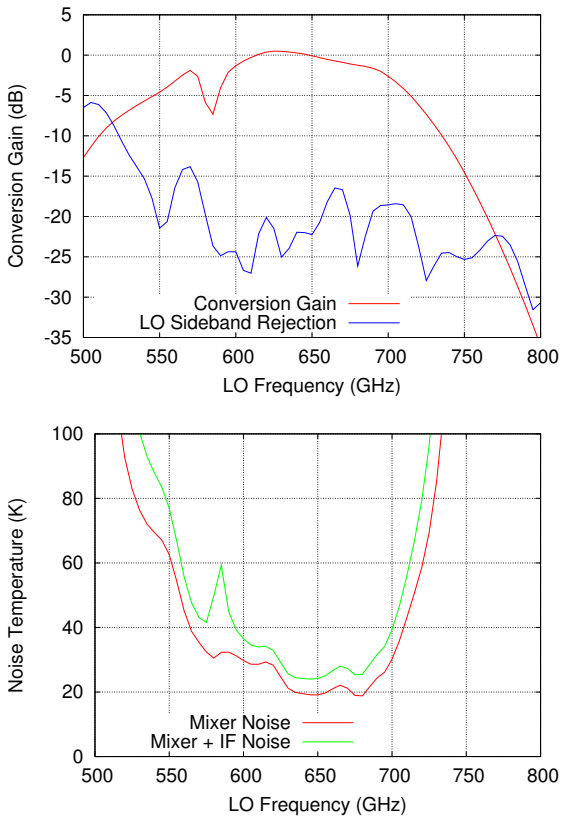

Fig. 12. Simulated performance of the balanced mixer as a function of LO frequency. LO power, bias voltage and IF frequency are fixed at a value that gives maximum conversion gain in the centre of the tuning.

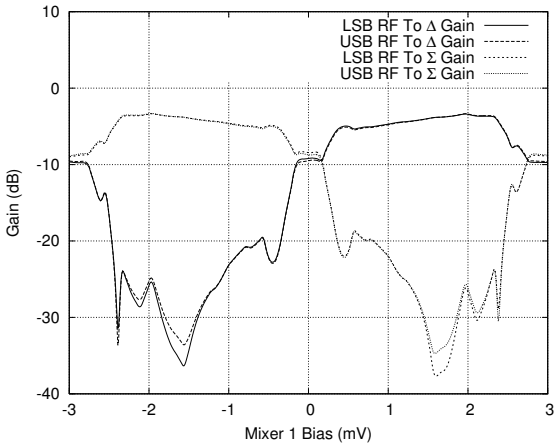

Fig. 13. Simulated conversion gain of the balanced mixer as a function of the bias voltage on one mixing element. By reversing the bias voltage on one mixing element the IF outputs are interchanged.

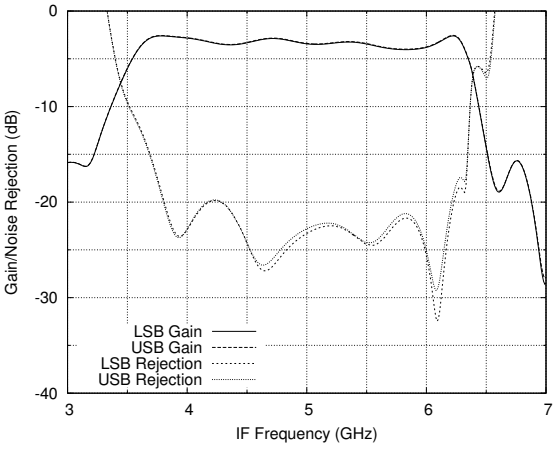

Fig. 14. Simulated noise performance of the balanced mixer across the IF frequency band.

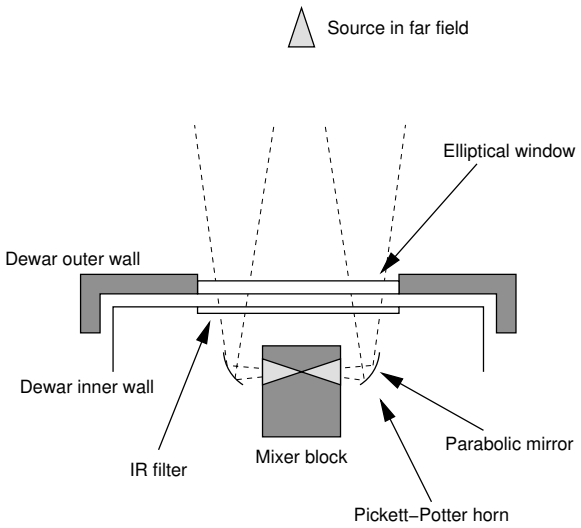

Fig. 15. Optical layout for testing the balanced mixer chip as a bolometric interferometer.

SuperMix simulations of previous finline mixers have predicted conversion gains comparable with measured results, but have consistently predicted receiver noise temperatures 2-3 times lower than the best measured results. If this again proves to be true for the balanced mixer, then we can reasonably hope to achiever receiver noise temperatures around 100 K with near unity conversion gain.

IV. Operation as a bolometric interferometer

The back-to-back finline layout has previously been used as the basis for bolometric interferometers at 350 GHz[6] and 150 GHz[10], using SIS and TES detectors respectively. The balanced mixer chip can also be operated as a bolometric interferometer by using each of the SIS mixing elements in the direct detection mode and the optical layout shown in fig. 15, although the mixer tuning circuits are not optimised for ultimate direct detection sensitivity.

The balanced mixer chip has one crucial advantage over the previously reported back-to-back interferometers, in that it uses a 3-dB quadrature hybrid coupler rather than a 15-20 dB parallel line coupler or a 180° hybrid coupler. In conjunction with the DC blocking capacitors, this allows simultaneous detection of both the sine and cosine fringes with no attenuation of either signal path.

By operating the balanced mixer as a bolometric interferometer with a coherent point source in the far-field, we can directly measure the amplitude and phase balance of the RF quadrature hybrid. Amplitude imbalances in the hybrid will reduce the visibility of the fringes, and phase imbalances will both reduce the visibility of the fringes and shift the sine and cosine fringe patterns relative to each other. Any difference in responsivities of the SIS detectors will also contribute to the amplitude imbalance, but it should be possible to separate this contribution out by biasing the detectors at different voltages.

Simulated fringes are shown in fig. 16 for two frequencies, firstly where the amplitude and phase are well matched, and secondly where they are poorly matched. These simulations were carried out in SuperMix, using a measured beam pattern

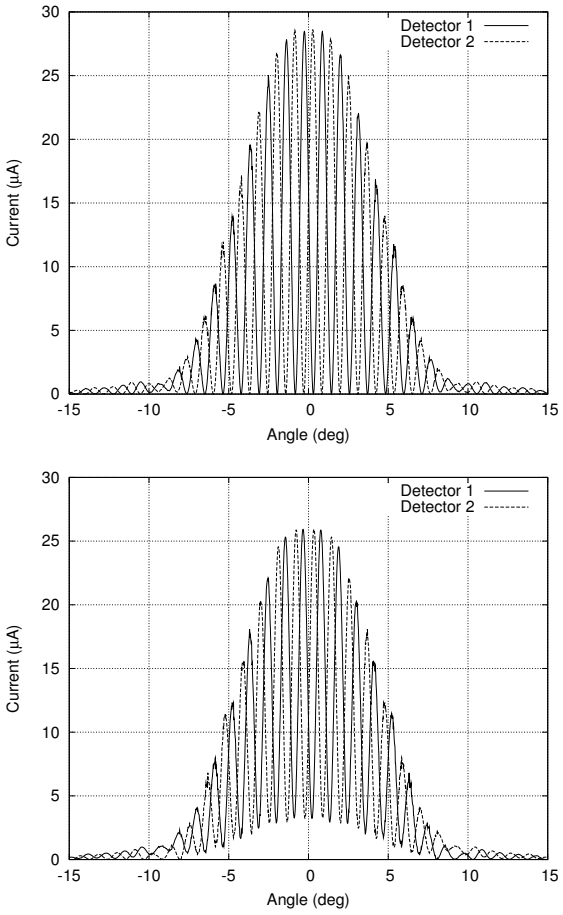

Fig. 16. Predicted fringes for the interferometer experiment when the amplitude and phase through the RF hybrid are well matched (660 GHz, top) and imbalanced (670 GHz, bottom).

of a Pickett-Potter horn-reflector antenna and the Sonnet *em* results for the RF quadrature hybrid.

V. Concluding remarks

We have presented the design of a single chip balanced mixer for the 600-720 GHz band. By basing the design on the back-to-back finline layout we have been able to use a simple, easy to machine mixer block in conjunction with high performance PPHR antennae and standard mixer chip fabrication techniques. Simulations of the performance of the balanced mixer lead us to expect very good performance, with near unity conversion gain and a reduction in noise temperature of about a factor of two over our previous finline SIS mixers in this frequency band, as well as a reduction in required LO power of at least 12 dB.

The successful operation of this balanced mixer design would enable us to consider a number of further developments. By using higher energy gap materials for some or all of the microstrip circuitry, a future mixer could be operated well above the gap frequency of niobium. The successful use of complex microstrip circuitry in a mixer will allow us to design more advanced compound mixers, such as sideband-separating or even balanced sideband-separating mixers. The back-to-back finline layout also lends itself naturally to use with photonic LO sources, particularly given the reduced LO power requirements of the balanced mixer design.

References

[1] D. M. Pozar, *Microwave Engineering, 2nd edition*. John Wiley & Sons, Inc., 1998.

[2] J. Kooi, A. Kovacs, F. Rice, M. Summer, J. Zmuidzinas, and T. Philips, "Heterodyne instrumentation development for the Caltech Submillimeter Observatory," in *Proc. SPIE*, vol. 5498, 2004.

[3] S. M. X. Claude, C. T. Cunningham, A. R. Kerr, and S.-K. Pan, "Design of a sideband-separating balanced SIS mixer based on waveguide hybrids," *ALMA Memo Series*, vol. 316, 2000.

[4] A. R. Kerr and S.-K. Pan, "Design of planar image separating and balanced SIS mixers," in *Proceedings of the Seventh International Symposium on Space Terahertz Technology*, 1996.

[5] A. R. Kerr, S.-K. Pan, A. W. Lichtenberger, N. Horner, J. E. Effland, and K. Crady, "A single-chip balanced SIS mixer for 200-300 GHz," in *Proceedings of the Eleventh International Symposium on Space Terahertz Technology*, 2000.

[6] E. S. Campbell, S. Withington, G. Yassin, C. Y. Tham, K. Jacobs, and S. Wolfe, "Single chip, beam combining, interferometric detector for submillimetre-wave astronomy," in *Proceedings of the Fourteenth International Symposium on Space Terahertz Technology*, p. 129, 2003.

[7] P. Kittara, P. K. Grimes, G. Yassin, S. Withington, K. Jacobs, and S. Wulff, "A 700 GHz antipodal finline mixer fed by a Pickett-Potter horn-reflector antenna," *IEEE Transactions on Microwave Theory and Techniques*, vol. 52, p. 2352, 2004.

[8] J. Ward, F. Rice, G. Chattopadhyay, and J. Zmuidzinas, "SuperMix: A flexible software library for high-frequency circuit simulation, including SIS mixers and superconducting elements," in *Proceedings of the Tenth International Symposium on Space Terahertz Technology* (T. W. Crowe and R. M. Weikle, eds.), p. 269, 1999.

[9] R. Knoechel and B. Mayer, "Broadband printed circuit $0°/180°$ couplers and high power inphase power dividers," in *IEEE MTT-S International Microwave Symposium Digest*, p. 471, 1990.

[10] G. Yassin, D. Goldie, L. Dunlop, S. Withington, and M. E. Jones, "A TES finline detector for bolometric interferometry," in *Proc. SPIE*, vol. 5498, 2004.

Session 4:

Systems I

Monday May 2, 14:00-15:40
Chairman: Heribert Eisele

Terahertz Applications Beyond Space Science

Peter H. Siegel, Caltech/JPL

Abstract:

After more than 30 years of focused applications in the space sciences area, Terahertz Technology is experiencing a true Renaissance. While major strides continue to be made in submillimeter wave astronomy and spectroscopy, the past few years have seen an unprecedented expansion of terahertz applications, components and instruments targeted *outside* of the space sciences. Broad popular interest in this unique frequency domain has emerged for the first time[1], spanning applications as diverse as biohazard detection and tumor recognition. Already there are groups around the world who have applied specialized Terahertz techniques to disease diagnostics[2], recognition of protein structural states[3], monitoring of receptor binding[4], performing label-free DNA sequencing[5] and visualizing contrast in otherwise uniform tissue[6]. A commercial terahertz imaging system has recently started tests in a hospital environment and new high sensitivity imagers with much deeper penetration into tissue have begun to emerge[7]. Solicitations for more sophisticated instruments and enabling terahertz components have filtered into US agency proposal calls from DoD and NASA, to NSF and NIH, and many new research groups have sprung up, both in the US and in Europe and Asia. This talk will broadly survey terahertz applications that may be less familiar, but equally interesting to a space scientist, with the hope of stimulating some crossover into Earth-based life sciences.

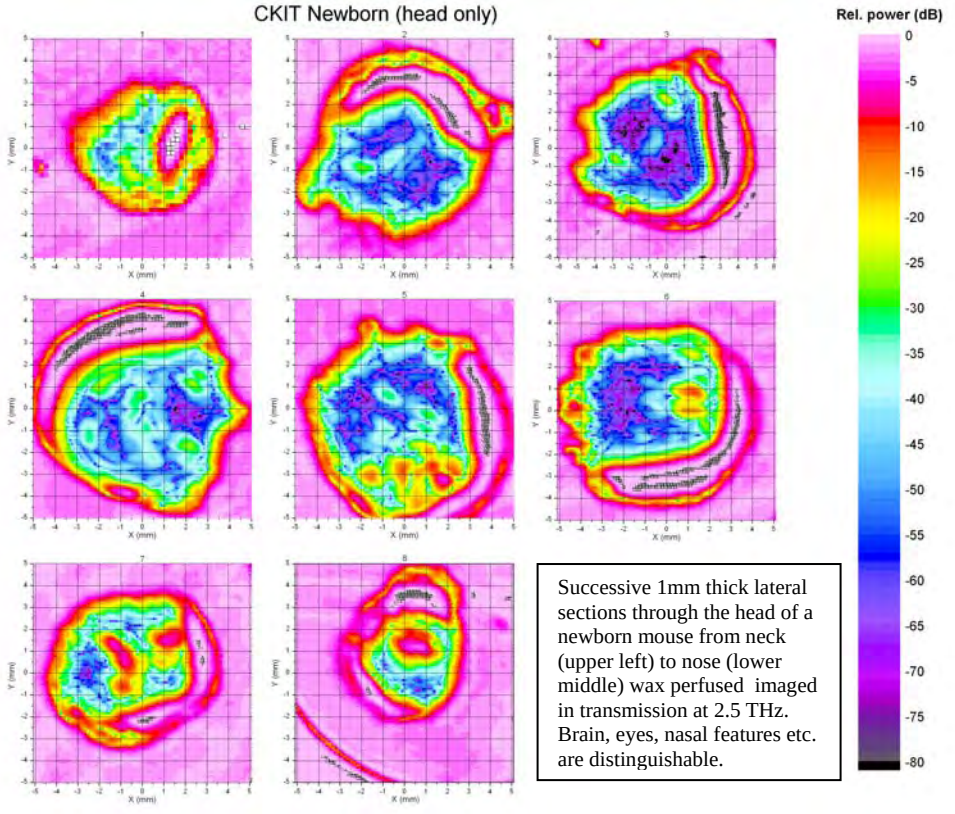

Successive 1mm thick lateral sections through the head of a newborn mouse from neck (upper left) to nose (lower middle) wax perfused imaged in transmission at 2.5 THz. Brain, eyes, nasal features etc. are distinguishable.

[1] P.H. Siegel, "Terahertz Technology in Biology and Medicine," IEEE Trans. MTT, vol. 52, no. 10, Oct. 2004, pp. 2438-2448.
[2] R.M. Woodward, V.P. Wallace, R.J. Pye, B.E. Cole, D.D. Arnone, E.H. Linfield and M. Pepper, "Terahertz Pulse Imaging of ex vivo Basal Cell Carcinoma," J. of Inv. Dermatology, vol. 120, no. 1, Jan. 2003, pp. 72-78.
[3] A. Markelz, S. Whitmore, J. Hillebrecht and R. Birge, "THz time domain spectroscopy of bimolecular conformational modes," Physics in Medicine and Biology, vol. 47, no. 21, 7 Nov. 2002, pp.3797-3805.
[4] S.P. Mickan, A. Menikhu, H. Liu, C.A. Mannella, R. MacColl, D. Abbott, J. Munch and X-C Zhang, "Label-free bioaffinity detection using terahertz technology," Physics in Medicine and Biology, vol. 47, no. 21, 7 Nov. 2002, pp.3789-3795.
[5] P. Haring Bolivar, M. Brucherseifer, M. Nagel, H. Kurz, A. Bosserhoff and R. Buttner, "Label-free probing of genes by time domain terahertz sensing," Physics in Medicine and Biology, vol. 47, no. 21, 7 Nov. 2002, pp.3815-3821.
[6] K.J. Seibert, T. Loffler, H. Quast, M. Thomson, T. Bauer, R. Leonhardt, S. Czasch and H.G. Roskos, "All-optoelectronic continuous wave THz imaging for biomedical applications," Physics in Medicine and Biology, vol. 47, no. 21, 7 Nov. 2002, pp.3743-3748.
[7] P.H. Siegel and R.J. Dengler, "Terahertz Heterodyne Imager for Biomedical Applications," SPIE Conf. on THz and GHz Electronics and Photonics III, vol. 5354, San Jose, CA, Jan 25-26, 2004.

GEO Atmospheric Sounder Technology Project

A. Emrich, Omnisys Instruments AB, Gruvgatan 8, 421 30 Göteborg, Sweden

ABSTRACT

Microwave and (sub) millimetre wave atmospheric sounders provide information on the distribution of radiation emitted by the atmosphere from which vertical profiles of temperature and humidity through the atmosphere may be obtained. Current generation of sounders are embarked on-board low Earth orbit (LEO) satellites for providing primarily meteorological data for numerical weather forecasting, and on the second level global observations for climate monitoring. Geostationary observations, unlike those from LEO satellites, have the key potential advantage to provide continuous coverage of the same region, which is essential for now casting.

A preliminary review of potential Geostationary Earth Orbit (GEO) missions, based of geophysical parameters, gave consideration to three main application areas for GEO sounding: numerical weather prediction (NTASK), climatology and now casting. In contrast to LEO microwave sounders in operation today, the proposed straw man GEO instrument uses many more channels that range in frequency from 89 GHz through to 874 GHz. Due to the large aperture size required to achieve a reasonable horizontal resolution, its use has so far been restricted to the case of Low Earth Orbit (LEO) satellites.

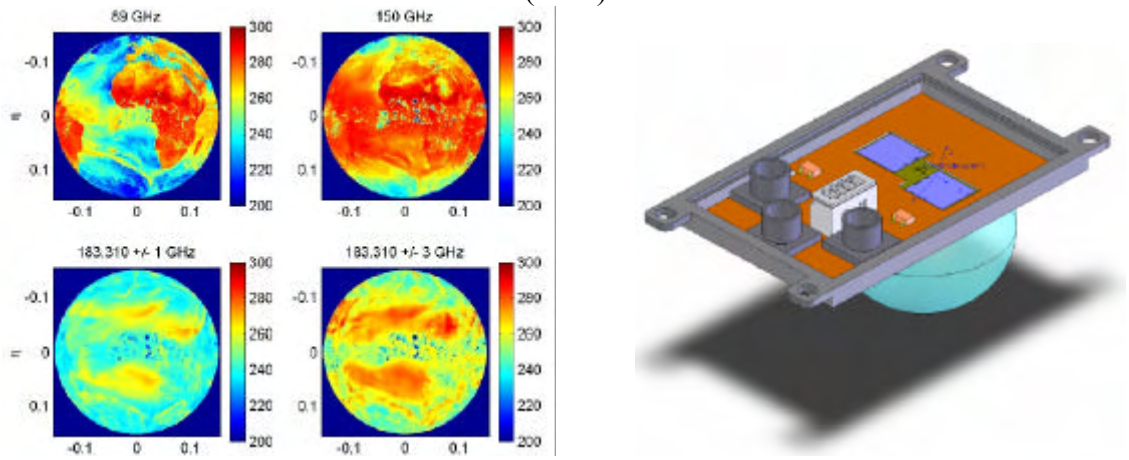

The earth seen in different frequency bands, and one receiver element for the 53 GHz band.

The overall objective of this activity is to develop and demonstrate enabling instrument concepts to achieve accurate observation at significant spatial resolution with microwave and (sub)millimetre wave sensors from Geosynchronous Earth Orbit (GEO). This will entail the development and demonstration of the required innovative technologies as part of a demonstrator.

Omnisys has lead an ESA study to select candidate breakthrough concepts to meet the requirements. The selected concept will be demonstrated and bread boarding of the critical technologies be performed during the second part of the study. The overall instrument concept will be presented as well as key technology development areas. In terms of performance, the specification is: 30 km resolution (400x400 map), covering the bands 53, 90, 119, 160, 183, 340, 380 GHz, and an update rate of 30 minutes. This will be accomplished with an instrument in the 200 kg / 300 W class, using 500+ (sub)millimeter receivers mounted on booms. The deployed booms stretch over an 8 meter diameter.

Femtosecond laser installation for terahertz pulse generation, detection and applications

R.A.Akhmedzhanov, A.I.Korytin, A.M.Sergeev and E.V.Suvorov
Institute of Applied Physics, Russian Academy of Sciences
Ulyanov str. 46, 603950 Nizhny Novgorod, Russia
e-mail: suvo@appl.sci-nnov.ru

Standard scheme of using femtosecond optical radiation for terahertz pulse generation and detection has been realized in the Institute of Applied Physics of Russian Academy of Sciences. Terahertz pulses are generated by nonlinear rectification of powerful optical radiation by crystal ZnTe plate and the waveform of THz pulses is registered by electrooptical sampling technique at similar ZnTe crystal; pulse repetition rate is 1 kHz. The main part of THz pulse energy is concentrated in a single field oscillation with characteristic temporal scale about 1 ps, the bandwidth of the pulse is comparable with its central frequency (~ 1 THz). According to estimates electric field intensity at the receiver crystal is about 20 kV/cm^2 and the peak power of THz pulse is about 3 kW (generation efficiency about 10^{-6}). Typical signal-to-noise ratio in the waveform measuring is 10^3.

First demonstration results are presented for measurements of absorption spectra for number of gases, solvents, protein solutions and medicine powders. Experimental scheme for Cherenkov generation of THz pulses from a laser spark produced by an axicon lens has been proposed and designed.

Dual frequency 230/690 GHz interferometry at the Submillimeter Array

Todd R. Hunter, John W. Barrett, Raymond Blundell, Robert D. Christensen, Robert S. Kimberk, Steve Leiker, Daniel P. Marrone, Scott N. Paine, D. Cosmo Papa, Nimesh Patel, Patricia Riddle, Michael J. Smith, T.K. Sridharan, C.-Y. Edward Tong, Ken H. Young and Jun-Hui Zhao
Harvard-Smithsonian Center for Astrophysics
60 Garden Street
Cambridge, MA 02138 USA
Email: thunter@cfa.harvard.edu

***Abstract*— The Submillimeter Array (SMA), a collaboration between the Smithsonian Astrophysical Observatory and the Academica Sinica Institute for Astronomy and Astrophysics of Taiwan, is an eight-element radio-interferometer designed to operate throughout the major atmospheric windows from about 180 to 900 GHz. In an effort to mitigate the effects of atmospheric instabilities which limit the phase coherence of the array especially in the higher frequency bands, the array was designed to allow simultaneous operation of a low frequency receiver (< 350 GHz) with a high frequency receiver (> 330 GHz). The overlap region of 330-350 GHz was included to facilitate dual polarization measurements in the frequency range considered to offer the highest sensitivity for continuum observations with the array.**

So far, the array is equipped with working SIS receivers covering the frequency ranges 176-250 GHz, 260-355 GHz, and 600-700 GHz, and single frequency operation has been routine in the lower two frequency bands for the past year. More recently, with the completion of IF hardware required to make full use of the SMA cross-correlator, dual receiver operation became possible. We have since made a number of Galactic and extra-galactic astronomical observations in dual-band mode with the hopes of using the 230 GHz receiver as a phase reference to enable improved interferometry in the 650 GHz band. We will present the current antenna and receiver performance, some of the first interferometric images in the 650 GHz receiver band, and our initial attempts at phase referencing.

I. Introduction

The Submillimeter Array (SMA), a collaboration between the Smithsonian Astrophysical Observatory and the Academica Sinica Institute for Astronomy and Astrophysics, is an eight-element, heterodyne radio-interferometer designed to operate throughout the major atmospheric windows from about 180 to 900 GHz. It is the first and only imaging interferometer to operate in the submillimeter band. The general design and operation of the SMA has been described previously [1]. Located near the 4200-meter summit of Mauna Kea, Hawaii, the array was dedicated in November 2003 and initial science results were collected in a 2004 special issue of *The Astrophysical Journal* [2]. The first SMA results at 690 GHz were published in 2004 based on observations of the carbon star IRC+10216 obtained with only three antennas [3]. Since that time, the second IF path of the SMA has been built and commissioned and improvements to the 690 GHz receivers and local oscillator (LO) control hardware have enabled fully-remote, dual-frequency operation for the first time. With this capability, the prospects for "phase referenced calibration" (i.e. scaling the measured atmospheric phase from a low frequency band to a high frequency band) can now be evaluated. This paper summarizes the present system and presents the first results obtained during a special observing campaign during January-February 2005.

TABLE I
Antenna performance as measured by holographic surface RMS (left column), and by aperture efficiency scans on celestial objects (right columns).

Antenna Number	RMS surface (μm)	Aperture efficiency (%) 230 (GHz)	345 GHz
1	15	77	68
2	14	74	67
3	15	75	61
4	18	73	64
5	20	75	60
6	22	74	60

II. System Details

A. Antenna performance

The SMA 6-meter antennas are composed of 72 machined aluminum reflector panels with 4 adjusting screws per panel. The surface is accurately measured (to 8 μm RMS) via near-field holography and the required screw adjustments to correct the surface are computed [4]. In preparation for 650 GHz work, all antennas were adjusted in this manner to improve the surface accuracy. As of February 2005, all antennas were better than 22 μm RMS with the best antenna being 14 μm RMS (see Table Table I). Confirmation of the antenna surface accuracy, especially at elevations different from the beacon (i.e. > 20 deg), has been obtained via aperture efficiency measurements on celestial objects (planets).

B. Optical alignment

In order to use two receivers simultaneously, the mixer feedhorns must be aligned on the sky to within a fraction of the primary beamsize of the low frequency receiver ($55''$

TABLE II
FEED OFFSET TERMS MEASURED ON THE SMA ANTENNAS.

Antenna Number	345 Rx vs 230 Rx A_1 ($''$)	345 Rx vs 230 Rx A_2 ($''$)	690 Rx vs 230 Rx A_1 ($''$)	690 Rx vs 230 Rx A_2 ($''$)
1	−0.2	+6.1	−2.7	+7.0
2	+4.3	+2.1	−0.85	+1.6
3	−0.7	−1.1	+4.1	−0.8
4	−5.3	+4.9	−2.2	+3.6
5	−3.9	−1.3	+4.8	−3.4
6	−0.1	+4.6	+4.4	+3.4

at 230 GHz, or $36''$ and 345 GHz). Alignment of the receiver feeds is done using near-field vector beam measurements in the laboratory [5]. This method produces beams aligned to within $5''$ on the sky, as demonstrated by pointing calibration performed in single-dish mode on each SMA antenna. Table II lists the feed offset terms measured on each of the six SMA antennas used during the recent 650 GHz campaign. The feed offsets are modelled by two parameters: the radial misalignment r in arcseconds, and the phase angle ϕ of this misalignment in degrees. These parameters are combined into two terms: $A_1 = rcos(\phi)$ and $A_2 = rsin(\phi)$, which translate into azimuth and elevation offsets: azoff = A_1sin(Elev) + A_2cos(Elev), eloff = A_1cos(Elev) - A_2sin(Elev). The repeatability of the feed offset measurements is $1-2''$. During dual-frequency observations, the antennas are pointed such that the high frequency receiver is aimed at the target. The largest resulting pointing error for the 230 GHz feed ($7''$) corresponds to less than 5% loss due to primary beam attenuation. At 345 GHz, the largest pointing error ($6''$) corresponds to less than 8% loss.

C. Mixer performance

In all three bands, the SMA receivers contain double-sideband mixers fabricated with niobium SIS junctions (cooled to 4.2 K) followed by low-noise HEMT amplifiers. The pumped I/V characteristics of these junctions in the field are shown in Figure 1. The IF of our receivers is 4-6 GHz, and the downconverter electronics and correlator can process the full 2 GHz of bandwidth in each sideband. The mixer performance in the IF passband was measured in each of the antennas via the Y-factor method. The passband response was recorded on a spectrum analyzer, first toward an ambient temperature load, and second toward a liquid nitrogen temperature load. A representative plot is shown in Figure 2. The typical receiver temperature (averaged across the IF band) was 300-400 K, or about ten times the quantum limit. In good dry weather conditions on Mauna Kea ($\tau_{225\mathrm{GHz}} < 0.05$), this level of performance results in system temperatures as low as 900-1200 K near zenith. As an example, Figure 3 shows a plot of the 684 GHz system temperatures and the 225 GHz zenith opacity vs. time during the nighttime observations of February 16, 2005.

D. Motorized LOs

The automation of the low-frequency (230 and 345 GHz) LO chains has been described previously [6]. The 690 GHz LO

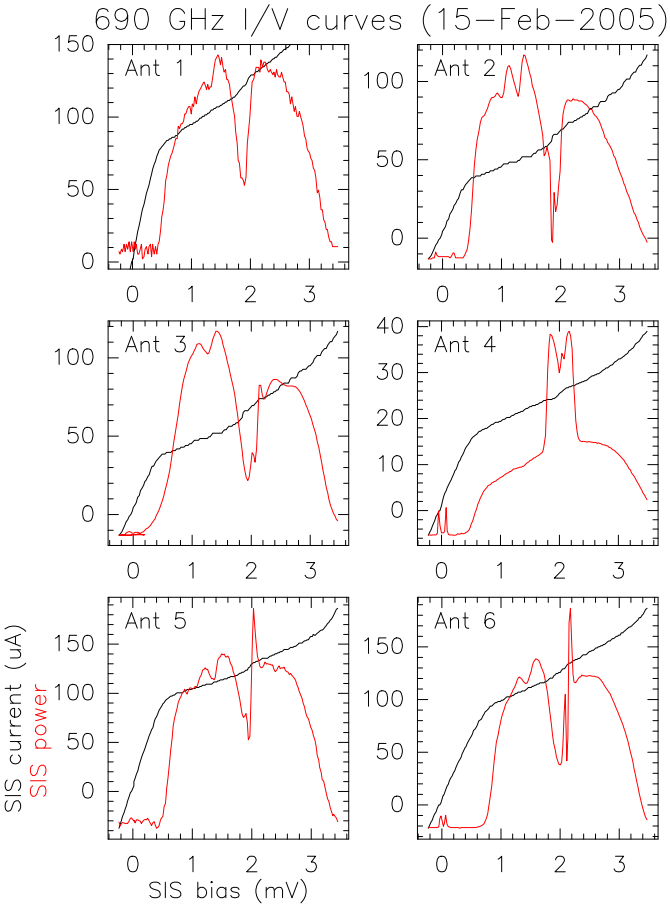

Fig. 1. SIS mixer current vs. bias voltage (black line) and SIS mixer power vs. bias voltage (red line) characteristics of the 650 GHz receivers on the SMA as measured remotely in the field. The SIS power is plotted in arbitrary units.

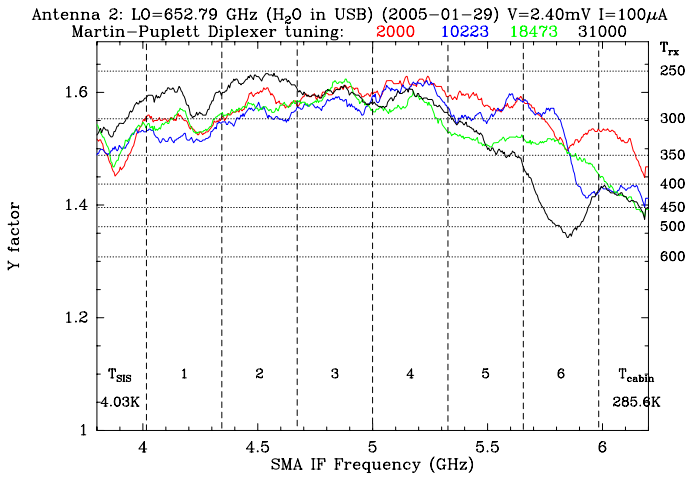

Fig. 2. Receiver temperature as a function of the IF passband (x-axis) and the Martin-Puplett diplexer tuning positions (colored lines) as measured with an HP8563 spectrum analyzer in the field in one of the SMA antennas. The data were obtained using the traditional y-factor method by taking the ratio of two traces: one observing an ambient temperature load and one observing a liquid nitrogen temperature load.

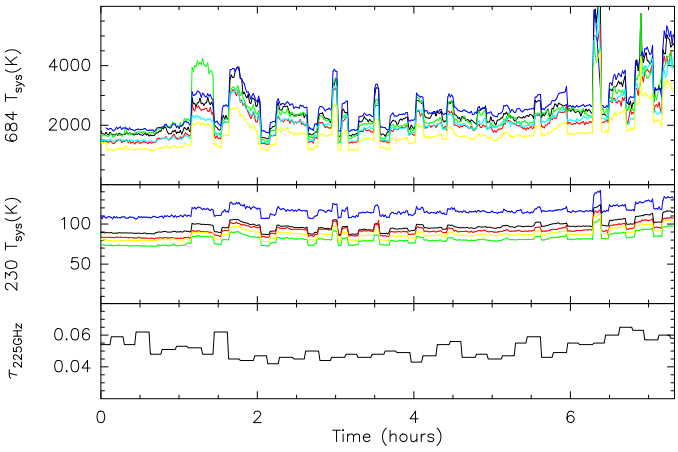

Fig. 3. System temperatures on each of the six antennas at 684 GHz (top panel) and 230 GHz (middle panel) during the night of Feburary 16, 2005. The maximum elevation of the target source (Sgr A*) was only 42 degrees above the horizon (i.e. 1.5 airmasses). For reference, the zenith opacity at 225 GHz as measured by the tipping radiometer at the Caltech Submillimeter Observatory is also plotted (lower panel).

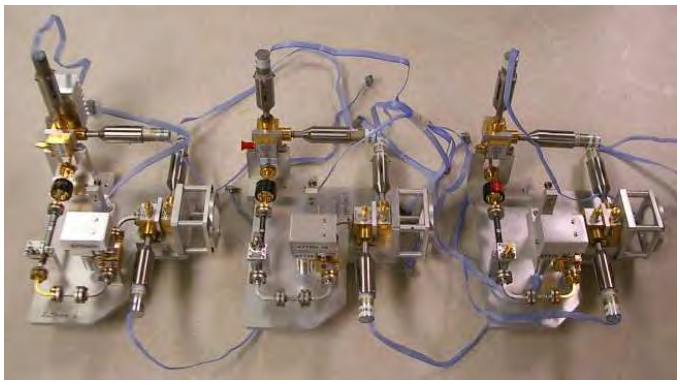

Fig. 4. Three of the six motorized 600-700 GHz LO chains installed on the SMA. At the top is the Gunn oscillator with two linear actuators at right angles to one another. Next is a waveguide isolator followed by a coupler to the PLL harmonic mixer. The vane attenuator is driven by a rotary motor via a gear assembly. The following doubler and tripler stages each have one linear actuator. The LO radiation exits through the lens at the right. Not shown is the Martin-Puplett diplexer which combines the LO and the signal ahead of the cryostat vacuum window.

chains have now been automated in a similar fashion. Each LO chain consists of six motorized components including a Gunn oscillator (2 motors), a vane attenuator (1 motor), a doubler (1 motor), a tripler (1 motor) and Martin-Puplett diplexer (1 motor). A photo three of the LO chains is shown in Figure 4.

E. Dual IF operation

One of the major challenges facing millimeter and submillimeter interferometers is fluctuations in atmospheric path length caused by water vapor [7]. Such path length changes result in phase changes which ultimately limit the angular resolution and sensitivity of the instrument. The standard technique of phase referencing at the observed frequency can remove slow drifts in atmospheric and instrumental phase (on timescales of minutes). However, as one observes at higher frequencies, the phase drifts increase in magnitude, the typical system sensitivities degrade, and the number of calibrators becomes sparse. All of these factors tend to limit the effectiveness of the standard phase referencing technique. The SMA telescope offers the benefit of two independent IF paths (via fiber optics) from the antennas to the correlator which allows simultaneous observations at two widely separated frequencies, or (eventually) dual-polarization observations in the 330-350 GHz range. Observations at different frequencies enable the possibility of simultaneous phase referencing from low frequency where the system sensitivity and stability are the best to high frequency where the tropospheric phase fluctuations are the largest. Recently, this concept has been applied successfully in astronomical very long baseline interferometry (VLBI) experiments by using non-simultaneous, but rapidly time-interleaved observations at 15, 43 and 86 GHz [8]. This interleaving concept has also been considered for use in the Atacama Large Millimeter Array (ALMA) in the future [9]. However, the major drawback of interleaved observations is the frequent receiver retuning which requires some finite amount of time during which the instrumental and atmospheric phases may change significantly. By design, the unique capability of the SMA of **simultaneous** observations at two frequencies offers the best chance at proving the utility of phase referencing in the submillimeter regime.

III. Observations and Results

A. Conditions and targets

A block of SMA time from January 25 to February 20, 2005 was dedicated to dual-frequency commissioning and observations. The first dual-frequency fringes with five antennas (ten baselines) were recorded on January 28 on the astronomical maser source W Hydra. The SiO J=5-4, $v = 1$ maser was observed at 215.596 GHz, and the H_2O $v_2 = 1, 1_{1,0} - 1_{0,1}$ maser was observed at 658.007 GHz. After this initial success, the sixth antenna became operational and the weather conditions became favorable for extensive observations of other astronomical targets from February 14 to 20. The array was configured in the "compact" formation which provides a synthesized beamwidth of 1.1 by 1.2 arcsecond (for sources of moderate northerly declination). Unprojected baseline lengths ranged from 16 to 69 meters. Observations in the CO J=6-5 transition were acquired of the nearby Classical T Tauri star TW Hydra, the protoplanetary nebula CRL618, the high-mass star-forming region Orion KL, the low-mass star-forming region IRAS 16293-2422 and the ultraluminous infrared galaxy Arp 220. The Galactic Center source Sgr A* was observed in the continuum at 684 GHz. Finally, the massive star-forming region G240.31+0.07 and the evolved star VY Canis Majoris were observed in the $C^{18}O$ J=6-5 transition. In each case, the typical on-source integration times were three hours. Detailed results from these observations will be presented elsewhere. As an example of the data quality, an image of the Galactic Center point source Sgr A* is shown in Figure 5. This image was produced via standard phase referencing at 684 GHz between

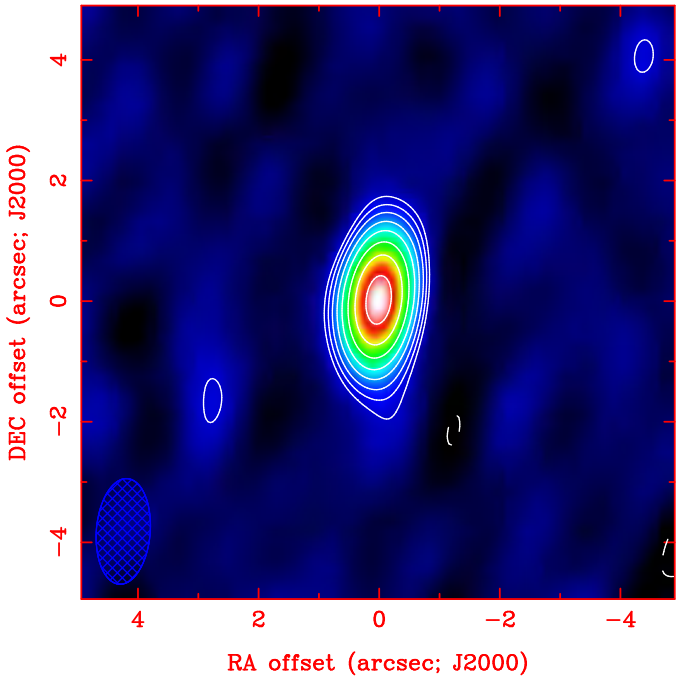

Fig. 5. Contour plot of the Galactic Center radio source Sgr A* observed in 684 GHz continuum emission. Levels are -5, -3.5, 3.5, 5, 7, 10, 14, 20, 28, and 40σ, with $\sigma = 0.06$ Jy and peak flux density of 2.7 Jy. One Jy is $10^{-26}\mathrm{Wm}^{-2}\mathrm{Hz}^{-1}$. Total integration time is about 3 hours. The synthesized beamwidth of the interferometer is shown in the lower left corner. The offsets are relative to the J2000 source position of 17:45:40.0409, −29:00:28.118.

the target and strong calibrators (in this case, Ganymede and Ceres, which were 68° and 41° distant, respectively), followed by phase-only self-calibration on the target itself.

B. Comparison of 230/690 GHz phase

Ultimately we are interested in whether the phase variations at $\nu_1 = 230$ GHz due to fluctuations in the water vapor column above the antennas can be used to calibrate the proportionally larger phase variations that these fluctuations cause at $\nu_2 = 690$ GHz. To first order, the expected scaling of the phase variations equals the ratio of the frequencies (i.e., the non-dispersive case). This is because the effect of introducing a small amount of water vapor above one antenna is to add a (nearly) frequency independent amount of excess propagation path L, which corresponds to a phase delay of L/λ radians where $\lambda = c/\nu$. So the ratio of phases in the two bands is $(L_1/\lambda_1)/(L_2/\lambda_2)$. If $L_1 \approx L_2$, then the ratio becomes $\lambda_2/\lambda_1 = \nu_1/\nu_2$. In fact, the actual value of L is a function of frequency, although it only varies significantly near strong atmospheric water lines [10], [11]. However, because the 650 GHz window sits between two major water lines, the variations are significant and one should not cancel L_1/L_2 in the above formula. So the actual phase ratio we expect is $(L_1/L_2)*(\lambda_2/\lambda_1)$. Figure 6 shows the theoretical ratio L_1/L_2 computed for observations in the 650 GHz band from the

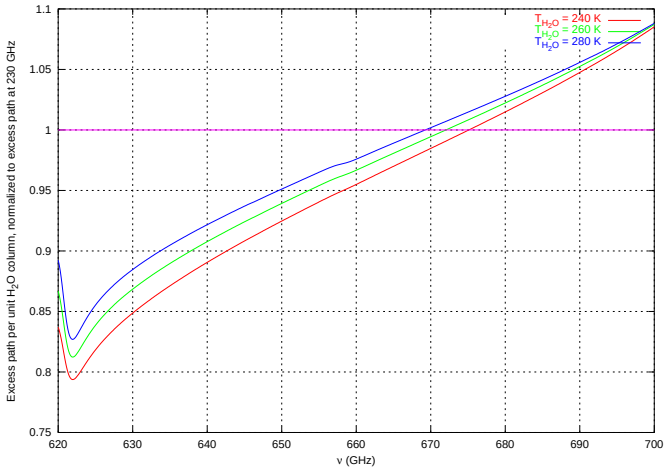

Fig. 6. Calculation of the theoretical excess path per unit water vapor column in the 620-700 GHz observing window, normalized to the excess path at 230 GHz. The three curves correspond to different water vapor temperatures in the model. The largest deviation from unity ratio occurs near water vapor lines, such as the $5_{3,2} - 4_{4,1}$ transition at 620.701 GHz.

summit of Mauna Kea[1]. The L_1/L_2 factor varies by about 15-20% across the tuning range of the SMA LOs (620-700 GHz), so it is not negligible.

The 230/690 SMA observations recorded on January 28, 2005 have been analyzed to search for correlations of phase between the two frequency bands. Figure 7 shows a time series comparison of the 215 GHz phase averaged across the central six spectral channels of the SiO maser line with the 658 GHz phase averaged across the central 21 spectral channels of the H_2O maser line. The baseline-based phase measurements were converted to antenna-based phases using the selfcal function of Miriad [13]. The gains were derived independently for each receiver band, using antenna 6 as the reference antenna, and are shown in Figure 8. The gains are plotted against each other in Figure 9 using the smavarplt function of Miriad, and the resulting linear regression results are listed in Table III. In summary, good correlations are seen on antennas 1, 2 and 3, with antenna 1 exhibiting a slope closest to the expected theoretical ratio (based on the model in Figure 6). Antenna 4 exhibited anomalous relative phases between the two frequency bands on many nights of the observing campaign, and clearly had some instrumental problem. Nevertheless, the fact that much of the phase data are well-correlated between the two bands is a promising sign for future phase referencing at the SMA. A similar analysis has been done with the lower-sideband continuum data on the minor planet Ceres ($diameter\ 0.5''$) observed for 3.5 hours on February 18, 2005 (see Figure 10). The linear regression results are also listed in Table III. Figure 11 shows a comparison of images of Ceres which demonstrates that phase transfer can be done successfully between the two receiver bands. The image in the left panel results from running selfcal on the 690 GHz data, and the signal-to-noise ratio is 267. The

[1]Based on calculations performed with the *am* atmospheric model [12], available at http://cfarx6.cfa.harvard.edu/am

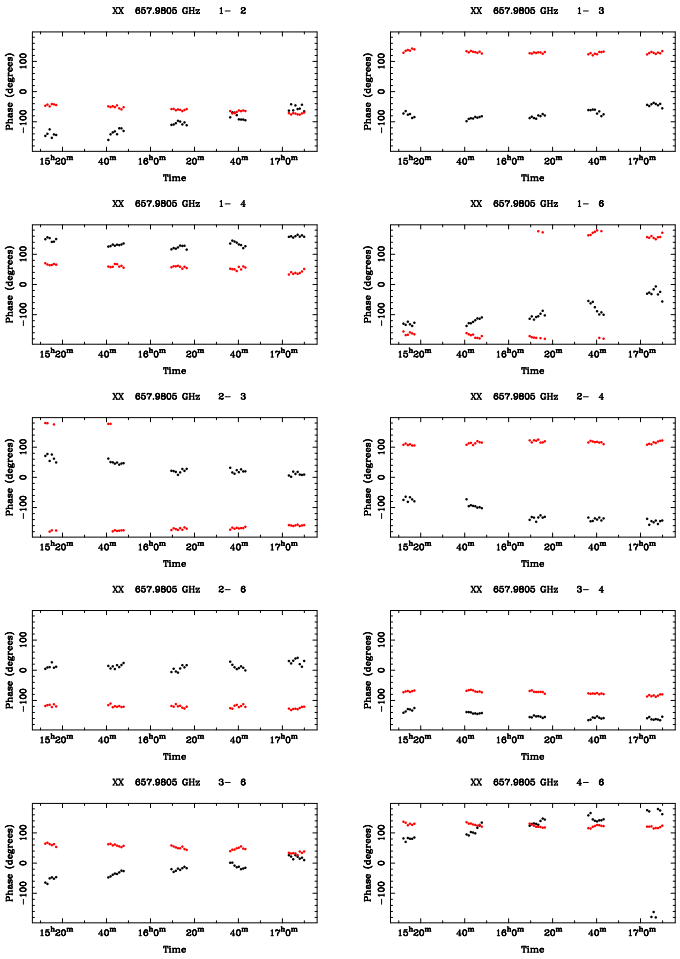

Fig. 7. Time series comparison of the spectral line maser phases of the evolved star W Hydra in the 215 GHz SiO maser (red dots) and the 658 GHz H_2O maser (black dots). The ten panels correspond to the ten different SMA baselines, as observed with five antennas on January 28, 2005.

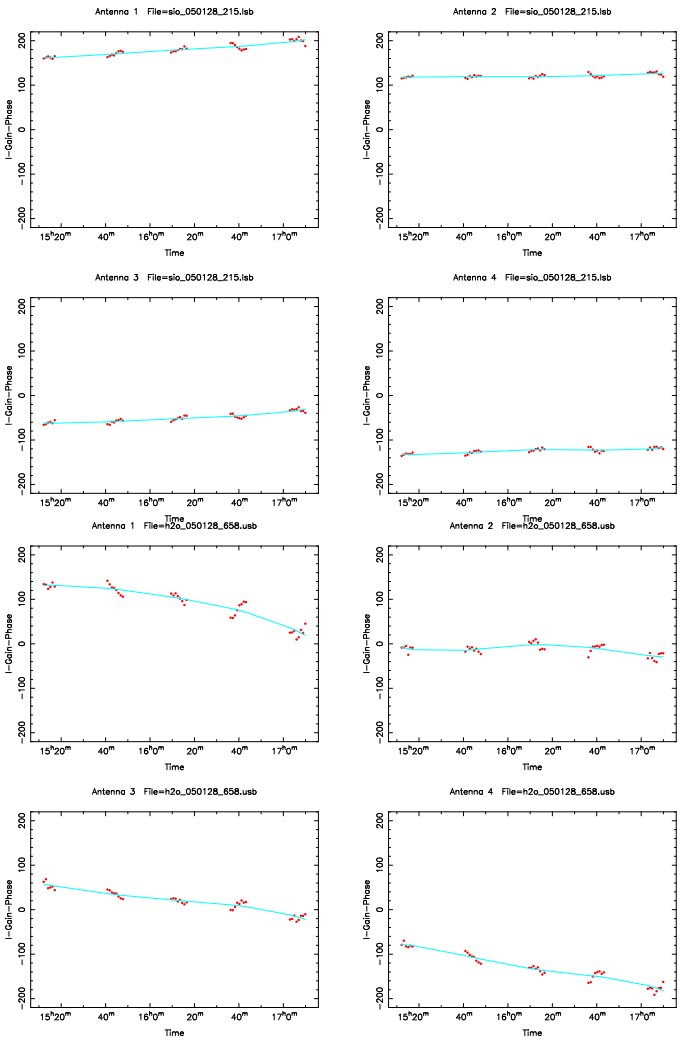

Fig. 8. Point-source antenna-based phase solutions for the SiO 215 GHz maser data (upper four panels) and the H_2O 658 GHz maser data (lower four panels) for W Hydra as observed on January 28, 2005. The reference antenna was antenna 6 whose phase was defined to be zero at all times (not shown). The phase data are plotted against each other in Figure 9.

image in the right panel results from running selfcal on the 230 GHz data, scaling the solutions to 690 GHz, and applying the scaled solutions to the 690 GHz raw data. In this case, the signal-to-noise ratio is 193.

IV. Conclusions

The SMA has successfully observed celestial sources in two frequency bands simultaneously (230 and 690 GHz). The first astronomical images with one arcsecond angular resolution in the 690 GHz band have been acquired. Initial observations of sources with strong maser lines in both bands demonstrate good correlation between the phases in the two widely-separated frequency bands, at least on most of the antennas. Although a number of instrumental issues with the SMA remain to be explored and improved, this initial result bodes well for future attempts at phase referencing the interferometer calibration from low frequencies to high frequencies in the submillimeter band (and perhaps the terahertz band), and thereby improving the ultimate sensitivity of traditional heterodyne interferometers at high frequencies.

TABLE III

Linear regression analysis of the 690 GHz band phase vs the 230 GHz band phase observed on W Hydra and Ceres

Source	Antenna	Sideband	Correlation	Slope
W Hydra (28Jan2005)	1	USB	0.97	−2.77
	2		0.76	−2.04
	3		0.96	−2.17
	4		0.86	−5.03
	theory		1.00	−2.90
Ceres (18Feb2005)	1	USB	0.97	2.81
	2		0.88	2.13
	3		0.95	2.08
	4		0.90	2.22
	5		0.97	3.14
	theory		1.00	3.15
Ceres (18Feb2005)	1	LSB	0.98	3.11
	2		0.86	2.22
	3		0.92	2.19
	4		0.79	2.37
	5		0.96	3.36
	theory		1.00	3.16

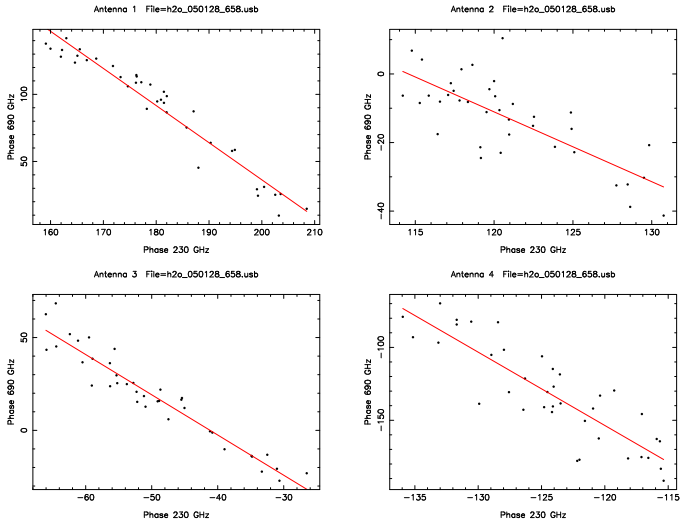

Fig. 9. Plot of the 658 GHz phase vs 215 GHz phase data from Figure 8 with linear regression fits overlaid. The negative slope results from the fact that the lower sideband SMA data are written with an opposite sign convention to the upper sideband SMA data. On antenna 1, the magnitude of the slope is close to the expected theoretical value of -2.90, as seen in Table III.

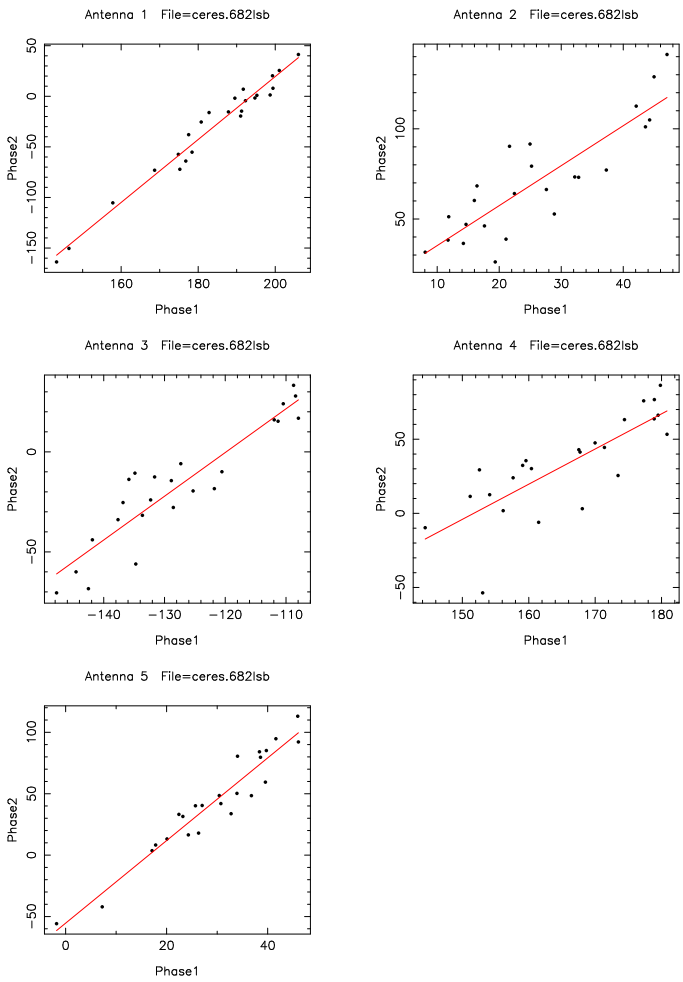

Fig. 10. Plot of the 682 GHz vs 221 GHz antenna-based continuum phase solutions of Ceres with linear regression fits overlaid. On antennas 1 and 5, the magnitude of the slope is close to the expected theoretical value of 3.15, as seen in Table III.

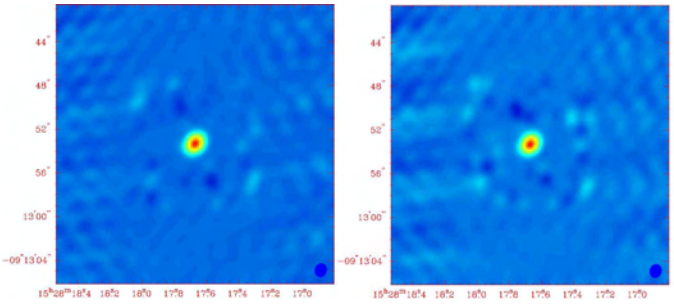

Fig. 11. Left image: the image resulting from a standard selfcal solution computed from the raw 690 GHz data of Ceres and applied to the same data. Peak = 3.53 Jy, rms=13 mJy, SNR=267. Right image: the result of taking the standard selfcal solution at 230 GHz, scaling it to 690 GHz via the slope and offset (Table III), and applying it the 690 GHz raw data. Peak = 3.34 Jy, rms=17 mJy, SNR=193. The degree to which the images are similar verifies the promise of this technique.

ACKNOWLEDGMENT

The authors would like to thank Irwin Shapiro for supporting the development of the SMA from its inception.

REFERENCES

[1] R. Blundell, "The Submillimeter Array – Antennas and Receivers," in *Fifteenth International Symposium on Space Terahertz Techonology*, 2004.

[2] P. T. P. Ho, J. M. Moran, and K. Y. Lo, "The Submillimeter Array," *The Astrophysical Journal Letters*, vol. 616, p. 1, 11 2004.

[3] K. H. Young, T. R. Hunter, D. J. Wilner, M. A. Gurwell, J. W. Barrett, R. Blundell, R. Christensen, N. Hirano, P. T. P. Ho, S. Y. Liu, K. Y. Lo, R. Martin, S. Matsushita, J. M. Moran, N. Ohashi, D. C. Papa, N. Patel, F. Patt, A. Peck, C. Qi, M. Saito, A. E. Schinckel, H. Shinnaga, T. Sridharan, S. Takakuwa, C. E. Tong, and D. Trung, "Submillimeter Array Observations of CS J = 14-13 Emission from the Evolved Star IRC+10216," *The Astrophysical Journal Letters*, vol. 616, pp. L51–L54, 11 2004.

[4] S. T. K., M. Saito, N. A. Patel, and R. D. Christensen, "Holographic surface setting of the Sub-millimeter Array antennas," in *Proceedings of the SPIE: Ground-based Instrumentation for Astronomy*, vol. 5495, 2004, pp. 441–446.

[5] C.-Y. Tong, D. V. Meledin, D. P. Marrone, S. N. Paine, H. Gibson, and R. Blundell, "Near-field vector beam measurements at 1 THz," *IEEE Microwave and Wireless Components Letters*, vol. 13, pp. 235–237, 2003.

[6] T. R. Hunter, R. W. Wilson, R. Kimberk, P. S. Leiker, and R. Christensen, "Receiver control for the Submillimeter Array," in *Proceedings of the SPIE: Advanced Telescope and Instrumentation Control Software II*, vol. 4848, 12 2002, pp. 206–217.

[7] O. P. Lay, "Phase calibration and water vapor radiometry for millimeter-wave arrays," *Astronomy and Astrophysics Supplement*, vol. 122, pp. 547–557, May 1997.

[8] E. Middelberg, A. L. Roy, R. C. Walker, and H. Falcke, "VLBI observations of weak sources using fast frequency switching," *Astronomy and Astrophysics*, vol. 433, pp. 897–909, 4 2005.

[9] M. A. Holdaway and L. D'Addario, "Simulation of Atmospheric Phase Correction Combined with Instrumental Phase Calibration," NRAO LAMA Memo Series, Tech. Rep. 803, 2003.

[10] A. Thompson, J. M. Moran, and G. W. Swenson, *Interferometry and Synthesis in Radio Astronomy*. Krieger Publishing Company, 1991.

[11] M. A. Holdaway and J. R. Pardo, "Atmospheric Dispersion and Fast Switching Phase Calibration," NRAO ALMA Memo Series, Tech. Rep. 404, 2001.

[12] S. N. Paine, "The *am* Atmospheric Model," Submillimeter Array Project, Tech. Rep. 152, 2004, http://sma-www.cfa.harvard.edu/private/memos/152-03.pdf.

[13] R. J. Sault, P. J. Teuben, and M. C. H. Wright, "A Retrospective View of MIRIAD," in *ASP Conference Series: Astronomical Data Analysis Software and Systems IV*, vol. 77, 1995, pp. 433–436.

Observations in the 1.3 and 1.5 THz Atmospheric Windows with the Receiver Lab Telescope

Daniel P. Marrone, Raymond Blundell, Edward Tong, Scott N. Paine, Denis Loudkov
Harvard-Smithsonian Center for Astrophysics
Email: dmarrone@cfa.harvard.edu

Jonathan H. Kawamura
Jet Propulsion Laboratory, California Institute of Technology

Daniel Lühr, Claudio Barrientos
Universidad de Chile

***Abstract*— The Receiver Lab Telescope (RLT) is a ground-based terahertz telescope; it is currently the only instrument producing astronomical data between 1 and 2 THz. The capabilities of the RLT have been expanding since observations began in late 2002. Initial observations were limited to the 850 GHz and 1.03 THz windows due to the availability of solid state local oscillators. In the last year we have begun observations with new local oscillators for the 1.3 and 1.5 THz atmospheric windows. These oscillators provide access to the $J = 11 \rightarrow 10$ and $J = 13 \rightarrow 12$ lines of ^{12}CO at 1.267 and 1.497 THz, as well as the [N II] line at 1.461 THz. We report on our first measurements of these high CO transitions, which represent the highest-frequency detections ever made from the ground. We also present initial observations of [N II] and discuss the implications of this non-detection for the standard estimates of the strength of this line.**

I. Introduction

Atmospheric absorption prevents astronomical observations from the ground at frequencies between 1 and 10 THz (300-30 μm), with the dominant contributor to the opacity being tropospheric water vapor. However, towards the ends of this frequency interval it is possible to find atmospheric windows at very dry locations. In particular, atmospheric transmission measurements between 1 and 3.5 THz show that a few strong windows open up under extremely dry conditions [1], [2]. An example of the atmospheric transmission at a very dry site under the best conditions is shown in Figure 1.

The Receiver Lab Telescope (RLT) is a ground-based terahertz telescope, located 40 km north of the ALMA site in northern Chile. The site, at an elevation of 5525 meters, shows some of the best terahertz weather in the world, with transmission as high as 50% observed in three supra-terahertz windows in the last year. The RLT is equipped with phonon-cooled HEB waveguide mixers for observations in four atmospheric windows between 800 GHz and 1.6 THz. Within these windows we have access to numerous atomic, molecular, and ionic lines, including seven transitions of ^{12}CO and ^{13}CO, the 809 GHz transition of [C I], and the 1.46 THz transition of [N II]. These bright lines are relevant to many topics in astronomy including star formation, the interstellar medium, and starburst/luminous infrared galaxies. Other, weaker lines that are unique to terahertz astronomy are also extremely interesting, in particular the 1.01 THz transitions of NH^+, an undetected molecular ion in the formation chain of ammonia,

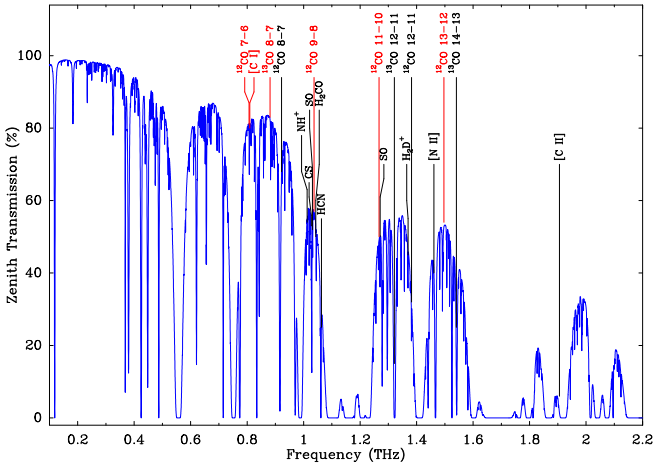

Fig. 1. Atmospheric transmission on Cerro Sairecabur on 24 January 2005 based on data from the Receiver Lab Fourier Transform Spectrometer (FTS) [2]. The FTS measures the sky emission spectrum from 300 GHz to 3.5 THz at 3 GHz resolution; this spectrum is then fit to an atmospheric model, which can be used to examine the transmission at full resolution. The model indicates that at the time of the measurement the precipitable water vapor (PWV) was only 93 μm. Several astronomically interesting lines are plotted for reference, including those detected by the RLT (in red). The few percent transmission at the 1.9 THz frequency of the [C II] line is unusual for this site, but suggests that even drier sites may provide access to this important line from the ground.

and the 1.37 THz ground-state transition of H_2D^+, a tracer of the molecule responsible for chemistry inside cold molecular cores. Astronomical interest in these and other lines has driven the development of several instruments for ground-based terahertz astronomy, as is discussed further in Section IV. Due to the atmospheric limitations at nearly all telescope sites, most of the lines in the RLT bands have not been observed from the ground (excepting, rarely, the 1.037 THz CO $J = 9 \rightarrow 8$ line [3]–[5]), and received little attention from the Kuiper Airborne Observatory (KAO) before it was decommissioned in 1995. Until the launch of Herschel in 2007-2008, or possibly the installation of the first heterodyne instruments on the Stratospheric Observatory For Infrared Astronomy (SOFIA, 2006-2007), these lines will only be observable from ground-based telescopes like the RLT or APEX.

The RLT and its first observations in the 1.03 THz window have been described in previous editions of these proceedings and elsewhere [5]–[8]. Here we discuss the first measurements

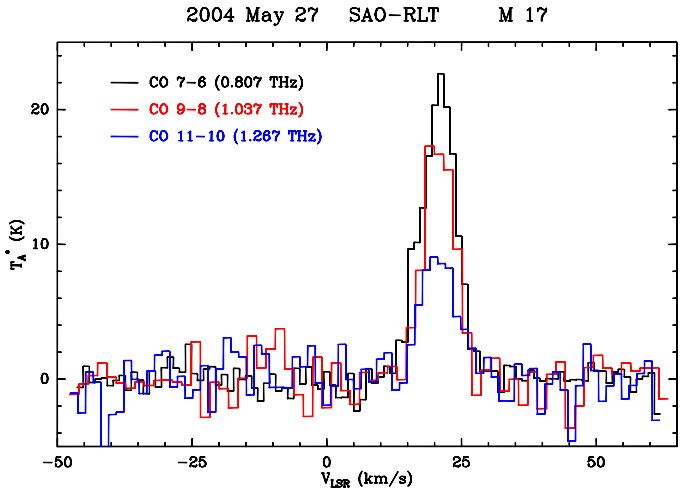

Fig. 2. CO emission detected in M17 from the RLT on 2004 May 27. At the time of this measurement, the ^{12}CO $J = 11 \rightarrow 10$ line was the highest frequency line ever detected from the ground.

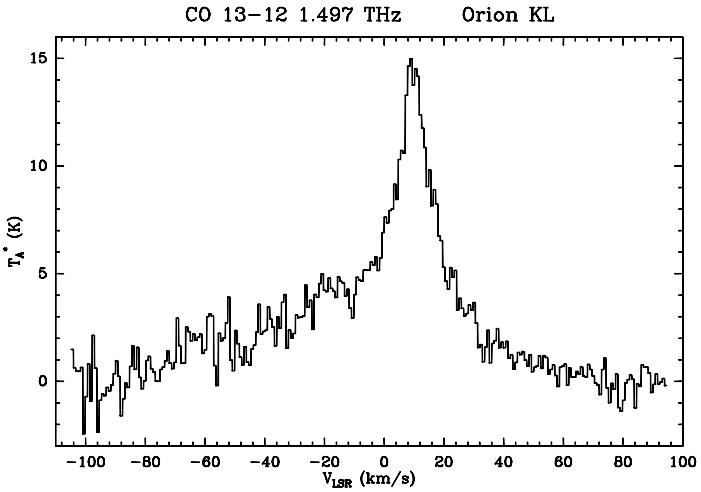

Fig. 3. ^{12}CO $J = 13 \rightarrow 12$ (1.497 THz) emission from Orion-KL, as measured with the RLT on 2004 December 17. The flux scale is somewhat uncertain because the telescope efficiency has not yet been measured at this frequency, but the amplitude matches higher frequency observations made with the KAO. This now stands as the highest frequency line detected from the ground.

made in the 1.3 and 1.5 THz windows, the highest-frequency astronomical detections made from the ground at radio frequencies, along with our first attempt at measuring the [N II] line at 1.46 THz.

II. Observations at 1.3 and 1.5 THz

In its first 18 months of operation the RLT was confined to observations in the 850 GHz and 1.03 THz windows. For much of this time we possessed a local oscillator (LO) source for the 1.3 THz window, but were prevented from using it by the RF bandwidth of the waveguide-coupled hot-electron bolometer mixer installed at the telescope. In May 2004 we installed a mixer with slightly larger RF bandwidth, sacrificing some performance in the low frequency windows to enable operation at 1.3 THz. On May 27 we obtained the first detection of an astronomical line in the 1.3 THz window, ^{12}CO $J = 11 \rightarrow 10$ at 1.267 THz. This line, along with two lower transitions observed in the same source on the same night, is shown in Figure 2. All three lines have the same velocity extent, as is expected for optically thick transitions, while the $J = 11 \rightarrow 10$ emission is weaker than the lower lines suggesting that the gas temperature is not high enough to thermalize the 365 K $J = 11$ rotational state.

Since this first observation, the RLT has routinely observed the CO $J = 11 \rightarrow 10$ line in other sources. The atmospheric conditions on Sairecabur allow regular observations of many high-frequency lines (^{12}CO $J = 7 \rightarrow 6$, $J = 9 \rightarrow 8$, and $J = 11 \rightarrow 10$, ^{13}CO $J = 8 \rightarrow 7$, and [C I]) that are difficult or impossible to detect at other observatories. These lines allow us to characterize the large-scale gas conditions in very warm sources where the lower energy transitions available from other telescopes are insensitive to the temperature.

RLT observations moved to even higher frequency in December 2004 with the arrival of an LO and receiver for 1.5 THz. The LO is on loan from the Jet Propulsion Laboratory and was constructed as a prototype for the HIFI instrument of the Herschel satellite [9]. The receiver was built and tested in the Receiver Lab and some of the testing is described elsewhere in these proceedings [10]. As of this writing, only two marginal nights have been available for observations at 1.5 THz with this receiver. Most of this time was reserved for the [N II] line, but several minutes were spent observing ^{12}CO $J = 13 \rightarrow 12$ at 1.497 THz to confirm that the receiver was functioning properly. A detection of this line in Orion-KL, using only 4 minutes on-source integration time, is shown in Figure 3. This detection represents the highest frequency line measured from the ground and the only line observed in the 1.5 THz atmospheric window.

III. Observations of [N II]

The 1.4611 THz [N II] line is one of the most important targets of ground-based terahertz astronomy. The FIRAS instrument [11] on the COBE satellite, which mapped the entire sky at low-angular and spectral resolution (7° beam, 5.4 GHz maximum spectral resolution), found that the [N II] lines at 1.46 and 2.46 THz (205 and 122 μm) were the brightest lines in the Galaxy after the 1.90 THz (157 μm) line of [C II] [12]–[14]. These two lines can be used together as a density probe for gas up to $\sim 10^3$ cm^{-3}, typical of the diffuse warm ionized medium [15]. The higher-frequency [N II] line has been studied in this galaxy and others at angular resolution comparable to that of the RLT (but much lower velocity-resolution) using the Long-Wavelength Spectrometer on the Infrared Space Observatory satellite [16]. This instrument was not sensitive to the 1.46 THz line and it is therefore poorly studied: there are only two published detections, both from the KAO [17], [18].

Ground-based telescopes at exceptional locations like the South Pole and the Atacama sites have access to this line in the 1.5 THz window, although the transmission is somewhat degraded by a nearby strong O_2 line at 1.4668 THz (at the line

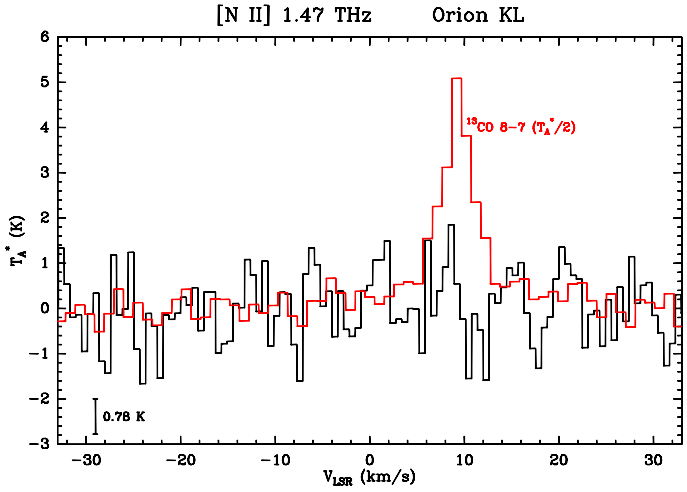

Fig. 4. [N II] in Orion-KL, with ^{13}CO $J = 8 \rightarrow 7$ (0.881 THz) overplotted as a rough velocity reference. The spectral rms is shown in the lower left.

center, $\tau_{O_2} \simeq 130$ for the South Pole and Sairecabur). The effect is worse at lower altitude where pressure-broadening increases the O_2 line width; at the South Pole it contributes an opacity of ~ 0.35 at the [N II] frequency, compared to ~ 0.16 at Sairecabur[1]. With our new 1.5 THz LO the RLT now has access to [N II], and observations of this line are now our key science goal.

As mentioned above, the 1.5 THz receiver arrived at the RLT in December 2004 shortly before the end of the observing year. The two nights available were somewhat below average for observations in this window, with transmission of 11-13% and 15-16%, respectively, at 1.461 THz. Orion-KL was well placed in the sky for our observations and contains an extended region of ionized gas, the edges of which contain strongly excited CO (see Figure 3), so we used this as our main source. We also briefly attempted NGC 2024 IRS5 and G270.3+0.8, using much less integration time and did not detect [N II] emission. The resulting spectrum at the [N II] frequency is shown in Figure 4, with ^{13}CO $J = 8 \rightarrow 7$ overplotted to indicate the velocity extent of another optically thin line in this source (although the CO emission traces slightly different gas). No detection is apparent. The observations of Orion-KL totaled 78 minutes on source and the rms on the spectrum is around 0.8 K, although the telescope efficiency has not been measured at this frequency and could be different from our (conservatively low) assumption. Higher efficiencies would place even more stringent limits on the line strength.

The lack of a detection of this line comes as something of a surprise to us; many groups have proposed ambitious studies of [N II] and it is expected to be quite bright. Of course, because there is little data on its strength on angular scales smaller than the large COBE beam one must make many assumptions to arrive at a predicted strength. The simplest argument (and one that is frequently used) is to take the [C II] line strength measured from the KAO and divide by ten, the average of [C II]/[N II] as observed by COBE [12]. In the case of Orion-KL the velocity-resolved [C II] observations of [20] suggest a brightness temperature of around 5 K, easily measured with our sensitivity. Our non-detection suggests that this common argument is too simplistic. In fact, the average over the whole sky is not representative of the [N II] and [C II] emission in a given smaller region because the two lines trace different gas. The [N II] line can be expected to be present over much of the sky at a low level, while the [C II] emission has a diffuse component but is most often found on the surfaces of molecular clouds, which fill a much smaller fraction of the sky. When averaged over the whole sky at low resolution, this difference in filling factor suppresses the [C II]/[N II] ratio, making this argument unreliable. A better estimate of the emission in a small patch of sky can be made from KAO observations of a somewhat analogous source, G333.6-0.2 [17]. Both [C II] and [N II] were detected in this source, with a line ratio of [C II]/[N II]$_{1.46THz} = 50$. Given this ratio, we may expect something closer to 1 K in Orion-KL, which is entirely consistent with our observations.

RLT observations have been suspended since January for the summer wet season known locally as “Bolivian Winter”. Operations resume in late April or early May with a new list of target sources. In particular, we are using ISO observations of the 2.46 THz line of [N II] to select our sources. Although COBE observations suggest that the Galactic average [N II]$_{1.46}$/[N II]$_{2.46}$ line ratio is approximately unity [14], in the individual sources we observe it is likely to be lower. In the high-density limit ($n > 10^3$ cm^{-3}) this ratio is around 0.1, and most gas in discrete sources will be at or above this density threshold. The ISO observations are not velocity resolved in most sources so the measured line fluxes cannot be directly inverted to obtain a peak line strength, but many sources with [N II] emission stronger than that observed in Orion have been obtained in the appropriate hour angle range.

IV. Prospects for THz Astronomy from the Ground

For the next two or more years, terahertz astronomy will only be possible from the ground. The Receiver Lab Telescope has now demonstrated observations of astronomical line radiation in all three of the atmospheric windows between 1.0 and 1.6 THz. From our site and nearby sites in northern Chile, the 1.5 THz window is likely to be the highest frequency window that will be regularly usable for astronomy. Observations of the transmission on very dry nights (multiple instances of PWV below 200 μm, including the 93 μm shown in Figure 1, have been been observed in the last year) suggest that from an even drier site one may be able to move to higher frequencies, including observations of the [C II] line at 1.9 THz. Proposed observations from Antarctic Dome A, for which measurements of submillimeter opacity are not yet available, may be able to make this step to higher frequencies if PWV predictions for this site are accurate.

Ground-based measurements will continue to have an important place in terahertz astronomy even in the era of SOFIA

[1]Based on calculations performed with the *am* atmospheric model [19], available at http://cfarx6.cfa.harvard.edu/am

and Herschel. First, telescopes on the ground can be much larger than is possible from airplanes or from space at similar cost. In the next year the 12-meter APEX telescope will begin observations above 1 THz with multiple receivers. Planning for an even larger telescope, the 25-meter Caltech-Cornell Atacama Telescope (CCAT), are underway. CCAT would achieve angular resolution around $2''$ at 1.5 THz, better than is now available from any single-aperture radio telescope, and almost an order of magnitude better than will be obtained from SOFIA or Herschel. Moreover, Herschel will lack receiver coverage between 1.25 and 1.41 THz, a gap that lines up well with the 1.3 THz atmospheric window. Sensitive observations from the ground, particularly with the angular resolution available from these larger telescopes, will access important science that Herschel will miss.

ACKNOWLEDGMENT

The authors thank the many current and former members of the Receiver Lab who have worked on bringing the RLT into existence and contributed to its operations in Chile, in particular, Hugh Gibson and Cosmo Papa. Site evaluation and RLT development could not have taken place without the ever present support of Irwin Shapiro, former director of the Center for Astrophysics. The project also owes a great deal to the many years of assistance provided by Jorge May and Leo Bronfman at Universidad de Chile. We also thank Imran Mehdi, John Ward, and their LO team for providing us with an oscillator for 1.5 THz observations. This work was performed for the Jet Propulsion Laboratory, California Institute of Technology, sponsored by the National Aeronautics and Space Administration. DPM acknowledges support from an NSF Graduate Research Fellowship.

REFERENCES

[1] S. Matsushita, H. Matsuo, J. R. Pardo, and S. J. E. Radford, "FTS Measurements of Submillimeter-Wave Atmospheric Opacity at Pampa la Bola II : Supra-Terahertz Windows and Model Fitting," *Pub. of the Astronomical Society of Japan*, vol. 51, pp. 603–+, Oct. 1999.

[2] S. Paine, R. Blundell, D. C. Papa, J. W. Barrett, and S. J. E. Radford, "A Fourier Transform Spectrometer for Measurement of Atmospheric Transmission at Submillimeter Wavelengths," *Pub. of the Astronomical Society of the Pacific*, vol. 112, pp. 108–118, Jan. 2000.

[3] J. R. Pardo, E. Serabyn, and J. Cernicharo, "Submillimeter atmospheric transmission measurements on Mauna Kea during extremely dry El Nino conditions: implications for broadband opacity contributions," *Journal of Quantitative Spectroscopy and Radiative Transfer*, vol. 68, pp. 419–433, Feb. 2001.

[4] J. Kawamura, T. R. Hunter, C.-Y. E. Tong, R. Blundell, D. C. Papa, F. Patt, W. Peters, T. L. Wilson, C. Henkel, G. Gol'tsman, and E. Gershenzon, "Ground-based terahertz CO spectroscopy towards Orion," *Astronomy & Astrophysics*, vol. 394, pp. 271–274, 2002.

[5] D. P. Marrone, J. Battat, F. Bensch, R. Blundell, M. Diaz, H. Gibson, T. Hunter, D. Meledin, S. Paine, D. C. Papa, S. Radford, M. Smith, and E. Tong, "A Map of OMC-1 in CO J = 9→8," *The Astrophysical Journal*, vol. 612, pp. 940–945, Sept. 2004.

[6] R. Blundell, J. W. Barrett, H. Gibson, C. Gottleib, T. R. Hunter, R. Kimberk, S. Leiker, D. Marrone, D. Meledin, S. N. Paine, R. J. Plante, P. Riddle, M. J. Smith, T. K. Sridharan, C. E. Tong, R. W. Wilson, M. A. Diaz, L. Bronfman, J. May, A. Otarola, and S. J. Radford, "Prospects for Terahertz Radio Astronomy from Northern Chile," in *13th International Symposium on Space Terahertz Technology, ed. C. E. Tong & R. Blundell*, 2002, pp. 159–166.

[7] D. P. Marrone, R. Blundell, H. Gibson, S. Paine, D. C. Papa, and C.-Y. E. Tong, "Characterization and Status of a Terahertz Telescope," in *15th International Symposium on Space Terahertz Technology, ed. G. Narayanan*, 2004, pp. 426–432.

[8] D. Marrone *et al.*, "A Ground-based Terahertz Observatory," 2005, in preparation.

[9] J. Ward, F. Maiwald, G. Chattopadhyay, E. Schlecht, A. Maestrini, F. Gill, and I. Mehdi, "1400 - 1900 GHz Local Oscillators for the Herschel Space Observatory," in *14th International Symposium on Space Terahertz Technology*, 2003, pp. 94–101.

[10] C.-Y. E. Tong, D. N. Loudkov, S. N. Paine, D. P. Marrone, and R. Blundell, "Vector Measurement of the Beam Pattern of a 1.5 THz Superconducting HEB Receiver," in *Sixteenth International Symp. on Space Therahertz Technology*, 2005.

[11] D. J. Fixsen, E. S. Cheng, D. A. Cottingham, R. E. Eplee, T. Hewagama, R. B. Isaacman, K. A. Jensen, J. C. Mather, D. L. Massa, S. S. Meyer, P. D. Noerdlinger, S. M. Read, L. P. Rosen, R. A. Shafer, A. R. Trenholme, R. Weiss, C. L. Bennett, N. W. Boggess, D. T. Wilkinson, and E. L. Wright, "Calibration of the COBE FIRAS instrument," *The Astrophysical Journal*, vol. 420, pp. 457–473, Jan. 1994.

[12] E. L. Wright, J. C. Mather, C. L. Bennett, E. S. Cheng, R. A. Shafer, D. J. Fixsen, R. E. Eplee, R. B. Isaacman, S. M. Read, N. W. Boggess, S. Gulkis, M. G. Hauser, M. Janssen, T. Kelsall, P. M. Lubin, S. S. Meyer, S. H. Moseley, T. L. Murdock, R. F. Silverberg, G. F. Smoot, R. Weiss, and D. T. Wilkinson, "Preliminary spectral observations of the Galaxy with a 7 deg beam by the Cosmic Background Explorer (COBE)," *The Astrophysical Journal*, vol. 381, pp. 200–209, Nov. 1991.

[13] C. L. Bennett, D. J. Fixsen, G. Hinshaw, J. C. Mather, S. H. Moseley, E. L. Wright, R. E. Eplee, J. Gales, T. Hewagama, R. B. Isaacman, R. A. Shafer, and K. Turpie, "Morphology of the interstellar cooling lines detected by COBE," *The Astrophysical Journal*, vol. 434, pp. 587–598, Oct. 1994.

[14] D. J. Fixsen, C. L. Bennett, and J. C. Mather, "COBE Far Infrared Absolute Spectrophotometer Observations of Galactic Lines," *The Astrophysical Journal*, vol. 526, pp. 207–214, Nov. 1999.

[15] F. P. Keenan, F. L. Crawford, W. A. Feibelman, and L. H. Aller, "Emission-Line Ratios for [N II] in Gaseous Nebulae and a Comparison between Theory and Observation," *The Astrophysical Journal Supplement Series*, vol. 132, pp. 103–106, Jan. 2001.

[16] P. E. Clegg, P. A. R. Ade, C. Armand, J.-P. Baluteau, M. J. Barlow, M. A. Buckley, J.-C. Berges, M. Burgdorf, E. Caux, C. Ceccarelli, R. Cerulli, S. E. Church, F. Cotin, P. Cox, P. Cruvellier, J. L. Culhane, G. R. Davis, A. di Giorgio, B. R. Diplock, D. L. Drummond, R. J. Emery, J. D. Ewart, J. Fischer, I. Furniss, W. M. Glencross, M. A. Greenhouse, M. J. Griffin, C. Gry, A. S. Harwood, A. S. Hazell, M. Joubert, K. J. King, T. Lim, R. Liseau, J. A. Long, D. Lorenzetti, S. Molinari, A. G. Murray, D. A. Naylor, B. Nisini, K. Norman, A. Omont, R. Orfei, T. J. Patrick, D. Pequignot, D. Pouliquen, M. C. Price, Nguyen-Q-Rieu, A. J. Rogers, F. D. Robinson, M. Saisse, P. Saraceno, G. Serra, S. D. Sidher, A. F. Smith, H. A. Smith, L. Spinoglio, B. M. Swinyard, D. Texier, W. A. Towlson, N. R. Trams, S. J. Unger, and G. J. White, "The ISO Long-Wavelength Spectrometer." *Astronomy & Astrophysics*, vol. 315, pp. L38–L42, Nov. 1996.

[17] S. W. J. Colgan, M. R. Haas, E. F. Erickson, R. H. Rubin, J. P. Simpson, and R. W. Russell, "Detection of the N II 122 and 205 micron lines - Densities in G333.6-0.2," *The Astrophysical Journal*, vol. 413, pp. 237–241, Aug. 1993.

[18] S. J. Petuchowski, C. L. Bennett, M. R. Haas, E. F. Erickson, S. D. Lord, R. H. Rubin, S. W. J. Colgan, and D. J. Hollenbach, "The N (II) 205 micron line in M82: The warm ionized medium," *The Astrophysical Journal*, vol. 427, pp. L17–L20, May 1994.

[19] S. N. Paine, "The *am* Atmospheric Model," Submillimeter Array Project, Tech. Rep. 152, 2004, http://sma-www.cfa.harvard.edu/private/memos/152-03.pdf.

[20] R. T. Boreiko, A. L. Betz, and J. Zmuidzinas, "Heterodyne spectroscopy of the 158 micron C II line in M42," *The Astrophysical Journal*, vol. 325, pp. L47–L51, Feb. 1988.

Terahertz Technology for ESPRIT – A Far-Infrared Space Interferometer

W. Wild, Th. de Graauw, A. Baryshev, J. Baselmans, J.R. Gao, F. Helmich, B.D. Jackson, V.P. Koshelets, P. Roelfsema, N.D. Whyborn, and P. Yagoubov

Abstract— In the Terahertz regime the angular (and sometimes spectral) resolution of observing facilities is still very restricted despite the fact that this frequency range has become of prime importance for modern astrophysics. ALMA (Atacama Large Millimeter Array) with its superb sensitivity and angular resolution will only cover frequencies up to about 1 THz, while the HIFI instrument for ESA'a Herschel Space Observatory will provide limited angular resolution (10 to 30 arcsec) up to 2 THz. Observations of regions with star and planet formation require extremely high angular resolution as well as frequency resolution in the full THz regime. In order to open these regions for high-resolution astrophysics we propose a heterodyne space interferometer mission, ESPRIT (Exploratory Submm Space Radio-Interferometric Telescope), for the Terahertz regime inaccessible from ground and outside the operating range of the James Webb Space Telescope (JWST). ESPRIT will employ heterodyne receivers from 0.5 to 6 THz.

The ESPRIT mission concept is described with an emphasis on Terahertz heterodyne receivers and cooling. The required technology development of mixers, local oscillators and integrated systems will be outlined.

***Index Terms*—Radio astronomy, Interferometry, Space technology, Submillimeter wave receivers.**

I. Introduction

The study of star and planet formation is one of the prime topics in modern astrophysics. Important questions include the physical conditions for star-formation to occur, the evolution of circum-stellar disks, the decoupling of dusty proto-planetary regions from the gas, and the chemistry that leads to the pre-biotic conditions of early Earth-like planets. In addition, we also would like to know what role star-formation, and in particular starbursts, play in external galaxies and how this interacts with the general interstellar medium.

The phenomena connected to star and planet formation are best studied in the far-infrared/Terahertz regime (0.5 THz to several THz). This wavelength range holds the most important spectral signatures of the material (atoms, ions, molecules) as it is processed. The low extinction at these long wavelengths allows unique observations of details of the star formation process, in particular during its early phases, when these regions are completely obscured by the surrounding dust.

The Earth atmosphere severely limits the possibility to observe at THz frequencies from ground-based observatories. ALMA will cover the atmospheric windows at very high angular resolution up to about 1 THz which is the limit for observations even from high-altitude sites (with the exception of a few small atmospheric windows around 1.3 and 1.5 THz accessible only from the very best sites on Earth).

Astronomical observations above 1 THz need to be done from space. However, all past, current and planned missions have limited angular resolution. The relatively small ratios of aperture diameter to wavelength, like for example in ISO, Spitzer Space Telescope and Herschel, provide only angular resolutions of the order of 5 arcsec in the 100μm region. This does not match the 0.1 arcsec resolution which is required for these studies. In order to achieve the required angular resolution, to investigate for example the distribution of key molecules in a circum-stellar disk, application of interferometer techniques in space is the only way forward. At the same time, high spectral resolution is required to measure the chemical composition, the dynamics and other physical conditions. In particular, studies of water and other hydrides, together with the isotopic/deuterated versions, are of prime interest for the star formation process.

A mission concept that combines all these capabilities is uniquely suited to address these questions: a free-flying, 6 element, far-infrared imaging interferometer using heterodyne detection: ESPRIT – the Exploratory Submm sPace Radio-Interferometric Telescope. After presentation of the mission concept, scienc goals and configuration aspects, we will outline the THz technology needed for such an instrument and the required development.

II. ESPRIT Mission Concept

Table I gives the main characteristics of ESPRIT. The 6-element interferometer will be in a free-flying configuration with precise metrology to determine the exact position of each satellite. The array will fly in a constantly moving configuration filling the u-v plane (see below). In a preliminary trade-off between signal strength, primary beam size and practical considerations, it appears that a 3.5 to 4

Manuscript received May 31, 2005.

The authors are with SRON Netherlands Institute for Space Research, Groningen and Utrecht, the Netherlands. (Corresponding author: W. Wild, phone +31-50-363 4074, fax +31-50-363 4033, W.Wild@sron.rug.nl).

W. Wild, Th. de Graauw, A. Baryshev, F. Helmich, and P. Roelfsema are also with the Kapteyn Astronomical Institute, University of Groningen, the Netherlands.

Th. de Graauw is also with Leiden Observatory, the Netherlands.

V.P Koshelets is with the Institute of Radio Engineering and Electronics, Russian Academy of Science, Mokhovaya 11, 125009, Moscow, Russia, and part-time with SRON Netherlands Institute for Space Research, Groningen, the Netherlands.

meter diameter of the primary mirrors would satisfy the overall mission goals.

TABLE I
MAIN CHARACTERISTICS OF ESPRIT

Telescope sizes	~ 3.5 meter ; off-axis
Number of elements	N =6 (15 baselines)
Frequencies	Spots in the range 0.5 – 6 THz (600 μm – 50 μm)
Projected baselines	~ 7- 200-1000 meter
Front Ends (0.5 – 1.5 THz)	SIS mixers, multiplier LO
Front Ends (1.5 – 6 THz)	HEB mixers, QCL as LO
System temperature	1000 K
IF bandwidth	> 4 GHz (goal 8 GHz)
F.O.V. / primary beam size	~ 6" at 100 μm
Spatial Resolution	0.02" at 100 μm
Pointing Requirements	accuracy: 0.2" measurement: 0.1"
Image Dynamic range	> 100
Spectral Dynamic range	> 1000
Correlator	4 sections of 1 GHz, each 128 channels
Configuration	Free-flying

From ground-based interferometer experience it is evident that in order to get an acceptable imaging capability one needs a minimum of 6 antenna elements. Each antenna will be equipped with a number of heterodyne receivers covering selected ranges between 0.5 and 6 THz (600μm to 50μm). The exact choice of frequencies will depend on the scientific priorities, and the number of receivers will depend on technical limitations (mass, size, cooling power etc.).

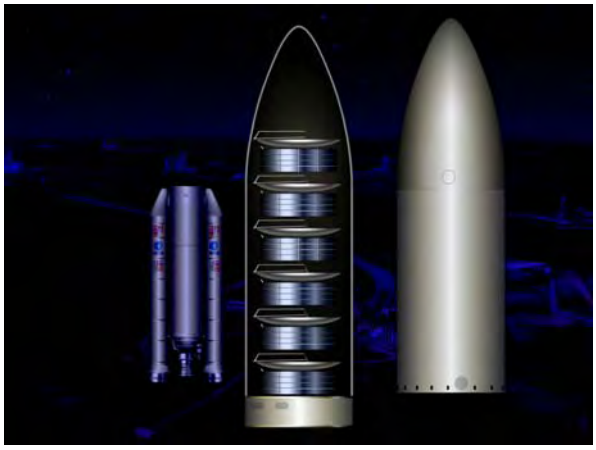

Fig. 1. The six elements of ESPRIT in an Ariane 5 faring. The telescope design has unfoldable subreflectors allowing dense packing and thus aiming for a single launch of the whole interferometer (artist conception).

A distributed correlator seems to be the most practical solution for this mission. Pointing requirements are proportional to the diffraction diameter and are roughly a factor of 10 more stringent than is being provided today in ESA's space missions. An important point is the aim to have all six satellites put into space with a single launch. A telescope design with subreflectors that unfold after leaving the launch vehicle in space would make this feasible (Fig. 1). ESPRIT is preferably situated in the Sun-Earth Lagrange point L2 about 1.5 million km from Earth because of thermal stability.

III. SCIENCE GOALS

The study of the formation and evolution of stars and solar systems is one of the main themes of modern astrophysics. In particular the indirect detection of more than 100 Jupiter-like extra-solar planets has enforced these studies and the development of missions. Although Spitzer and JWST will address these subjects in detail, there is a clear missing link in these studies. This concerns mainly the epoch before the objects are becoming strong IR emitters. And Herschel, although the largest space telescope planned for the FIR, will have a too modest angular resolution (ranging from 6 to 40 arcsec) for unraveling the star/planet formation process.

The most critical and unique spectral lines for studying this process are from H_2O, H_3O^+, OI, C^+, N^+, CH, OH, CH^+, and their isotopes including their deuterations. ESPRIT will trace the movements and spatial distribution of the ionic and molecular material and its specific components, from cold dark pre-stellar clouds through the final stages of star formation process. In particular measuring the distribution of water in the pre-stellar clouds and proto-planetary nebulae and disks is crucial, not only for its unique diagnostics but also for assessing the cloud's thermal conditions during its evolution.

Similar observations of circum-stellar material of evolved stars are most relevant for understanding the evolution of extra-solar planetary systems. In this sense the detection by SWAS of circum-stellar water vapor towards the evolved carbon-rich star IRC10216 is very interesting. The most plausible explanation for the presence of the amount of detected water vapor is evaporation of ice on Kuiper Belt type objects by the central star. ESPRIT will have sufficient sensitivity to detect in detail many of these objects.

The facility will be the high-frequency/short-wavelength complement of the ground-based ALMA, without any atmospheric attenuation and disturbance in phase and transmission. It will be a follow-up mission of ISO-LWS, SWAS, ODIN, SIRTF, ASTRO-F, Herschel-PACS and -HIFI and of MIRI on JWST. Nevertheless, with the rapid development and increase of observing capabilities of ground-based and space/airborne facilities it will be important to update the scientific case as new discoveries are made.

IV. INTERFEROMETER CONFIGURATIONS

The six satellites of ESPRIT will be positioned in space in a three dimensional configuration. By combining the down converted and digitised signals of the elements in a correlator a set of complex visibilities are obtained corresponding to different locations in the sky fourier transform plane. Thus by fourier transforming these visibilities an image of the sky is obtained. Different configurations are being studied. A simple radial expansion and contraction of the array does not yield a high-quality beam, whereas a combined movement of radial expansion

together with overall rotation of the array results in a more uniform u-v coverage and thus a "better" synthesized beam (Fig. 2). Clearly more detailed studies will have to determine the best strategy for moving the individual satellites.

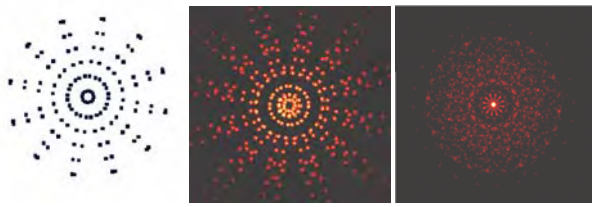

a) b) c)

Fig. 2. One example of a possible ESPRIT array configuration which rotates while it expands and contracts. a) Motion of ESPRIT elements, b) Resulting u-v coverage, c) Synthesized beam.

It is anticipated that ESPRIT will make use of small ion thrusters like FEEPs (Field-Emission Electric Propulsion) . Due to weight and power constraints it will not be possible to move the satellites very quickly. Therefore the thrust and duration of each thrust period determines the velocity each telescope will get and thus limits the number of instantaneous configurations, within one observing run for a particular source. Likely it will typically take several days before the array has expanded from its smallest configuration to its full size of around 1 kilometre.

V. Front End Technology for ESPRIT

A. Heterodyne Receivers

The focal plane instrumentation of ESPRIT will consist of cryogenic heterodyne receivers. Two types of mixer technology will be used: from 0.5 to about 1.3 or 1.5 THz SIS mixers offer best sensitivity, and above 1.5 THz up to 6 THz HEB mixers are the best choice. Both types of mixer have been space qualified (up to 1.9 THz) for Herschel-HIFI and will be flown in 2007 (see next section).

Fig. 3 shows a block diagram for two channels (one SIS with integrated LO, and one HEB). ESPRIT will cover as many spots in the frequency range from 0.5 to 6 THz as possible within the technical limitations (such as volume, mass, cooling capacity etc.). In addition, a low frequency channel (80…200 GHz) will be included for phase calibration. Since the astronomically observable velocity width scales inversely with the observing frequency for a given IF bandwidth, a large IF bandwidth of the receiver is important at THz frequencies. For example, a 4 GHz IF bandwidth corresponds to only 200 km/sec at 6 THz, and an 8 GHz IF bandwidth still provides only 400 km/sec velocity coverage.

The performance of a heterodyne front-end is largely determined by three components in the system: the local oscillator, the mixer, and the IF amplifier chain:

- LO: The LO must provide sufficient power to drive the mixer (typically 10's of μW), must be spectrally pure, and must be stable. The tuning range of the LO is also critical to the tuning range of the receiver.

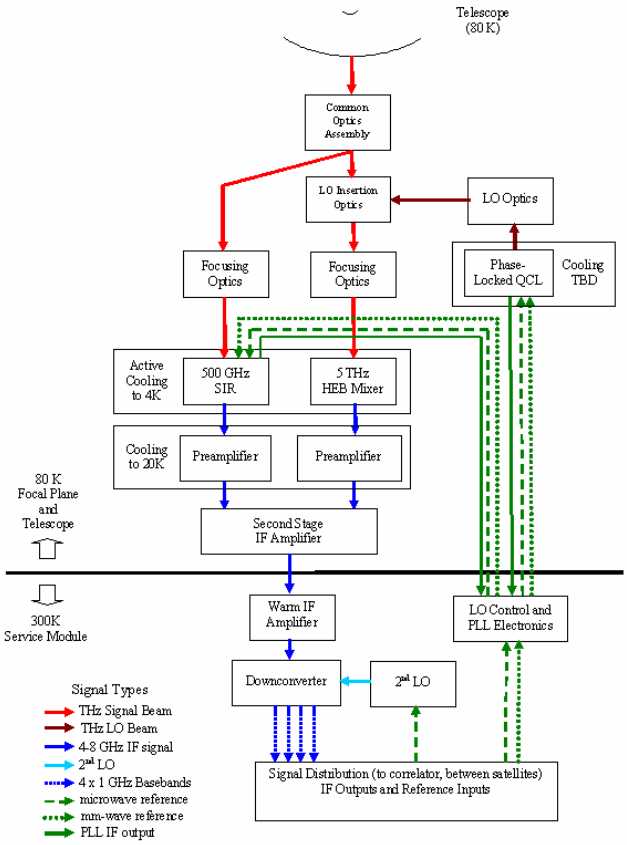

Fig. 3. Functional block diagram for an ESPRIT front-end (here for two channels) and the satellite IF systems.

- Mixer: The noise and gain of the mixer dominate the sensitivity of a high-frequency heterodyne receiver (especially for a space-based instrument that is not affected by an atmosphere or cryostat windows). The mixer may also limit one or both of the RF tuning range and IF bandwidth of the receiver.
- Cryogenic IF amplifier: The noise contribution of the IF amplifier chain (especially the "pre-amp" which immediately follows the mixer) is an important part of the overall system noise budget, while its bandwidth may limit the IF bandwidth of the receiver.

The state-of-the-art of these components and the required development / improvements for ESPRIT will be discussed in the following sections.

TABLE II
Space Qualified Heterodyne Technology for HIFI-Herschel

	Band 1 to 5	Band 6
Mixer type	SIS	HEB
Frequency	0.48-1.25 THz	1.4 – 1.9 THz
IF	4 – 8 GHz	2.4 – 4.8 GHz
Local oscillator	Multiplier chain	Multiplier chain
Sensitivity	3 - 5 hν/k	20 hν/k
Status	Space qualified	Space qualified

B. Mixers and local oscillators up to 2 THz

SIS and HEB mixers as well as multiplier chain local oscillators have been developed and space qualified for Herschel-HIFI covering the range up to 2 THz, with a 4 and

2.4 GHz IF bandwidth, respectively. Table II and Fig. 4 give an overview. During the last few years the multiplier chain LO development for HIFI has progressed significantly. For details on the current status of high-frequency multiplier chain LOs see [4]-[6].

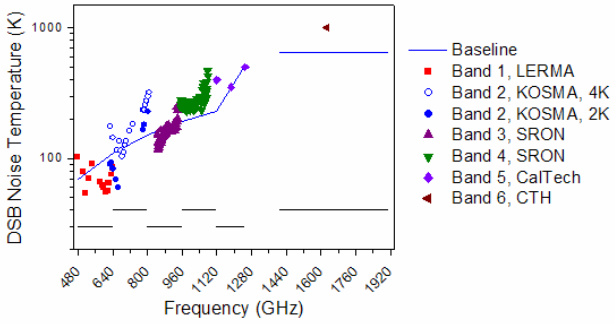

Fig. 4. DSB noise temperatures of the HIFI mixers (Bands 1-5: SIS; Band 6: HEB), Sep 2004.

For ESPRIT some development in the areas of noise temperature and IF bandwidth would be required. The sensitivity of the ESPRIT interferometer depends to a large extent on the front end noise with the mixer being the most important element. Mixer noise temperatures have improved significantly over the past years, in particular for SIS mixers, and it is desirable that continued development further decreases the mixer noise. Concerning HEB mixers, improvement of the mixer noise is required for ESPRIT. Present state-of-the-art noise temperatures are around 8-10 times the quantum limit (Fig. 5).

For ESPRIT an IF bandwidth of up to 8 GHz or even more is desirable. Extending the IF bandwidth of the SIS mixers is possible, 8 GHz has been achieved up to 720 GHz [1], [2]. However, reaching 8 GHz IF bandwidth for the HEBs needs more development work. For both types of mixers a development to integrate mixers and pre-amp could simplify the instrument. Another development, the use of superconducting integrated receivers (SIR) with the (flux flow) local oscillator located on the same chip as the mixer, as is developed by Koshelets et al. [3], could lead to more compact receivers.

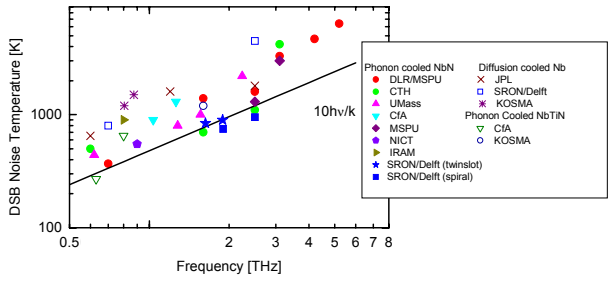

Fig. 5. State-of-the-art DSB noise temperatures of HEB mixers from 0.6 to 5.3 THz. Best results correspond to about 10 hv/k (compilation by Gao et al. and Huebers).

At present a SIR channel at 650 GHz is developed for the balloon-based atmospheric mission TELIS (Terahertz and submm limb sounder, see Yagoubov et al. [7] and reference therein). Fig. 6 shows the chip containing all major elements of a heterodyne receiver. Based on the results of this development, the SIR could become an interesting option for some of the ESPRIT frequency channels with the corresponding advantages in terms of mass, size, and lower system complexity.

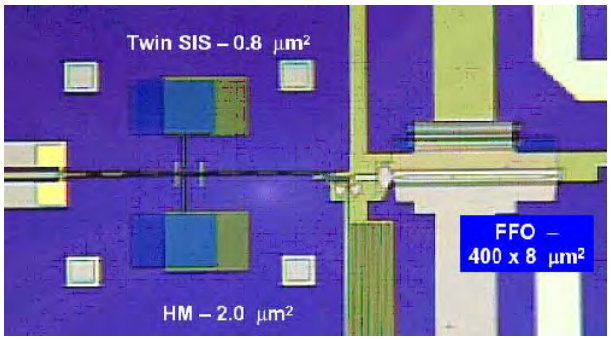

Fig. 6. Microscope photograph of a central part of the SIR chip (field of view is about 1.5mm by 1.0mm). All main elements of the Integrated Receiver (double-dipole twin SIS mixer, Flux Flow Oscillator and Harmonic Mixer) are present.

C. *Mixers and local oscillators above 2 THz*

Above 2 THz a number of HEB systems have been demonstrated in the lab by various groups, but none has been used for astronomical observations due to a lack of suitable (space) platforms. All of these systems have been operated at specific frequencies with a small tuning range (due to the use of a laser LO) and fairly low IF bandwidth (typically 2-3 GHz, or less). The highest demonstrated frequency is 5.3 THz. Fig. 5 shows reported noise temperatures with best values around 8-10 hv/k. For ESPRIT, both a larger IF bandwidth and lower noise temperatures will be needed. An extension of the IF bandwidth (ideally 8 GHz) and improved sensitivity (to ~ 3 hv/k) will require development work. Note that the drop in demonstrated sensitivities at 3 THz is due to the bulk of developments to-date being aimed at receivers for 2.5 THz or less – it does not reflect a limitation of the HEBs themselves.

The Local Oscillator development for Herschel-HIFI has pushed the operation of multiplier chains driven by high-power millimeter-wave sources to 2 THz. With some effort this could probably be extended to 3 THz. Coming from the mid-IR side of the spectrum, the recent successful development of Quantum Cascade Lasers (QCL) has opened up the possibility for heterodyne receivers operating at 6 THz (=50μm). QCLs have been demonstrated in CW operation in the THz range from 2.1 to 4.7 THz with output powers of several hundred μW to tens of mW (an HEB mixer only requires ~0.5 to 1 μW of LO power). The tuning range is on the order of 10 GHz and thus quite limited. The line-width of a QCL is small - 30 kHz has been measured. These characteristics make QCLs interesting THz local oscillators, and first experiments using a QCL as LO in a heterodyne system have been performed recently. For a THz heterodyne receiver system issues like phase-locking, tuning range and stability need to be considered and investigated. Furthermore, since the QCL chips are very small (millimeter size) and fairly compact integrated systems could be developed possibly containing many QCL chips for one mixer, to overcome the tuning range limitation.

D. IF amplifiers

Existing cryogenic IF amplifiers provide bandwidths of up to 8 GHz (with discrete elements) or beyond (with MMIC-based designs) with very good noise temperatures (below 5 K). For HIFI, IF amplifiers in the 4-8 and 2.4-4.8 GHz ranges have been space qualified. For ESPRIT, existing designs may be either used directly or modified to accommodate a different IF range, depending on the exact IF range and bandwidth requirements. Integration of the first IF amplifier with the mixer might reduce system complexity.

E. Telescope, optics and front-end cooling

The cooling requirements for ESPRIT can be divided in several components like telescope cooling, detector cooling and everything in between. It is beyond the scope to provide a complete overview of the ESPRIT cooling and a careful system study is mandatory. However, the requirements of a number of key system components can be considered.

1) Telescope cooling requirements

While older FIR telescopes relied on liquid Helium for the cooling of the telescope to suppress the telescope's own background, newer ones rely on passive cooling, as is the case for the Herschel telescope. The advantage is clear: since the telescope dish doesn't have to fit in the helium cryostat it can be larger, such that the size of the telescope dish is now mainly determined by the mass of the dish itself and the space available in the launch vehicle. Cooling of the Herschel telescope (3.5m) is done passively by radiating heat away into cold deep space. Although it is not yet certain what the final temperature of the telescope will be, studies show that it will be close to 70-80K. Note that due to the heterodyne nature of HIFI, it is the least susceptible of the Herschel instruments to the telescope background radiation. This advantage is also available to ESPRIT, so an 80K dish is sufficient. Since it is assumed that the ESPRIT telescope will be similar in size to that of Herschel, very similar passive cooling is needed.

2) Front-end optics cooling requirements

The front end optics for ESPRIT are expected to be at similar temperatures as the telescope dish. Due to the heterodyne nature of ESPRIT, thermal background and stray-light problems are not expected, but standing waves may occur if parallel surfaces exist within the light paths. Detailed quasi-optical modeling would show whether and how standing waves could be avoided, even at temperatures of 70-80K. Note that for Herschel-HIFI the Focal Plane temperature of 15K is sufficient to keep the background low, and although some parallel surfaces do exist within HIFI, the standing wave amplitudes are within reasonable bounds.

3) Front-end electronics cooling requirements

The SIS and HEB mixers will need to be cooled to 4K or below (with dissipation powers of less than a mW each), while the IF pre-amplifiers will need to be cooled to at least 20K (dissipation ~ 8mW per pre-amp). The second-stage IF amplifiers may be heat-sunk to the passively cooled front-end optics, at about 70-80 K (dissipation ~ 10 mW per amplifier).

TABLE III
COOLING REQUIREMENTS FOR ESPRIT THZ RECEIVERS

Temperature level	**One receiver with 2 mixers and LO**	
Between 30 K and 120 K	LO (QCL)	2.5 W
70 K	2 Amplifiers	20 mW
25 K	2 Pre-amplifiers	16 mW
4.2 K	2 Mixers	0.5 mW
	Parasitics	1 mW

The local oscillators (multiplier chain and/or QCL) may require active cooling, with operating temperatures between 30 and 120K. The QCLs will have power dissipations on the order of 1 W.

An overview of the cooling requirements for THz receivers is given in Table III for observations at one frequency dual polarization (i.e. using two mixers per satellite). These estimates apply only to the active channels (the instrument will likely operate with 1 or 2 active channels and several inactive channels at any one time) and do not include the mechanical support structure of the cryostat. A more detailed thermal design is needed to evaluate the overall heat-loads in the cryostat, front-end, and cable harnesses.

In order to achieve a long life time of ESPRIT, the active cooling of the front-end electronics to 4 K will require the use of mechanical, sorption/Joule-Thompson or similar coolers. The thermal stability of this 4K temperature level may also form an important aspect of the cooler design.

While a study needs to be conducted to show the exact figures for passively cooling the telescope and the optical bench, the real technology step lies in space-qualifying coolers such as now developed e.g. at the University of Twente (Netherlands) and elsewhere. Since the cooling of the front-ends is critical, this should receive early attention, but it should also be noted that many missions require similar technology, and studies dedicated to the cooling of these missions will provide the necessary knowledge for ESPRIT.

The bias and control electronics for the front-end electronics can be located with the other warm electronics. If it is defined as part of the front-end, the 2nd LO (which down converts individual sub-bands of the 4-8 or 4-12 GHz IF band to a common lower-frequency base band that is then sampled in the correlator) can also be located with the other warm electronics.

VI. CONCLUSION: WHAT IS NEEDED FOR ESPRIT

Concerning THz receiver and cooling technology for ESPRIT, the following technology steps are needed:

- *SIS Mixers:* Further improvement of noise temperatures is desirable. An IF bandwidth of 8 GHz, now demonstrated for mixers up to 720 GHz, should also be possible beyond that frequency. The frequency limit for quantum-limited SIS receivers should be pushed up to 1.5 THz or even higher.

- *HEB mixers:* Noise temperatures should be optimized to comply with the science requirements (T<1000 – 1500K at 100 μm / 3 THz), preferably up to 6 THz. IF bandwidths should be increased to at least 4 GHz, with a goal of 8 GHz.
- *Multiplier chain LO:* The development should be pushed to 3 THz. A decrease in system complexity is desirable.
- *QCL LOs:* Demonstration as a heterodyne LO is needed, including investigations of phase-locking, tuning range, and stability. The possibility to improve tuning range by parallel combinations of QCLs should be investigated. Power and cooling requirements for optimized QCLs should be investigated.
- *IF amplifiers:* Existing designs can be used or modified for use.
- *Front-end cooling:* Space-qualified coolers with low mass and power consumption as well as high thermal stability are required. Needed temperature levels are 4 K, 25 K, 70 K, and a TBD level between 30 and 120 K for QCL cooling (depending on QCL properties).

REFERENCES

[1] A. Baryshev, E. Lauria, R. Hesper, T. Zijlstra, and W. Wild, "Fixed-tuned waveguide 0.6 THz SIS mixer with wide band IF," in: R. Blundell and E. Tong (Eds.), Proc. of the 13th Int. Symposium on Space THz Technology, Havard University, Cambridge, MA, USA, March 26-28, 2002, pp. 1-10.

[2] R. Hesper et al. "Design and development of a 600-720 GHz receiver cartridge for ALMA Band 9", these Proceedings.

[3] Koshelets et al., "Superconducting Submm Integrated Receiver with Phase-Locked Flux-Flow Oscillator for TELIS", these Proceedings.

[4] J. Ward et al., "Local Oscillators from 1.4 to 1.9 THz", these Proceedings

[5] G. Chattopadhyay, E. Schlecht, J. Ward, J. Gill, H. Javadi, F. Maiwald, and I. Mehdi, "An All Solid-State Broadband Frequency Multiplier Chain at 1500 GHz," IEEE Transactions on Microwave Theory and Techniques, vol. 52, no. 5, pp. 1538-1547, May 2004.

[6] A. Maestrini, J. Ward, J. Gill, H. Javadi, E. Schlecht, G. Chattopadhyay, F. Maiwald, N. R. Erickson, and I. Mehdi, "A 1.7 to 1.9 THz Local Oscillator Source, IEEE Microwave and Wireless Components Letters," vol. 14, no. 6, pp 253-255, June 2004.

[7] P.A. Yagoubov, W.-J. Vreeling, H. van de Stadt, R.W.M. Hoogeveen, O.V. Koryukin,V. P. Koshelets, O.M. Pylypenko, A. Murk "550-650 GHz spectrometer development for TELIS", these Proceedings.

Session 5:

Poster session

Monday May 2, 17:00-19:00
Chairmen:
Harald Merkel, Jan Stake, Josip Vukusic

Poster session I:

Systems

Quasi-Optical Verification of the Band 9 ALMA Front-End

M. Candotti*, A. M. Baryshev†, N. A. Trappe*, R. Hesper†, J. A. Murphy*, J. Barkhof†
*National University of Ireland, Maynooth, Co. Kildare, Ireland
Email: Massimo.Candotti@nuim.ie
†9700 AV Groningen, The Netherlands
Email: A.M.Baryshev@sron.rug.nl

***Abstract*— The front-end optical design for band 9 (600 to 720GHz) of the Atacama Large Millimeter Array (ALMA) is now completed. A frequency independent design approach is used to couple radiation to the two orthogonal polarized mixed detectors from the large 12m ALMA Cassegrain telescope. As it is a heterodyne receiver, two local oscillator beam paths are integrated into the front-end optical system. Due to the large number of interferometer elements (64 antenna units) to be built, installed and maintained in the remote site of the Atacama Desert, reliability of the optical system should be ensured. A modular and compact optical design is also important. In addition a cheaper fabrication process is considered, at these more tolerant higher frequencies, by milling the mirror surfaces near the surface roughness limit. In this paper we verify the optical design and estimate system efficiency by means of experimental measurement and software simulation comparisons. Precision planar scans of near field beam patterns (amplitude and phase) have been measured. Experimental beam measurements were taken at the output of the mirror coupling system (telescope focal plane location) for both polarization paths and for both local oscillator beam guides. At the same measurement locations, software simulations of a highly accurate geometrical model of the mirror coupling system were predicted using the commercial package GRASP8©. These comparisons at some fundamental locations along the beam paths, allow the assessment of the quasi-optical beam coupling system design. The local oscillator power budget analysis is carried out from results obtained using GRASP8©. In the conclusion we summarize the current status and describe future analysis plans.**

I. Introduction

The work presented in this paper is a continuation of the optical design and later verification of the optical coupling mirror system for the ALMA band 9 system. This activity has started with the evaluation of a basic prototype of a two mirror coupling system [1], resembling the real optical design. In this initial work most of the attention was aimed at the evaluation of the mirror surface milling technique adopted. In fact, in order to minimize costs and improve system modularity, a a minimum surface roughness accuracy of $7\mu m$ RMS was choose and obtained with conventional CNC machines. By means of experimental measurements and later on also with software electromagnetic analysis [2], it was proven that these mechanical project choices were satisfactory operation of band 9. In phase one of the analysis the conceptual design was verified completely. Tight distance tolerances of $40\mu m$ were chosen to insure the optimum optical component alignment without the need for optical alignment with a laser beam. In this paper we then analyze measured and simulated data of the final optical coupling system to be mounted in to the band 9 cryostat, but at the room temperature. In section II we present a brief description of the optical coupling system project. The interested reader could have more information on this topic by reading [3]. Sections III and IV will describe respectively the measurement setup used to scan intensity and phase of the near field at the focal plane (FP) location and the electromagnetic software model implemented in GRASP8©. Measured data at two different frequencies (606 and $668GHz$) are then compared and analyzed with related software predictions at the same frequencies and location in section V. In this section a Gaussian Beam Mode Analysis (GBMA) is also carried out for the Co-Polar (Co-P) components. Due to the excellent agrement between measured (experimental) and software (theoretical) data is it then possible to make some system performance predictions using the simulation tool. An example is reported in section VI dealing with the Local Oscillator (LO) power budget requirements. Further work and conclusions are finally considered at the end of this paper.

II. Optical coupling system

The telescope has to be coupled to the mixer corrugated horn with an illumination edge taper of $12dB$ at the secondary reflector. A series of two ellipsoidal mirrors were designed in order to refocus the horn field distribution twice and achieving the desired edge taper. Since there are two orthogonal linear polarized signals detected from the sky, the coupling system is in fact exactly duplicated for both of the two polarization channels. This is also the case of the LO signal injection system. The procedure used to design all the optics for this coupling system is based on geometrical optics techniques. The choice of the bending angles for the mirrors coupling the horn to the telescope is not only dictated by the requirements of compactness inside the cryostat, but in a way that minimize the beam distortion at the output of the system [3].
In figure 1 we can see how the sky signal and LO signal are coupled to the mixer horn from the telescope FP and the LO feed respectively for both polarizations. The chief ray path from $M3$ (common to both configurations) to the antenna subreflector is following an off-axis trajectory since it has an inclination of 0.94° respect the telescope axis. This is due to the fact that the band 9 cryostat window

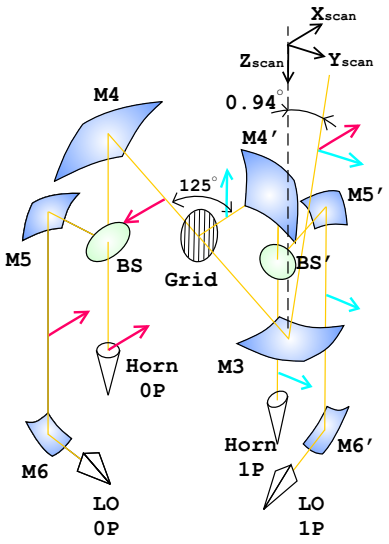

Fig. 1. Sketch of the optical coupling system for ALMA band 9.

TABLE I
MEASUREMENT SETUP FEATURES.

Electrical properties		
Gunn diode freq.	$[GHz]$	$100-120$
Multiplication chain, x2-x3	[GHz]	$600-720$
Output power	$[\mu W]$	60
Dynamic range	$[dB]$	$50-60$
Detector		Super Lattice Electronic Device
Amplitude stability	$[\%/hr]$	± 2
Phase stability	$[^\circ/hr]$	± 20
Scanner ranges and resolution		
X,Y,Z travel ranges	$[mm]$	100
Step accuracy	$[\mu m]$	5
Alignment accuracy		
X and Y offset	$[mm]$	± 0.1
Z offset	$[mm]$	± 0.2
X and Y rotations	$[^\circ]$	< 0.05
Z rotation	$[^\circ]$	< 0.1

is located off-axis in FP to accommodate the other ALMA channels. The $1P$ polarization beam path is a copy of the mirror system at the right side of the grid and rotated by 125° clockwise respect the incident point at the grid. The grid than works in reflection for the $1P$ polarization (linearly polarized on the plane of the $M3$ $M4$ ellipsoidal axis) and in transmission for the $0P$ polarization (orthogonally polarized respect $1P$). A beam splitter is located between $M4$ ($M4'$) and the mixer horn aperture with an inclination of 45° such as the linear polarized electric field is perpendicular to the plane of incidence. Another series of ellipsoidal mirrors, $M5$ ($M5'$) and $M6$ ($M6'$), are used to quasi-optically couple the LO signal source located at the $90K$ stage in the cryostat. The LO antenna is a diagonal horn. This kind of feed presents a optimum Gaussian beam coupling of 84% that allows, with a proper beam guide, efficient power coupling with the mixer horn.

III. MEASUREMENT SETUP

The measurement setup is a planar near-field antenna measurement based on radio heterodyne detection method using a vector network analyzer. Phase and intensity measures are then possible within the accuracies described in table I. Scan and optical mirror block alignment and parallelism are achieved by means of a theodolite in conjunction with well referenced point locations on the mirror block. In this way is then possible to establish a planarity (parallelism) relation within the scan stages and the mirror block. Autocollimation processes reflecting the theodolite laser beam, ensure parallelism. A set of cross-references drawn with know position on the mirror block to respect the $M3$ chief ray incident point, help to locate the source horn (held on the scan stages) in front of this incident point. By centering the scan to a set of 2 reference crosses aligned along the X or Y axis on the mirror block and reading the scan position, it is possible to fix the mirror block rotation around the Z axis, setting its Z tilt in order to correct rotation displacements. The precise alignment of the measurement system with the accuracies described in table I is difficult and the detailed information on the procedures used are not given in this paper.

IV. SOFTWARE MODEL

Theoretical modelling and analysis were carried out by using different complementary techniques, from basic geometrical optical ray tracing, GBMA and vector field analysis with the commercial package GRASP8©. Ray tracing performed by means of ABCD law gives the essential information of a quasioptical system. From the optical design distances between objects in the system and single optical elements characteristics, such as focal length of the mirrors, slant length R_h and aperture diameter of the corrugated horn, it is possible to describe how the fundamental Gaussian beam behaves along the optical path. For instance, radius w and radius of curvature R of the beam are traceable at each location between optical elements. The waist of the beam is than determined at each refocusing location depending on the frequency f. This technique treats the optical system as a paraxial system, without considering any diffraction effect due to truncations occurring at reflecting surfaces. Despite this limitations this method is a highly effective first order design and analysis tool. A more sophisticated software model can be implemented using GRASP8©. This is basically a software making use of Physical Optics (PO) approximations for the electromagnetic field computation. This technique allows to have vector information of the electromagnetic field in any location in the system under analysis. Its results are base on the full based Green's Maxwell equation solution considering the induced currents such as the electromagnetic field acts locally on the surface like a plane wave.The limits of applicability of this assumptions require scatters being large and smooth having a surface radius of curvature in terms of wavelength bigger than

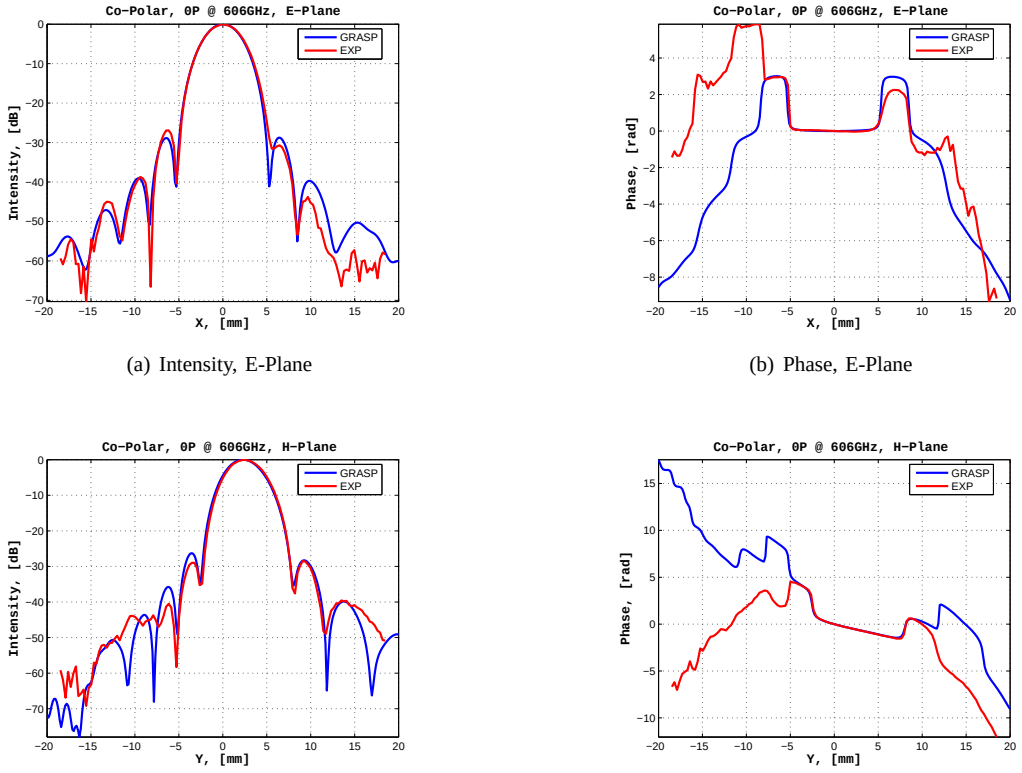

(a) Intensity, E-Plane

(b) Phase, E-Plane

(c) Intensity, H-Plane

(d) Phase, H-Plane

Fig. 2. Experimental and software data comparison of the $0P$ polarization signal at $606GHz$. Intensity and phase at E- and H- plane. Measured plane at $145mm$ from the chief ray incident point on $M3$.

6λ. This is our case since all the mirrors were designed taking into account a minimum clearance of at least $5w$ as stated in section II. From experimental measurement comparisons and previous analysis using this software [4] it turned out that PO gives accurate results for the system being analyzed. Using one of the features of GRASP8©, mirror rims can be modelled on the basis of actual mirror production drawings. Therefore the evaluation of the electromagnetic field will produce high fidelity beam pattern, describing mirror edge diffraction. Grids and apertures in GRASP8© can also be analyzed allowing the evaluation of polarization and truncations effects respectively. Using GBMA a more detailed picture of the beam quality at the FP location can be obtained.

Particular attention has been paid to the description of the input field at the mixer horn aperture location. It has been seen that a simple Gaussian beam model of the horn electric field distribution with a proper waist, does not predict either the sidelobes and the main-beam distortions along the optical path. A better way to improve the input field is to assume the field at the corrugated horn aperture plane as a truncated Bessel function with a spherical phase front [7]. Despite this choice improved the quality of the simulated beams, there is still no information on the Cross-Polar (Xs-P) component at the horn aperture, since only the Co-Polar (Co-P) field is described by the truncated Bessel function. A further improved representation of the electric field at the horn aperture was achieved by applying mode matching techniques developed initially in [5] and expanded in [6]. The horn is regarded as a large number of waveguide sections in succession, which match the profile of the horn. Waveguide modes are tracked through the horn and power conserved. This technique has the advantage of describing Co-P and Xs-P at the aperture plane of a corrugated horn from the detailed mechanical drawings. Thus, we obtained a complete field description at each particular frequency of interest for the mixer horn. With this input field distribution the results from GRASP8© take also into account how the Xs-P level evolve along the optical path. As an example of accuracy of this model, coupling the Co-P component resulting from the procedure previously described, with a fundamental Gaussian at the horn aperture[1] at the frequency of $668GHz$, a Gaussian power coupling coefficient of 97.72% was obtained. This value is very close to the model of a truncated Bessel function (98%) given in [7].

V. Experimental and Software Data Analysis

The aim of this section is to analyze beam electrical field distributions of the $0P$ and $1P$ beams at the FP from data obtained by real measurement and also software electromagnetic simulations. The measurement plane, both in the experiment

[1]Virtual waist of $1.05mm$ inside the horn calculated at the frequency of $668GHz$.

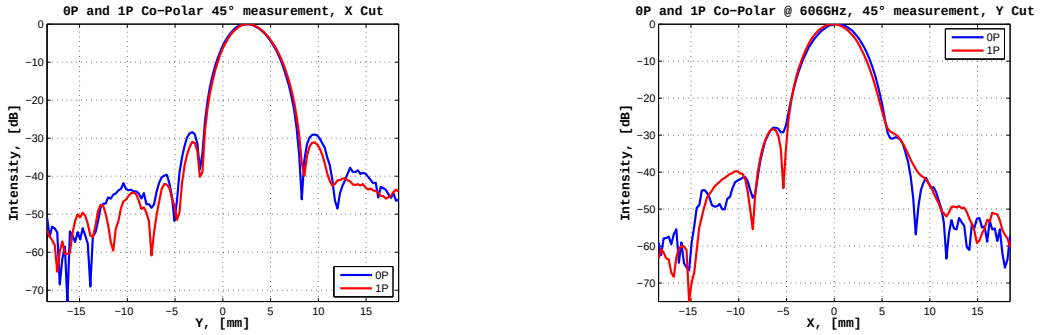

(a) X Cut (b) Y Cut

Fig. 3. Experimental $45°$ measurement comparison.

set-up and in the software model, is a plane normal to the telescope axis with the center of the co-ordinate system located $145mm$ in front of the chief ray intersection point on $M3$ (see figure 1). In this frame the beams are coming parallel to the $Y-Z$ plane and with a slope of $0.94°$. By having the same measurement plane definition and relying on the measurement alignment accuracy, we can visually compare experimental and software set of data obtained at the scan location.

A. E-Plane and H-Plane Field cuts comparisons

In figure 2 and 4 we show the direct comparison between experimental and simulated electromagnetic field at the E- and H-plane respectively for the $0P$ and $1P$ configuration. Figure 4 refer to a measurement involving the beam passing through an aperture emulating the cryostat window and it will be explained in the end of this section. These pictures refer to the frequency of $606GHz$, but other measurements where also taken at the higher frequency of $668GHz$. From these intensity and phase comparisons there is in general a good agrement with both phase and intensity distributions with high accuracy even at off-axis points from the main beam. This means that the measured beam is not diffracted by mechanical struts surrounding it. The five times the beam radius clearance design rule is respected along the whole optical path.

A particular measurement was carried out with the scanning source rotated at $45°$ to respect the two signal polarizations coming out from $M3$. In figure 3(a) and 3(b) the X and Y scan cuts are plotted on top of each other for a measurement at the frequency of $606GHz$. These plots show the two beams coming at the FP at the same location, indicating that the behavior of the two polarization signals is correct. At higher frequencies such behavior should be even smaller due to less diffraction effects.

B. Fundamental Gaussian beam mode analysis

A more qualitative analysis of the output beams could be made by means of GBMA. From the data distribution we can see how much the real beam is close to a fundamental Gaussian (fitting procedure), but also how much of the power of the real beam couples with the nominal fundamental Gaussian beam at the FP location. First we fit the field distribution with a fundamental Gaussian beam of unknown parameters. We carry out an overlap integral at the desired plane and vary the parameters of the Gaussian beam so as to maximize power coupling with the experimental or simulated field of interest. By maximizing the power coupling the equivalent Gaussian that best matches the field is obtained.

$$K = \left| \frac{\int_S E_m^* G ds}{\sqrt{\int_S E_m^* E_m ds \int_S G^* G ds}} \right|^2 \tag{1}$$

Equation (1) gives the amount of power coupled between the measured field E_m and a fundamental Gaussian beam G. In general a fundamental Gaussian beam is described by a waist w_0 located in a certain point in the space. Additional displacement offsets along the 3 axis (x_{Offset}, y_{Offset}, z_{Offset}) and tilts in x and y (θ_x and θ_y), give further degrees of freedom in order to define a beam in the space that best fit E_m. Considering the Gaussian distribution with a spherical phase front

$$\begin{aligned} G(x,y,z;w,R) = & \left(\frac{2}{\pi w}\right)^{0.5} \cdot \exp\left(-\frac{(x^2+y^2)}{w^2}\right) \cdot \\ & \cdot \exp\left(-j\pi\frac{(x^2+y^2)}{\lambda R}\right) \cdot \\ & \cdot \exp(j\phi_0) \cdot \exp\left(-j\frac{2\pi z}{\lambda}\right) \end{aligned} \tag{2}$$

where beam radius w, radius of curvature R and phase shift ϕ_0 depend on z [7], it is possible to include displacement and tilts of the plane wave phase front term (i.e. the beam direction) by using the following projections

$$x' = x_{Offset} + x\cos\theta_x \tag{3}$$
$$y' = y_{Offset} + y\cos\theta_y \tag{4}$$
$$z' = z_{Offset} + x\sin\theta_x + y\sin\theta_y \tag{5}$$

Using this projection we can move the fundamental Gaussian and also varying the waist w_0, to maximize power coupling (1). If displacements, tilts and waist are left free to vary and we apply the maximization of K, we obtain a set of these parameters describing which is the fundamental Gaussian

TABLE II
FUNDAMENTAL GBMA AT $606GHz$

$f = 606GHz$		Experimental $0P$	Experimental $1P$	Software $0P$	Software $1P$	Expected
Gaussucity,	[%]	98.15	98.31	98.19	97.99	~ 98
w_0,	$[mm]$	3.00	2.95	2.98	2.98	2.96
x_{Offset},	$[mm]$	0.06	0.26	0.00	-0.10	0.00
y_{Offset},	$[mm]$	2.58	2.85	2.45	2.45	2.47
θ_x,	[°]	0.06	-0.04	0.00	0.14	0.00
θ_y,	[°]	1.00	0.88	0.99	0.99	0.94

TABLE III
FUNDAMENTAL GBMA AT $668GHz$

$f = 668GHz$		Experimental $0P$	Experimental $1P$	Software $0P$	Software $1P$	Expected
Gaussucity,	[%]	98.56	98.66	98.16	97.97	~ 98
w_0,	$[mm]$	2.82	2.74	2.70	2.70	2.67
x_{Offset},	$[mm]$	0.10	0.28	0.00	-0.09	0.00
y_{Offset},	$[mm]$	2.58	2.86	2.44	2.44	2.46
θ_x,	[°]	0.06	0.02	0.00	0.13	0.00
θ_y,	[°]	1.02	0.94	0.98	0.98	0.94

beam that best fits E_m. In table II and III the results of this procedure are shown for the two measured and simulated data set at 606 and $668GHz$. If instead we consider what the ideal beam should be at the FP location, we find the power coupling efficiency between E_m and G. By setting the offsets in such a way they describe the nominal fundamental Gaussian beam at the FP for a certain frequency, we obtain coupling efficiencies shown in table IV. The values of waist at the FP come from the ABCD analysis at the chosen frequencies. However if we leave only z_{Offset} free to vary, we found a value of z_{Offset} that tell us what is the defocusing along the telescope axis, of E_m with respect to the location of the nominal fundamental Gaussian at the FP waist position. In table V we list the defocousing of the measured and simulated beams at the FP. Such levels of defocuosing are not be worrying since as pointed out in [3], by means of repositioning the secondary mirror of the Cassegrain system, it is possible to bring the efficiency back to optimal levels.

C. Cryostat window effects

One of the big concerns in coupling the feed beam with the telescope is in fact its passage through the cryostat window. This window usually has to be as small as possible to avoid scattering of ambient temperature radiation into the receiver.

TABLE IV
COUPLING WITH THE NOMINAL GAUSSIAN AT THE FP, [%]

f, $[GHz]$	nominal w_0, $[mm]$	Experimental $0P$	Experimental $1P$	Software $0P$	Software $1P$
606	2.96	97.84	95.90	98.14	97.65
668	2.67	97.73	95.46	98.11	97.64

TABLE V
DEFOCUSING AT THE FP, $[mm]$

f, $[GHz]$	Experimental $0P$	Experimental $1P$	Software $0P$	Software $1P$
606	1.4	1.7	1.6	0.3
668	-1.4	-0.3	1.1	0.1

As a first attempt to investigate the effects of the cryostat window we carried out a measurement with a circular aperture at the cryostat window location. The aperture diameter was $20mm$ and centered $150mm$ from $M3$ chief ray intersection point. In figure 4 is shown the comparison between experimental measurement and software result for the $1P$ polarization, obtained introducing such kind of aperture in the GRASP8© model. Despite the simplified experiment, it is clear that the window aperture in itself does not introduce noticeable diffraction effects on the main beam.

VI. LO POWER BUDGET

One of the features of GRASP8© is the ability to give the power spill-over efficiency at each of the scatters through the signal path. The Co-P linear polarized electric field at the LO diagonal horn aperture plane using equation (7.52) of [7]. Propagating this field from the diagonal horn aperture through $M4$, $M5$ and the Beam Splitter (BS) we obtain the total path spill-over and the field distribution of the LO signal at the mixer horn aperture. The BS is a thin slab of Mylar ($13\mu m, n = 1.73$). The power reflection coefficient was calculated at the frequencies of 600, 660, $720GHz$ (average of 6%), considering that the LO signal is perpendicular to the plane of incidence. Thus after spill-over and reflection at the BS, the LO signal reaches the mixer horn aperture with a certain aperture efficiency. Finally, with an average LO power at the diagonal horn aperture of $40\mu W$, we show in table VI what is the level of LO power arriving at the mixer horn aperture. These power levels are sufficiently high to pump the mixer, since its minimum power level requirement is about $0.5\mu W$. Furthermore, slight misalignments of the LO optics could be also tolerated.

TABLE VI
TOTAL LO POWER REACHING THE MIXER HORN WITH $40\mu W$ INPUT POWER. $[\mu W]$

f, $[GHz]$	$0P$	$1P$
600	1.84	1.84
660	2.21	2.21
720	2.61	2.61

VII. FURTHER WORK AND CONCLUSION

In this paper we analyzed the optical coupling system for the ALMA band 9 front-end. Experimental and simulated data agree very well. The field distribution (both intensity and

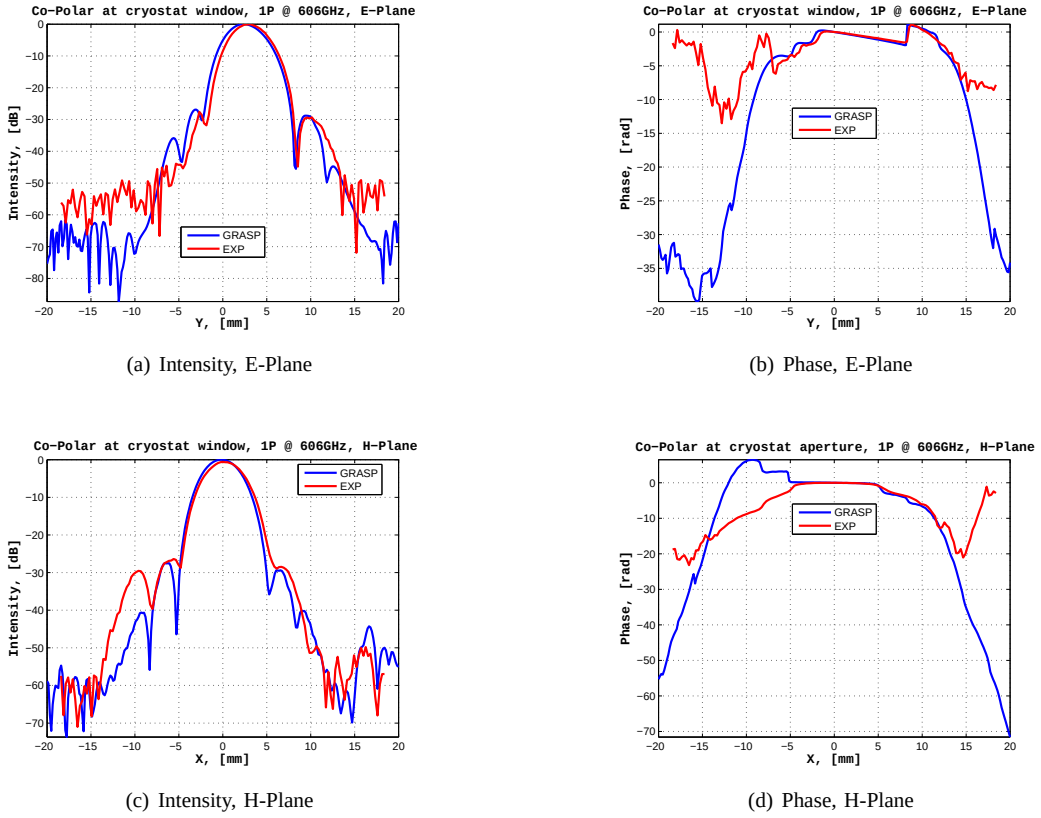

(a) Intensity, E-Plane

(b) Phase, E-Plane

(c) Intensity, H-Plane

(d) Phase, H-Plane

Fig. 4. Experimental and software data comparison of the $1P$ polarization signal at $606GHz$ after passing through the Cryostat window. Intensity and phase at E- and H- plane. Measured plane at $155mm$ from the chief ray incident point on $M3$.

phase) have been calculated and compared for the two polarization configurations. From visual comparison it is evident that the measured beams does not suffer from mechanical strut diffraction effects, since the beam shapes resemble the simulated ones. A fundamental Gaussian beam mode analysis was carried out, indicating that the beams are behaving as expected, maintaining a good level of power coupling efficiency with the nominal fundamental Gaussian at the FP. A slight defocusing effect was illustrated, but within the range of tolerance which can be corrected by movement of the secondary along the telescope axis. The LO beam guide was analyzed to deduce the level of LO signal power effectively reaching the mixer horn aperture. The overall analysis shows that the optical coupling system is working properly respecting the design specification in order to be coupled with the Cassegrain antenna. It was not shown here, but it has been seen that both $0P$ and $1P$ signals are reaching the secondary with the required edge taper of $12dB$, as well as a cross-polar level at the FP less than $20dB$. The telescope coupling efficiency evaluation and further analysis of the beams coming out from the cryostat window will be part of the next phase of work in assessment of the ALMA band 9 optical front-end.

ACKNOWLEDGMENT

The authors would like to thank the European Southern Observatory (ESO) for financing the ALMA band 9 receiver development.

REFERENCES

[1] A. Baryshev, M. Carter, W. Jellema, R. Hesper, *Design and evaluation of ALMA band 9 quasi-optical system*, Proc. of the 5^{th} Int. Conf. on Space Optics, 30 March - 2 April 2004, Toulouse, France. Ed.: B. Warmbein. ESA SP-554, Noordwijk, NetherlandsL ESA Publication Division, ISBN 92-9092-865-4, p. 365-371.

[2] A. Baryshev, M. Carter, M. Candotti, N. A. Trappe, J. A. Murphy, *Verification of the optical design for band 9 of the ALMA receiver*, Proceedings of the 29^{th} Int. Conf. on Infrared and Millimeter Waves and 12^{th} Int. Conf. on THz Electronics, Univ. of Karlsruhe, Karlsruhe (Germany), Sep. 27 - Oct. 1, 2004.

[3] A. Baryshev, W. Wild, *ALMA band 9 optical layout*, ALMA Memo 394, September 2001.

[4] M. Candotti, G. Cahill, T. Finn, W. Jellema, J. Lavelle, J. A. Murphy, C. O'Sullivan, N. A. Trappe, *Quasi-Optical Verification of the Focal Plane Optics of the Heterodyne Instrument for the Far-Infrared (HIFI)*, Proc. of the SPIE Astronomical Telescopes and Instrumentation Symposium, 21 - 25 June 2004, Glasgow, Scotland (UK).

[5] A. D. Olver,P. J. B. Clarricoats, A. A. Kishk and L. Shafai, *Microwave Horns and Feeds*, IEEE Press, 1994.

[6] J. A. Murphy, R. Colgan, C. O'Sullivan, B. Maffei, P. Ade, *Radiation patterns of multi-moded corrugated horns for far-IR space applications*, Infrared Physics and Technology, Vol. 43, p. 515 - 528, 2001.

[7] P. F. Goldsmith, *Quasioptical Systems: Gaussian beam quasioptical propagation and applications*, IEEE Press, New York, 1997.

STEAM (Stratosphere-Troposphere Exchange And climate Monitor)

A. Emrich, Omnisys Instruments AB, Gruvgatan 8, 421 30 Göteborg, Sweden

ABSTRACT

Mankind's influence on the atmosphere of the planet Earth has expanded in recent decades from the local scale of urban pollution to global scale effects such as the ozone hole. Global problems require global monitoring and global solutions.

The widespread use of 3D-models for predicting the effects of future changes in the atmosphere necessitates validation of the models with measurements.

STEAM is an explorer concept that can provide a unique global data set in the region 5-25 km by measuring, simultaneously, target species such as O3, H2O, ClO and CO within a very fine vertical grid (1-2 km) and a fine horizontal grid along the satellite track (30-50 km).

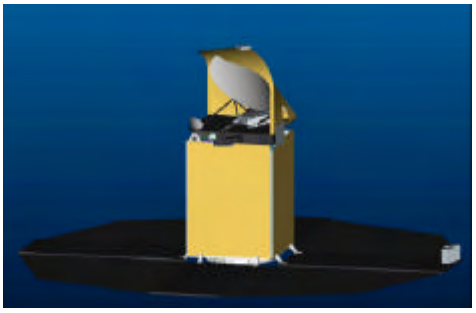

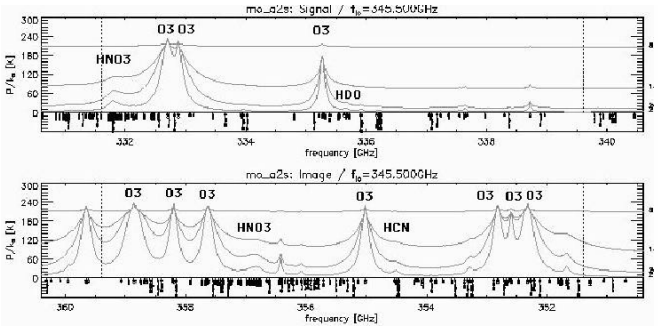

STEAM will measure molecular thermal emission spectra at sub-millimetre wavelengths. The instrument consists of a telescope that views thermal emission from the atmospheric limb imaged by a small linear array of receivers in the instrument platform. The incoming radiation from the Earth's limb is down converted in each mixer and amplified in low noise amplifiers. Spectrometers measure the spectral power density across each band.

Compared to Odin we do not foresee a need for power demanding active cooling and fundamentally pumped mixers. This makes it possible to build a very much-simplified system with mixers directly fed by the telescope and pumped via wave-guides. It is then possible to build a multi-beam system and use novel tomographic methods to overcome one major limitation of the current limb-scanning technique — the poor horizontal resolution.

The efficacy of topography has been successfully demonstrated using the Odin near-IR limb imager. To keep the crowding of the focal plane reasonable, not more than 8-12 mixers will be used. The reduction in sensitivity due to a non-optimum mixer configuration is compensated by the increase in integration time enabled by multiple mixers

The STEAM instrument will be presented on system level and key subsystems will be described in detail.

The same technology can meet the requirements for other proposed instruments, such as MASTER, CIWSIR and MAMBO. Implementations concepts for these instruments will also be presented.

Terahertz transmitted spectral imaging for some drugs

Cunlin Zhang , Zhenwei Zhang
Department of physics，Capital Normal University
Xisanhuan Beilu 105, 100037 Beijing, China

Abstract

THz wave imaging is a new and promising technology for non-destructive testing. Due to the most drugs have several or one at least own absorption frequency at 0.2~2.5THz, THz imaging will be become a power method for drug inspecting. In this paper, some drugs, such as heroin, cocaine and so on, are inspected and imaged. Due to the diversity of samples and the complicacy of surroundings of hiding samples in the practical applications, several signal processing approaches based on classical transmitted scanning imaging setup and Fourier transformation are adopted to exact inspect hiding samples, including time-domain maximum-amplitude （minimum-amplitude） imaging, time-domain peak-to-peak amplitude imaging, time-domain time delay imaging, frequency-domain fixed frequency amplitude(power) imaging, as well as frequency–domain fixed frequency phase imaging, are discussed and compared. The results indicate that imaging making use of drug’s finger spectrum at terahertz band is a promising and applied method for drug inspecting.

Keywords: Terahertz, THz imaging, image processing, drug

The Band 7 Cartridge (275-373GHz) for ALMA

S.Mahieu, B.Lazareff, D.Maier, M.Carter, and S.Claude

IRAM, Grenoble, France

The ALMA frontends are designed for ten frequency bands, of which four are currently budgeted. Each frequency band is implemented as a dual-polarization modular cartridge. IRAM is responsible for designing the Band 7 cartridge covering the signal frequency range 275–373 GHz, and for building 8 pre-series units. The cartridge must meet a number of specifications, including SSB noise temperature less than 133K, but also total power stability, optical beam coupling, etc…

The Band 7 cartridge comprises, within a cylindrical support structure, several elements:

- Cold refocusing optics, including polarization diplexing;
- Two sideband separating mixer units, reported separately in this Conference;
- Four intermediate frequency amplifiers (4–8 GHz), designed by Centro Astronómico de Yebes;
- Two cryogenic frequency triplers (VDI);
- Bias circuits.

We will present some key design issues, notably the optics, and experimental results.

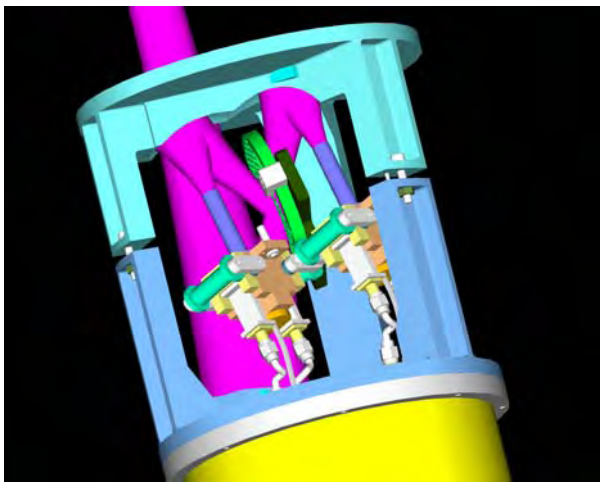

Left: The complete cartridge. Right: A CAD rendering showing the 4K part of the cartridge: optics, mixers, signal beams; one part has been removed for clarity.

Biochemical sensing application of photonic crystal based devices in the far-infrared regime

Hamza Kurt[a)] and D. S. Citrin[a,b)]
[a]School of Electrical and Computer Engineering, Georgia Institute of Technology, Atlanta, Georgia 30332-0250
hkurt@ece.gatech.edu
[b]Georgia Tech Lorraine, Metz Technopole, 2-3 rue Marconi, 57070 Metz, France

Peculiar properties of PC open up the potential applicability of them for bio-sensing purposes. We carried out electromagnetic simulations of two-dimensional photonic-crystal waveguide (PCW) and coupled-resonator optical waveguide (CROW) structures created by changing the radii of air holes in a given row to investigate the effects in the terahertz region of the electromagnetic spectrum of introducing small quantities of molecules, such as DNA, in the air holes. The terahertz interaction with the analyte is modeled as a Lorentz medium. The finite-difference time-domain method with recursive convolution is used for numerical analyses. Low group velocity around the photonic band edge and electric-field enhancements in the low-index medium enable significantly enhanced interaction of guided light with the molecular sample. The sensitivity dependence on the CROW structure parameters, such as intercavity distance and cavity type (donor/acceptor), is investigated for the effects in the terahertz region of the electromagnetic spectrum of introducing small quantities of molecules in the air holes. Introducing the absorptive material into the low-index medium greatly affects the shape of the propagating modes of the CROW and the transmitted electric field. The shift of the resonant frequency also depends linearly on the refractive index changes for off-resonant case (dispersive effect). The proposed device is predicted to exhibit sensitivity enhancement over bulk systems and requires a small analyte volume of picoliters.

The spectroscopic change in the transmission spectrum with the sample inserted into the air holes in the waveguide region is monitored to ascertain the effect of and the direct electromagnetic-matter interaction. The guided propagating signal interacts with the dispersion and absorption of the photonic crystal (PC) containing the biological material, which provides the sensing mechanism. The long effective path length over which the terahertz pulse interacts with the biological material was ensured without increasing the actual structure size by ensuring that the propagating mode in the band gap region has low group velocity. Moreover the field was confined largely within the holes where the biological material is placed.

Based on our detailed simulations (results will be presented in the conference), PCW's and CROW for bio-sensing applications are found to be promising. Low group velocity and localization of light in these structures result in enhanced terahertz absorption by DNA molecules (the specific example treated in this study) within the low refractive index medium. Compared with the freespace (bulk) approach, device size can be reduced dramatically, less sample material is needed, and an integrated system can be made with PC's; hence, different molecules could be analyzed simultaneously.

Compact Optical Assemblies for Large-Format Imaging arrays

G. Yassin, S. B. Sørensen, and P. K. Grimes

Abstract—

Compact telescopes with ~1m diameter primary, have recently been employed in the Cosmic Microwave Background (CMB) investigations. Some of these telescopes are designed to measure the CMB polarization at an angular scale of a few arcminutes. Considering that the polarization signal is extremely weak, the radiation pattern needs to be circular, with very low cross polarization. In this paper, we compare the performance of two compact dual-reflector systems, fed by a relatively large focal plane array, at millimetre wavelengths. We consider the case where the apertures of the feeds are forced to lie on a planar surface, allowing only the central feed to be exactly on focus. This geometry is chosen in order to make the fabrication of the feed array block easier. Our simulation show that Compact Range Antenna (CRA) has a much better performance than the more commonly employed offset Gregorian configuration. We illustrate that the CRA provides a circular beam with extremely low cross polarisation, even when the antenna is fed by more than 200 feeds, at 90 GHz.

I. Introduction

The effort to increase the sensitivity of astronomical receivers is an important on-going research activity and considerable effort has already been invested to improve the performance of the single pixel detector. Recent advances in detector technology led to the development of detectors with background- limited sensitivity. Additional sensitivity therefore can only be achieved by increasing the number of detectors.

A recent motivation for further performance improvement, came from the emergence of new Cosmology instruments that attempt to measure the CMB polarization. The sensitivity of these instruments needs to be two orders of magnitude better than existing CMB anisotropy telescopes in order to detect the B-mode component, which is the signature of primordial gravitational waves [1]. Several instruments are now being designed or built including PLANCK, BICEP, EBEX, QUAD and CLOVER [2]. Although the design strategy and frequency coverage of these instruments differ substantially, they all have a key common feature: they employ a focal plane detector array feeding a compact optical assembly. Consequently, a lot of care is needed in designing the optics since the beams formed by the feeds at the edges of the array can exhibit high sidelobes, cross polarization and distortion by aberrations.

In this paper, we compare the performance of two offset compact optical assemblies that have been considered for large format imaging arrays, at millimetre and submillimetre wavelengths. The first is the Compact Range Antenna (CRA), which has a concave hyperboloidal subreflector and the second is the Gregorian that has an ellipsoidal subreflector. Each assembly has a parabolic primary and is fed by approximately 200 corrugated feeds array at 90 GHz.

The radiation pattern of each antenna will be analysed employing the rigorous Physical Optics (PO) method as implemented in the software package GRASP. In each case, the design parameters will be optimised for minimum cross-polarization and beam distortion by forcing the Mizuguchi condition.

II. Method of Design and Analysis

A. The Physical Optics Method

The Physical Optics method is a powerful tool in computing scattering from reflectors of finite conductivity. The method is now commonly employed in both the analysis and design of antennas and complex optical systems that comprise several reflectors. Calculation of the radiated fields is done in two steps:

1. Find the equivalent currents induced on the reflector surface.
2. Calculate the fields radiated by those currents.

The total field at any point may be written as the sum of incident and scattered fields:

$$\mathbf{E} = \mathbf{E}^i + \mathbf{E}^S$$

The induced current in PO, are found assuming that only the geometrically bright region is illuminated by the sources.

For a perfect conductor, the tangential component of the electric field vanishes on the reflector surface hence the induced current at any point is given by:

$$\mathbf{K}^{PO} = \begin{cases} \mathbf{n} \times \mathbf{H} = 2\mathbf{n} \times \mathbf{H}^i & \text{on illuminated surface} \\ 0 & \text{on the Shadow surface} \end{cases}$$

$$\mathbf{K}^{*PO} = 0 \quad \text{Everywhere}$$

G. Yassin is with the Sub-dept. of Astrophysics, University of Oxford, Denis Wilkinson Building, Keble Road, Oxford, OX1 3RH, UK. (e-mail: ghassan@astro.ox.ac.uk).

S. B. Sørensen is with TICRA Engineering Consultants Læderstræde 34DK-1201 Copenhagen Denmark (e-mail: sbs@ticra.com).

P. K. Grimes is with the Sub-dept. of Astrophysics, University of Oxford, Denis Wilkinson Building, Keble Road, Oxford, OX1 3RH, UK. (e-mail: pxg@astro.ox.ac.uk).

where $\mathbf{K}^{PO}$ and $\mathbf{K}^{*PO}$ are respectively the electric and magnetic current densities, $\mathbf{H}^{i}$ is the incident magnetic field on the reflector and **n** is a unit vector normal to the surface. The above expression was derived by asuming a tangential plane at the point of interest and using the images method.

Following the calculation of the current at any point on the geometrically illuminated surface, the fields at any point can be found by re-writing the fields from Maxwell equations using the equivalence method:

$$\mathbf{E} = \mathbf{E} + i\omega\mathbf{A} - \frac{\nabla\nabla.\mathbf{A}}{i\omega\varepsilon\mu}$$

$$\mathbf{H} = \mathbf{H}^{i} + \frac{1}{\mu}\nabla \times \mathbf{A}$$

where **A** is the electric vector potential given by:

$$\mathbf{A} = \frac{\mu}{4\pi}\iint \mathbf{K}^{PO}\frac{e^{ikR}}{R}dS$$

in the above expression $R = |\mathbf{r} - \mathbf{r}'|$ where r is the observation point, r' is the integration variable over the surface and the integration is carried out over the illuminated surface.

It is worthwhile noting that while the radiated fields by the currents are calculated exactly, the induced currents themselves are found using two approximations, first by assuming that the geometrical shadow region does not radiate (which is clearly untrue) and then by neglecting the current non-uniformity near the edges. It turns out however that for apertures of several wavelengths across, the Physical Optics method is extremely reliable in both far- and near-field calculations [3]. Moreover, for very small apertures, the PO method can be supplemented by the Physical Theory of Diffraction correction (PTD) [4], to yield very accurate results in practical systems.

B. Design Hints

Offset parabolic systems normally have poor cross polarization performance and high aberrations. In dual reflector systems, therefore it is common to compensate for that by forcing the Mizuguchi condition:

$$\tan\left(\frac{\psi_f}{2}\right) = M_0 \tan\left(\frac{\alpha}{2}\right)$$

where Ψ_f is the angle between the feed and subreflector axes, α is the angle between the axes of the two reflectors and M_0 is given by

$$M_0 = \frac{e+1}{e-1}$$

Where *e* is the eccentricity of the subreflector.

Another constraining quantity is the effective focal length given by:

$$f_e = fM_0\frac{1+\tan^2\left(\frac{\alpha}{2}\right)}{1+M_0^2\tan^2\left(\frac{\alpha}{2}\right)}$$

Where *f* is the focal length of the main reflector. In what follows we shall describe our effort to design a CRA for CLOVER. Here, the feeds in the array are all pointing orthogonal to the telescope beam imposing the condition:

$$\alpha + \psi_f = 90^{\circ}$$

The actual choice of the two angles depends on the system design and an example of that is given in Fig. 1 with the requirements of primary diameter of 1.6 m at 90 GHz.

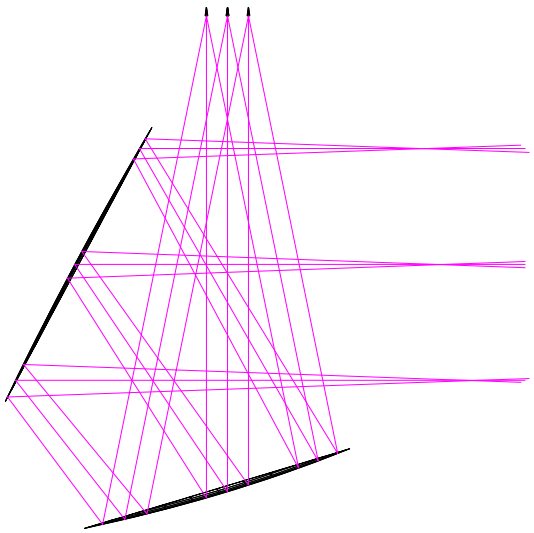

Figure 1 GRASP ray tracing of a CRA illuminated by three feeds in the plane of asymmetry (x-z plane).

Taking a ratio $f_e / D \approx 2$ which is typical for this system, we have α = -65 and *e* = -2.06748. The design of the system was then taken from the optimised ratios: $f/D = 4.5,\ 2c/D = 6.3$

The final design parameters are given in Table 1.

Primary diameter (D)	1.6 m
Primary focal length (*f*)	7.2 m
Eccentricity of subreflector (e)	-2.06748
Distance between foci of subreflector (2c)	10.08 m
Angle between feed and subreflector axes (ψ_f)	25°
Angle between primary and subreflector axes	65°

Table 1: Design parameters of the CRA system

III. Simulated Results

The following simulations were made for a hexagonal array of 216 corrugated horns illuminating the CRA described in Table 1. Each feed is assumed to have a Gaussian beam with an edge taper of 14.4° at –12 dB. This corresponds to a feed aperture diameter of about 18 mm. Assuming a feed wall thickness of 1.25 mm, the outer feed centre will be located at 164 mm away from the centre of array. Below, is a GRASP simulation pattern of the central feed showing the E-plane and the H-plane cuts, as well as the cross polarization.

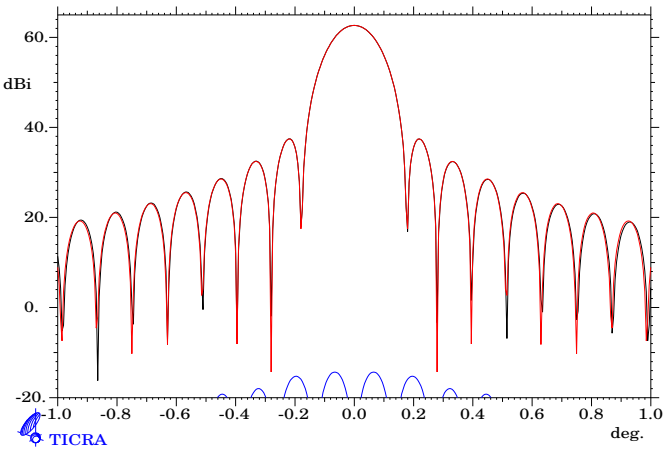

Figure 2: Radiation pattern of the CRA when illuminated by the central feed at 90 GHz. Notice that Notice that the E and H-planes are identical and that the cross polarisation is below –70 dB.

Next we compare the radiation patterns resulting from the outer feeds along the axis of symmetry (y-axis) and asymmetry (x-axis). The results are shown in Fig. 3.

Notice that the cross polarisation level has now risen to just below –40 db and that the main beam is no longer circular below approximately –20 db. However, the level of cross polarisation and beam distortion remain acceptable considering that the feed apertures are not exactly located in the focal plane. We should emphasize however that the shift of the centres in the top patterns of Fig. 3 is the result of misalignment in the cut coordinate system orientation and hence should be ignored.

Finally we compare the performance of the CRA with the Offset Gregorian antenna, which is employed in PLANCK. A ray diagram of the system is shown in Fig.4. The design parameters of this antenna were taken from "GRASP Technical Manual" and are shown in Table 2.

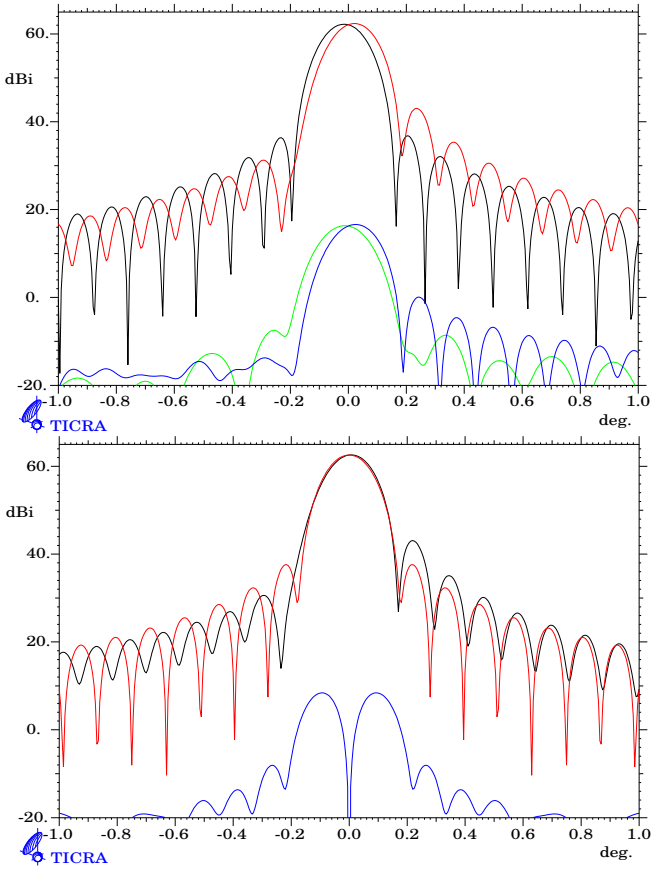

Figure 3: Radiation pattern of the CRA when it is illuminated by the outer feeds, 164 mm away from the centre in the y-direction (top) or in the x-direction (bottom). This corresponds to a hexagonal array of 217 feeds.

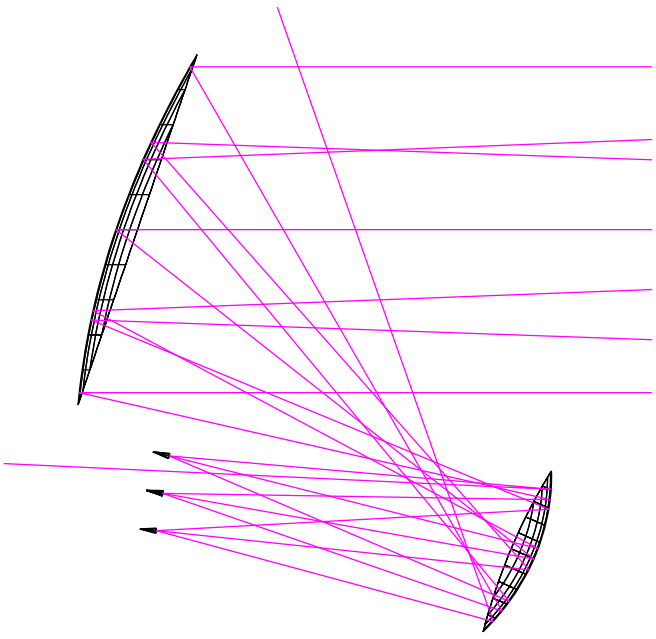

Figure 4: GRASP ray tracing of the offset Gregorian antenna.

Frequency	90 GHz
Primary diameter (D)	1.6 m
Primary focal length (f)	1.6
Eccentricity of subreflector (e)	0.5
Distance between foci of subreflector (2c)	1.2 m
Angle between feed and subreflector axes (ψ_f)	-14.92°
Angle between primary and subreflector axes	5°

Table 2: Design parameters of the CRA system

We recall that in the CRA, the outer feed scanned the beam by 2.8 degrees. Since the F/D ratio for the GRA is 2.96 the outer feed needs to be located at 231 mm from the centre in order to have the same scan angle. Another way of looking at it is to require that the two antennas have the same beamwidth. For that to happen, we need to under-illuminate the GRA by the effective focal lengths ratio. This requires horns of larger aperture diameter by approximately the same ratio, and hence the outer feed will be further displaced by the distance quoted above. The feed opening angle towards the subreflector is now smaller, giving a taper of -12 dB at 9.7 degrees. The simulated pattern of this system is shown in Fig. 5. Her we can easily see that the circularity of beam is no longer satisfactory and that the cross polarization level has risen to -35 db. This is despite the fact that the outer feeds were only shifted by 173.2 mm instead of 231 mm (to have the same number of feeds as the CRA) and that those feeds were also tilted towards the centre in order to have a reasonable spill-over (as can be seen from Fig. 4).

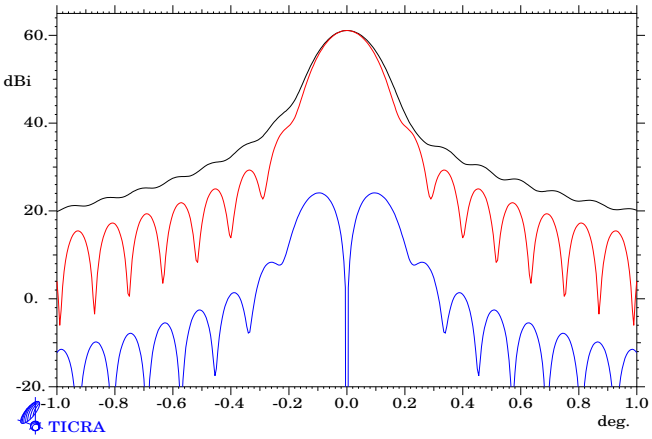

Figure 5 (a): Simulated beam patterns for the offset Gregorian system with the feed shifted 173.2 mm in the x direction

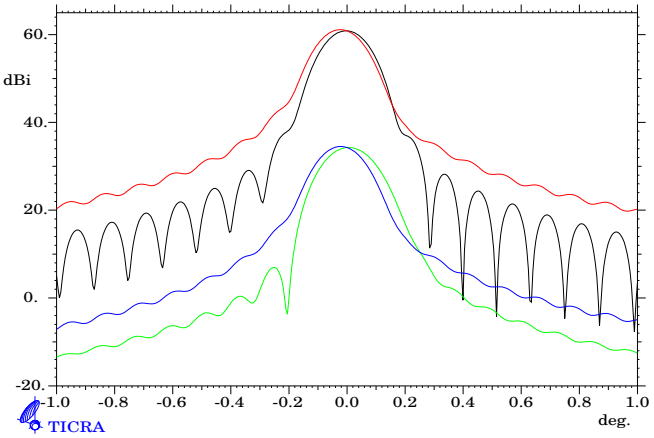

Figure 6 (b): Simulated beam patterns for the offset Gregorian system with the feed shifted 173.2 mm in the y direction

IV. Conclusions

We investigated the performance of compact optical assemblies when fed by a large focal plan arrays. Our simulations show that for a typical CMB telescope operating at 90 GHz and a –3db full beamwidth of 8.4 arcminutes, the Compact Range Antenna gives excellent performance even when the array is not exactly located on the focal surface. The Gregorian system however, does not seem to be suitable for large beam scanning.

References

[1] W. Hu and M. White, astro- ph/9706147, (1997)

[2] Johansen. P. M, (1996): "Uniform Physical Theory of Diffraction equivalent edge currents for truncated wedge strip, " IEEE Trans Antenna Propagat. Vo. 44, no. 7, pp. 989-995.

[3] Yassin, G., Ade, P. A. R., Calderon, C., Challinor, A. D., Dunlop, L., Gear, W. K., Goldie, D. J., Grainge, K. J. B., Griffin, M. J., Jones, M. E., Lasenby, A. N., Maffei, B., Mauskopf, B. P. D., Melhuish, S. J., Orlando, A., Piccirillo, L., Pisano, G., Taylor, A. C., and Withington, S., (2004): `` CLOVER: The CMB Polarization Observer)'' To appear in the proceedings of the 15th International Symposium on Space Terahertz Technology, April 27-29, UMASS, USA

[4] Yassin, G., Withington, S., O'Sullivan, C., Murphy, J. A., Peacocke, T. P. Jellema, W. and Wesselius, P. R., (2002): ``Electromagnetic modelling of submillimetre-wave systems," To appear in the Proc. 14th International Symposium on Space Terahertz Technology, 26–28 March, Harvard-Smithsonian Centre for Astrophysics, USA

.

A Prototype Terrestrial Terahertz Imaging System

Ric Zannoni, K.S. Yngvesson, F. Rodriguez-Morales, J. Nicholson, D. Gu, E. Gerecht,

***Abstract*—Interest in alternative imaging, with an emphasis on medical and security applications, is increasing. The terahertz spectrum is beginning to be explored for these applications. A prototype scanning imaging system is described here. This system currently operates at 1.6 THz and uses a HEB as a heterodyne detection element. Object scanning is accomplished by using an oscillating mirror running at 8 Hz with a scanning angle of 30º. Theoretical calculations for this system yield a thermal resolution of better than 0.5 K with an integration time of 1 ms. This calculation is based on a system noise temperature of 1000 K at the image and neglects the effects of system gain fluctuations. At this time, the system's RMS thermal noise level is 1 K with an integration time of 1 second. A major component of the system is IF gain stabilization through active LO power control. Currently, the LO power control is under development. Completion of this subsystem is likely to greatly enhance thermal resolution. Further improvements--specifically, faster scan rates optimized to the stabilized IF output--can then be pursued.**

***Index Terms*—HEB, hot electron bolometer, THz, terahertz, imaging.**

I. Introduction

For the purposes of the prototype imaging system described here, terahertz (THz) video imaging is defined, minimally, as scanning a 1 m x 2 m object with 20 mm resolution at a rate of 10 frames per second. Under these criteria, hot electron bolometer (HEB) heterodyne systems have advantages over other systems. For example, in terahertz time domain spectroscopy (THz-TDS), video imaging is currently not possible due to limitations of delay line speed and difficulties in forming arrays. With these limitations, THz-TDS systems produce an image in a time on the order of minutes [1].

A 640 GHz imaging system was recently demonstrated that used Schottky diode mixers [2]. Schottky diode mixers require a LO power on the order of 1 mW, which makes this system impractical for the multi-pixel arrays needed to achieve video rate imaging. Conversely, the LO requirement of an HEB mixer is on the order of 1 μW, which is well-suited for the arrays needed in a video rate system. Schottky direct detectors have to contend with large 1/f noise [3]. Room-temperature niobium (Nb) direct detectors have an RMS noise-equivalent input temperature fluctuation level (NEΔT) of about 100K [4] with an integration time of 100 ms. Current HEB technology yields an NEΔT of 0.5 K with an integration time of 1 ms. These values assume that the contributions from gain fluctuations are small. The system proposed here actively compensates for these fluctuations on two levels.

R. Zannoni, K. S. Yngvesson, F. Rodriguez-Morales, J. Nicholson, and D. Gu, are with the Department of Electrical and Computer Engineering, University of Massachusetts, Amherst

E. Gerecht is with the National Institute of Standards and Technology, Boulder CO, and with the Department of Electrical and Computer Engineering, University of Massachusetts, Amherst

.

II. Referenced Line Scanning Imager

A. Overview

The Referenced Line Scanning Imager (RLSI) under development at University of Massachusetts—Amherst (UMASS) combines techniques from many disciplines into a unique arrangement. The system is diagramed in Fig. 1. A multifaceted rotating mirror, producing one scan per facet, scans the object. Between the facets are reference loads used for real-time calibration. The thermal radiation from the object is combined with the LO, produced by a gas laser, and is mixed at the HEB array. The HEBs are constant voltage biased, and the current is stabilized with the LO. The signal from the reference load controls the back-end gain.

B. Rotating Mirror and Optics Configuration

The specifications for the system given in the introduction require that we detect radiation from 100 (vertical) x 50 (horizontal) pixels. The HEB array is oriented horizontally, and the rotation of the mirror scans the object vertically, producing signals corresponding to 100 pixels from each array element in each scan. The number of array elements determines the number of vertical scans required. We propose a linear array of 25 elements. We would first scan the 25 horizontal pixels in the left half of the object, and then the 25 pixels in the right half. Thus, two scans will cover the entire image. To achieve the alternating left/right scans, alternating facets of the rotating mirror are at offset angles in the horizontal plane. A 30-degree field width requires a 15-degree mirror angle articulation. Therefore, a mirror with 24 facets at alternating angles could be employed. The scanning action is rotational rather than reciprocating, making very high scan rates achievable. This leaves open the possibility of multiple scans per frame. The system uses as a reference a square wave with a period of T_{ref} equal to the frame rate (100 ms) divided by the number of vertical pixels (100). The mirror rotation is locked to this reference. Between each facet is a black body reference load. The signal from the reference is used to normalize the pixels and stabilize the back-end gain.

There are also focusing elements (offset paraboloidal mirrors) between the object and the HEB (not shown). In a future system capable of imaging at greater distances (say 25 meters) the rotating mirror would be positioned near the focus of a Cassegrain reflector system with sufficiently large main reflector diameter to produce the required resolution of 20 mm on the object.

C. HEB Bias

The HEB mixer uses a constant voltage bias. The bias current is sensed and sent to a proportional integral derivative (PID) control. The error signal from the PID

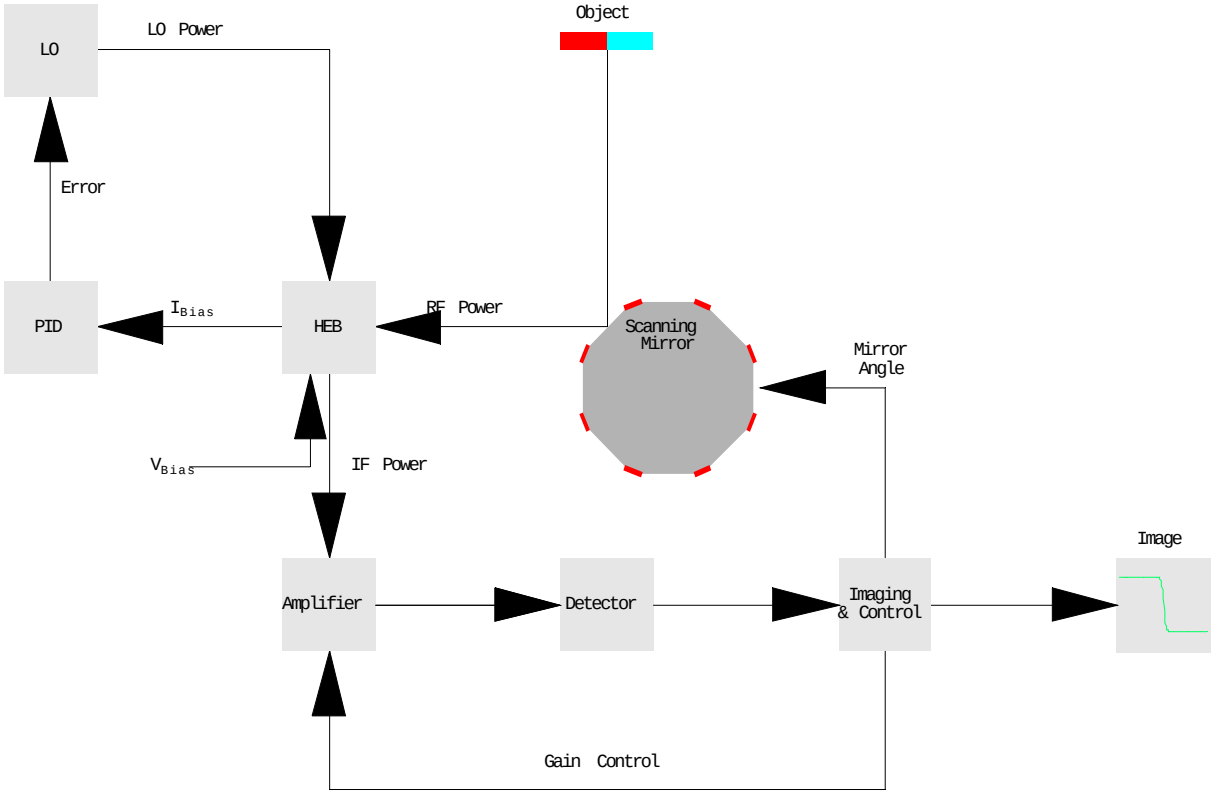

Figure 1. Block diagram of the proposed Reference Line Scanning Imager

control trims the LO power. An acousto-optical modulator in the FIR pump beam controls the LO power. The PID time constant is 1 ms, which effectively stabilizes the bias point during scanning.

D. Demodulation

All pixel levels are simultaneously demodulated from the raw signal of the detector. Each pixel is demodulated as follows. From the T_{ref} signal a pulse is produced with positive width equal to T_{ref}. This pulse has a phase shift appropriate for the pixel. A product is formed between the raw signal and the pulse. The difference between this product and the level from the reference load is the pixel level. The signal from the reference load is leveled by a feedback loop with the back-end amplifier gain. The image size is 100 pixels x 50 pixels, containing a total of 5,000 pixels. With a 25-element array, an integration time of 0.5 ms is afforded. This integration can be an average of multiple scans or a single scan. Current HEB technology can achieve a noise temperature of 1,000 K with a bandwidth of 4 GHz. By the radiometer formula, an RMS input noise level of 0.7 K is expected. With an average image temperature of 300 K, this is a signal-to-noise ratio of better than 400:1. This is an improvement by a factor of four over a much slower photomixing technique used by Siebert, *et al.* [4]. Their 3,072 pixel image forms in about 11 minutes with a signal-to-noise ratio of 100:1.

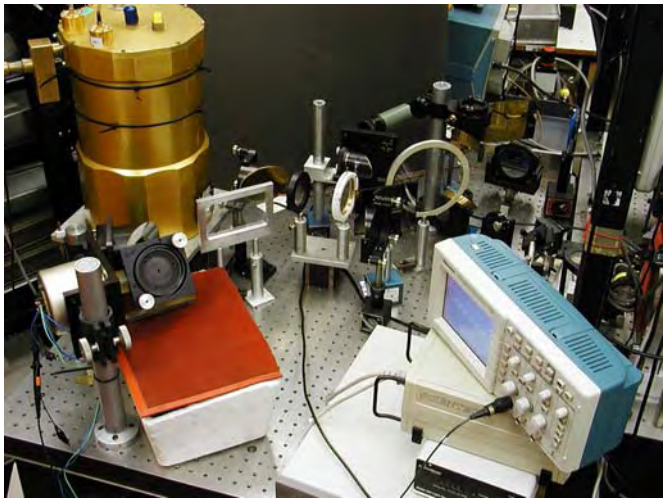

Figure 2. Photograph of current prototype imager.

III. Current Prototype

A. Description

The currently operating prototype is a test bed for many of the systems in the RLSI. The optical design is pictured in Fig. 2 and can be explained with reference to Fig. 3. In this single element system a line of the image is scanned

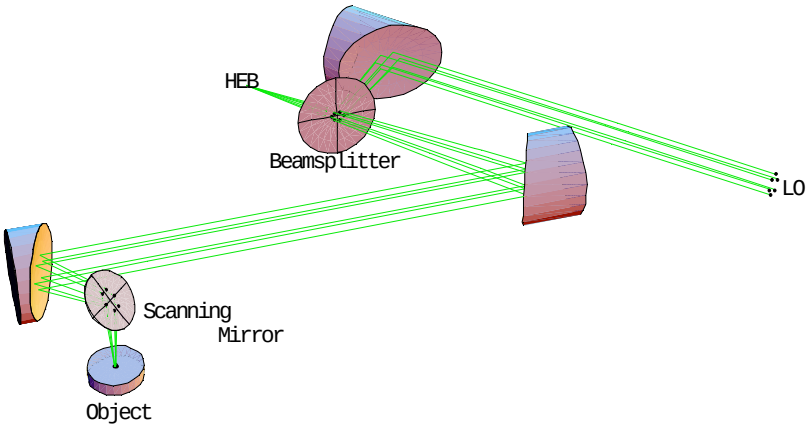

Fig. 3 Optical diagram for the prototype imager.

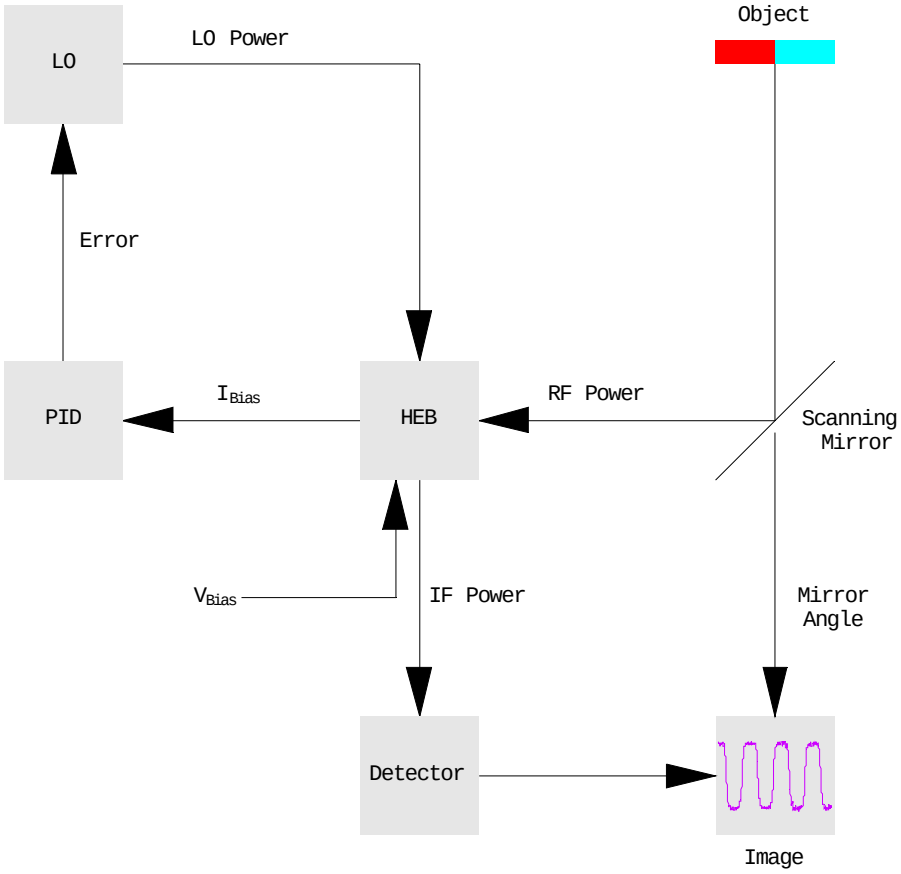

Figure 4. Block diagram showing signal processing for the prototype imager.

with an *oscillating* mirror running at 8 Hz. The mirror is driven with a triangle wave, which also triggers the sweep of the digitizer (Tektronix Digitizing Oscilloscope type 11403A), where the image of the line scan is formed. The scan angle is 30 degrees. The imaged area is a 50 mm line approximately 100 mm from the oscillating mirror. Signal processing is diagrammed in Fig. 4 and described as follows. The amplified IF signal from the HEB covers a bandwidth of 0.5 GHz to 4 GHz, and is rectified with a standard microwave detector. This signal is low-pass filtered to the pixel acquisition time and then applied to the vertical input of the digitizer. The digitizer then averages over a set

number of sweeps. The HEB current lock is currently being tested.

B. Results

The measured noise temperature of the HEB used in this system was 3,500 K at the image. We employ an HEB integrated in a mixer block, with an MMIC IF amplifier similar to the elements we used in the focal plane array described in [6]. At the time the images presented here were recorded, the HEB current lock had yet to be integrated. Nevertheless, the results from this simplified system are encouraging. In Fig. 5, an integration time of 1 s is used to image a transition from an absorbers at 280 K to one at 77 K.

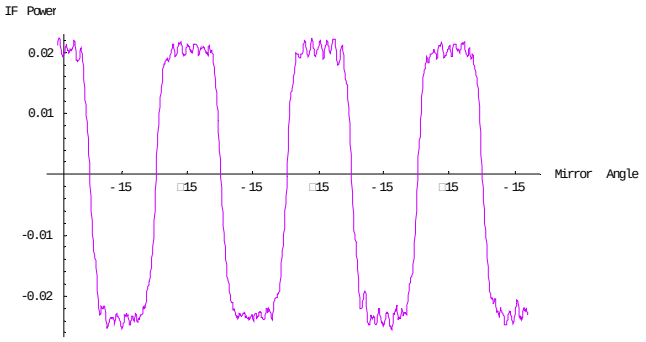

Figure 5. Test recording from the prototype imager with a split object at 280 K and 77 K, respectively.

The image records a peak-to-peak level of 43 mV for a ΔT of 200 K. From this, a responsivity of 0.2 mV K^{-1} is inferred. Using the same experimental setup to record an image of a steel bar in thermal equilibrium with a 280 K background, the image in Fig. 6 was recorded.

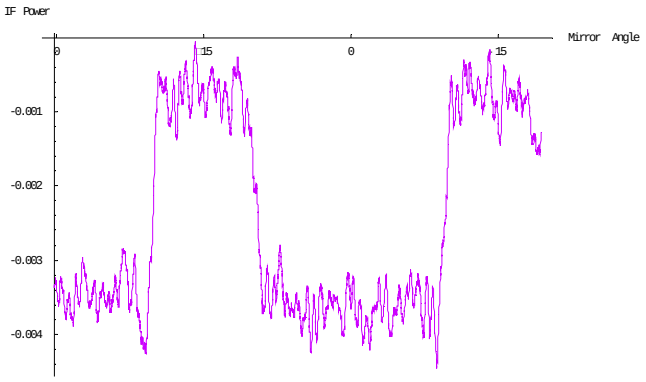

Figure 6. Image of a steel bar over a 280 K background. The lowest signal is due to the steel bar.

The peak-to-peak level in the latter image is 3 mV, which translates to a ΔT of approximately 15 K. The steel bar was measured by a conventional thermometer to be in thermal equilibrium with the 280 K background absorber it rested on. The peak-to-peak noise in this image is less than 1 mV or 0.3 mV RMS. Therefore, the fluctuation level at the system input is equivalent to a thermal signal of less than 1.5 K RMS. This value is far greater than what would be expected from the radiometry formula (0.06 K). A portion of the noise level in the recorded signal may still be due to pick-up of 60 Hz and other interfering signals. We also expect that we are seeing the result of system gain fluctuations that we are now beginning to combat with the HEB current lock. Preliminary tests of the current lock show a dramatic reduction in the measured Allan variance of the detected IF power. We define the normalized Allan deviation as follows. Sampling the IF power, the vector, $\{P_1, \ldots, P_N\}$, is formed with sample time Δt. The mean of X equals:

$$<X> = <\{X_1, \ldots, X_N\}> = \frac{1}{N}\sum_{i=1}^{N}[X]_i$$

When the least integer function is defined as [.], then

$$m = [\frac{N}{j}]$$

We also define

$$\delta_j = \{<\{P_1, \ldots, P_j\}>, <\{P_{j+1}, \ldots, P_{2j}\}>, \ldots, <\{P_{j(m-1)+1}, \ldots, P_m\}>\}$$

and we can now express the standard Allan variance as:

$$\sigma_j^2 = \frac{1}{2m}\sum_{k=1}^{m-1}([\delta_j]_k - [\delta_j]_{k+1})^2$$

Finally, we define the dimensionless normalized Allan deviation:

$$\sigma_j = \frac{\sqrt{\sigma_j^2}}{<P>}$$

When we use a bandwidth of 250 MHz, the normalized Allan deviation (with an integration time of 0.1 s) is reduced from 1.3 10^{-3} (with the current lock off) to 6.8 10^{-5} (with the lock on).

III. Future Progress

The integration of the HEB current lock is presently underway. With this completed, we expect the noise to be greatly reduced.

Replacing the oscillating mirror with the rotating mirror is the next advancement. This arrangement will allow the system to be tested at video scan rates. Amplifier back-end gain leveling can also be enabled once the rotating mirror is operational.

Array development is progressing concurrently. A three-element array has already been tested [6], and we believe that a 10-element linear array is within reach. With all these components in place, the full capability of the RLSI system can be ascertained.

We are collaborating with the National Institute of Standards and Technology (NIST) in Boulder, CO in a

related project where a 700 GHz HEB imaging system is also being built. This work is described in [7].

REFERENCES

[1] D. Mittleman, *Sensing with Terahertz Radiation*, New York: Springer-Verlag, 2003, pp. 120.

[2] Robert J. Dengler, Anders Skalare, and Peter H. Siegel, "Passive and Active Imaging of Humans for Contraband Detection at 640 GHz," *2004 IEEE Intern. Microw. Symp.,*, pp. 1591-1594.

[3] E. N. Grossman, et al., "Concealed weapons detection system using uncooled, pulsed imaging arrays of millimeter-wave bolometers," *SPIE Proc*., vol. 4373, p. 7, 2001. Also ibid, p. 64.

[4] E. R. Brown, "A system-level analysis of Schottky diodes for incoherent THz imaging arrays*," Solid State Electronics*, vol. 48, pp. 2051-2053, 2004.

[5] K. J. Siebert, H. Quast, R. Leonhardt, T. Löffler, M. Thomson, T. Bauer, and H. G. Roskos, "Continuous-wave all-optoelectronic terahertz imaging," *Applied Physics Letters*, vol. 80(16), April 2002.

[6] Fernando Rodriguez-Morales, K. Sigfrid Yngvesson, Eyal Gerecht, Niklas Wadefalk, John Nicholson, Dazhen Gu, Xin Zhao, Thomas Goyette, and Jerry Waldman, "A Terahertz Focal Plane Array Using HEB Superconducting Mixers and MMIC IF Amplifiers" Microwave and Wireless Component Letters, IEEE Microwave and Wireless Components Letters, Vol. 15, No. 4, April 2005, pp 199-201.

[7] Eyal Gerecht, Dazhen Gu, Sigfrid Yngvesson, Fernando Rodriguez-Morales, Ric Zannoni, and John Nicholson, "HEB heterodyne focal plane arrays: a terahertz technology for high sensitivity near-range security imaging systems", SPIE Defense and Security Symposium, Orlando Florida. March 28 – April 1, 2005.

Reflective Terahertz Imaging at the ENEA FEL Laboratory

A.Doria, G.P. Gallerano, M. Germini[1], E.Giovenale, G. Messina, I. Spassovsky[2]
L. D'Aquino[*]

ENEA- Advanced Physics Technologies, P.O. Box 65, 00044 Frascati – Italy
(*) ENEA – Trisaia Research Center, 75026 Rotondella (MT) - Italy
(1) ENEA-student
(2) ENEA-ICTP Fellow

THz radiation penetrates most dielectric materials and is specifically absorbed by organic substances. As in the case of microwaves metals are completely opaque to THz radiation, and polar liquids such as water are strong absorbers. The absorption and reflection properties of water in the THz region make possible new applications of THz radiation for monitoring the hydration state of plants on a laboratory scale as well as on the field. Moreover, unlike microwaves, focusing a THz beam to a submillimeter spot is straightforward. All such properties make THz radiation a powerful tool to provide high contrast in imaging applications in environmental studies.

The development of both transmissive and reflective THz imaging is under way at ENEA-Frascati employing a THz Compact Free Electron Laser (THz C-FEL). This source provides 130 GHz coherent radiation with an output power of 1.5 kW in 4 μs pulses at a maximum pulse repetition rate of 10 Hz. The high peak power available makes the FEL particularly suitable for long range detection. Different setup have been tested at different levels of spatial resolution to image objects from a few centimeter square to larger sizes. In this paper we demonstrate an example of reflection imaging. Using a hybrid setup in reflection we have obtained 0.4 mm spatial resolution at 130 GHz: the FEL radiation is coupled first into a focusing cone and then into a WR6 directional coupler. The reflected signal is detected by a diode with 14 dB attenuation. Images of different samples will be presented together with considerations on how to optimize the contrast and the maximum achievable resolution.

The Band 7 Cartridge (275-373 GHz) for ALMA

S. Mahieu, B. Lazareff, D. Maier, M. Carter, AL. Fontana and S. Claude

***Abstract*—IRAM is responsible for designing the ALMA Band 7 cartridge covering the signal frequency range 275-373 GHz, and for building 8 pre-series units. The cartridge must meet a number of specifications, including SSB noise temperature less than 133K, but also total power stability, beam pattern, etc… We present in this paper some of the challenging issues met during the design and prototyping of the cartridge, and experimental results obtained so far.**

I. Introduction

The Atacama Large Millimeter Array (ALMA) will be a radio telescope with 64 antennas. It is under construction in the Atacama desert in northern Chile. The front end for ALMA will consist of a 4-K cryostat with ten insertable receivers called cartridges covering the frequency range 31 to 950 GHz. Each cartridge will operate simultaneously in two linear polarizations. A block diagram of the Band 7 cartridge is given in Figure 1 and an overall view of the #1 cartridge is given in Figure 2.

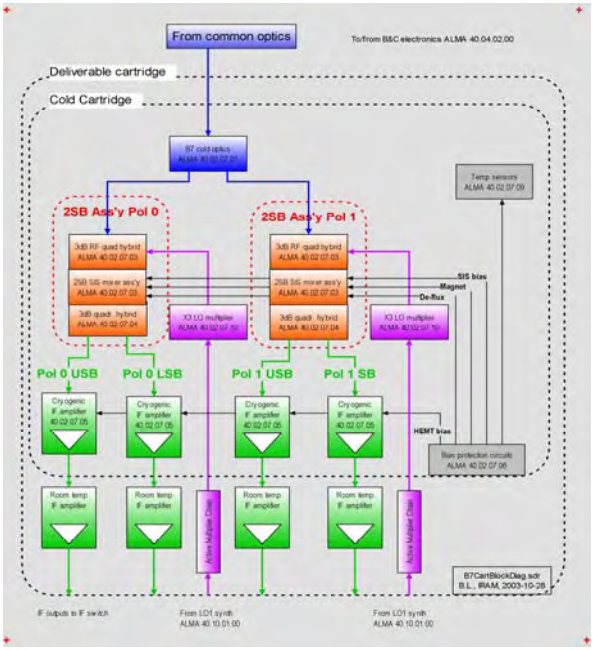

Figure 1: Band 7 cartridge block diagram

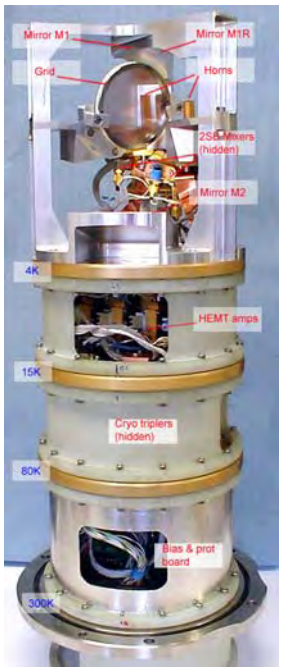

Figure 2: Complete Band 7 Cartridge #1

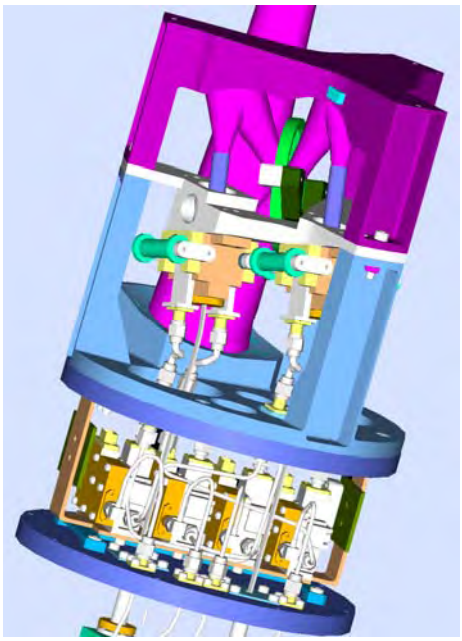

Figure 3. 4K stage: optics, 2x2SB mixer assemblies; 15K stage: 4x HEMT amplifiers (thermalized to 4K).

The cartridge consists in three cold stages with operating temperatures of 4K, 20K and 90K and a room temperature baseplate which is the interface between the vacuum and the air. The stages are supported by G10 glass fiber tube spacers. The four plates and GFRP tubes constitute the blank cartridge, designed and supplied within the ALMA project by Rutherford Appleton Laboratories (UK)

- The 4 K assembly comprises:
  - The cold optics, consisting of three off-axis elliptical mirrors and a polarization diplexing grid, designed to achieve near-optimum coupling of the cartridge to the telescope within prescribed tolerances;
  - The two dual-sideband (2SB) mixer assemblies (see Maier et al this conference);
  - A thermal sink for the four HEMT amplifiers;
  - Mechanical structures to support these elements in the adequate positions within tolerances.
- The 15 K stage only provides thermal shunts for wiring, IF coaxial cables, and LO waveguides, as well as mechanical (thermally insulated) support for the HEMT amplifiers.

- The 90K stage has the two LO triplers, wiring thermal shunts mounted on it.
- The 300 K baseplate supports the ESD protection board and the IF, DC and LO feedthroughs.

II. 4 K Optics and Support Assembly

A. Requirements

The constraints for the design of the optical train were to: a) couple to the f/D=8 optics of the telescope with an edge taper of 10dB, independent of wavelength over the operating band; b) perform polarization diplexing; c) provide a clear aperture of 5w (fundamental Gaussian mode) at each optical element (mirrors, grid); d) last but not least, fit within a cylinder of ∅170mm×H475mm (from 300K baseplate).

Furthermore, the cartridge beam should point to the center of the subreflector, with a global tolerance of 6mrad, which corresponds to 1.2% loss of spillover efficiency. Out of that global budget, 4mrad are allocated to the cartridge optics.

B. Optical train.

To minimize risk and development effort, the decision was made to realize the polarization diplexing using a grid rather than an orthomode transducer. The space limitations led to a design where each mixer horn is coupled to the Cassegrain focal plane by two off-axis elliptical mirrors, labeled M1 and M2 (counting from the horn towards the sky), and the polarization-separating grid is placed between M1 and M2; accordingly, there are actually two identical mirrors M1 and M1R (see Figure 2 and Figure 3). The two 2SB mixers have parallel orientations, while being coupled to orthogonal polarizations on-sky. A first design was made based on fundamental Gaussian mode analysis, with a goal of 12dB edge taper; further multimode analysis performed by Tham and Withington (Cambridge University) showed that, as expected, the actual edge taper was very close to 10dB, and led to small adjustments of the parameters.

	Diam.	***L (axial)***		***d-to-next***
Horn	6.0	45.68		38.0
	R_{source}	$2\times\theta$	R_{image}	***d-to-next***
M1	44.58	40°	61.01	157.0
M2	108.12	25°	268.38	

The fact that these optical elements are cooled to 4K prompts the question of the impact of contraction on performance. The answer is: nil, and can be best explained by a thought experiment. Stage 1: cool down the optics, and adjust the wavelength by the same amount as the dimensions (~0.5%); because electromagnetics is scale-invariant, the far-field *angular* pattern is unchanged. Stage 2: restore the original wavelength; because the design is wavelength-independent, the angular beam pattern is again unchanged.

Both the prototype and the #1 optics have been verified at room temperature using the IRAM antenna range and Schottky mixers. Using the complex (amplitude and phase) measurements acquired in the measurement, the far-field pattern has been derived, and is shown below

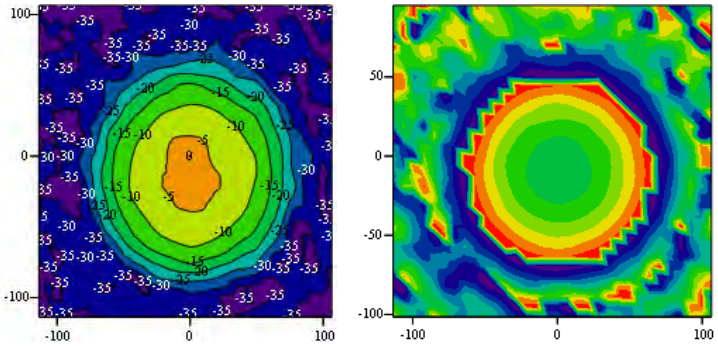

Figure 4. Far field pattern of the optics, derived from complex (amplitude and phase) near-field measurements. Frequency: 330GHz, polarization: P0 (grid reflecting). Left: amplitude, contour interval 5dB; right, phase. Angular units: milliradians. The vertical offset (-0.955°=-16.7mrd) is required for aperture plane alignment from the off-axis cartridge location in the focal plane.

C. Cold optics mechanical design

In order to avoid the buildup of tolerances, the 4K mechanical supports and optical mirrors assembly has been machined out of bulk metal, with a reduced parts count to minimize the tolerance buildup. This design consists of just three main parts:

1. Bottom level: bottom plate, mirror M2, and bottom halves of three vertical legs;
2. Middle: a three-arm star extending to the vertical legs, and holding the two 2SB mixer assemblies and the grid;
3. Top level: top half of the vertical legs, and the two M1 mirrors.

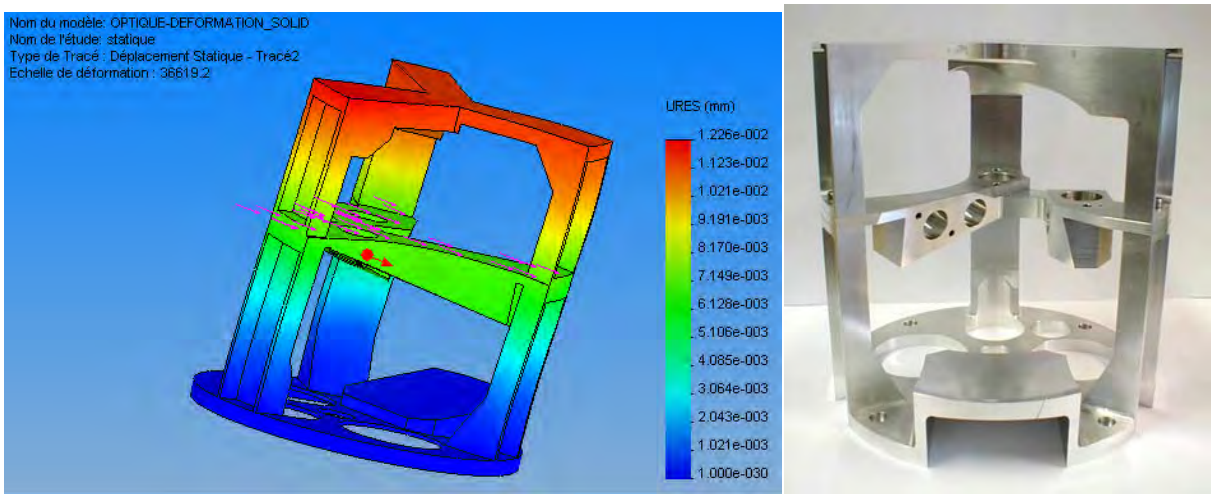

Figure 5. Left: Cold optics under gravitational load; maximum deformation 12μm; right: the actual part

D. *Tolerance analysis*

A cold optics internal tolerance analysis has been performed. This includes gravity deformations of the structure loaded by its payload (0.7kg mass on the center piece), see Figure 5, and machining/assembly tolerances. An analysis was made of the sensitivity of the beam direction to various misalignments of the optical elements; this was combined with the results of the gravity deformation analysis and estimates of machining tolerances on modern CNC equipment (≈10μm for individual contributions). While this does not prove the correctness of the analysis, antenna range measurements of both the prototype and the #1 pre-production cartridge show that the beam orientation is within the 4mrd tolerance.

Table 1. Summary of tolerance analysis. Beam deviation from nominal, milliradians.

Cartridge			***System***
RSS	*Worst case*	*Spec*	*Spec*
1.3	3.5	4.0	6.0

III. WIRING

A. *Requirements*

The wiring is intended to carry voltages and currents to and from various electronic components, to supply electric power and to monitor voltages. Beyond that basic role, it must be reliable, noise-free, provide low voltage drop, add minimum heat load to cryogenic stages from conduction and Joule heating; and outgas below prescribed limits

B. *Choice of wiring material and diameter*

Minimizing the sum of conduction and Joule heating leads to conflicting requirements from the two individual terms, regarding the wire diameter. We have determined an optimum diameter for various metals, as a function of current load and length. We find that the thermal load (conduction+Joule) at optimum diameter is virtually the same for all metals (Wiedemann-Franz). On the other hand for, e.g., copper, the optimum diameter is impractically small. We chose 0.2mm diameter manganin for small currents and 0.2mm diameter brass for high currents (coils, heaters).

C. *ESD protection and routing board*

In order to protect the cartridge sensitive components (i.e. SIS junctions and HEMT amplifier transistor) from both excessive DC bias and electro static discharges (ESD); we need a protection board at the cartridge bias input. ESD protection is realized by parallel-connected 2-terminal devices with appropriate threshold voltages

D. *Harnesses and connectors*

All the harnesses are made from braids consisting of 8 twisted pairs (manganin of brass, see above). Heat sinking at each temperature stage is realized (for each 8-twisted-pair braid) by inserting the braid in a two-piece OFHC copper clamp, with the inner space filled with Stycast 2850FT. Compared with discrete heat sinks that break the physical continuity of the wiring, this construction requires less manpower and is more reliable

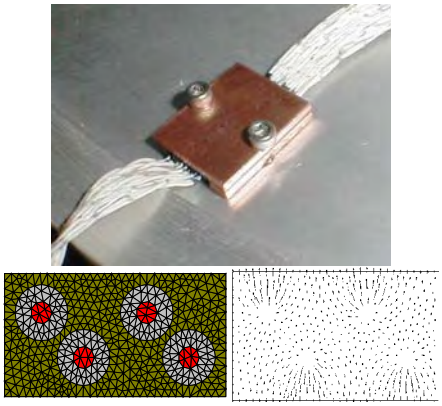

Figure 6. Wiring heat sink: device and FE conduction modeling.

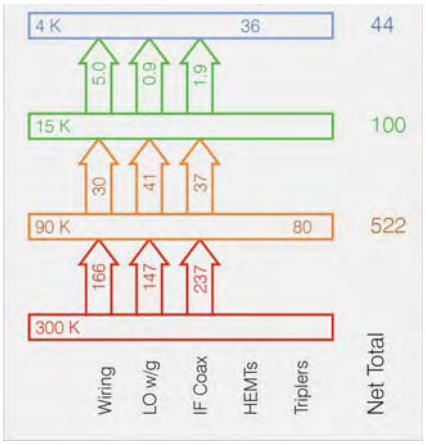

Figure 7: Thermal Budget

Together with the thermal resistance of the wires from the next-higher temperature stage, the thermal conductance of the shunt acts as a resistive divider. Based on modeling, the worst case ΔT between the heatsunk wire and stage is 0.5K for the 80K sink, and much smaller at lower temperatures. The measured difference in the worst case is 1K.

IV. LO PATH INSIDE THE CARTRIDGE

A. *Design choices.*

The LO power enters the cartridge at 1/3 the final frequency (90-120GHz approx). Transport to the cryogenic triplers (one for each polarization) is via a stainless steel (low thermal conduction) gold plated (low RF loss) WR10 waveguide. We have experimentally verified that with 1μm gold plating the increase in thermal conductivity is negligible, while the RF losses are close to that of a copper waveguide. From the output of the triplers to the 2SB mixers, fundamental mode stainless steel would have prohibitive losses, and is near impossible to gold plate inside. We have decided to use overmoded stainless steel WR10 waveguide. Because the optics imposes a 15° bend, and because of the issues discussed below, we have left that waveguide unplated, to keep a controlled amount of loss.

The power to drive the cryo tripler is supplied by the AMC (active multiplier chain), designed and built within the ALMA project by NRAO (USA); the cryo tripler itself is designed and built by Virginia Diodes, Inc (USA).

B. *Overmoded waveguide: resonant absorption caused by bends.*

In an overmoded waveguide, bends introduce coupling between the fundamental mode and overmodes. We have performed a study of these couplings, as a function of the two dimensionless parameters: a/λ and R/a, where a is the waveguide width and R the bend radius. In our case, the two ends of the overmoded waveguide are terminated by transitions to fundamental-mode guide: overmodes are trapped in a resonant cavity; this will give rise to absorption dips in the main transmission path.

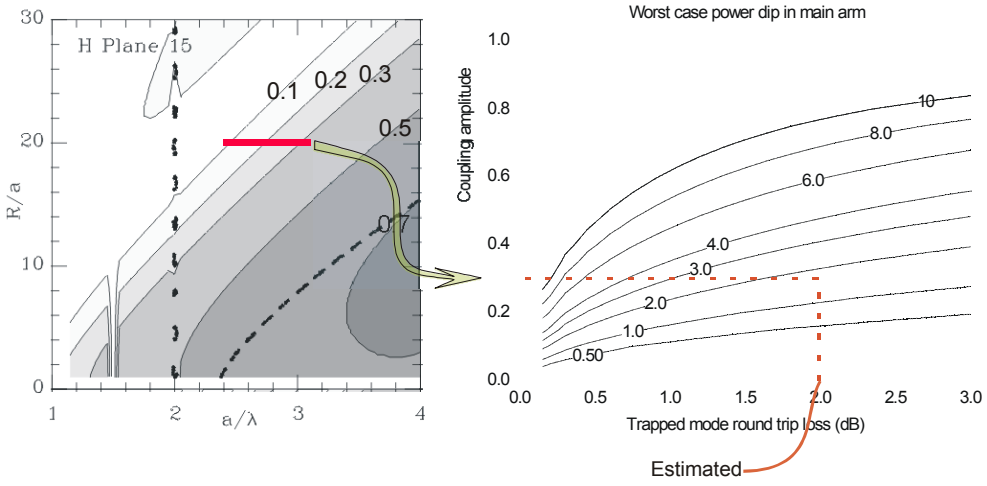

Figure 8 : Design graphs for the 15° bent, overmoded LO waveguide. Left: coupling amplitude from TE10 to TE11/TM11; right: the worst case resonant loss is found to be less than 2dB.

V. IF Subsystem Description

A. Requirements

- The contribution of the IF subsystem to the global noise budget should be as small as possible; in view of the large electronic gain of the HEMT amplifier, the noise contribution of the IF is essentially determined by the input noise of the HEMT.
- The contribution of the IF susbsystem to the cartridge gain and phase instabilities should be as small as possible, allowing the global budget to remain within the envelope of the specs.
- The gain of the IF chain should be such that — including allowance for the gain dispersion of all elements in the signal chain, including the mixer — the output level at the interface between the cartridge and the FE subsystem IF switch should be between –40dBm and –27dBm.
- The design should be robust, with easy access to any of the component and ensure that critical components are interchangeable; in particular, the warm cartridge assembly should be interchangeable independently from the cold cartridge, while still meeting the specifications.
- Finally, no more than 36 mW must be dissipated on the 4K stage.

B. Signal chain implementation

The IF chain comprises:

- A three stage cryogenic amplifier designed and built by C.A. Yebes (Spain). Gain 38dB (typ), noise 5K (max).
- A 2 stage room-temperature amplifier with 25 dB of gain (nominal), mounted outside the cartridge (warm cartridge assembly).

C. Thermal Stress Relief (IF and LO paths):

During the cryostat cool-down, the cartridge body as well as the components fitted into it will contract. The amount of contraction will vary depending on the temperature and manufacturing material used. A diagram illustrating the cumulative deflection in the IF path is shown in the Figure 9

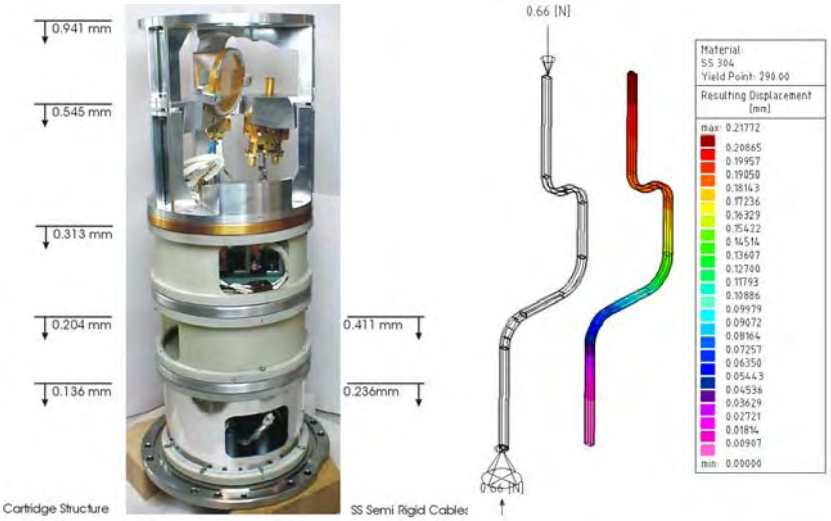

Figure 9 Left: Cartridge and stainless steel semi rigid cable no-load deflection due to thermal contraction. Right: IF coaxial cables and stainless steel waveguides have been bent to accommodate the differential contraction with minimal stress. Waveguides between the tripler and the mixer have no extra bends; the compliance is provided by the support of the tripler.

VI. Results

A. Receiver noise.

The receiver noise of cartridge #1 has been measured a) integrated over the 4-GHz bandpass, for each of the two polarization channels, for LSB and USB; b) at every 4GHz in LO frequency, across the IF bandpass, with a 0.1GHz stepping.

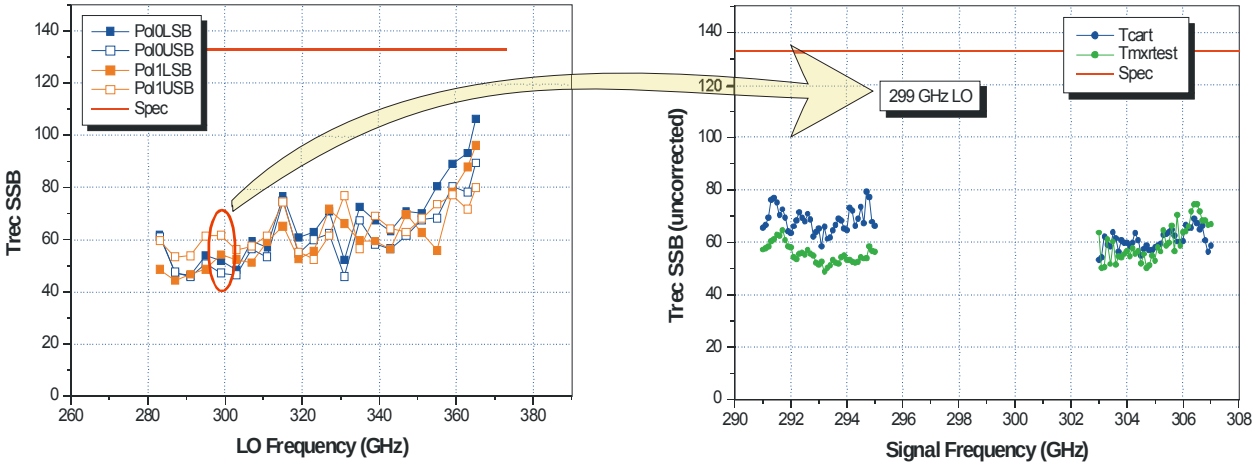

Figure 10. Left: receiver noise integrated over the IF bandpass; right: receiver noise across the IF bandpass, for an LO frequency of 299GHz, polarization 1, LSB and USB; blue: cartridge measurements; green: the same 2SB assembly as measured in the mixer test set (see Maier et al, this conference).

B. Image rejection.

The image rejection has not yet, at the time of writing been measured in the cartridge. Measurements performed in the 2SB mixer test station show, however, that the 10dB specification is generally met, except for a few combinations of LO frequency and IF frequency (see Maier et al, this conference). However, the significant margin by which the noise specification is met ensures that the scientifically significant figure of merit of SSB noise is within requirements in all cases.

C. Cartridge Gain Stability

The stability specification is defined by the Allan variance, that must be less than $4\ 10^{-7}$ between 0.1s and 1s. This corresponds to an Allan deviation ($\sqrt{\text{var}}$) $6.3\ 10^{-4}$. The measured stability is within the specification; it is, however, worse (for the same 2SB mixer) than measured on the mixer test set; this needs further investigation.

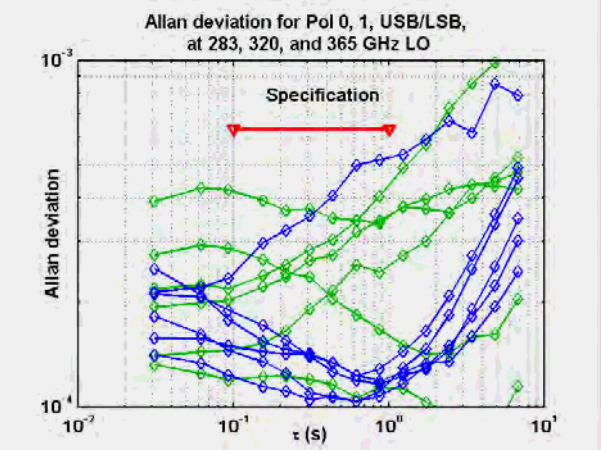

Figure 11: Total Power Stability, Allan deviation measured in the pre-production cartridge#1.

VII. Conclusions

We have designed and built a compact, modular, low-noise cartridge covering the signal frequency band 275-373 GHz, compliant with the requirements of the ALMA project. At the time of writing, the first pre-series cartridge is undergoing pre-delivery tests. The cartridge has been found to meet the specifications that have been tested so far.

Development of a 1.8THz receiver for the TELIS instrument

U.Mair(1), N.Suttiwong(1), H.-W.Hübers(2), A.D.Semenov(2), H.Richter(2), G.Wagner(1) and M.Birk(1)
(1) Remote Sensing Technology Institute, DLR Oberpfaffenhofen (2) Institute for Planetary Exploration, DLR Berlin-Adlershof

A new state-of-the-art balloon borne three channel (500GHz, 625GHz, 1.8 THz) cryogenic heterodyne spectrometer will allow enhanced limb sounding of the Earth's atmosphere within the submillimeter and far-infrared spectral range. The instrument, called TELIS (TErahertz and submm LImb Sounder), is being developed by a consortium of major European institutes that includes the Space Research Organisation of the Netherlands (SRON), the Rutherford Appleton Laboratory (RAL) in the United Kingdom and the Deutschen Zentrum für Luft- und Raumfahrt (DLR) in Germany (lead institute). TELIS will utilise state-of-the-art superconducting heterodyne technology and is designed to be compact and lightweight, while providing broad spectral coverage, high spectral resolution and long flight duration (24 hours duration during a single flight campaign). Target species are key atmospheric short-lived radicals such as OH, HO2, ClO, BrO together with stable constituents such as O3, HCl and HOCl.One of the three channels (developed by DLR) will focus on the measurement of the OH-triplett at 1.8 THz. Low noise NbN based Hot Electron Bolometers will be used as heterodyne mixing elements. Recently the laboratory version of the TELIS heterodyne receiver (using a far infrad laser as LO source) has been set up and first gas cell measurements have sucessfully been carried out . The current status of the THz-channel development in the framework of the TELIS project will be presented.

Modulation Transfer Function in Terahertz FPAA Quasi-Optical Imaging Systems

Leonid V. Volkov, Alexander I. Voronko, Natalie L. Volkova
Secomtech Ltd., 24/2, 125, Prospect Mira, Fryazino,
Moscow region, 141196, Russia, (E-mail: leon_volkov@mail.ru)

Nowadays MMW, THz and even IR quasi-optical imaging systems based on usage of focal plane antenna array (FPAA) gain acceptance for lots of applications including remote sensing, weapons and explosive detection, surveillance, different radar applications, etc. The receiving elements of the FPAA may exhibit different performance: antenna-coupled detectors/mixers, antennas connected with mixers through impedance-matching circuits (waveguides), antennas connected with direct amplification and detection MIMIC circuits, etc. It is obvious that spatial and sampling features of the FPAA and the FPAA-based imaging systems mainly depend on both focusing lens properties and characteristics of the array antennas [1-4]. In present work factors determining spatial resolution of quasi-optical imaging systems based on usage of focal plane antenna arrays are considered in detail. Rigorous analytical expressions for point spread functions (PSF) and modulation transfer functions (MTF) of FPAA receiving elements and the imaging system as a whole are derived both for spatially-coherent (radars) and spatially-incoherent imaging systems (including radiometric cameras) and for any kind of radiation polarization. Accurate PSF and MTF functions are calculated for long horn antenna and resonance-dipole antenna. Further, combined effects of image formation, sampling and reconstruction in focal plane antenna array (FPAA) MMW /THz imaging systems are rigorously analyzed. Formalism of average modulation transfer functions for sampled imaging systems is applied for MTF analysis of both the subsystems and the entire FPAA MMW/THz imaging system and for any kind of radiation polarization. Possibilities of usage of accurately calculated PSFs of the FPAA imaging systems for further advancement of super-resolution algorithms. The developed approach may be effectively used for computer aided design of MMW/THz FPAA imaging systems being able to consider combined effects of imaging, sampling and reconstruction procedures.

References

1. A. Murphy, R. Radman, Int. Journ. of Infrared. and Millimeter Waves , vol.9, N8,1988, pp.667-703.
2. L. V. Volkov, A.I.Voronko, N.L. Volkova, Radioengineering (Russia), N8, 2003, pp. 67-80.
3. L.V.Volkov, A.I.Voronko,N.L.Volkova, SPIE Def.&Security Symp., Orlando 2004, Proc.V.2 5410B-42.
4. L.V. Volkov, A.I.Voronko, N.L.Volkova, Conf. Digest of 29th International Conference of Infrared and Millimeter Waves and 12th International Conference on Teraherz Electronics, Karlsruhe, Germany, 2004, pp.743-744.

Quasi-optical characterization of low-dielectric constant thin film in the sub-terahertz region

Roman Tesař[1] and Etsuo Kawate
National Institute of Advanced Industrial Science and Technology (AIST)
1-1-1, Central 2, Umezono, Tsukuba, Ibaraki 305-8568, Japan

***Abstract*— Dielectric properties of materials important for production of high-speed electronic devices are studied in the sub-terahertz region. For characterization of a thin SiO_2 film we have developed the Grazing Angle Etalon (GAEA) method [1]. Theoretical calculations are based on recurrence relations for transmittance and reflectance coefficients of multilayer system [2].**

I. Introduction

Let a *s*-polarized plane wave is incident at angle θ_0 on a plane-parallel plate. Interference of electromagnetic waves in the plate results in periodically located maxima and minima in the transmittance spectra. Maximum intensity appears when the phase difference δ between the incident and transmitted beam fullfills the condition [2], [3]

$$\delta = \frac{2\pi}{\lambda} nd\cos\theta = m\pi, \quad m = 1, 2, 3, ... \qquad (1)$$

where λ, θ, n and d are wavelength of the incident light, angle of refraction, index of refraction and thickness of the plate, respectively. The maxima are sharper and the distance between them is larger for higher angle of incidence θ_0, whilst their height remains constant (Fig. 1). The narrowing of peaks is caused by an increased reflectivity of the plate surfaces at grazing angles of incidence. The distance between the maxima is enlarged since the effective optical thickness is decreased by factor $\cos\theta$ and condition (1) is satisfied at higher frequencies.

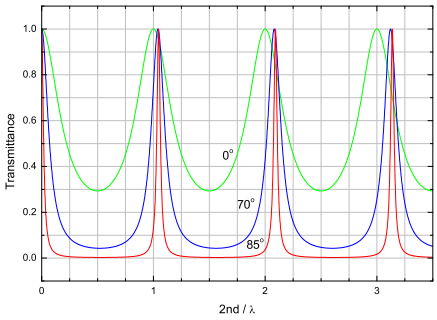

Fig. 1. Transmittance spectra calculated for a plane-parallel silicon substrate.

In Fig. 2 we show a transmission peak in the silicon substrate calculated for several angles of incidence and *s*-state of polarization. If the substrate is coated with a SiO_2 thin film, position of the peak shifts slightly towards lower frequencies. The presence of the small shift is manifested in the relative transmittance spectra by a maximum-to-minimum structure which becomes larger with increasing incident angle, as can be seen in Fig. 3. The best fit of the theoretical curves to measured relative transmission data may be used to determine the complex refractive index n_f and dielectric constant $\epsilon_f = n_f^2$ of the film. The technique described above is called Grazing Angle Etalon (GAEA) method [1].

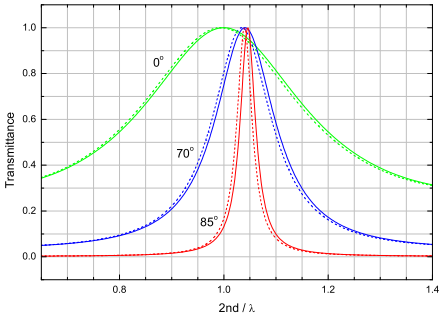

Fig. 2. Position of the transmission peak in bare (–) and coated (- -) substrates.

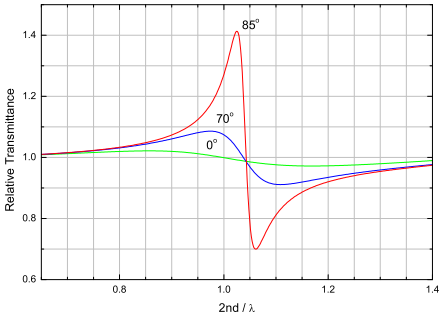

Fig. 3. Maximum-to-minimum structure in the relative transmission.

II. Experiment

The sample was a non-doped silicon wafer 700 μm thick, 100 mm in diameter coated on both sides with 2 μm thin SiO_2 films. Thickness of the silicon substrate was selected to obtain one peak in the measured frequency range. The thin SiO_2 films were prepared by thermal oxidation of the Si wafer at 1200°C. Half of the films areas were removed from both sides of the wafer using hydrogen fluoride acid.

[1]Institute of Physics ASCR, Cukrovarnická 10, 162 53 Praha 6, Czech Republic

The experimental setup used for measurement of transmission is shown in Fig. 4. The source of millimeter waves comprised the signal generator connected to the frequency multiplier chain by a RF cable. The waves in the 50-75 GHz frequency band were transmitted to a free space using a horn antenna, focused by lenses and, after passing through the sample, were focused to horn antenna receiver equipped with a Schottky diode detector. Amplitude modulation of the generator output at 20 kHz allowed easy signal detection by a lock-in amplifier and a fast spectra scanning.

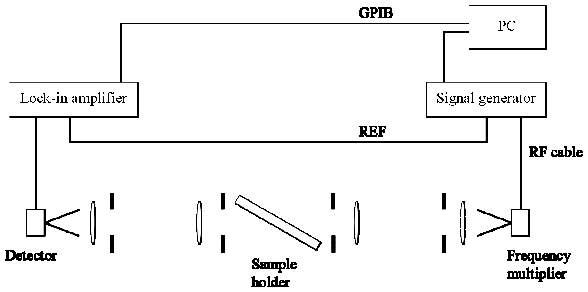

Fig. 4. The transmission measurement setup.

III. Results

Measured spectra of relative transmission defined as the ratio of transmission of the substrate coated with the film to that of the substrate without film are shown in Fig. 5. Dashed lines represent theoretical calculations for *s*-polarized waves incident at grazing angles of 70°, 75° and 80°, film thickness d_f = 2μm on both sides of substrate, index of refraction n_f =2.0+0.4i and substrate parameters d =700μm and n = 3.4+0i. The theoretical curve agrees fairly well with the experimental data for θ_0 = 70°. At higher angles of incidence the measured spectra are distorted by some additional oscillations, but their overall shape seems to be consistent with the theory. From the index of refraction we obtain the complex dielectric constant of the SiO_2 film $\epsilon_\mathrm{f} = n_\mathrm{f}^2$ = 3.84 + 1.6i. Whereas the real part of the dielectric constant shows good agreement with the data published by other authors [4], the imaginary part indicates rather high loss in the film under study. We estimate the complex refractive index on the assumption that there is only one maximum-to-minimum structure in the relative transmittance spectrum. With the increasing real part of refractive index, the difference between maximum and minimum of the relative transmittance is increasing. When the imaginary part is zero, the middle point of relative transmittance remains unity. However, with the increasing imaginary part of the refractive index, the middle point moves below unity. In our opinion a superposition with another structure, which is seen in Fig. 5 (b) and (c), may be responsible for the lower value of the middle point and the higher estimate of the imaginary part of the refractive index.

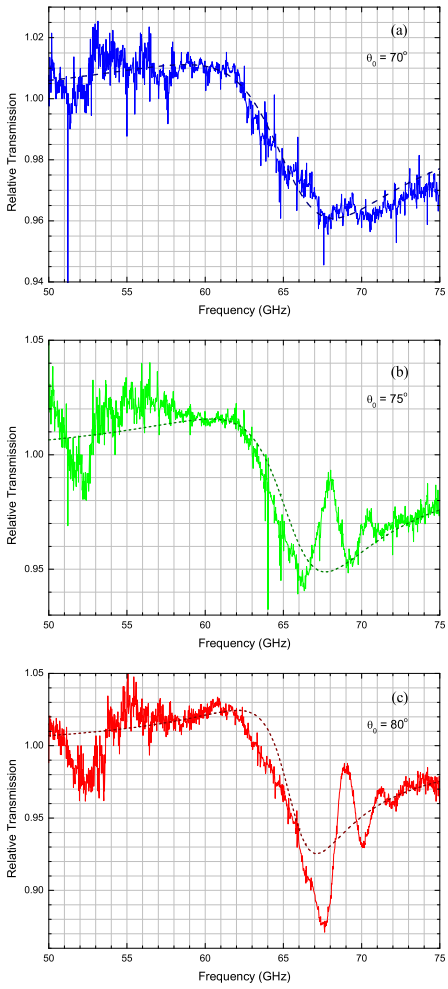

Fig. 5. Measured (–) and calculated (- -) relative transmission spectra of SiO_2 thin film on the silicon substrate.

IV. Conclusion

Despite of the problems mentioned in the previous section, the Grazing Angle Etalon (GAEA) method [1] seems to be suitable for extracting material constants of thin films from the measured relative transmition spectra. The method attains enhanced sensitivity at grazing angles of incidence and makes possible to characterize low-dielectric constant thin films even when $n_\mathrm{f} d_\mathrm{f} \ll \lambda$ and other quasi-optical methods are hardly applicable.

Acknowledgment

This work is supported by R&D system for supporting regional small and medium enterprises of MITI.

References

[1] E. Kawate and K. Ishii, Appl. Phys. Lett. **84** (2004) 4878.
[2] O. S. Heavens: *Optical properties of thin solid films* (Butterworths, London, 1955).
[3] M. Born and E. Wolf: *Principles of Optics* (Pergamon, Oxford, 1975).
[4] J. W. Lamb: "Miscellaneous data on materials for millimeter and submillimetre optics", Int. J. Infrared and Millimeter Waves, **17** (1996) 1997-2034.

Evaluation of a 640 GHz Cryo-Receiver for Limb Emission Sounder JEM/SMILES

Masumichi Seta and Takeshi Manabe
National Institute of Information and Communications Technology, Tokyo184-8795, Japan

Ken'ichi Kikuchi, Seikoh Arimura, Yasunori Fujii, Ryouta Sato, Toshiyuki Nishibori, Hiroyuki Ozeki, Akinobu Okabayashi, and Junji Inatani
Japan Aerospace Exploration Agency,Tsukuba, Ibaraki 305-8505 Japan

We are developing a 640 GHz SIS receiver for JEM/SMILES. SMILES is an instrument to observe ozone layer in limb sounding method from the International Space Station. SMILES aims to realize the most sensitive 640 GHz heterodyne receiver for space use. The design goal of the receiver noise was 500 K in SSB. The sensitivity is dominated by the noise of a mixer, the noise of a first low noise amplifier, and the loss in input optics. We had developed a SIS mixer with a DSB noise temperature of 65 K. We also had developed a cooled 20 dB amplifier for 11-14 GHz IF band with a noise of 16 K. The mechanical 4 K cooler for SMILES has cooling capability of 20 mW at 4.5 K stage. It was one of the difficulties for a receiver for space use to integrate the mixers and amplifiers into such a limited cooling capability cryo-receiver while keeping low noise requirement of 500 K. Strict specifications of heat load for the cooler restrict freedom in design for optics and IF output cable from the mixer. A diameter of window for RF signal is limited to be 25 mm and three IR filters are inserted on the RF path. Zitex is selected for the IR filters to minimize dielectric loss for less than 0.15 dB. We developed a beryllium-copper IF cables for connection between the SIS mixer and the 20 K cooled amplifier for satisfying thermal load requirement of 1.6 mW into the 4 K stage. The loss of IF signal is 0.4 dB that is much smaller than conversion loss 6.5 dB of the mixer. The SSB system noise of the receiver is designed to be 480 K evaluated at input port of the ambient temperature optics.

The engineering model of the 640 GHz receiver has been manufactured. The noise temperature of the cryo-receiver was evaluated to be 200 K in DSB by the Y-factor method. The noise is now mainly determined by the noise for the SIS mixer of 65 K, the conversion gain of -6.5 dB of the mixer, and the noise for the cooled amplifiers of 16 K. The DSB 200 K noise is upper limit for realizing SSB noise of 480 K after assembling the ambient temperature optics with 0.7 dB loss on the cryo-receiver. It may be possible to reduce the noise further by decreasing physical stage temperature for the SIS mixer and a modification of IF circuit of the SIS mixer.

The effect of vibrations during launch on the cryo-receiver was examined by comparing frequency characteristics of the noise before and after random vibration test. There was no significant change in the frequency characteristics of the noise.

We concluded that our design and the EM for the cryo-receiver fulfilled requirement in noise for the space qualified 500 K noise 640 GHz heterodyne receiver.

Design and development of a 600-720 GHz receiver cartridge for ALMA Band 9

R. Hesper, B. D. Jackson, A. M. Baryshev, J. Adema, K. Wielinga, M. Kroug, T. Zijlstra, G. Gerlofsma, M. Bekema, K. Keizer, H. Schaeffer, J. Barkhof, F. P. Mena, A. Koops, R. Rivas, T. M. Klapwijk, and W. Wild

Abstract— **This paper describes the design of the Band 9 receiver cartridges for the Atacama Large Millimeter Array (ALMA). These are field-replaceable heterodyne front-ends offering high sensitivities, 602-720 GHz frequency coverage, 4-12 GHz IF bandwidths, and high quasioptical efficiencies. Because the project will ultimately require 64 cartridges to fully populate the ALMA array, two key aspects of the design of the Band 9 cartridge have been to take advantage of commercial manufacturing capabilities and to simplify the assembly of the cartridge. Preliminary test results of the first (prototype) cartridge are also presented.**

***Index Terms*—radio astronomy, submillimeter wave receivers, superconductor-insulator-superconductor mixers**

I. Introduction

The Atacama Large Millimeter Array (ALMA) is a collaboration between Europe, North America, and Japan to build an aperture synthesis telescope with 64 12-m antennas at 5000 m altitude in Chile [1]. In its full configuration, ALMA will observe in 10 bands between 30 and 950 GHz, and will provide astronomers with unprecedented sensitivity and spatial resolution at millimetre and sub-millimetre wavelengths.

Band 9, covering 602-720 GHz, is the highest frequency band in the baseline ALMA project, and will thus offer the telescope's highest spatial resolutions. Furthermore, sub-mm observations with Band 9 of ALMA will provide complementary information to observations with the observatory's lower frequency bands, due to the fact that sub-mm line observations typically probe warmer, denser material than mm-wavelength observations, while continuum observations over a broad range of frequencies will better constrain dust temperatures.

The ALMA Band 9 cartridge is a field-replaceable unit containing the core of a 600-720 GHz heterodyne front-end. Primary requirements of the Band 9 cartridges include:

- double side-band (DSB) operation with $T_{N,rec}$ = 169 K over 80% of the 614-708 GHz LO frequency range;
- an intermediate frequency (IF) bandwidth of 4-12 GHz with low power variation across the band (6 dB peak-to-peak and 4 dB within any 2 GHz) and a total output power level of -37 to -24 dBm;
- detection of two orthogonal linear polarizations with cross-polarization levels of -20dB;
- 90% coupling of the cartridge's optical beam to the telescope secondary;
- long lifetime and high reliability; and
- the design must be consistent with the need for series production of 64 cartridges.

This paper presents the design of the first (prototype) Band 9 cartridge, together with results of first-light tests.

II. Cartridge Design Overview

The overall design of the Band 9 cartridge is highlighted in Figure 1. The Band 9 cartridge contains a electronically tunable LO, low-noise DSB superconductor-insulator-superconductor (SIS) mixers, and a low-noise, broad-band IF chain. These are combined in a compact opto-mechanical structure that interfaces with the ALMA cryostat. Each of these elements in the cartridge design is discussed in the following sections.

A. Basic Cartridge Structure

The basic structure of the cartridge body is defined by the design of the ALMA cryostat from the Rutherford Appleton Laboratory [2]. It consists of 4 plates separated by thermally

Manuscript received May 30, 2005. This work was coordinated by the Netherlands Research School for Astronomy (NOVA) under contract to the European Southern Observatory (ESO) (contract 73072/MAP/03/8632/GWI).

R. Hesper, A. M. Baryshev, J. Adema, G. Gerlofsma, M. Bekema, J. Barkhof, F. P. Mena, A. Koops, and W. Wild are with the Kapteyn Astronomical Institute, Landleven 12, 9747 AD Groningen, The Netherlands.

B. D. Jackson, K. Keizer, H. Schaeffer, and W. Wild are with the SRON Netherlands Institute for Space Research, Landleven 12, 9747 AD Groningen, The Netherlands. (corresponding author: B.D. Jackson; phone: +31-50-363-8935; fax: +31-50-363-4033; e-mail: B.D.Jackson@ sron.rug.nl)

R. Hesper, B. D. Jackson, A. M. Baryshev, J. Adema, T. Zijlstra, G. Gerlofsma, M. Bekema, K. Keizer, J. Barkhof, F. P. Mena, and A. Koops are with the Netherlands Research School for Astronomy (NOVA), Postbus 9513, 2300 RA, Leiden, The Netherlands.

M. Kroug, T. Zijlstra, and T.M. Klapwijk are with the Kavli Institute for Nanoscience, Faculty of Applied Science, Delft University of Technology, 2628 CJ Delft, The Netherlands.

K. Wielinga is with Mecon Engineering B.V., Postbus 679, 7000 AR Doetinchem, The Netherlands.

R. Rigas is with the Technische Universität München, 80290 München, Germany.

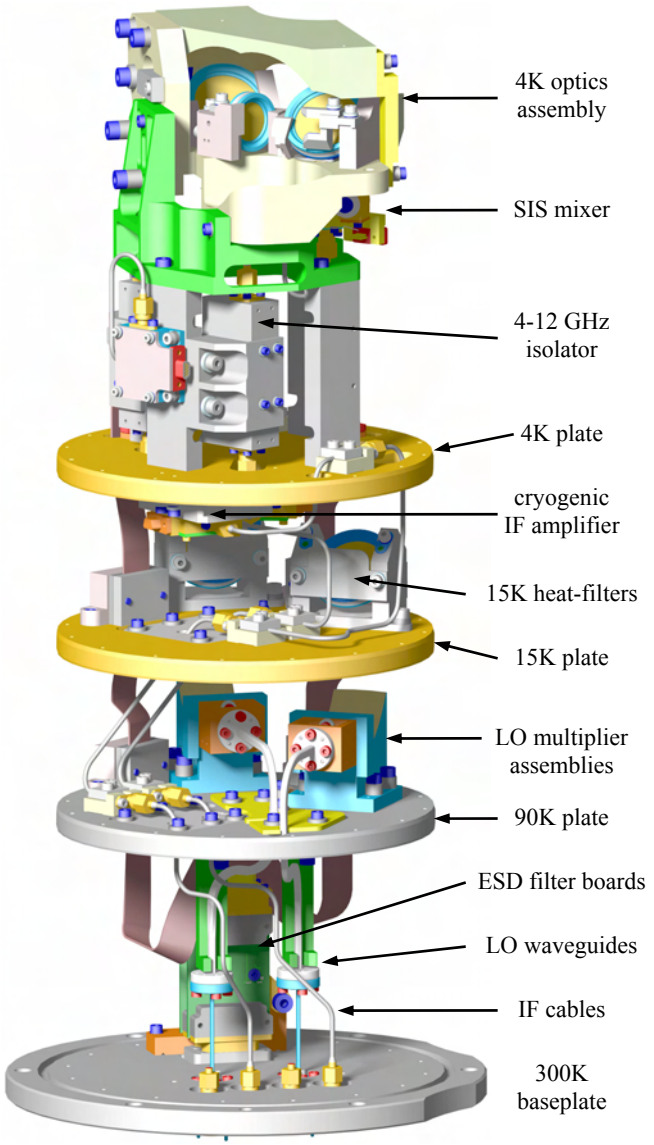

Fig. 1 – Layout of the ALMA Band 9 cartridge. The fibre-glass cylinders that separate the cartridge's four temperature levels are not shown.

insulating fibre-glass cylinders (not shown in Figure 1 to allow the cartridge's internal components to be seen). The lowest plate – the baseplate – is a vacuum flange in the base of the cryostat, while the 3 cold plates (at 90, 15, and 4 K) are connected to the cold plates of the ALMA cryostat by flexible thermal links (on the cryostat side of the interface).

B. Local Oscillator Injection

The ALMA Band 9 local oscillator (LO) is an electronically-tunable solid-state LO based on mm-wave (100-120 GHz) power amplifiers and Schottky diode frequency multipliers.

As described in [3], the LO signal is generated in a YIG oscillator operating at 16-20 GHz, followed by an active multiplier chain (x6). A portion of the output of the active multiplier is coupled into a phase-lock loop which phase-locks the 6th harmonic of the YIG oscillator to an externally

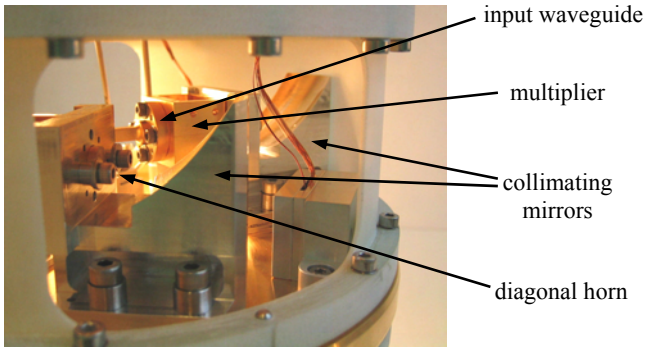

Fig. 2 – The LO multiplier assemblies mounted on the 90K stage of the first cartridge. The front of the diagonal horn of the nearest assembly is visible, as is the integrated x2x3 multiplier of the rear assembly.

generated reference signal. The remainder of the output from the active multiplier chain is coupled into the power amplifier unit, which amplifies, splits, and then further amplifies the signal to produce 2 high-power mm-wave outputs. The power of these two channels can be independently adjusted to allow the drive level of the cartridge's 2 SIS mixers to be independently tuned.

The output from the power amplifiers enters the cartridge via vacuum feedthroughs (with a thin Kapton windows sealing the cryostat vacuum), and is transported to the cartridge's 90K stage via WR8 waveguides. Short, straight sections of gold-coated thin-walled stainless steel waveguide are used as thermal breaks, while longer, bent sections of coin silver waveguide are used to accommodate differential thermal expansion between the cartridge's 300 and 90K stages.

The 90K stage contains 2 integrated x2x3 LO multipliers [4] that frequency multiply the 100-120 GHz outputs of the power amplifiers to produce the 600-720 GHz LO power that drives the cartridge's SIS mixers (see Figure. 2). This high frequency LO signal is optically coupled from the 90K stage to the 4K optics assembly via a diagonal horn and collimating mirror at 90K and an infrared heat-filter in the 15K stage. Within the cold optics assembly, each of the LO beams is refocussed and coupled into the mixer via a thin (14 μm) Mylar beamsplitter located in the optical beam in front of the mixer.

The YIG oscillator, active multiplier chain, and mm-wave power amplifiers, together with their associated control electronics and phase-lock loop are contained in a warm cartridge assembly that bolts to the outside of the cartridge baseplate (not shown in Figure 1). The warm cartridge assembly, including the LO components that it contains, together with the cold frequency multipliers, are developed and produced by the National Radio Astronomical Observatory (NRAO) and Virginia Diodes Inc. (VDI).

C. 4K Optics Assembly

The 4K optics assembly combines and focuses the incident astronomical beam from the ALMA telescope and the two LO beams originating on the 90K stage into two SIS mixers. As

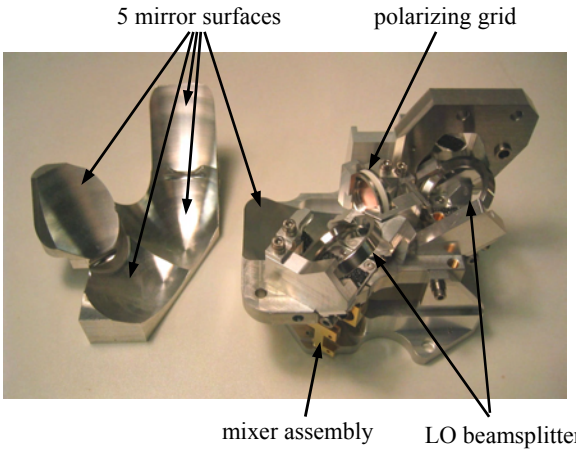

Fig. 3 – ALMA Band 9 optics assembly. The optics assembly is composed of two primary blocks – the upper block (left) contains 4 of the 5 mirror surfaces; while the lower block (right) contains 1 mirror surface plus the polarizing grid, 2 LO beamsplitters, and the 2 mixer assemblies.

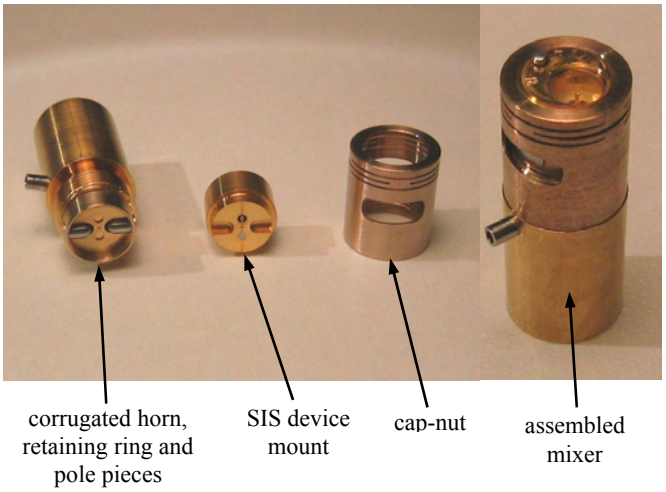

Fig. 4 – ALMA Band 9 SIS mixer. (left) The components of the mixer, including the new cap-nut with a multi-section spring cut into its walls. (right) The assembled mixer. The pin inserted into the horn is used for rotational alignment of the mixer in the mixer mount. (see Figure 5)

is described in more detail in [5], the beam from the telescope is refocussed by a common mirror and then split into to linear polarizations with a polarizing grid. Each linearly polarized signal beam is then focussed into a single SIS mixer, with a beamsplitter between the focussing mirror and the mixer being used to inject the local oscillator beam.

In total, the 4K optics assembly thus contains five mirrors, a polarizing grid, and two LO beamsplitters, which must be packed into a compact assembly to fit within the available space. Because of the complexity of this assembly, and its criticality to the overall performance of the Band 9 cartridge, specific attention has been paid in the design to making the assembly as easy as possible to manufacture and assemble. In particular, the system has been designed without any means for alignment of either the optics or the grid and beamsplitter mounts. As seen in Figure 3, this has been accomplished by machining four of the five mirrors into a single aluminum block (the upper block in Figure 1), with the fifth mirror and the mounting interfaces for the grid and beamsplitter mounts in the second (bottom) block. The alignment accuracy and optical quality of the cartridge's optical beam is thus determined by the accuracy with which these blocks are machined. However, as is shown in [5], the accuracy of modern precision CNC machines is sufficient to ensure that the desired optical performance is obtained.

D. SIS Mixers and Mixer Mounts

The incident astronomical signal is detected by two orthogonally polarized DSB SIS mixers to both maximize sensitivity, and to allow the polarization of the incident signal to be measured. The RF design and performance of the SIS mixers used in the ALMA Band 9 cartridge is described in [6]. As described previously and shown in Figure 4, the core of the mixer contains a corrugated horn (from Radiometer Physics [7]) and a SIS device mount that are clamped together by a so-called cap-nut that threads onto the horn, clamping the device mount to the back of the horn. A centering ring and two magnet pole pieces are used to both center and rotationally align the backpiece with respect to the horn. One new feature that has been introduced to this design is a multiple-section leaf spring that is machined into the side-walls of the phosphor bronze cap-nut (see Figure 4). This spring ensures that tightening the cap-nut onto the horn produces a controlled clamping force between the horn and device mount.

The SIS mixer slides into a mixer mount (see Figure 5) that contains the SMA connector for the mixer's IF output and all of the mixer's auxiliary circuitry, including an electromagnet for suppressing the Josephson effect in the SIS junctions, a contact spring that makes electrical contact to a resistive de-flux heater soldered into the SIS device mount, and a temperature sensor. This separation of the critical RF components of the mixer from the mixer mount ensures that the two halves can be separately assembled and tested, so as to

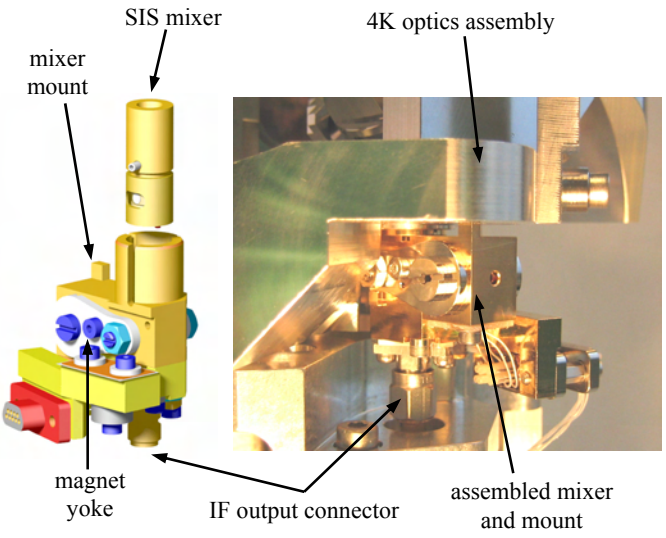

Fig. 5 – ALMA Band 9 mixer mount and mixer. (left) A 3-D model of the mixer and mixer mount. (right) An assembled mixer mounted in the 4K optics assembly of the first cartridge.

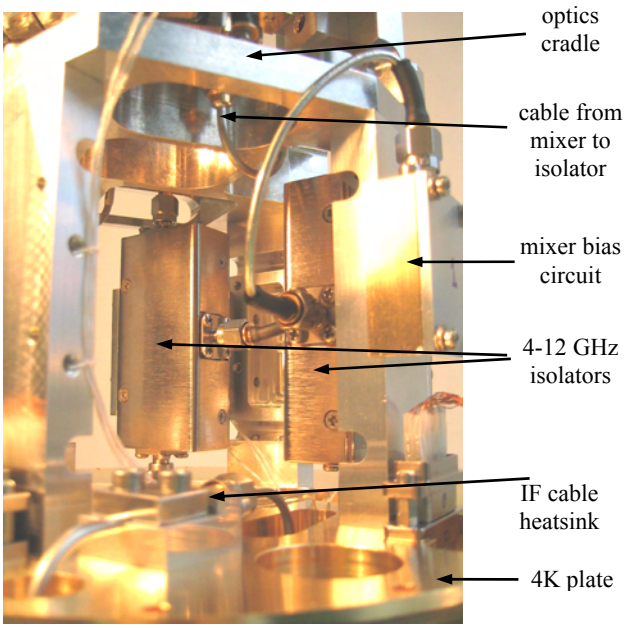

Fig. 6 – Two 4-12 GHz isolators from Pamtech [8] mounted on the 4K level of the first Band 9 cartridge. Note that the RF load port of the isolator has a DC connection to its RF input port, allowing the isolator to be used as a bias-T for the DC bias to the mixer.

further streamline the assembly (and eventual repair) of the cartridge. The mixer mount also provides an opto-mechanical interface between the mixer's corrugated horn and mounting holes that are bored in the 4K optics assembly.

E. Low-Noise 4-12 GHz IF Chain

Two of the significant technical challenges in the Band 9 cartridge are the requirement for a 4-12 GHz IF band and a low variation in output power across the IF band. Because the mixer and cryogenic amplifier are being designed and built independently, this has required the development of 4-12 GHz isolators (at Pamtech [8]) to suppress reflections in the cables between the mixer and the amplifier. As seen in Figure 6, the two isolators (one per mixer) are mounted on the side of the optics assembly's support legs. One additional feature of the 4-12 GHz isolator is that the RF load port has a DC connection to the signal input port, which allows the isolators to be used as bias-T's for supplying DC bias to the SIS mixers.

The cartridge's first-stage IF amplifiers are three-stage InP HEMT amplifiers mounted on the bottom of the cartridge's 4K stage. The 4-12 GHz amplifier that is under development at the Centro Astronomico de Yebes should offer an input noise temperature of ~ 5 K and 30 dB of gain, with < 9 mW of power dissipation per amplifier [9]. 4-8 GHz amplifiers are being used for preliminary tests of the cartridge while the 4-12 GHz amplifiers are being developed.

In order to ease assembly of the cartridge, the IF output from the cryogenic amplifier is coupled via a cable to top of the cartridge's 4K stage, where it is heat-sunk with a cable clamp and a bulkhead connector. Stainless steel cables are

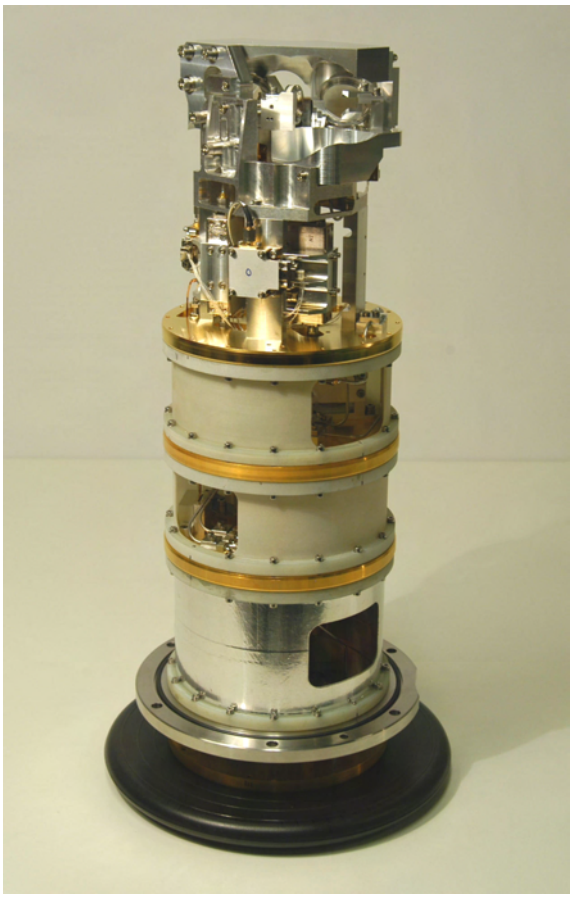

Fig. 7 – The first (prototype) ALMA Band 9 cartridge.

then used to couple the IF output signal out of the cartridge via bulkhead connectors and heat-sinks on each of the 15 and 90K stages and vacuum feedthroughs in the cartridge baseplate. Hand-formable semi-rigid cables with aluminum outer conductors are used to connect the components on the 4K stage (mixer-to-isolator, isolator-to-amplifier, and amplifier-to-bulkhead), due to their low loss and to minimize thermal-mechanical stresses.

The noise contributions of the ALMA front-end's IF system, including cabling and the IF switch that is used to select the active band, are minimized by placing a second-stage IF amplifier in the warm cartridge assembly that contains the warm LO components. A commercial amplifier is used for this purpose.

F. Opto-Mechanical Design

The cartridge components are built into a rigid opto-mechanical structure based upon the basic cartridge body from RAL (see Figure 7). With only a few exceptions, aluminum is used for all optical and mechanical components, in order to minimize the total mass of the cartridge and minimize differential thermal expansion. One notable exception to this is the 4K plate, which is copper, as defined by the design of the ALMA cryostat. Due to concerns about the potential effect of differential contraction on the alignment of the optics assembly (the two mirror blocks are aluminum), the optics are

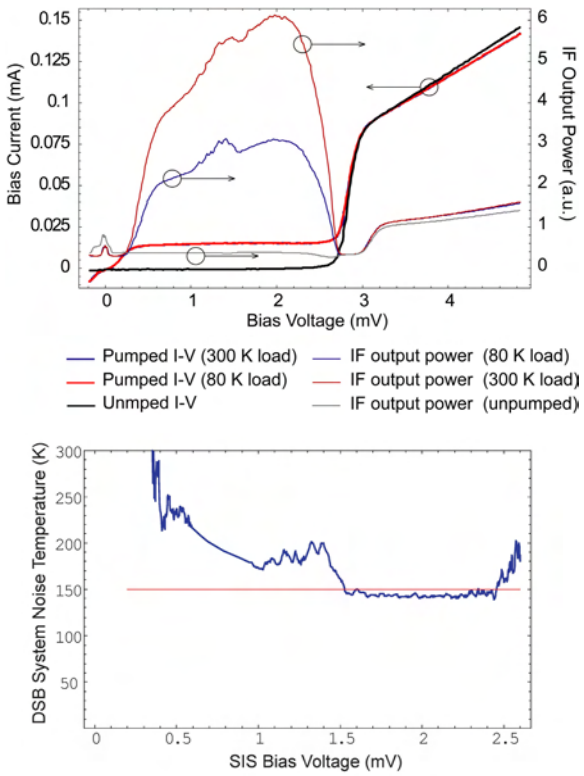

Fig. 8 – (top) Measured mixer bias current and IF output power as a function of bias voltage for one channel of the first cartridge, with and without LO power applied (at 638 GHz), and with LO power while looking at a hot (300 K) and cold (77 K) blackbody load. (bottom) DSB receiver noise as a function of bias voltage calculated from the hot and cold IF output power curves above. The mixer is driven by an external LO, coupled into the cartridge via an external beamsplitter. The optimum noise temperature of < 150 K is below the required level (169 K), despite the additional noise contributed by the external beamsplitter.

connected to the 4K plate by four rectangular posts that are flexible in the radial direction (to and from the centre of the cryostat), but stiff in the transverse direction. This geometry allows the posts to rigidly centre the optics assembly relative to the cartridge body, while also accommodating differential thermal expansion between the optics assembly and the 4K plate.

Because the cartridge will ultimately need to be produced in quantities of ~64 units, the cartridge design has been developed with the goal of simplifying its manufacturing and assembly. This is most strongly seen in the design of the 4K optics assembly described above. However, it also applies more generally to the cartridge as a whole – two of the primary design goals have been to maximize the use of standard commercial manufacturing methods (and standard commercial parts, where possible), and to minimize the assembly work that is required after commercially manufactured parts have been received.

III. First-Light Results

Manufacturing and assembly of the first (prototype) cartridge has been completed (see Figure 7), and testing of the cartridge is now proceeding. Figure 8 presents first-light measurements of the sensitivity of one channel of the first cartridge pumped by an external LO (and thus including additional noise contributed by an external beamsplitter). In particular, the measured SIS mixer bias current and the receiver's IF output power are plotted as a function of SIS bias voltage, with and without LO power (at 638 GHz) and looking at a hot (300K) and cold (80K) blackbody load. The DSB receiver noise temperature that is calculated from the measured IF output power is also shown. From this plot, it is seen that even with the additional noise contributed by the external beamsplitter, the measured receiver noise is still below the $T_{N,rec}$ = 169 K that is required. Measurements are now proceeding over a wider range of frequencies, and using the internal LO.

These measurements were performed at a mixer temperature of ~ 2.8 K (the base temperature of the cartridge test cryostat provided by the National Astronomical Observatory of Japan, NAOJ). The IF output from the cartridge is amplified, filtered with a YIG filter (with a bandwidth of 50 MHz at a center frequency of 6 GHz), and then detected with a power meter. The receiver noise temperatures are calculated from the measured IF output power and the blackbody load temperatures in the Rayleigh-Jeans limit. The external beamsplitter is 40 µm thick, offering an LO injection efficiency of ~ 10% for this polarization.

IV. Conclusion

The ALMA Band 9 cartridge is a low-noise SIS receiver covering the 602-720 GHz atmospheric window with low noise and a broad (4-12 GHz) IF band. Due to the large number of cartridges that will ultimately be needed for the ALMA project, the design of the cartridge has been optimized to take advantage of the capabilities of modern precision CNC machining to ease its manufacturing and assembly. First-light heterodyne sensitivity measurements at a single LO frequency have also been presented.

Acknowledgment

The authors would like to thank W. Boland, E. van Dishoeck, and G.-H. Tan for their support for the work presented here.

References

[1] Gie Han Tan and R. Kurz, "The Atacama Large Millimeter Array," in: Proc. of 3rd ESA Workshop on Millimetre Wave Technology and Applications: Circuits, Systems, and Measurement Techniques ESA WPP 212, ESA, Noordwijk, Netherlands, 2003, pp. 107-12.

[2] A. Orlowska, M. Harman, and B. Ellison, "Receiver Cryogenic System," Ch. 6 in: J. Baars (Ed.), ALMA Construction Project Book Version 5.50, 2002.

[3] E. Bryerton, K. Saini, M. Morgan, D. Thacker, and T. Boyd, "Development of Electronically Tuned Local Oscillators for ALMA", 30th International Conference on Infrared and Millimeter Waves and 13th International Conference on Terahertz Electronics, Sep. 2005.

[4] J. Hesler, "Submillimeter Wave Sources and Receivers: Creating a Practical Technology Base," presented at the 16th Int. Symposium on Space THz Technology – ISSTT 2005, Chalmers University of Technology, Göteborg, Sweden, May 2-4, 2005.

[5] M. Candotti, A. Baryshev, N. Trappe, R. Hesper, J.A. Murphy, and J. Barkhof, "Quasi-Optical Verification of the Band 9 ALMA Front-End," presented at the 16th Int. Symposium on Space THz Technology – ISSTT 2005, Chalmers Univerisity of Technology, Göteborg, Sweden, May 2-4, 2005; and A. Baryshev, R. Hesper, K. Wielinga, G. Gerlofsma, and M. Carter, "Design and verification of ALMA Band 9 receiver optics," in: G. Narayanan (Ed.), Proc. of the 15th Int. Symp. on Space THz Technology, Univ. of Massachusetts, Amherst, MA, April 27-29, 2004, pp. 433-440.

[6] A. Baryshev, E. Lauria, R. Hesper, T. Zijlstra, and W. Wild, "Fixed-tuned waveguide 0.6 THz SIS mixer with wide band IF," in: R. Blundell and E. Tong (Eds.), Proc. 13th Int. Symp. on Space THz Technology, Harvard University, Harvard, MA, Mar. 26-28, 2002, pp. 1-10.

[7] RPG Radiometer Physics GmbH, Birkenmaarstrasse 10, 53340 Meckenheim, Germany.

[8] Passive Microwave Technology, Incorporated, 4053 Calle Tesoro, Suite A, Camarillo, CA 93012, USA.

[9] I. Lopez-Fernandez, J. D. Gallego Puyol, A. B. Cancio, and F. Colomer, "New trends in cryogenic HEMT amplifiers for radio astronomy," presented at the Int. Science and Technology Meeting on the Square Kilometer Array, Berkeley, CA, July 9-13, 2001.

Investigations of mixers noises on semiconductor superlattices

D.G. Paveliev*, Yu. I. Koshurinov*, A.N. Panin**, V.L. Vaks**

*N.I.Lobachevsky Nizhniy Novgorod State University,

**Institute for physics of microstrutures Russian Academy of Sciences, Nizhniy Novgorod,Russia

Application of diodes on semiconductor superlattices in mixers allows increasing their high operating frequency in comparison with mixers on Schottky diodes. It is known that mixers on semiconductor superlattices have higher output noises in comparison with mixers on Schottky diodes. It is explained by presence of carrier's negative mobility zone at volt-ampere characteristic of diodes on semiconductor superlattices. It is possible to increase output noises or optimize signal-to-noise rates of output signal in IF circuit by taking the working area on volt-ampere characteristic of diodes on semiconductor superlattices. The both modes have practice interest. The first mode is suitable for obtaining the uniform broadband noise. The second one is necessary for obtaining maximum signal-to-noise rate in the IF circuit. The experimental set for investigations of semiconductor superlattice mixers characteristics in THz-band was designed for study of these modes of semiconductor superlattices diodes. This set consists of the BWO signal source with PLL system of a band more the 0,7 THz and a heterodyne. The both signals were applied to the mixer on semiconductor superlattices diodes. The superlattice noises dependence on the signal power was taken in IF circuit.

Non-spherically-decaying radiation from an oscillating superluminal polarization current: possible low-power, deep-space communication applications in the MHz and THz bands

J. Singleton[1], A. Ardavan[2], H. Ardavan[3], J. Fopma[2] and D. Halliday[2]
[1]National High Magnetic Field Laboratory, TA35, MSE536, Los Alamos National Laboratory, Los Alamos, NM 87545, USA.
[2]Department of Physics, University of Oxford, Oxford OX1 3PU, UK.
[3]Institute of Astronomy, University of Cambridge, Cambridge CB3 0HA, UK.

The emission of electromagnetic radiation from a superluminal (faster-than-light in vacuo) charged particle was first studied by Sommerfeld in 1904. However, the Special Theory of Relativity was published a few months later; prevailing scientific opinion then effectively curtailed the research field until Ginzburg and coworkers pointed out in the 1980s that no physical principle forbids emission by extended, massless superluminal sources. A polarization current density ($d\mathbf{P}/dt$; see Maxwell's fourth equation) can provide such a source; the individual charged particles creating the polarization do not move faster than c, the speed of light, and yet it is relatively trivial to make the envelope of the polarization current density to do so.

Based on these principles, we have constructed a practical realization of an accelerated, oscillating superluminal source [1,2]. This provides precise control of the source speed over the range c to $2c$ and emits radiation chiefly at frequencies ~0.6 THz [1,2]. As described in theoretical [3,4] and experimental [1,2] papers that explore the physics of the practical machine, the emitted radiation has many unusual characteristics, including: (i) the intensity of some components decays as the inverse of the distance from the source, rather than as $1/(\text{distance})^2$ (i.e. these components are *non-spherically-decaying*); (ii) the emission is tightly beamed, the exact direction of the beam depending on the source speed; and (iii) the emission contains very high frequencies not present in the synthesis of the source. Note that the non-spherically-decaying components of the radiation do not violate energy conservation. They result from the reception, during a short time period, of radiation emitted over a considerably longer period of (retarded) source time; their strong electromagnetic fields are compensated by weak fields elsewhere [1].

In this presentation, we shall describe recent calculations and measurements that explore the geometry of the non-spherically-decaying radiation. We show that the emission occupies a very small polar angular width of order 0.8 degrees in the far field. Based on these findings, we suggest that a superluminal source could act as a highly directional transmitter of MHz or THz signals over very long distances. Such a machine would have very low power requirements compared to a conventional transmitter, making it suitable for communication to and from deep space probes.

[1] A. Ardavan *et al.*, *J. Appl. Phys.* **96** 4614 (2004).
[2] J. Singleton *et al.*, *IEEE Conference Digest* **04EX857**, 591 (2004).
[3] H. Ardavan *et al.*, *J. Opt. Soc. Am. A* **20**, 2137 (2003).
[4] H. Ardavan et al., *J. Opt. Soc. Am. A* **21**, 858 (2004).

Analytical modelling of THz frequency multipliers and mixers based on Schottky diodes

Oliver Nipp[1], Viktor Krozer[1], Jesús Grajal de la Fuente[2], José Vicente Siles Pérez[2], and Bruno Leone[3]

[1] Electromagnetic Systems EMI, OerstedDTU, Technical University of Denmark, DK-2800 Lyngby, Denmark, email: vk@oersted.dtu.dk and with ATHENE e.V., Merckstrasse 25, D-64297 Darmstadt

[2] ETSIT, Universidad Politecnica Madrid, Ciudad Universitaria s/n, 28040 Madrid, Spain, email:jesus@gmr.ssr.upm.es and with ATHENE e.V., Merckstrasse 25, D-64297 Darmstadt

[3] Bruno Lenone is with the ESA/ESTEC, Keplerlaan, Noordwijk, The Netherlands

***Abstract*— We present an analytical Schottky diode model implemented into commercial CAD simulator for accurate simulation of frequency multipliers and mixers. The model is verified against our numerical model and measurements. We have found good agreement between measured and simulated results. It is demonstrated that the model could become a prediction and circuit design tool of choice due to its efficiency.**

Future generation of MMIC-based multiplier and mixer circuits for THz frequencies demand for simulation tools, which include circuit design and accurate device simulation. Currently, such tools are not commercially available. With the rapid development of GaAs processes significant progress has been reported for multipliers. Similar results are expected from integrated mixer circuits. Planar Schottky diodes are important for Earth observation and atmospheric sensing missions.

This paper demonstrates as analytical physical Schottky diode model for frequency multipliers and mixers. This activity is part of ESA's effort towards Schottky diode technology with the according design tools. In previous work we have presented simulated results for frequency multipliers for the Herschel platform [1], [2].

The analytical physical Schottky diode model employed here has been published in previous publications [3], [4] with numerous modifications. The model is implemented into Agilent ADS2003C environment as a senior device model. It is supported by an equivalent numerical model described earlier [1]. The numerical model has been substantially improved and will be a subject of a different contribution.

Figure 1 shows the cascaded efficiency for a frequency multiplier chain. It can be seen that the overall efficiency can still be improved, as compared to measured results achieved today. Based on these results combined multiplier mixer circuits will be demonstrated at the conference.

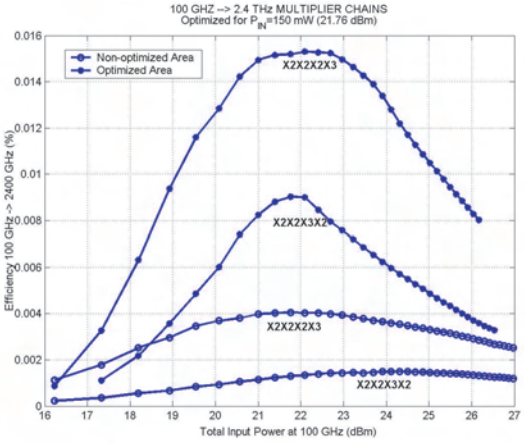

Fig. 1. Simulated and measured cascaded effi ciency versus the power level at 100 GHz.

REFERENCES

[1] J. Grajal, J. S. Prez, V. Krozer, E. Sbarra, and B. Leone, "Analysis and design of Schottky diode multiplier chains up to terahertz frequencies," in *Proc. Joint 29th International Conference on Infrared and Millimeter Waves and 12th International Conference on Terahertz Electronics*, (Karlsruhe, Germany), September 27 - October 1, 2004. invited keynote talk.

[2] V. Krozer and E. Sbarra, "THz LO generation with frequency multipliers," in *Proceedings of the Conference on Post herschel Perspectives 2003*, (Madrid, Spain), Sept. 2003.

[3] A. Jelenski, A. Grüb, V. Krozer, and H. L. Hartnagel, "New approach to the design and the fabrication of THz Schottky barrier diodes," *IEEE Trans. Microwave Theory & Techniques*, vol. MTT-41, no. 4, pp. 549–557, 1993.

[4] V. Krozer and A. Grüb, "A novel fabrication technique and process simulation by an analytical model for near-ideal epitaxial Pt/GaAs Schottky barrier diodes," *Solid-State Electronics*, vol. 37, no. 1, pp. 169–180, 1994.

Poster session II:

Detectors

Submillimeter wave detection using Josephson fluxonic diode

Farshid Raissi

K. N. Toosi University of Technology, P. O. BOX 16315-1355, Tehran 16314, Iran

raissi@kntu.ac.ir

We present simulation results on 0.5-0.8 THz detection properties of Josephson Fluxonic Diode (JFD) in its avalanche multiplication mode. JFD is a long Josephson junction to which a spatially reversing magnetic field is applied. Vortices fill half of the junction and antivortices fill the other half. JFD has a forward and a reverse bias mode of operation depending on the direction of bias current. Forward bias corresponds to a voltage state and reverse bias corresponds to a short circuit. When reverse biased, if the magnitude of magnetic field is larger than a threshold value and bias current is large enough, vortex and antivortex pairs are generated at the center and a voltage state is created. This phenomenon is similar to avalanche breakdown in semiconductor pn junctions. And similar to avalanche photodiodes it can be used to detect electromagnetic radiation. The interesting property of JFD is that the frequency and strength of the radiation necessary for pair-generation depends on the magnetic field and bias current.

Any radiation which affects Cooper pair density, the strength of magnetic field, or can modulate the bias current can cause pair generation. By biasing the junction at a certain current a predetermined frequency can be detected. Changing the bias current then changes the detected frequency. There are several advantages associated with JFD compared to regular quasi-particle SIS junctions. Such advantages include: a relatively large size comparable to radiation wavelength causing a better match to radiation, much larger voltage and currents at the operating point, and the ability to detect a very wide range of frequencies up to infrared and X-rays.

An Integrated Array Antenna for a TES Imaging Radiometer: General Concept and Simulations

Sergey V. Shitov, Alexander N. Vystavkin, *Member, IEEE*

***Abstract*—We are developing an imaging radiometer based on concept of direct connection of superconducting TES detector to a planar antenna. To control a large-dimension imaging array, multiplexing procedure via method of projection is suggested; the antenna array and the image are rotating reciprocally in their common plane during the signal integration process. Each crossed double-slot antenna feeds two TES detectors integrated in the central part of the antenna via a combination of microstrip and coplanar transmission lines. The instantaneous bandwidth of 50% is estimated for 5-Ω TES detector tuned at 600 GHz. The coupling circuit with overlapping RF feed-lines demonstrated cross-talk interference below -30 dB. Infinite expansion of the array is possible while the number of output leads can be minimized to N + M for N by M array; the continuous signal integration is available for all pixels. The design and analysis are performed using commercial EM-software.**

***Index Terms*—Bolometer, imaging array, method of projection, slot antenna, transition edge sensor.**

I. Introduction

A superconducting transition-edge sensor (TES) bolometer [1]-[3] consists of a radiation absorbing element attached to a superconducting film with a transition temperature T_c, which is weakly coupled to a heat sink at temperature $T_0 \approx T_c/2$. The superconducting film is heated by a bias source to an operating point within superconducting transition, where its resistivity is very sensitive to temperature changes. Since the bias voltage is fixed, the bias current through the TES is temperature-sensitive (optical signal sensitive), and it can be coupled to an ultra-low-noise amplifier based on a superconducting quantum interference device (SQUID amplifier).

Manuscript received May 2, 2005. This work was supported in parts by the by Russian State Program "Support of Leading Scientific Schools in Russia" (grant 1548.2003.2) and Program for Basic Research "Problems of Radio Physics" (Department of Physical Sciences, Russian Academy of Science) in direction "Applications in Terahertz Range".

S. V. Shitov is now with the National Astronomical Observatory of Japan, Mitaka, Tokyo 181-8588, Japan, on leave from the Institute of Radio Engineering and Electronics, Russian Academy of Sciences, Moscow 125009, Russia (phone: +81-422-34-3629; fax: +81-422-34-3817; e-mail: sergey@alma.mtk.nao.ac.jp, sergey@hitech.cplire.ru).

Alexander N. Vystavkin is with the Institute of Radio Engineering and Electronics, Russian Academy of Sciences, Moscow 125009, Russia (e-mail: vyst@hitech.cplire.ru).

The voltage bias introduced by Irwin [4] provides a negative electrothermal feedback, which stabilizes the temperature of the TES at the operating point on the transition. The electrothermal feedback keeps the total power input constant. This negative-feedback TES bolometer has advantages of good linearity and wider bandwidth; they can be produced by thin-film deposition and optical lithography, so they are suitable for large format arrays.

The absorption of RF power can be realized either directly within radiation absorption pads [5]-[10] or via combination of antennas and transmission lines heating the absorber. The antenna-coupled TES bolometer development [11]-[15] is just beginning, and it still tends to employ traditional thermally isolating legs or very thin membranes. Fortunately, the small area of integrated antenna terminations makes possible using TES absorber directly deposited on the silicon substrate without any legs for thermal isolation. At temperatures 0.1 K, the weakness of the electron-phonon interaction impedes the flow of heat from the metal into the dielectric substrate and can provide values of thermal conductance that are appropriate for low-background astronomical bolometers.

In our antenna-integrated TES, similar to [16]–[18], the extra weakening of the electron–phonon interaction is assumed via Andreev electron-reflection effect at the interface between the submicron-size absorber and leads of the antenna made from a higher-Tc superconductor (Nb). For our Mo/Cu absorber (Tc = 0.1-0.3 K) [19] operating within its superconductor transition region, the RF current from antenna assumed to be the source of hot electrons within the absorber. The heat escape from the absorber is limited by the above-mentioned Andreev mirrors, and the goal of producing bolometers with NEP $\approx 10^{-18}$ W $Hz^{1/2}$ and below can be set.

To control a large-dimension imaging array, the multiplexing procedure via method of projection, when the array and the radiation source image are rotating reciprocally in their common plane, is suggested [20]. Since the sky objects usually emit both polarizations, the projections method needs both polarizations to be analyzed. To receive both polarizations independently, a crossed double-slot antenna (CDSA) is used [21], but unlike in [15], we assume direct connection of TES to the leads of antenna.

To read and amplify output signals from the array, a concept of SQUID-amplifier working in a frequency

multiplexing mode [22] is being developed as a part of the imaging array research. The method of projections allows for minimizing the number of output leads to N + M for N × M array, since it assumes the connection of all detectors within a row and a column in parallel for their bias voltages and output currents. To resolve a 2-D image, the rotation of the image in respect to the array is assumed using, for example, a K-mirror system. Note that a full-time signal accumulation is possible for all elements of the imaging array.

Present paper describes our approaches for designing a practicable array antenna, which can work with TES detectors at submillimeter wavelength.

II. Details of Design

A. Antenna Packaging

The distance between elementary antennas can be found using requirements for their beams' overlapping. The beams' overlapping level can be defined according to desired sampling technique. We have chosen the under-sampling factor of four that allow the space between neighboring beams is just enough for accommodating another beam. This means that complete mapping of the image can be achieved via two samplings for each axis: to fill in a 2-D image four samplings are needed. The intersection level (taper level) is chosen at about -10 dB for two reasons. 1) Such low taper allow for clear separation of two neighboring pixels of the image, which has high pixel-to-pixel contrast. 2) High taper (say, -3 dB) means direct (on-chip) interference (cross-talk) of the integrated antennas via common RF currents that is in contrary with the wish of high-resolution imaging. Fig. 1 presents the antenna package with separation of 2λ (center-to-center) that provide low cross-talk between all components of the array as shown in Fig. 2. The extremely low cross-talk between the two polarizations of a crossed double-slot antenna (CDSA) is illustrated in Fig. 3 via the visualization of the current density distribution.

B. RF Coupling Circuit and DC Interconnections

Each pixel of the array contains two coupling circuits feeding two TES detectors integrated in the central part of the CDSA. These two circuits must overlap as shown in Fig. 3. Since the polarization separation properties of the two antennas (of the CDSA), each detector is sensing only one polarization. To connect each slot-antenna to its own TES detector, the combination of microstrip and coplanar waveguides is used. Since the output impedance of a slot antenna is about 50 Ω that is essentially higher than the resistance of the TES detector (0.5-5 Ω), a careful impedance transformation has to be considered. We have found that the problem of RF coupling of the low-resistive TES detectors is somewhat similar to the well-known problem of coupling SIS detectors [3]. The impedance of a small (low-resistive) TES is presumably reactive (inductive), and it needs to be tuned with a capacitive tuner, which can be provided by

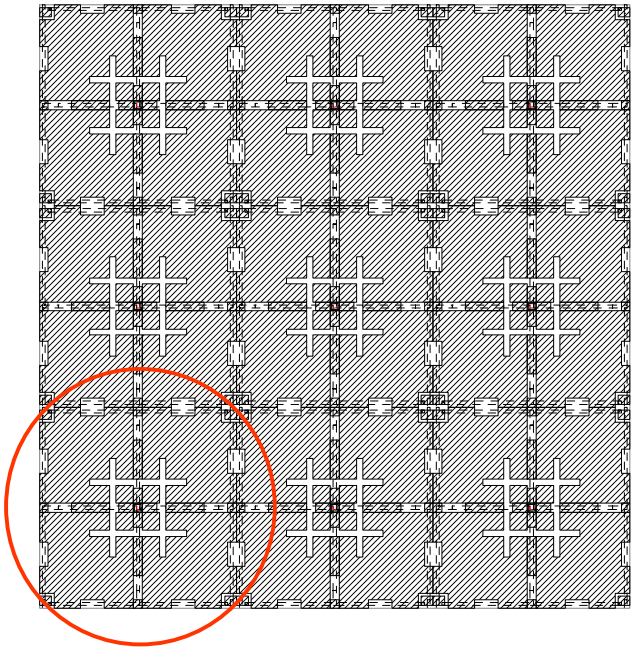

Fig. 1. Layout of array antenna. Each crossed double-slot antenna provides an elementary cell (pixel) marked by circle. Infinite multiplication is possible while keeping same complexity of the wiring.

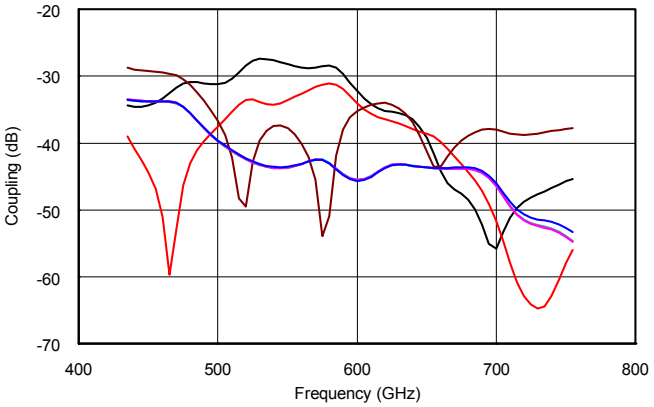

Fig. 2. Parasitic coupling between neighboring antenna elements of the array from Fig. 1. Simulation performed for CDSA positioned in the corner of the chip.

a fraction of a microstrip line (L < λ/4). We have estimated the bandwidth of about 50% for a 5-Ohm TES detector tuned for central frequency 600 GHz as shown in Fig. 4. Note that a narrower RF bandwidth (narrow-band filtering) can be provided simply via extra inductance in series with TES that result in higher Q-factor of the circuit.

To achieve the best symmetry on the two detector circuits, their overlapping is arranged on the base of coplanar waveguide (CPW) that allow for using only two metal layers as shown in Fig. 5. The CPW solution helps to minimize the asymmetry of the detectors in respect to the ground plane. In spite heavy cross-talk interference between overlapping CPW lines looks highly probable, we estimated the cross-talk below -30 dB at 600 GHz as presented in Fig. 6. Extra measures

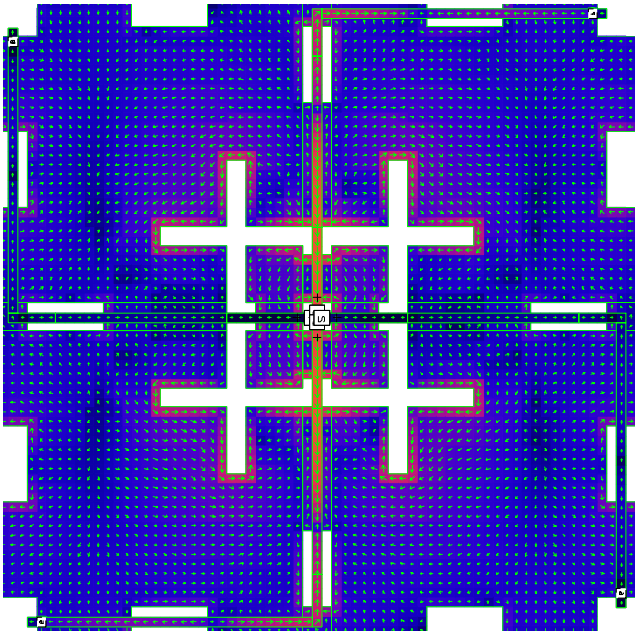

Fig. 3. RF currents at 600 GHz for the cell-antenna from Fig. 1 (simulation). Red and blue colors present high and low current density accordingly. Microstrip lines in the wiring layer provide both RF coupling and DC filtering.

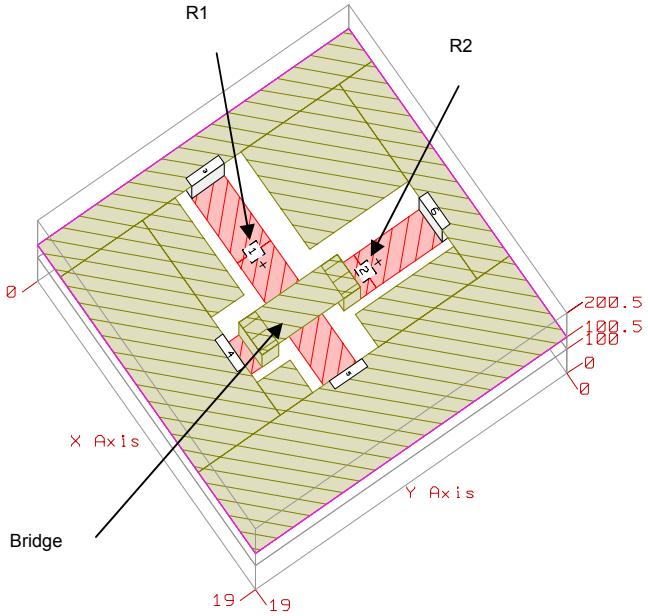

Fig. 5. Design of cross-line region providing best cross-talk isolation; internal ports R1 and R2 stand for two TES-detectors. Absolute symmetry of the structure is not possible, since detectors cannot be fabricated on top of each other.

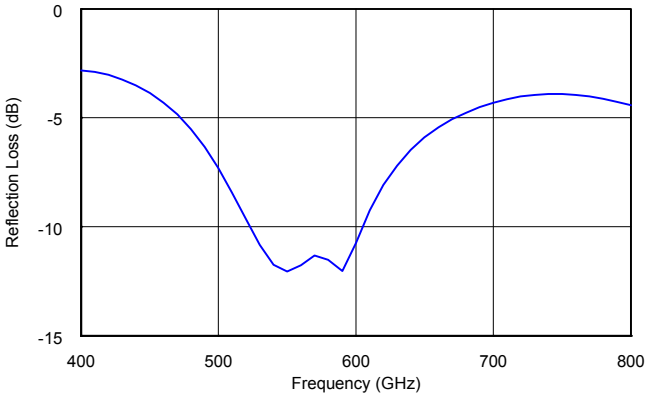

Fig. 4. Simulation of antenna coupling with 5-Ohm TES bolometer.

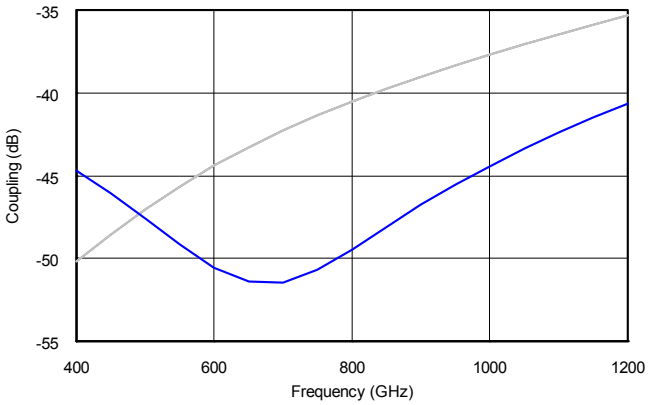

Fig. 6. Cross-talk level for the overlapping RF circuits from Fig. 5 (simulation). Result of improvement in cross-talk isolation at about 600 GHz is presented by the two curves that achieved via careful design of the asymmetric cross-hole as shown in Fig. 5.

can be taken for further reducing of the cross-talk as illustrated in Fig. 5 and Fig. 6.

The DC filters of the antennas (RF band-stop filters) are designed using alteration of λ/4-long CPW and microstrip waveguides that is clearly seen in Fig. 3. The CPW lines are formed by opening λ/4-long holes in the ground plane of the microstrip lines. The extensions of the RF filters at horizontal and vertical directions (see Fig. 3) form the DC bias/output signal wires, which are connecting all detectors in parallel for each column and for each row of the antenna array. This allow for virtually infinite expansion of number of pixels in the array without essential growing of complexity of the DC bias/read-out circuit. The presented simulations, including the antennas' impedance, are performed using commercial 2.5-D electromagnetic software ("Microwave Office" [23]).

C. Optical System and Cryostat

It is known that most of planar antennas are the low-gain antennas which have a very broad beam (typically wider than 90 degrees). To couple such antennas to the high-gain telescope beam, an intervening optics is necessary. The most advanced techniques of printed antennas employ the immersion-type lenses: hyper-hemispherical or truncated elliptical lenses [24]. It is important that the elliptical lens can work in the diffraction limit. This means it can offer the ultimate gain providing the beam waist at its aperture. Fig. 7 presents the optical concept for the integrated antenna array from Fig. 1 placed on the back of a truncated ellipsoid. We are going first try a small 9-pixel array of 3 by 3 pixels. To

achieve low spherical aberrations, the diameter of ellipsoid is estimated as 25 mm for our case.

To reduce the heat load to the milli-Kelvin stage and the detector, the infra-red (IR) filters are necessary along with proper focusing of the array beam at the smallest possible apertures of the thermal shields of the cryostat. The pure mono-crystalline silicon is a good material for both low-loss terahertz optics and efficient IR filters. The preliminary design concept shown in Fig. 7 assumes two long-focusing silicon lenses as the intervening optics in combination with three additional IR filters (scattering filters of narrow-band mesh filters).

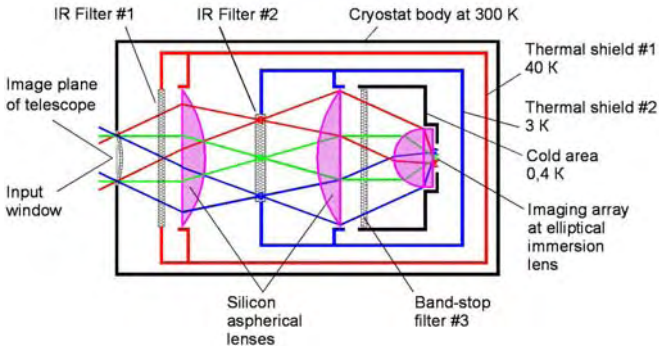

Fig. 7. Optical scheme of the imaging array TES-radiometer mounted within the ultra-low temperature cryostat.

ACKNOWLEDGMENT

Authors thank B. Karasik, H. Matsuo and M. Ishiguro for fruitful discussions.

REFERENCES.

[1] P. L. Richards, "Bolometric detectors for space astrophysics," in *Proc. Far-IR, Sub-MM, and MM Detector Workshop*, vol. NASA/CP-2003-211 408, J. Wolf, J. Farhoomand, and C. R. McCreight, Eds., 2003, pp. 219–223

[2] P. L. Richards, C. R. McCreight, "Infrared detectors for astrophysics," *Physics Today*, February 2005, pp. 41-47.

[3] J. Zmuidzinas, P. L. Richards, "Superconducting detectors and mixers for millimeter and submillimeter astrophysics," *Proc. IEEE*, 2004, v. 92, pp. 1597-1616.

[4] K. Irwin, "An application of electrothermal feedback for high-resolution cryogenic particle-detection," *Appl. Phys. Lett.*, vol. 66, no. 15, pp. 1998–2000, 1995.

[5] J. Gildemeister, A. Lee, and P. Richards, "Monolithic arrays of absorber-coupled voltage-biased superconducting bolometers," *Appl. Phys. Lett.*, vol. 77, no. 24, pp. 4040–4042, 2000.

[6] D. J. Benford, G. M. Voellmer, J. A. Chervenak, K. D. Irwin, S. H. Moseley, et al., "Thousand-element multiplexed superconducting bolometer arrays," in *Proc. Far-IR, Sub-MM, and MM Detector Workshop*, vol. NASA/CP-2003-211 408, J. Wolf, J. Farhoomand, and C. R. McCreight, Eds., 2003, pp. 272–275.

[7] W. Duncan, W. S. Holland, M. D. Audley, M. Cliffe, T. Hodson, et al., "SCUBA-2: Developing the detectors," in *Proc. SPIE, Millimeter and Submillimeter Detectors for Astronomy*, vol. 4855, T. G. Phillips and J. Zmuidzinas, Eds., Feb. 2003, pp. 19–29.

[8] J. Gildemeister, A. Lee, and P. Richards, "A fully lithographed voltage-biased superconducting spiderweb bolometer," *Appl. Phys. Lett.*, vol. 74, no. 6, pp. 868–870, 1999.

[9] D. J. Benford, M. J. Devlin, S. R. Dicker, K. D. Irwin, P. R. Jewell, et al., "A 90 GHz array for Green Bank Telescope, Nuclear Instruments and Methods in Physics Research," *Proc. of the 10th Intern. Workshop on Low Temperature Detectors – LTD-10,* Genoa, Italy, July 7-11, 2003, pp. 387-389.

[10] J. E. Ruhl, P. A. R. Ade, J. E. Carlstrom et al., "The South Pole Telescope," *Proc. SPIE (Intern. Symp. Astronomical Telescopes)*, 2004 [Online]. Available: www.spt.uchicago.edu/extweb/spt_spie_2004.pdf.

[11] S. Schwarz and B. Ulrich, "Antenna-coupled IR detectors," *J. Appl. Phys.*, vol. 48, no. 5, pp. 1870–1873, 1977.

[12] M. Nahum and P. Richards, "Design analysis of a novel low-temperature bolometer," *IEEE Trans. Magn.*, vol. 27, pp. 2484–2487, Mar. 1991.

[13] J. Mees, M. Nahum, and P. Richards, "New designs for antenna coupled superconducting bolometers," *Appl. Phys. Lett.*, vol. 59, no. 18, pp. 2329–2331, 1991.

[14] C. L. Hunt, J. J. Bock, P. K. Day, A. Goldin, A. E. Lange, et al., "Transition-edge superconducting antenna-coupled bolometer," in *Proc. SPIE, Millimeter and Submillimeter Detectors for Astronomy*, vol. 4855, T. G. Phillips and J. Zmuidzinas, Eds., Feb. 2003, pp. 318–321.

[15] M. J. Myers, A. T. Lee, P. L. Richards, D. Schwan, J. T. Skidmore, et al., "Antenna-coupled arrays of voltage-biased superconducting bolometers," in *Proc. 9th Int. Workshop Low Temperature Detectors*, vol. 605, F. S. Porter, D. McCammon, M. Galeazzi, and C. K. Stahle, Eds., 2002, pp. 247–250.

[16] B. Karasik, W. McGrath, H. LeDuc, and M. Gershenson, "A hot electron direct detector for radioastronomy," *Supercond. Sci. Tech.*, vol. 12, no. 11, pp. 745–747, 1999.

[17] B. Karasik, W. McGrath, M. Gershenson, and A. Sergeev, "Photon noise-limited direct detector based on disorder-controlled electron heating," *J. Appl. Phys.*, vol. 87, no. 10, pp. 7586–7588, 2000.

[18] B. S. Karasik, B. Dalaet, W. R. McGrath, J. Weu, M. Gershenson, and A. V. Sergeev, "Experimental study of superconducting hot-electron sensors for submm astronomy," *IEEE Trans. Appl. Supercond.*, vol. 13, pp. 188–191, June 2003.

[19] A. N. Vystavkin, S. A. Kovtonyuk, A. G. Kovalenko, "Experimental study of superconducting transition in a molybdenum-copper thin film structure showing the proximity phenomenon and the estimation of the sensitivity of TES bolometers on the basis of such a structure," *Nuclear Instruments and Methods in Physics Research*, 2004, vol. A 520, pp. 289-292.

[20] A. N. Vystavkin, A. V. Pestriakov, "The multiplexing of signals in direct detector arrays using projections method," *Nuclear Instruments and Methods in Physics Research,* 2004, vol. A 520, pp. 562-565.

[21] G. Chattopadhyay and J. Zmuidzinas, "A dual-polarized slot antenna for millimeter waves," *IEEE Trans. Antennas Propagat.*, vol. 46, pp. 737–737, May 1998.

[22] J. Yoon, J. Clarke, J. Gildemeister, A. Lee, M. Myers, et al., "Single superconducting quantum interference device multiplexer for arrays of low-temperature sensors," *Appl. Phys. Lett.*, vol. 78, no. 3, pp. 371–373, 2001.

[23] Microwave Office 2004 Design Suite [Online]. Available: http://www.appwave.com/products/mwoffice/

[24] D. Filipovic, S. Gearhart, and G. Rebeiz, "Double-slot antennas on extended hemispherical and elliptic silicon dielectric lenses," *IEEE Trans. Microwave Theory Tech.*, vol. 41, pp. 1738–1749, Oct. 1993.

Characteristics Measurements of Supersensitive Direct Detector Receivers of Submillimeter Waveband Region Using Planck Radiation Source

Alexander N. Vystavkin, *Member, IEEE,* Andrey V. Pestriakov, and Eugeny A. Vinogradov

Abstract—**A blackbody radiating at the temperatures and frequencies corresponding to the relationship $T \approx \hbar\omega/k$ which is valid when the radiation power spectral density is described by the Planck formula, is considered. This blackbody is used to measure the spectral characteristics and noise equivalent power of low-temperature ($T \approx 0.3…0.1$ K) direct detectors. The above relationship corresponds to the submillimeter waveband and temperatures ranging from several Kelvins to 40...50 K. It is suggested that the blackbody be placed in the cryostat cold area near a direct detector to prevent external thermal radiation which may overheat a low temperature refrigerator being employed. A measurement technique is developed which involves a Fredholm equation of the first kind and regularization methods.**

Keywords—M*illimeter- and submillimeter-wave direct detectors, super low temperature detectors, super high sensitive radiation detectors, spectral characteristics measurements, noise equivalent power measurements.*

I. Introduction

DURING the investigation and development of supersensitive low temperature direct detector receivers of submillimeter waveband region a need of measurements of their spectral and sensitivity characteristics is arising. We interpret the receiver as the direct detector, for instance, bolometer, the planar matching antenna into which the direct detector is incorporated (coupled) at submillimeter waves together with input and blocking filters, resonant circuit etc. or without them as well as focusing lens, for instance, immersion lens In the process of choice a measurement method the following circumstances have to be taken into account. The first: said direct detectors have to work at very low temperatures (0.3 – 0.1 K) to achieve super high sensitivity. The submillimeter radiation feeding in from outside to a refrigerator with measurement purposes is complicated problem because it is difficult to filter ambient background thermal radiation which will overheat the refrigerator strongly. The latter could not cope with intensive heat influx. The second: the radiation power value feeding in to the receiver, for instance, from a spectrum analyzer, has to be below of higher level of receiver dynamic range, i.e. before the beginning of non-linear portion of its signal characteristic. For existing now super low temperature submillimeter direct detectors [1] this limit may be two-three orders higher than their noise equivalent power, i.e. $NEP \approx 10^{-18}$ W/Hz$^{1/2}$ or less.

With the purpose to overcome said difficulties we propose to mount the black body source in cold area of receiver cryogenic system, for instance, inside the precooling cryostat at temperature 4.2 K, or to another place at lower temperature. The black body source has to be equipped with the heater and thermometer to be heated from units to ~ 40…50 K as well as with not complicated quasioptical system forming collimated radiation beam directed to the receiver. Using formulae from [2] we obtain the expression for the radiation power spectral density of black body thermal radiation at frequency ω from area S_{rad} in spatial angle $\Delta\Omega$:

$$p(\omega,T) = S_{rad} \cdot \Delta\Omega \cdot \frac{k^3T^3}{4\pi^3c^2\hbar^2} \cdot \frac{x^3}{e^x - 1}, \qquad (1)$$

where $x = \hbar\omega / kT$, $\hbar \cong 1.054 \cdot 10^{-34}$ J·s – Planck constant, $k \cong 1.38 \cdot 10^{-23}$ J/K – Boltzmann constant, and $c \cong 2.998 \cdot 10^8$ m/s – light speed in vacuum. The maximum of expression $y_\omega = x^3/(e^x - 1)$ takes place at $x_m \cong 2.85$ and is $y_{\omega m} \cong 1.415$. The position of this maximum at frequency f_m is connected with temperature as

$$f_m = (kx_m / 2\pi h)T \cong 0.594 \cdot 10^{11}\ T(\mathrm{K})\ \mathrm{Hz}, \qquad (2)$$

Manuscript received May 2, 2005. This work was supported in part by the Russian Council on Leading Scientific Schools under Grant No. SSCH-1548.2003.2 and by the Department of Physical Sciences of Russian Academy of Sciences in frames of the Program "Problems of Radiophysics" – section "The Development of Terahertz Frequency Band".

A. N. Vystavkin (corresponding author: phone: 7-095-203-25-05; fax: 7-095-203-84-14; e-mail: vyst@hitech.cplire.ru), and A. V. Pestriakov are with the Institute of Radioengineering and Electronics of Russian Academy of Sciences, 11 Mokhovaya Street, 125009 Moscow, Russian Federation.

E. A. Vinogradov is with the Institute of Spectroscopy of Russian Academy of Sciences, Troitsk, 142092 Moscow Region, Russian Federation.

what is one of forms of Wien shift law [2]. In accordance with (2) when the temperature changes from 4.2 to 50 K the frequency f_m moves from $f_m \cong$ 249.5 GHz ($\lambda \cong 1.2$ mm) at $T = 4.2$ K to $f_m \cong 2.97$ GHz ($\lambda \cong 0.1$ mm), i.e. the radiation power density maximum moves trough all submillimeter waveband range. One may estimate the radiation power value of said thermal radiation source in frequency band Δf in vicinity of frequency f_m keeping in mind that $P_{rad} \cong p_{\omega m} \cdot \Delta\omega = p_{\omega m} \cdot 2\pi\Delta f$. Substituting $p_{\omega m}$ from (1) at $y_\omega = y_{\omega m}$ we have

$$P_{rad} \cong 1.415 \cdot S_{rad} \cdot \Delta\Omega \cdot \Delta f \cdot (k^3 T^3 / 2\pi^2 c^2 \hbar^2).$$

For instance at S_{rad} = 0.1 cm^2, $\Delta\Omega \cong 10^{-2}$ sr and $\Delta f = 0.05 f_m$ Hz the calculation gives $P_{rad} \cong 1.75.10^{-14}$ and $P_{rad} \cong 2.44.10^{-10}$ W for 4.2 and 50 K respectively. These values, especially near to 50 K, could be higher than indicated above possible radiation power level. It can be reduced making S_{rad} and $\Delta\Omega$ smaller. Keeping in mind the variation of radiation power along whole submillimeter waveband region it is necessary to provide for several, at least two, black body source apertures.

The described circumstances give good possibility to measure the characteristics of supersensitive low temperature direct detector receivers of submillimeter waveband region using black body thermal radiation source with variable temperature from ~ 1 to ~ 50 K ($T \gg \hbar\omega / k$) and several apertures. We have named it by ***the Planck radiation source*** (PRS) in conformity with the characteristics measurements of said above receivers. This possibility and initial relations including the equation (3) (see below) were formulated in [3].

Below the methods of measurement of the spectral characteristics and the noise equivalent power (*NEP*) of said above receivers using the PRS are considered.

II. SPECTRAL CHARACTERISTICS MEASUREMENTS.

Not losing the common formulation of the problem we consider the method of spectral characteristics measurements of submillimeter receivers using the PRS applying it for the direct detector based on the electron heating in transition edge sensor (TES bolometer) with Andreev electron reflection [1]. The output current (detected signal) $|\Delta I|$ of such direct detector when the radiation power P_{abs} absorbed is: $|\Delta I| = S_I \cdot P_{abs}$, where S_I is current responsivity of direct detector**.** For a direct detector receiver with spectral characteristic (transfer function) $k(\omega)$ one may obtain the receiver current response:

$$\left|\Delta I(T)\right| = S_I \cdot P_{abs}(T) = S_I \int_{\omega_{\min}}^{\omega_{\max}} k(\omega) \cdot p(\omega, T) d\omega, \quad (4)$$

where $\omega_{\min}$ and $\omega_{\max}$ are lower and higher limits of chosen frequency range for spectral characteristic measurement and $p(\omega,T)$ is determined by (1). We rewrite (4) in the next form

$$Ak(\omega) = \int_{\omega_{\min}}^{\omega_{\max}} p(\omega, T) \cdot k(\omega) d\omega = I(T),\ T_{\min} \le T \le T_{\max}, \quad (5)$$

where $T_{\min}$ and $T_{\max}$ are lower and higher limits of chosen temperature range of the PRS, for instance 4.2 K and 50 K, and $I(T) = \left|\Delta I(T)\right| / S_I$. The equation (5) is the Fredholm integral equation of first kind with non-precisely given right side (measurement errors, noise) [4, 5]. The solving methods of such equations for various applied problems using regularizing methods, for instance Tikhonov method, are well developed [4-6]. We have followed by well known approach [6] when the problem is reduced to the boundary problem for Euler equation:

$$\left.\begin{aligned} &\int_{\omega_{\min}}^{\omega_{\max}} k(\omega) \cdot \bar{p}(\omega, T) d\omega + \alpha\{k(\omega) - qk''(\omega)\} = g(\omega), \\ &k(\omega_{\min}) = 0, \quad k(\omega_{\max}) = 0, \\ &\bar{p}(\omega, T) = \int_{T_{\min}}^{T_{\max}} p(t, \omega) \cdot p(t, T) dt, \\ &g(\omega) = \int_{T_{\min}}^{T_{\max}} p(t, \omega) \cdot I(t) dt. \end{aligned}\right\} \quad (6)$$

In this case we have replaced the initial equation (5) with the equation with stabilizer $\alpha\{k(\omega) - qk''(\omega)\}$ which permits to find approximate solution but stable for small variations of measured data at some positive stabilizer parameters α and q. For calculations the equation (6) is replacing with its difference equivalent at the even grid with increment i besides the middles of segments are accepting as grid nodes, i.e.:

$$i = (\omega_{\max} - \omega_{\min}) / n, \quad t_z = 0,5 \cdot i + (z-1) \cdot i, \quad (7)$$
$$z = 1, 2, ..., n.$$

As the result we obtain the difference equation:

$$\sum_{j=1}^{n} \bar{p}(\omega_j, T_z) \cdot i \cdot k(\omega_j) + \alpha \cdot k(\omega_z) +$$
$$+\alpha \cdot q \cdot \frac{2 \cdot k(\omega_z) - k(\omega_{z-1}) - k(\omega_{z+1})}{i^2} = g(\omega_z). \quad (8)$$

The solution of this equation is reducing to the solution of linear equation set with amount of frequency and temperature sampling points usually from 32 to 512. Main difficulties during the solving of this problem are the large range of data variation and the large amount of variational parameters using for the stability providing and the solution precision improvement.

We have computer simulated the solution of problem of spectral characteristic $k(\omega)$ measurement of mentioned above direct detector receivers for various forms of $k(\omega)$. The set of transfer function was given analytically. They were substituted to (5) and $I(T)$ for T = 4.2 – 50 K were calculated for each of them. After that using calculated

$I(T)$ the reverse problem was solved by described above method using the equation (8). The obtained transfer functions were compared with initial ones as the result of what the conclusion on the method effectiveness was made. At Fig. 1 the example of results of simulation with the transfer function $k(f)$ in form of resonant circuit

$$k(f) = Q^2 / [Q^2(1 - f^2 / f_0^2)^2 + f^2 / f_0^2] \qquad (9)$$

with resonance frequentcies f_0 = 150 GHz and f_0 = 2000 GHz and the quality Q = 20 are given. At first the search of a position and form of the direct detector response in wide frequency band was made (Fig.1,a,b) during the reverse problem solving. Then the frequency band was narrowed in accordance with determined approximate position and form and the procedure was repeated. This permitted to determine the position and the form.of response more precisely. The result of such repeated procedure for resonant transfer function for f = 2000 GHz is given at Fig. 1,c. The peak of reconstructed curve is ~ 20% less and width is ~ 20% larger in comparison with initial curve. Similar differences take place for another Q's: for instance ~ 10% for Q = 10 and ~ 5% for Q = 5. At the same time it was found that the relation $A[k(f)] \cong 1/Q$, where $A[k(f)]$ is the area under curve $k(f)$, takes place as for initial so for reconstructed transfer characteristics. Knowing the value of $A[k(f)]$ we may correct with sufficient precision the curve width and the peak height in necessary direction. The similar results in respect of peak heights and curve widths were obtained for the transfer functions in form of Gaussian, parabola and Π-shape curves what gives possibility to conclude that form of the transfer function is not so important. It was possible to reconstruct without difficulties the transfer functions in presence of up to five percent noise in the measured current as well as for double-peak curve of two coupled resonant circuits. All these approve the normal work of measurements method using the PRS up to $Q \approx 100$. Measurement simulation result for double-resonance spectral characteristic is given at Fig. 2. One may see that PRS method has acceptable frequency resolution.

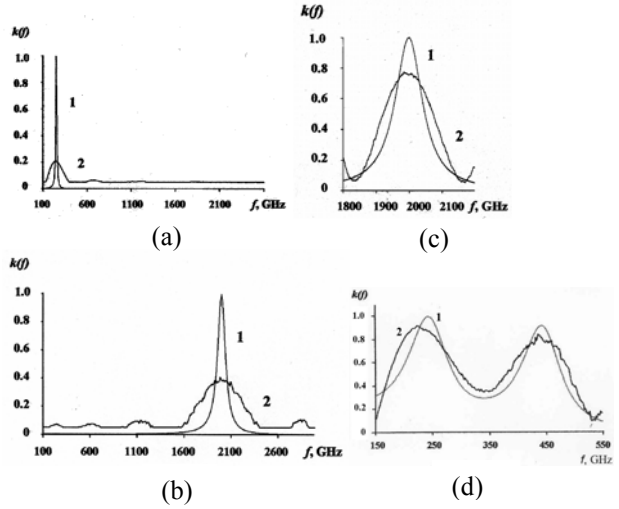

Fig. 1. The results of computer simulation with the spectral characteristic in form of resonant circuit with Q = 20: (a) and (b) – the search of position and form for f_0 = 150 GHz and f_0 = 2000 GHz respectively, (c) – the refining of the position and the form for f_0 = 2000 GHz; the same for double-resonance characteristic (d); **1** – initial and **2** – resulting spectral characteristic.

Acttual measurements of the receiver spectral characteristic should involve measurements of dependence $|\Delta I(T)|$ instead of $I(T)$ in (5). Then, spectral characteristic $k(\omega)$ in (5) must be replaced by the function $K(\omega) = S_I Lk(\omega)$. Here, factor L characterizes the receiver (including detector and matching elements) losses. It is assumed that these losses slightly depend on frequency only within the frequency range of the measured spectral characteristic of a receiver. Function $K(\omega)$ is a solution of (5) and can be represented in the form

$$AK(\omega) = \int_{\omega_{\min}}^{\omega_{\max}} p(\omega, T) K(\omega) d\omega = |\Delta I(T)|, \qquad (10)$$

$$T_{\min} \le T \le T_{\max},$$

The amplitude of obtained function $K(\omega)$ is equal to $K(\omega)_{\max} = S_I L = S_{Iopt}$. This value corresponds to the optical current response of a direct detector. The dividing of $K(\omega)$ by $S_I L$ yields dimensionless spectral characteristic $k(\omega)$; the dividing of $K(\omega)_{\max}$ by S_I yields microwave (optical) loss L by a direct detection receiver.

III. *NEP* MEASUREMENTS

The standard method of receivers *NEP* measurements at microwave frequencies is the well known method of cold/warm loads (sources). This method is working at frequencies and temperatures when $x << 1$ ($\hbar\omega \ll kT$), i.e. when the relation (1) becomes

$$p(\omega, T) \cong S_{rad} \cdot \Delta\Omega \cdot (\omega^2 / 4\pi^3 c^2) \cdot kT$$

(Rayleigh-Jeans formula) what means that $p(\omega, T) \propto T$. At frequencies and temperatures when $\hbar\omega \sim kT$ there is no proportionality between $p(\omega, T)$ and T and the method of cold/warm loads is not valid. Instead of the using two temperatures of the radiation source, in our case of the PRS, we propose to use two apertures of this radiation source. Then the absorbed powers by the receiver will be proportional to S_{rad}. It is convenient to set such PRS temperature when the radiation frequency corresponding to the maximum of its spectral radiation density will coincide with the middle of of receiver frequency bandwidth. These data are known from the foregoing measurements of the receiver spectral characteristic. In this case the *NEP* measurement will consist of measurement of two output signals at two apertures and hash width at the receiver output. Then the hash width has to be expressed in thermal power units of the PRS.

When realizing the described measurement method using the PRS in conformity with definite direct detector receiver design the additional examination is needed. This is important, for instance, when the receiver design comprises planar antenna/antennas matching an incident

radiation with the detector/detectors [1]. We consider, as an example, the radiation beam passing in optical camera of a possible imaging radiometer (Fig. 2) from the telescope output through lenses to antenna array with direct detectors (for

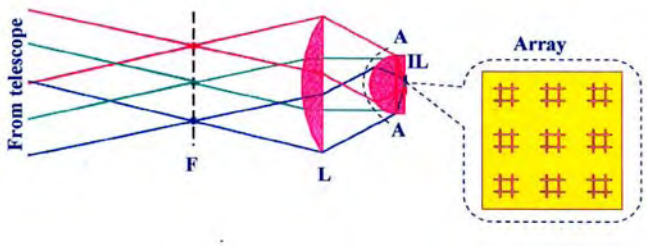

Fig. 2. Simplified scheme of a possible submillimeter imaging radiometer optical camera with 3×3 detector array: F is the telescope focal plane, L is the intermediate lens, IL is the immersion lens focusing radiation beam onto the antennas-detectors array.

instance, bolometers) coupled into antennas. The beam passing in vicinity of antenna array, moreover, from antennas to detectors of course can not be described in conception of geometrical optics: the examination in conception of wave optics is needed. It has to be done actually with the purpose to construct the optical camera with maximum possible radiation power transmission factor from the immersion lens input to detectors. Setting this problem apart we may formulate the problem of direct detector receiver characteristics measurement in conformity with considered case choosing the surface AA (Fig. 2) as an input of the receiver. Exactly in this place the spectral characteristic and noise equivalent power of receiver have practical importance. If so, whole presented above consideration has to be applied on the basis of conception that the surface AA (Fig. 2) is the receiver input. It is necessary to emphasize that spectral characteristics of receiver pixels are determined first of all by frequency characteristics of separate matching antennas with detectors. Losses in each pixel will worsen the receiver *NEP*. Both characteristics are determined in the measurement procedure as described above. We suppose that characteristics of each pixel have to be measured. Keeping in mind the optical camera scheme shown at Fig. 2 it is necessary to repeat that we have to create a precisely collimated radiation beam in the optical measurement scheme corresponding to the receiver array structure.

ACKNOWLEDGMENT

Authors thank V. V. Shevchenko and V. A. Cherepenin for useful discussions.

REFERENCES

[1] A. N. Vystavkin, "Supersensiting hot-electron microbolometer with Andreev electron reflection phenomenon for submillimeter radio astronomy", *Radiotekhnika i Elektronika* (in Russian), 2001, v. 46, # 7, pp. 806-815.

[2] D. V. Sivukhin, "Physics (general textbook)" v. IV "Optics", Ch. X "Thermal radiation".(in Russian), *"Nauka" Publishing House,* Moscow, 1985,

[3] E. A. Vinogradov, A. N. Vystavkin, § 8.6 in the Annual report № 2 on the project 1239 of the ISTC "Investigation and development of the ultrahighsensitive terahertz frequency band hot-electron S-LN-S microbolometer microbolometer for extra atmosphere astrophysics observations and measurements", April 16, 2002.

[4] A. N. Tikhonov, V. Ya. Arsenin, "Methods of solution of ill-conditioned problems" (in Russian), *"Nauka" Publishing House,* Moscow, 1986.

[5] A. F. Verlan', V. S. Sizikov, "Integral Equations: Methods, Algorithms, Proframs" (in Russian), *"Naukova Dumka" Publishing House,* Kijev, 1986.

[6] A. V. Gontcharsky, A. M. Cherepashchuk, A. G. Yagola, "Computational methods of astrophysics reverse problems solving" (in Russian), *"Nauka" Publishing House,* Moscow, 1978.

Detection of Terahertz radiation using large Niobium detector arrays

Simon Doyle, Chris Dunscombe, Philip Mauskopf
Department of Physics and astronomy
Cardiff University
Cardiff
Email: Simon.Doyle@Astro.cf.ac.uk

Zaid Aboush, Adrian Porch
Department of Electrical Engineering
Cardiff University
Cardiff
Email:PorchA@cf.ac.uk

***Abstract*— Kinetic Inductance Detectors (KIDs) made from Niobium are an attractive solution for constructing large detector arrays working at temperatures achievable using only modest cryogenic equipment. In a high Q resonant structure, generation of non-equilibrium quasiparticles upon photon absorption causes a change in complex impedance of the superconducting thin film making up the resonator. This change in complex impedance is observed through a shift in the resonant frequency or a phase change of a microwave probe signal. Fabricating KIDs of varying resonant frequencies means they can be easily multiplexed and therefore lend themselves to use in large detector arrays. Here we present results from the fabrication and testing of simple resonant structures created from Niobium thin films and cooled to 4.2 K. We discuss the design and optimisation of antenna coupled and lumped element Niobium KIDs for use in the detection of THz radiation.**

I. Introduction

Kinetic Inductance Detectors (KIDs) are capacitively coupled superconducting transmission lines that effectively measure the quasiparticle density of the superconductor. The equilibrium quasiparticle density can be perturbed by a change in temperature of the resonator or by direct absorption of a photon above the gap energy $2\Delta/h$. This change in quasiparticle density will alter the complex impedance of the resonator and hence its resonant frequency. The change in resonant frequency is proportional to the kinetic inductance L_k which is increased with reduction of the centre strip width or thickness. This change in resonant frequency will also give rise to a change in the phase of a fixed tone microwave probe signal of frequency equal to that of the resonator's resonant frequency f_0. This change in phase for a given shift in resonant frequency is enhanced by the overall unloaded Q factor of the resonator and its coupling coefficient g[1].

The fundamental limiting factor of a KID is the noise associated with the random generation and recombination of quasiparticles in the resonator. This noise is proportional to the quasiparticle life time τ_{qp}, which depends on the superconducting material and temperature[2]. The quasiparticle lifetime also provides a lower limit for the time constant of a KID. However this limit is realistically inaccessible due to the electronic ring-down time of high Q circuits. Owing to the longitudinal current distribution of a half wave resonator the response of a KID demonstrates a position dependence which is greatest for an absorption event occurring half way along the centre strip. For a quarter wave resonator the optimal position for photon absorption occurs at the shorted end of the centre strip. There have been various solutions proposed for both antenna coupling and quasiparticle trapping using quarterwave resonators. In this paper we discuss the theoretical performance of a Niobium KID operating at modest cryogenic temperatures.

II. Microwave details of a KID

The favoured resonator geometry for KIDs is the coplanar waveguide resonator (shown in fig1). Unlike microstrip or stripline devices, the impedance of the coplanar waveguide resonator (CPWR) can be set by altering the gap width (s) alone provided that the substrate thickness $d \gg s$. The flexibility of such a structure allows us to set a centrestrip width (w) to whatever we desire and still have control over the impedance of the resonator for matching to an antenna or our microwave probe source. For most applications a characteristic impedance Z_0 of 50Ω is desirable which requires a s/w ratio of 0.142 for a CPWR on sapphire ($\epsilon_r \approx 9.4$) . The impedance of the resonator is further modified by the fact it is decoupled from the line by a gap of capacitance C_g. This now give an input impedance on resonance of Z_0/g where g is the coupling coefficient given by $g \approx 8\pi Q(f_0 C_g Z_0)^2$ [1]

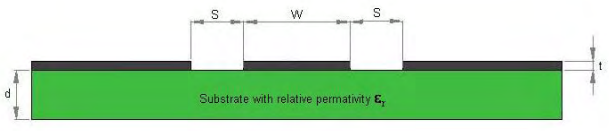

Fig. 1. Schematic of a Coplanar waveguide cross section

The resonant frequency of a half wave CPWR or any transmission line resonator is set by the centre strip length (l) and effective dielectric constant (ϵ_{eff}) and can be calculated by

$$f_0 = \frac{c}{2l\sqrt{\epsilon_{eff}}} \quad (1)$$

Equation 1 contains a factor of 4 in the denominator for a quarter wave resonator. For a CPWR where the substrate thickness $d \gg s$, ϵ_{eff} is given by $(1+\epsilon_{substrate})/2$.

At resonance $\mid S_{11} \mid = (1-g)/(1+g)$ giving zero reflection for a critically coupled resonator. The phase shift of S_{11} close to resonance is given by

$$\Delta\phi \approx \frac{4gQ}{1-g^2}\frac{\Delta f}{f_0} \tag{2}$$

Equation 2 shows the change in phase of S_{11} for a given shift in frequency from resonance is scaled by Q and $1/1-g^2$. Although g and Q are not independent variables g can in principal be set to any value by altering the size of the capacitive gap. This potentially gives us a large shift in phase for a relatively small shift from the resonant frequency. Making use of this control of g provides a measurable phase shift for a given shift from resonant frequency without the need for ultra high Q resonators.

III. Detector performance

The performance of a KID depends ultimately on two parameters; the shift in resonant frequency (Δf_0) upon photon absorption and the microwave response to Δf_0. The microwave response has been explained in the last section and demonstrates a need for a high Q resonator close to being critically coupled. The shift in resonant frequency is governed purely by the change in kinetic inductance ΔL_k. The total kinetic inductance for a CPWR can be calculated from the Cooper pair density in the centre strip and by considering a change in superconducting electron density (n_s) by -1 in a small volume of the centre strip δV we calculate the ratio of $\Delta L_k/L_k$ to be:

$$\frac{\Delta L_k}{L_k} = \frac{1}{n_s}\frac{J_0^2}{\int J^2 dV} \tag{3}$$

Here the value J_0 is the local current density at the point where n_s is reduced by 1. The volume integral of$J^2 dv$ accounts for the non-uniform current distribution across the strip width. Equation 3 is modified to take in to account the non-uniform current distribution along the centre strips length to give:

$$\frac{\Delta L_k}{L_k} = \frac{1}{n_s}\frac{2}{s_{eff} l} \tag{4}$$

Here s_{eff} gives an effective cross-sectional area of the centre strip and is given by $\int J^2 dv/J_0^2$. Due to the long diffusion length of a quasiparticle once created (up to 1mm [3]), means that for a thin narrow strips s_{eff} becomes the cross-sectional area of the strip Wt. Equation 4 can now be written as

$$\frac{\Delta L_k}{L_k} = \frac{1}{n_s}\frac{2}{V} \tag{5}$$

where V is the volume of the centre strip. The resulting shift in resonant frequency can be calculated by $\Delta f_0 \approx -f_0 \frac{\Delta L_k}{2L}$ where L is the total inductance of the strip [1]. L is dominant over L_k so we can write

$$\frac{\Delta f_0}{f_0} \approx -\frac{\beta k}{2 n_s V} \tag{6}$$

Here $k = \Delta L_k/L$ and β is a dimensionless factor that accounts for the proportion of L_k not provided by the centre strip and is typically in the range of 0.6 to 0.85 for CPWR geometries [1]. Re fering back to equation 2 we can calculate the phase shift of S_{11} for $n_s \rightarrow n_s - 1$ as

$$\Delta\phi \approx \frac{4gQ}{1-g^2} - \frac{\beta k}{2 n_s V} \tag{7}$$

Values for Q can be derived from the Mattis-Bardeen result for complex conductivity and shows a suppression of Q with a increase in L_k; $Q_c = (2/\pi k)\exp(\Delta(0)/k_b T)$. This suppression of the conductor quality factor (Q_c) is offset by the larger shift in f_0 for stuctures with a larger L_k so does not effect the overall phase shift for a change in n_s. Rewriting equation 7 in terms Q_c we can write the complete expression for $\Delta\phi$ as:

$$\Delta\phi \approx \frac{4g\beta}{\pi(1-g^2)}\frac{1}{n_s V}\exp\left(\frac{-\Delta(0)}{k_b T}\right) \tag{8}$$

Equation 8 holds well until Q_c reaches the limit set by the surface resistance ($R_{s,0}$) of the resonator. In high quality Nb films $R_{s,0}$ can be as low as $10n\Omega$ which modifies Q_c by $Q_c \approx \omega\mu_0\lambda/2kR_{s,0}$ which is $\approx 10^6$ to 10^7 at 10GHz. The total Q for the resonator is also reduced by radiative losses and substrate losses. The latter can be reduced by using low loss substrates such as sapphire.

The fundamental noise source in a KID comes from the random generation and recombination of quasiparticles in the superconducting resonator and is governed by the quasiparticle life times (τ_{qp}) and densities (N_{eq}). The generation-recombination noise equivalent power (NEP_{gr}) is given by $NEP_{gr} = 2\Delta\sqrt{N_{eq}\tau_{qp}}$ [2]. Theoretical values for τ_{qp} as a function of T are given by Kaplan [3]

$$\frac{1}{\tau_{qp}} = \frac{\pi^{1/2}}{\tau_0}\left(\frac{2\Delta}{k_b T_c}\right)^{5/2}\left(\frac{T}{T_c}\right)^{1/2} exp\left(\frac{-\Delta(0)}{k_b T}\right) \tag{9}$$

$\tau_0 = 0.149 \times 10^{-9} s^{-1}$ for Niobium [3]. Calculating the NEP_{gr} from equation 9 for a strip of volume $\approx 1000\mu m^3$ predicts an NEP_{gr} of $10^{-19} W\sqrt{Hz}$ at 1K. This result is consistent with Sergeev and Karasik [2] . τ_{qp} will also dictate the fundamental time constant for the detector. Fig 3 shows a decrease in $\tau_{qp}$with a reduction in temperature. The value of τ_{qp} can be as short as 10^{-9} at 4.2K however the electronic ringdown time is scaled by Q ($\tau_{ring} = Q/\pi f_0$). In order to make the electronic ringdown time comparable with τ_{qp} for a 10GHz resonator we would need to suppress Q down to about 30.

IV. Applications

For terahertz radiation, Niobium resonators are capable of providing low noise detectors at modest cryogenic temperatures. At 1K a Nb KID can have an NEP_{gr} as low

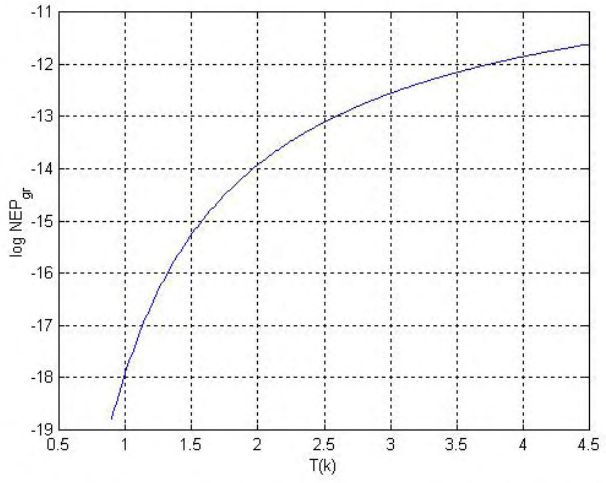

Fig. 2. calculated NEP_gr for a $1000\mu m^3$ strip from 0.9 to 4.5K

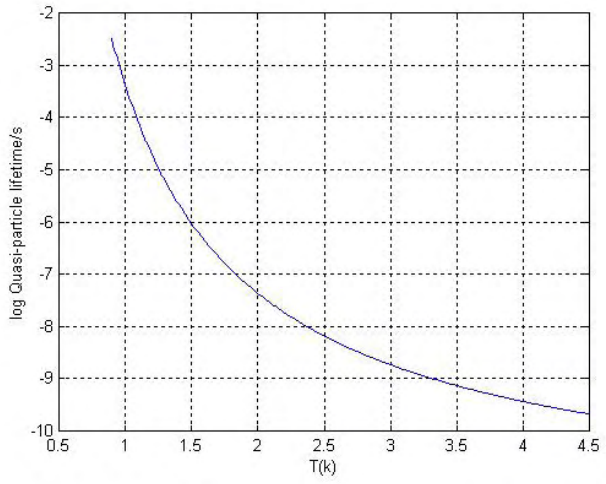

Fig. 3. calculated NEP_gr for a $1000\mu m^3$ strip from 0.9 to 4.5k

as $10^{-19}W/\sqrt{Hz}$ whereas an Aluminium equivalent would need to be cooled to around 130 mK to achieve the same NEP_{gr}. Aluminium KIDs have been considered for mm wave applications and arrangements have been proposed for Aluminium KIDs using Niobium antennas and microstrip lines to couple in photons of energy $2\Delta_{Al} < h\nu < 2\Delta_{Nb}$ [4]. For a Niobium KID working in the terahertz region we would need to use an normal metal antenna and microstrip line to couple in the photon power. This arrangement would be lossy at THz frequencies so keeping the microstrip lines short would be necessary in order to detect low power signals. Another solution to couple power on to the centre strip is to use slot antennas etched in to a gold layer deposited on to the ground planes of the CPWR but seperated by a dielectric layer. This gold layer will suppress the Q by a factor proportional to the dielectric thickness and the quality of the gold film. This suppression of Q could be offset by altering the coupling coefficient g to regain a phase sensitivity to Δf_0. Finally using a lumped element resonator can provide an absorbing area with a uniform current distribution, hence removing the position dependance of the detector. Lumped element resonators tend to have lower Q values compared to their distributed component counterparts, which again could be offset by altering g. A lumped element resonator could be used with a feed horn or a hemi-spherical lens in an arrangment similar to that of the spiderweb bolometer.

V. Results

Measuring the unloaded Q factor of a resonator (Q_u) requires an accurate measurement of the insertion loss (IL). Q_u can be deduced from the loaded Q (Q_L) using the following

$$Q_u = \frac{Q_L}{1-|S_{21}|} \quad \text{where} \quad |\ S_{21}\ | = 10^{\frac{-IL}{20}} \tag{10}$$

$|\ S_{21}\ |$ is governed by the coupling and for a strongly coupled CPWR will heavily load Q. The results shown in fig 4are for the loaded Q of a 12mm Niobium resonator. Although this line is superconducting and should have a theoretical Q_u of order 10^4 we can see the effects of being over coupled. The measured Q_L for this line is around 100. To avoid over coupling and measure a value closer to Q_u far weaker coupling is required. This can be achieved by increasing the capacitive gaps at each end of the resonator.

The resonant frequency f_0 for this line was 4.7 GHz which is in accordance with equation‘1

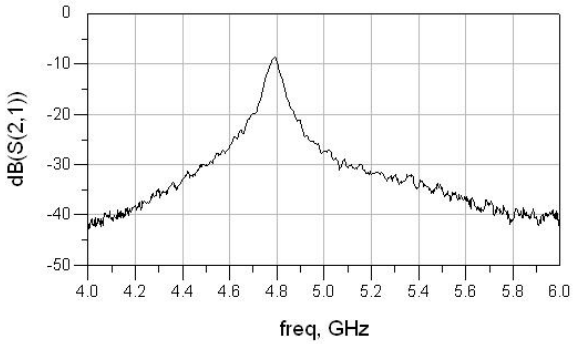

Fig. 4. Example of a over-coupled Nb resonator at 4.2K

VI. Conclusion

Niobium KIDs theoretically have very low noise at 1K and would make an ideal terahertz detector. Along with low noise properties, KIDs have the potential to be multiplexed in to large arrays reducing the electronic complexity on the cold stage to a simple 2-port RF coupling. In comparison to an Aluminium KID the Niobium KID requires simpler cryogenics and could be run using simple sorption coolers

running in an open cycle (permanent 1K stage) mode. Gold slot antennas could allow efficient coupling of THz radiation to a Nb resonator providing the Q factor is not suppressed beyond a point we can adjust for by altering (g). Alternatively lumped element resonators could act a multimode free space absorbers for terahertz radiation. We are currently simulating various Nb THz KID geometries to optimise both the coupling and quality factors for distributed and lumped element devices.

ACKNOWLEDGMENT

Mr Vic Haynes, Miss Nicola Whitehouse and Mr Douglas Haig

REFERENCES

[1] S. Porch, P. Mauskopf, S. Doyle, and C. Duscombe, "Calculations of the characteristics of coplanar resonators for kinetic inductance detectors," in *Applied Super Conductivity*, October 2004.

[2] A. Sergeev, B. Karasik, I. Gogidze, and V. Mitin, "Ultrasensitive hot-electron kinetic-inductance detectors," *AIP Conf. Proc. 605: Low Temperature Detectors*, vol. 605, pp. 27–30, Feb. 2002.

[3] S. B. Kaplan, C. C. Chi, D. N. Langenberg, J. J. Chang, S. Jafarey, and D. J. Scalapino, "Quasiparticle and phonon lifetimes in superconductors," vol. 14, pp. 4854–4873, Dec. 1976.

[4] B. Mazin, "Microwave kinetic inductance detectorsl," Ph.D. dissertation, Californian Institute of Technology, Nov. 2004.

A Cold Electron Bolometer using a Two-Dimensional Electron Gas Absorber

Ian Bacchus, Phil Mauskopf,
Martin Elliott, Dmitry Morozov, and Chris Dunscombe
School of Physics and
Astronomy
Cardiff University
Cardiff, CF24 3YB, UK
Email: Ian.Bacchus@astro.cf.ac.uk

Mohamed Henini
School of Physics and
Astronomy
University of Nottingham
Nottingham NG7 2RD, UK

***Abstract*— We describe a new type of Terahertz (THz) detector using a two-dimensional electron gas (2DEG) hot electron bolometer [1] where the temperature of the electrons read out using superconducting tunnel junctions connected to the 2DEG (similar to a SINIS detector). We present measurements of the electron-phonon thermal conductivity in a high-mobility GaAs/AlGaAs 2DEG sample at 4.2 K as a function of electron temperature and magnetic field. From these measurements we estimate the sensitivity of an element in a filled array of S-2DEG-S detectors at 4.2 K to be approximately $10^{-14}\ W/\sqrt{Hz}$ with a response time of 1 ns. Using measured parameters for the normal resistance of the S-2DEG-S contacts, we calculate the effect of using a voltage bias to cool the electrons in the absorber significantly from a 300 mK base temperature. In this configuration, these detectors can achieve sufficient sensitivity to detect individual THz photons.**

I. Introduction

The next generation of space instruments for FIR/THz astronomy will require a new detector technology that combines (i) sensitivity, (ii) speed, (iii) linearity, (iv) multiplexability and (v) can easily be fabricated in large-format filled arrays. For this reason, several groups are developing new generations of ultra-sensitive detectors such as bolometers using Silicon Nitride thermal isolation and transition- edge superconducting thermometers (TES) (e.g. SRON private communication) or superconducting Kinetic Inductance Detectors (KIDs) (e.g. Mazin, et al., SPIE or Doyle, these proceedings).

Here, we describe a new type of THz detector similar in design to the cold electron bolometer (CEB) consisting of sub-micron size normal metal absorber capacitively coupled via Normal metal/Insulator/Superconductor (NIS) tunnel junctions [2]. We find that using a 2-dimensional electron gas (2DEG) instead of the normal metal strip as the absorbing medium allows (i) simultaneous optimisation of the thermal and electrical properties of the absorber by modification of the electron density and mobility in the 2DEG, (ii) $\simeq 10^5$ times lower thermal conductivity per unit area than in a normal metal absorber for the same impedance and therefore do not require sub-micron dimensions to have good sensitivity. For these reasons, 2DEG CEBs or HEBs are a good candidate for filled arrays of ultra-sensitive bolometers with free-space absorbers (not requiring antennas).

The thermal and electrical properties of electrons in 2DEGs have been measured at low temperatures by a variety of methods ([3], [4])We present precise measurements of the electron-phonon coupling in a high mobility 2DEG sample using multiparameter fits to the Shubnikov-DeHaas oscillations of conductivity vs. magnetic field. From these fits, we estimate the sensitivity of a 2DEG bolometer vs. temperature.

The structure of our sample 2DEG is similar to the 2DEG hot electron bolometer (HEB) described by Yngvesson [5]. Layers of doped and undoped GaAs and AlGaAs are grown via molecular beam epitaxy (MBE), a sketch of this is shown in Figure 1. The discrepancy in the layers' Fermi energy levels gives rise to energy barriers between the layers (Fig 2). Such an energy barrier keeps the electrons trapped in the donor layer until we liberate them with a light pulse. These electrons are bumped into a two-dimensional energy well that lies in the undoped buffer layer of GaAs; they lack sufficient energy to escape this well and are trapped there, forming a 2DEG. The details of the doping and thicknesses of the AlGaAs and GaAs layers determine the mobility and density of carriers in the 2DEG. The mobility is a measure of electrical conductivity per electron and for a high-mobility 2DEG can be thousands of times higher than the conductivity per electron in a metal film. A fixed impedance per square absorber made from a 2DEG requires a much smaller density of electrons per square than a normal metal.

The thermal conductivity between electrons and phonons in an absorber with area, A, at low temperatures follows:

$$G_{\rm ep} = 5\Sigma n_e A T^4 \qquad (1)$$

where Σ, the is a material dependant constant and $n_e A$ is the total number of electrons. The value of Σ for carriers in semiconductors is an order of magnitude smaller than in metals. Therefore, the total electron-phonon conductivity for a 2DEG absorber will be up to 10^5 times lower per unit area than for a metal absorber. A bolometer using a 2DEG absorber is subject to the same equations as more conventional bolometers [6]. Specifically, its NEP^2 is given by the sum of its Johnson,

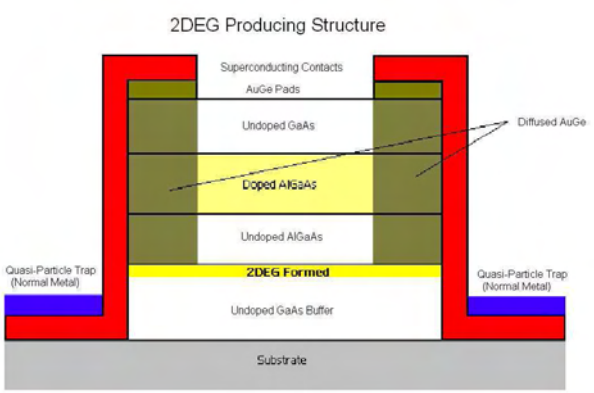

Fig. 1. Cross-sectional sketch of a 2DEG producing structure, not to scale. Shown is what will be our final configuration, with superconducting contacts. We used ohmic contacts for this experiment.

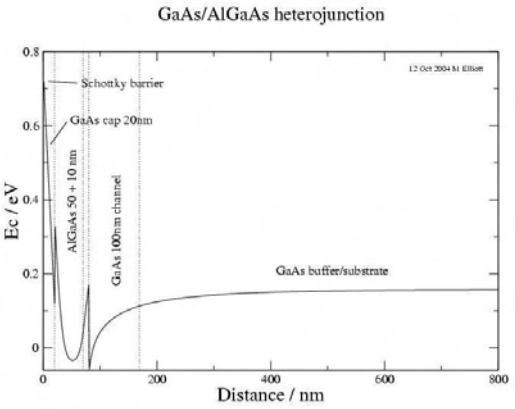

Fig. 2. Schematic of conduction band of semiconductor stack. The Fermi level is indicated by 0 eV.

photon, and amplifier noise. For the sake of this experiment, we are looking at the phonon noise exclusively:

$$NEP^2_{phonon} = 4k_B T_e^2 G \tag{2}$$

Where T_e is the electron temperature and the thermal conductivity of the electron gas $G = IV/T_{electron} - T_{lattice}$. IV is the power dissipated in the 2DEG. Determination of the zero magnetic field electron temperature is determined by zero field IV and resistance vs. temperature curves. A resistance vs. temperature curve for a 2DEG shows that the resistance increases linearly according to the equation $R = R_o + \alpha T_e$, where $\alpha = dR/dT$. We have found through experiment that our α is about 3.4 Ohms/Kelvin and our baseline resistance about 115 Ohms.

To determine the electron-phonon thermal conductivity in our 2DEG sample , we measured the electron temperature as a function of the power dissipated in the 2DEG. At low temperatures, a 2DEG will exhibit Shubnikov de Haas (SdH) oscillations [7]–[15]:changes in the value of resistivity with respect to the magnetic field. We determine the electrical (IV) power dissipated by applying a bias voltage to the 2DEG and a resistor in series. The current running through the system is determined by measuring the voltage drop across the bias resistor and the resistivity of the 2DEG is calculated from this current and the voltage drop across the 2DEG. The tests were done at liquid helium temperature (4.2 K) and the magnetic field swept from 0-12 Tesla. Application of the magnetic field gives rise to Landau levels [10],

$$E_{Landau} = \hbar\left(\frac{eB}{m^*}\right)\left(n + \frac{1}{2}\right) = \hbar\omega_c\left(n + \frac{1}{2}\right), \tag{3}$$

where ω_c is the cyclotron frequency. The widths of the Landau levels are determined by the Heisenberg uncertainty relation for energy, $\Delta E \Delta t \leq \hbar/2$, where the time concerned is the lifetime of an electron in the given energy level. As the field increases, the Landau level spacing increases. In an ideal system, we would be able to operate at a temperature of 0 K, guaranteeing all the electrons in the 2DEG are at or below the Fermi level; hence only electrons at the Fermi level would be available to conduct. As we increase the magnetic field, the Fermi energy level of the 2DEG sees the Landau levels moving past. When the Fermi level is between Landau levels, the system is at a quantum plateau where the longitudinal conductivity and resistivity of the 2DEG are simultaneously zero, so we get no longitudinal voltage drop. If the electrons in the 2DEG are too warm, they will partially occupy many levels above that of the Fermi energy, meaning some electrons will be at the same energy level as a Landau level at all times so the observer won't see any oscillations in the resistivity.

The SdH effect is well described theoretically by the 'Lifshitz-Kosevich' formula in which the oscillatory part of the resistance can be expressed as a Fourier-like expansion [7]–[9],

$$\frac{\Delta\rho_{xx}(T_e, B)}{\rho_0} = \sum_r A_r X_r \exp(-Krm^* T_D/B) \times \cos(2\pi r F/B + \phi_r) \tag{4}$$

where ρ_0 is the zero-field resistance, F is the SdH frequency, related to the 2D electron density n_s by $F = (h/2e)n_s$. The terms A_r and ϕ_r are amplitude and phase factors for each harmonic number r. The electron effective mass m^* is $0.067m_e$ for the GaAs-based 2DEGs examined here, and $T_D = \hbar/2\pi k_B \tau$ is the so-called temperature and is related to the scattering lifetime τ of electrons in the quantised Landau levels. The fundamental constant $K = 2\pi^2 k_B/\hbar m_e e = 1.613 \times 10^3 1$ T(K kg)$^{-1}$

Central to our experiments is the thermal damping factor [7], [15]

$$X_r = \frac{Krm^* T_e/B}{\sinh(Krm^* T_e/B)} \tag{5}$$

arising from the Fermi-Dirac distribution of states around the Fermi level, and which contains all the temperature dependence of the SdH effect. From this factor, by examining the SdH effect as power is dissipated in the sample, it is possible

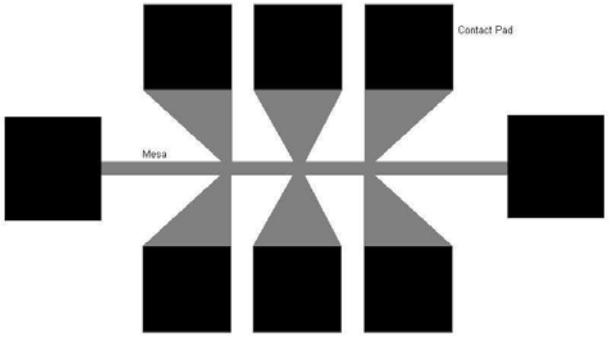

Fig. 3. Sketch of 2DEG mesa structure, not to scale. In our measurements, the bias current was applied via the longitudinal contact pads. The transverse pads were used to measure the longitudinal and transverse (Hall) voltages along the 2DEG.

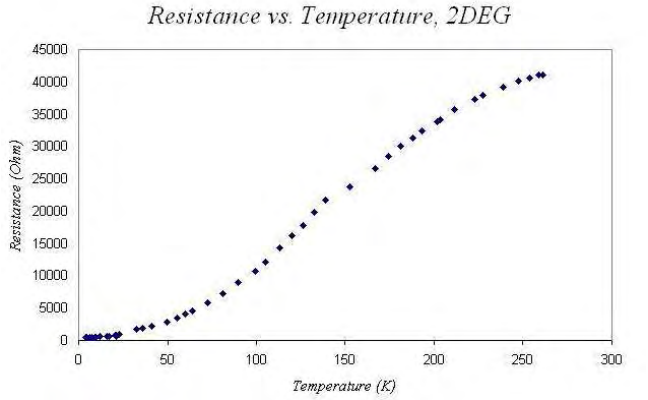

Fig. 4. The resistance of the 2DEG is directly related to its temperature, which rises as the power dissipated in the 2DEG increases, but for low currents, this change is negligible.

to calculate the electron temperature T_e, if all other quantities in equation (4) are known.

II. Experimental

Measurements were performed on Hall bars prepared at Nottingham University. The 2DEG sample consisted of the following layers: 170$\mathring{A}$ GaAs cap layer, 400$\mathring{A}$ silicon-doped AlGaAs layer, 400 $\mathring{A}$ AlGaAs spacer layer, 2μm GaAs buffer layer, and a semi-insulating GaAs substrate. The structure was wet-etched to form a mesa. Metallic contacts were added for the sake of applying voltages and reading out. The mesa area was approximately $50\times1200\mu\text{m}^2$. The longitudinal contact pads are $300\times350\mu\text{m}^2$, while the transverse pads are $300\times 300\ \mu\text{m}^2$ (see Fig. 3). Standard low-frequency, constant current, four-terminal ac measurements of the longitudinal ρ_{xx} and transverse ρ_{xy} resistance were made at 4.22 K in the bore of a 12 tesla superconducting magnet. We determined the sample power from its resistance and the current (as determined by measuring the voltage V_b across a 100 kΩ series resistor).

Typical low-field SdH oscillations are shown in figure 5. The periodicity of the oscillations corresponds to an electron number density of $2.47\times10^{15}\text{m}^{-2}$, in good agreement with simultaneous measurements of the Hall resistance in this sample, which gave a number density of $2.51\times10^{15}\text{m}^{-2}$. Although oscillations occur up to the highest field measured (the filling factor $\nu = 1$ occurs around 9.5 tesla), detailed analysis of these data is complicated by spin-splitting of the oscillations, and by slight inaccuracies in the Hall bar geometry, so is not presented here.

III. Results and Analysis

As the resistance of the 2DEG changes, so, too, must the power dissipated within it (Fig. 4); the electron temperature will therefore vary as the magnetic field changes. However, at sufficiently low bias voltages, the change in the electron temperature over the course of the experiment will be negligible, so we take a curve at low fields and fit it with that assumption. From that curve, we find via the fit values for the

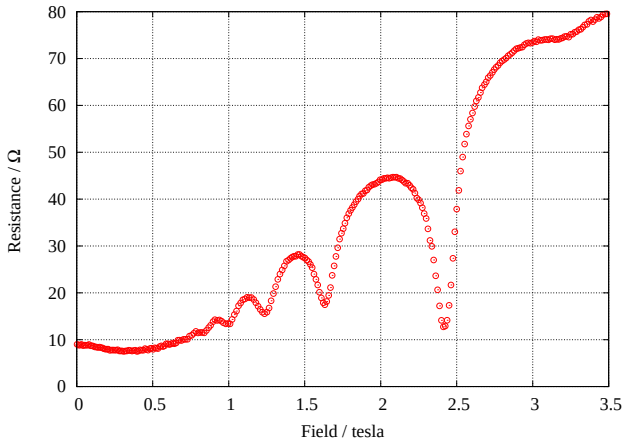

Fig. 5. Field variation of the magnetoresistance of a 2DEG sample at a temperature of 4.22 K for negligible power dissipation.

Dingle temperature, the SdH frequency, the phase factors, and the harmonic coefficients. The two-step analysis process was as follows.

1) First, equation (4) was used to fit the SdH data (with typically 3 to 10 harmonics depending on field range) at sufficiently low current with negligible dissipation, where we can assume that $T_e = 4.22$K, the known temperature of the sample helium bath. This yielded 3-10 amplitudes and phases, a Dingle temperature T_D and a frequency F (also an offset, linear and quadratic term in $\rho(B)$ to allow for the non-oscillatory part of the magnetoresistance).
2) The data at higher dissipation was then analysed, with T_e alone as the adjustable fitting parameter. This is justified for small temperature rises since all other terms are essentially temperature independent.

It is worth pointing out that most theories [9] find the amplitude factors A_r all equal to 4, but Vavilov and Aleiner [8] indicate that this is not generally true, and our experiments confirm that it is essential to use them as fitting parameters

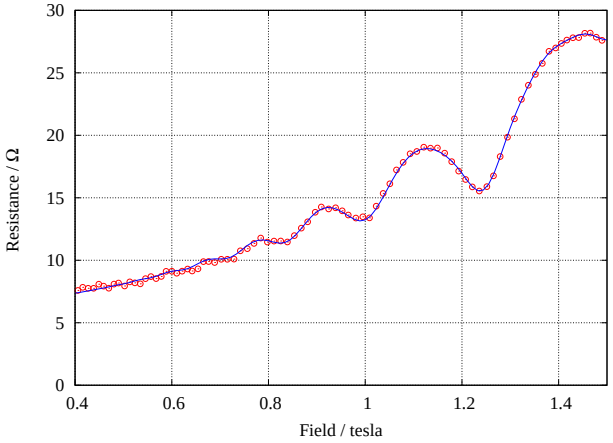

Fig. 6. Analysis of the low-field portion of figure 5. The sample current was approximately 0.23μA. A 4-harmonic fit of equation (4) with fixed temperature 4.22 K. was made, yielding a Dingle temperature T_D=1.17$\pm$0.17 K.

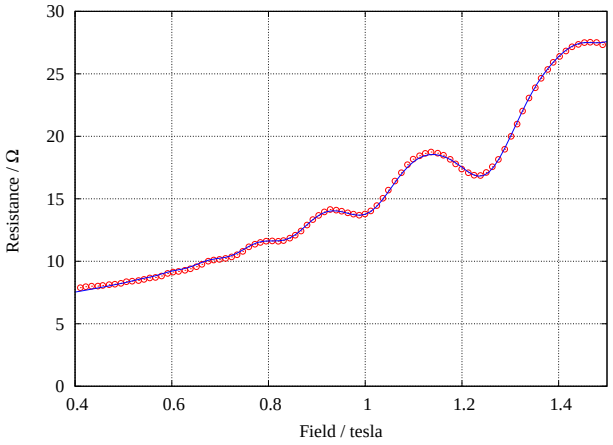

Fig. 7. Analysis of low-field SdH oscillations with a sample current of approximately 5μA. A 4-harmonic fit with $T = 4.76 \pm 0.02$K is shown.

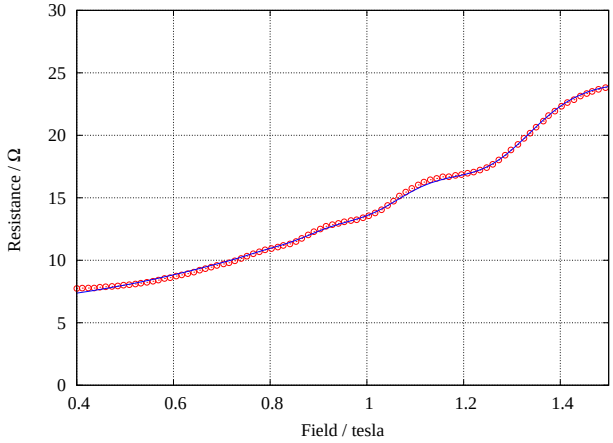

Fig. 8. Analysis of low-field SdH oscillations with a sample current of approximately 10μA. A 4-harmonic fit with $T = 7.01 \pm 0.09$K is shown.

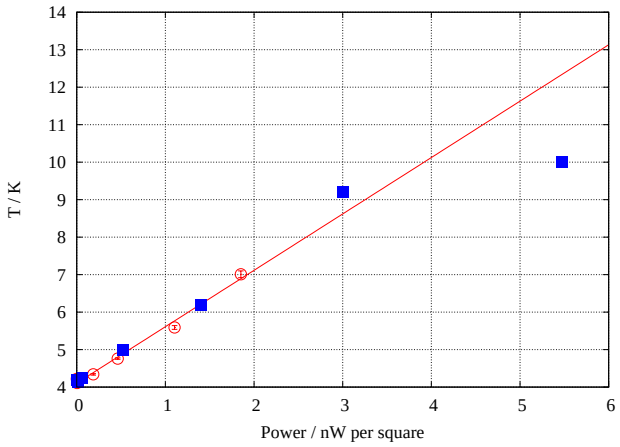

Fig. 9. Electron temperature versus sample power, derived from the low-field SdH fit (red circles) and high-field fit (blue squares). A linear fit 1.50 ± 0.06 K/nW to the low-field points is shown.

to describe the SdH oscillations sasifactorily. Most previous analyses have avoided this issue by using very low-field or higher temperature data, where the harmonic terms are negligible. We also let the phase terms ϕ_r be adjustable fitting parameters, even though they are known theoretically, because they are rather sensitive to magnet hysteresis and error in the field.

In Figure 6 we show the results of Step 1 of the fitting procedure and gives a very satisfactory fit to the SdH data. The Dingle temperature found corresponds to a scattering lifetime of 1.04 ps or 'quantum mobility' $\mu_q = e\tau/m^*$ of 2.73 m^2/Vs.

The results of Step 2 are illustrated in Figures 7 and 8. They show the decrease in SdH oscillation amplitude as the ac drive current through the sample is increased. Excellent fits to the data are produced using the same parameters as obtained in the first fit, but with temperature as the single adjustable parameter. The poorer quality of the fits at higher bias voltages is due to variations in power dissipation that become more acute at higher electron temperatures.

Finally a graph of the temperature rise in the 2DEG as a function of power dissipated. Included are data from high and low magnetic field fits. The greater variations in the resistivity in the high field oscillations mean that the constant electron temperature assumption is less valid there. With the addition of the heating effects at higher currents, the high field data deviates from the trend even more severely. Even so, there is a compelling agreement with low and high field data for lower power dissipation levels (lower currents).

Ian Bacchus
28 Apr 2005

IV. Conclusion

The resistivity of a 2DEG undergoing SdH oscillations can be very accurately modeled using the 'Lifshitz-Kosevich' formula and assuming that the electron temperature doesn't

change with the resistivity. While ignoring electron heating leads to rather poor overall fits at high bias voltages, low field fits are fairly accurate. High field fits are similarly impaired by the assumption of constant electron temperature, but low bias voltage, high field fits agree with the trend evident from the low field data. Our data points to an electron heating rate of 1.50±0.06 K/nW/square at 4.2 K. A 1 mm^2 2DEG absorber would therefore have an electron-phonon thermal conductance of about 10^{-7} W/K. This absorber used with an ideal electron thermometer would give a detector NEP of approximately $10^{-14}W/\sqrt{Hz}$ with a response time of 1 ns (τ=C/G). By taking into account the area and electron density of our 2DEG, we calculate a G of 5.45×10^{-15} W/K per electron. This is in good agreement with Appleyard [12], who gets 1.5×10^{-14} W/K per electron. In addition, the low electron-phonon coupling of the 2DEG absorber enables efficient cooling of the electrons well below the lattice temperature through the use of superconductor-2DEG-superconductor contacts. This effect has been shown to work in highly doped thin silicon films [16]. The 2DEGs should work better than silicon due to their higher mobilities and lower densities of carriers. Detectors of this type would potentially have sufficient sensitivity ($10^{-21}W/\sqrt{Hz}$) to resolve individual THz photons. Future work will probe the thermal and electrical properties of the 2DEGs and superconducting contacts at sub-Kelvin temperatures.

ACKNOWLEDGMENT

The authors would like to thank Jasbinder S. Chauhan of the University of Nottingham for his assistance, advice, and hospitality. Mohamed Henini acknowledges support from the Engineering and Physical Sciences Research Council (United Kingdom)

REFERENCES

[1] J.-X. Yang, F. Agahi, D. Dai, C. F. Musante, W. Grammer, K. M. Lau, and K. S. Yngvesson, "Wide-bandwidth electron bolometric mixers: A 2deg prototype and potential for low-noise thz receivers," 1993.

[2] D.-V. Anghel and L. Kuzmin, "Capacitively coupled hot-electron nanobolometer as far-infrared photon counter," 2003.

[3] G. Gol'tsmann and K. Smirnov, "Electron-phonon ineraction in a two-dimensional electron gas of semiconductor heterostructures at low temperatures," 2001.

[4] R. R. Schliewe, A. Brensing, , and W. Bauhofer, "Contactless heation of two-dimensional electron gas systems by strip-line guided microwaves," 2001.

[5] K. S. Yngvesson, "Ultrafast two-dimensional electron gas detector and mixer for terahertz radiation," 2000.

[6] P. L. Richards, "Bolometers for infrared and millimeter waves," 1994.

[7] Y.-W. Tan, J. Zhu, H. L. Stormer, L. N. Pfeiffer, K. W. Baldwin, and K. W. West, "Measurements of the density-dependent many-body electron mass in two dimensional GaAs/AlGaAs heterostructures," *Phys Rev Lett*, vol. 94, no. 1, p. 016405, 2005. [Online]. Available: http://link.aps.org/abstract/PRL/v94/e016405

[8] M. G. Vavilov and I. L. Aleiner, "Magnetotransport in a two-dimensional electron gas at large filling factors," *Phys Rev B (Condensed Matter and Materials Physics)*, vol. 69, no. 3, p. 035303, 2004. [Online]. Available: http://link.aps.org/abstract/PRB/v69/e035303

[9] P. T. Coleridge, "Inter-subband scattering in a 2D electron gas," *Semiconductor Science and Technology*, vol. 5, no. 9, pp. 961–966, 1990. [Online]. Available: http://stacks.iop.org/0268-1242/5/961

[10] Y. Kawano, H. Takenouchi, and S. Komiyama, "Highly sensitive and tunable detection of far-infrared radiation by quantum hall devices," 2001.

[11] P. Ramvall, N. Carlsson, P. Omling, L. Samuelson, W. Seifert, and Q. Wang, "Tuning of the single-particle relaxation time of a high mobility electron gas in a gainas/inp quantum well," 1997.

[12] N. Appleyard, J. Nicholls, M. Y. Simmons, W. R. Tribe, and M. Pepper, "Thermometer for the 2d electron gas using 1d thermopower," 1998.

[13] M. A. Zudov, R. R. Du, J. A. Simmons, and J. L. Reno, "Shubnikov de haas-like oscillations in millimeterwave photoconductivity in a high-mobility two-dimensional electron gas," 2001.

[14] A. A. Verevkin, N. G. Ptitsina, G. M. Chulcova, G. N. Gol'tsman, and E. M. Gershenzon, "Determination of the limiting mobility of a two-dimensional electron gas in algaas/gaas heterostructures and direct measurement of the relaxation time," 1996.

[15] Y. Ma, R. Fletcher, E. Zaremba, M. D'Iorio, C. T. Foxon, and J. J. Harris, "Energy-loss rates of two-dimensional electrons at a gaas/algaas interface," 1991.

[16] A. Clark, N. A. Miller, A. Williams, S. T. Ruggiero, G. C. Hilton, L. R. Vale, J. A. Beall, K. D. Irwin, and J. N. Ullom, "Cooling of bulk material by electron-tunneling refrigerators," 2005.

Hot Electron Bolometer Development for a Submillimeter Heterodyne Array Camera

Matthew O. Reese, Daniel F. Santavicca, Luigi Frunzio, Daniel E. Prober

***Abstract*—We are developing Nb diffusion-cooled Hot Electron Bolometers (HEBs) for a large-format array submillimeter camera. We have fabricated Nb HEBs using a new angle deposition process. We have characterized these devices using heterodyne mixing at 20 GHz. We also report on optimizations in the fabrication process that improve device performance.**

***Index Terms*—Hot Electron Bolometers, superconductivity proximity effect, electron-beam fabrication**

I. Introduction

A superconducting microbridge connected to thick, normal metal contacts forms the active element of the superconducting Hot Electron Bolometer (HEB), which has demonstrated promising performance as a terahertz detector.[1-5] HEBs have several desirable characteristics: unlike SIS tunnel junctions, they are not limited by the gap frequency;[6] they require very small local oscillator power; their simple geometry, with low stray impedance, facilitates integration in multi-pixel arrays; and they have demonstrated IF bandwidth as large as 9 GHz.[1-5]

Recently, we have focused on fabricating diffusion-cooled niobium HEBs. These devices are being developed to be part of a large format array camera for use in the 810 GHz atmospheric window on the Heinrich Hertz Telescope operated by the University of Arizona. This can serve as a model for future THz camera designs. We require a reasonably sharp resistive transition of the superconductor, a critical temperature (T_c) of 4-5 K to operate in a pumped ^{4}He cryostat, and contact pads that either do not superconduct or have a much lower T_c than the bridge. Here we present our new fabrication process along with initial characterization results.

II. Fabrication Method

The essential goal has been to produce Nb HEBs using a single lithographic patterning and no cleaning step between the deposition of our Nb and normal metal. (Here we use Al, because $T_{bath}>T_{c,Al}$). Our structure is patterned as shown in Fig. 1. We use a converted Scanning Electron Microscope (FEI Sirion XL40) to expose a pattern in a 380 nm thick monolayer of 950K polymethyl methacrylate (PMMA) spun on a substrate of silicon or fused silica. [When using fused silica, we evaporate 10-15 nm of Al on top of our PMMA before e-beam writing, to reduce charging effects. Before developing our resist, we remove the Al with 5 minutes in MF-312 developer (4.9% by volume tetra methyl ammonium hydroxide in water), then arrest the process with 20 s in isopropyl alcohol (IPA).] Developing is done in a solution at 25°C of 1:3 methyl isobutyl ketone:IPA for 20 s in an ultrasonic bath, arrested by 20 s in IPA in ultrasound. The substrate is then blown dry with N_2. The sample is loaded into a Kurt J. Lesker Supersystem III Series multi-sputtering and evaporation system with a base pressure of ~10^{-6} Pa. First the 2" diameter Nb target is pre-sputtered for 2 min in an Ar plasma with a power of 350 W and a pressure of 0.17 Pa and a flow rate of ~82 sccm. The sample is then ion beam cleaned by Ar with current of 4.7 mA for 15 s using a 3 cm Kaufman-type gun to help adhesion to the substrate. Then, a Nb film is

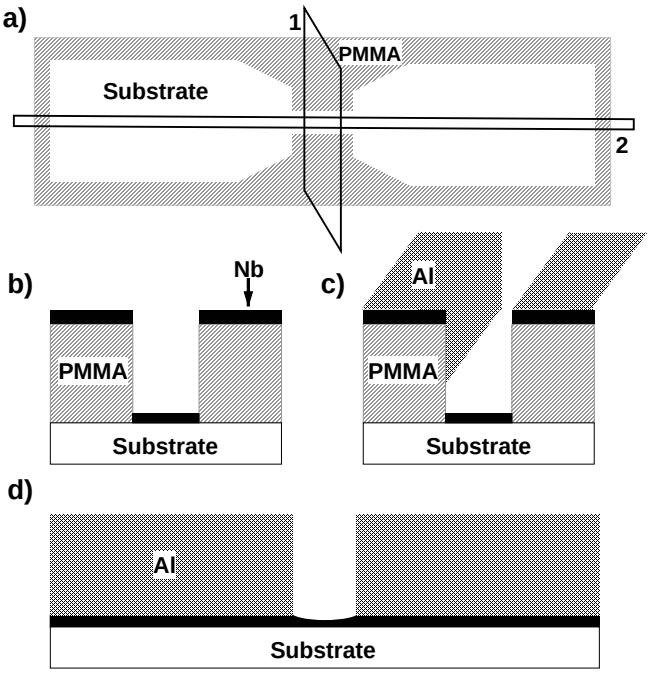

Fig. 1. Deposition process: a) e-beam pattern PMMA, top view [Side views of slice 1: Fig. b&c, slice 2: Fig. d], b) sputter Nb, c) angle evaporate Al, Al sticks on side of resist in bridge region, d) final result after liftoff. The Nb in the bridge center is slightly thinner than the contact region (see text).

Manuscript received October 19, 2005. This work was supported by NSF-AST, NASA-JPL, and a NASA Graduate Student Research Fellowship for M. O. Reese.

All authors are in the Department of Applied Physics of Yale University, New Haven, CT 06520-8284 USA. All correspondence should be directed to Daniel Prober (phone: 203-432-4280; fax: 203-432-4283; e-mail: daniel.prober@ yale.edu).

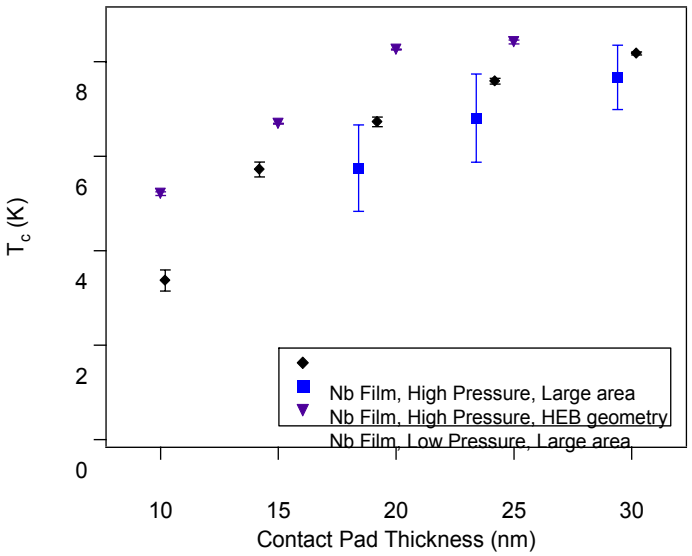

Fig 2. Transition temperature of Nb Films with no Al on top. The error bars represent the onset and completion of the transition (T_c is defined as the center of the transition). The points are spread out horizontally to allow easier viewing, and suggest the error in thickness measurements. The thicknesses are 10, 14, 19, 24, and 30nm, measured in the contact pad region.

sputtered for 9 s, using the same parameters as stated above. And then with as little delay as possible (typically ~3 min.), we angle evaporate 200 nm of Al at 1 nm/s. Lift-off is done in hot acetone (50°C) for one hour, followed by 2 min in ultrasound.

III. Results and Optimizations

A. Monolayer Resist

Our fabrication development originally used a bilayer resist process (PMMA on top of the copolymer MMA) designed to allow clean liftoff. This works well with sputtered Nb and even with the directionality of evaporated Al films. However, while liftoff was clean, our sputtered Nb HEBs had broad resistive transitions. This resulted from the non-directional nature of sputtering. The Nb spread out to the base of the bottom resist layer, which had undercut of 50-100 nm. Hence, the center of a 200 nm wide bridge was only ~60% of the thickness of the contact pads, from spreading of the Nb after it had passed through the narrow opening in the top resist layer.

Using a single layer of resist significantly reduced the effect of Nb spreading. As the bridge becomes increasingly narrow (<1 μm), however, reduction of the bridge thickness is still observed. This can be seen in Fig. 2 by the broadening of the resistive transitions for narrow bridges. This effect is due to the sputter process and the geometry of the PMMA slot used to form the HEB. Sputtering is a non-directional process. In a large opening in the resist pattern, sputtered material from every direction will reach the substrate. In a narrow opening, a fraction of the incident Nb will not have a line of sight to the substrate, thereby reducing the deposited thickness in the center of the wire compared to the contact pad region. This reduced thickness leads to a broader and lower temperature transition for the bridge compared to the contact pads.

	Estimated Nb Thickness	Base Pressure	Δt: Nb→Al
HEB A	10 nm	4 x 10^{-5} Pa	35 min
HEB B	10 nm	4 x 10^{-5} Pa	6 min
HEB C	12 nm	1 x 10^{-5} Pa	37 s

Table I. Fabrication parameters for the Hot Electron Bolometers appearing in Fig. 3.

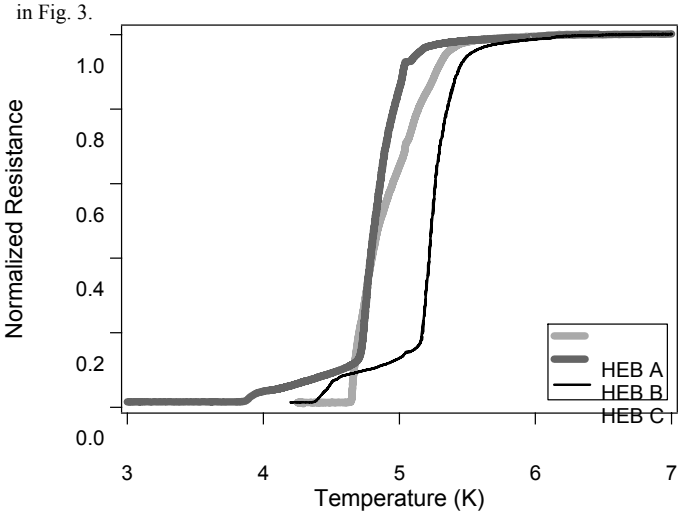

Fig 3. Normalized resistance versus temperature curves for three HEBs. See Table for details on fabrication parameters. Notice the foot structure for devices B and C due to the contact pads. The broad resistive transition of Device A may be a result of poor suppression in the contact pads as well.

B. Improved Nb

We were able to improve the quality of our thin film Nb, as determined by its T_c, by lowering our Ar plasma pressure and at the same time increasing the dc power [See Fig. 2]. Our original values were 0.53 Pa/270 W; our new values are 0.17 Pa/350 W. This increased our deposition rate from 1.0 nm/s to 1.25 nm/s and may have reduced the film stress and thus improved the quality.[7]

C. Suppression of Superconductivity in the Contact Pads

We want to form a clean interface in our contact pads, thereby ensuring good suppression of the superconductivity in the thin Nb under the thick Al. The presence of a superconducting energy gap in the pads would inhibit the ability of hot electrons to diffuse off the bridge. Because the proximity effect has a strong dependence on both the thickness of the Nb and Al films as well as the transparency of the interface between them, it can be difficult to achieve good suppression.[8,9] We found that the thicknesses of our Nb and Al films, as well as the length of time between their depositions, significantly affect suppression.

We first achieved good suppression in the contact pads (while still having an acceptably high T_c in the bridge) by reducing the time delay between depositions. Our improved Nb films have increased T_c and reduced ΔT_c. This allows for sufficiently thin (10 nm) Nb films, which are more readily suppressed. We also use a thick (200nm) normal metal film. By reducing the base pressure of our system from 4 x 10^{-5} to 1x 10^{-6} Pa, we were able to make the time interval between depositions relatively unimportant. With P = 10^{-6} Pa we could get the same suppression if we waited 30 s or 30 min. With

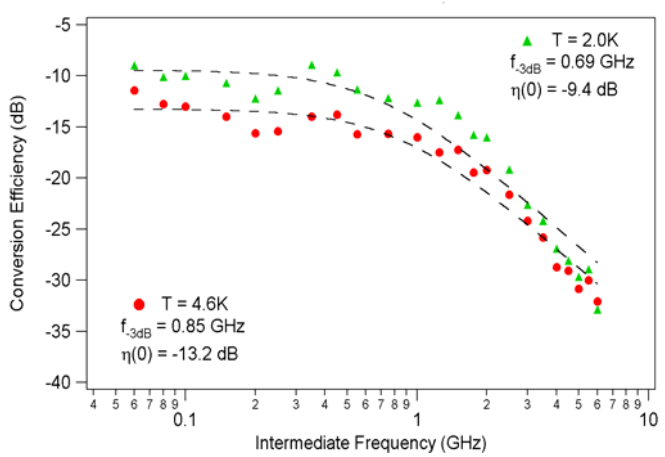

Fig 4. IF Conversion efficiency of HEB C with bandwidth above and below the transition of the suppressed contact pads. The contact pads in this sample had a T_c=4.4K.

our higher quality Nb film parameters and 200 nm Al, at a base pressure of 4 x 10^{-5} Pa, we made two batches of devices with a long (HEB A) and shorter (HEB B) time interval between the Nb and Al depositions to illustrate the importance of interface transparency [Fig 3].

HEB A has a single, somewhat spread out transition. The contact pads have a higher onset transition temperature than the bridge, because the contacts pads are thicker than the bridge, and only weakly suppressed. HEBs B and C each had short intervals between depositions and each has two distinct transitions. The higher temperature transition is the bridge transition; the second is the transition of the suppressed contact pads. The transition temperature of the contact pads (~3.8 K for HEB B, ~4.4K for HEB C which had thicker Nb) agrees with that of Nb-Al bilayers, made during the same deposition but measured separately. The finite resistance in the contact pads is due to the large number of squares in the rf choke structure in our device geometry.

D. Improved Bandwidth

To illustrate the importance of good suppression of the superconductivity of the contact pads, we provide bandwidth measurements in the overpumped regime, where the critical current is suppressed by the local oscillator power. These were performed at temperatures above and below the T_c of the contact pads. These data are from HEB C, a 400 nm long device, from the same cooldown [Fig. 4]. These results were obtained by heterodyne mixing at 20 GHz following the techniques described in Ref. 9. We used wirebonds, however, instead of a flip-chip process to connect the device. The difference in conversion efficiencies between the two curves can be explained by the typical increase of conversion efficiency as the bath temperature is lowered to $T_{bath} \approx T_c/2$.[10] There is an observed increase of ~15% of the IF bandwidth when the contact pads are normal, at T=4.6 K. The reduced bandwidth at T=2 K may be due to hot electrons at energies less than the gap of the contact pads that cannot easily diffuse off the nearly normal bridge. This would increase the thermal response time and thus reduce the IF bandwidth. At 4.6 K, the gap in the contacts is zero and all the hot electrons are able to leave the bridge rapidly. The bandwidth, to the authors' knowledge, has not previously been observed to exhibit any temperature dependence in a diffusion-cooled device. A 2 GHz bandwidth is desirable, and can readily be achieved by reducing the bridge length to about 250 nm.[10]

IV. Future Plans

In the future, we seek to reduce the T_c of the contact pads beyond our present reduction, thereby allowing us to operate at 2 K and maximize both conversion efficiency and bandwidth. We also plan to investigate the mixer noise and conversion efficiency at 345 GHz, in measurements at the University of Arizona.

Acknowledgment

We thank Bertrand.Reulet, Lafe Spietz, and John D. Teufel for helpful discussions.

References

[1] E. M. Gershenzon, et. al., Sov. Phys. Supercond. **3**, 1990, 1582.
[2] D. E. Prober, Appl. Phys. Lett. **62**, 1993, 2119.
[3] J. J. A. Baselmans et. al., Appl. Phys Lett. **84,** 2004, 1958
[4] R. A. Wyss,, et. al., Proc. 10th Intl. Symp. Space Terahertz Tech, 1999, 215
[5] B. S. Karasik, et. al., IEEE Trans. Appl. Supercond. **7**, 1997, 3580
[6] M. Bin, et. al., IEEE Trans. Appl. Supercond. **7**, 1997, 3584
[7] S. Knappe, C. Elster, H. Koch, J. Vac. Sci. Technol. A **15,** 1997, 2158
[8] J. M. Martinis, et. al., Nucl. Instrum. Methods A **444**, 2000, 23
[9] D. Esteve, et. al, "Correlated fermions and transport in mesoscopic systems", eds. T. Martin, G. Montambaux, and J. T. T. Van (1996)
[10] P. J. Burke, et. al., Appl. Phys. Lett. **68**, 1996, 3344
[11] P.J. Burke, Ph.D Thesis, Yale University, 1998, accessible from http://www.yale.edu/proberlab/alumni.html

A Concept of Cold Electron Bolometer Mixer

Mikhail A. Tarasov and Leonid S. Kuzmin

***Abstract*— A novel type of phase-sensitive Terahertz heterodyne detector with Cold Electron Bolometer (CEB) sensor is proposed. In CEB mixer a normal metal absorber of sub-micrometer size is terminated to planar antenna via superconductor-insulator-normal metal (SIN) junctions. Such mixer combines advantages of Hot Electron Bolometer (HEB) mixer such as high signal frequency and low LO power, and advantages of SIS mixer such as low noise, high IF and immunity to small temperature variations. At the same time it avoids drawbacks of HEB and SIS such as sensitivity to magnetic field interference, additional noise due to Josephson effect and superconducting transition.**

***Index Terms*—cold electron bolometers, hot electron bolometers, terahertz mixers, power mixers.**

I. Introduction

At present there are two main types of most sensitive superconducting mixers in submm-wave or THz frequency range. First is SIS mixer approaching a noise temperature about 100 K that is of a few quantum limits T_n^q=hf/k at frequencies up to about 1 THz [1]. Above the energy gap frequency 700 GHz of Nb with transition temperature 9 K or twice as high for NbN with T_c=15 K, the noise temperature increase greatly above frequency 0.7 or 1.4 THz. Hot electron bolometer-mixer HEBM [2] is alternative type of mixers that can operate well above 1 THz with noise temperature about 1000 K that can be approximated as T_n~10hf/k [3]. The mechanism of operation for HEBM is much different from a conventional switching mixer in which conductance is modulated by LO frequency. In HEBM resistance can not be modulated with so high frequency, bolometer is too slow to follow THz frequency. Instead it detects the average of interference signal, similar to what happens in Fourier Transform Spectrometer with Michelson interferometer and Goley cell as a sensor. The HEB mixer performance is limited by intrinsic losses in superconductor-normal metal interface due to proximity effect, excess noise in the region of hot spot, overheating of bolometer by dc and RF biases.

In this paper we present a concept of novel device that can overcome limitations of both types of superconducting mixers. A Cold Electron Bolometer-Mixer (CEBM), see Fig. 1, combines elements of SIS and HEB, it consists of a normal metal (or weak superconductor) strip of absorber terminated to electrodes by superconducting tunnel junctions of SIN type as in conventional cold electron bolometer [4]. Contrary to conventional operation of CEB as a direct bolometer in millikelvin temperature range, in the case of CEBM it operates at liquid helium temperature that increase the response frequency from 10-100 MHz to about 1 GHz that is acceptable as IF. In this paper we compare operation of cold electron bolometer in coherent and noncoherent operation modes and show the difference of conventional switching mixer and power mixer.

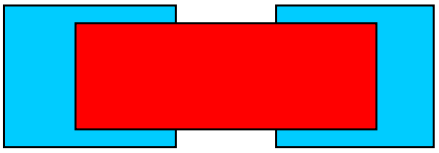

Fig. 1. Schematic view of SINIS for CEB mixer. Electrodes are superconducting, absorber (in the center) is normal metal. Gap between electrodes is 1 μm, size of overlap (tunnel junctions) is 1x1 μm^2.

II. Coherent and Incoherent Detection at MM and Submm Waves

There are two basic methods to detect radiation: coherent one that is arranged by mixers and incoherent that utilizes direct detectors and bolometers.

There are two basic types of incoherent detectors, in first one incoming photons generate single or multiple charge carriers, in second one incoming radiation is converted to heat. First class is presented by photoconductors and discharge tubes, in which an incoming photon excites a carrier into a semiconductor's conduction band, or in vacuum between cathode and anode. In bolometers the incoming radiation elevates the temperature of a sensitive thermometer. The characteristic of absorption determines the frequency range and usually absorber and thermometer are separated in so-called composite bolometers. Microwave radiation directly accelerates electrons in hot electron bolometers, heating the electron gas into a range where the electron mobility is energy dependent. Thermodynamic temperature of the electron gas T_e is higher than the lattice temperature, and changes in current are proportional to the electron mobility $\Delta i \sim V/\Delta r \sim V/(ne\mu(E))$.

Manuscript received April 30, 2005. This work was supported in part by Swedish agencies VR, STINT, by INTAS under Grant 01-686, ISTC project 3174 and the President Grant for Scientific School 1344.2003.2

M.A.Tarasov is with the Institute of Radio Engineering and Electronics of Russian Academy of Sciences, Moscow 125009, Russia (phone: 7-095-2032784; fax: 7-095-2038414; e-mail: tarasov@hitech.cplire.ru).

L.S.Kuzmin is with the Department of Microtechnology and Nanoscience, Chalmers University of Technology, Gothenburg SE-412 96, Sweden (phone: 46-31-7723608, fax: 46-31-7723471, e-mail: leonid.kuzmin@mc2.chalmers.se).

In coherent receiver the input signal frequency is converted by mixing with monochromatic local oscillator in a nonlinear element. The receiver is phase coherent because the phase relation of incoming signal to LO is preserved in the output signal. Mixers can be divided into two different classes. The first one can respond to the signal and LO frequencies separately, it is so-called switching mixer. Schottky diodes and SIS tunnel junctions are most popular mixers of this type. The second type is class of power mixers, which responds to the total power. These mixers do not respond separately to the individual fields, but measure the interference, which brings the difference frequency in the total power. Hot electron bolometers and photoconductors fall into this class. Classical heterodyne mixers, or switching mixer, generate output signals at sums and differences of input frequencies and their harmonics. In quantum detector the shape of IV curve is irrelevant, they produce one charge carrier per incident phonon.

Phase coherent methods preserve the phase information of the incoming signal, but at the cost of imprecision in the intensity (number of phonons) in the incoming radiation. Phase incoherent methods are capable of counting photons, but consequently destroy the phase information in the signal. The reason for this is a wave-particle duality of electromagnetic radiation. The Heisenberg uncertainty principle can be expressed as

$$\Delta E \cdot \Delta t \geq \hbar / 2 \qquad (1)$$

The intensity can be rewritten in terms of number of photons N, and time in terms of phase φ, so $\Delta E = hf \cdot \Delta N$ and

$$\Delta t = \frac{\Delta\varphi}{\omega} = \frac{\Delta\varphi}{2\pi f}$$

which brings the relation $\Delta E \cdot \Delta t = hf \cdot \Delta N \frac{\Delta\varphi}{2\pi \cdot f} \geq \frac{\hbar}{2}$, that shows simple relations of amplitude and phase uncertainty

$$\Delta N \cdot \Delta\varphi \geq \frac{1}{2} \qquad (2)$$

It means that it is generally impossible to simultaneously determine both the phase and number of photons to arbitrary high precision. Another important consequence is that, in principle, incoherent detection is more sensitive than coherent, because sensitivity is ΔN and $\Delta N > \frac{1}{2\Delta\varphi}$

III. Conventional Heterodyne Mixers

A classical switching mixer generates output signals at frequencies equal to the sum and difference of input frequencies. Usually the difference frequency between the LO and the signal is of main interest. The LO is a large signal that shifts the mixer's bias point on a nonlinear IV curve as a function of time. The signal amplitude is small and does not affect the bias point, but interacts with the mixer as with a passive nonlinear element with resistance depending on LO frequency. The shift by LO of bias point changes the resistance that can be presented as a Fourier series at LO harmonics, the main component is

$G(t)=G_0+G_1(A,\omega_{LO})Cos(\omega_{LO}t)$

The signal voltage will produce the output current

$I(t)=G(t)V_sCos\omega_st=G_0V_sCos\omega_st+0.5G_1V_s[Cos(\omega_s+\omega_0)t+Cos(\omega_s-\omega_0)t]$

in which the down-converted signal is

$$I_{if}=0.5G_1V_sCos(\omega_s-\omega_0)t \qquad (3)$$

Numerical example see in Fig. 2. To calculate the output power one should take into account the mismatch of source and input impedances

$K=4R_sR_l/(R_s+R_l)^2$

The last relation shows the fundamental limit on conversion efficiency in any resistive mixer: in the optimal case the source power is shared in equal parts by source and load impedances that bring the maximal conversion efficiency of –3 dB.

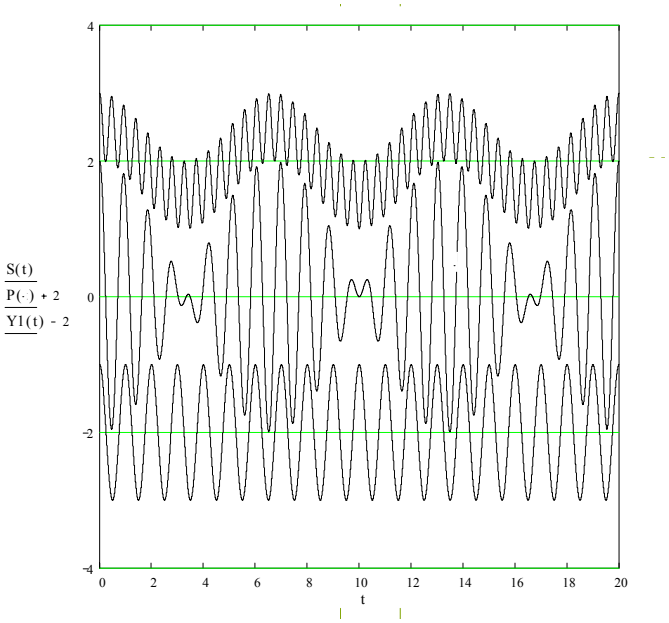

Fig. 2. Conversion process for switching and power mixer. Lower trace Y=Cos(f1·t) is initial signal, middle S=Y1+Y2 is a sum of two cosin terms in the power mixing, and upper trace P=Y1·Y2 is a product of multiplying of two cosin terms in switching mixer

IV. Power Mixers

The power mixer can be viewed as a combination of power detector and interferometer in which signal and local oscillator fields interfere to form the interference pattern with rapidly varying interfered component. The general case, when LO power is much greater the signal power, the analysis can be reduced to a simple one when both amplitudes are equal

$E(t)/E_{LO}=Cos\,\omega t+\alpha Cos(\omega+\delta)t=(1-\alpha)Cos\omega t+\alpha[Cos\omega t+Cos(\omega+\delta)t]= E1+E2$

The last term E2 brings the interference pattern that can be converted to natural form:

$$E2 = Cos\omega t + Cos(\omega+\delta)t = 2\cdot Cos\frac{2\omega+\delta}{2}t\cdot Cos\frac{\delta}{2}t \qquad (4)$$

These two components E1 and E2 of combined fields independently heat our slow bolometer and produce power

$$P=\overline{\frac{E_1^2}{R}+\frac{E_2^2}{R}}=\overline{\frac{(1-\alpha)^2}{R}Cos^2\omega t}+\overline{\frac{4\alpha^2}{R}Cos^2\left(\frac{2\omega+\delta}{2}t\right)\cdot Cos^2\frac{\delta}{2}t}=$$

$$=\frac{(1-\alpha)^2}{R}\left(\frac{1-Cos2\omega t}{2}\right)+\frac{4\alpha^2}{R}\left(\frac{1-Cos(2\omega+\delta)t}{2}\right)\left(\frac{1-Cos\delta t}{2}\right)$$

which brings after averaging in the signal frequency time scale the IF power

$$P(t)=\frac{(1-\alpha)^2}{2R}+\frac{\alpha^2}{R}-\frac{\alpha^2}{R}Cos\delta t \qquad (5)$$

which can be clearly explained for equal levels of power α=1

$$P(t)=(E^2/R)(1-Cos\delta t) \qquad (6)$$

It means that output power varies from zero to maximum, and its average is

$$P=E^2/2R+E^2/2R=E^2/R$$

that is the sum of equal initial powers. If LO power is larger, the interference term automatically will interact only with the equal amplitude. It means that required power for detection of low signal is equally low. If it is required to have a large dynamic range, then the amplitude of available at bolometer-mixer input should be equal to the maximum amplitude of the expected input signal. The HEBM operation can be explained with the above model, and our proposed CEBM can also be viewed as a power mixer that is too slow to follow the LO frequency, but fast enough to detect IF response at difference frequency. Numerical illustration to these equations is given in Fig. 2 and Fig. 3.

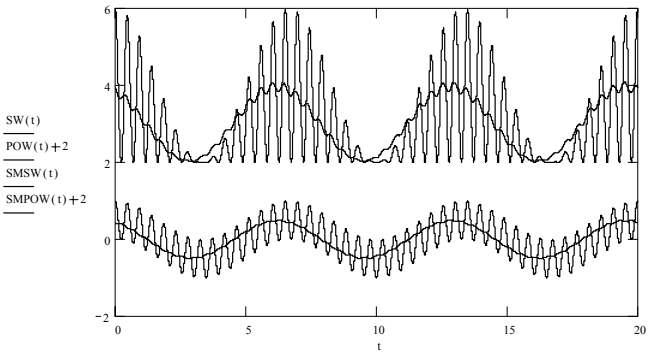

Fig. 3. Power and switching mixing after squaring. Integration of both signals brings the same down-converted frequency. Upper dependencies were calculated for power mixing after squaring and after averaging. Lower dependencies – for switching mixer.

V. COLD ELECTRON BOLOMETER AS MIXER

When operate at millikelvin temperatures CEB demonstrate rather slow response in a megahertz range due to reduced electron-phonon interaction and slow cooling of the overheated electrons. With increase of temperature the e-p interaction power increases as $P_{ep}=\Sigma\nu(T_e^5-T_{ph}^5)$ in which is Σ material constant, ν is volume, T_{ph} is phonon temperature, T_e is electron temperature.

An effective thermal time constant without electrothermal feedback (electron cooling) can be estimate from the simple relation

$$\tau_0=C_\nu/G_{ep},\ \tau=\tau_0/(L+1)$$

in which $C_\nu=\nu\gamma T_e$ is heat capacity of the absorber, $G_{ep}=5\Sigma\nu Te^4$ is electron-phonon thermal conductance, $L=G_{cool}/G_{ep}$ is ETF gain. The estimated values of effective time constant are10 μs at 100 mK and 150 ps at 4.2 K. With ETF they can be reduced by a factor of 10 to 1000. These values are in the range of commercial cooled RF amplifiers with the noise temperature below 10K.

The conversion efficiency can be estimated from the basic principles of electron cooling: if we have incoming heating power P_{sig} it will be completely compensated by electron cooling to have the same electron temperature. One electron of current roughly removing the energy of kT, and it means, that $P_{cool}=P_{sig}=kT\cdot\Delta I/e$, or $\Delta I=eP_{sig}/kT$. Power absorbed in the IF load can be estimated from simple Joule heating by IF current at bias voltage close to the gap voltage. That is for two junctions in series $P_{IF}=2V_\Delta\cdot\Delta I=2eV_\Delta\cdot P_{sig}/(kT)$, Finally the power gain $G=P_{IF}/Psig=2eV_\Delta/kT=eV_{2\Delta}/kT$ and it means that contrary to classical mixer with 3 db conversion losses as the best, for CEBM we can have a moderate power gain.

Noise performance in first approximation can be deduced from the shot noise of SIN junction at the output port (input assume as noiseless, it is just real resistance of metal strip). Current shot noise at the output is $I_n^2=2eI\cdot\Delta f$ and it can be recalculated into power as $P_n\approx 2eIR\cdot\Delta f\approx 2eV_\Delta\cdot\Delta f=kT_n\cdot\Delta f$ from which we can obtain the output noise temperature $T_n^{out}=eV_{2\Delta}/k$ that is about 30 K in the case of Nb. If we can also take into account the above estimated conversion gain $G=eV_{2\Delta}/kT$ one can obtain a very optimistic estimation of noise temperature referred to the input $T_n=T$.

Power matching to the input signal is much easier compared to SIS mixer, in CEBM or SINIS we do not need to compensate the intrinsic capacitance of tunnel junction, its impedance is rather low and we have mainly real resistance of metal absorber (normal metal film) that is terminated to the planar antenna. In this case it is very easy to achieve perfect impedance matching, even in the wide frequency range.

For IF matching the problem is essentially the same as for SIS mixer, and it can be solved for SINIS in the same way. For estimations of resistances and capacitances we can take characteristics of regular SIS junctions with AlOx barrier [5] that are characterized by the R_nA product (A is an area, R_n is normal resistance of the junction) in the range 25-30 $\Omega\cdot\mu m^2$, that corresponds to the current density of 7-8 kA/cm^2, and specific capacitance 70 fF/μm^2. For the junction of 1 μm^2 area the resistance can be about 30 Ω and capacitance 70 fF.

At IF=1.5 GHz it brings capacitive impedance of about 1500 Ω and dynamic resistance about R_n=30 Ω, while the absorber should be about 70 Ω to match THz signal to complementary planar antenna. Finally at IF we need to match 130 Ω of SINIS to 50 Ω of amplifier that can be done by a coplanar matching transformer. Losses at the IF port in the case of 70 Ω absorber will be about 3 dB. If we apply the advanced technology of AlN tunnel barrier [6], that allows to obtain the RnA product down to 1 $\Omega\cdot\mu m^2$, in this case the problem of IF matching is easy solved. The IF impedance will be equal to normal resistance of absorber that is chosen to be 70 Ω for matching to complementary planar antenna at signal frequency.

VI. Design and Studies of CEB

We designed and fabricated CEB sensors in a simple technology of angle evaporation through suspended mask. Normal metal absorber was made of Cu film and superconducting electrodes are made of Al. Bolometers were integrated with log-periodic and double-dipole antennas. The view of the SINIS sample with log-periodic antenna is presented in Fig. 4. Absorber in this sample is relatively long, about 10 μm. Samples were measured at temperature 280 mK that is below transition temperature of Al. The estimated time constant for such samples at this temperature is about 1 MHz. Reducing the length of bolometer down to 1 μm and replacing Al with Nb or NbN will allow to increase temperature over 4.2 K and increase response frequency over 1 GHz. According to our estimations it is possible to achieve IF in CEBM up to 10 GHz.

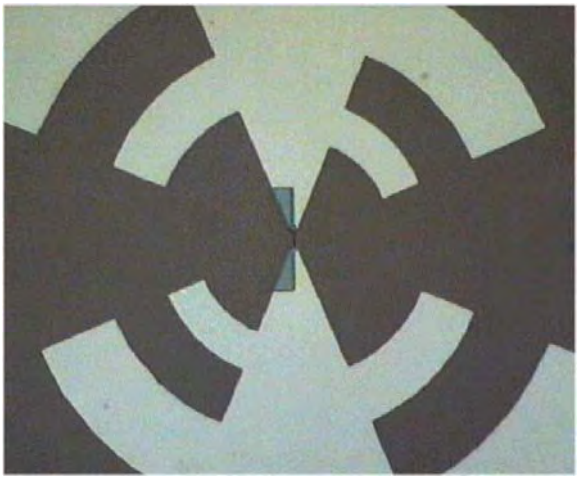

Fig. 4. CEB integrated with log-periodic antenna.

Voltage and current responses of CEB are presented in Fig. 5, and frequency response in Fig. 6. For details of these measurements and sample layout see also [7]. These dependences illustrate capability of SINIS sensor to detect submm-wave radiation at frequencies around 2 THz that is much above the gap frequency of of Al and with Noise Equivalent Power (NEP) below $2 \cdot 10^{-17}$ W/Hz$^{1/2}$. The electron-phonon relaxation time for the sample with Cu absorber at temperature 300 mK can be estimated as

$\tau_{ep}=20/T^3$ ns=1 μs ,

which is reduced to 0.36 ns at 4.2 K. By changing absorber material and thickness this value can be reduced further in the same way as in HEB mixers.

To summarize, earlier it was demonstrated that SINIS sensor can be used as incoherent detector. High sensitivity was achieved at millikelvin temperatures using ^{3}He sorption cooler. Now we propose to use the same SINIS as coherent detector for spectroscopy in Terahertz frequency range. With Nb or NbN junctions, AlN barrier and reduced length of absorber it is possible to increase intermediate frequency up to few gigahertz at ambient temperature 4.2 K.

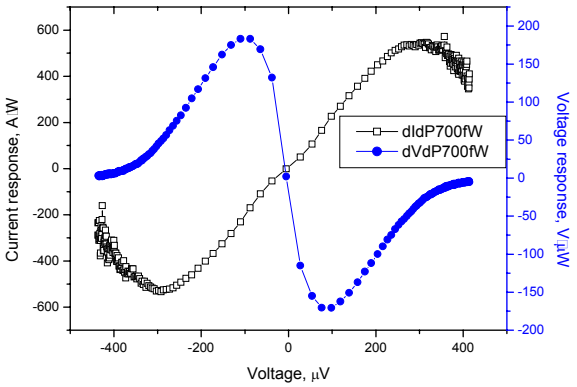

Fig. 5 **C**urrent and voltage response of CEB on applied power.

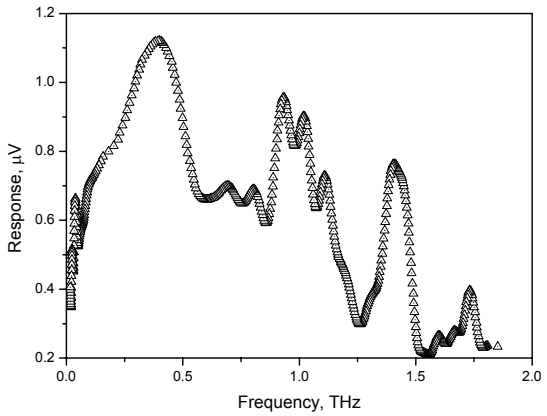

Fig. 6 Spectrum response of CEB in bolometer mode.

References

[1] A.Karpov, D.Miller, F.Rice, J.A.Stern, B.Bumble, H.G.LeDuc, J.Zmuidzinas, "Low noise SIS mixer for far infrared radio astronomy", *Proc. of SPIE*, vol. 5498, (2004), pp. 616-621.

[2] E.M.Gershenson, M.E.Gershenson, G.N.Goltsman, A.Lul'kin, A.Semenov, A.Sergeev, "Limiting characteristics of high-speed superconducting bolometers", *Journal of Techn. Phys*, vol. 59, N 2, (1989), pp. 111-120.

[3] T.M.Klapwijk, R.Barends, J.R.Gao, M.Hajenius, J.J.A.Baselmans, "Improved superconducting hot-electron bolometer devices for the THz range", *Proc. of SPIE*, vol. 5498, (2004), pp. 129-139.

[4] L.Kuzmin, I.Devyatov, D.Golubev, "Cold-electron bolometer with electron microrefrigeration. The general noise analysis", *Proc. SPIE*, vol. 3465, (1998), p.193.

[5] L.V. Filippenko, S.V. Shitov, P.N. Dmitriev, A.B. Ermakov, V.P. Koshelets, and J.R. Gao, "Integrated Superconducting Receiver: fabrication and yield", *IEEE Trans. on Appl. Supercond.*, vol. 11, N 1, pp. 816-819, (2001).

[6] P.Dmitriev, I.Lapitskaya, L.Filippenko, A.Ermakov, S.Shitov, G.Prokopenko, S.Kovtonyuk, V.Koshelets, "High quality Nb-based tunnel junctions for high frequency and digital applications", *IEEE Trans Appl. Supercond.*, vol. 13, N 2, (2003), pp. 107-110.

[7] M.Tarasov, L.Kuzmin, E.Stepantsov, I.Agulo, A.Kalabukhov, Z.Ivanov, T.Claeson, "Terahertz spectroscopy by Josephson oscillator and SINIS bolometer". *JETP Letters*, vol.79, N 6, 2004, pp. 298-303.

Shapiro-steps in $Bi_2Sr_2CaCu_2O_8$ (Bi2212) intrinsic Josephson Junctions (IJJ)

Single crystals and thin films of very anisotropic high-transition-temperature superconductors (HTS) show Josephson coupling in the c-axis direction between adjacent (clusters of) Cu-O planes [1]. Bi2212 belongs to this group of compounds and single crystals are composed of large series arrays of Josephson tunnel junctions in the c-axis direction. Mesas composed of a few (even one) or up to thousands of these intrinsic Josephson junctions (IJJ) can be patterned in the crystal to make devices. IJJ could be attractive both for SIS-mixers due to the large gap frequency and as voltage standards, due to the stacked nature of the junctions, making it possible to add Shapiro steps in series easily up to the Volt range. Shapiro steps have been detected for frequencies up to 2,5 THz [2], results which might be used for designing a Josephson voltage standard based on HTS.

In this work, we present preliminary results on both fabrication and measurements on IJJ coupled to Bow-tie and log-periodic antennas operating in the range of 300 GHz. The IJJ are fabricated from single crystals of Bi2212, by using photolithography and ion-beam etching. A wiring layer contacts the mesas and also forms the structure of the antennas. Fig. 1 shows a photo of one of our devices. A measurement of this device at 300 GHz is presented in Fig. 2, where the Shapiro steps are clearly seen.

We are now working on improving the coupling of the device to the antenna and to the external quasi-optical set-up to bring the operating frequency up to beyond a THz.

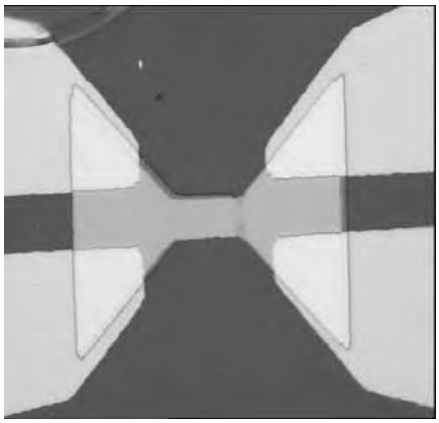

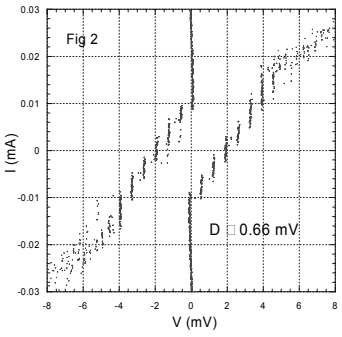

Fig. 1 (left) Photograph of one of our devices. The single crystal Bi2212 can be seen on the middle of the sapphire substrate. The IJJ are located in the bridge in centre of the structure.
Fig. 2 (right) Current voltage characteristic of a device with 20 IJJ. Up to 7 Shapiro steps at 300 GHz can be seen in this plot.

[1] R. Kleiner, F. Steinmeyer, G. Kunkel, and P. Mu¨ller, Phys. Rev. Lett. **68**,2394 □1992.
[2] H.B Wang, P.H Wu and T. Yamashita, "Terahertz responce of intrinsic Josephson junctions in high Tc superconductors" Phys. Rew. Lett. 87, 107002

Attowatt Sensitivity of the Capacitively-Coupled Cold Electron Bolometer

Ian Jasper A. Agulo, Leonid S.Kuzmin, and Michael A. Tarasov

***Abstract*—We have fabricated and characterized the Cold-Electron Bolometer (CEB) in the current-biased mode. We measured the bolometer responsivity and the noise equivalent power (NEP) by applying a modulated heating current through the absorber. The frequency of modulation varied from 35 Hz to 2 kHz. The best responsivity of 1.5×10^{10} V/W was obtained at 35 Hz. NEP of better than 10^{-18} W/Hz$^{1/2}$ was measured for modulation frequencies above than 100 Hz. The background power load and the bolometer time constant was also estimated using the experimental device parameters.**

***Index Terms*—Cold-Electron bolometer, Noise Equivalent Power, Responsivity, SIN tunnel junction**

I. Introduction

The highest level of requirements for detectors in the near future will be determined by the proposed NASA missions SPIRIT, SPECS and SAFIR. The detector goal is to provide noise equivalent power down to 10^{-20} W/Hz$^{1/2}$ [1] over the 40 – 500 μm wavelength range in a 100x100 pixel detector array with low power dissipation array readout electronics. To the author's knowledge, the transition-edge sensor (TES) with a strong electrothermal feedback [2,3] is the current detector technology of choice. However, the limitations in its sensitivity are excess noise, saturation and overheating from the dc power for the feedback. To achieve high sensitivity, the concept of the Cold-Electron Bolometer (CEB) with strong electrothermal feedback [4] has been proposed.

Manuscript received May 31, 2005. This work was supported by The Swedish Research Council (Vetenskapsrådet), The Swedish Foundation for International Cooperation in Research and Higher Education (STINT), and the Swedish Institute (SI).

I. J. A. Agulo is with the Quantum Device Physics Laboratory, Department of Microtechnology and Nanoscience, Chalmers University of Technology SE-41296 Gothenburg, Sweden, on leave from the Department of Physics, University of the Philippines Baguio, Gov. Pack Road, 2600 Baguio City, Philippines (e-mail: ian.agulo@ mc2.chalmers.se).

L. S. Kuzmin is with the Quantum Device Physics Laboratory, Department of Microtechnology and Nanoscience, Chalmers University of Technology SE-41296 Gothenburg, Sweden, and is also affiliated to Moscow University, Nuclear Physics Institute, 119899 Moscow, Russia (corresponding author: +46(31)-772-3608; fax: +46(31)-772-3471; e-mail: leonid.kuzmin@mc2.chalmers.se).

M. A. Tarasov is with the Quantum Device Physics Laboratory, Department of Microtechnology and Nanoscience, Chalmers University of Technology SE-41296 Gothenburg, Sweden (e-mail: mikhail.tarasov@mc2.chalmers.se).

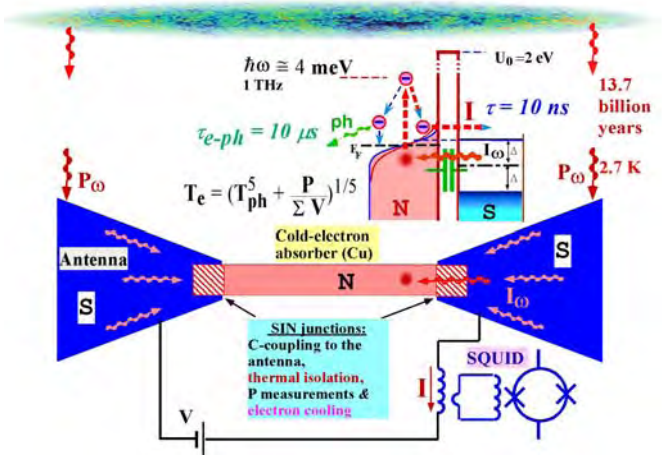

Fig. 1. Principle of the CEB. Radiation from space is detected by the antenna, which then focuses the incoming signal to the absorber. The electromagnetic signal goes through the superconductor-insulator-normal metal (SIN) tunnel junctions, and its energy is transferred to the normal metal electrons. The relaxation of electron energy occurs in two ways. The first is relaxation by electron-phonon interaction, and the second is extraction of hot electrons from the normal metal by the cooling current of the SIN tunnel junction. The fastest process determines the bolometer response. The ideal case would then be the electron cooling due to SIN tunnel junctions to be the dominant process.

The CEB concept is based on the direct electron cooling of the absorber that serves as a negative electrothermal feedback for the incoming signal. The electromagnetic signal is first detected by the antenna. It then goes through the superconductor-insulator-normal metal (SIN) tunnel junctions to the normal metal absorber. The energy is then absorbed by the electrons in the absorber. One electron has obtained an energy equal to the energy of one photon. The first step in the relaxation process is due to electron-electron interaction. At this point, there is a number of hot electrons with high energies.

The next step in the relaxation of energy is brought about by two processes. The first process is due to electron-phonon interaction in the absorber. The second is due to electron cooling by the SIN tunnel junctions. The ideal case would be to transfer all the high energy electrons through the tunnel junctions, which is seen as a current response.

To make this response as close to ideal as possible, we employed proximity traps to enhance the electron cooling of the absorber, which serves as a negative electrothermal feedback. This type of feedback keeps the electron temperature below the phonon temperature. This improves the detector responsivity and sensitivity. The feedback also

increases the dynamic range of the device.

II. Theory of the Cold-Electron Bolometer

The non-equilibrium theory of the hot-electron bolometer (HEB) is explained in detail by Golubev and Kuzmin [5]. In this HEB, the absorber is capacitively-coupled to the antennae through SIN tunnel junctions. As described previously, the electron temperature, T_e in the CEB is kept well below phonon temperature, T_{ph}. This is achieved by improving the geometry of the superconducting electrodes such that there is more volume for tunneled quasiparticles to diffuse into, or by adding normal metal traps adjacent to the superconducting electrodes [6], [7]. The only effect of this is to increase the cooling power of the SIN tunnel junction. This cooling power is well described in equation (2) below and no change in any of the expressions below is necessary to account for conceptual differences between the HEB and the CEB.

As previously stated, the electron temperature of the absorber is related to the power of the incoming radiation, which we are interested in measuring. In order to determine the electron temperature of the normal metal absorber, one has to take into account all the contributions to the heat load to the absorber. The dominant power contribution at a given bias voltage at a certain temperature will determine the electron temperature. This can be attained by solving the heat balance equation, as shown below.

$$c_v \nu \frac{dT}{dt} + \Sigma \nu \left(T_e^5 - T_{ph}^5\right) + P(V, T_e, T_S) = P_0 + \frac{V^2}{R_s} + \delta P(t) \qquad (1)$$

where $c_v = \gamma T_e$ is the specific heat of the normal metal, ν is its volume, $\Sigma\nu(T_e^5 - T_{ph}^5)$ is the heat flow from the electron to the phonon sub-system in the normal metal, Σ is the electron-phonon coupling constant dependent on the material used, ν is the volume of the absorber, V^2/R_S is the heat load due to the subgap leakage resistance, R_S, P_0 is the background optical power load of the bolometer, $\delta P(t)$ is the incoming rf power. The cooling power, $P(V, T_e, T_S)$, of the SIN tunnel junction is given by:

$$P(V, T_e, T_S) = \int dE E \left[\Gamma_{N\to S}(E) - \Gamma_{S\to N}(E)\right] \qquad (2)$$

In the calculations, the temperature of the superconductor, T_S is assumed to be equal to the phonon temperature, T_{ph}. In general, this is not the case and heating of the superconducting electrodes should be considered. However, we are interested in the region below the superconducting gap where the absorber is cooled due to the dominant cooling power of the tunnel junction.

A bolometer is characterized by its responsivity and sensitivity and its time constant. In the current-biased mode, the responsivity, S_V, is described by the voltage response to an incoming power

$$S_V(\omega, I) = \frac{\delta V_\omega}{\delta P_\omega} = \frac{-\dfrac{\partial I/\partial T}{\partial I/\partial V}}{-i\omega c_V \nu + 5\Sigma\nu T_e^4 + \dfrac{\partial P}{\partial T} - \dfrac{\partial I/\partial T}{\partial I/\partial V}\dfrac{\partial P}{\partial V}} \qquad (3)$$

The noise is characterized by the Noise Equivalent Power (NEP), which is the net effect of all the sources referred to the input of the bolometer. The total NEP is the sum of three components given by

$$\mathrm{NEP}^2_{\mathrm{total}} = \frac{\left\langle \delta V_\omega^2 \right\rangle_{\mathrm{amp}}}{S_V^2(0, I)} + 10 k_B \Sigma V \left(T_e^6 + T_{ph}^6\right) + \mathrm{NEP}^2_{\mathrm{NIS}} . \qquad (4)$$

The first term on the right hand side is the NEP due to the amplifier given by the voltage noise of the amplifier divided by the voltage response of the bolometer to applied power. The second term is the NEP associated with the heat flow between electrons and phonons. The last term is the NEP associated with NIS tunnel junction. Theory predicts that the CEB should be able to show a sensitivity of 10^{-19} W/Hz$^{1/2}$. This paper demonstrates a sensitivity of better than 10^{-18} W/Hz$^{1/2}$ at 100 mK in the current-bias mode.

The CEB for dc characterization is composed of four superconductor-insulator-normal metal (SIN) tunnel junctions. The outer SIN junctions serves as a capacitive coupling of the absorber to the antenna, as thermal isolation and as electron coolers of the absorber. All these three functions work for the improvement of the responsivity and the sensitivity of the bolometer. Chouvaev, et. al. [8] reported that the improvement is due to the isolation of the device from the external interferences picked-up by the lead wires. Jochum, et. al. [9] demonstrates the significance of the temperature of the normal metal to the increased sensitivity of detectors which utilize SIN tunnel junctions. The inner SIN junctions serve to measure the temperature of the normal metal. For this purpose, these junctions should have minimal influence on the device. To do this, the inner tunnel junctions were designed to have smaller area in comparison to the outer tunnel junctions.

As was mentioned, the detector sensitivity is improved by electron cooling of the absorber. The addition of normal metal traps adjacent to the outer SIN tunnel junctions greatly enhances the electron cooling. In our previous work [6], [7], we demonstrated a decrease in electron temperature by almost 200 mK with the use of the normal metal traps. With all these

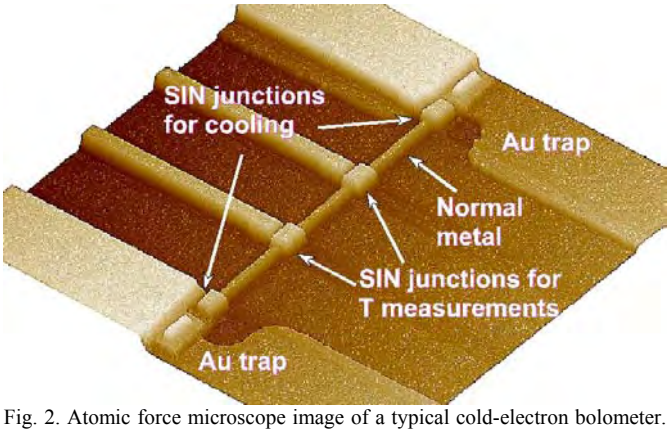

Fig. 2. Atomic force microscope image of a typical cold-electron bolometer. The outer SIN tunnel junctions cools the electrons in the normal metal. This electron cooling is enhanced by the Au traps in proximity to the cooling junctions. The inner SIN tunnel junctions acts as a thermometer to measure electron temperature in the absorber.

TABLE I
LIST OF EXPERIMENTAL PARAMETERS

	Area (μm2)	Normal Resistance (kΩ)	Zero-bias Resistance (MΩ)
Outer SIN tunnel junctions	0.45	4.3	8.4
Inner SIN tunnel junctions	0.06	14.5	21.2
Normal metal absorber	0.11 μm^3 [a]	0.063	-

Measured parameters at 20 mK. The normal resistance corresponds to the asymptotic resistance for large bias currents.

[a]The volume of the absorber is the important parameter as it is directly coupled to the absorbed power and therefore to the sensitivity of the device.

things in consideration, we have fabricated our device as follows.

III. FABRICATION OF THE DEVICE

The CEB is fabricated by e-beam lithography using two-layer resist technology, and two-angle evaporation. 0.2 μm PMMA on top of 0.8 μm Copolymer were exposed to 80 pA of beam current with a dose of 315 $\mu C/cm^2$. PMMA was developed in Toluene:IPA=1:3 and Copolymer in Ethoxylacetate:Ethanol=1:5 to create the masks for the device pattern. The normal metal traps and the bolometer device were made in two separate vacuum cycles. In the first vacuum cycle, 10 nm of chromium, followed by 30 nm of gold, and finally 10 nm of palladium were thermally evaporated to make 50 nm of normal metal trap. Cr was used for better adhesion of Au to the SiO_2 substrate. Pd was used as a buffer layer between Au and Al when they are in contact with each other. In time, Au reacts with Al forming an alloy that increase the contact resistance, which is naturally undesirable.

In the second vacuum cycle, the aluminum electrode was thermally evaporated at an angle of 55º relative to the surface normal upto a thickness of about 60 nm. The tunnel barrier was formed by oxidizing the electrode for 2 minutes at a pressure of $5x10^{-2}$ mbar. The normal metal absorber was created by evaporating 30 nm of chromium and then 30 nm of copper at an angle of 0º. Cr was used to improve the impedance matching of the antennae to the normal metal and also for better adhesion of Cu to the substrate. The measured resistance of the absorber was about 60 Ω. Table 1 lists down the pertinent experimental parameters of the CEB. Fig. 2 shows a typical schematic of the CEB using a scanning probe microscope.

The sample was measured in an Oxford dilution refrigerator. Measurements were performed in the current-biased mode. The current source consisted of a symmetric voltage source in series with bias resistors ranging from 200 kΩ to 20 GΩ. This provides us the possibility to measure large voltage ranges to measure the asymptotic resistances of the junctions, and also their subgap and zero-bias resistances. The high-ohmic bias resistances also provide some amount of protection from external interference.

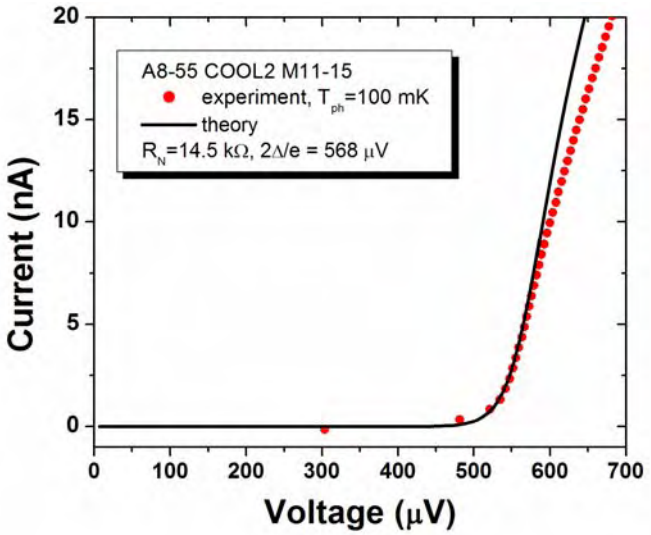

Fig. 3. Current-voltage characteristic of the tunnel junction used for response measurements (the inner pair) at T_{ph}=100 mK (circles). The measured normal state resistance was 14.5 kΩ and the subgap resistance was 21.2 MΩ. The superconducting gap, 2Δ=568 μeV, was estimated by fitting the theoretical curve (solid line) with the experimental curve.

IV. RESULTS AND ANALYSIS

A. I-V Characteristics

Fig. 3 shows the current-voltage characteristic of the inner tunnel junctions, which was used as the response junctions. The superconducting gap voltage of 568 μeV for the aluminum electrode was estimated by fitting the theoretical estimate with the experimental data. The solid line shows the theoretical fit. It is in very good agreement in the region of the gap. As the voltage increases from the gap voltage, the discrepancy between the theory and experiment increases. Moving further away from the gap (not shown), the discrepancy then decreases, and the experimental curve follows the asymptotic line corresponding to the normal state resistance of the tunnel junction pair. We believe that the discrepancy is due to nonuniformity of the gap in the tunnel junction.

B. Bolometer Responsivity, dV/dP

The basic idea in measuring bolometer responsivity in the current-biased mode is the determination of the voltage response corresponding to an input power. We have used both dc input power and modulated input power with frequencies from 35 Hz to 2 kHz, and measured voltage response in both cases.

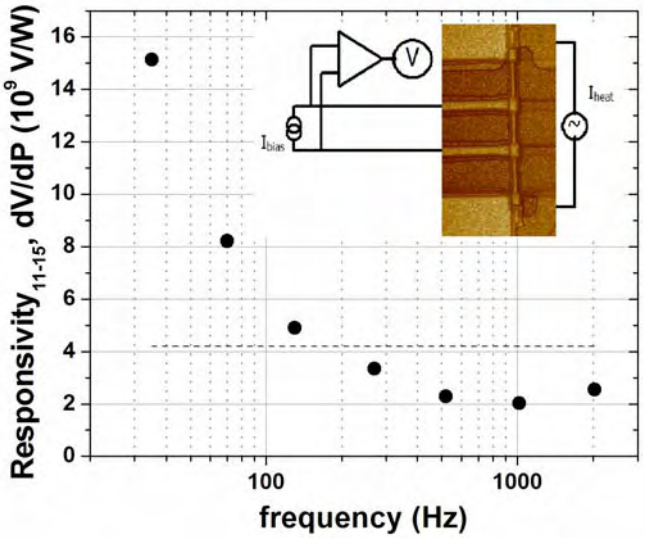

Fig. 4. Measured responsivity of the inner tunnel junctions at T_{ph}=100 mK (circles) for modulation frequencies from 35 Hz to 2.02 kHz. Using the experimental parameters, the theoretical curve (dashed line) predicted a responsivity of 4.2x10^9 V/W. (Inset) A view of the measurement scheme for responsivity.

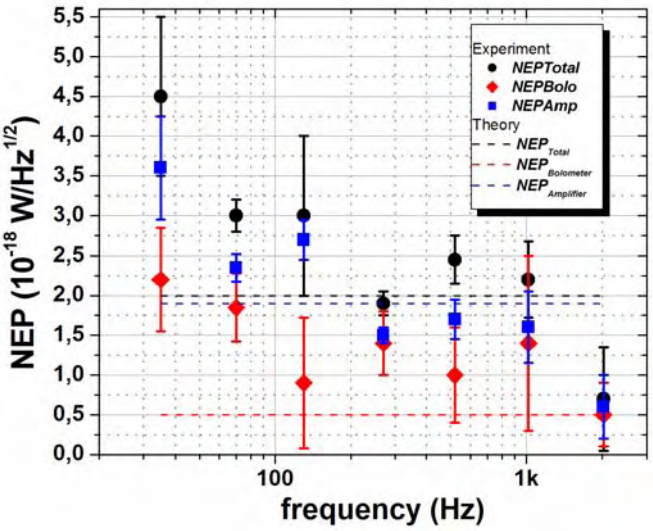

Fig. 6. Measured noise equivalent power (*NEP*) of the inner tunnel junctions for modulation frequencies from 35 Hz to 2.02 kHz. The dashed lines show the theoretical estimations using the experimental parameters. The bolometer *NEP* is clearly better than 10^{-19} W/Hz$^{1/2}$ for modulation frequencies above 100 Hz. Theory predicts 5x10^{-19} W/Hz$^{1/2}$ for the given experimental parameters.

To measure the response of the inner junctions, we applied the input power to the outer junctions. The technique with dc input power requires sweeping an external current bias to the outer junctions. Using its I-V characteristic, we can determine how much power we are applying to the absorber. The corresponding voltage response is measured for different bias currents of the inner junctions. Using the I-V characteristic of the inner junctions, the maximum responsivity, *dV/dP* can then be plotted as a function of the bias voltage.

In the modulation technique, a modulated bias current is applied to the outer tunnel junctions. Using its I-V characteristic, the magnitude of the input power can be obtained. We have then measured the voltage response using the SR830 lock-in amplifier by sweeping the bias to the inner tunnel junctions. Figure 4 shows the result of our measurement of responsivity for different frequencies using the modulated heating power. The highest value of the responsivity obtained at 35 Hz was measured to be 1.5x10^{10} V/W. The attenuation of the filter lines in the dilution refrigerator is the most probable reason for the observed dependence of responsivity on frequency. The dashed line shows the responsivity computed from theory using the experimental parameters. Theory gives the value for maximum responsivity of 4.2x10^9 V/W.

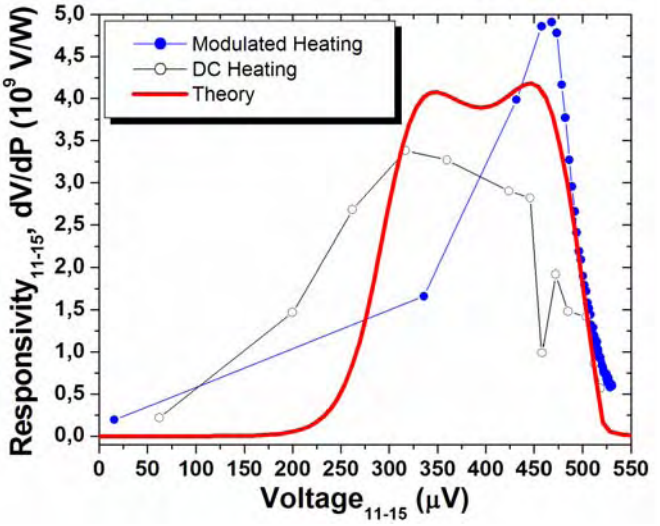

Fig. 5. Comparison between the two techniques of measuring the bolometer responsivity and the theoretical estimation.Very good agreement between experiment and theory can be seen in the region near and below the superconducting gap voltage.

Fig. 5 shows comparison between responsivities measured using dc heating power, modulated heating power of 0.2 fW for f = 120 Hz and the theoretical result from the experimental parameters. In the region below the gap where it is expected to have good electron cooling, both experimental curves agree well with the theory.

C. Bolometer NEP

The next step in the characterization was to measure the *NEP* of the bolometer. It can be only be measured indirectly by subtracting the amplifier NEP from the total NEP, i.e.

$$NEP_{total}^2 = NEP_{bolometer}^2 + NEP_{amplifier}^2 \qquad (5)$$

The total *NEP* and the amplifier *NEP* is obtained by the dividing the responsivity by the total noise and the amplifier noise, respectively, as described in (4). Fig. 7 shows the measured total *NEP*, amplifier *NEP*, and bolometer *NEP* as a function of frequency of modulated heating. We have observed bolometer *NEP* to be better than 10^{-18} W/Hz$^{1/2}$ for modulation frequencies greater than 100 Hz. Theoretical estimations give NEP_{total} = 2x10^{-18} W/Hz$^{1/2}$, $NEP_{amplifier}$ = 1.8x10^{-18} W/Hz$^{1/2}$, and $NEP_{bolometer}$ = 5x10^{-19} W/Hz$^{1/2}$ (shown in dashed lines).

Fig. 7 shows the *NEP* as a function of voltage at f = 1.02 kHz in comparison to theory. Below the gap region, we see a good qualitative agreement between experiment and theory to within the accuracy of measurement.

The main limitation to our measurement of bolometer NEP is the large noise contribution of the amplifier. This can be improved by using an amplifier with lower voltage noise, or a cold amplifier to reduce its thermal noise. Another method would be to improve the noise temperature by operating the amplifier with higher source impedance. The source impedance for a typical amplifier such as OPA111 is in the order of MΩ. However, the resistance of our device is in the order of kΩ at the optimal bias. To achieve the high source impedance, the superconducting CEB (SCEB) is proposed [10]. In the SCEB, the operating point would be in the region between the difference and the sum gap. In that region, the impedance is in the order of MΩ, which is desirable for the operation of a room temperature amplifier with lower noise temperature. In addition, analysis of the CEB made by Golubev and Kuzmin [5] show that the voltage-biased regime is optimal for better responsivity and sensitivity.

D. *Estimation of time constants*

To fully characterize the bolometer, we estimated the time constants of the electron-phonon interaction and the extraction of normal metal electrons due to cooling by the SIN tunnel junctions using the experimental parameters. The time constant is given by

$$\tau = \frac{\gamma T_e \nu}{\partial P_{total} / \partial T} \qquad (6)$$

where

$$\partial P_{total}/\partial T = \partial P_{e-ph}/\partial T + \partial P_{cool}/\partial T \qquad (7)$$

For the normal metal absorber, we used γ=9.77 J/μm^{3}K^2 for copper. Fig. 8a shows our estimation for all relevant voltage ranges. In the subgap region where the dynamic resistance is high, the dominant process is clearly the interaction due to electron-phonon coupling. As the bias approaches the superconducting gap, the electron cooling begins to take over. In region just below the gap, the dominant process is the cooling of the SIN tunnel junctions. This is more clearly depicted in fig. 8b.

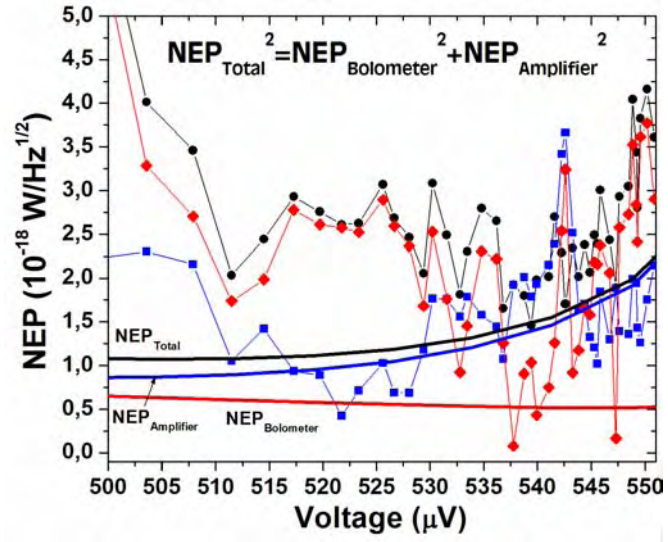

Fig. 7. The measured noise equivalent power (*NEP*) near and below the superconducting gap voltage for f = 1.02 kHz in comparison to theoretical prediction. In the region near the gap, there is a good qualitative agreement between experiment and theory.

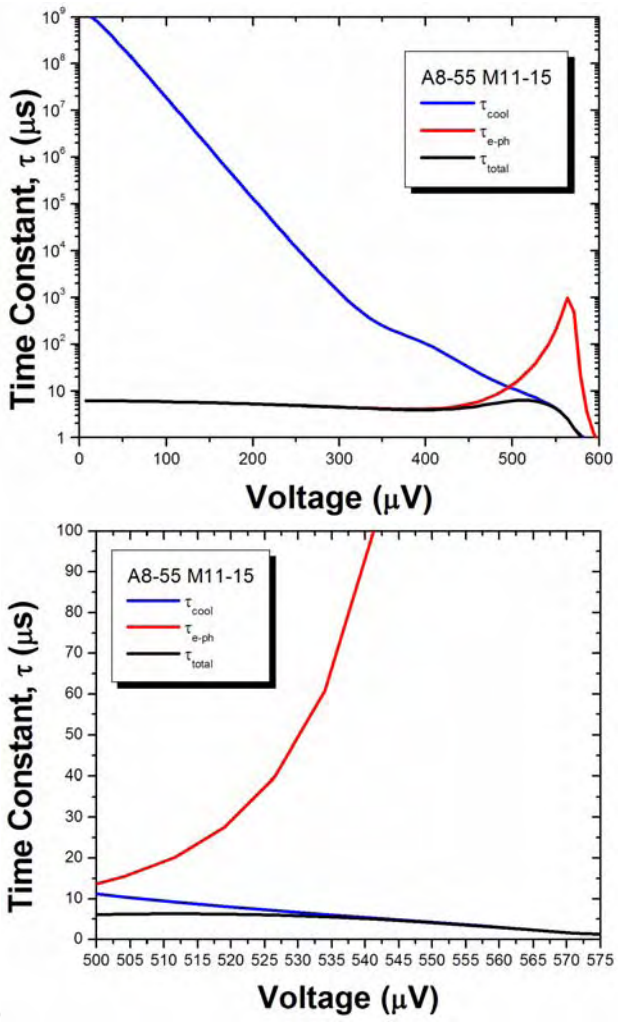

Fig. 8. Estimation of time constants using the experimental parameters. (a) In the subgap region, the dominant process is due to the electron-phonon coupling. (b) In the region near and below the gap, the dominant process is the electron cooling due to the SIN tunnel junctions.

V. CONCLUSIONS

We have fabricated and characterized the cold-electron bolometer (CEB). We have measured the responsivity by applying an input power from a modulated heating current for frequencies from 35 Hz to 2.02 kHz. The best value of the responsivity obtained was 15x10^9 V/W for f = 35 Hz. We have also measured the noise equivalent power of the bolometer. For modulation frequencies greater than 100 Hz, the measured *NEP* is better than 10^{-18} W/Hz$^{1/2}$. Theory gives good agreement with the experimental results in the region

near and below the superconducting gap voltage. In this region, the estimated time constant is mainly due to the strong electron cooling of the normal metal absorber by the SIN tunneling junction.

ACKNOWLEDGMENT

We would like to thank Dmitry Golubev for extensive and enlightening discussions on the theoretical part of this work.

REFERENCES

[1] D. Leisawitz et al., "Scientific motivation and technology requirements for the SPIRIT and SPECS far-infrared/submillimeter space interferometers", SPIE 2000.

[2] K. Irwin, "An application of electrothermal feedback for high-resolution cryogenic particle detection," *Appl. Phys. Lett.*, vol. 66, no. 15, pp. 1998-2000, Apr. 1995.

[3] A. Lee, P. Richards, S. W. Nam, B. Cabrera, K. D. Irwin, "A superconducting bolometer with strong electrothermal feedback," *Appl. Phys. Lett*, vol. 69, no. 12, pp. 1801-1803, Sep. 1996.

[4] L. Kuzmin, "Ultimate cold-electron bolometer with strong electrothermal feedback," *Proceedings of SPIE -- Millimeter and Submillimeter Detectors for Astronomy II*, vol. 5498, pp. 349-361, Oct. 2004.

[5] D. Golubev and L. Kuzmin, "Non-equilibrium theory of a hot-electron bolometer with normal metal-insulator-superconductor tunnel junction," *J. of Appl. Phys*, vol. 89, no. 11, pp. 6464-6472, Jun. 2001.

[6] I. J. Agulo, L. Kuzmin, M. Fominsky, and M. Tarasov, "Effective electron microrefrigeration by superconductor-insulator-normal metal tunnel junctions with advanced geometry of electrodes and with normal metal traps," *Nanotechnology*, vol. 15, no. 4, pp. S224-S228, Apr. 2004.

[7] L. Kuzmin, I. J. Agulo, M. Fominsky, A. Savin, and M. Tarasov, "Optimization of electron cooling by SIN tunnel junctions," *Supercond. Sci. Technol.*, vol. 17, pp. S400-S405, May 2004.

[8] D. Chouvaev, L. Kuzmin, and M. Tarasov, "Normal-metal hot-electron microbolometer with on-chip protection by tunnel junctions," *Supercond. Sci. Technol.*, vol. 12, no. 11, pp. 985-999, Nov. 1999.

[9] J. Jochum, C. Mears, S. Golwala, B. Sadoulet, J. P. Castle, M. F. Cunningham, O. B. Drury, M. Frank, S. E. Labov, F. P. Lipschultz, H. Netel, and B. Neuhauser, "Modeling the power flow in normal conductor-insulator-superconductor junctions," *J. of Appl. Phys.*, vol. 83, no. 6, pp. 3217-3224, Mar. 1998.

[10] L. Kuzmin, "Superconducting Cold-electron bolometer with proximity traps," *Micr. Eng.*, vol. 69, no. 2-4, pp. 309-316, Sep. 2003.

Fabrication and characterization of UTC-PDs for THz-wave generation

Josip Vukusic*, Per Olof Hedekvist** and Jan Stake**

**Institut d'Electonique de Micro´electronique et de Nanotechnologies, Universit´e des Sciences et Technologies de Lille, E-mail:vukusic@mc2.chalmers.se*
***Department of Microtechnology and Nanoscience, Chalmers University of Technology,*

The uni-travelling-carrier photodiode (UTC-PD)[1] has demonstrated the ability of combining high output power with large bandwidth. This is due to the fact that the absorption takes place in the p-region instead of the intrinsic region as for the traditional pin-diode. By shifting the absorption towards the p-contact we shorten the limiting transit time of the holes, thereby gaining speed and postponing the onset of current saturation. Besides the potential use in fiber optic links [2] the UTC-PD has also attracted attention as the principal component in photo-mixing schemes, ranging from 100 GHz [3] to 1 THz [4] in output frequency.

We aim at presenting preliminary results on single UTC-PD components covering fabrication and characterization. An approach for generating high output powers will also be proposed, involving closely packed UTC-PD-antenna (2D/1D) arrays. The ultimate goal is to demonstrate compact, efficient, tunable, high output power THz-wave emission.

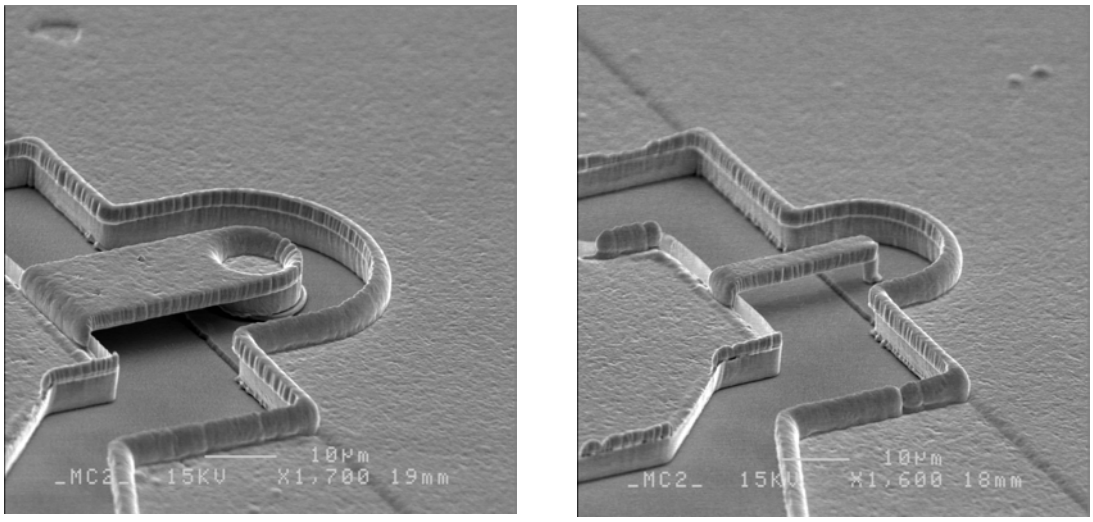

Figure 1. Scanning electron microscopy (SEM) images showing the largest and smallest of the processed UTC-PDs

[1] T. Ishibashi, N. Shimizu, S. Kodama, H. Ito, T. Nagatsuma, and T. Furata, "Uni-Travelling-Carrier Photodiodes," *Proc. UEO-OSA*, pp. 83-87, 1997.

[2] M. Gustavsson, P. O. Hedekvist, and P. A. Andrekson, "Uni-Travelling-Carrier Photodiode Performance with X-band Modulation at High Optical Power', to be published in *Microwave and Wireless Components Lett.*, 2005.

[3] H. Ito T. Nagatsuma, A. Hirata, T. Minota, A. Sasaki, Y. Hirota, and T. Ishibashi, "High-Power Photonic Millimetre Wave Generation at 100GHz using Matching-Circuit-Integrated Uni-Travelling-Carrier Photodiodes*", IEE Proc. Optoelectron.*, Vol. 150, No 2, pp. 138-142, April 2003.

[4] F. Nakajima, T. Furuta, and H. Ito, "High-Power Continuous-Terahertz-Wave Generation using Resonant-Antenna-Integrated Uni-Travelling-Carrier Photodiode", *Eletron. Lett*, No. 20, pp. 1297-1298, Sept. 2004.

Poster session III:

SIS

A new multibeam receiver for KOSMA with scalable fully reflective focal plane array optics

T. Lüthi*, D. Rabanus*, U. U. Graf*, C. Granet† and A. Murk‡
*KOSMA, I. Physikalisches Institut, Universität zu Köln, Zülpicher Strasse 77, 50937 Köln, Germany
Email: luethi@ph1.uni-koeln.de
†CSIRO ICT Centre, PO Box 76, Epping NSW 1710, Australia
‡Institute of Applied Physics, Universität Bern, Sidlerstrasse 5, 3012 Bern, Switzerland

***Abstract*— We are developing a new submillimeter heterodyne array receiver for the KOSMA 3m telescope on Gornergrat, Switzerland. In order to facilitate assembly and maintenance, the receiver consists of two self-contained 3×3 beam cartridge-type receiver modules. They employ new focal plane array optics which are both fully reflective and scalable in frequency as well as in the number of beams. So far, a first 345 GHz focal plane array optics prototype has been realized and its near field patterns have been measured.**

We describe the overall receiver design and present the focal plane array optics as well as the measured focal plane beam patterns.

I. Introduction

Heterodyne multibeam receivers greatly improve the mapping performance of millimeter and submillimeter telescopes. As the noise temperature of single-beam receivers approaches the quantum limit, a further increase in mapping speed requires multibeam receivers. However, there should be made no compromises resulting in an increased noise temperature of the individual receiver channels. The mapping time for a given area and a desired sensitivity increases with the square of the receiver noise temperature, but decreases only linearly with the number of receivers.

Today, there already exist several operational heterodyne array receivers at short millimeter and submillimeter wavelengths (e.g. SMART [1], HERA [2], PoleSTAR [3]). SMART is a dual-frequency/eight-beam receiver operating at 490 and 810 GHz, used as a facility instrument at the KOSMA 3m telescope on Gornergrat, Switzerland [4]. In order to replace the telescope's older 230/345 GHz dual-frequency/single-beam receiver, we are developing a 2×9 beam array receiver. It is based on two self-contained 3×3 beam cartridge-type receiver modules [5]. The modular receiver design not only facilitates assembly and maintenance, it also allows a rapid adaptation to the seasonal observation conditions. For the dry winter months the receiver modules can be easily replaced with higher-frequency units.

The receiver modules employ a new focal plane array optics which is fully reflective, thus avoiding the absorption and reflection losses of dielectric lenses. It is scalable both in frequency as well as – for the first time with a fully reflective array – to an arbitrary number of beams. So far, a first 345 GHz focal plane array optics prototype has been realized and its near field patterns have been measured.

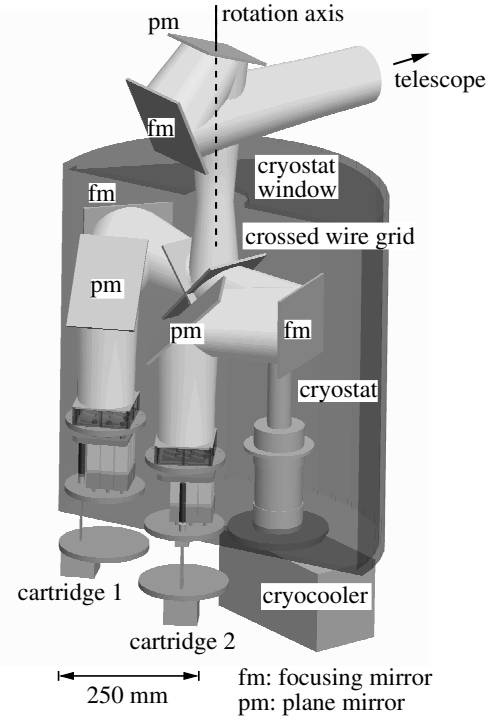

Fig. 1. General layout of the array receiver. The cryostat uses a two-stage cryocooler (50 and 4 K). Not shown are the inner radiation shields, thermal links and the support structure. The indicated beam contour is the envelope of all nine beams at 345 GHz.

In this paper we describe the overall receiver design and present the focal plane array optics and the first measured focal plane beam patterns.

II. Receiver Overview

In order to fit into the limited space available at the KOSMA 3m telescope the instrument has to be very compact. A general overview of the receiver layout is shown in Fig. 1. The telescope focal plane is re-imaged by a Gaussian telescope into the cryostat, with a pupil at the location of the cryostat window in order to minimize the window size. The warm optics consist of two mirrors (one focusing and one plane mirror) mounted at the telescope's Nasmyth port.

Inside the cryostat the telescope signal is split into two orthogonal polarizations by crossed wire grids, followed by

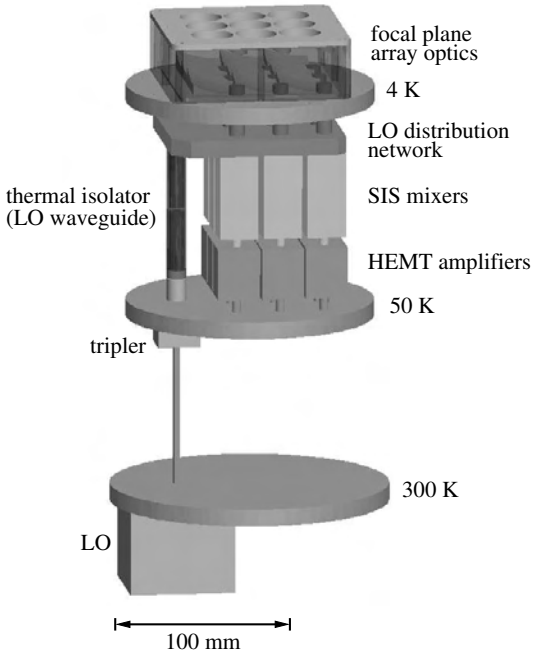

Fig. 2. General layout of the receiver modules. Not shown are the IF/DC cables and the cartridge support structure.

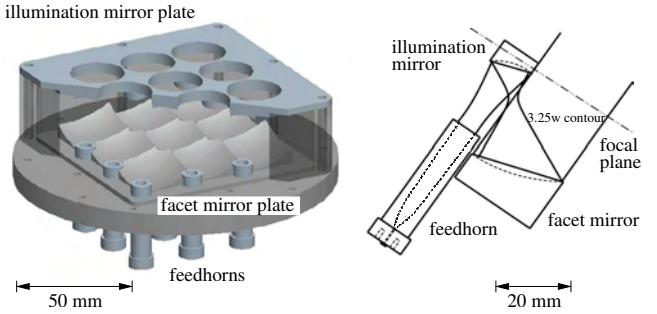

Fig. 3. 3×3 beam focal plane array optics (left) and optics unit-cell with the 3.25 w beam contour (right). Aside from the feedhorns the focal plane array optics consists of only three major parts: two plates with all the facet and illumination mirrors, respectively, and a spacer frame.

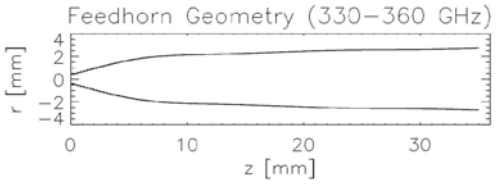

Fig. 4. Optimized feedhorn profile for the 330–360 GHz band.

the second focusing mirror of the Gaussian telescope and a further plane mirror. Finally, the beams are coupled through two focal plane array optics into the individual feedhorns. This folded optics design allows a very compact optical layout.

Image de-rotation will be accomplished by a rotating cryostat (e.g. [6]), thus eliminating the need for an external image rotator. However, this leads to a varying relative alignment of the focusing off-axis mirrors of the Gaussian telescope. Therefore the two focusing mirrors will have to be optimized in order to minimize the resulting aberrations [2].

The cryostat houses two self-contained 3×3 beam cartridge-type receiver modules. The cartridge concept with automatic thermal link was introduced for the ALMA receivers [5], [7] and is also highly advantageous for array receivers. Assembly and maintenance are facilitated considerably, and the receiver modules are easily replaced in order to adapt to seasonal observation conditions.

Each module (Fig. 2) consists of the focal plane optics, feedhorns, sideband-separating SIS-mixers, HEMT-amplifiers and local oscillator. The local oscillator will be a synthesizer/multiplier chain at ambient temperature, with the final tripler at cryogenic temperature (50 K). Thermal isolation of the LO-waveguide between the 50 and 4 K stage will be accomplished either by a microwave bandgap joint [8] or two face-to-face feedhorns. The LO distribution network to the nine mixers will be realized entirely in waveguide technology, which allows a compact optical design as no quasioptical diplexer is required.

III. Focal Plane Array Optics

The focal plane optics match the beams of the feedhorns to those provided by the telescope. They should have low loss and be compact in order to match the space requirements of a cartridge-type receiver module. In order to avoid the absorption and reflection losses of dielectric lenses, it is desirable to use fully reflective optics. However, fully reflective array receivers so far offered a maximum of four rows of beams per optics module, as they used feedhorns located beside their individual off-axis mirrors (e.g. [1], [9]). In our setup, however, the beams are arranged on a rectangular grid, with the feedhorns and small illumination mirrors located in the gaps between the individual beams (Fig. 3 left). Thus, for the first time with fully reflective optics, the array is scalable to an arbitrary number of beams.

The optics unit-cell (Fig. 3 right) consists of the feedhorn (w_0=1.8 mm) and the elliptical illumination and facet mirrors (f=7.4 and 21.2 mm, respectively). The reflection angles are 35 deg. As the illumination mirror is located at only ∼one third of the far-field distance $2D^2/\lambda$ from the feedhorn, the latter, a smooth-walled spline-profile feedhorn, is optimized to produce a Gaussian beam on the illumination mirror, 22 mm in front of its aperture. The optimization method [10] varies the spline-profile, computes the resulting beam pattern via a mode-matching algorithm and compares it to the pattern to be met. Thus, feedhorns can be customized for a wide range of applications. Additionally, the smooth-walled feedhorns can be manufactured considerably easier than corrugated ones, which is an important cost-saving factor for array receivers that use large numbers of feedhorns. The optimized feedhorn profile for the 330-360 GHz band is shown in Figure 4.

As a compromise between a short mapping time and high complexity we have chosen a 3×3 beam arrangement. Additionally, this provides a center pixel to facilitate pointing, and the rectangular beam arrangement allows efficient on-the-fly

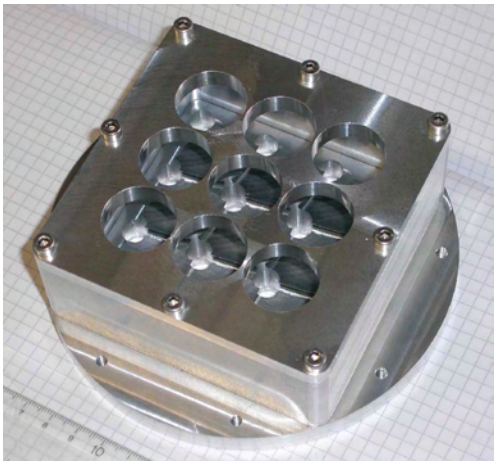

Fig. 5. 345 GHz focal plane array optics prototype.

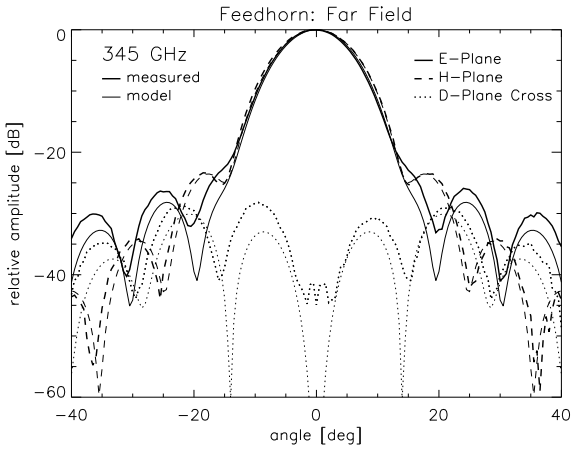

Fig. 6. E- and H-plane co-polar, and D-plane (45°) cross-polar radiation pattern of the feedhorn at 345 GHz. Bold curves: measurements, thin curves: simulation.

mapping (equidistant sampling when the array is inclined by 18.4 deg with respect to the scanning direction, [2]).

In order to minimize the need for optical alignment, large optical sub-assemblies are machined monolithically, using CNC milling techniques. Aside from the feedhorns, the focal plane optics consist therefore of only three major parts: two plates with all the facet and illumination mirrors, respectively, and a spacer frame.

The focal plane array optics were designed using a 3D-CAD software (*Pro/Engineer Wildfire*) and simulated with a physical optics beam propagation software [11]. In order to check the design, a first 345 GHz prototype has been built (Fig. 5) and its focal plane beam patterns have been measured.

IV. Measurements

Both the feedhorn and focal plane patterns were measured in amplitude and phase with a scanning vector network analyzer from *AB-Millimetre*. The signal-to-noise ratio was 50–60 dB. We obtained 1D scans at 330, 345 and 360 GHz, as well as 2D scans at 345 GHz. All scans were repeated with the probes moved $\lambda/4$ away from the device under test, in order to correct for standing waves.

From the measured amplitude and phase the parameters of the best fitting Gaussian beam were obtained by maximizing the coupling integral of the measured beam pattern to a fundamental mode Gaussian. We thus obtained the waist radius w_0 and location z, as well as lateral and pointing offsets of the measured beams.

A. Feedhorn

Angular cuts of the feedhorn radiation pattern (far field) were obtained by rotating the feedhorn around its calculated phase center. The 345 GHz radiation pattern is shown in Figure 6: In H-plane, the agreement between the measurement (bold curves) and the simulation (thin curves) is excellent. In E-plane, we measure a slightly increased side-lobe level. Cross polarization (D-plane) is also slightly higher than simulated. A similar behavior is also observed at 330 and 360 GHz, with the best agreement between measurements and simulations at 330 GHz. The far-field cuts clearly show that the feedhorn works as specified down to -20 dB over the whole bandwidth of 330-360 GHz, and is well suited for use in our focal plane array optics.

At 345 GHz, we also measured the near field radiation pattern in the plane of the illumination mirror, 22 mm in front of the feedhorn aperture. These measurements were obtained with a rectangular waveguide-probe (0.4 mm$\times$0.8 mm) on a planar xy-scanner. Again, measurements and simulation agree well, and we find w_0=1.8 mm. The waist is located 2.8 mm *outside* the aperture plane (simulation: 2.6 mm), which opens the possibility to use two of these feedhorns also as a thermal isolator for the LO-waveguide. As the waist is located outside the feedhorn, two of them can be joined face-to-face with a 5.6 mm gap in between. The alignment requirements of two coupling Gaussian beams are much less stringent than those of a microwave bandgap joint [8]. However, we still have to evaluate the effect of the slightly changing waist location with frequency, as well as possible resonances of higher order modes [12].

B. Focal Plane Array Optics

The E-plane of the feedhorn is inclined by 45 deg with respect to the unit-cell's symmetry plane (y-plane in Fig. 7 left). This orientation is best suited for the subsequent mounting of the mixer blocks and the LO-distribution network.

We obtained 1D scans at 330, 345 and 360 GHz of the center beam (1), as well as 2D scans of the center and a corner beam (2) at 345 GHz. All these measurements were made in the near field with a planar scanner 100 mm in front of the array focal plane.

The 2D patterns of both measured beams agree well down to the -40 dB level. The power pattern of the center beam is shown in Figure 7. It corresponds well to a Gaussian down to the -20 dB level, below which is a slight asymmetry in

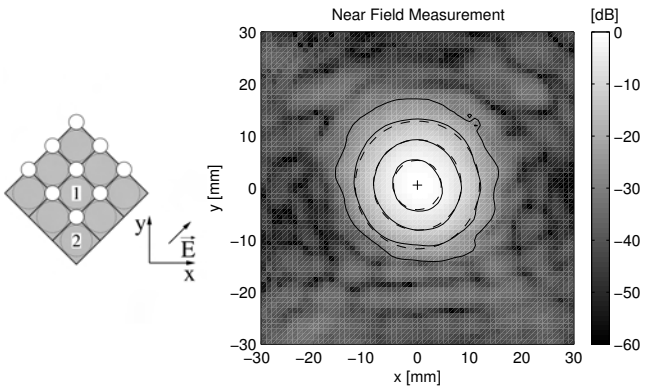

Fig. 7. Coordinate system for the focal plane array measurements (left) and center beam power pattern measured 100 mm in front of the array focal plane. The contour levels are -3, -10, -20 and -30 dB. Also shown is the center (+) and the contours (dashed lines) of the best fitting Gaussian beam.

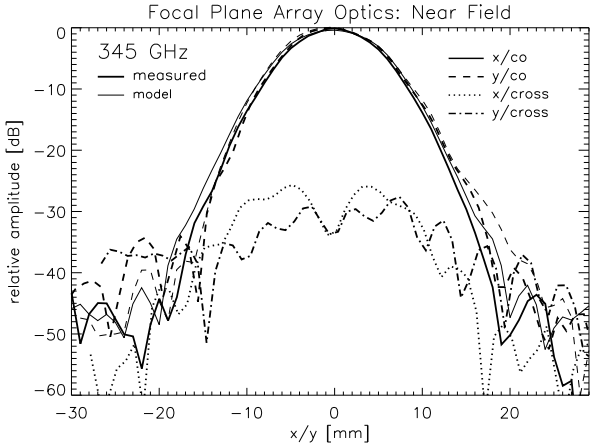

Fig. 8. Linear cuts along the x- and y-plane of the 345 GHz power pattern. Bold curves: measurements, thin curves: simulation (only shown for co-polarization).

y-direction (i.e. the asymmetric direction of the optics unit-cell). The X-shaped structure at the -40 dB level is due to the basically square shape of the facet mirrors, truncating the beam at $\geq$3.25 w. From the best fit to a Gaussian beam (dashed) we obtain w_0=7.0 mm with an asymmetry between the x- and y-direction of $\sim$3.6% and a Gaussicity $\geq$98%. The focal plane beam separation is thus $\sim$3.6 w_0, which translates into $\sim$2.3 HPBW on the sky. The linear scans at the other frequencies yield beam waists of 7.4 and 6.7 mm at 330 and 360 GHz, respectively. Thus, the beam waist scales well with the wavelength.

Linear cuts of the center beam at 345 GHz are shown in Figure 8. Cross-polarization is well below -25 dB. Also indicated is the simulated co-polar power pattern, which is slightly broader than measured. Indeed, the measured beam waist of 7.0 mm is slightly less than simulated ($\sim$7.2 mm). This difference does not affect the functionality of the focal plane array optics. However, simulations indicate that it might be due to an alignment error between the illumination and facet mirror plates. If this can be confirmed by mechanical sampling of the mirror surfaces, it will be easily corrected by a modified spacer frame. The array should then reach its nominal performance with a beam separation of 3.4 w_0 in the focal plane, corresponding to $\sim$2.2 HPBW on the sky.

V. Conclusions

We are developing a new submillimeter array receiver for the KOSMA telescope, based on cartridge-type receiver modules. The receiver modules employ new fully reflective focal plane array optics, thus avoiding the absorption and reflection losses of dielectric lenses. They are scalable both in frequency and – for the first time with a fully reflective array – to an arbitrary number of beams. A 345 GHz 3×3 beam optics prototype was built and successfully tested. The measured focal plane beams exhibit a Gaussicity of $\geq$98% and best fit a Gaussian beam with a waist radius w_0 of 7.0 mm at 345 GHz. This corresponds to a focal plane beam separation of 2.6 w_0, or 2.3 HPBW on the sky.

Acknowledgments

This research is supported by Swiss National Science Foundation under grants PBBE2-106793 and 200020-100167, Deutsche Forschungsgemeinschaft under grant SFB 494, and by the ministry of science of the state Nordrhein-Westfalen.

References

[1] U. U. Graf, S. Heyminck, E. A. Michael, S. Stanko, C. E. Honingh, K. Jacobs, R. Schieder, and J. Stutzki, "SMART: The KOSMA Sub-Millimeter Array Receiver for Two frequencies," in *Thirteenth International Symposium on Space Terahertz Technology*, vol. 4855. Harvard University, Mar. 2002, pp. 143–152.

[2] K.-F. Schuster, C. Boucher, W. Brunswig et al., "A 230 GHz heterodyne receiver array for the IRAM 30 m telescope," *A&A*, vol. 423, pp. 1171–1177, Sept. 2004.

[3] C. Walker, C. Groppi, D. Golish et al., "PoleStar: An 810 GHz Array Receiver for AST/RO," in *Proceedings of the 12th International Symposium on Space Terahertz Technology*, 2001, pp. 540–552.

[4] C. Kramer, C. G. Degiacomi, U. U. Graf, R. E. Hills, M. Miller, R. Schieder, N. Schneider, J. Stutzki, and G. Winnewisser, "The new KOSMA 3m telescope," in *Proc. SPIE*, vol. 3357, 1998, pp. 711–720.

[5] W. Wild, J. Payne, J. W. Lamb et al., ALMA Project Book, Chapter 5, Tech. Rep., 2002.

[6] R. Güsten, G. Ediss, F. Gueth et al., "CHAMP – The Carbon Heterodyne Array of the MPIfR," in *Proc. SPIE*, vol. 3357, Mar. 1998, pp. 167–177.

[7] A. Orlowska, M. Harman, and B. Ellison, ALMA Project Book, Chapter 6, Tech. Rep., 2001.

[8] J. L. Hesler and N. Horner, "A Broadband Waveguide Thermal Isolator," *ALMA memo 469*, Tech. Rep., 2003.

[9] D. Rabanus, U. Graf, M. Philipp, J. Stutzki, and A. Wagner, "Cryogenic Design of KOSMA's SOFIA Terahertz Array Receiver (STAR)," *SPIE: Airborne Telescope Systems*, vol. 5498, pp. 473–480, 2004.

[10] C. Granet, G. L. James, R. Bolton, and G. Moorey, "A Smooth-Walled Spline-Profile Horn as an Alternative to the Corrugated Horn for Wide Band Millimeter-Wave Applications," *IEEE Transactions on Antennas and Propagation*, vol. 52, pp. 848–854, Mar. 2004.

[11] S. Heyminck, "Entwicklung und Test von optimierten Phasengittern für Submillimeter Mehrkanal-Empfänger," Master's thesis, I. Physikalisches Institut, Universität zu Köln, 1999.

[12] W. Jellema, S. Withington, N. Trappe, J. A. Murphy, and W. Wild, "Theoretical and Experimental Study of High-Q Resonant Modes in TeraHertz Optical Systems," in *Joint 29th International Conference on Infrared and Millimeter Waves and 12th International Conference on Terahertz Electronics*, 2004, pp. 805–806.

Linearity Measurements of the 640 GHz SIS Mixer for JEM/SMILES

A. Murk*, K. Kikuchi†, and J. Inatani†
*Institute of Applied Physics, Universität Bern, Sidlerstrasse 5, 3012 Bern, Switzerland
Email: axel.murk@mw.iap.unibe.ch
†Japan Aerospace Exploration Agency, Tsukuba, Ibaraki, Japan

***Abstract*— The nonlinearity of SIS mixers is a critical issue for several new instruments which aim for high accuracy. One of them is the submillimeter wave limb emission sounder JEM/SMILES which will observe the spectral transition lines of various stratospheric trace gases. In this paper we present a perturbation technique which was used to determine the nonlinearity of its 640 SIS mixer. The measurements showed that the incremental gain compression of the mixer is about 0.7% when looking at 300 K black-body radiation.**

I. Introduction

The nonlinearity of SIS mixers is a critical issue for several upcoming missions which aim for high accuracy. The calibration plan for the HIFI instrument of the Herschel Space Observatory [1] mentions that up to 6% gain compression could be expected from a 300 K thermal source, depending on the bandwidth of the mixer. For a 230 GHz SIS mixer of the ALMA project a nonlinearity of 1% has been determined [2].

The JEM/SMILES instrument [3] is a submillimeter wave limb sounder for atmospheric research on board of the International Space Station. It will measure the spectral emission lines of the stratospheric trace gases O_3, HCl, ClO, BrO and others in two frequency bands around 625 and 650 GHz. Besides an unprecedented sensitivity for the weak emission lines SMILES also has the goal to reach an absolute measurement accuracy of 1%. A nonlinearity of its SIS mixers would lead to a systematic calibration error of the radiometric measurements. In this paper we propose a perturbation method which can be used to measure the nonlinearity of SIS mixers or other receiver components. We have used this method to test the engineering model of the JEM/SMILES mixer.

The SIS mixer of our experiments was fabricated in Nb/Al-AlOx/Nb technology. It has a parallel connecte twin-junctions (PCTJ) design [4] optimized for 640 GHz. Typical values of the SIS junctions are an area of about 1.2×1.2 mm^2, a current density of 7.5 kA/cm^2 and a normal resistance of 20 Ω. The mixer has a double-sideband noise temperature of typically 200 K over an IF bandwidth of 11–13 GHz.

II. Experimental Setup

The authors A. R. Kerr et al. have described theory [5] and measurements [2] of SIS mixer saturation. For their experiments with a 230 GHz SIS mixer they injected a small CW signal via a waveguide coupler and observed the suppression of its IF amplitude when the thermal noise input to the mixer was chopped between a hot and a cold black-body radiation source. They found an incremental gain compression of 1% by the ambient temperature load. They also identified additional systematic measurement artifacts of 0.5% from the nonlinearity in their IF chain and of 0.5% caused by standing waves between the mixer and the surface of the liquid nitrogen of the cold load.

We tried similar measurements with the JEM/SMILES mixer. This mixer, however, is not equipped with a waveguide coupler because of the much higher frequency of 640 GHz, and the CW test signal had to be injected quasi-optically via a dielectric beam splitter. The SIS mixer and the low-noise IF amplifiers were cooled in our test cryostat by a closed cycle Gifford-McMahon refrigerator which caused significant mechanical vibrations and IF power fluctuations with a 1 Hz periodicity. The stability of this setup was not good enough to detect nonlinearities at the 0.5% level. For that reason we used an alternative ”perturbation method” to determine the gain compression.

In our test setup the field of view of the mixer is terminated through a quasi-optical network either on a cold or a hot black-body radiator. These targets consist of THz absorbers immersed in liquid Nitrogen or at 300 K ambient temperature and they define the thermal noise backgrounds T_C and T_H, respectively. A dielectric beam splitter with a small coupling ration is used to inject a significantly smaller modulated noise

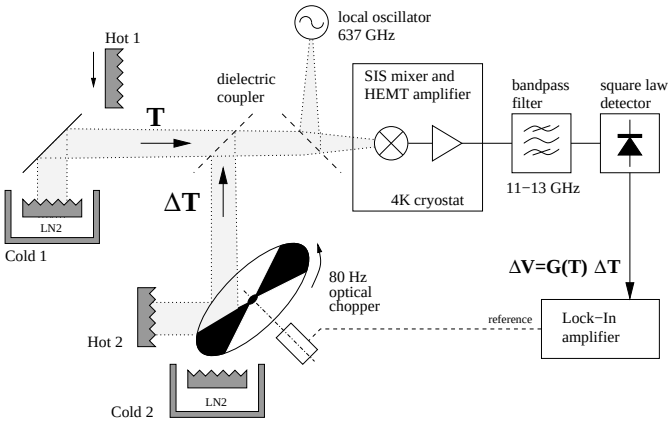

Fig. 1. Schematic measurement setup for the linearity tests.

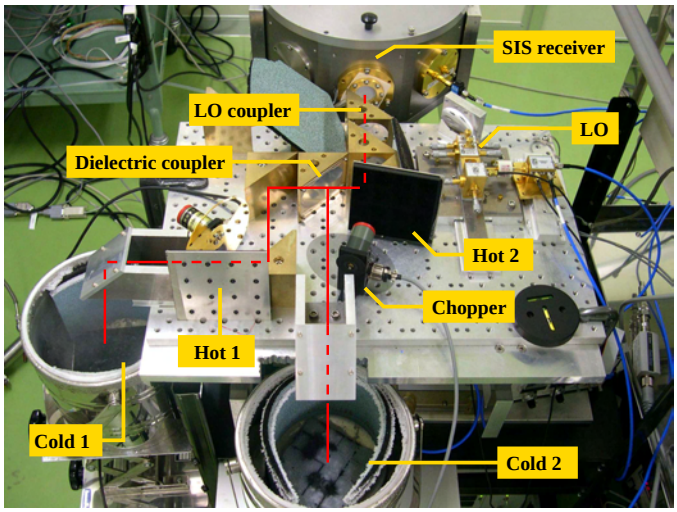

Fig. 2. Optical layout with two hot and two cold loads, optical chopper and dielectric couplers. Additional focusing mirrors are not shown in the schematic in Fig. 1.

offset ΔT which is generated with an optical chopper and an additional pair of hot and cold black-bodies. A second beam splitter is used to inject the signal of the phase-locked 637 GHz local oscillator. The IF signal is amplified by two cryogenic HEMT amplifiers, which are also included in our linearity tests. A 2 GHz wide bandpass filter centered at 12 GHz selects the same IF band that will be used for SMILES. The total power of the IF signal is measured with a fast square-law diode detector which results in an output voltage $V\,(T + \Delta T)$. The amplitude of the modulated signal ΔV is monitored with a Lock-In amplifier which is phase synchronized with the optical chopper. The schematic overview of the test setup and its quasi-optical layout are given in figures 1 and 2, respectively.

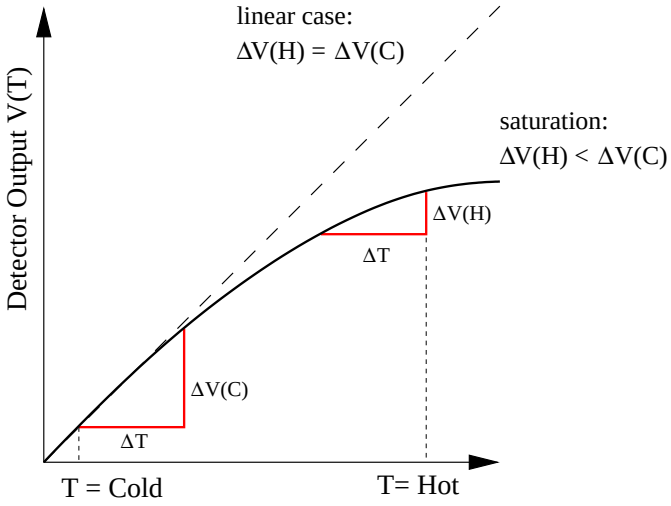

Fig. 3. Measurement principle of the linearity tests. A modulated noise offset ΔT is added to different thermal backgrounds T. The resulting modulated output voltage ΔV of the IF detector remains constant for a linear system, but gets slightly suppressed with increasing T in the case of nonlinearities.

Figure 3 shows the principal idea behind this perturbation method. For a linear system, ΔV is independent from the noise background T, and the Lock-In response will remain constant when T is switched from the cold to the hot load. Any saturation effects of the receiver or the detector, however, will decrease ΔV at the hot background: $\Delta V(T_{\mathrm{H}}) < \Delta V(T_{\mathrm{C}})$. Similar to the measurements with CW test signal this determines the incremental, and not the large signal gain compression of the system for a certain input level. As long as the nonlinearities are small, the latter will be approximately half of the incremental compression [2].

The advantages of our method are that the values of T and ΔT must not be known precisely, and that no waveguide coupler and no additional CW submillimeter wave source are required. It is also less sensitive to standing waves which can cause problems with a CW tests signal. The main drawback, however, is that the sensitivity of our measurements is limited by the gain fluctuations of the system. In our case, with the optical chopper running at about 80/ Hz, the integration time of the Lock-In amplifier had to be in the order of 3s to achieve a sufficient signal-to-noise ratio. As a result the minimum switching period for the background T was about 30 s, and the gain of the complete setup needs to be stable over these timescales. Otherwise any gain fluctuation leads to a similar relative change of ΔV. It turned out that the stability of our test setup was always worse than 0.1%, mostly because of the 1 Hz cycle of the mechanical refrigerator, the frequency stability of the chopper and variations of the room temperature. Figure 4 gives an example for these fluctuations. It shows the normalized Lock-In output voltage of a measurement were T remained on the hot load for 120 s.

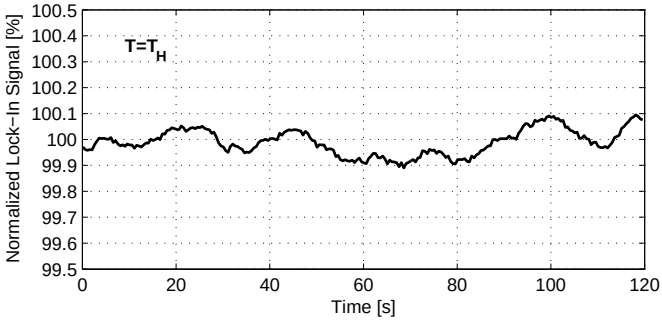

Fig. 4. Example of the instability of the normalized Lock-In output voltage. For this measurement, the noise background remained fixed on the hot load T_H and the time constant of the Lock-In amplifier was set to 3 s.

III. Measurement Results

Figure 5 shows three independent measurements during which the hot load was replaced manually by the cold load for about 30 s. For each of the measurement series the Lock-In output was normalized with the values where T was on the cold load. With the thermal background of the hot load the signal is suppressed by about 0.5%. The true incremental gain compression is slightly larger because of the finite coupling

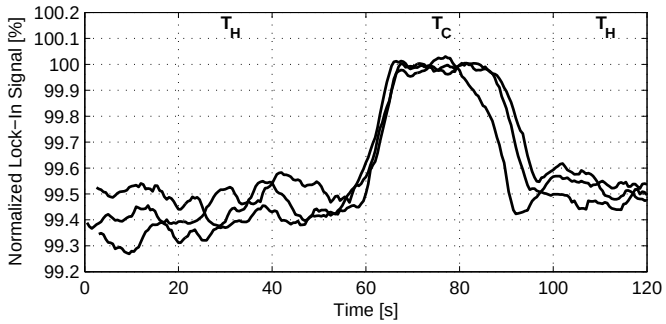

Fig. 5. Linearity measurements where the noise background was switched from the hot load T_H to the cold load T_C for a period of about 30 s and then back. The Lock-In signal has been normalized with the T_C values. The $\sim$0.5% suppression during the T_H observation results from the SIS receiver saturation by the 300 K background.

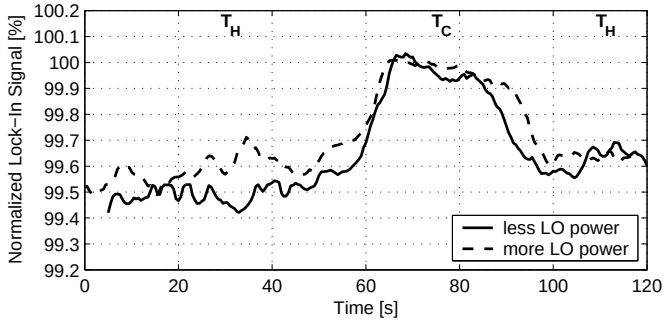

Fig. 6. Linearity measurements where the LO power had been increased or decreased from its optimum level. In this case saturation is slightly lower than in Fig. 5.

ratio of the beam splitter, and also because a small nonlinearity will be already present at the cold load. When the 20% coupling ratio of the beam splitter is taken into account we can estimate that the nonlinearity caused by the 300 K background is about 0.7%.

To study how the nonlinearities are affected by the bias conditions of the SIS mixer the measurements were repeated with different settings of the local oscillator power. For the nominal operation conditions, which maximize the IF power and the noise performance, the LO power is adjusted until the SIS bias current is 45 μA at a constant bias voltage of 1.9 mV. Figure 6 shows measurements with two different LO power levels which led to a $\pm$15 μA increase or decrease of the bias current. In both cases the observed nonlinearity is slightly lower than for the optimum bias conditions.

Care has to be taken that the measurements are not affected by nonlinearities of the IF chain or of the detector. This was done by adding enough fixed attenuators to keep them well below their saturation level. We have confirmed with a similar measurement technique that the effect of the detector nonlinearity is less than 0.1%. For these tests the small modulated offset was injected in the IF chain and the noise background was varied over a wide range using a step attenuator. Figures 7 and 8 show this test setup and the measurement results of two different detectors, respectively.

Another possible measurement artifact are reflections at the calibration loads. Both loads were made of TK-RAM absorbers [6] which have a reflectivity in the order of -50 dB, but from the cold loads reflections of up to -21 dB can be expected from the surface of the liquid nitrogen. In [2], the standing waves between the SIS receiver and the liquid nitrogen caused a periodic modulation of about 0.5% depending on the changing nitrogen level in the load. In our case ΔT consists of broadband noise, and similar standing waves from the coherent reflections will lead to a periodic baseline ripple with a period of less than 150 MHz, corresponding to the distance between the SIS receiver and the liquid nitrogen surface. Averaged over the whole 2 GHz bandwidth of our measurement, this will only have a marginal effect on the linearity tests.

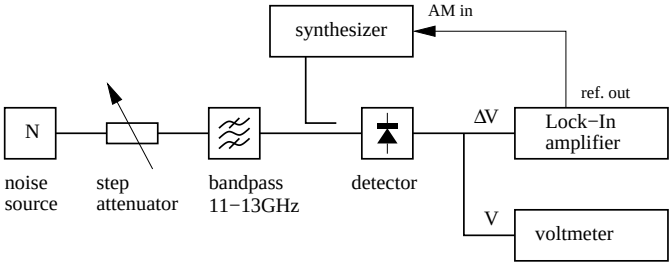

Fig. 7. Measurement setup to determine the detector nonlinearity.

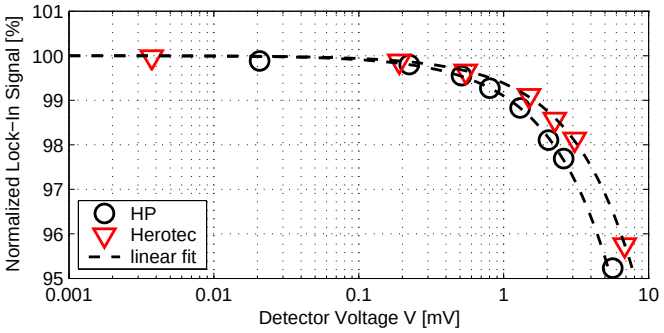

Fig. 8. Test results for the nonlinearity of two different diode detectors. The SIS linearity tests were done at a detector voltage below $V(T_H) < 0.2$ mV where its linearity is better than 0.1%.

IV. Discussion

The theoretical investigation of SIS mixer saturation described in [5] allows to estimate the incremental gain compression as a function of $S_{\rm in}^2 = (e/Nhf)^2\, G_0\, P_{\rm sig} R_{\rm L}$, where N is the number of junctions in series, f the local oscillator frequency, G_0 the small signal gain of the mixer, $P_{\rm sig}$ the signal input noise power, and $R_{\rm L}$ the IF load impedance seen by the SIS mixer.

The input noise power from the hot load is expressed as $P_{\rm sig} = kT_{\rm H}B$, where B is the input noise bandwidth. Since the SIS mixer was designed to have the relative bandwidth of 12.5%, we may estimate $B = 80$ GHz. This is almost consistent with a measurement result from Fourier transform spectroscopy [7]. Based on the other measurements, we also estimate an SIS mixer gain of -7 dB on average over the band. Finally the IF load impedance is assumed to be 50 Ω over the extended frequency range 0 Hz to B. Thus we obtain $S_{\rm in}^2 = 4.4 \cdot 10^{-4}$ for our SIS mixer. According to the model in [2] this corresponds to an incremental gain compression of 1.8%. This is more than twice as much as the results of our measurements, but it is most likely that this discrepancy can be explained by the uncertainty of our rough estimates. Especially the assumption of a constant load impedance over the full bandwidth seems to be rather unrealistic. The small improvement of the linearity after the increase or decrease of LO power can be explained by the reduced mixer gain at these settings.

V. Conclusions

We determine the incremental gain compression of a 640 GHz SIS mixer with a perturbation technique in which a small modulated noise signal is added quasi-optically to different noise backgrounds. First measurements of an engineering model of the SIS mixer for the JEM/SMILES mission showed that the nonlinearity which is caused by a 300 K thermal background is in the order of 0.7%. The actual flight hardware can have a different characteristic because it contains an improved IF matching circuit [8] and different HEMT amplifiers. For that reason similar linearity tests are planned for the final JEM/SMILES receiver subsystem.

Our current measurements have an uncertainty in the order of $\pm$0.1% because of the limited stability. One reason for this are the strong 1 Hz fluctuations caused by the cooler of the test facility. The real JEM/SMILES receiver has a better space qualified 4 K cooler which operates with a faster compressor cycle ($>$15 Hz) and which has been designed to minimize mechanical vibrations [9]. For that reason it can be expected that the linearity tests of the complete SMILES receiver can be done with a higher precision. Laboratory tests in a liquid Helium bath cryostat should be even more stable. Further improvements could be achieved by temperature stabilization of the diode detector.

The best way to overcome the stability problems is to use an automated switching mirror for changing the noise background T between hot and cold. This would allow to decrease the time constant of the Lock-In amplifier and to average the ratio of many cold/hot measurements. In our current setup this was not possible because the loads were replaced manually, but for the tests of the complete system a computer controlled switching mirror will be used.

The JEM/SMILES mission plan requires that the linearity of the SIS receiver is better than 1%. Our measurements have confirmed that the current mixer design fulfills this requirement. The linearity of the complete receiver in space will be even better than our results because of the sideband filter which is included in its optics. It will always terminate the image band on the cold sky, whereas the noise background was present in both sidebands during our laboratory tests.

References

[1] D. Teyssier and M. Pérault, "HIFI calibration plan," Tech. Rep. LRM-ENS/HIFI/PL/2000-001, Issue 1, SRON, Groningen, NL, Oct. 2003.

[2] A. R. Kerr, J. Effland, S. Pan, G. Lauria, A. W. Lichtenberger, and R. Groves, "Measurement of gain compression in SIS mixer receivers," in *Proc. 14th International Symposium on Space Terahertz Technology*, (Tucson, AZ), Apr. 2003.

[3] SMILES Science Team, "JEM/SMILES Mission Plan, version 2.1," tech. rep., Japan Aerospace Exploration Agency, Tsukuba, JP, Nov. 2002. available at http://smiles.tksc.jaxa.jp.

[4] T. Noguchi, S. C. Shi, and J. Inatani, "An SIS mixer using two junctions connected in parallel," *IEEE Trans. Appl. Supcond.*, vol. 5, p. 2228, June 1995.

[5] A. R. Kerr, "Saturation by noise and CW signals in SIS mixers," in *Proc. 13th International Symposium on Space Terahertz Technology*, (Cambridge, MA), Mar. 2002.

[6] Thomas Keating Instruments Ltd., "Space qualified tessalating THz RAM." http://www.terahertz.co.uk/.

[7] K. Kikuchi, Y. Fujii, and J. Inatani, "Simple FTS measurement system for submillimeter SIS mixer," *International Journal of Infrared and Millimeter Waves*, vol. 23, pp. 1019–1028, 2002.

[8] K. Kikuchi, S. Arimura, J. I. Y. Fujii, T. Suzuki, A. Iwamoto, and A. Yamamoto, "Impedance matching of 640 GHz SIS mixer in a high IF band of 11-13 GHz," in *Proc. 16th International Symposium on Space Terahertz Technology*, (Göteborg, SE), May 2005.

[9] K. Narasaki, S. Tsunematsu, S. Yajima, A. Okabayashi, J. Inatani, K. Kikuchi, R. Satoh, T. Manabe, and M. Seta, "Development of cryogenic sustem for JEM/SMILES," in *Proc. The Cryogenic Engineering Conference and the International Cryogenic Materials Conference*, (Anchorage, AK), Sept. 2003.

A SIS Mixer for ALMA Band 10: Development Concept

Sergey V. Shitov, Takashi Noguchi, Teruhiko Matsunaga, Tomonori Tamura, Andrey V. Uvarov, Ilya A. Cohn, and Tetsuo Hasegawa

***Abstract*—Conceptual design of waveguide and quasioptical mixers for ALMA Band-10 is presented along with SIS chip performance estimates. A combination of NbTiN/Al tuning circuit with the Nb-based high current density SIS junctions employing AlN tunnel barrier ($A = 0.5\ \mu m^2$, $J_c = 15 - 20\ kA/cm^2$) is suggested as the base-line. The following parameters are expected for a 20-Ω SIS mixer: $G_m = -7.5 \ldots -9$ dB, $T_m < 200$ K (DSB), $P_{LO} < 1\ \mu W$ at 950 GHz. Tunerless full-height waveguide (280 μm × 140 μm) mixer will employ a single-side chip probe-antenna configuration. A chip-package concept is under development for quick mounting (replacement) of serial mixers. Quasioptical mixers will be used for material research and as an option for a weak LO source. A quasioptical balanced mixer can reduce LO power requirement down to only 3-5 μW for the whole two-polarized cartridge along with essential simplification of its optical scheme. The IF range of 4-12 GHz is simulated successfully for the quasioptical mixers.**

***Index Terms*—Balanced mixer, quasioptical mixer, SIS mixer, slot antenna, SNAP process.**

I. Introduction

THE Band-10 (787 – 950 GHz) is currently the highest frequency range of Atacama Large Millimeter and Submillimeter Array (ALMA) [1], which employs the quantum-noise-limited SIS mixers [2]. The difficult point in designing the front-end mixer is that whole frequency range spreads far above the gap-frequency of Nb (≈ 700 GHz), so this material cannot be used for tuning circuit of a SIS junction; the use of normal metals or higher gap-frequency superconductors has to be considered [3]. To achieve the ALMA Band-10 specification for the receiver noise temperature in the double-side-band regime (DSB), $T_{RX} \leq 230$ for 80 % of the band and $T_{RX} \leq 345$ K for any point of the band [4], both the SIS junction technology and the materials for the tuning circuit must be selected very carefully.

There are not many choices for a beam launcher. The corrugated horn antenna is known for its high-quality beam properties. In spite of severe mechanical tolerances, which are about 10 μm, the feasibility of corrugated horn antennas is proven within 800-1000 GHz frequency range by a number of experiments (e.g. HIFI and ASTE projects) [5], [6]. The waveguide approach applies severe mechanical requirements also to the mixing chip: typical dimensions of the chip will be about $500 \times 50 \times 30\ \mu m^3$. This makes chips difficult to process/handle and may slow down the research phase of the project.

Another approach is the well-known integrated lens-antenna [7], [8]. Although the beam quality of known lens-antennas is not as good as for horn launchers, this direction is growing rapidly mainly due to much simpler mixer mechanics, shorter fabrication run and easier chip handling, while the receiver noise can be as low as for waveguide mixers. The analysis of an ideal corrugated feed estimated total sidelobes of the ALMA system antenna at ≈ 20 dB [9] that is just few dB lower than the sidelobes of a practicable elliptical silicon lens-antenna SIS mixer [8]. It means that the final (system) difference between the horn-antenna (waveguide) and the lens-antenna SIS mixers can be a marginal issue.

The output port capacitance of a SIS chip can be essential, so advanced electromagnetic design is needed for efficient coupling of the signal within intermediate frequency (IF) band of 4-12 GHz. A narrower IF band of 4-8 GHz is allowed in the case of single-side-band (SSB) operation. The tunerless method of the side-band separation is developed and tested for waveguides at millimeter wavelengths using two identical mixers and RF/IF 3-dB hybrid couplers [10]. However, this method seems difficult to implement, since not only very small mechanical tolerance is needed to balance the mixers, but also because of essential signal loss in a rectangular single-mode waveguide at terahertz frequencies.

Another difficult point is the submillimeter local oscillator (LO) compatible with the ALMA cartridge concept. Recent solid-sate tunerless sources based on chain multipliers are hardly able to deliver the LO power higher than 10-20 μW

Manuscript received May 2, 2005. This work was supported in part by the ALMA-J Office, National Astronomical Observatory of Japan.

S. V. Shitov is with the National Astronomical Observatory of Japan, Mitaka, Tokyo 181-8588, Japan, on leave from the Institute of Radio Engineering and Electronics, Russian Academy of Sciences, Moscow 125009, Russia (phone: +81-422-34-3629; fax: +81-422-34-3817; e-mail: sergey@nao.ac.jp).

T. Noguchi, T. Matsunaga, T. Tamura and T. Hasegawa are with the National Astronomical Observatory of Japan, Mitaka, Tokyo 181-8588, Japan (e-mail: Takashi.Noguchi@nao.ac.jp, teru@nro.nao.ac.jp, tomonori.tamura@nao.ac.jp, tetsuo.hasegawa@nao.ac.jp).

Andrey V. Uvarov and Ilya A. Cohn are with the Institute of Radio Engineering and Electronics, Russian Academy of Sciences, Moscow 125009, Russia (e-mail: uvarov@hitech.cplire.ru, cohn@hitech.cplire.ru).

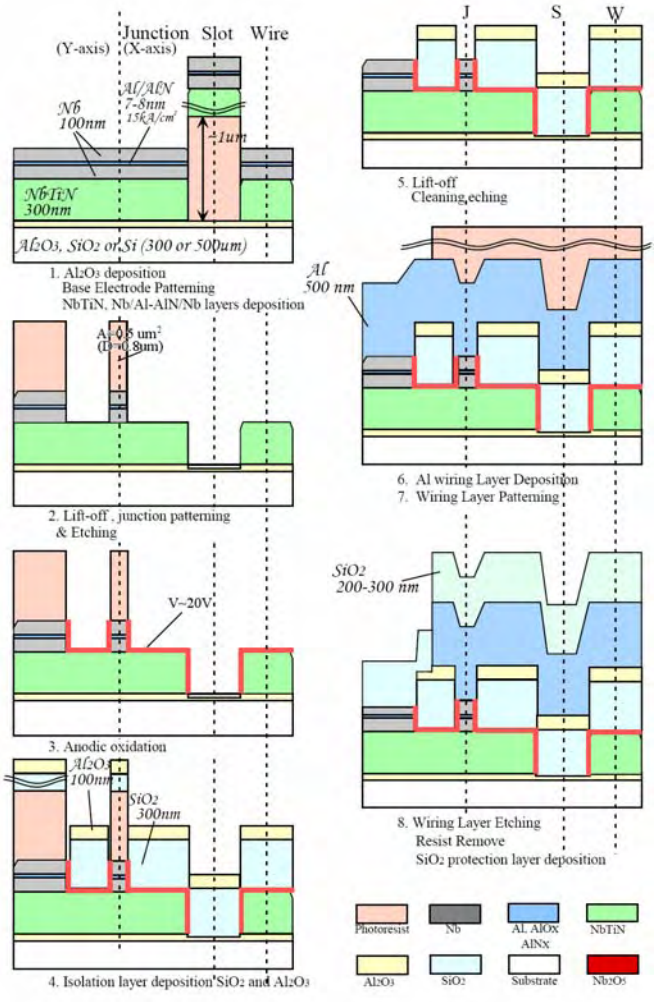

Fig. 1. SIS junction fabrication flow-charts for SNAP technique.

Fig. 2. The g-Line Stepper machine (top) and developed sub-micron photoresist patterns within one-shot exposing area of 3.5 x 3.5 mm^2 (bottom).

within the desired frequency range [11] that is not sufficient even for a state-of-the-art SIS mixer, if input beam-splitter is used. The LO powers of order of 200 μW are still a unique and narrow-band issue [12]. This is why the balanced SIS mixer approaches [13], [14] could be of great interest.

In present paper we discuss the development of the SIS mixer and the front-end optics for ALMA Band-10. Conceptual designs for waveguide and quasioptical mixers are presented along with SIS chip performance estimates.

II. Approaches and Details of Design

A. SIS Junction Fabrication and Mixer Performance

The ALMA 'mass production' has to account for assurance issues for SIS junctions and other components of the RF circuit. To easier achieve the specified (wide) RF frequency range, the Nb-based high current density submicron-size SIS junctions with AlN tunnel barrier [15] (A = 0.5 μm^2 or 0.8 μm diameter, J_c= 15 - 20 kA/cm^2) are being fabricated at NAOJ using SNAP technique (presented in Fig. 1) and the new 4-target RF/DC deposition plant (from Ulvac) along with the projection g-Line Stepper machine (shown in Fig. 2). Since the previous experimental results [16]-[19], the NbTiN/SiO_2/Al microstrip is accepted as the base-line for the tuning circuit. The electromagnetic simulation of the RF circuit demonstrated that the traditional Al_xO_y barrier SIS junctions (A = 0.8 μm^2 or 1 μm diameter, J_c= 10 - 12 kA/cm^2) can also suit the ALMA specifications. The calculations using Tucker's theory (3-port model includes the quantum reactance) [2] predict the following parameters for a 20-Ohm SIS mixer: G_m= -7.5…- 9 dB (3-dB loss of the tuning circuit with RF sheet resistivity of 0.1 Ω/sq included), T_{RX} < 200 K (DSB) (for realistic value T_{IF} < 10 K) and P_{LO} < 1 μW at 950 GHz (no optics loss included). The example of simulation data is presented in Fig. 3.

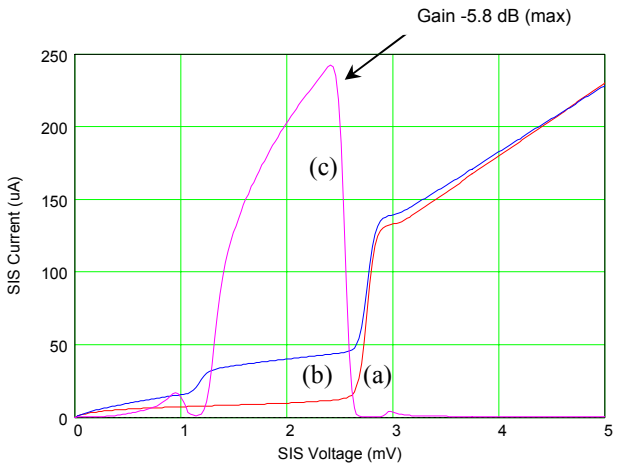

Fig. 3. Simulated IV-curves: un-pumped (a) and pumped (b). The simulated gain of SIS mixer at 950 GHz is presented by (c).

B. *Waveguide Mixer*

The suggested tunerless full-height waveguide (280 μm × 140 μm) mixer will employ a single-side probe-antenna [20] as shown in Fig. 4. The coplanar waveguide at the IF output facilitates the wide IF band: the RF chokes are grounded, so they do not contribute to the output capacitance. A chip-package concept (see Fig. 5) assumes a SIS junction staying within its particular waveguide mount (chip-package) for repeatable tests; there no need to dismount good chip for testing another one. The new chip can use its own package. Many mixers can be pre-certified at RF using the common parts of only one mixer block – the corrugated horn antenna and the fix-tuned backpiece.

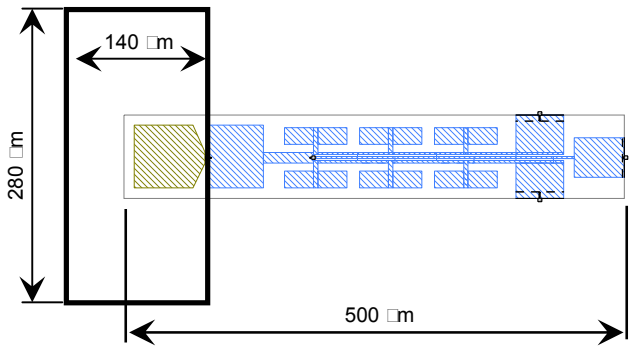

Fig. 4. Probe-antenna chip mounted in full-height waveguide (scheme).

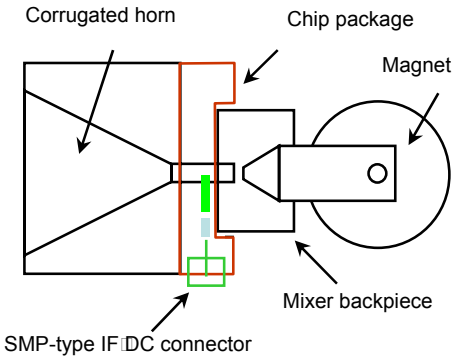

Fig. 5. Chip packaging concept for waveguide mixer.

C. *Quasioptical Mixers*

Since quasioptical chips are easier to process, and they can be handled with much less caution, the lens-antenna mixer can be used as a handy test platform for SIS junctions and tuning circuits (materials). It is worth to note that high-quality epitaxial films from NbN for terahertz-range applications [21] can be grown presumably on the high-dielectric MgO substrate (ε = 9.6), which are difficult to use with waveguides.

We are going to use the quasi-optical mixing structure presented in Fig. 6 to facilitate the waveguide SIS mixer

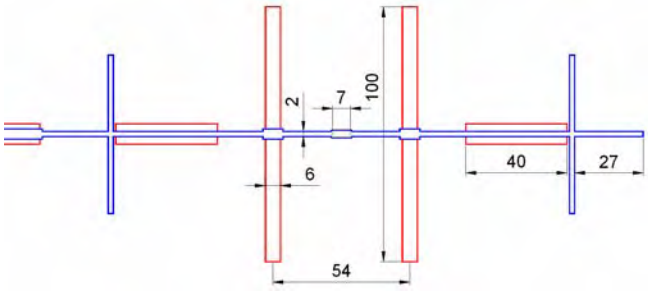

Fig. 6. Layout of quasioptical SIS mixer based on a double-slot antenna.

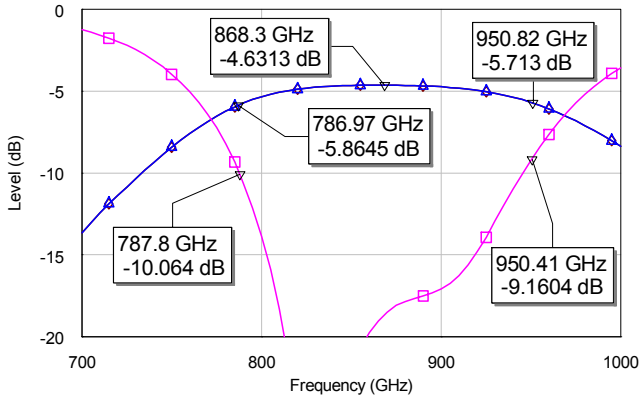

Fig. 7. Signal coupling (top curve) and reflection (bottom curve) for the QO mixer from Fig. 6 (simulation). The coupling level has to be corrected up for 3 dB, since two equal SIS junctions are used.

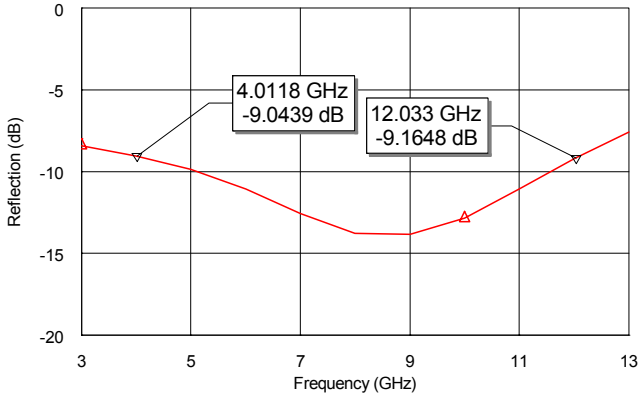

Fig. 8. Output port (IF signal) coupling to a 50-Ω load for the QO mixer from Fig. 6 (simulation).

development. Simulations predict good performance of such mixer as shown in Fig. 7, which employs the twin-junction tuning circuit [22]-[24]. It is important to note that in spite of larger size of the chip (larger circuit), the IF range of 4-12 GHz is simulated successfully for the quasioptical mixers as shown in Fig. 8. However, this smooth figure seems realistic only in the case of the integrated IF amplifier [25].

A quasioptical balanced mixing structure (QBM) from Fig. 9 can be accepted as the main option in the case of weak LO. The new scheme of QBM is using two crossed double-slot antennas [13], which separate orthogonally polarized LO

and signal. The LO power is injected symmetrically to the signal slot-antennas via integrated RF interface providing anti-phased IF signals at two twin-junction SIS mixers. We estimated essential reduction of LO power requirements down to only 2-3 μW for the whole two-polarized cartridge as presented in Table I.

The implementation of the balanced mixer allows for essential simplification of the optical scheme of the cartridge as presented in Fig. 10. It is important that the launching beam angle can be defined via proper design of the elliptical lens, which is the only non-flat optical element between the SIS mixer chip and the sub-reflector of the telescope.

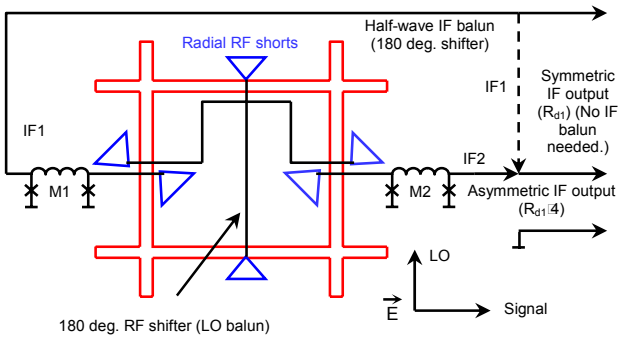

Fig. 9. Conceptual scheme of balanced quasioptical SIS mixer employing the crossed double-slot antenna and two twin-junction detectors. Polarizations for signal and local oscillator are shown at the bottom.

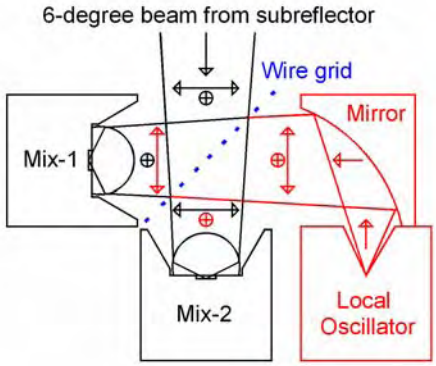

Fig. 10. Optical scheme of double-polarized receiver cartridge employing two balanced SIS mixers (Mix-1 and Mix-2) from Fig. 9 (simplified).

TABLE I
LO REQUIREMENTS FOR CARTRIDGE WITH BALANCED MIXERS

LO frequency (GHz)	RF Power before 3 dB loss (μW)	Coupled RF power (μW)	Mixer gain, Gm/after 3 dB loss (dB)	Optimum LO voltage (α_{RF}) (a.u.)	DSB T_{RX} (K)
780	1.9	0.8	-5 / -8	0.64	-
865	2.3	1.12	-5.2 / -8.2	0.70	-
950	2.8	1.28	-5.8 / -8.8	0.70	198

ACKNOWLEDGMENT

Authors thank Y. Sekimoto, S. Asayama, M. Sugimoto and M. Ishiguro for many fruitful discussions.

REFERENCES

[1] A. Wooten, "Atacama large millimeter array (ALMA)," *Proc. SPIE, Large Ground-Based Telescopes*, vol. 4837, pp. 110–118, Feb. 2003. ALMA memo series [Online]. Available: http://www.alma.nrao.edu/memos

[2] J. R. Tucker and M. J. Feldman, "Quantum detection at millimeter wavelengths," *Rev. Mod. Phys.*, vol. 57, no. 4, pp. 1055–1113, 1985.

[3] G. Delange, J. Kuipers, T. Klapwijk, "Superconducting resonator circuits at frequencies above the gap frequency," *J. Appl. Phys.*, vol. 77, no. 4, pp. 1795–1804, 1995.

[4] *Front-End Sub-System Technical Specifications.* ALMA Internal Report.

[5] *HIFI Band 3 and 4* [Online]. Available: http://www.sron.rug.nl/hifi_b34/

[6] *ALMA memo series* [Online]. Available: http://www.alma.nrao.edu/memos/html-memos/alma458/memo458.pdf

[7] G. Rebeiz, "Millimeter-wave and terahertz integrated-circuit antennas," *Proc. IEEE*, vol. 80, pp. 1748–1770, Nov. 1992.

[8] D. Filipovic, S. Gearhart, and G. Rebeiz, "Double-slot antennas on extended hemispherical and elliptic silicon dielectric lenses," *IEEE Trans. Microwave Theory Tech.*, vol. 41, pp. 1738–1749, Oct. 1993.

[9] *Receiver Optics Design Electromagnetic Analysis.* ALMA Internal Report.

[10] V. Vassilev, V. Belitsky, R. S. Booth, "New sideband separation SIS mixer for ALMA," *Proc. SPIE, Radio Telescopes*, vol. 4015, pp. 567–573, July 2000.

[11] *Virginia Diodes Inc.* [Online]. Available: http://www.virginiadiodes.com

[12] F. Maiwald, J. C. Pearson, J. S. Ward, E. Schlecht, G. Chattopadhyay, J. Gill, R. Ferber, R. Tsang, R. Lin, A. Peralta, B. Finamore, W. Chun, J. Baker, R. J. Dengler, H. Javadi, P. Siegel and I. Mehdi, "Solid-State Terahertz Sources for Space Applications," [Online]. Available: http://www.submm.caltech.edu/~goutam/ps_pdf_files/irmm_04.pdf

[13] G. Chattopadhyay and J. Zmuidzinas, "A dual-polarized slot antenna for millimeter waves," *IEEE Trans. Antennas Propagat.*, vol. 46, pp. 737–737, May 1998.

[14] A. Kerr, S.-K. Pan, A. Lichtenberger, N. Horner, J. E. Effland, K. Crady, "A single-chip balanced SIS mixer for 200–300 GHz," in *Proc. 11th Int. Symp. Space Terahertz Technology*, 2000, pp. 251–259.

[15] B. Bumble, H. G. LeDuc, J. A. Stern, K. G. Megerian, "Fabrication of Nb/AlN/NbTiN junctions for SIS mixer applications," *IEEE Trans. Appl. Supercond.*, vol. 11, pp. 76–79, Mar. 2001.

[16] M. Bin, M. C. Gaidis, J. Zmuidzinas, T. G. Phillips, H. G. LeDuc, "Low-noise 1 THz niobium superconducting tunnel junction mixer with normal metal tuning circuit," *Appl. Phys. Lett.*, vol. 68, pp. 1714–1716, 1996.

[17] J. W. Kooi, J. A. Stern, G. Chattopadhyay, H. G. LeDuc, B. Bumble, J. Zmuidzinas, "Low-loss NbTiN films for THz SIS mixer tuning circuits," *Int. J. IR and MM Waves*, vol. 19, pp. 373–383, 1998.

[18] B. Jackson, A. Baryshev, G. de Lange, J. Gao, S. Shitov, N. Iosad, T. Klapwijk, "Low-noise 1 THz superconductor–insulator–superconductor mixer incorporating a NbTiN/SiO/Al tuning circuit," *Appl. Phys. Lett.*, vol. 79, no. 3, pp. 436–438, 2001.

[19] S. Shitov, B. Jackson, A. Baryshev, A. Markov, N. Iosad, J. Gao, T. Klapwijk, "A low-noise double-dipole antenna SIS mixer at 1 THz," *Physica C*, vol. 372, no. 1, pp. 374–377, 2002.

[20] J. Kooi, G. Chattopadhyay, S. Withington, F. Rice, J. Zmuidzinas, C. Walker, G. Yassin, "A full-height waveguide to thin-film microstrip transition with exceptional RF bandwidth and coupling efficiency," *Int. J. IR MM Waves*, vol. 24, no. 3, pp. 261–284, 2003.

[21] Y. Uzawa, Z. Wang, and A. Kawakami, "Terahertz NbN/AlN/NbN mixers with Al/SiO/NbN microstrip tuning circuits," *Appl. Phys. Lett.*, vol. 73, no. 5, pp. 680–682, 1998.

[22] V. Belitsky and M. Tarasov, "SIS junction reactance complete compensation," *IEEE Trans. Magn.*, vol. 27, pp. 2638–2641, Mar. 1991.

[23] T. Noguchi, K. Sunada, J. Inatani, "An SIS mixer with integrated tuning circuit (II) - A proposal of SQUID-type mixer," *Proc. 39th Spring Meeting of the Japanese Society of Appl. Physics,* Tokyo, Japan, March 1992, p. 76.

[24] J. Zmuidzinas, H. G. LeDuc, J. A. Stern, and S. R. Cypher, "Two junction tuning circuits for submillimeter SIS mixers," *IEEE Trans. Microwave Theory Tech.*, vol. 42, pp. 698–706, Apr. 1994.

[25] S. Padin, D. P. Woody, J. A. Stern, H. G. LeDuc, R. Blundell, C. E. Tong, and M. W. Pospieszalski, "An integrated SIS mixer and HEMT IF amplifier," *IEEE Trans. Microwave Theory Tech.*, vol. 44, pp. 987-987–990, June 1996.

Impedance Matching of 640 GHz SIS Mixer in a High IF Band of 11-13 GHz

Ken'ichi KIKUCHI [1], Seikoh ARIMURA [1], Junji INATANI [1], Yasunori FUJII [1], Toshiaki SUZUKI [2], Akiko IWAMOTO [2], and Akihito YAMAMOTO [2]

[1] Japan Aerospace Exploration Agency (JAXA), Tsukuba, Ibaraki 305-8505, Japan
[2] Mitsubishi Electric TOKKI Systems Corporation, Kamakura, Kanagawa 247-0065, Japan

Two 640 GHz SIS mixers are used for SMILES(*), an atmospheric research mission to be aboard the International Space Station. Those SIS mixers are operated at a relatively high IF band of 11-13 GHz, which is selected from the scientific reason of the mission. That high IF frequency, however, makes it more difficult to match the SIS device to the subsequent 50 Ω IF line. In addition to an impedance difference in real part, parasitic effects due to bonding wires, RF choke circuit as well as the capacitance of the SIS junctions will play an important role. When the IF matching is poor, the SIS mixer under test often exhibits significant gain ripples in its IF characteristics.

A solution for that is to insert a proper impedance transformer between the SIS mixer device and the IF output port and compensate the undesirable parasitic effects. To experimentally derive the output impedance of the SIS device, we have repeated measurements of the receiver gain with respect to an SIS device combined with several different types of matching transformers. We utilized the set of data with different IF characteristics to determine the SIS mixer parameters by means of a fitting technique. This has worked well and allowed us to establish the SIS mixer model to reproduce the measured data. An example of the comparison between the measured data and model is shown in Figure 1.

With a proper impedance transformer designed based on the above fitting results, we successfully realized a small ripple and better flatness in the gain profiles of the mixer.

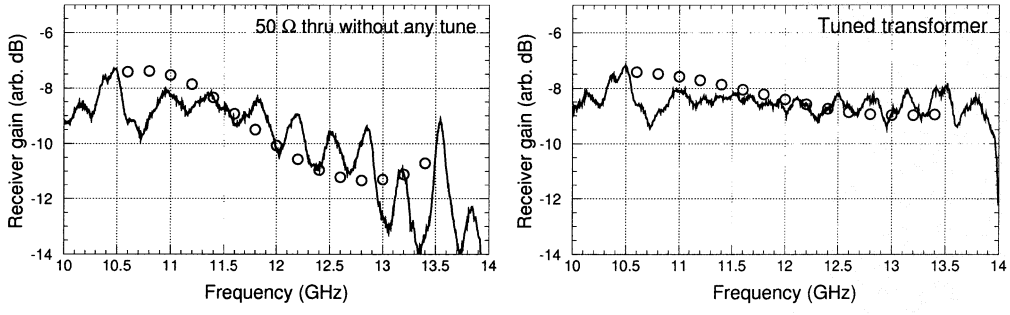

Figure 1: Example of SIS receiver gain with 50 Ω through transformer (*left panel*), and with tuned transformer based on fitting result (*right*). Solid lines show the measured data and open circles are fitted models.

* Superconducting Submillimeter-wave Limb-emission Sounder. See http://smiles.tksc.jaxa.jp/ for detail.

Design of a Multi-beam Focal Plane Array SIS Receiver for 86-115 GHz band

Moon-Hee Chung[1], Vladimir B. Khaikin[2], Hyo-Ryoung Kim[1], Changhoon Lee[1], Kwang-Dong Kim[1], and Kiwon Park[1]
[1]TRAO (Taeduk Radio Astronomy Observatory), South Korea
E-mail: mhchung@trao.re.kr
[2]The Special Astrophysical Observatory of RAS, Russia

***Abstract*— the noise temperature of existing millimeter-wave receivers is already within two or three times quantum noise limit. One of practical ways to increase the observation speed of single dish radio telescope without longer integration time is use of multi-beam focal plane array receiver as demonstrated in several large single dish radio telescopes. In this context the TRAO (Taeduk Radio Astronomy Observatory), which operates a 14 m Cassegrain radio telescope, is planning to develop a 4 x 4 beams focal plane array SIS receiver system for 86-115 GHz band. Even though millimeter-wave HEMT LNA-based receivers approach the noise temperature comparable to the SIS receiver at W-band, it is believed that the receiver based on SIS mixer seems to offer a bit more advantages. The critical part of the multi-beam array receiver will be sideband separating SIS mixers. Employing such a type of SIS mixer makes it possible to simplify the quasi-optics of receiver. Otherwise, a SSB filter should be used in front of the mixer or some sophisticated post-processing of observation data is needed. In this paper we will present a preliminary design concept and components needed for the development of a new 3 mm band multi-beam focal plane array receiver.**

***Index Terms*— multi-beam feed, sideband-separating SIS mixer, focal plane array receiver**

I. Introduction

The TRAO(Taeduk Radio Astronomy Observatory) 14 m radio telescope is located at about 110 meters above sea level in the central region of South Korea. Because of the low altitude of the observatory site and lossy radome enclosing the radio telescope, the observation frequency band of the TRAO 14 m telescope is restricted to lower than 200 GHz. In general the noise temperature contributed by the atmosphere and the antenna itself is greater than around 300 K across the operation band. The noise contribution of the system except the receiver portion is far higher than the noise temperature of SIS mixer- based receivers for 3 mm and 2 mm bands. This implies that the efforts of decreasing the single-beam receiver's noise temperature do not greatly benefit the observation efficiency in terms of mapping speed when performing the observation of large extended sources like molecular clouds or galactic plane. Since many millimeter and submillimeter-wave observatories faced the same problem, over the last two decades several multi-beam focal plane array receivers at millimeter and submillimeter wavelengths have been constructed [1]-[8] and proved the promising performances compared to the single-beam receivers. The multi-beam focal plane array receiver became a radio astronomical instrument of choice for the single dish millimeter and submillimeter-wave telescope [9]. One of the main rationales of developing the multi-beam focal plane array receiver is to dramatically improve the mapping speed. In addition to the increased mapping speed, another benefit is to make possible the cancellation of the atmospheric fluctuations in continuum observations. In this context, the TRAO is planning to develop a multi-beam focal plane array receiver for 3mm band.

The image rejection or sideband separation in the spectral line observations is imperative in order to eliminate the atmospheric noise or unwanted signal noise from the image band. Earlier multi-beam receivers based on Schottky or SIS mixers utilized quasi-optical devices for the single sideband diplexing [2], [3], [4], [7] or a technique of backshort adjustment of the SIS mixer for achieving the image rejection [5], [8]. A cryogenic HEMT LNA-based multi-beam array receiver for 3 mm band employed a technique of choosing very wide IF frequencies to ease sideband separation problems [6]. In conjunction with the advance of millimeter-wave waveguide design and fabrication techniques, the sideband-separating SIS mixer using waveguide structure for 3 mm and 1 mm bands has been progressed during the past few years. These waveguide type sideband-separating SIS mixers have been developed by several groups [10]-[14] and the laboratory demonstrations and a test observation [15] indicated that the sideband-separating SIS mixer technology is mature enough to be applied to multi-beam array receivers. Employing such a sideband separating SIS mixer enables the optics of multi-beam array receiver to be simpler than previous quasi-optical scheme-based receivers for the image rejection and the operation of multi-beam focal plane array receiver becomes easier. On the other hand, as shown in [6], recent progress of millimeter-wave HEMT LNA also provides another option for multi-beam array receiver developments.

The detailed technical designs for components needed in the multi-beam focal plane array SIS receiver are now under way. In this paper we describe our design philosophy concerning the input optics, sideband separating SIS mixer, LO system and IF amplifier.

II. Antenna Modeling

The radio telescope of the TRAO is a classical Cassegrain type and the secondary focus is located just before the vertex of the primary reflector. The Cassegrain F/D is 4.074. Below are the antenna parameters of the TRAO radio telescope.

Diameter of the main dish (cm)	1371.6
Diameter of the secondary mirror (cm)	108.6
Prime focal distance (cm)	508
Interfocal distance (cm)	462.3
Illumination semi-angle (deg)	7.02
Feed taper (dB)	-13/-10

For the simulation of the multi-beam radiation pattern of the 14 m telescope and calculation of some other antenna characteristics (illumination, aperture, spillover, sidelobe efficiencies, beam overlapping level, etc.), FOPAS (Focal Plane Array Simulation) program has been applied [23]. FOPAS uses GO+PO approach and takes into account the geometry of dual reflector radio telescope, expected aperture distribution or beam pattern of ideal broadband feed, the feed removal from the focus and off-axis aberrations. Some results of the simulation are given in Fig. 1-3.

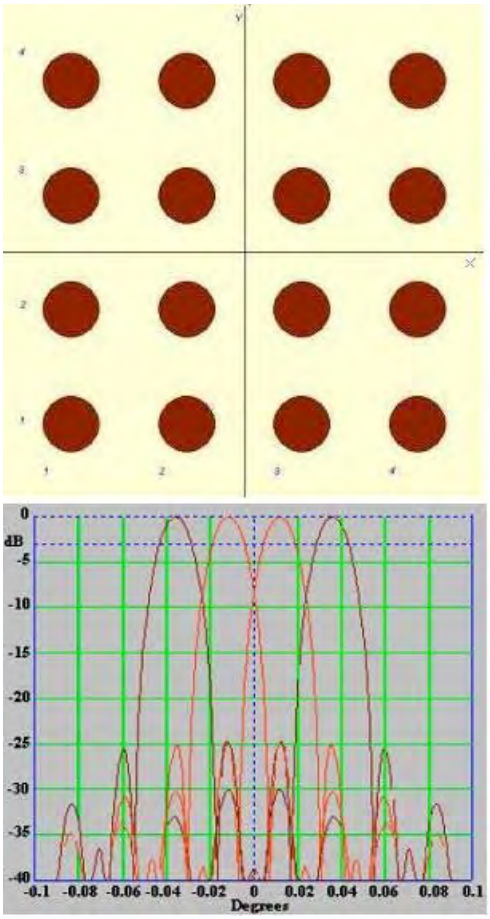

Fig. 1. Position of array feeds (top) and beam patterns of the array at 100 GHz (bottom)

The long focal length of TRAO Cassegrain type telescope with m = (e+1)/(e-1) = 11 gives negligible aberrations for off-axis beams. Given the telescope optics, the minimum

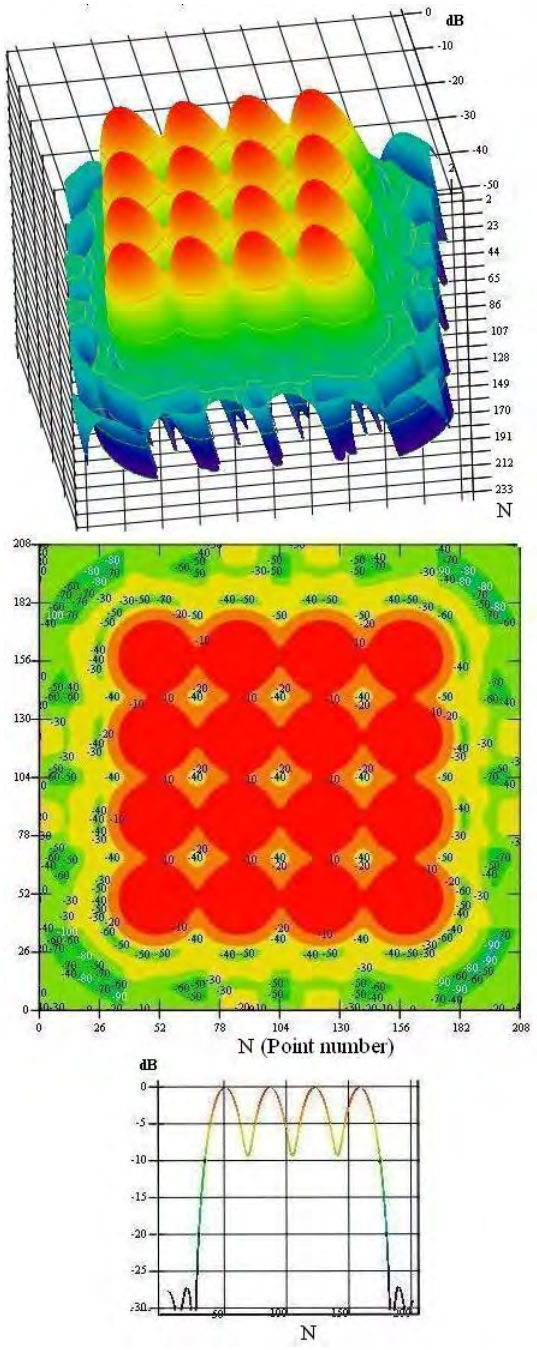

Fig. 2. 3D 4 x 4 beam pattern of TRAO 14 m telescope at 100 GHz (top) with -10 dB feed taper, isolines (middle), and cut view (bottom)

feed spacing in the secondary focus is 25 ~ 27 mm which provides beam separation larger than 100 arcsec and beam overlapping level -12 ~ -11 dB. With closer feed spacing, spillover/sidelobe efficiency falls while the antenna temperature increases. Therefore an additional input optics is needed in a multi-beam mode to reduce beam separation, beam overlapping level, antenna temperature and cross-talk effect as well. In the multi-beam simulation we used the feed spacing 23.5 mm which must be provided by the additional input optics with an ellipsoidal mirror. For more accurate simulation PO+GO+GTD approach must be used to take into account all the mirrors and diffraction effect in the input optics.

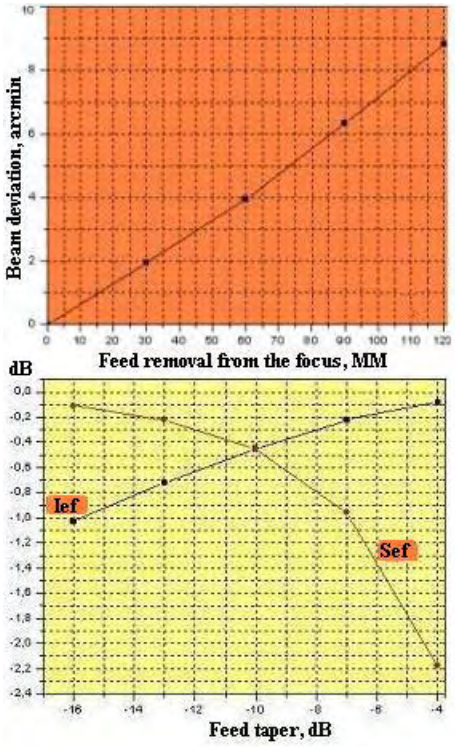

Fig. 3. Beam deviation dependence on the feed removal from the focus (top), illumination and spillover efficiencies as a function of feed taper (bottom)

III. Input Optics

Considering the fact that the main goal of multi-beam focal plane array receiver is to increase the mapping speed, how to configure the input optics of multi-beam array receiver is one of the most important design issues. To make the sampling on the sky as close as possible, it seems better to pack the mixer module as closely as possible. But some spacing constraints arise from the physical dimensions of the sideband-separating mixer block which is relatively larger compared with a single DSB mixer block and the cross-talk among the adjacent feedhorns. One method to avoid the above problem is to interleave the opposite polarizations of the two sub-arrays, which was already used by other groups [2], [3]. In the current design we make use of the similar approach to deploy the feedhorn-mixer modules of the array, that is, 16 beams are divided into two groups: horizontal and vertical polarization groups each containing 8 feedhorn-mixer modules. Another issue in designing of the input optics of multi-beam array receiver is concerned with the image rotation. Recently the OTF technique has been widely used for mapping observation. If such an OTF observation technique is employed, it's not needed to have an image rotator in the multi-beam array receiver. The combination of multi-beam array receiver and OTF observation technique will offer a powerful observation capability for the mapping of large extended sources.

The overall layout of the input optics of multi-beam focal plane array receiver is depicted in Fig. 4. The main function of the optics is to perform the polarization interleaving on the

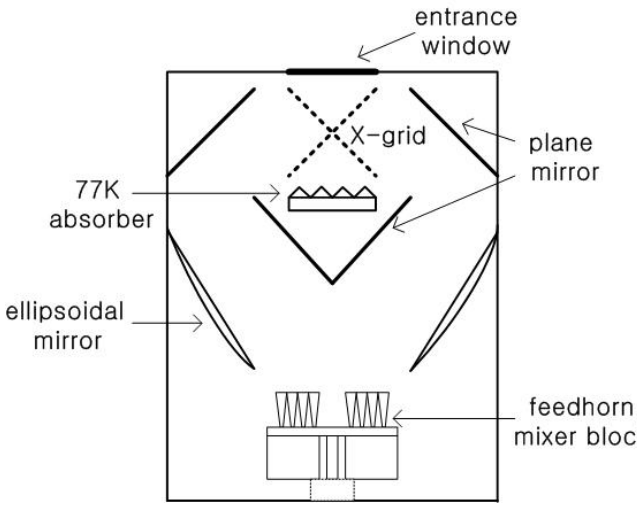

Fig. 4. Layout of optical scheme

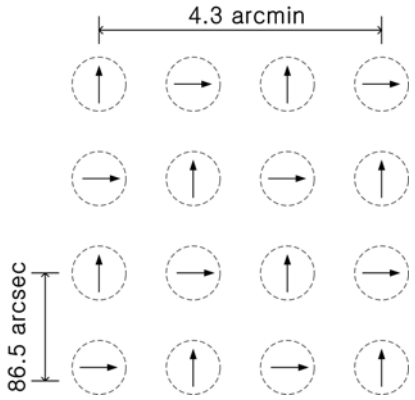

Fig. 5. Beam footprint on the sky of the multi-beam focal plane array receiver at 100 GHz

sky and match the beams from the feedhorns to the required beam waist for the optimum illumination on the subreflector. The input beam is divided into two orthogonal polarizations via an X-grid through which the infrared radiation falls on 77 K absorber. Without this scheme a huge thermal load caused by the infrared would impinge on the cold stage. The optics has a symmetric structure for both polarizations. The sub-array for each polarization consists of 8 feedhorn-mixer blocks. The diameter of feedhorn is around 22 mm and corrugated circular horns will be used for its well-known properties and performance. The maximum field of view of multi-beam focal plane array receiver can be determined by the allowable antenna gain degradation due to the lateral displacement of the feed at Cassegrain focal plane. The spacing between the adjacent beams and the entrance window located near the Cassegrain focus are decided to be 23.5 mm and about 100 mm diameter, respectively. The antenna gain decrease due to the off-axis displacement in the 4 x 4 beams configuration is practically negligible and the main constraint of the field of view is rather the physical dimensions of multi-beam array receiver. The plate scale of the TRAO 14 m telescope is 3.69 arcsec/mm and the spacing of beams on the sky is 86.5 arcsec as shown in Fig. 5. The beam spacing is about 1.73 x FWHM at 100 GHz. The most

critical part of the input optics is to design a single large off-axis ellipsoidal mirror as shown in Fig.4. The requirement of maintaining good image qualities over the field of view leads to take a different mirror design approach compared to the single-beam mirror optics. The design technique involves modifying the basic ellipsoidal mirror's geometric foci while keeping other properties fixed in order to improve the off-axis imaging across the field of view at the expense of a slight degradation of the on-axis image as explained in [16]. So, the modified ellipsoidal mirror has a larger size and more axisymmetric section than the original basic ellipsoidal mirror. Optimizing the geometry of ellipsoidal mirror is being carried out by using commercially available software such as Zemax to calculate the Strehl ratios across the field of view.

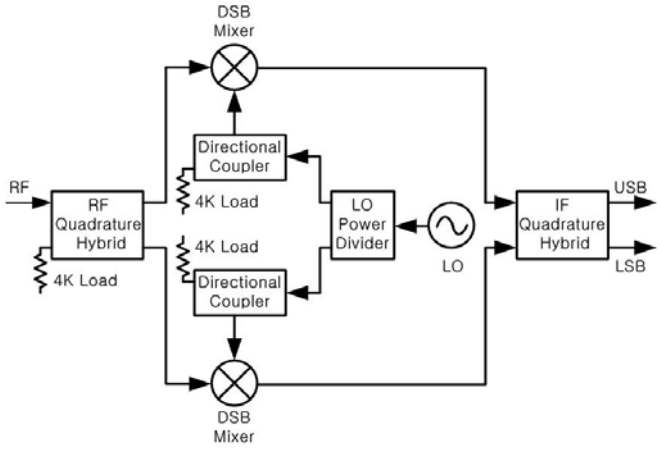

Fig. 6. Schematic diagram of the sideband separation mixer

IV. SIDEBAND-SEPARATING SIS MIXER

In the spectral line observation the sideband separation or image rejection is necessary to practically suppress the unwanted noise from the image band. Until recently the methods of sideband separating at millimeter and submillimeter wavelengths were use of quasi-optical devices or relying on sophisticated software. But over the past few years several groups have developed sideband-separating SIS mixers for 100 GHz and 230 GHz bands using waveguide technology and demonstrated very encouraging performances [10]-[14]. So, we decided to employ sideband-separating SIS mixers in the multi-beam focal plane array receiver. As shown in Fig. 6, a sideband separating mixer module comprises two quadrature hybrids for RF and IF, directional couplers, in-phase power divider, and two DSB mixers. The DSB mixer is a tunerless SIS mixer which has no need of using mechanical tuner. We can fabricate the RF quadrature hybrid, directional couplers, in-phase power divider, and DSB mixers in a single E-plane split-block component of which two halves have a symmetric structure. The RF quadrature hybrid and directional couplers are an E-plane branch-line coupler type. Considering the integration of 16 mixer modules in a limited space, the physical size of the mixer module is a critical issue and now the sideband separating mixer block is being optimized to have a compact size which enables ease of assembling and maintaining the sub-array unit. The design goal of single sideband separating SIS mixer is as follows.

RF band	86 – 115 GHz
SSB noise temperature	< 60 K
IF band	4 – 8 GHz
Image rejection ratio	> 10 dB

V. LO, IF AMPLIFIER AND OTHER PARTS

In the summary below we briefly mention other parts needed for the multi-beam focal plane array receiver. The LO signal generation for simultaneously pumping the 16 SSB SIS mixers (or 32 DSB SIS mixers) at 3mm band doesn't appear to be a greatly difficult task thanks to the very small LO power requirement of SIS mixer itself and the advancement of the millimeter-wave solid-state MMIC technology [18]. What makes LO power problem sophisticated is rather how to distribute and adjust the LO power for each SIS mixer which is supposed to demand different LO power level. An encouraging experience of shared LO power adjustment for a waveguide type array SIS receiver was reported by other group [8] and a further work for this LO adjustment problem is required. The IF amplifier scheme must be as simple and compact as possible due to a large number of mixer elements in the array receiver. One of the candidates for such a goal is to integrate MMIC amplifier like WBA13 chip into the mixer module [19], so that the cryogenic isolator is not necessary between mixer and IF amplifier and assembling of the IF amplifiers into the mixer modules can be very simplified. As reported in the literature, WBA13 is a very low noise and ultra wideband cryogenic MMIC amplifier which seems appropriate for the IF amplifier across 4-8 GHz. If the thermal isolation between the SIS mixer and IF amplifier chip is made for the power dissipation of amplifier not to influence the physical temperature of the SIS junctions, such a scheme can make assembling of the mixer and IF amplifier module very simpler. Another issue is concerned with cooling system. We have used a Daikin CG308SC cryocooler since several years and its cooling capacity is about 3W at 4 K which is believed to be sufficient for cooling the whole SIS mixers to 4K.

VI. CONCLUDING REMARKS AND FUTURE WORKS

Figure 7 illustrates a 3D drawing of the proposed receiver system in this paper. This is a preliminary design concept and there remain many technical works to be done. The development project of the multi-beam focal plane array SIS receiver is now in the phase of detailed designs. Because of the relatively wide field of view, the proposed multi-beam focal plane array receiver may be suitable for survey observation programs. In addition to the above plan, a multi-beam array receiver employing cooled HEMT LNA is being proposed in parallel for the TRAO 14 m telescope [17]. Both multi-beam focal plane array receivers can be used for mapping in continuum and spectral line observations which also include a search for Spectral Spatial Fluctuations (SSF) of Cosmic Microwave Background (CMB). SSF of the CMB temperature must be a result of an interaction of primordial

molecules (LiH, H_2D^+, HeH) with CMB and proto-objects moving with peculiar velocities relative to the CMB [20] – [22]. SSF detection will lead to the discovery of the cosmological molecules which can help us to explore Dark Ages epoch of the early universe ($10 < z < 300$) and physical properties of Dark Matter and Dark Energy.

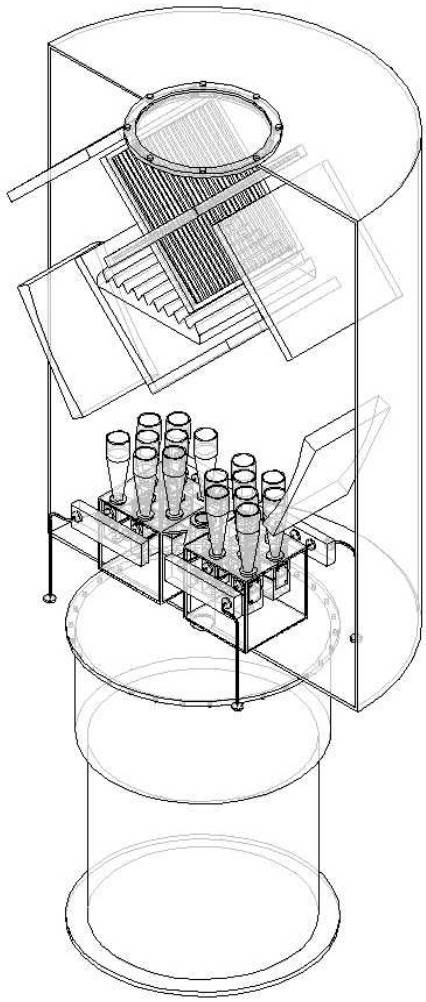

Fig. 7. 3D drawing of the proposed multi-beam focal plane array receiver

ACKNOWLEDGMENT

The authors are very grateful to Jae-Ock Cha for the 3D drawing of the multi-beam focal plane array SIS receiver described in this paper.

REFERENCES

[1] J. M. Payne, "Multibeam receiver for millimeter-wave radio astronomy," *Rev. Sci. Instr.* 59(9), pp. 1911-1919, 1988.

[2] N. R. Erickson, P. F. Goldsmith, G. Novak, R. M. Grosslein, P. J. Viscuso, R. B. Erickson, C. R. Predmore, "A 15 Element Focal Plane Array for 100 GHz," *IEEE Trans. Microwave Theory Tech.*, vol. MTT-40, pp. 1-11, 1992.

[3] R. Güsten, H. Hauschildt, G. A. Ediss, C. Kasemann, N. J. Keen, H. Mattes, M. Pilz, M. Scherschel, G. Schneider, C. K. Walker, H. Knoepfle, K. H. Gundlach, "A 16-element 480 GHz Heterodyne Array for the Heinrich-Hertz Telescope (HHT)," *Multi-Feed Systems for Radio Telescopes*. (D. T. Emerson and J. M. Payne, Eds), ASP Conference Series, vol. 7, 1995.

[4] J. F. Johansson, "SISYFOS – A project Presentation and Progress Report," *Multi-Feed Systems for Radio Telescopes*. (D. T. Emerson and J. M. Payne, Eds), ASP Conference Series, vol. 7, 1995.

[5] K. Sunada, T. Noguchi, M. Tsuboi, J. Inatani, "A Focal Plane Array Receiver for the NRO 45-M Telescope," *Multi-Feed Systems for Radio Telescopes*. (D. T. Emerson and J. M. Payne, Eds), ASP Conference Series, vol. 7, 1995.

[6] N. R. Erickson, R. M. Grosslein, R. B. Erickson, S. Weinreb, "A Cryogenic Focal Plane Array for 85-115 GHz using MMIC Preamplifiers, " *IEEE Trans. Microwave Theory Tech.*, vol. MTT- 47, pp. 2212-2219, 1999.

[7] C. Groopi, C. Walker, C. Kulesa, G. Narayanan, K. Jacobs, U. Graf, R. Schider, J. Kooi, "Heterodyne Array Development at the Univeristy of Arizona," *Proc. 14th Int'l. Symp. on Space Terahertz Tech.*, April 2003.

[8] K.-F. Schuster, C. Boucher, W. Brunswig, M. Carter, J.-Y. Chenu, B. Foullieux, A. Greve, D. John, B. Lazareff, S. Navarro, A. Perrigouard, J.-L. Pollet, A. Sievers, C. Thum, H. Wiesemeyer, "A 230 GHz heterodyne receiver array for the IRAM 30 m telescope," *Astronomy & Astrophysics*, 423, pp.1171-1177, 2004.

[9] P. F. Goldsmith, C.-T. Hsieh, G. R. Huguenin, J. Kapitzky, E. L. Moore, "Focal Plane Imaging Systems for Millimeter Wavelengths," *IEEE Trans. Microwave Theory Tech.*, vol. MTT- 41, pp. 1664-1675, 1993.

[10] S. M. X. Claude, "Sideband-Separating SIS Mixer for ALMA Band 7 -275-370 GHz," *Proc. 14th Int'l. Symp. on Space Terahertz Tech.*, 22-24 April 2003.

[11] S. Asayama, T. Noguchi, H. Ogawa, "Sideband-Separating SIS Mixer at 110 GHz for the measurement of atmospheric ozone," *Proc. 14th Int'l. Symp. on Space Terahertz Tech.*, April 2003.

[12] A. R. Kerr, S.-K. Pan, E. F. Lauria, A. W. Lichtenberger, J. Zhang, M. W. Pospieszalski, N. Horner, G. A. Ediss, J. E. Effland, R. L. Groves, "The ALMA Band 6 (211-275 GHz) Sideband-Separating SIS Mixer-Preamplifier," *Proc. 15th Int'l. Symp. on Space Terahertz Tech.*, 2004.

[13] V. Vassilev, V. Belitsky, C. Risacher, I. Lapkin, A. Pavolotsky, E. Sundin, "Design and Characterization of a Sideband Separating SIS Mixer for 85-115 GHz," *Proc. 15th Int'l. Symp. on Space Terahertz Tech.*, 2004.

[14] G. Narayanan, R. Grosslein, V. Kodipelli, V. Fath, D. Lydon, P. Deshpande, "A Dual Polarization Sideband Separation SIS Receiver for the Large Millimeter Telescope," *Proc. 15th Int'l. Symp. on Space Terahertz Tech.*, 2004.

[15] S. Asayama, K. Kimura, H. Iwashita, N. Sato, T. Takahashi, M. Saito, B. Ikenoue, H. Ishizaki, N. Ukita, "Preliminary Tests of Waveguide Type Sideband-Separating SIS Mixer for Astronomical Observation," *ALMA Memo* #481, Nov. 24, 2003

[16] E. Serabyn, "A Wide-Field Relay Optics System for the Caltech Submillimeter Observatory," *Int. J. Infrared Millimeter Waves*, pp. 273-284, 1997.

[17] V. B. Khaikin, M.-H. Chung, V. N. Radzikhovsky, S. E. Kuzmin, S. V. Kaplya, "Simulated characteristics of 14 m MM TRAO telescope with multi-element FPA at 85-115 GHz," *Proceedings of Cosmion-2004*, 2005.

[18] M. Morgan, S. Weinreb, N. Wadefalk, and L. Samoska, "A MMIC-based 75-110 GHz signal source, " *IEEE MTT-S Intl. Microwave Symp. Digest*, pp. 1859-1862, Seattle, WA, 2002.

[19] G. Engargiola, A. Navarrini, R. L. Plambeck, N. Wadefalk, "Simple 1 mm receivers with fixed tuned double sideband SIS mixer and wideband InP MMIC amplifier," *SPIE* vol. 5498, pp. 556-566, 2004.

[20] V. K. Dubrovich, *Astron. Letters*, 3, 243, 1977.

[21] V. K. Dubrovich, *A&A*, 324, 27, 1997.

[22] V. Khaikin, A. Luukanen, V. Dubrovich, "Instrumental and atmospheric noise in MM-wave ground based SSF experiment," *Cosmology and Gravitation J.*, 2005, in presss.

[23] V. Khaikin, "Simulation of antenna characteristics of MM-wave radio telescopes with multibeam FPA," *Proceedings of 28th ESA Antenna Workshop on Space Antenna Systems and Technologies*, Nordwijk, The Netherlands, May, 2005.

Development of a 385-500GHz SIS Mixer for ALMA Band 8

Wenlei Shan, Shinichiro Asayama, Mamoru Kamikura , Takashi Noguchi,
Shengcai Shi and Yutaro Sekimoto

***Abstract*—In this paper, we report on the design and experimental results of a fix-tuned Superconductor-Insulator-Superconductor (SIS) mixer for Atacama Large Millimeter/submillimeter Array (ALMA) band 8 (385-500GHz) receivers. Nb-based SIS junctions of a current density of 10kA/cm^2 and one micrometer size (fabricated with a two-step lift-off process) are employed to accomplish the ALMA receiver specification, which requires wide frequency coverage as well as low noise temperature. Parallel-connected twin junctions (PCTJ) are designed to resonate at the band center to tune out the junction geometric capacitance. A waveguide-microstrip probe is optimized to have nearly frequency-independent impedance at the probe's feed point, thereby making it much easier to match the low-impedance PCTJ over a wide frequency band. The SIS mixer demonstrates a minimum double-sideband receiver noise temperature of 3 times of quantum limits for an intermediate-frequency range of 4-8GHz. The mixers were measured in band 8 cartridge with a sideband separation scheme. Single-sideband receiver noise below ALMA specification was achieved over the whole band.**

***Index Terms*—Atacama Large Millimeter/submillimeter Array, noise temperature, SIS Mixer, wideband performance.**

I. Introduction

THE Atacama Large Millimeter Array (ALMA) is a millimeter/sub-millimeter wave interferometer to be located at an altitude of about 5000 meters in Llano de Chajnantor, Chile. To be the most sensitive and highest spatial resolution radio interferometer in the world, ALMA is composed of 64 12-meter and 12 7-meter antennas equipped with the most sensitive receivers. The ALMA covers the frequency range of 31-950GHz, which is divided into 10 separate bands coinciding with those transparent atmospheric windows. This division also allows the optimization of both noise performance and optical coupling at all frequencies. The ALMA receivers from 84 GHz adopt superconducting SIS (superconductor-insulator- superconductor) mixers. The front end of an ALMA receiver includes SIS mixers, a LO (local oscillator) subsystem, IF amplifiers and all necessary optical components, all put inside a self-contained module known as cartridge. The SIS mixers are primarily responsible for the sensitivity of the total cartridge. The ALMA receiver specification requires the band 8 receiver's double-sideband (DSB) noise temperature to be below 4 times the quantum limit over 80% of the band, with an intermediate frequency (IF) bandwidth of 8GHz in total per polarization.

To relax the ALMA requirement of having an 8GHz IF bandwidth, we designed the ALMA band 8 receiver on the basis of a sideband separation(2SB) scheme using a quadrature hybrid and two identical DSB SIS mixers. Similar design has been adopted for the ALMA band 4 mixers developed in NAOJ [1]. Since the RF bandwidth is of our most concern, great efforts have been made to achieve wideband response for each component of the SIS mixer including the SIS junctions, junction's tuning structure, impedance transformers and waveguide-microstrip probe. We also designed a compact fix-tuned mixer block unit incorporating with a superconducting magnet, which is easy to assemble and maintain in the band 8 cartridge.

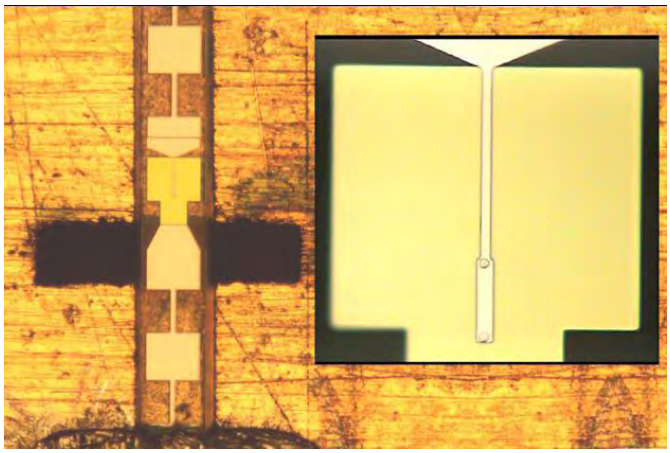

Fig. 1. A mounted mixer chip viewed from the mixer's backshort. Waveguide size is 508×127μm and chip size 120×60μm. Microstrip probe couples RF and LO signals from a half-reduced waveguide. The insect shows the detail of the PCTJ tuning structure.

Wenlei Shan is with Nobeyama Radio Observatory, National Astronomical Observatory of Japan, Nobeyama, Nagano, Japan, 384-1305. He is also with Purple Mountain Observatory, National Astronomical Observatories of China, Nanjing, China. (e-mail: shawn@nro.nao.ac.jp)

Mamoru Kamikura, Shinichiro Asayama, Yutaro Sekimoto and Takashi Noguchi are with National Astronomical Observatory of Japan, Mitaka, Tokyo 181-8588, Japan. (e-mail: sekimoto.yutaro@nao.ac.jp , noguchi@nro.nao.ac.jp)

Shengcai Shi is with Purple Mountain Observatory, National Astronomical Observatories of China, Nanjing 210008, China. (e-mail: shengcai@public1.ptt.js.cn)

II. SIS Mixer Design

A. Design of Waveguide-microstrip Probe

The SIS mixer design was divided into two independent sub-sections corresponding to different transmission media, namely waveguide-microstrip probe based on a 60μm-thick quartz substrate and superconducting microstrip circuit based on a 300nm-thick SiO_2 thin film. These two sub-sections are independently optimized to be wideband with different simulation tools.

As an antenna inside waveguide, the waveguide-microstrip probe couples the LO and RF signals into a quasi-TEM-mode microstrip line. In general there are three types of designs for such a probe, which have been adequately discussed by several authors [2]-[4]. The most commonly used one is a bow-tie probe with its feed point at the center of waveguide. Although this type of probe can reach 30% bandwidth, its feed-point impedance is rather high (about 100Ω) even if the waveguide height is largely reduced to suppress high-order modes. This disadvantage results in difficulty of wideband matching to low-impedance SIS junctions. Single-side probe [2] is found to be of low impedance and wideband with full-height waveguide. However this type of probe requires close location of the DC/IF ground to the mixer's IF port, which may bring uncertainty to the IF-circuit design and difficulty of DC/IF grounding especially for small mixer chips. Here we adopted a probe design proposed by S.C. Shi et al.[4] for the ALMA band 8 mixers. With the feed point moving outside waveguide and adding one section of impedance transformer, the feed-point impedance can be reduced to below 30Ω. Note that the waveguide height is half reduced to extend the matching bandwidth. The photograph of a mounted mixer chip is shown in Fig. 1. The junction's tuning structure (i.e., parallel-connected twin junctions, PCTJ) is also shown.

The probe was optimized together with the mixer's IF chock filter by a 3D electromagnetic field simulator (Ansoft HFSS).

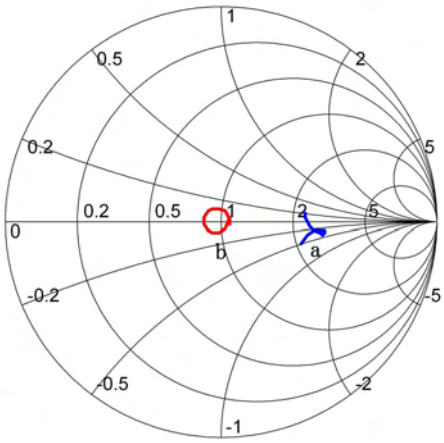

Fig. 2. Impedance seen at the feed point (curve a) and embedding impedance seen by the PCTJ (curve b). The smith chart is normalized to 13Ω(PCTJ's normal resistance) and the frequency range is 385-500GHz.

The goal is to achieve uniform RF impedance at the probe's feed point and low leakage of RF signal to the mixer's IF port within the frequency range of 385-500GHz. The optimized feed-point impedance and the impedance seen by twin SIS junctions (i.e., tuning circuit adopted here) are shown in Fig. 2.

B. Design of SIS Junction and Tuning Structure

The feed point impedance obtained by the preceding method acts as source impedance in this design process. To make good matching between this source impedance and the SIS junction circuit, we have to tune out the junction's geometric capacitance and make use of an impedance transformer.

Parallel connected twin junctions (PCTJ) [5], between which an inductive tuning microstrip line is situated (shown in Fig. 1), were employed to tune out the junction's geometric capacitance. This tuning scheme is favored because of its simple structure and relatively high input impedance. The bandwidth of the PCTJ tuning structure is limited by its quality factor Q=ωRC. Here ω is the center frequency, R is the RF resistance of individual SIS junction that is close to the junction's normal-state resistance at 500GHz band, and C is the junction's capacitance. Since the RC product is inversely proportional to the junction's current density (Jc), high Jc is preferred to have a wideband RF response (corresponding to a low Q). On the other hand, a large R is desirable to reduce the impedance-transform ratio so as to achieve a wideband performance. Based on the above considerations as well as limitations of junction fabrication, we adopted SIS junctions of a current density of 10kA/cm^2 (ωRC =5) and measuring 1μm in diameter. The normal-state resistance of each SIS junction is about 26Ω and the junction's specific capacitance is estimated to be 90fF/μm^2.

Based on the quantum mixing theory [6] with a 5-port approximation and a calculating model for thin-film superconducting microstrip lines [7], we developed a simulation tool to optimize the tuning inductive microstrip line and impedance transformer in order to minimize the receiver noise temperature while keeping good RF coupling and avoiding instability due to oscillations in RF and IF passes over the whole frequency band.

The length of the inductive tuning microstrip line was finally reduced by 15% taking account of the current spreading around the two SIS junctions. In fact, this spreading inductance was simulated numerically by calculating the phase of reflection coefficient of a thin-film microstrip line short-circuited by a conductive pole, which has the same transaction profile as the SIS junction. This modification is important to achieve a correct center frequency for PCTJs that employ a short tuning microstrip line at sub-millimeter wavelengths.

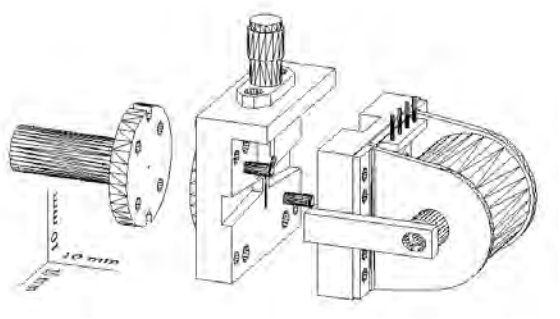

Fig. 3. Mechanical design of the mixer block. Superconducting magnet is fixed onto the backshort part by screws to form a single unit and biased through a 4-pin connector.

C. Mixer Block Design

We aimed to design a mixer block of compactness and assembling simplicity as well as good performance. The DSB mixer block shown in Fig. 3 consists of a diagonal horn, a taper part, a centering ring which aligns the horn with the taper part (not shown), a backshort piece and a superconducting magnet. Since sufficient magnetic field is necessary to suppress the Josephson effect at the 500GHz band, the two arms of the superconducting magnet yoke were designed to locate 1mm away from the mixer's junction chip for a good coupling of magnetic-field flux from the coil to the SIS junctions. The magnetic field at the junctions was designed to be larger than 300 Gauss, which produces approximately two flux quanta in a 1μm-diameter junction. The total number of winding is about 3500 to 4000 with a 0.125mm-diameter Cu-cladding NbTi wire. Experimental results show that a current as small as 30mA was sufficient to suppress the Josephson current of a 1μm SIS junction. The superconducting magnet frame was fixed onto the backshort piece to form a single unit and biased through a 4-pin connector.

The 2SB scheme can be readily assembled with two DSB mixer blocks and a RF hybrid (Fig. 4). Except for the disadvantages of its bulk in size and associated transmission loss in the waveguide as well as the loss at waveguide flanges, this configuration provides great convenience to evaluate the performance of each part in the 2SB unit especially when the measurement result is not as good as expected.

D. RF Hybrid Design

A RF hybrid shown in Fig. 5, which includes a quadrature branch line coupler and two branch line in-phase LO dividers, is a scaled version of RF hybrid of Band 4 2SB mixer developed in NAOJ. The quadrature coupler employs a six-branch line structure with branch width 67μm and spacing 163μm (Fig. 6). The measured S-parameters plotted in Fig.7 were found to be in good agreement with those simulated ones. Two 2-slot branch line couplers with a coupling coefficient -17dB were employed to feed the two DSB mixers of equivalent power of same phase.

III. SIS Junction Fabrication

The 500-GHz Nb SIS junctions were fabricated by incorporating SNEP (Selective Niobium Etching Process) with the anodization technique on crystalline quartz substrates [8]. The barrier was formed by the oxidation of a 7nm-thick Al film with 3.3 Pa Ar+10%O_2 for 30 minutes to achieve a critical current density of around 10kA/cm^2. The quality measured by the ratio of sub-gap resistance to normal-state resistance was typically 15.

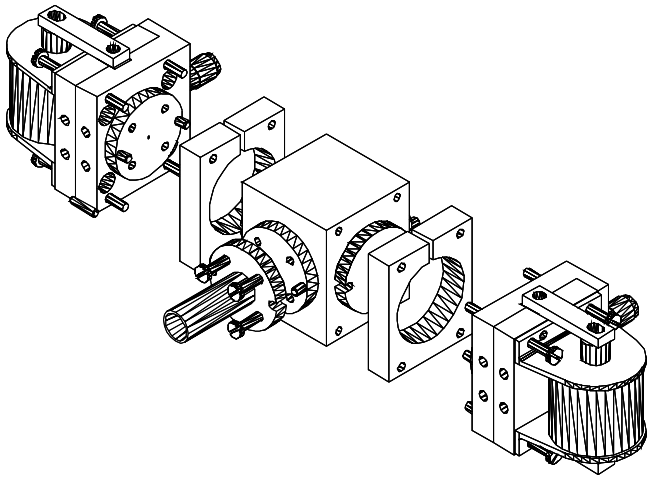

Fig. 4. Mechanical drawing of 2SB mixer assembly. It includes two DSB mixer blocks, a RF hybrid, two centering rings and a feed horn.

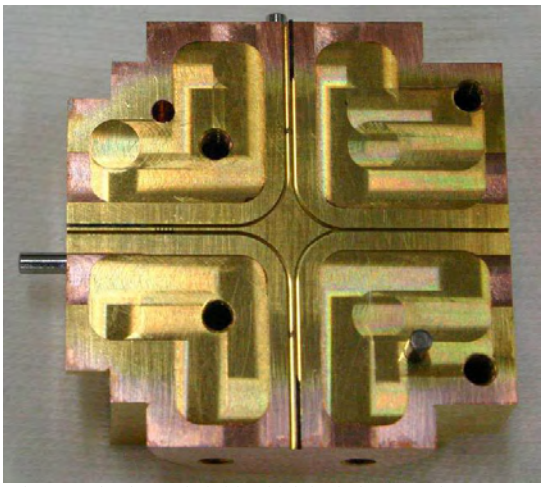

Fig. 5. Photograph of a RF hybrid, which includes a quadrature coupler and two LO dividers.

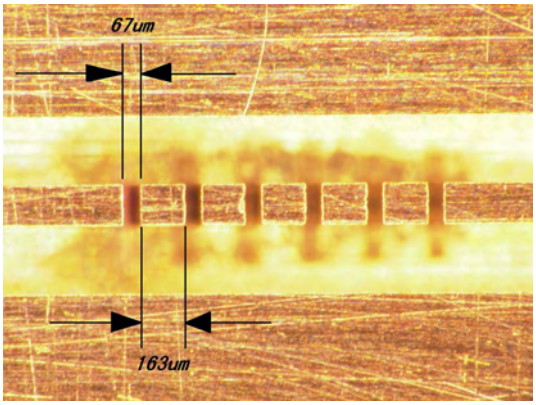

Fig. 6. Photograph of a 6-branch line quadrature coupler with branch width 67µm and spacing 163µm

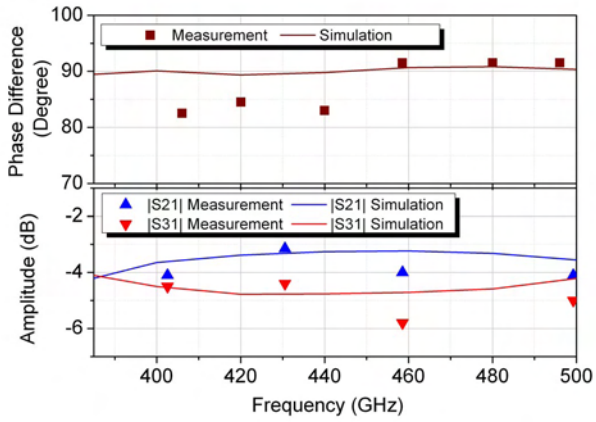

Fig. 7. Measured S parameters and simulated ones of a 6-branch line quadrature coupler.

To achieve good yield and uniformity, two photo masks with circular patterns of 1µm and 3µm in diameter, respectively, were employed to form the junction's contact hole. The 1µm pattern was defined by a g-line (635nm) stepper with high dimensional accuracy. The junction area was then isolated by reactive ion etching (RIE) combined with anodization. Then the whole wafer was covered by an 80nm SiO_2 and a 20nm Al_2O_3 protection layer. After a lift-off process, the 3 µm photoresist pattern was coaxially overlapped to the contact hole by a ultra-violet mask aligner with the second mask. Remaining 250nm of SiO_2 is deposited and a second lift-off process exposed the contact hole for wiring layer connection. The thickness of insulator deposition was adjusted according to subsequent etching consumption to form 300nm SiO_2 in total.

IV. Measurement Setup

The ALMA band 8 DSB mixers were measured in a 4-K Gifford-McMahon/Joule-Thomson mechanical cryocooler. An isolator with a built-in bias-T, inserted between the SIS mixer and a 4-8GHz low noise amplifier, was cooled to 4K to reduce the thermal noise injection from its terminated port. An off-axis ellipsoidal mirror with an edge-taper of 30dB was put on the 4K stage to refocus the beam from the diagonal horn onto an external hot (300K) /cold (liquid nitrogen) load. A 100µm-thick polyimide film was used as the vacuum window, while a 150µm-thick Zitex sheet cooled at the 70K stage blocked the infrared radiation. A 12.5µm-thick polyimide film was used as a beam splitter, coupling the LO signal generated by a Gunn oscillator followed by two Schottky-diode doublers with a factor of -15dB.

V. Measurement Results And Discussion

A. DSB Receiver Noise

Typical I-V and IF responses with hot and cold loads are shown in Fig. 8. With a magnet driving current of 30mA, no additional noise induced by the Josephson current was found. We used a standard Y-factor measurement technique to determine the receiver noise temperature. All presented noise temperatures were uncorrected for the optics loss, and a Callen/Welton formula [9] was used to obtain the black-body radiation temperatures. A noise temperature of 60K at the band center and 120K at the band edges are demonstrated in Fig. 9.

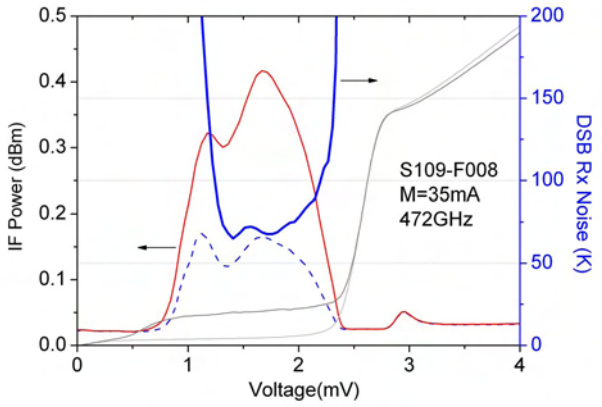

Fig. 8. Typical I-V curve and IF output power (left) at 472GHz with magnet driving current 30mA. The noise temperature is also plotted as a function of bias voltage.

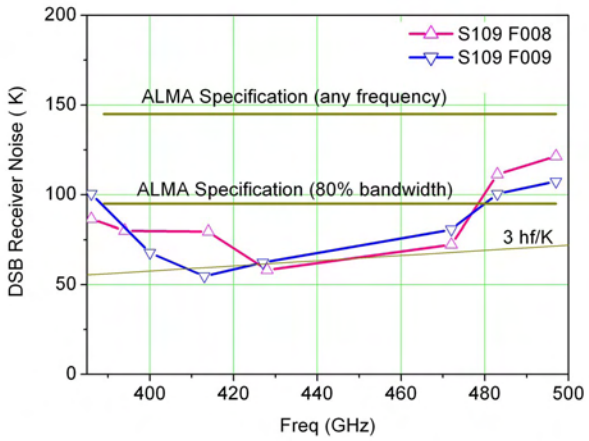

Fig. 9. DSB receiver noise of two typical band 8 mixers. In a wide frequency range, the receiver noise is as low as 3 times of quantum limits.

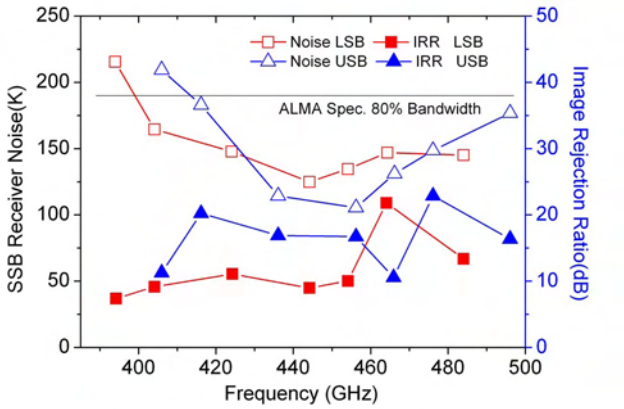

Fig. 11. SSB receiver noise and image rejection ratio of Band 8 cartridge

The measurement results demonstrate a wide bandwidth, which benefits from employing high current density, small-sized SIS junctions and wideband design of the mixer chip. The best performance is well located at the band center, indicating an accurate design of the PCTJ's tuning inductance. The intermediate frequency (IF) noise, calculated to be 15K, is mainly contributed by a 2-stage GaAs based HEMT low noise amplifier (LNA) and the isolator before it. We expect that the IF noise contribution can be further reduced by adopting InP based LNA, which can ordinarily reaches 5K noise temperature at 4-8GHz band.

Receiver noise was also measured as a function of IF as shown in Fig. 10. Due to standing waves between SIS mixer and isolator the receiver noise varies about 10% around the average value over the whole IF band.

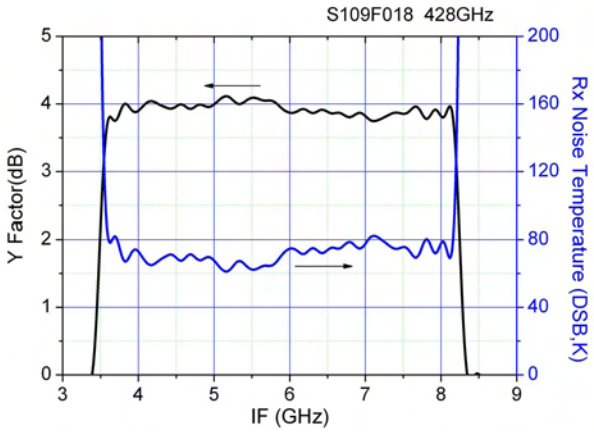

Fig. 10. Receiver noise as a function of intermediate frequency. Ripples are due to standing waves between SIS mixer and isolator.

B. Sideband Separation Receiver Noise and Image Rejection Ratio (IRR)

A 2SB assembly was measured to evaluate the mixer performance in the qualification model of Band 8 cartridge. The SSB noise temperature and image rejection ratio are plotted in Fig.11. Noise temperatures below ALMA specification was achieved over the whole band from 385GHz to 500GHz. The loss of RF hybrid, which was thought to contribute a lot to overall receiver noise, turns out to be much smaller than estimated. The IRR of 10dB~20dB was achieved. The large difference between IRR measured at lower sideband and higher sideband is possibly caused by unbalanced conversion gain of the two mixers , which were individually measured beforehand.

C. Determining the Embedding Impedance of SIS Mixers

The embedding impedance seen by PCTJ was determined experimentally with the "RF voltage match" method [10]. We improved the method so that it can treat PCTJ structure. Fitting process was performed with pumped IV curves at several frequencies. At each frequency three IV curves at different pumping levels were fitted respectively and the average value was adopted. The embedding impedances for three mixers are plotted in a Smith chart (Fig. 12), which is normalized by PCTJ normal resistance. Good matching between PCTJ and signal source can be found though the three curves do not agree well, which is due to the combination of mixer mounting misalignments, mixer block fabrication errors, uncertainty of PCTJ parameters as well as the fitting errors of this method itself .

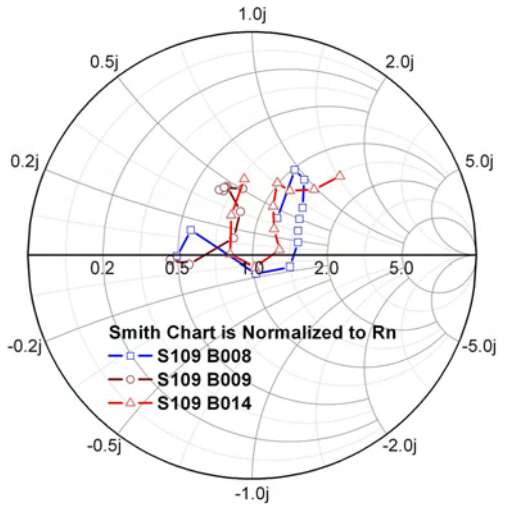

Fig. 12. Fitted embedding impedance of three mixers. Results indicate good matching between PCTJ and signal source.

VI. Conclusion

We have designed a wide-band, low noise SIS mixer for ALMA Band 8. DSB receiver noise as low as 3 time quantum limits has been demonstrated. The SSB receiver noise measured in a Band 8 cartridge is below the ALMA specification over the whole band. The good RF performance is attributed to accurate design of PCTJ embedding impedance and the tuning microstrip line as well as adopting high current density one micrometer size SIS junctions.

Acknowledgment

We are grateful to T. Matsunaga and T. Takizawa for their great help of junction fabrication, M. Tomimura, Y. Iizuka, N. Satou, T. Kamba and J. Li for receiver measurement assistance. This work was partly supported by the NSFC under Contracts No. 20030001-10390163 and No. 10303008, and the CAS under Contract No. KJCX2-SW-T2.

References

[1] S. Asayama, H. Ogawa, T. Noguchi, K. Suzuki, H. Andoh and A. Mizuno, "An Integrated sideband-separating SIS mixer based on waveguide split block for 100GHz band," *ALMA Memo* 453, Available: http://www.alma.nrao.edu/memos

[2] A.V.Raisanen, W.R. McGrath, D. G. Grete, and P. L. Richards, "Scaled model measurements of embedding impedances for SIS waveguide mixers," *Int. J. Infrared and Millimeter Waves*, vol. 6, 1985, pp1169-1189

[3] G. Tassin and S. Withington, "Analytical expression for the input impedance of a microstrip probe in waveguide," *Int. J. Infrared and Millimeter Waves*, vol. 17, 1996, pp1685-1705.

[4] S. C. Shi and J. Inatani, " A waveguide-to-microstrip transition with a DC-IF return path and an offset probe,", *IEEE Trans. Microwave Theory and Techniques* , vol. 45, March 1997, pp442-446

[5] T. Noguchi, S. C. Shi, and J. Inatani, "Parallel connected twin SIS junctions for millimeter and submillimeter wave mixers: analysis and experimental verification," *IEICE Trans Electronics*, vol. E78-C, 1995, pp481-489.

[6] Tucker J.R. "Quantum limited detection in tunnel junction mixers," *IEEE J. Quantum Elec*, vol. 15, 1979, pp1234-1258.

[7] W. H. Chang, "The inductance of a superconducting strip transmission line," *J. Appl. Phys.* , vol. 50, 1979, pp8129-8134

[8] T. Noguchi, A. Sakamoto, and S. Ochiai, "Fabrication of sub-micrometer -sized SIS junctions," *IEICE Technical Report*, SCE93-64, 1994.

[9] H.B. Callen and T. A. Welton, "Irreversibility and generalized noise," *Phys. Rev.*, vol. 83, July 1951, pp34-40.

[10] Anders Skalare, "Determining embedding circuit parameters from DC measurements on quasiparticale mixers," *Int. J. Infrared and Millimeter Waves*, vol. 10, 1989, pp1339-1353.

Variable capacitors in meander-suspended superconducting microbridge technology for high frequency applications

M. Schicke[1], A. Navarrini[2], and K.-F. Schuster[1]

[1]IRAM, Institute de Radio Astronomie Millimetrique, 300 Rue de la Piscine, 38406 St Martin d'Hères, France
[2]Radio Astronomy Lab (RAL), University of California, 601 Campbell Hall, Berkeley CA 94720-3411, USA

Abstract— **Variable capacitors in the fF to pF capacitance range are very interesting for high frequency applications like variable filters, couplers, resonators, etc. Our recent development permits to use meander-like suspensions for electrostatically actuated microbridges in Niobium (Nb) technology (see Fig. 1). The surface mounted fabrication procedure allows for integration of these devices with the standard Nb tunnel diode fabrication process as used for radio astronomical heterodyne detectors and superconducting electronic circuitry. We present the fabrication procedure, first meander suspended devices with a low actuation voltage range, and two filter designs for 22 GHz tunable band pass filters.**

***Index Terms*—variable capacitors, Nb, microbridge, MEMS (MicroElectroMechanical Systems), tunable filters**

I. Introduction

The development of superconducting RF MEMS is motivated by the possibility of compact and reliable tuning elements with very low loss. In recent work we developed a fabrication technology for surface mounted Niobium MEMS, which is compatible with the low temperature (<150°C) fabrication procedure of Nb-Al/AlOx-Nb SIS tunnel diodes, used in heterodyne high frequency mixers operated at 4 K. This permits the planar integration of the filters and detectors. In a simple geometry of a first design (see Fig. 1), the suspension of 700nm thick bridge layers was very rigid and required high actuation voltage. Thinner bridge layers (200nm to 300nm) revealed a strong differential stress. Due to the stress-induced deformation the bridge layers obtained a undesirable rigidity (saddle-like structure, see inset of Fig. 1). Nevertheless a considerable height variation at bias voltages of less than 50 V could be achieved. The working principle of microbridges with a thin bridge layer has already been demonstrated for test capacitors with areas close to 100µm×100µm and an air gap of 5 µm. The capacity (some tens of fF) of these devices could be varied by more than 10% by applying a voltage of 45V [1]. In this paper we describe the successful solution of the remaining stress problem which allows us to reduce the actuation voltage to ~10 V.

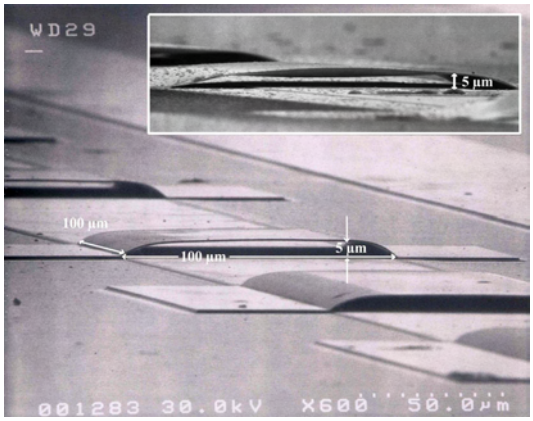

Figure 1: Example of a simple Nb thin film bridge. The Nb film of the bridge is 700 nm thick. The inset shows the extreme bending of a bridge layer with only 240nm thickness and the reduced height due to stress in the Nb film.

II. MEMS fabrication procedure

Most superconducting circuits and mm-wave detectors are based on superconducting Nb [2, 3]. Compared with galvanically grown bridge layers, sputtered Nb air bridges have the advantage, that the same techniques can be used as for the other parts of the superconducting circuitry.

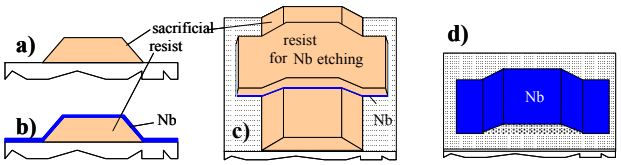

Figure 2: Fabrication process for sputtered Nb air bridges.

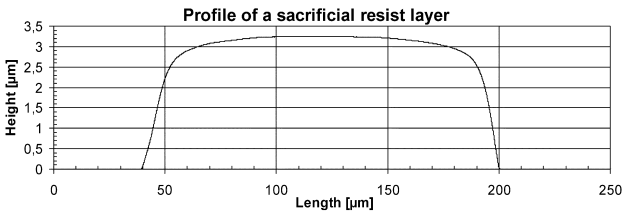

Figure 3: Profile of a sacrificial resist layer after flood exposure and development measured with a Dektak 8 profilometer.

After patterning of the attracting electrode using any suitable technique (e.g. lift-off or etching), a crucial step consists in the preparation of the sacrificial layer, which defines the bridge profile (Fig. 2a). Here, the photoresist AR-4000/8 (ALLRESIST) is used, giving an initial resist thickness of 5 µm. The pre-exposure bake is done for 30 minutes at 85°C in a convection oven. To obtain sufficiently smooth edges, the resist is baked 4 h at 94°C (flow bake) after development. Recent optimizations using proximity instead of contact exposure improved the edge smoothness and the total process time and hence replaced the flow bake. With an additional flood exposure the resist height can be adapted to a desired value. A resist profile can be seen in Fig. 3.

In the second step, the Nb layer is sputtered by DC-magnetron sputtering in periods of 5–10 s deposition and 5 min pause (Fig. 2b). Different step times have been chosen in order to examine a possible correlation with the film stress. The pauses are needed to reduce surface heating and thus deformation or polymerization of the resist layer.

The bridge widths and form of the suspensions are defined in the third step with a photo resist etch mask. For a good coverage of the structures, we use again the thick resist. Through this resist mask, which covers the surface of the Nb bridges, the non-covered parts of the Nb layer are etched by ICP (Inductively Coupled Plasma) etching, as shown in Fig. 2c [4].

In the final step, the resist is washed away in 70°C hot acetone (Fig. 2d).

Applying this new technique, bridges with Nb layers of 1.5 µm thickness were fabricated with lengths of 50–200 µm and widths of 50–1080 µm. A Nb film sputtered on top of the sacrificial resist layer prepared without flow bake shows a bending diameter of 1–2 mm. Taking a simple two-layer model one can estimate the compressive stress in the lower layer to be of the order of 100–200 MPa. This indicates that the film bending within the lengths of the bridges is much less pronounced than for 700 nm thick films with a bending diameter of 10–20 µm, corresponding to compressive stress of a few GPa. We tentatively explain this phenomenon with a strong stress gradient within the lower few hundred nm of the film thickness, whereas the upper part has almost no stress and serves therefore as stabilization. This effect can possibly be explained with the expansion and shrinking of the sacrificial resist layer during deposition and cooling, respectively, which might be more pronounced for the first hundreds of nm Nb thickness than for the last ones.

III. Meander-suspended Microbridges

Thin film structures from Niobium have great rigidity as can be seen from the Young's modulus of 105 GPa. This fact and the possibility to etch thick Nb layers highly anisotropically by ICP etching with helium substrate cooling opened the opportunity to introduce meander-like spring suspensions for variable capacities (see Fig. 4). With this type of suspension the spring constant can be adjusted through the meander dimensions.

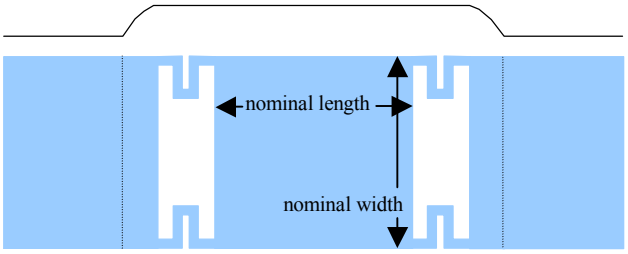

Figure 4: Schematic of a meander-suspended microbridge.

The fabrication of differently sized test bridges with differently sized meander suspensions showed that bridges with lengths of up to 100 µm and widths of up to 600 µm could be fabricated yielding more than 80% (see Fig. 5), whereas the bridges longer than 200 µm were often sticking on the ground after the washing of the sacrificial resist layer. With the actual recipe the bridge height can be chosen between 2 µm and 7 µm, but tests indicate that bridge heights down to 1 µm might be achievable.

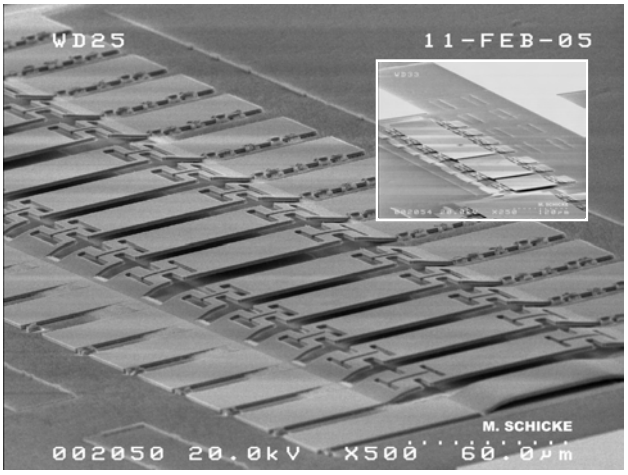

Figure 5: Series of 50µm-bridges with different meander dimensions. The bridge height is 3 µm and the Nb film thickness is 1.5 µm. In the inset a series of 100µm-bridges with widths from 180 µm to 600 µm can be seen.

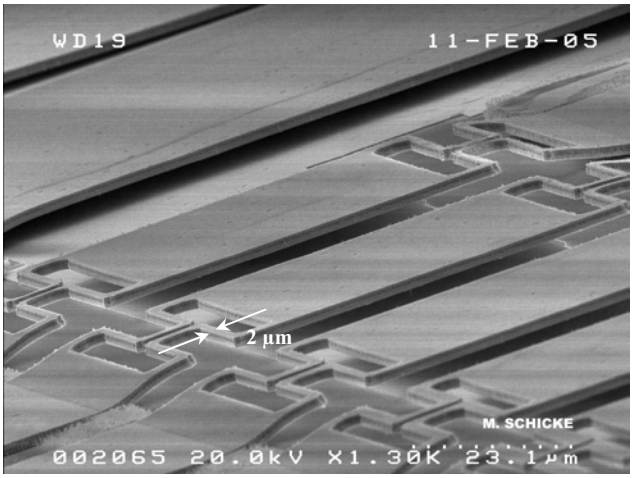

Figure 6: Series of 50µm-bridges with 2 µm wide meanders.

It has been demonstrated that even bridges with meander widths of 2 µm could be fabricated (see Fig. 6). Measurements of the capacitance were done with an Agilent LCR meter in a 4-point configuration. The variation of differently sized test bridges gave very promising results, as can be seen on Fig. 7. Only the 100x100 µm^2 bridges with meanders larger than 4 µm and shorter than 25 µm had their pull-in point above 40 V. From the capacitance value of the 150µm-bridge one can deduce an effective unbiased bridge height after release of 1 µm instead of 3 µm given by the thickness of the sacrificial resist layer. We explain this reduced height with the bending of the Nb bridge layer.

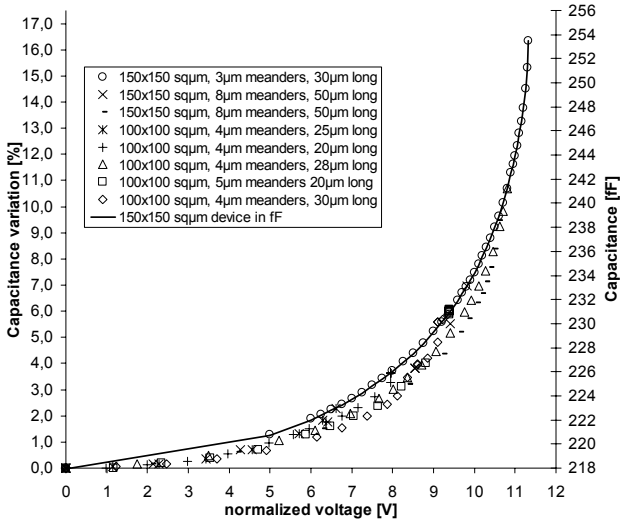

Figure 7: Capacitance of different meander-suspended microbridges as a function of the actuation voltage. The continuous line belongs to the right scale and the voltage scale shows the real voltages applied to this device. Points belong to various devices and capacity (left scale) has been normalized in order to show the similarity in actuation behavior.

IV. Band Pass Filters

The two filter chips, shown in Fig. 8, have been realized on quartz substrates with dimensions of 0.2×1.0×7.7 mm^3. Each of them has been synthesized starting from a lumped element model consisting of series inductors and parallel capacitors, which have been successively transformed in short sections (l<<λ) of, respectively coplanar waveguides (CPW) and microbridge lines. The electrodes underneath the bridges have almost the same size as the bridges. Both filters are optimized to provide maximum tuning frequency range when the air gaps of the microbridges are decreased from their nominal (unbiased) value of 2.5 µm down to the minimum of ~1.7 µm, expected when the maximum bias voltage is applied.

The filters were optimized using the commercial software ADS [5]. The microbridge structures and the effects of discontinuities between these sections and the CPW sections were modeled with Sonnet [6] and were successively included in ADS for global optimization of the filters. The superconducting effects, that slightly modify the transmission line properties due to the field penetration depth inside the 150 nm thick Nb layers, were taken into account in the electromagnetic simulations. The input and output sections of both filters are 50 Ω CPW with 260 µm wide central conductor

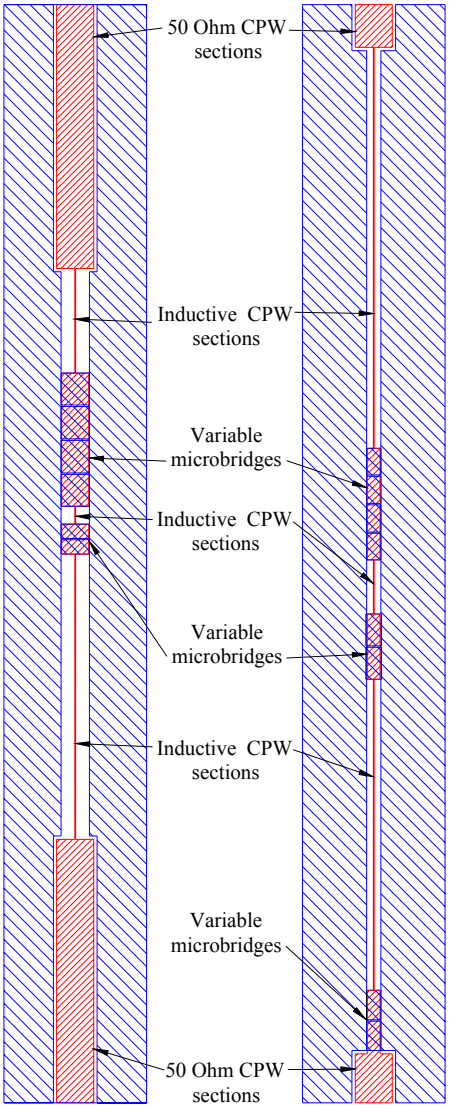

Figure 8: View of bandpass tunable filter chips: a) of order 5, b) of order 6.

and 23 µm gap to adjacent ground electrodes. The microbridges of each filter have all the same length (200 µm in the filter of order 5, 100 µm in the filter of order 6). The maximum width of the microbridges is 224 µm, and the narrowest central strip of the CPW sections is 5 µm. Because of the shorter microbridge length, the filter of order 6 can be realized with a higher yield than the other one, which has, nevertheless, the advantage that it can be tuned over a wider frequency range.

The results of the simulations for the transmitted amplitudes of the two filters under biased and unbiased conditions are shown in the Figs. 9 and 10. The central frequency of the filter can be tuned continuously within the respective range. The 3-dB fractional bandwidth of the filter is about 3% and varies only slightly with the voltage applied to the microbridges (between 670 MHz and 760 MHz). The estimated insertion losses are very low (< 0.3 dB), and vary little with bridge height. The off resonance isolation is below -17 dB.

First filter devices have been fabricated (Fig. 11) and are about to be measured.

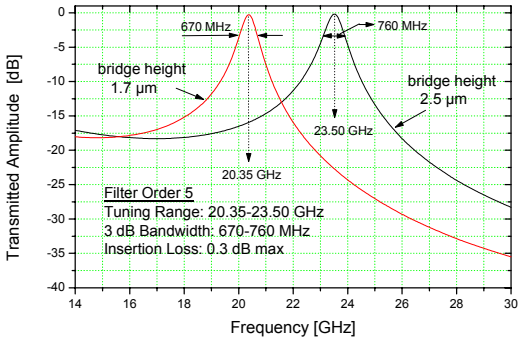

Figure 9: Transmitted amplitude of the filters of order 5 for two different air bridge heights: 2.5 µm (no voltage applied), and 1.7 µm (maximum voltage).

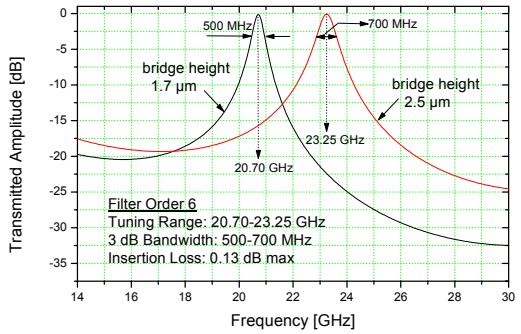

Figure 10: Transmitted amplitude of the filters of order 6 for two different air bridge heights: 2.5 µm (no voltage applied), and 1.7 µm (maximum voltage).

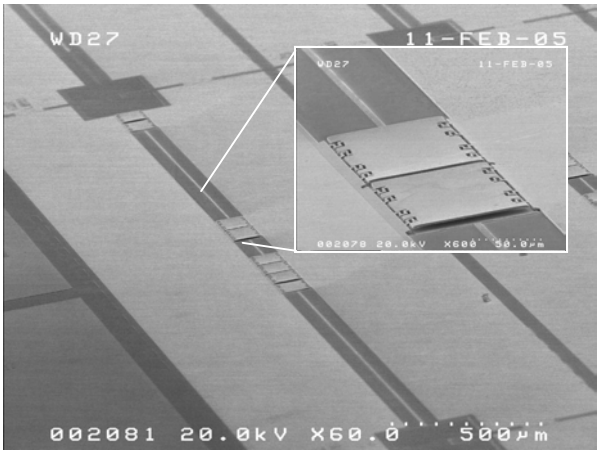

Figure 11: A 22 GHz band pass Filter device of order 6.

V. Outlook

One important aspect of variable microwave filter devices is the tunability band. The relative band of tunability is proportional to the relative variation ΔC/C of the micro-bridge's capacitance obtained by applying an actuation voltage or not. The value ΔC/C can be considerably increased by using a dielectric layer with high dielectric constant between the microbridge and the ground plane, as shown in Figure 12.

The capacitance C_{off} (no voltage applied) of two plane conductors separated by a distance h1+h2, where h1 is an air gap and h2 is a dielectric (AlN for example), is equivalent to a series of two capacitors C1 and C2 where C1 is the

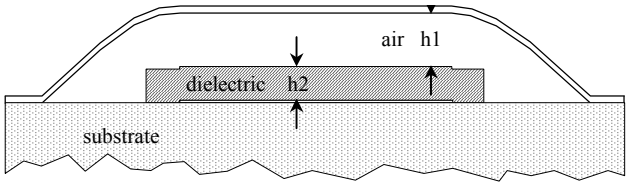

Figure 12: Schematic of a microbridge with additional dielectric layer.

capacitance of two conductors separated by a gap of air h1, and C2is the capacitance of two conductors separated by a h2 thick dielectric. The maximum relative variation of the capacitance is given by: $\Delta C/ C_{off} = (C2-C_{off})/C_{off} = \varepsilon_r\, h2/h1$. For example, if we use air only (with no dielectric) like in our 22 GHz filter design, with $\varepsilon_r=1$, h1=0.8 µm, h2=1.7 µm, we get: $\Delta C/ C_{off}=47\%$. If we add a dielectric layer of AlN ($\varepsilon_r=4.6$, [7]) with h2=1.7 um, and air h1=0.8 um, we obtain $\Delta C/C_{off}=216\%$.

Therefore, future improvements will include separation of actuation electrodes from tuned capacities. Topological variations of either top or ground electrodes can lead to much wider tuning ranges. Finally, dielectric layers will further improve tuning ranges and at the same time resolve problems of electrical isolation and sticking.

VI. Acknowledgements

The authors would like to thank A. Salvador Matar for his help in process optimization and T. Scherer for many helpful discussions. This project has been supported by ADIXEN-ALCATEL Vacuum Technology.

VII. References

[1] M. Schicke and K.F. Schuster, "Integrated Niobium Thin Film Air Bridges as Variable Capacitors for Superconducting GHz Electronic Circuits",*IEEE Trans. on Appl. Supercond.*, Houston, Texas, USA, June 2003.

[2] J. Zmuidzinas and P.L. Richards, "Superconducting Detectors and Mixers for Millimeter and Submillimeter Astrophysics", *Proceedings of the IEEE*, Vol. 92, No. 10, October 2004.

[3] K.H. Gundlach and M. Schicke, "SIS and bolometer mixers for terahertz frequencies", *Supercond. Sci. Technol.* 13 R171-R187, 2000.

[4] K.F. Schuster et al., "Inductively coupled plasma etching of Nb, NbN and Ta", 2005, submitted to Journal of Vacuum Science and Technology B.

[5] ADS (Advanced Design System), Agilent Technologies, http://eesof.tm.agilent.com/products/adsoview.html

[6] Sonnet Software, Inc., 1020 Seventh North Street, Suite 210, Liverpool, NY 13088, USA, http://www.sonnetsoftware.com

[7] Y. Goldberg, "Properties of advanced Semiconductor Materials GaN, AlN, InN, BN, SiC, SiGe", Eds. M.E. Levinshtein, S.L.Rumyantsev, M.S. Shur, John Wiley & Sons, Inc. New York, 2001, 31-47.

Design of a Sideband Separation Receiver for 500 GHz

Raquel Monje, Christophe Risacher, Vessen Vassilev and Victor Belitsky

Group for Advanced Receiver Development (GARD), Department of Radio and Space Science with Onsala Space Observatory, Chalmers University of Technology, MC2, S 412 96, Gothenburg, Sweden

Abstract — **We describe design of a sideband-separating superconductor-insulator-superconductor (SIS) mixer for the APEX telescope Band 3, 385 – 500 GHz. The mixer design combines waveguide components and on-chip local oscillator (LO) injection. The receiver used quadrature scheme where the RF signal is divided equally with a 90°-phase shift by a waveguide 3 dB hybrid with novel design using several microstrip probes. The LO is divided using an in-phase or 180-degree waveguide E-plane Y-junction. The output waveguides of the hybrid are coupled to the mixer SIS junctions through an E-probe based on waveguide-to-microstrip transition with integrated bias-T. A directional coupler for the LO and RF signals, the SIS junction, the tuning circuitry lines and the bias-T are integrated on a single mixer chip. We use a novel component, an ellipse termination to provide easy and high-performance on-chip LO injection.**

Index Terms — **SIS mixer, sideband separating receiver, waveguide-to-microstrip transition.**

I. Introduction

The Atacama Pathfinder Experiment (APEX) will have a suite of heterodyne receivers for spectroscopy and bolometer arrays for continuum observations across the range from 200 GHz - 1.5 THz divided in different bands. For band 3 (385 - 500 GHz), sideband separation (2SB) SIS mixer is chosen. This technology provides better sensitivity for spectral line observation than double sideband (DSB) [1]. Besides, DSB observations may lead to spectral line-confusion or degrade the system noise temperature and the receiver sensitivity with strong absorption bands falling into the image band. This is a driving reason to choose this technology considering that some of the important molecules for this band are very close to telluric absorption line, as in the case of deuterated water, HDO, with its fundamental transition frequency at 465 GHz.

In the proposed design, sideband separation is achieved using a quadrature scheme. The configuration used in the presented work is shown schematically in Figure 1. The RF signal is divided equally with 90° phase difference, and the local oscillator (LO) is symmetrically split and applied to 2 identical DSB mixers 180 degree phase difference. The mixers outputs at intermediate frequency (IF) are connected to IF cryogenic amplifiers followed by a quadrature 3 dB hybrid. Since one of the sidebands is combined in phase and the other out of phase, sideband cancellation occurs and both sidebands appear separated. Alternative scheme considers the hybrid inputs take the mixer IF signals directly while the outputs of it is connected to cryogenic IF Low Noise Amplifiers (LNA).

The mixer chip design is based on the previous development of a 2SB mixer for 85-115 GHz using a combination of waveguide components and on-chip LO injection [2], whose results confirm the capability of such integrated structure.

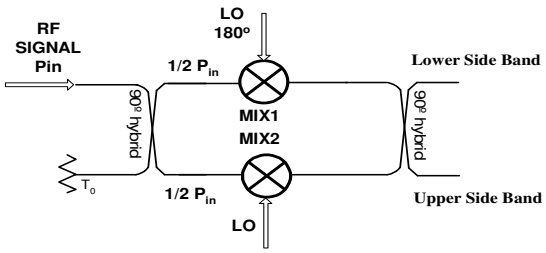

Fig. 1. Sideband-separation mixer configuration for Band 3.

II. Waveguide Quadrature Hybrid

The quadrature hybrid is used to divide equally the RF signal with a 90° phase difference. At these frequencies the branch dimensions become very small, and thus conventional waveguide 3 dB branch line coupler is extremely difficult to machine. We designed a waveguide hybrid using several microstrip probes inspired by the design with broad-wall coupling [3]. Our design provides 3 dB coupling using 6 E - field probes in each waveguide combined with short microstrip line optimized to obtain a maximum RF bandwidth. The probes are placed on quartz ($\varepsilon_r = 4.34$) with substrate dimensions of about 310 μm x 120 μm x 50 μm. The distance between the two probes is a quarter of wavelength in order to provide 90° phase difference between port 3 and port 4.

This kind of hybrid will be built into the mixer block using a split-block technique. The back-piece part of the mixer block will accommodate the microstrip probes oriented parallel to the electric field and the termination of the idle port of the hybrid.

Figure 2 shows the HFSS simulated parameters of this structure, the magnitude imbalance is of ± 0.5 dB around -3 dB in the band of interest (385-500 GHz). Whereas, the return losses and isolation are better than -15 dB. Our study of the tolerances reveals that the displacement of the branch-

line substrate along the y-axis allows a deviation of ± 10µm without changing the coupler performance any noticeable.

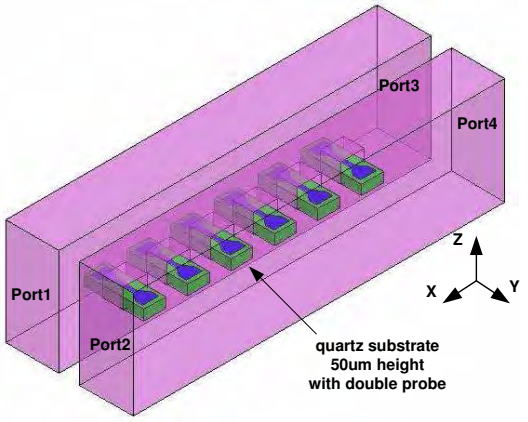

Fig. 2. 3 dB Quadrature hybrid with 6 microstrip branches sections using broadband probes.

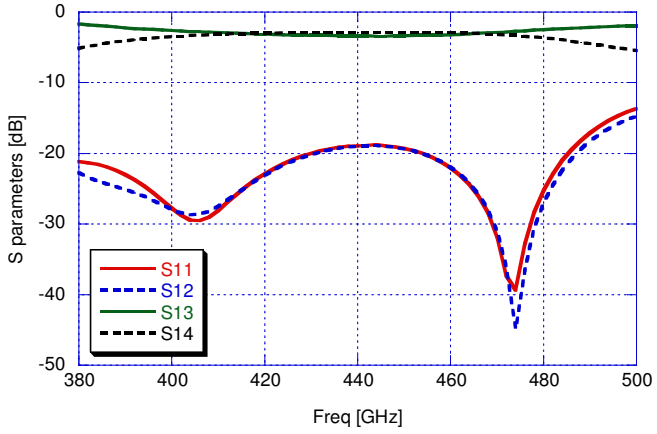

Fig. 3. S-parameters from the simulation, coupled signals (port 3 and 4) are about -3 dB and the return loss and isolation (port 1 and 2) better than -15 dB.

III. Waveguide-to-Microstrip Transition

The proposed waveguide-to-microstrip transition is made of a full-height waveguide, a fixed waveguide backshort, an E - probe with an integrated bias-T [4] using choke filters. With the aim of adding an isolated port for DC and IF signals, we connect the E-probe wide side via a $(2n+1)\lambda/4$ long line to the choke filter at the other side of the waveguide (Fig. 4). This provides isolation of the port and minimize its influence on the performance of the waveguide-to-microstrip transition because the lane has length of an odd number of quarter wavelengths and at the waveguide wall plane, the line ends on a choke structure, providing RF ground for the high impedance line and port for DC and IF signals. The quartz substrate used for this design will have a thickness of 50 µm and width of 150 µm. The RF probe is shaped in order to achieve a broadband matching between the waveguide and the probe output and to obtain as low impedance as possible at the microstrip port. According to our simulations the impedance observed at the microstrip is approximately 30 Ω see insert Figure 4, the 30 Ohm normalized Smith Chart, we can observe the "tear drop" shaped frequency dependent input impedance of the microstrip.

The probe structure is oriented perpendicular to the Pointing vector in the waveguide with an airgap underneath the substrate (see Figure 4). This airgap increases the cutoff frequency of the dielectric channel and therefore, it allows us to increasing the substrate width. The dimensions of the airgap are 10 µm x 120 µm, deeper gap will produce the excitation of higher modes. The simulated results shown in Figure 5 predict an insertion loss less than -0.05 dB and a return loss better than -15 dB at the entire band.

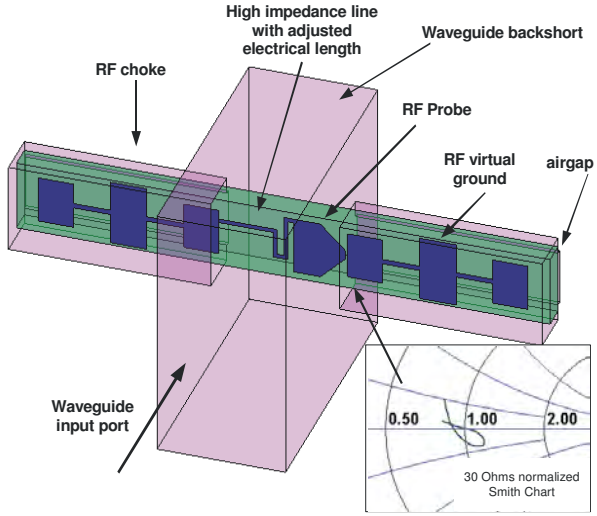

Fig. 4. Schematic drawing of the waveguide-to-microstrip transition and the 30 Ohm normalized Smith Chart showing the frequency dependent impedance at the output of the probe.

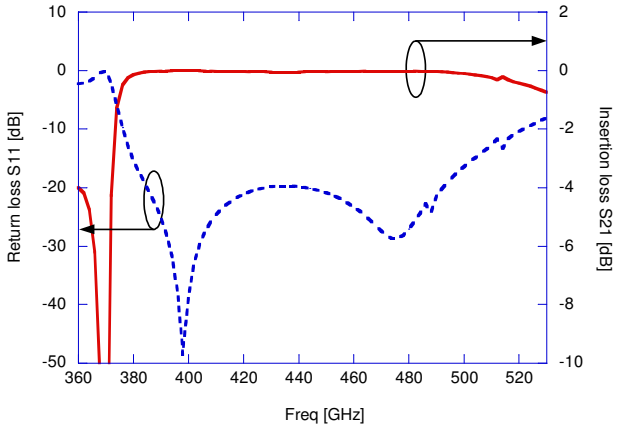

Fig. 5. Simulated results: upper curve is the insertion loss and lower curve is the return loss.

V. Mixer Block Description

The main mixer block part containing the LO in-phase power divider and the RF 3 dB coupler will be split in two parts following the split block technique, Figure 6 shows

one half of the mixer chip. The mixer blocks attached laterally to this structure will house the mixer chip together with the magnetic field concentrators for the Josephson effect suppression and all IF and the DC bias circuitry.

For the LO in-phase power divider is an E-plane Y-junction with a 3-section Chebyshev transformer from a rectangular to square waveguide has been chosen [5] due to its good performance. The radius used in this structure is equal to 0.6 mm providing a very compact design.

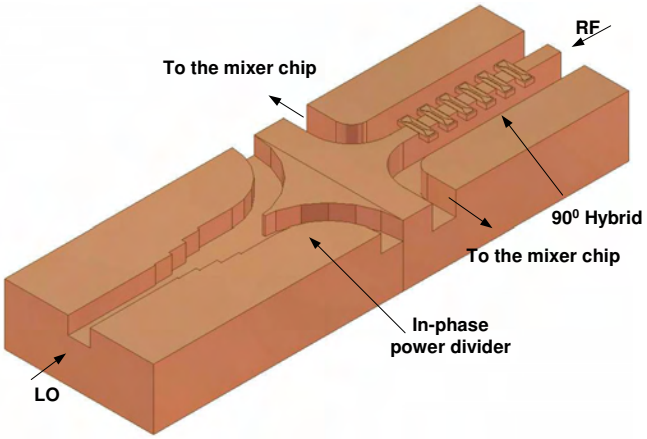

Fig. 6. Drawing of one half of the mixer block containing the LO in – phase power divider and the RF 3-dB coupler.

IV. On Chip LO Directional Coupler

The LO directional coupler, shown in Figure 7, is integrated on the mixer chip, this configuration presents a compact and alternative solution to the branch waveguide couplers that in order to provide such a weak coupling the branch waveguides should become extremely small and therefore very difficult to fabricate.

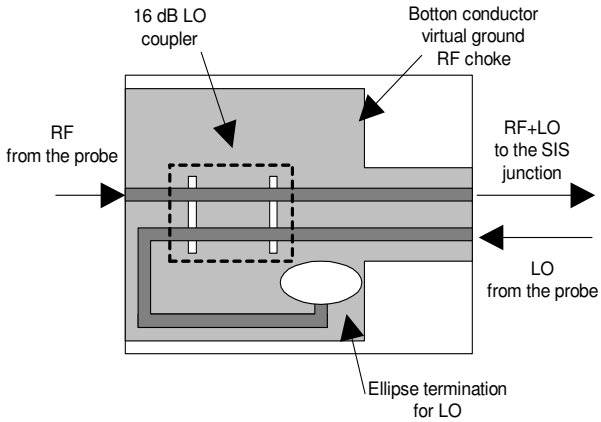

Fig. 7. Schematic drawing of the LO directional coupler with two perforations slot-holes and the ellipse termination for the idle LO port

The two in-phase LO output from the splitter will enter the mixer chip through a waveguide-to-microstrip probe at the opposite end of the RF probe, and it will be coupled to the RF path through a 16 dB directional coupler. The LO directional coupler is made with superconducting lines coupled via lumped links, the two perforations slot-holes in the ground plane on the same substrate as the SIS junction and the RF tuning circuitry. The LO idle line is terminated with an elliptical termination [5], which provides a very high and wideband performance. This termination is made of a resistive material having a sheet resistance equal to the impedance of the line [6].

VI. Conclusion

We present the design of a sideband separation mixer for 385-500 GHz. The mixer design introduces a novel 3 dB coupler, combining waveguide and microstrip components. Furthermore, the mixer include some other novel components as a waveguide probe with integrated bias-T, allowing to extract IF signals and to inject DC current as well as a high-performance ellipse termination for the LO. The first test of the receiver is planned for the beginning of 2006.

Acknowledgement

The authors would like to acknowledge Dr. Denis Meledin, GARD OSO, for his support of our modeling effort. Professor Roy Booth was always providing us with remarkable support and encouragement for successful completion of this work.

This work is part of APEX Project and is supported by the Swedish Research Council and the Wallenberg Foundation by their respective grants. EU FP6 RadioNET AMSTAR program provides support for these research activities.

References

[1] P. R. Jewell and J. G. Mangum, “System temperatures single versus double sideband operation and optimum receiver performance”, *International Journal of Infrared and Millimeter Waves*, Vol. 20, No 2, pp. 171-191, May 1999.

[2] V. Vassilev and Victor Belitsky, “Design of sideband separation SIS mixer for 3 mm band”, Proceedings of the Thirteenth International Symposium on Space Terahertz Technology, pp. 373-382, San Diego, February 2000.

[3] A. R. Kerr and N. Horner,“A Split-Block Waveguide Directional Coupler”,ALMA Memo 432, 26 Aug. 2002.

[4] Christophe Risacher Vessen Vassilev, Alexei Pavolotsky and Victor Belitsky, “Waveguide-to-microstrip transition with integrated Bias-T”, IEEE Microwave and Wireless Components Letters”, Vol.13, No. 7, July 2003, pp. 262–264.

[5] Raquel R. Monje, Vessen V. Vassilev, Alexey Pavolotsky and Victor Belitsky, “High Quality Microstrip Termination for MMIC and Millimeter-Wave Applications”, to be presented at the International Microwave Symposium, June 12-17, 2005, Long Beach, California.

[5] Monje, R., Vassilev, V., Belitsky, V., Risacher, C., Pavolotsky, A. “High Performance of Resistive Thin-Film Termination for Microstrip Lines”, Conference Digest *29th International Conference on Infrared and Millimeter Waves and 12th International Conference on Terahertz Electronics*, September 2004, pp 699-700.

Cryogenic LNA Characterization with SIS Junction as a Noise Source

E. Sundin, A. Pavolotsky, C. Risacher, V. Vassilev and V. Belitsky

***Abstract*—Radio astronomy heterodyne receivers based on SIS mixers and hot electron bolometers always use cryogenic low-noise IF amplifiers. Modern HEMT-based amplifiers have the noise temperature of a few Kelvin. In order to have good understanding of the system noise contribution it is of interest to characterize IF amplifier noise accurately. Another important reason why one should know the noise temperature of the amplifier more accurately is that this is the main parameter, which drives the amplifier design and thus is of a greater importance for cryogenic amplifier development. Widely used cold attenuator (CA) method includes several unrecoverable sources of errors such as losses in the coaxial cables, temperature dependences, temperature gradients and accuracy in measurement of the attenuators physical temperature. The error of the CA-method is of the order of ±0.5 Kelvin. This can be as much uncertainty as almost 30% of the measured amplifier noise temperature.**

This paper describes a way to improve the accuracy of the LNA characterization by using a SIS-junction as a source of shot-noise. When SIS junction biased in the linear part above the gap, the equivalent noise temperature of the shot-noise is dependent on the bias voltage and the fundamental physical constants only. The result is an extremely well defined source of noise. However, the most challenging part of this is the losses due to matching to a 50 Ω coaxial line, which is typical interface of an LNA. In order to reduce the complexity of the design and remove the need of matching network, the SIS junction should be manufactured with normal state resistance $R_n \equiv 50\Omega$. Additionally, in order to provide a wideband operation of such precession noise source a special matching circuitry is necessary to ensure the source impedance will be matched within desired frequency band of 3 - 10 GHz.

***Index Terms*— Amplifier noise, Cryogenic electronics, Noise measurement, Superconductor-insulator-superconductor devices**

I. Introduction

In most radio astronomy front-ends cryogenic low noise (LNA) HEMT amplifiers are used as a second IF stage following the superconducting mixer. For observations up to around 100 GHz HEMT can be used as a front-end. Noise temperature of the IF amplifiers (4-8 GHz) in use is typically about 5K and depending on available transistors 2-3K can be achieved [1].

The purpose of this project is to increase the accuracy for the noise characterization of the cryogenic amplifiers that is developed and built by our group. It can be used to characterize one amplifier to be a reference to compare or calibrate the usual measurement setup or directly used for amplifier characterization. The current method in use is the cold attenuator and [2] shows that the accuracy is about ±0.74K. Considering that the measured values are expected to be in the range of 4-5 K, this error is quite large to give desirable accurate measurements. Y-factor method used to make the characterization employs a noise source placed outside the cryostat; with the use of an attenuator at the amplifier input the influence of errors in loss estimation in cabling to the amplifier is reduced. Another method considered in [2] is the hot-cold method employing a variable temperature load placed inside the cryostat. The Y-factor is used also here but the physical temperature of the input load is changed inside the cryostat. Better accuracy, about ±0.40K, is estimated [2] but the change between the hot and cold states is more time consuming procedure as well as the loss with the thermal gradient in the cable connecting the load and the amplifier under the test.

The current project is based on using a superconducting tunnel junction, SIS, as source of shot-noise. Physical constants and the bias voltage define the power of the shot-noise, and thus the equivalent load temperature is defined precisely when the junction is operated in the linear region of its current-voltage characteristic above the gap voltage. The advantage of this idea compared to the usual hot-cold method is that all parts have the same physical temperature and thus no thermal gradient affecting the accuracy is presented, see Fig. 1. Consequently, the SIS noise source can be directly connected to the amplifier, which reduces possible errors in estimations of cable losses and connectors, also the change between hot and cold load occurs much quicker. Since the structure is based on superconductivity the operating temperature must be well below 9K since Niobium-based SIS is used. We have chosen dip-stick measurements, when the source and amplifier is immersed into liquid Helium providing quick method with well-known physical temperature, though the size and mechanical design of Device Under Test (DUT) is strictly limited to the Dewar's neck. In comparison the cryostat

Manuscript submitted May 2005

This work is a part of the APEX Project, supported by the Swedish Research Council and the Wallenberg Foundation by their respective grants.

Authors are with the Group for Advanced Receiver Development (GARD), Centre for Astrophysics and Space Science, Chalmers University of Technology, 412 96 Gothenburg, Sweden. Phone: +46 31 772 1833; fax: +46 31 772 1801; e-mail: erik.sundin@ chalmers.se.

method requires a cryocooler supporting 4K instead of our current 12K, but the mechanic design is less restricted.

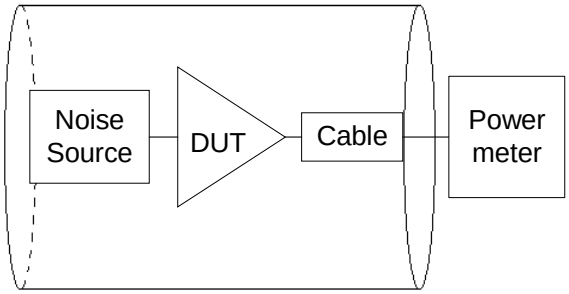

Fig. 1. Schematic of Y-factor measurement setup, where the source is placed close to the device under test and at same ambient temperature as the DUT.

II. SOURCE

The concept of this work is to use a SIS junction as the source of noise. The technique has been used since beginning of 90's as a built-in IF diagnostic system for the SIS receivers [3]. Instead, we use the SIS junction primarily for the purpose of generating noise to be able to perform accurate Y-factor measurements. Since this is the main purpose, the design can be optimized to reach as good as possible coupling between the junction and the output connector without trade-offs. When a junction is biased in its linear region, above the gap voltage, the current fluctuations when $hf << eV_0$ is given by [4] as

$$\left\langle i^2 \right\rangle = 2 \cdot e \cdot I_{bias}(V_{bias}) \cdot B \cdot \coth\left(\frac{e \cdot V_{bias}}{2 \cdot k \cdot T}\right) \quad (1)$$

where e is the electron charge, V_{bias} is the DC voltage over the junction, B is the bandwidth, k is Boltsman's constant and T is the ambient temperature. At low temperature and in the linear region the coth-term becomes unity. The shot-noise generated by the junction when biased in the linear region is defined by

$$Te = \frac{e \cdot V_{bias}}{2 \cdot k}. \quad (2)$$

This results in a linear slope of the noise temperature of Te≅5.8 K/mV. Variable load temperature Y-factor measurements can be done with the source temperature of about 20-60 Kelvin for the "cold load" bias slightly above the gap and for the "hot load" at a higher voltage, up to 10 mV. The design has been done to be reasonable insensitive to variations in the processing of the SIS structure and mounting the sample in the holder. The SIS structures are produced in-house with Nb-based tri-layer thin film processing. Substrate is crystal quartz to ensure good thermal properties since the bias point will be higher than normally used in mixers, see Fig. 2.

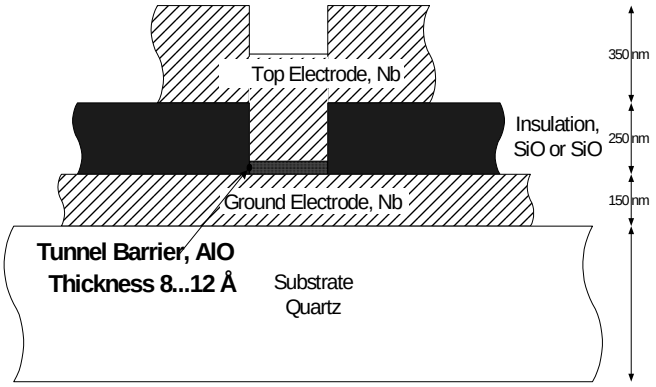

Fig. 2. Cross-section of a SIS junction used as source. Structure is built on quartz substrate with thickness of 150 micrometer. Layer thickness starts at 150 nanometer and increases with 100 nm per layer.

III. DESIGN

A. Electrical design

Considering the chip itself, the first layout was done in Agilent ADS where tuning and tests of different approaches are quick and easy. In the schematic mode in ADS no care is taken about coupling between the closely spaced components. As a complement, HFSS was used to get more accurate model of the circuit. Results from HFSS were exported to S-parameters and used in ADS since the junctions parasitics have to be taken in to account. The reason is that the layout needed to be divided into two parts since the junction should be embedded inside the model, it is also quicker to smaller simulations and combine them when a change is done only in one part of the circuit instead of redo the simulation for the complete structure. To make the source matched to the standard 50 ohm, the SIS junction is designed to have a normal state resistance (R_n) of 50 ohm. This solution with such high R_n was chosen instead of designing a matching network for a typical R_n in the range 5-15 ohms. Thus, no matching of the impedance needs to be done, and the circuit layout will consist of a fewer components and so both design/simulation will be simpler and more accurate. The actual R_n of the manufactured junction compared with the designed can differ a bit. In general, a common solution to increase the R_n is thermal annealing at 130-150 degrees Celsius. Aiming at an R_n slightly lower, say 45 ohm, the sample can be heated in a controlled way until a good result is achieved.

First idea was to have a simple chip and an external bias network, but small variations in connections from bond wires seemed to have much influence on the performance and required precise control over bonding. It was therefore decided to remove the bias network such that the bond wires to be of less influence, see Fig. 3. The chip size become 2.5 mm x 5.5 mm and is connected to the SMA connector by joining the connector against the chip with pressing pure indium in between. The same method is used for the connection to the ground. Biasing is done with 4-wire method and is DC current controlled.

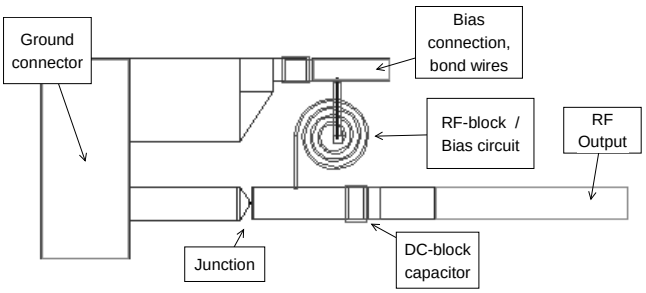

Fig. 3. Layout of the chip. To reduce the influence of shape and exact placement of bond wires, parts of the bias network is placed on the chip. This is the reason why the inductor is integrated on the chip.

B. Dip-stick

For the measurements to be done with the dip-stick the allowed dimensions were limited by the opening diameter of the Dewar, which is 50 mm, some margin is obviously needed. structure to be cooled should preferable be light to reduce the consumption of liquid helium. This limited also the design of the amplifier to be measured, and the current design had to be modified to fit in to this size. The probe part of the dip-stick is made to be flexible in sense of further changes or to be used in other projects as well if needed.

IV. MEASUREMENTS

The measurement setup consists of current source, voltmeter, power meter (power meter or spectrum analyzer) and a computer (see Fig 4) with GPIB interface to control the setup. For the first tests a spectrum analyzer was used to measure over the spectrum (3-9 GHz), also a power meter with a band-pass filter for 4.0-4.5 GHz were tested. Designed bandwidth for the amplifier is 4-8 GHz. Corrections for losses and noise contribution in the cables and the room temperature amplifier were done. More care should be taken to take the linearity and eventually offsets in to account, also R_n of the used chip was 37 ohm instead of the aimed 50 ohm and no correction were done for that in this first test.

Measurements done with the spectrum analyzer has the advantage to show the whole band for the amplifier. With the drawback of unreliable results since each point has small bandwidth and even with averaging results varies quite a lot. The results with use of a power meter were much more stable since a band-pass filter of 500 MHz was used. For now only a filter with center frequency close to the edge of band were available, instead of in the middle, which would give more reliable value of gain and noise temperature. A drawback with this approach is clearly that different filters is needed depending on which frequency should be measured.

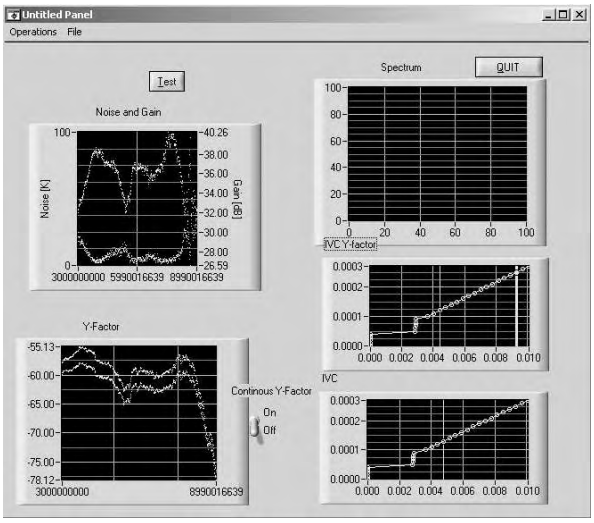

Fig 4. Print screen from the program written in LabWindows. Graphs shows the calculated DUT gain and noise temperature, the measured spectrum from the analyzer and the IVC of the junction with the used bias points used for the cold and hot load.

V. CONCLUSION

A new method for characterization of cryogenic low noise amplifiers were presented and tested experimentally. According to the first measurements the method seems promising, although much more care should be taken to provide and keep high accuracy of characterization.

ACKNOWLEDGMENT

The authors would like to thank D. Meledin for diceing of wafers and S-E. Ferm for hardware work, both at GARD. Thanks also to professor Roy Booth for providing support and encourage.

REFERENCES

[1] C. Risacher, E. Sundin, V. Perez Robles, M. Pantaleev, V. Belitsky, "Low noise and low power consumption cryogenic amplifiers for Onsala and APEX telescopes", *Proceedings of Gaas 2004*, pp. 378-378, 11-12 October 2004, Amsterdam, The Netherlands.

[2] C. Risacher, M. Dahlgren, V. Belitsky, "A low noise 3.4-4.6 GHz amplifier", in *Proc. GigaHertz 2001 Symposium*, November 26-27, 2001, Lund, Sweden; available on the web Http://gard04.mc2.chalmers.se/papers/GHz2001.pdf

[3] D. P. Woody, "Measurement of the noise contributions to SIS heterodyne receivers", *IEEE Transactions on Applied Superconductivity*, vol. 5, No. 2, June 1995.

[4] V.Vassilev "Development of a Sideband Separating SIS Mixer Technology for MM-Wavelengths", Ph.D. thesis, Dept. of radio and space sci. Chalmers Univ. Of Tech. pp. 48-54. 2003

Design of a side-band-separating heterodyne mixer for band 9 of ALMA.

F. P. Mena*, J. Kooi†, A. M. Baryshev*, C. F. J. Lodewijk‡, and W. Wild*
*Space Research Organization of The Netherlands and Kapteyn Institute
University of Groningen, Landleven 12, 9747 AD Groningen, The Netherlands
†California Institute of Technology, MS 320-47 Pasadena, California 91125, USA
‡Kavli Institute of Nanoscience
Delft University of Technology, Lorentzweg 1, 2628 CJ Delft, The Netherlands

***Abstract*— A side-band-separating (SBS) heterodyne mixer has been designed for the Atacama Large Millimeter Array (ALMA) 602-720 GHz band, as it will present a great improvement over the current double-side-band configuration under developed at the moment. Here we present design details and the results of extensive computer simulations of its performance. The designed SBS mixer exploits waveguide technology. At its core it consists of a quadrature hybrid, two LO injectors, and three dumping loads. The entire structure has been analyzed in a linear circuit simulator with custom code written to accurately (verified by HFSS finite element simulations) model the hybrid structures. This technique permitted an optimization of the dimensions and the study of the consequences of deviations from the ideal situation. It is estimated that the tolerances in several of the components should be kept at less than 3 μm. Important parts of the design are the dumping loads which, due to the involved dimensions, are not easy to implement. Therefore, we have also designed a simple load which is rather large compared with the waveguide making it relatively easy to realize at such small dimensions. It consists of a large cavity at the end of the waveguide and filled with an absorbing material. A simulation of its performance shows that besides its simplicity it can have a reflectivity as low as -40 dB if the appropriate material is used.**

I. Introduction

A well known improvement over double-side-band (DSB) mixers is the side-band separating (SBS) configuration. Contrary to to the DSB mixers, the later permits the separate detection of the upper and lower RF band frequencies. Despite this important advantage, it is not always implemented at high frequencies as the involved dimensions for the required components are prohibitory small. This is particularly true in the range corresponding to ALMA band 9 (602-720 GHz) and, hence, DSB mixers are currently being developed. However, the current state-of-the-art technology is such that, we believe, it will permit the implementation of SBS heterodyne mixers at even these high frequencies. We, therefore, have designed a heterodyne mixer in the SBS configuration containing a quadrature hybrid. The proposed waveguide structure has been extensively modeled assuming perfect load terminations. This modeling has permitted an optimization of the structure dimensions for the range corresponding to ALMA band 9. Deviations from the optimal dimensions have also been studied, which suggest that for a good performance the tolerances of several of the components have to be kept at around 3 μm. Moreover, in this article, we also propose a new design for the waveguide termination loads that will be an important component of the hybrid mixer. A new design for the loads is necessary due to the small dimensions involved. We show that with this new design a reflectivity as low as -40 dB can be achieved if the appropriate material is used.

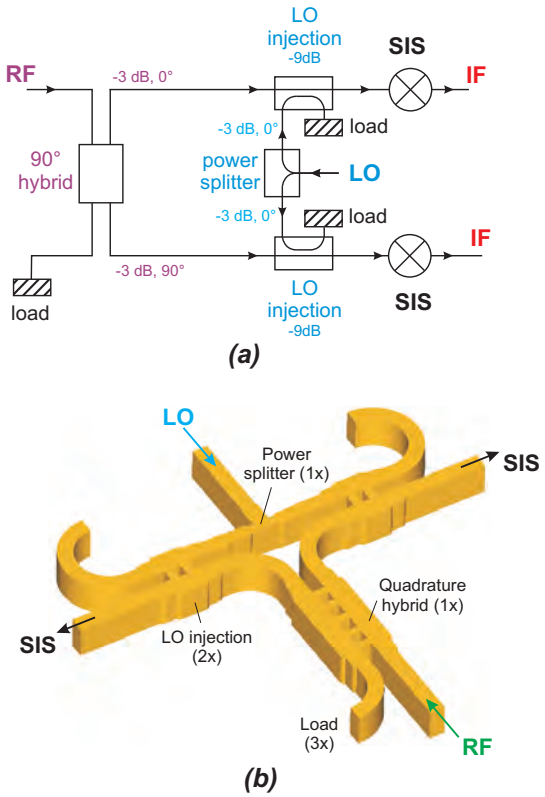

Fig. 1. *(a)* Diagram of the chosen configuration for a SBS mixer. *(b)* Core of the proposed waveguide implementation. The transversal dimensions of the waveguide are 145×310 μm.

II. Design

A. Quadrature Hybrid

A layout of the chosen configuration and the proposed implementation for the SBS mixer are shown in Fig. 1. The core of the suggested mixer consists of a quadrature hybrid, two LO injectors, and three dumping loads. Although a balanced

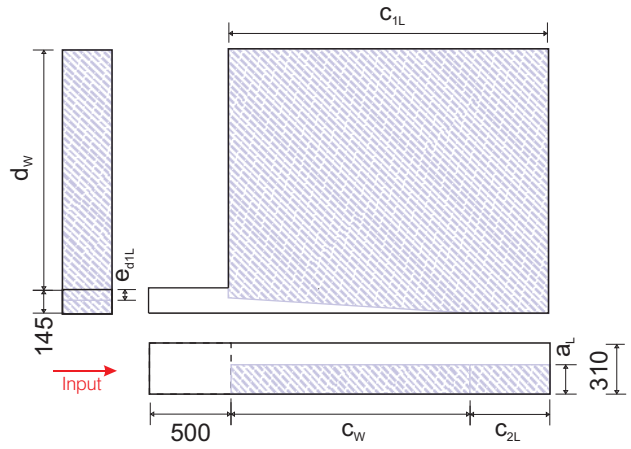

Fig. 2. Proposed design for a waveguide load (all dimensions are in μm). At the end of the waveguide, a large cavity is built which, in turn, is partially filled with an absorbing material (gray lines). The figure also shows the parameters that have been changed during the simulations.

TABLE I
PARAMETERS OF THE LORENTZ OSCILLATOR USED TO SIMULATE THE TRANSMISSION DATA OF REF. [2].

ϵ_∞	ω_o	ω_p	γ
-	GHz	GHz	GHz
4.2	15300	14220	207900

mixer containing a 180° hybrid has superior fundamental and intermodulation product suppression capabilities, its 90° counterpart is simpler and, thus, easier to implement at this frequencies [1].

B. Load

The load presented here consists of a cavity at the end of the waveguide and which is partially filled with an absorbing material. The design is depicted in Fig. 2 where the space filled with the absorbing material is represented by gray lines. This geometry should be relatively easy to make as the the largest dimensions are designed to be parallel to the splitting plane of the block. Moreover, the dimensions of the load itself are suitable to be machined by conventional means.

One candidate to be used as absorbing material is the commercially available epoxy MF112 [2], [3]. From published transmittance data [2], we have modeled its dielectric function in this frequency range with one Lorentz oscillator [4]. The corresponding parameters (presented in Table I) were used in the simulations presented in the following section.

III. SIMULATION AND RESULTS

A. Quadrature Hybrid

The construction presented in Fig. 1 has been analyzed in a linear circuit simulator with custom code written to accurately model the hybrid structures. The results were verified by HFSS finite element simulations. This has the advantage that the effect of non-ideal termination impedances may be examined. In the ideal situation, the SIS junctions are well matched to the probe impedance and the waveguide terminations are ideal. This maybe regarded as an ”upper performance limit”. In the non-ideal situation the port mismatch is chosen to be 25% (-12 dB return loss).

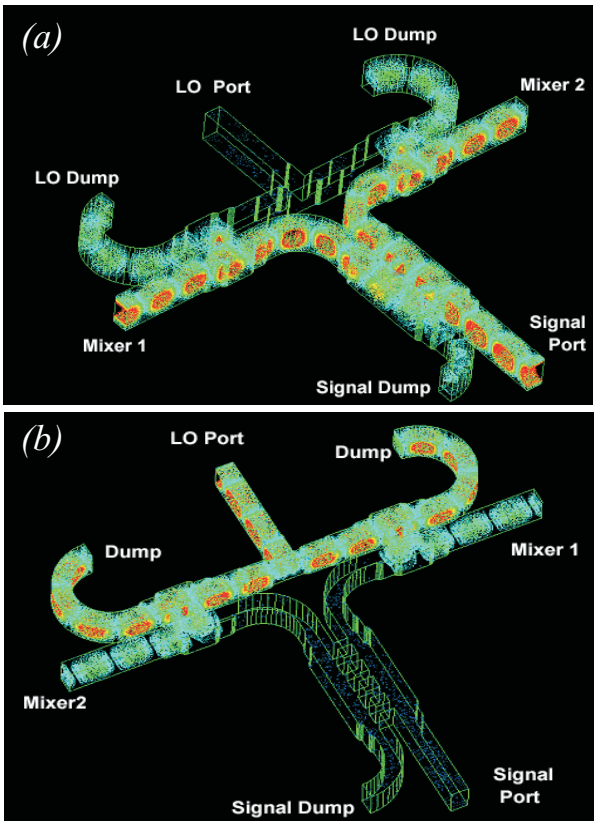

Fig. 3. *(a)* Electric field distribution with the signal port excited. The input signal is split 50% with a 90° phase difference between the two output ports. By design approximately 10% of the LO signal is coupled into the signal path. *(b)* Electric field distribution with the LO port excited. Approximately 10% of the available LO power couples to the mixer path, with the remaining 90% of the LO terminated. In both cases the simulation frequency is 660 GHz.

The results of the simulations are summarized in Figures 3 through 5. First, to illustrate how the various components of the proposed hybrid perform in the ideal situation, in Fig. 3 we show the electric field distributions when *(a)* the signal and *(b)* the LO ports are excited independently. In the former case, the input signal is split 50% with a 90° phase difference between the two output ports. By design approximately 10% of the LO signal is coupled into the signal path, and it follows from reciprocity that 90% of the signal will couple to the LO path (dump). The loss of 10% was deemed acceptable. When the LO port is excited, approximately 10% of the available LO power couples to the mixer path, with the remaining 90% of the LO terminated. It has to be noted that the device will operate at 4 K.

Figure 4 shows the sideband rejection ratio in the ideal (upper limit) and non-ideal situations (lower limit). Note that the latter case although includes power and phase imbalances, it does not include IF and mixer gain imbalances. Finally,

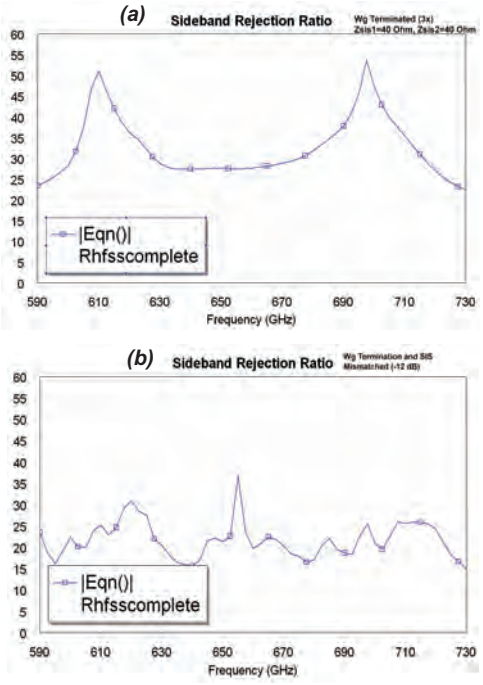

Fig. 4. Sideband rejection ratio in the *(a)* ideal and *(a)* non-ideal situations. In the non-ideal scenario, the SIS junction and waveguide termination are presumed to be mismatched by 25% (Return loss = -12 dB). The results include power and phase imbalances, however do not include IF and mixer gain imbalances.

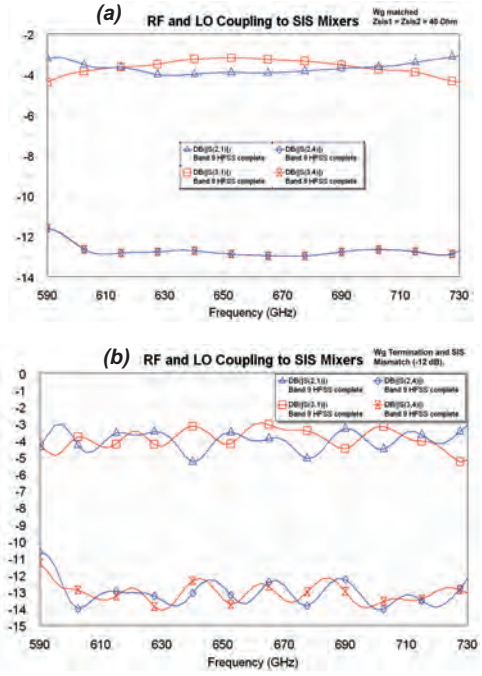

Fig. 5. RF and LO coupling to the SIS junctions in the *(a)* ideal and *(b)* non-ideal cases.

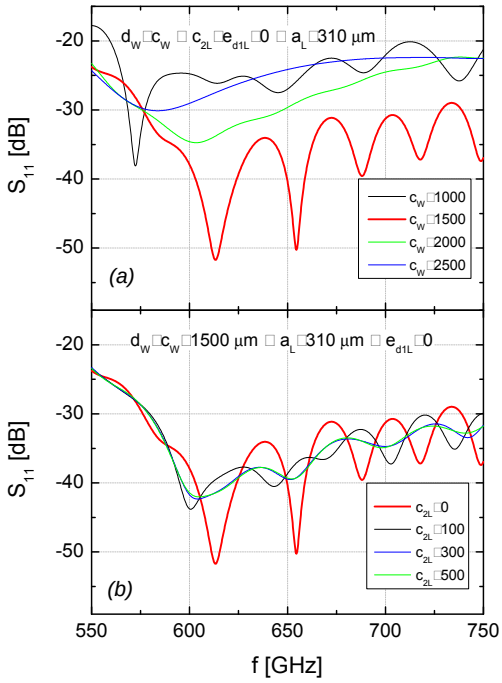

Fig. 6. Resulting S_{11} coefficient when the dimensions *(a)* c_W and *(b)* c_{2L} are varied.

Fig. 5 presents the RF and LO coupling to the SIS junctions in both cases. The LO power coupling balance is critically dependent on both LO dumps having the same termination impedance. In turn this will affect the pumping level of the individual mixers and their mixer gain (mixer gains ought to be closely matched).

B. Load

The one-port system depicted in Fig. 2 was simulated in CST Microwave Studio [5] with the load material simulated according the parameters given in Table I. The geometrical parameters varied during the simulations are length of the load cavity (c_W), cavity width (d_W), height of the load (a_L), and matching between the waveguide and the load material (e_{d1L}). All of them are also shown in Fig. 2. In the first place, by varying c_W and d_W (with $a_L = 310$ and $c_{2L} = e_{d1L} = 0$), we have found that the overall lowest reflectivity is achieved when $c_W = d_W = 1500$ μm (Fig. 6a). At that values, the reflectivity shows a series of oscillations that are rapidly *washed out* by increasing c_{2L} (Fig. 6b).

Our load design is prone to two kinds of errors, air gaps ($a_L < 310$ μm) and geometrical mismatches between the waveguide and the load ($e_{d1L} \neq 0$). These errors have been simulated and the results are presented in Fig. 7a. The load performance is not degraded substantially in the presence of large air gaps. As shown in Fig. 7a, a gap as large as half the waveguide height, still produces a reflectivity bellow -20 dB. Regarding the geometrical mismatch e_{d1L}, small changes

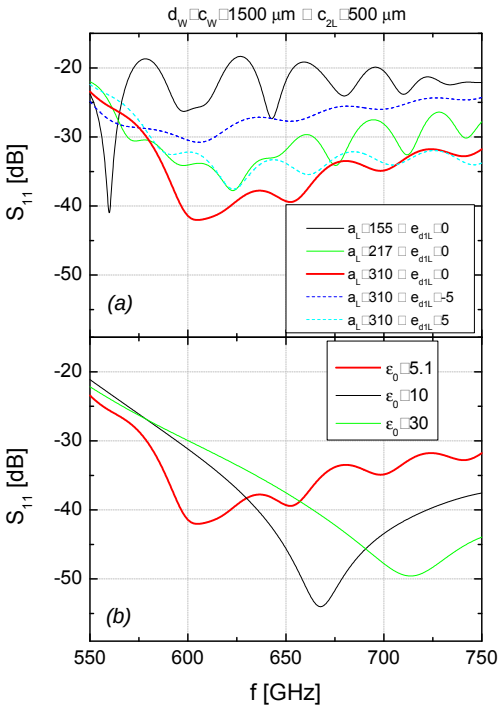

Fig. 7. Simulation of the load performance when : *(a)* mounting errors ($a_L < a$; $e_{d1L} \neq 0$) are present and *(b)* different materials are used.

in both directions produce a rather large degradation of the performance of the load. However, errors as large as 20 μm produce still a reflectivity below -20 dB (not shown here).

Finally, we have modeled the performance of the load with different materials. This have been simulated by changing the Lorentz model given in Table I. The specific parameter changed is the static value of the dielectric function ($\epsilon_0 \equiv \epsilon(0) = \epsilon_\infty + \frac{\omega_p^2}{\omega_0^2}$). Fig. 7b shows the results that demonstrate the ability of our design to perform efficiently with a wide range of materials.

IV. Conclusions

In conclusion we have presented a design for a side-band-separating mixer for the frequency region corresponding to ALMA band 9. Its ideal and non-ideal properties have been presented from which it is estimated that tolerances in some of the components should be as low as 3 μm. We think these tolerances are achievable with state-of-the-art micromachining, which is confirmed by the first promising attempts [6]. A design of a new load has also been presented. Its relatively large dimensions respect to the waveguide make it appropriate for high frequencies. Moreover, the results of the simulations indicate that the design is very robust as can tolerate rather large mounting errors and a wide variety of absorbing materials.

References

[1] J. W. Kooi, A. Kovacs, B. Bumble, G. Chattopadhyay, M. L. Edgar, S. Kaye, R. LeDuc, J. Zmuidzinas, and T. G. Phillips, *Heterodyne Instrumentation Upgrade at the Caltech Submillimeter Observatory*.
[2] G. A. Ediss, A. R. Kerr, H. Moseley, and K. P. Stewart, "FTS Measurements of Eccosorb MF112 at Room Temperature and 5 K from 300 GHz to 2.4 THz", ALMA Memo 273, 2 September 1999.
[3] http://www.eccosorb.com/.
[4] F. P. Mena and A. Baryshev, "Design and Simulation of a Waveguide Load for ALMA-band 9", ALMA Memo 513, 5 January 2005.
[5] http://www.sonnetusa.com/.
[6] Private communication, Radiometer Physics GmbH, http://www.radiometer-physics.de.

Broadband Fix-tuned Receivers Using Same Block

Faouzi Boussaha, Morvan Salez, Yan Delorme, Benoit Lecomte, Frédéric Dauplay, Alexandre Féret, Jean-Michel Krieg, Joseph Spatazza[1], Christine Chaumont[2], Michel Chaubet[3]

***Abstract*—We present the performances of two sensitive submillimeter receivers operating in distinct bandwidth ranges: 330-540 GHz and 430-660 GHz, by using a unique robust, assembly-friendly, space-qualified fix-tuned mixer block. Only the corrugated horns and SIS devices have been swapped. The Fourier Transform Spectrometry measurements show 50% frequency bandwidth and the uncorrected measured DSB noise temperatures were less than 7 times the quantum limit in both cases.**

***Index Terms*—Fix-tuned mixer block, twin SIS junction, broad bandwidths.**

I. Introduction

Low noise fix-tuned broad band heterodyne receivers are needed for many projects presently in progress: HIFI heterodyne instrument for space-based telescope Hershel and ground-based interferometer ALMA composed of 64 12-m antennas. Within the framework of HIFI channel 1, i.e 480-640 GHz frequency range, Salez et al [1] have developed a high-performance SIS mixer producing state-of-the-art results; i.e they obtained noise performances better than 3 times the quantum limit over the whole 30% bandwidth. They have used a space-qualified fix-tuned mixer block, in which was mounted an SIS chip fabricated at IRAM [2]. In this paper, we present similar high-performance measurement results at 330-540 GHz, i.e a bandwidth including ALMA band 8, using same robust block. Indeed, HIFI band 1 block has a peculiarity that only the feedhorn section is frequency-band dependant, housing the horn itself, the waveguide transition, the waveguide and the substrate channel, forming a single part (see below). Switching from HIFI band 1 to ALMA band 8 simply meant swapping the corrugated horn and the SIS chip and keeping the rest of the mixer unit identical. In order to compare the performances, we also present FTS and heterodyne measurements obtained with mixer using SIS circuit designed according to Paris observatory fabrication process and operating in HIFI channel 1 band.

Faouzi Boussaha, Morvan Salez, Yan Delorme, Benoit Lecomte, Frédéric Dauplay, Alexandre Féret, Jean-Michel Krieg are with LERMA - Observatoire de Paris, 61 avenue de l'Observatoire 75014 Paris – France (phone: +33-1-40512069; fax: +33-1-40512085; e-mail: faouzi.boussaha@obspm.fr).

[1]CNRS-INSU, Division Technique, 1 place Aristide Briand, 92195 Meudon – France

[2]GEPI-Pôle Instrumental-Observatoire de Paris, 61 avenue de l'Observatoire 75014 Paris – France

[3]CNES - BP 2220, 18 avenue Edward Belin 31401 Toulouse Cedex 4 – France

II. Receivers

A. Mixer Block

As seen in Fig. 1, our mixer block is divided into two functional components: (a) component including DC supply circuit, the 4-8 GHz IF circuit and the coils, (b) horn component in which is placed the mixer device. It is made up of copper corrugated horn, the waveguide transition, the waveguide and the substrate channel thus forming a single part. The local oscillator (LO) and RF signals are conveyed to the mixer chip via a half-height rectangular waveguide. The mixer device is fabricated on a fused quartz substrate, placed into a channel perpendicular to the waveguide as shown in figure 1-c. The table 1 summarizes the principal horn component dimensions and substrate thickness according to the bands.

TABLE 1 HERE

The waveguide/substrate transition allowing quasi-TEM-mode in microstrip line is realized by a bow-tie antenna whose impedance is real ~ 50 + j0 Ω over the two frequency bands, thanks to the optimisations using CST-Microwave Studio [3]. Made of the simple plain flat metal part, the backshort, which is into component (a), closes both the substrate channel and the waveguide-end and comes to contact the block (b) between the air-gap of a cryoperm core (see fig. 1-c). In both cases, the microstrip faces the backshort.

FiG. 1 HERE

Consequently, the block manufacturing and assembly are deeply simplified. The undesirable Josephson currents are suppressed by a magnetic field, which is generated by NbTi superconductive wire coiled around a cryoperm core made of a single piece and folded into the proper shape. The IF coupling is provided by an optimized microstrip-to-coaxial 90° transition using a spring bellow, allowing a simple and fast mixer block mounting procedure and avoiding the risks of electrical contact disruption during cool-downs. The principles of this compact (32x32x40 mm^3) and light (67 g) mixer block

design have been well described in [4]. It is machined by SAP: Société Audoise de Précision [5]. As we mentioned above, the mixer block, initially developed for HIFI space instrument, was space qualified by submitting to vibration tests, electromagnetic compatibility (EMC) tests, and thermal cycling tests between 360 K and 4.2 K. It successfully passed all these tests.

B. Detectors and fabrication

The mixer devices are based on double Nb/AlO_x/Nb junction tuning circuit [6-7]. We chose an average current density of 10 kA/cm². The devices were initially optimised to operate in ALMA Channel 8 band: 380-500 GHz and HIFI Channel 1 band: 480-640 using same techniques employed for HIFI channel 1 developments [8-10]. The junction areas are respectively 1.3x1.3 µm² with $R_n \approx 10\ \Omega$ and 1.4x1.4 µm² with $R_n \approx 6\ \Omega$. The intrinsic capacitance measured is C_J=81 fF/µm². The voltage gap is ~ 2.82 mV. Their quality defined as the ratio of the subgap current at 2 mV to the normal resistance ratio (R_{SG}/R_n) is ~ 15 average.

FiG. 2 HERE

All SIS devices were fabricated at Paris observatory facility using standard SNEP (Selective Niobium Etching Process) technique [11] based on standard optical lithography process. The 0.2 µm niobium base electrode, the 0.01 µm aluminium, and 0.1 µm upper niobium films are DC sputtered. The tunnel barrier is built by thermal oxidation of the aluminium layer, using pure O_2 before upper niobium deposition. The bow-tie antenna and RF filters were defined by photolithography technique. A 0.25 µm SiO layer was evaporated to isolate the junction's area and to make a dielectric for RF tuning circuits. The photolithography follow-up the lift-off of 0.35 µm counter-electrode niobium allows to connect the junctions and to define the upper electrode of the RF tuning circuits. It was DC sputtered. Finally, a 0.2 µm gold film was evaporated in order to obtain the electrical contact.

III. Results

The SIS mixer is cooled down to 4.2 K in a cryostat. The IF signal is amplified by a 4-8 GHz cryogenic HEMT preamplifier. A current of less than 10-mA was sufficient to produce a flux of two quanta ($2\Phi_0$), allowing the quasi-total suppression of Josephson effect. The IF matching is provided by a 50-Ω microstrip line on an alumina board, contacting a coaxial SMA plug at 90°. The local oscillator signals were provided by two solid-state sources which cover the 385 to 500 GHz range. On their quasioptical path, RF and LO signals encounter a 13-µm mylar beam splitter, a 25-µm mylar cryostat window, a 250-µm Zitex infrared filter and two cold elliptical mirrors before arriving at the mixer feedhorn.

A. Fourier Transform Spectroscopy

Direct detection responses, obtained by FTS measurements, reveal a 50 % relative bandwidth in both cases as shown in Fig. 3. The measurements were made without vacuum environment. We note the water transitions at 385 GHz and 557 GHz, as two clear absorption features.

B. Heterodyne measurements

Fig. 4-c and 4-d show the uncorrected DSB receiver noise temperatures measured over a 385-500 GHz and 490-700 GHz frequency range. Below 385 GHz, the measurements were not possible due to lack of LO source operating at these frequencies. DSB receiver noise temperature is measured by standard Y-factor method: $Y=P_{hot}/P_{cold}$ where P_{hot} and P_{cold} are respectively the measured IF output power using hot (298 K) and cold (170K) blackbody sources as the input signal. The IF output power versus DC bias voltage for both load temperatures are shown in Fig. 5.

FiG. 3 HERE

FiG. 4 HERE

For the lower band, the noise temperatures are relatively homogeneous over the whole bandwidth.The lowest noise temperature is 95 K measured at 474 GHz and the highest is 142 K at 385 GHz. For the higher band, the DSB noise temperatures were below 160 GHz expect at 641 GHz where we measured 190 K. This increase is due to the very low output power of our LO chain at this frequency. The quasioptical contribution was estimated around 40 K using the intersecting lines technique [12]. The IF noise is about 15 K, as deduced using the shot noise in the twin SIS junctions as a calibrator. In this case, the corrected noise temperatures; i.e subtracting the quasioptical loss contribution, are equivalent to about 3 times the quantum limit.

FiG. 5 HERE

IV. Conclusion

We have measured two fix-tuned mixers designed to operate in two different band frequencies: 385-500 GHz and 480-640 GHz, using the same mixer unit. It was possible thanks to judicious concept of the mixer block where only the corrugated horn is swapped. The FTS measurements showed a relative bandwidth of 50% in both cases. The uncorrected DSB noise temperatures are between 95 and 142 K for lower band and between 97 -190 K for the higher band at 4.2 K. In addition, we expected similar performances for any wide band from 200-800 GHz using the same Nb process, by simply manufacturing band-specific front sections consisting each of the adequate corrugated feedhorn, waveguide and SIS device.

Acknowledgment

This work has been funded by the Centre National de la Recherche Scientifique (CNRS)-Institut National des Sciences de l'Univers (INSU). The french space agency CNES has funded the HIFI channel 1 project and has co-funded with CNRS this development. We would like to thank G. Beaudin,

J-M. Lamarre, Y. Viala and P. Encrenaz for their continued support and I. Peron and K.F. Shuster for their fruitful discussions.

REFERENCES

[1] M. Salez , Y. Delorme, B. Lecomte, I. Péron, F. Dauplay, A. Féret, J. Spatazza, J.-M. Krieg, K. Schuster " Space-qualified SIS mixers for Herschel Space Observatory's HIFI Band 1 instrument ", ISSTT2005

[2] Institut de RadioAstronomie Millimétrique, 300 rue de la Piscine, Domaine Universitaire 38406 Saint Martin d'Hères, France

[3] Computer and Simulation Technology : www.cst.com

[4] M. Salez, Y. Delorme, I. Peron, B. Lecomte, F. Dauplay, F. Boussaha, J. Spatazza, A. Féret, J-M. Krieg, K. Schuster, "A 30% bandwidth tunerless SIS mixer of quantum-limited sensitivity for Herschel/HIFI band 1", Millimeter and Submillimeter Detectors for Astronomy, Hawaii, USA, SPIE Proc.Vol.485522-28 août 2002.

[5] Société Audoise de Précision, Z.A du pont 81500 Ambres, France

[6] J. Zmuidzinas, H. G, LeDuc, J. A. Stern, and S. R. Cypher, "Two-Junction Tuning Circuits for submillimiter SIS Mixer", IEEE Trans. Microwave Theory Tech, vol. 42, pp. 698-706, 1994.

[7] V. Y. Belitsky, M. A. Tarasov, S. A. Kovtonjuk, L. V. Filipenko, and O. V. Kaplunenko, "Low noise completly quasioptical SIS receiver for radiosatronomy at 115 GHz", Int. J. Infrared and Millimeter wave, Vol. 13, pp. 389-396, Apr. 1992.

[8] Gurvitch, M. A. Washington, H. A. Huggns, Appl. Phys. Lett., No. 42, p. 472, 1987.

[9] M. Salez, Y. Delorme, M. H. Chung, F. Dauplay, "Simulated performance of multi-junction parallel array SIS mixers for ultra broadband submillimeter-wave applications", Proc. 11th International Symposium on Space Terahertz Tech. 343. May 2000.

[10] M. Salez, Y. Delorme, F. Dauplay, B. Lecomte, I. Peron, K. Schuster, "Design and evaluation of a fix-tuned 30% bandwidth SIS receiver for FIRST/HIFI band 1 (480-640 GHz) and other space applications", WOLTE 4 : Proc. 4th European Workshop on Low Temp. Electron., ESTEC, Noordwijk, The Netherlands, 21-23 june 2000.

[11] F. Boussaha, Y. Delorme, M. Salez, M.H. Chung, F. Dauplay, B. Lecomte, J.-G. Caputo, V. Thevenet "A superconductor parallel junction array mixer for very wide band heterodyne submillimeter-wave spectometry", Proc. 13th International Symposium on Space Terahertz Tech, pp. 291-297, 2002.

[12] R. Blundell, R. E. Miller, and K. H. Gundlach, "Understanding noise in SIS receiver", Int. Journal of Infrared and millimeter wave, Vol. 13, No. 1, 1992.

TABLE I
PRINCIPAL HORN COMPONENT DIMENSIONS

	ALMA Band 8	HIFI Band 1
Substrate thickness (µm)	60	50
Channel width (µm)	160	130
Rectangular Waveguide (µm)	500x125	400x100

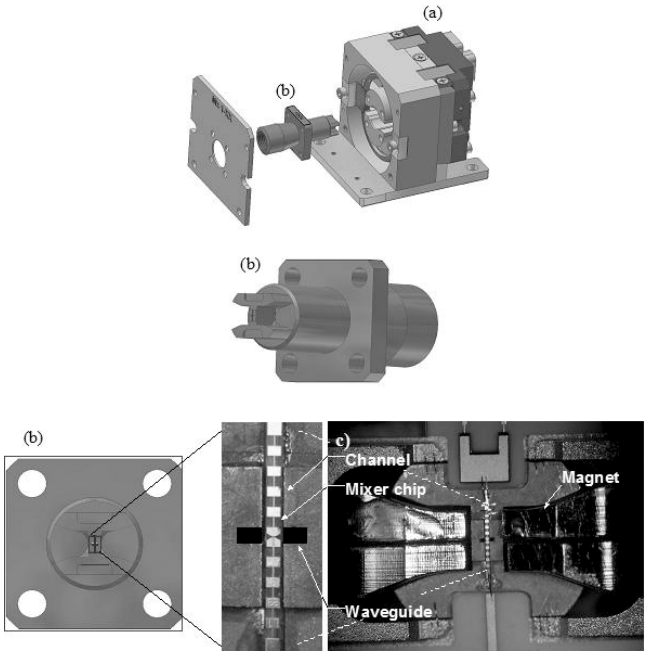

Fig. 1. Views of our mixer block: (a) component including DC supply circuit, the 4-8 GHz IF circuit and the coils, (b) horn component made up of corrugated horn, the waveguide transition, the waveguide and the substrate channel . View (c) shows mixer chip placed into substrate channel perpendicular to the waveguide and the magnet.

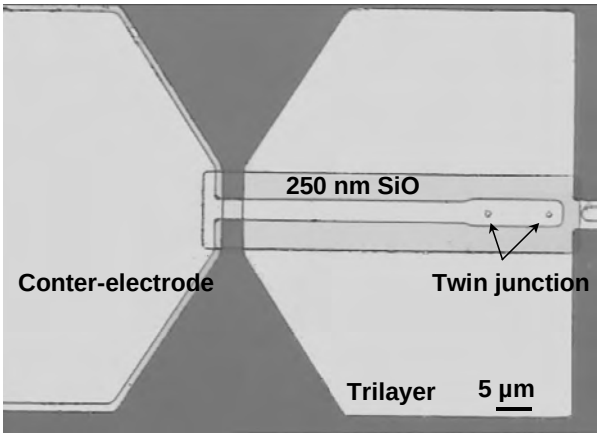

Fig. 2. Optical microscope image of twin parallel. The $Nb/AlO_x/Nb$ SIS junctions are 1.3x1.3 µm².

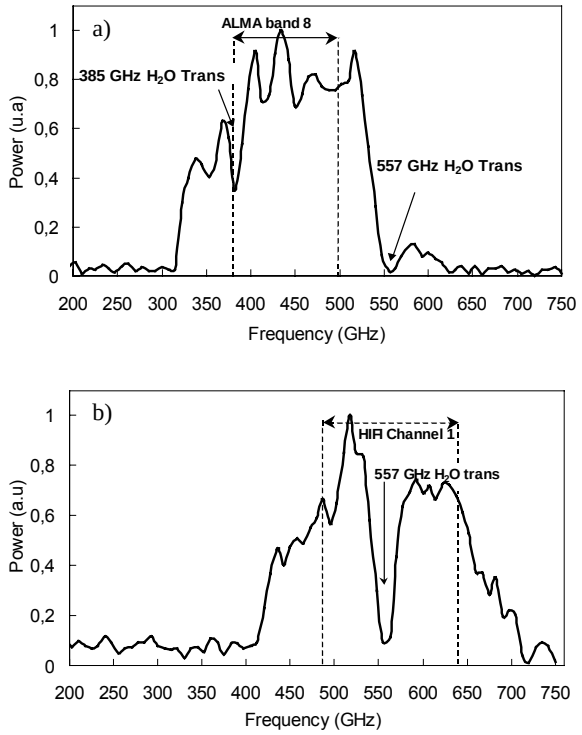

Fig. 3. Direct detection response of two mixers using same mechanical block by swapping only the horns. The measurements were made without vacuum at 4.2 K.

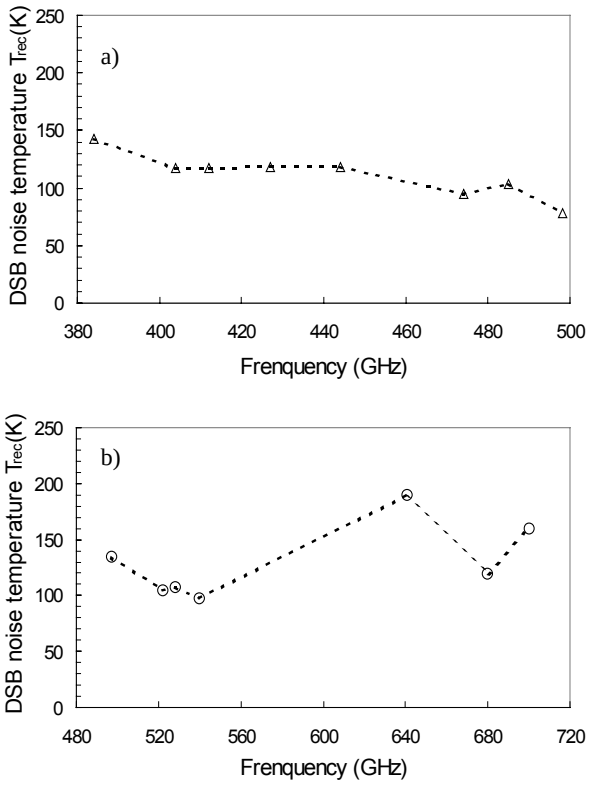

Fig. 4. Uncorrected DSB noise temperatures receiver versus frequency of two mixers measured at 4.2 K.

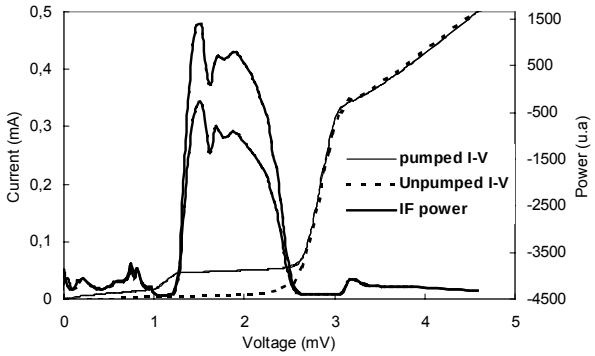

Fig. 5. IF output powers, unpumped and pumped I-V curves versus voltage bias for ALMA device at 385 GHz using hot (298K) and cold (170K) loads.

Results and Analysis of HIFI Band 2 Flight Mixer Performance

R. Teipen, M. Justen, T. Tils, M. Schultz, S. Glenz, P. Pütz, K. Jacobs, C.E. Honingh
Kölner Observatorium für Submillimeter-Astronomie, KOSMA
I. Physikalisches Institut, Universität zu Köln
Zülpicher Straße 77, 50937 Köln, Germany
Email: rteipen@ph1.uni-koeln.de

***Abstract*— We present the flight mixers for Band 2 of the HIFI instrument on the Herschel satellite observatory [1], [2]. Three flight mixers are produced, tested and delivered. They are shown to be fully space qualified by environmental tests on identical prototypes. After subtracting the noise of the optics and external IF-components the RF-performance requirements for the receiver-noise inside the instrument ($T_{Rec} = T_{Mix} + 10\ \mathrm{K}/G_{Mix}$) of 110 K at 636 GHz and 150 K at 802 GHz are met for 75% of the band within an assumed error of ±15 K in noise temperature. The IF-output power variation is well below 2 dB. The limits in performance of the fabricated devices are analyzed and compared with theory [3]. Possible noise mechanisms are discussed and estimated.**

The mixing elements are SIS-devices (single Nb/Al_2O_3/Nb-Junctions) with a current density of 13-14 kA/cm^2 with a NbTiN/SiO_2/Nb-matching circuit, which are fabricated at KOSMA [4], [5]. Waveguide environment and probe are designed by simulation with a 3D-simulation software, which is also used to investigate the detailed IF performance. The waveguide blocks and the IF circuits are also fabricated in house.

I. Introduction

In this paper we present the SIS mixers for band 2 of the HIFI instrument for the Herschel satellite observatory. The performance for HIFI is specified as 110-150 K input noise temperature over the 636-802 GHz band for the mixer and the low noise 4-8 GHz amplifier (T_{IF}=10 K) together. In addition to these performance requirements, the mixer design is subjected to numerous environmental constraints to insure the reliable operation of the mixer during test, launch and operation.

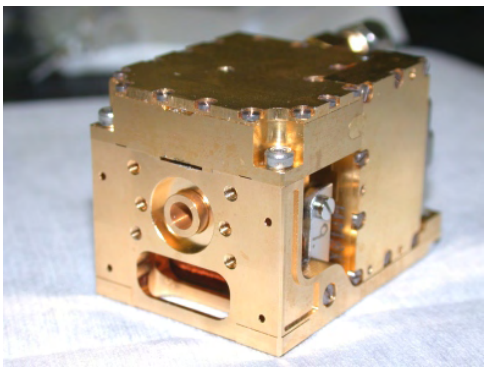

Fig. 1. Photo of mixer flight model hardware for HIFI frequency band 2.

II. Mixer Design

As part of a space project the mixer unit has to comply to the given interfaces of the rest of the instrument. The performance requirements for the different components of the mixer *especially RF- and IF-performance* have to be met. At the same time all components have to fulfill specific environmental requirements: thermal hardness during bake-out before launch, mechanical stability during launch and reliability during operation in space etc. In order to achieve the requirements for each single component of the mixer a modular mechanical design was applied. So one component could be tested, improved or exchanged without a complete redesign of the entire mixer.

A. Mechanical Design

The whole mixer has to fit into an envelope of $32 \times 32 \times 45$ mm^3. The maximum allowed mass is 80 g. A sketch of the major components is given in figure 2.

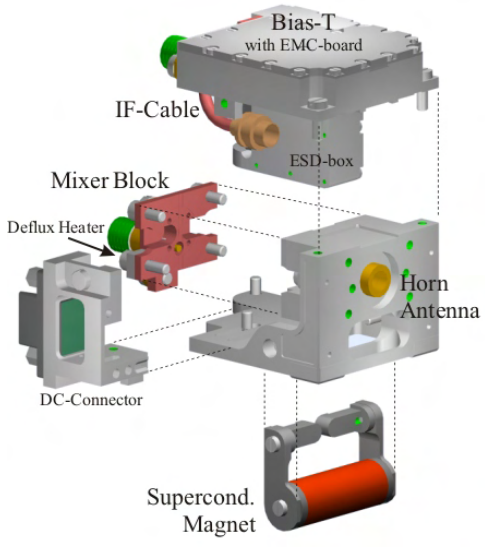

Fig. 2. The components of the mixer are mixer block with heater and SIS-device, horn antenna with bracket, bias-T with ESD- and EMC-protection, DC-connector and super-conducting magnet.

The mixing SIS-device is in the substrate channel across the waveguide of the the copper fixed tuned waveguide mixer

block. Details of the block and the mounting of the SIS-device are given in [6]. The mass of the block is reduced to meet the HIFI mass budget. For selection of the devices, the performance of an SIS-device could first be tested in its mixer block in another test mixer environment. The mixer blocks with the best devices were assembled with the flight hardware.

The mixer block and its waveguide is connected and positioned to the corrugated feed horn and its bracket via dowel pins and screws. The horns were fabricated by Radiometer Physics [7] for a center frequency of 720 GHz (for characterization see [8], [9]). Fabrication tolerances in the outer reference cylinder of the horns were compensated by adapting a dedicated bracket for each horn.

The mixer block is connected to the bias-T with an SMA connector and semi rigid cable. In the bias-T the DC connections are protected against electro-static discharge (ESD) and shielded against electro-magnetic interference (EMI). The bias-T consists of two compartments: one compartment (on top of the mixer) for the DC-connection to the semi rigid cable with the EMI-protection and a second compartment besides the mixer block with a circuit for protection against ESD from the DC-connector to the sensitive mixer device.

To suppress the Josephson effects in the SIS-junction a superconductive magnet is used. The maximum allowed current here is 10 mA, which leads to a magnet of 10,000 turns of 70 μm thick NbTi copper cladded wire. The pole pieces are out of pure iron ($\geq$99.9 %).

The second DC-connector (front left in figure 2) provides the electrical connection for the mixer deflux heater, consisting of a thermally well connected 1.5 kΩ SMD resistor, and the magnet current.

B. RF-Design

The SIS-device is located in a substrate channel perpendicular to the waveguide. An asymmetric stripline waveguide probe couples the radiation to stripline modes and is integrated with an RF-blocking filter. The impedance of the waveguide

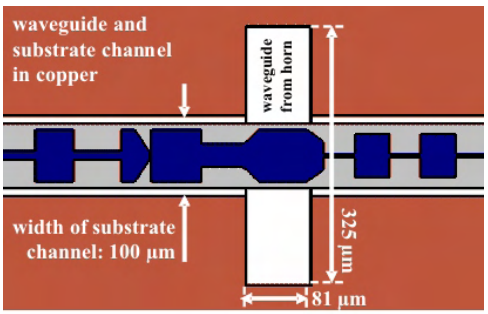

Fig. 3. Schematic concept of the asymmetric stripline waveguide probe, optimized for low waveguide impedance ($\approx$ 30 Ω).

probe is determined and optimized by a full electro-magnetic 3-dimensional time domain analysis software [10]. A sketch of the optimized waveguide model is given in figure 3.

To couple the radiation from the waveguide in the SIS-junction, a three step transformator as resonant matching circuit is used. It transforms the waveguide impedance to the lower impedance of the junction and compensates the intrinsic capacitance of the junction.

As mixing element in the HIFI frequency band 2 (636–802 GHz) superconductor-isolator-superconductor junctions (SIS) are used. The layout of the devices is depicted in figure

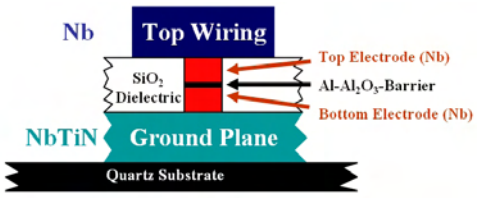

Fig. 4. Cross section of an SIS junction of a HIFI mixer chip

4. As junction electrode material in this frequency region the well known material Niobium can still be used. The Nb/Al-Al_2O_3/Nb junction is embedded in an NbTiN/SiO_2/Nb resonant microstrip tuning circuit, processed on a fused quartz substrate.

For a good coupling a lossless stripline would be ideal. A superconductor with a gap-frequency well above the frequency band 2 is NbTiN. Optimum coupling with negligible losses in the stripline would be with NbTiN as ground-plane and top-wiring. Because this causes heat trapping due to Andreev-reflection at the interface of the the Nb-electrode with the NbTiN-wiring [11], the top-wiring is made of Niobium despite the losses of this material above 700 GHz, which makes cooling of the Nb junction electrode via the top-wiring possible.

Aluminium top-wiring which could be used as an alternative for Nb shows a better conduction than Nb above 750 GHz, but would give a considerably worse performance below 750 GHz, and especially below 700 GHz. So for an optimum overall band performance Nb is the best choice. In addition Nb is also more rugged than aluminum as a top electrode material, which is an advantage for environmental testing. The NbTiN quality which is determined by the critical temperature and the DC resistivity at 20 K was improved compared to the process described in [4] by heating the substrate to 400°C during the reactive magnetron sputtering process of this layer.

The stringent requirements on the RF performance of the mixer demand in particular an accurate junction definition (size and alignment) in addition to a low loss integrated tuning circuit. Variations in the junction area shift the center of the frequency band, where the matching circuit is optimum. A variation in the junction width of Δl_{SIS}=0.1 μm, which is typical for UV-lithography, results in a shift of the frequency band of $\approx$15 GHz or a relative reduction in power coupling at a fixed frequency of $\gtrsim$30 %. With a relative bandwidth of 23 % and the stringent performance requirements for the mixers this means, a variation in junction width of Δl_{SIS}=0.1 μm results in a performance which is far from the specification (see figure 5). For a broadband matching there is a high priority to produce devices with a definite submicron junction area. This is achieved by the use of electron-beam lithography and

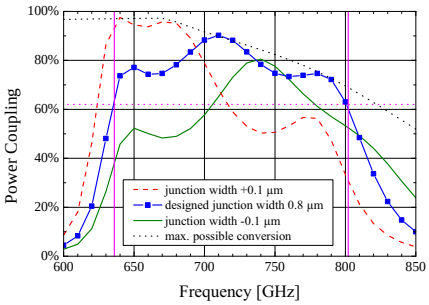

Fig. 5. Analysis of variation in junction width. A change of Δl_{SIS}=0.1 μm results in a strong shift of the frequency band. If e.g. the value of 62 % is assumed as the necessary power coupling to meet the specification the optimized matching circuit with a junction area of (0.8 μm)^2 is above this threshold for the whole band. If the junction width changes with Δl_{SIS}=$\pm$0.1 μm, for more than 50 % of the frequencies the power coupling is too low which results in higher noise.

a subsequent chemical mechanical polishing step, which is described in detail in [5].

The conduction of NbTiN and Nb was calculated after the theory of Mattis-Bardeen [12]. The power coupling is calculated from the surface impedances of the striplines including fringe effects [13] and step inductances [14] with KOSMA inhouse software, developed in the course of several years of experience. The calculated power coupling for an optimum broad-band matching circuit is already given in figure 5 (filled squares). Design parameters for the junction are a current density of 15 kA/cm^2 and a gap-voltage of 2.75 mV. Junctions are calculated for areas from (0.8 μm)^2 to (1.0 μm)^2.

C. IF-Design

The mixerblock and the bias-T are connected via SMA connectors and a 50 Ω semi rigid cable. So these two parts of the IF chain in the mixer unit can be optimized and measured separately. The IF path insde the mixerblock is shown in figure 6. The plot in Figure 7 shows the matching for the IF

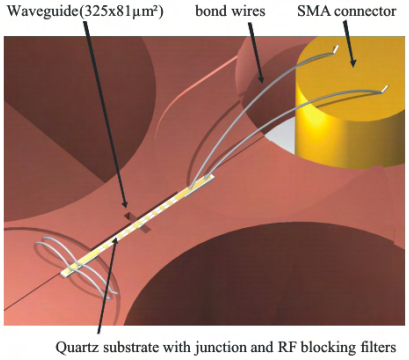

Fig. 6. The IF path in the mixerblock.

signal from the junction to the SMA connector calculated in a EM 3D simulation for different junction impedances. Reliable standard wire bonding of the mixerchip to the SMA still results

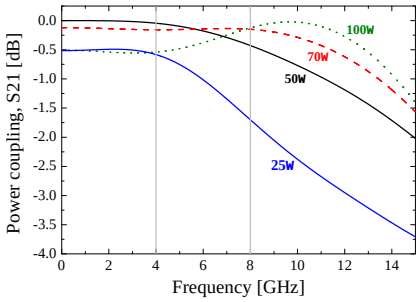

Fig. 7. Calculated IF coupling from the junction dynamic impedance to the SMA connector of the mixerblock.

in a good match up to approximately 10 GHz, provided the junctions dynamic impedance is between 50 and 100 Ω. The signal is then guided through a semi rigid SMA cable from the mixerblock to the bias-T circuit.

The main challenges in designing the bias-T were to find an extremely reliable solution for all connections avoiding single point failures, to provide good ESD protection, ample shielding and EMI filtering, and furthermore to place everything including bias- and IF-connectors mandatory on the backplane all in the tight envelope and weight constraints. The cable which ensures a flexible connection between the copper mixerblock and the aluminium bias-T box is directly flanged to the box. The inner conductor is connected via two thin strands to the microstrip line. This flexible connection assures stability under thermal and vibrational stress and saves the space and weight of another (SMA) connector.

To avoid damage by ESD while the mixer is integrated into the FPU all bias lines have RC filters in a 2nd separate compartment. In combination with additional microstrip filters they protect the mixer chip from EMI of other spacecraft instruments through the unshielded wiring in the HIFI dewar. The compartments need to be completely shielded with the exception of a tiny hole for the bias line to prevent crosstalk between the different filter sections.

All parts of the bias circuit are designed using analytical models, 3D simulation technique and network analyzer measurements of real models. A model of the bias-T with the critical SMA to microstrip transitions and EMI filtering circuits is shown in figure 8. The metal pillar between the bottom and the lid of the box shorts out a box resonance around 6.5 GHz.

III. Environmental and Performance Tests

Most of the environmental tests were made during the qualification process of the mixers with qualification models (QM), which are prototypes for the later flight models (FM). The IF- and RF-performance tests were made with the FMs.

A. Environmental Tests

To test the influence of EMI in a ”noisy” satellite environment and the shielding of the bias-lines from the IF-ouput by

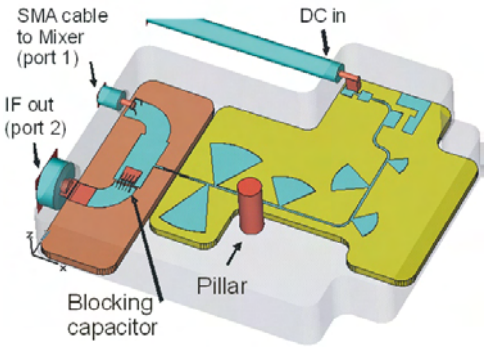

Fig. 8. 3D model used for simulations of the IF performance of the bias-T. The pillar in the box center suppresses a box resonance within the IF band.

the EMI filter inside the bias-T, the bias-lines where connected to unshielded cables of ≈1 m length and exposed to cw-radiation. The power coupling measured at the IF-output is given in figure 9. The coupling inside the IF-band is below

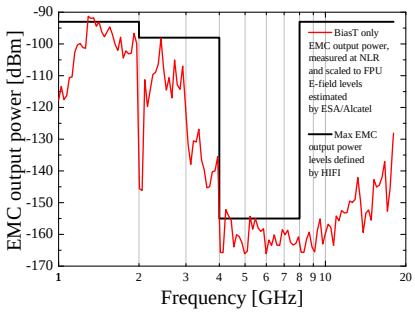

Fig. 9. RF coupling via unshielded bias-cables vs. frequency of cw-radiation

the allowed EMI levels.

The QMs were also were tested in a long 144 hours bake-out test at a temperature of 83 °C. The current density of the devices was reduced by ≈10 %. The mixer noise temperature did not change more than 10 K. Although the absolute error of the mixer noise temperature is 15 K, this difference value of 10 K with the same measurement setup and same correction terms for optics and IF-contribution is reliable. This change in mixer noise lower than 10 K is within the allowed tolerance.

As a test for the mechanical stability during the launch of the satellite a vibration-test at cryogenic (77 K) and room-temperatures with QM- and FM-mixers were made. At random and sine vibration levels the mixers did not show significant resonances.

B. RF-Performance

The three devices with the best RF-performance during the pre-tests were chosen and then tested in the FM-brackets with FM-bias-T at 2.9 K ambient temperature. From these three FMs FM1 and FM3 showed the best performance. FM2 is used as an attrition mixer. Here only the results of FM1 and FM3 are presented.

1) FTS-Measurement: To characterize the RF-bandpass of the mixers Fourier-Transform-Spectrometer measurements were made with a commercial instrument [15]. The measurements were made in voltage-detection mode with a 75 μm mylar beamsplitter which was characterized before with a separate internal DTGS-detector. The measured coupling for FM1 and FM3 corrected for the transmission of the internal beamsplitter is shown in figure 10. The lower band edge of the

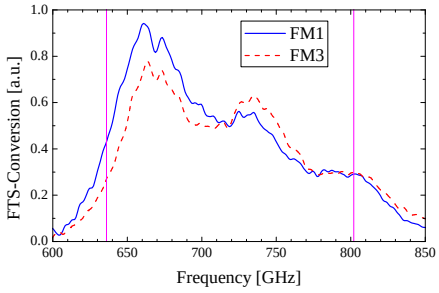

Fig. 10. FTS-conversion vs. frequency, corrected for FTS-beamsplitter

FM3 is shifted to higher frequencies by $\Delta\nu$ ≈10 GHz with respect to the FM1. One can clearly see that the structure is similar to the designed curves in figure 5).

2) Heterodyne Measurements: The receiver noise temperature of the system was measured with a standard hot-cold-setup (hot: 295 K, cold: 77 K black-body load). As local oscillator frequency-locked solid-state LOs were used [7]. To couple load signal and LO-radiation into the 2.9 K dewar, a 12 μm mylar beamsplitter was used. The dewar window is a 0.44 mm teflon-window. As IR-shield one layer Zitex G 108 (thickness 0.20 mm) was used [16]. The transmission of the three optics components was characterized with the FTS. For the beamsplitter under 45° the transmission was measured polarization dependent with a polarization grid.

A typical hot-cold-measurement is shown in figure 11. At

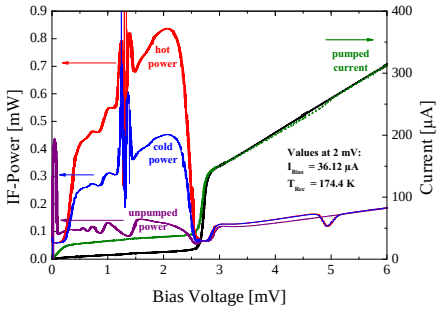

Fig. 11. IF-power and device current of FM1 at 642 GHz vs. bias-voltage

1.3 mV in the pumped IF-power one can see the Shapiro-steps which are not suppressed totally in this measurement.

The resulting receiver noise temperatures for FM1 and FM3 are shown in figure 12 (top). The shift in the frequency band

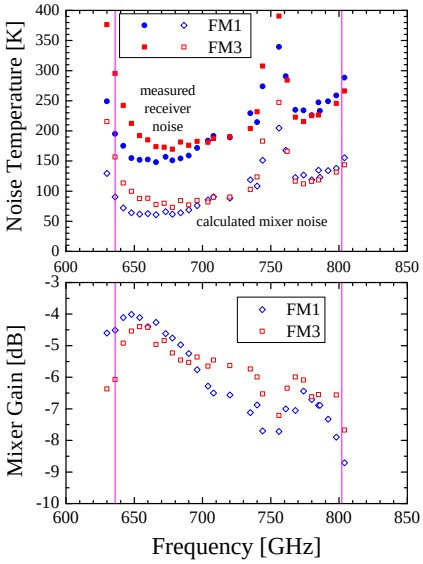

Fig. 12. Measured receiver noise for FM1 and FM3 (filled squares and diamonds) and calculated mixer noise and mixer gain (open squares and diamonds). The increased noise at ≈750 GHz is a result of the water absorption in the non-evacuated signal path. This feature is not seen in the evacuated FTS-measurement (figure 10).

of FM3 with respect to FM1 which was already seen in the FTS-measurements is reproduced in the noise measurement. The corrections for the optics vary from 48 K to 58 K with RF-frequency. The corrections for the IF-chain (5.5 K) are obtained from a hot-cold measurement of the IF-chain with a 50 Ω resistance load and a standard Schott-noise fit of the unpumped IF-output power vs. bias-voltage. All calculations were made after the Callon-Welton formula (see [17]).

The baseline for the HIFI-project is defined for a receiver assuming optics with 100 % transmission and IF-contribution of 10 K. The resulting receiver noise temperature ($T_{Rec,HIFI} = T_{Mix} + 10\ \mathrm{K}/G_{Mix}$) is plotted and compared with the baseline in figure 13. The error of these values is ±15 K because of

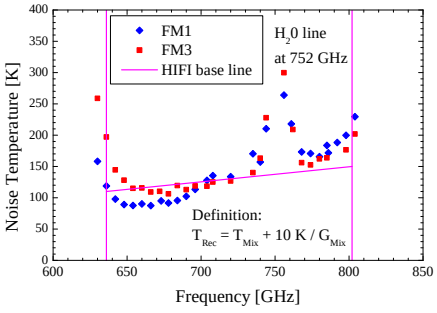

Fig. 13. Calculated HIFI receiver noise assuming 10 K IF-noise vs. LO-frequency and HIFI baseline.

the tolerances of accuracy in the measurements of the optics- and IF-contribution. Within this error the HIFI receiver noise for the to FM-mixers matches the baseline for 75 % of the frequency band.

C. IF-Performance

The IF-performance of the bias T was separately measured with a network analyzer at room temperature. The measured values are shown in figure 14. One sees a very good agreement

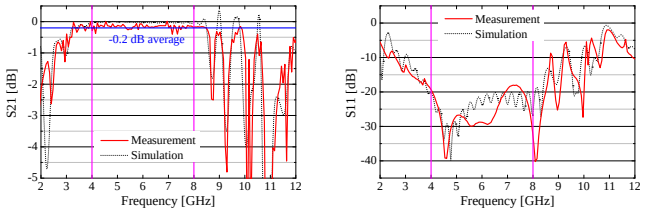

Fig. 14. Transmission (left) and reflection (right) of bias-T. Measurements with network analyzer as solid line, 3D simulation (CST Microswave Studio) as dashed line.

of the measurements with the 3D-simulated data. The contribution of the bias-T to the IF noise, measured separately at 3K, is lower than 1K.

During the RF-measurement with the mixers also IF-resolved measurements with a spectrum-analyzer were made. Hot and cold IF output power were measured as a function

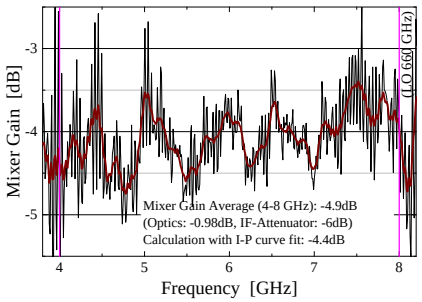

Fig. 15. Calculated mixer gain vs. IF-frequency measured with spectrum analyzer. The IF-ripple is well below 2 dB. The bold line is an average over the data to eliminate random noise.

of IF-frequency. For the measurement at an LO-frequency of 660 GHz the calculated mixer gain is plotted in figure 15. The maximum ripple over the IF-band is found by this method to be well below 2 dB for the whole RF frequency band.

IV. Noise Analysis

After comparison of the FTS-data, mixer noise and mixer gain with the calculated conversion using the measured material parameters (ρ=80 $\mu\Omega$cm and T_c=13.8 K), including the measured dc-values for normal resistance R_N and gap voltage V_{Gap} a current density of 13–14 kA/cm^2 is obtained for both FM devices. The shape of the coupling curves only fits if an additional geometrical shift of the matching circuit with respect to the SIS-junction of Δl=+0.5 μm and a broadening

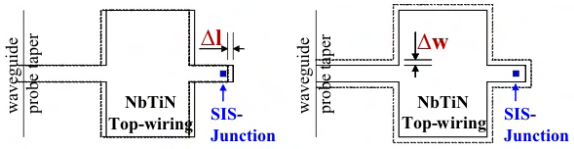

Fig. 16. Influence of variation in fabrication: absolute positioning accuracy Δl, stripline broadening Δw.

of the striplines of Δw=+0.2 μm is assumed (for definition see figure 16). These values are in the reasonable range for the fabrication tolerances. In this analysis the parameters are not fully determined. For example a higher current density j_c can be compensated by a lower Δw and vice versa. But after reviewing photographs of devices from the same row of the batch the given values are reasonable.

Based on this analysis an embedding impedance can be estimated for both devices and the mixer noise be calculated from the DC voltage-current characteristics after Tucker's theory [3]. The results are given in figure 17. Here the

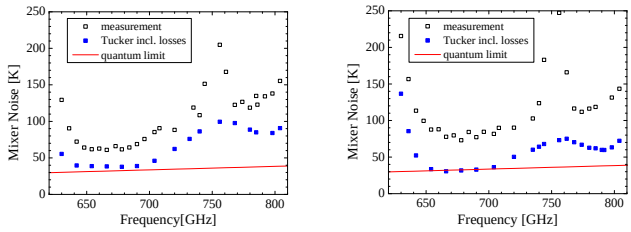

Fig. 17. Mixer noise of FM1 (left) and FM3 (right) after Tucker's theory (filled squares) and values from measurement (open squares).

pump power levels are taken to comply with the optimum levels in the measurement, which complies with the optimum theoretical power-levels. The band edges agree quite well in measurement and theory, but the absolute values of the noise do not comply with the measured values. There are several possible reasons for the discrepancy. According to [18] there can be a factor of 1.5 in mixer noise temperature because of multiple Andreev reflection in pinholes for this type of device (ν_{LO}=700 GHz, j_c=13–14 kA/cm^2, R_{subgap}/R_N=9). This would to a great extent explain the big difference from theory to the measurement. In addition to that the quality data for the stripline materials Nb and NbTiN are measured dc at single layers, not striplines. Losses at the interfaces and possible partial step coverage are not included.

V. Conclusion

Three mixers were fabricated, assembled and tested by KOSMA for the HIFI band 2 and delivered to the project. The modular design of the mixers is favorable to testing optimizing and space qualification of separate components within limited time schedule. The RF-baseline is met for 75 % of the frequency band. Losses and additional noise yield a factor $\lesssim$2 of the theoretically possible mixer noise. So additional analysis is necessary and optimization of the devices is still possible for future projects. The IF-performance fulfills the requirements.

Acknowledgment

Thanks to SRON (National Institute for Space Research, NL) QA, J. Evers. – This Project was supported by DLR (Deutsches Zentrum für Luft- und Raumfahrt, Germany), grants 50 OF 0001 2, 50 OF 9902 4.

References

[1] G. L. Pilbratt, "The Herschel Mission, Scientific Objectives, and this meeting," in *The Promise of the Herschel Space Obervatory*, G. L. Pilbratt, J. Cernicharo, A. M. Heras, T. Prusti, and R. Harris, Eds., 2001, pp. 13–20.

[2] T. de Graauw and F. P. Helmich, "Herschel-HIFI: The Heterodyne Instrument for the Far-Infrared," in *The Promise of the Herschel Space Obervatory*, G. L. Pilbratt, J. Cernicharo, A. M. Heras, T. Prusti, and R. Harris, Eds., 2001, pp. 45–51.

[3] J. R. Tucker and M. J. Feldman, "Quantum detection at millimeter wavelenghts," *Rev. Mod. Phys.*, vol. 57, no. 4, pp. 1055–1113, 1985.

[4] S. Glenz, M. Justen, P. Pütz, R. Teipen, T. Tils, C. Honingh, and K. Jacobs, "Broadband NbTiN based SIS mixers for HIFI band 2," in *Digest 27th Int. Conf. on Infrared and Millimeter Waves*. IEEE, September 2002, pp. 257–258.

[5] P. Pütz, S. Glenz, C. E. Honingh, and K. Jacobs, "Progress in SIS device fabrication for HIFI mixer band 2 at KOSMA," in *Proc. 13th Int. Symp. on Space Terahertz Technology*, 2002, pp. 383–390.

[6] S. Haas, S. Wulff, D. Hottgenroth, C. E. Honingh, and K. Jacobs, "Broadband array SIS mixers for 780-880 GHz with aluminum tuning circuits," in *Proc. 11th Int. Symp. on Space Terahertz Technology*, 2000, pp. 95–104.

[7] RPG Radiometer Physics GmbH, D-53340 Meckenheim, Germany, Internet: www.radiometer-physics.de.

[8] A. Murk and A. Magun, "Characterization of corrugated horn antennas for HIFI," in *25th ESA Workshop on Satellite Antenna Technology*. ESTEC, Noordwijk, NL, Sept. 2002, pp. 159–164.

[9] T. Tils, A. Murk, D. Rabanus, C. E. Honingh, and K. Jacobs, "High performance smooth-walled horns for THz waveguide applications," in *Proc. 16th Int. Symp. on Space Terahertz Technology*, 2005.

[10] CST Microwave Studio from CST GmbH, Bad Nauheimer Str. 19, D-64289 Darmstadt, Germany. Internet: www.cst.de.

[11] B. Leone, B. D. Jackson, J. R. Gao, and T. M. Klapwijk, "Geometric heat trapping in niobium superconductor-insulator-superconductor mixers due to nobium titanium nitride leads," *Appl. Phys. Lett.*, vol. 76, no. 6, pp. 780–782, February 2000.

[12] D. C. Mattis and J. Bardeen, "Theory of the anomalous skin effect in normal and superconducting materials," *Phys. Rev.*, vol. 111, no. 2, pp. 412–417, 1958.

[13] K. C. Gupta, R. Garg, and I. J. Bahl, *Microstrip Lines and Slotlines*. Dedham: Artech House, 1979.

[14] R. K. Hoffmann, *Integrierte Mikrowellenschaltungen*. Berlin: Springer Verlag, 1983.

[15] Fourier Transform Spectrometer "IFS 66v/S" from Bruker Optik GmbH, Rudolf-Plank-Str. 27, D-76275 Ettlingen, Germany, Internet: www.brukeroptics.de.

[16] Vendor: Saint-Gobain Performance Plastics GmbH, Delmenhorster Strasse 20, D-50735 Cologne, Germany, Internet: www.saint-gobain.de.

[17] A. R. Kerr, "Suggestions for revised definitions of noise quantities, including quantum effects," *Microwave Theory and Techniques, IEEE Transactions on*, vol. 47, no. 3, pp. 325–329, Mar 1999.

[18] P. Dieleman, "Fundamental limitations of THz niobium and niobiumnitride SIS mixers," Dissertation (PhD thesis), Rejksuniversiteit Groningen, NL, 1998.

Space-qualified 4 K Cooler for 640 GHz SIS Receiver of SMILES

J.Inatani(1), A.Okabayashi(1), K.Kikuchi(1), R.Sato(1), T.Manabe(2), M.Seta(2), S.Tsunematsu(3), S.Yajima, and K.Narasaki(3)
(1) Japan Aerospace Exploration Agency, Tsukuba, Ibaraki 305-8505, Japan.
(2) National Institute of Information and Communications Technology, Koganei, Tokyo 184-8795, Japan.
(3) Sumitomo Heavy Industries, Ltd., Niihima, Ehime 792-8588, Japan.

We have built and tested a proto-flight model (PFM) of the 4 K cooler and its cryostat for SMILES 640 GHz SIS receiver. Tests have been conducted for the cooler and cryostat in mechanical, thermal and electric aspects, and also for the RF performance of SIS receiver accommodated in the cooler. Those tests have shown the cooler system meets all the specifications of the SMILES receiver.
The cooler system is composed of a two-stage 20 K Stirling cooler and a Joule-Thomson 4 K cooler. Narasaki et al. reported the design of those components and the cryostat in detail as well as the results of space-qualification tests at the CEC/ICMC conference, Anchorage, Sept. 21-26, 2003. Since then we have accumulated experience of running the cooler system while conducting the submillimeter receiver performance tests over the noise temperature, gain stability, quasi-optical characteristics and others. We are now confident on the cooling performance and its repeatability. Two SIS mixers are kept at a physical temperature that is adjustable below 4.5 K as shown in Fig.1. Its stability is better than 7 mK (peak-to-peak), which is limited by the variation of the room temperature that is not expected in orbit. We have also investigated the effects of mechanical vibrations and magnetic fluxes due to the compressors: the Stirling compressor is working at 15 Hz and the JT at 30 Hz. Although we find significant oscillations at these frequencies in DC bias lines of the SIS mixer, they are too small to affect the mixer performance. From the viewpoint of optical alignment, we measured the movement of the 4 K stage during the cool-down and warming-up periods. It is found repeatable and has been put into the whole mechanical alignment process of the cryostat. Those measured characteristics of the SMILES 4 K cooler will be reported with an emphasis on the effects to the SIS receiver performance.

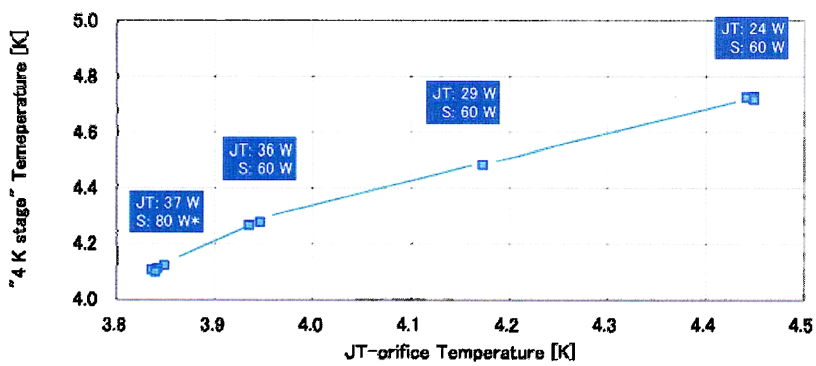

Fig.1 Temperatures of the cryostat "4 K" stage and JT orifice are adjustable by means of the AC power put into the JT and Stirling compressors (given in each box).

Poster session IV:

HEB

Development of a Quasi-Optical NbN Superconducting HEB Mixer

W. Zhang, L. Jiang, Z.H. Lin, Q.J. Yao, J. Li, S.C. Shi, S.I. Svechnikov, Yu. B. Vachtomin, S.V. Antipov, B.M. Voronov, N.S. Kaurova, and G.N. Gol'tsman

Abstract—**In this paper, we report the performance of a quasi-optical NbN superconducting HEB (hot electron bolometer) mixer measured at 500 and 850GHz. The quasi-optical NbN superconducting HEB mixer is cryogenically cooled by a 4-K close-cycled refrigerator. Measured receiver noise temperature at 850 and 500GHz are 3000K and 2500K respectively with wire grid as beamsplitter, while the lowest receiver noise temperature is found to be approximately 1200K with Mylar film. The theoretical receiver noise temperature (taking into account the elliptical polarization of log-spiral antenna) is consistent with measured one. The receiver noise temperature and conversion gain with 15-μm Mylar film as the beamsplitter at 500GHz are thoroughly investigated for different LO pumping levels and dc biases. The stability of the mixer's IF output power is also demonstrated.**

***Index Terms*—Close-cycled 4K refrigerator, NbN HEB mixers, wire grid, elliptical polarization, U-factor**

I. Introduction

Superconducting HEB mixers have demonstrated good performance at terahertz frequencies. The DSB noise temperature of phonon-cooled superconducting HEB mixers is approaching eight times the quantum limit ($8h\nu/k$) [1] and the required LO power is as low as one microwatt. Some ongoing projects (including ground-based TREND [2], airborne SOFIA [3], and spaceborne Herschel [4]) will benefit from the technology of superconducting HEB mixers.

To suit long-period operations such as astronomical and atmospheric observations, it is of particular interest to investigate the behaviors of superconducting HEB mixers cooled by a close-cycled 4-K refrigerator. It has been indeed demonstrated that phonon-cooled NbN superconducting HEB mixers can survive such a cooling circumstance [5]. In this paper, a quasi-optical NbN superconducting HEB mixer is measured at 500 and 850GHz with a close-cycled 4-K refrigerator. The theoretically calculated receiver noise temperature as a function of the wire angle of wire grid was in good agreement with the measured one due to the elliptical polarization of log-spiral antenna [6]. Its performance is thoroughly investigated for different LO pumping levels and dc biases at 500GHz. In addition, the stability of IF output power of the quasi-optical NbN superconducting HEB mixer is examined.

Manuscript received May 2, 2005. This work was supported by the NSFC under Contracts No. 10390163 (20030001) and No. 10211120645, the CAS under Contracts No. KJCX2-SW-T2 and No. GFCX-YJ-06, and the RFBR under Contract No. 04-02-39016.

W. Zhang, L. Jiang, Q. J. Yao, Z. L. Lin, Ji. L, and S. C. Shi are with Purple Mountain Observatory, NAOC, CAS, Nanjing, China. Phone: 86-25-83332203; fax: 86-25-83332206; e-mail: l.jiang@mwlab.pmo.ac.cn.

S. I. Svechnikov, Y. B. Vachtomin, S.V. Antipov, B. M. Voronov, N.S. Kaurova, and G. N. Goltsman are with Department of Physics, Moscow State Pedagogical University, Moscow, Russia

II. Measurement Setup

As shown in Fig. 1, the quasi-optical NbN superconducting HEB mixer measured is made up of a log spiral antenna and an ultra-thin NbN film bridge across the antenna's feed point. The log spiral antenna couples the RF and LO signals to the thin NbN film bridge, where mixing happens via some heat exchanges between electron and phonon. The thin NbN film, measuring about 3.5-nm thick, was deposited by dc magnetron sputtering on a heated high resistivity silicon substrate, while its bridge area, measuring 0.2-μm long and 2.4-μm wide, was fabricated through e-beam lithograph. The thin NbN film bridge had a normal resistance of 100 Ω and a critical current of 190 μA at 4.2 K. And its critical temperature and transition width were 9.6 K and 0.9 K, respectively.

The quasi-optical NbN superconducting HEB mixer was firstly glued onto a hyper-hemispherical silicon lens (of a diameter 12.7 mm, with no anti-reflection layer). The silicon lens with the superconducting HEB mixer was then put into a copper mixer block, which includes a 50-Ω microstrip line with its one port connected to the HEB mixer chip (via Indium)

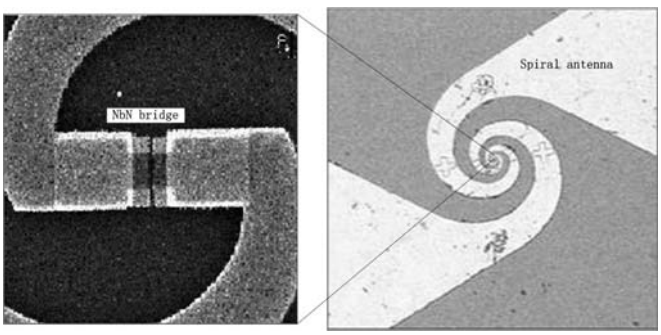

Fig. 1 Photograph of a quasi-optical NbN superconducting HEB mixer chip. The NbN bridge measures 2.4-μm wide, 0.2-μm long and 3.5-nm thick.

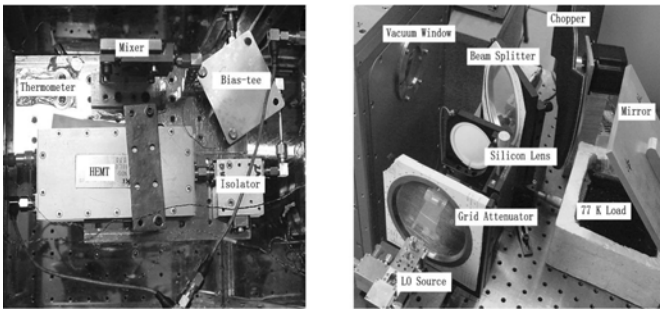

(a) (b)

Fig. 2 Photograph of the measurement setup, with (a) inside the cryostat and (b) outside view.

and the other to the IF&DC output port. The whole mixer was mounted onto the 4-K cold plate of the close-cycled cryostat (as shown in Fig. 2a).

We used the conventional Y-factor method to measure the noise performance of the quasi-optical NbN superconducting HEB mixer. The measurement setup is shown in Fig. 2b. A beam splitter made of a 15-μm thick Mylar film or wire grid couples the RF signal from a chopper (indeed a 295-K and 77-K blackbody) and the LO signal from a 850-GHz BWO or 500-GHz solid state source (Gunn plus x6 multiplier). The RF and LO signals are incident onto the hyper-hemispherical silicon lens through a vacuum window (100-μm Mylar film on the 300-K shield of the close-cycled cryostat) and an IR filter (two layers of Zitex G108 on the 40-K shield). The hyper-hemispherical lens focuses the RF and LO signals to the HEB mixer chip. The IF output signal goes through a bias-tee, a 1.2-1.8 GHz cooled HEMT low noise amplifier (including an isolator on the 4-K cold plate), a room-temperature amplifier (45-dB gain), a bandpass filter (1.55±0.085 GHz), and is finally detected by a square-law detector of a sensitivity of 1 mV/μW.

III. Measurement Results

3.1 Noise temperature at 850GHz with BWO

Since the output power of our BWO at 850 GHz was too small to pump the I-V curve, we chose wire grid (fabricated from tungsten with wire diameter and space of 10 μm and 25 μm respectively) as beamsplitter to measure the receiver noise temperature. The measured optimal DSB receiver noise temperature was 3000K at the point 0.75mV and 36μA (shown in Fig. 3). During the experiment we found that the IF output power was not so stable, so we measured the correlation between the IF output power and BWO cathode voltage by measuring the voltage across a 500-Ω resistor in series with BWO (shown in Fig. 4). The IF output power is in good agreement with the voltage across the 500-Ω resistor in series with BWO during the period of 10 minutes, which led us to measure the receiver noise temperature at 500GHz.

3.2 Noise temperature at 500GHz with wire grid as beamsplitter

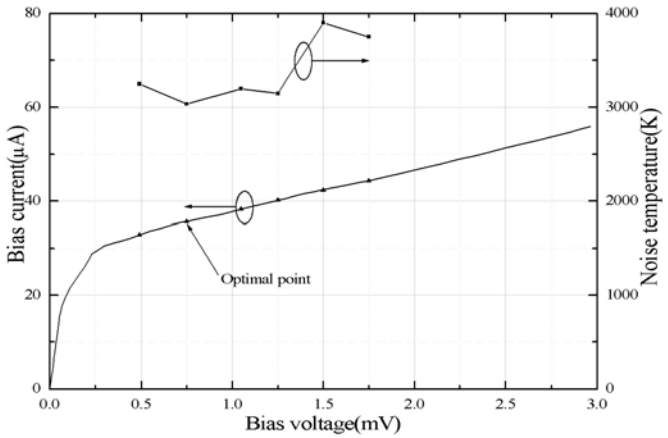

Fig.3 Measured receiver noise temperature along the optimal I-V curve at 850GHz

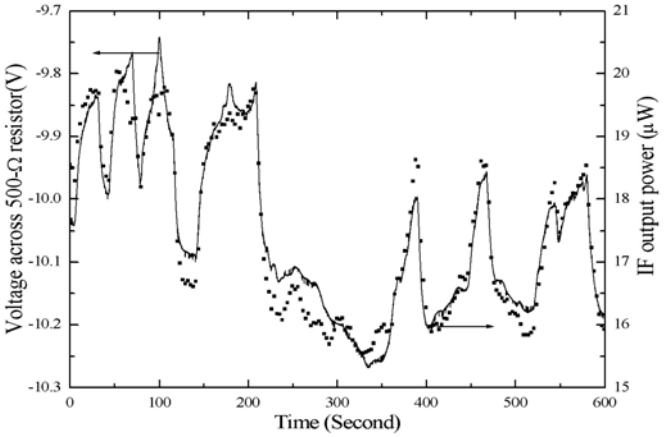

Fig.4 Dependence of IF output power on the voltage cross the 500Ω resistor in series with BWO.

Then we measured the receiver noise temperature at 500GHz with solid-state source (gun oscillator plus 6x multiplier) as LO source. The measured DSB receiver noise temperature T_{rec} at 500 GHz for different wire angles at the same bias point (V_{bias} =0.87 mV and I_{bias}= 38 μA) is exhibited in Fig. 5. The lowest receiver noise temperature of 2700K was obtained when the wire angle was tuned to -50 degree (i.e., counterclockwise from the vertical direction), and T_{rec} deteriorated drastically with the increment of the wire angle. It had been demonstrated that the log-spiral antenna integrated with hyper-hemispherical lens was elliptical polarization. There was an angle of about 25 degree between the line along the tapered section of the antenna and the long axis of the elliptical polarization, and the axis ratio was 1.3 and 3 at 1.4 and 2.5 THz, respectively [6]. Given the fact that the position of our HEB mixer was clockwise tilted about 15 degree from vertical direction due to not so good alignment, measured results were consistent with polarization of log-spiral antenna. Assumed that the axis ratio of elliptical polarization of log-spiral antenna is 1.25 at 500GHz and the long axis is 40 degree clockwise from the vertical direction, we theoretically calculated the receiver noise temperature. The Y factor is given by the following formula

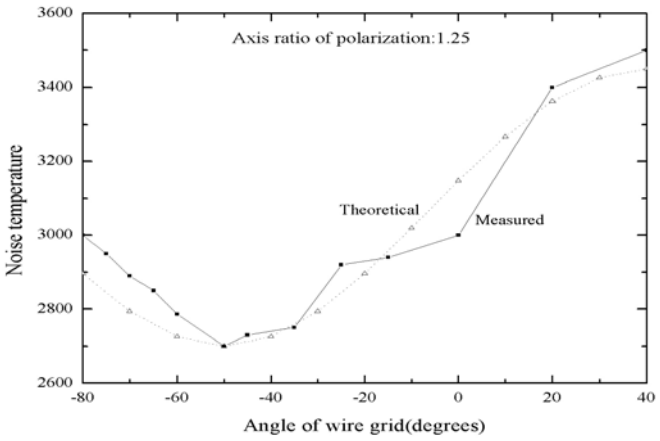

Fig. 5 Measured and theoretical receiver noise temperature

$$Y = \frac{(300+T_m)*S*A+300*R*B}{(77+T_m)*S*A+300*R*B} = \frac{300+T_m+300*R/S*B/A}{77+T_m+300*R/S*B/A} \quad (1)$$

where T_m is the equivalent input noise temperature, S and R are the transmission and reflection coefficient of wire grid (S=R=0.5), while A and B are the coupling coefficient of transmitted (E field vertical to wire) and reflected (E field parallel to wire) load signal due to elliptical polarization of log-spiral antenna. So the measured receiver noise temperature T_{rec} is given by

$$T_{rec} = \frac{300-77*Y}{Y-1} = T_m + 300*R/S*B/A = T_m + 300*B/A \quad (2)$$

The contribution of LO chain to the total receiver noise temperature (300*B/A) is between 240 and 375K while the wire grid was rotated, which cannot be neglected as thin Mylar film as beamsplitter (~30K) [7].

The noise temperature after correcting the loss of wire grid and polarization influence of log-spiral antenna can be given

$$T_{mr} = T_m * 0.5 * A \quad (3)$$

The lowest noise temperature after such correction is 1230K at the direction when transmitted E field signal can be optimally coupled to HEB mixer (i.e. wire vertical to the long axis of elliptical polarization), which should be constant. The theoretical receiver noise temperature is also shown in Fig. 5, which is consistent with measured one.

3.3 Noise temperature at 500GHz with 15-μm thick Mylar film as beamsplitter

In order to improve the transmission coefficient of beamsplitter and reduce the contribution of LO chain to the total receiver noise temperature, we replaced the wire grid with 15-μm thick Mylar film to measure the receiver noise temperature (DSB, T_{rec}) of the quasi-optical NbN superconducting HEB mixer for different LO pumping levels and dc biases. The measurement results (with no corrections) are plotted in Fig. 6a. Obviously, the lowest receiver noise temperature in the stable region appears 1200 K at 500 GHz (biased at 0.7 mV and 25 μA) and the area giving similar noise performance is quite large. The LO power absorbed by the HEB device was estimated to be 366 nW by an isothermal

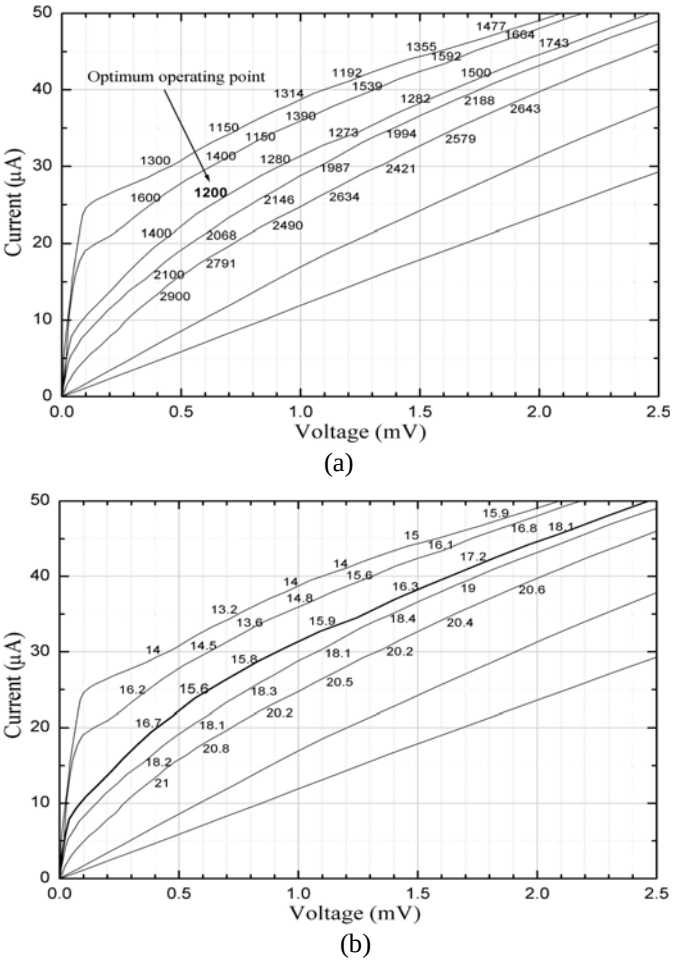

Fig. 6 Uncorrected receiver noise temperature (a) and conversion loss (b) for different LO pumping levels and dc biases.

technique [8]. At the optimal point we also measured noise temperature with wire grid as beamsplitter (as shown in Tab.1), the corrected noise temperature with wire grid is the same as that with Mylar film after correction the contribution (300*R/S) of LO chain and the influence of transmission coefficient (S) of beamsplitter, where we ignored the effect of elliptical polarization of log-spiral antenna since it's too small.

We also evaluated the total conversion loss (L_{total}) of the quasi-optical NbN superconducting HEB mixer using a U-factor technique [9]. This U-factor technique assumes that HEB devices in the superconducting state have a zero IF impedance at zero dc bias. With this assumption, the U-factor, defined as a ratio between the IF output powers at its operating point (P_{295}) and zero dc bias (P_{sc}), is written as

$$U = \frac{P_{295}}{P_{sc}} = \frac{T_{295}+T_{rec}}{T_{bath}+T_{if}} \frac{2}{L_{total}} \quad (4)$$

where T_{295} and T_{bath} are effective radiation temperatures derived from Callen-Welton formula for the physical temperatures of 295 K and 4.2 K at the measurement frequency, respectively, and T_{if} is the equivalent input noise temperature of the IF chain (assumed to be 20 K here). The

total conversion loss is therefore given by

$$L_{total} = \frac{2(T_{295} + T_{rec})}{U(T_{bath} + T_{if})} \quad (5)$$

Fig. 6b shows the calculated mixer conversion losses (with no corrections) of the quasi-optical NbN superconducting HEB mixer corresponding to different LO pumping levels and dc biases.

Tab.1 Comparison of noise temperature with wire grid and Mylar film

Beam Splitter	Trans. &Ref.	T_{rec}	Contribution of LO chain	T_m	Corrected T_m
Wire grid	0.5,0.5	2500	300	2200	1100
Mylar	0.96,0.04	1200	12.5	1187.5	1140

Tab. 2 Loss and equivalent noise temperature of the quasi optical components.

Component	Loss (dB)	Physical Temp. (K)	Noise Temp. (K)
Beam splitter	0.2	295	14.5
Vacuum window	1.25	295	102.4
Zitex filter	0.2	40	2
Si lens, reflection	1.55	4	7.7
Si lens, absorption	0.1	4	
Lens antenna	0.5	4	

To understand how good the intrinsic performance of the quasi-optical NbN superconducting HEB mixer is, we calculated or estimated the losses and noise contributions of individual quasi-optical components. The results are summarized in Tab. 2. Clearly the vacuum window has considerable loss and noise contribution. We indeed found that after correcting the losses and noise contributions of individual components before the quasi-optical NbN superconducting HEB mixer, the lowest receiver noise temperature was only 445 K.

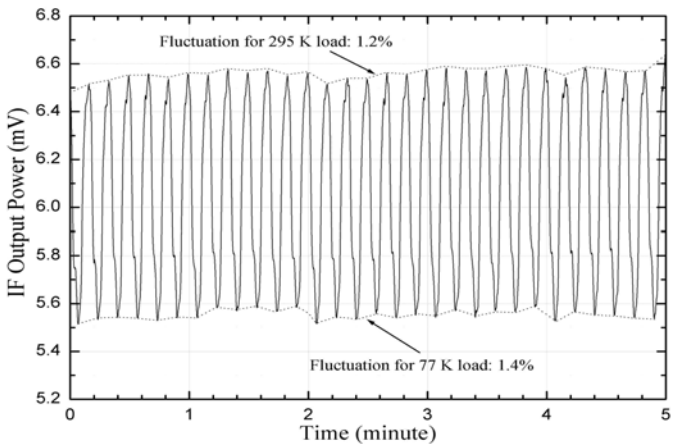

Fig. 7 Measured IF output power for a 295-K and 77-K load chopped at 0.1 Hz.

Finally, we studied the stability of IF output power of the quasi-optical NbN superconducting HEB mixer cooled by a 4-K close-cycled refrigerator. We recorded the IF output power when doing the Y-factor measurement. As displayed in Fig. 7 (for 5 minutes), it is rather stable, giving fluctuation of 1.2% for the 295-K load and 1.4% for the 77-K load.

IV. Conclusion

We have investigated the performance of a quasi-optical NbN superconducting HEB mixer at 500 and 850GHz, when it is cooled by a 4-K close-cycled refrigerator. The lowest receiver noise temperature was 3000K with wire grid as beamsplitter at 850GHz. The theoretical total receiver noise temperature was in good agreement with measured one at 500GHz for different wire grid angles. The lowest receiver noise temperature is about 1200 K and 2500K with no correction corresponding to Mylar film and wire grid as beamsplitter at 500GHz, while they are coincident after correcting the contribution of LO chain and the influence of transmission coefficient of beamsplitter. This HEB mixer demonstrates a fairly large range of good mixer performance for both LO pumping and dc bias. The corrected receiver noise temperature was reduced to 445 K after correcting the losses and noise contributions of individual components before the HEB mixer. Furthermore, this HEB mixer exhibits fairly good stability even working with a close-cycled cryocooler. It will be very beneficial to real applications.

V. Acknowledgement

The authors would like to thank Prof. J. Chen of Nanjing University for lending a 500-GHz local oscillator. L.J. thanks D.R. Yang, W.M. Chen, W. Miao, and Y. Luo for technical support. This work was supported by the NSFC under Contracts No. 10390163 (20030001) and No. 10211120645, the CAS under Contracts No. KJCX2-SW-T2 and No. GFCX-YJ-06, and the RFBR under Contract No. 04-02-39016.

References

[1] J. J. A. Baselmans, M. Hajenius, J. R. Gao, T. M. Klapwijk, P. A. J. de Korte, B. Voronov and G. Gol'tsman, "Doubling of sensitivity and bandwidth in phonon cooled hot electron bolometer mixers," *Applied Physics Letts.*, Vol. 84, No. 11, pp. 1958-1960, 2004.

[2] K.S. Yngvesson, C. F. Musante, M. Ji, F. Rodriguez, Y. Zhuang, E. Gerecht, M. Coulombe, J. Dickinson, T. Goyette, J. Waldman, C. K. Walker, A. Stark, and A. Lane, "Terahertz receiver with NbN HEB device (TREND)-A low-noise receiver user instrument for AST/RO at the south pole," *Proc. of 12th International Symposium on Space Terahertz Technology*, San Diego, pp. 262-285, 2001.

[3] H.-W. Huebers, A. Semenov, J. Schtibert, G. Gol'tsman, B. Vornov, E. Gershenzon, A. Krabbe, and H. P. Roser, "NbN hot electron bolometer as THz mixer for SOFIA," *Proc. SPIE vol. 4014 (Airborne Telescope Systems)*, pp. 195-202, March 2000.

[4] Th. de Graauw and F. P. Helmich, "Herschel-hifi: the heterodyne instrument for the far-infrared," *Proc. of Symposium "The Promise of the Herschel Space Observatory,"* Toledo, Spain, December 2000.
[5] L. Jiang, J. Li, W. Zhang, Q. J. Yao, Z. L. Lin, S. C. Shi, Y. B. Vachtomin, S.V. Antipov, S. I. Svechnikov, B. M. Voronov and G. N. Goltsman, "Characterization of NbN HEB mixers cooled by a close-cycled 4 Kelvin refrigerator," *IEEE Trans. Appl. Supercond.*, June 2005, in press.
[6] P. Yagoubov, W. –J. Vreeling, and P. de Korte, "Characterization of an integrated lens antenna at terahertz frequencies," *Proceedings of 12th International Symposium on Space Terahertz Technology*, San Diego, pp. 193-204, 2001.
[7] Goutam Chattopadhyay, Frank Rice, David Miller, Henry G. LeDuc and Jonas Zmuidzinas, "A 530-GHz balanced mixer," IEEE microwave and guide wave letters, vol.9, No. 11, pp.467-469, Nov. 1999.
[8] G.N. Gol'tsman et al, "NbN hot electron superconducting mixers for 100 GHz operation," *IEEE Trans. Appl. Supercond.*, vol. 5, March 1995.
[9] S. Cherednichenko et al, "1.6 THz heterodyne receiver for the far infrared space telescope," *Physica C: Superconductivity and its Applications*, 372-376:427-431, 2002.

Balanced Waveguide HEB Mixer for APEX 1.3 THz receiver

Denis Meledin, Miroslav Pantaleev, Alexey Pavolotsky, Christophe Risacher, Victor A. Perez Robles, Victor Belitsky, Vladimir Drakinskiy and Sergey Cherednichenko

Abstract— **We present results on the design and construction of a waveguide balanced Hot Electron Bolometer (HEB) Terahertz mixer for Atacama Pathfinder EXperiment (APEX), band T2 covering 1250-1390 GHz frequency range. In the proposed design, a waveguide balanced mixer is realized using a quadrature scheme. The two identical HEB elements are integrated with RF choke filters, DC-bias, IF circuitry, and fabricated from 4 nm thick NbN film deposited on a crystalline quartz substrate with dimensions of 1100 µm×70 µm×17 µm. We have designed and fabricated an input 3 dB quadrature waveguide hybrid. For its fabrication, we use micromachining approach to achieve low insertion loss and symmetrical division of the RF and local oscillator (LO) power within the band of interest. We plan to use two HEB mixer configurations with different probe impedance values of 55, 70 Ohm within 1250-1390 GHz frequency range.**

***Index Terms*—balanced mixer, terahertz radio astronomy, hot-electron bolometer mixer.**

I. Introduction

THE APEX 12 single dish telescope located at Chajnantor Plato, in Northern Chile will be equipped with heterodyne and bolometric receivers for radio astronomical observations at the frequency range 211 – 1500 GHz [1]. According to recent atmospheric measurements, the three windows centered at 1.03, 1.35 and 1.5 THz show transmission as high as 40% under favorable conditions on this site [2]. Currently, there is only one ground-based submillimeter telescope successfully operating at frequencies above 1 THz [3].

In this paper, we present progress of our development of the waveguide balanced HEB mixer intended for APEX band T2 covering 1250 - 1390 GHz frequency range with a central frequency of 1320 GHz.

The balanced scheme of HEB mixer has a number of benefits over a single-ended mixer. Among them, for instance, are good rejection of LO amplitude modulation noise and better LO power handling capabilities [4]. On the other hand, the high operating frequencies, above 1 THz, introduce significant difficulties for manufacturing waveguide components, and make balanced design less attractive.

The prototype's design of waveguide balanced HEB mixer for APEX 1.3 THz receiver proposed in [9] is revised significantly. In the current paper, we present important improvement in mixer components design and fabrication. Figure 1 shows the quadrature scheme of our balanced HEB mixer. The 3 dB quadrature waveguide hybrid couples the RF signal and LO to the individual identical HEB mixers. The outputs from the HEB mixers at intermediate frequency (IF) are connected to cryogenic IF low noise amplifiers (LNA). These LNAs 2-4 GHz designed at GARD use 50 Ω-matched inputs in order to improve system noise temperature by avoiding circulators [5]. A commercial 180° IF hybrid combines IF outputs from the both mixers. The resulting IF signal is collected at one of the IF hybrid outputs, and the amplitude component of the sideband LO noise is terminated at the other output. Placing the LNAs before the IF hybrid should improve the system noise performance by the reduction of the additional noise caused by the IF hybrid insertion loss. In contradistinction to the previous mixer design [9], we do not use an additional cryogenic LNA following the IF hybrid. Moreover, the isolation of the balanced mixer depends on the amplitude and phase imbalance of the two IF amplifiers.

II. Waveguide 90° Hybrid

The input waveguide 3dB hybrid providing LO injection and RF signal distribution between two HEB mixers with 90° phase shift, is designed compatible with the split-block technique. The splitting takes place through the plane of symmetry in the middle of the waveguide's broad walls. Therefore, possible imperfect contact between two halves will not affect the

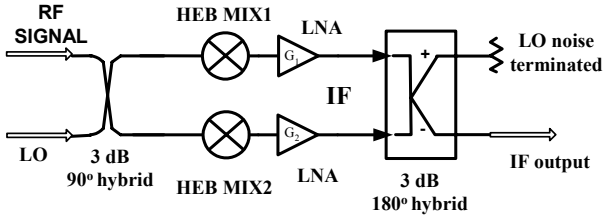

Fig.1. Scheme of the balanced HEB mixer

Manuscript submitted May 2005.

Denis Meledin, Miroslav Pantaleev, Alexey Pavolotsky, Christophe Risacher, Victor A. Perez Robles, and Victor Belitsky are with Group for Advanced Receiver Development (GARD), MC2, Chalmers University of Technology, S-412 96, Gothenburg, Sweden. (the first author's phone: +46 31 772 1842, fax: +46 31 772 1801; e-mail: meledin@oso.chalmers.se).
Vladimir Drakinskiy and Sergey Cherednichenko are with Microwave Electronics Laboratory, MC2, Chalmers University of Technology, S-412 96, Gothenburg, Sweden.

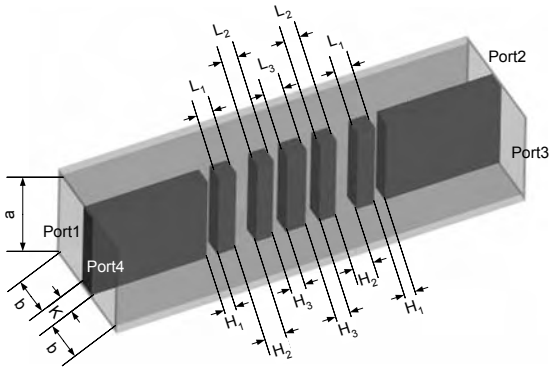

Fig.2. The waveguide hybrid with six branches. The main waveguide size is 180 μm (dimension *a*) by 90 μm (dimension *b*). Values of *K*, L_n, H_n were varied to achieve the optimal configuration of the coupler at *K*=50 μm, H_1=21 μm, H_2=35 μm, H_3=25 μm, L_1=44 μm, L_2=41 μm, L_3=45 μm.

hybrid's performances.

In order to ensure fractional bandwidth of about 20%, we intend to use a six-section hybrid. Drawing of the proposed hybrid design is shown in Fig.2. The increased number of branches makes the fabrication difficult because the required dimensions become too small to be produced with sufficient accuracy using conventional machining techniques.

The design variables are the heights of the branches (H_n), the spacing between branches (L_n), and the distance between the main waveguides (*K*). The main waveguide dimensions a=180 μm and b=90 μm are fixed. Thus, for each half of the split-block the waveguide depth channel has to be 90 μm. The limit of branch guide height H_n is chosen to be as low as 20 μm.

To analyze the hybrid performance, the hybrid was represented as a series of E-plane T-junctions interconnected by waveguides. On the initial stage of the design, we applied a numerical matrix method based on circuit theory [6], [7]. Then final optimization of the hybrid performance was carried out by using HFSS™[8]. The optimal configuration of the hybrid is achieved with the following values of the design variables: *K*=50 μm, H_1=21 μm, H_2=35 μm, H_3=25 μm, L_1=44 μm, L_2=41 μm, L_3=45 μm. In Figure 3, the lines show S_{21}, S_{31}, S_{11}, and S_{41} values obtained from HFSS simulations. As we mentioned above, the amplitude and phase symmetry at the two ports of the hybrid is crucial for good isolation between the mixers. For the optimal design parameters, amplitude imbalance, $S_{31} - S_{21}$, and phase difference, ϕ_{31}-ϕ_{21}, at the outputs of the hybrid are better then 0.5 dB and 0.5°, correspondingly, within the 1250-1390 GHz band.

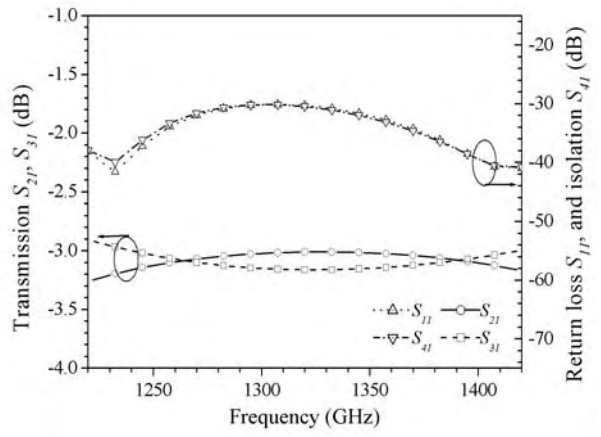

Fig.3. Results of HFSS simulations of the hybrid S-parameters at the optimal design variables.

In our previous paper [9], we found that the amplitude imbalance between port 2 and 3 of the hybrid over the required band became not acceptable if all structure dimensions has been produced with a linear error as small as 2 μm. Therefore, the required dimension tolerances along with high quality of the waveguide walls surface (better than 0.1 μm at 1.3 THz) prompts to use a micromachining method for fabrication the hybrid. In order to achieve the required machining precision, we use photolithography of thick SU-8 [10] photoresist combined with the copper electroplating. This fabrication method was discussed in a greater detail in [11], and has shown good dimension reproducibility with accuracy of better than 2 μm. The hybrid made using this technology is shown in Fig. 4a, b.

III. HEB MIXER DESIGN

The key and extremely important part of our heterodyne receiver is a pair of phonon-cooled HEB waveguide mixers based on NbN film deposited on 150 μm thick crystalline quartz substrate. For these films, the typical critical temperature is about 9.5 K with transition widths of 0.6-0.7 K. The film is patterned using e-beam lithography to form the bolometer elements of 0.1-0.2 μm long and 1-2 μm wide. With those dimensions, the measured mixer's room-temperature resistance is within a range of 100-130 Ω. The normal-state resistance, R_N, is about 15% higher than the room-temperature value. Critical current value is close to 140 μA at 4.2 K bath temperature.

For a balanced mixer, each HEB should have very similar DC and noise characteristics to guaranty better balance and the LO noise rejection. The HEB element is integrated with the "hammer" type RF filters, DC-bias circuitry, and IF leads on an individual crystalline quartz substrate with dimensions of

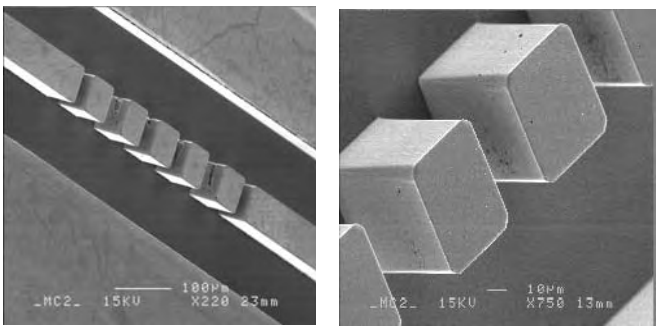

a). b).

Fig.4a, b. SEM pictures of the hybrid's halves fabricated from copper, and split through the plane of symmetry at the middle of the main waveguides broad walls.

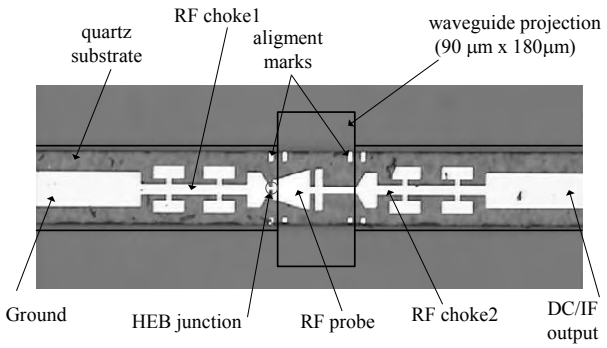

Fig.5. The layout of the individual HEB mixers integrated with RF filters, DC-bias, and IF circuitry on an individual crystalline quartz substrate with dimensions of 1000 μm x70 μm x17 μm

1000 μm x70 μm x17 μm. Both substrates will fit into a suspended microstrip channel across the broad wall of full height 180 μm x 90 μm waveguide inside a copper mixer block with fixed 70 μm backshort. The individual HEB mixer layout is shown in Fig.5. In the probe design, the input RF signal coming from waveguide port is coupled to the HEB junction by E-type probe, and appeared to be isolated from DC bias/IF output port using RF choke [12]. Good match over wide frequency band with no needs to reduce the waveguide height makes the "one side" probe's configuration attractive especially for THz frequencies. The 17 μm thickness of quartz substrate is chosen to prevent propagation of waveguide mode to the IF port.

We have two designs of the RF probe providing different embedding impedance to the HEB elements of about 55 Ohm (type A), 70 Ohm (type B) within the receiver frequency band, as shown on the Smith chart in Fig. 6. The HFSS simulation results show that RF probe impedance is purely real in

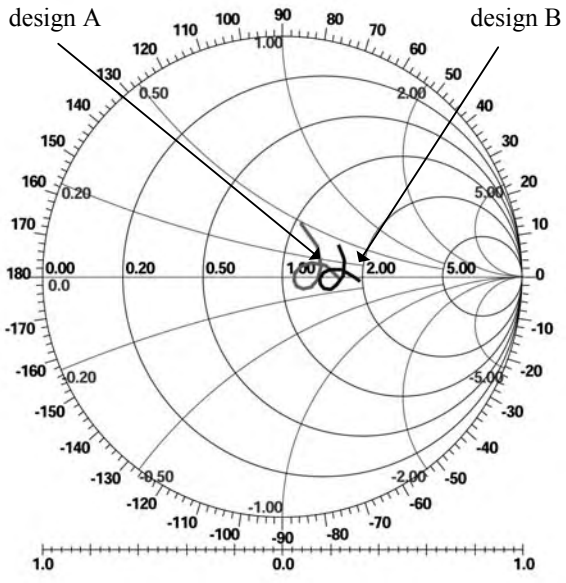

Fig.7. Smith chart normalized to 50 Ohm with RF probe impedance values at the HEB junction input for two probe designs: type A (gray curve) and type B (black curve). The frequency range is from 1220 to 1420 GHz.

frequency range from 1248 to 1392 GHz for the both proposed designs.

The mixer block is under machining at our workshop, and we expect that the first measurements results of the 1.3 THz mixers will be reported soon.

IV. Conclusion

We have achieved a final stage of the development of a waveguide balanced HEB 1.3 THz receiver for APEX Band T2. We have successfully designed and fabricated 1.32 THz waveguide 3 dB 90°-hybrid. According to the detailed HFSS simulations, the required values of the amplitude and phase imbalance at the coupler's outputs have been achieved.

We have designed two types of RF probe with different embedding impedance to the HEB elements of about 55 and 70 Ohm in 1250-1390 GHz frequency range. The first batch of NbN HEB mixers with the two types of RF probe has been fabricated and prepared for further measurements.

V. Acknowledgment

The authors thank B. Voronov and G. Goltsman, Moscow State Pedagogical University for deposition of NbN films, A. Kalaboukhov, Chalmers University of Technology for the hybrid photomask preparation.

This work is a part of APEX Project, and is supported by Swedish Research Council and Wallenberg Foundation by their respective grants. EU FP6 RadioNET AMSTAR program provides also support for these research activities.

VI. References

[1] APEX project on web http://www.oso.chalmers.se/oso/apex/index.html.

[2] S. Paine, et al., "A Fourier transform spectrometer for measurement of atmospheric transmission at submillimeter wavelengths," *Publications of the Astronomical Society of the Pacific*, vol. 112, pp 108-118, Jan. 2000.

[3] D. Marrone, J. Battat, F. Bensh, R. Blundell, M. Dias, H. Gibson, et al., "A map of OMC-1 in CO J=9→8," *Astrophys. J.,* vol. 612, pp. 940-945, September 2004.

[4] S. A. Maas, Microwave Mixers, 2nd edition. Boston, MA: Artech House, 1993.

[5] C. Risacher, E. Sundin, V. Perez Robles, M. Pantaleev, and V. Belitsky," Low noise and low power consumption cryogenic amplifiers for Onsala and APEX telescopes", presented at European Microwave Week 2004, Amsterdam, October 2004.

[6] Hiroya Andoh, Shinichiro Asayama, Hideo Ogawa, et al., "Numerical matrix analysis for performances of wideband 100 GHz branch-line couplers," *Int. Jour. of Infr. and Mill. Waves,* vol. 24, no. 5, pp. 773-788, May 2003.

[7] N. Marcuvitz, *Waveguide Handboo*k, New York: McGraw Hill, 1951.

[8] Agilent Technologies, 395 Page Mill Road, Palo Alto, CA 94304 USA.

[9] Pantaleev, D. Meledin, A. Pavolotsky, C. Risacher, and V. Belitsky, "Design of a Balanced Waveguide HEB Mixer for APEX 1.32 THz Receiver", presented at the 15th International Symposium on Space Terahertz Technology, Northampton, MA, USA, April 2004.

[10] MicroChem Corp., 1254 Chestnut Street, Newton, MA 02464 USA.

[11] A. Pavolotsky, D. Meledin, C. Risacher, M. Pantaleev, V. Belitsky, "Micromachining approach in fabricating of THz waveguide components", to be published in *Microelectronics J." Circuits and Systems".*

[12] C. Risacher, V. Vassilev, A. Pavolotsky, V. Belitsky, "Waveguide-to-microstrip transition with integrated Bias-T", *IEEE Microwave and Wireless Components Letters*, vol.13, no. 7, July 2003, pp. 262-264.

Lifetimes of NbN Hot Electron Bolometer mixers.

M. Hajenius, Z.Q. Yang, J.J.A. Baselmans and J.R. Gao.

***Abstract*— Superconducting NbN hot electron bolometer mixers have become the only sensitive heterodyne detectors operating at frequencies far above 1 THz. Since their application will be mainly in space, the reliability of such mixers becomes a key issue. In this paper we report measurements of the resistance and the superconducting critical current as a function of time under normal laboratory conditions for a period of one year as well as the resistance versus time under a harsh condition (85 ^oC/ 85 $\%$ relative humidity). The devices studied are small volume twin slot antenna coupled NbN HEB mixers. By defining the lifetime during which the room temperature resistance increases by 15 $\%$, we find that the lifetime of standard devices is only half a year in normal atmosphere, which is insufficient for space applications. However, by introducing an additional passivation on the standard devices, the lifetime becomes longer than one year. The advantage of applying the passivation layer is further confirmed by the 85/85 accelerated tests.**

***Index Terms*— Superconducting, NbN, HEB mixers, Lifetime, Space Qualification, Passivation layer, SiO_2.**

I. Introduction

NBN HEB detectors currently demonstrate the best characteristics for heterodyne astronomical observations at frequencies above 1.5 THz [1], [2]. Since the earth's atmosphere is largely opaque in this range the mixers will primarily be used from space (e.g. HIFI on HERSCHEL space telescope [3]) or from high elevations. Obviously, reliable detector operation of the NbN based HEBs is crucial to the success of such missions. However, in contrast to standard semiconductor devices, very few is known about the lifetime of mixer structures based on extremely thin (NbN) superconducting films.

According to the American Society for Testing and Materials (ASTM), the service lifetime of materials, devices, or systems is the exposure time at which degradation occurs below a prescribed or required value, i.e. a total failure or a failure to perform at a preassigned value. Still, no such criteria have been established for NbN HEB mixers yet. It is clear that deterioration of superconducting properties eventually imposes questionable device operation and even failure. The increase in room temperature resistance (R_{300K}) is found as a good indicator for this deterioration. We choose a 15 $\%$ increase in R_{300K} as prescribed limit.

The (required) lifetime is in general coupled to the precise conditions under which the device is kept or treated. Two conditions are of special interest: Firstly under normal atmosphere at room temperature and secondly under vacuum at 85 ^oC. For space applications, the mixers should be able to survive many integration, transport and storage steps. The total duration of exposure to normal atmosphere can be between one to five years [4]. The resistance to more extreme conditions, i.e. baking at 85 ^oC for at least 72 hours [4] under vacuum is required as a standard method to assure vacuum hardness of the system. We note that several other conditions (e.g. thermal cycling) remain undiscussed here since they proved to be unproblematic.

M. Hajenius, Z.Q. Yang, J.J.A. Baselmans, and J.R. Gao are with the SRON National Institute for Space Research, Sorbonnelaan 2, 3584 CA Utrecht, The Netherlands.

M. Hajenius and J.R. Gao are also with the Kavli Institute of NanoScience Delft, Faculty of Applied Sciences, Delft University of Technology, Lorentzweg 1, 2628 CJ Delft, The Netherlands.

II. Devices

The HEB devices under consideration are based on sputtered NbN thin films on a pure Si substrate with an intended thickness of 3.5 nm prepared at MSPU, Moscow. The unprocessed NbN has a critical temperature (T_c) between 8.6 - 9.3 K depending on the film and precise location on the wafer, a sheet resistance ($R_{sheet,300K}$) of 600 Ω at 300 K, and a resistance ratio RRR $(R_{sheet,300K}/R_{sheet,16K})$ of 0.8. After processing the bulk film degrades marginally: The $R_{sheet,300K}$ of the film, of a large structure is slightly higher; 650 Ω, the T_c is reduced < 0.5 K, and a critical current (I_c) of 900 μA for an 8 μm wide structure is measured.

Below we discuss the fabrication process of the devices as lifetime may depend on its details.

The NbN films are contacted to the antenna structure by the contact pads. The contact pads are defined by E-beam lithography using a double layer PMMA resist system, which requires in total 10 minutes baking at 120 ^oC. After development, an Oxygen plasma clean is performed, just long enough to remove resist remnants. Next, a short physical Ar^+ etch is performed followed by in situ deposition of 10 nm of $NbTiN$ and 40 nm Au. We note that the exact contacting procedure is crucial [6], [7] to device performance. See Fig. 2

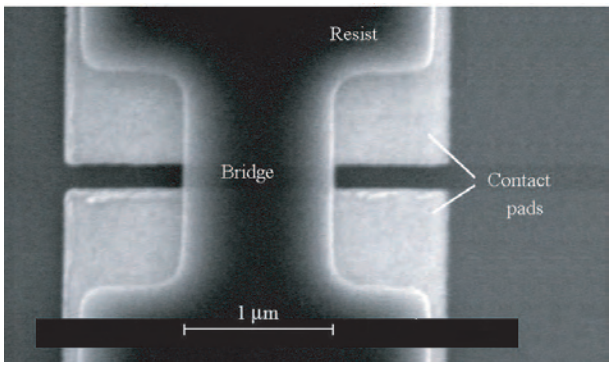

Fig. 1. SEM picture showing a Topview of the HEB bridge structure. The HEB consists of the NbN bridge in the middle contacted by two large contactpads on either side. The HEB bridge is protected by negative resist on top.

for a cross-section of the contactpads. To define the twinslot antenna, a single layer Negative resist is spun, requiring 3 minutes baking at 90 ^oC and after E-beam exposure a 3 minutes 110 ^oC postbake. After development with MF322 for 9 minutes and Oxygen plasma clean we evaporate 5 nm Ti for adhesion and 150 nm Au to constitute the antenna. Liftoff is done in PRS3000 at 90 ^oC for two minutes in combination with ultrasonic agitation, followed by 5 minutes ultrasonic agitation in Acetone. Finally, the bridge is defined by E-beam lithography using a 500 nm thick SAL601 negative resist etch mask. After 7 minutes development in MF322 we perform an Oxygen plasma clean to remove resist remnants. The final etch is performed by RIE using CF_4 + O_2, with a 20 $\%$ overetch. After RIE etching, a short Oxygen etch is performed to oxidize any remaining material on the surface. After the final etch, the remaining SAL601 etch mask is about 300 nm thick and is left on the device. The completed bridge measures 150 nm in length and 1.0 um to 2.0 um in width, see Fig. 1. This concludes fabrication for ”standard” devices.

To reduce the aging effect, to be discussed shortly, we introduce a passivation layer on top of the active region of the HEB. This layer consists of 500 nm thick SiO_x ($1.5 < x < 2.0$). The Devices *with* passivation layer experience only one additional fabrication step which consists of SiO_x sputter deposition using a SiO_2 target. Note that the sample is pumped down 24 hours before deposition. An elevated mask is used to cover only a 200 μm x 200 μm region around the bridge *with* SiO_x. The SAL601 resist remains on the bridge in order to avoid chemical reactions between SiO_x and NbN. Care is taken to avoid heating of the substrate during the SiO_x deposition.

Shortly after fabrication, such devices (1 μm wide) have a $R_{sheet,300K}$ around 800 to 900 Ω and (I_c) around 70 μA. These values are found for both devices *with* and *without* passivation layer. Note that this is higher and lower respectively than values for a big film after processing. The reason for this is not clear to us. Note however that devices are typical and are taken from several batches with mixer performance $>$ 10 $\%$ from the best.

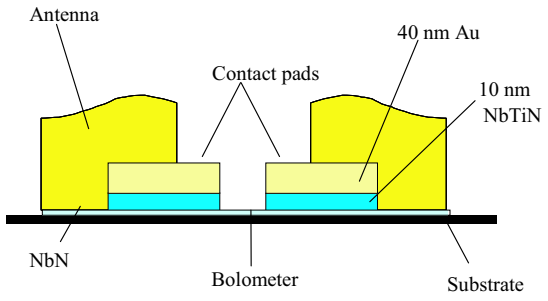

Fig. 2. Cross-sectional drawing of the HEB structure as shown from the top in Fig. 1. The cross-section reveals the composition of the contactpads, consisting of the NbN with 10 nm NbTiN on top followed in situ by 40 nm Au. Note that the resist protecting the NbN bridge is not shown.

III. Lifetime in laboratory conditions

Lifetime measurements of NbN HEBs are performed in standard laboratory conditions, 20 ^oC and 65 $\%$ relative humidity (RH). The R_{300K} as well as the superconducting properties are measured at certain intervals in time. Fig. 3 shows the typical resistance versus temperature (RT) and Fig. 4 the current versus voltage (IV) measurements for a device *without* passivation layer. It becomes clear from Fig. 5 how the resistance increases while T_c and I_c decrease for longer exposure. To show this trend for more devices, the R_{300K} and I_c of several devices *without* passivation layer versus exposure time is shown in Fig. 5. Note that the readily measured R_{300K} reliably indicates the degradation of superconducting properties. Specifically, the standard devices (*without* passivation layer) show an increase in resistance of about 0.1-0.3 Ω per day. Over a period of one year the R_{300K} is expected to increase about 7-30 $\%$ (10-50 Ω). The average lifetime of the devices *without* passivation layer is thus about half a year, well below the required one year. The 15 $\%$ increase in R_{300K} matches with a substantial 30 $\%$ average reduction in I_c.

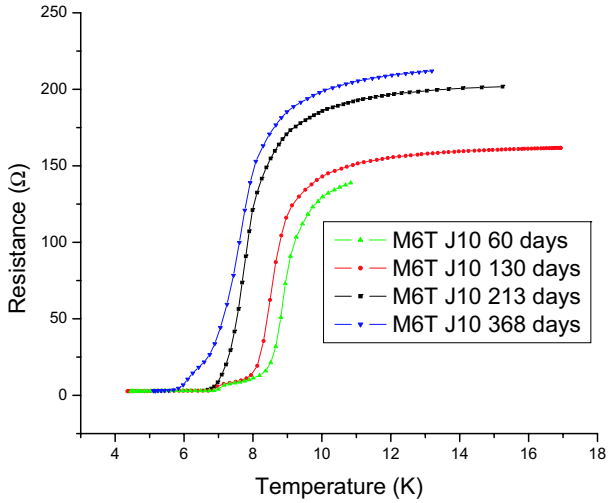

Fig. 3. Resistance versus Voltage plot of device J10 of batch M6T measured at several intervals, indicated in days after fabrication.

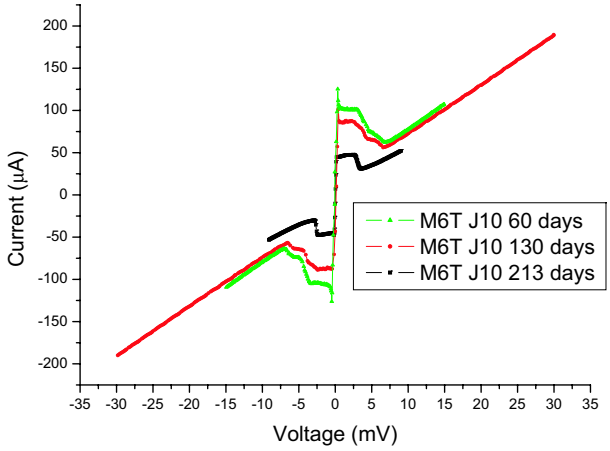

Fig. 4. Current versus Voltage plots of device J10 of batch M6T measured at several intervals, indicated in days after fabrication.

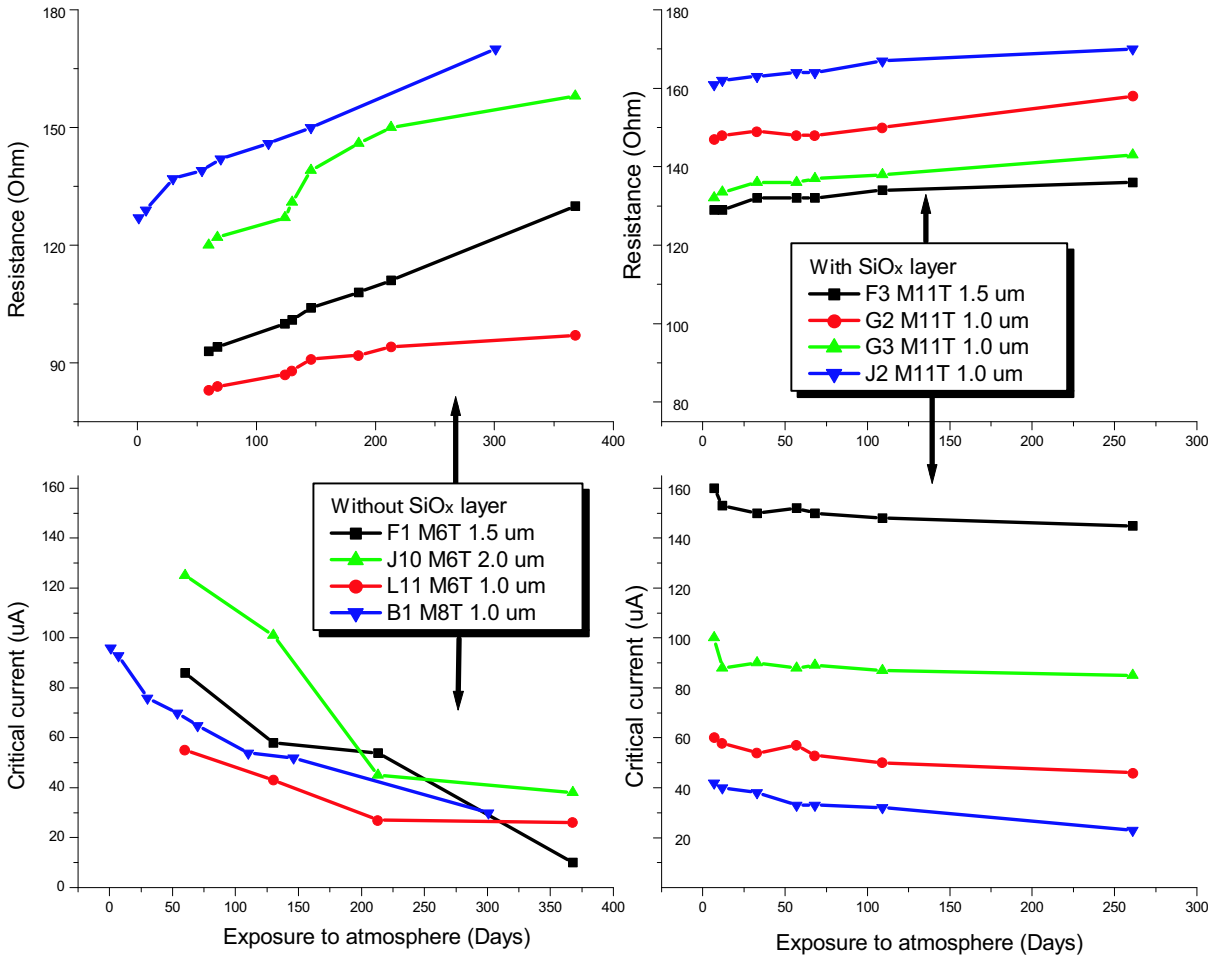

Fig. 5. Normal state resistance at 300 K (top panels) and critical current at 4.2 K (lower panels) versus exposure time in atmosphere at 300 K and 65 % RH. Left panels are for devices *without* passivation layer, right panels for devices *with* SiO_x passivation layer.

By storing devices in vacuum, we found that the aging effect is reduced considerably. This indicates that O_2 and H_2O in normal atmosphere are likely ingredients of the aging. However, during integration of HEB mixers into the instrument, applying vacuum is impractical. This motivates the introduction of a capping layer to reduce the aging effects, similar to the SiO passivation layer proposed by Kawamura et al. for Nb HEBs [8]. Fig. 5 shows the dramatic improvement in lifetime by using SiO_x passivation layer, in which the resistance increases less than 10 % during approximately one year storage in the laboratory. This is also reflected by no more than 10-15 % decrease of I_c for the same storage time.

IV. Accelerated lifetime tests.

A standard method to determine the lifetime of semiconductor devices is the "accelerated test" at 85 ^oC and 85 % relative humidity (RH). Then, applying a well established model to predict the lifetime under normal conditions. This method can not apply to NbN HEB mixers since such model is lacking. We merely make use of the accelerated lifetime test to compare the devices *with* and *without* passivation layer. We performed accelerated lifetime tests at 85 % RH and 85 ^oC. The R_{300K} as function of exposure time is shown in Fig. 7. The R_{300K} in Fig. 7 increases exponential-like over time for both devices *with* as well as *without* passivation layer. The 15 % increase in R_{300K} of devices *without* passivation layer is reached on average after 29 hours and only after an average of 60 hours

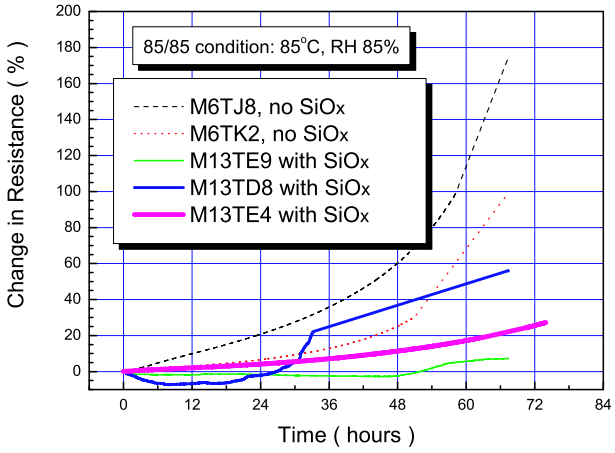

Fig. 7. Accelerated aging test by monitoring the device resistance under a harsh 85 ^oC - 85 % relative humidity environment as a function of time. The R_{300k} of the devices is close to 150 Ω, except for device J8 which has a R_{300k} of 100 Ω.

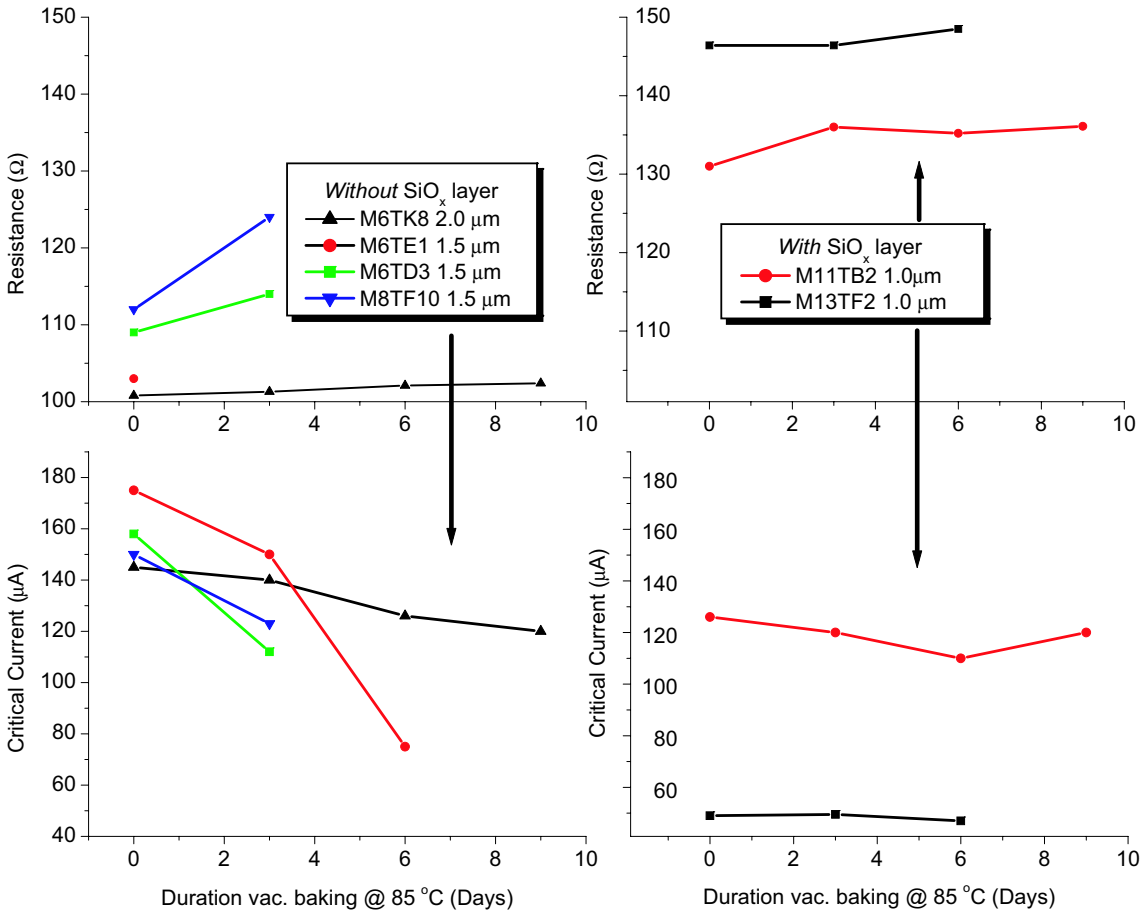

Fig. 6. Normal state resistance at 300 K (top panels) and critical current at 4.2 K (Lower panels) versus baking time in days at 85 ^oC and $6 \cdot 10^{-5}$ mB. Left panels are for devices *without* passivation layer, right panels for devices *with* SiO_x passivation layer.

for devices *with* passivation layer. This confirms the advantage of using the SiO_x passivation layer.

V. Lifetime under bake-out conditions.

Devices were baked at 85 ^oC under vacuum conditions ($6 \cdot 10^{-5}$ mB) using a rotary pump. The baking was interupted for characterisation of R_{300K} and I_c. Fig. 6 shows R_{300K} and I_c as a function of baking time. For devices *without* passivation layer, R_{300K} increases between 5 % and 20 % for a duration of 9 days. Critical current decreases from 10 % to 60 % after 9 days baking. Although some devices *without* passivation layer hardly change, the limit of 15 % R_{300K} increase is exceeded for others. Moreover, the atmospheric pressure during bake-out may be much higher than used in this baking test. Consequently the deterioration of the device performance of devices *without* passivation layer may be even more severe. Again, devices *with* passivation layer show reduced deterioration as can be seen in Fig. 6. R_{300K} increases less than 10 % and I_c decreases less than 20 % for 9 days of baking at 85 ^oC. It is interesting to note that a device with low critical current density (J_c) *with* passivation layer shows almost unchanged I_c after a maximum of 6 days baking. We note that pumping down the oven 24 hours before starting the heater is advantageous in reducing device degradation. Baking has been performed to a maximum of 9 days.

As part of the baking tests we also measure the influence on RF performance. Fig. 8 shows the mixer noise temperature

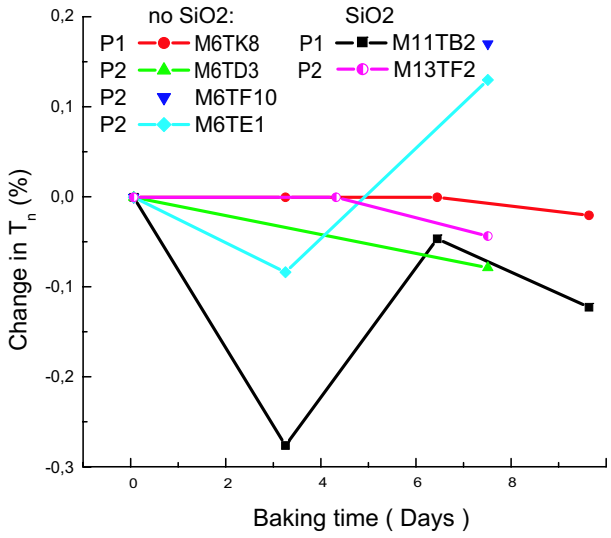

Fig. 8. Relative changes of the noise temperature with baking time in days for devices *with* and *without* passivation layer. P1 indicates the procedure that the heating was switched on 24 hours after the pumpdown was started. P2 indicates that the heater was started several hours after the pumpdown was started. In both cases the pressure during baking was about $6 \cdot 10^{-5}$ mB

(T_n) for different durations of baking. Also here we compare between devices *with* and *without* passivation layer. We find that T_n can either decrease or remain unchanged after short baking times of 2-3 days. When baking is resumed, after a total of 6 days of baking the T_n will increase again. Devices *with* passivation layer generally show largest decrease of T_n after 3 days while after 6 days the increase in T_n is small compared to before baking. The exact reason for this is not clear. However, DC characterization suggests an improvement of the contacts by short baking (e.g. 3 days) in competition with film degradation for longer baking times [9].

VI. Conclusions.

The resistance and superconducting critical current of standard NbN HEB devices in normal atmosphere *without* passivation layer show a severe deterioration over a period of about one year. Based on this data, a practical definition for the lifetime is established which equals the duration at which the R_{300K} has increased by 15 $\%$. Using this definition we find that standard devices *without* passivation layer have a lifetime of about half a year, which is insufficient for (space) applications. In contrast, devices with a 500 nm thick SiO_x passivation layer have prolonged lifetime in atmosphere to more than one year. The advantage of introducing the passivation is further confirmed by accelerated lifetime tests. The devices *with* the passivation layer show lifetimes at least a factor of two longer than those *without*.

References

[1] E.M. Gershenzon, G.N. Goltsman, I.G. Gogidze, A.I. Eliantev, B.S. Karasik and A.D. Semenov, *Millimeter and submillimeter range mixer based on electronic heating of superconducting films in the resistive state*, Sov. Phys. Supercondcutivity **3**, 1582 (1990).

[2] D.E. Prober, *Superconducting terahertz mixer using a transition -edge microbolometer*, Appl. Phys. Lett. **62**, 2119 (1993).

[3] http://www.esa.int/science/herschel.

[4] B. Jackson, J. Evers, K. Wafelbakker, *"Environmental Test Levels for the HIFI Mixers"*, Doc. no.: FPSS-00276, Issue: 1.1, Category: 3, (2002).

[5] M. Hajenius, J.J.A. Baselmans, J.R. Gao, T.M. Klapwijk, P.A.J. de Korte, B. Voronov and G. Gol'tsman, "low noise NbN superconducting hot electron bolometer mixers at 1.9 and 2.5 THz", Superconductor Science and Technology, **17**, 224 (2004).

[6] M. Hajenius, J.J.A. Baselmans, J.R. Gao, T.M. Klapwijk, P.A.J. de Korte, B. Voronov and G. Gol'tsman, *"low noise NbN superconducting hot electron bolometer mixers at 1.9 and 2.5 THz*", Superconductor Science and Technology, **17**, 224 (2004).

[7] J.J.A. Baselmans, J M.Hajenius, R. Gao, T.M. Klapwijk, P.A.J. de Korte, B. Voronov, G. Gol'tsman. "*Doubling of sensitivity and bandwidth in phonon cooled hot electron bolometer mixers*", Appl. Phys. Lett. **84**, 1958, (2004).

[8] J. Kawamura, B. Bumble, D.G. Harding, W.R. McGrath, P. Focardi, R. LeDuc, "*1.8 THz superconductive hot-electron bolometer mixer for Herschel*, Proceedings of the SPIE, **4855**, pp. 355-360, (2002).

[9] Z.Q. Yang, M. Hajenius, J.J.A. Baselmans, T.M. Klapwijk, J.R. Gao, B. Voronov, G. Gol'tsman, "*Improved Performance of NbN hot electron bolometer mixers by vacuum baking*", This proceedings.

Improved sensitivity of NbN hot electron bolometer mixers by vacuum baking

Z.Q. Yang*, M. Hajenius*†, J. J. A. Baselmans†, J.R. Gao*†,
T. M. Klapwijk†, B. Voronov‡ and G. Gol'tsman‡
*SRON National Institute for Space Research, Sorbonnelaan 2, 3584 CA Utrecht, The Netherlands
†Kavli Institute of NanoScience Delft, Faculty of Applied Sciences, Delft University of Technology,
P.O. Box 5046, 2600 GA Delft, The Netherlands
‡Physics department, Moscow State Pedagogical University, Moscow 119435, Russia

***Abstract*— We find that the sensitivity of heterodyne receivers based on superconducting hot-electron bolometer (HEB) increases by 25 − 30% after baking at 85 ^{o}C and in a high vacuum. The devices studied are twin-slot antenna coupled HEB mixers with a small NbN bridge of 1×0.15 μm^2. The mixer noise temperature, gain, and resistance versus temperature curve of a HEB before and after baking are compared and analyzed. We show that baking reduces the intrinsic noise of the mixer by 37 % and makes the superconducting transition of the bridge and the contacts sharper. We argue that the reduction of the noise is due to the improvement of the transparency of the contact/film interface. The lowest receiver noise temperature of 700 K is measured at a local oscillator frequency of 1.63 THz and a bath temperature of 4.3 K.**

I. Introduction

In recent years phonon-cooled hot electron bolometer (HEB) mixers have matured as the only sensitive heterodyne detector for the frequency range from 1.5 to 6 THz [1], [2], [3], [4]. HEBs based on thin superconducting NbN film with a fast electron-phonon cooling are particularly attractive due to their high sensitivity and large intermediate frequency (IF) bandwidth. Theoretically it has been predicted that such mixers could have nearly quantum noise limited sensitivity [5]. However, the best double sideband (DSB) receiver noise temperature ($T_{rec,DSB}$) reported so far is 950 K at 2.5 THz, corresponding to 8 $h\nu/k_b$, where h is Plank's constant, ν the frequency, and k_b Boltzmann's constant. This result was achieved in a spiral-antenna coupled large NbN HEB (4×0.4 μm^2) mixer by cleaning the surface of the NbN film and depositing a superconducting NbTiN interlayer and a standard Au layer as the contacts during fabrication [4], [6]. By applying the same contacts, a $T_{rec,DSB}$ of 900 K has been obtained in a twin slot antenna coupled small NbN HEB (1×0.15 μm^2) mixer at 1.6 THz [7]. Despite of the fact that similar result has been reproduced in devices fabricated in other runs, fluctuations in the sensitivity have been observed among a large number of batches. We report here that the sensitivity of "poor" NbN HEB mixers can be improved by vacuum baking. To understand the result, we monitor and analyze the dc properties, the mixer noise temperature, and the mixer conversion gain before and after baking.

II. Experimental

The NbN HEB mixers studied in the present work are fabricated using a standard thin NbN film (with an intended thickness of 3.5 nm) on a Si substrate with a superconducting transition temperature T_c of 9.5 K, and coupled by a twin-slot antenna designed for 1.6 THz (see the inset of Fig. 1). The superconducting bridge of the mixer is 1 μm wide and 0.15 μm long and the contacts are made of Au/NbTiN. Before deposition of the contact layers, a short O_2 plasma etch is first applied to remove resist remnants and then a short in-situ Ar sputter etch is introduced to clean the film surface. We anticipate this to be a critical step technologically, which can result in the fluctuations of the interface quality from batch to batch. The fabrication process is very similar to our early work [6], except for the definition of the antenna and a passivation layer. The passivation SiO_2 layer of 500 nm is sputtered on top of the active region of the HEB mixer, to prevent the aging effect in normal lab conditions. Although several devices were measured, we focus here on the one showing a normal state resistance (R_N) of 153 Ω at 16 K and a slightly reduced T_c of around 9 K. Vacuum baking has been performed in an oven connected to a turbo pump. Before switching on and setting it to 85^{o}C, the oven has been pumped for 24 hours and the pressure reached 10^{-5} mbar. Under these conditions the devices were baked for 72 hours.

We measure the receiver noise temperature, the gain, and the dc resistance versus temperature (RT) curve before and after baking. We use a RF (radio frequency) test setup for a typical Y-factor measurement. A standard quasi-optical technique is applied to couple RF signal from the free space to the HEB. The HEB chip is glued on the backside of an elliptical silicon lens. The lens is placed in a metal mixer block, thermally attached to the 4.2 K cold plate of a vacuum cryostat. Blackbody signal sources (Eccosorb) are used as the signal, which defines a hot load at 295 K and a cold load at 77 K. The signal is combined with the local oscillator (LO) signal via a 3.5 μm thick Mylar beam splitter. Both of the signals transmit further into the lens though a 1.1 mm thick HDPE window (RF loss of -1.1 dB) and a Zitex G104 (-0.45 dB) heat filter at 77 K. The LO source is an optically pumped gas laser at 1.63 THz and is attenuated with a rotatable grid. The IF signal

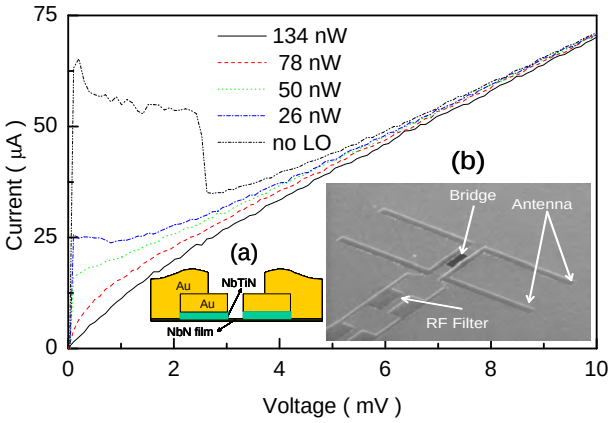

Fig. 1. Current-voltage characteristics of a NbN HEB mixer without and with LO power, before baking. In the inset: a) a cross-section view of the bridge and the contacts of the HEB mixer; b) a top view of the HEB mixer before the deposition of the SiO_2 layer, where the bridge, antenna, and RF filter structure are indicated. The transmission line (not indicated) connects the HEB to the antenna.

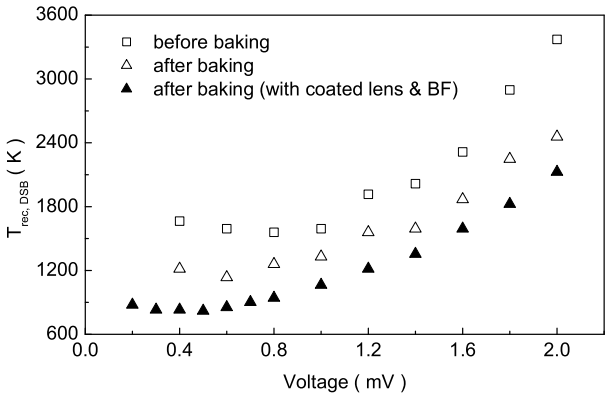

Fig. 2. Receiver noise temperature (DSB) of the HEB mixer as a function of bias voltage obtained before and after baking. Symbol notation: open squares and up-triangles - before and after baking measured on an uncoated lens; closed up-triangles - after baking measured using a coated lens and a cold bandpass filter.

is amplified by a low noise amplifier with 40 dB gain and a noise temperature of 5 K. The signal is further amplified by a room temperature amplifier with 41 dB gain and is filtered in a 80 MHz bandwidth at 1.4 GHz before detection with a power meter. The Y-factor used for calculating the receiver noise temperature, is the ratio of the measured IF output powers responding to the hot and cold loads [8]. The dc resistance is measured using a standard lock-in technique.

III. Results and Discussion

A. Current-voltage characteristics

In Fig. 1 we plot the current-voltage (IV) curves without and with applying LO power before the device is baked. We measured also the unpumped and pumped IV curves after baking and find a small reduction of the critical current from 68 μA to 65 μA and a small (4 Ω) increase of R_N. However, the pumped IV curves are similar. In particular, the optimal IV curve, where the lowest noise temperature is obtained, remains unchanged. Based on the IV curves at different pumping levels, the LO power absorbed by the HEB is estimated using the isothermal technique [9]. The optimal LO pumping level is around 50 nW for both cases.

B. DSB receiver noise temperature

The $T_{rec,DSB}$ calculated according to the Callen-Welton definition [8] are plotted in Fig. 2 as a function of bias voltage at the optimal LO power before and after baking. Note that in both cases an uncoated Si lens is used and the total RF loss in the signal path is -4.35 dB. As indicated in the figure, the $T_{rec,DSB}$ after baking decreases significantly over the whole voltage bias range. At the optimal bias point (0.6 mV), the $T_{rec,DSB}$ decreases by 27% and becomes 1050 K, which is slightly lower (7%) than the previous best result for the case of the uncoated lens [7]. Similar improvement was observed in four other devices, showing a decrease of $25-30\%$ in $T_{rec,DSB}$.

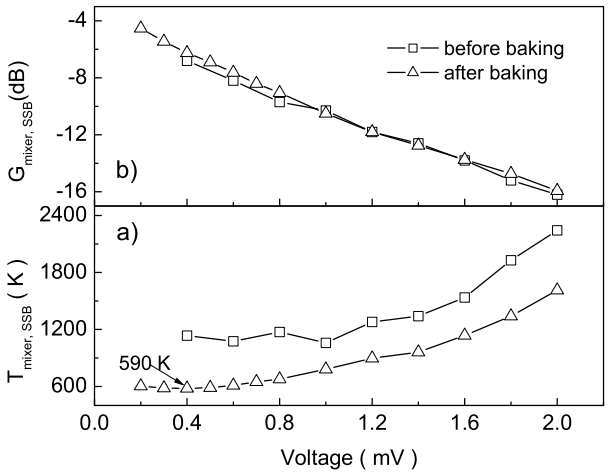

Fig. 3. Mixer noise temperature (SSB) and conversion gain (SSB) of the HEB mixer as a function of bias voltage. The open squares denote the value before baking; the open up-triangles - after baking.

C. SSB mixer noise temperature and conversion gain

$T_{rec,DSB}$ reflects the effective noise temperature of a cascade of the optics (all of the optical components and the transmission efficiency of the atmosphere), mixer, and IF amplifier. After subtracting the contributions from the optics and IF amplifier, we derive the single sideband (SSB) mixer noise temperature $T_{mixer,SSB}$ and the SSB mixer conversion gain $G_{mixer,SSB}$, which are plotted as a function of bias voltage in Fig. 3. We observe that, after baking the mixer gain changes rather small. Around the optimal bias point, it increases less than 13%. The mixer noise temperature $T_{mixer,SSB}$ decreases by 44%. The lowest $T_{mixer,SSB}$ found is 590 K. Since the output noise of a HEB equals to $T_{mixer} \times G_{mixer}$, the baking in essence reduces the intrinsic noise by 37%.

D. Device resistance versus temperature curve

We assume that the coupling of the RF signal via the antenna and transmission line into the HEB remains unchanged

after baking. This is supported by the gain data and by the measured direct response of the HEB by Fourier Transform Spectroscopy, which shows essentially the same spectrum after baking. To understand the reduction of the noise, we need to look closely at the changes of the HEB itself. For this reason, we measured its RT characteristics before and after baking. The result is given in Fig. 4, together with the derivative of resistance dR/dT (in the inset). We observe three superconducting transition features in the RT curve and define T_c (the highest) for the bridge, T_{c1} (the middle) for the contact pads, and T_{c2} (the lowest) for the transmission line/RF filter structure according to an early study [10]. These values in our case correspond to the peak positions in the dR/dT. As one can see, baking certainly affects the bridge, reducing the T_c and the transition width ΔT_c as well. We determine the exact values using the broken line method [5] and list them in table I. The baking also makes also the superconducting transition in the RT curve at T_{c1} (the contacts) and T_{c2} (the transmission line/RF filter structure) considerably sharper, indicated clearly by both RT and dR/dT curves.

E. Discussions

Before we attempt to associate the RT behaviour to the reduced noise, we briefly describe another baking experiment in similar HEBs, but from two good batches. These devices show good sensitivity as in [7] and relatively sharp RT curves as the one in Fig. 4 after baking. In this case, the baking gives either no effect or improves T_{rec} slightly. We notice that the RT (T_c and ΔT_c) of the bridge behaves in a very similar way as the one shown in Fig. 4, but not the transition associated to the contacts. The latter stays the same. Thus, we do not consider the change of RT in the bridge as a possible explanation. Instead, we ascribe the reduced noise to an improvement of the contact/film interface. The sharper transition in the contacts suggests a more homogeneous contact/film interface. This fact recalls the results of the previous work [4], [6], that different cleaning and contact structure can influence the performance of the mixer significantly.

To fully explain our result, one requires a theoretical model which is able to calculate the gain and noise by including the resistive transition, the contacts, and noise sources. Such a model is in progress [11], [12], [13], [14], but not fully applicable yet. An offshoot of our experiment is that we can prove that the lumped element model [5] based only on the superconduction transition of the bridge seems to be not applicable to our case. In this model, the mixer noise temperature is dominated by the thermal fluctuation noise T^{TF}_{Mixer}, which is given by $T^{TF}_{Mixer} \propto T_c$. The mixer gain is given by $G_{Mixer} \propto T_c/\Delta T_c$. Using the inputs from table I, after baking the T_{mixer} is expected to decrease by 3.5 %, while the G_{Mixer} should increase by 57 % (2.0 dB), which disagree the measured T_{mixer}(44 %) and the G_{Mixer} (13 % (0.6 dB)).

To determine the ultimate receiver noise temperature of the device after baking, we reduce the RF loss (1 dB) in the optics by applying a Si lens coated with an antireflection layer of 29 μm thick Parylene C. In addition, we also add

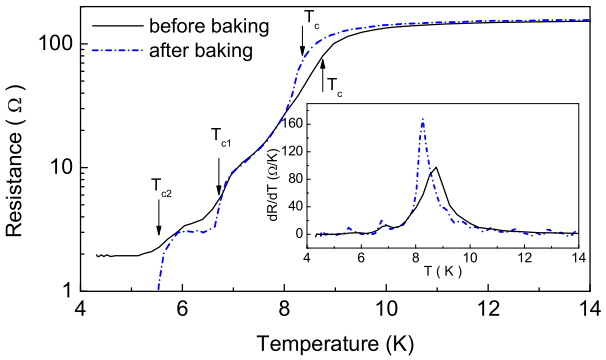

Fig. 4. The resistance (R) of the HEB mixer as a function of temperature before (solid line) and after (dash-dotted line) baking. T_c, T_{c1} , and T_{c2} correspond to the transition temperature of the bridge, the contact pads and the transmission line/the RF filter structure respectively (see Fig. 1). The inset shows the dR/dT as a function of temperature.

TABLE I
RELEVANT PARAMETERS FOR THE SUPERCONDUCTING TRANSITION IN THE BRIDGE BEFORE AND AFTER BAKING

Parameter	Before baking	After baking
T_c[K]	8.68	8.37
ΔT_c[K]	1.55	0.95

a metal mesh RF bandpass filter with an effective bandwidth of 200 GHz centered at 1.6 THz, mounted on the 4.2 K cold plate, which filters the hot/cold load power and thus reduces the direct detection effect of broadband radiation [15]. This effect, which can reduce a Y-factor, is particularly important in the case of the small volume HEBs. The measured new receiver noise temperature is also plotted in Fig. 2. We observe that the receiver noise temperature further decreases, with the lowest $T_{rec,DSB}$ of 740 K around the optimal operating point (0.4 mV). In this case the total optical loss is -3.87 dB. By flushing the signal path with dry N_2 gas, which reduces loss of 0.3 dB due to the water absorption in the air, we measured a $T_{rec,DSB}$ of 700 K (not shown in Fig. 2), corresponding to 9 $h\nu/k_b$. This value is identical to the record sensitivity reported in a spiral-antenna coupled large (4×0.4 μm^2) HEB mixer at the same frequency [3], [16].

IV. CONCLUSION

In conclusion, we have demonstrated that baking can reduce the receiver noise temperature of NbN HEB mixers. The analysis shows that the baking reduces the intrinsic noise of the mixer by 37 %, but gives little effect on the mixer gain. Based on the RT before and after baking, we attribute the improvement in sensitivity to the role of the contact/NbN interface. The lowest measured receiver noise temperature is 700 K at 1.63 THz. The IF impedance and gain of the same device as a function of frequency have also been measured and are reported in a separated paper by Kooi *et al* [17].

ACKNOWLEDGMENT

We acknowledge H. Hoevers, P.A.J. de Korte, J. Kooi, R. Barends, B. Jackson, and A. Baryshev for stimulating discussions and W.J. Vreeling for his assistance during the measurement. The work is supported partly by RadioNet and partly by INTAS.

REFERENCES

[1] E.M. Gershenzon, G.N. Golt'sman, I.G. Gogidze, A.I. Eliantev, B.S. Karasik and A.D. Semenov, "Millimeter and submillimeter range mixer based on electron heating of superconducting films in the resistive state", *Sov. Phys. Superconductivity*, vol. 3, pp. 1582, 1990.

[2] A.D. Semenov, H.-W. Hübers, J. Schubert, G.N. Golt'sman, A.I. Elantiev, B.M. Voronov, and E.M. Gershenzon, "Design and performance of the lattice-cooled hot-electron terahertz mixer", *J. Appl. Phys.*, vol. 88, no. 11, pp.6758-6767, 2000.

[3] S. Cherednichenko, P. Khosropanah, E. Kollberg, M. Kroug, and H. Merkel, "Terahertz superconducting hot-electron bolometer mixers", *Physica C*, vol. 372-376, pp. 407-415, 2002.

[4] J.J.A. Baselmans, M. Hajenius, J.R. Gao, T.M. Klapwijk, P.A.J. de Korte, B. Voronov and G. Gol'tsman., "Doubling of sensitivity and bandwidth in phonon cooled hot electron bolometer mixers", *Appl. Phys. Lett.*, vol. 84, pp. 1958-1960, 2004.

[5] B.S. Karasik and I. Elantiev, "Noise temperature limit of a superconducting hot-electron bolometer mixer", *Appl. Phys. Lett.*, vol. 68, pp. 853-855, 1996.

[6] M. Hajenius, J.J.A. Baselmans, J.R. Gao, T.M. Klapwijk, P.A.J. de Korte, B. Voronov and G. Gol'tsman., "Low noise NbN superconducting hot electron bolometer mixers at 1.9 and 2.5 THz", *Supercond. Sci. Technol.*, vol. 17, S224-228, 2004.

[7] J.J.A. Baselmans, M. Hajenius, J.R. Gao, P.A.J. de Korte, T.M. Klapwijk, B. Voronov and G. Gol'tsman, "Doubling of sensitivity and bandwidth in phonon cooled hot electron bolometer mixers", *Proc. of the SPIE, vol. 5498: Millimeter and Submillimeter Detectors for Astronomy II*, by J. Zmuidzinas, W. S. Holland, S. Withington, Editors, 23-25 June 2004, Glasgow, Scotland, UK, p. 168-177.

[8] A.R. Kerr, "Suggestions for Revised Definitions of Noise Quantities, Including Quantum Effects", *IEEE Trans. on Microwave Theory and Techn.*, vol. 47, no. 3, pp. 325-329, 1999.

[9] H. Ekström, B.S. Karasik, E.L. Kollberg, and K.S. Yngvesson, "Conversion gain and noise of niobium superconducting hot-electron mixers", *IEEE Trans on Microwave Theory and Tech.*, vol. 43, pp. 938-947, 1995.

[10] M. Hajenius, R. Barends, J.R. Gao, T.M. Klapwijk, J.J.A.Baselmans, A. Baryshev, B. Voronov and G. Gol'tsman. "Local resistivity and the current-voltage characteristics of Hot Electron Bolometer mixers", *IEEE Trans. on Appl. Super.*, in press, 2005.

[11] D. Wilms Floet, E. Miedema, T.M. Klapwijk, and J.R. Gao, "Hotspot mixing: A framework for heterodyne mixing in superconducting hot-electron bolometers", *Appl. Phys. Lett.*, vol. 74, pp. 433-435, 1999.

[12] H. Merkel, P. Khosropanah, P. Yagoubov, and E. Kollberg,"A hot spot mixer model for superconducting phonon-cooled HEB far above the quasiparticle bandgap", *Proceedings of the 10^{th} International Symposium Space Terahertz Technology*, Charlottesville, March 16-18, 1999, pp. 592-606.

[13] T.M. Klapwijk, R. Barends, J.R. Gao, M. Hajenius, and J.J.A. Baselmans, "Improved superconducting hot-electron bolometer devices for the THz range", *Proc. of the SPIE, vol. 5498: Millimeter and Submillimeter Detectors for Astronomy II*, by J. Zmuidzinas, W. S. Holland, S. Withington, Editors, Glasgow, Scotland, UK, 23-25 June 2004, pp. 129-139.

[14] R. Barends, M. Hajenius, J.R. Gao, and T.M. Klapwijk, "Direct correspondence between HEB current-voltage characteristics and the current-dependent resistive transition", *The 16th Int. Symp. on Space Terahertz Technology*, Göteborg, Sweden, 2-4 May 2005, (preprint).

[15] J.J.A. Baselmans, A. Baryshev, S.F. Reker, M. Hajenius, J.R. Gao, T.M. Klapwijk, B. Voronov and G. Gol'tsman, "Direct detection effect in small volume hot electron bolometer mixers", *Appl. Phys. Lett.*, vol. 86, pp.163503-163505, 2005.

[16] M. Kroug, S. Cherendnichenko, H. Merkel, E. Kollberg, B. Voronov, G. Gol'tsman, H.W. Hübers, H. Richter, "NbN hot electron bolometric mixers for terahertz receivers", *IEEE Trans. on Appl. Supercond.*, vol. 11, pp. 962-965, 2001.

[17] J. W. Kooi, J. J. A. Baselmans, J. R. Gao, P. Dieleman, Z. Q. Yang, A. Baryshev, M. Hajenius, G. de Lange, and T. M. Klapwijk, "IF Impedance and Mixer Gain of Phonon Cooled Hot-Electron Bolometers and the Perrin-Vanneste/Nebosis Two Temperature Model", *The 16th Int. Symp. on Space Terahertz Technology*, Göteborg, Sweden, 2-4 May 2005, (preprint).

An investigation of the performance of the waveguide superconducting HEB mixer at different RF embedding impedances

D. Loudkov, C.-Y.E. Tong, R. Blundell, N. Kaurova, E. Grishina, B. Voronov, G. Gol'tsman

***Abstract* — We have conducted an investigation of the performance of superconducting hot-electron bolometric (HEB) mixer at 800 GHz as a function of the embedding impedance of the waveguide embedding circuit. Using a single half-height mixer block, we have developed three different mixer chip configurations, offering nominal embedding resistances of 70, 35, and 15 Ohms. Both the High Frequency Structure Simulator (HFSS) software and scaled model impedance measurements were employed in the design process. Two batches of HEB mixers were fabricated to these designs using 3-4 nm thick NbN thin film. The mixers were characterized through receiver noise temperature measurements and Fourier Transform Spectrometer (FTS) scans. Briefly, a minimum receiver noise temperature of 440 K was measured at a local oscillator frequency 850 GHz for a mixer of normal state resistance 62 Ohms incorporated into a circuit offering a nominal embedding impedance of 70 Ohms. We conclude from our data that, for low noise operation, the normal state resistance of the HEB mixer element should be close to that of the embedding impedance of the mixer mount.**

***Index Terms*— Hot-electron bolometer mixer, Embedding impedance, Fixed-tuned waveguide receiver,**

I. Introduction

HOT Electron Bolometer (HEB) based receivers currently offer the highest sensitivity above 1.2 THz. These receivers have been selected for a number of astronomical instruments in the Terahertz frequency range [1-5]. The lowest receiver noise temperatures reported for laboratory prototypes are of the order of $(10h\nu/k)$ [6, 7].

In the design of HEB mixers, it has been generally assumed that the impedance of the HEB element is real. This impedance is considered to be close to the DC bias resistance at frequencies between the 3 dB gain roll-off and the energy gap of the superconducting film [8, 9]. At higher frequencies the film appears as a normal conductor and therefore, it may be logical to assume that the impedance at Terahertz frequencies is just the normal state resistance of the HEB element [10]. According to the BCS theory the relation between the energy gap at absolute zero and the critical temperature of a superconductor is: $2\Delta_0=3.52k_BT_c$. With $T_c=10$ K, the frequency corresponding to the superconducting energy gap is 0.74 THz. Since the HEB mixer operates in the resistive state, heated by DC bias current and incident Local Oscillator (LO) power, the effects of superconductivity are suppressed. It follows that the gap frequency is shifted down to lower frequencies. However, there exist only limited experimental data to support these assumptions.

We present an investigation of the optimal RF impedance of the waveguide HEB mixers designed for a center frequency of 0.8 THz. The devices were fabricated from 3.5 nm thick Niobium Nitride (NbN) film. We compare the performances of three different mixer chip designs, which present different source impedance to the HEB mixers.

II. Chip design for the waveguide HEB mixer

A scaled model was used to evaluate designs for our 0.8 THz waveguide mixer. The scaled model dimensions were 160 times larger than those of the actual mixer block such that model measurements were made at around 5 GHz. The mixer block design was adopted from mixer assembly of fixed tuned SIS mixer developed for the SubMillimeter Array telescopes [11, 12].

Three mixer chip configurations were designed by the High Frequency Structure Simulator (HFSS) software and confirmed by the scaled model measurements. The nominal impedances of these 3 designs are: 70 Ω (Design A), 35 Ω (Design B), and 15 Ω (Design C). The impedance value of design A is chosen to be close to the HEB mixer normal state resistance (R_N). For design C the embedding impedance is closest to the DC resistance at the optimal bias point (R_{DC}). With these three designs, the embedding impedances cover most of the range of interest for the HEB mixer.

At the target frequency of 800 GHz (5 GHz on the scaled model), the calculated complex impedances for the 3 designs are: 69 - j8 Ω, 37 + j2 Ω, 14 – j7 Ω respectively. All three

D. Loudkov is with the Moscow State Pedagogical University, Moscow, Russia, 119992 (e-mail: dloudkov@cfa.harvard.edu).

C.-Y. E. Tong is with the Harvard-Smithsonian Center for Astrophysics, Cambridge, MA 02138 (e-mail: etong@cfa.harvard.edu).

R. Blundell is with the Harvard-Smithsonian Center for Astrophysics, Cambridge, MA 02138 (e-mail: rblundell@cfa.harvard.edu).

N. Kaurova is with the Moscow State Pedagogical University, Moscow, Russia, 119992 (e-mail: nkaurova@mail.ru).

E. Grishina is with the Moscow State Pedagogical University, Moscow, Russia, 119992 (e-mail: Grishina@front.ru).

B. Voronov is with the Moscow State Pedagogical University, Moscow, Russia, 119992 (e-mail: bmvoronov@mail.ru).

G. Gol'tsman is with the Moscow State Pedagogical University, Moscow, Russia, 119992 (e-mail: goltsman00@mail.ru).

designs employ the same mixer chip dimensions and the mechanical design of the mixer block is also the same. The only difference lies in the detailed geometry of the electrodes of the HEB element which forms the coupling structure to the wave propagating down the waveguide. Consequently, the mixer chips are interchangeable and all three types of chip can be fabricated and processed, lapped and diced, at the same time on a single wafer.

The embedding impedance at the mixer feed point is derived from the scaled model vector measurement using the 3-standard de-embedding method [13]. For each design we first measure the reflection coefficient at the input port of the scaled model mixer mount with the mixer feed point terminated using the 3 known standards: an open, a short, and a 50 Ω chip resistor. The embedding impedance is related to these reflection coefficients through the relation:

$$Z_{emb} = Z_r(\Gamma_o - \Gamma_r)/(\Gamma_r - \Gamma_s),$$

where Z_{emb} is the embedding impedance seen at the HEB mixer feed point, Z_r = 50 Ω, and Γ is the measured reflection coefficient at the mixer input port for the three terminations: open (o), short (s) and 50 Ω resistive (r) load. We obtained reasonable agreement between the impedances obtained by scaled model measurements and the impedances obtained by HFSS simulations.

III. HEB MIXERS

A photo mask incorporating all three designs was prepared, and e-beam lithography was used to fabricate two batches of mixer elements with dimensions 3×0.15 μm^2 and 3×0.18 μm^2 on 3-4 nm thick NbN film [14]. The critical temperature of superconducting transition, T_C, was about 10 K for the measured samples. All of the tested mixers have normal state resistances (R_N) of around 60 Ω, extracted from the over-pumped current-voltage characteristics at 4.2 K.

Devices from batches I and II demonstrate considerable differences in their optimal bias conditions. For example, the DC resistance at the optimal bias point, defined as $(R_{DC} = V_{bias}/I_{bias})$, is generally around 24 Ω for mixers from batch I but it is about 15 Ω for batch II devices. Also, the differential resistance at the optimal bias point for batch I mixers ranges from 100 to 125 Ω, but for batch II devices this generally lies between 60 and 90 Ω. We believe that this behavior reflects variations in film quality between batches and a variation in contact resistance across the superconductor - normal metal interface.

Table I summarizes the characteristics of the HEB devices used in our experiments. The receiver input bandwidth (BW) was estimated from Fourier Transform Spectrometer (FTS) scans, which was made by using the mixer as a direct detector. For the receiver noise measurements (T_{RX}) we used an IF of 1.5 GHz, and included an isolator between the mixer and low-noise amplifier to present an in-band impedance of about 50 Ω to the mixer. Y-factor measurements were performed in the frequency range from 770 GHz to 860 GHz with frequency step about 10 GHz using the same experimental set-up. The minimum noise temperature measured for each device (Min T_{RX}) is given in the last column of Table 1. These values are close to 10*hv/k*, for mixer designs A and B, and are consistent with the highest reported sensitivities for this type of mixer [6, 7].

TABLE I
HEB MIXER CHARACTERISTICS

Device[a]	Z_{emb} (Ω)	R_{DC} @ opt bias (Ω)	R_N (Ω)	Input BW (GHz)	Min. T_{RX} (K)
AI#8	70	15	62	350	440
AI#17	70	14	72	350	480
AII#2	70	26	58	350	530
BI#13	35	13	50	330	470
BII#1	35	26	60	330	560
CII#13	15	21	51	220	603
CI#14	15	13	62	200	780

[a]The first letter of the device type indicates the chip design (A, B, or C), the roman numeral I or II indicates the batch number.

In figures 3, 4 and 5 we display the frequency response obtained from FTS scans for a variety of devices and the results of the Y-factor measurements (for 295K and 77K input loads to the receiver) are overlaid on the frequency response. From the FTS spectra, we note a low frequency cut-off, at around 600 GHz, which is due to the waveguide dimensions. Since the exact width and thickness of the individual mixer chip dictates the onset of higher order modes, the high frequency response of the mixers (above ~ 900 GHz) does not show a definite pattern.

In Fig. 3, we compare the response of two mixer chips of design A. We note a significant difference in performance between mixers AI#8 and AII#2, even though they possess almost identical R_N and critical current of 0.238 mA.

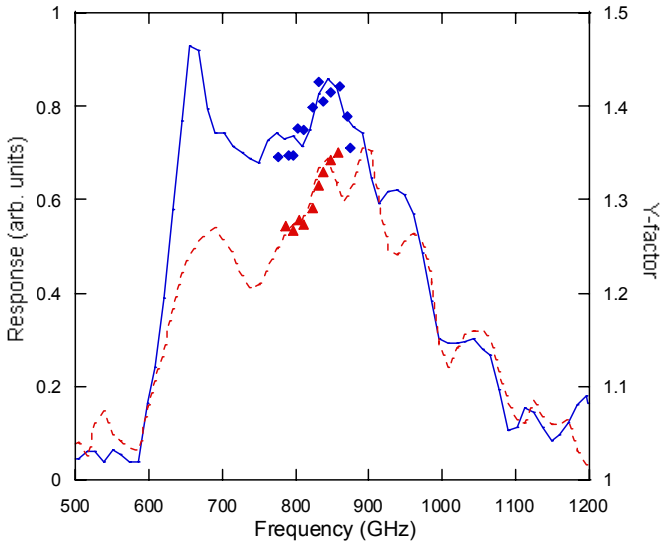

Fig. 3. Direct detector response and Y-factor values (symbols and right axis) of design A HEB mixers. The solid line and diamond symbols are for mixer AI#8, dashed line and triangles for mixer AII#2.

This suggests that some other additional, batch-dependent parameters play an important role in determining overall mixer performance. In other words, it is only possible to make a fair comparison of the performance of the different mixer designs from within a given batch.

In Fig. 4 we compare the FTS response of the three mixer types from the batch I. Referring to Table I, these mixers all have similar values of R_N. Mixer AI#8 has the best sensitivity among all of the measured devices. For example, at a local oscillator frequency of 850 GHz we measured a Y-factor of 1.42. This corresponds to a DSB receiver noise temperature of 440 K, or about 11 *hν/k*. The input bandwidth for this mixer of ~ 350 GHz is also quite wide.

Mixer BI#13 has similar sensitivity and RF bandwidth to AI#8. This can be explained by the fact that the normal state resistance of each mixer is close to the embedding impedance. For device AI#8, the match between R_N and the nominal embedding impedance of 70 Ω is better than 20 dB, and for BI#13, with a normal resistance of 50 Ω and a nominal embedding impedance of 35 Ω, we have a match of about 15 dB. Mixer CI#14 is significantly less sensitive and it has a narrower bandwidth than type A or B devices. For this mixer, the match between R_N and the nominal embedding impedance of 15 Ω is only about 5 dB. Interestingly, the 13 Ω DC resistance of this mixer at the optimal bias point is quite close to the nominal embedding impedance of 15 Ω for the type C mixer.

Clearly for devices with R_N ~ 60 Ω, designs A and B are better. This suggests that the optimal embedding impedance for low-noise performance should be close to the normal state resistance of the HEB element, not its DC resistance. However, the available data also suggest that the performance is not a very sharp function of the impedance match. Most likely, a match of better than 10-12 dB is quite sufficient.

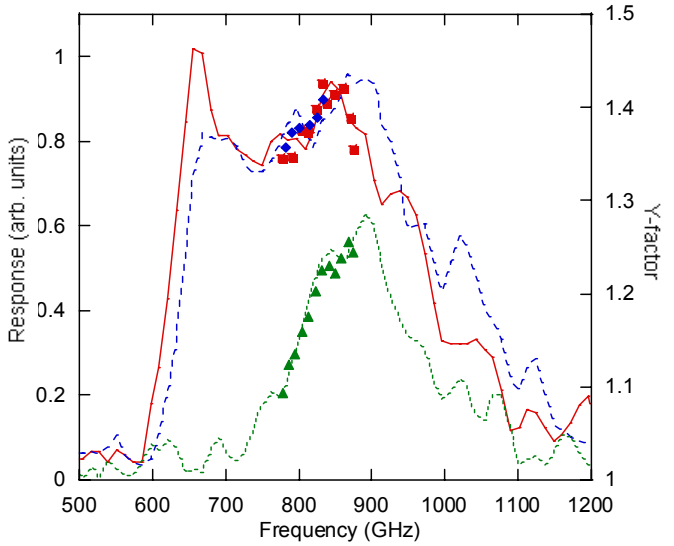

Fig. 4. Direct detector response and Y-factor (symbols and right axle) of the three types HEB mixer from batch I. The solid line and squares are for mixer AI#8, dashed line and diamonds for mixer BI#13, and dotted line and triangles for mixer CI#14.

In Fig. 5 we compare the performances of another set of devices, this time from batch II. Referring once more to Table I, the normal state resistance of these devices (AII#2, BII#1 and CII#13) has an almost identical spread to those from batch I. Mixers AII#2 and BII#1 have similar normal resistance (58 Ω and 60 Ω) and identical critical current (0.237 mA) which indicate similar critical temperatures of the superconducting transition. Nevertheless, these two mixers possess different RF characteristics. The poorer performance of the type B mixer at low frequencies is undoubtedly a result of the difference in embedding impedance of the 2 mixer chips. At around 800 GHz, mixer CII#13 offers sensitivity close to that of the other two mixer types. However, it is less sensitive at low frequencies, and its RF bandwidth is much reduced. We can conclude that operating a mixer with R_N significantly different to the embedding impedance generally results in a reduction in sensitivity and RF bandwidth.

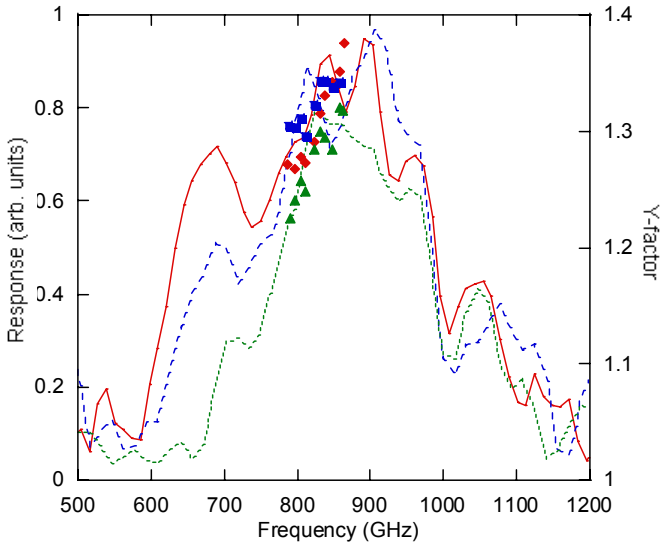

Fig. 5. Direct detector response and Y-factor (symbols and right axle) of the three types of HEB mixer from batch II. The solid line and diamonds are for mixer AII#2, dashed line and squares for mixer BII#1, and dotted line and triangles for mixer CII#13.

IV. Summary

We have designed and fabricated three different types of waveguide HEB mixer chips, with nominal embedding impedance levels of 70 Ω, 35 Ω and 15 Ω. For the mixer AI#8 with normal resistance value of 62 Ω, designed for an embedding impedance of 70 Ω, we have measured a DSB receiver noise temperature of 440 K at a local oscillator frequency 850 GHz. This corresponds to a sensitivity close to $10h\nu/k$. Type A mixers offer an input bandwidth of about 350 GHz.

By comparing the sensitivity and frequency response of the different mixer types, we find that HEB mixers operate best with a normal state resistance close to that of the embedding network. However, RF performance is not a critical function of the match, but for $R_N >> Z_{emb}$ the receiver sensitivity drops and the available input bandwidth is also reduced.

Our experimental data also confirms that other factors, such as film quality and contact resistance at the superconductor – normal metal interface can have a significant impact on the performance of the HEB mixer receiver.

REFERENCES

[1] D. Meledin, D. Marrone, E. Tong, H. Gibson, R. Blundell, S. Paine, C. Papa, M. Smith, T. Hunter, J. Battat, B. Voronov, and G. Goltsman, "A 1-THz superconducting Hot-Electron-Bolometer Receiver for Astronomical Observations." *In press IEEE Trans. On Microwave Theory and Tech.*, vol. 52, no. 10, October 2004.

[2] D. Marrone, R. Blundell, H. Gibson, S. Paine, D. C. Papa, C.-Y. E. Tong, "Characterization and Status of a Terahertz Telescope." *Proc. of the 15th International Symposium on Space Terahertz Technology*, Northampton, Massachusetts, USA, April 27-29, 2004.

[3] K. Yngvesson, C. Musante, M. Rodriguez, Y. Zhuang, E. Gerecht, M. Coulombe, J. Dickinson, T. Goyette, J. Waldmann, C. Walker, A. Stark, A. Lane, "Terahertz receiver with NbN HEB device (TREND) – a low noise receiver user instrument for AST/RO at the south pole." *Proc. of the 12th Intern. Symposium on Space THz Technology*, p.26, San Diego, CA, 2001.

[4] S. Cherednichenko,M. Kroug, H. Merkel, P. Khosropanah, A. Adam, E. Kollberg, D. Loudkov, G. Gol'tsman, B. Voronov, H. Richter, H.-W. Huebers, "1.6 THz heterodyne receiver for the far infrared space telescope", *Physica C*, Volume 372, p. 427-431, August 2002.

[5] A. Semenov, H. Richter, K. Smirnov, B. Voronov, G. Gol'tsman, H.-W. Hübers, "The development of terahertz superconducting hot-electron bolometric mixers", *Superconductor Science and Technology*, Volume 17, Issue 5, pp. S436-S439, 2004.

[6] C.-Y. E.Tong, J. Stern, K. Megerian, H. LeDuc, T.K. Sridharan, H. Gibson, R. Blundell, "A Low-noise NbTiN Hot Electron Bolometer Mixer." *Proc. of the 12th International Symposium on Space Terahertz Technology*, pp. 253-261, San Diego, CA, 2001.

[7] M. Kroug, S. Cherednichenko, M. Choumas, H. Merkel, E. Kollberg, B. Voronov, G. Goltsman, D. Loudkov, H. W. Hubers, H. Richter, "HEB quasioptical heterodyne receiver for terahertz frequencies," *Proc. of the 12th International Symposium on Space Terahertz Technology*, pp. 244-253, San Diego, CA, 2001.

[8] H. Ekström, B. Karasik, E. Kollberg, S. Yngvesson, "Conversion gain and noise of niobium superconducting hot-electron bolometer mixers," *IEEE Trans. Microwave Theory and Tech*., pp. 938-947, vol. 43, no. 4, april 1995.

[9] B. S. Karasik, A. I. Elantev, "Analysis of the noise performance of a hot-electron bolometer mixer," 6th *International Symposium on Space Terahertz Technology*, pp. 229-247, Pasadena, CA, 1995.

[10] H.Ekstrom, E.Kollberg, P.Yagoubov, G.Goltsman, E.Gershenzon, and S.Yngvesson, "Gain and Noise Bandwidth of NbN Hot Electron Bolometric Mixers," Appl.Phys.Lett., 70(24), 16 June 1997.

[11] E. Tong, R. Blundell, S. Paine, D.C. Papa, J. Kawamura,R. Leombruno, X. Zhang, and J. Stern, H. LeDuc, "Design and characterization of a 250-350-GHz fixed-tuned superconductor-insulator-superconductor receiver," *IEEE Trans. Microwave Theory Tech.*, vol. 44, pp. 1548-1556, 1996.

[12] J. Kawamura, R. Blundell, E. Tong, D.C. Papa, T. Hunter, S. Paine, F. Patt, G. Goltsman, S. Cherednichenko, B. Voronov, and E. Gershenzon, "Superconductive hot-electron bolometer mixer receiver for 800 GHz operation," *IEEE Trans. Moicrowave Theory Tech.*, vol. 48, pp. 683-689, 2000.

[13] W. Zhang, C.-Y.E. Tong, S.C. Shi, "Scaled model measurement of the embedding impedance of a 660-GHz waveguide SIS mixer with a 3-standard deembedding method," *IEEE Microwave & Wireless Components Lett*., vol. 13(9), pp. 376-378, Sept. 2003.

[14] D. Meledin,C.-Y. E. Tong, R. Blundell, N. Kaurova, K. Smirnov, B. Voronov, G. Gol'tsman, "Study of the IF bandwidth of NbN HEB mixers based on crystalline quartz substrate with an MgO buffer layer", *IEEE Trans. Applied Superconductivity*, Vol. 13, p. 164, June 2003.

A 585 GHz Diffusion-Cooled Niobium Hot-Electron Bolometric Mixer Element for Imaging Applications

Lei Liu, Robert M. Weikle, II, Arthur W. Lichtenberger, Acar Isin, and Bascom S. Deaver, Jr.

***Abstract*— Two prototype silicon-supported niobium hot-electron bolometric (HEB) mixers have been designed and fabricated for operation at 585 GHz. The HEB's are integrated into annular slot antennas that incorporate low-pass filters (LPF's). In these prototype designs, two impedance-matching schemes are proposed to optimize the embedding impedance presented to the mixer element. One scheme employs a simple quarter-wavelength impedance transformer while an alternative approach utilizes two d-HEB's fabricated in series at the feed-point of the annular slot. To reduce the footprint of the circuit and permit high packing density, a compact LPF design that significantly reduces circuit size is introduced. DC test results, including R-T and I-V measurements, indicate successful fabrication of the d-HEB's. A quasi-optical mixer block has been fabricated for RF measurements. Preliminary measurements of conversion gain, coupling efficiency, and noise temperature are presented and demonstrate promising performance of these single-element HEB mixers for imaging array applications.**

***Index Terms*— Hot-electron bolometer, heterodyne receiver, annular slot antenna, imaging array.**

I. Introduction

SUPERCONDUCTING hot-electron bolometers (HEB's) with high sensitivities have been a subject of great interest over the past few years for submillimeter receivers in radio astronomy [1][2][3]. These devices are especially attractive for frequencies above the superconducting gap of niobium superconductor-insulator-superconductor (SIS) receivers ($\sim$ 700 GHz). Compared to phonon-cooled HEB's, *diffusion-cooled* HEB's (d-HEB's) have shorter device lengths ($L < L_{\mathrm{e-ph}}$, where $L_{\mathrm{e-ph}}$ is the mean free path for inelastic electron-phonon scattering), which allow hot electrons to out-diffuse to contact pads before scattering to the substrate. Due to the superconducting d-HEB's merits (i.e., broad IF bandwidth, low noise temperature and high sensitivity), single element receivers and mixers employing these devices have been proposed and studied by a variety of research groups [4][5][6]. However, few of the RF circuit designs utilized in these receivers have been suitable for imaging arrays — an application that can reduce observing and processing time by recording imaging information in parallel. The slot-ring antenna (SRA) provides a compact and attractive structure for this application, making it an ideal candidate for high resolution imaging arrays (see fig. 1) [7][8].

L. Liu, R.M. Weikle, II, and A.W. Lichtenberger are with the School of Engineering and Applied Science, University of Virginia, Charlottesville, VA 22904-4743, U.S.A. A. Isin and B.S Deaver, Jr. are with the Department of Physics, University of Virginia, Charlottesville, VA 22904-4714, U.S.A.

This work was supported by the National Science Foundation under grant AST-0242525 and the U.S. Army National Ground Intelligence Center under grant DASC01-01-C-0009.

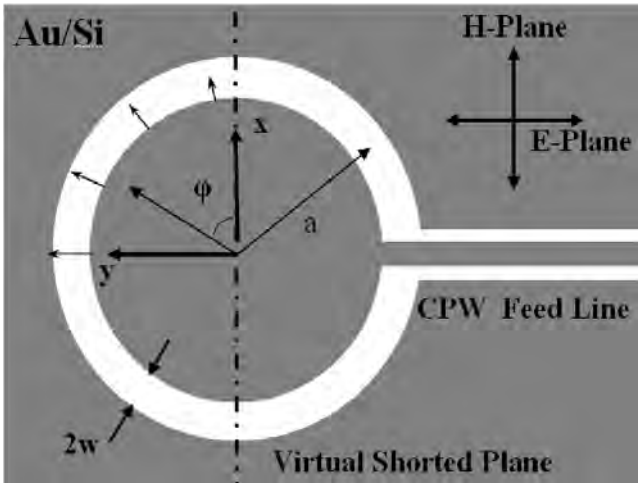

Fig. 1. Measured and simulated second harmonic conversion loss versus the number of diode pairs.

In this paper, the design of a quasi-optical single-element mixer operating at 585 GHz is presented that consists of a SRA and superconducting d-HEB integrated on a single silicon chip. The fabrication process employs electron-beam lithography (EBL). DC test results are presented in this paper as well as RF measurements and characterization.

II. Mixer Design

Gerecht *et al*, first developed a SRA coupled HEB mixer based on NbN phonon-cooled microbridges [9][10]. For the mixer described in this paper, two impedance-matching schemes are proposed to optimize power coupling from the SRA's to the mixer elements. One scheme employs a simple quarter-wavelength impedance transformer while the alternative approach utilizes two d-HEB's fabricated in series at the feed-point of the SRA. The aspect ratio of the HEB's are chosen to present an optimum impedance to the antenna, while keeping an upper limit on the individual device lengths that is less that the mean freee path for inelastic electron-phonon scattering ($L_{\mathrm{e-ph}}$). Silicon is chosen as the mixer substrate because of its relatively high dielectric constant ($\epsilon_r = 11.7$), which results in high directivity and efficiency for the receiving antenna [12][14]. The SRA is designed to operate at 585 GHz and has a radius, a, of 36 μm and a slot width, 2w, of 2.6 μm.

ADS momentum simulations of the slot-ring antenna performance is shown in Fig. 2. The designed SRA has a 3-dB bandwidth of approximately 100 GHz (16%). At 585 GHz, the real and imaginary parts of the antenna input impedance

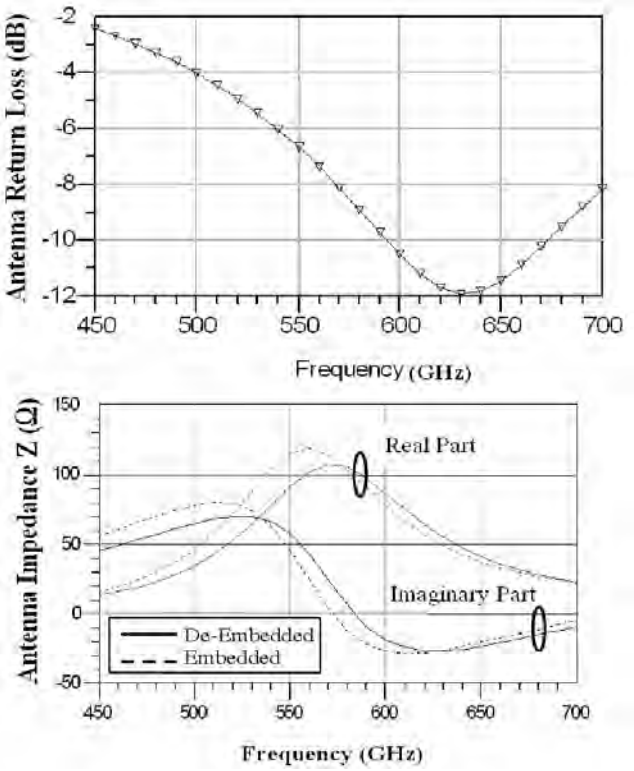

Fig. 2. Measured and simulated second harmonic conversion loss versus the number of diode pairs.

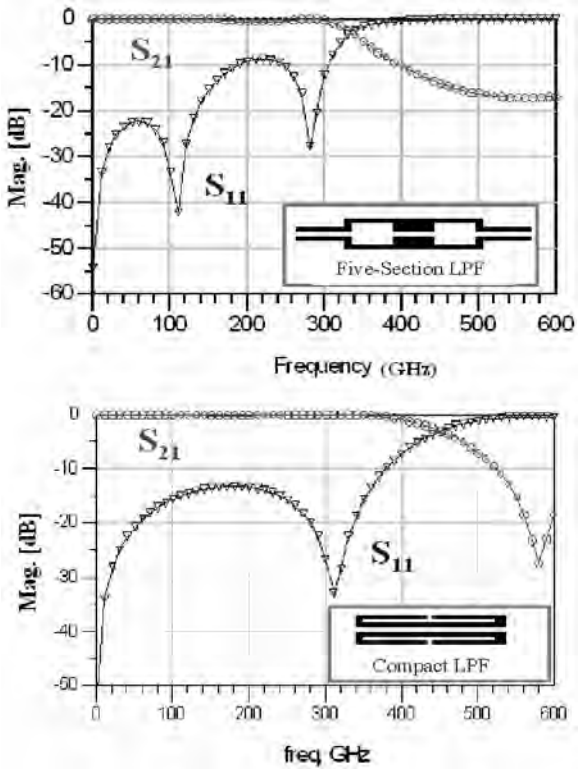

Fig. 3. Circuit model of one section of the distributed balanced doubler. Z_{Slotline} and Z_{CPW} are the unloaded slotline and CPW transmission line impedances respectively, and ℓ is the spacing between the diode pairs. Series resistance, junction capacitance and other lumped elements associated with the varactor (including parasitic bondwire inductance) are included in the diode model.

are 100 Ω and approximately zero, respectively. Consequently, impedance matching to the devices is relatively straightforward because the superconducting HEB bridge is expected to be a purely resistive device. A d-HEB with resistance as high as 100 Ω, however, requires nearly 3 squares of Nb thin film (10 nm thick with a sheet resistance of 35 Ω/square in the normal state). Hence, the resulting device length approaches that of the inelastic electron-phonon mean free path, $L_{\mathrm{e-ph}}$. Because the resolution of the Nanometer Pattern Generation System (NPGS) employed at the University of Virginia is approximately 100 nm, the resulting device could well exceed the maximum length for diffusion cooling. As a result, two different schemes are proposed to match the 100 Ω antenna impedance to the HEB bridge in the mixer design. The first scheme employs a simple quarter-wavelength impedance transformer (scheme-I) while the second utilizes two HEB microbridges fabricated in series (each with a normal-state resistance of 50 Ω) and connected by a gold cooling pad (scheme-II).

Conventional high/low stepped-impedance low-pass filters (LPF's) are typically used for mixer circuits because they are simple to design and implement. For high insertion loss in the stopband, many stages are normally used, thus increasing size of the overall circuit. In the present design, a compact LPF is introduced that significantly reduces circuit size [11]. Fig. 3 shows the s-parameters (simulated with ADS Momentum) of a conventional 5-step LPF (258 μm in length) and one-cell of the compact LPF structure (108 μm in length). In the compact LPF, the RF signal at 585 GHz is suppressed by 30 dB while the overall circuit length is reduced by 55% (from 330 μm to 180 μm). Moreover, the compact LPF can be placed anywhere in the IF output circuits, which permits flexibility in design.

Fig. 5(a) shows a diagram of a quasi-optical HEB mixer mounted on an extended hemispherical silicon lens with radius $R = 4.5$ mm. The lens focuses incident radiation onto the SRA. Radiation patterns of the SRA on silicon lens are calculated using the ray-tracing technique of Filipovic [14]. Shown in Fig. 3(b) are the E-plane patterns for various extension lengths. An extension length of 1600 μm is chosen to achieve the highest antenna directivity while keeping an acceptable Gaussian coupling efficiency [14].

III. Fabrication

The HEB fabrication used in this work is based on a process developed by the University of Virginia's Superconducting Device and Materials Research Group [15]. The process begins with sputtering of a niobium/gold (10 nm/10 nm) bi-layer onto a Si wafer, followed by a standard lift-off process to define the base layer. The base layer consists of the slot-ring antenna, lowpass filter and tuning circuits. These are based on coplanar waveguide with a 200 nm thick Au layer.

After the base layer is defined, the mixing element - the HEB bridge - is fabricated using a two-step electron-beam lithography (EBL) process. In the first step, a bilayer PMMA (950/495) is spun on the base layer as the resist structure. The

-HEB cooling pads patterns are then directly written by an electron-beam controlled by the NPGS. The trilayer Nb/Au/Nb (10 nm/50 nm/10 nm) cooling pads are hence generated and the Nb microbridge length is defined after a lift-off process. During the second EBL step, the HEB bridge is first patterned by the NPGS. A Au/Nb (20 nm/20 nm) bilayer is deposited, and after lift-off, a bridge is left spanning the cooling pads.

Reactive-ion etches (RIE) are then performed to remove the unwanted metal layers, leaving a Nb bridge between the gold cooling pads. The length of the HEB bridge is chosen to be approximately 200 nm, a value well below the inelastic electron-phonon scattering length, resulting in a diffusion-cooled HEB device. The bridge width can be modified to produce the desired device resistance for circuit matching since the sheet resistance for 10 nm thick Nb film is known to be 35 Ω/square in the normal state [15].

Fig. 5 shows typical fabrication results for the scheme-I and scheme-II mixer circuits. In fig. 5(a), the one-square HEB bridge (HEB-A1-4) is fabricated at the end of the quarter-wave transformer with a device length of 240 nm and a device width of 237 nm, resulting in a device resistance of 35 Ω. In 5(b), the HEB bridge width is designed to be 175 nm, and the lengths of the two series HEB bridges are equal to be 250 nm. However, the measurement shows that in the mixer in fig. 5(b) (HEB-B1-4), the left-hand side HEB length is 266 nm and the right-hand side one is 230 nm. Additional measurements have demonstrated that this is not an exceptional case, but a common phenomenon with our fabrication process. This is attributable to the displacement of the alignment markers and the e-beam writing position. Because the IF bandwidth of the mixer will be determined by the longer HEB bridge ($f_{3\ \mathrm{dB}} = \pi D/2L^2$) [16], two identical series HEB bridges with equal device lengths are preferred to achieve impedance matching while maximizing the IF bandwidth.

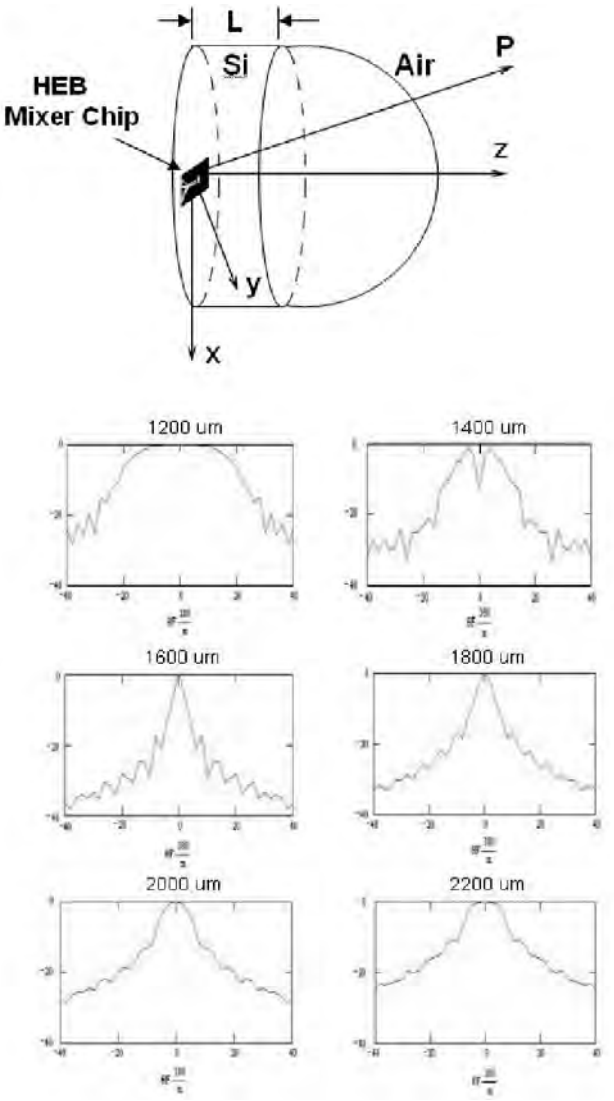

Fig. 4. Measured and simulated second harmonic conversion loss versus the number of diode pairs.

IV. Measurements

Room temperature probe station measurements show the resistance of the one-square Nb microbridge in Fig. 5 a is approximately 70 Ω (with the RF circuit and transformer contributing approximately 20 Ω). This result agrees with theoretical predictions, once the residual resistance ratio (RRR $\sim$ 2 in our case) of thin Nb film is taken into account. To further explore the superconducting properties of the Nb film HEB, R-T curve measurements of the mixer HEB-A1-4 are performed and shown in Fig. 6(a). A sharp resistance transition from the superconducting state to the normal state is observed at a critical temperature $\mathrm{T_c} = 5.4$ K with a transition width $\Delta \mathrm{T_c} \sim 0.5$ K. Shown in Fig. 6(b) is the low temperature I-V curve of this device measured at 4.7 K. The critical current is around 120 μA, corresponding to a $J_c \sim 5.1 \times 10^6\ \mathrm{A/cm^2}$, comparable to the results reported by other groups. The normal state resistance is 29 Ω, implying a thicker-than-designed Nb thin film has been fabricated, resulting in a smaller-than-expected sheet resistance.

The IF output consists of a coplanar transmission line fabricated on a Si wafer with a thickness of 1.1 mm. This results in a total lens-supported antenna extension length of approximately 1.6 mm. A quasi-optical mixer block to support the IF substrate/HEB chip is fabricated from brass and installed into an HD-3(8) dewer system for cryogenic testing and RF measurements. Fig. 7 shows the diagram of the RF measurement system used to measure the mixer parameters including conversion gain, coupling efficiency, and noise temperature. In this system, a VDI 576–640 GHz Frequency Extension Module (courtesy of Virginia Diodes, Inc.) is employed to provide the LO power. A hot/cold load is used to measure the system Y-factor. Both the LO and RF are coupled into the cryogenic dewar through a set of lenses and mirrors. Inside the dewar, the quasi-optical mixer block is placed before a teflon window and biased from a bias-T. The IF signal is output to an isolator and low noise amplifier (LNA) before being fed to an external (room temperature) IF chain for data processing.

Prior to performing the Y-factor measurement, pumped I-V curves at 585 GHz (Fig. 8) are measured by coupling into the dewar the LO signal. As expected, the critical current

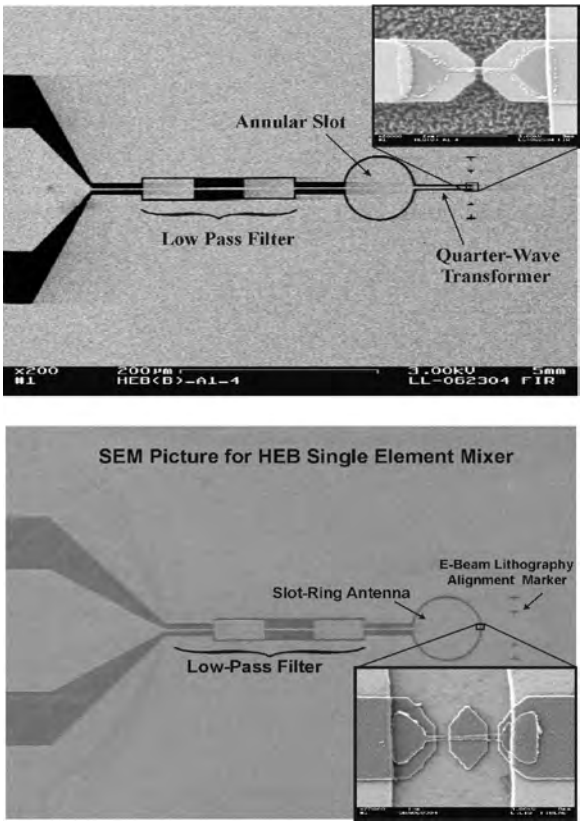

Fig. 5. Measured and simulated second harmonic conversion loss versus input frequency for 6 diode pairs.

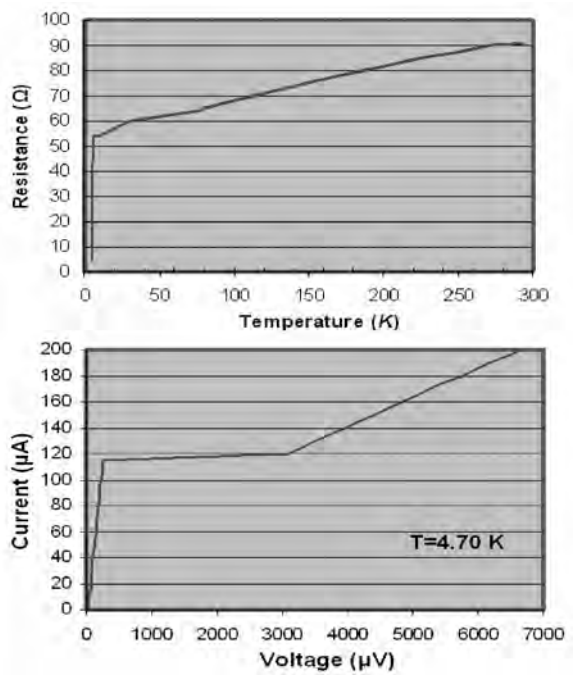

Fig. 6. Measured and simulated second harmonic conversion loss versus input frequency for 6 diode pairs.

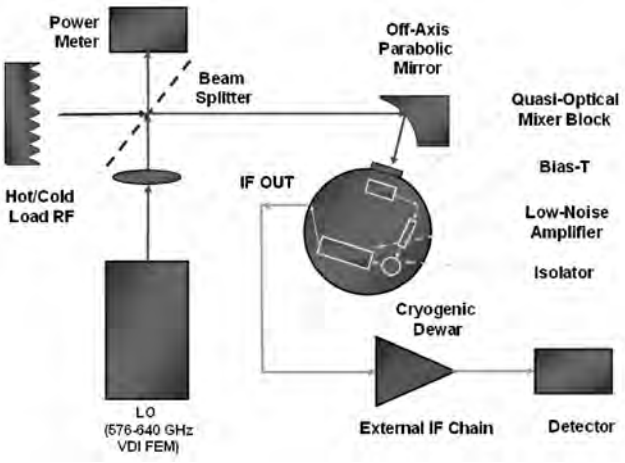

Fig. 7. Measured P_{in} v. P_{out} at the fundamental, second, and third harmonics for the distributed balanced doubler. The input power is 27 dBm (500 mW) and the peak output power at the second harmonic is 22.6 dBm (180 mW)

decreases with increasing LO power. The HEB device is saturated (i.e., behaves as a pure resistance) at a LO power of P4, indicating the entire Nb microbridge is pumped from the superconducting state into the normal state.

The frequency response of the system is measured with an amplitude-chopped LO. The response of the HEB is maximum at 600 GHz and a second maximum occurs at 615 GHz. These are likely attributable to the transmission characteristic of the mesh-filter and the frequency response of the SRA, respectively. These peaks are slightly shifted from their designed values. The measured E-plane radiation pattern of the SRA-coupled HEB is shown in Fig. 9 and the main beam demonstrates good agreement with calculation.

V. Discussion

In this paper, a SRA-coupled 585 GHz d-HEB mixer for imaging array applications has been designed and fabricated. To optimize the power coupling from the SRA to the mixing element, two impedance matching schemes have been proposed. A compact LPF structure has been introduced to provide for a more compact mixer for future imaging array applications.

DC and RF measurements demonstrated the successful design and fabrication of the SRA-coupled d-HEB mixer. The parameters at 585 GHz including coupling efficiency, noise temperature and conversion gain will soon be fully investigated for evaluation of the mixer performance. Future work also includes investigation of mutual coupling between adjacent SRA's and expansion of the single HEB mixer to a full imaging array.

Acknowledgment

The authors would like to thank colleagues in the Far-Infrared Receiver Laboratory and the UVA Microfabrication Laboratory for valuable discussions and assistance.

References

[1] D. E. Prober, "Superconducting terahertz mixer using a transition-edge microbolometer," *Appl. Phys. Lett.*, vol. 62, pp. 2119-2121, 1993.

[2] H. Ekström, B.S. Karasik, E.L. Kollberg, and K.S. Yngvesson, "Conversion gain and noise of Niobium superconducting hot-electron-mixers," *IEEE Trans. Microwave Theory Tech.*, vol. 43, no. 4, pp. 938-947, Apr. 1995.

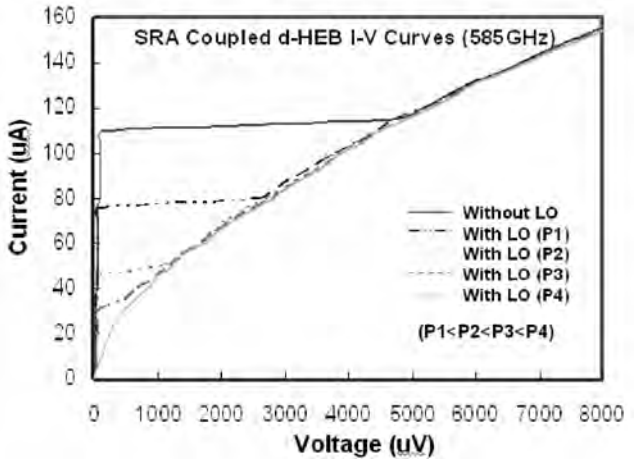

Fig. 8. Measured P_{in} v. P_{out} at the fundamental, second, and third harmonics for the distributed balanced doubler. The input power is 27 dBm (500 mW) and the peak output power at the second harmonic is 22.6 dBm (180 mW)

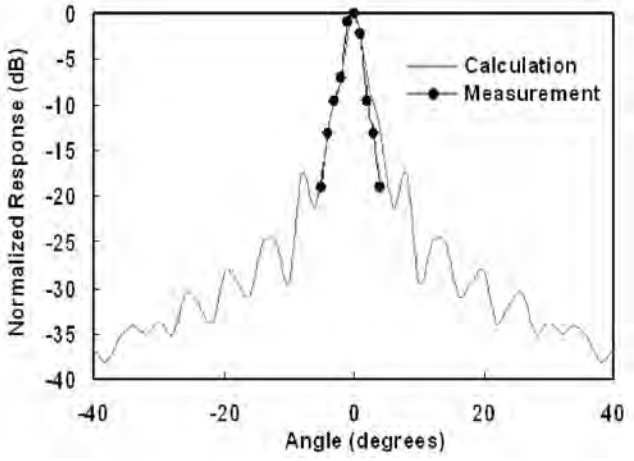

Fig. 9. Measured P_{in} v. P_{out} at the fundamental, second, and third harmonics for the distributed balanced doubler. The input power is 27 dBm (500 mW) and the peak output power at the second harmonic is 22.6 dBm (180 mW)

[3] B. S. Karasik and A. I. Elantiev, "Noise temperature limit of a superconducting hot-electron bolometer mixer," *Appl. Phys. Lett.*, 68 (6), Feb. 1996.

[4] A. Skalare, W. R. McGrath, B. Bumble, H.G. LeDuc, "Receiver measurements at 1267 GHz using a diffusion-cooled superconducting transition-edge bolometer," *IEEE Trans. Appl. Supercon.*, vol. 7, no. 2, June 1997.

[5] W. F. M. Ganzevles, L. R. Swart, J. R. Gao, P. A. J. de Korte, T. M. Klapwijk, "Direct response of twin-slot antenna-coupled hot-electron bolometer mixers desined for 2.5 THz radiation detection," *Appl. Phys. Lett.*, vol. 76, no. 22, May 2000.

[6] W. F. M. Ganzevles, J. R. Gao, D. Wilms Floet, G. de Lange, A. K. van Langen, L.R. Swart, T.M. Klapwijk, and P. A. J. de Korte, "Twin-slot antenna coupled Nb hot electron bolometer mixers at 1 THz and 2.5 THz," *Proc. 10th Int. Symp. On Space Terahertz Technology*, University of Virginia, Charlottesville, USA, March 16-18, 1999, pp. 246.

[7] C.E. Tong, and R. Blundell, "An annular slot antenna on a dielectric half-space," *IEEE Trans. Antennas and Propagation*, vol. 42, no. 7, pp. 967-974, July 1994.

[8] S. Raman and G.M. Rebeiz, "Single- and dual-polarized millimeter-wave slot-ring antennas," *IEEE Trans. Antennas Propagat.*, vol. 44, no. 11, pp. 1438-1444, Nov. 1996.

[9] E. Gerecht, D. Gu, X. Zhao, J. Nicholson, F. Rodriguez-Morales, and K.S. Yngvesson, "Development of NbN terahertz HEB mixers coupled through slot-ring antennas," *Proc. 15th Int. Symp. On Space Terahertz Technology*,University of Massachusetts, Amherst, 2004.

[10] F. Rodriguez-Morales, K.S. Yngvesson, E. Gerecht, N. Wadefalk, J. Nicholson, D. Gu, X. Zhao, T. Goyette, and J. Waldman, "A terahertz focal plane array using HEB superconducting mixers and MMIC IF amplifiers," *IEEE Microwave and Wireless Comp. Lett.*, vol. 15, no. 4, pp. 199–201, April 2005.

[11] J. Sor, Y. Qian, and T. Itoh, "Miniature low-loss CPW periodic structures for filter applications," *IEEE Trans. Microwave Theory Tech.*, vol. 49, no. 12, pp. 2336-2341, Dec. 2001.

[12] D.B. Rutledge, D.P. Neikirk, and D.P. Kasilingam, "Integrated-circuit antennas," *Infrared and Millimeter Waves*,, vol. 10, Chap. 1, Academic Press Inc. 1979.

[13] R. E. Collin, *Antennas and Radiowave Propagation* New York McGraw-Hill, ch.4, 1985.

[14] D.F. Filipovic, S.S. Gearhart, and G.M. Rebeiz, "Double-slot antennas on extended hemispherical and elliptical silicon dielectric lenses," *IEEE Trans. Microwave Theory Tech.*, vol. 41, no. 10, Oct. 1993.

[15] R. B. Bass, "Hot-electron bolometers on ultra-thin silicon chips with beam leads for a 585 GHz receiver," Ph.D. dissertation, University of Virginia, May 2004.,

[16] I. Siddiqi, A. Verevkin, D.E. Prober, A. Skalare, B.S. Karasik, W.R. McGrath, P. Echternach, and H. G. LeDuc,, "Noise and conversion efficieny of Aluminum superconducting hot-electron bolometer mixer," *IEEE Trans. Appl. Supercon.*, vol. 11, no. 1, March 2001.

Effect of the direct detection effect on the HEB receiver sensitivity calibration

S. Cherednichenko, V. Drakinskiy, T. Berg, E. Kollberg, I.Angelov.

***Abstract*—We analyze the scale of the HEB receiver sensitivity calibration error caused by the so called "direct detection effect". The effect comes from changing of the HEB parameters when whey face the calibration loads of different temperatures. We found that for HIFI Band 6 mixers (Herschel Space Observatory) the noise temperature error is of the order of 8% for 300K/77K loads (lab receiver) and 2.5% for 100K/10K loads (in HIFI). Using different approach we also predict that with an isolator between the mixer and the low noise amplifiers the error can be much smaller.**

***Index Terms*—HEB, mixer, terahertz, noise temperature.**

I. Introduction

1.4-1.7 THz and 1.6-1.9 THz NbN Hot-Electron Bolometer (HEB) mixers [1] are intended for Band 6 of the HIFI instrument of the Herschel Space Observatory [2]. A number of other radioastronomical projects, such as APEX, TELIS, SOFIA, involve the same HEB mixers [3]. One of the crucial requirements is the calibration accuracy of the receiver noise temperature which for HIFI is of the order of 1 %. Noise temperature calibration will be done using 10 K and 100 K "cold"-"hot" loads placed in the receiver beam way after the dual-way diplexer (the telescope signal is split for two mixers of different polarization). The calibration loads are broadband black body sources. The radiation is coupled to the HEB mixers via relatively broadband planar double- slot antennas. The overall single –mode hot-cold signal power, incident on the mixer, is estimated from the Planck law as 3 nW, i.e. not negligible comparing to the LO power incident on the mixers (200÷300 nW). The electron temperature of the HEB is proportional to the absorbed RF+LO power. An IF signal is generated by the electron temperature oscillations caused by the mixing of the LO and the RF waves. Therefore, for different RF input powers (for the hot and the cold loads) the HEB mixer is at different electron temperatures and hence has different gain and noise. Depending on the HEB volume, the critical current, the RF bandwidth of the antenna, the change of the mixer electron temperature is seen on the mixer bias current (in case of the voltage bias). The shift of the HEB's bias current is traditionally called "a direct detection effect" since it is just this current modulation which is used for the response read-out of all bolometric direct detectors. Although, the linearity of HEB mixers' response to hot-cold load has been verified up to 1000 K for the smallest NbN HEBs (a number of papers have been published), the direct detection effect modifies the Y-factor and introduces a systematic error in the receiver noise temperature calibration. In this paper we discuss different techniques to calibrate out the direct detection effect.

Manuscript received May 30, 2005. This work was supported the Swedish National Space Board.

Authors are with the Microwave Electronic Laboratory, MC2, Chalmers University of Technology, SE-412 96, Gothenburg, Sweden, (corresponding author S.Cherednichenko, e-mail: serguei.cherednichenko@ mc2.chalmers.se).

II. Direct detection effect

A. The noise temperature error

A typical HEB receiver DSB noise temperature at 1.63 THz is shown in Figure 1 on an example of the Band 6 Low mixer of the HIFI instrument of the Herschel Space Observatory. We build up the discussion in this paper based on the results obtained for this mixer, which is similar to the Flight Mixer to be installed in HIFI.

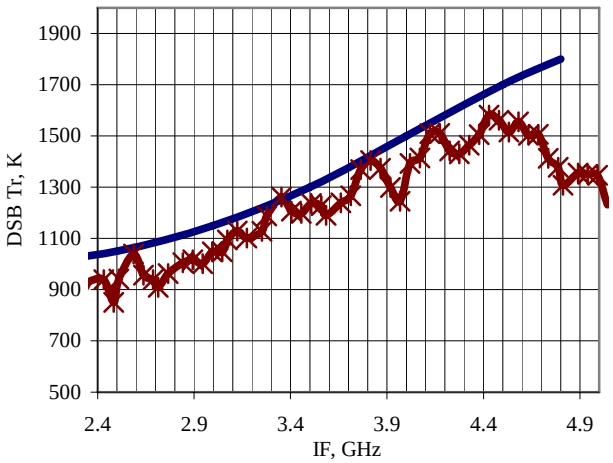

Figure 1.HIFI Band 6 Low HEB receiver noise temperature at 1.63 THz LO frequency, corrected for the input optics loss.

The receiver sensitivity is measured with the Y-factor technique. Y-factor, corresponding to the noise temperature of 1000 K is about 0.8 dB (see Figure 2). In order to obtain a certain noise temperature measurements accuracy the Y-factor error shall not exceed the corresponding value. In Figure 3 we calculate the Y-factor error as a function of Tr which leads to

1%, 5%, and 10% of the noise temperature error. From this figure we can see that the Y-factor shall be measured with the accuracy better than 0.01dB in order to achieve the Tr error as low as 1% at 1000 K level. It relaxes to 0.035dB for the Tr error of 5%.

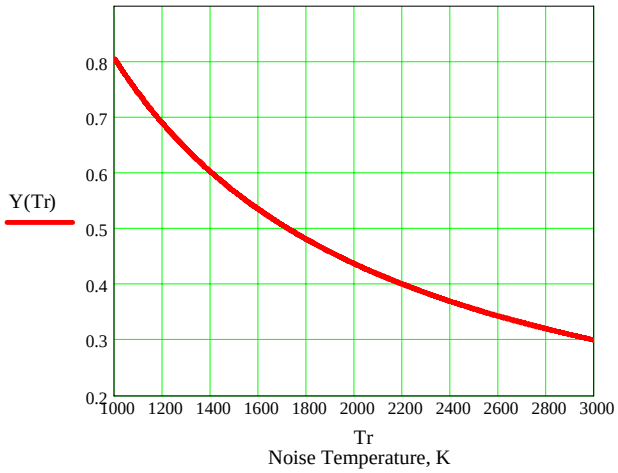

Figure 2. Y-factor versus noise temperature.

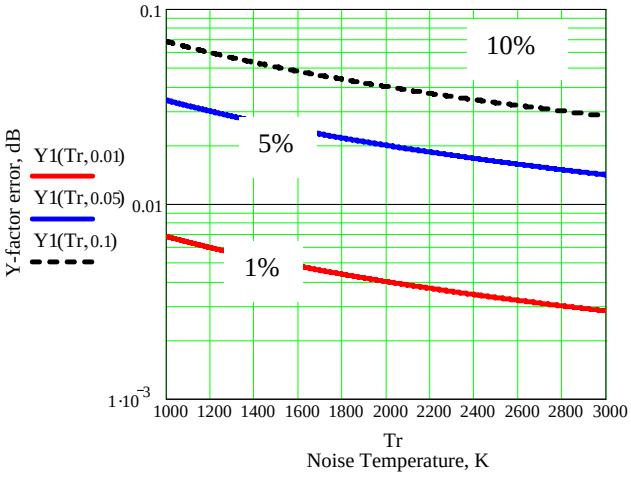

Figure 3. Y-factor error corresponding to the 1%, 5% and 10% of the noise temperature error as a function of the receiver noise temperature.

B. RF power coupling to the mixer

Single mode black body power coupled to the HEB mixer is defined by the antenna RF bandwidth. In our investigation, a 1.6THz double slot antenna was used of the same type as for the HIFI Band 6 Low mixers. The antenna is used in its low impedance resonance in order to facilitate an efficient matching to an HEB mixer which normal state impedance (resistance) is of the order of 50÷100 Ohm. Low impedance resonance for DSAs is much more broad comparing to the high impedance resonance (it is opposite as for the double dipole antennas) and reaches relative bandwidth of about 30% [4]. Its RF band was measured by a Fourier Transform Spectrometer (FTS) with the HEB as a direct detector (see Figure 4, solid line) (see also [5]). The obtained curve was approximated with a function I(f), and the coupled black body power was calculated as

$$P(T) = \int_{0.5}^{3} \varepsilon(f,T) \cdot I(f) \cdot df \,,$$

where

$$\varepsilon(f,T) = hf \frac{1}{\exp\left[\frac{hf}{kT}\right] - 1}$$

is the single mode black body power spectral density.

In the band of the discussed antenna and at assumed optical losses [6] the 300 K (77 K) load produces about 2.8 nW (1.6 nW) referenced to the silicon lens input.

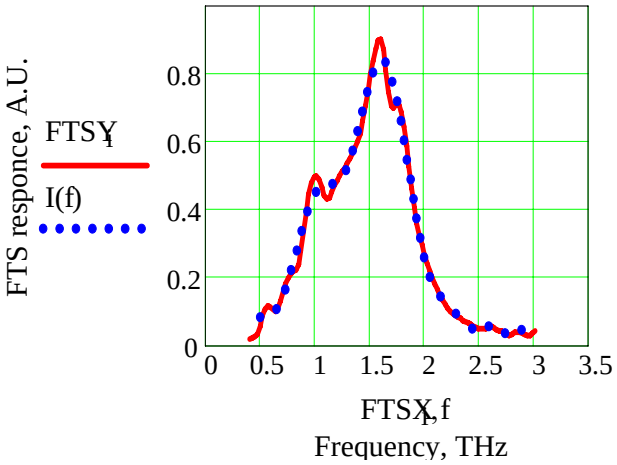

Figure 4. 1.6THz double slot antenna RF band (solid) and an approximation curve (dots).

The LO power referred to the Si lens is of the order of 100-200 nW for the discussed HEB mixers at 4.2 K bath temperature. Such large uncertainty of the required LO power is caused by the difficulty to measure 1.6THz beam power at such low power levels. Even when a thin beam splitter is used with reflectivity of a few percent, the transmitted power is only of the order of 10÷20 μW. The LO power increases the electron temperature from the bath temperature (4.2 K) up to Tc (9 K). A set of the IV-curves corresponding to different LO power values incident on the mixer is shown in Figure 5. The LO power tuning range is about 3dB from the highest IV to the lowest IV shown in the figure. Equivalently, the change from the cold (77 K) load to the hot (290 K) load changes the IV curve as shown in Figure 6. The higher input load corresponds to the higher dc resistance, i.e. lower current at the constant voltage biasing regime.

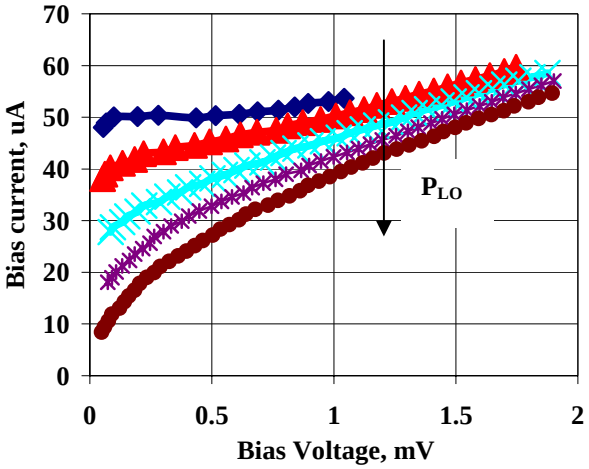

Figure 5. Current – voltage curves under different LO power levels (mixer faces the hot load).

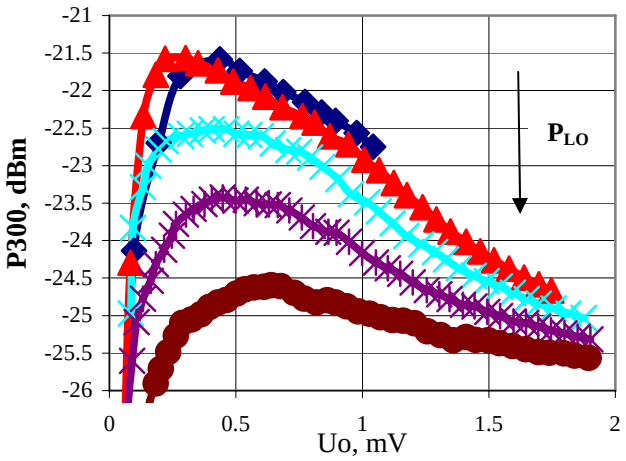

Figure 7. Receiver output power vs bias voltage at different LO power levels. The mixer is loaded on 290 K input load.

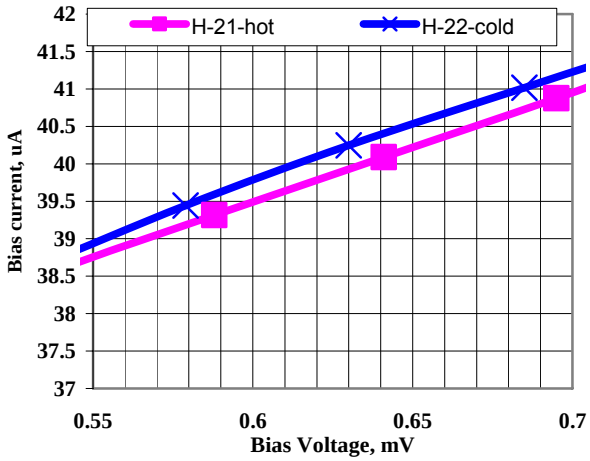

Figure 6. Current –voltage curves under the hot (lower) and the cold(higher) loads. The shown bias area corresponds to the minimum mixer noise temperature.

The mixer output power, P_{if}, consists of the down converted (from RF to IF) input signal and the mixer output noise: $P_{if}=P_{load}\ G\ +T_{out}$. The output power corresponding to the IV curves from Figure 5 is shown in Figure 7. As P_{load} changes from 300K to 77K , the IF output change is:

$$dP_{if}= dP_{load}\ G – P77\ dG – dT_{out}, \qquad (1)$$

dG and dT_{out} is caused by the change of bias current dI (see Figure 6), and for an ideal HEB mixer (no direct detection effect) both dG and dT_{out} shall be zero.

If dI=0, then both dG=0 and dT_{out}=0. In this case dP_{if} is caused by the heterodyne response, i.e. $dP_{load}\ G$. If dI>0, then dG>0 and dT_{out}>0.

In this case, dP_{if} is reduced, hence the Y-factor. The impact of the direct detection effect on the Y-factor measurements depends on the bias current shift (dI), and how strong the G(I) and Tout(I) functions are. For the discussed mixer dI=0.25 μA at the bias point corresponding to the lowest mixer noise temperature (shown in Figure 6).

It has been suggested to define the Tout(I) dependence from Figure 7 assuming that the mixer gain does not change with the current (for small dI values), i.e. dG=0. The obtained correction factor for $dT_{out} = \frac{\partial P_{300}}{\partial I} dI$ was applied to the Equation 1 and the corrected Y-factor was obtained. This method was qualitatively used to analyze the direct detection effect scale by many authors and quantitavely was also applied in [7]. But in this case an uncertainty remains that the mixer gain G shall be LO power dependent, and by changing the LO power the gain changes as well. Especially, this method is valid if the mixer gain is assumed to be bias current independent, which is not quite obvious.

We would like to verify this technique and discuss alternative methods to take into account the direct detection effect.

III. Experiment-I

We investigated two methods to compensate the HEB electron temperature shift at different input loads: by a resistive heater and by an RF heater. In both cases the LO frequency was 1.63 THz.

As a resistive heater we used a high power resistor mounted on the mixer unit. The mixer bias voltage was 0.6mV. In this case the LO power was constant and the mixer bath temperature was changed.

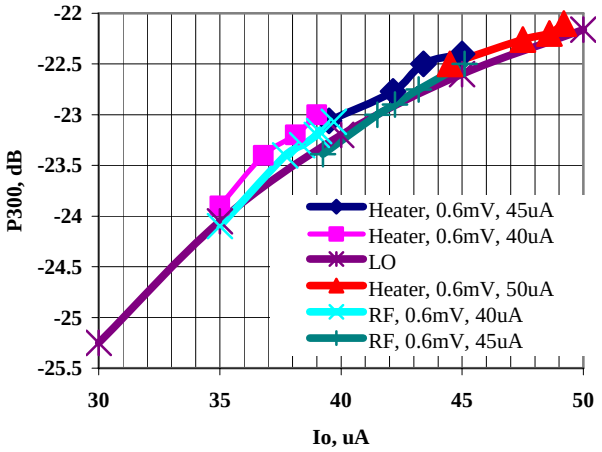

Figure 8. Receiver output power vs bias current at a fixed bias voltage. The bias current was changed by changing the mixer bath temperature.

The applied heating was not very strong and it caused the bias current reduction at maximum by 5 μm at around each used bias current. The measurement were carried out at LO power levels corresponding to the IVs from Figure 5.

The RF heating was applied from a 600 GHz backwards wave oscillator. The BWO beam was inserted into the LO beam path with a second beam splitter. The RF heating occurs via the photon absorption by the electrons with the consequent heat removal by the phonons, i.e. in the heat balance equation the input power changes. While with the resistive heater the bath temperature changes (the border conditions of the heat balance equation). Since these two processes are not identical both heating mechanisms have to be investigated.

For comparison we have also measured P_{if} vs bias current when tuned with the LO power (at the constant bath temperature and the input load). This is shown in Figure 8 with a long solid line. The data obtained for the constant LO power (tuned by the heater and the BWO) are shown with the filled diamonds and the crosses, correspondingly.

For the first approximation, for all three bias current tuning (LO, heater, and BWO) the $P_{if}(I)$ curves coincide with each other. This might be indicating that the method of [7] could be correct. $\delta P_{300}/\delta I$ is about 0.2dB/μA. Since dI, caused by the direct detection is of the order of 0.2 μA, then dT_{out}=0.04dB. The receiver noise temperature (including input optical losses) is 1700 K, and from Figure 3 we see that 0.04dB Y-factor error corresponds to about 8% of the noise temperature error.

We see that dI= 0.2 μA is caused by the 2.8 nW - 1.6 nW= 1.2 nW signal from 300K/77K calibration loads. HIFI calibration loads have bath temperatures of 100 K and 10 K. Since in HIFI the optical loss from the loads to the mixer lens is very low, the mixer will face 0.74 nW input signal change referenced to the silicon lens input. This is a factor of 2 lower than for the lab receiver. Therefore, it will cause 0.02 dB Y-factor error. Since in this case we refer the Y-factor to the silicon lens (not to the calibration loads like for the lab receiver, through the lossy air, the vacuum window and the IR filters), then the receiver noise temperature is about 1000 K (calibrated for the lab receiver input losses). From Figure 3 we obtain that for this noise level 0.02dB Y-factor error corresponds to 2.5% noise temperature error.

IV. Experiment-II

When no direct detection is present the IF signal change when 300K load is replaced with 77 K load is caused by the heterodyne response and log(P300)-log(P77) is positive (we monitor the IF signal in logarithmic scale, i.e. in dBm). While, as it is seen from Figure 7 the $P_{if}(I)$ and G(I) have a positive gradient, at least at the bias area with the maximum HEB sensitivity. Therefore, the direct detection effect reduces the Y-factor. Of course, during the astronomical observations the input signal power will be much less than the calibration loads power. However, it is important to understand the scale of the direct detection effect influence on the HEB calibration for more accurate power measurements of the astronomical sources.

A possible solution would be to eliminate the heterodyne response and look at the log(P300)-log(P77) caused by the bias point shift only. From Figure 4 once can see that at 2.6 THz the double slot antenna response drops nearly to zero. The FIR laser, which we used as the LO source, has a 2.6THz line with the output power of a few mW. We could pump our mixer at this frequency with the same 3 μm Milar beam splitter as for the 1.6 THz experiment. The HEB IV curves for these two LO frequencies are absolutely identical as it seen from Figure 9.

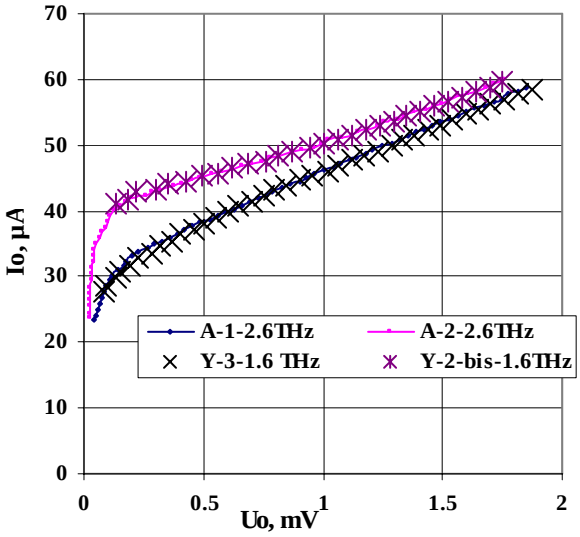

Figure 9. HEB IV-curves pumped to the optimal state with the 1.6 THz LO (crosses) and with the 2.6 THz LO (solid) (IVs with two different LO powers are shown).

This is because both frequencies are much above the energy gap frequency of the used thin NbN superconducting film ($T_c \approx 9$ K). However, the direct detection effect scale is defined by the calibration loads power coupled to the mixer. This

remained unchanged since it is the same mixer-antenna which is used. The observed dI change for 2.6 THz was the same as for 1.6 THz as the loads switched from 300 K to 77 K.

As we have mentioned, for 2.6 THz LO frequency with the 1.6 THz DSA HEB mixer, the mixer gain shall be nearly zero due to the drop of the antenna efficiency. From Eq.1 we shall see that dP_{if} is caused by the direct detection effect only and the measured Y-factor log(P300)-log(P77) shall be negative (or zero if no direct detection effect is present). Surprisingly we observed a positive Y-factor of the order of 0.05÷0.1 dB (for different samples). Since in Chapter III we have estimated the direct detection effect on the Y-factor as -0.04 dB, it results in the real Y-factor (measured Y-factor plus direct detection calibration) of the order of 0.1-0.15dB at 2.6 THz, which seems to be too high for such low antenna efficiency as shown in Figure 4.

We shall note that Band 6 mixers of HIFI instrument will operate without IF isolators between the mixers and the LNAs. The reason is unavailability of cryogenic isolators for the 2.4-4.8 GHz band. In our measurements we used an Alcatel HIFI prototype LNA without an isolator as well. Therefore, the LNA input is directly loaded with the HEB mixer which IF impedance changes in a wide range through the discussed IF band [8]. An important HEB parameter defining the HEB IF impedance is the mixer dV/dI at the operation point. As for the IVs from Figure 9 the dV/dI changes with the bias point. It causes the HEB impedance to change. A model of a InP HEM amplifier (Chalmers design) was used in order to estimate how sensitive the LNA gain is to the input load impedance. Preliminary calculations show that the LNA gain increases by 0.6 dB when the input load impedance increases from 50 Ohm to 60 Ohm. Of course, the impedance change associated with the direct detection effect is not more than 1 Ohm, however our modeling was quite simplified as well. It shall also mean that the direct detection error introduced into the Y-factor shall be intermediate frequency dependent.

In order to check the discussed phenomenon we introduced a 4-8 GHz isolator between the HEB and the LNA. The LNA band was 2.4-4.8 GHz, hence the LNA-isolator common band was 4-4.8 GHz. We compared the experiment at 2.6 THz, discussed in this chapter, with such isolator and without it. Intermediate frequency was 4 GHz in both cases. We observed a positive Y-factor of 0.05dB without the isolator, and no distinguished Y-factor with the isolator. The set of curves as in Figure 7 has to be recorded for the LNA with the isolator and $P_{300}(I)$ shall be compared for the case without the isolator. This is planned for the future.

V. Conclusion.

Direct detection effect is defined as the shift of the HEB bias current when the 300 K calibration load is switched to 77 K load. The shift is caused by the heating of the HEB by the black body power absorbed by the HEB via the double slot antenna. The bias current shift introduces an error into the Y-factor measurements. Different techniques can be used in order to figure out the scale of the effect from the measured dI value. Using a simplified method we obtain that this effect gives about 8% noise temperature error for the Band 6 Low mixers of the HIFI instrument (Herschel Space Observatory). For these mixers an error of 2.5 % is expected when the calibration loads with 100 K and 10 K (as in HIFI) are used (assuming no coupling loss from the loads to the mixer).

A clear evidence of the bias current shift effect on the HEB-LNA matching has been observed when comparing the results with and without the IF isolator. A more thorough investigation is needed in order to understand the scale of the effect quantitatively. An isolator, covering the entire IF band (2.4-4.8 GHz), might be an option in order to minimize the Y-factor error.

Acknowledgements.

For the HEB mixers we used NbN films deposited at Moscow State Pedagogical University (Russia). The work was supported by Swedish National Space Board in the frame of the HEB Mixers for Herschel Space Observatory project.

References:

[1] E. M. Gershenzon, G. N. Gol'tsman, I. G. Gogidze, A. I. Elant'ev, B. S. Karasik and A. D. Semenov, "Millimeter and submillimeter range mixer based on electronic heating of superconducting films in the resistive state", Sov. Phys. Superconductivity, 3, 1582, 1990

[2] http://sci.esa.int/sciencee/www/object/index.cfm?fobjectid=34682

[3] U.Mair et al in this Prceedings; and D.Meledin at al in this Proceedings.

[4] M. Kominami, D. M. Pozar, and D. H. Schaubert, "Dipole and slot elements and arrays on semi-infinite substrates," IEEE *Trans. Antennas Propagal.* vol. 33, pp. 600-607, June 1985.

[5] D. Loudkov, P. Khosropanah, S. Cherednichenko, A. Adam, H. Merkel, E. Kollberg, G. Gol'tsman, "Broadband Fourier Transform Spectrometer (FTS) measurements of spiral and double- slot planar antennas at THz frequencies", *Proc. 13th*. International Symposium on Space Terahertz Technology, *Cambridge, MA , March 2002*

[6] Air loss: 0.6dB, vacuum window 0.7dB, IR filter (at 77K) 0.3dB, IR filter (at 10K) 0.3dB.

[7] Baselmans, J.J.A.; Hajenius, M.; Gao, J.R.; Baryshev, A.; Kooi, J.; Klapwijk, T.M.; Voronov, B.; de Korte, P.; Gol'tsman, G.;" NbN hot electron bolometer mixers: sensitivity, LO power, direct detection and stability", IEEE Trans.Appli. Supercond., IVolume 15, Issue 2, Part 1, June 2005 Page(s):484 - 489

[8] H.Ekström, B.Karasik, E.Kollberg, and K.S.Yngvesson, "Conversion gain and noise of niobium superconducting hot-electron –mixers", IEEE Trans., MTT, vol 43, n.4, 1995.

Air-Bridge Integrated Slot-Ring Antennas for HEB Devices: New Fabrication Techniques*

Dazhen Gu, Eyal Gerecht, Xin Zhao, and Sigfrid Yngvesson

***Abstract*—In order to develop multi-pixel focal plane arrays at terahertz frequencies based on hot electron bolometer (HEB) technology, special consideration must be given to the power coupling configuration. Tunable terahertz local oscillator (LO) sources have insufficient power to bias large arrays of HEB mixers. We are developing a new quasi-optical coupling structure consisting of a slot-ring antenna and an elliptical silicon lens. The goal of the project is to eliminate the need for a beam splitter or diplexer and to couple both LO beam and signal beam directly to the antenna. This direct coupling can be achieved by setting the polarizations of the LO and signal beams to be orthogonal to each other. The IF power is extracted through a coplanar waveguide (CPW) that includes a stub filter to prevent the loss of terahertz power from the slot-ring. Discontinuities in the CPW structure cause even symmetry modes to propagate. An air-bridge ground plane structure can prevent the propagation of such undesirable modes, through which terahertz and IF power may be lost. Although slot-ring antennas, including air-bridges, have been used successfully at much lower frequencies, they present a fabrication and design challenge at terahertz frequencies. We have developed a complex fabrication technique for the construction of HEB devices at the terminals of air-bridge integrated slot-ring antennas.**

***Index Terms*— HEB devices, quasi-optical coupling, slot-ring antenna, terahertz receivers.**

I. Introduction

TERAHERTZ radiation, with frequencies between those of millimeter waves and the infrared, exhibits unique properties for radio astronomy, biomedical, and homeland security applications. A number of terahertz technologies for use in imaging, remote sensing, and spectroscopy, are under development [1-5]. All these applications rely on reliable terahertz sources that can provide sufficient power and high tunability. The main terahertz source technologies are listed below.

A. Far-infrared Lasers

Far-infrared (FIR) lasers consist of a tunable Fabry-Perot cavity optically pumped by a continuous wave carbon dioxide (CO_2) laser [6]. Optically pumped lasers can operate at many frequencies, which fully cover the terahertz range (from 300 GHz to 10 THz). FIR lasers are used primarily only in laboratory research because of their bulky size and difficulty of operation. Although there are many spectral lines corresponding to different frequencies of operation, FIR lasers lack sufficient tunability. A custom-designed FIR laser system, under operation at the UMass Terahertz Laboratory, is shown in Fig. 1(a).

B. Harmonic Multipliers

Harmonic multipliers have been widely used in RF circuits from megahertz frequencies to gigahertz frequencies. Recent development of Gallium Arsenide (GaAs) Schottky diode harmonic multipliers has pushed this technology into the terahertz regime. Driven by millimeter wave synthesizers, harmonic multipliers can directly multiply the frequency up to terahertz frequencies. However, the available output power from harmonic multipliers decreases with increasing frequency. The best harmonic multiplier source at about 700 GHz can generate one hundred microwatts of output power, which is barley sufficient to provide biasing power for a small number of detectors, but insufficient for focal plane arrays with a medium or large number of detectors. Harmonic multiplier sources generate less than 10 μW at frequencies above 1 THz but have a significant advantage over other terahertz sources in terms of their size (very mobile), ease of use, and tunability. Fig. 1(b) shows a commercially available multiplier source.

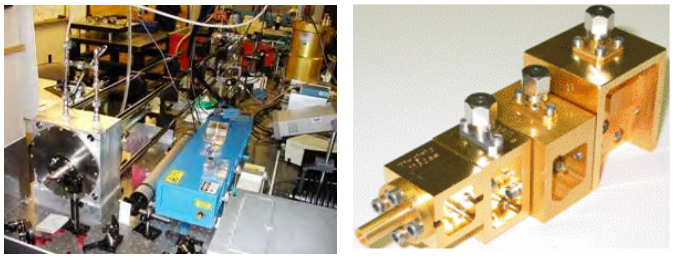

(a) (b)

Fig. 1. Terahertz sources: (a) far-infrared laser; (b) harmonic multiplier.

*Work partially supported by U.S. Government; not protected by U.S. copyright.

D. Gu and E. Gerecht are with the National Institute of Standards and Technology, Boulder, CO 80305 USA (phone: 303-497-3939; fax: 303-497-3970; e-mail: dau@ boulder.nist.gov).

X. Zhao and S. Yngvesson are with the Electrical and Computer Engineering Department, University of Massachusetts, Amherst, MA 01003 USA.

C. Quantum Cascade Lasers

Quantum cascade lasers (QCL), invented by scientists at Bell Labs for optical wavelengths, are under development at terahertz frequencies [7]. QCLs usually consist of so-called quantum wells which include a few hundred molecular beam epitaxy (MBE) grown layers of nanometer-thin alloy materials, such as gallium and aluminum compounds. These quantum wells are arranged in a QCL device as a waterfall structure with each layer at a lower energy level than the one before. When an electric current flows through a QCL device, the electrons jump from one energy level to another, rather than moving smoothly between levels, and similarly the electrons tunnel from one layer to the next going "through" rather than "over" energy barriers separating the wells. This cascading effect produces sufficient gain in the QCL. The frequency of the QCL can be tuned by adjusting the thickness of the layers. Although QCLs have become a well-established radiation source technology for the mid-infrared region, the output power level at frequencies lower than 3 THz is still very small. QCLs operate at cryogenic temperatures, and temperature instability will result in a frequency shift. QCLs are not currently commercially available.

Harmonic multiplier sources are the most promising technology for mobile terahertz imagers. A two-dimensional terahertz imaging system employing a harmonic multiplier source is under development at the National Institute of Standards and Technology in collaboration with the UMass Terahertz Laboratory.

To efficiently utilize the power from a multiplier source at terahertz frequencies, we developed a quasi-optical design based on a slot-ring antenna and an elliptical silicon lens. The LO injection scheme, shown in Fig. 2, will be used to pump the state-of-the-art hot electron bolometer (HEB) mixers. By fabricating the HEB device at a location of 45 degrees with respect to the slot input, the polarizations of LO and signal beams can be set orthogonal to each other. The signals are then combined using a wire grid instead of a beam splitter. In order to eliminate the spurious slot-line mode propagating through the IF channel, an air-bridge structure is required to be integrated with the slot-ring antenna. The small dimensions of the slot-ring antenna at terahertz frequencies require a new fabrication process. This paper describes the design of an air-bridge integrated slot-ring antenna and the new fabrication process for such structures.

II. Antenna and Filter Design

Slot-ring antennas have been used in millimeter-wave receivers with balanced mixer configurations [8][9]. When these structures are used for sub-millimeter-wave applications, the power loss due to substrate modes becomes increasingly important. A convenient way to eliminate substrate modes is to place the slot-ring antenna substrate on a dielectric lens having roughly the same dielectric constant [10]. The lens acts as an effective dielectric half-space. Most of the power (about 97 %) radiates into the dielectric half-space. The power radiating outwards into the vacuum side (3 %) contributes 0.1 dB to the total system noise figure [11]. The design of a slot-ring antenna with a resonance frequency centered at 1.56 THz was reported in a previous publication [12]. The impedance of the antenna, with a ring radius of 13.5 μm and a slot width of 2 μm, was simulated to be 90 Ω. In the following subsections, theoretical calculations of the radiation pattern of the slot-ring antenna and S-parameters of the stub filter are discussed.

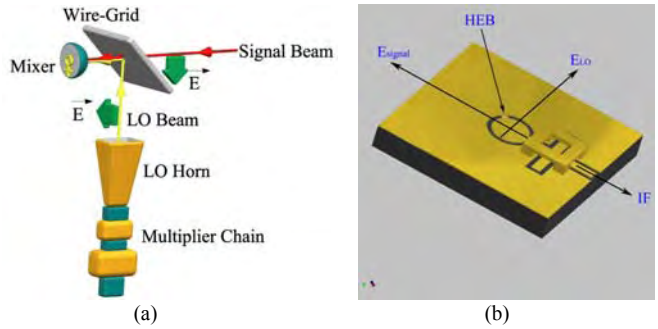

Fig. 2. (a) LO injection scheme; (b) slot-ring antenna with an air-bridge design.

A. Radiation Pattern of Slot-ring Antenna with Lens

In order to obtain the radiation pattern of the slot-ring antenna on a silicon lens, we first calculate the far-fields of the antenna without the presence of the lens, and then add the effects of the lens. At the resonance frequency, the circumference of the slot-ring is close to one guided wavelength ($1.07\lambda_g$). The magnitude of the electric field in the slot has a sinusoid distribution and varies only along the azimuthal angle. Therefore, the slot-ring can be equivalently viewed as a magnetic current loop with its magnitude given by

$$\boldsymbol{M}(\varphi) = \boldsymbol{M}_0 \cos(\boldsymbol{ka}\varphi), \tag{1}$$

where k is the propagation constant, a is the radius of the slot-ring, and φ is the azimuthal angle. The aperture radiation pattern can be calculated from the effective magnetic and electric current densities [13]. Starting from Eq. (1), we can derive the far-field radiation pattern as

$$\boldsymbol{E}_\theta(\theta,\varphi) \sim \boldsymbol{J}_1'(\boldsymbol{ka}\cdot\sin\theta)\cdot\cos\varphi \text{ and} \tag{2}$$

$$\boldsymbol{E}_\varphi(\theta,\varphi) \sim \frac{\boldsymbol{J}_1(\boldsymbol{ka}\cdot\sin\theta)}{\boldsymbol{ka}\cdot\sin\theta}\cdot\cos\theta\cdot\sin\varphi, \tag{3}$$

where $k=k_d=2\pi/\lambda_d$ for the dielectric side and $k=k_0=2\pi/\lambda_0$ for the vacuum side, J_1 is the first order Bessel function of the first kind and J_1' is its first derivative.

The silicon lens functions as a beam-focusing element, and hence will reshape the far-field radiation pattern. We used a ray-optics approach and a two-dimensional Fourier transform to include the effects of the lens [14]. At the interface between

the dielectric lens and the vacuum, the field components in spherical coordinate system are transformed to the cylindrical coordinate system (see Fig. 3). On the dielectric side, it is convenient to use the spherical coordinate system for a point source, which is the slot-ring antenna. In order to calculate the far-field pattern, we need to integrate the electromagnetic fields on the two dimensional plane just outside of the dielectric lens. This requires us to use a cylindrical coordinate system on the vacuum side. The electric fields of the point source (E_θ and E_φ) are therefore transformed to the fields on the plane (E_ρ and E_φ) as follows:

$$E'_\rho(\rho,\varphi') = E_\theta(\theta',\varphi')\cdot\frac{n-\cos\theta'}{(n-1)f}t_\theta\cdot\frac{1}{r} \text{ and} \quad (4)$$

$$E'_\varphi(\rho,\varphi') = E_\varphi(\theta',\varphi')\cdot\frac{n-\cos\theta'}{(n-1)f}t_\varphi\cdot\frac{1}{r}, \quad (5)$$

where f is the distance from the slot-ring antenna to the top of the lens, n is the dielectric constant of the silicon lens, and t_θ and t_φ are the field transmission coefficients through the interface between the lens and the vacuum half-space. Subscripts θ and φ correspond respectively to the elevational and azimuthal directions.

In terms of the far-field radiation, we are concerned about the relative pattern rather than the absolute value. Eq. (4) and Eq. (5) are then simplified as follows:

$$\boldsymbol{E}'_\rho(\theta',\varphi') \sim \boldsymbol{J}'_1(\boldsymbol{ka}\cdot\sin\theta')\cdot\cos\varphi'\cdot\boldsymbol{t}_\theta\cdot\frac{1}{\boldsymbol{r}} \text{ and} \quad (6)$$

$$\boldsymbol{E}'_\varphi(\theta',\varphi') \sim \frac{\boldsymbol{J}_1(\boldsymbol{ka}\cdot\sin\theta')}{\boldsymbol{ka}\cdot\sin\theta'}\cdot\cos\theta'\cdot\sin\varphi'\cdot\boldsymbol{t}_\varphi\cdot\frac{1}{\boldsymbol{r}}. \quad (7)$$

The final far-field pattern can be obtained by integrating on the closed surface, just outside of the lens (s'). The electrical fields, E_θ and E_φ, are then expressed as follows:

$$\boldsymbol{E}_\theta \sim (1+\cos\theta)\iint_{s'}\left[\boldsymbol{E}'_\varphi\sin(\varphi-\varphi')+\boldsymbol{E}'_\rho\cos(\varphi-\varphi')\right] \cdot\boldsymbol{e}^{\boldsymbol{jk}\rho\sin\theta\cos(\varphi-\varphi')}\rho\cdot\boldsymbol{d}\rho\boldsymbol{d}\varphi' \quad (8)$$

$$E_\varphi \sim (1+\cos\theta)\iint_{s'}\left[E'_\varphi\cos(\varphi-\varphi')-E'_\rho\sin(\varphi-\varphi')\right] \cdot e^{jk\rho\sin\theta\cos(\varphi-\varphi')}\rho\cdot d\rho\cdot d\varphi'. \quad (9)$$

The terms of E_ρ' and E_φ' in Eq. (8) and Eq. (9) can be substituted by Eq. (6) and Eq. (7).

Fig. 4 shows the far-field radiation patterns as calculated from Eq. (8) and Eq. (9). The beam in the H-plane is slightly wider than the one in the E-plane and therefore agrees with the results obtained by [8]. The simulated side lobe levels (SLLs) of 15.7 dB in the E-plane and 19.7 dB in the H-plane are also similar to the results of [8]. Another important characteristic of the radiation pattern is the 3 dB beamwidth of the main lobe. The 3dB beamwidth of the main lobe is less than 3° for both the E-plane and the H-plane (see Fig. 4).

B. Performance of Bandstop Filter with Air-bridge

We chose a double-stub bandstop filter because of its advantages of being less prone to picking up RF/LO radiation. Two quarter-wavelength long open-circuit stubs are placed one quarter-wavelength away from the slot-ring antenna and form the bandstop filter. The open-circuit is therefore transformed to the interface between the CPW and the slot-ring antenna. Such filters introduce even-symmetry modes of propagation due to discontinuities in the CPW structure. These even modes can cause extra loss to the LO and the RF, resulting in higher LO power requirements as well as a higher receiver noise temperature. In order to suppress the undesirable modes, an air-bridge structure is fabricated on top of the double-stubs to form an elevated ground plane.

A number of simulations were performed to study the performance of the double-stub filter and then optimize its dimensions. Fig. 5 shows the simulation results of the

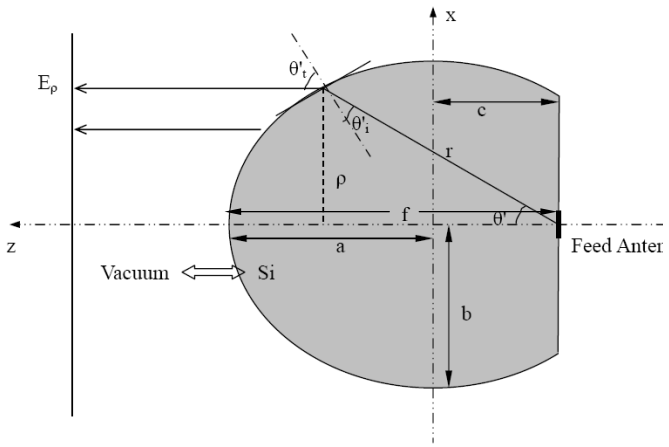

Fig. 3. Illustration of a silicon lens as a beam reshaping element.

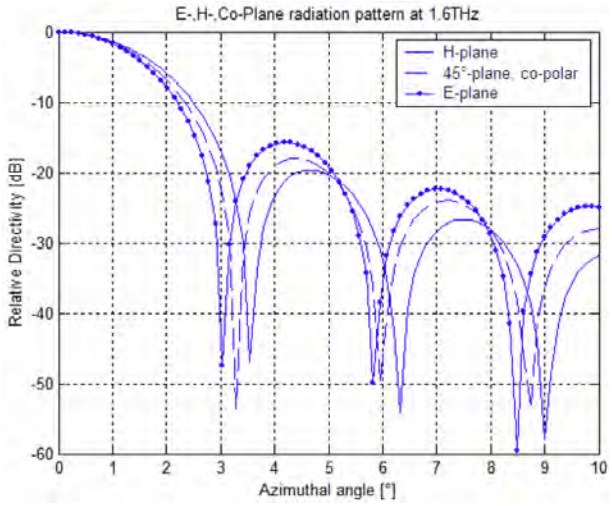

Fig. 4. Far-field radiation pattern of the lens-integrated, slot-ring antenna.

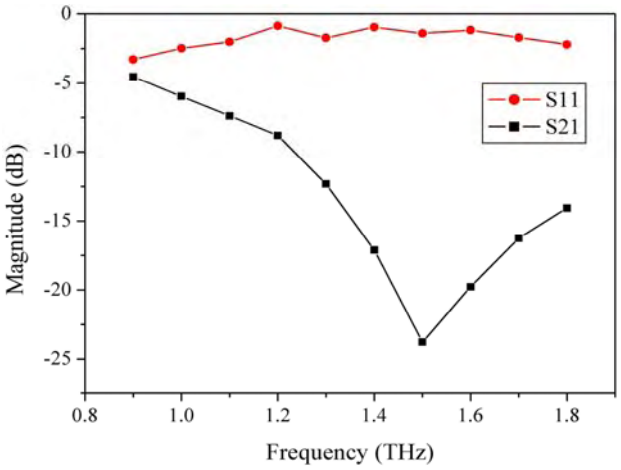

Fig. 5. Simulation results of the air-bridge integrated stub filter.

bandstop filter S-parameters. The insertion loss (S_{21}) at the center frequency (1.5 THz) is about 25 dB. The insertion loss without the air-bridge structure is less than 15 dB at the center frequency. This 10 dB difference in the insertion loss demonstrates the effectiveness of the air-bridge structure.

III. Fabrication Process

HEB devices were fabricated on a NbN film 3.5 nm thick, that was deposited on a silicon substrate by DC magnetron sputtering. The active region of the NbN strip is 4 µm wide by 0.5 µm long. Fig. 6 shows the main steps of the fabrication process. We fabricated the device using an advanced stepper lithography instrument. Such a system utilizes ultra-short (365 nm wavelength) UV light to reduce diffraction and thus achieve higher resolution. Furthermore, the stepper instrument contains lenses of high numerical aperture designed to project the exposure light with a reduction of image size on the wafer by a factor of five. We have also introduced a bi-level lift-off process that improves the yield of the critical submicron lift-off step. In addition to the standard photoresist, the chip is first coated with a layer of MicroChem [15] lift-off resist (LOR). At a specific pre-bake temperature, the LOR layer produces a sideways undercut distance of 0.1 to 0.2 µm, which ensures good lift-off with thin film edge quality without flakes or fences.

After the metallization and lift-off steps, a strip of photo resist was patterned on the device in order to protect it from the reactive ion etch (RIE) process. This step is designed to remove the excess NbN film.

Next, a backside alignment window for the lens positioning was patterned. This step was performed using a standard contact aligner and an infrared camera for aligning the window on the back side of the silicon substrate. After the titanium-gold layer was deposited on the chip in an E-beam evaporation chamber, an additional lift-off step was performed to open the window.

Once the fabrication of the device was completed, the air-bridge was constructed. Fig. 7 illustrates the two main steps

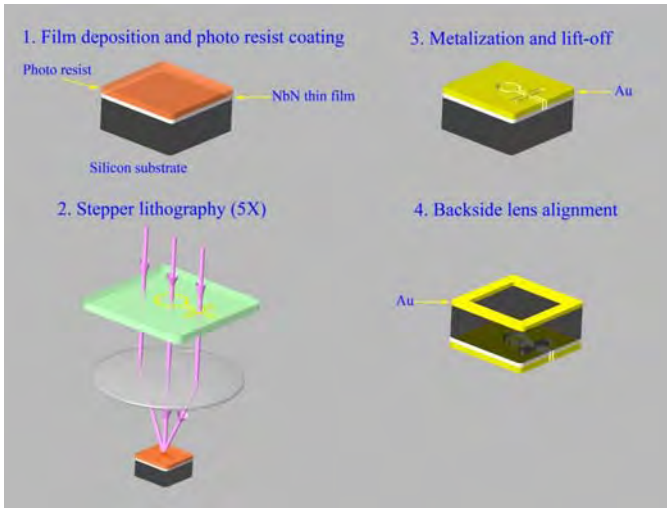

Fig. 6. Illustration of the HEB device fabrication steps.

involved in the fabrication of the air bridge structure. The air-bridge structure, which consists of 6 µm tall posts and 3 µm thick spans, was constructed by a gold electroplating process. This step was carried out by use of a commercially-available noncyanide electrolytic solution (TECHNI-GOLD 25 MAKEUP ES [15]) at a temperature of 60 °C. The thickness of the electroplated gold is controlled by the plating time, with the current density fixed at 2 mA/cm^2. The resulting electroplating rate is 0.11 µm/min. To form a 6 µm thick sacrificial layer to realize the standing posts and elevated spans, a thick photo resist (SPR 220-7 [15]) was coated and patterned by means of the UV stepper lithography equipment. The patterned sacrificial layer was thermally cured at 115 °C in order to de-gas the photoresist. After the electroplating step, a titanium-gold layer was coated onto the chip by E-beam metallization. This titanium-gold layer provides electro-contact for the following gold plating step. Next, an additional thick photoresist layer (SPR 220-3 [15]) was spun on and patterned to form a 3 µm thick sacrificial layer. After the photoresist was cured in the oven at a temperature of 120 °C for 5 minutes, 3 µm thick gold was electroplated on to form the spans. Finally, the whole chip was immersed in a photoresist remover solution (NANO Remover PG [15]) at a

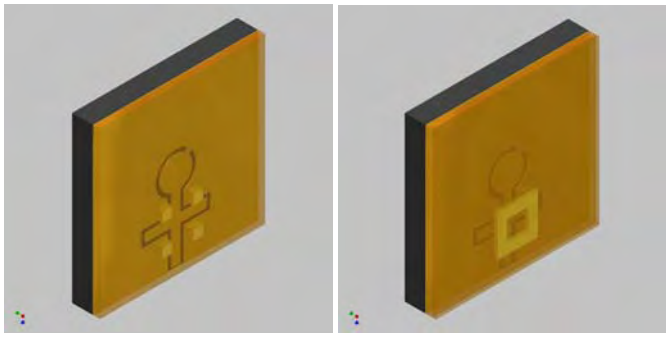

(a) (b)

Fig. 7. Two gold electroplating steps for constructions of the air-bridge. (a) 4 posts; (b) spans.

temperature of 60 °C in order to remove the photoresist and the excess metal. Ultra-sound agitation may be used to accelerate the lift-off step.

The entire electroplating process was carried out in a Process Systems International (PSI) Excellite 9000 [15] plating bath. Plating cell configurations utilize a rotating wheel (cathode), where one wafer can be attached, along with reciprocating anodes. During plating, as the wafer rotates, the anodes move continuously from left to right and vice versa, and a high precision pulse DC power supply provides rectification. In our setup, the device chip was held on a dummy wafer using purified bee's wax. The bee's wax melts at around 80 °C. Since the electroplating process is performed at 60 °C, the bee's wax provides sufficient adhesion.

IV. Results

The fabrication process described above was first optimized on the test wafer in order to produce a functioning air-bridge structure in the absence of an HEB device. The optimization process resulted in a robust air-bridge structure with a yield of better than 95 %. The resistance between the air-bridge structure and the ground plane on the device substrate was less than 5 Ω. After the evaluation of the air-bridge structure on the test wafer, we proceeded with a working HEB device fabricated on a silicon substrate. Extra care is required when the air-bridge structure is fabricated on an actual HEB device. The yield drops to about 75 %. The HEB devices fabricated on the NbN film exhibited a resistance of 90 to 100 Ω compared with a slot-ring antenna resistance of about 90 Ω. A good resistance match between the slot-ring antenna and the device is highly desirable in order to achieve a good power coupling efficiency.

Scanning electron microscope photographs of the air-bridge integrated slot-ring antenna and an HEB device are shown in Fig. 8. The images were taken on the JEOL 6400 SEM [15] system. Photos (a) and (b) were taken with the sample stage tilted at 45 degrees, while photos (c) and (d) were taken as the stage tilted at 75 degrees. The air-bridge structure appears to be very uniform and robust. This is also verified by the fact that the air-bridge survived the ultra-sound agitation step, known to be very violent and destructive.

V. Conclusion

An air-bridge integrated slot-ring antenna has been designed for operation at 1.6 THz. Numerical calculations of the antenna radiation pattern show a narrow beamwidth (~3°) of the slot-ring antenna at the center frequency. From the simulation, the air-bridge integrated stub filter exhibits a good bandstop characteristic with a rejection of 25 dB at the center frequency.

We have demonstrated a new fabrication technique for making an air-bridge integrated slot-ring antenna with an HEB device. Further characterization of the HEB device in terms of power coupling and noise temperature measurements is on-going. Future multi-pixel focal plane arrays for terahertz imaging may utilize the quasi-optical configuration demonstrated here.

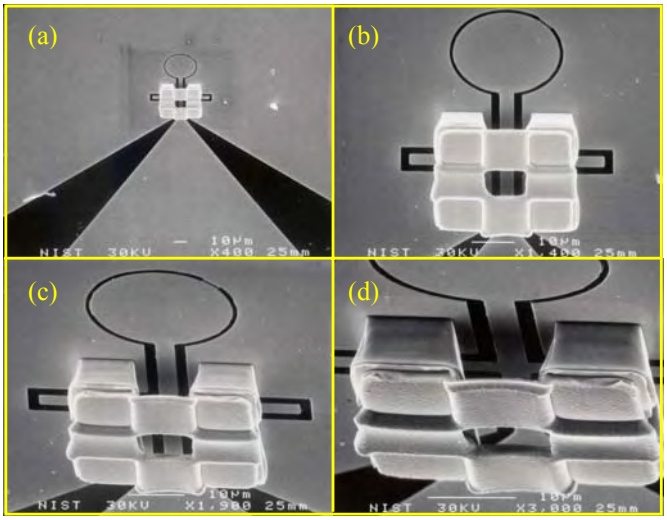

Fig. 8. SEM images of a slot-ring device and an air-bridge structure.

Acknowledgment

This work was supported by grants from NASA and the National Institute of Standards and Technology in Boulder, CO.

References

[1] S. Wang and X.C. Zhang, "Pulsed terahertz tomography," Journal of Physics D – Applied Physics, vol 37 (4), pp R1-R36, Feb 2004.

[2] R. Hoogeveen, Overview of TELIS system. Available: http://www.sron.nl/www/code/eos/telis/telis.php?1=1&menuID=1127

[3] T. Nagashima, K. Takata, S. Nashima, H. Harima and M. Hangyo, "Measurement of electrical properties of GaN thin films using Terahertz-time domain spectroscopy," Japanese Journal of Applied Physics Part 1, Vol 44 (2), pp 926-931, Feb 2005.

[4] E. Gerecht, et al, " Development of TREND- a low noise receiver user instrument at 1.25 THz to 1.5 THz for AST/RO at the South Pole," 14th Intern. Symp. Space THz Tech., Tucson, AZ, Apr. 2003.

[5] S. Cherednichenko, M. Kroug, H. Merkel, P. Khosropanah, A. Adam, E. Kollberg, D. Loudkov, G. Gol'tsman, B. Voronov, H. Richter, and H.-W. Huebers, "1.6 THz Heterodyne Receiver for the Far Infrared Space Telescope", Physica C, Superconductivity and its Applications, 372-376: pp. 427-431, 2002.

[6] E. R. Mueller, Terahertz radiation: application and sources. Available: http://www.aip.org/tip/INPHFA/vol-9/iss-4/p27.html

[7] J. Faist, et al, "High power mid-infrared (~ 5 µm) quantum cascade lasers operating above room temperature," Applied Physics Letter, Vol 68 (26), pp. 3680-3682, June 1996.

[8] S. Raman and G. M. Rebeiz, "Single- and dual-polarized millimeter-wave slot-ring antennas", IEEE Transaction on Antennas and Propagation, Vol 44 (11), pp 1438-1444, Nov 1996.

[9] C. E. Tong and R. Blundell, "An annular slot antenna on a dielectric half-space," IEEE Transaction on Antennas and Propagation, Vol 42(7), pp 967-974, July 1994.

[10] D. B. Rutledge, D. P. Neikirk and D. P. Kasilignam, "Integrated circuit antennas," Infrared and Millimeter-Waves, Vol 10, K. J. Button, Ed., pp. 1-90, Academic Press, New York, 1983.

[11] X. Zhao, "Integrated Antenna for THz Hot Electron Bolometer Mixers", Master Thesis, Electrical and Computer Engineering, University of Massachusetts Amherst, Feb. 2005.

[12] E. Gerecht, D. Gu, X. Zhao, J. Nicholson, F. Rodriguez-Morales, and S. Yngvesson, "Development of NbN terahertz HEB mixers coupled through slot-ring antennas," 15th Intern. Symp. Space THz Technology, Northampton, MA, Apr. 2004.
[13] C. A. Balanis, Antenna Theory – analysis and design, 2nd edition, John Wiley & Sons, Inc. 1997.
[14] D. F. Filipovic, S. S. Gearhart, and G. M. Rebeiz, " Double-slot antennas on extended hemispherical and elliptical silicon dielectric lenses," IEEE Transaction on Microwave Theory and Technology, vol 41, pp 1738-1749, Oct. 1993.
[15] Products and companies named here are cited only in the interest of complete scientific description, and neither constitute nor imply endorsement by NIST or by the US government. Other products may be found to serve just as well.

Performance Improvement of Integrated HEB-MMIC Receivers for Multi-Pixel Terahertz Focal Plane Arrays

Fernando Rodriguez-Morales, Eyal Gerecht, Dazhen Gu, Richard Zannoni, Sigfrid Yngvesson, Niklas Wadefalk, and John Nicholson.

***Abstract*— Phonon-cooled NbN HEB mixers have been successfully integrated with InP MMIC IF amplifiers to produce low-noise HEB-MMIC receivers. Noise temperatures of less than 1,600 K and receiver noise temperature bandwidths of at least 4 GHz (measured at 1.6 THz) have earlier been demonstrated for this type of integrated receivers. Our configuration eliminates the need for isolators which require very large areas on the IF circuit. In this paper, we are presenting recent results from ongoing measurements of these integrated receivers. We propose using different matching schemes for the MMIC LNA that will help reduce the size of the IF circuitry. Small circuit size is a desirable feature for focal plane arrays. Next, we propose a linear terahertz FPA with an increased number of HEB pixels based on the integrated miniaturized design. Lastly, we describe a frequency multiplexing scheme formulated to significantly reduce the number of IF lines required in a large imaging array. The proposed multiplexing scheme utilizes the very broad bandwidth (12 GHz) presently demonstrated for MMIC low-noise IF amplifiers.**

***Index Terms*— HEB mixers, integrated terahertz receivers, MMIC low-noise amplifiers.**

I. Introduction

In contrast to the large arrays available for detection in the visible and infrared, the majority of the instrumentation available for terahertz heterodyne detection is still based on single-pixel receivers. Hot electron bolometer (HEB) receivers, in particular, are an excellent choice to achieve near quantum-limited noise performance. The main technological challenges for building array receivers at these frequencies encompass receiver miniaturization, LO power reduction, and minimization of the DC-power consumption in the cryogenic IF circuitry. Complicating the matter, the issue of IF impedance matching needs to be addressed before a practical HEB focal plane array can be constructed. Let us think about the most common and general configuration for an HEB terahertz receiver. This configuration is illustrated in Fig. 1. Typically, the HEB mixer and the IF low-noise amplifier (LNA) are placed in independent blocks connected through a short coaxial cable. The experienced designer knows that if an isolator is not added to the receiver chain, the system will seriously suffer from standing waves between the mixer and the IF LNA.

This work was supported by NASA through the Langley Research Center under contract NAS1-01058 and CONACyT, Mexico.

F. Rodriguez-Morales, E. Gerecht, D. Gu, R. Zannoni, K.S. Yngvesson, and J. Nicholson are with the University of Massachusetts, Amherst, MA, USA; N. Wadefalk is with the California Institute of Technology, Pasadena, CA, USA.

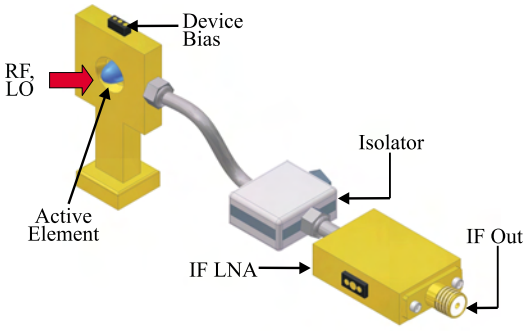

Fig. 1. Typical HEB receiver configuration.

Unfortunately, including an isolator is not an optimal solution for multiple receiver systems. Isolators occupy a significant physical space apart from increasing the thermal load. Moreover, the widest bandwidth that can be achieved with currently available isolators is at most one octave.

We have developed miniaturized receivers with the HEB mixers integrated in close proximity with InP MMIC amplifiers (Fig. 2). This configuration is compact, broadband and with reasonably low DC-power utilization. The HEB and the MMIC are contained in the same housing, without requiring an isolator. These receivers represent the core of the focal plane array described in [1]. Our recently developed terrestrial terahertz imaging system [2], [3] also makes use of this technology.

In this paper, we are presenting results from ongoing measurements of the current performance of these integrated receivers, as well as their prevailing limitations. Next, we propose a 3x2 terahertz FPA based on a new design, in which the receivers have been further miniaturized. The proposed prototype can be easily extended to a linear array with 10 or more elements, suitable for near-range imaging applications. Lastly, we describe a frequency multiplexing scheme formulated to significantly reduce the number of IF lines required in a large imaging array. The proposed multiplexing scheme utilizes the extremely wide bandwidth attainable with state-of-the-art MMIC LNAs.

II. Receiver Characterization

A. Overview of the HEB/MMIC Integrated Receivers

The integrated receiver configuration has been put together in a mixer block unit, as shown in Fig. 3. The mixer elements

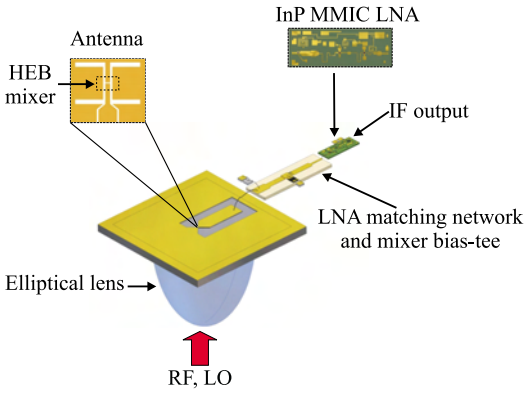

Fig. 2. Integrated HEB receiver configuration.

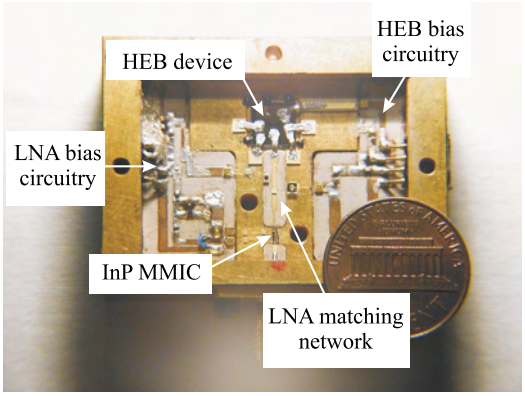

Fig. 3. Inside view of the integrated quasi-optical receiver.

are phonon-cooled NbN HEBs integrated with planar twin-slot antennas. The PHEBs have been fabricated on silicon substrates. The IF amplifiers are 3-stage InP MMIC chips. These chips (denoted WBA-13) have been developed by Weinreb and Wadefalk [4] at JPL/Caltech. The MMICs require an input matching network for optimum noise performance. In our circuit, the matching network is a multi-stage microstip transformer. All the bias and IF circuitry is included in the same housing, resulting in a very compact design. Relevant details on the construction of these receivers can be found in [5].

B. Measurement Setup

The main objective of the measurements described here is to show how the performance of these integrated receivers has been improved in comparison with previously presented results. The two parameters of interest for this analysis are the double-sideband noise temperature , T_{sys}, and the receiver bandwidth.

We measured T_{sys} as a function of IF frequency, using the standard Y-factor method. We have a broadband IF back-end that allows us to perform noise measurements over a very wide frequency range. The LO source was a CO_2-pumped far infrared (FIR) laser system. We used a 6 μm thick mylar beam splitter as the diplexer between the LO and the signal beam. The measurements were performed using a 1.63 THz laser line, which runs on difluoromethane gas.

III. Measurement Results

A. Noise Performance

Fig. 4 shows the noise performance of a test HEB device measured at 1.6 THz using two different configurations. The solid line represents the prediction for the simple receiver configuration (Fig. 1) obtained using the standard model. In the first measurement the standard receiver configuration was used with no isolator in the IF chain. This curve presents two sharp peaks at 3.25 GHz and 6.5 GHz, respectively. Calculations showed that the location of the peaks was associated with the length (approximately 15 cms) of the stainless steel coax cable that connected the MMIC LNA module with the HEB mixer block. The presence of these peaks is not unexpected and

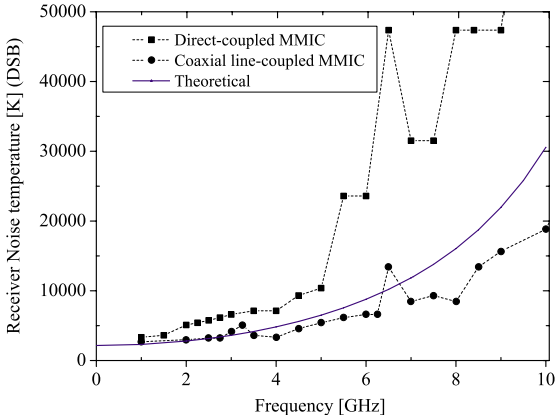

Fig. 4. Comparison between performance of the different receiver configurations. The response of the integrated configuration is before optimization.

is consistent with similar measurements performed by other groups [6]. The second measurement was completed using the integrated receiver configuration (Fig. 2) with the MMIC and the HEB located in the same plane. The difference between the two measurements at the low IF frequencies is mostly due to a slight degradation suffered in the critical current of the NbN film. This parameter changed about 10% between measurements. The differences in performance at the upper end of the band were first attributed exclusively to mismatch between the MMIC LNA and the HEB. However, impedance mismatch is only a partial justification. It was later found that the bias resistor for the first stage's gate of the MMIC (in the integrated configuration), exhibited poor performance beyond 5 GHz. This had a strong impact on the MMIC noise temperature. The abrupt increase in the noise for frequencies larger than the noise bandwidth was aggravated by the low self-resonant frequency (SRF) of other components in the IF circuitry, in particular the spiral inductor used for the HEB mixer bias-tee.

Fig. 5 shows the measured noise response of five different detectors, all measured at 1.6 THz. The noise temperatures are clearly different for each detector. Since the HEB specimens were all fabricated from different film, these differences are not unexpected. What is more important in this set of measurements is the difference in the smoothness of noise

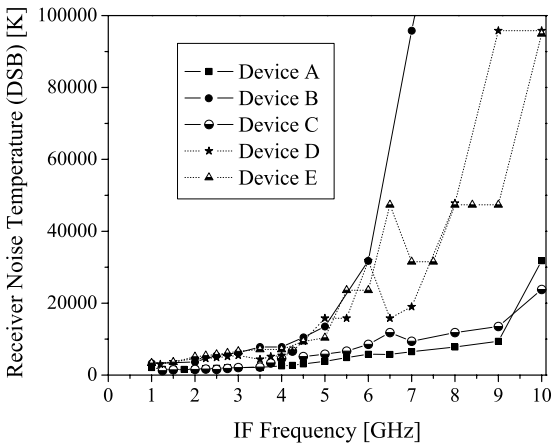

Fig. 5. Measured performance of different devices using the integrated configuration.

performance. The dotted lines (devices D and E) indicate the use of IF circuitry with poor performance. Devices A, B, and C show the improved performance of the integrated configuration after optimization. From these results, we may conclude that the microwave properties of the components used in the IF circuitry plays a very important role in the performance of the integrated receiver.

B. Receiver Bandwidth

An important figure of merit used to describe quantitatively the bandwidth performance of any HEB receiver, is the the noise bandwidth, N_B. This parameter is defined as the frequency at which the noise temperature doubles with respect to the zero IF value. N_B can be obtained by inspection from the experimental noise data. A different figure of merit is introduced in this paper for the same purpose, the effective bandwidth, B_{eff}. This parameter can be obtained by integrating the expression for the inverse of ΔT^2_{rms} in the well-known radiometer equation,

$$\frac{1}{\Delta T^2_{rms}} = \int_{f_o}^{\infty} \frac{1}{T^2_{sys}(f)}\, df \cdot \tau = \frac{B_{eff} \cdot \tau}{T^2_{sys}(f = f_o)} \qquad (1)$$

$$B_{eff} = T^2_{sys}(f = f_o) \cdot \int_{f_o}^{\infty} \frac{1}{T^2_{sys}(f)}\, df \qquad (2)$$

where τ is the integration time, f_o is the lowest frequency of operation of the MMIC IF amplifier (close to 0.5 GHz for the WBA-13), and $T_{sys}(f)$ is obtained by fitting the measured noise temperature response to a polynomial in f.

Table I presents a summary of important results obtained for the five devices measured in the integrated mixer block. The widest effective bandwidth obtained corresponds to 5 GHz for device A, which also had a very competitive noise temperature. The best trade-off between sufficiently low noise and wide bandwidth will be achieved when the interaction between the LNA and the HEB is better understood and modeled.

TABLE I

NOISE AND BANDWIDTH PERFORMANCE OF DIFFERENT DEVICES TESTED USING THE INTEGRATED HEB/MMIC CONFIGURATION.

Device #	NT (at 1 GHz)	N_B GHz	B_{eff} GHz
A	1600 K	4.5	5.0
B	3200 K	3.5	3.0
C	1200 K	3.4	2.9
D	3000 K	4.2	3.8
E	3500 K	3.0	2.2

IV. FURTHER INTEGRATED RECEIVER IMPROVEMENTS

A. Matching Network Design

It has been mentioned that the MMIC LNA used in our receivers requires an external input matching network (IMN) for best noise performance. In particular, this IMN should be designed to provide a conjugate match over the bandwidth of interest. Since the input impedance of the LNA is mainly dominated by the gate-to-source capacitive reactance of the first HEMT transistor, the IMN should behave as a series inductor. It is thus reasonable to think of substituting the microstrip transformer by a lumped-element matching network in order to further reduce the size of the prototype. The difficulty that arises from this approach is finding (or making) chip inductors that can cover the entire frequency range of interest. Large inductors typically have low SRF, while small inductors do not present enough reactance at low frequencies. A set of circuit simulations has been performed using models for the best inductors available in the market [7], [8]. Thus far, this analysis appears to indicate that the incorporation of such inductors in the LNA circuitry has a negative impact on the performance of the MMIC, causing the noise temperature to rise rapidly with frequency. Concurrently, Wadefalk has performed microwave measurements on these inductors [9], finding that the models provided by the manufacturers correspond to a best case approximation. The measured performance appears to be below the manufacturer's specifications. The satisfactory performance of the inductors used for matching purposes is more critical than that of the RF-choke in the mixer bias-tee. Substituting the IMN with a circuit based on these inductors would therefore produce a serious deterioration in the overall receiver performance. We are currently investigating other design possibilities to overcome the lack of commercially available broadband inductors.

In the first place, if one can make the IF impedance of the HEB high enough (100-200 Ω) at the operating point, our simulations indicate that the requirements for the external IMN become relaxed. Accurate measurements need to be performed in order to determine exactly how the HEB impedance of an actual receiver mixer can be made high enough. Another possibility is to use wire-bonds as inductive elements, as is often done in microwave and mm-wave circuit design. Fig. 6 shows the simulated performance of the WBA-13 LNA for different input matching conditions. The solid curve represents the original response, using the microstrip matching transformer. The dotted line was obtained by using a 800 μm long wire-bond

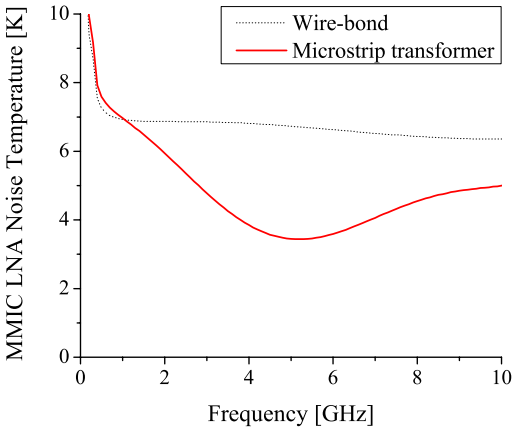

Fig. 6. Simulated noise performance of the LNA using bond wires as inductive elements for input conjugate match. The solid line indicates the original response using the microstrip transformer.

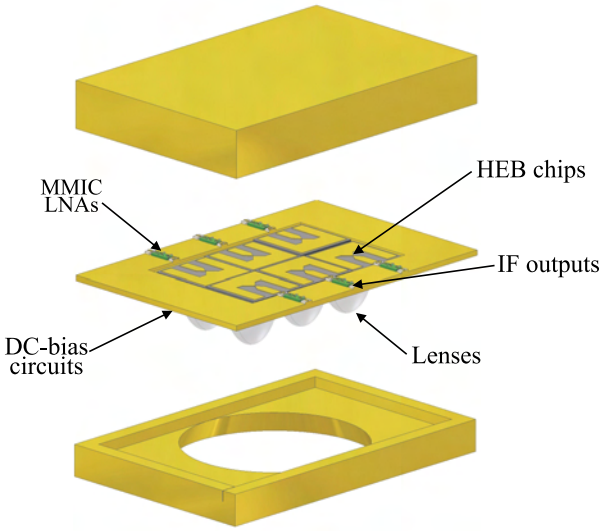

Fig. 7. Prototype 3x2 HEB focal plane array.

(25 μm diameter) as a series inductor for the input, in place of the microstrip circuit. Although the noise temperature obtained in the second case is higher, it is still low enough to not affect the performance of the integrated receiver in a significant way. An extra increase in the LNA noise temperature is expected after the effect of the integrated mixed bias-tee is accounted for in the simulation. This increase, however, is roughly 1K throughout the band. This holds provided that the resistors used in the 4-wire HEB biasing scheme present a high SRF. High quality microwave resistors are readily available from a variety of vendors, so this does not represent a major pitfall. Further measurements will demonstrate the adequateness of this approach. The preliminary simulation results obtained for this part are certainly promising.

B. New Prototype FPA

After finding the most appropriate substitute for the microstrip transformer, a new focal plane array prototype will be constructed. The concept of this 3x2 element FPA is illustrated in Fig. 7. This array will be useful to test the functionality of a number of new design features and can be easily extended to a larger number of elements. The DC-bias circuitry is on the opposite side from the MMICs. The connections between the two sides are made with glass beads. One side of the bead is soldered to the printed circuit board underneath the chips, while the other side is wire-bonded to the gate and drain pads of the MMICs. The HEB device is biased on a similar fashion. This technique has been sucessful in producing multichip modules with up to 20 MMICs [9]. We will continue to use 4-mm diameter elliptical lenses. The spacing between radiating elements will be set to the minimum possible, which has been found to be close to the diameter of the lens [1]. This FPA will be optimized for near-range scanning applications, relevant to security and and medical imaging.

V. Frequency Multiplexing

Another important concern in the design of FPAs comes to play as we desire to increase the number of elements in the array. A primary difficulty resides in how to multiplex the IF outputs for individual pixels. Having one coaxial line per active element becomes impractical in a large multiple receiver system. We are developing a frequency division multiplexing scheme in which each detector's output, IF_n, is mixed with a microwave signal F_{LOn} (Fig. 8). The microwave LO signals can be produced by means of inexpensive voltage controlled oscillators (VCOs) operating at room temperature. These signals are combined and injected into the cryostat through a single coax line. The F_{LO} signals are then separated inside the dewar by using a filter bank and connected to their corresponding mixer. The mixing of the FPA IF outputs is performed in order to assign a narrow bandwidth channel to each detector. Each channel is centered at a different frequency in order to make a distinction between different elements. All the mixer outputs are fed to a power combining network, and further amplified by a broadband MMIC amplifier. A single coaxial line is required for the signal containing all the FPA outputs. Individual pixel IF outputs can be recovered outside the cryostat by means of filtering.

This scheme is advantageous over other alternatives, specially since the multiplexer is not required to operate at 4K. The mixers can be based on inexpensive Schottky diodes and fabricated on a special purpose MMIC. This would make the entire multiplexer compact, based in a multi-chip module configuration. Future developments are expected to further increase the bandwidth of the MMIC amplifiers, which will make the multiplexing scheme even more effective.

VI. Conclusion

An extensive set of measurements has been performed on the integrated HEB-MMIC receiver configuration we have developed. A significant improvement in the receiver bandwidth has been achieved compared to the results presented in last year's symposium. Effective receiver bandwidths up

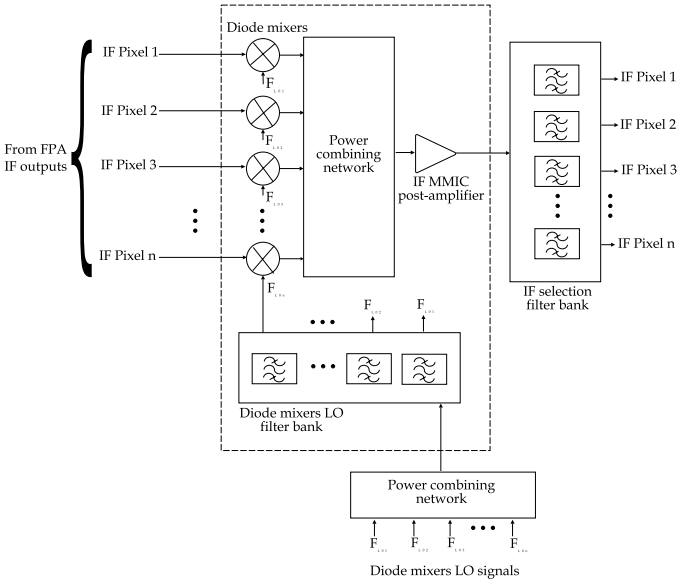

Fig. 8. Block diagram of the proposed frequency multiplexing scheme.

to 5 GHz can now be achieved using this configuration. The integrated quasi-optical detectors provide an important advantage for multi-pixel focal plane arrays. The incorporation of a different input matching scheme for the MMIC LNA is being investigated. This change will result in the further miniaturization of the receivers. A new 3x2 element FPA has been proposed. This system will incorporate the new matching mechanism and a variety of other features. The proposed array will be used for THz imaging and can be easily extended to a larger size array.

A frequency multiplexing scheme has been proposed to reduce the number of IF lines required for an array with a large number of quasi-optical detectors.

ACKNOWLEDGMENT

We would like to thank Dr. Sander Weinreb for supplying the MMIC chips. Mr. Pourya Khosropanah is gratefully acknowledged for fabricating some of the devices measured in this paper.

REFERENCES

[1] F. Rodriguez-Morales, K. S. Yngvesson, E. Gerecht, N. Wadefalk, J. Nicholson, D. Gu, X. Zhao, T. Goyette, and J. Waldman, “A Terahertz Focal Plane Array Using HEB Superconducting Mixers and MMIC IF Amplifiers,” *IEEE Microw. Wireless Comp. Lett.*, vol. 15, no. 4, pp. 199–201, Apr. 2005.

[2] R. Zannoni, S. Yngvesson, F. Rodriguez-Morales, J. Nicholson, D. Gu, and E. Gerecht, “A Prototype Terrestrial Terahertz Imaging System.” in *This symposium*.

[3] E. Gerecht, D. Gu, S. Yngvesson, F. Rodriguez-Morales, R. Zannoni, and J. Nicholson, “HEB Heterodyne Focal Plane Arrays: A Terahertz Technology for High Sensitivity Near-range Security Imaging Systems,” in *SPIE Defense and Security Symposium*, March 2005–April 2005.

[4] D. DeBoer and D.-J. Bock, “The Allen Telescope Array: Splitting the Aperture,” *IEEE Microw. Mag.*, vol. 5, no. 2, pp. 46–53, Jun. 2004.

[5] F. Rodriguez-Morales, S. Yngvesson, E. Gerecht, N. Wadefalk, J. Nicholson, D. Gu, X. Zhao, T. Goyette, and J. Waldman, “A prototype focal plane array with HEB mixer elements and MMIC IF amplifiers.” in *Proc. 15th Int. Symp. Space Terahertz Tech., Northampton, MA*, Apr. 2004.

[6] T. Berg, S. Cherednichenko, H. Merkel, E. Kollberg, and J. Kooi, “IF Impedance Optimization of HEB’s for Band 6 at the Herschel Space Observatory.” in *This symposium*.

[7] “US Microwaves Inc.” http://www.usmicrowaves.com/.

[8] “Piconics Inc.” http://www.piconics.com/.

[9] N. Wadefalk, Private communication.

Aging Investigation of NbN Hot Electron Bolometer Mixers

Pourya Khosropanah, Vladimir Drakinskiy, Sergey Cherednichenko, Therese Berg

Department of Microtechnology and Nanoscience (MC2)
Microwave Electronics Laboratory
CHALMERS UNIVERSITY OF TECHNOLOGY
412 96 Gothenburg, Sweden
Email: pourya.khosropanah@mc2.chalmers.se

***Abstract*— This work presents an aging investigation of NbN HEB mixers in usual lab conditions and also in high temperature and high relative humidity environment. A variety of devices have been fabricated using different combinations of resist (SAL), Si, SiO_2 and SiN single and multi-layer for bolometer protection. In the accelerated aging tests the degradation is monitored by measuring the DC resistance of the devices during the test. The results show that using multi-layer protection increases the device lifetime significantly.**

I. Introduction

NbN HEB mixers are to be used for band 6 low (1.410-1.700 THz) and band 6 high (1.700-1.920 THz) of the HIFI instrument (Heterodyne Instrument for Far-Infrared) [1] on the Herschel Space Observatory [2] due to launch 2007. This will be the first time that HEB mixers are used on a space mission. The double side band receiver noise temperature using these mixers are below 1000 K with 5-6 GHz IF bandwidth and they require less than 500 nW of local oscillator power [3].

Since the assembling of the flight mixer units is now in progress, they will be stored for about two years before the launch. This raises questions concerning the degradation of the mixer chips during this period. This work presents our attempts to estimate the HEB lifetime with different protection layers by comparing the accelerated aging test results in high temperature and high relative humidity with the available data concerning degradation of the devices in usual lab conditions. An independent similar investigation is presented in [4]. Here, a variety of devices have been fabricated using different combinations of Si, SiO_2, SiN and resist multi-layers for bolometer protection. Some of these devices are stored in ordinary lab environment and their resistance and the critical current have been measured regularly, in some cases for a period of two years. In the accelerated aging tests the resistance of devices are monitored while exposed to high temperature and high relative humidity. The increase of resistance and decrease of critical current are the measures of device degradation.

II. Device Fabrication

The device fabrication is done by several consecutive electron beam lithography steps followed by metallization and lift off, where small contact pads, antenna and the large contact pads are patterned. 5 nm Ti followed by 80 nm of Au is deposited for small contact pads. The antenna and large pads are made from 5 nm of Ti and 200 nm Au. Then a protection layer is defined over the bolometer bridge by one more lithography step. This is to protect the NbN film in the bolometer bridge during the ion milling. In the last step the NbN is etched away using Ar ion milling from the whole wafer except from the bolometer bridge and under the antenna and pads. Figure 1 shows the SEM picture of a bolometer integrated with double slot antenna for 1.6 THz. A variety of devices have been fabricated using different combinations of Si, SiO_2, SiN and resist (SAL) multi-layer for bolometer protection. The shapes and the thicknesses of these layers are illustrated in figures 2 and 3. The resist (SAL) is a negative resist and the protection layer is defined by the e-beam writing. The Si and SiN layers are made by magnetron sputtering and the SiO_2 layer is deposited using e-beam evaporation. In both cases the bolometer protections are formed using lift off technique. The first protection layers is in rectangular shape and covers the bolometer bridge together with parts of the small contact pads. The second and the third protection layers are in circles which cover the whole center part of the device.

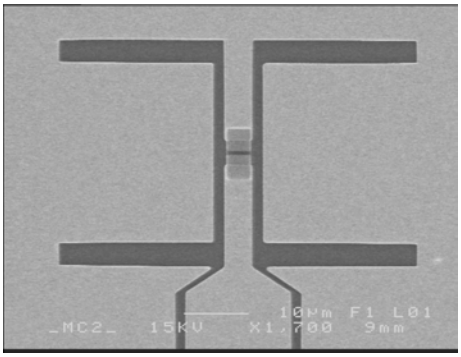

Fig. 1. HEB integrated with double slot antenna for 1.6 THz

III. Device Degradation in Lab Condition

The HEB devices degrade by time. The degradation appears as increase of resistance and decrease of critical current.

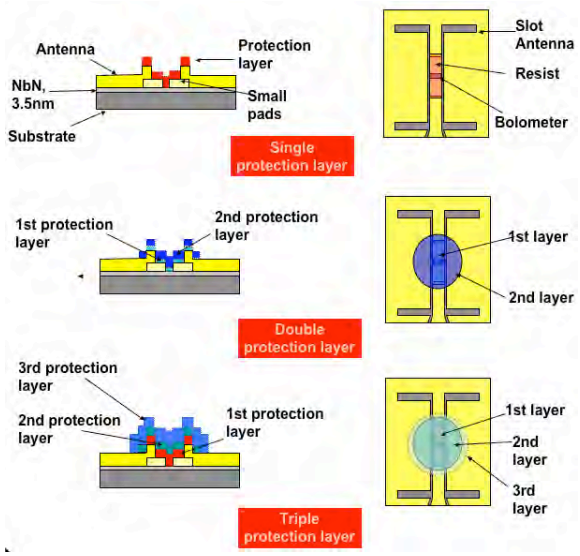

Fig. 2. Protection layers over the bolometer bridge

A number of devices have been stored under ordinary lab conditions in air (around 20°C and 30% RH). The resistance and critical current of these devices have been measured periodically which is summarized in table I.

Although these data show the tendency for the Si+Si double layer protection to be more resistant against aging, the result is not yet conclusive and the accelerated aging tests seems necessary.

IV. Receiver Noise Temperature and Mixer Degradation

In order to see the degradation effect on the mixer performance, receiver noise temperature have been measured two times using the same mixer chip. The mixer was fabricated in February 2004 and kept in desiccator until April 2004 when it was mounted in the HIFI mixer unit and measured for the first time. Then it was stored on the shelf at about 20°C and 30% RH until August 2004, when the second test was performed. During this time the device resistance increased by 5% and the

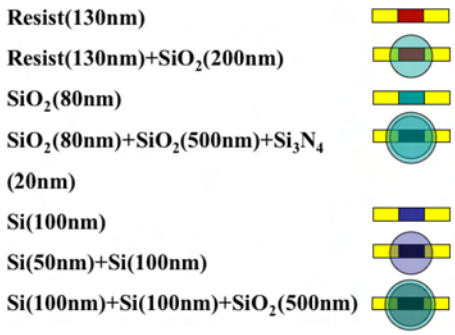

Fig. 3. Variety of HEB protection layers and their thicknesses

TABLE I
HEB degradation in room temperature and 30% RH

Protection	Time (Month)	dR/R (%)	dI/I (%)
SAL	12	20	30-50
SAL	16	30	50
SAL	24	50	60-70
SAL+SiO_2	7	3-13	5-12
SiO_2	7	15	8
Si+Si	6	2-5	6-9

measured critical current decreased by 10%. Figure 4 shows the double side band receiver noise temperature in these two occasions together with the HIFI specification limit. As we see, the mixer performance was not much affected by this level of degradation and the receiver noise temperature is within acceptable limit. The device used in this test has a resist (SAL) protection layer for the bolometer.

V. Vacuum Baking Test

141 hours of vacuum baking was done with 3 devices with resist (SAL) protection. The pressure of 10^{-4} mbar was achieved with 2 hours of pre-pumping and temperature was kept constant at 90°C on the hotplate where devices were placed. As it is shown in table II, the resistance and the critical current of these devices did not changed significantly during the test, which means that the heating effect on device degradation in the absence of air is negligible and not affected by temperature.

VI. Accelerated Aging Test at 85°C-85% RH

Several devices with a variety of bolometer protection layers were kept in 85°C-85% RH for over 100 hours. The resistance of these devices was monitored during this time. Figure 5 summarizes the result of these tests. The devices with resist (SAL) protection have the shortest lifetime. Although

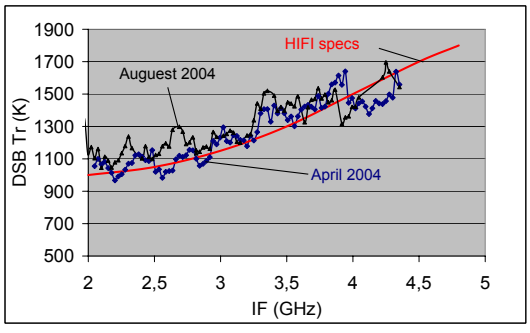

Fig. 4. DSB receiver noise temperature measured twice with about 5 month time difference using the same HEB chip stored in about 20°C and 30% RH during this time.

TABLE II
VACUUM BAKING TEST AT 90°C FOR 141 HOURS

Device ID	R (Ω) before	R (Ω) after	I_C (μA) before	I_C (μA) after
A	87	85	134	132
B	95	93	140	137
C	93	92.5	130	118

there is a diversity in their performance, they all severely degrade within first 10 hours and before all the other type of devices. Adding an extra layer of SiO_2 improves the life time significantly. There is a clear difference in lifetime when the SAL protection is replaced by Si or SiO_2. However, the major improvement occurs when double layer Si+Si or triple layer SiO_2+SiO_2+SiN is used which increase the lifetime of HEB by almost an order of magnitude.

A number of devices were periodically exposed to 10 hour of 20°C-20% RH following by 10 hours of 85°C-85% RH for about 120 hours of total time. As is shown in figure 6, the devices with SAL protection were degraded faster than the devices with Si+Si double protection layer. We can also see that the degradation stops (constant resistance) during 20°C-20% RH and starts again when at 85°C-85% RH.

VII. ACCELERATED AGING TEST AT 65°C-85% RH

In order to see the temperature effect on the degradation of HEB, a number of devices with SAL and Si+Si protection were exposed to 65°C-85% RH for over 100 hours. As is shown in figure 7, the devices with SAL protection were affected much faster that the devices with Si+Si double protection layer. Comparing this result with the outcome of the 85°C-85% RH (figure 5), one can see that the degradation in 65°C happens considerably slower than in 85°C.

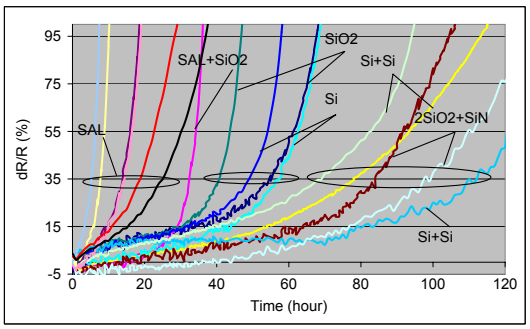

Fig. 5. Accelerated aging test at 85°C-85% RH

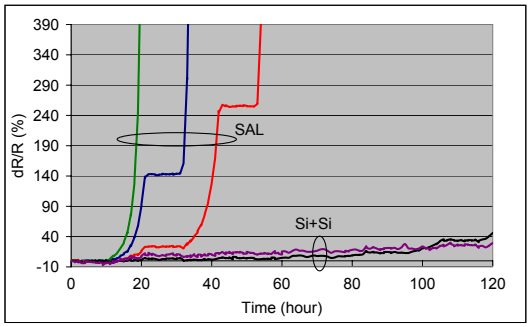

Fig. 6. Periodical aging test: 10 hour of 20°C-20% RH following by 10 hours of 85°C-85% RH repeated for about 120 hours.

VIII. ACCELERATED AGING TEST AT 50°C-85% RH

Only devices with resist (SAL) protection were used in a 50°C-85% RH aging test. The reason was that they were expected to have shorter lifetime and therefore more practical to test at lower temperature. Using other devices with double or triple layer protection in this test requires very long testing time which is cumbersome. As is shown in figure 8, the devices are degraded in a much slower pace compared with degradation at 65°C and 85°C. The diversity of degradation rate in here is similar to what we see in figure 5 for SAL devices.

IX. DISCUSSIONS AND CONCLUSION

The 130 nm thick resist (SAL) used traditionally as top layer does not provide good protection against aging. Adding a 200 nm layer of SiO_2 on top of the SAL provides a somewhat better protection layer. Replacing the SAL by Si or SiO_2 increases the HEB lifetime dramatically. Our measured results show that Si-Si double layer or SiO_2-SiO_2-SiN triple layer

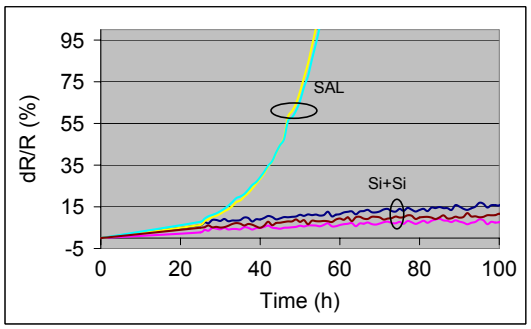

Fig. 7. Accelerated aging test at 65°C-85% RH

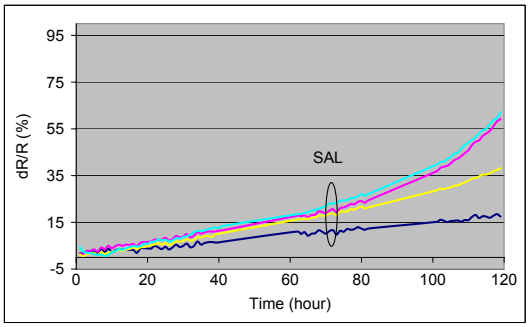

Fig. 8. Accelerated aging test at 50°C-85% RH

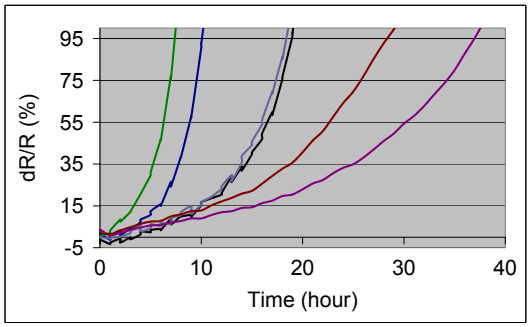

Fig. 9. Spread of data for accelerated aging test at 85°C-85% RH for devices with SAL protection

provides the best protection layer compared with the others mentioned above.

Baking test (90°C in vacuum) did not show any degradation of devices. This means that the main cause of degradation is the humidity and the process is accelerated at higher temperature.

There is a spread of data for the lifetime of similar devices. As it is shown in figures 9 not all devices with SAL protection behave exactly the same. It is also observed that 1 out of 9 tested devices with Si+Si protection and very similar characteristics surprisingly had a short lifetime (see figure 10). This means that although statistically there is a clear advantage in using multi-protection layers, we cannot assure that every single device of this type will have a long lifetime. Therefore, it is necessary to develop a method to select the flight mixers in a way to be sure about their lifetime.

Comparing the resistance of devices under 85°C-85% RH test with the similar devices degraded in usual lab condition, one can estimate that every hour of accelerated aging test corresponds to about 1 to 1.5 month of shelf time storage. Based on this result for devices with double or triple protection layers, it takes well above 2 years time until the degradation affects the mixer performance. This means that there is no problem with the aging of HEBs during the assembling time of the Herschel Space Observatory.

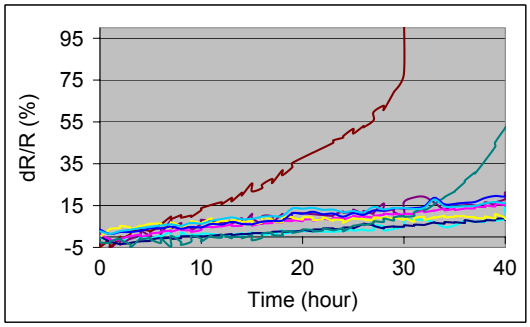

Fig. 10. Accelerated aging test at 85°C-85% RH for devices with Si+Si protection. 1 out of 9 had a short lifetime.

ACKNOWLEDGMENT

The authors would like to thank Saab Ericsson Space and specially Ulf Storm for our fruitful collaboration.

REFERENCES

[1] Th. de Graauw and F.P. Helmich. Herschel-hifi: "the heterodyne instrument for the far-infrared". In *proceedings of Symposium "The Promise of the Herschel Space Observatory", Toledo, Spain*, December 2000.

[2] G.L. Pilbratt, J. Cernicharo, A.M. Heras, T. Prusti, and R. Harris. The Herschel mission, scientific objectives. In *proceedings of Symposium "The Promise of the Herschel Space Observatory", Toledo, Spain*, pages 13–20, December 2000.

[3] S. Cherednichenko, P. Khosropanah, A. Adam, H. Merkel, E. Kollberg, D. Loudkov, G. Golt'sman, B. Voronov, H. Richter, and H.-W. Hübers. 1.4-1.7 THz NbN hot-electron bolometer mixer for the Herschel Space Observatory. In *Proceedings of SPIE, Millimeter and submillimeter detectors for astronomy*, pages 361–370, 2002.

[4] M. Hajenius, Z.Q. Yang, J.J.A. Baselman, J.R. Gao, B. Voronov, and G Gol'tsman. Towards space qualified NbN hot electron bolometer mixers. In *This proceedings: proceedings of 16th International Symposium on Space Terahertz Technology*, 2005.

Development of Phonon-Cooled NbTiN HEB Heterodyne Mixers for GREAT

S. Bedorf, P. Muñoz, T. Tils, C. E. Honingh and K. Jacobs

***Abstract*— The current development status of Niobium-Titanium Nitride (NbTiN) HEB mixers, for example for the GREAT receiver on SOFIA, is presented for both waveguide and quasi-optical mixers for 0.8, 1.9 and 2.7 THz LO frequency. For the waveguide mixers at 0.8 and 1.9 THz the HEBs are made on 2μm thick silicon nitride membranes which are suspended in a substrate channel perpendicular to the waveguide.**

For the quasi-optical mixer at 2.7 THz the devices are fabricated on Si-substrates and are integrated into spiral- and double-slot antennas and used with an extended hemispherical silicon lens. Our measurements show that the waveguide/membrane mixers work well at both 800 GHz and 1.9 THz.

To increase the required IF bandwidth we are developing thin NbN films. The first results of the NbN thin film development are presented in the paper.

I. Introduction

CURRENTLY, state-of-the-art phonon-cooled HEBs are usually made of Niobium Nitride (NbN) thin films, but results at 800 GHz [1] and above 1 THz [2] have shown that Niobium Titanium Nitride (NbTiN) can be used as well. The physical and chemical properties of NbTiN and NbN thin films are closely related and quite similar. Recently it was shown experimentally that the response of a phonon-cooled HEB depends strongly on the nature of the contact from the active superconductor to the Au-leads. By cleaning this interface and by inserting a thin superconducting layer, an increase in IF bandwidth and a reduced level of LO power was observed in [3].

We have investigated the influence of different clean processes and contact pad materials on the DC characteristics of NbTiN HEBs. Also, we present RF measurements of devices which have been fabricated using this approach.

Two types of mixer designs are presented in this work, a quasi-optical mixer based on an extended hemispherical silicon lens integrated with a logarithmic spiral antenna and a waveguide mixer based on 2 μm thick silicon nitride membranes which are suspended in a substrate channel.

II. Device Fabrication

Both kinds of mixers are based on 4-5 nm thin NbTiN films which are deposited on high resistivity silicon substrates for the quasi-optical design and a Si_3N_4 membranes for the waveguide design by DC reactive magnetron sputtering using a $Nb_{78\%}Ti_{22\%}$ alloy sputtering-target in a mixture of Ar and N_2.

S. Bedorf, P. Muñoz, T. Tils, C. E. Honingh and K. Jacobs are with KOSMA, I. Physikalisches Institut, Universität zu Köln, Zülpicher Str. 77, 50937 Köln, email: bedorf@ph1.uni-koeln.de

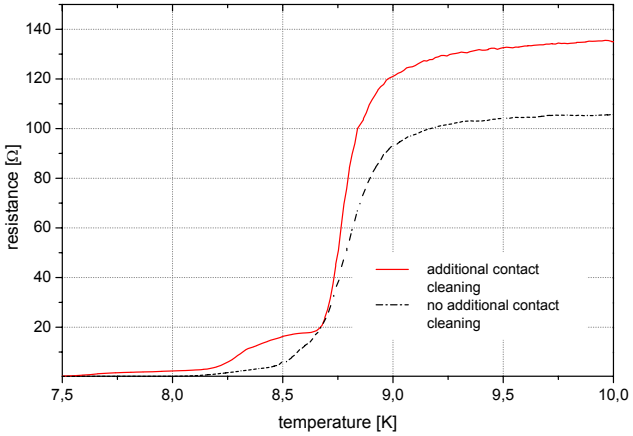

Fig. 1. Resistance versus temperature curves of two devices with and without additional cleaning of the interface area.

The substrate is heated to 600°C during deposition. The deposition process is optimized to yield a critical temperature T_c of 8-8.5 K for 4-5 nm films. The film has a normal-state resistance of approximately 300 Ω per square. The active area of the HEB is defined by electron beam lithography to form a microbridge about 0.4 μm long and 2 μm wide.

The nature of the contacts determines the interface transparency between the bolometer and the contact structure. Cleaning the interface leads to a better control over the interface.

The cleaning process consists of an oxygen plasma etching step, followed by an argon physical plasma etching step. To restore the superconducting film properties that might be affected by the cleaning process, a NbTiN layer (10 nm) is deposited on top of the contact area. The result is shown in the resistance versus temperature (RT) curve in Figure 1.

Two different superconducting transitions are observed, one due to the NbTiN bridge itself and the lower transition due to the interface between the pads and the NbTiN bridge. [4]. The parts of the bridge close to the contact pads show a reduction of the critical temperature T_c associated with a superconducting proximity effect, which is influenced by the interface transparency. Devices with additional cleaning show a larger resistance at the lower transition. A higher value of the resistance at the lower transition is caused by a larger proximity effect and therefore indicates a better interface transparency. A better interface transparency gives less RF losses and could improve the HEB sensitivity and LO requirement. This is indeed observed for NbN HEB devices.

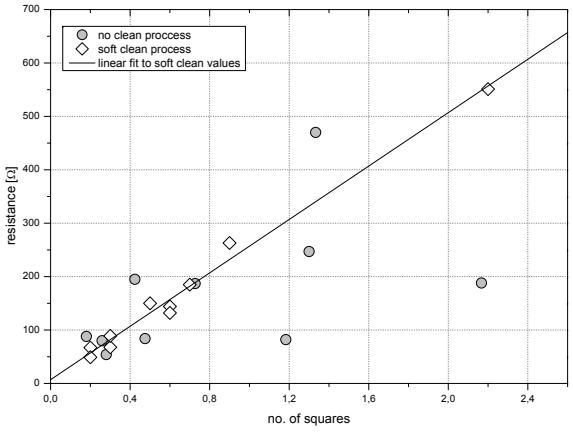

Fig. 2. Resistance versus nominal bridge dimension (in number of squares) for devices with and without additional cleaning

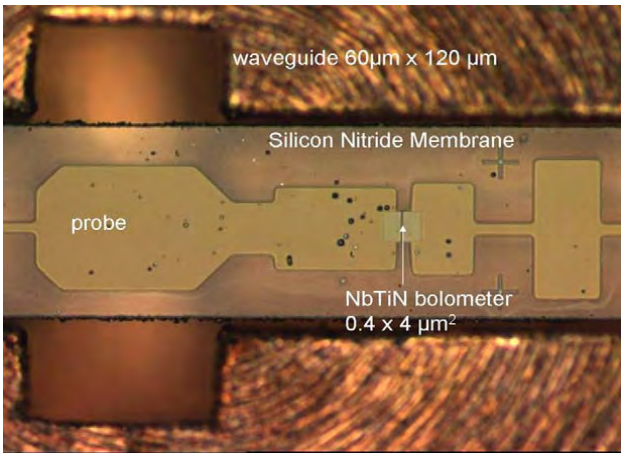

Fig. 3. 1.9 THz bolometer mixer with 0.4 x 4 μm NbTiN HEB device. The horn antenna is removed and the device metallization is seen through the backside of the transparent 2 μ SiN membrane

HEB devices with different lengths have been fabricated to investigate more precisely the influence of cleaning the interface. Figure 2 shows the nominal bridge dimension in number of squares versus the resistance for HEB devices with and without additional cleaning. The dashed line is a linear fit to the resistance values for the devices with additional cleaning. Devices with additional cleaning show very little deviation from the linear behavior, while devices without additional cleaning show a significant deviation from the linear scaling which is attributed to an uncontrolled contact resistance. The contact resistance for HEB devices with additional cleaning is 7 Ω, indicated by the y-axis intercept of the linear fit. Devices with an additional cleaning of the interface show a much better reproducibility in the values of the normal state resistance.

III. RF Measurements

All devices used for the RF measurements are devices with an additional cleaning of the interface as described above. For the waveguide mixer, the membrane with the HEB is flip-chip bonded to a silicon frame. This frame is subsequently mounted in a standard fixed tuned waveguide mixer block. Figure 3 shows the inner part of the waveguide 1.9 THz HEB mixer.

For the quasi-optical mixer the substrate with the HEB device is clamped onto the flat side of an extended hemispherical silicon lens.

The noise performance of the mixers was measured at 800 GHz. The uncorrected receiver noise T_{rec} as a function of the intermediate frequency (IF) is measured using the standard Y-factor method. The local oscillator (LO) source for 800 GHz is a solid state LO with an output power of max. 30 μW. The signal and the LO radiation are superimposed by a 50 μm Mylar beamsplitter (44% reflection) for the quasi-optical mixer and 13 μm (8.8% reflection) Mylar beamsplitter for the waveguide mixer.

The lowest measured DSB receiver noise-temperature is T_{rec} = 650 K for waveguide mixer. The quasi-optical mixer shows a higher receiver noise temperature of T_{rec} = 3000 K at 800 GHz. Figure 4 shows the measured receiver noise

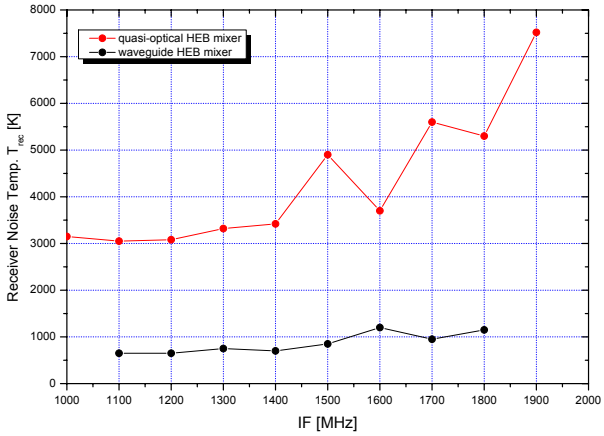

Fig. 4. Noise temperature versus IF at 800 GHz for waveguide and quasi-optical NbTiN HEB mixer

temperature at 800 GHz LO frequency versus IF frequency for both mixer types. The device size of HEB used for the quasi-optical is 2.8 x 0.5 μm and 4.5 x 0.35 μm for the waveguide mixer. The noise bandwidth is found to be approximately 1.5 GHz for both mixers. As the devices are very similar, the reason for the decreased sensitivity is a yet unknown coupling loss.

We have used a Fourier Transform Spectrometer (FTS) to measure the spectral response of the 1.9 THz waveguide mixer. In figure 5 the FTS measurement is shown and compared to simulated data. The simulation is done in CST Microwave Studio [5]. From the calculated impedance versus frequency the coupling factor is obtained by matching the impedance data to the normal state resistance of this specific device, in this case 34 Ω.

For the measurement the optical path is evacuated to approx. 1 mbar. The measured bandwidth is smaller than the predicted one. The drop of the coupling factor at 1.6 THz is probably a feature of the measurement setup. The simulated bandpass correspond fairly well to the measurement.

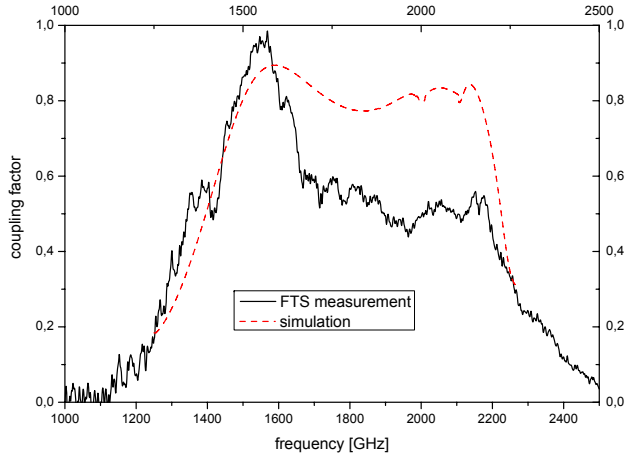

Fig. 5. Spectral response of the 1.9 THz waveguide HEB mixer measured by FTS in direct detection mode as function of frequency. The dashed line indicates the simulation.

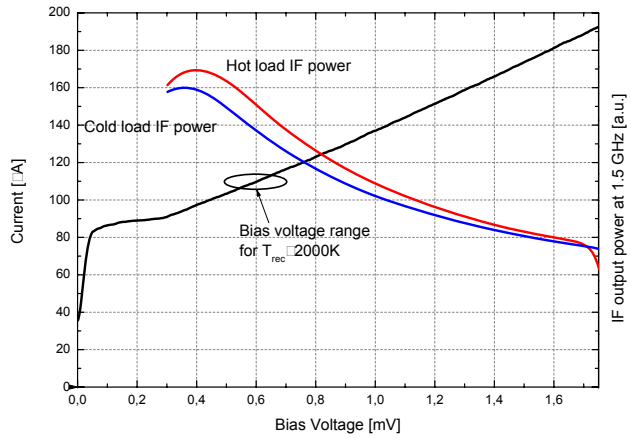

Fig. 6. Current-voltage (IV) curve of the 1.9 THz NbTiN waveguide HEB mixer with LO power at 1.75 THz. The HEB device size is 0.4 x 4 μm. Also shown is the IF output power in response to hot (295K) and cold (77K) loads placed at the receiver input.

First experiments of a 1.9 THz waveguide HEB mixer were performed at 1.75 THz using a FIR laser as LO source. The CO_2 laser is tuned on a 9P36 line and pumps the methanol line at 170.57 μm wavelength. The current-voltage (IV) characteristic of the 0.4 x 4 μm device with LO power at 1.75 THz is shown in Figure 6. Also shown in Figure 6 is the receiver output in response to hot and cold loads. The optimal sensitivity is achieved at a bias voltage of 0.5 - 0.7 mV and a bias current of roughly 110 μA. The uncorrected measured noise temperature at this bias point is about 2000 K. A beam splitter with 29% reflection loss was used which adds substantially to the mixer noise.

For the GREAT receiver the 1.9 THz waveguide mixer will be pumped using a BWO with a frequency tripler as LO. The estimated LO power of the BWO with the frequency tripler is max. 2.4 μW. A Martin-Puplett-Interferometer was used to superimpose the LO and the signal radiation. Figure 7 shows the current-voltage characteristics of the 1.9 THz waveguide HEB mixer with and without LO power. This is our first time to pump the 1.9 THz waveguide mixer using a BWO with a frequency tripler. Form Figure 7 we see that it is possible to pump the device almost to normal state resistance, demonstrating the possibility to use the BWO with frequency tripler as LO source for the GREAT receiver.

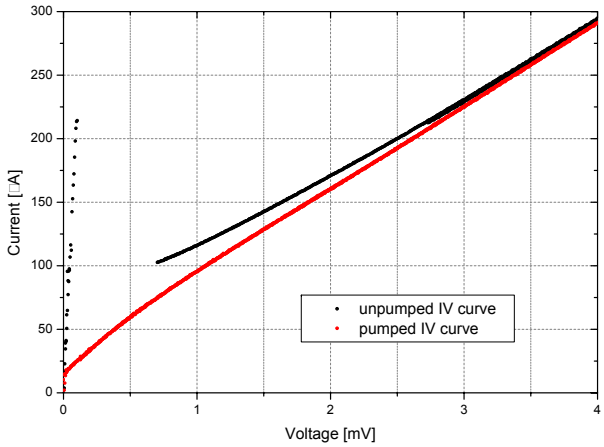

Fig. 7. The I-V curves of the 1.9 THz waveguide HEB mixer with and without LO power at 1.9 THz using a BWO with a frequency tripler.

IV. NbN HEB mixers

The NbTiN HEBs fabricated for GREAT show a rather limited noise bandwidth of about 1.5 GHz. The HEB devices fabricated on thin Si_3N_4 membranes do not show a different IF noise bandwidth than the devices fabricated on much thicker Si wafers. That indicates that the cooling mechanism to the substrate of the waveguide mixer is not the limiting factor for the IF bandwidth of these mixers. An experiment in collaboration with Delft University of Technology, Physics of NanoElectronics (R. Barends) indicated an intrinsically slower electron-phonon τ_{e-ph} interaction for NbTiN compared to NbN. Even though the actual IF bandwidth of the NbTiN HEB devices could only be measured with an appropriate IF system, the results of this work show that NbTiN is potentially inferior in bandwidth to NbN. To increase the IF bandwidth for the GREAT HEB mixers, 3-4 nm thin NbN films, fabricated at KOSMA, will be used for the next generation of our HEB mixers.

The thin NbN films are deposited onto 350 μm high resistivity Si substrates. The NbN films are deposited by DC magnetron sputtering in a Ar/N_2 atmosphere. For the thin films a low sputtering rate of 2-5 Å/s is desired. Therefore, a small constant current of 0.3 A is used.

Figure 8 shows the resistance versus temperature (RT) curves for 4 and 5 nm thin NbN films on high-resistivity Si. The 4 nm thin films which will be used for the HEB device fabrication have a critical temperature T_c = 8.7 K and a transition width of ΔT_c = 1.7 K. The surface resistance of the 4 nm thin films is about 800 Ω. The deposition rate is 2 Å per second.

To deposit 4 nm thin NbN films with these characteristics, substrate heating is essential. Substrate heating is achieved by

using a PBN/Pyrolytic (PG) resistance heating element with an operating temperature up to 1800°C.

The influence of heating the substrate during deposition on the superconducting properties of 5 nm thin NbN films is shown in Figure 9. Heating the substrate up to 600°C significantly increases the critical temperature T_c from 8.1 K at ambient temperature to 9.4 K. The transition width ΔT_c becomes slightly smaller.

In order to verify the uniformity of the critical temperature T_c across the wafer, a 30 x 30 mm wafer was cut into three 10 x 30 mm pieces after the deposition. The critical temperature was measured at distances of 5 mm across the wafer slice to get an indication of the large-scale critical temperature distribution across the wafer. Figure 10 shows the resistance versus temperature diagram of the 5 different position on the center part of a split wafer. The NbN film is about 4 nm thick. The identifiers A2-A6 and B6-B7 indicate contact positions on the wafer in 5 mm distance, respectively. Although the critical temperature T_c of the wafer is lower than the expected T_c for a 4 nm thin NbN film, figure 10 clearly shows that the critical temperature and the resistance ratio R_{300}/R_{20} remains constant, indicating that the film thickness is very uniform across the 10 x 30 mm wafer. The resistance in this diagram varies because the four-point probe distance was different for each measurement point.

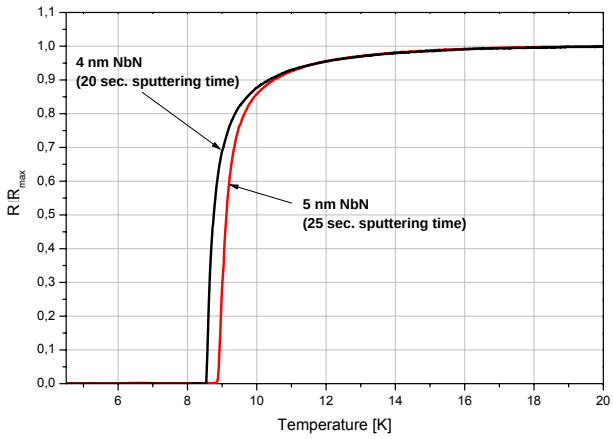

Fig. 8. Resistance versus temperature curves of 4 and 5 nm thin NbN films on high-resistivity Si.

V. Conclusion

We have demonstrated receiver noise temperature of 650 K and 3000 K at 800 GHz for waveguide on suspended Si_3N_4 membrane and quasi-optical mixers respectively. The IF noise bandwidth is 1.5 GHz for both mixers. The comparable IF-bandwidth for Si and Si_3N_4 substrates indicates that the present IF bandwidth is dominated by intrinsic NbTiN film parameters. The additional cleaning of the interface did not improve the noise temperature or the IF bandwidth compared to previous HEB batches fabricated without additional cleaning. Cleaning the interface area however shows a much better reproducibility of the normal state resistance.

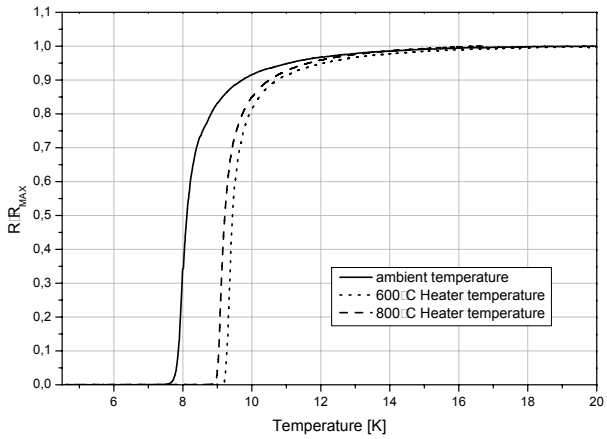

Fig. 9. R(T) curves for 5 nm ultrathin NbN films on Si-substrates for different temperatures during deposition.

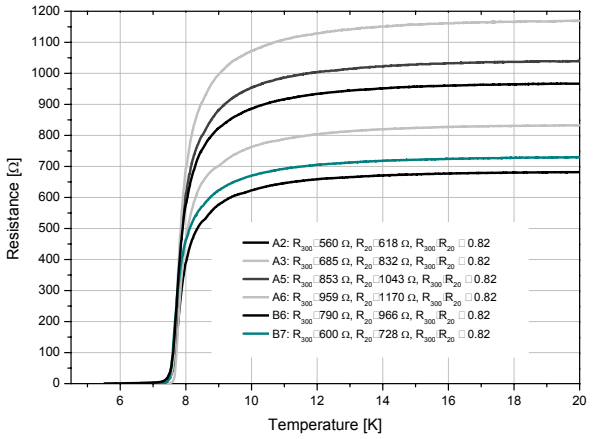

Fig. 10. Resistance versus temperature of a 4 nm thin NbN film measured across a 10 x 30 mm large wafer. The identifier A2-A6 and B6-B7 are contact positions on the wafer in 5 mm distance respectively.

The first heterodyne measurements of the 1.9 THz waveguide GREAT HEB receiver based on NbTiN showed an uncorrected receiver noise temperature of $T_{rec} \approx 2000$ K using a FIR laser as LO source. It is also possible to pump the 1.9 THz HEB mixer using a BWO with a frequency tripler. Receiver noise temperature measurements using the BWO will follow.

To increase the required IF bandwidth of the GREAT HEB mixers we are developing thin NbN films. The first results of 4 nm thin NbN films on high-resistivity Si show a critical temperature of T_c = 8.7 K and a sheet resistance of $R_\square \approx 800\ \Omega$. The large-scale critical temperature distribution is very uniform across the wafer. The next batch of our HEB devices will be fabricated based on 4 nm thin NbN on Si and Si_3N_4.

Acknowledgment

This development has been supported by the Deutsche Forschungsgemeinschaft (grant Sonderforschungsbereich SFB 494).

REFERENCES

[1] Tong C E, Stern J, Megerian K, LeDuc H, Sridharan T K, Gibson H, Blundell R, "A Low-noise NbTiN Hot Electron Bolometer Mixer", in *12th Intern. Symp. Space THz Technology*, 2001.

[2] Khosropanah P, Bedorf S, Cherednichenko S, Drakinskiy V, Jacobs K, Merkel H, Kollberg E, "Fabrication and Noise Measurements of NbTiN Hot Electron Bolometer Heterodyne Mixers at THz Frequencies", in *14th International Symposium on Space Terahertz Technology*, 2003.

[3] Baselmans J J A, Hajenius M, Gao J R, Klapwijk T, de Korte P A J, Voronov B, Gol'tsman G, "Doubling of sensitivity and bandwidth in phonon cooled hot electron bolometer mixers", *Appl. Phys. Lett.*, vol. 84, no. 11, 2004.

[4] Hajenius M, Baselmans J J A, Gao J R, Klapwijk T M, de Korte P A J, Voronov B, Gol'tsman, "Low noise NbN superconducting hot electron bolometer mixers at 1.9 and 2.5 THz", *Supercond. Sci. Technol.*, vol. 17, pp. 224–228, 2004.

[5] CST, "Computer Simulation Technology", *Microwave Studio 5.0*, http://www.cst.com.

FTS measurement of a 2.5 THz double-slot antenna on SiO_2/Si_3N_4 membrane

J. Baubert, P. Khosropanah,V. Desmaris, V. Drakinskiy, P. Pons, P. Calmon, H. Merkel, M. Salez

Abstract— **Membrane-based NbN HEB mixers are being developed for new type of receivers. Taking advantage of the quasi-optic design allowed by the membrane, those detectors are expected to show numerous advantages and permit to easily design and process double-slot antennas up to several THz. This work presents the FTS measurements made with a membrane-based double-slot antenna, designed at 2.5 THz, and using an NbN HEB mixer.**

As HEB mixers on SiO2/Si3N4 membranes are recent innovative devices, new technological challenges are faced, which limit the overall processing yield to about 30%. In order to improve the processing yield, we have developed a new processing procedure, which we present also in this paper. The results collected allow us to have high expectations.

***Index Terms*— heterodyne receiver, HEB mixer, stress-less membrane, coupling efficiency, low-cost space applications, quasi-optic array design.**

I. INTRODUCTION

Receivers for astronomical observation above 1 THz have been developed the last years, such as the ground-based radio telescope in the south pole TREND, the airborne-based observatory SOFIA or the space-based Herschel observatory All these observatories use NbN Hot Electron Bolometer on bulk Silicon chips [1, 2], since it has been demonstrated to be the best mixing element at above 1.4 THz, showing better noise performances than SIS [3, 5], an intermediate frequency about 4 GHz [6, 7] and LO power requirement around a few hundreds of mW [8].

Detection of submillimeter lines of OH and HD at 2.5 and 2.7 THz presents a high interest for radioastronomers [9]. Observations of the 112μm ground-state rotational transition of the deuterated hydrogen molecule, HD, with SOFIA will allow the derivation of the abundance profile of deuterium across the Galactic disk and nearby galaxies, thereby providing critical information on the star formation history of these systems. The fundamental OH doublet at 119 μm [10] is of special interest. The hydroxyl radical is one of the most important molecules in interstellar chemistry. It is vital for understanding the water chemistry, since it is both a precursor of water production and a product of water destruction.

At those very high frequencies, the fabrication of waveguides becomes very difficult. In recent years, the micromachining technology has been proposed for the fabrication of millimeter wave circuits on very thin dielectric membranes [11]. We chose then a quasi-optic design, with a HEB mounted on a freestanding SiO2/Si3N4 membrane, for plethora of reasons: it allows us to use a mirror instead of a silicon lens (and anti-reflection coating), decreasing the overall noise temperature, the structure of the antenna is enlarged and the processing at very high frequencies is made easier, a back-short can be added at $\lambda/4$ to double the antenna gain.... such a device on a membrane has been studied already in a few papers [12, 14].

Planar antennas are usually used to couple the RF power to the bolometer and it is mandatory to experimentally determine the RF bandwidth of those antennas. Fourier Transform Spectrometer is usually used for this type of investigation [15].

II. SIMULATIONS

On silicon wafers, the dimensions of the double-slot antenna are defined by scaling method [16]. The slot length L is usually taken equals to $0.3\lambda_0$, the distance between slots S equals to $0.17\lambda_0$ and the width of the slots W equals to $0.02\,\lambda_0$.

At 2.5 THz, λ_0 equals 120 μm, and the slot length L_1 should then be equal to 40 μm on Silicon. Since the membrane thickness 1.4 μm < $0.04\lambda_0$ (4.8 μm), no influence is expected from the membrane [17]. From equation 1, we find a factor of 2.55 between the substrate and the membrane. Then, we should find from the simulations $L=L_1*2.55=102$ μm.

$$L/\lambda_0 = \frac{0.48.A}{\sqrt{\frac{\varepsilon_r + 1}{2}}} \qquad (1)$$

After simulation with CST microwave studio [18], the resonance has been found for a slot length equals to L=91 μm,

Manuscript received April 10, 2005. This work was supported in part by Radionet-Amstar.

J. Baubert is with the LERMA & Chalmers T.U (phone: 0317725035; e-mail: jbbaubert@ yahoo.fr).

P. Khosropanah, is with Chalmers T.U (phone: 0317721621; e-mail: pourya.khosropanah@ mc2.chalmers.se).

V. Desmaris is with Chalmers T.U (phone: 031771896; e-mail: Vincent.desmaris@ mc2.chalmers.se).

which is smaller than the theory, but reflect the influence of the dielectric membrane.

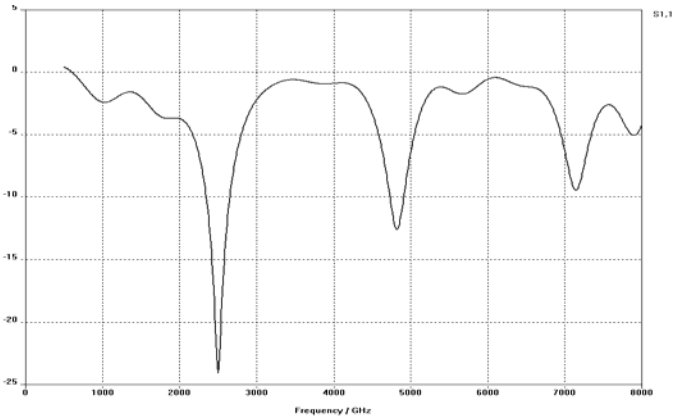

Fig. 1. S11 parameter from the Double-Slot antenna on membrane at 2.5 THz

III. MEASUREMENTS

3.1 Absorption

Atmosphere contains numerous gases which absorb microwave radiations coming from the sky. The absorption depends on the air pressure and humidity. Indeed, higher atmosphere suffer less from the absorption than low atmosphere. That's why submillimeter ground-based telescopes are located in high altitude and dry air environment. Our receiver will be placed on SOFIA Telescope flying at 14 km above the sea level, in the ionosphere.

But FTS measurement has to be made on ground. Around 2.5 THz, absorption is severe (Fig.2). One needs to design and build a vacuum chamber FTS. Still the air path from the vacuum chamber to the cryostat will attenuate the signal, according to the sea level atmospheric absorption, which is due to chemicals, such as CO and H_2O gases.

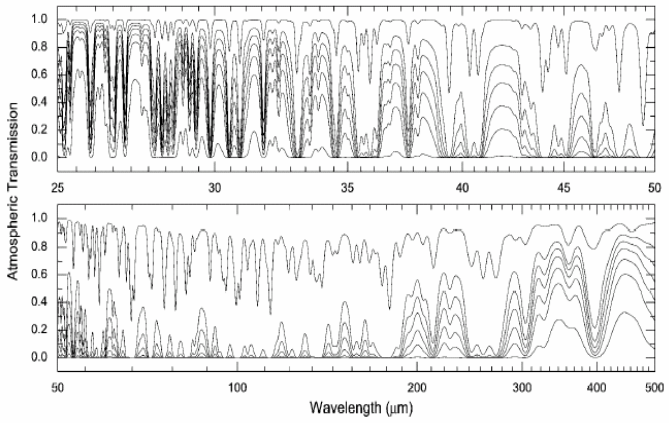

Fig. 2: Atmospheric absorption at 0 km and 14 km

3.2 Setup

We present in this paragraph the Fourier Transform Setup (Fig.3). All the system is placed under vacuum, to avoid to much absorption lines at those frequencies. An Hg lamp is chopped and illuminates with a large range of frequencies. A stepper motor moves the movable mirror. The cryostat is places in front of the FTS output and the biased signal is connected to a lock-in amplifier locked on the chopped signal frequency. The beam coming out is a Gaussian beam large enough to have a good coupling with the lens.

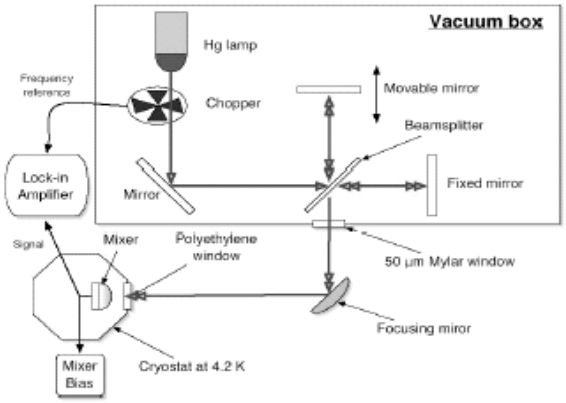

Fig. 3: FTS Setup

A Mylar beam splitter with a thickness of 50 μm was used in order to obtain sufficient signal-to-noise ratio at frequencies above 1 THz. For the spectral measurements, the HEB was constant-voltage biased.

The device temperature was set at the transition edge temperature at ~ 7 K, using a heater.

The mixer unit used for the measurement is quasi-optic (Fig.4). It uses a Silicon lens, and the chip is glued at the back of the lens. A pin is connected to the IF pad to take the IF signal out.

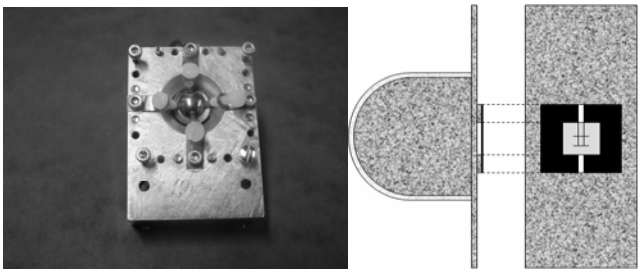

Fig. 4: Chip mounting in mixer unit

3.3 Measurements

The FTS is operated in a step and integration mode with an integration time of 1 s. The measured interferogram is then apodized by a cosine squared apodization function. Finally the Fourier transform of the apodized interferogram gives the spectrum response of the antenna at 2.5 THz (Fig.5).

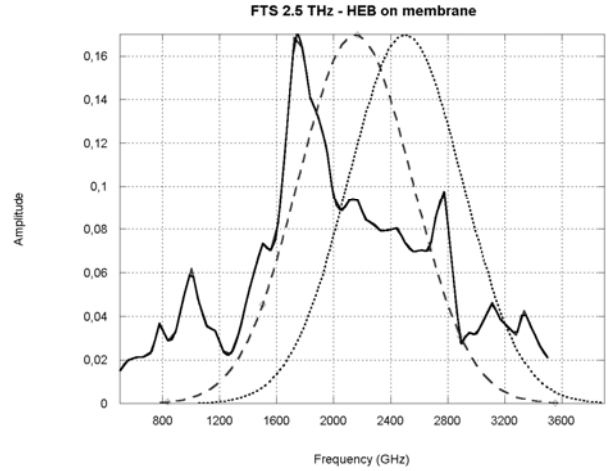

Fig. 5: 2.5 THz FTS response

The FTS maximum frequency measured was 6 THz, the number of step was 200 and the resolution was 2 cm^{-1} (60 GHz).

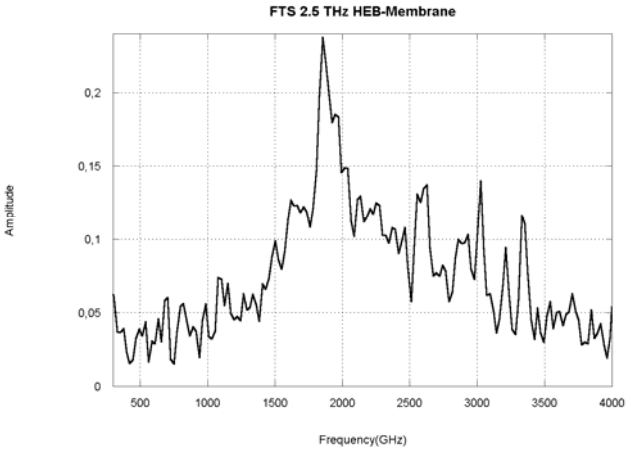

Fig. 6: 2.5 THz FTS response

Here is another FTS measurement of the same device, but the number of step was 1000 with a resolution of 0.4 cm^{-1} (12GHz). (Fig, 6)

From [10], we can compare the absorption lines contained in the air path between the vacuum chamber and the cryostat window. Table 1 summarizes the theoretical and observed absorption lines.

Ther.Freq.	1.66	1.93	2.41	2.50
Obs. Freq.	1.664	1.921	2.414	2.507
Ther.Freq.	2.67	2.77	2.88	3.00
Obs. Freq.	2.671	2.78	2.88	2.97

Table 1: Molecular transition lines comparaison

As we can see on fig. 5 and 6, the RF response of the double-slot antenna is not Gaussian as it should be in theory. We think the radiation encountered reflections in the air gap contained between the silicon lens and the double-slot antenna, as can be seen on Fig. 4. In order to confirm this explanation, we measured the FTS RF response of this antenna, taking exactly the same dimensions, but placing the antenna on a bulk Silicon substrate. In that way, we will be able to observe the shape of the RF response, but at lower frequencies. Result is shown in Fig.7.

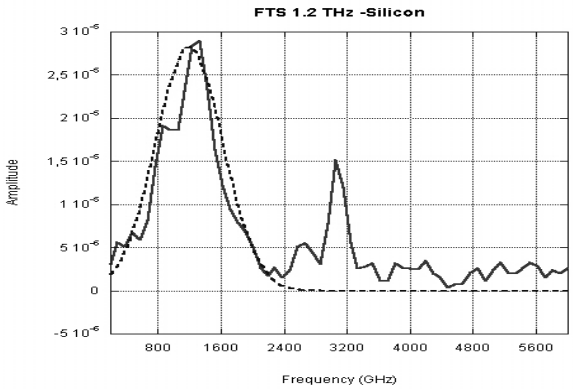

Fig. 7: FTS response on Silicon

The shape is very close to the one it should be in theory, which means that we encountered some reflections at 2.5 THz, due to the air gap between the Silicon lens and the dielectric membrane.

3.4 Discussion

We can now calculate the central frequency of the RF response at 2.5 THz (see Fig. 5), and compare it with the theoretical one. We find out a shift of 12 % (2.2 THz instead of 2.5 THz), which correspond to the shift of 15 % observed by Neto *et al* in [19] at same frequency. The simulations are then verified and the shift of 12 % remains unexplained. Another result is that the substrate is not the cause of this shift, since we observe it as well on a membrane-based antenna.

From the FTS measurement on Silicon, it is found out a central frequency of 1.2 THz. The central frequency observed on a membrane is 2.2 THz. If the membrane would not have influenced the RF response of the antenna, we would have found out a central frequency on Silicon of 1 THz. It means that the antenna responds to higher frequencies. The antenna structure on membrane is then smaller than it would be in free air. The simulations have then taken into account the action of the dielectric membrane on the antenna dimensions. Logically, the factor between RF response on Silicon and membrane should then be lower than 2.55 (from equation 1). Actually, it is found out a factor of 1.83. The membrane indeed acts as would do a semi-infinite bulk substrate of refraction index of 1.65.

IV. MEMBRANE PROCESS

4.1 Membrane Process

A SiO_2/Si_3N_4 1.4 µm thick membrane is deposited on both faces of a 4" wafer in Toulouse and sent to Chalmers. After NbN film deposition and HEB processing in Chalmers facilities, the membrane on the back face has to be removed (window opening). This step is done by Reactive Ion Etching (RIE). The next step is to remove the Silicon until reaching the SiO_2 membrane on the top face. This is achieved by using the patented "Bosh" process. Fig. 3 & 4 show the result on the top face without any pattern and the view from the back-side with the antenna patterns which are on the front side.

Fig. 3: front side

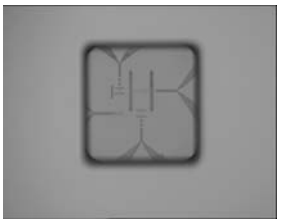

Fig. 4: back side

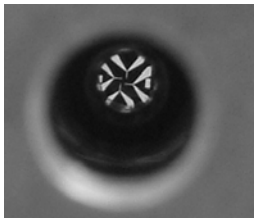

Fig. 5: chip in mixer unit

Fig. 5 shows the same antennas than figure 4, mounted into the quasi-optic mixer block. The view is from the back side where a back-short can be inserted. This mixer block design should avoid reflection or standing waves for future measurements.

5.2 *Process procedures*

It has been tried to deposit NbN films on chips with a membrane already etched, in order to expose the HEB to less process steps. T_c was not as good as a dummy sample placed in the same condition for comparison. It would be due to the temperature on the membrane which seems to be not as high as it is on a bulk silicon chip.

Almost 70% of the devices degrade or die during the membrane process, even if shorted. A solution has been found out and experimented. The last step of HEB process (NbN Ion etching) has been done after the membrane process. All devices successfully passed this procedure and show good I-Vs.

V. CONCLUSION

We have reported in this paper the FTS measurements of double-slot antennas designed at 2.5 THz on SiO_2/Si_3N_4 1.4 µm thick membrane, and on bulk Silicon substrate. A shift of 12 % from the expected central frequency has been observed and a factor of 1.83 has been found out between the two RF responses on the two different substrates. It means that the simulations are correct, but that the dielectric membrane influences the RF behaviour of the antenna. That will be taken into account to redesign the antenna dimensions.

Future investigation has to be made to confirm this factor of 1.83, by measuring FTS of double-slot antenna designed for 4.7 THz on membrane. Moreover, noise bandwidth measurement can be done with an antenna radiating at 2.5 THz on membrane.

REFERENCES

[1] E.M. Gershenzon, G.N. Goltsman, I.G. Godize, Y.P. Gusev, A.I. Elantev, B.S. Karasik, A.D. Semenov, "Millimeter and Submillimeter Range Mixer Based onElectronic Heating of Superconducting Films in the Resistive State," Superconductivity, 3, pp. 1582-1597, 1990

[2] D.E Prober, superconducting terahertz mixer using a transition-edge microbolometer, Appl. Phys. Letter 62(17), (1997), p2119.

[3] P. Yagoubov, M. Kroug, H. Merkel, E. Kollberg, G. Gol'tsman, A.Lipatov, S. Svechnikov and E. Gershenzon, "Quasioptical NbN phonon cooled hot electron bolometric mixers with low optimal local oscillator power", Proc. 9th Int. Symnp. on Space Terahertz Technology, Pasadena, CA, 131 (1998).

[4] P. Yagoubov, M. Kroug, H. Merkel, E. Kollberg, G. Gol'tsman, S. Svechnikov and E. Gershenzon, "Noise temperature and Lo power requirement of NbN phonon-cooled hot electron bolometric mixers at Terahenz frequencies", Submitted to Appl. Phys. Leu., 1998.

[5] A. Skalare, W.R. McGrath, B. Bumble and H. G. LeDuc, "Noise and RF bandwidth measurements of a 1.2 THz HEB heterodyne receiver", Proc. 8fh hit. Symp. on Space Terahertz Technology, Cambrige, MA, 47, (1997).

[6] P. Yagoubov, G. Gol'tsman, B. Voronov, L. Seidman, V. Siomash, S. Cherednichenko, and E. Gershenzon. "The Bandwidth of HEB Mixers Employing Ultrathin NbN films on Sapphire Substrate", Proc. 7th Int. Syrtzp. on Space Teruhertz Technology, Charlottesville. VA, 290, (1996).

[7] S. Cherednichenko, P. Yagoubov, K. n'in, G. Gol'tsman and E. Gershenzon, ''Large bandwidth of NbN phonon cooled hot-electrcin bolometer mixers on supphire substrates", Proc. 8th Inf. Sytnp. on Spuce Terahertz Technology, Cambrige, MA, 245, (1997).

[8] S.Cherednichenko et al. "Local oscillator power requirement and saturation effects in NbN mixers," 11th ISSTT, Ann Arbour, Michigan, May 2000, pp. 379-388

[9] www.sofia.usra.edu

[10] http://www.mpe.mpg.de/ir/ISO/linelists/Molecular.html

[11] J. Sor et al., Electronics letters, 36, p.1, 2000.

[12] A hot-spot model for membrane-based HEB mixer J. Baubert, H. Merkel, M. Salez Proceeding of 13th International Symposium on Space Terahertz Technology, 2002. Tucson, Arizona.

[13] Membrane-based HEB mixer for THz applications J. Baubert, M. Salez,Y. Delorme, P. Pons, G. Goltsman, H. Merkel, B. Lecomte Proceeding of the SPIE International Symposium on Microtechnologies for the New Millennium 2003. Maspalomas, Gran Canaria, Canary Islands, Spain. Proc. SPIE Int. Soc. Opt. Eng. 5116, 551 (2003)

[14] Millimeter wave HEB mixers on membrane: Theory - fabrication process - resultsJ. Baubert, M. Salez, Y. Delorme, P. Pons, G. Goltsman, H. Merkel, B. Lecomte Proceeding of MEMSRF 2003, Toulouse, France.

[15] P.F Goltsmith "Quasi optical systems", IEEE Press, 1998, p. 204

[16] Dipole and slot elements and arrays on semi-infinite substrates Kominami, M.; Pozar, D.; Schaubert, D. Antennas and Propagation, IEEE Transactions Volume 33, Issue 6, Jun 1985 Page(s):600 - 607

[17] D.F Filipovic, S.S. Gearhart, G.M Rebeiz, "Double-slot antennas on extended hemispherical and elliptical dielectric lenses", IEEE Trans. On Microw. Th. And Tech., Vol 41, n 10, Oct 1993

[18] CST & HFFS simulation for membrane-based HEBs in array configuration J. Baubert, M. Salez, Y. Delorme, P. Pons, G. Goltsman, H. Merkel, B. Lecomte SPIE "Astronomical Telescopes" June 2004.

[19] R.A Wyss, A. Neto, W.R Mc Grath, Submillimeter spectral response of twin-slot antennas coupled to HEB, Proc. Os 11th ISSTT, Ann Arbor, MI, May 1-3, 2000.

Optical Investigation of ultra-thin NbN films for phonon-cooled Hot-Electron-Bolometers (HEB)

T.A. Scherer[1], M. Schicke[1], R. Blundell[2] and K.-F. Schuster[1]

[1] IRAM, Institut de Radio Astronomie Millimétrique, 300 Rue de la Piscine, 38406 St Martin d'Hères, France
[2]SAO, Smithsonian Astrophysical Observatory, Cambridge, MA, USA

Abstract— **We investigate ultra-thin NbN films by means of spectroscopic ellipsometry and Raman spectroscopy. These measurements give important information on thickness dependent structural properties and phonon density of states. Thus first steps towards a microscopic understanding of the physics of phonons in these films and their coupling to the substrate can be made. As an ultimate goal we search to relate optical measurements with the specific performance of HEBs and in particular the IF bandwidth of HEB mixers. This work is part of a larger project to optimize NbN films for HEB applications including a relatively large number of deposition parameters. Within this parameter study a first surprising result is that a native Si <100> surface is non-optimal for good superconductive properties of NbN films.**

***Index Terms*—Hot-Electron-Bolometer (HEB), NbN, Raman-spectroscopy, superconducting properties**

I. INTRODUCTION

HEB mixer devices based on superconducting NbN films have been manufactured by various groups [1,3,4,5,6,7, 15,16,17,18,19,20]. One of the main limitations of HEB mixers for THz spectroscopy remains the relatively small IF bandwidth (~3-4 GHz) resulting in an exceedingly small Doppler-velocity range for astronomical applications. According to current understanding, the IF bandwidth of phonon-cooled HEBs is largely determined by the time scales on which phonons escape from the thin film into the substrate. Apart from film thickness, sound speed and acoustic matching between film and substrate play therefore a major role. Unfortunately, so far only very little is known about these parameters and most often these parameters have been freely adjusted to more complex measurements or have been derived from bulk values. To optimize films and devices it is however necessary to develop a detailed microscopic picture of the phonon escape process. On one side this requires modeling which takes into account the particular situation of phonons in very thin films. On the other side it is mandatory to search for measurements which allow direct access to the structure and dynamics of films with thickness below 5 nm. Due to the relative strong absorption of light in NbN films, optical investigations are surface sensitive. In this paper we present first results of spectral ellipsometry and Raman scattering and discuss preliminary interpretations of these measurements.

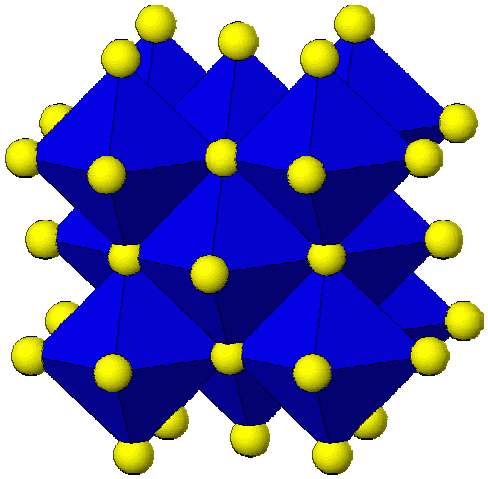

Fig.1. Lattice structure of an ideal fcc NbN single crystalline film. The spheres correspond to the nitrogen atoms. The niobium atoms are located in the center of the bi-pyramids. We found that the Raman-scattering cross-section of this material is sufficient for investigations of ultra-thin films.

II. FILM PREPARATION AND PARAMETER SPACE

In the standard process of IRAM, thin NbN films are deposited from a 4 inch niobium target by 13.56 MHz RF magnetron sputtering technique on a 2 inch substrate in a nitrogen / argon / methane atmosphere (pressure: 0.852 Pa, flow Ar: 46 sccm, flow N_2: 2.7 sccm, flow CH_4: 0.6 sccm, power 240 W). The deposition is made at room temperature. The small amount of methane improves the superconducting properties of the NbN film [6,7]. However, carbon build into the films by this process might influence the device performance.

As a first approach before a more general parameter study we try to understand the thickness dependence of optical and electrical properties of the films.

The dependence of the optical constants n and k at room temperature of NbN and the superconducting transition temperature on thickness and on partial methane pressure during the deposition will be discussed in the following chapters. A first attempt to use silicon as appropriate substrate material will be discussed.

III. Spectral Ellipsometry and Raman Spectroscopy

The evaluation of the phonon cooling mechanism by an acoustic matching approach using the long wavelength properties as derived from bulk materials might not be optimal for ultra-thin NbN films. These films have usually polycrystalline or amorphous lattice structure [6,9]. Film stress and lattice disturbances can lead to important variations in the acoustic properties and the very small NbN film thickness will lead to changes in the phonon density of states.

Fig. 2 shows wavelength-dependent ellipsometric measurements of the optical constants n and k of ultra-thin NbN films on fused quartz with 15 nm MgO seed layer [13]. An indication that important, thickness-dependent structural and electronic evolution is taking place is given by the thickness-dependent complex refractive index. For a higher film thickness a shift of the minimum in the refractive index n down to lower wavelengths λ can be observed.

NbN is Raman-active. For NbN films the wavelength dependent Raman scattering depth δ_R is entirely dominated by the strong absorption :

$$\delta_R(\lambda) = \frac{1}{2} \cdot \frac{\lambda}{4\pi \cdot k(\lambda) \cdot n(\lambda)} \qquad (1)$$

Raman scattering measurements of NbN are therefore surface sensitive. For the wavelength of He-Ne laser (λ = 632.817 nm) the corresponding scattering depth is about $\delta_R \approx 8$ nm.
We investigated NbN films by confocal Raman scattering setup with a spot diameter of 1 μm. To avoid heat-related oxidation effects of NbN in air we used a low laser power of P = 6.5 mW.

First Raman measurements have been reported in [1,11]. Fig. 3 shows the Raman-spectra of ultra-thin NbN films of different thickness as measured at room temperature. The right panel illustrates the corresponding bulk NbN phonon dispersion relation between Γ and X as measured by neutron diffraction methods [12]. A first information about the film structure is given by the very strong signal from acoustic phonons. This indicates a violation of the momentum conservation due to grain sizes in the nm range. Former X-ray diffraction measurements show similar grain sizes [7,9]. For such polycrystalline films the Raman signal form of acoustic phonons is a good indicator of the phonon density of state (DOS).

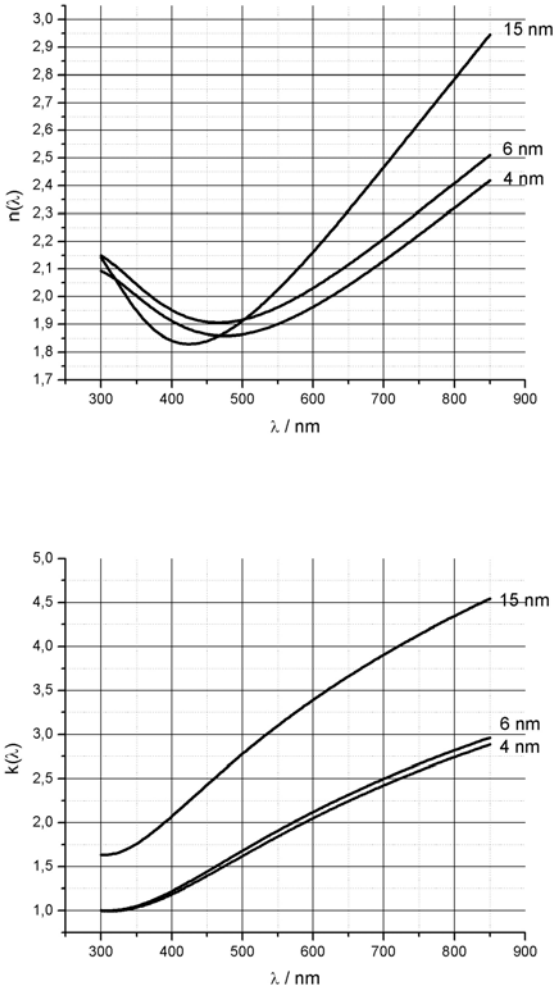

Fig. 2. Wavelength dependent ellipsometric measurements of the optical constants n and k of ultra-thin NbN films on fused quartz with a 15 nm MgO seed layer.

For films of a thickness less than 3 nm a shift to higher frequencies and simultaneously a considerable broadening of the acoustic DOS peak can be observed. This effect can be either due to stress or phonon confinement.

IV. Superconducting Properties

In a second step we have studied the superconducting properties of reactive sputtered ultra-thin NbN films. An important parameter is the critical temperature T_c of the NbN film obtained by DC transport measurements. We investigated the dependence of the resistivity R(T) as function of the temperature T for various film thickness and for different lattice-stabilizing methane contents in the sputter gas atmosphere during the deposition process. The dependencies are shown in Fig. 4.

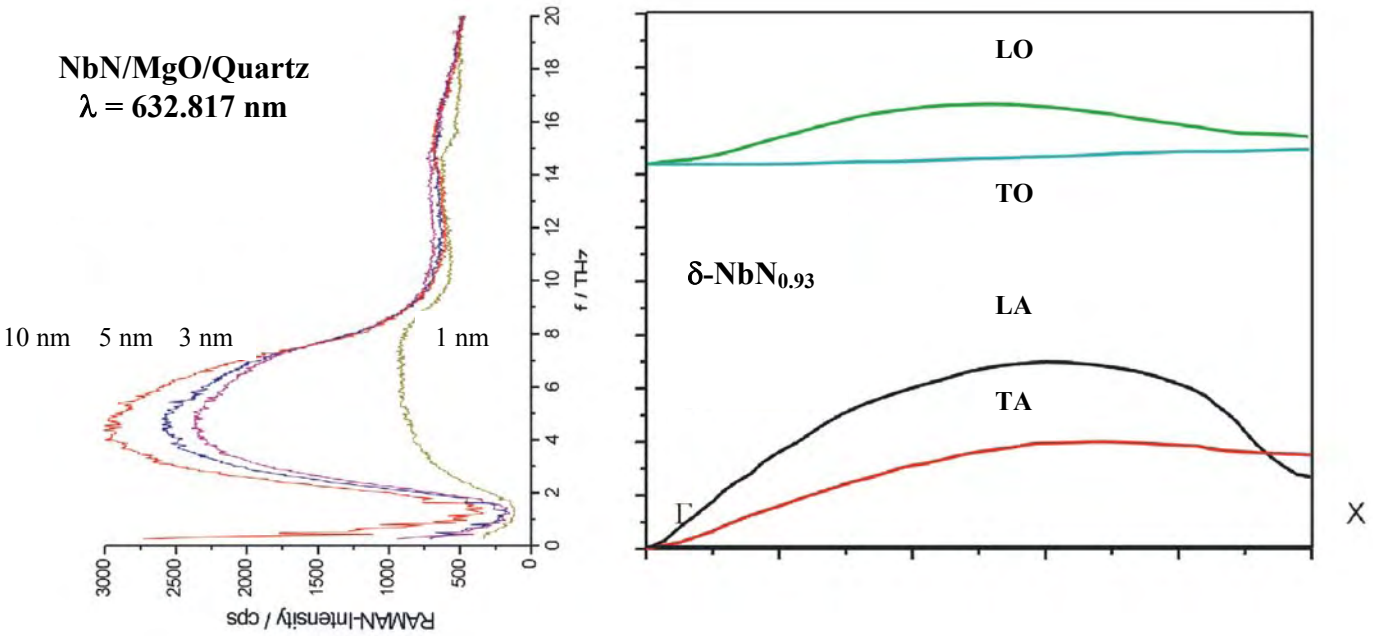

Fig. 3. Raman-spectra of ultra-thin NbN films and the corresponding NbN phonon-dispersion relation.

Real HEB devices use a NbN film thickness between 3.5 nm and 5 nm. The critical temperature in this range is about Tc ≈ 9 – 11 K. The standard methane flow in the IRAM deposition process is 0.6 sccm CH_4 for a gas mixture of 46 sccm argon and 2.7 sccm nitrogen. The total deposition pressure is p = 0.85 Pa. For a higher methane flow the critical superconducting temperatur is increased.

To improve the thermal properties of HEB devices we take into account different substrate materials. A first attempt is the use of (100)-orientated silicon substrates. The surface of pure silicon is covered by a native SiO_x layer [14]. The quality of reactive sputtered NbN on silicon substrates shows a dependence of the resistivity R(T) from the cleaning process of an argon plasma, illustrated in Fig. 5.

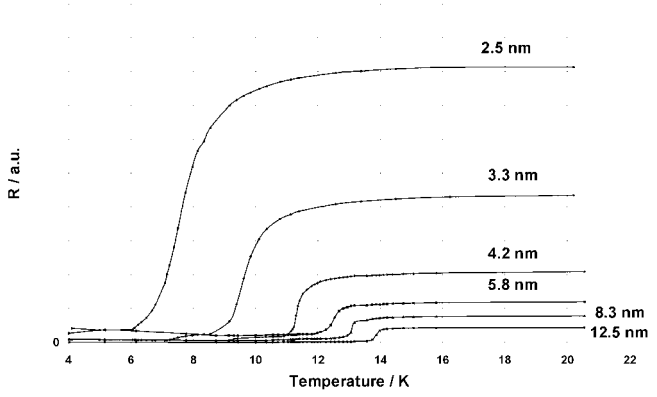

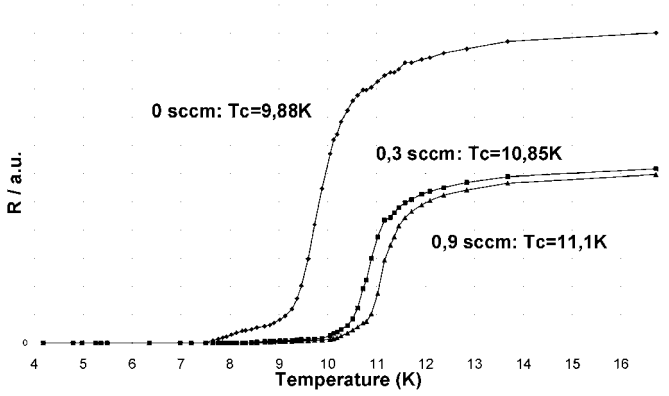

Fig. 4. Dependence of the resistivity R(T) of ultra-thin NbN films on fused quartz with 15 nm MgO seed layer for different thickness and lattice carbon content. The thickness of the NbN film is about 4 nm.

It is remarkable that without cleaning the resistivity is lower than with cleaning procedure.

V. Conclusion

Optical investigations by means of ellipsometry and Raman spectroscopy of ultra-thin NbN films can reveal information on structural and electronic properties. Our measurements indicate important interface stress for NbN films as grown on MgO buffer layers.

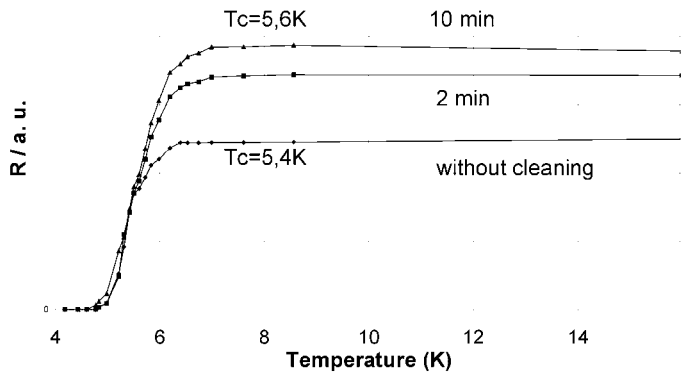

Fig. 5. Temperature dependence R(T) of 4 nm thick NbN films on (100)-oriented silicon substrate without MgO seed layer with different argon plasma cleaning time. The plasma power was 50 W (13.56 MHz RF) at 2 Pa (50 sccm) Ar pressure. The power density for the cleaning process is about 2.5 W/cm^2.

Ellipsometry indicates a thickness dependence of refractive index which is likely due to structural inhomogeneity. Films on clean Si <100> show reduced superconducting properties as compared to Si substrates with native oxide, an effect which is likely due to the large lattice mismatch between NbN and Si.

ACKNOWLEDGMENT

The authors would like to thank J. Kreisel, ENSPG, Grenoble for the assistance during the Raman measurements, S. Mougel, IRAM for the DC transport measurements of the NbN thin films and S. Peters, SENTECH, Berlin for the wavelength dependent ellipsometry. This work is part of the *EU-FP6-Radionet-AMSTAR* project.

REFERENCES

[1] T. A. Scherer, M. Frommberger, M. Schicke, K. Schuster, Institut de RadioAstronomie et Millimétrique (IRAM) Grenoble, "Development of Phonon Cooled Hot-Electron-Bolometers (HEB) for Applications in THz Radioastronomy", 2004 Joint 29th Int. Conf. On Infrared and Millimeter Waves and 12th Int. Conf. On Terahertz Electronics, Univ. of Karlsruhe, Germany, Sept. 27 – Oct. 1, 2004, pp. 447 – 448, ISBN 0-7803-8490-3

[2] S.B. Kaplan, "Acoustic matching of superconducting films to substrates", J. Low Temp. Phys., Vol. 37, (3/4), 1979.

[3] E. M. Gershenzon et al., "Millimeter and submillimeter range mixer based on electronic heating of superconducting films in the resistive state", Supercond. Vol. 3, no. 10, 1990.

[4] E. M. Gershenzon et al., "Electron-phonon interaction in ultrathin Nb films", Sov. Phys. JETP, vol. 70, no. 3, 1990.

[5] Y. P. Gousev et al., "Broadband ultrafast superconducting NbN detector for electromagnetic radiation", J. Appl. Phys., vol. 75, no. 7, 1994.

[6] M. Frommberger, "Herstellung und Charakterisierung supraleitender Nb und NbN Hot-Electron Bolometer Mischerelemente", PhD thesis, Univ. Koeln, Shaker-Verlag, ISBN 3-8265-9440-1, June 2001.

[7] M. Schicke, "Superconducting Mixer Elements for Terahertz Frequencies", PhD thesis, Univ. Hamburg, VDE-Verlag, ISBN 3-8007-2470-7, Nov. 1998.

[8] S. Cherednichenko et al., "Large bandwidth of phonon-cooled bolometer mixers on sapphire substrates", 8th Int. Symp. on Space Terahertz Technol., Harvard University, March 1997.

[9] B. Plathner, "Frequenzmischer-Elemente fuer Ueberlagerungs-empfaenger oberhalb 600 GHz", PhD thesis, Techn. Univ. Muenchen, March 1996.

[10] M. Born and E. Wolf, "Principles of Optics", Pergamon Press, 6th edition, 1993.

[11] X-J. Chen et al., "Pressure-induced phonon frequency shifts in transition-metal nitrides", to be published in Phys. Rev. B.

[12] A.N. Christensen et al., "Phonon Anomalies in Transition Metal Nitrides : δ-NbN", Solid State Comm., vol. 31, no. 11, 1979.

[13] SENTECH, Berlin, Ellipsometry by H. Witek, B. Gruska and S. Peters.

[14] H. Lueth, "Surfaces and Interfaces of Solid Materials", 3rd Springer Study Edition, 1995.

[15] J. Kawamura, R. Blundell, C.-Y. E. Tong, D. Cosmo Papa, T. R. Hunter, S. N. Paine, F. Patt, G. Gol'tsman, S. Cherednichenko, B. Voronov, E . Gershenzon,"Superconductive Hot-Electron Bolometer Mixer Receiver for 800 GHz Operation", IEEE Trans. Microw. Theory and Techn., 1999.

[16] A. Semenov, H. Richter, K. Smirnov, B. Voronov, G. Gol'tsman, H.-W. Huebers,"The development of terahertz superconducting hot-electron bolometric mixers", Supercond. Sci. and Technol., Vol. 17,, pp. 436 – 439, 2004.

[17] D. Wilms Floet, E. Miedema, T. M. Klapwijk, J. R. Gao, "Hotspot mixing: A framework for heterodyne mixing in superconducting hot-electron bolometers", Appl. Phys. Lett. Vol. 74, No. 3, pp. 433 – 435, 1999.

[18] J. J. A. Baselmans, M. Hajenius, J. R. Gao, T. M. Klapwijk, P. A. J. de Korte, B. Voronov, G. Gol'tsman, "Doubling of sensitivity and bandwidth in phonon cooled hot electron bolometer mixers", Appl. Phys. Lett., Vol. 84, No. 11, 2004.

[19] H. F. Merkel, P. Khosropanah, S. Cherednichenko, E. Kollberg, "Comparison of the Noise Performance of NbTiN and NbN Hot Electron Bolometer heterodyne mixers at THz Frequencies", 14th Intern. Symp. On Space THz Technol. ISSTT 2003, pp. 31 – 32, 2003.

[20] M. Frommberger, P. Sabon, M. Schicke, F. Mattiocco, K.-F. Schuster, "Fabrication and Characterization of Hot-Electron Bolometers for THz Applications", IEEE Trans. On Appl. Supercond., Vol. 11, No. 1, 2001.

Poster session V:

Sources

Analysis and Design of Si Terahertz Transit-Time Diodes

Xiaochuan Bi, Jack R. East, Umberto Ravaioli and George I. Haddad

***Abstract*—This paper presents a numerical simulation of a Si MITATT diode working in the submillimeter-wave and lower terahertz frequency range. Both the drift-diffusion model and full band Monte Carlo model are used to investigate the diode DC, small signal and large signal properties. Simulation shows that the Si MITATT diode is not limited by the dead-space of the impact ionization. For the diode under study, the same structure is capable of generating significant RF power at both 200 GHz and 300 GHz.**

***Index Terms*—Transit-Time Diode, Monte Carlo Simulation, Terahertz Frequency**

I. Introduction

THE terahertz frequency range of the electromagnetic spectrum holds great promise for many applications including sensing, imaging, and communications [1]. However the availability of solid-state power sources with reasonable power levels is well recognized as one of the major obstacles for system applications in this frequency range. Two-terminal devices hold record performance in terms of power generation capability, particularly at higher millimeter- and submillimeter-wave frequencies. They also have the potential of reaching terahertz frequencies and generating significant power levels. Fig. 1 shows the state-of-the-art experimental results of transit-time diodes in cw mode [2, 3].

Most recent work focuses on developing GaAs TUNNETT diodes [3, 4] partially because of the availability of mature material growth technology and quiet noise behavior, but the power is inferior to Si IMPATT diodes [5-7] and inadequate for terahertz system applications. The reasons come from the moderate efficiency of TUNNETT mode operation and material properties. The GaAs figure of merit, $(F_c \times v_{sat})^2$, is half of that of Si, where F_c is the critic field and v_{sat} is the saturation velocity. Wide bandgap materials, GaN and SiC for example, and new device structures have attracted attention to improve the power performance, but they are still limited by present fabrication techniques. In this paper we analyze transit-time diode operation in the terahertz frequency range but focus on the power generation from Si MITATT diodes [8] which have a lower noise measure than IMPATT diodes. Simulation shows that Si MITATT diodes are capable of generating significant power in the terahertz frequency regime.

X. Bi, J. R. East and G. I. Haddad are with the Solid-State Electronics Laboratory, Department of Electrical Engineering and Computer Science, The University of Michigan at Ann Arbor, Ann Arbor, MI 48109-2122 USA (e-mail: xbz@engin.umich.edu; jeast@eecs.umich.edu; gih@eecs.umich.edu).

U. Ravaioli is with the Beckman Institiue and ECE Department, University of Illinois at Urbana-Champaign, Urbana, IL 61801 USA (e-mail: ravaioli@uiuc.edu).

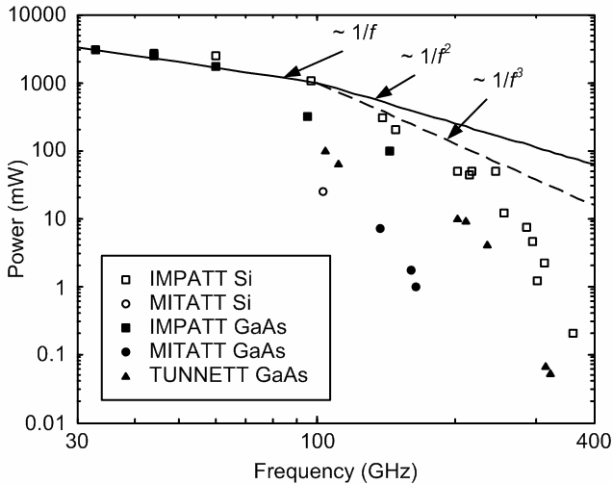

Fig. 1. State-of-the-art RF power levels from transit-time diodes under cw operation in the frequency range from 30 to 400 GHz.

II. Small Signal Model and Numerical Simulation Technique

A. Small signal Model

To operate a Si transit-time diode in the MITATT mode, the generation region electric field needs to be low, normally below 2 MV/cm, to minimize the tunneling [2]. A minimum generation region width is needed to satisfy the breakdown condition $\int \alpha dx = 1$, where α is the ionization coefficient. For the terahertz application, the diode total width is small in order to create a desired drift angle, and therefore the generation region width is relatively large. The Gilden-Hines model for the generation region [9], as shown in Fig. 2(a), assumes a narrow generation region and it is no longer applicable. The Misawa model [10], as shown in Fig. 2(b), should be used instead to account for the transit-time effect in the generation region. The extra negative resistance $-R_g$ comes from the transit time delay in the generation region.

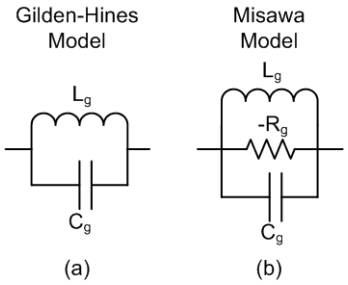

Fig. 2. Equivalent small signal circuit for the generation region.

B. Drift-Diffusion Model

The above small signal models explain transit-time diode operation in the linear region. However large signal models are needed to analyze nonlinear effects, design physical structures and estimate RF power generation [11]. The simplest one is the drift-diffusion model which solves the following continuity equations and Poisson's equation numerically,

$$\frac{\partial p}{\partial t} = g - \frac{1}{q}\frac{dJ_p}{dx},$$

$$\frac{\partial n}{\partial t} = g + \frac{1}{q}\frac{dJ_n}{dx},$$

$$\frac{dF}{dx} = \frac{q}{\varepsilon_s}\left[p - n + N_D - N_A\right],$$

where

$$J_p = q\mu_p pF - qD_p\frac{dp}{dx},$$

$$J_n = q\mu_n nF + qD_n\frac{dn}{dx}.$$

The g is the total generation-recombination rate. For the MITATT mode operation where both tunneling and avalanche effects exist, g becomes

$$g = g_a + g_t,$$

where g_a is the avalanche generation rate and g_t is the interband tunneling rate using the Kane's model [12]. The small recombination rate can be ignored.

$$g_a = \frac{1}{q}\left(\alpha_n|J_n| + \alpha_p|J_p|\right),$$

$$g_t = A_T F^2 \exp\left(-B_T/F\right).$$

C. Monte Carlo Model

As the frequency approaches the terahertz regime, the carrier transient transport time is comparable to the carrier transit time, and the drift-diffusion model is no longer reliable because of the equilibrium transport assumption. The Monte Carlo (MC) method can be used instead. For low field transport, the electron energy is small and close to the band edge. Therefore the Si bandstructure can be simplified as six equivalent ellipsoidal valleys along the X directions, as shown in Fig. 3. However for high field transport as in the MITATT diode, the electrons distribute in the whole Brillouin zone, and the full bandstructure must be used to describe the density of states and carrier dynamics [13]. The full band MC model used in this paper is described elsewhere [14] which includes the avalanche generation. In addition, the tunneling generation is introduced by adding electrons and holes into the diode according to the tunneling probability using the Kane's model.

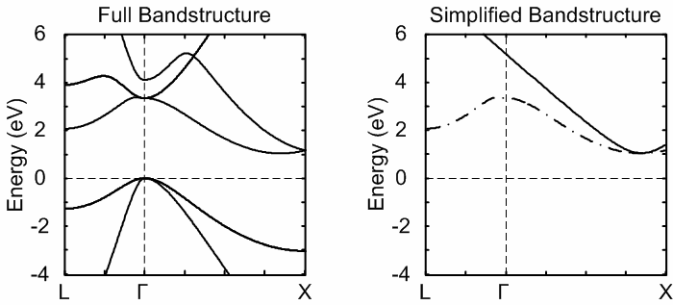

Fig. 3. Si bandstructure. The left one shows the real bandstructure. The right one shows the simplified bandstructure used in a three-valley Monte Carlo program.

D. Discussion

The above three models are used in this paper to analyze the Si MITATT diode operation. The drift-diffusion model is used to generate quick numerical solutions and the Misawa model is used to explain the device physics. The full band MC model is more accurate predicting carrier dynamics in the terahertz frequency but requires much longer simulation times. Therefore it is used to confirm the result from the drift-diffusion model. Simulation shows that the drift-diffusion model is useful to predict MITATT diode operation in the terahertz frequency range with proper estimation of generation region width as discussed in section III.

III. MITATT Mode Operation

A. Impact Ionization

The avalanche process dominates the carrier generation in MITATT mode operation where new carriers are created by the electron and hole impact ionization. In this section the time and space response of the impact ionization is discussed.

Impact ionization is fast, even in the terahertz frequency range, in the sense that the response time for the impact ionization is less than 0.1 ps when driven by a small signal electric field over a DC value of 1 MV/cm, as simulated from the full band MC model. The time for an electron or hole to gain 1 eV of energy is 0.1 about ps if it moves at 10^7 cm/s in a field of 1 MV/cm. Once the carrier accumulates enough energy, it quickly creates a new electron-hole pair due to the large scattering rate for the impact ionization.

But the impact ionization is limited by the dead-space within which the ionization coefficient is zero [15]. The dead-space is associated with the distance required to acquire the initial threshold energy, about one half times of bandgap

energy, to create a new electron-hole pair in order to conserve both energy and momentum. However, later simulation shows that the dead-space only degrades the diode operation by making the generation region wider.

B. DC Results

The drift-diffusion model and full band MC model were used to simulate a Si double drift region (DDR) transit-time diode as shown in Fig. 4. The asymmetric doping profile is used to accommodate the different properties of electrons and holes, yet it is achievable with current growth techniques. To make the comparison more valid, the material parameters used for the drift-diffusion model, the saturation velocities and ionization coefficients, are generated from the full band MC model.

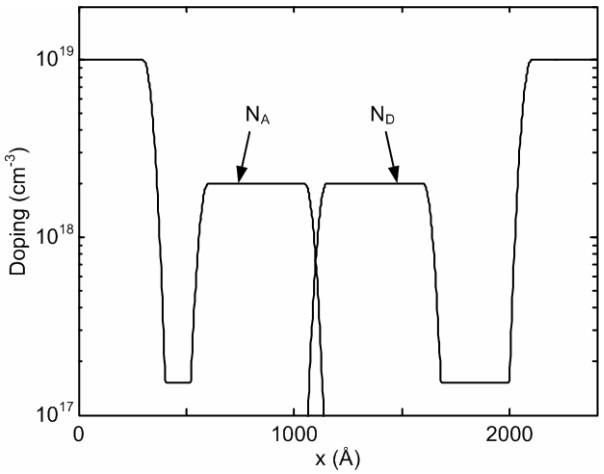

Fig. 4. Si transit-time diode structure.

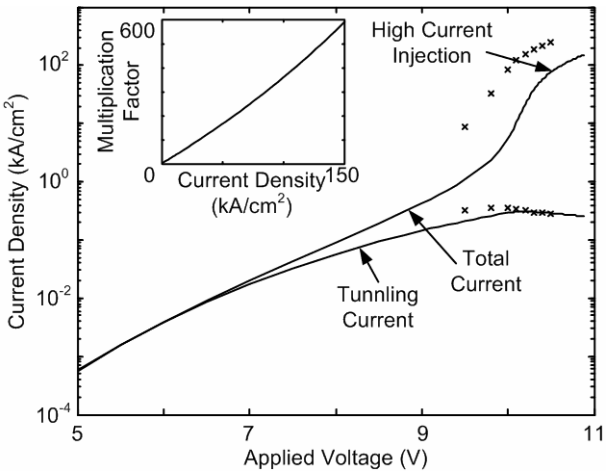

Fig. 5. I-V curve of the diode. The solid lines are from the drift-diffusion model and the x's are from the MC model. The inset shows the multiplication factor as a function of current density from the drift-diffusion model.

Fig. 5 shows the diode DC I-V curves at 500 K. Although the breakdown voltages are slightly different from the two models, both results give similar current curves. The multiplication factor M_a is 600 at a current density of 150 kA/cm^2 and therefore the diode operates in the MITATT mode. The multiplication factor M_a is defined as the total current J_{TOT} divided by the tunneling current J_t, i.e. $M_a \equiv J_{TOT}/J_t$.

An important difference is that the avalanche generation in the MC model are shifted from the central high field generation region towards the outside low field contact regions, resulting in a wider effective generation region, as shown in Fig. 6. This difference comes from the fact that the carriers need space to accumulate energy and release energy. The voltage drop across the shifted space is about the bandgap energy which is the threshold energy needed for impact ionization.

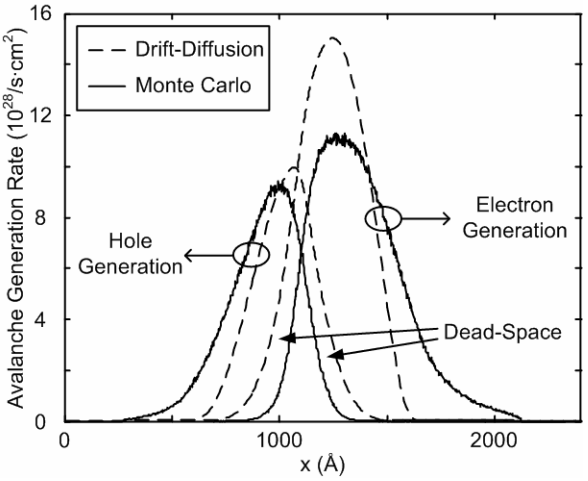

Fig. 6. Avalanche generation rate at current density of 150 kA/cm^2.

C. Small signal Results

The small signal simulation shows a good match between the drift-diffusion model and the full band MC model, as shown in Fig. 7. The reason is that the Si relaxation times are very short compared to the rate of change in the electric field, so the equilibrium transport assumption is still reasonable. One difference is that the avalanche region width is larger from the full band MC model, resulting in smaller negative conductance and larger bandwidth. Nevertheless the drift-diffusion model and hence the Misawa model still give reasonable results.

Although the generation region is not localized, the diode provides negative conductance which comes from the avalanche delay, and the transit-time delay exists both in the drift region and in the generation region. Because the non-localized avalanche region holds the transit-time effect over a wide frequency range, the negative conductance is wideband, as explained from the Misawa model.

The injection current phase angle is shown in Fig. 8. The injection phase angle increases quickly as the avalanche generation starts, and when the current is dominated by the avalanche generation, the injection phase angle is relatively constant. Therefore the power generation from the MITATT

diodes is similar to the IMPATT diodes, as shown in the following large signal results.

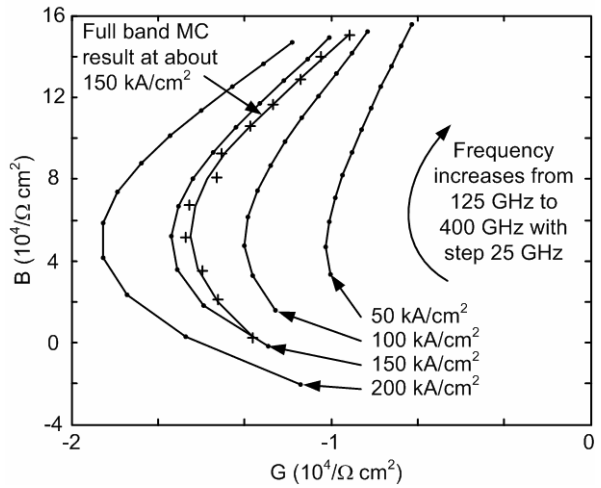

Fig. 7. Diode small-signal admittance G+*i*B.

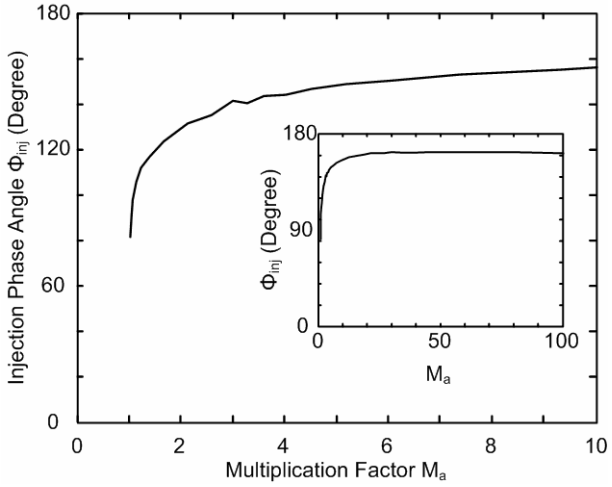

Fig. 8. Injection current phase angle.

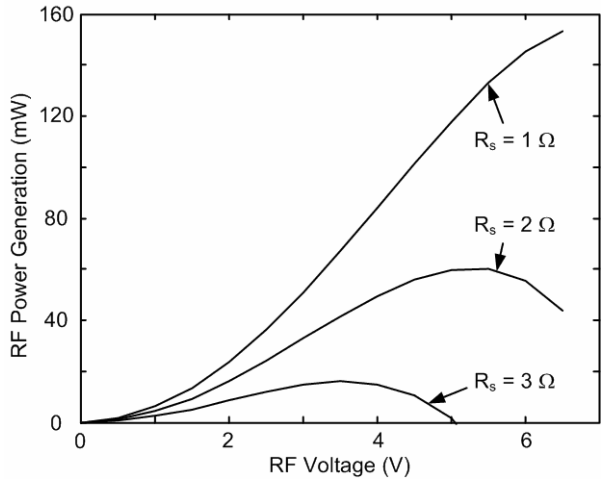

Fig. 9. RF power generation from the Si MITATT diode for different R_s at 200 GHz. J_{DC} = 150 kA/cm^2, r = 6 μm. The contact resistance is 0.9 Ω if the contact resistivity is 10^{-6} Ω·cm^2.

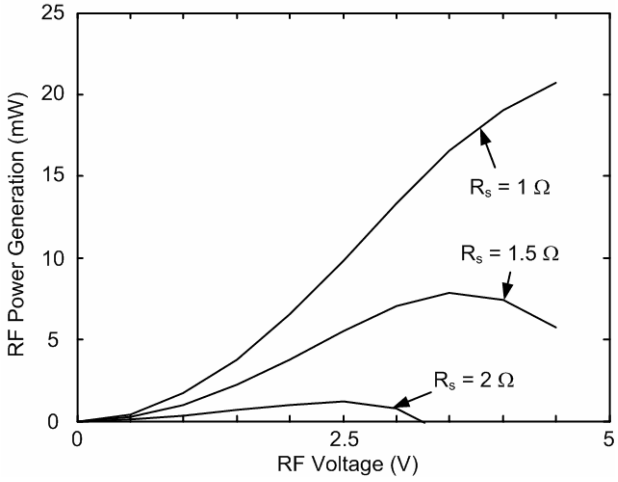

Fig. 10. RF power generation from the Si MITATT diode at 300 GHz. J_{DC} = 175 kA/cm^2, r = 4 μm. The contact resistance is 2 Ω if the contact resistivity is 10^{-6} Ω·cm^2.

D. Large-Signal Results

Because the negative conductance is wideband, the same Si MITATT diode is capable to generate RF power at both 200 GHz and 300 GHz by choosing different device areas, as predicted by the drift-diffusion model. Fig. 9 and Fig. 10 show the power generation for different parasitic losses R_s. The DC current density is increased slightly at 300 GHz in order to increase the negative conductance and therefore RF power generation.

The RF power generation decreases rapidly as R_s increases. Therefore low loss is important. For the transit-time diode, the R_s is dominated by the Ohmic contact resistance and 10^{-6} Ω·cm^2 for the contact resistivity is a conservative number for Si. Much lower resistivity has been reported [16] and even better results can be achieved from a forward biased Schottky contact [17]. Therefore it is possible to reduce the parasitic loss below 1 Ω for both cases.

Although the drift-diffusion model overestimates the RF power generation because the actual avalanche region width is wider and the negative conductance is smaller, the full band MC model shows the diode can still generate significant power at 200 GHz for similar bias condition, as shown in Fig. 11. Actually the power prediction is close to the published Si IMPATT diode data on Fig. 1 at the same frequency range which makes the results reasonable [5-7]. If biased at a higher current density, significant RF power can be expected from 300 GHz as well, as shown in Fig. 12.

IV. CONCLUSION

This paper analyzes Si transit-time devices working in the frequency range from 150 GHz to 400 GHz. Although the drift-diffusion model assumes equilibrium transport, it still gives reasonable results compared with more accurate full band Monte Carlo model. The reason is that the dead-space of

the impact ionization does not limit the Si MITATT diodes operation in this frequency range. It decreases the diodes negative conductance but increases the bandwidth as well. Simulation shows that the Si MITATT diode under study can produce useful power from 200 GHz up to 300 GHz.

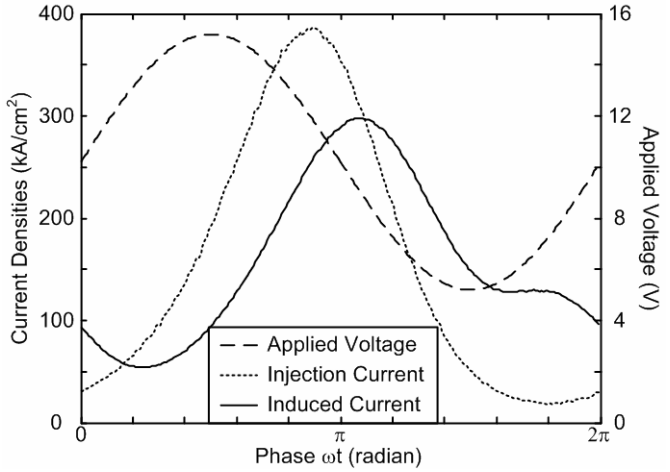

Fig. 11. Large signal operation from the full band MC model at 200 GHz. V_{DC} = 10.2 V, V_{RF} = 5 V, J_{DC} = 157 kA/cm^2, r = 6 µm, R_s = 1 Ω, P_L = 54 mW, η = 3 %.

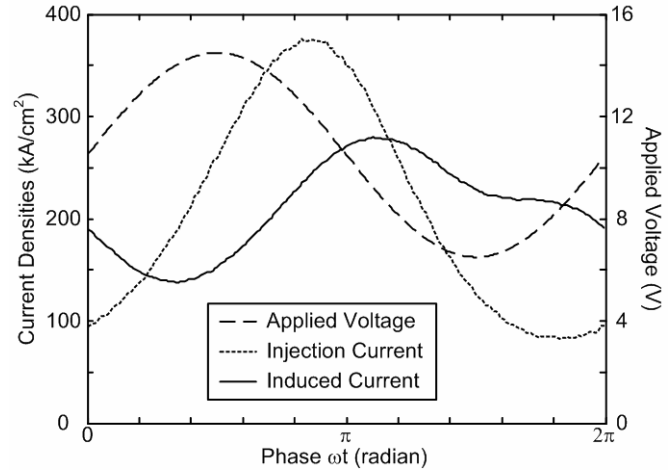

Fig. 12. Large signal operation from the full band MC model at 300 GHz. V_{DC} = 10.5 V, V_{RF} = 4 V, J_{DC} = 211 kA/cm^2, r = 4 µm, R_s = 1 Ω, P_L = 20 mW, η = 1.8 %.

ACKNOWLEDGMENT

This work was supported by ARO under the MURI Program Number DAAD-19-01-1-0622. The authors would like to acknowledge the NSF Network for Computational Nanotechnology for the Monte Carlo codes. The authors would like to thank Dr. Jasprit Singh for helpful discussions.

REFERENCES

[1] Haddad, G.I., J.R. East, and H. Eisele, *Two-Terminal Active Devices for Terahertz Sources*, in *Terahertz Sensing Technology*, M.S. Shur, Editor. 2003, World Scientific.

[2] Eisele, H. and G.I. Haddad, *Active Microwave Diodes*, in *Modern Semiconductor Device Physics*, S.M. Sze, Editor. 1998, John Wiley & Sons, Inc. p. 343-407.

[3] Plotka, P., et al., *240-325-GHz GaAs CW Fundamental-Mode TUNNETT Diodes Fabricated With Molecular Layer Epitaxy.* IEEE Trans. Electron Dev., 2003. **ED-50**(4): p. 867.

[4] Eisele, H., A. Rydberg, and G.I. Haddad, *Recent Advances in the Performance of InP Gunn Devices and GaAs TUNNETT Diodes for the 100-300-GHz Frequency Range and Above.* IEEE Trans. Microwave Theory Tech., 2000. **MTT-48**(4): p. 626.

[5] Chang, K., W.F. Thrower, and G.M. Hayashibara, *Millimeter-Wave Silicon IMPATT Sources and Combiners for the 110-260-GHz Range.* IEEE Trans. Microwave Theory Tech., 1981. **MTT-29**(12): p. 1278.

[6] Chao, C., et al., *Y-Band (170-260 GHz) Tunable CW IMPATT Diode Oscillators.* IEEE Trans. Microwave Theory Tech., 1977. **MTT-25**(12): p. 985.

[7] Ino, M., T. Ishibashi, and M. Ohmori, *C. W. Oscillation with p^+-p-n^+ Silicon IMPATT Diodes in 200 GHz and 300 GHz Bands.* Electron. Lett., 1976. **12**(6): p. 148.

[8] Elta, M.E. and G.I. Haddad, *Mixed Tunneling and Avalanche Mechanisms in p-n Junctions and Their Effects on Microwave Transit-Time Devices.* IEEE Trans. Electron Dev., 1978. **ED-25**(6): p. 694.

[9] Gilden, M. and M.E. Hines, *Electronic Tuning Effects in the Read Microwave Avalanche Diode.* IEEE Trans. Electron Dev., 1966. **ED-13**(1): p. 169.

[10] Misawa, T., *Multiple Uniform Layer Approximation in Analysis of Negative Resistance in p-n Junction in Breakdown.* IEEE Trans. Electron Dev., 1967. **ED-14**(12): p. 795.

[11] Scharfetter, D.L. and H.K. Gummel, *Large-Signal Analysis of A Silicon Read Diode Oscillator.* IEEE Trans. Electron Dev., 1969. **ED-16**(1): p. 64.

[12] Kane, E.O., *Zener Tunneling in Semiconductors.* J. Phys. Chem. Solids, 1959. **12**: p. 181.

[13] Fischetti, M.V. and S.E. Laux, *Monte Carlo Analysis of Electron Transport in Small Semiconductor Devices Including Band-Structure and Space-Charge Effects.* Phys. Rev. B, 1988. **38**(14): p. 9271.

[14] Hess, K., ed. *Monte Carlo Device Simulation: Full Band and Beyond.* The Kluwer International Series in Engineering and Computer Science. 1991, Kluwer Academic Publishers.

[15] Kim, K. and K. Hess, *Simulations of Electron Impact Ionization Rate in GaAs in Nonuniform Electric Fields.* J. Appl. Phys., 1986. **60**(7): p. 2626.

[16] Janega, P.L., J. McCaffrey, and D. Landheer, *Extremely Low Resistivity Erbium Ohmic Contacts to n-Type Silicon.* Appl. Phys. Lett., 1989. **55**(14): p. 1415.

[17] Urteaga, M., et al., *Submicron InP-Based HBTs for Ultra-High Frequency Amplifiers*, in *Terahertz Sensing Technology*, M.S. Shur, Editor. 2003, World Scientific.

Superconducting Submm Integrated Receiver with Phase-Locked Flux-Flow Oscillator for TELIS

Valery. P. Koshelets, Pavel N. Dmitriev, Andrey B. Ermakov, Lyudmila V. Filippenko,
Oleg V. Koryukin, Andrey V. Khudchenko, Mikhail Yu. Torgashin,
Pavel A. Yagoubov, Ruud W.M Hoogeveen, and Wolfgang Wild

***Abstract*—We present results of a single-chip superconducting integrated receiver development for the Terahertz Limb Sounder (TELIS) balloon project. TELIS is a collaborative European project to build a three-channel heterodyne balloon-based spectrometer for measuring a variety of the stratosphere constituents. The Superconducting Integrated Receiver (SIR) comprises in one chip a planar antenna integrated with a superconductor-insulator-superconductor (SIS) mixer, a superconducting Flux Flow Oscillator (FFO) acting as Local Oscillator (LO) and a second SIS harmonic mixer (HM) for FFO phase locking. An improved design of the FFO for TELIS has been developed and optimized. A free-running linewidth between 9 and 2 MHz has been measured in the frequency range 500 – 710 GHz. As a result the spectral ratio of the phased-locked FFO varies from 35 to 90 % correspondingly, ensuring that at least half of the phase-locked FFO power in the primary frequency range for TELIS (550-650 GHz). The FFO performance required for successful TELIS operation is discussed. New generation of the SIR for TELIS with improved FFO performance has been developed and preliminary tested. It is important to ensure that tuning of a phase-locked (PL) SIR can be performed remotely by telecommand. For this purpose a number of approaches for the PL SIR automatic computer control have been developed. Preliminary measurements give an uncorrected double side band (DSB) noise temperature of about 200 K measured at 2.1 K with the FFO phase-locked at 660 GHz. The effect of FFO linewidth imperfections on retrieval procedure is discussed.**

***Index Terms*— Submillimeter wave integrated receivers, phase-locked oscillators, Josephson junctions, superconducting devices.**

Manuscript received May 2, 2005.

The work was supported in parts by the RFBR projects 03-02-16748, INTAS project 01-0367, ISTC projects # 2445, 3174 and the President Grant for the Scientific School 1344.2003.2.

V.P. Koshelets, P.N. Dmitriev, A.B. Ermakov, L.V. Filippenko, O.V. Koryukin, A.V. Khudchenko, and M.Yu. Torgashin are with the Institute of Radio Engineering and Electronics, Russian Academy of Science, Mokhovaya 11, 125009, Moscow, Russia; they are also partially with the Space Research Organization of the Netherlands (SRON), P.O. Box 800, 9700 AV Groningen, the Netherlands, (telephone: 7-095-2032784, e-mail: valery@hitech.cplire.ru)

P. Yagoubov, R. Hoogeveen, *and W. Wild* are with the Space Research Organization of the Netherlands (SRON), P.O. Box 800, 9700 AV Groningen, the Netherlands, (telephone: 31-50-3634074, e-mail: P.A.Yagoubov@sron.rug.nl).

I. Introduction

TELIS (Terahertz and submm Limb Sounder) [1] is a collaborative European project that combines three independent receiver channels, selected to yield maximum science output and to provide the most complete map of atmospheric species ever measured from one platform. The channels sharing the same front-end optics are located inside one helium-cooled cryostat and operate at 500 GHz, 550–650 GHz and at 1.8 THz. The 550 - 650 GHz channel is based on a phase-locked Superconducting Integrated Receiver (SIR) [2]. SIR is an on-chip combination of a low-noise SIS mixer with quasioptical antenna, a superconducting Flux Flow Oscillator (FFO) [3] acting as a Local Oscillator (LO) and an SIS harmonic mixer (HM) for FFO phase locking.

The FFO is a long Josephson tunnel junction with a unidirectional flow of fluxons caused by applied dc magnetic field and bias current. The velocity and density of the fluxons and thus the power and frequency of the emitted signal may be adjusted independently by tuning bias current and magnetic field. The SIR microcircuits are fabricated from a high quality Nb-AlOx-Nb tri-layer on a Si substrate. The FFO is connected to a double-dipole or double-slot antenna/mixer with a microstrip transmission line, which contains a number of rf-coupling and dc-blocking elements. Both the SIS mixer and the FFO are provided with local magnetic fields via integrated control lines.

In order to obtain frequency resolution required for practical application of a heterodyne spectrometer (of at least one part per million) an integrated local oscillator (LO) must be phase-locked to an external reference. To achieve this goal a concept of the integrated receiver with phase-locked loop (PLL) has been developed [4] and experimentally proven. Following this concept a 350 GHz single-chip receiver has been designed, fabricated and successfully tested [5], [6], showing the frequency resolution of the receiver as good as 10 kHz. The effect of SO_2 gas spectral line broadening as measured by this spectrometer for a laboratory gas cell demonstrated the feasibility of such device for practical applications [6], although this SIR could operate only at almost fixed frequencies on Fiske steps.

There is a number of important issues that have to be addressed to SIR design and its operation. First of all it is a challenge to realize the ultimate performance of separate superconducting elements after their integration in a single-chip device. Also it is important to ensure that operation and tuning of a phase-locked (PL) SIR can be provided distantly. The knowledge of exact parameter values of the frequency locked (FL) and phase-locked (PL) FFO is required for correct retrieval procedure. The last issue is related to the fact that FFO linewidth has Lorentzian shape both at higher voltages on the flux flow step (FFS) [5] and at lower voltages in the resonant regime on the Fiske steps (FS's) [7]. It means that the free-running ("natural") FFO linewidth in all operational regimes is determined by the wideband thermal fluctuations and the shot noise. This is different from most of traditional microwave oscillators where the "natural" linewidth is very small and the observed linewidth can be attributed mainly to external fluctuations. All these issues will be discussed in this report.

II. SIR Design and Results of the First RF Tests

A key element of the 650 GHz channel is the SIR [2] that comprises in one chip (size of 4 mm*4 mm*0.5 mm) a low-noise SIS mixer with quasioptical antenna (double dipole or double slot) and a superconducting Flux Flow Oscillator (FFO) acting as LO. The receiver chip is placed on the flat back surface of the elliptical silicon lens. A quarter-wave back reflector chip is installed behind the double-dipole antenna to obtain a beam of high efficiency and good symmetry. To achieve the required instantaneous bandwidth of 550-650 GHz with emphasis on 600-650 GHz frequency range, a side-feed twin-SIS mixer with 0.8 μm^2 junctions is implemented. Microphotograph of the central part of the SIR chip with double dipole antenna is presented in Fig. 1.

The SIR microcircuits of this design have been preliminary tested as a receiver [8] showing at the first time a possibility to realize the PL SIR concept at high frequencies above boundary [9] where FFO operates in a real Flux-Flow regime and continuous frequency tuning is possible (this boundary is of about 450 GHz for Nb-AlOx-Nb tunnel junctions).

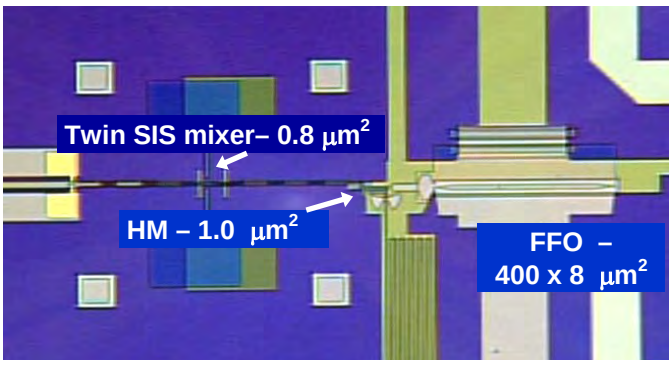

Fig. 1. Central part of the SIR chip with double-dipole antenna, twin SIS-mixer and harmonic mixer for FFO phase locking.

It was also found that due to insufficient coupling between FFO and SIS/HM the SIR phase-locking is possible only at some specific frequencies. For example, results presented in Fig. 2 - 4 have been measured at bath temperature of 2.1 K. In this case a reasonably good pumping for both SIS and HM was realized at FFO frequencies from 500 to 680 GHz. It was impossible to get a good pumping of the SIS mixer at bath temperature of 4.2 K at 670 GHz, where the best sensitivity was measured by FTS. The reason is losses in the SIR microstrip lines at frequencies close to the gap value of Nb (note that temperature of the SIR chip is usually a little higher than that of the bath).

Dependence of the experimentally measured Y-factor on the FFO frequency and FFO bias current is shown in Fig. 2. The data were measured by specially developed data acquisition system for Integrated Receiver TEst and CONtrol (IRTECON) [9]. We used a rotating hot/cold load chopper (frequency of about 11 Hz), tunable IF YIG filter (bandwidth of about 40 MHz) and fast power meter. Such procedure (for all frequencies of interest) takes usually of about 20 minutes for fixed SIS-mixer bias voltage (2.2 mV for data shown in Fig. 2). It was also possible to optimize the bias voltage of the SIS mixer for each FFO bias point; in this case a complete scan requires 2-3 hours. From the data presented in Fig. 2 DSB receiver noise temperature can be re-calculated (see Fig. 3). Note that there is a wide range of the FFO bias currents (i.e. FFO power) where Y-factor is close to maximum; it makes possible the selection of optimal conditions for HM operation.

To investigate frequency resolution of the receiver we have measured the signal of the synthesizer multiplied by super-lattice structure developed by D. Paveliev from University of Nizhny Novgorod (see report at this conference). The results of these measurements are presented in Fig. 4; one can see that recorded signal is a convolution of the delta-function provided by synthesizer with phase-locked spectra of the FFO.

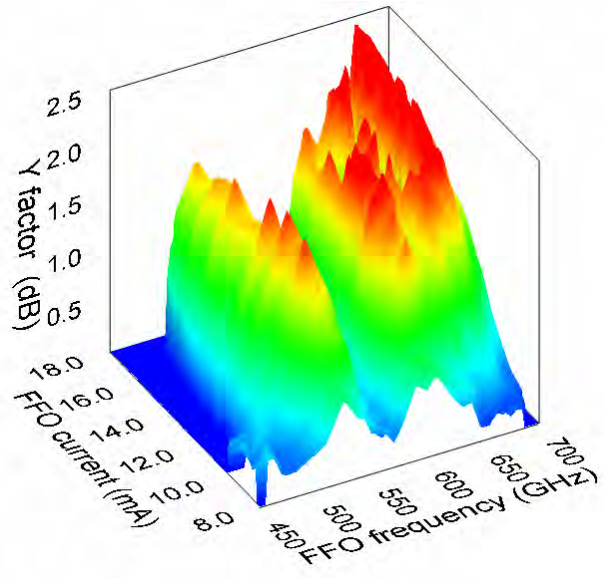

Fig. 2. Y-factor of the SIR as a function of FFO frequency and FFO bias current (T= 2.1 K, V_{SIS} = 2.2 mV, IF = 4.3 GHz).

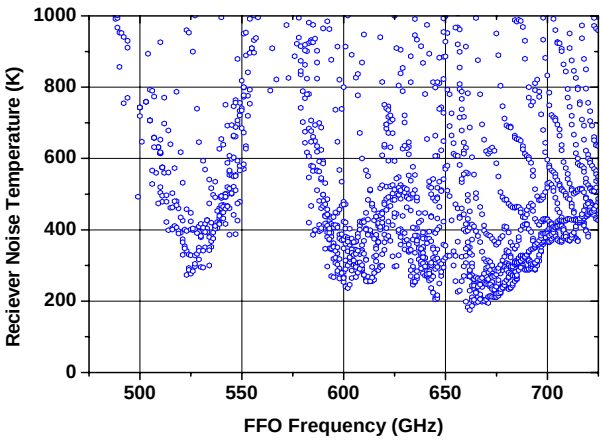

Fig. 3. Uncorrected DSB noise temperature of the SIR as a function of FFO frequency measured at different FFO bias currents that results in various SIS pumping level (T_{BATH} = 2.1 K, V_{SIS} = 2.2 mV, IF = 4.3 GHz).

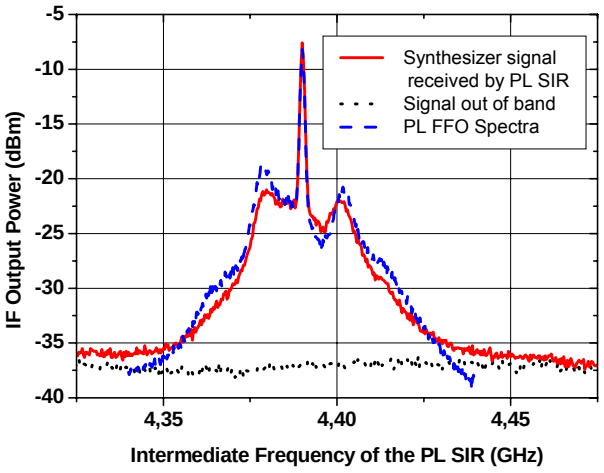

Fig. 4. Signal of multiplier driven by synthesizer (17.967 GHz * 37 = 664.8 GHz), measured by TELIS SIR with FFO phase-locked at 660.4 GHz – solid line. For the trace shown by dotted line the signal of the synthesizer is shifted by 5 MHz to be out of IF band. Dashed line – spectrum of the PL FFO, measured at HM IF output and frequency translated.

For the first SIR designs it was impossible to realize a PL SIR operation in the whole TELIS frequency range mainly because of two important problems: 1) insufficient pumping of the SIS-mixer and/or the HM at some frequencies; 2) influence of the 22-24 GHz synthesizer power, applied to HM on the SIS-mixer operation. The high harmonics (up to 30th) of the synthesizer is mixed in the HM with FFO signal and down-converted signal is used by the PLL system to stabilize FFO frequency. The synthesizer power required for HM operation is rather high; at some frequencies a part of that power "leaked" to the SIS-mixer that resulted in smearing of the SIS IVC and considerable deterioration of the SIR performance. To overcome these problems a new design of SIR microcircuit has been developed. The main features of the new design are: novel construction of the matching elements, decreased (submicron) area of SIS and HM junctions, etc. Results of the tests of these microcircuits at DC are presented below.

III. DC Tests of the TELIS SIR of the New Design

There is a number of important requirements for the FFO properties to make it suitable for application in the phase-locked SIR. Obviously an FFO should emit enough power to pump an SIS mixer taking into account a specially designed mismatch of about 5-7 dB between the FFO and SIS mixer, introduced to avoid leakage of the input signal to the LO path. Implementation of the improved matching circuits and submicron junctions both for SIS and HM allows to deliver enough FFO power for the optimal operation of these devices (see Fig. 5 – 7, where an SIS-mixer pumping is illustrated; that is the most important for low noise SIR operation). Note that the 22-24 GHz synthesizer provides pumping for HM while FFO power is a signal that should be down-converted, so even moderate HM pumping by FFO (5-10 % of the HM Ig, where Ig is a current jump at the gap voltage Vg) is enough [10] to ensure large enough signal to noise ratio (SNR) at the IF output and consequently efficient FFO phase locking.

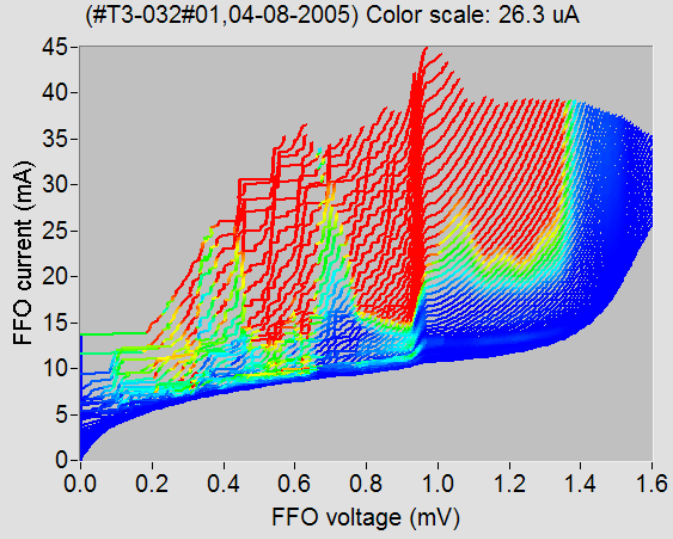

Fig. 5. IVCs of the FFO of T3 design measured at different CL currents; the pumping of the SIS-mixer is shown by color scale (red color corresponds to pumping level > 25% of SIS Ig), see Fig. 8, 9.

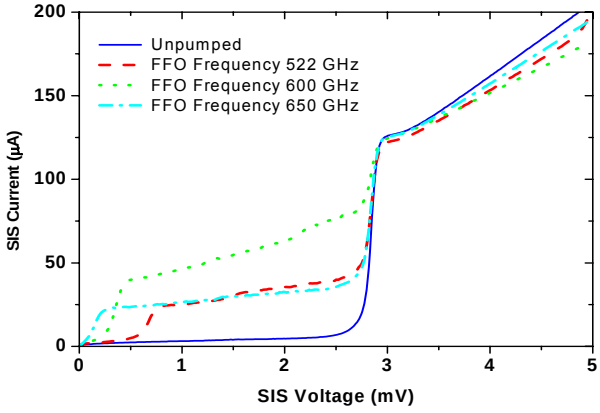

Fig. 6. IVCs of the SIS-mixer of T3 design: solid line - unpumped, dashed, dotted and dash-dotted – pumped by FFO at frequencies 522, 600 and 650 GHz correspondingly.

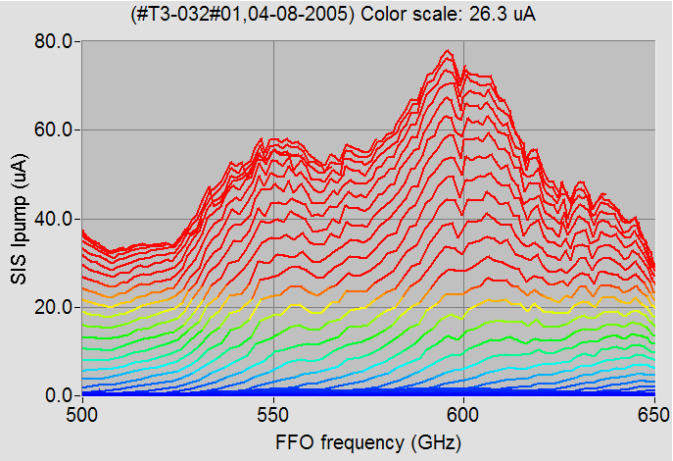

Fig. 7. Pumping of the SIS-mixer as a function of FFO frequency at different FFO CL currents. The pumping level > 25 % of Ig (> 26.3 μA) is realized in the TELIS-SIR frequency range 500 - 650 GHz.

IV. Dependence of the FFO Linewidth on its Parameters

Even for ultra wideband PLL system an effective regulation bandwidth is limited by the cable length (about 7 MHz for typical PL loop length of two meters). It means that free-running FFO linewidth has to be well below 10 MHz to ensure stable FFO phase locking with reasonably good spectral ratio (SR) - the ratio between the carrier and total power emitted by FFO, determines quality of FFO phase locking. For example, only about 50 % of the FFO power can be phase-locked by the present PLL system at the free-running FFO linewidth of 7 MHz. Low spectral ratio results in considerable error in resolving the complicated line shape [8]. Thus sufficiently small free-running FFO linewidth is vitally important for realization of the phase-locked SIR for TELIS.

Previous measurements [11] have demonstrated considerable increase of the FFO linewidth with FFO current density. It contradicts with the simplified consideration: the increase of the FFO current density should result in an increase of the total FFO bias current and a decrease of the FFO differential resistance. Since the FFO linewidth is proportional to $R_d^2 * I_b$, the increase of the FFO current density has to be accompanied by the decrease of the measured FFO free-running linewidth. In reality the increase of the linewidth is caused by the fact that decrease of the differential resistance is smaller than expected [11]. High value of the current density ($J_c \geq 8$ kA/cm^2) is important for wide-band operation of an SIS mixer at submm wave range. The discussed above increase of the FFO linewidth with current density creates serious problem in design and development of SIR chips. Implementation of two separate tri-layers with different current densities - one for the SIS mixer (high J_c) and the other for the FFO (lower J_c) might be a solution. We have successfully tested and verified this approach for SIR TELIS microcircuits.

Recently it was shown [10] that for all frequencies of interest the FFO linewidth considerably decreases with increasing FFO width (consequently, the spectral ratio is getting much higher). Furthermore, there is no visible saturation of this effect in the studied range of FFO widths up to 28 μm. In principle such behavior is quite explainable according to existing theoretical models: FFO linewidth, proportional to $R_d^2 * I_b$, has to go down with an increase of the FFO width since it should result in an increase of total FFO bias current and in decrease of the FFO differential resistance. Fortunately, in contrast to the case of changing of the FFO current density, the R_d value indeed decreases more or less inversely proportional to I_b. Of course, one can expect saturation of the linewidth decrease and deterioration of the FFO behavior at further width increase (for example, due to appearance of the transversal modes). Since there is no reliable theory the optimal value of the FFO width has to be determined experimentally.

Dependences of the free-running FFO linewidth and SR of the phase-locked FFO on the FFO frequency measured at constant bias current of 32 mA for FFO as wide as 28 μm are presented in Fig. 8. Abrupt increase of the linewidth at the FFO frequency of about 450 GHz is caused by the effect of Josephson self-coupling (JSC) [12]. The JSC considerably modifies FFO properties at voltages $V \approx V_{JSC} = 1/3 * Vg$ (V_{JSC} corresponds to 450 GHz for a Nb-AlO_x-Nb FFO) and results in larger internal damping at voltages $V > V_{JSC}$ that significantly complicates phase locking of the FFO at frequencies just above V_{JSC}.

Note that for the wide FFO its centerline is shifted from the edge of the bottom electrode that results in considerable decrease of the R_d^{CL} value. Furthermore, larger overlapping of the electrodes for wider FFO presumably provides more uniform bias current distribution – due to much smaller inductance of the overlapping electrodes. Presented results are very encouraging and these modifications of the FFO have been already implemented in the TELIS SIR chips.

In conclusion, an improved design of the FFO for TELIS has been developed and optimized. Free-running linewidth value from 9 to 2 MHz has been measured in the frequency range 500 – 710 GHz. As a result the spectral ratio of the phase-locked FFO varies from 35 to 90 % correspondingly, ensuring that at least half of FFO power is phase-locked in the primary frequency range for TELIS 550-650 GHz.

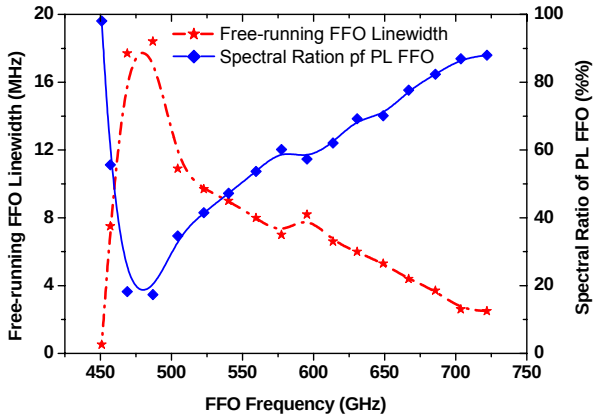

Fig. 8. Free-running linewidth and SR of PL FFO of a new design as a function of FFO frequency (FFO width = 28 μm; RnS = 30 Ohm*μm^2).

V. Remote Optimization of the PL SIR Operation

It is important to ensure that tuning of a phase-locked SIR can be provided distantly. Equally important is to determine in flight the main parameters of the FFO at specific bias conditions (without complicated spectrum measurements). The knowledge of such parameters as "free-running" linewidth (FRL) for the frequency locked FFO and spectral ratio (SR) for the phase-locked FFO are required for correct retrieval procedure. It was shown [10] that the SR value for the given PLL system is determined by the free-running FFO linewidth: these two quantities are unambiguously related. So only one value (SR or FRL) has to be measured in flight to ensure retrieval procedure.

To adjust in flight the PL FFO operation (and to determine the resulted SR of the PL FFO) a computer controlled PLL system with a specially designed monitoring channel "IF level output" has been developed by Institute for Physics of Microstructure, Russian Academy of Science (Nizhny Novgorod, Russia). The dc signal at this output of the PLL system is proportional to the power measured by a detector with 0.8 MHz band-pass filter at 400 MHz. This DC signal is proportional to the PL FFO spectral ratio (see Fig. 9) [8]. Furthermore, the constant of proportionality does not depend on FFO bias current and is the same for FFOs of quite different design (see Fig. 9). It means that SR can be determined in flight if the power level is kept constant.

It is possible to optimize the HM tuning by monitoring the "IF level output" in the PL regime while the HM bias voltage and/or the synthesizer power are being adjusted (see Fig. 10) [8]. It is clear from Fig. 10 that there is a number of closely spaced local maximums. The height of these maximums is almost equal in quite a large range of parameters, so any of these peaks can be used for PL SIR operation. On the other hand the "valleys" between peaks are quite deep and precise tuning of the parameters (HM bias voltage, synthesizer power) is required. At the synthesizer power of about 10dBm (power delivered to HM is of about 1 μW) the spacing between peaks became twice as small compared to optimal – this corresponds to crossover from the quasiparticle to Josephson mode of HM operation. As a matter of fact, no significant difference between these two regimes has been found; almost the same signal to noise ratio (SNR) and consequently Spectral Ratio can be realized. On the other hand the requirement to minimize cross talk between pumped HM and SIS-mixer forced us to use mainly the Josephson mode of HM operation for present PL SIR measurements.

From Fig. 10 one can see that tuning of the single-junction HM is reasonably smooth for both HM bias voltage and synthesizer power; tuning by the PLL gain level is even smoother. Note that all dependences are very well reproducible. Thus it seems that fine-tuning of HM regimes may be accomplished during the flight remotely by simple algorithms. It is important that phase locking regime can be automatically restored if the HM mode is adjusted to one of the optimal peaks.

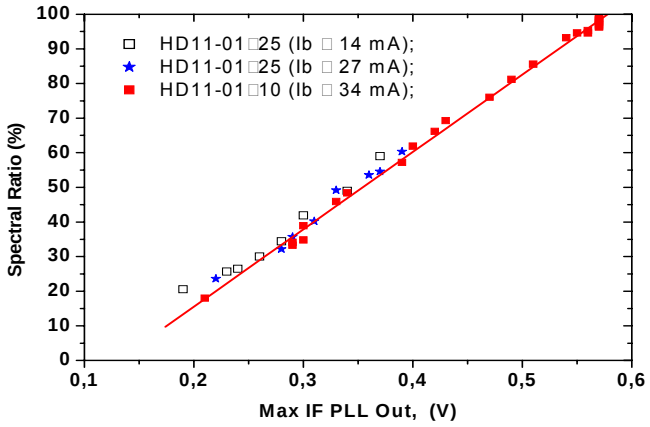

Fig. 9. Spectral ratio of the PL FFO on IF level output of the PLL system measured for the FFOs of different design.

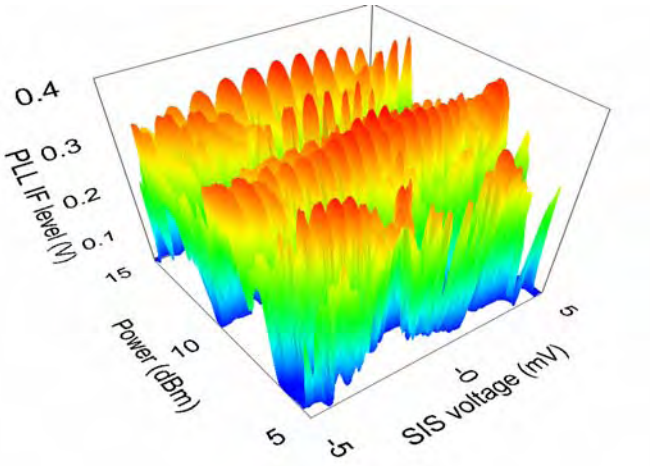

Fig. 10. 3-D diagram for HM operational parameters measured by PC controlled PLL. The level of IF-out PLL signal is represented by color scale; note that normal PL operation is possible at IF levels larger than 250 mV.

VI. Retrieval: Influence of FFO Spectrum Imperfection

The output mixer product depends on FFO spectral properties. Initial source spectrum is distorted due to FFO spectrum imperfections. To assess the impact of an imperfect FFO spectrum on trace gas profile retrieval in TELIS a model based on the SMART retrieval code (Sub Mm Atmospheric Retrieval of Trace gases) is used. The basic of the SMART is as follows: a database contains spectroscopic information of many trace gases present in the atmosphere. When the value of density or volume-mixing ratio is given, as well as temperature, pressure and viewing geometry a synthetic spectrum can be calculated [13]. This so-called forward model has been verified and validated in the ASUR (Airborne Sub-millimeter SIS Radiometer) project. Retrieval simulations are performed by "creating" a SMART spectrum and its comparison with a measured one. So in this retrieval model the good prior knowledge is used.

In the case when the prior knowledge about measured spectrum is absent different deconvolution methods can be used. We tested one of them (Fourier-quotient method). This

method often leads to an ill-posed problem [14]. For example this method cannot be used for present frequency locked FFO, because of strong noise amplification after deconvolution. However our calculations show, that all retrieval methods work well enough in the case of PL FFO spectra with SR > 50%. Noise is "amplified" by approximately a factor of two (see Fig. 11); for these calculations we added Gaussian noise at the SIR output (T_{Add} = 1 K). This added noise corresponds to SSB noise temperature of the SIR = 1000 K, 1 MHz band and integration time of 1 sec. In flight FFO spectrum is not exactly known. To simulate this situation different PL FFO spectra are used for the forward convolution while retrieval calculations are made for one spectrum with SR = 80.4% (see Fig. 12). For the realistic added noise T_{Add} = 0.4 K the 2% uncertainty in the SR value results in less than 2 % error after deconvolution.

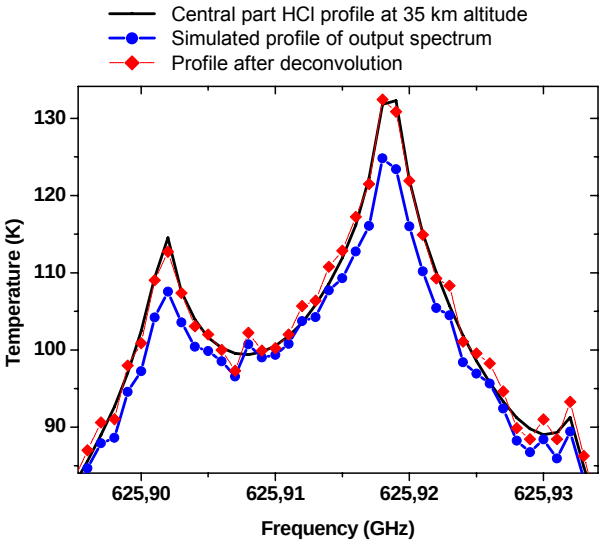

Fig. 11 Results of deconvolution of HCl line. Solid line - input spectrum (central part of HCl spectrum at altitude 35 km). Circles – simulated output spectrum (convolution of the input spectrum with spectrum of PL FFO, SR=80.4 %, plus added gaussian noise T = 1 K). Diamonds - result of deconvolution of simulated output spectrum with spectrum of PL FFO.

VII. Conclusion

The concept of the PL SIR for TELIS has been experimentally proven. New generation of the SIR microcircuits for TELIS has been developed and preliminary tested, showing a performance approaching to TELIS requirements.

Acknowledgment

Authors thank Thijs de Graauw and Avri Selig for fruitful and stimulating discussions as well as Vladimir Vaks, Victor Khodos, Oleksandr Pylypenko and Dimitry Paveliev for development of the dedicated components for TELIS.

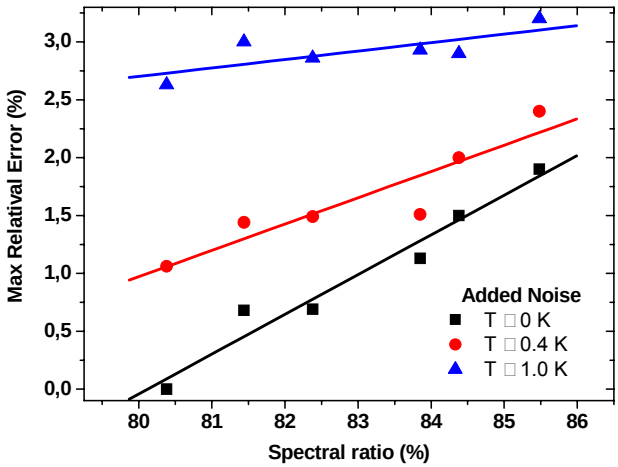

Fig. 12. Results of deconvolution (retrieval model) of the HCL line with experimentally measured PL FFO spectrum (SR=80.4%) for three different temperature of added noise. In forward model the experimental PL FFO spectra with SR from 80.4% to 85.5% are used.

References

[1] U. Mair *et al*, "TELIS – development of a new balloon borne THz/submm heterodyne limb sounder," presented at the 13-th International Symposium on Space Terahertz Technology, Harvard University, March 26-28, 2002.

[2] V. P. Koshelets and S. V. Shitov, "Integrated Superconducting Receivers," *Superconductor Science and Technology*, vol. 13, pp. R53-R69, 2000.

[3] T. Nagatsuma, K. Enpuku, F. Irie, and K. Yoshida, "Flux-flow type Josephson oscillator for mm and submm wave region," *J. Appl. Phys.*, vol. 54**,** p. 3302, 1983, see also Pt. II: *J. Appl. Phys.* vol. 56**,** p. 3284, 1984; Pt. III, *J. Appl.*

[4] V. P. Koshelets *et al.*, "Flux Flow Oscillators for Sub-mm Wave Integrated Receivers," *IEEE Trans. on Appl. Supercond.*, vol. 9, no. 2, pp. 4133-4136, 1999.

[5] V. P. Koshelets *et al*, "Towards a Phase-Locked Superconducting Integrated Receiver: Prospects and Limitations," *Physica C*, vol. 367, pp. 249-255, 2002.

[6] S. V. Shitov *et al.*, "An Integrated Receiver with Phase-Locked Superconducting Oscillator," *IEEE Trans. on Appl. Supercond.y*, vol. 13, no. 2, pp. 684-687, June 2003.

[7] V. P. Koshelets *et al.*, "Radiation Linewidth of Flux-Flow Oscillators", *Supercond. Sci. Technol.*, vol. 14, p. 1040 - 1043, 2001.

[8] V. P. Koshelets *et al.*, "Superconducting Integrated Receiver for TELIS", *IEEE Trans. on Appl. Supercond.y*, vol. 15, no. 2, June 2005..

[9] A.B. Ermakov, S.V. Shitov, A.M. Baryshev, V.P. Koshelets, W. Luinge, "A data acquisition system for test and control of superconducting integrated receivers", *IEEE Trans. on Appl. Supercond.*, **v.11,** No 1, pp. 840-843, (2001).

[10] V. P. Koshelets *et al.*, "Optimization of the Phase-Locked Flux-Flow Oscillator for the Submm Integrated Receiver", *IEEE Trans. on Appl. Supercond.y*, vol. 15, no. 2, June 2005.

[11] V. P. Koshelets *et al.*, "Superconducting Phase-Locked Local Oscillator for Submm Integrated Receiver", *Supercond. Sci. Technol.*, vol. 17, p. 127-131, 2004.

[12] V. P. Koshelets, S. V. Shitov, A. V. Shchukin, L. V. Filippenko, J. Mygind, and A. V. Ustinov, "Self-Pumping Effects and Radiation Linewidth of Josephson Flux Flow Oscillators", *Phys Rev B*, vol. 56, p. 5572-5577, 1997.

[13] R. Hoogeveen, "Impact of FFO spectrum on trace gas retrievals," Technical note, TLS-SRON-TN-2004-027, Jan 2005.

[14] J. L. Starck, E. Pantin and F. Murtagh, "Deconvolution in Astronomy: A Review", Publications of the Astronomical Society of the Pacific, **v. 114**, 1051–1069, October 2002

Multi-Anode Frequency Triplers at Sub-Millimeter Wavelengths

Alain Maestrini, Charlotte Tripon-Canseliet, John Ward, Hamid Javadi, John Gill, Goutam Chattopadhyay, Erich Schlecht, and Imran Mehdi

***Abstract*—We report on the design methodology of fix-tuned split-block waveguide balanced frequency triplers working at 300, 600 and 900 GHz. They feature four to six GaAs Schottky planar diodes in a balanced configuration. A 6-anode 300 GHz tripler, a 6-anode 560 GHz tripler and a 4-anode 900 GHz tripler will be fabricated with JPL membrane technology in order to minimize dielectric loading and ensure accurate thickness of the substrate. A 4-anode 600 GHz tripler was fabricated with JPL substrateless technology that delivers 0.8-1.6mW in the 540-640 GHz band at room temperature. When cooled to 120K this tripler delivers 2-4mW from 540 to 640 GHz.**

***Index Terms*—local oscillator, varactor, Schottky diode, frequency multiplier, frequency tripler, submillimeter wavelength.**

I. Introduction

WIDE BAND frequency triplers with high efficiency are highly desirable to build THz sources based on a cascade of frequency multipliers. A demonstration of the feasibility of a ×2×3×3 chain in the band 1.7-1.9 THz has already been presented in [1]. The present paper will discuss the design methodology of wideband multiple anode triplers. Focus will be put on a 260-340 GHz fixed-tuned tripler that will be used as the first stage of a future ×3×3×3 chain to 2.7 THz. Similar multipliers have been designed for higher frequencies: a 6-anode 510-590 GHz tripler and a bias-able 4-anode 900 GHz tripler that will be used as the second stage of a future 2.7 THz chain. The integrated circuits for these multipliers are currently being fabricated in the JPL Micro Device Laboratory. A 4-anode 540-640 GHz balanced tripler has already been fabricated with JPL substrateless technology and delivers 0.8-1.6mW in the 540-640 GHz band at room temperature [2].

II. Accurate 3D modeling of the multipliers

Since the mid-90's works of Tuovinen, Erickson [3] and Hesler [4] on the design of millimeter and submillimeter-wave multipliers and mixers using commercial 3D field solvers such as Ansoft HFSS, the accuracy of the calculations has been greatly enhanced, in part by the improvement of the codes themselves but much more by the exponential increase in computer processing speed and memory. It is now possible to resolve very fine details of the multipliers with a ratio in excess of 1:10,000 between the smallest and the largest dimensions. This capability is of prime importance to model details such as the passivation layers with thickness typically ranging between 0.1 and 0.3 µm, depending on the process, or to model the air-bridges which are only one to a few micrometers wide. Other dimensions of the same circuit can reach a millimeter or more. The definition of the micro-coaxial probe, used as an Ansoft HFSS wave-port to measure the fields and calculate the impedance seen at the exact location of the Schottky contact [4], also requires very fine details. In our model we included the passivation layers and we set the gap between the inner and the outer conductor of the micro-coaxial probe to 0.1 µm to accurately model the parasitic capacitance of the Schottky diode.

III. Topology and design steps for wide band frequency triplers

1. Topology: the triplers are split-block waveguide designs that feature four to six Schottky planar varactor diodes, monolithically fabricated on a GaAs-based substrate (3 to 5 µm thick membrane or 12 µm thick for a "substrateless" device) and connected in series at DC (see Fig. 1). The chips are inserted between the input and the output waveguides in a channel. An E-plane probe located in the input waveguide couples the signal at the fundamental frequency to a suspended microstrip line that can propagate only a quasi or true TEM mode (depending on the design, dielectric may or may not be present in the channel). This line has several sections of low and high impedance used to match the diodes at the input and output frequency and to prevent the third harmonic from leaking into the input waveguide. The third harmonic produced by the diodes is coupled to the output waveguide by a second E-plane probe.

Inside the chip-channel, the circuit is symmetrical except for small asymmetries introduced by the physical structure of the Schottky diodes. Given the symmetry of the excitation, the odd harmonics are generated on a TEM mode and the even harmonics are trapped in a virtual loop (the line of diodes) provided that the suspended microstrip line cuts-off the parasitic TE mode. More detail about this topology can be found in [5].

A. Maestrini is with Laboratoire des Instruments et Systèmes d'Ile de France - Université Pierre et Marie Curie, 4 place Jussieu, case 252, 75252 Paris cedex 5, France, and is associated with Laboratoire d'Etude du Rayonnement et de la Matière en Astrophysique, Observatoire de Paris, France. Email : alain.maestrini@lisif.jussieu.fr

J. Ward, J. Gill, H. Javadi, E. Schlecht, G. Chattopadhyay, I. Mehdi are with the Jet Propulsion Laboratory, California Institute of Technology, MS 168-314, 4800 Oak Grove Drive, Pasadena, CA 91109, USA.

C. Tripon-Canseliet is with LISIF - Université Pierre et Marie Curie, France.

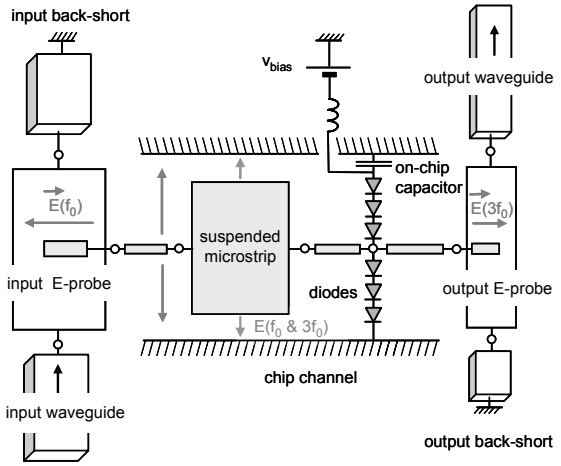

Fig. 1: block diagram of the 300 GHz balanced tripler. Inside the chip channel, only a quasi-TEM mode can propagate at all the frequencies of interest.

2. Design method: detailed explanations of the design methodology are given in [2]. In summary, the first step is to optimize the diode cell that consists of the part of the circuit that includes the diodes, a section of the chip-channel and two sections of the propagating line at the center of the chip (see Fig. 2). The optimization is performed using 3D electromagnetic codes like Ansoft HFSS and harmonic-balance codes like Agilent ADS. The optimum diode junction capacitance and bias voltage are determined at the same time.

This optimization is performed for a given input power and output frequency. The doping level is crucial because it defines the breakdown voltage which is the main parameter that controls the power handling capability per anode. Time domain non-linear simulations have been performed to check the waveform of the voltage across the diodes in order to determine the maximum input power and optimum bias voltage. For our 6-anode 300 GHz tripler and our 6-anode 560 GHz tripler the design doping is $2 \cdot 10^{17}$ cm^{-3} to allow 70 to 80 mW of input power to be safely handled. The doping for the 4-anode 600 GHz is $1 \cdot 10^{17}$ cm^{-3} to allow 100 to 120 mW to be safely handled. For the 4-anode 900 GHz tripler the doping is $5 \cdot 10^{17}$ cm^{-3}, which will limit the maximum safe input power to the 15 to 18 mW range.

The second step is to optimize the input and output matching circuit using on-chip and waveguide matching elements. This is done by first optimizing the circuit at the center of the band of interest using non-linear simulations. A minimum of matching elements is used. The bandwidth is then extended by adding to the input and output waveguides a succession of sections of high and low impedances. As the matching circuit in the input and output waveguide are independent, it is possible to use linear simulations.

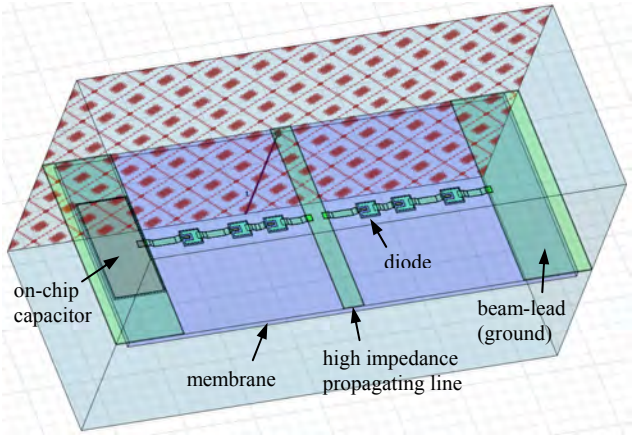

Fig. 2: diode cell used to optimize the channel cross-section dimensions, the location of the 6 anodes and the air-bridge size. One of the HFSS ports is shown in the back side of the diode cell.

3. Design of a high efficiency wideband 300 GHz tripler: using this methodology, we designed a high power 6-anode 260-340 GHz tripler to be used to drive a 2.7 THz LO chain (see Fig. 3). The expected peak efficiency is 12% at room temperature with a -3dB bandwidth of 25%. A very good balance between the diodes at the input and the output frequencies has been successfully achieved (see Fig. 4). The performance is expected to greatly increase upon cooling: at 120K, the conversion efficiency of the multiplier is expected to reach 20% at 300 GHz.

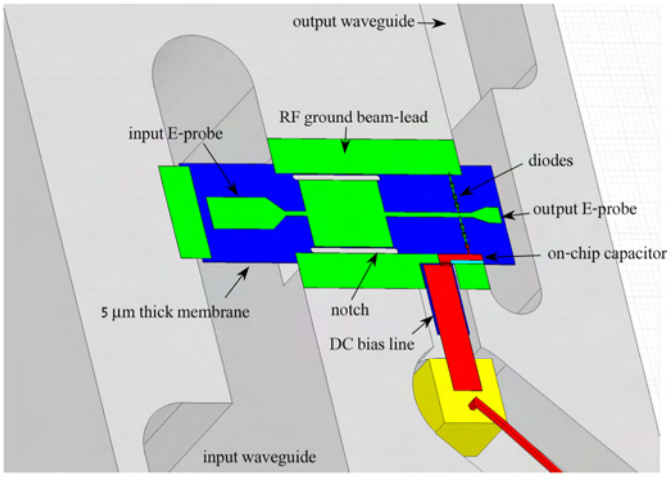

Fig. 3: 3D view of the bottom part of the waveguide block with the 260-340GHz tripler chip installed. The device is fabricated on a 5µm thick GaAs membrane substrate. It features 6 Schottky diodes in a balanced configuration. The chip is held by two beam leads. RF grounding and DC reverse bias are provided using an on-chip capacitor. The complete input matching waveguide-circuit (not shown) consists of several reduced-height rectangular waveguide sections and several standard-height rectangular waveguide sections. The waveguide backshorts and steps are not represented to their optimized positions.

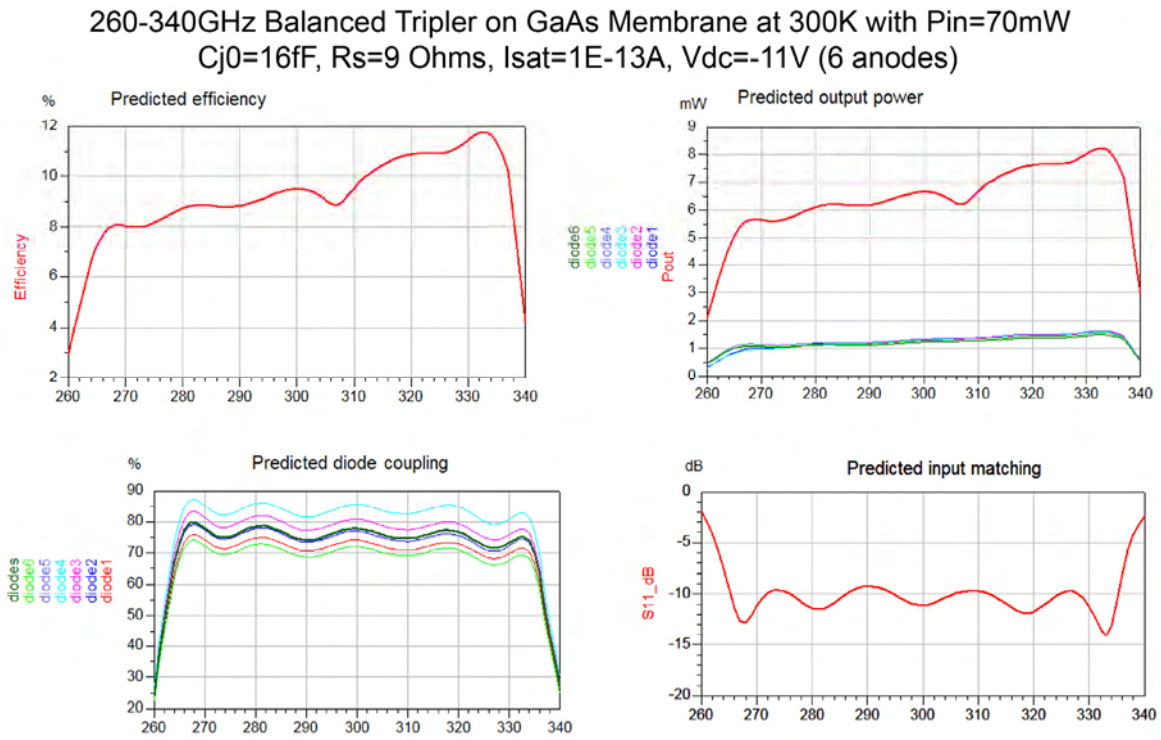

Fig. 4: Predicted performance of the 6-anode 260-340GHz balanced tripler at room temperature with 70 mW of input power. When cooled to around 120K the conversion efficiency of the multiplier is expected to reach 20% at 300 GHz. The coupling at the input frequency is calculated for each diode (left and bottom curves). The calculated output power per diode is shown on the right and top curves along with the total output power.

Conclusion

In recent years, tremendous progress has been made in the design methodology and the fabrication of submillimeter Schottky diode-based circuits. We recently demonstrated a wideband high power 540-640 GHz balanced tripler which concept was used to design a family of next-generation balanced triplers using up to 6 anodes and for frequencies ranging from 300 GHz to 900 GHz.

Acknowledgements

The authors are grateful for the helpful technical discussions with Dr. Peter Siegel and Dr. John Pearson. The research described in this publication was carried out in part at the Jet Propulsion Laboratory, California Institute of Technology, under a contract with the National Aeronautics and Space Administration.

References

[1] A. Maestrini, J. Ward, J. Gill, H. Javadi, E. Schlecht, G. Chattopadhyay, F. Maiwald, N.R. Erickson, and I. Mehdi, "A 1.7 to 1.9 THz Local Oscillator Source," *IEEE Microwave and Wireless Components Letters*, Vol. 14, no. 6, pp. 253-255, June 2004.

[2] A. Maestrini, J. Ward, J. Gill, H. Javadi, E. Schlecht, C. Tripon-Canseliet, G. Chattopadhyay and I. Mehdi, "A 540-640 GHz High Efficiency Four Anode Frequency Tripler," to be published in IEEE-MTT, 2005.

[3] J. Tuovinen, N.R. Erickson, "Analysis of a 170 GHz frequency doubler with an array of planar diodes," *IEEE Trans. Microwave Theory Tech.*, Vol. 43, no. 4, pp. 962–968, April 1995.

[4] J. Hesler, "Planar Schottky diodes in submillimeter-wavelength waveguide receivers," Ph.D. dissertation, faculty of the School of Engineering and Applied Science, University of Virginia, January 1996.

[5] S.A. Maas, "Non-linear Microwave Circuits," Artech House, 1988.

Design, Fabrication and Characterisation of High Power HBV Diodes

Tahereh Arezoo Emadi*, Josip Vukusic†, Mattias Ingvarson*, Mahdad Sadeghi*,
Tomas Bryllert*, Arne Øistein Olsen* and Jan Stake*
*Department of Microtechnology and Nanoscience, Microwave Electronics Laboratory,
Chalmers University of Technology, SE-412 96 Göteborg, Sweden
Email: arezoo.emadi@mc2.chalmers.se
Telephone: +46 31 7721836
Fax: +46 31 164513
†Université des Sciences et Technologies de Lille,
Institut d'Electronique de Micro-électroniqueet de Nanotechnologie,
Département hyperfréquences et semi-conducteurs, France

***Abstract*— We present design and analysis of material structures and device geometries for heterostructure barrier varactor diodes (HBVs) for high-power frequency multipliers. The methods aim at finding optimum epitaxial layer structures with respect to diode power handling capability and efficiency. A distributed device geometry for further increasing the output power levels whilst maintaining acceptable device temperatures is also presented. Finally, an electro-thermal HBV model with the ability of incorporating temperature-dependent device parameters is used to simulate the introduced devices, followed by a design example of a 3×4-barrier high-power HBV diode.**

I. Introduction

Applications in the millimeter wavelength range have in the last decades increased, e.g. radio astronomy, high-speed wireless communications, medical and biological imaging and surveillance systems, but a major problem at these frequencies is the lack of power sources. One promising approach is to use a frequency multiplier [1] with high-power heterostructure barrier varactors (HBVs) [2], [3], as HBVs use a heterojunction as a blocking element and therefore several barriers can be grown epitaxially, to increase the breakdown voltage and thereby the power handling capacity. This property favors HBVs rather than Schottky diodes for high-power, high-order frequency multiplication [4], [5]. The vast majority of HBV multipliers this far have been tripler circuits and efficiencies of 12% at the output frequency of 250 GHz in InP-based system have been achieved [6], [7].

State-of-the-art high-frequency HBVs are fabricated using $In_{0.53}Ga_{0.47}As/In_{0.52}Al_{0.48}As$ on semi-insulating InP substrates [8]. This system offers higher electron velocities and mobilities compared to GaAs-based systems, which means lower series resistance and higher conversion efficiency. For higher input powers more barriers need to be stacked, resulting in a comparatively thick epitaxial layer. However, because of the strong correlation between HBV performance and material properties, the main difficulty is to maintain a high quality when growing thick epitaxial layers. Also, in high-power applications, a large amount of input power is dissipated as heat in the devices, resulting in high temperatures, causing high leakage currents and self-heating problems in HBVs [9]. The main disadvantage of using an InP lattice matched system in high-power applications is the poor thermal conductivity that causes a high temperature inside the mesa, leading to a lower efficiency [10]. Therefore the maximum allowable absorbed power per barrier is limited by the maximum acceptable temperature inside the mesa. One solution could be to fabricate HBVs on substrates having a higher thermal conductivity [11], or to apply a distributed topology structure that improves the heat transfer through the device patterned on an InP-based [12]. We here introduce parameters important for the diode performance for high-power applications, and present design methods for epitaxial layer structures, circuits, materials and geometries in order to reach high power handling capabilities and diode efficiencies. In order to assess and analyze the designs, we perform simulations using an electro-thermal model which updates the device temperature and temperature-dependent device parameters self-consistently [13]. Finally, we present a 3-barrier HBV material, Chalmers MBE995, designed for high output power level, with a wide and smooth I-V curve and a maximised elastance swing which would result in higher efficiency.

II. Device Model

A. Basic Principle

A general InP-based HBV layer structure is shown in Table I. The modulation and barrier layers consist of InGaAs and InAlAs, respectively. The layer sequence 2-5 can be repeated N times to create an N-barrier HBV. This structure with a pseudomorphic (3nm) AlAs layer in the center of the barrier has a high potential barrier, resulting in a very low leakage current [14].

The performance of a varactor device is associated with the dynamic cut-off frequency, f_c, which determines the conversion efficiency [15].

$$f_c = \frac{S_{max} - S_{min}}{2\pi R_s} \tag{1}$$

TABLE I
A TYPICAL ONE-BARRIER HBV LAYER STRUCTURE

Layer No.	Layer	Thickness [nm]	Doping level [cm^{-3}]
7	Contact	200	$\sim 10^{19}$
6	Modulation	400	6×10^{16}
5	Spacer	5	undoped
4	Barrier	20	undoped
3	Spacer	5	undoped
2	Modulation	400	6×10^{16}
1	Buffer	500	$\sim 10^{19}$
	Substrate		

where S_{max} and S_{min} are the maximum and minimum elastance, respectively, during a pump cycle and R_s is the series resistance.

For a typical HBV the parallel plate capacitor model can be used to estimate the elastance,

$$S = \frac{1}{C} = \frac{N}{A}\left(\frac{b}{\varepsilon_b} + \frac{2s}{\varepsilon_d} + \frac{w}{\varepsilon_b}\right) \tag{2}$$

Here N is the number of barriers, A is the cross sectional area, b, ε_b, s and ε_d are the thickness and permittivity of the barrier and spacer layer, respectively, and w is length of the depleted region.

The series resistance is voltage-dependent through the extension of the depleted region and also depends on the device geometry, material parameters and the temperature. For a planar HBV with two series-connected mesas, Figure 1, the series resistance can be estimated as

$$\begin{aligned} R_s(T) = {} & R_{mesa}(T) + R_{buffer}(T) + R_{cl}(T) \\ & + R_c + R_{finger} \end{aligned} \tag{3}$$

where R_{mesa} is the resistance of the layers inside the mesa, R_{buffer} is the spreading resistance in the buffer layer, R_{cl} is the resistance of the contact layers, R_c is the ohmic contact resistance, and R_{finger} is the resistance of the air bridges.

Any of these resistances can be calculated as

$$R = \frac{t}{A\sigma} \tag{4}$$

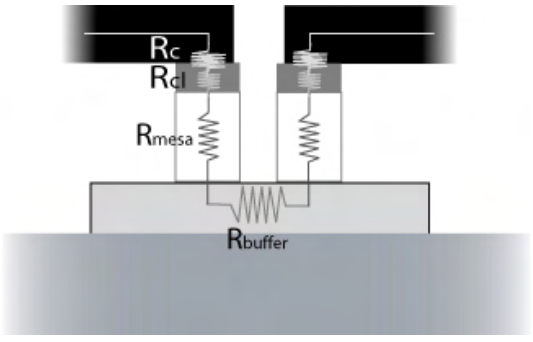

Fig. 1. Contributions to the series resistance of a planar HBV diode.

where t is the thickness and σ is the electrical conductivity of the layer. The electrical conductivity depends on the doping concentration and the electron mobility as

$$\sigma = q \cdot N_d \cdot \mu_e(N_d, T) \tag{5}$$

where $\mu_e(N_d, T)$ is the electron low-field mobility, calculated from the following empirical model [16]

$$\mu_e(N_d, T) = \mu_{min} + \frac{\mu_{max}(T_0)(\frac{T_0}{T})^{\theta_1} - \mu_{min}}{1 + \left(\frac{N_d}{N_{ref}(T_0)(\frac{T}{T_0})^{\theta_2}}\right)^{\lambda}}. \tag{6}$$

Here μ_{min}, μ_{max}, N_{ref}, λ, θ_1 and θ_2 are fitting parameters available for most common III-V materials, and $T_0 = 300K$.

B. Electro-Thermal Model

Simple analytical expressions can be used for initial estimations and investigations about thermal properties, but in order to properly design and analyze HBVs, especially for high-power applications, it is necessary to employ combined electrical and thermal simulations. Here we demonstrate the use of an electro-thermal model, implemented in Agilent Advanced Design System (ADS) [13].

The voltage across an HBV as a function of the charge Q stored in the device is calculated from the quasi-empirical Chalmers HBV model [17]

$$\begin{aligned} \frac{V(Q)}{N} = {} & \frac{bQ}{\varepsilon_b A} + 2\frac{sQ}{\varepsilon_d A} \\ & + \text{Sign}(Q) \cdot \left(\frac{Q^2}{2qN_d\varepsilon_d A^2} \right. \\ & \left. + \frac{4k_B T}{q}\left(1 - exp\left[- \frac{|Q|}{2L_D A q N_d} \right]\right)\right) \end{aligned} \tag{7}$$

where k_B is the Boltzmann constant, q is the elementary charge, and L_D is the intrinsic Debye length. The displacement current is

$$i(t) = \frac{\partial Q}{\partial t}. \tag{8}$$

For GaAs-based HBVs that exhibit relatively low effective barrier height, the conduction current is dominated by thermionic emission [9], [17], but for InP-based HBV devices, the current transport is rather dominated by electron tunnelling through the barrier.

By using an equivalent electro-thermal circuit, the device temperature T can be treated like any other control voltage [18]. Now, the electrical properties of an HBV can be modeled with harmonic balance simulations using the equivalent circuit in Figure 2 (left) together with (7), combined with appropriate expressions for the conduction current and the series resistance. The thermal resistance R_{th} is calculated by using 3-D finite element simulations. The thermal capacitance C_{th} models the thermal storage of the device, so that the thermal time constant is $\tau_{th} = R_{th} \cdot C_{th}$.

The thermal properties are modeled with the electro-thermal equivalent circuit displayed in Figure 2 (right). We have implemented the electro-thermal model in ADS by using an extra nonlinear port.

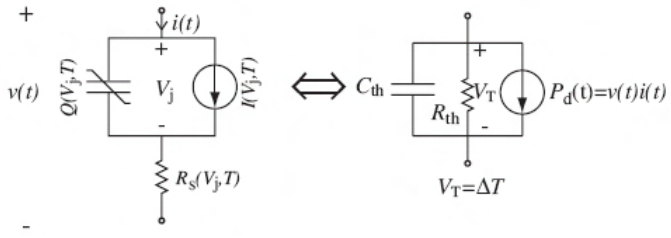

Fig. 2. Electrical equivalent (left) and electro-thermal equivalent circuit model (right) for harmonic balance simulations.

C. Thermal Resistance and Device Geometry

It is obvious that the power handling capacity of the conventional HBV is limited to the maximum allowable temperature inside the active part of the diode for a certain amount of input power [10]. We have calculated the temperature distribution for conventional planar HBVs using 3-D finite element simulations. We assume that 1200 mW is absorbed in the device. The total required number of barriers needed to be able to handle this power level is considered to be 12 [10], which, in a conventional planar HBV, are divided equally into two series-connected mesas, see Figure 3. Since the HBV is to be flip-chip mounted onto the embedding circuitry, only the contacting pads are assumed to be perfectly heat-sunk, and due to symmetry reasons only a quarter of the geometry is displayed.

As can be seen in Figure 3 the maximum rise temperature for this power level is $230°$C, higher than the acceptable level, which is approximately $150°$C.
The thermal resistance, R_{th}, is calculated by using 3-D finite element simulations and equal to the maximum rise temperature divided by the total dissipated power in the device, $R_{th} = 190\ K/W$.

III. Results

A. Distributed Geometry

In order to lower the temperature to an acceptable level, we propose the topology shown in Figure 4 [12]. This geometry consists of 16 mesas, 4 connected in parallel and 4 in series. This gives a thinner epitaxial thickness which is also advantageous from a material growth point of view, since it is difficult to realize a thick, high-quality material in this particular material system.

Figure 4 shows that the maximum temperature has decreased substantially, to $115°$C. This is mainly because of the heat source being distributed over a larger area. The distance between the fingers is larger for the inner pair. This is to avoid a higher temperature on these two fingers compared to the ones at the periphery. Also, in each finger, the two inner mesas are not connected directly, because of the gold pad extending down to the substrate to divert heat more efficiently for the innermost mesas. The distance between two nearest mesas is chosen as short as possible with respect to limitations in processing and parasitic capacitances, since a wider separation increases the series resistance in the structure, and thereby lowers the diode conversion efficiency.
By using 3-D finite element, the thermal resistance is calculated $R_{th} = 100\ K/W$ for this kind of distributed geometry, which is lower than in the case of conventional planar HBV.

B. Epilayer Structure Optimization

The performance of an HBV device depends on the dynamic cut-off frequency, which is the main figure of merit for pure varactor multipliers. Another parameter which influences the device performance is the conduction current, especially in GaAs-based systems. A Poisson/Schrödinger calculation of the current density for a single-barrier InP-based HBV as a function of the barrier thickness shows that the barrier thickness which gives the lowest conduction current by including a thin central AlAs layer inside the barrier is around $20nm$, this thickness for GaAs-based HBV is about $15nm$ [14].

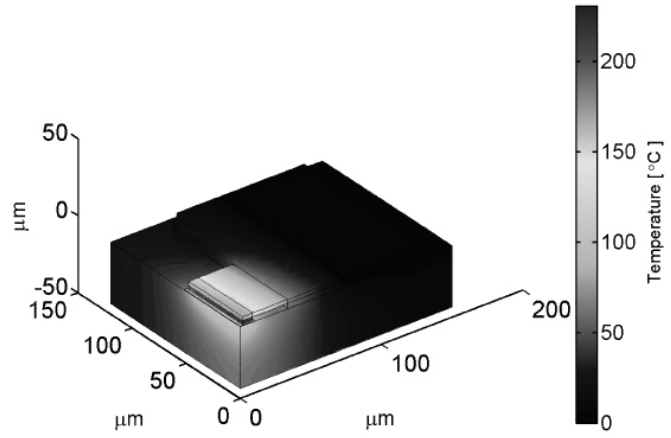

Fig. 3. Temperature distribution for a conventional planar HBV, InGaAs on InP substrate.

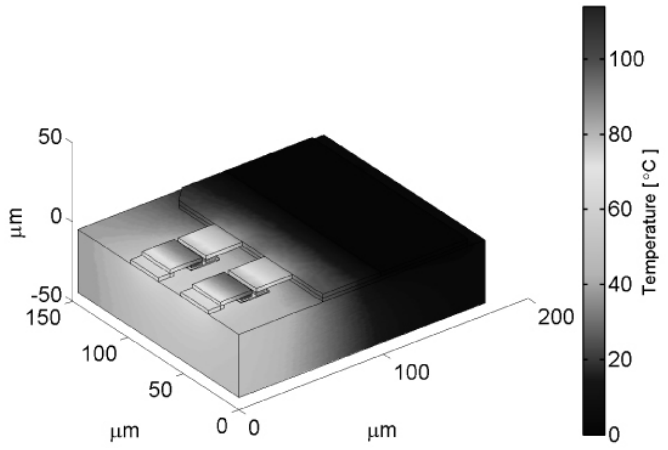

Fig. 4. Temperature distribution for the novel InGaAs on InP HBV, consisting of 16 mesas.

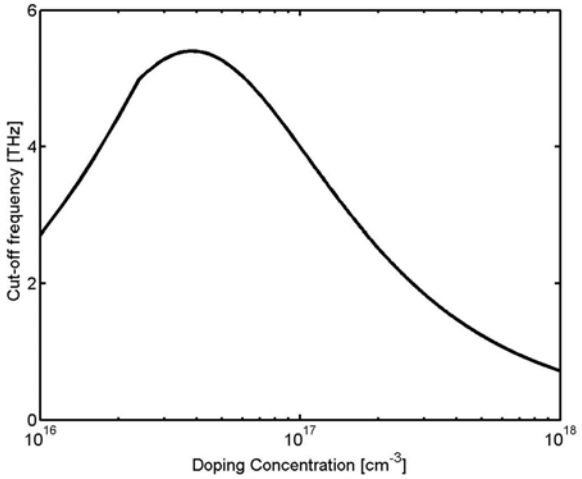

Fig. 5. Cut-off frequency for a 3-barrier planar HBV versus doping concentration.

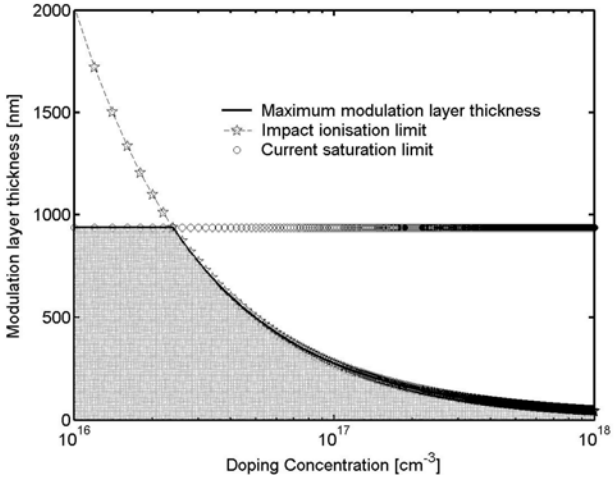

Fig. 6. Maximum modulation layer thickness versus doping for both impact ionization and current saturation conditions.

From (1) it can be seen that for optimizing the efficiency, one should maximize the elastance swing, $S_{max} - S_{min}$, and minimize the series resistance, R_s.

The maximum elastance, S_{max}, is directly proportional to the modulation layer thickness. However, a thicker layer leads to a higher series resistance which results in a lower efficiency. For high-power applications the thickness of the modulation layer is determined by considering impact ionization at high electric fields, while still making sure that it is thinner than current saturation thickness limit [19].

For impact ionization, the maximum modulation layer thickness can be calculated as

$$w_{max} = \frac{\varepsilon_d E_{d,max}}{qN_d} \tag{9}$$

where $E_{d,max}$ is the maximum electric field in the modulation layer at the voltage where breakdown occurs and can be described as

$$E_{d,max} = \frac{a}{1 - b\log\left(\frac{N_d}{N_{d,ref}}\right)} \tag{10}$$

where $a = 3{\times}10^7$, $b = 0.28$ and $N_{d,ref} = 1.5{\times}10^{16} cm^{-3}$ are the fitting parameters for Chalmers MBE InP based materials. Current saturation limits the thickness according to

$$w_{max} \approx \frac{v_{max}}{8 f_p} \tag{11}$$

where v_{max} is the saturated electron velocity [19], [20].

From (1), (2) and (9) we observe a necessary trade-off between doping concentration and thickness of the modulation layer, in order to achieve an optimum cut-off frequency and thereby the highest efficiency. Figure 5 shows how f_c and thereby η vary with doping concentration for a certain number of barriers, in this case a 3-barrier planar HBV with four series-connected mesas distributed in four fingers and a total diode cross sectional area of $700 \mu m^2$, Figure 4.

The modulation layer thickness has been calculated according to (9) for each value of doping concentration so that impact ionization occurs before current saturation. Figure 6 shows the modulation layer thickness versus doping concentration for a 3-barrier material.

The series resistance of the active part of the diode also varies with the doping, where R_{buffer} and R_{mesa} constitute the main contributions to the total resistance, respectively, especially for structures with thin buffers. According to (3), the total resistance can be calculated for a given area and doping concentration value with the respective maximum modulation layer thicknesses.

The device breakdown voltage depends on the doping level and the related maximum modulation thickness, and can be described as

$$V_{BD,max} = N\varepsilon_d E_d \left(\frac{b}{\varepsilon_b} + \frac{2s}{\varepsilon_d} + \frac{w_{max}}{2\varepsilon_d} \right). \tag{12}$$

The breakdown voltage and thereby the power handling capacity can also be increased by increasing the number of barriers, limited by the maximum allowed temperature inside the mesas [10].

C. Design Examples

We now use the presented optimization methods and then the electro-thermal model to further demonstrate the design of high-power HBV diodes. The material structure is optimized for a 100 GHz frequency tripler. We assume the distributed geometry, Figure 4, with 3-barrier mesas and a total cross sectional device area of $A = 700 \mu m^2$. Plot of the cut-off frequency versus the doping concentration obtained from the models presented shows that $N_d = 7{\times}10^{16} cm^{-3}$ gives the highest cut-off frequency. This corresponds to a modulation layer thickness of $370nm$, which is thinner than the current saturation limit, and a total breakdown voltage of $90\ Volt$.

This InP-based material, Chalmers MBE995, has been grown, with a slight difference in doping, $N_d = 1{\times}10^{17}\ cm^{-3}$. To verify the quality, a test diode consisting of one mesa has been

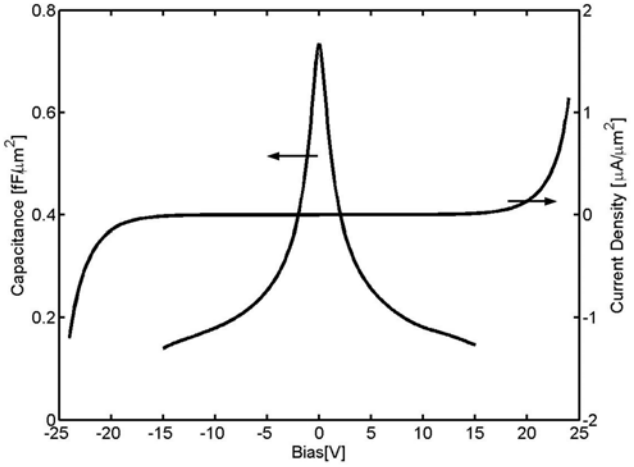

Fig. 7. C-V and I-V for a high power designed material, Chalmers MBE995.

fabricated by using this material, Figure 7 shows C-V and I-V measurements for this 3-barrier diode. This device has a breakdown voltage of $24\ Volt$, and an excellent C_{max}/C_{min} ratio of 5.2.

SEM image of the high power diode with distributed geometry, Figure 4, is shown in Figure 8.

For this material, we have used the electro-thermal model [13]to estimate the diode efficiency and the maximum temperature inside the device for a certain input power level for a pump frequency of 33 GHz.

The series resistance is calculated with (3) with considering four series-connected mesas distributed in four fingers, Figure 4, and assuming $R_c{\cdot}A = 100\mu m^2$ per mesa. The room temperature value is 4Ω and the increase in the series resistance due to self-heating is approximately 14%.

The conversion efficiency excluding circuit losses with and without effect of junction temperature is shown in Figure 9a and the corresponding junction temperature is displayed in Figure 9b. Approximately $2W$ of input power can be handled by this device without reaching the breakdown voltage per barrier or an unacceptable device temperature.

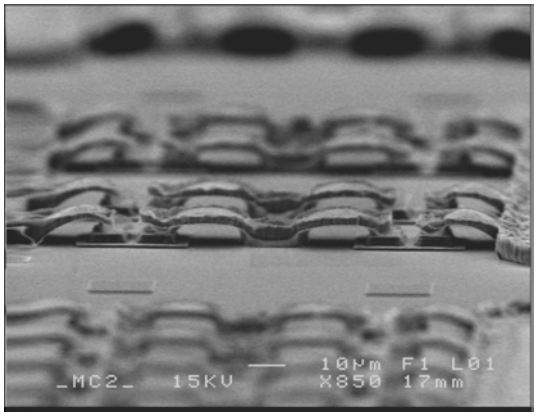

Fig. 8. SEM image of high power HBV diodes.

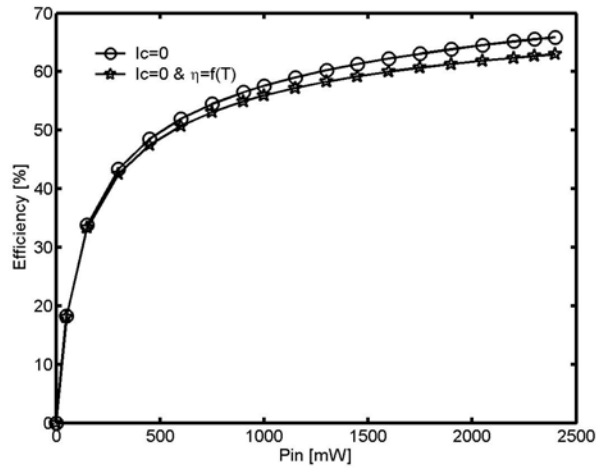

(a)

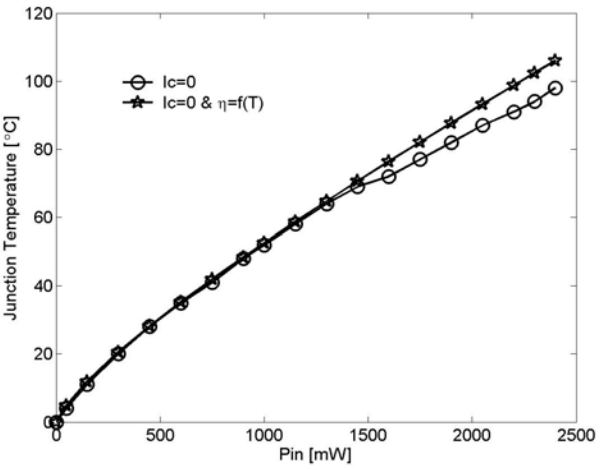

(b)

Fig. 9. Simulated diode efficiency (a) and the corresponding junction temperature (b) for a 12-barrier high-power HBV, Chalmers MBE995, with an area of $A = 700\mu m^2$ distributed in four fingers.

IV. Conclusions

To be able to handle high input power levels with HBV diode multipliers for millimeter and submillimeter wavelength applications, we have presented a device model, a material structure optimization method, and a temperature-dependent electro-thermal model. To further decrease the maximum temperature rise in the device we have also presented a distributed geometry for which thermal calculations show that the maximum temperature is drastically decreased compared to the conventional planar HBV. Finally, using the presented models, a high-power InP-based material has been designed and fabricated. The measured DC characteristics are excellent. The electro-thermal model has been employed to simulate the diode performance of the fabricated material and to further demonstrate the design method.

V. Acknowledgment

This work has been supported by the European Space Agency through the project HBV Devices and MMICs, the Swedish Defence Research Agency, FOI, through the Nano Technology program, the EU INTERACTION program and SSF-HSEP.

References

[1] A. Rahal, E. Boch, C. Rogers, J. Ovey, and R.G. Bosisio. "Planar multi-stack quantum barrier varactor tripler evaluation at W-band". *Electronics Letters*, 31(23):2022 – 3, 1995.

[2] E. Kollberg and A. Rydberg. "Quantum-barrier-varactor diodes for high-efficiency millimetre-wave multipliers". *Electronics Letters*, 25(25):1696 – 1698, 1989.

[3] S.M. Nilsen, H. Groenqvist, H. Hjelmgren, A. Rydberg, and E.L. Kollberg. "Single barrier varactors for submillimeter wave power generation". *IEEE Transactions on Microwave Theory and Techniques*, 41(4):572 – 579, 1993.

[4] T.W. Crowe, W. Peatman, P. Wood, and X. Liu. "GaAs Schottky barrier diodes for THz applications". *IEEE MTT-S International Microwave Symposium Digest*, 2:1141 – 1144, 1992.

[5] N.R. Erickson. A 1650-1900 GHz tuneable source. In *Proceeding of the 14th International Symposium Space Terahertz technology*, pages 64–72, 2003.

[6] R. Meola, J. Freyer, and M. Claassen. "Improved frequency tripler with integrated single-barrier varactor". *Electronics Letters*, 36(9):803 – 804, 2000.

[7] X. Melique, A. Maestrini, P. Mounaix, M. Favreau, O. Vanbesien, J.M. Goutoule, G. Beaudin, T. Narhi, and D. Lippens. Record performance of a 250 GHz InP-based heterostructure barrier varactor tripler. *Electronics Letters*, 35(11):938–939, 1999.

[8] T. Bryllert, A.Ø. Olsen, J. Vukusic, T.A. Emadi, M. Ingvarson, J. Stake, and D. Lippens. "11% efficiency 100 GHz InP-based heterostructure barrier varactor quintupler". *Electronics Letters*, 41(3):131 – 132, 2005.

[9] J. Stake, L. Dillner, S.H. Jones, C. Mann, J. Thornton, J.R. Jones, W.L. Bishop, and E. Kollberg. "Effects of self-heating on planar heterostructure barrier varactor diodes". *IEEE Transactions on Electron Devices*, 45(11):2298 – 303, 1998.

[10] M. Ingvarson, B. Alderman, A.Ø. Olsen, J. Vukusic, and J. Stake. "Thermal constraints for heterostructure barrier varactors". *IEEE Electron Device Letters*, 25(11):713 – 15, 2004.

[11] L. Dillner, J. Stake, and E.L. Kollberg. "Heterostructure barrier varactors on copper substrate". *Electronics Letters*, 35(4):339 – 41, 1999.

[12] T.A. Emadi, J. Vukusic, M. Ingvarson, A.O. Olsen, T. Bryllert, E. Kollberg, and Jan Stake. "High power HBV multipliers for F- and G- band applications". *Conference Digest of the 2004 Joint 29th International Conference on Infrared and Millimeter Waves and 12th International Conference on Terahertz Electronics*, pages 319 – 320, 2004.

[13] M. Ingvarson, J. Vukusic, A.Ø. Olsen, T.A. Emadi, and J. Stake. An electro-thermal HBV model. *Accepted to International Microwave Symposium*, 2005.

[14] Y. Fu, J. Stake, L. Dillner, M. Willander, and E.L. Kollberg. "AlGaAs/GaAs and InAlAs/InGaAs heterostructure barrier varactors". *Journal of Applied Physics*, 82(11):5568 – 72, 1997.

[15] P. Penfield and R.P Rafuse. V*aractor Applications*. The M.I.T. Press, 1962.

[16] M. Sotoodeh, A.H. Khalid, and A.A. Rezazadeh. "Empirical low-field mobility model for III-V compounds applicable in device simulation codes". *Journal of Applied Physics*, 87(6):2890 – 2900, 2000.

[17] L. Dillner, J. Stake, and E.L. Kollberg. Modelling of the heterostructure barrier varactor diode. In *Procceding of the International Semiconductor Device Research Symposium*, pages 179–182, 1997.

[18] S.A. Mass. N*onlinear* M*icrowave and* RF C*ircuits*. Artech House, 2nd edition, 2003.

[19] E.L. Kollberg, T.J. Tolmunen, M.A. Frerking, and J.R. East. Current saturation in submillimetre-wave varactors. *IEEE Transaction on Microwave Theory and Techniques*, 40(5):831–838, 1992.

[20] J. Stake, S.H. Jones, L. Dillner, S. Hollung, and E.L. Kollberg. "Heterostructure-barrier-varactor design". *IEEE Transactions on Microwave Theory and Techniques*, 48(4, pt.2):677 – 82, 2000.

Beam Pattern Measurements on Quantum Cascade Lasers Operating at 2.8 THz

Aurèle J.L. Adam, J. Niels Hovenier, Irmantas Kasalynas, Tjeerd O. Klaassen, Jian-Rong Gao, Benjamin S. Williams, Sushil Kumar, Qing Hu, Ekaterina E. Orlova and John L. Reno

***Abstract*—Quantum cascade lasers operating in the THz region are of great potential interest as local oscillators for THz heterodyne detection. To assess the applicability of this new source as LO, a study of the properties of the emitted radiation, like beam shape and optical phase front, is very important. In this paper we will present results of the beam profile of 'metal-metal' cavity QCL's using the conical section method, designed for spherical antenna pattern measurements. It appears that, contrary to earlier waveguide based simulations, the beam patterns show strong angular intensity oscillations.**

***Index Terms*—Beam profile, Local oscillator, Quantum cascade laser, THz radiation**

I. Introduction

THE development of TeraHertz technology has been severely hindered by the lack of versatile sources. For long, one had to rely on bulky optically pumped far-infrared lasers or on complicated systems based on either frequency *multiplication* of high frequency microwave radiation (typically 80–100GHz) or on generation of radiation at the frequency *difference* of two (VIS/NIR) diode lasers. The quest for new sources has resulted recently in the development of the Quantum Cascade Laser (QCL) [1]. After the first demonstration of emission in the mid-infrared range ($\lambda \approx 4$ μm; 75 THz)[2], now Quantum Cascade Lasers (QCL) are operating CW in the THz range, down to 2.1 THz ($\lambda \approx 143$ μm)[3]. These sources are very promising as local oscillators for heterodyne detection, especially for frequencies above 2 THz where the usual frequency multiplier systems do not provide enough output power. In order to use the QCL for that purpose, apart from the frequency and power stability, one also needs to investigate the pattern of the emission beam. This latter issue is very important because, in order to keep the electrical dissipation of these cryogenic devices low, the dimensions of the active region should be reduced as much as possible. As a result, the dimensions of the waveguide cavity may turn out to be of the order of, or even smaller than, the emission wavelength. We will report for instance on the beam pattern of a QCL, emitting at $\lambda = 107$ μm, with a 650 x 25 x 10 μm^3 metal-metal cavity. A set-up has been build to measure the beam pattern of QCL's in the near- and far field region. It consists of a Helium flow cryostat with optical windows, offering a wide angle of view (up to 120º full cone angle). The THz intensity is measured using a pyroelectric detector, mounted on a two-axis rotation system. We will report on beam patterns of QCL bars with a metal-metal cavity of various dimensions, emitting at 2.8 THz.

A.J.L. Adam, J.N. Hovenier, I. Kasalynas, T.O. Klaassen and J.R. Gao are with the Kavli Institute of NanoScience, Faculty of Applied Sciences, Delft University of Technology, Lorentzweg 1, 2628 CJ Delft, The Netherlands. (phone:+31.15.2786136 ; fax:+31.15.2783251;e-mail: t.o.klaassen@tnw.tudelft.nl)

B.S. Williams, S. Kumar and Q. Hu are with the Department of Electrical Engineering and Computer Science and Research Laboratory of Electronics, Massachusetts Institute of Technology, Cambridge MA 02139, U.S.A.

E.E. Orlova is with the Institute for Physics of Microstrucutres, Russian Academy of Sciences, GSP-105, 603950 Nizhny Novgorod, Russia

J. L. Reno is with the Sandia National Laboratories, Albuquerque, NM 87185-0601, U.S.A

II. THz. Laser samples

A number of different design types for the basic heterostructure module as well as for the cavity of THz QCL's exists. The heterostructure design employed for the THz QCL's used in this research is based on resonant LO-phonon scattering to selectively depopulate the lower radiation level, while maintaining a long upper level lifetime, see fig. 1 [4,5]. The cavity of this QCL, operating at 2.8 THz, is of the metal-metal type, fabricated using a copper-to-copper thermo-compression bonding technique [5,6].

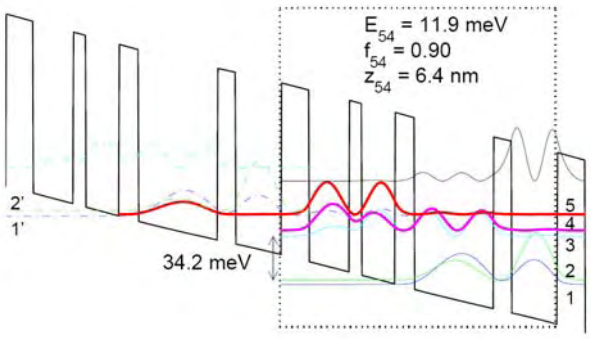

Fig. 1. Energy level scheme of the AlGaAs/GaAs heterostructure module. Lasing at about 2.8 THz occurs between levels 5&4

The advantage of such a metal-metal type of waveguide structure is two-fold. First of all, a better heat contact of the

active region with the cold plate can be obtained. Secondly, and most important, the optical mode remains confined to the active region of the QCL. This is in contrast with the Semi insulating (SI) surface plasmon cavity, where a considerable part of the laser mode occurs in the non-active GaAs substrate. The active, MBE grown, region in both cases is about 10 µm thick whereas the SI substrate is 200-300 µm thick. (see fig.'s 2 and 3).

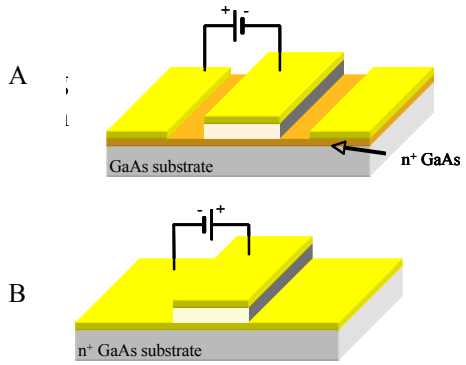

Fig. 2. Schematics of the semi-insulating surface plasmon waveguide (A) and the metal-metal waveguide (B)

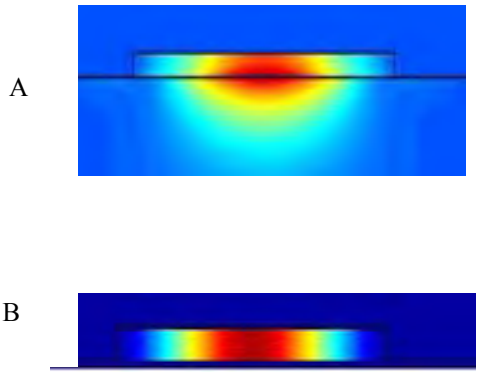

Fig. 3 Schematics of the transverse optical mode patterni n A: the semi-insulating surface plasmon waveguide, and B: the metal-metal waveguide

This optimum overlap of optical field and gain volume results in a consistently lower threshold gain for the metal-metal cavity than for the surface plasmon cavity for laser frequencies in the 1 – 7 THz range [7]. This enables a larger reduction of the active volume for the metal-metal cavity than for the SI surface plasmon cavity. As the thickness of the active region is set by the MBE growth limitations to be about 10 µm, a reduction in active volume means a reduction of width x length of the laser bar. This leads to a proportional reduction of the threshold electrical excitation power of the laser. In view of the need for cryogenic cooling of these THz QCL's, minimizing the heat load of the laser is of crucial importance. Especially for its use as local oscillator for heterodyne detection in space applications, CW operation with the lowest possible cooling budget is required.

In fact, for the smallest metal-metal cavity QCL on which we report here, with dimensions of 10 x 25 x 670 µm^3, CW operation at a record cold plate temperature of 97 K has been observed [5].

In figure 4 the I-V curve at T=7K is shown, together with the optical emission power as a function of the driving current for various cold plate temperatures. The threshold current at T = 7K is 60 mA@ 12V, leading to a minimum electrical input power of 720 mW. Strong and stable CW laser emission occurs for an electrical excitation power of only 1W! At liquid Nitrogen temperature (T=77K) an output power of 400 µW is realised with an input power of 1.2 W.

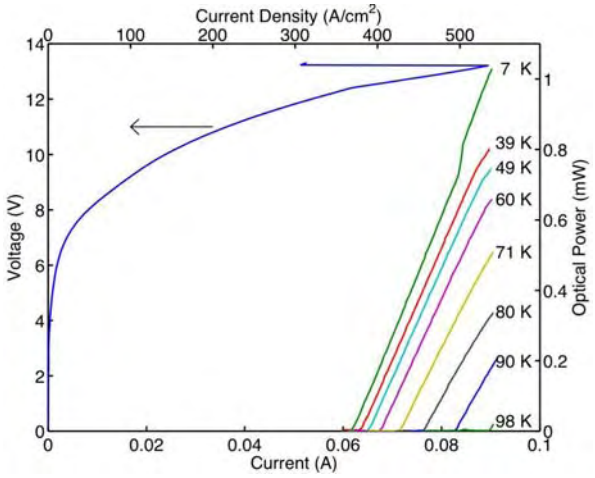

Fig. 4. I/V curve and I/L characteristics as a function of cold plate temperature of a 10 x 25 x 670 µm^3 laser operating in CW mode at 2.8 THz

The spectra presented in Fig.5 were taken in the pulsed mode (2 ms pulse length @ 40 Hz rep. rate), but are essentially equal to those taken under CW operation. Two distinctly different emission lines (at 2.76 and 2.81 THz) are observed at low temperature for different driving currents. Their frequency difference (1.89 cm^{-1}) proves that these are two longitudinal modes originating from the same transverse mode in this 0.67 mm long cavity with an index of refraction n = 3.95.

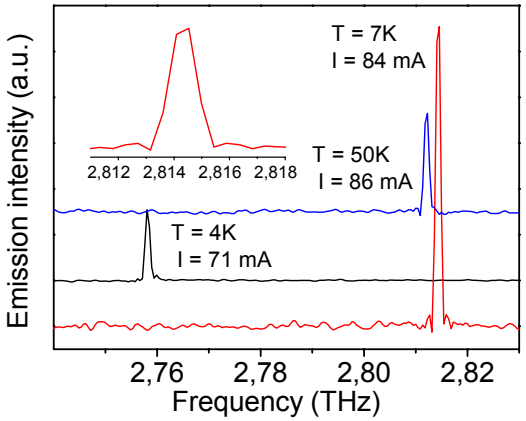

Fig. 5. Spectrum of the 10 x 25 x 670 µm^3 laser operating in CW mode.

The frequency width of the emission (see insert) is of the order of 1 GHz, and set by the resolution of the FT spectrometer. A shift towards lower frequency with increasing temperature is observed (up to about 10 GHz for T_{max} =95 K), mainly resulting from the change in dielectric constant of the active material. Apart from a small intermediate current range,

the emission is single mode, and can be used for LO purposes. To illustrate the importance of the width of the cavity for (transverse) mode control, in Fig. 6 spectra for a 10 x 40 x 1180 μm^3 laser sample, produced from the same wafer material, are shown. In this case only for near threshold currents single mode emission is observed, whereas in general a complicated multi mode structure occurs.

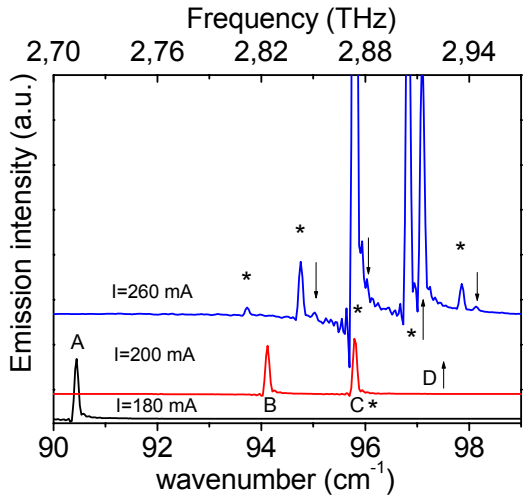

Fig. 6 . Spectra for various driving currents of the 10 x 40 x 1180 μm^3 sample; CW operation at 10 K Four different transverse modes (A-D) are present. Additional longitudinal modes occur for the C (*) and D(↑) transverse modes.

II. Experimental set-up

The quantum cascade laser samples are cooled using a LHe flow cryostat (Fig. 7) with either a high density polythene - or a z-cut quartz window. With the sample near the Φ = 50 mm window an effective full cone field of view of about 120^0 is obtained. The QCL is operated in the long-pulsed mode with a 250 Hz rep. rate and a 1ms pulse duration, in order to facilitate the use of a simple room temperature pyroelectric detector,

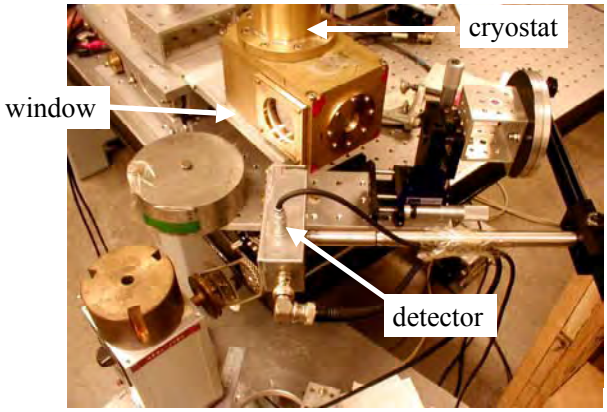

Fig. 7. Picture of the heart of the experimental set-up

and a lock-in amplifier to reduce the noise. The detector with a sensor diameter of either 2 or 5 mm, is placed in a two-axis rotation system (Fig.'s 7,8), similar to that employed in the conical section method for spherical antenna pattern measurements. The emission is monitored throughout the total solid angle of view at a constant - but adjustable - distance from the QCL. The detector movements and the recording of the signal are computer controlled. Inside the cryostat THz absorbing surfaces have been placed to avoid radiation emitted from the uncoated end facet to reflect and disturb the measured intensity pattern resulting from the forward emission.

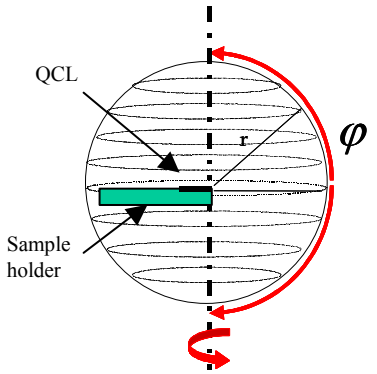

Fig. 8. Schematic view of the measurement configuration, defining the angles θ and φ

III. Results

In Fig. 9 the results of such a beam pattern measurement on the 10 x 25 x 670 μm^3 laser bar is shown. The detector is placed at 60 mm distance from the QCL. The results are presented in an equi-rectangular projection (θ,φ).
The emission is very small in the φ < 0 area, although the mounting of the QCL at the sample holder does not prevent radiation from the end face of the bar to reach the detector.

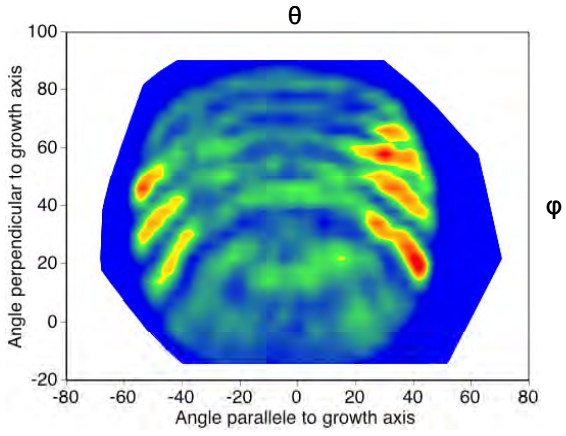

Fig. 9. Experimental beam pattern of the 10 x 25 x 670 μm^3 laser bar.

The beam pattern is clearly structured and not directive at all. Intensity maximums are situated on rings centered around the QCL pointing direction (θ=0°, φ=0°). The radiation emitted in that pointing direction is weak.
Preliminary experiments on laser samples with a larger length and/or width show a different, but similar structured, ring-like intensity patterns. We have carefully checked that this beam pattern is not the result of spurious reflections or to absorption or interference in the optical windows.

Beam pattern simulations based on a model for the THz emission from the front facet of a 10 μm thick metal-metal waveguide (of infinite width and length) show that the output power should change only very slowly and monotonously with the angle φ, perpendicular to the substrate [7]. Such a model clearly does not describe the emission pattern of these QCL's.

A new model is being developed to describe this peculiar angular dependence of the emission intensity of this type of sub-wavelength laser bars. The far-field pattern is calculated taking into account the emission from both the end facets and the side facets. The simulation gives a ring like intensity pattern with divergence angles fitting the experimental data.

A full description of the model will be published elsewhere.

REFERENCES

[1] R. Köhler, A. Tredicucci, F. Beltram, H. E. Beere, E. H. Linfield, A. G. Davies, D. A. Ritchie, R. C. Iotti, and F. Rossi, "Terahertz semiconductor-heterostructure laser", Nature London **417**, 156-159 (2002).

[2] J. Faist, F. Capasso, D.L. Sivco, C. Sirtori, A.L.. Hutchinson, A.Y. Cho, „Quantum Cascade Laser", Science **264**, 553-556 (1994).

[3] B.S. Willaims, S. Kumar, Q.Hu and J.L. Reno, „Resonant-phonon terahertz quantum-cascade laer operating at 2.1 THz (λ≈ 141μm)", Electr. Lett. **40,** 431-433 (2004)

[4] B.S. Williams, H. Callebaut, S. Kumar, Q. Hu, J.L. Reno, "3.4 THz quantum cascade laser based on longitudinal-optical-phonon scattering for depopulation", Appl. Phys. Lett. **82**, 1015-1017 (2003).

[5] Q. Hu, B.S. Williams, S. Kumar, H. Callebaut, S. Kohen and J.L. Reno, "Resonant-phonon-assisted THz Quantum Cascade Lasers with Metal-Metal Waveguides", accepted for publication in Semiconductor Science and Technology **20(7)** (2005)

[6]] B.S. Williams, S. Kumar, H. Callebaut, Q. Hu, J.L. Reno, "Terahertz quantum-cascade laser at λ≈ 100 μm using metal waveguide for mode confinement", Appl. Phys. Lett. 83, 2124-2126 (2003).

[7] S.Kohen, B.S. Williams and Q. Hu, " Electromagneticmodeling of terahertz quantum cascade laser waveguides and resonators" , J. Appl. Phys. **97**, (2005)

Radiation Properties of New Laser based on Electric Chemical Luminescence of Weak Electrolytes with Activators

B.P. Yefimov, M.O. Khorunzhiy, A.N. Kuleshov
Institute for Radiophysics and Electronics of NAS of Ukraine
12 Ac. Proscura st., 61085 Kharkov, Ukraine, e-mail: jean@ire.kharkov.ua

***Abstract*— The experimental results of new laser based on electric chemical luminescence effect in weak electrolytes are given in this paper. We described the model and measuring method of discharge processes taking place in active medium. The radiation in visible range and the radiation of hard photons were experimentally observed. It is shown that discharge processes leads to the creation of plasmoids with spherical form in the air above the model**.

***Index Terms*— Active medium, radiation, electrical discharge, plasmoid, lens.**

I. Introduction

THIS work is dedicated to experimental investigations of radiation properties of new laser based on weak electrolytes, which are the active medium. Such electrolytes' pumping is produced by electrical energy reserved in capacitors battery. To obtain a weak electrolyte we added small quantity of acids and salts in distilled water, which act as activators in electric chemical reactions and displacement reactions. Water presence in weak solutions had an influence on discharge characteristics and radiation parameters, particularly, on discharge duration and pick value of discharge current.

It is well-known fact [1] that radiation spectrums corresponding to active medium of complex molecules in comparison with linear spectrum have wider structure. It is explained due to a complex character of inside motion in molecule. It means electronic, oscillatory and rotatory spectrums. In our experiments due to the complex behavior dynamics of water solution of acids and salts, which are the active medium of new laser, we paid much attention to an explanation of radiation mechanisms from the position of creation of conditions to make population inversion on rotatory and oscillatory molecule levels corresponding to radiation spectrums in visible and infrared wave ranges.

Given research can be useful not only from practical point of view. It extends fundamental knowledge on the nature of discharge processes taking place in complex liquid mediums, which are accompanied by all kinds of ionizing and electromagnetic radiation.

II. Model Description

The model described in [2, 3] served as a basis for our research. Our experimental model for discharge process investigations is shown in fig. 1. The difference between our model and model described in [2, 3] is other placement of electrodes and their dimensions. Considering a necessary of high electric stability of electrode 3 we changed its placement. It is put into water medium through the container bottom as it is shown in fig. 1. It allows us to save the electrical symmetry of electrodes in solution. The placement of another (ring) electrode 2 can be varied in solution limits. A polyethylene container is clear for visual observation with the same dimensions (diameter 170 mm and height 200 mm) as in [2, 3].

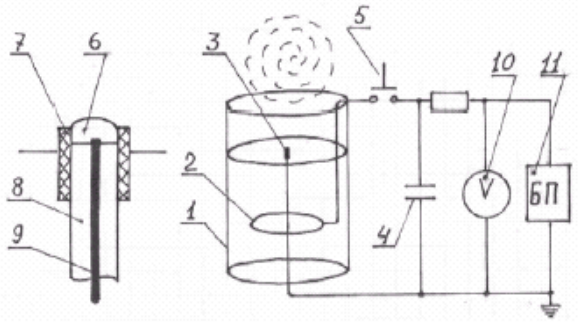

Fig. 1. Plasmoid creation device: 1 – polyethylene container, 2 – ring electrode, 3 – central electrode, 4 – capacitor battery, 5 – switch, 6 – solution drop, 7 – quartz tube, 8 – conductor insulation, 9 – cuprum conductor, 10 – kilovolt meter, 11 – constant voltage model.

Another difference is the possibility of ring electrode placement variation along vertical symmetry axis. It means that we can change the distance from ring electrode to liquid-air boundary and container bottom. We can vary electrical resistance of discharge interval "ring electrode – liquid surface" by these variations of electrode placement in container volume. The electrical scheme using in research, its compounds and requirements for them (allowable voltage and current values) are the same as in [2, 3]. The capacitor battery with capacity 500 micro Farads was charged by constant voltage model 11 up to 6 kV that corresponds to potential energy 9 kJoules. The discharge of capacitor battery was

between electrodes 2 and 3 by circuit closing through discharger 5.

III. Experimental Results

The research of new sources of electromagnetic radiation in short wave range from infrared to roentgen frequency spectrum allow us to detect new laser effect appearing in electrolytes that is based on electric chemical luminescence. In this connection we have carried out experiments of discharge processes in weak electrolyte solutions with impurities. As the result of these experiments we observed new physical phenomena unknown in scientific literature. It lies in:

--The radiation in the form of distant light beam appeared as the result of electrical discharge process in a container with

Fig. 2. The radiation from the electrolyte container (convex lens).

electrolyte that is registered by digital camera (fig. 2).

--Further investigations showed that the radiation is a beam of corpuscles (particles) with significant penetrability in different materials such as Cu, Pb, Fe, St etc. and also dielectrics.

--The property of corpuscular radiation focused by the variation of the form of container with electrolyte. It is shown that the radiation from a container in the form of convex lens is focused and the radiation from a container in the form of concave lens is defocused (fig. 3).

--Electrical discharge in electrolyte is accompanied by electromagnetic radiation of roentgen range.

New laser principle is based on a mechanism of electrical discharge influence on a medium, which is a weak electrolyte with activators (impurities). This regime is similar to electric chemical luminescence occurring in three stages:

--Dissociation of electrolyte molecules with activators in solution under the action of electric field.

--Further chemical energy liberation caused by molecule recombination and excitation of activator molecules.

--Excited molecule return to basic state with a radiation of electromagnetic field quantum.

The mechanism of corpuscular radiation is more complex and need further researches.

The analysis of experimental results allows us to make following conclusions:

--Distilled water with low conductivity (resistance is 300-500 kOhms) as dielectric does not demonstrate both creation of plasmoid and radiation.

--Insertion of small quantity of impurities (donors or acceptors) creates needed conditions to get optimal electrical discharge. In our experiments we used impurities Cl, Mg, Cu, S etc. resulting electrolyze reaction in water with some drops of acids (sulfuric, hydrochloric etc.). Obtained values of conductivity and water molecule mobility create optimal conditions for discharge accompanied both spherical plasmoid and corpuscular radiation of strange nature.

--In experiments we observed whole water volume glowing that can be explained as population inversion of electronic, oscillatory and rotatory levels of water molecules

Fig. 3. The radiation from the electrolyte container (concave lens).

resulting electrical pumping and further radiation.

IV. The Phylosophy Of Experiments

There were two regimes of discharge:

1) If central cuprum electrode 9 overflows the drop surface 6 then electrical discharge occurred above the water surface with both light and acoustic energy liberations recalling blast. There was considerable quantity of ozone in the air. To photograph this process we have to use collection of light filters. Discharge photos are shown in fig. 4. The discharge was uniformly glowing plasma creation with a life time about several milliseconds. Gas was heated up to 5000 – 6000 K. We suppose that such great discharge power connected with water molecule dissociation on atomic hydrogen and oxygen with presence of air components (nitrogen, carbon etc.). Bonding energy of water molecule is 0,5 eV corresponding to gas temperature of splitting about 6000 K.

2) The central electrode 9 is inside the drop. Closing the discharge switch whole potential energy of capacitor battery concentrates in a drop. At the same time the leader stream forms and propagates along solution-air boundary. The plasma

blast is released from solution volume and further glowing plasmoid separates form this plasma blast and flies in the air. This process was registered by digital camera with 25 frames

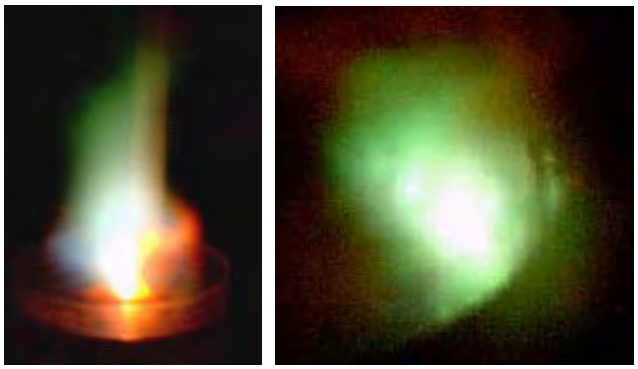

Fig. 4. The discharge on the electrolyte-air boundary with two voltages: left picture – 4.6 kV and right picture – 6 kV.

per second (frame width is 40 ms).

The dynamics of plasmoid development is shown in fig. 5. Life time of visible plasmoid equals 6 frames, i.e. 0,24 s. There are four frames satisfactory illustrating this process. Favorable regimes of plasmoid creation is in a discharge voltage range from 3,5 to 4,6 kV. We experimentally investigate regimes accompanied by plasma blowout in a range from 2 kV to 6 kV. The discharge process decelerates in low voltage that was registered on oscilloscope current curve. It was established that both the duration of plasmoid creation process and its life time depends on not only electrical regime. It depends on electrolyte volume, ring electrode 1 square, temperature of surrounding air and liquid medium. We carried out in experiments in active medium varying its temperature from 273 K to 343 K. It was established that plasmoid life time was in 2 – 3 times greater when electrolyte temperature is 273 K.

At a high temperature the plasma blowout is faster and the plasmoid form is not exactly a sphere. Increased life time of plasmoid at a low water temperature can be explained as in summary of [2, 3]. Hydrated plasma as puff of hot and moist air with lower temperature then surrounding air replenishes its internal energy from more hot air that allow them to make their life time longer.

It should be noticed that discharge process depends on charging circuit time constant. Both parallel connection and a concatenation of noninductive resistances with the same conductivity as water were investigated. In the case when electrical charge partially leaves capacitor plate (about 1/6 stays) then discharge time can be determined as

$$i = \frac{dq}{dt} = -\frac{q_0}{T}\exp\left(-\frac{t}{T}\right) = -\frac{u_0}{r}\exp\left(-\frac{t}{T}\right)$$

where t – current time, T – circuit time constant, r – discharge interval resistance, q – capacitor charge.

Used water resistance is in the range 1 – 1,2 kOhms. Circuit constant is 0,5 sec for r=1 kOhm and C=0,5 mFarads. Then time of discharge from q to $q/6$ is 0,9 sec (U=6 kV *and* U=1 kV). This discharge time can be two times shorter with parallel switched resistance 1 kOhm and it can be two times longer with the same boosting resistance. At that the discharge

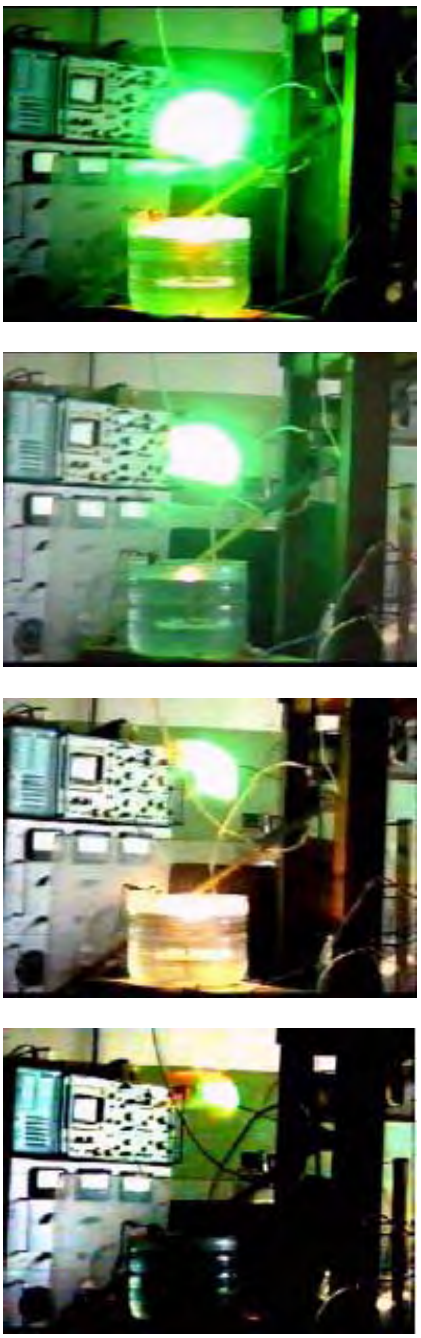

Fig. 5. The dynamics of the spherical plasmoid creation registered by digital photo camera with 25 frames per second.

power changes and can be adjusted by value U_0.

It was imperative to detect the radiation of the electrical discharge on the electrolyte-air boundary. Toward this end the discharge placement was surrounded by opaque envelopes with photo paper. It is clear that visible radiation from polarized water (weak electrolyte) in clear polyethylene container can not spoil this photo paper. Experimental results show that the discharge creates a radiation of not only visible range, which is registered in photo paper as spots and tracks of different configuration. It is clear that this radiation is

harder then the radiation of visible range. It must be the soft roentgen. Several photos of radiation are shown in fig. 6.

We should notice that such radiation was registered only above water container (above discharge) and from the bottom of container. It is necessary to use specific devices and methods for more detailed measurements of radiation properties and its parameters. Now we are carrying out such experiments and measurements.

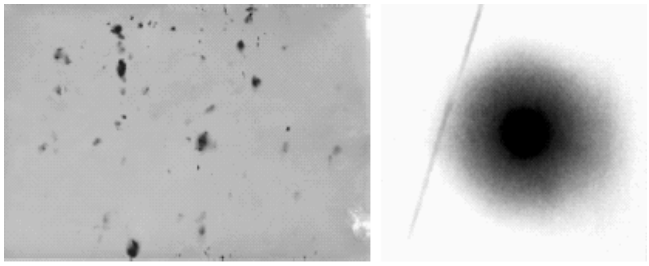

Fig. 6. Typical tracks of radiation registered in photo paper: left picture – discharge voltage is 4,6 kV and right picture – discharge voltage is 6 kV.

Also there is another main question about the intensity of liquid medium glowing. Authors of [2, 3] consider this glowing as the result of the recombination of ions concentrated in hydrated clusters of spherical plasmoid and there is no information about liquid medium glowing. In the other hand great number of our experimental results show that the process of liquid medium glowing starts long before plasmoid creation as it is shown in our photos. Liquid medium polarization, which is registered by visible glow, appears not in the form of cone (from ring electrode base to the vertex of cone in the point electrode 2). Liquid medium polarization appears as glowing disks in whole volume of a solution from the container bottom to a surface (fig. 7). At the moment when whole cylindrical spout is in the form of single glowing object the liquid medium is ready to create a plasmoid. This mechanism acts even if ring electrode diameter is less then the container diameter.

Fig. 7. One of the final states of liquid medium polarization and its glowing at the moment of plasmoid creation.

V. Conclusion

Given experimental research shows that hydrated plasma is not good studied matter state. It depends on surrounding air, many other parameters of discharge medium, particularly, its temperature and conductivity. We carried out experiments in a wide energy range from 9 to 2 kJoules with voltages up to 6 kV. The focusing property of discharge process defined by electrolyte container form is found out. Both ionizing and electromagnetic radiation with hard photons are detected. To explain discovered properties of discharge process we apply electric chemical luminescence phenomenon.

References

[1] *Physical encyclopedic dictionary*/ ed. A.M. Prokhorov. M.: Sov. Enc. – 1984.

[2] A.E. Yegorov, S.I. Stepanov, "Long-living plasmoid – an analogue of ball lightning in moist air," *JTF*., vol. 72, n. 12, 2002, p.p. 102-104.

[3] A.E. Yegorov, S.I. Stepanov, G.D. Shabanov, "Demonstration of ball lightning in the laboratory," *UFN*, vol. 174, n. 1, 2004, p.p. 107-109.

[4] G.N. Gestrin, A.N. Kuleshov, B.P. Yefimov, "On Conditions of Creation of Long-Living Electron Bunches in Motz Undulator and Other Systems," *Conference Digest of the 2004 Joint 29th Int. Conf. on IRMMW and 12th Int. Conf. on THz Electronics*, Sept. 27 - Oct. 1, 2004, Karlsruhe, Germany, p.p. 611-612.

Superlattice frequency multiplier for generation of sub-terahertz radiation

B. I. Stahl, K. F. Renk, A. Rogl, T. Janzen
Institute of Applied Physics, University of Regensburg, 93040 Regensburg, Germany

D. G. Pavel'ev, Yu. I. Koshurinov
Department of Radiophysics, Nizhny Novgorod State University, Nizhny Novgorod, Russia

V. Ustinov, A. Zhukov A. F.
Ioffe Physico-Technical Institute, St. Petersburg, Russia

We report on a GaAs/AlAs superlattice frequency multiplier. It delivered continously tunable cw-radiation at the 3rd harmonic frequency (~300GHz, power ~100μW) of a microwave pump field with a conversion efficiency of about 4%; also at higher harmonics, radiation was observed. The nonlinear electron transport properties of the superlattice were due to Bragg reflections of miniband electrons at the superlattice planes. The problem of impedance matching to the waveguide system is discussed. The presented superlattice frequency multiplier seems to be a promising candidate for small, room temperature operated solid-state cw radiation sources at sub-terahertz and terahertz frequencies.

Superconductor – Insulator - Superconductor (SIS) and Hot Electron Bolometer (HEB) pumping with LT-GaAs based photonic local oscillators.

I. Cámara Mayorga , P. Muñoz Pradas, M. Mikulics, A. Schmitz, C. Kasemann, P. van der Wal, K. Jacobs and R. Güsten.

Abstract—Two astronomical heterodyne receivers - SIS at 450 GHz and HEB at 750 GHz – were successfully pumped. A photonic local oscillator fabricated with LT-GaAs was illuminated by two NIR semiconductor lasers, creating a beat frequency in the submm range. SIS junction I-V characteristics for two different LO power pump levels demonstrate that the power delivered by the photomixer is sufficient to pump an SIS mixer with an acceptable safety margin.

In order to investigate that the photonic LO does not add significant internal noise to the mixer, we compared SIS-receiver noise temperatures -from hot / cold measurements-using a conventional solid-state LO and a photonic LO. A Martin-Puplett diplexer (MPD) was used to inject the LO signal into the signal path. In both cases, the system noise temperature was identical ($T_{receiver}$=170 K).

Additionally, the photomixer was used as an LO in a heterodyne mixing experiment with a phonon-cooled HEB mixer from 650 GHz to 750 GHz. For this purpose, the circularly polarized output signal from a spiral antenna photomixer was transformed to a lineal polarization by a MPD and mixed with a Hot-Cold Load in a second MPD, making the overall losses of the quasioptical design approximately 20 %. The HEB mixer consisted of a NbTiN bridge (approx 4.5 x 0.4 x 0.004μm³) on a Si_3N_4 membrane fabricated at KOSMA.

Experiments realized under cryogenic conditions show that the power can be still considerably increased as to be sufficient for successful pumping of astronomical mixers in the supra-THz range.

Keywords: *Index Terms*— **LT GaAs, Photonic local oscillators, Terahertz, SIS, HEB, photomixers**.

Manuscript received May 25 2005. This work was supported by the the "Deutsche Forschungsgemeinschaft" through grant SFB 494

I. Cámara Mayorga, A. Schmitz, C. Kasemann, P. van der Wal and R. Güsten are with the Max Plack Institut für Radioastronomie. Auf dem Hügel 69, 53121 Bonn, Germany. Phone: +49 228 525342; fax: +49 228 525229; e-mail: imayorga@ mpifr-bonn.mpg.de.

P. Muñoz Pradas, K. Jakobs and E. A. Michael are with the 1. Physics Institute, University of Cologne, Zülpicher Str. 77, 50937 Köln, (Germany)

M. Mikulics is with the Institute of Thin Films and Interfaces (ISG-1), Research Center Jülich, 52425 Jülich, Germany

I. Introduction

Terahertz generation by photonic techniques like difference-frequency mixing in ultrafast low-temperature grown GaAs (LT GaAs) photodetectors has been studied extensively during the last decade [1]. The huge bandwidth offered by one photomixing device (from DC to several THz) has a tremendous potential for many applications as radioastronomy, THz imaging, high resolution spectroscopy, skin cancer detection, security, defence, etc.

The progress made in fabrication of LT-GaAs photomixers has leaded to carrier lifetimes below 0.5 ps at moderate bias voltages. This is important for operation in the supra-THz range because (together with the RC constant for MSM photomixers) it limits the 3 dB cutoff frequency of the device by $(2\pi\tau)^{-1}$ where τ is carrier recombination lifetime.

In this paper we report on activities regarding photomixing as a Local Oscillator (LO) source for heterodyne detection in radio astronomy. The aim of these preliminary experiments is to allow the integration of a photonic LO in:

- GREAT (German Receiver for Astronomy at Terahertz Frequencies), which will be a first-generation dual-channel heterodyne instrument for high resolution spectroscopy aboard SOFIA (Stratospheric Observatory For Infrared Astronomy).
- APEX, the Atacama Pathfinder Experiment.

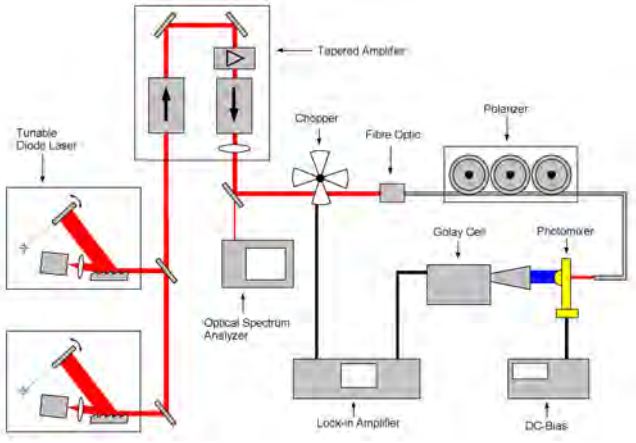

Fig. 1. Schematic diagram of the measurement system

II. OPTICAL HETERODYNE MIXING

A. *Photomixer section.*

As shown in figure 1, the scheme for optical heterodyning consisted of two near infrared (NIR) 780nm continuous-wave (CW) single mode lasers in Littman configuration (New Focus, model Velocity 6312), where at least one laser diode was tunable to make frequency selection possible. The output signal of the lasers ~6mW was combined and amplified in a tapered laser amplifier (Toptica TA100), which provided up to 0.5W of combined power.

The beam was then coupled into a single mode optical fiber and to an optical spectrometer to monitor frequency difference and to guarantee an equal power distribution between the two colors. To avoid optical feedback to the lasers and amplifier, optical isolators were included in the setup as well fiber optics with APC connectors (>60dB reflection losses).

(a)

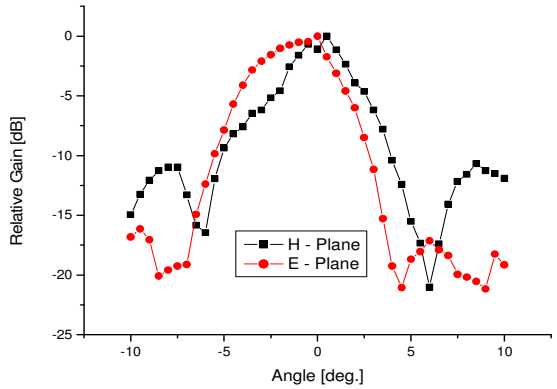

(b)

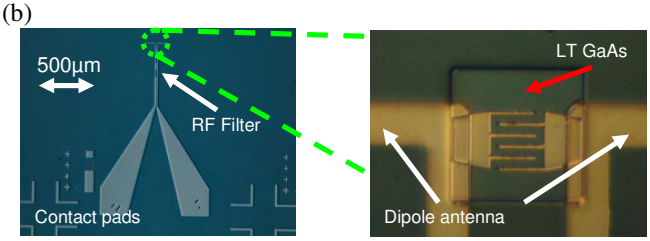

Fig. 2. (a) E-plane and H-plane power patterns measured for a λ dipole in resonance at 450 GHz. The high resistivity Si substrate has a hyperhemispherical form to reduce the divergence of the beam. (b) Microphotograph of the dipole antenna and finger structure of the photoactive area.

The fiber optic was positioned to achieve an optimal photomixer illumination with a piezoelectric actuator. This device allowed a fine (~100nm) position control in three axes. The air gap between fiber optic and photomixer substrate acts as a Fabry-Perot etalon. To cancel out this effect, the air gap was filled with an optical adhesive [2] [3], which has a similar refraction index as the fiber optic, pigtailing the fiber optic to the photomixer. This step also inhibited the negative influence of mechanical vibrations which misaligned the fiber optic at large timescales and restricted the reproducibility of our experiments.

Once the two colors interfere on the photoactive area, electron-hole pairs are generated and immediately separated by the applied bias voltage. Details on the underlying physics phenomena may be found elsewhere [4], [5], [6]. The ultrashort carrier lifetime of LT-GaAs enable the photogenerated carriers to "follow" the envelope of the optical power. Since the photoactive area was patterned in the feed point of a resonant or broadband antenna, the beat signal was radiated to free space. The high dielectric constant of the GaAs photomixer substrate (ε_r=12.8), prevents the signal from being radiated backwards to the fiber optic. Its hyperhemispherical form avoided the formation of surface modes and provided acceptable beam directivity [7], [8].

B. *Mixing experiment with a SIS at 450 GHz.*

The power performance and noise temperature of our photomixers was tested with a SIS mixer.

It is well known that a photomixers have a high internal resistance [9] and thus impedance matching is difficult. For this reason, high radiation resistance antennas are preferable. A full wave dipole antenna shows a higher radiation resistance (~210 Ω on a GaAs Substrate) than a broadband logarithmic spiral antenna (~73 Ω on a GaAs Substrate). The polarization of a dipole is lineal; having the same orientation as the dipole itself and its gaussicity is higher than in case of spiral antenna. Our SIS mixer was only sensitive to linearly-polarized signals [10], which favored the use of a dipole antenna.

The above mentioned characteristics motivated our group to perform a SIS mixer pumping experiment with a dipole antenna photomixer. Measurements of E and H planes show goog gaussicity and low sidelobes (figure 2).

I-V characteristics at 450 GHz for two different LO power pump levels are shown in Figure 3. With a photocurrent of 0.6 mA and a NIR optical power of 70 mW, the RF power generated was a factor 3 under device burnout, so that an acceptable safety margin was available to operate the photonic LO.

In order to investigate wether the photonic LO does add significant internal noise to the mixer, we compared receiver noise temperatures -from hot/cold measurements- using a con-

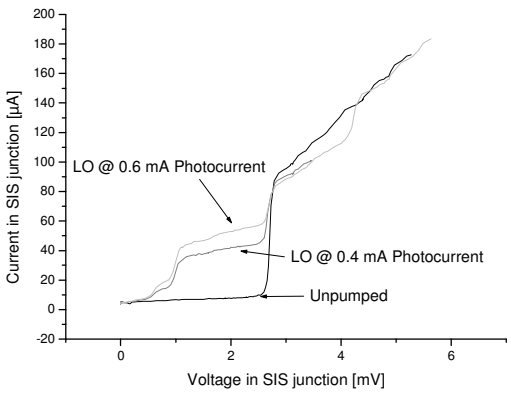

Fig. 3. The I-V curve of the SIS mixer in absence of LO signal and pumped by a photonic LO signal at 450GHz for different powers.

ventional solid-state LO and the photonic LO. A Martin-Puplett diplexer (MPD) was used to inject the LO signal into the signal path. The divergent beam from the MPD output was transformed to a convergent beam with a plane-convex Teflon lens.

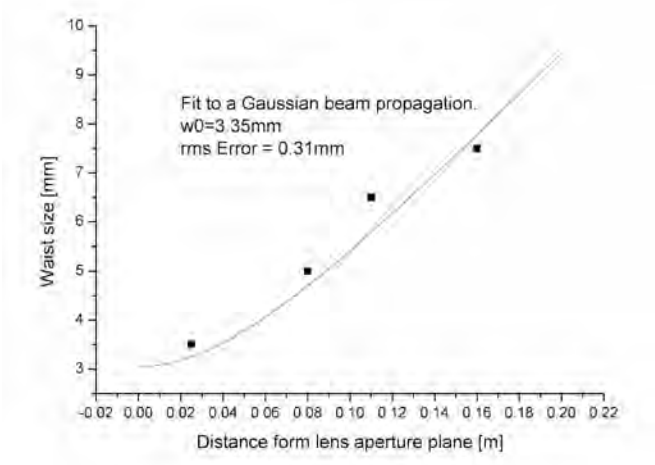

Fig. 4. The waist size was measured at different distances from the photomixer lens aperture plane. The data points were fitted to a Gaussian beam propagation curve. From the fit, the minimum waist (beam waist) w0 was extracted. The dimensions of the photomixer substrate lens were calculated to synthesize an ellipse. The position of the beam waist coincides with the lens-to-air interface.

The double sideband (DSB) noise temperature of the photomixer and solid state LO was measured at an intermediate frequency band of 2 to GHz. The result was identical ($T_{receiver}$ = 170 K). In contrast to cascading multipliers, the noise contribution of a photonic LO is not expected to increase with frequency because the THz is directly generated by optical mixing of two laser signals, a process which is frequency independent.

C. Mixing experiment with a HEB at 750 GHz.

Once having tested the performance of our photonic LO with an SIS mixer, a more challenging experiment with a HEB at 750 GHz was proposed.

At theses frequencies no resonant antenna photomixer device was available so we used a photomixer with integrated logarithmic spiral (broadband) antenna.

The HEB consisted of a NbTiN bridge on a Si_3N_4 membrane with dimensions approximately 4x0.4x0.004 µm³. Its design frequency was 750 GHz.

The membrane waveguide HEB mixer used for the experiment was sensitive for vertical polarization. The 3.3mm beam waist position was located at the Dewar window. To make an optimum quasioptical coupling design, the beam parameters of the photomixer beam were previously measured.

A computer controlled motorized translation stage in three axes was designed. Our RF power detector, a Golay cell, was installed with an iris diaphragm that was setup to achieve sufficient spatial resolution while obtaining an acceptable S/N ratio in the power detection. The beam was spatially characterized from measurements at different distances from the photomixer. A fit to a theoretical Gaussian-beam propagation was performed and the beam waist radius was extracted giving as result 3.3 mm (see figure 4). This result was similar to the beam waist of the HEB mixer, simplifying considerably the quasioptical design .

The immediate problem associated with the use of a spiral antenna is the need of transforming its circular polarization to vertical, in order to match the vertical polarization of the HEB mixer.

Two Martin-Puplett diplexers were used. The first transformed the polarization form circular to linear. The other MPD was used to inject Hot/Cold load for noise temperature measurements.

To assure that beam truncation doesn't play a major role, the ratio between beam to aperture diameter at the output of the Martin-Purplett diplexer was computed giving as result 1/3, which corresponded to -77.8dB spillover loss.

The quasioptical design of figure 5, which is symmetrical due to the identical beam waists of photonic LO and HEB mixer, uses an off-axis paraboloidal mirror with a focal length of 250mm.

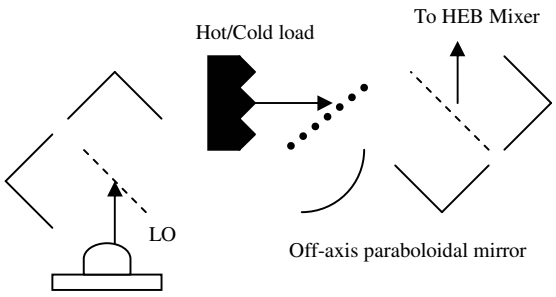

Fig. 5. Schematic of the quasioptical setup. A first MP diplexer transforms the circular polarization from the log-spiral antenna photomixer to vertical. The paraboloidal mirror makes the diverging LO beam convergent. The second MP diplexer injects the hot/cold load signal.

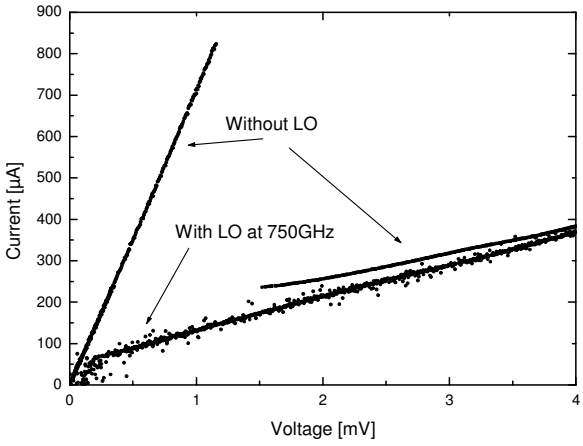

Fig. 6. IV-Characteristics of the HEB without LO power and pumped by the photomixer at 750GHz. The serial resistance originates at the IF-Filter of the HEB.

Figure 6 represents the IV characteristics of the HEB mixer with photonic LO power and without. The scatter results from standing waves and microphony.

The photomixer was illuminated by 70mW NIR power and the photocurrent was 1.7mA, generating 450nW of RF power, which is near the photomixer burnout point. At the output of the quasioptical system, the RF power was 375 nW, which represents 20% quasi-optical and water absorption losses.

The absorbed RF power was calculated by the isothermal method in the HEB to be 300 nW, which is congruent with this measurement.

In case of using a resonant antenna design photomixer, the expected power could be higher by a factor of 3, due to its higher radiation resistance. Also the gaussicity and lineal polarization would simplify the quasioptical setup.

III. FUTURE WORK.

Next we will perform pump experiments at higher frequencies with Hot Electron Bolometer mixers operated at 1.4 THz. For these purposes, dipole antenna design photomixers will be processed. Since the frequency roll-off of the photomixer drops 40dB/dec from 1THz, the photomixers will be operated at higher laser power and bias voltages to generate sufficient LO power. To avoid device burnout, our cryogenic setup [10] will be used.

On the other hand, we will work on the reduction of our laser diode linewidth in order to achieve a sub-mm wave linewidth smaller than 100 KHz.

REFERENCES

[1] E. R. Brown, K. A. Mcintosh, F. W. Smith, M. J. Manfra, and C. L. Denis, Measurements of optical-heterodyne conversion in low-temperature-grown GaAs. App. Phys. Lett. 62, 1207 (1992).

[2] Norland Optical Adhesive 61.

[3] S. Verghese, K. A. McIntosh, E.R. Bown, Optical and terahertz power limits in the low-temperature-grown GaAs photomixers. App. Phys. Lett. 71, 2743 (1997).

[4] E. R. Brown, F. W. Smith, and K. A. McIntosh, Coherent millimeter-wave generation by heterodyne conversion in low-temperature-grown GaAs photoconductors, J. Appl. Phys. 73, 1480 (1993).

[5] E. R. Brown, K. A. McIntosh, F. W. Smith, K. B. Nichols, M. J. Manfra, C. L. Dennis, and J. P. Mattia, Milliwatt output levels and superquadratic bias dependence in a low-temperature-grown GaAs photomixer, Appl. Phys. Lett. 64, 3311 (1994).

[6] N. Zamdmer and Qing Hu, K. A. McIntosh and S. Verghese, Increase in response time of low-temperature-grown GaAs photoconductive switches at high voltage bias. Appl. Phys. Lett. 75, 2313 (1999).

[7] D. B. Rutledge, D. P. Neikirk, and D. P. Kasilingam, "Integrated circuit antennas," *Infrared and Millimeter-Waves*, K. J. Button, Ed. New York: Academic, 1983, vol. 10, pp. 1–90.

[8] D. F. Filipovic, S. S. Gearhart, and G. M. Rebeiz, "Double slot antennas on extended hemispherical and elliptical silicon dielectric lenses," *IEEE Trans. Microwave Theory Tech.*, vol. 41, pp. 1738–1749, Oct. 1991.

[9] S. Verghese,a) K. A. McIntosh, S. Calawa, W. F. Dinatale, E. K. Duerr, and K. A. Molvar, Generation and detection of coherent terahertz waves using two Photomixers. Appl. Phys. Lett. 73, 3824 (1998).

[10] I.Cámara Mayorga, M. Mikulics, A. Schmitz, P. Van der Wal, R. Güsten, M. Marso, P. Kordos, H. Lüth. *An Optimization of Terahertz Local Oscillators based on LT-GaAs Technology*. Proceedings of SPIE Volume: 5498, pp. 537 (Millimeter and Submillimeter Detectors for Astronomy II. SPIE, Glasgow 2004). Editors: Jonas Zmuidzinas, Wayne S. Holland, Stafford Withington.

Terahertz Generation in Free Space and in Waveguide Partially Loaded With Nonlinear Crystal

A S Nikoghosyan[ac], E M Laziev[a], R M Martirosyan[a], A A Hakhoumian[a], J M Chamberlain[b], R A Dudley[c], N N Zinov'ev[c,d]

[a]Department of Microwave Engineering, Yerevan State University, 1 Alex Manoogian Str., Yerevan 375025, Armenia, *nika@ysu.am*
[b]Department of Physics, Rochester Building, Science Laboratories, University of Durham, Durham DH1 3LE
[c]National Physical Laboratory, Queens Road, Teddington, Middlesex TW11 0LW, UK
[d]Solid State Electronics Division, A.F. Ioffe Physical Technical Institute of RAS, 26 Polytechnicheskaya Str., 194021 St Petersburg, Russia

To trigger the enormous application potential of the teraherz (THz) band an efficient powerful source of coherent THz radiation is an essential requirement. The efficiency of difference frequency generation (DFG), a widely used approach to generate broadband THz radiation, depends on the condition of wave synchronism. The use of waveguide was suggested in [1] to enhance the wave synchronism by increasing the phase velocity of terahertz radiation in waveguide. This helps to reduce the differences in refractive indices at THz and pump frequencies incurred by dispersion and to bring some of waveguide modes closer to synchronism. In this report we demonstrate this enhancement achieved at THz frequencies using a partially loaded by a nonlinear crystal terahertz waveguide. In this case the nonlinear crystal, $LiNbO_3$, works as a nonlinear frequency convertor in the combined structure "waveguide + crystal".

We present the experimental results on THz generation in a waveguide partially loaded with $LiNbO_3$ crystal using 50 fsec pulses Ti:sapphire laser. The outgoing radiation in the band 0.1-2.7 THz as the superposition of H_{mo} [1,2] modes was detected with a free space electro-optic setup. Following the experimental results we present a review on the theoretical calculations. The results have shown an order of magnitude enhancement of terahertz generation in the waveguide structures comparing with positioning samples in free space.

1. A.S.Nikoghosyan, Kvant.Electron. (Moscow) [Sov. J.Quantum Electron],15, 569, 1988
2. G.Galiot, S.P. Jamison, R.W. McGowan, D.Grischkowsky.J.Opt.Soc.Am.B.Vol17, p.851-863,2000

Numerical Simulation of Photoconductive Dipole Antennas: the Effect of the DC bias Striplines

Kamran Ezdi, Thomas Kleine-Ostmann, Martin Koch

Institut für Hochfrequenztechnik
Technische Universität Braunschweig, Schleinitzstrasse 22,
D-38106 Braunschweig, Germany

***Abstract*— We perform numerical simulations to evaluate the effect of the dc bias striplines on the performance of photoconductive dipole antennas. We find that the resonance frequency and the maximum of the input impedance of the antenna shift to lower frequencies as the length of the striplines is increased. In addition, we compare the performance of impedance matched antennas with that of more realistic antennas which are characterised by a severe mismatch between source and antenna structure.**

***Index Terms*—photoconductive dipole antennas, photomixing**

I. INTRODUCTION

Photoconductive dipole antennas are widely used to optoelectronically generate and detect pulsed and continuous wave (CW) THz radiation [1-4]. They consist of a piece of semiconductor onto which metal structures are deposited. These structures can be of different shapes corresponding to different antenna designs. One of the most popular designs is the dipole antenna which exhibits a resonant behaviour and on which we focus in this paper. The typical structure of a photoconductive dipole antenna is shown in figure 1.

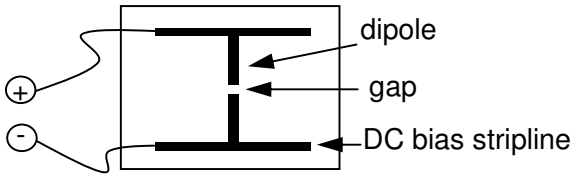

Fig. 1 Schematic drawing of a photoconductive dipole antenna.

To use the antenna as a THz emitter a bias is applied to the dipole through two parallel striplines. The dipole structure with a typical length between 50 and 200 µm is interrupted by a small gap whose width is typically 10 µm. Due to the applied bias, the field strength within the gap amounts to several kV/cm. To operate the antenna, carriers are optically excited within the gap. The excitation can be either pulsed, using femtosecond laser pulses, or continuous wave (CW), if the output of two single CW laser diodes is superimposed in the gap region. The carriers are accelerated in the bias field which gives rise to a small current that is the source for THz radiation. While the first excitation mechanism produces broadband THz pulses and is used in THz time-domain spectroscopy, the latter is referred to as photomixing, and it generates CW THz radiation. In both cases the role of the antenna is to effectively radiate the terahertz energy.

Over the last few years a lot of theoretical and experimental work has been done on the analysis of photoconductive dipole antennas. Jepsen et al have used the Drude-Lorentz theory to model the photo-current in the semiconductor and compare the predictions of theory to experimental results [5]. Tani et al have experimentally compared the radiation performance of different types of antennas using the Finite Difference Time Domain (FDTD) method [6]. Cai and coworkers have pointed out that the efficiency of THz antennas can be enhanced by using pointed contacts [7].

However, in the typical design shown in Fig. 1, the striplines act as an end capacitance and affect the dipole resonance. Here, we use a commercial software package to investigate this effect. We find that the resonance frequency and the maximum of the input impedance of the antenna shift to lower frequencies as the length of the striplines is increased.

In addition, we investigate a second aspect: one of the main design challenges in using THz antennas with photomixers is the severe impedance mismatch between the high internal impedance of the photoconductor and the much lower input impedance of the antenna structure. It is almost impossible to achieve impedance matching with such a big difference. It was pointed out by Duffy et al. in 2001 that the most effective way to optimise the radiated THz energy is to increase the input resistance of the antenna [8].

As we will show here, our simulations confirm this statement. In essence, the maximum THz power is not radiated at the antenna resonance obtained for the matched case, but at

* corresponding author: email kezdi@wave.ihf.ing.tu-bs.de (Kamran Ezdi), phone +49 5313912010/ fax+49 5313912045

the frequency where the antenna input impedance has a maximum. i.e. at the frequency of the lowest impedance mismatch.

II. Software and Methodology.

We use the software package Computer Simulation Technology (CST) to simulate the antenna and stripline structures. CST works on the finite integration technique developed by Weiland. It is based on the idea of using the integral, rather than the differential form, of Maxwell's equations in the discretisation. The program requires considerable computing power, hence it is the advent of powerful computers that has made the use of this technique possible. CST is widely used to simulate antenna and stripline structures in the GHz range. Since the finite integration method is frequency-independent, CST is expected to give accurate results also at THz frequencies.

We assume a dipole antenna with a length of 200 μm deposited on a GaAs substrate. In the 5 μm gap between the two arms of the dipole a current source, in the form of a discrete port, is introduced and the appropriate boundary conditions are specified. The current source simulates the current in the photoconductive gap. The first run of the simulation is carried out with the default value of the source internal impedance (50 Ω). The result of the simulation gives the value of the input impedance of the antenna. The source impedance is then matched to this value and a second simulation run is carried out to get results for a matched source-load situation.

The striplines are introduced incrementally to the structure. For each incremental length of stripline the procedure outlined above is repeated; the incremental lengths are added until they reach the ends of the substrate. For each incremental length, results for the reflection-coefficient S_{11}, the far-field radiation pattern, the antenna current and the input impedance of the antenna are obtained.

Although the simulations for the matched case are quite instructive they are in a sense purely academic as real antennas have a severe mismatch between the photomixer and antenna. In a second run we simulate the mismatched case where the source impedance is set to a more realistic value of 10 kΩ.

III. Results and Discussion

The resonance frequency of a dipole antenna on a dielectric half space can be approximated by the following expression [9]:

$$\lambda_{eff} = \frac{\lambda}{\sqrt{\varepsilon_{eff}}}$$

where $\varepsilon_{eff} = \frac{1+\varepsilon_r}{2}$ is the *effective* permittivity.

For a 200 μm dipole on a GaAs substrate (ε_r=13), the above rule-of-thumb predicts a resonance frequency of 280 *GHz*. This compares with the following plot for a matched antenna from the simulation.

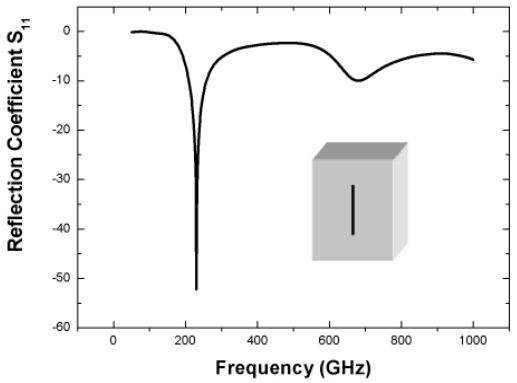

Figure 2. Reflection Coefficient for a 200 μm dipole

The difference between the predicted (280 *GHz*) and simulated (230 *GHz*) values can be attributed to the fact that the rule-of-thumb applies to dipoles of very small widths, while the simulated antenna has a finite width of 10 μm.

It is observed that increasing the length of the striplines shifts the resonance frequency of the antenna to lower values. In other words the electrical length of the antenna is increased. The plots below show the progressive shift to lower frequencies as the length of the striplines increases.

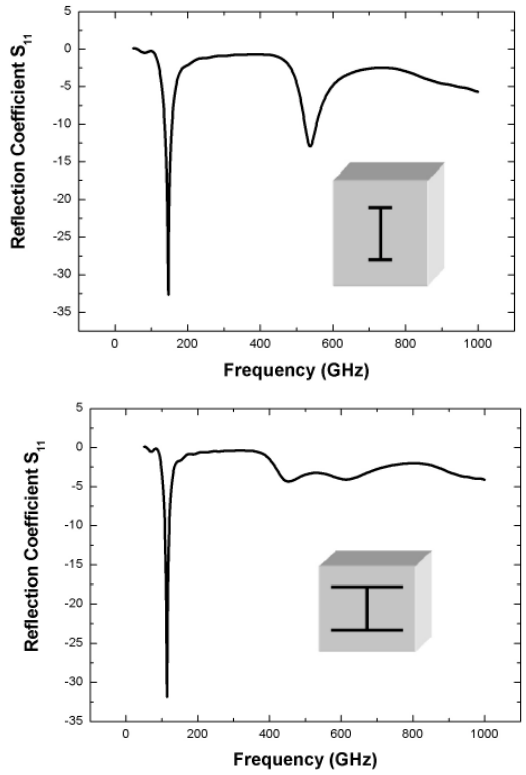

Figure 3. Reflection Coefficient for a 200 μm dipole with increasing stripline length.

This behaviour can be explained by the fact that adding the striplines amounts to adding end capacitance to the antenna, which lowers the resonance frequency of the antenna. The decrease of the resonance frequency with increasing stripline length is shown in figure 4.

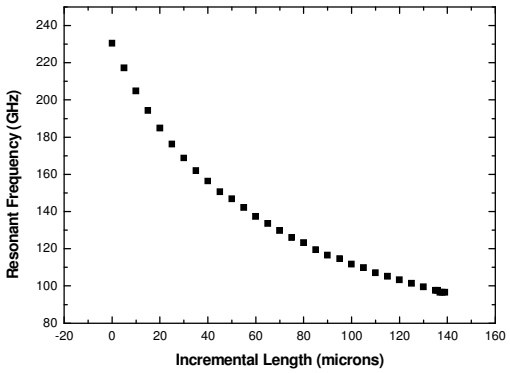

Figure 4. Decrease of the resonance frequency with increasing stripline length

The input impedance of the antenna at resonance was also investigated and was found to be in agreement with the value predicted by the rule-of-thumb. The value of the input resistance of a dipole antenna on a GaAs half-space is given by

$$R_{in} = \frac{75}{\sqrt{\varepsilon_{eff}}} = 28\Omega$$

where 75 Ω is the well-known value of the input resistance of a dipole radiating in free space. As can be seen from figure 5 the input resistance of the dipoles decreases with the increasing length of striplines.

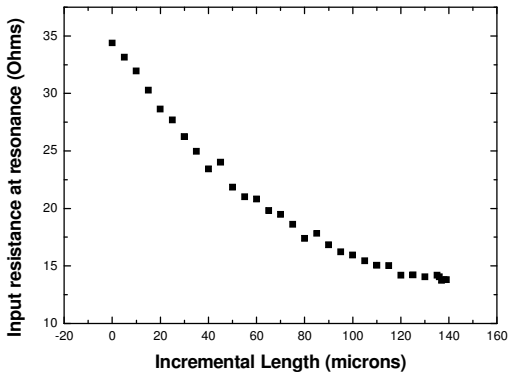

Figure 5. Decrease if input resistance with increase in stripline length.

The simulated radiation pattern of the antenna confirms the well-known fact that most of the power is radiated into the dielectric. Figure 6 shows the simulated radiation pattern of a dipole without striplines on a GaAs substrate. The substrate is positioned in the upper half space.

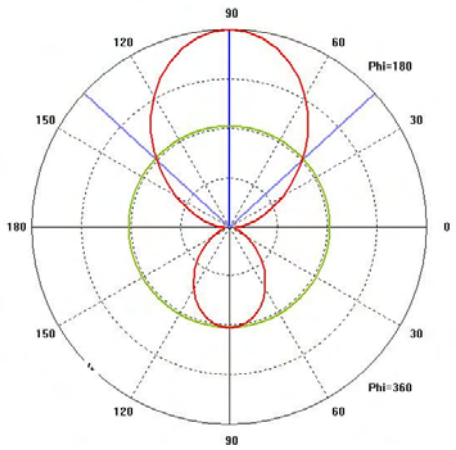

Figure 6. 2-D radiation pattern of a dipole antenna on GaAs half space

As already stated, the resistance of photomixers is very high. Therefore, to simulate the actual situation as closely as possible, a second simulation run was carried out with the source impedance set to a value of 10kΩ. Figure 7 shows the reflection coefficients for three of the structures with different stripline length. As expected the generation of THz radiation is much less efficient as compared to the matched case. While values of more than –50 db were observed in the minimum of S_{11} for the matched case (Fig. 2) the values for the heavily mismatched case are always smaller than –1dB. Furthermore, the resonances are much broader for the mismatched source-antenna system.

It is interesting to note that the impedance mismatch has an interesting effect on the resonance frequency. Like in the matched case it shifts to lower frequncies with increasing stripline length. Yet, in the mismatched case the resonance frequency is always higher. The bare dipole, for example, now has a resonance frequency around 350 GHz. Interestingly, this frequency corresponds to a maximum in the real part of the antenna input impedance (not shown). This leads to the conclusion that the THz generation for a mismatched source-antenna system is most efficient at the frequency of the smallest impedance mismatch between antenna and source and not at the antenna resonance frequency that is observed in the matched case. This has important implications for the antenna design. To design the dipole length of a THz emitter antenna that has a resonance at 1 THz one should not apply the rule-of-thumb given above (or corrections of that taking into account the striplines) but make the arms of the dipole somewhat longer.

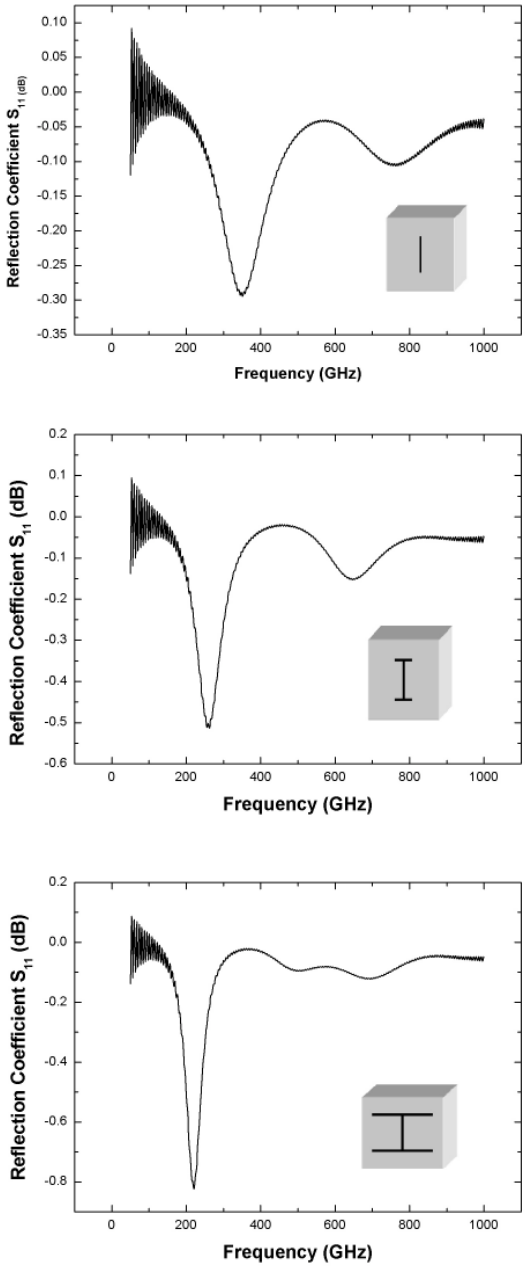

Figure 7. Shift towards lower resonance with increasing stripline length for mismatched structures

IV. SUMMARY

In summary we have studied the effect of the striplines on the performance of the dipole antenna using the simulation software CST. We find that the resonance frequency and the maximum of the input impedance of the antenna shift to lower frequencies as the length of the striplines is increased. We have also investigated the effect of an impedance mismatch between the photoconductor and the dipole antenna as this is the real life case.

V. REFERENCES

[1] P. R. Smith, D. H. Auston, and M. C. Nuss, "Subpicosecond photoconducting dipole antennas," *IEEE J. Quantum Electron.* Vol. 24, p. 255, 1988

[2] J. E. Pedersen, S. R. Keiding, C. B. So rensen, P. E. Lindelhof, W. W. Rühle, and X. Q. Zhou, "5 THz bandwidth from GaAs-on-silicon photoconductive receiver," *J. Appl. Phys* .Vol 74, p. 7022-7024, 1993

[3] M. Tani, K. Sakai, and H. Mimura, "Ultrafast Photoconductive Detectors Based on Semi-Insulating GaAs and InP," *Jpn. J. Appl. Phys.* Vol 36, p. 1175-1178, 1997

[4] S. Matsuura, M. Tani, and K. Sakai, "Generation of coherent terahertz radiation by photomixing in dipole photoconductive antennas," *Appl. Phys. Lett*. vol. 70, no. 5, p. 559, 3 February 1997

[5] P. U. Jepsen, R. H. Jacobsen and S. R. Keiding, "Generation and Detection of terahertz pulses from biased semiconductor antennas*," J. Opt. Soc. Am B*., Vol. 13, No. 11, p. 2424, November 1996

[6] M. Tani, S. Matsuura, K. Sakai, and S. Nakashima, "Emission Characteristics of Photoconductive Antennas based on Low-Temperature-Grown GaAs and Semi-Insulating GaAs" *Applied Optics*, vol. 36, No. 30, p. 7853, 20 October 1997

[7] Y. Cai, I Brener, J. Lopatta, J. Wynn, L. Pfeiffer, and J. Federici, "Design and performance of singular electric field terahertz photoconducting antennas," *Appl. Phys. Lett*. vol. 71, no. 15, p. 2076, 13 October 1997

[8] S. M. Duffy, S. Verghese, K. A. McIntosh, A. Jackson, A. C. Gossard and S. Matsuura, "Accurate Modeling of Dual Dipole and Slot Elements Used with Photomixers for Coherent Terahertz Output Power," *IEEE Trans. Microwave Theory Tech*., vol.49, no. 6, p.1032, June 2001

[9] C. R. Brewitt-Taylor, D. J. Gunton, and H. D. Rees, "Planar antennas on a dielectric surface," *Electron. Lett.,* vol. 12, pp. 729-731, Oct.1, 1981

OPTIMIZATION SUBMILLIMETER-WAVE ORBOKLYSTRON OSCILLATORS

A.A. Kurayev, A.V. Aksenchyk
Belarusian State University of Informatics and Radioelectronics
6, P.Brovki str., Minsk-220027, Republic of Belarus
e-mail: kurayev@bsuir.unibel.by

V.D. Yeryomka
Usikov Institute for Radiophysics and Electronics
of National Academy of Sciences of Ukraine,
12, Ac.Proscura St., Kharkiv, Ukraine, 61085,
e-mail: yeryomka@ire.kharkov.ua

The generating capability of submm-wave oscillators operating at 200 to 1360 GHz is provided by widely used BWOs that allow the output signal power to be produced from units to tens of mWatts [1, 2]. The technological limit achieved by submm-wave BWOs is dictated by the series factors. Orotrons [3] and orbotrons [4] are currently in the stage of laboratory investigations.

The present paper deals with one of the trends in developing orbotrons, specifically with the klystron interaction mechanism responsible for generating oscillations and multiplying a frequency with a high factor (over 1000 GHz). A multibeam klystron-type orbotron arrangement delivers a considerable high power of an electron flow within a device. A non-linear discrete-interaction model presented in [5] has been utilized in the course of computational procedures. This model uses the relativistic equations of motion in the system t, t_0 at one-dimensional approximation. To simulate an electron beam a large-size particle method is employed. Voltages around slots are distributed according to the normal law, with a distribution center around the last slot. For the calculation purposes we assume a voltage V_1 at the 1-*st* slot and a voltage V_n at the last slot. Then the voltage at the $k-th$ slot is calculated by the formula $V_k = V_n \exp\left[\left(\frac{X_k - X_n}{X_1 - X_n}\right)^2 Ln\,\frac{V_1}{V_n}\right]$ where X_k is the distance between the centers of the 1-*st* and $k-th$ slots.

	f [GHz]	V_0 [kV]	I_0 [A]	P_{5out}, W	N_b	N	h, *cm*	Δ, *cm*	d, *cm*	L, *cm*
A1	200	3	0.1	3	4	5	0.02	0.01	0.01	0.5
A2	100	3	0.5	7	8	7	0.02	0.01	0.01	0.5

The voltages $V_1 \ldots V_n$ at the slots and the lengths of drift interaction between the slot were optimized. The remaining parameters are listed in Table bellow: V_0 - acceleration voltage; I_0 - operating current of an electron flow; P_{nout} -output power at a submm-wave band; N_b - the number of electron beams, beam channel width h; ribbon-shaped EB thickness Δ; EB width L; interaction gap slot width d; number of slots N. The results were obtained from designing two-stage devices operating at 200 GHz in the first stage and 1000 GHz in the second one (prototype A1) as well as the devices operating at 100 and 1000 GHz (prototype A2 –see Tabl.) respectively. The oscillator construction provides for smooth electric tuning of an output frequency signal over a range of around 20%. The versions of multibeam orbotron-klystrons which were reffered to in the paper hold great promise, because they provide an excellent basis for developing submm-wave oscillators that are operated at frequencies between 500 and 2000 GHz.

References

[1]. E.M.Gershenzon, M.B.Golant, A.A.Negirev, V.S.Saveljev. *Backward wave oscillators of mm and submm wave bands.* (in Russian). Ed. N.D. Devjatkov. - Moscow, Radio i svjaz'. 1985. - 136 p. [2]. L.Ives, C. Kory, J. Neilson, e. a. "Development of TeraHertz Backward Wave Oscillators". *IVEC'2004. Monterey. USA. Conf. Dig. p.67-68. 2004.* [3]. V. G. Bratman, F.S. Rusin. Orotron of Submm Wave Band . *Proc. 28th Int. Conf. IRMMW'2003.* [4]. V.D.Yeryomka, A.A. Kuraev, A.K. Sinitsyn. Orbotrons - multibeam oscillators of villimeter and submillimeter waves", (in Russian), in *Proc. 14-th Int.Conf."Microwave & Telecommunication Technology"* Sevastopol: Weber Publishing Co*: 2004, p.199-202.* [5]. A.V. Aksenchik, A.A. Kuraev. *High-Power Microwave Devices with Discrete Interaction (Theory and Optimization).* (in Russian). Minsk: Besprint, 2003, 376 p.

Monolithic approach of terahertz HBV-based multipliers

M.F. Foulon, D.A. Yarekha, X. Mélique and D. Lippens
Institut d'Electronique de Microélectronique et de Nanotechnologies
Université des Sciences et Technologies de Lille
Avenue Poincaré, BP 60069, 59652 Villeneuve d'Ascq Cedex, France

Introduction: Heterostructure Barrier Varactors have demonstrated excellent performances in the millimetre wave spectrum with well defined advantages in terms of (i) C-V symmetry, (ii) lack of bias voltage and (iii) possibility to epitaxially and planar integrated several barriers in series [1]-[3]. The main drawback related to a low semiconductor barrier height for AlGaAs-based devices, with respect to the metal Schottky counterpart, has been overcome with the fabrication of high performance InP-based heterotructures solving by this way the device-related problems. In this paper, we addressed the circuit-related issues in connection with the fabrication of monolithic devices aimed at operating at Terahertz. This work is carried out in the framework of an ESA contract with the University of Lille as prime, where the epilayers are grown and where monolithic devices are fabricated on the basis of full wave analyses and advanced technologies (MBE, e-beam, RIE,...).

Integrated Circuit's approach and related issues: There are several advantages associated with the fabrication of monolithic devices. First of all, the fact to work under fixed tuning avoids the tedious mounting of the devices with the benefit of a better knowledge of the device embedding. At last, this permits to decrease dramatically the diode series resistance, which impacts dramatically the frequency capability of the device, notably by means of vertical integration techniques. Figure 1 thus shows a scanning electron micrograph of a monolithic circuit fabricated at IEMN. The active devices integrate four barriers (two during the growth and two by planar integration as shown in inset) and have demonstrated state-of-the-art performance in the upper part of the millimeter wave spectrum at 288 GHz.

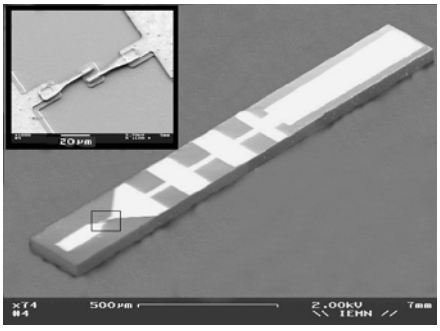

Fig. 1: SEM view of a device monolithically fabricated onto a quartz substrate

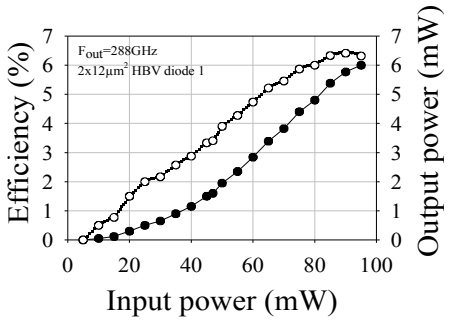

Fig. 2 : Performance of a 288GHz tripler

Upper operation frequencies targeted, that is to say between 500 GHz and 1 THz, require to further study the electromagnetic behaviour of propagation media in order to avoid multimoding by mode matching [4] and to limitate the overall losses with fixed tuned matching circuit, mainly at the input of the non-linear diode. From this side, membrane-like approach and thin film BCB technologies are currently investigated in our laboratory.

[1] T. David, S. Arscott, J.-M. Munier, T. Akalin, P. Mounaix, G. Beaudin and D. Lippens, Monolithic integrated circuits incorporating InP-based heterostructure barrier varactors, IEEE MWCL, 2002
[2] T. Bryllert, A.O. Olsen, J. Vukusic, T.A. Emadi, M. Ingvarson, J. Stake and D. Lippens, 11% efficiency 100 GHz InP-based heterostructure barrier varactor quintupler, Electronics Letters, 2005
[3] Qun Xiao, Yiwei Duan, J.L. Hesler, T.W. Crowe and R.M. Weikle, A 5 mW and 5% efficiency 210 GHz InP-based heterostructure barrier varactor quintupler, IEEE MWCL, 2004
[4] T. Decoopman, X. Melique, O. Vanbesien and D. Lippens, A taper filtering finline at millimeter wavelengths for broadband harmonic multiplication, IEEE MWCL, 2003

Analysis of multiplier with a novel symmetric ferroelectric varactor

Pär Rundqvist*, Andrei Vorobiev*, Spartak Gevorgian* † and Erik Kollberg*
*Department of Microtechnology and Nanoscience
Chalmers University of Technology
SE-412 96 Göteborg, Sweden
Email: par.rundqvist@mc2.chalmers.se
†Microwave and High Speed Electronics Research Center
Ericsson AB,
SE-431 84 Mölndal Sweden

***Abstract*— This work is aimed at investigating the potential of $(\mathrm{Ba,Sr})\mathrm{TiO_3}$ ferroelectric varactors in frequency multipliers in the 100 GHz to several THz region. There has been an increasing interest frequency generation in this frequency band in recent years. An equivalent circuit is introduced with a voltage dependent capacitance $\mathrm{C(V)}$, constant resistances and constant inductance components, to describe the impedance and multiplier behavior over a wide frequency range. The measured C-V curve is similar to that of the Heterostructure Barrier Varactors (HBV). The components values are extracted using a random optimisation method. As the thin film measurements are limited to frequencies below 50 GHz, the equivalent circuit parameters are also fitted using measured bulk data. The cut-off frequency is approximately 3 THz, which is slightly higher than initially obtained with HBVs. Harmonic balance simulations show an efficiency of around 5% for a 3x300 GHz multiplier. Our results show that the ferroelectric varactor has an interesting potential for applications in frequency multipliers at submillimetre waves and THz frequencies.**

I. Introduction

In recent years there has been an increasing interest of power generation in the lower THz region [1]. The main applications are within science, spectroscopy, radio astronomy and future communication technologies. However at frequencies of one to a few THz, there is a drop in output power of the currently available sources. This region is known as the THz gap.

Several techniques are under investigation to fill this gap, including varactor multipliers. The varactor multipliers can be divided into two categories depending on the appearance of the C-V curve, symmetric or asymmetric. A typical example of the asymmetric C-V curves is displayed by Schottky diodes. A Schottky diode in a multiplier will therefore generate both even and odd harmonics. The Heterostructure Barrier Varactor (HBV) on the other hand displays a symmetric C-V curve. The absence of even harmonics in a symmetric varactor multipliers simplifies the realisation of higher order multiplier circuits. The potential of HBV varactors has already been proven in real circuits [2].

For multiplier applications the limiting properties of varactor are the breakdown voltage, resistive losses, and the tunability of the capacitance (magnitude and shape) [3]. Ferroelectric varactors using $(\mathrm{Ba,Sr})\mathrm{TiO_3}$ (BST) have high breakdown voltage, very low resistive losses, considerable tuning, high speed and are easily scalable [4], [5], [6]. Apart from this, BST varactors are integratable on Si and have a rather simple structure compared to the HBV [7]. It should be pointed out that in ferroelectric materials the change in capacitance is due to field dependent polarisation. In semiconductor devices the capacitance changes due to electrons moving causing a depleted region. There is a certain inertia in electrons that are not present when moving polarisations. All of this makes the ferroelectric varactor a promising candidate for multipliers in the THz gap.

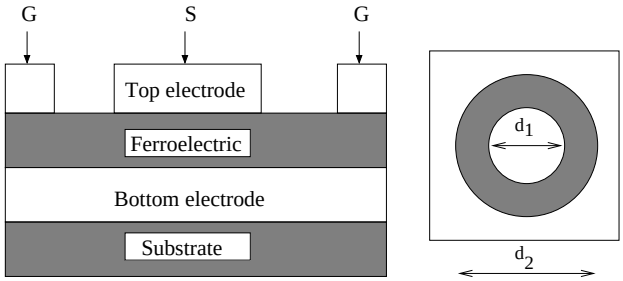

(a) Cross section (b) Layout

Fig. 1. Cross section (a) and layout (b) of the varactor.

In this paper we investigate the potential of a ferroelectric varactor made from $(\mathrm{Ba,Sr})\mathrm{TiO_3}$ in a frequency multiplier using harmonic balance simulations.

II. Experimental

High resistivity ($\rho_{Si} = 5\mathrm{k\Omega \cdot cm}$) platinized silicon $\mathrm{Pt/TiO_2/SiO_2/Si(100)}$ was used as substrate. Pt (50 nm)/Au (500 nm) bottom electrode films were deposited by e-beam evaporation at room temperature. 300 nm BST was deposited by pulsed laser ablation from a $\mathrm{Ba_{0.25}Sr_{0.75}TiO_x}$ target at 650° C and 0.4 mBar oxygen pressure using a KrF examiner laser (λ = 248 nm, τ =30 ns) operating at 10 Hz with an energy density of 1.5 $\mathrm{J \cdot cm^{-2}}$. After deposition, the sample was cooled down to room temperature at 950 mBar oxygen pressure. The Au (500 nm)/Pt (50 nm) top electrode films were

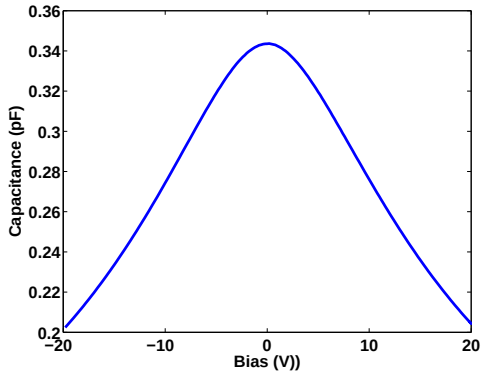

Fig. 2. Capacitance vs. DC bias at 1 MHz.

also deposited by e-beam evaporation at room temperature, Fig. 1(a). The top electrodes were patterned with a lift-off process. The layout of the top electrode consists of a central circular patch (d_1 =10 μm or d_1 =30 μm in diameter) and a co-centric outer electrode with d_2 =150 μm internal diameter as seen in Fig. 1(b). The size of the outer electrode can be considered infinite (5x5 mm).

The C-V characteristic was measured at 1 MHz using an HP LCR meter on a $d_1 = 30$ μm electrode. S_{11} was measured using a Vector Network Analyser between 45 MHz and 45 GHz connected to a top electrode with $d_1 = 10$ μm in diameter. The size of the outer electrode is for both structures d_2 =150 μm. The capacitance, tunability and $\tan\delta$ were extracted from the S_{11} measurement using methods presented in a previous work [8].

III. The equivalent circuit

The C-V curve shown in Fig. 2 is measured at 1 MHz. Note that the capacitance is measured using the larger (d_1 =30 μm) top electrode. The capacitance is easily rescaled to a (d_1 =10 μm) top electrode, in order to be easy comparable to the high frequency measurements, using Eq. 1. The capacitance of a parallel plate varactor is calculated as:

$$C = \frac{\epsilon_0 \epsilon S}{t} \tag{1}$$

where S is the surface area of the top electrode; t is the thickness of the ferroelectric film; $\epsilon_0 = 8.85 \cdot 10^{-12}$ (F/m) is the dielectric constant of the vacuum and ϵ ($\epsilon_{max} \approx 200$) is the permittivity of the ferroelectric film. The rescaled capacitance is used in further simulations.

Fig. 3(a) shows the capacitance of the varactor at 0 V and at 15 V DC-bias. It can be seen that the permittivity is frequency independent between 100 MHz and 45 GHz both at 0 V and 15 V. By comparing Fig. 3(a) and Fig. 2 we see that the maximum and minimum of capacitance is preserved. The tunability is calculated as:

$$T = \frac{C(V_{Max}) - C(V_{Min})}{C(V_{Max})} = \frac{C(E_{Max}) - C(E_{Min})}{C(E_{Max})} \approx 41\% \tag{2}$$

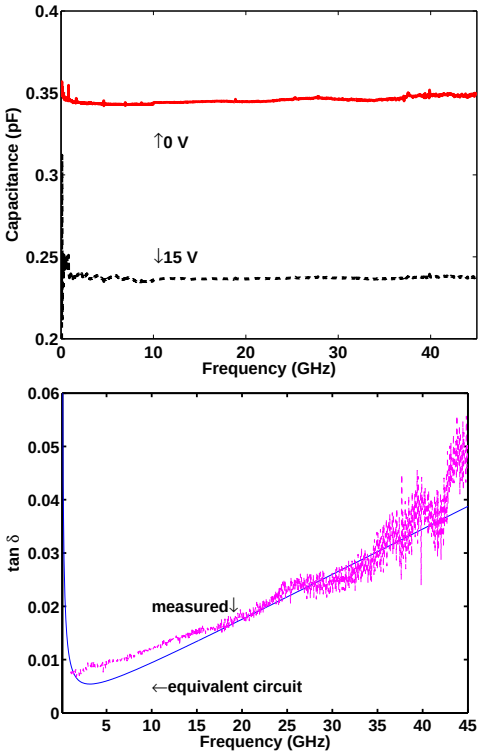

Fig. 3. The capacitance at 0V and 15v dc bias (a) vs. frequency. Measured and calculated (from the equivalent circuit) $\tan\delta$ (b) vs. frequency.

which is also frequency independent. We can anticipate a larger tunability with more applied DC bias. As these measurements are limited in frequency, due to the measurement set up, we have to rely upon STO bulk data [9], [10] for an extrapolation to higher frequencies. The bulk permittivity is essentially frequency independent up to 3 THz.

In Fig. 3(b) $\tan\delta$ can be seen as a function of frequency. $\tan\delta$ for the Device Under Test (DUT) is 0.04 at 45 GHz. However from [8] we can calculate that $\tan\delta$ in the film is 0.015 at 45 GHz. The intrinsic losses for bulk BST is 0.002 at 10 GHz and room temperature [10]. This means that the extrinsic losses are about 5 times higher than the intrinsic losses at 10 GHz. The origin of the fundamental (intrinsic) loss is the interaction of the ac-field with the phonons of the material. The extrinsic losses are associated with coupling of the ac-field with defects. Among the known extrinsic loss mechanisms those listed below are considered as significantly contributing to the loss in the tunable microwave materials [6], [11]:

1) Loss owing to charged defects.
2) Universal relaxation low mechanism.
3) Quasi-Debye contribution induced by random-field defects.

The pure intrinsic losses are increasing as f^1 [6] and the extrinsic losses, due to charged defects, increases as $f^{1/3}$ [11], [13]. The losses in the electrode increases as $f^{1/2}$ [11]. The extrinsic losses are dominating at lower frequencies and the intrinsic at higher .

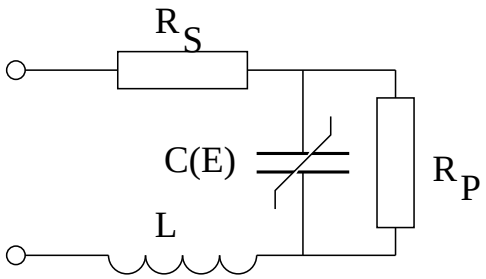

Fig. 4. Simplified equivalent circuits of the varactor.

With the measured and extracted results we now can determine an equivalent circuit. The capacitance is already found in Fig. 3(a). Looking at the physical structure in Fig. 1(a) and 1(b) we arrive at a rather complex equivalent circuit, which can be simplified [8]. The simplified circuit is shown in Fig. 4. The reason for an inductance in the equivalent circuit is to model the increase in $\tan\delta$ appearing in STO up to 3 THz [9]. The parameter values are found using a random optimisation method and comparing both thinfilm and bulk data. The voltage independent values are $L = 8.3$ fH, $R_S = 0.11\ \Omega$, $R_P = 3000\ \Omega$ and the capacitance varies in between $C_{Min} = 0.20$ and $C_{Max} = 0.34$ pF. From these parameters $\tan\delta$ can be calculated:

$$\tan\delta = \frac{Re(Z)}{Im(Z)} \tag{3}$$

the result is plotted as equivalent circuit in Fig. 3(b). Now that all the parameters in the equivalent circuit are determined we can calculate the cut-off frequency useful for comparison to other varactors.

$$f_c = \frac{1/C_{Min} - 1/C_{Max}}{2\pi R_S} \tag{4}$$

In the above equation the inductance and parallel resistance are neglected. We can now see that the cut-off frequency is 3 THz, which is the same order as for HBVs [2], [3]. The limit of 20 V in voltage swing is mainly due to the measurement set-up. We estimate by using a higher applied voltage we would reach $C_{Min} = 0.17$ pF. This would increase the cut off frequency 40 %. Even if the cut-off frequency is an important figure-of-merit regarding a varactor in a multiplier, it does not say everything. As already stated the shape of the C-V curve has a substantial influence on the varactor performance [3]. The C-V dependence in Fig. 2 can be considered as symmetric and can be therefore be described as [12]:

$$C(E) = 3.4 \cdot 10^{-13} + 1.5 \cdot 10^{-3} E^2 \tag{5}$$

Equation (5) is expressed in the electric field E(V/m) instead of applied bias voltage because of the scalability of ferroelectric varactors. If the fringing fields are ignored then the top electrode can be made as small as manufacturing tolerances (1 nm). However the fringing field must be included when the radius of the top electrode becomes comparable to the thickness [12]. The minimum thickness of the ferroelectric

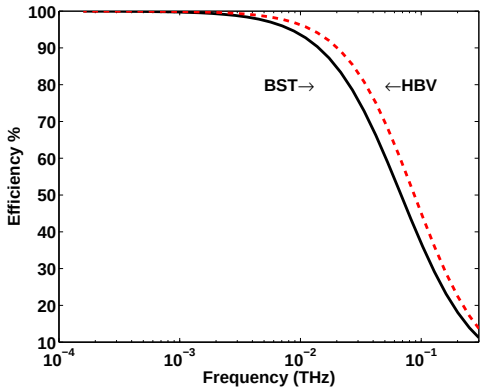

Fig. 5. The conversion efficiency for the tripler as a function of the pump frequency f_p

film is limited by the dead-layer effect [7], [11]. The dead-layer is caused by an approximately 20 nm thick layer in the ferroelectric, close to a metal electrode. This sets the lowest limits of the film thickness. The nature of dead layers are not completely understood but is usually associated with interdiffusion, chemical reactions, contamination and/or structural defects in the metal/ferroelectrics interfaces [13]. The problem is most pronounced in the ferroelectric film close to the bottom electrode. The influence of the dead layer can be reduced by using a $SrRuO_3$ (SRO) interlayer [11]. A SRO interlayer will increase $\tan\delta$. However also the capacitance (two times) and tunability (> 60 %) will increase. The cut-off frequency, however, will be approximately the same as without SRO interlayer [14].

IV. Tripler performance

An in-house harmonic balance (HB) simulator was used to calculate the conversion efficiency for the third order harmonics. We used 15 dBm input power, the C-V dependence in Eq. (5), (Fig. 2) and the equivalent circuit shown in Fig. 4 in the simulations. The resulting efficiency is shown in Fig. 5. Also shown is a curve for the empirical expression for HBV tripler:

$$\eta = \frac{100}{1 + \alpha(\frac{n \cdot f_p}{3 \cdot f_c})^\beta} \tag{6}$$

Where $\alpha = 200$ and $\beta = 1.5$ are empirically determined and n is the order of the multiplication [15]. These results are confirmed for higher frequencies by a commercially available ADS HB simulator. The efficiency for the ferroelectric varactor is close to 100% for lower frequencies with a rapid decrease as the frequencies approaches the cut-off frequency. This is in correspondence with results presented on HBVs [3]. Compared to these HBVs the series resistance R_S is lower but the tunability is also lower. One major contributor to the lower tunability is material defects in the ferroelectric thin film, strains and film interfaces to metal electrodes.

V. Accuracy

When making HB simulations, the accuracy of the parameters involved is very important. In a previous paper we reported

that the error in both C and $\tan\delta$ is less than $\pm 10\%$ [8]. As R_S is derived from the S_{11} measurement in the same manner as C, the error can be estimated to be less than $\pm 15\%$. The HB simulations are very sensitive to error in R_S [3]. If we start by considering the possible error in the cut-off frequency Eq. (1), we have:

$$\Delta f_c < |f_c \frac{\Delta R_S}{R_S}| + 2|f_c \frac{\Delta C}{C_{Min}}| \approx 0.35 f_c \qquad (7)$$

This shows that the error in cut-off frequency can be as large as 35% or 1 THz. As we have seen before the efficiency is very dependent on the cut-off frequency and thereby R_S and C. Dillner et al have investigated the large influence in the efficiency of any change in R_S. [3].

VI. Discussion and conclusion

This work is aimed at investigating the potential of $(\mathrm{Ba,Sr})\mathrm{TiO}_3$ ferroelectric devices for THz multiplier applications. A simple equivalent circuit is used to achieve foundations for harmonic balance simulations. The equivalent circuit ($L = 1.5$ fH, $R_S = 0.11\Omega$, $R_P = 3000\Omega$, $C_{Min} = 0.20$ and $C_{Max} = 0.34$ pF) is designed to describe the frequency dependence of both $\tan\delta$ and the impedance of the device. The cut-off frequency of the device is approximately 3 THz, which is of the same order of magnitude as the HBVs. Harmonic balance simulations show an efficiency of around 5 % for a 3x300 GHz multiplier. All this put together shows that the ferroelectric varactor has potential for frequency multipliers in the THz region. However the results are very dependent on material properties, the losses increased and the tunability decreased for thin films compared to bulk. At the same time the integration of a simple technology on Si is vital for future applications.

Our results show that the ferroelectric varactor has an interesting potential for applications in frequency multipliers at submillimetre waves and THz frequencies.

Acknowledgment

This work was supported by Swedish Strategic Research Foundation SSF (Oxide and HSEP Research center), VR project components for future microwave systems, Ericsson AB and Vinnova (PIDEA/Pacific boat). Thank you Bahar M. Motlagh and Sten Gunnarsson for the help with ADS and Jan Stake for help with the in-house HB simulator.

References

[1] P. H. Siegel, *"Terahertz technology in biology and medicine"* IEEE trans Microwave Theory and Techn. 52, no 10 2438 (2004).

[2] M. Ingvarsson, A. Ø. Olsen, J. Stake, *"Design and analysis of 500 GHz heterostructure barrier varactor quintuplers"* Proc. 14th international symposium on space terahertz tech. 2003.

[3] L. Dillner, J. Stake, E. L. Kollberg *"Analysis of symmetric varacrtor frequency multipliers"* Microwave Opt. Techn. Lett. Vol 15.

[4] S. Gevorgian, E. Kollberg, *"Do we really need ferroelectrics in paraelectric state only in electrically controlled microwave devices?"* Asia-Pacific Microwave Conference Proceedings, APMC, 2000, p 23

[5] A. Vorobiev, P. Rundqvist, K. Khamchane, S. Gevorgian, *"Silicon substrate integrated high Q-factor parallel-plate ferroelectric varactors for microwave/millimeterwave applications"* Appl Phys Lett 83, 3144 (2003).

[6] A. K. Tagantsev, V. O. Sherman, K. F. Astafiev, J. Venkatesh, N. Setter *"Ferroelectric materials for microwave tunable applications"* J. Electr. Cer. Vol 11, pp. 5-66 (2003).

[7] R. York, A. Nagra, E. Erker, T. Taylor, P. Periaswamy, J. Speck, S. Streiffer, O. Auciello, *"Microwave integrated circuits using thin-film BST"* IEEE International Symposium on Applications of Ferroelectrics, v 1, 2000, p 195-200.

[8] P. Rundqvist, A. Vorobiev, S. Gevorgian, *"Non-destructive microwave characterisation of ferroelectric films on conductive substrates"* Intrg. Ferroelectr. 60:1-19, 2004.

[9] J. Petzelt, T. Ostapchuk, I. Gregora, I. Rychetsky, S. Hoffmann-Eifert, A. V. Pronin, Y. Yuzyuk, B. P. Gorshunov, S. Kamba, V. Bovtun, J. Pokorny, M. Savinov, V. Porokhonskyy, D. Rafaja, P. Vanek, A. Almeida, M. R. Chaves, A. A. Volkov, M. Dressel, R. Waser, *"Dielectric, infrared, and Raman response of undoped $SrTiO_3$ ceramics: Evidence of polar grain boundaries"* Phys. Rev. B (Condensed Matter and Materials Physics), v 64, n 18, 1 Nov. 2001, p 184111/1-10.

[10] K. Bethe, Philips Res. Repts. Suppl. 2, 74, Eindhoven, Netherlands: N. V. Philips' Gloeilampenfabrieken, 1970, pp. 55-97.

[11] A. Vorobiev P. Rundqvist S. Gevorgian, *"Microwave loss mechanism in $Ba_{0.25}Sr_{0.75}TiO_3$ thin film varactors"* J. Appl. Phys.

[12] J. Im, S. K. Streiffer, O. Auciello, A. R. Krauss, *"$Ba_xSr_{1-x}Ti_{1+y}O_{3+z}$ interface contamination and its effect on electrical properties"* Applied Physics Letters, v 77, n 16, 16 Oct. 2000, p 2593-5

[13] P. Rundqvist, A. Vorobiev, S. Gevorgian, *"Large Signal Circuit Model of Parallel-Plate Ferroelectric Varactors"* European Microwave Conference, Amsterdam Nederlands, EuMC Oct, 2004.

[14] P. Rundqvist, A. Vorobiev, S. Gevorgian, *"Influence of $SrRuO_3$ interlayer in ferroelectric BST varactors"* To be published.

[15] J. Stake, S. H. Jones, L. Dillner, S. Hollung, E. L. Kollberg, *"Heterostructure-barrier-varactor design"* IEEE Trans. on Microwave Theory Tech, vol. 48, pp 677 - 682, 2000

A low-temperature-grown (LT) GaAs based photomixer as a local oscillator (LO) for a hot electron bolometer (HEB) mixer at 700 GHz

E. A. Michael,[a] P. Munoz,[a] I. Camara Mayorga,[c] M. Mikulics,[b] K. Jacobs,[a] C. E. Honingh,[a] R. Schieder,[a] R. Güsten,[c] and J. Stutzki [a]

[a] *1. Physics Institute, University of Cologne, Zülpicher Str. 77, 50937 Köln, Germany*
[b] *Institute of Thin Films and Interfaces (ISG-1), Research Center Jülich, 52425 Jülich, Germany*
[c] *Max-Planck-Institute for Radioastronomy, Auf dem Hügel 69, 53121 Bonn, Germany*

A LT-GaAs based traveling-wave photomixer [1, 2] was applied to pump a NbTiN-based membrane-mounted and waveguide-integrated HEB mixer of 2 μm^2 area. [3,4]
To couple most of the LO power to the mixer, a Martin-Puplett diplexer was used together with a Gaussian telescope, consisting of two 90°-offaxis mirrors transforming the beam waist of the photomixer to the one of the mixer horn. The diplexer, situated in between the two mirrors, showed a transmission of 75% at an IF of 1.1 GHz in the right polarisation. The Gaussicity of the photomixer bow-tie antenna beam pattern was calculated to 65 %. With 1 µW output of the photomixer the HEB was pumped to estimated 70 % of the optimal level at which it was characterised with a multiplier-LO and showed T_{sys}=1200 K. The sub-optimal pump level led to T_{sys}=1500K, which is only moderately increased. According to the above numbers the estimated power was 500 nW at the HEB dewar window in the fundamental Gaussian mode, while the absorbed power in the HEB was determined to 300 nW with the isothermal method.
Apart from the experiment with the HEB, best photomixer samples were shown to produce 2µW of power at 700 GHz, which, according to the above results, must be sufficient power for pumping the investigated HEB optimally. The THz power was measured with a calibrated large-area 4.2K-InSb-bolometer with a Winston cone, which is sensitive also to the calculated 35% of higher modes from the photomixer antenna.
Operated near their voltage and IR power limits our photomixer chips where found to have a statistical life-time of a few days due to electrostatically attracted dust particles in a normal laboratory atmosphere, because a protective IR antireflection coating was not applied up to now due to its poor reproducibility. However, ultimate photomixers will be manufactured with this antireflection coating and thus will be more durable.

References:

[1] E. A. Michael, M. Mikulics, M. Marso, P. Kordoš, H. Lüth, B. Vowinkel, R. Schieder, J. Stutzki, “Large-area traveling-wave LT-GaAs photomixers for LO application”, Millimeter and Submillimeter Detectors for Astronomy II, June 23-25 2004, Glasgow, Scottland, UK, Proceedings of the SPIE 5498, p. 525 (2004)

[2] E. A. Michael, M. Mikulics, M. Marso, B. Vowinkel, R. Schieder, and P. Kordos, “Large-area traveling-wave photonic mixers for increased continuous terahertz power”, Appl. Phys. Lett. 2005, in press

[3] P. Munoz et al., to be published

[4] S. Bedorf, et al, this conference

On Possibilities of Real-Time Millimeter/Terahertz Three-Dimensional Imaging of Remote Concealed Objects

Leonid V. Volkov, Alexander I. Voronko, Natalie L. Volkova
Secomtech Ltd., 24/2, 125, Prospect Mira, Fryazino,
Moscow region, 141196, Russia, (E-mail: leon_volkov@mail.ru)

Usage of MMW/THz imaging systems for remote stealth screening of suspect individuals at entries is of growing interest. Passive imaging systems exploiting only natural MMW/THz emission within observable scene are not quite effective for indoor inspections due to low brightness temperature contrast. The authors have proposed two novel active MMW/THz quasi-optical imaging techniques which are taking into account peculiarities of reflections of the MMW/THz radiation with most objects of interest and intensively exploiting possibilities of state-of-the-art transceiver apparatus for the radiation. The first technique [1] is intended for remotely forming two-dimensional (2D) images of enhanced quality and extended information content. It is based on concealed object illumination with encoded multi-parameter radiation, formation of distinct partial images and digital synthesis of resulting images. The technique was experimentally confirmed by the authors and a prototype is currently under development. The second technique [2] allows to remotely form three-dimensional (3D) images of concealed objects with spatial localization/ substitution of strong reflections appearing due to hard/wet clothes and skin. It is based on focusing of object-reflected radiation onto focal plane array (FPA) by means of lens, thereby it is exploited stepped frequency radar approach for illuminating the object and further coherent detection of portions of focused radiation being spatially distinctly sampled with FPA elements in the lens focal plane (Fig.1). Fourier Transformation of complex signal sets each of which is distinctly received with particular FPA element allows to reconstruct 3D (volume) image of objects which is disposed within space layer near sharply focused object surface. The first experiments realizing aforesaid technique in its one-element monostatic realization were performed in [3]. This paper outlines the theory of the 3D imaging system operation and presents analysis of factors limiting possibilities of quasi-optical 3D imaging .

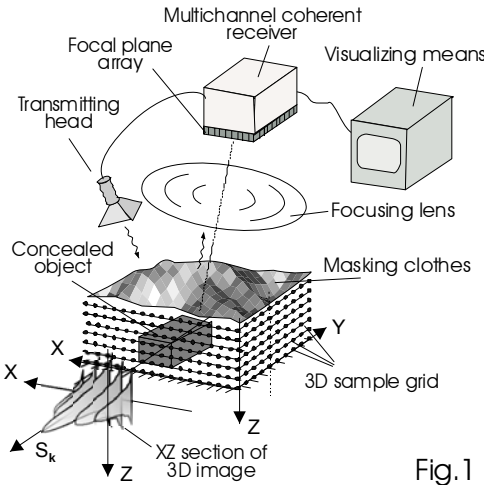

Fig.1

References

1. L.V.Volkov, A.I.Voronko,N.L.Volkova, Proc.of European Microwave Conf. 2003, Munich, v.**2,** pp. 531-534.
2. L.V.Volkov, etc, PCT WO 03/098262 A1 , 27 November 2003.
3. J. Detlefsen, etc., Proc. of European Radar Conf.2004, Amsterdam, pp.279-282.

Phase Synchronization of BWO SubTHz Frequency Range, Applying Superlattice Harmonic Mixer

Vladimir L. Vaks, *Member, IEEE,* Dmitry G. Paveliev, *Member, IEEE,* Yu. I. Koshurinov, Valery P. Koshelets, *Member, IEEE,* Alexander N. Panin

***Abstract*— We report generation of a signal of 667-857 frequency range by means of a synthesizer of 15-20 GHz frequency range. Frequency of the reference is multiplied 30-45 times by means of mixer based on superlattice structures. The mixer is used at the room temperature.**

***Index Terms*—THz frequency range, phase synchronization, superlattice structures, diode**

I. INTRODUCTION

THE great interest to the THz frequency range is caused by new possibilities for investigations, first of all, in high resolution microwave spectroscopy. These investigations substantially stimulate a lot of researches, for example radio-astronomical ones [1].

However, this region is one of the least explored ranges. Until recently, it was difficult to efficiently generate and detect THz radiation. Most THz sources were either low-brightness emitters such as thermal sources, or cumbersome, single-frequency molecular vapor lasers. The only source of wide-range coherent THz radiation – backward wave oscillator (BWO) – generates till 1200 GHz. Recently, however, there has been a progress in THz technology due to the using of optical techniques such as femtosecond laser [2]. Application of such sources, based on femtosecond lasers, allow to create THz spectrometers [2], which are capable to solve various problems, for instance studying of biological molecules [3], liquids [4,5] and solids [6,7]. Although it is worth pointing out, that spectral resolution is worse than 1 cm^{-1}. It is insufficient for the high resolution spectroscopy naturally. Necessary condition of high spectral resolution is a source having narrow line and accurate control of frequency. Spectroscopic requirements to frequency parameters and spectrum of the high quality source are usually determined by necessity of resolving of Doppler broadened lines ($\sim 10^{-6}$) and finding of frequencies and its displacement to within $\sim 10^{-8} \div 10^{-10}$.

Usually such a system - frequency synthesizer – represents a system of proportional multiplication (based on phase lock of generators of various ranges) of reference synthesizer frequency (as a rule of centimeter range). This system fulfils the requirements described above. Its frequency stability is near 3×10^{-10} c^{-1}, comparative spectral width is about 3×10^{-10} at l =1 mm. The first frequency synthesizer, described in [8], had 6 multiplication rings. In general, as nonlinear element in harmonic mixers of GHz frequency range planar semiconductors Schottky diodes (SD) are used [9-15]. However application of these diodes in the THz region requires increase of limiting frequency of the diode, f_p, (a frequency which determines the upper limit of working range of diode). Unfortunately it is quite difficult due to some restrictions. On the one hand the limiting frequency is given by peculiarities of processes in semiconductors, particularly by inertness of flight of electrons (for Schottky barrier). Time of flight for the best SD is about 1 ps [14]. On the other hand, the limiting frequency is specified for the most part by influence of parasitic capacitance of diode, C, and series resistance, R_s ($f_p = 1/2\pi R_s C$). The latter consists of resistance of semiconductor thickness, contact junction and outputs of diodes. Capacity of Schottky diode, which active area is several mkm, is not less than 3 fF [12-14]. Decrease of the series resistance by increasing of alloyage is restricted to the concentration of 5×10^{17} ?? $^{-3}$ [13, 14].

More short response time and lesser capacities can be obtained by making planar diodes based on semiconductor superlattice structures (DSS) [16,17]. Current-voltage characteristic of the superlattice structures has negative differential conductivity till to several THz [11,12]. All these peculiarities of the superlattice structures make them attractive for investigations, since generators, mixers, detectors based on these structures, can be used for elaboration of new sources and detectors of THz radiation.

In the paper [21] there was done a comparison between planar diodes based on the superlattice structures and planar

Manuscript received July, 6 2005.

This work was supported by RFBR (project 03-02-17088), Program of Physical Science Department RAS (project "Problems of radiophysics"), ISTC (project 2445) and INTAS (project 367).

Vladimir L. Vaks and Alexander N. Panin are with the Institute for Physics of Microstructures of Russian Academy of Sciences (IPM RAS), GSP-105, 603950 Nizhny Novgorod, Russia (phone:+7-8312-607-648; fax: +7-8312-385-553; e-mail: vax@ipm.sci-nnov.ru).

Valery P. Koshelets, is with the Institute of Radio Engineering and Electronics (IREE RAS), Russian Academy of Sciences, 101999 Moscow, Russia (e-mail: (e-mail: valery@hitech.cplire.ru).

Dmitry G Paveliev and Yu. I. Koshurinov are with N.I.Lobachevsky Nizhniy Novgorod State University, GSP-20, 603950 Nizhniy Novgorod, Russia (e-mail: pavelev@rf.unn.ru).

Schottky diodes. To do it a special method was applied [22], which allows managing without THz detectors. According to the method a diode is treated with signals of two mm sources, which have different frequencies F_s and F_p. Low-frequency signal of beating, f_{if}, (between harmonics mF_s and nF_s, where m,n are integers) is intensified by low-noise amplifier and observed on a screen of a spectral analyzer. Tuning the frequencies F_s and F_p and observing displacement of f_{if} on the screen of analyzer, one can determine harmonic numbers m, n, appearing in the diode. For studying diode's characteristics in the mm frequency range, the diodes were put into metallic single-mode waveguides of 80 ÷120 GHz. Block diagram includes two synthesizers (80 ÷120 GHz and 115÷150 GHz), set of attenuators, low-noise amplifier of 1÷2 GHz frequency range, spectral analyzer of 0.1÷2 GHz and constant-current source. Maximal harmonic frequency observed for diodes based on superlattice structures was 3000 GHz, but for SD it was 1800 GHz. Experimental dependence of signal strength of beating on the harmonic's number was approximated by a power polynomial with index of power -5.3. For DSS the index of power was -3.6 (see Fig 1).

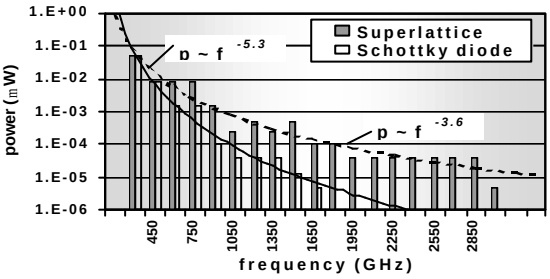

Fig. 1. Experimental dependence of the signal power on the harmonic's number for Schottky diode and diode based on superlattice structures. It was approximated by a power polynomial.

Therefore, planar diodes based on alloyed superstructures can be used for construction of THz sources. Let us consider application of amplifiers based on DSS for stabilization of subTHz generator.

At present phase lock systems of BWO utilizing harmonic mixers based on SD with automatic tuning with respect to reference source of frequency range 8÷18 GHz. In this system phase lock is realized on 16 ÷26 harmonics of reference synthesizer HP 8673 E with output power 20 mW. In the phase lock systems of BWO of frequency range 380÷1000 GHz harmonics 4÷10 of synthesizers (78 ÷118 GHz and 118÷178 GHz) are used.

II. EXPERIMENT

Below we describe phase lock loop system of 526÷714 GHz frequency range of BWO OV-80 and phase lock loop system of 667 ÷ 857 GHz of BWO OV-81, where harmonic mixer based on DSS was applied. In latter phase lock synchronization is fulfilled with respect to 30th and 44th harmonics of reference synthesizer of 8÷20 GHz frequency range. Beforehand we measured characteristics of multipliers, based on DSS to use them as THz sources till 2.5 THz. Also there were done measurements (till 1 THz) of characteristics of harmonic mixers based on DSS for the phase lock of BWO. Earlier measurements of the properties of multipliers based on DSS shown, that necessary power of input signal must be 12 ÷20 mW. To optimize a work of DSS, we investigated possibility of operation of multipliers, based on DSS, under voltage. To study dependence of characteristics of DDS on voltage there was used frequency synthesizer (of 8÷18 GHz, with output power to 100 mW) as an input signal source. Application of such a synthesizer allowed comparing characteristics of DDS in two different regimes: with and without bias.

As a result of the experiment we established that supply of bias causes decrease of necessary power of input signal, but the noise of output signal increases and some points of frequency range have frequency modulation of output signal. The latter indicates a bad balancing of reference generator's channel and input of multiplier based on DSS. We carried out qualitative measurements of noises of harmonic mixers on DSS in channel of intermediate frequency. The results shown that if a commercial amplifier M42136 "Saljut" (with noise coefficient k =2 dB at t=25^{0}C) is used as intermediate-frequency amplifier, mixer's noise is higher than one of the multiplier per 5 dB. The measurements were done by Hewlett Packard E4402B. Conversion ratio of harmonic mixer of input signal (power 0.5 mW, frequency 844 GHz) with 44th harmonic of reference generator (power 20 mW, frequency 19.175 GHz) is 80 dB.

Block diagram of the BWO phase-lock loop system for OV-80 and OV-81 is shown on pic.2.

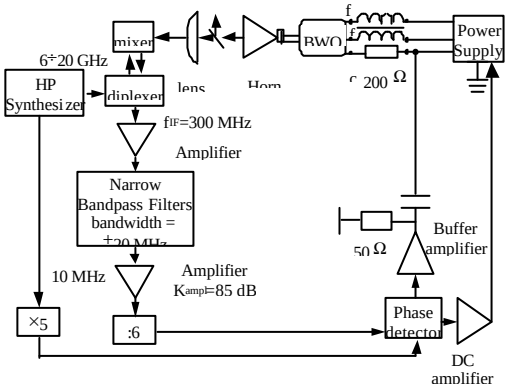

Fig. 2. Block diagram of the BWO phase-lock loop system

As a reference generator we apply a synthesizer of frequency range 0.01 ÷20 GHz in the set-up. In the frequency range of 667 ÷857 GHz synchronization is obtained at the 37th and 44th harmonics of reference synthesizer. The intermediate frequency channel consists of three multipliers M42136 and band-pass filter with bandwidth 40 MHz at the frequency 300 MHz. The total gain constant of intermediate-frequency

amplifier is 85 dB. To improve a noise-to-signal ratio incoming to the frequency-phase detector, the bandwidth of intermediate frequency channel is chosen as narrow as possible, but it is taken into account bandwidth of signal, which is generated by BWO freely. This bandwidth is 20 MHz. Control of the BWO frequency is done by two-channel scheme.

Command of frequency-phase detector is divided on two channels: low-frequency one (0-40 kHz) and high-frequency channel (higher than 40 kHz). Frequency-phase detector is built on a chip PE3236 of Peregrine with reference frequency 50 MHz. Control of BWO frequency at low-frequency channel is realized by high-voltage power supply. Command of high-frequency channel is given to a cathode of BWO trough disjunctive capacity. Such a control scheme of BWO let one obtain maximum broad synchronization range of 5 MHz.

Spectral analysis of characteristics of PLL BWO is done at the signal of intermediate frequency. On fig.3 the spectrum of signal of intermediate frequency (at a frequency 300 MHz) of BWO output signal (on a frequency 844 GHz) is presented. The measurements are done by spectrum analyzer ROHDE SCHWARZ 1093.4495.30.

Our results of investigation of the BWO synchronization and characteristics of harmonic mixers based on DSS give a possibility to obtain BWO synchronization (till 1 THz), applying the presented method.

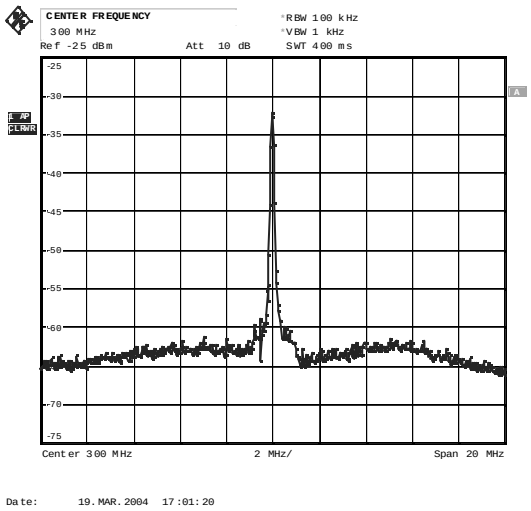

Fig.3. Line shape of PLL spectral power density. Center frequency is 300 MHz, Ref is -25 dBm, Att. is 10 dB, RBW is 100 kHz, VBW is 1 kHz, SWT is 400 ms.

REFERENCES

[1] Winnewisser, J.Mol.Sctruc., 408/409, 1 (1997).

[2] A.G.Davies, E.H.Linfield, M.B. Johnston, Phys.Med.Biol., 47, 3679 (2002).

[3] A. Markelz, S.Whitmire, J.Hillebrecht, R. Birge, Phys.Med.Biol, 47, 3797 (2002).

[4] R.McElroy, K.Wynne, Phys.Rev.Lett., 79, 3078 (1997).

[5] G.Haran *et al* , Chem.Phys. Lett. 274, 365 (1997).

[6] Y.Y. Divin *et al*, Physica C, 372-376, 416 (2002).

[7] H. Murakami, *et al*, Physica C, 367, 322 (2002).

[8] V.L.Vaks, L.I.Gershteyn, A.V.Maslovskiy. Submillimeter frequency synthesizer. // Pribory i technika eksperimenta, ? 6, p. 210-202 (1984) (in Russian)

[9] *Microwave semiconductor devices and their circuit applications*, ed. by H. A. Watson (N.Y.-Toronto-London-Sydney, McGraw-hill Book Company, 1969)].

[10] *Spectroscopic techniques for far-infrared, submillimetre and millimeter waves*, ed. by D. H. Martin (Amsterdam, North-Holland Publishing Company, 1967)].

[11] J.A. Calviello. IEEE Trans. Electron Devices, **ED-26**, 1273, (1979).

[12] F. Lewen, R. Gendriesh, I. Pak, D.G. Paveliev, M. Hepp, R. Schieder, G. Winnerwisser. Rev. Sci. Instrum., **69**, 32 (1998).

[13] F. Maiwald, F. Lewen, B. Vowinkel, W. Jabs, D.G. Paveljev, M. Winnerwisser, G. Winnerwisser. IEEE Microwave and Guided Wave Letters, **9**, 198 (1999).

[14] F. Maiwald, F. Lewen, V. Ahrens, M. Beaky, R. Gendriesch, A.N. Koroliev, A.A. Negirev, D.G. Paveliev, B. Vowinkel, G. Winnewisser. J. Mol. Spectrosc., **202,** 166 (2000).

[15] C.-I. Lin, A. Vogt, M. Rodriguez-Gironés, A. Simon, H.L. Hartnagel. Pt/n-GaAs Schottky Diodes using InAs-Electrode for THz-Applications. *Annual Report*, p. 33, (1998).

[16] Brandl, E. Schomburg, R. Scheuerer, K. Hofbeck, J. Grenzer, K.F. Renk, D.G. Pavel'ev, Yu. Koschurinov, A. Zhukov, A. Kovsch, V. Ustinov, S. Ivanov, P.S. Kop'ev. Appl. Phys., 73, 3117 (1998).

[17] E. Schomburg, K. Hofbeck, R. Scheuerer, M. Haeussler, K.F. Renk, A.-K. Jappsen, A. Amann, A. Wacker, E. Scholl, D.G. Pavel'ev, Yu.Koschurinov. Phys. Rev. B, **65**, 155320 (2002).

[18] L. Esaki, R. Tsu. IBM J. Res. and Dev., **14,** 61 (1970).

[19] S. Winnerl, E. Schomburg, J. Grenzer, H.-J. Regl, A. A. Ignatov, A. D. Semenov, K.F. Renk, D.G. Pavel'ev, Yu. Koschurinov, B. Melzer, V. Ustinov, S. Ivanov, S. Schaposchnikov, P.S. Kop'ev. Phys. Rev. B, **56**, 10303 (1997).

[20] F.Maiwald, F.Lewen, V.Ahrens, M.Beaky, R.Gendriesch, A.N.Koroliev, A.A.Negirev, D.G.Paveliev, B.Vowinkel, and G.Winnewisser, Journal of Molecular Spectroscopy 202,166-168 (2000).

[21] D.R.Woods, R.G.Strauch, Proc. IEEE, 54, 673 (1966).

[22] V.P.Koshelets, A.B.Ermakov, S.V.Shitov, P.N.Dmitriev, L.V.Filippenko, A.M.Baryshev, W.Luinge, J.Mygind, V.L.Vaks, D.G.Pavelèv, Applied Superconductivity, IEEE Trans. on Appl. Supercond., **v.11,** No 1, pp. 1211-1214, (2001).

Poster session VI:

Components

Design curves for the Picket-Potter horn-reflector antenna for THz applications

A. Airalucksanawong, S. Wangsuya, P. Kittara and G. Yassin

email: tepcy@mahidol.ac.th, ghassan@astro.ox.ac.uk

A feed may be considered suitable for high performance THz detectors if it satisfies the following requirements: 1. efficient coupling of radiation from telescopes to the detector. 2. easy to fabricate. Conventionally, THz detectors have employed corrugated horn to couple radiation from the telescope to the detector since they are known to have low side lobes and cross polarization levels over a substantial fractional bandwidth. It is well known, however, that fabrications of corrugated horns at THz frequencies are difficult since several corrugation per wavelength are needed in order to guarantee a pure hybrid mode over a large bandwidth.

In previous papers [1,2], we describe a feed called the Pickett-Potter horn (PPH) antenna which has only a single step discontinuity at the horn throat. We have demonstrated that this antenna exhibits a performance which is comparable to corrugated horns over a fractional bandwidth of 15%. Analysis of the Pickett-Potter horn (PPH) antenna was carried out using the modal matching technique. The radiation patterns of the horn are then calculated using a diffraction theory method. To collimate the beam, we place the phase centre of the horn at the focus of a 90-degree offset parabolic reflector to form a Pickett-Potter horn-reflector (PPHR) antenna. To find radiation patterns of the PPHR antenna we propagate the horn field into the projected aperture using a conformal mapping method.

From the discussion above, we notice that calculating the radiation pattern of the PPHR antenna exactly is quite involved. In this paper, we present design formula, procedures and graphs that allow computing the radiation pattern of the PPH and PPHR antennas. For example, we shall provide design curves that give optimized horn parameters for a required radiation patterns. This includes the step dimension, the input waveguide radius and the horn parameters as function of the phase error scaled to wavelengths. We shall also give analytical expression that relates the beamwidths of the PPH to that of the PPHR antenna.

[1] P. Kittara *et al*, "A Pickett-Potter horn-reflector antenna for submillimetre-wave applications," *Proc. 11th ISSTT*, pp. 598-607, 2000
[2] P. Kittara *et al*, "A 700-GHz SIS Antipodal Finline Mixer Fed by a Pickett–Potter Horn-Reflector Antenna", *IEEE Trans. Microwave Theory Tech*., 52(10), pp. 2352-2360, Oct. 2004

Integrated Planar Antennas at Terahertz Waves

A. Semenov, H. Richter, B. Günther, H.-W. Hübers, J. Karamarkovic

***Abstract* — We present the terahertz performance of integrated lens antennas consisting of a double-slot or a log-spiral planar feed and a synthesized elliptical lens. The radiation pattern and the impedance of the planar feeds are computed using the method of moments; the collimating action of the lens is modeled using the physical-optics approach based on the Huygens principle. In the frequency range from 1.5 to 3 THz (double-slot feed) and 0.6 to 5 THz (log-spiral feed) the measured antenna efficiency and radiation pattern correspond fairly well with the results of simulations approving this simulation technique as a reliable tool for the antenna design.**

***Index Terms*—planar antennas, impedance, beam pattern**

I. Introduction

Exploring the terahertz frequency range becomes an important trend in planetary science, astronomy and security research. For terahertz receivers the planar integrated quasioptical technology is expected to be a preferable alternative to wave-guide based front ends. Although corrugated horns can be fabricated for frequencies up to 2.5 THz, they are getting more expensive to manufacture and the effect of misalignments becomes more severe when the frequency increases. Recent progress in nano-structuring and micro-machining allows reliably producing and aligning planar antenna structures on dielectric surfaces with an accuracy sufficient for the terahertz range. Log-periodic, log-spiral, double-slot and double-dipole feed antennas integrated with quartz or silicon lenses have been shown to successfully couple radiation in the frequency range from 30 GHz to 5.2 THz. However, designing an integrated quasioptical front-end requires reliable modeling of the feed-antenna performance. A semi-analytical, lumped element technique that was implemented so far provides results inconsistent with the experimental data at frequencies above a few terahertz [1]. The main reason, e.g. for a double-slot feed, is that this technique neglects frequency-dependent parasitic impedances appearing at the points where virtual lumped elements are connected to each other. As a result, experimentally verified resonance frequencies of the double-slot feeds do not coincide with the computed resonance frequencies. Although the discrepancy can be partly relaxed taking into account the geometric inductance of the detector used for experimental evaluation, the remaining inconsistence is rather large. This obstacles the feed design and engineering of the entire integrated antenna.

In this work we have applied the method of moments (MoM) to the entire feed structure including the slots as well as imbedding and interconnecting elements. The MoM solution was then used as an input for the physical-optics ray-tracing (PORT) procedure to obtain the beam parameters of the integrated lens antenna. The performance of integrated antennas was experimentally evaluated in combination with a hot-electron bolometer. We compare simulated and measured performance of integrated antennas with double-slot planar feeds and complementary log-periodic planar feeds and verify this technique at frequencies from 1.5 THz to 3 THz and from 0.6 to 5.2 THz, respectively.

II. Simulation Procedure

A. Feed antennas

The full wave method of moments reveals the current and charge density distribution in the antenna by solving numerically Maxwell equations with boundary conditions on a virtual mesh superimposed on the real structure. The fields at an arbitrary observation point can be computed via scalar and vector potentials generated by the source densities. We used the FEKO software package [2] that combines the accurate method of moments with the physical optics approach and the uniform theory of diffraction to obtain fields radiated by our planar feeds. We applied this technique to the double-slot and log-periodic planar feeds printed on the plane boundary of a dielectric. The geometry of the feeds used in this study is defined in Fig. 1, 2, the sizes of the feeds are shown in Table I

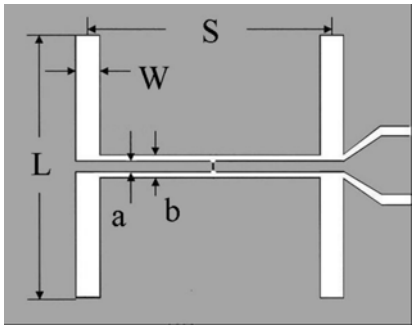

Fig. 1. Layout of a double-slot feed antenna. Gray color denotes the gold layer, white color – the dielectric. The bolometer (or the excitation slit) is located in the middle of the co-planar line connecting vertical slots.

A. Semenov, H. Richter, B. Günther and H.-W. Hübers are with the DLR institute of Planetary Research, 12489 Berlin, Germany. (corresponding author e-mail: Alexei.Semenov@dlr.de)

J. Karamarkovic is with the Faculty of Civil Engineering and Architecture, University of Nis, Serbia and Montenegro, fizika@gaf.ni.ac.yu

TABLE I
SIZES OF THE STUDIED DOUBLE-SLOT FEEDS.

Feed	a, μm	b, μm	L, μm	S, μm	W, μm
TWS1	2	4	60	32	4
TWS2	2.2	3.3	40	21	2.2
TWS3	2	4	33.5	20	2.4
TWS4	2.2	3.3	46	24	3
TWS5	3.6	2.4	30	17	2.4
TWS6	2	4	50	28	3.6
TWS7	3.6	5.1	55	30	3
TWS8	2	4	46	28	3

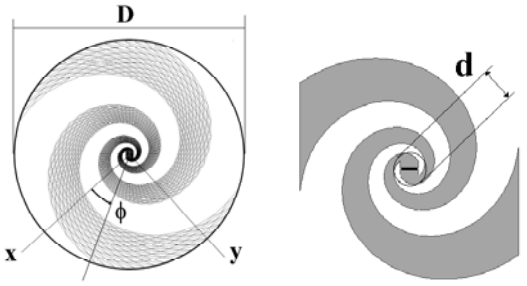

Fig. 2. Left: Full structure of the spiral feed and the mesh used for the MoM simulation. The angular position of the beam-cut is defined by the azimuth angle ϕ. Right: The smallest size *d* of the feed and the excitation slit. The parameter a = 0.36 [3] was chosen to build the arms of the feed antenna according to $R = R_0 \exp(a\,\phi)$ with ϕ been the angle and *R* the distance from the geometric center of the feed.

TABLE II
SIZES OF THE STUDIED LOG-SPIRAL FEEDS.

Feed	D, μm	d, μm
DLR_a	48	2.25
DLR_c	130	11.2

and Table II. MoM simulations were made for feeds on Si half-space cut out from a 70-nm thick gold layer.

B. Current Distribution

Double Slot: For simulations we chose the squared gold sheet with a size of 100 x 100 μm^2 that contained a double-slot feed positioned in the center of the square. We applied a uniform voltage excitation along the infinitesimally thin slit cut in the middle of the co-planar waveguide across its central line. Fig. 3 (left) shows the distribution of high-frequency 2.5 THz current in the TWS2 feed as resulted from MoM simulation. An excess current appears around the connections between the co-planar waveguide and slots. This contradicts to the lumped-element semi-analytical model, which suggests the smallest current density near the central part of each slot. The excess current modifies the feed impedance that changes the resonance frequency of the antenna.

Log-spiral: We applied a uniform excitation along the infinitely thin slit in the geometric center of the feed (Fig. 2, right panel). The overall size of a log-spiral feed is defined by the outer and the inner diameter. The outer diameter (*D*) is the diameter of the smallest circle that encompasses the feed structure. The inner diameter (*d*) is the smallest diameter where the arms still obey the spiral equation. Connecting terminals are formed inside the circle having the diameter *d*.

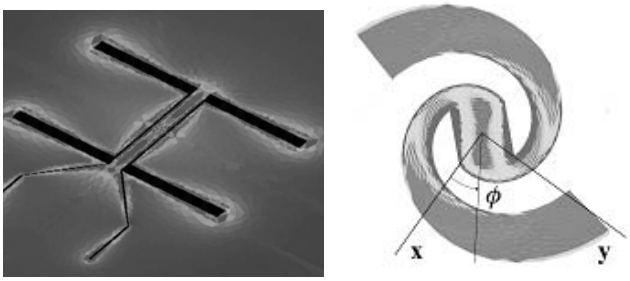

Fig. 3. Left: Distribution of the high-frequency current in the feed TWS2 obtained with MoM. Black denotes the dielectric. Right: Distribution of the high-frequency current in the spiral feed.

The electric current distribution in the central part of the DLR_c feed obtained by the MoM is shown in Fig. 3 (right panel). As it was expected, due to the skin effect [4] the high-frequency current flows mostly along the edges of the feed structure.

C. Antenna Impedance

Double Slot: The simulated impedance for the feed TWS2 is shown in Fig. 4 (upper panel). The frequency dependence of the real and imaginary parts of the feed impedance seen from the excitation slit has a certain similarity to the frequency dependence of the impedance computed for two slots without connecting co-planar waveguide [5]. However, changes introduced by the co-planar waveguide are clearly visible. The radiation coupling efficiency of the feed antenna reaches the maximum value when the imaginary component of the impedance becomes zero. For TWS2 feed corresponding resonance frequency appears approximately between 2.2 THz and 2.5 THz. In the receiving mode, the frequency resulting in the best coupling additionally depends on the impedance of the detector connected to the feed.

Log-Spiral: The simulated antenna impedance is shown in Fig. 4 (lower panel). In the whole frequency range of simulation the impedance of our feed antennas has a non-negligible imaginary component. That contradicts to the simple theory suggesting a real impedance for a free-standing complementary planar antenna. For the DLR_c feed in the frequency range up to 2.5 THz, the real part of the impedance remains almost constant and exceeds noticeably the imaginary component. Thus this antenna may be qualified as frequency-independent only in the frequency interval from 1 THz to 2.5 THz.

D. Bolometer Impedance

In order to compare the measured and simulated performance of our antennas we also modeled the impedance

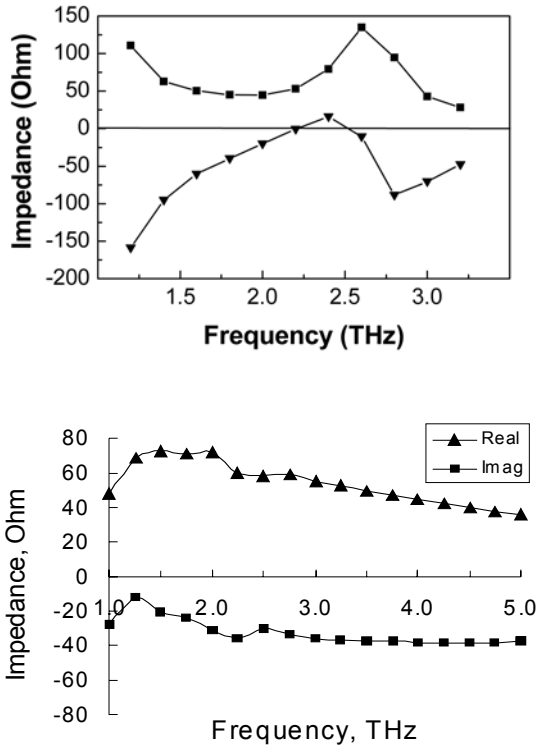

Fig. 4. Upper panel: Real (squares) and imaginary (triangles) components of the impedance computed for the TWS2 feed. Lower panel: Impedance of a log-spiral feed DLR_c. Lines are guides for the eye.

of the hot-electron bolometer, which was used for the experimental evaluation. Assuming a frequency independent conversion efficiency of the bolometer and taking into account the skin effect in the bolometer itself [5], we derived the complex HEB impedance Z_B. This results in the following antenna gain G

$$G = \frac{4Z_{B1}(Z_1 + Z_K) + Z_{B2}Z_2}{(Z_1 + Z_{B1} + Z_K)^2 + (Z_2 + Z_{B2})^2} M \qquad (1)$$

$$Z_B = R_n \frac{w(1+j)}{4\delta} \coth\left[\frac{w(1+j)}{4\delta}\right] = Z_{B1} + jZ_{B2}$$

where $Z_A = Z_1 + j\,Z_2$ is the impedance of the feed, R_n is the normal dc resistance of the bolometer, Z_K is the contact resistance and $\delta = (2\mu_0\omega/\rho)^{1/2}$ and ρ are the skin depth and the normal-state resistivity of the bolometer, respectively. The factor M accounts for coupling losses, which have been estimated using attenuation of optical elements [4]. Fig. 5 shows the impedance computed according Eq. 1 for a 2-μm wide bolometer. Even for a relatively small HEB, the imaginary part of the impedance compares with the real part at frequencies above 1 THz. Since the contact resistance for a particular specimen is not well known, for gain simulations we used $Z_K = 0.4\ R_n$. For the integrated antenna including planar feed and HEB, maximum power is delivered to the HEB in case of the conjugate matching: $Z_{B2} = -Z_2$.

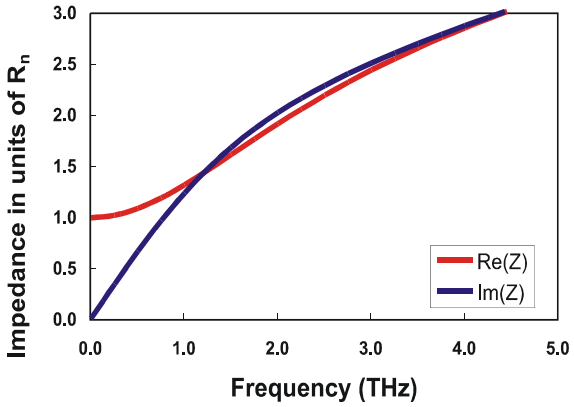

Fig. 5. Calculated impedance of the 2-μm wide HEB.

E. Ray-Tracing

Given the Rayleigh distance less than one millimeter, the surface of a lens with a diameter of few millimeter appears in the far-field regime of the feed. Therefore, as an input for the PORT procedure we used the far-field results delivered by the MoM simulations. The electric and magnetic fields at the surface inside the lens were decomposed into the s- and p-components. Then each component was multiplied with an appropriate Fresnel transmission coefficient and the resulting components were combined again to obtain the electric E and magnetic H fields just outside the lens. Equivalent electric and magnetic sources outside the lens were defined [6] as

$$\vec{J}_S = \vec{n}1 \times \vec{H} \quad and \quad \vec{M}_S = -\vec{n}1 \times \vec{E} \qquad (2)$$

where $\boldsymbol{n1}$ is the unit vector normal to the lens surface. The electric field at the observation point at a distance r from the running point on the surface, $\boldsymbol{e}_r$ being the unit vector of this distance, was obtained by integrating over the lens surface A

$$\vec{E} = \frac{j k_0}{4\pi\,\omega\,\varepsilon_0} \times \qquad (3)$$

$$\iint_S \left[\vec{J}_S - \left(\vec{J}_S \cdot \vec{e}_r\right)\vec{e}_r + \frac{1}{Z_0}\left(\vec{M}_S \times \vec{e}_r\right)\right] \frac{e^{-j k_0 r}}{r} dA$$

with k_0, Z_0 and ω been the free-space wave-vector, the impedance of free space and the angular frequency, respectively. We computed the beam profile formed by an extended hemi-spherical lens (radius $R_L = 6$ mm, index of refraction $n = 3.42$) with different extension lengths ε.

Results for the TWS6 feed at 1.9 THz are shown in Fig. 6. The –3 dB width of the main lobe reaches the minimum of 1.55° for $\varepsilon = 2.4$ mm while the side-lobes drop to the lowest level at $\varepsilon = 2.5$. An acceptable level (-14 dB) of side lobes and an almost Gaussian shape of the main lobe are both achieved for an intermediate extension length of 2.45 mm that brings

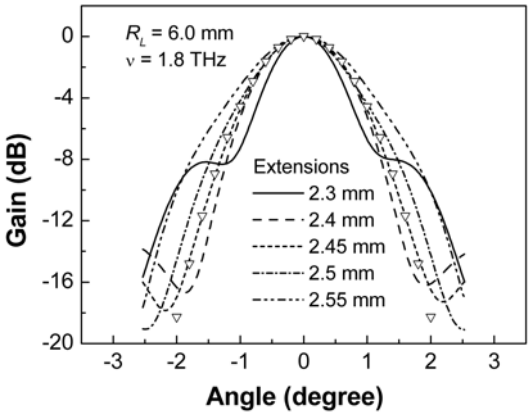

Fig. 6. Computed by E-plane 1.8-THz beam profile of the TWS6 feed integrated with a 6 mm radius lens with different extension lengths. Triangles show an analytical Gaussian profil.

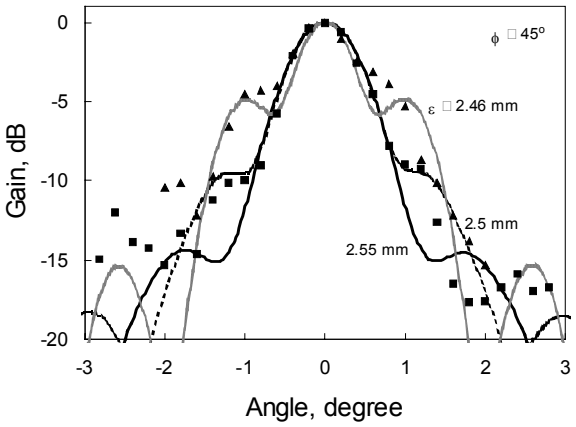

Fig. 8. Radiation pattern of integrated lens antennas with the DLR_a feed at 2.5 THz. Experimental data are shown by squares for scans at ϕ = 45° and by triangles for scans at ϕ = 135°. The lines present the result of MoM + PO ray-tracing simulations. Extension lengths are marked at the curves.

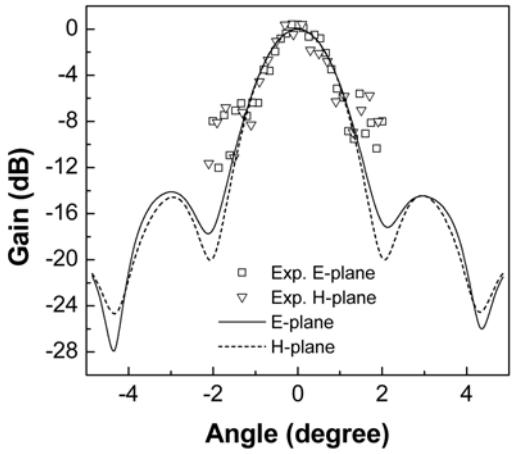

Fig. 7. Simulated (lines) and experimentally measured (squares and triangles) beam pattern of the integrated antenna with the TWS6 feed at 1.9 THz. The extension length in both cases was 2.45 mm.

the feed to the most distant focal point $\varepsilon = R_L/(n\text{-}1)$ of a corresponding synthesized elliptical lens [7]. At this optimal extension length the simulated beam profile of the integrated antenna is practically the same in both E- and H-planes down to –15 dB level (Fig. 6). However, an accuracy of the feed positioning better than 100 μm is required in order to keep side-lobes below -10 dB.

III. Experiment

We evaluated experimentally the performance of integrated lens antennas in the receiving mode. Hot-electron bolometers were incorporated in the planar feed and operated as either heterodyne or integrating direct detector. The feed was printed on a 350 μm thick Si substrate from a 70 nm thick gold film. HEBs were fabricated from a superconducting NbN film with a nominal thickness of about 4 nm and a sheet resistance of ≈ 600 Ohm just above the superconducting transition. Fabrication details are presented elsewhere [4]. A typical bolometer had an area of one tenth of a square, i.e. the width W = 1.8 μm amounted at ten times the length, and the corresponding normal-state resistance R_n = 60±6 Ohm as determined by the accuracy of the manufacturing process. The substrate carrying the feed with the bolometer was glued with its back-side onto the flat optically polished side of an extended hemispherical silicon lens. The lens had a radius of 6 mm. A 2.1-mm extension of the lens together with the substrate thickness positioned the feed in the more distant elliptical focus. The lens with the HEB was mounted in a dewar with optical access through a wedged TPX vacuum window and a cold (77 K) quartz filter.

In the heterodyne regime, the intermediate frequency signal was amplified and registered within a bandwidth of 75 MHz centered at 1.5 GHz. An optically pumped FIR gas laser providing lines at frequencies 0.69, 1.63, 2.53, 3.1, 4.3 and 5.2 THz was used as a local oscillator (LO). Signal radiation and LO radiation were superimposed by a 6 μm thick Mylar beam splitter. The double sideband (DSB) noise temperature of the receiver was measured by the Y-factor method. Hot and cold loads (Eccosorb) at 293 K and 77 K alternatively covered the antenna beam. The beam pattern of the integrated antenna was measured with a small 5-mm high-pressure mercury lamp moving in the far field of the integrated antenna. The output heterodyne signal was recorded as a function of the lamp position.

Fast-Fourier-Transform (FTS) measurements were performed with the mixer kept at the middle of the superconducting transition and operated in the direct detection regime. We used an interferometer with a 12-mm thick Mylar beam splitter and a mercury discharge lamp as radiation

source.

A. Experimental Data versus Simulation

Double-Slot: The measured beam pattern of the integrated lens antenna with the TWS6 feed at 1.9 THz is shown in Fig. 7 along with the computed beam profiles. Due to the large distance betwen the lamp and the antenna, the nose was relatively high not allowing us to reach side-lobe level. However, an overall width of the mail lobe corresponds fairy well with the results of simulation.

Log-spiral: Experimentally measured radiation pattern of integrated lens antennas with the DLR_a feed at 2.5 THz is shown in Fig. 8 along with the computed beam profiles. The sensitivity at 2.5 THz was relatively low resulting in a high noise level that did not allow us to clearly distinguish side-lobes. Another reason is that the 0.3° angular size of our hot-source was comparable to the angular spacing of the side lobes. However, the shape of the measured radiation pattern agrees with the results of simulations.

B. Comparison with FTS spectra

For all studied feeds, we have found a reasonably good agreement between measured FTS spectrum, system noise temperatures and simulated frequency dependence of the antenna gain.

Double slot: Data for three selected feeds are presented in Fig. 9 (upper panel). Measured noise temperatures correlate better with simulated gain spectra than with FTS spectra, which are systematically shifted to lower frequencies. We speculate, that this shift may be due to the difference between the HEB impedance in the heterodyne and the direct detection mode. Another outcome of our study also noticed in Ref. 1 is that commonly used design rules [9] to achieve the resonance wavelength λ_0, i.e. $L \approx 0.33\ \lambda_0$, $S = 0.17\ \lambda_0$ and $W = 0.05\ \lambda_0$, practically result in a double-slot feed with a somewhat larger resonance wavelength. The difference gradually grows with the operation frequency.

Log-spiral: The lower panel of Fig. 9 compares the simulated gain and the reciprocal noise temperature for integrated antennas with two different log-spiral feeds. There is a good match through the whole frequency range besides the lowest frequency where the device performs better than the simulation predicts. We suggest that the actual conversion efficiency of a HEB increases at frequencies smaller than the frequency corresponding to the energy gap of NbN.

IV. Conclusion

In conclusion, we have demonstrated that the full method of moments applied to the entire feed structure and combined with the physical-optics ray-tracing technique adequately models both the radiation coupling abilities and the beam pattern of an integrated lens antenna at terahertz frequencies. The approach can be used as an engineering tool for the design of quasioptical front-ends in the state-of-the-art heterodyne receivers.

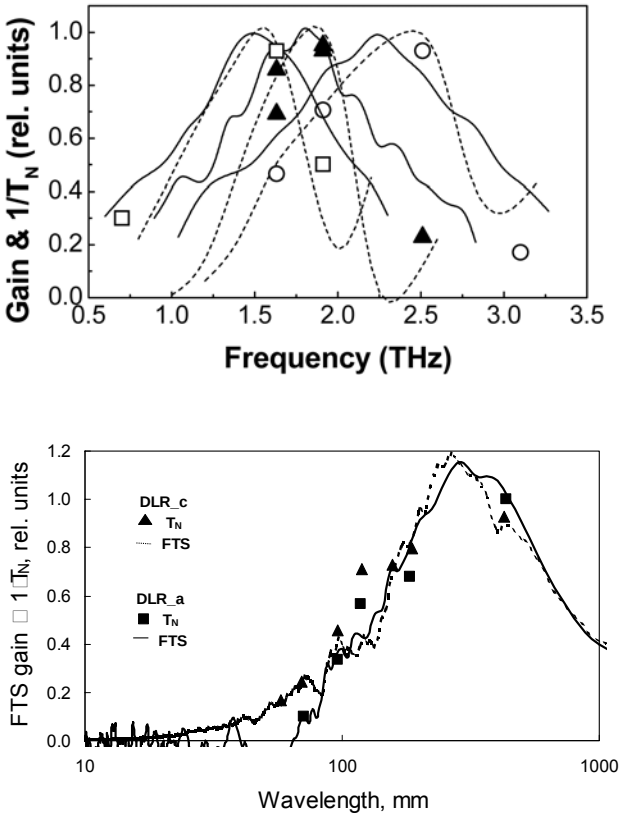

Fig. 9. Upper panel: Simulated gain versus frequency for the double-slot feeds (dotted lines), experimentally measured FTS spectra (solid lines) and reciprocal noise temperature of integrated antennas with (from left to right) TWS1 (squares), TWS6 (triangles) and TWS2 (circles) feeds. Lower panel: FTS spectra and reciprocal noise temperatures of integrated antennas with log-spiral feeds.

References

[1] R.A. Wyss, A. Neto, W.R. McGrath, B. Bumble, H. LeDuc, in Proceedings of the 11th Int. Symposium on Space Terahertz Technology, Uni. of Michigan, Ann Arbor, MI, pp. 388-397, May 2000.

[2] FEKO: a computer code for the analysis of electromagnetic problems, http://www.feko.info/.

[3] Yu. P. Gousev, A. D. Semenov, E. V. Pechen, A. V. Varlashkin, R. S. Nebosis, and K. F. Renk, "Broadband coupling of terahertz radiation to an YbaCuO hot-electron bolometer mixer," Supercond. Sci. Technol. Vol. 9, pp. 779-787, 1996.

[4] A. D. Semenov, H.-W. Hübers, J. Schubert, G. N. Gol'tsman, A. I. Elantiev, B. M. Voronov, and E. M. Gershenzon, "Design and Performance of the Lattice Cooled Hot-Electron Terahertz Mixer," Journal of Applied Physics, vol. 88, pp. 6758-6766, December 2000.

[5] M. Kominami, D.M. Pozar and D.H. Schaubert, *IEEE Transactions on Antennas and Propagations* **33**, 600 (1985).

[6] J.A. Balanis, *Antenna Theory: Analysis and Design*, John Wiley & Sons, Inc., pp. 448-450, 1982.

[7] D.F. Fillipovic, S.S. Gearhart, G.M. Rebeiz, *IEEE Transactions on Microwave Theory and Techniques* **41**, 1738 (1993).

[8] M. Bin, M.C. Gaidis, J. Zmuidzinas, T.G. Philips, H.G. LeDuc, *Appl. Phys. Lett.* **68**, 1714 (1996).

The Multiplexing of Signals in Direct Detector Arrays using the Combination of Projections and Frequency Domain Biasing Methods

Alexander N. Vystavkin, *Member, IEEE,* Andrey V. Petriakov

Abstract—**A new method of signal multiplexing in submillimeter super low temperature direct detector arrays is proposed. This method makes it possible to sharply reduce the number of wires connected to direct detectors and SQUID's in the super low temperature area, significantly decrease the required number of SQUID based readout amplifiers, and substantially reduce the contribution of the SQUID and detectors noise and simplify connections of bolometers and SQUID's as compared to other known multiplexing methods.**

Keywords—M*illimeter- and submillimeter-wave direct detectors, super low temperature detectors, super high sensitive radiation detectors, signal and biasing multiplexing.*

I. Introduction

ARAYS of super low temperature (T ≅ 0.3 - 0.1 K) direct detectors of *N*×*N* dimension up to 100×100 and more are needed in radio astronomy for observations and measurements of distributed submillimeter radiation sources. Large amounts of wires (up to tens of thousands) have to be led into low temperature area of the cryogenic system for lead-in the bias voltage to detectors and lead-out the detected signals from them. This will bring the influx of excessively large thermal power through wires to the low temperature refrigerator which will not cope with it definitely. To solve this problem various methods of the multiplexing (commutation, concentration, group transmission and subsequent separation) of signals in direct detector arrays are proposed and realized [1, 2].

The Andreev reflection hot-electron bolometers with superconducting transition edge sensor or sensor based on SIN-junctions are examples of such direct detectors [3]. In the first said detector which is used in our subsequent consideration, the current decrement $|\Delta I|$ (detected signal) in each moment in each bolometer of the array is connected with the absorbed radiation power P by expression [4]

$$|\Delta I| = (1/V) \cdot P, \qquad (1)$$

where V is fixed bias voltage applied to bolometer.

The readout and amplifying of detected signals in direct detector array is realized using SQUID's with ultimately high current sensitivity. On their level the multiplexing is based, for instance, on time division [1] or on frequency division [2].

II. Signal multiplexing using projection method

We propose a novel method of the signal multiplexing in array of receiving elements with direct detectors which are connected for this purpose in parallel in set of rows and sums of detected signals in rows are read out by one SQUID in each row (Fig. 1). The detected signals are integrated over readout time. The image of observed radiation and the array are rotated

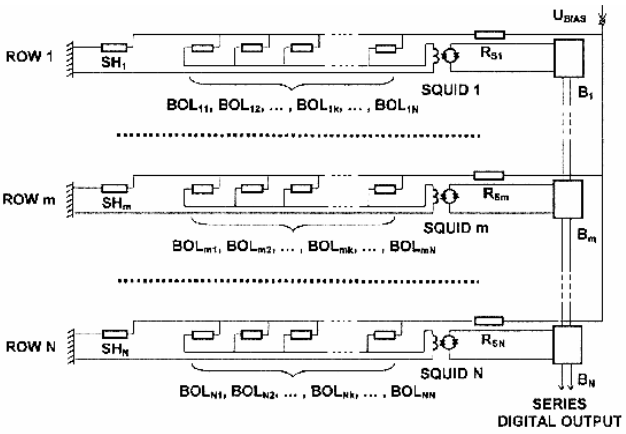

Fig. 1. Parallel electrical connection of bolometers with output to the SQUID-amplifier in each row: BOL_{mk} – bolometers with similar resistances R_{Bmk} and transition edge temperatures [4], SH_m – shunts feeding bolometers with fixed bias voltage V, R_{Sm} – series resistances of biasing circuits, $\{B_m\}$– projections acquisition system (block of SQUID-electronics, analog-to-digital converter and data parallel-to-series digital converter in each row for data transmission bus). Feedback circuits of SQUID's are not shown.

Manuscript received May 2, 2005. This work was supported in part by the Russian Council on Leading Scientific Schools under Grant No. SSCH-1548.2003.2 and by the Department of Physical Sciences of Russian Academy of Sciences in frames of the Program "Problems of Radiophysics" – section "The Development of Terahertz Frequency Band".

A. N. Vystavkin (corresponding author: phone: 7-095-203-25-05; fax: 7-095-203-84-14; e-mail: vyst@hitech.cplire.ru), and A. V. Pestriakov are with the Institute of Radioengineering and Electronics of Russian Academy of Sciences, 11 Mokhovaya Street, 125009 Moscow, Russian Federation.

reciprocally in their common plane fixing the array (or the image) at angle steps. The final procedure is the reconstruction of the initial image from the set of the detected signal sums gathered from all rows at all reciprocal angles using algorithms of the computer tomography [5]. We interpret the receiving element as the direct detector and the matching antenna into which the direct detector is incorporated (coupled) at microwave (in our case – submillimeter) frequency. The array of receiving elements based, for instance, on four-slot matching antennas with double polarization [6] is more adequate for proposed method in order not to lose the information on the difference in radiation intensity in two polarizations during reciprocal rotation of image and receiving elements array. The rotation of receiving elements relative to the image can be realized by means of the rotation of the telescope around its main optical axis. One may imagine some other methods, as optical-mechanical (Fig. 2) or electronic-optical, of rotation of image relatively to the array, what is equivalent to the rotation of the array relatively to the image.

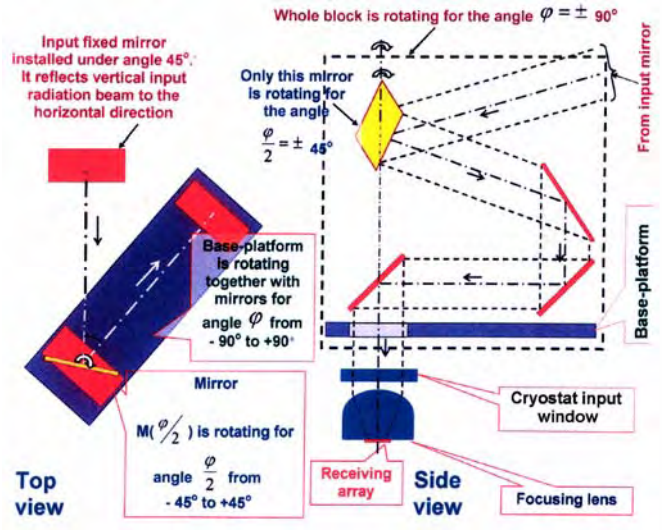

Fig. 2. A scheme of possible optical-mechanical rotating device providing the rotation of an image for angle from 0 to 180^0 relatively to the detector array in their common plane. It is possible to rotate the radiometer relatively its optical axis.

The fixed bias voltage for all bolometers in row is supplied from one shunt resistance (Fig. 1) like in case of single TES bolometer [7] and its value is determined by the expression $1/R_{SH} >> \sum 1/R_{BOLk}$ in each row. The system stability is providing by choice of this resistance in accordance with an expression $1/R_{SH} + \sum 1/(R_{dif})_{BOLk} > 0$, where $(R_{dif})_{BOLk}$ is the negative differential resistance of each bolometer connected into fixed-voltage bias circuits in each row [7]. The summing of all detected signals in each row is realizing in input coil of SQUID readout-amplifier, one in each row for N bolometers. By this reason the drastic reducing of amounts of wires leading in, the bias to bolometers and feed-back signals to SQUID's, and leading out, detected signals, is achieved. The amount of SQUID's themselves is reducing strongly as well.

The sets of current decrements (detected signals) sums in rows at different angles θ of reciprocal positions of array and image can be named projections in a similar as in the computer tomography [5]. Exactly by this reason we have given the name of proposed multiplexing method. Portions of radiation power coming to each of receiving elements of array can be described by the table $\{P_{mk}\}_\Theta$ where k is number of detector in row and m is number of row. The subindex Θ means that we have the number of radiation power parts sets corresponding to different reciprocal angles between the array and the image. A corresponding table of current decrements $\{\Delta I_{mk}\}_\Theta$ calculated through (1) is obtained. A detector noise current of approximately similar value is added to each current decrement ΔI_{mk}. By the reason of large sum (N~100) of current decrements ΔI_{mk} (detected signals) flowing to the input coil of one SQUID its noise can be neglected. The result of the summing detected signals and corresponding noise currents is the following table:

$$\left\{ \sum_k \Delta I_{1k} + \sqrt{N\overline{I_n^2}}, \ldots \quad \sum_k \Delta I_{mk} + \sqrt{N\overline{I_n^2}}, \ldots \quad \sum_k \Delta I_{Nk} + \sqrt{N\overline{I_n^2}} \right\}_\Theta . \qquad (2)$$

(direction of ξ coordinate →)

The set of sums (2) like in the computer tomography are projections in (ξ, θ) coordinates [5]: θ is current value of the rotation angle of the receiving element array relatively to the image, ξ is current coordinate along given projection set. Besides we see from (2) that the signal-to-noise ratio at the output of row is $\sim\sqrt{N}$ times higher than at the output of single bolometer what is one more advantage of the proposed multiplexing method.

The reconstruction of images is realized by the method of convolution and back-projections. Algorithms of this procedure are well developed and described [5]. They may be applied for our case without extra efforts when to express the searching for unknown (reconstructing) radiation power field not by discrete data field of parts $\{P_{mk}\}$ but by continuous power density field $p(x, y)$, where x and y are coordinates in the common plane of the image and receiving elements. Sets of discrete functions being current decrements sums values in the table (2) also have to be approximated with distributions of detected $\iota(\theta,\xi)$ and noise currents $\varsigma(\theta,\xi)$ where ι is linear density of current decrements and ς is linear density of noise currents. We define the projection from function $p(x, y)$ to the family of lines $L(\theta,\xi)$ as:

$$\iota(\theta,\xi) = (1/V) \int_{L(\theta,\xi)} p(x,y)ds. \qquad (3)$$

The factor $1/V$ takes into account the relation between ι and p following from (1). The derivation of the radiation power density distribution $p(x,y)$ from the projections set (3) is the ill-conditioned inverse problem of mathematical physics and Tikhonov regularizing method can be proposed for its solution in accordance with which the derivation of equation (3) can be obtained as [8]

$$p(x,y)=\frac{1}{\pi}V\int_{\theta=0}^{\theta=0+\pi}d\theta\int_{-\infty}^{+\infty}K_\alpha(\xi-\xi')\imath(\theta,\xi')d\xi', \qquad (4)$$

where the convolution kernel is introduced through its Fourier image as

$$\left.\begin{aligned}K(\xi)&=\int_{-\infty}^{+\infty}K_\alpha(\omega)\cdot e^{-i\omega\xi}\,d\omega\\ K_\alpha(\omega)&=|\omega|/(1+|\omega|^{2r})\end{aligned}\right\}$$

where α is regularization parameter, and r is regularization rate.

The additive random current noise expressed like total detected signal current in form of linear current density ς has to be added into the reconstruction algorithm (4)

$$p(x,y)=\frac{1}{\pi}V\int_{\theta=0}^{\theta=0+\pi}d\theta\int_{-\infty}^{+\infty}K_\alpha(\xi-\xi')\imath(\theta,\xi')d\xi'+$$
$$+\frac{1}{\pi}V\int_{\theta=0}^{\theta=0+\pi}d\theta\int_{-\infty}^{+\infty}K_\alpha(\xi-\xi')\varsigma(\theta,\xi')d\xi', \qquad (4')$$

where $\varsigma(\theta,\xi)$ is the noise component of projection under the current angle in given direction. In this way the algorithm transforms the noise components of the projection linearly into noise components of the reconstructed image in the same way as signal components. This means that the signal-to-noise ratio in the reconstructed image will be the same as in projections and consequently the mentioned above advantage in signal-to-noise ratio will remain.

We have computer simulated the procedure of signal multiplexing in the array of N×N = 100×100 receiving elements by described method. We have used image of M33 Galaxy obtained at wavelength 100 μm (Fig. 3,a) [11] as primary one. Omitting simulation details, its results are given at Fig.3,b. One may see that the signal multiplexing procedure using projections method is working normally.

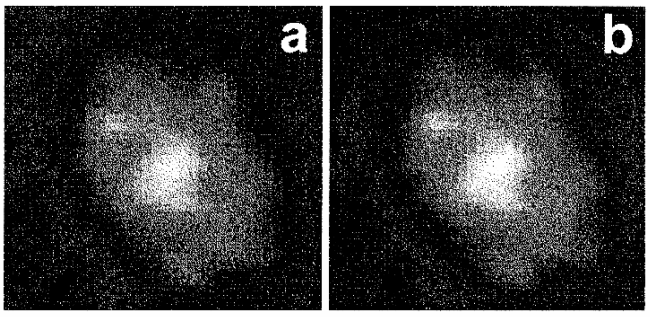

Fig. 3. (a) Primary image of M33 Galaxy, obtained at λ=100 μm [10]; (b) Simulation results of the projections multiplexing procedure using the image of M33 Galaxy as initial one.

II. COMBINATION OF PROJECTIONS AND FREQUENCY DOMAIN BIASING METHODS

Further development of the multiplexing scheme using the projection method is its combination with the frequency domain biasing method proposed by Berkeley group [2]. In said method each single bolometer is biased with its own frequency (Fig. 4). The frequency comb is amplifying by one or very small amount of SQUID. Signals are separated by lock-ins.

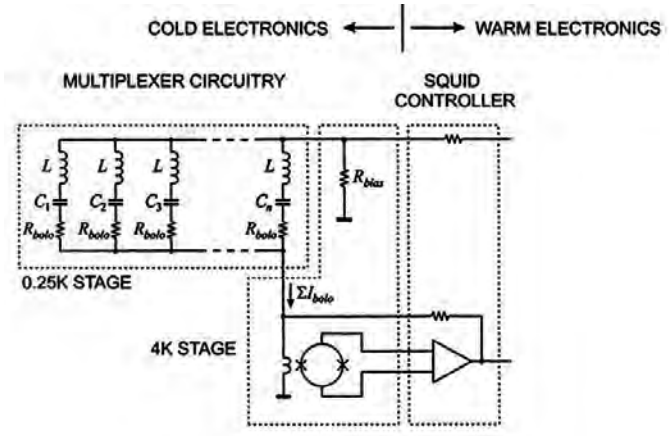

Fig. 4. Scheme of frequency domain multiplexing method.

We propose to put a row of N bolometers (Fig. 5) connected in parallel instead of each single bolometer R_{bolo} in accordance with previous method. This gives combination of advantages of both methods.

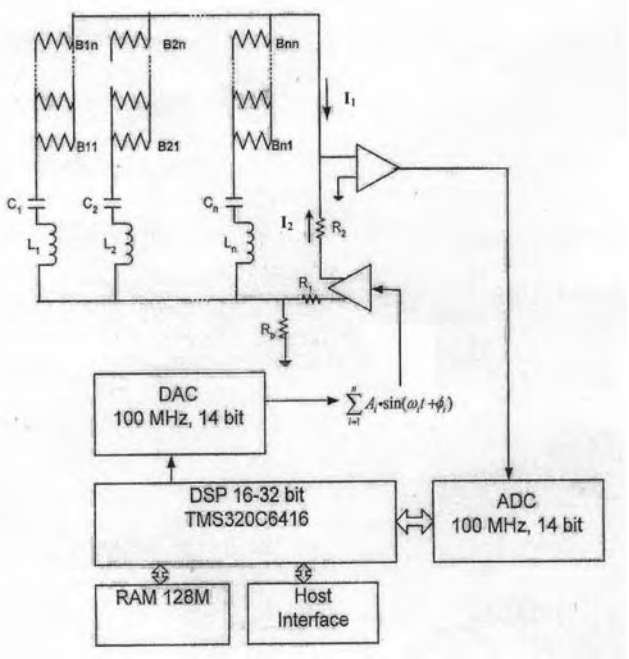

Fig. 5. Scheme of the bolometer connection and biasing in the combined multiplexing method.

In this scheme the separation of signals from rows is realized in the digital signal processor (DSP) in multifrequency lock-in mode. The frequency current comb I_2 compensates the pedestal of the current comb I_1 containing signals. Computer simulation results of operation of 29-channel lock-in amplifier

(scheme is given above) having one SQUID` and frequency

of discretization 150 MHz are shown at Fig. 6.

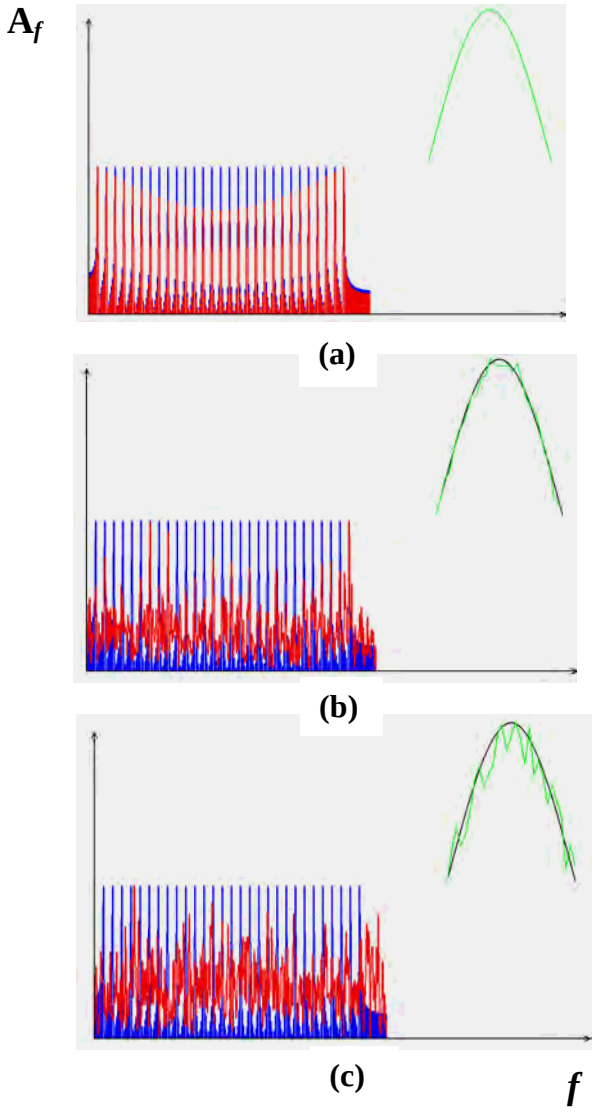

Fig. 6. Results of operation computer simulation of the scheme shown at Fig. 5. At the left of each picture – input and outout frequency combs; at the right-top – initial and processed signal distributions along a bolometers row without noise (a) and in the presence of noise with noise-to-signal ratio N/S = 1 (b) and N/S = 50 (c).

One may see from Fig. 6 that that the multifrequency lock-in amplifier operation is efficient. Existing DSP's permit an operation up at 128 frequency channels: array, i.e. in our case for array of 128 x 128 detectors. However by the reason of SQUID bandwidth restriction (~ 1 MHz) the scheme has to be divided for 4 sections with one SQUID in each section.

It is possible to conclude that the projection method and the frequency domain biasing method complement one another.

ACKNOWLEDGMENT

Authors thank S. V. Shitov and P. L. Richards for useful discussions.

REFERENCES

[1] K. D. Irwin, M. D. Audley, J. A. Beall, J. Beyer, S. Deiker, W. Doriese, et al., "In-focal-plane SQUID multiplexer", *Nuclear Instruments and Methods in Physics Research,* A 520, 2004 (Proc. of the 10th Intern. Workshop on Low Temperature Detectors – LTD-10, Genoa, Italy, July 7-11, 2003), pp. 387-389.

[2] J. E. Ruhl, P. A. R. Ade, J. E. Carlstrom, H. M. Cho, T. Crawford, M. Dobbs, et al., "The South Pole Telescope", *Proc. SPIE (Intern. Symp. on Astronomical Telescopes)*, 2004.
www.spt.uchicago.edu/extweb/spt_spie_2004.pdf.

[3] A. N. Vystavkin, "Supersensiting hot-electron microbolometer with Andreev electron reflection phenomenon for submillimeter radio astronomy", *Radiotekhnika i Elektronika* (in Russian), 2001, v. 46, # 7, pp. 806-815.

[4] A. N. Vystavkin, A. G. Kovalenko, S. A. Kovtonyuk. "Study of superconducting transition in a Mo/Cu thin film structure and estimation of sensitivity of SUBMM waveband region TES bolometers on the basis of such a structure, *This Symposium*.

[5] W. Swindel and S. Webb, "X-ray transmission computer tomography", in "The Physics of Medical Imaging", Ed. by S. Webb, *Adam Hillier Publ. House,* Bristol and Philadelphia, 1988.

[6] G. Chattopadhyay and J. Zmuidzinas, "A dual-polarized slot antenna for millimeter waves," *IEEE Trans. Antennas Propagat.*, May 1998, v.. 46, pp. 737–737.

[7] K. D. Irwin, "An application of electrothermal feedback for high resolution cryogenic particle detection", *Appl. Phys. Lett.,* 1995, 10 April, 66 (15), pp. 1998-2000.

[8] A.N. Tikhonov, V.Ya. Arsenin, Methods of solution of ill-conditioned problems (in Russian), Moscow, "Nauka", 1986.

[10] I.B. Rubashov, A.A. Timonov, A.V. Pestriakov, Doklady Akademii Nauk SSSR (in Russian), 1981, v.258, №4, pp.846-850.

[9] IPAC-NASA, M33-Spiral Galaxy,
http://sirtf.caltech.edu/Education/Messier/m33.html.

MEASUREMENT OF DIELECTRIC LOSSES IN CVD DIAMONDS IN MILLIMETER WAVE BAND AT LOW TEMPERATURES

V.N. Derkach, G.P. Ermak, R.V. Golovashchenko, S.V. Nedukh, O.S. Plevako, S.I. Tarapov, A.V. Varavin
Usikov Institute of Radiophysics and Electronics of National Academy of Sciences of Ukraine,
12 Ac. Proskura St., Kharkov, 61085, Ukraine
e-mail: derkach@ire.kharkov.ua, tarapov@ire.kharkov.ua

The problem of output windows in gyrotrons and of analogous input windows in fusion reactor for realization of initial heating of plasma is the most critical in Project of ITER. Therefore necessity of high-quality radiotransparent materials are great [1]. Recently detailed investigation of properties CVD diamonds characterized by low dielectric and thermal losses, especially with increasing of frequency, is required. One of most precise techniques of measurement of such materials is the method of disk dielectric resonator (DDR) with whispering gallery modes (WGM) [2].

We designed the experimental cryogenic complex for measurement of properties of low loss dielectrics in the millimeter wave band (30-150 GHz) and at temperatures T=0.6-300 K [3]. Complex includes cryogenic and electrodynamical modules. Refrigerator is manufactured as a "top-loading refrigerator", enabling one to change a sample during the experiment without increasing the temperature. Electrodynamical module provides the location and the effective excitation of the DDR. The DDR is manufactured with the optical precision from the material under test. Spectrums and field characteristics of DDR were registered by using of an automatic measuring test-bench. High-Q $EH_{mn\ddot{a}}$ modes with n=0 and were used as working modes.

Model experiments for measurement loss tangent tan$d$ for several promising technological materials (sapphire, semiconductors, CVD-diamonds) are carried out. We investigated two CVD diamond samples, produced by General Physics Institute of Russian Academy of Sciences (1) (d=20.6 mm, h=0.34 mm) and by DeBeers Company (2) (d=18.02 mm, h=1.85 mm) in a frequency band 60-115 GHz and at temperatures 4.2-300 K. With decreasing of temperature tan$d$ decrease from $1.7\cdot10^{-4}$ (300 K) to $1.3\cdot10^{-4}$ (4.2 K) for sample 1 and from $9\cdot10^{-5}$ (300 K) to $5\cdot10^{-5}$ (4.2 K) for sample 2 at frequencies about 112 GHz.

Thus the values of loss tangents of diamonds which perspective for use as output and input windows of high frequency powerful devices are measured. The experimental results are summarized in the graphic and tabulated forms.

The work is partially supported by STCU project 1916.

[1] A.Ibarra and E.R.Hodgson, Nuclear Instruments and Methods in Physics Research B, vol. 218, 2004, pp. 29–35.
[2] J.Krupka, K.Derzakowski, A.Abramowicz, M.E.Tobar, R.G.Geyer, IEEE Trans. on MTT, vol. 47, no. 6, 1999, pp. 752-759.
[3] V.N.Derkach et al., Conf. Digest of the Joint 29th Int. Conf. on Infrared and Millimeter Waves and 12th Int. Conf. on Terahertz Electronics; Sept.27–Oct.1, Karlsruhe, Germany, 2004, pp.211–212.

Orthomode Transducer with Waveguide Ports and Balanced Coaxial Probes

G. Engargiola and A. Navarrini

***Abstract*—We describe measurements and simulations of a K-band orthomode transducer (OMT) consisting of orthogonal balanced coaxial probes in a circular waveguide linked by coaxial transmission lines to balanced coaxial probes in orthogonal WR42 waveguides. Over most of the frequency range 18 – 26 GHz, the reflection coefficient is < –12 dB and the cross-polarization coupling is <-30 dB. The insertion loss is ~0.4 dB at room temperature.**

To operate at 200-270 GHz, this OMT must be scaled so that the phase imbalance of the matched coaxial transmission lines is less than 15^0, equivalent to a line length difference of less than 0.0015-in, to mitigate periodical resonances. Probes must be located with 0.001-in accuracy. We predict an insertion loss of 0.25 dB at 4K.

***Index Terms*— Radio astronomy, Coaxial transmission lines, Polarimetry, Waveguide transitions.**

In a radio astronomical receiver, an orthomode transducer can link a single scalar feedhorn to two independent detectors, where each detector couples signal from one of two mutually orthogonal polarizations [1]. Recent examples of compact orthomode transducers demonstrated to work well at millimeter wavelengths [2] are based on the Bøifot orthomode junction [3], which includes a tapered septum in a square waveguide to direct $TE_{0,1}$ and $TE_{1,0}$ modes into separate rectangular waveguides. We explore the possibility that polarization separation at these frequencies can be done with balanced orthogonal coaxial probes in a circular waveguide, instead. Teflon coated wire with ~0.012-in diameter can be placed in narrow channels machined in metal to make low-loss coaxial transmission lines linking coaxial waveguide probes. In this paper we describe measurements and simulations of a K-band scale model orthomode transducer with coaxial probes to measure electromagnetic performance in relation to fabrication tolerances. The results are extrapolated to millimeter wavelengths.

I. Design

Fig. 1 shows an internal view of our orthomode transducer design. Incoming radiation of arbitrary polarization couples into a circular waveguide of diameter 0.455-in. Orthogonal, balanced probes made of Teflon-covered wire enter the circular waveguide wall through four square apertures of width 0.120-in. The wire has a circular cross section with an insulator diameter of 0.117-in and a central conductor diameter of 0.036-in. The four probes lie in a plane displaced 0.13-in (~1/4 λ_g) in front of a fixed circular waveguide backshort. The wire itself was made from Belden RG-402/U type coaxial cable by etching away the outer conductor with nitric acid. Balanced probes for the WR42 waveguide-to-coax transitions, made from the same Belden wire, are 0.068-in long – with a 0.034-in gap between probes – and lie in a plane 0.107-in in front of a fixed backshort cavity.

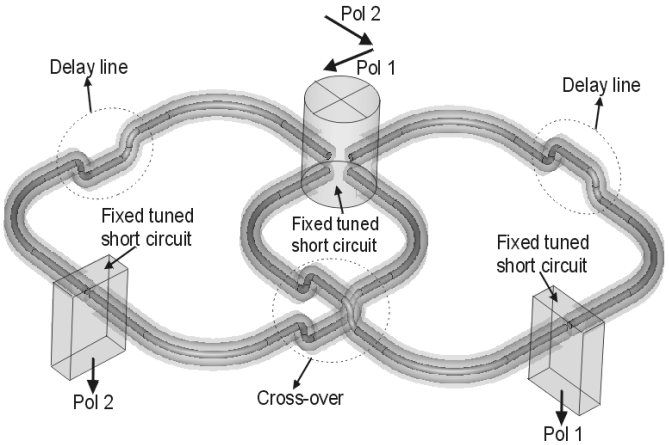

Fig. 1 Internal view of the orthomode transducer showing the input circular waveguide to four-probe coaxial line transition, the cross-over, the delay lines, and the two WR42 waveguide to dual-probe coaxial line transitions at the output.

Transmission lines with 50 Ω impedance are formed by capturing the stripped Belden cable in a symmetrically split channel with 0.120-in x 0.120-in square cross section. Matched transmission lines link coaxial probes formed by wire extensions into waveguide.

The split view of the orthomode transducer (Fig. 2) shows the circular and rectangular waveguides, the coaxial transmission line channels, the delay lines, and the cross-over region. The coaxial lines without their external conductors are seen in the block to the right. The transmission lines are confined largely to a single plane. However, at one position the lines must cross over. Delay lines are used to compensate for the added electrical length due to vertical deflection at the crossover.

The electromagnetic software Microwave Studio from CST, based on the finite integration technique was used to optimize the coax-to-waveguide transitions and simulate the performance of the entire structure, shown in Fig. 1.

The authors are with the Radio Astronomy Laboratory, University of California, Berkeley, CA 94720 USA (e-mail: greg@astron.berkeley.edu).

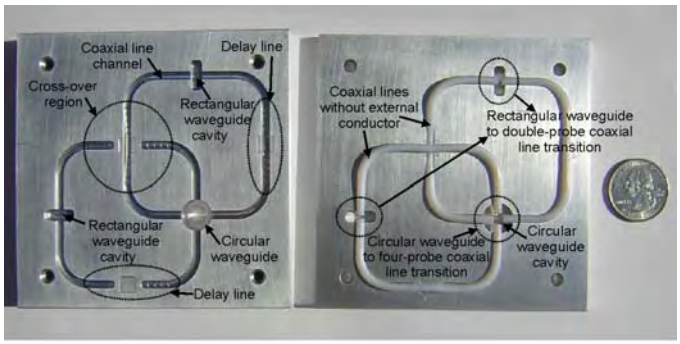

Fig. 2 Internal view of the two aluminum blocks of the orthomode transducer shows the circular and rectangular waveguides, the coaxial line channels, the delay lines, and the cross-over region. The coaxial lines are installed on the block shown on the right.

We assumed a dielectric constant ε_r of 2.05 for the FEP Teflon wire insulation, a conductivity of 6.1 x 10^7 S/m for the silver coated wire core, and a conductivity of 3.5 x 10^7 S/m .

II. K-band Measurements, Fabrication Errors, and Mode Conversion

If two coaxial transmission lines which link two anti-symmetric probe pairs differ in length, they will transform the probe impedances Z_p differently. This will cause reflections at the waveguide-coaxial probe transitions. These reflections can trap RF energy in 1-d modes on the coaxial transmission lines with guide wavelengths $\lambda_g = 2L/m$, where L is the length of the line and m is the mode index. If the two arms of the polarization channel are of slightly different length, sharp resonances appear. When the length of the coaxial lines in the orthomode transducer is 3.42-in, then modes with indices 15 - 22 will occur in K-band.

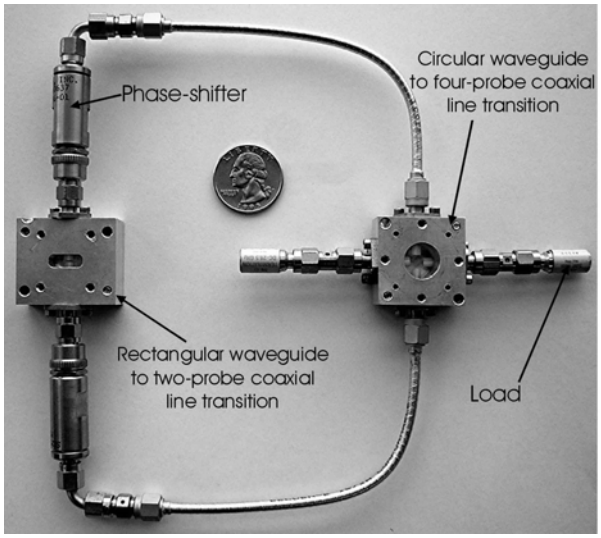

Fig. 3 Orthomode transducer assembled from separable components. Shown are waveguide-coaxial probe transitions, SMA semiflex cables, and Semtech, Inc coaxial phase-shifters. The circuit was used to study resonances due to trapped modes in coaxial transmission lines due to phase imbalance.

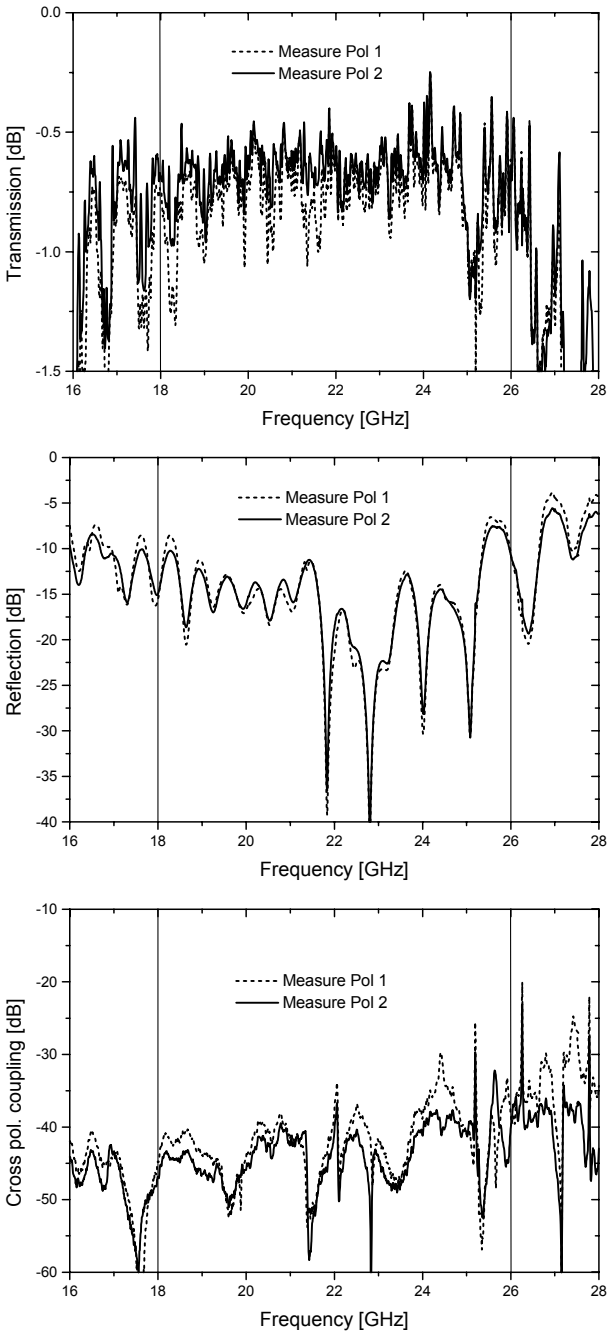

Fig. 4 Measured transmission, reflection, and cross polarization coupling of the separable orthomode transducer for polarization channels Pol. 1 (dashed line) and Pol. 2 (solid line). Measured insertion loss is ~0.65 dB across most of K-band. Reflection amplitude varies between –13 dB at K-band edges and –26 dB at band center. Cross polarization coupling is –30 dB to -40 dB.

To study the origin of the modes, we constructed an orthomode transducer, shown in Fig.3, from separable components. Measurements of the separable orthomode transducer are shown in Fig. 4. The performance of the orthomode transducers shown in Figs. 2 & 3 is comparable, with the exception that the insertion loss of the separable orthomode transducer is somewhat greater (-0.65 dB) than that of the integrated one (-0.4 dB). Both devices have a return loss less than –12 dB and a cross polarization coupling of less than –30 dB over most of the band.

The orthomode transducer functions as a 180^0 power divider (the circular waveguide-coaxial probe transition) in series with a 180^0 power combiner (the coaxial probe-WR 42 transition) linked by equal lengths of transmission line. Any difference in coaxial cable lengths Δ will unbalance the phase of the two lines by $k\,\Delta$, where k is the wave-number of the signal, resulting in a reduced transmission of 10 log ½ (1+ cos k Δ) dB for the recombined signal.

In Fig. 5 the results of deliberately unbalancing the coaxial transmission line arms of Pol. 1 are shown. The phase shifters were used to effectively increase one of the line lengths 0.020-in (~20^0 at 22 GHz) relative to the other. This produces eleven ~1 dB insertion loss resonances spaced at ~0.8 GHz intervals (mode indices m = 23, 24, …, 33) and reduces the average transmission by –0.13 dB. Simulation and measurement both show an insertion loss of ~-0.65 dB. Also, simulation and measurement show nearly identical insertion loss resonances.

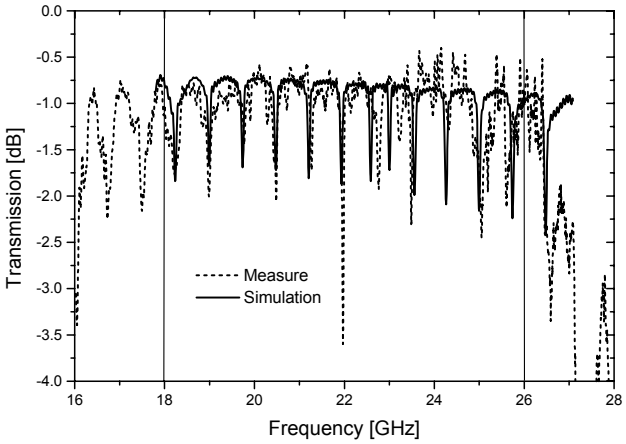

Fig.5 The transmission characteristic for a single polarization channel of the separable orthomode transducer for the case where the coaxial transmission lines have been deliberately unbalanced by 0.020-in, resulting in a 20^0 phase difference at 22 GHz. Prominent resonances arise at ~0.8 GHz intervals. The CST Microwave Studio simulations of the equivalent integrated orthomode transducer circuit predict results remarkably similar to measurement.

In Fig. 6 we present at high resolution (Δf ~ 2 MHz) a typical transmission resonance profile as a function of phase imbalance between the coaxial arms of a single polarization channel. From top to bottom the transmission profiles correspond to phase imbalances which vary from 0^0 to 50^0, where the curves are plotted at 5^0 intervals. As expected, the curves shift to lower frequencies with increasing phase (or line length) imbalance; the profiles get deeper and wider, indicating a rising level of mode conversion [4].

In addition to the unbalanced coaxial line we mention the effect of fabrication errors on the probes. As stated in Section II (a) anything that breaks the four-fold symmetry of the four-probes to circular waveguide coupling structure has the potential to excite higher order modes. However, in K-band only the TM_{01} and the TE_{21} modes can be coupled. Due to the

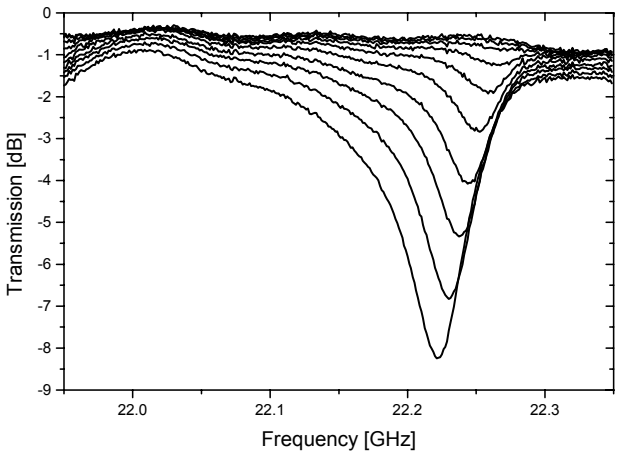

Fig. 6 A typical transmission resonance profile measured as a function of phase imbalance between the coaxial arms of a polarization channel. From top to bottom, the phase imbalance varies from 0^0 to 50^0, with curves plotted at 5^0 intervals.

anti-symmetric phasing of the probes, the TM_{01} mode can couple only very weakly to the fundamental TE_{11} mode, even for substantial probe fabrication errors. Moreover, the TE_{21} mode if excited affects only a very narrow section of the pass-band at 25.195 GHz. More importantly is how probe asymmetries interact with the 1-d coaxial modes. When the probes in either waveguide transition have incorrect lengths or positions they will become reflective discontinuities, trapping energy in coaxial transmission line modes. We tested a number of cases using CST Microwave Studio simulations: for example, probes deflected off-axis (causing azimuthal offsets) by 0.005–0.010-in or probes made unequal (shifting the gap between probes off-center) by 0.005–0.010-in. We find that, provided the coaxial transmission lines are equal length, probe defects have a minor effect on insertion loss. Unequal length diametrically opposite probes will excite a series of coaxial transmission line modes but the amplitude of the resonances will be ~0.1 dB; they barely excite the TE_{21} mode. Probes with azimuthal deflections are much more effective at coupling energy to the TE_{21} mode, but as mentioned before this represents limited insertion loss in the band.

III. Scaling Coaxial Orthomode Transducer to Millimeter Wavelengths

The insertion loss of the coaxial transmission lines in the orthomode transducer scaled for operation at λ = 1 mm must be of an acceptably low level for the device to be useful for astronomical measurements. This can be estimated by combining theory and measurement. When we immersed in liquid nitrogen a straight 3.42-in section of coaxial transmission line identical in length and cross section to those shown in Fig.2, the insertion loss declined from a room temperature value of 0.35 dB to 0.20 dB at 77 K.

An approximation for the losses can be estimated using simple formulas by assuming that both the inner and outer conductors have circular cross sections of radii R_i and R_o, where we set $R_o \sim w/2$, the half-width of the square channel.

The attenuation of the coaxial line α_T equals the sum of the conductor loss α_c and dielectric loss α_d given by (expressed in dB/m):

$$\alpha_c = 8.686\,[(\nu\,\mu_l/\pi\sigma_i)^{1/2}\,1/R_i + (\nu\,\mu_o/\pi\sigma_o)^{1/2}\,1/R_o]/4\,Z_0 \quad (1)$$

$$\alpha_d = 8.686\,\pi\,\nu\,(\varepsilon_r)^{1/2}\tan(\delta)/c \quad (2)$$

Here, $\sigma_{i,o}$ indicates the DC electrical conductivity of the metals, $\mu_{i,o}$ the magnetic permeability of the conductors, Z_0 the characteristic impedance of the line, *c* the speed of light in vacuum, tan (δ) the loss tangent of the dielectric, and ν is the frequency in Hz.

Using room temperature values of σ_i = 6.3 10^7 S/m for silver, σ_o = 3.5 10^7 S/m for aluminum, and tan(δ) = 4 10^{-4} for Teflon, we calculate a loss at 22 GHz of α_T = 2.7 dB/m, where α_c = 1.6 dB/m and α_d = 1.15 dB/m. This gives a total insertion loss of 0.25 dB for a 3.42-in length of 0.120-in diameter coaxial line. If we assume that the conductor losses α_c scale as $T^{0.5}$, then α_c(77K) is approximately 0.4 dB/m [2]. The larger contribution to α_T at cryogenic temperature comes from the temperature independent α_d, and α_T(77K)~1.5 dB/m. The total predicted loss at 77 K for the 3.42-in coaxial line is 0.16 dB. The predicted relative reduction in α_T (~40 %) due to cooling is consistent with the reduction in loss measured when the coaxial line fixture is immersed in liquid nitrogen.

The losses at λ = 1 mm for the coaxial cable can be estimated by rescaling by ~10 the dimensions of the lines used in K-band but now assuming a gold outer conductor, where σ_o = 4.26 10^7 S/m at room temperature. The room temperature losses at 230 GHz estimated by the model for a section of Rubadue wire in a channel are α_T = 19.2 dB/m, where α_c = 7.2 dB/m and α_d = 12.0 dB/m. For a 0.34-in long section of coaxial line, this gives a total loss of 0.17 dB. Ohmic losses will be reduced by a factor of 3 to 4 upon cooling gold to cryogenic temperature, according to Wollack [2], which reduces α_c(4K) to 2.1 dB/m. This results in a total loss of α_T(4K) ~ 14.1 dB/m or an insertion loss of 0.13 dB for our 0.34-in long coaxial lines.

For satisfactory performance, we conclude from scaling the K-band results that wire length and placement in a 230 GHz orthomode transducer must be correct to within approximately 0.001-in.

Connecting to the rectangular and circular waveguide ports requires adequate separation between the ports to allow the attachment of three waveguide flanges. A slight modification of the orthomode transducer geometry makes this simple, as shown in Fig. 7. The circular and rectangular waveguide ports emerge from orthogonal sides of the orthomode transducer, instead of opposite faces, as shown in Fig. 2. Note that the rectangular waveguides are split along the E-plane. Another consequence of this modification is that the coaxial lines can be made much shorter. This reduces the insertion loss of the orthomode transducer and the number of coaxial line modes which can be supported as a result of line length errors.

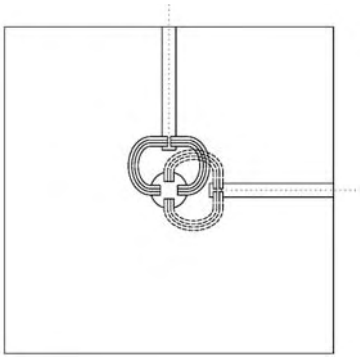

Fig. 7 Proposed geometry of a coaxial orthomode transducer which operates at millimeter wave frequencies. The circular and rectangular waveguides immerge from orthogonal sides of the orthomode transducer, instead of the same side, as shown in Figs. 1 & 2.

The dimensions of the waveguide flanges set the minimum external dimensions of the orthomode transducer. If a standard UG-387M/U flange with 0.75-in external diameter is used, the rectangular waveguide sections have lengths on order of half this value. We estimate that the room temperature loss associated with the attenuation of the single TE_{10} mode in a ~0.35-in long section of gold-plated WR3.7 is 0.45–0.66 dB/in, using Formula 1.66 in Harvey [5] substituting half of the dc gold conductivity. This corresponds to an insertion loss of 0.16–0.23 dB for a ~0.35-in section of rectangular waveguide, that reduces to 0.05–0.07 dB upon cooling the waveguide to 4 K. We estimate that the attenuation of the TE_{11} mode in the circular waveguide, which must be approximately the same length as the rectangular waveguides, is nearly the same (see Formula 1.79 [5]). Hence, for either polarization channel, the combined loss of the input circular waveguide, the coaxial lines, and the output rectangular waveguide is 0.23 – 0.27 dB. In comparison, Wollack [6] measures an insertion loss of ~0.4 dB for a Bøifot-style orthomode transducer fabricated for operation at λ = 1 mm. The noise temperature increase due to 0.25 dB insertion loss at 4 K in front of a SIS receiver with 30 K noise temperature is only 2 K.

REFERENCES

[1] G. Engargiola and R. L., Plambeck, "Tests of a planar L-band orthomode transducer in circular waveguide," *Review of Scientific Instruments*, vol. 74, issue 3, pp 1380-1382, 2003.

[2] E. J., Wollack, W., Grammer and J. Kingsley, "The Bøifot Orthomode Junction," Alma Memo no. 425, May 2002.

[3] A. M., Bøifot, E., Lier and T., Schaug-Pettersen, "Simple and Broadband Orthomode Transducer," *Proc. IEE*, vol 137, no. 6, pp. 396 – 400, 1990.

[4] R. G., Meadow, "An Absorption Resonance Method for Measuring Mode
Conversion Coefficients of Overmoded Waveguide Components," *Int. J. Electronics*, vol. 34, no. 6, pp. 837-848, 1973.

[5] A. F., Harvey "Microwave Engineering," Academic Press Inc. London, 1963, pp. 15.

[6] E. J., Wollack, and W., Grammer, "Symmetric Waveguide Orthomode Junctions," *Proceedings of the 14th. International Symposium on Space Terahertz Technology*, Tucson, Arizona, Apr. 2003, pp 169-176.

Terahertz waveguide mixer development with micromachining and DRIE

P. Pütz, T. Tils, K. Jacobs and C. E. Honingh

***Abstract*—Simple waveguide mixers have been fabricated up to 1.9 THz in traditional technology. Advanced mixer concepts such as sideband separation or balancing demand more complicated and precise waveguide technology. Mixer development at KOSMA is based on a dual fabrication technology approach. On the one hand we have extended our traditional, CNC lathe based, metal micro machining capabilities. We will present micro milling results of 490 GHz waveguide couplers with ±5 µm precision. On the other hand deep reactive-ion etching (DRIE) of silicon for fabricating waveguides as a new, very powerful technology is explored. This will be demonstrated with successfully fabricated 1.9 THz waveguide structures. Feature reproducibility, given by the photolithography based processes, is ±1 µm, which is sufficiently precise up to frequencies of 10 THz. Features with two different etch depths, such as a waveguide with substrate channel, have been successfully fabricated by using a dual masking scheme.**

***Index Terms*— DRIE, feedhorn, heterodyne receivers, micromachining, mixers, terahertz, waveguide**

I. Introduction

KOSMA has developed a THz waveguide mixer with proven performance up to 1.9 THz [1]. This mixer is a rather straightforward modification of the standard KOSMA SIS mixer design that has demonstrated its good performance in numerous occasions up to 880 GHz in the past [2], [3]. The hardware of the standard design is composed of three main components. First is a solid copper block with a stamped fixed backshort waveguide cavity and a cut substrate channel feature on its face side, which is all machined at the KOSMA workshop. Second is a Pickett or Potter type electroformed feedhorn with integrated waveguide transition manufactured by RPG [4], which is mounted perpendicularly onto the block's face. Third is a lapped Si frame on which the only 2 µm thin Si_3N_4 membrane is flip-chip bounded and enables careful alignment of the device into the waveguide cavity without risking breakage of the fragile membranes (see Fig. 1 for a close-up of the modified mixer block with mounted device) [5], [6].

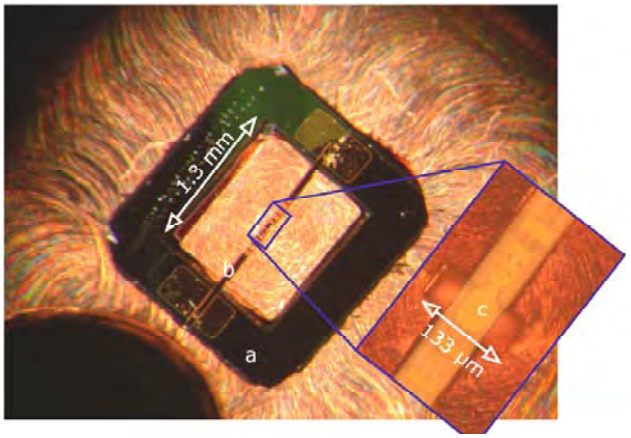

Fig. 1. Close-up of the center of a KOSMA 1.9 THz waveguide mixer block (feedhorn removed). Depicted are (a) the Si frame centering (b) the Si_3N_4 membrane based superconducting HEB device in the substrate channel and (c) a close-up of the waveguide probe in the waveguide.

As a mixing device for THz application we use a phonon-cooled superconducting Hot-Electron Bolometer also completely fabricated in-house.

Although this design works, it is necessary to completely rethink mixer design, in particular when THz array applications, e.g. STAR on SOFIA, are targeted. First the frame mount approach works for a single-pixel application but is too critical and time-consuming for an observatory array receiver. Second the metal machining of the waveguide and substrate channel features is lacking sufficient precision, speed and yield for reproducible volume fabrication of array mixer units.

II. Future KOSMA THz waveguide mixers

A. More mature designs

Our goal is a mixer design mature enough to include features like balancing and high IF output for array applications up to an operating frequency of several THz. The general approach is to use the newly available plasma based deep-reactive ion etch (DRIE) of Si wafers for the small, high frequency structures, which is novel to submillimeter and THz waveguide mixer fabrication. This is made possible by the latest addition to KOSMA cleanroom processing equipment, an inductively coupled plasma (ICP) etcher [7].

This work was supported in part by the Deutsche Forschungsgemeinschaft (DFG), grant SFB494, and the European Union , grant FP6-Radionet.

T. Tils, K. Jacobs and C. E. Honingh are with the Kölner Observatorium für Submm-Astronomie (KOSMA), I. Physikalisches Institut der Universität zu Köln, Zülpicher Str. 77, 50937 Köln, Germany (email: lastname@ph1.uni-koeln.de).

P. Pütz was with KOSMA. He is now with the Steward Observatory Radio Laboratory (SORAL), University of Arizona, 933 N. Cherry Avenue, Tucson, AZ 85721 USA (e-mail: ppuetz@as.arizona.edu).

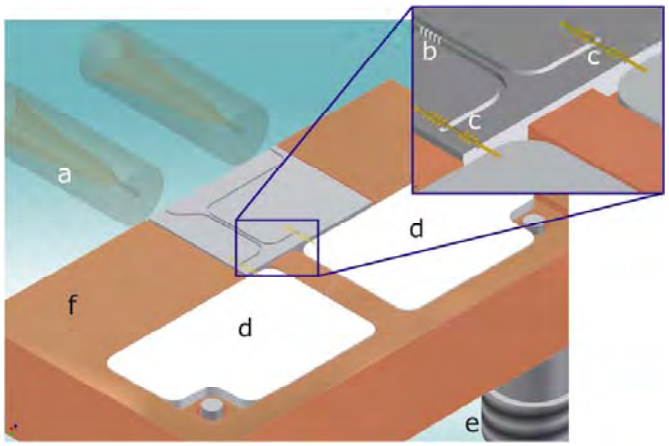

Fig. 2. Conceptual 3D rendering of the hybrid test mixer for 1.4 THz. The individual components are (a) the smooth-walled feedhorn, (b) the DRIE micromachined silicon insert with branchline coupler and mixer waveguide, (c) the devices on membranes with beamleads, (e) the SMP type output connector and (f) the copper support block.

Larger scale, lower frequency structures will be machined with refined metal milling on a CNC lathe. For THz frequencies this leads to a hybrid mixer design, which has a DRIE structured Si wafer insert with the waveguide and substrate channel features and a metal support block to accommodate the insert, the IF board and the dc and IF connectors (Fig. 2). The mixer will be of an E-plane split-block type.

A 1.4 THz balanced mixer is being constructed to demonstrate this hybrid design approach, and in parallel the metal micromilling processes is being improved while manufacturing branchline couplers for new 490 GHz mixers.

For maximum performance and ease of mounting in later array mixer units the mixing elements will be beamlead supported Si or Si_3N_4 membrane devices [8], [9]. The beamleads will also deliver RF and IF ground to the device.

B. Improved feedhorn performance

Feedhorn reproducibility is an additional issue for THz frequencies. Currently, the highest performance feedhorns are typically of the corrugated type, as e.g. for Band 1–4 of the HIFI instrument of the Herschel Space Observatory, and are fabricated through an electroforming process at RPG. The corrugations of the feedhorn become mechanically unreliable for THz frequencies and, more importantly, pose a significant additional effort during feedhorn fabrication. Feedhorn alignment onto the waveguide cavity has to be precise to a few micrometers at 1.9 THz, which is difficult to achieve with a typical dowel pin type interface. A simpler more precise and reproducible alignment scheme is required for the feedhorns and, at least for the high frequencies, should favor a split-block type approach with the feedhorn directly machined into the mixer block. In this case the alignment accuracy between feedhorn and waveguide features is determined by the precision of the machining process. Then only the split-block half alignment itself remains critical.

Hence we are investigating two new routes for THz compatible feedhorns, again with reproducibility and ease of volume production for array mixer units in mind.

First we have investigated the performance of smooth-walled type feedhorns fabricated with the same electroforming technique as the corrugated ones [10]. The performance of these horns is excellent even though of the vastly simplified fabrication [11]. The alignment concept for these horns remains the conventional at first.

Second, avoiding the horn / waveguide alignment for the high frequency range, is the laser micromachining (LMM) process of split-block corrugated feedhorn features into Si [12], [13]. This process uses a powerful laser in combination with a chlorine environment to write 3D features directly into a Si wafer with a few micrometer precision by means of scanning optics. As this micromachining process is only available for the THz mixer community at the Steward Observatory Radio Laboratory (SORAL), U. of Arizona, a close collaboration between KOSMA and SORAL has been set up. In combination with the DRIE process it seems possible to fabricate all critical mixer features in Si and enabling sufficiently precise waveguide features up to 10 THz.

III. Fabrication

Several areas need to be investigated for the hybrid mixer fabrication.

A. Metal micromilling

We are currently improving our CNC lathe milling process. The goal is to mill features down to 50 µm to ±3 µm precision. This would enable a very precise fit of the silicon inserts in the mixer block and additionally permit the use of metal milled branchline waveguide couplers up to 800 GHz.

B. Silicon micromachining of planar structures

We have started developing the Si DRIE process for waveguide fabrication and have principally demonstrated its ability to precisely reproduce structures defined by the photolithographic masking process to better than two micrometers for very high aspect ratio features. One principal limitation of the DRIE process is that it can only yield planar features normal to the wafer surface and only on one depth level per DRIE process step. A one level structure could e.g. be a hybrid coupler for a balancing or sideband separating mixer.

Because a waveguide environment composed of a waveguide cavity and substrate channel is a two-level structure, a two step DRIE process is required with two masking layers.

C. Silicon micromachining of tapered and stepped structures

Stepped and tapered Si structures are micromachined with the LMM system at SORAL. As this process is rather slow when compared to DRIE, large area planar structures should be avoided. The current LMM systems can write structures with 3 µm resolution within a 2 mm × 2 mm scanning field, and a new, higher resolution system is being finalized which will provide a 10× higher resolution but with equally reduced scanning field.

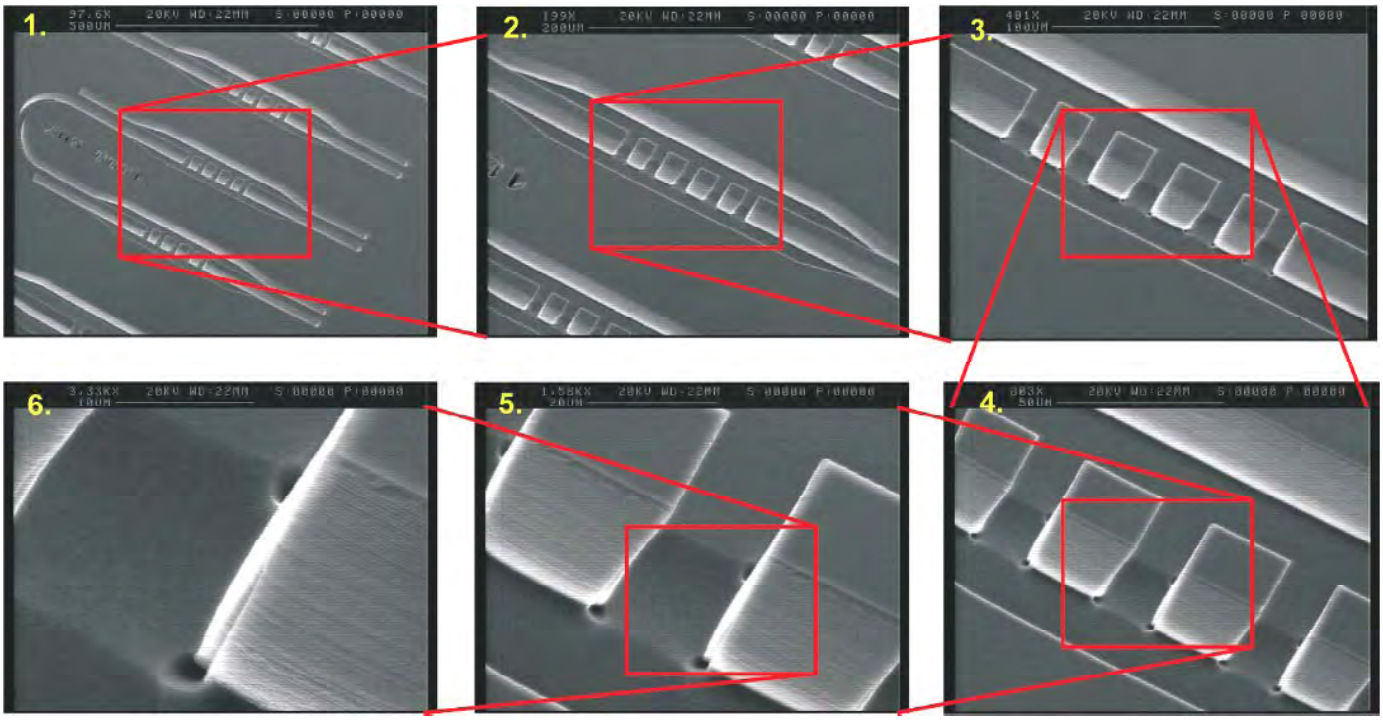

Fig. 3. SEM micrograph zoom in sequence onto a Si DRIE 1.9 THz branchline coupler. The scale bar on the last micrograph measures 10 µm. Etch depth is 55 µm. Note the low sidewall roughness of the Bosch process. The view is inclined by approx. 45°.

D. Additional considerations

The Si features need to be plated with Au. For typical high-aspect ratio waveguide features sidewall coverage needs to be investigated as well as the cryo compatibility. Resulting from our experience gained from constructing the HIFI Band 2 mixer we opted for 200 nm sputter-deposited Au on top of 50 nm sputter-deposited Al. DRIE structured Si wafers were cycled 10× in LN2 and then several times to LHe temperature in vacuum, according to HIFI specifications. Microscopic inspection of the Au surface revealed no noticeable change such as peeling or discoloring and tape pull tests showed no difference in adhesion strength before and after the cooling cycles.

Dependent on the mixer block design a concept for precise feedhorn alignment needs to be developed. For the silicon insert split-block alignment could be achieved through self-aligning the Si pieces by means of additional DRIE structures.

IV. Silicon Micromachining of THz Structures

DRIE is executed with a time-multiplexed process, also known as the Bosch process, in our inductively coupled reactive-ion etcher [14]. The process switches between an etch and a deposition (passivation) cycle every few seconds which results to near-perfect vertical etching, i.e. high aspect ratio structures for several hundred micrometers. The resulting scalloping of the sidewalls is so small that is not of concern, as can be seen on the last SEM micrograph of the zoom in sequence onto a 1.9 THz branchline coupler in Fig. 3. Remarkably the process leaves no residue. Time averaged etch rate is typically 5 µm/min.

The lateral feature size reproducibility of this process therefore is determined by the photolithography process used for defining the etch mask and is ±1 µm. The etch depth is computer controlled in-situ during the DRIE with means of a dual beam interferometer to < 1 µm.

For two-level structures we have developed a dual masking scheme process with uses two DRIE steps. The process has been optimized to prevent formation of a burr at the step between the two levels (Fig. 4).

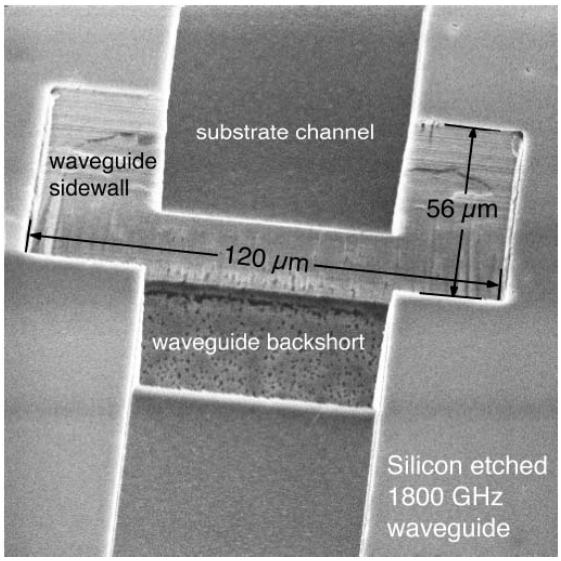

Fig. 4. SEM micrograph of a 1.9 THz two-level Si DRIE waveguide-substrate channel structure. Note that the dual masking process has been optimized to prevent formation of a burr between the waveguide and the substrate channel.

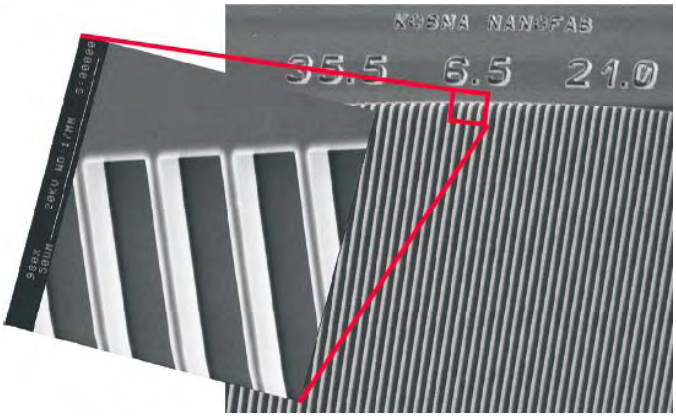

Fig. 5. SEM micrographs of DRIE etched antireflection structures on a Si window. The large numbers give the target values for period, bar width and etch depth. Note the absence of any residue from the DRIE process.

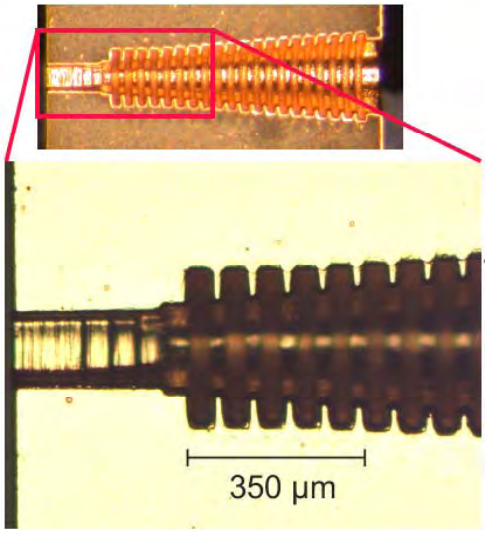

Fig. 6. Microscopic view of a LMM 1.9 THz feedhorn half. The feedhorn is gold plated. The lower image shows a close-up of the neck area with the waveguide transformer section.

Fig. 5 depicts another application for Si DRIE. Si is one of the materials with the lowest losses in the 1–2 THz range and therefore very interesting as e.g. the dewar window material. Due to its high dielectric constant some kind of antireflection coating is required. Structuring precise periodic structures into the Si can serve this purpose [15].

What we have learned up to now is that the DRIE process is extremely powerful. It is a very fast structuring method and due to its precision and reliability most suitable for volume production of array mixer units.

LMM feedhorns are now available from SORAL. Fig. 6 shows a microscopic view onto a 1.9 THz feedhorn half that already has been Au plated. Judging from the microscopic inspection feature size reproducibility and precision of this sample horn is good enough for this frequency, even though this feedhorn was machined with the lower resolution LMM system.

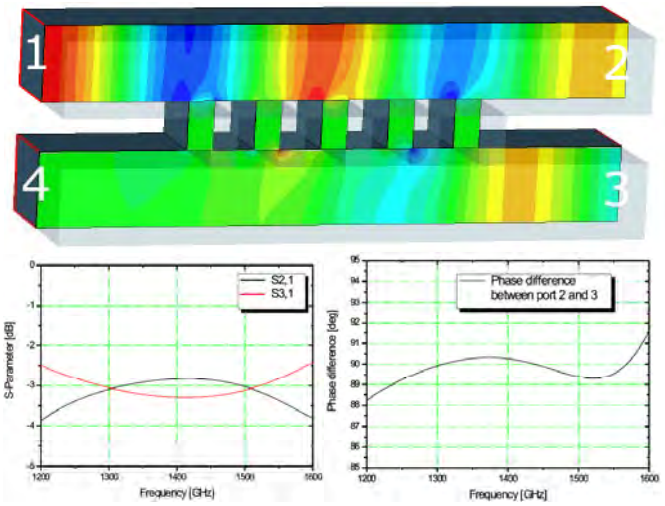

Fig. 7. Simulation of an optimized 1.4 THz branchline coupler. Port 1: input; Port 2: -3 dB output; Port 3: -3 dB output with 90 degree phase difference to Port 2; Port 4 is terminated by a load. Top depicts the field distribution in the coupler structure and plots below show the results for S21 and S31 as well as phase difference.

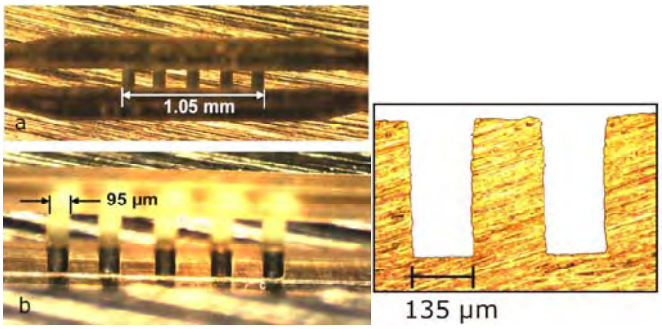

Fig. 8. Microscopic view of CNC lathe machined metal branchline couplers. Right: (a) depicts a top and (b) a tilted side view of the 490 GHz structures. Right: Microscopic cross-section of the same branchline coupler. (Milling tool diameter: 100 µm, milling tool rotation speed: 70000 rpm)

V. Design of Waveguide Structures

Waveguide structures such are designed and optimized with CST Microwave Studio 3D EM simulation software [16]. Fig. 7 shows the simulation results of the optimized 3 dB 90 degree branchline waveguide coupler for the 1.4 THz balanced mixer [17], [18]. The top part of the figure depicts the field intensity distribution through the coupler structure, whereas the plots below show that S21 and S31 are 3±0.5 dB and the phase balance between ports 2 and 3 is within ±1.7 degrees for the simulated frequency range 1.2–1.6 THz.

VI. Prototyping at 490 GHz

As an intermediate step we are currently optimizing the machining process for 490 GHz branchline couplers for a single-sideband mixer project. Currently we can machine the couplers to ±5 µm precision which is sufficient for this frequency (Fig. 8).

VII. Conclusion

We believe that our dual technology approach for the mixer hardware should make reproducible fabrication of wideband waveguide based mixers possible to 10 THz. The use of metal micromilling techniques for fabrication of mixer housings, as well as for (lower frequency) less critical waveguide features, in combination with silicon micromachined waveguide inserts is powerful enough for volume production of THz array mixer hardware.

Acknowledgment

We like to thank Stephan Wulff for maintaining the cleanroom facilities and for bringing forward important contributions to process development. We also like to thank Michael Schultz for his superb skills in 3D CAD design and mechanical engineering. We are grateful towards Bettina Deckert for carefully conducting the thermal cycling tests. Last but not least the very high standard in fine mechanical machining being consistently attained by the KOSMA workshop under supervision from Matthias Mondt is pivotal to these and all other developments.

References

[1] S. Bedorf, P. Munoz, C. E. Honingh, K. Jacobs. Development of phonon-cooled NbTiN HEB heterodyne mixers for GREAT. Published in these proceedings.

[2] C. E. Honingh, S. Haas, D. Hottgenroth, K. Jacobs, and J. Stutzki. Low noise broadband fixed tuned SIS waveguide mixers 660 and 800 GHz. IEEE Trans. Appl. Supercond., 7:2582–2586, 1997.

[3] P. Pütz, S. Glenz, R. Teipen, T. Tils, N. Honingh, K. Jacobs, A. Hedden, C. Kulesa, C. E. Groppi, and C. K. Walker. High Sensitivity 810 GHz SIS Receivers at AST/RO. J. Zmuidzinas, W. S. Holland, and S. Withington, editors, Proc. SPIE, Vol. 5498, Millimeter and Submillimeter Detectors for Astronomy II, pages 509–516. SPIE, The International Society for Optical Engineering, 2004.

[4] Radiometer Physics GmbH (RPG). http://www.radiometer-physics.de.

[5] M. Brandt, P. P. Muñoz, J. Stodolka, T. Tils, C. E. Honingh, and K. Jacobs. Superconducting Hot Electron Bolometers on fused quartz and on freestanding Silicon Nitride membrane strips. Proceedings of the 6th European Conference on Applied Superconductivity (EUCAS), pp. 2978–2985, Sorrento, Italy, September 2003. Institute of Physics Publishing.

[6] S. Bedorf, P. Munoz, M. Brandt, P. Pütz, N. Honingh, and K. Jacobs. Development of phonon-cooled NbTiN HEB heterodyne mixers for THz applications. Digest 29th Int. Conf. on Infrared and Millimeter Waves and 12th Int. Conf. on Terahertz Electronics, pp. 455–456, 2004.

[7] Oxford Instruments Plasma Technology. Plasmalab System 100. http://www.oxford-instruments.com.

[8] R. B. Bass, A. W. Lichtenberger, R. M. Weikle, S.-K. Pan, E. Bryerton, C. K. Walker, Ultra-Thin Silicon Chips for Submillimeter-Wave Applications. Proceedings of the 15th International Symposium on Space THz Technology, Northampton, MA, April 2004

[9] A. B. Kaul, B. Bumble, K. A. Lee, H. G. LeDuc, F. Rice, and J. Zmuidzinas. Fabrication of wide-IF 200 – 300 GHz superconductor–insulator–superconductor mixers with suspended metal beam leads formed on silicon-on-insulator. J. Vac. Sci. Technol. B, 22(5):2417–2422, 2004.

[10] C. Granet, G. L. James, R. Bolton, and G. Moorey. A Smooth-Walled Spline-Profile Horn as an Alternative to the Corrugated Horn for Wide Band Millimeter-Wave Applications. IEEE Trans. on Ant. and Prop., 52(3):848–854, March 2004.

[11] T. Tils, A. Murk, D. Rabanus, C. E. Honingh, and K. Jacobs. High performance smooth-walled horns for THz waveguide applications. Published in these proceedings.

[12] C. K. Walker, G. Narayanan, H. Knoepfle, J. Capara, J. Glenn, A. Hungerford, T. M. Bloomstein, S. T. Palmacci, M. B. Stern, J. E. Curtin, Laser micromachining of silicon: a new technique for fabricating high quality terahertz waveguide components. Proceedings of the 8th International Symposium on Space Terahertz Technology, eds. R. Blundell, E. Tong, pp. 358-376, 1997.

[13] A. Hedden, C. K. Walker, D. Golish, C. Drouet d'Aubigny, C. Groppi, C. Kulesa, D. Prober, J. W. Kooi, G. Narayanan, A. Lichtenberger, A. Datesman, Applications of Laser Micromachining Technology to THz HEB Array Development. Proceedings of the 15th International Symposium on Space THz Technology, Northampton, MA, April 2004.

[14] F. Laermer and A. Schilp, Patent DE4241045 (U.S. Pat. No. 5,501,893), 1994.

[15] A. Wagner-Genter, K. Jacobs, U. Graf, and D. Rabanus. Low-loss THz window. Published in these proceedings.

[16] CST. Computer Simulation Technology. Microwave Studio 5. http://www.cst.com.

[17] S. M. X. Claude, C. T. Cunningham, A. R. Kerr, and S.-K. Pan. Design of a Sideband-Separating Balanced SIS Mixer Based on Waveguide Hybrids. ALMA Memo Series, #316. 2000.

[18] K. S. Srikanth, and A. R. Kerr. Waveguide Quadrature Hybrids for ALMA Receivers. ALMA Memo Series, #343. 2001.

The potential of dielectric mirrors as key elements in future non-line-of-sight indoor terahertz communication systems

R. Piesiewicz, K. Baaske, K. Gerlach, M. Koch, T. Kürner

Abstract— **We present results of transfer matrix simulations of the reflectivity of dielectric mirrors in the THz range. The potential of dielectric mirrors as key elements in future non-line-of-sight indoor communication systems is demonstrated with ray-tracing simulations. The channel properties are derived for the case when dielectric mirrors are used as wall paper and for the case without them. Our simulations show that the indirect transmission paths between a transmitter and a receiver will provide a significantly enhanced signal coverage when mirrors are present.**

Index Terms — **submillimeter wave communication, terahertz systems, dielectric mirrors, ray tracing, channel characterization**

I. Introduction

Short range wireless communication systems are expanding at a rapid rate, finding applications in offices, congested urban areas and homes. The development of wireless local area networks is accompanied by an increasing demand for higher data rates. This in turn entails the necessity to develop communication systems which operate at higher frequencies. Currently WLAN work at a few GHz, while systems operating at several ten GHz appear already feasible. It can be expected that wireless short-range communication networks will soon push towards the THz frequency range and that systems which support very large bandwidth communications with gigabit data rates will be developed in a few years time.

Since THz radiation is strongly absorbed by the atmosphere and free-space path losses are high, working distances may be short and individual THz pico-cells may cover only single rooms or one building at the most. Furthermore, these systems will require high directivity antennas and hence will depend on an unobstructed line-of-sight between a transmitter and a receiver. However, a practical indoor THz communication system must be robust against shadowing, as moving people or other objects may block the direct line of sight link. Thus, for reliable operation, such a system should also allow non-line-of-sight (NLOS) transmissions, realized with directed reflections from the walls or other objects. Considering the small wavelengths in the THz range and the roughness of indoor walls, it can be expected that such reflections have significant diffuse contributions. Hence, the power will be inefficiently scattered, the directivity of antennas will be lost and it will be rather difficult to obtain gigabit data rates. Recently, flexible all-plastic mirrors, supporting specular reflections in the THz range have been demonstrated [1]. They are cheap and easy to produce and can be used as frequency selective wall-paper to enhance the reflectivity of walls and hence facilitate NLOS communication in a THz cell.

This paper is organized as follows. In Section II we discuss the fundamentals of dielectric mirrors and the transfer matrix approach to calculate their reflectivity. In Section III the results of transfer matrix simulations of the mirror reflectivity for different angles of incidence, polarization and frequencies are shown. Furthermore, the influence of the variation of the mirror parameters on its reflectivity is investigated. In Section IV the potential of dielectric mirrors is shown with ray-tracing simulations of indoor terahertz channel parameters for the cases with and without them. Section V concludes the paper.

II. Dielectric Mirrors

Dielectric mirrors are well known from optical frequencies. They consist of a stack of pairs of different dielectric materials. In Fig. 1 a structure consisting of 3.5 pairs is displayed [2].

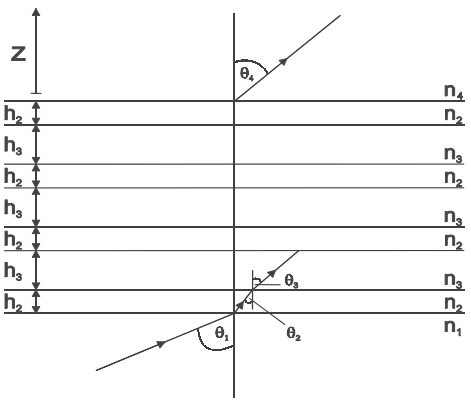

Fig. 1. Schematic of a dielectric mirror consisting of 3.5 pairs [2].

R. Piesiewicz and T. Kürner are with the Institut für Nachrichtentechnik, Braunschweig University of Technology, Braunschweig, Germany (e-mail: piesiewicz@ifn.ing.tu-bs.de). K. Baaske, K. Gerlach and M. Koch are with the Institut für Hochfrequenztechnik, Braunschweig University of Technology, Braunschweig, Germany

The layer designated by n_2 and h_2 occurs four times whereas the layer designated by n_3 and h_3 appears three times resulting in 3.5 alternating layers. The two materials involved have refractive indexes of n_2 and n_3 ($n_2 > n_3$) and thickness of h_2 and h_3. In Fig. 1 n_1 is a refractive index of an ambient medium and n_4 that of a substrate medium.

In the following we consider a plane wave incident at an angle θ as depicted in Fig. 1. At each transition from one refractive index to another the wave is partially transmitted and partially reflected. If the condition

$$n_2 h_2 = n_3 h_3 = \frac{\lambda_0}{4} \tag{1}$$

holds, the optical thickness of the two materials matches. It means that all reflected components including those originating from internal reflections interfere constructively at the given free-space wavelength of λ_0 and odd order multiples (1,3,5, …) of λ_0. This condition potentially results in a very high reflectivity of a mirror.

The reflectivity and transmission of a mirror can be calculated by determining the propagation of a plane wave through the stratified medium with the help of a transfer matrix, the so called characteristic matrix.

The characteristic matrix of a single layer is given by

$$M_j = \begin{bmatrix} M_{11} & M_{12} \\ M_{21} & M_{22} \end{bmatrix} = \begin{bmatrix} \cos\delta_j & \dfrac{-i\sin\delta_j}{p_j} \\ -ip_j\sin\delta_j & \cos\delta_j \end{bmatrix} \tag{2}$$

where $\delta_j = \dfrac{2\pi}{\lambda_j} n_j h_j \cos\theta_j$ is the optical thickness of each layer, λ_j denotes wavelength in the given medium and θ_j is the angle of refraction in the j_{th} layer [3]. Depending on the layer referred to, j takes on the values of 2 or 3, whereas i is the square root of –1. In (1) p_j is given by

$$p_j = n_j \cos\theta_j \tag{3}$$

for TE polarized waves and by

$$p_j = \frac{\cos\theta_j}{n_j} \tag{4}$$

for TM polarized waves. The characteristic matrix M_{23} of one double layer with n_2, n_3, h_2, h_3 can be expressed by $M_{23}=M_2M_3$. Thus, the characteristic matrix of the dielectric mirror consisting of a stack of N double layers has the following form

$$M_{N(23)} = \underbrace{M_{23} \cdot M_{23} \cdots M_{23}}_{Ntimes} \tag{5}$$

The reflection coefficient of a mirror can be obtained from (5) and is given by

$$r = \frac{(M_{11} + M_{12}p_4)p_0 - (M_{21} + M_{22}p_4)}{(M_{11} + M_{12}p_4)p_0 + (M_{21} + M_{22}p_4)} \tag{6}$$

where p_0, p_4 are the values for ambient and substrate media corresponding to (3) and (4) for TE and TM polarization respectively. The elements of M in (6) refer to the characteristic matrix of the multilayer structure in total.

A transmission measurement for a structure which contains 4.5 pairs of materials with the following parameters: $n_2=2.6$, $h_2=200\mu m$, $n_3=1.33$, $h_3=130\mu m$ [2] is shown in Fig. 2.

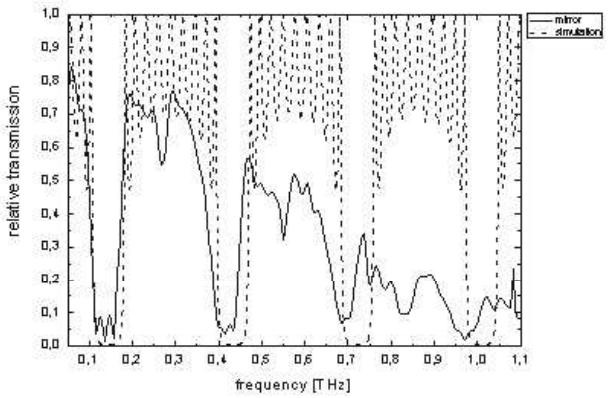

Fig. 2. Results of transmission measurement and simulation of a dielectric mirror with $n_2=2.6$, $h_2=200\mu m$, $n_3=1.33$, $h_3=130\mu m$ [2].

The solid line in Fig.2 shows results of mirror measurements. The transmission of the measured mirror decreases with the increase in frequency which can be attributed to the scattering. However, the foils were arbitrarily taken from commercially available ones. No emphasis was put on the quality of the material. The dashed line in Fig. 2 shows the simulation of the mirror transmission. The discrepancy between the measurement and the simulation of the mirror can be attributed to the measurement error of the mirror parameters on one hand and to the fact that constant values of the refractive indexes were taken for the foils and no account was made for their frequency dependence.

III. Results of Mirror Reflectivity Simulations

For applications in directed NLOS communication scenarios a dielectric mirror should have good reflective properties in a broad range of angles of incidence. Such a mirror is called omni-directional and can be obtained by a proper choice of its parameters, i.e. refractive indexes and thickness of layers [4].

In the following, a mirror designed for a center frequency of 300 GHz is investigated for its reflective properties. The chosen frequency corresponds to a relatively low atmospheric

attenuation and hence would be a good candidate for a carrier frequency for the potential THz communication system. The mirror is composed of 8.5 pairs of foils with refractive indexes of $n_2=2.5$, $n_3=1.5$ and thickness $h_2=107\mu m$, $h_3=178\mu m$.

A. *Frequency and angular dependence of the mirror reflectivity*

The results of simulations of the mirror reflectivity are presented in Fig. 3 and 4 for TE and TM polarization respectively. The reflectivity is shown as a function of frequency for different angles of incidence.

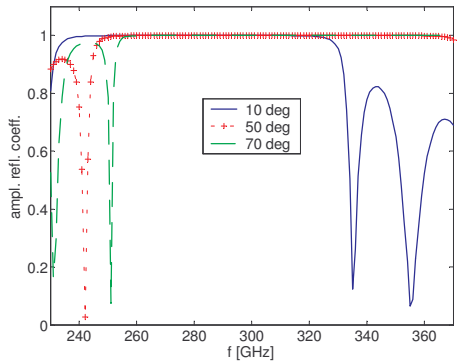

Fig. 3. Mirror reflectivity for TE polarization as a function of frequency for angles of incidence of 10, 50 and 70 degrees.

As can be seen from Fig. 3 and 4 the mirror has an excellent reflectivity over a wide frequency band for all angles. In the case of TE polarization the reflectivity band is centered around 300 GHz with a width exceeding 60 GHz. In the case of TM polarized waves the bandwidth, for which the mirror has very good reflective properties is smaller and amounts to 40 GHz.

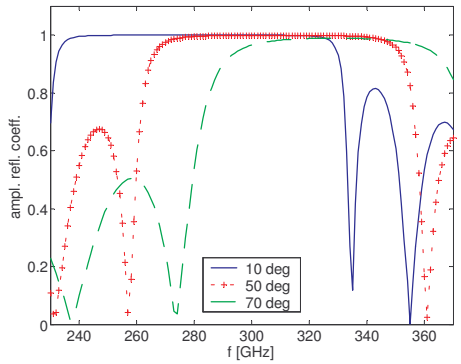

Fig. 4. Mirror reflectivity for TM polarization as a function of frequency for the angle of incidence of 10, 50 and 70 degrees.

The simulation results of the mirror reflectivity as a function of angle of incidence are shown in Fig. 5 and 6 for different frequencies and for TE and TM polarization, respectively.

Fig. 5 and 6 show the omni-directional character of the presented mirror. In the case of TE polarized waves the mirror shows excellent reflective properties in the whole range of angles of incidence and over bandwidth of 60 GHz. In the case of TM polarization the mirror is highly reflecting for the angles of incidence up to 50 degrees if the same bandwidth is considered. Yet, for a smaller bandwidth the mirror is a good reflector up to angles of 90 degrees.

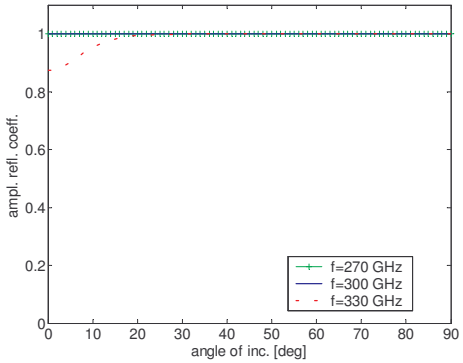

Fig. 5. Mirror reflectivity for TE polarization as a function of angle of incidence for the frequencies of 270, 300 and 330 GHz.

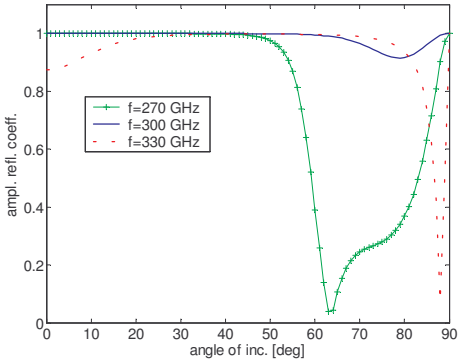

Fig. 6. Mirror reflectivity for TM polarization as a function of angle of incidence for the frequencies of 270, 300 and 330 GHz.

B. *Thickness variation of the dielectric layers*

The thickness of the dielectric layers can deviate from the nominal values. In the following we investigate the influence of a variation of h_2 and h_3. Fig. 7 and 8 show the reflectivity of the mirror at 300 GHz as a function of the angle of incidence and the variation of the thickness of h_2 for TE and TM polarization, respectively. The thickness variations are in the range of ±25% around the nominal value of 107µm.

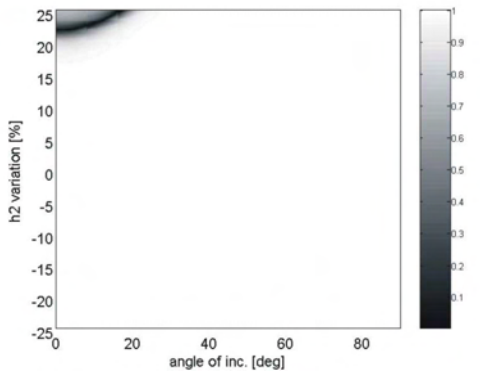

Fig. 7. Mirror reflectivity for TE polarization as a function of the angle of incidence and the variation of the thickness of layer 2.

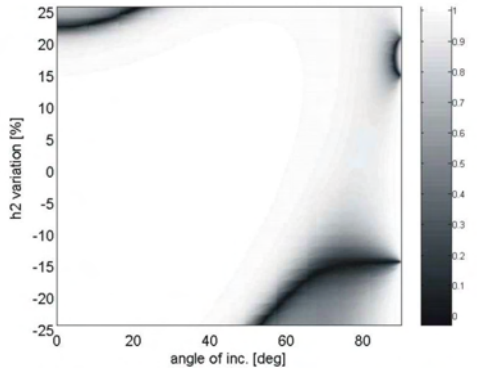

Fig. 8. Mirror reflectivity for TM polarization as a function of the angle of incidence and the variation of the thickness of layer 2.

In the case of TE polarization the mirror reflectivity is less than one only for large positive thickness variations of layer 2 and small angles of incidence. In the case of TM polarization considerable negative thickness variations of layer 2 result in a reflectivity reduction for large incidence angles.

In Fig. 9 and 10 the reflectivity of the mirror at 300 GHz is shown as a function of the angle of incidence and a variation of the thickness h_3 for TE and TM polarization, respectively. The thickness variations are again in the range of ±25% around the nominal value. A comparison with Fig. 7 and 8 shows that thickness variations of layer 3 have similar effect as variation of layer 2.

C. *Variation of the refractive index of the mirror layers*

In analogy to the thickness variations also the refractive index of mirror layers can deviate from the nominal values. In the following, we investigate the influence of a variation of n_2 and n_3 on the mirror performance. Fig. 11 and 12 show the reflectivity of the mirror at 300 GHz as a function of the angle of incidence and the variation of n_2 for TE and TM polarization, respectively. The n_2 variations are in the range of ±25% around the nominal value of 2.5. In the case of TM polarization negative variations of n_2 greater than 5 % result in a reflectivity reduction. Large angles are more heavily affected. In contrast, reflections under TE polarization are much more immune to variations of the refractive index of layer 2.

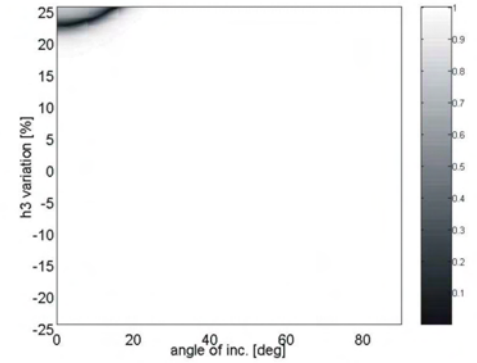

Fig. 9. Mirror reflectivity for TE polarization as a function of the angle of incidence and the variation of the thickness of layer 3.

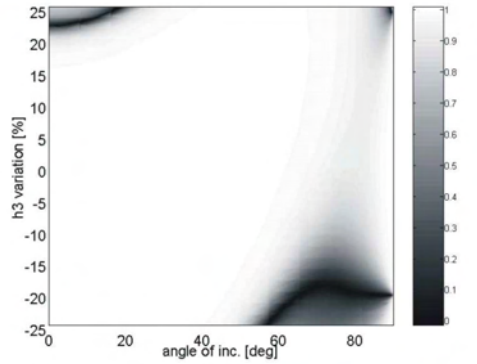

Fig. 10. Mirror reflectivity for TM polarization as a function of the angle of incidence and the variation of the thickness of layer 3.

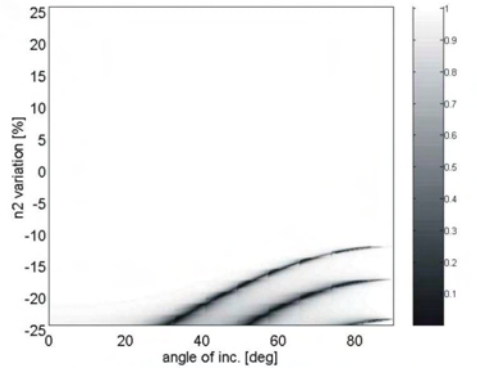

Fig. 11. Mirror reflectivity for TE polarization as a function of angle of incidence and variation of refractive index of layer 2.

In Fig. 13 and 14 the reflectivity of the mirror at 300 GHz is shown as a function of the angle of incidence and the variation of n_3 for TE and TM polarization, respectively. The n_3 variations are in the range of ±25% around the nominal value of 1.5. Here, in the case of TE polarization positive variations of n_3 greater than 15 % result in reflectivity reduction, especially at small angles. In the case of TM polarization both negative and positive variations of n_3 lead to a reduced reflectivity. Large angles are more affected for negative variations, whereas small angles are more for positive ones.

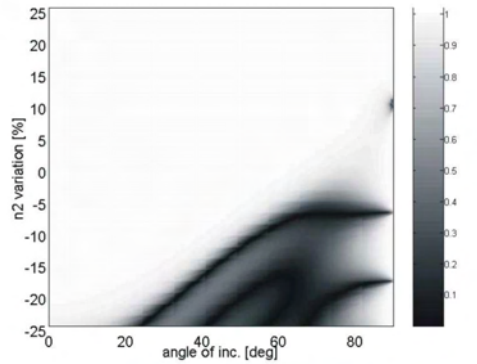

Fig. 12. Mirror reflectivity for TM polarization as a function of the angle of incidence and the variation of refractive index of layer 2.

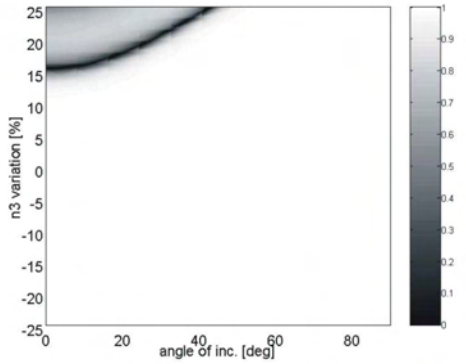

Fig.13 Mirror reflectivity for TE polarization as a function of the angle of incidence and the variation of the refractive index of layer 3.

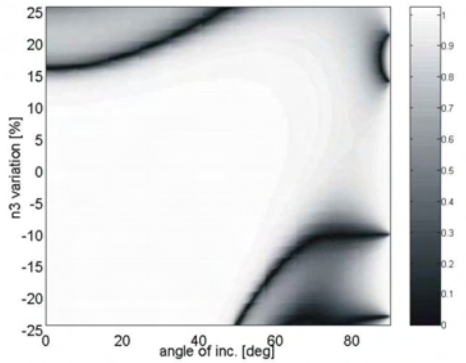

Fig. 14. Mirror reflectivity for TM polarization as a function of the angle of incidence and the variation of the refractive index of layer 3.

IV. Ray-tracing simulations

In the following we present ray-tracing simulations which are preformed to demonstrate the potential of dielectric mirrors as key elements in future non-line-of-sight indoor communication systems at terahertz frequencies. A possible THz communication scenario is shown in Fig. 15. The simulated room is without furniture and there are windows on one of the walls. The walls are covered with plaster. The transmitter, with an output power 0 dBm is centered on the ceiling in the middle of the room with dimensions 6m x 5m x 2.5m. The receiver is about one meter above the ground in the plane z=0.95m. Ray-tracing simulations are performed for the frequency of 300 GHz to derive the properties of the THz propagation channel [5]. The channel characteristics are simulated for the case when dielectric mirrors are used as wall paper and for the case that the walls are made of plaster.

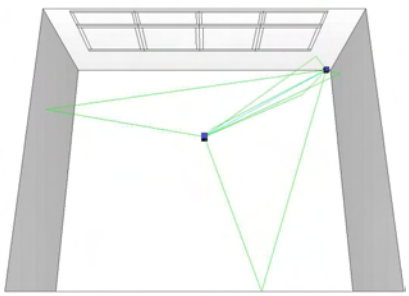

Fig. 15. Three dimensional view of the simulated THz cell scenario.

Fig. 16 and 17 show the power distribution in the plane of the receiver which arise from electromagnetic waves with TM polarization that are reflected once. Fig 16 shows the power level for the case that that walls are covered with dielectric mirrors and Fig. 17 shows the same for the case that no mirrors are present and the walls are covered with plaster. The reflectivity of plaster was measured in a THz-TDS (terahertz time-domain spectrometry) reflection set-up in the 70 – 400 GHz frequency range for different angles of incidence. The measurement results were incorporated as interpolated reflectivity functions into the ray-tracing simulations.

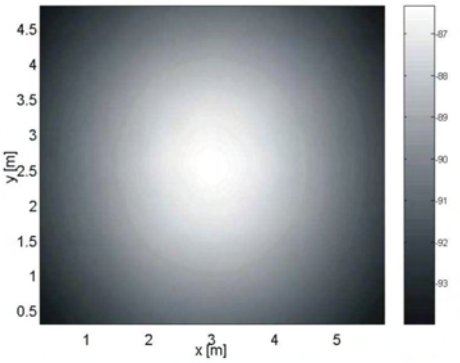

Fig. 16. Power distribution in dBm in the plane z=0.95m of the receiver arising from once-reflected paths. It is assumed that the electromagnetic waves have TM polarization and that the walls are covered by mirrors.

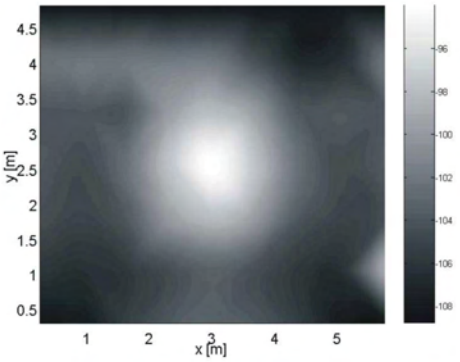

Fig. 17. Power distribution in dBm in the plane z=0.95m of the receiver arising from once-reflected paths. It is assumed that the electromagnetic waves have TM polarization and that the walls are made from plaster.

When the walls are covered with mirrors the received once-reflected power varies between –87 and –94 dBm. If the walls are covered with plaster the received power is considerably lower and varies between –95 and –108 dBm.

If mirrors are present we obtain essentially the same results for TE polarization. Yet, if the walls are covered by plaster the results are different. Fig. 18 shows that case. Note, that the signal level varies between –96 and –98 dBm and is much higher than that displayed in Fig. 17. This difference results from the fact that the reflectivity of TE waves is always higher than that of TM waves. Also the variation of the received power is not as pronounced as for the case of TM polarization. This can be attributed to the non existence of a Brewster angle for TE waves. Nonetheless, the received power level for once-reflected TE waves is considerably smaller if the walls are

covered with plaster than if they are covered with mirrors.

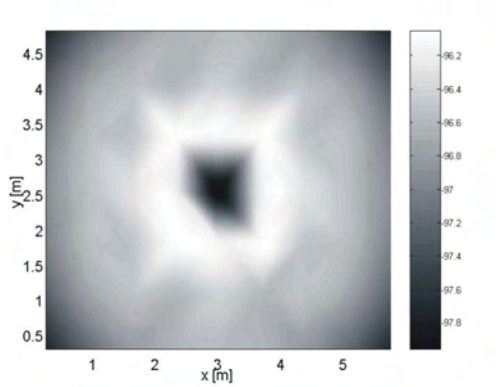

Fig. 18. Power distribution in dBm in the plane z=0.95m of the receiver arising from once-reflected paths. It is assumed that the electromagnetic waves have TE polarization and that the walls are made from plaster.

V. Conclusion

We have presented the results of transfer matrix simulations of the reflectivity of dielectric mirrors in the THz range. A proper choice of the layer thickness and the index of refraction allows us to construct a quasi omni-directional mirror that shows excellent reflective properties for a broad range of incidence angles for both TE and TM polarization. The presented mirror was simulated for a center frequency of 300 GHz. The bandwidth, over which it shows good reflective properties is around 40 GHz. Such mirrors are cheap, easy to produce and could be used as wall paper to enhance the reflectivity of walls in order to facilitate non-line-of-sight propagation in future gigabit data rate THz communication cells.

Furthermore, ray-tracing simulations were performed to derive propagation channel characteristics for the case when walls are covered with dielectric mirrors and for the case without them. Our simulations show that indirect transmission paths between a transmitter and receiver, supported by dielectric mirrors will provide better signal coverage in future THz cells and will make the THz communication channel much more robust against shadowing.

Acknowledgment

We acknowledge discussions with Thomas Kleine-Ostmann and Frank Rutz.

References

[1] D.Turchinovich, A.Kammoun, P.Knobloch, T.Dobbertin, M.Koch, “Flexible all-plastic mirrors for the THz range,” *Applied Physics Letters A*, vol. 74, 2002, pp. 291-293.

[2] H. Vahle, “New materials for dielectric mirrors in the THz frequency range,” B.S. thesis, Inst. für Hochfrequenztechnik., Braunschweig Univ., Braunschweig, Germany, 2004.

[3] M. Born, *Principles of Optics*, Cambridge, Cambridge University Press, 1998, pp. 58-64

[4] M.Mansuripur, “Omni-directional Dielectric Mirrors,” *Optics & Photonics News*, September 2001, pp. 46-50

[5] R.Piesiewicz, J.Jemai, M.Koch, T.Kürner, “THz channel characterization for future wireless gigabit indoor communication systems,” *Intl. Symp. on Integrated Optoelectronic Devices*, *Terahertz and Gigahertz Electronics and Photonics IV*, January 2005, San Jose, USA

High performance smooth-walled horns for THz waveguide applications

Thomas Tils*, Axel Murk+, David Rabanus*, C.E. Honingh*, Karl Jacobs*
*KOSMA, I. Physikalisches Institut, Universität zu Köln
Email: tils@ph1.uni-koeln.de
+Institute of Applied Physics, University of Bern

***Abstract*— For the coupling from free space to waveguide corrugated horns are presently the optimum choice. Currently the extension of the waveguide technology towards THz frequencies, e.g. with silicon micromachining techniques, looks very promising, which increases the demand for THz horns. The HIFI project has shown that even at submm frequencies it is not easy to manufacture reliable corrugated horns for cryogenic applications. For small corrugations it is difficult to avoid fluid inclusions in the corrugations during electroforming. In addition experience has shown that dust or small metal particles can easily settle in between the corrugations and are very difficult to remove. Smooth-walled horns do not have these disadvantages. We will present measurements of a prototype smooth-walled horn for 756-924 GHz. The horn is designed by C. Granet [1] and manufactured by RPG [2]. The measurements were done at 800, 840 and 860 GHz with an AB-mm vector network analyzer at the University of Bern. We have also simulated the performance of the horn in CST Microwave Studio [3]. The simulation results are in a good agreement with the measured data. With the same measurement setup we measured a corrugated horn for the HIFI band 2 Mixer Unit. We conclude that we can replace the corrugated horn by a properly designed smooth-walled horn without significant loss of performance. This is an important step towards building THz waveguide mixers.**

I. Introduction

The fabrication of corrugated horns at THz frequencies is complicated by its small dimensions. For example at 1.9 THz (GREAT receiver for SOFIA [4]) the corrugations are smaller than 25 μm. In general a metal mandrill of the horn-inside is machined, subsequently electroformed, and then removed by etching. The madrills itself are already a major challenge for THz frequencies, but in addition during the electroforming process corrosive fluid inclusions may be formed in the narrow corrugations that break corrugations of the horn for example when it is thermally cycled. Although a method has been found in the course of the HIFI project [2] to avoid the inclusions for horns up to 1.1 THz this method is expensive, time consuming and rather dependent on workmanship. Another method would be, if the mandrill can still be machined, to fill the mandill corrugations by other methods than electroforming [5] or fabricate the horns in split block technique by silicon micro machining [6] and metal plate them afterwards. Both methods are also time consuming, expensive and/or require large investments.

To overcome the limitations imposed by the corrugations Granet et al. at the ICT centre, CSIRO, Australia, have developed a method [1] for optimizing the shape of a smooth-walled spline-profile feed horn to overcome these limitations imposed by corrugations. The optimizing method allows to model feed horns that produce good Gaussian beam shapes at a certain distance from the horn. This method is an algorithm that varies the spline-profile and checks the resulting antenna pattern via a mode matching algorithm for compliance with the pattern to be met. A resulting horn profile is shown in figure 1.

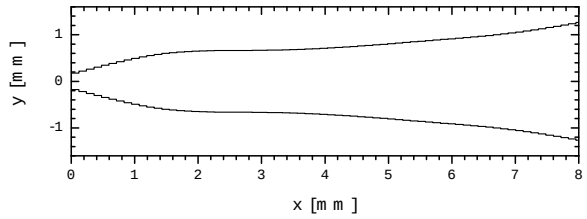

Fig. 1. *Horn profile of the smooth-walled horn for 840 GHz center frequency.*

This technique makes it possible to manufacture high performance feed horns considerably easier than up to now. That is especially interesting since at KOSMA, besides the efforts at submm frequencies, there are (array) instruments being developed at 1.4 and 1.9 THz, and the development of this feed horn technology mitigates the difficulties that arise from the high frequencies. To validate the horns we have measured the pattern of a smooth-walled horn with a center frequency of 840 GHz with a vector network analyzer. With the same set-up, within the HIFI project we have done also measurements at a HIFI band 2 corrugated horn. To calculate the horn performance we use a 3D field simulation. This is a good check for the measurement results and helps to include machining tolerances into the calculation. We also used the simulation to compare the smooth-walled horn and the corrugated horn which are designed for different center frequencies.

II. Measurement

The complex beam patterns of the horn antenna were measured with a vector-network analyzer from *AB-Millimetre*

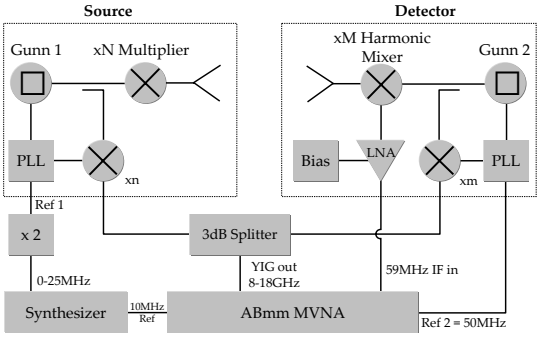

Fig. 2. *Measurement setup, the horn under test is mounted at the detector*

[7]. Coherent submm radiation is generated by a phase-locked Gunn oscillator using harmonic multiplication and transmitted to free space with a potter horn antenna. Although the horn radiates polarized radiation, a grid is used to be sure there is no radiation with the wrong polarization present at the horn under test. This is primarily important for the cross polarization measurement. The horn under test is feeding a harmonic Schottky diode mixer which is pumped by a second Gunn oscillator. This oscillator is phase-locked to the same reference signal as the first one (Fig. 2). A small frequency offset is maintained between the two oscillators which allows heterodyne detection of amplitude and phase with high dynamic range. The far-field distance $2D^2/\lambda$ of the horns under test is the largest in the case of the corrugated horn at 800 GHz with 80 mm. All measurements described in this paper were done at a distance between the source and the test horn of around 200 mm. The measurement test setup comprises a rotational stage where the feed horn under test is mounted with its phase center close to the rotation axis of the stage. Seen from the device under test the transmitter rotates on a spherical surface. This corresponds to the definition for the coordinate system of Ludwig 3 [8] as it is used in the next section for the 3D-simulation.

TABLE I
DESIGN PARAMETERS OF BOTH HORNS. A = APERTURE; F_r = FREQUENCY RANGE; F_c = CENTER FREQUENCY

smooth-walled horn			corrugated horn		
A [mm]	F_r [GHz]	F_c [GHz]	A [mm]	F_r [GHz]	F_c [GHz]
2.9	756-924	840	3.86	620-820	720

The single mode waveguide is tapered via a transition block towards the waveguide with different dimensions of the room temperature Schottky mixer. The signal source is mounted on a x-y-z-linear stage which allows to change the horn-to-horn distance with a relative accuracy of about a micron. To reduce the influence of standing-wave patterns, the signal source linear stage is moved 4 times about $\lambda/4$ towards the horn under test, with an angular sweep at each position. The retrieved amplitude and phase information then allows to correct for standing waves [9].

We have done measurements of the corrugated horn at 625,

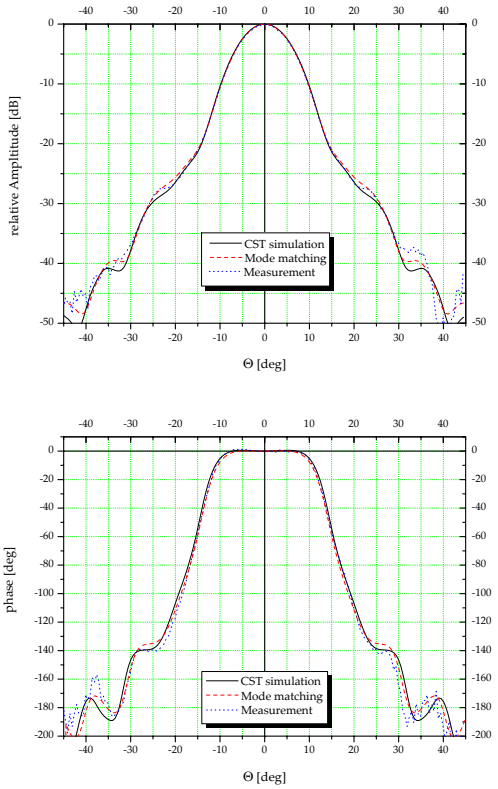

Fig. 3. *The simulation results and measured data are in excellent agreement, here in H-plane for 800 GHz at the smooth-walled horn*

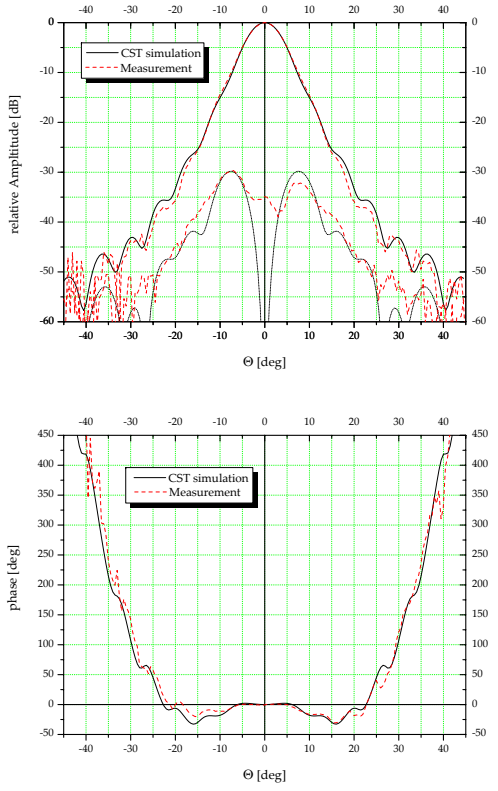

Fig. 4. *The data of the corrugated horn and the simulation match equally well, here in D-plane for 800 GHz*

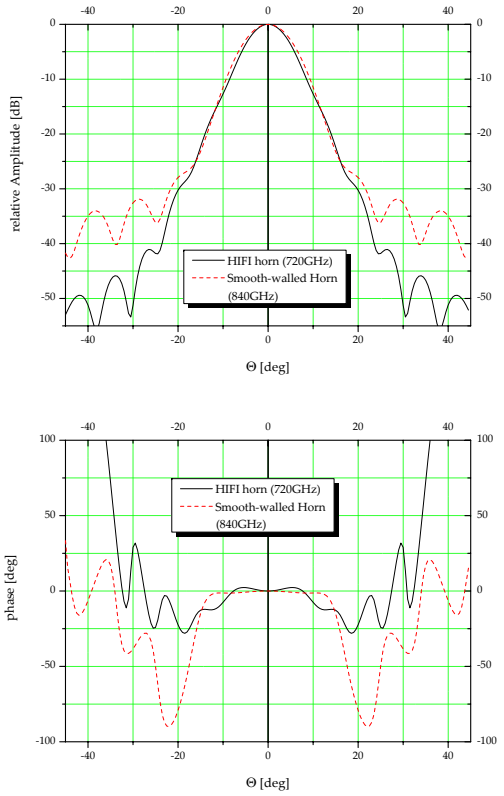

Fig. 5. *The data of the smooth-walled horn compared to the data of the corrugated HIFI horn in E-plane. Both at their respective center frequency.*

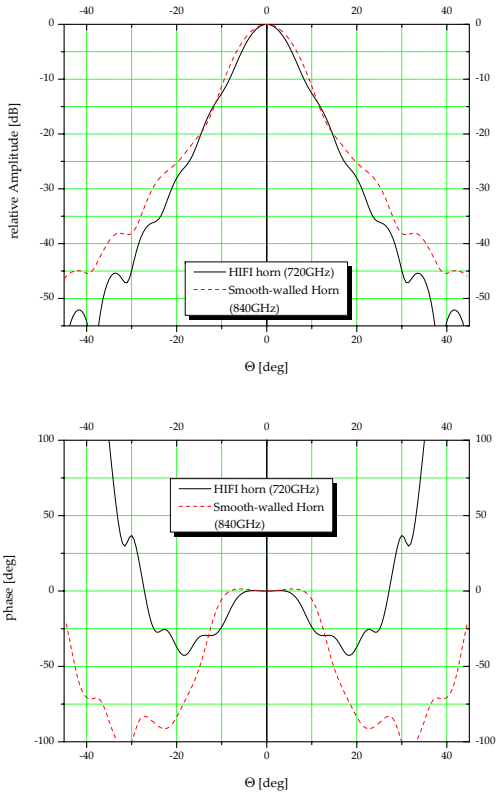

Fig. 6. *The data of the smooth-walled horn compared to the data of the corrugated HIFI horn in H-plane. Both at their respective center frequency.*

714 and 800 GHz. Near the band center ($F_C = 720$ GHz) at 714 GHz we have only measurements with a dynamic range of approx. 25 dB. The smooth-walled horn is tested at 800, 840 and 860 GHz. The range was limited by the frequency range of the source oscillator (795 - 860 GHz). For all measurements a Gunn with multipliers is used as a source. The design parameters of both horns are shown in table I. To measure E-, H- and D-plane the horn and the source (with grid) is rotated around the longitudinal axis by respectively 90 and 45 deg. Further detailes about the measurements of the smooth-walled horn are given in [10].

III. 3D Simulation

For the 3D simulation the transient solver of CST Microwave Studio is used. This is a time domain solver which calculates the development of fields through time at discrete locations and at discrete time samples. It calculates the transmission of energy between the exiting port and open space of the investigated structure. The far-field components are derived from the calculated fields inside the horn. The software makes the calculation of patterns for arbitrary frequencies in every plane possible. As already mentioned in section II the definition by Ludwig 3 is used to get the 1D data in E-, H- and D-plane. In this definition the vertical and horizontal

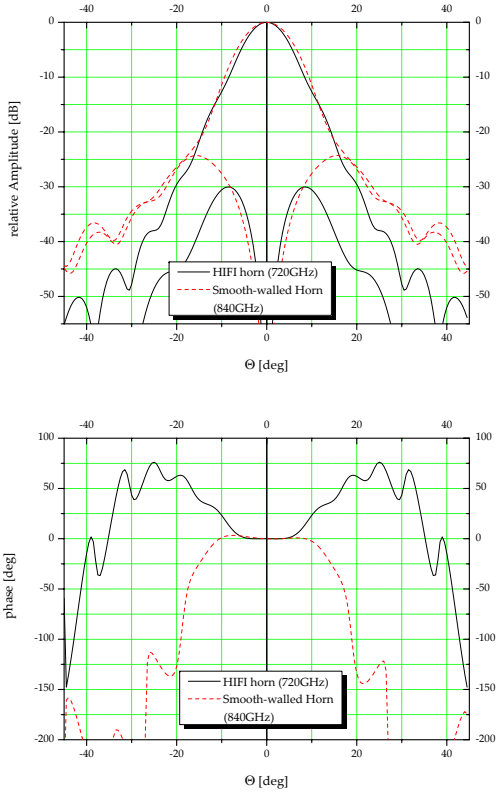

Fig. 7. *The data of the smooth-walled horn compared to the data of the corrugated HIFI horn in D-plane. Both at their respective center frequency.*

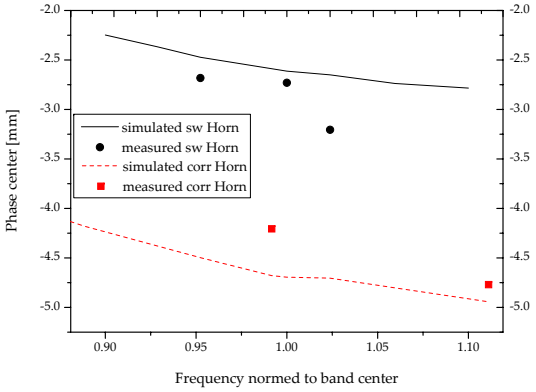

Fig. 8. *Distance of phase center to horn aperture*

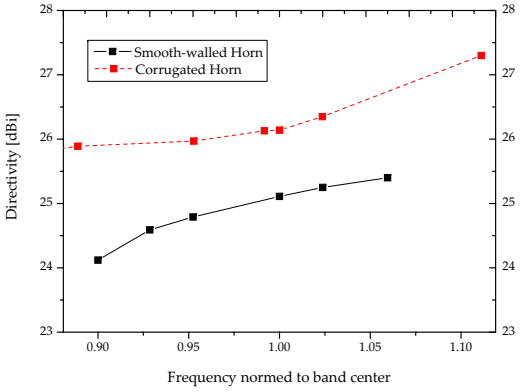

Fig. 10. *Directivity for both horns*

components are calculated as follows:

$$E_{horizontal} = E_\Theta \cos\phi - E_\phi \sin\phi \quad (1)$$

$$E_{vertical} = E_\Theta \sin\phi + E_\phi \cos\phi \quad (2)$$

The phase is calculated using the real (Re) and imaginary (Im) part of the signal measured at a certain position:

$$\angle E = \arctan\left(\frac{Im(E)}{Re(E)}\right) \quad (3)$$

An illustration of the coordinate system is shown in figure 9. In addition the 3D simulation gives us the field distribution inside the horn. An advantage to the mode matching method is the possibility to simulate fabricational imperfections like a burr. We have done it successful for interpretation of measurements within the HIFI project. A comparison of the simulation with measured data is done for 625 and 800 GHz at the corrugated horn and for 800, 840 and 860 GHz at the smooth-walled horn. The simulated data are in excellent

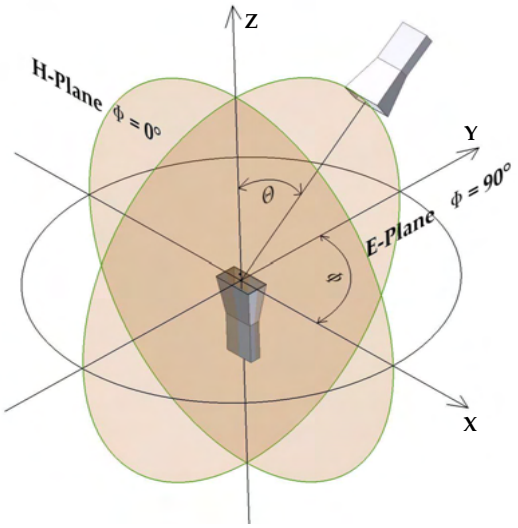

Fig. 9. *The Ludwig 3 coordinate system as it is used in the simulation with CST Microwave Studio. The coordinates are fixed with the horn under test.*

agreement with the measured data, examples are given in figure 3 and 4. For the smooth-walled horn we have additional results calculated with mode matching by C. Granet. These data correspond also well with the measurements.

Because the two horns have different center frequencies (see table I) a comparison of both horns is done with simulated data at the center frequencies (figure 5-7). The beam width of both horns is comparable, the side lobe level of the smooth-walled horn is at an angle of 40 deg approx. 10 dB higher than at the corrugated horn. Also the cross polarization level is higher (5 - 10 dB) at the smooth-walled horn. The main criterion for the phase is, that it is flat over an angle as large as possible, because this will simplify to design the optical components like mirrors etc.. This claim is satisfied by the smooth-walled horn very well. In addition, it is of advantage if the phase center lies in the same position over the frequency range. The phase center is calculated in Microwave Studio. It is used the phase of the phi or theta component of the electric field and the calculation is limited by an angle of 50 degrees around the main lobe. The phase center is calculated from phase values in E-Plane. To compare this data with the measurement, the measured phase is fitted to the simulated data by

$$\Delta\Phi = 2\pi\frac{\Delta z}{\lambda}(1 - \cos\Theta) \quad (4)$$

with the axial offset $\Delta z \ll z$ [11]. At the smooth-walled horn is the variation of the phase center position comparable with the corrugated horn. In figure 8 is shown, that the drift in the phase center is comparable for both horns. The plot shows also some measured points, of which the accuracy is limited by the mounting of the horns, that is not more exact than 1 mm. In addition the directivity (simulated in Microwave Studio) is evaluated. The directivity of an antenna is defined as the ratio of the radition intensity in a given direction from the antenna to the radiation intensity averaged over all directions. At this the radiation intensity is given by the power radiated per unit solid angle $P(\Theta, \phi)$ by the antenna divided by the

total radiated power P_{total}:

$$D(\Theta, \phi) = 4\pi \cdot \frac{P(\Theta, \phi)}{P_{total}} \quad (5)$$

The directivity (figure 10) for the smooth-walled horn is 1 to 1.5 dBi less than for the corrugated horn. This is a design parameter, therefore it is possible to optimize a smooth-walled horn for this requirement for a dedicated application.

IV. Conclusion

High quality phase and amplitude measurements of a HIFI Band 2 corrugated horn and a novel smooth-walled horn are presented. The data are compared to mode matching calculations and to full 3D electromagnetic simulations. Data and simulations are in excellent agreement. The 3D simulation is used to compare the smooth-walled horn and the corrugated horn. Their performance is comparable. The easier machining of the smooth-walled horn is bought at the expense of a little smaller directivity. The phase flatness is similar. Smooth-walled horns are a good choice to replace corrugated horns, especially for applications in the THz range; because they are much easier to manufacture with standard technique.

Acknowledgements

The authors would like to thank Christophe Granet for the design and mode matching calculations of the smooth-walled horn. In addition, we thank RPG for the production of the prototype. This research is supported by DLR under grant 50 OF 0001 2, Swiss National Science Foundation under grant PBBE2-200020-100167 and by the *Deutsche Forschungsgemeinschaft* through grant SFB 494.

References

[1] C. Granet, G. L. James, Fellow, R. Bolton and G. Moorey. *A Smooth-Walled Spline-Profile Horn as an Alternative to the Corrugated Horn for Wide Band Millimeter-Wave Applications.* IEEE Transations on Antennas and Propagation, 52(3):848854, 2004.

[2] RPG. *Radiometer Physics GmbH.* http://www.radiometer-physics.de.

[3] CST. *Computer Simulation Technology.* Microwave Studio 5.0, http://www.cst.com.

[4] GREAT. *German REceiver for Astronomy At Terahertz.* on SOFIA *Stratospheric Observatory For Infrared Astronomy*, http://www.sofia.usra.edu/Science/instruments/instruments_great.html.

[5] B. N. Ellison, M. L. Oldfield, D. N. Matheson, B. J. Maddison, Mann and C. M. Smith (1994): Internat. Seminar on Terahertz Electronics (Part II), Lille, France, June 13-14

[6] C. Walker and A. Lichtenberger. *A New Laser Micromachining System for the Fabrication of THz Waveguide and Quasi-Optical Components* Proceedings of the Eleventh International Symposium on Space THz Technology, May 2000

[7] P. Goy and M. Gross *Vector Transceiver for mmWAVE Antennas* 20th ESTEC Workshop on Millimetre Wave Antenna Technology and Antenna Measurements, 1997.

[8] A. C. Ludwig. *The Definition of Cross Polarization* IEEE Trans. Antennas Propagat. vol. AP-21, no. 1, pp. 116-119, January 1973.

[9] A. Murk and A. Magun. *Characterization of corrugated horn antennas for HIFI* 25th ESA Antenna Workshop on Satellite Antenna Technology, 2002.

[10] D. Rabanus, C. Granet, A. Murk and T. Tils. *Measurement of properties of a smooth-walled spline-profile feed horn around 840 GHz* Infrared Physics and Technology, to be published in 2005.

[11] C.A. Balanis. *Horn Antennas, Chapter 8 in* Antenna Handbook (Y.T. Lo and S.W. Lee, eds.) Van Nostand Reinold Co., New York, USA, 1988.

Transmission Measurements of Infrared Filters for Low-Noise Terahertz Receiver Applications

D. Loudkov, C.-Y. E. Tong, D. P. Marrone, S. Ryabchun, S. N. Paine, and R. Blundell

Abstract — **Infrared (IR) filters are very important to the efficient operation of cryogenic receivers. Usually, such filters are mounted on the radiation shield of the cryostat to reduce the heat load to the 4 K stage. Insufficient filtering may cause the temperature of the mixing element in a receiver to be excessively warm, leading to degradation in sensitivity. These filters should be effective in blocking the room temperature IR radiation from outside the cryostat, yet should be transparent across the desired signal frequency band. In the Terahertz frequency range, which is close to the infrared, it is difficult to find an inexpensive low-loss material that can provide the required IR blocking capacity.**

We present transmission measurements, made using a Fourier Transform Spectrometer (FTS), of a number of potential infrared filters between 0.4 and 1.6 THz. The filters tested include the widely-used, Teflon-based, Zitex-A and Zitex-G films, alkali halide based infrared filter, and crystalline quartz coated with Parylene, and polyethylene films.

***Index Terms*—Infrared filters, Zitex, LDPE, Crystalline quartz, Antireflection coating, Parylene.**

I. INTRODUCTION

HETERODYNE receivers for terahertz spectroscopy are showing noise performance close to the fundamental quantum noise limit [1, 2]. These low noise cryogenic receivers require infrared (IR) filters to reduce the thermal loading to the cryostat. Since terahertz mixers have generally higher conversion loss, any input losses introduced by the filter material will further increase the conversion loss of the front-end mixer and would cause substantial degradation to the receiver noise temperature. Therefore, it is important to find an inexpensive low-loss material that can provide the required IR blocking capability and yet transparent to terahertz radiation.

The double-side-band receiver noise temperatures of a 1.5 THz waveguide Hot Electron Bolometer (HEB) receiver are displayed for the cases when two different IR filters were used (Fig.1) [3]. With multi-layer Zitex (expanded Teflon) filter, we obtained higher noise temperature than a full-wave thick crystalline quartz slab. This demonstrates that the choice of low loss and IR filter is critical to the operation of terahertz receivers [4-7].

Transmission measurements were performed for various IR filters using a Fourier Transform Spectrometer (FTS). The samples were inserted in one arm of the Martin-Puplett interferometer which is placed in a vacuum chamber to eliminate the effects of atmospheric absorption [8]. Our set-up also allows us to cool the sample to perform measurements at cryogenic temperatures.

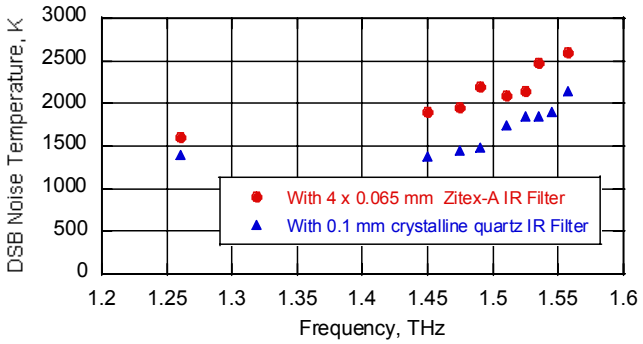

Fig. 1 Receiver noise temperature of a 1.5 THz HEB receiver using two different IR filters mounted on the 4.2 K cold plate [3]. Lower noise temperatures are obtained with the full-wave crystalline quartz filter, centered at around 1.45 THz, than the four layer Zitex-A filter.

II. DIELECTRIC FILM IR FILTERS

Infrared filters based on dielectric films, such as Teflon-based Zitex, are widely used in cryogenic terahertz receivers. We have tested two types of Zitex (type A and G). Zitex-A is a Teflon sheet perforated with pores that are generally bigger than 10 μm in diameter. Zitex-G is made of very fine sintered Teflon spheres, yielding pores that are generally smaller than 10 μm in diameter. Transmission measurements of 0.37 mm thick films are shown in Fig. 2. Clearly, the transmission Zitex- G film is substantially better above 0.6 THz.

Zitex films are useful as IR filters because the transmission of radiation in Teflon drops dramatically at frequencies above 5 THz [9]. However, since Zitex films are porous, a few layers are required to achieve reasonable IR blocking. This also leads

D. Loudkov is with the Moscow State Pedagogical University, Moscow, Russia, 119992 (e-mail: dloudkov@cfa.harvard.edu).

C.-Y. E. Tong is with the Harvard-Smithsonian Center for Astrophysics, Cambridge, MA 02138 (e-mail: etong@cfa.harvard.edu).

D. P. Marrone is with the Harvard-Smithsonian Center for Astrophysics, Cambridge, MA 02138 (e-mail: dmarrone@cfa.harvard.edu).

S. Ryabchun is with the Harvard-Smithsonian Center for Astrophysics, Cambridge, MA 02138 (e-mail: sergey_ryabchun@yahoo.co.uk).

S. N. Paine is with the Harvard-Smithsonian Center for Astrophysics, Cambridge, MA 02138 (e-mail: spaine@cfa.harvard.edu).

R. Blundell is with the Harvard-Smithsonian Center for Astrophysics, Cambridge, MA 02138 (e-mail: rblundell@cfa.harvard.edu).

to reduction in the signal transmission in the frequency band of interest. It is noted that if the transmission for a single layer is 95%, due to absorption loss, then the use of four layers will yield a transmission of 81%.

We have also made measurements on an IR filter made of polyethylene loaded with powdered alkali halide crystals [10]. Scattering of mid-IR radiation by powdered crystals is the basis of operation of this type of IR filter [11]. The sample is dark grey in color and its thickness is 0.42 mm. As shown in Fig. 3, the measured transmission coefficients do not show much dependence in temperature in the frequency range 0.4 – 1.6 THz. Based on these data, the estimated complex refractive index is $n = 1.61 + i0.003$. It should be noted that the sinusoidal frequency response of this filter may limit its applicability to wide-band low noise receivers at Terahertz frequencies. For narrow band operation, it is important to choose an appropriate thickness for the filter.

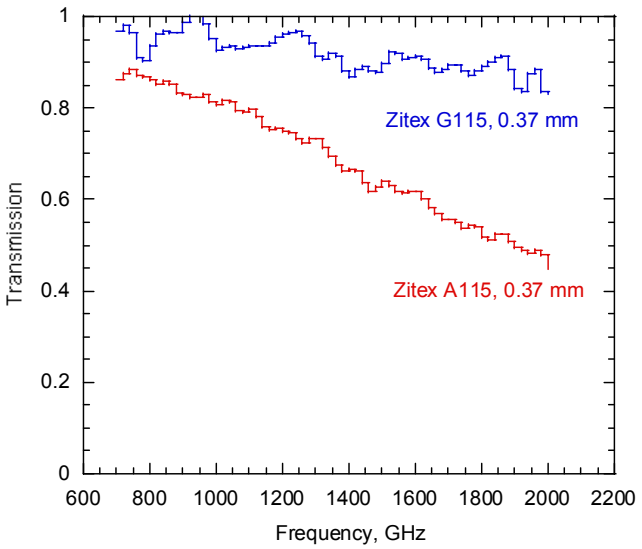

Fig. 2 Measured power transmission coefficients of Zitex-A115 and Zitex-G115 at 295 K.

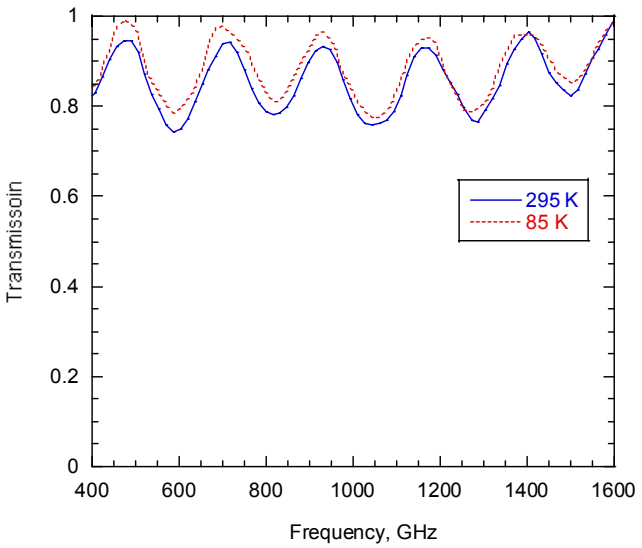

Fig. 3 Measured power transmission coefficient of the polyethylene loaded with alkali halide IR filter.

The measured transmission coefficient of a sheet of low density polyethylene (LDPE) film 0.47 mm thick at 295 K is shown in Fig. 4. The experimental data shows very good agreement with the theoretical complex index of $n = 1.51 + i0.002$. These results also agree with the reported properties of LDPE [6] and indicate the reliability of our measurements. LDPE is quite transparent to infrared radiation and it is not a candidate for a stand alone IR filter but as seen in the next section, it can be used as a matching layer for other materials.

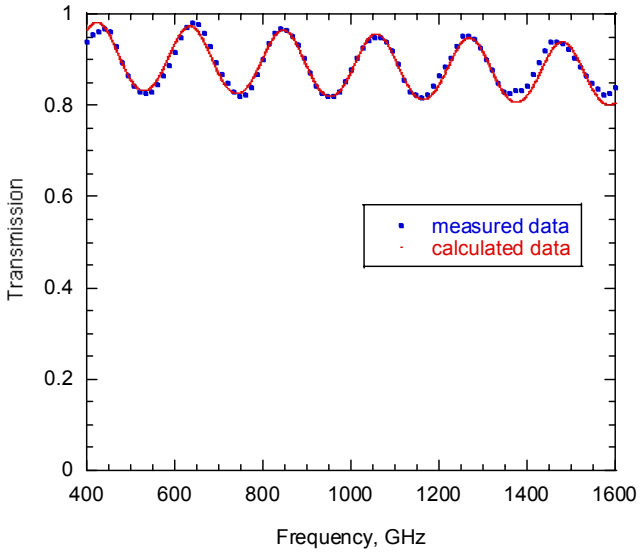

Fig. 4 Power transmission coefficient of a 0.47 mm thick LDPE sheet at 295 K.

III. Uncoated and Coated Crystalline Quartz

IR filters are usually placed inside a cryostat on the low temperature radiation shields for effective IR blocking. The filtering materials are therefore subjected to heating by either room temperature radiation or radiation originating from higher temperature stages. This may produce non-uniform temperature profile due to poor thermal conductivity. From this point of view, crystalline materials with much higher thermal conductivities, like quartz, are preferable.

Crystalline quartz is a very good IR filter candidate because it is essentially opaque to wavelengths around 10 μm, the peak of the black body radiation from ambient sources. As illustrated in Fig. 1, the use of a half-wave or full-wave slab of crystalline quartz allows for very good matching to the RF signal. However, such a thin piece of quartz (0.1 mm thick for a 1.5 THz full-wave plate) is very fragile. On the other hand, the use of a thick uncoated slab of crystalline quartz is not practical due to multiple internal reflections inside the quartz. The transmission coefficient of a 3.1 mm thick crystalline quartz slab is presented in Fig. 5. By fitting to the data, we obtained the complex index of $n = 2.1 + i0.0006$.

The standard ways of reducing reflection losses are surface grooving or application of an antireflection coating. The latter is chosen because it is fairly time consuming to mechanically create fine grooves. Two materials were tested as the coating

layer: Parylene and LDPE. Silicon lenses coated by Parylene have been previously reported and show good improvement over uncoated lenses [12, 13]. Parylene coating was applied by vapor deposition in a vacuum chamber. This procedure is generally performed by a specialized coating company. In contrast, coating by LDPE can be done in any laboratory by baking a sandwich of LDPE and quartz under pressure for several hours. Since quartz and LDPE have significantly different thermal contraction coefficients, the LDPE matching layer tends to peel off the quartz disk when cooled to low temperatures. In order to limit the strain caused by differential contraction, we have scored the LDPE matching layer with a dicing saw to produce an array of square patches (5 x 5 mm). These grooves allow the LDPE coated quartz disk to withstand thermal cycling.

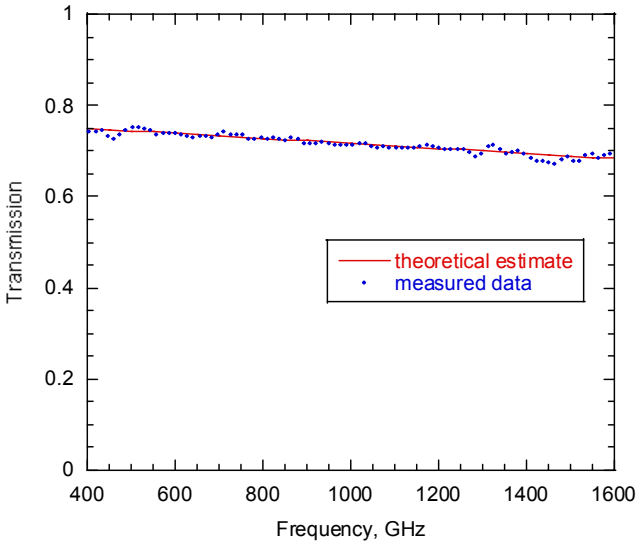

Fig. 5 Transmission coefficient of a 3.1 mm thick crystalline quartz slab.

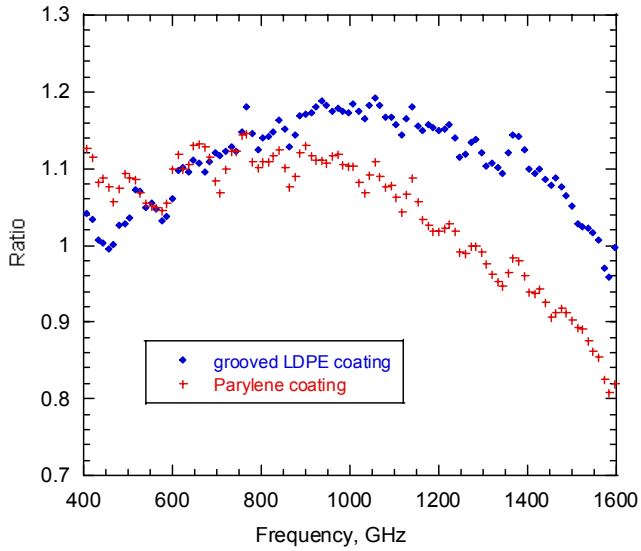

Fig. 6 Transmission ratio of an antireflection coated crystalline quartz window to an uncoated one. Two samples are presented with the Parylene coating and the grooved LDPE coating.

Using 3 mm thick crystalline quartz disks, we measured the transmission coefficients of crystalline quartz filters coated with Parylene and with LDPE. In Fig. 6, we plot the ratio of the measured transmission coefficients of the coated filter to uncoated one as a function of frequency. The two samples have slightly different center frequency of operation because of the thicknesses of the matching layer. The LDPE coating clearly provides better signal coupling. However, we have observed small variations in the optical properties of the LDPE films from different batches.

The transmission of the quartz window with grooved LDPE coating on both sides is presented in Fig. 7. The thickness of the coating was 0.13 mm and the thickness of the quartz disk was 2.9 mm. The complex refractive index was estimated by the fitting the calculated data to the measured data. The best correlation of the theoretical calculations and measured data was achieved for the refractive indices of $n = 1.5 + i\,0.002$ and $n = 2.1 + i0.0003$ for the polyethylene and quartz respectively. This corresponds to a loss tangent of 2.6×10^{-3} for LDPE. These losses are higher then that reported in [6], possibly due to the grooves and changes in the LDPE density during coating process.

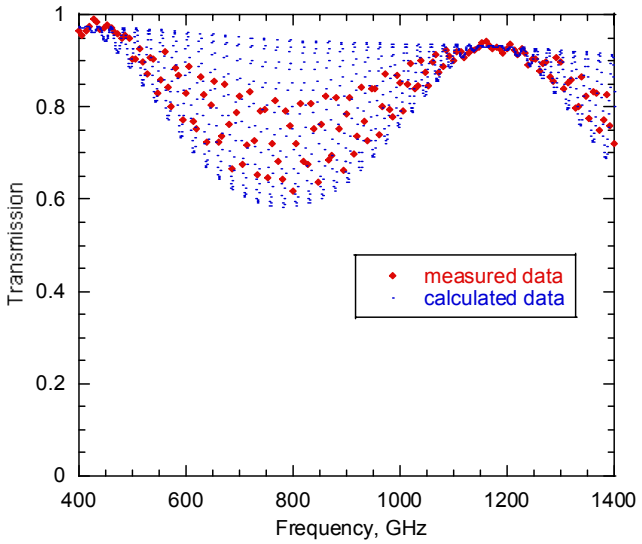

Fig. 7 Transmission of the crystalline quartz window coated with grooved LDPE film.

Calculated and measured transmissions of the quartz window with Parylene antireflection coating are shown in Fig. 8. The crystalline quartz slab was 3.1 mm thick and the Parylene film was 0.14 mm thick. The estimated refractive index of Parylene are $n = 1.62 + i\,0.025$ and $n = 2.1 + i0.0003$. This gives a loss tangent of 3×10^{-2}. Clearly, LDPE is a lower loss material in this frequency range.

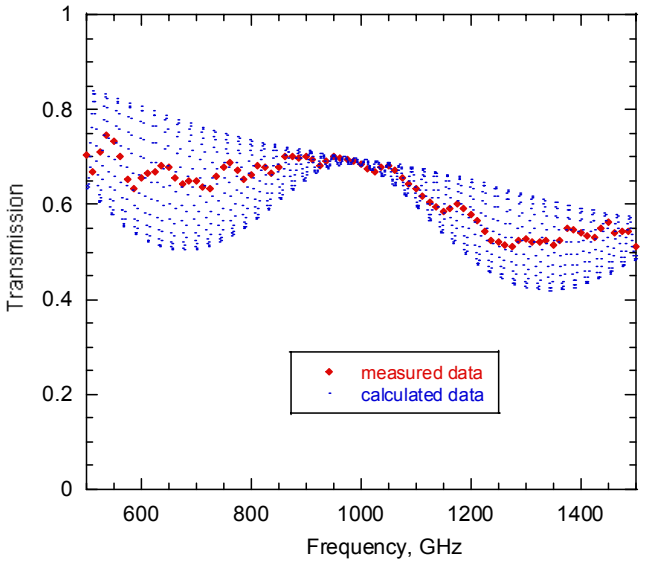

Fig. 8 Transmission of the crystalline quartz window coated with Parylene film.

IV. Summary

We have conducted investigations based on FTS measurements of the optical properties of different materials. Investigations of Teflon based IR filters show that G-type Zitex has lower losses than Zitex-A above 0.6 THz.

The FTS transmission measurements also show that the performance of a crystalline quartz IR filter with grooved low density polyethylene coating is better than one with Parylene coating. The estimated loss tangent is 3×10^{-2} for Parylene and 2.6×10^{-3} for LDPE in covered frequency range. The calculated data shows good overlap with measured one.

The crystalline quartz IR filter with grooved LDPE antireflection coating may be a good alternative to the widely used multilayer Zitex filters. However variations in the refractive index of LDPE must be considered in the matching layer design.

References

[1] B.D. Jackson and T.M. Klapwijk, "The current status of low-noise THz mixers based on SIS junctions", *EUCAS 2001*, *Physica C*, 372-376 (2002) 368-373.

[2] G.Gol'tsman, D.Loudkov, "Terahertz Superconducting Hot-Electron Bolometer Mixers and Their Application in Radio Astronomy", *Radiophysics and Quantum Electronics*, v. 46, Issue 8, 2003, p. 604.

[3] C.-Y. E. Tong, D. Meledin, D. Loudkov, R. Blundell, N. Erickson, J. Kawamura, I. Mehdi, and G. Gol'tsman, "A 1.5 THz Hot-Electron Bolometer Mixer Operated by a Planar Diode Based Local Oscillator", *2003 IEEE MTT-S Digest*, 2003.

[4] D.J. Benford, J.W. Kooi & E. Serabyn, "Spectroscopic Measurements of Optical Materials Around One Terahertz," 1998, *Proc. 9th International Symposium on Space Terahertz Technology*, p.405, Pasadena, 1998.

[5] D.J. Benford, M.C. Gaidis, J.W. Kooi, "Transmission properties of Zitex in the infrared to submillimeter," *Proc. 10th International Symposium on Space Terahertz Technology*, p. 405, Charlottesville, 1999.

[6] James W. Lamb "Miscellaneous data on materials for millimetere and submillimetre optics," *Int. J. of Infrared and Millimeter Waves*, p. 1997, Vol. 17, No. 12, 1996.

[7] C.-Y. E. Tong, J. Kawamura, T. Hunter, D.C. Papa, R. Blundell, M. Smith, F. Patt, G. Gol'tsman and E. Gershenzon, "Successful operation of 1 Thz NbN hot-electron boblometer receiver," *Proc. of 11th Int. Symp. on Space Terahertz Tech.,* p. 49, Ann Arbor, Michigan, May 2000.J.

[8] Kawamura, S. Paine, D.C. Papa, "Spectroscopic measurements of optical elements for submillimeter receivers," *Proc. 7th Int. Symp. Space THz Tech.*, pp. 349-355, Univ. Virginia, Charlottesville, VA, Mar. 1996.

[9] D. Loudkov, P. Khosropanah, S. Cherednichenko, A. Adam, H. Merkel, E. Kollberg, G. Gol'tsman "Broadband Fourier Transform Spectrometer (FTS) Measurements of Planar Antennas at THz Frequencies", *Proc. of the 13th International Symposium on Space Terahertz Technology*, Cambridge, p. 373, MA, USA, Mar 2002.

[10] supplied by QMC Instruments, U.K.

[11] Y. Yamada, A. Mitsuishi, and H. Yoshinaga, *J. Opt. Soc. Am.,* **52**, 17 (1962) or E.V. Loewensten, and D.R. Smith, "Far Infrared," *American Institute of Physics Handbook, 3rd Edition,* pp. 6-277, McGraw-Hill, 1982.

[12] M. Kroug, S. Cherednichenko, E. Choumas, H. Merkel, E. Kollberg, , H.-W. Hubers, H. Richter, D. Loudkov, G. Gol'tsman, B. Voronov, "HEB Quasioptical Heterodyne Receiver for Terahertz frequencies," *Proc. of the 12th, International Symposium on Space Terahertz Technology*, San-Diego, CA, Feb 2001, p. 244

[13] M. Ji, S. Yngvesson, A.J. Gatesman, and J. Waldman, "Study of Parylene as anti-reflection coating for silicon optics at THz frequencies," *Proc. of 11th Int. Symp. on Space Terahertz Tech*., p. 21, Ann Arbor, Michigan, May 2000

Optimization of sub-100 nm InP HEMT technology

Jan Grahn, Malin Fridman, Mikael Malmkvist, and Anders Mellberg

Chalmers University of Technology, MC2, Microwave Electronics Laboratory,
SE-412 96, Göteborg, Sweden

Introduction

At high mm-wave frequencies, the InP HEMT amplifier technology provides the lowest noise and highest power. The technology is critical both for ground-based ultra-low noise receivers (IF amplifiers in radio astronomy) and in several scientific missions probing outer space. The InP HEMT technology, however, is not wide-spread and detailed data on device performance are scare, in particular for scaled HEMT devices below 100 nm. We here report results from a 50/70 nm InP HEMT technology.

Results

An InP pseudomorphic HEMT technology with 70 nm gate length has been developed. The epitaxial HEMT structure was grown using an in-house InGaAs-InAlAs-InP MBE. Dc and rf performance as a function of epitaxial parameters has been studied, in particular gate-to-channel distance. This has resulted in devices with f_{max} > 400 GHz and g_m > 1500 mS/mm, see Fig. 1 for g_m(Vg) as a function of gate-to-channel distance. The extrinsic cut-off frequency f_T was 180 GHz..

Dedicated modeling and experimental studies for the InP HEMT process have also been performed for thin-film TaN resistors, dry etching of via holes and MIM capacitance models. MMIC demonstrators have been fabricated in a microstrip process using 50 nm InP HEMTs. See Fig. 2 for a photograph of a one-stage broadband feedback amplifier exhibiting a gain of more than 8 dB from 0 to 42 GHz.

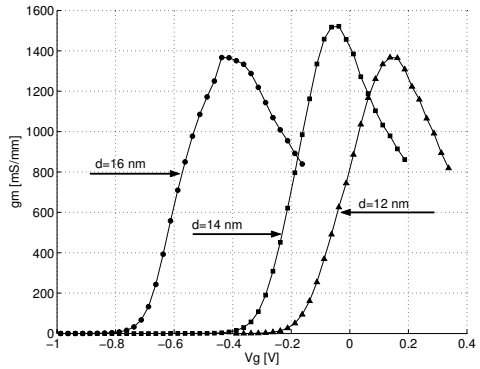

Fig. 1. Transconductance vs. gate voltage for V_{ds}=1.5 V.

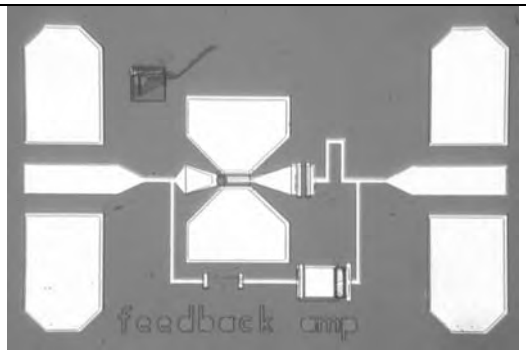

Fig. 2. A MMIC broadband amplifier based on 50 nm InP HEMT technology.

The Development of Rectangular Aperture Dichroic Plate Filters for Sharp Image Rejection in Heterodyne Receivers

B. Alderman, G. Kergonou, B. N. Ellison, and P. G. Huggard

Millimetre Wave Technology Group
Rutherford Appleton Laboratory
Chilton,
OX11 0QX, UK

Email: B.E.J.Alderman@rl.ac.uk

We report on the development of a new fabrication technique for the formation of an electrically thick array of rectangular apertures in a metal plate. Theoretical and experimental results are compared to good agreement. As image rejection filters, these structures demonstrate improved performance compared with previously used circular aperture arrays. Furthermore, the ability to form rectangular apertures increased the number of degrees of freedom in the design, allowing the filter to accommodate wide-angle reflection whilst retaining sharp sideband rejection. This technique has been used to realise filters working in the range from 500 GHz to 1.8 THz.

Drilling an array of circular holes in a thick metallic substrate is usually used to form these filters. This technique is readily available for devices operating at wavelengths of order 1 mm, but becomes more difficult at terahertz frequencies as the dimension of the hole reduces and the number of holes typically increases. To make our filters, slots are cut in a resin layer, which has been deposited on a metal substrate. Electroplating is used to fill the slots and the filter is then detached and the resin removed.

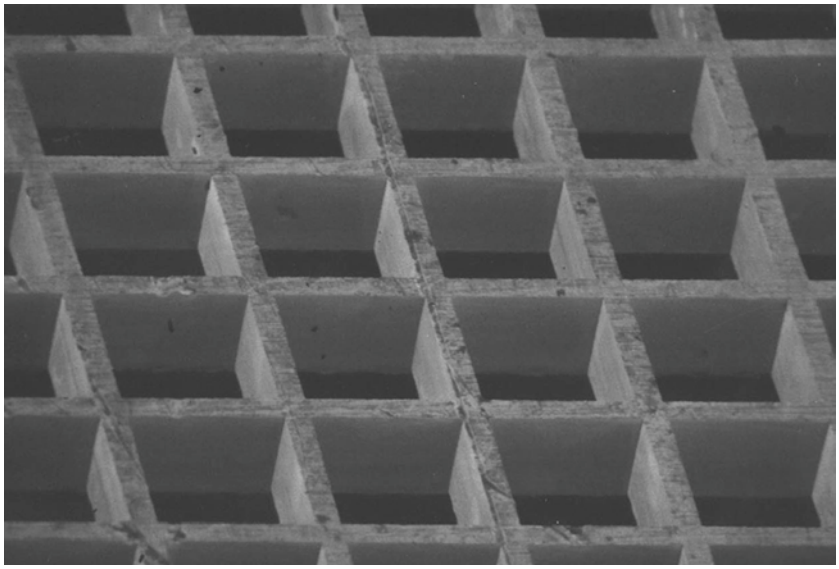

Fig.1: Square aperture dichroic filter for 500 GHz. The holes measure 430 x 430 μm^2

Low Loss THz Window

Armin Wagner-Gentner, K. Jacobs, U.U. Graf, and D. Rabanus
KOSMA, 1.Physikalisches Institut
University of Cologne, Germany
Email: wagner@ph1.uni-koeln.de

***Abstract*— This paper presents a method how to manufacture a low loss window applicable for THz frequencies. The window is made out of high resistivity silicon ($3k\Omega cm$, $n = 3.42$ and $\alpha = 0.1/cm$). Reflective loss due to the impedance mismatch between the substrate and free space is overcome by etching (Bosch-process) rectangular grooves of depth $\lambda/4$ into the substrate as an antireflection (AR) layer. Simulation of the AR-layer was done by using a transmission line analogue and the *Scatter*-program written by R. Padman. FTS measurements yield a transmittance greater than 96% at 2.1 THz and a bandwitdh of 400 GHz (1.9-2.3THz) with 90% transmission.**

I. Introduction

In the THz range, standard polymer windows (e.g. HDPE, Mylar) have high absorption. Conversely, substrates transmitting THz radiation (e.g. quartz, silicon, germanium) have extremely high dielectric constants. For these materials, AR-coatings are needed to minimize reflection losses. This can be done by coating both window surfaces with a material of thickness $\lambda/4$ and refractive index $n_{AR} = \sqrt{n}$. Coatings with the required dielectric constants are very rare. Unfortunately, most of them have poor transparency in the THz frequency range (e.g. PE, Parylene, Teflon) leading to high absorption losses. Precisely manufactured HDPE windows are only slightly worse than a Parylene coated silicon window (for example) in the THz range (1). In addition, AR-coatings are not always easily applicable to the window substrate. Especially in the case of cryogenic temperatures, glued or sintered materials may peal off under temperature cycling. Fig. 1 gives an overview of appropriate THz window designs.

A second method to match the impedance of the window material to free space is to design artificial dielectrics with a refractive index of $\sqrt{n}$ by cutting a well defined topology of $\lambda/4$ depth into the substrate. The generated dielectric constant is a function of the filling factor and can be calculated. Theories for 1D structures like rectangular-, multistep-, triangular- and sin-wave-grooves [1][2] and 2D structures like rectangles and holes [3]. are known. For wavelengths up to 400 GHz, grooved HDPE can be fabricated with common manufacturing techniques such as CNC milling. However, the needed sub-wavelength structures of about 6 microns at 1.9 THz are quite difficult to manufacture conventionally.

Rectangular grooves were manufactured into high resistivity silicon by using the Bosch-process to keep the fabrication process simple and to get high transmission at THz frequencies.

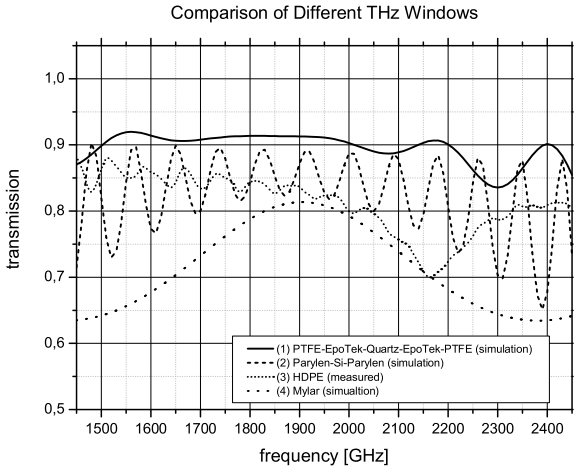

Fig. 1. (1) Theoretical transmission of PTFE glued on z-cut crystal quartz: $25\mu m$ PTFE, $5\mu m$ Epo-Tek-301, $500\mu m$ quartz, $5\mu m$ Epo-Tek-301 and $25\mu m$ PTFE. (2) Calculation for Parylene coated silicon: $24.38\mu m$ Parylene, $527\mu m$ silicon and $24.38\mu m$ Parylene. (3) Measured (FTS - Bruker) transmsission of $1.29mm$ HDPE. (4) Simulated data of $90\mu m$ Mylar.

II. Theory

Theories to calculate 1D or 2D AR-structures are given by [1][2] and [3]. In both cases, the topology models the dielectric constant of the substrate, thus artificial dielectrics can be designed. It should be noted, that 1D structures are polarisation dependent and birefringent [4], whereas 2D structures are not.

Raguin et al. [1] developed the 2nd order effective medium theory (EMT), which allows the calculation of the dielectric constant of rectangular grooves as a function of the filling factor $f = b/p$ (see Fig. 2). The groove geometry is defined as shown in Fig. 3.

The groove depth d equals a quarter wavelength of the incident wave (λ_0) in the window material:

$$d = \frac{\lambda_0}{4\sqrt{n_s}} \tag{1}$$

The grating equation sets an upper bound on the period-to-wavelength ratio, since the 2nd order EMT is only valid as long as only the zeroth diffraction order propagates:

$$\frac{p}{\lambda_0} \leq \frac{1}{\beta(n_s + n_i)} \tag{2}$$

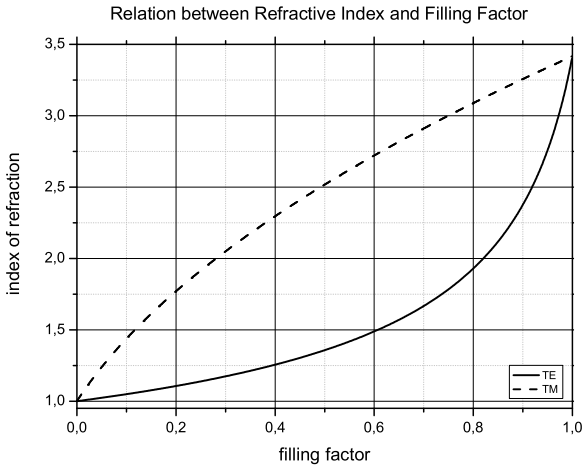

Fig. 2. Dependency between the filling factor and the resulting refractive index for an incident TE and TM wave. For calculation of $n(f)$ see [1]

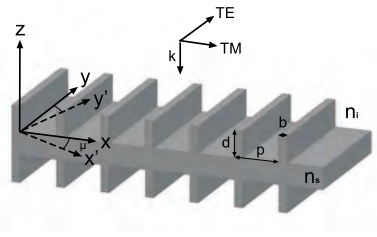

Fig. 3. Rectangular grooves as an example of a polarization dependent 1D-structure matching the impedance of the substrate with refractive index n_s to free space (n_i). Groove pitch p, depth d and tooth width b. The incident wave propagates in k-direction with rotation angle μ with respect to the groove pitch vector.

The design constant β, describes how much smaller the ratio p/λ_0 is than the critical value $1/(n_s + n_i)$. For ease of manufacturing β should be close to unity. Values of β less than unity allow the propagation of higher diffraction orders, hence 2nd order EMT fails.

III. Simulation

Simulation of the artificial dielectric is possible by using a simple transmission line analogue (Fig. 4), as long as $\beta \geq 1$ for any wavelength in a given frequency range, angle $\mu = 0°$ and the k-vector is perpendicular to the surface.

The transmission line method can not be properly used when β drops below 1 in the analyzed frequency band, because higher-order diffraction waves start to propagate. In this case the transmissivity should be calculated by solving Maxwell's Equations. Here, the FORTRAN-Code *Scatter*, written by R.

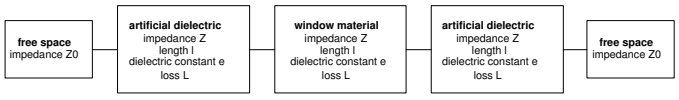

Fig. 4. Transmission line

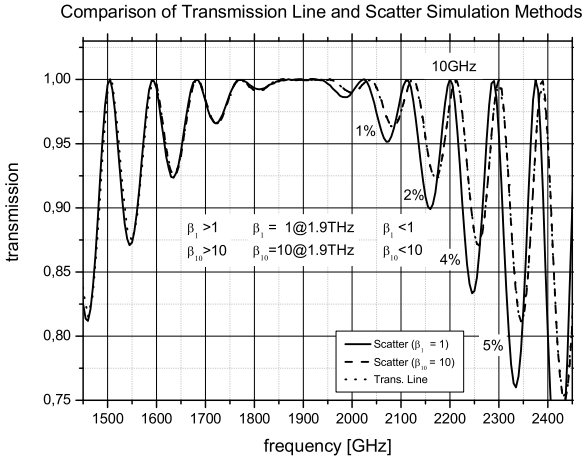

Fig. 5. Simulation of a grooved silicon ($n = 3.42$) window. Design frequency 1.9THz ($\lambda_0 = 158\mu m$). *Scatter*: $\beta_1 = 1$, i.e $p = 35.5\mu m$, $b = 6.5\mu m$ and $d = 21\mu m$ and $\beta_{10} = 10$, i.e. $p = 3.6\mu m$, $b = 0.8\mu m$ and $d = 21\mu m$. The maximum error using the transmission line analogue is only 2% within the band pass of 90% transmission.

Padman [5], is used. But a comparison of both simulation methods for a 1.9THz window shows, that the error introduced by the transmission line model is small for $\beta < 1$. At 2.075THz the error is only 1%, accompanied by a 10GHz frequency shift of the extremum (see Fig. 5). The error is a consequence of Eq. 2, since for the given period-to-wavelength ratio at 1.9THz, β drops under unity for frequencies greater than 1.9THz. At 2.075THz β decreases to ≈ 0.93. Identical simulation results are achievable if (for example) $\beta \geq 10$ at the design frequency.

The *Scatter* program also allows the computation of the transmission for different angles, μ. But as can be seen in Fig. 6, the groove orientation with respect to the E-field vector is not critical. Misalignment of $5°$ yields 3% loss only.

Much more critical is the groove depth. Taking Eq. 1 into account, one can see that the frequency of maximum transmission at a design frequency of 1.9THz is shifted by ≈ 80GHz per μm depth variation.

IV. Design constraints

The KOSMA single pixel 1.9THz heterodyne HEB-receiver channel on GREAT, operated on the SOFIA airborne observatory, needs a low loss THz window, because observation time on the stratospheric telescope is expensive. Loss from the cryostat window should be as low as possible, no more than 10%. Due to safety reasons the window must support a pressure load of 3.5bar with a clear aperture of 25mm.

V. Measurements

First, a stress analysis of a fixed mounted $527\mu m$ thick silicon wafer under a pressure load of 3.5bar at a clear aperture of 25mm was made. A subsequent single burst test approved

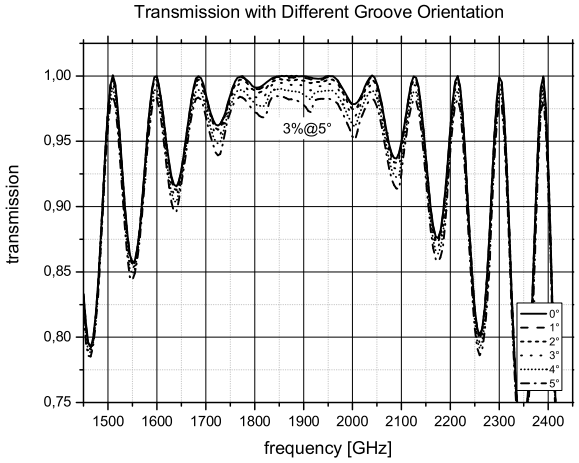

Fig. 6. Loss due to misalignment of the grooves with respect to the polarization vector of the incident wave (3% loss for 5° only!). *Scatter* simulation data with $\beta_1 = 1$, i.e $p = 35.5\mu m$, $b = 6.5\mu m$ and $d = 21\mu m$.

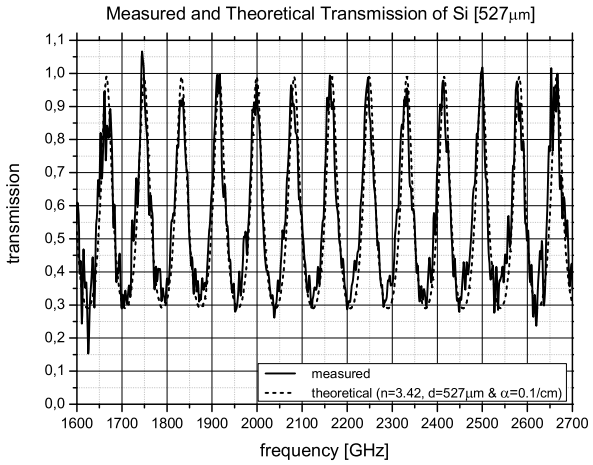

Fig. 7. FTS measurements yield a refractive index of $n = 3.42$ and an absorption of $0.1/cm$ for $3k\Omega cm$ silicon.

the preceding calculations and yielded a possible pressure load greater than 4bar.

In a next step, the refractive index and the absorption of high resistivity silicon was measured by using a Bruker FTS (see Fig. 7). The values obtained for the refractive index and absorption are $n_s = 3.42$ and $\alpha = 0.1/cm$, appropriate for the manufacture of a 1.9THz window with up to 98% transmittance, when reflective loss is minimized by a lossless AR-layer.

Based on the theory [1] a rectangular groove AR-structure for high resistivity silicon was calculated ($\beta = 1$ at 1.9THz: $p = 35.5\mu m$, $b = 6.5\mu m$ and $d = 21\mu m$). The transmission was simulated with the *Scatter* program. Then, the grooves were dry-etched by using the Bosch-process. The dry reactive

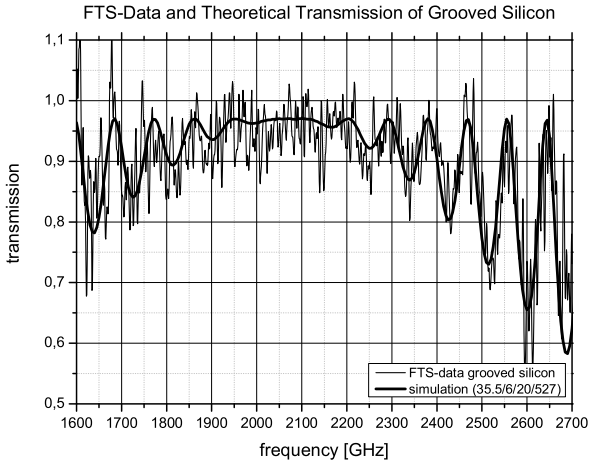

Fig. 8. Measured FTS data of our first dry-etched silicon cryostat window for THz-frequencies. Theoretically predicted transmission for a structure of b = 6m, p = 35.5m and d = 20m on 527m thick silicon is overlaid.

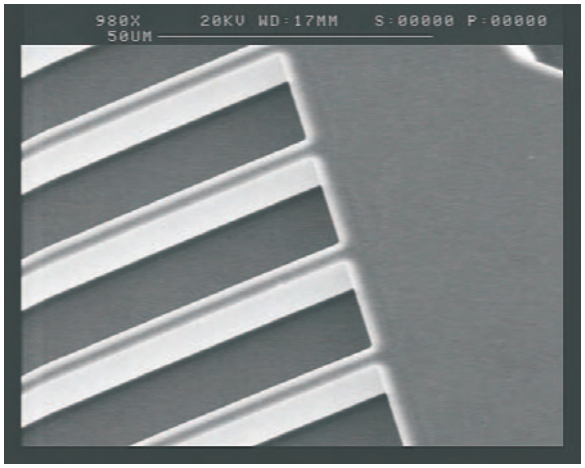

Fig. 9. SEM picture of our first low loss THz window. The rectangular groove AR-structure can be seen.

ion etching process ensured the accuracy needed for the structure ($< 1\mu m$ for all dimensions) and kept the fabrication process simple. Fig. 8 shows fitted data ($p = 35.5\mu m$, $b = 6\mu m$ and $d = 20\mu m$) together with measured FTS data of our first device. As can be seen, maximum transmittance of more than 96% could be achieved. The 90% transmission bandwidth was found to be 400GHz. An SEM image of the etched grooves is shown by Fig. 9.

VI. Conclusion

Rectangular grooves, working as an AR-coating, were manufactured into high resistivity silicon ($3k\Omega cm$, $n = 3.42$ and $\alpha = 0.1/cm$). Silicon was used to keep the fabrication process simple (Bosch-process) and to get high transmission at THz frequencies. The topology was simulated by using a transmission line analogue and R. Padmans *Scatter* program. Theoretical predictions and FTS measurements of our

first 1.9THz device are shown in Fig. 8. As can be seen, transmittance was found to be more than 96% at 2.1THz and the bandwidth within 90% transmission was 400GHz (1.9-2.3THz). The band pass shift to higher frequencies is a consequence of the etched groove depth, which is difficult to control. In addition, the etched tooth width b is a little bit smaller than calculated ($6\mu m$ instead of $6.5\mu m$), leading to a slightly different filling factor, hence to a smaller refractive index n_{AR} as needed for a perfect matching layer.

The mechanical design constraints, clear aperture of 25mm under a pressure load of 3.5bar, are satisfied. The result of a single burst test yields a possible pressure load greater than 4bar.

ACKNOWLEDGMENT

This work is supported by the *Deutsche Forschungsgemeinschaft* through grant SFB 494, and by the ministry of science of the state Nordrhein-Westfalen.

REFERENCES

[1] D. Raguin and G. Morris, "Analysis of antireflection-structured surfaces with continous one-dimensional surface profiles," *Applied Optics*, vol. 32, no. 14, pp. 2581–2598, 1993.

[2] ——, "Antireflection structured surfaces for the infrared spectral region," *Applied Optics*, vol. 32, no. 7, pp. 1154–1167, 1993.

[3] S. Biber, J. Richter, S. Martius, and L. Schmidt, "Design of artificial dielectrics for anti-reflection-coatings," European Microwave Week. Munich, 2003.

[4] D. Mawet, J. Baudrand, C. Lenaerts, V. Moreau, P. Riaud, D. Rouan, and J. Surdej, "Birefringent achromatic phase shifters for nulling interferometry and phase coronagraphy," in *ESA SP-539: Earths: DARWIN/TPF and the Search for Extrasolar Terrestrial Planets*, 2003.

[5] R. Padman, *Program SCATTER - A Program for the Calcualtion of Plane-Wave Propagation in a Stratified Anisotropic Dielectric*, CSIRO Division of Radiophysics Internal Report RPP 2031(L), December 1976.

[6] C. Englert, M. Birk, and H. Maurer, "Antireflection coated, wedged, single-crystal silicon aircraft window for the far-infrared," *IEEE Transactions on Geoscience and Remote Sensing*, vol. 37, no. 4, pp. 1997–2003, 1999.

[7] H.-W. Hübers, J. Schubert, A. Krabbe, M. Birk, G. Wagner, A. Semenov, G. Gol'tsman, B. Voronov, and E. Gershenzon, "Parylene anti-reflection coating of a quasi-optical hot-electron-bolometric mixer at terahertz frequencies," *Infrared Physics and Technology*, vol. 42, pp. 41–47, 2001.

[8] M. Ji, C. Musante, S. Yngvesson, A. Gatesman, and J. Waldman, "Study of parylene as anti-reflection coating for silicon optics at THz frequencies." Proc. of the 11th Int. Symp. of Space THz Technol., 2000.

[9] R. Padman, *Program SCATTER for the Analysis of Dielectric Matching Layer*, National Radio Astronomy Observatory Charlottesville, Virginia, Electronic Division Technical Note No. 155, 1989.

Passive Polarization-Sensitive Outdoor MMW Imaging

Leonid V. Volkov, Alexander I. Voronko, Natalie L. Volkova
Secomtech Ltd., 24/2, 125, Prospect Mira, Fryazino,
Moscow region, 141196, Russia, (E-mail: leon_volkov@mail.ru)

Quasi-optical systems operating at millimeter wave and terahertz radiation spectral ranges due to penetrative properties of the radiation are able to provide essential information on observable objects when visual and infrared imaging systems are not effective [1-2]. Both passive and active MMW/THz imaging systems have demonstrated their ability to detect objects beneath individual clothes in surveillance indoor applications. Thereby passive systems are essentially effective for imaging outdoor scenes [3] which exhibit enough brightness temperature contrast for system operation.

Fig.1

In this paper possibilities of polarization-sensitive passive quasioptical imaging of complicated outdoor scenes under various environmental condition are experimentally investigated. For the goal a multifunctional experimental imaging system has been developed (Fig.1). In the system a polysterene lens with diameter 60 cm and focal length 1 m is used as a focusing lens. Mechanically scanning precise positioner being under computer control provides oversampled imaging with factor 16x for 94 GHz radiation. Radiometer receiver is microprocessor-controllable unit with stabilization of internal temperature for providing stable long–time action. Its operating frequency is 94 GHz, temperature sensitivity is less then 0.1 K /s. Sample time per pixel is changeable by computer program (from 0.1 s to 5 s and more). The input horn antenna of the receiver is supplied with polarization grid exhibiting cross-polarized component transmisivity less then 10^{-2}. (Radiometric receivers for 140 GHz and 220 GHz are currently under development). The system is provided with computer controllable mechanical unit for rotating the receiver around the optical axes with accuracy 0.5^0 for polarization imaging and shifting one along the optical axes with accuracy 0.5 mm for sharp focusing. Imaging system possibilities have allowed to reveal peculiarities of MMW polarization imaging. Particularly it was shown that metallic-like objects may be better detected within terrain by means of analysis of its polarization-distinct images (or images consisting of coherence matrix elements).

References.

1.A Luukanen,V.-P. Viitanen, SPIE Conf on Passive MMW Imaging Technology, 1998, V.3378, pp.36-44.
2. L. V. Volkov, A.I.Voronko, etc., Radioengineering (Russia), N8, 2003, pp.67-80.
3. R. M. Smith, etc., Microwave Journal, March 1996, pp.22-32.

Session 6:

Sources II

Tuesday May 3, 8:30-10:25
Chairman: Jan Stake

Submillimeter Wave Sources and Receivers; Creating a Practical Technology Base

Jeffrey Hesler, Thomas Crowe, Dave Porterfield and William Bishop

Virginia Diodes Inc.
Charlottesville, VA 22902
www.vadiodes.com

To meet the requirements of new generations of scientific projects, there is a need for broadband, compact, rugged and reproducible sources and receivers at submillimeter wavelengths. For example, the Atacama Large Millimeter Wave Array (ALMA) requires electronically tunable sources covering the range 100 GHz to 1000 GHz with individual bandwidths of up to 25%. As another example, CoSSIR, an instrument developed at Goddard Space Flight Center to measure cirrus-cloud and water vapor profiles, has a need for ultra-compact rugged receivers up to 870 GHz. This talk will discuss the development of sources and receivers applicable to these and other projects. The ultimate goal of this research is to create a technology base that expands the use of the terahertz spectrum to more routine but equally important scientific and military measurements, and in the longer term to enable a wide range of commercial applications.

A series of full-waveguide band tunerless multipliers, including doublers, triplers and quintuplers, have been developed at frequencies up to 1.7 THz. These multipliers use no bias, and have a very simple construction, thus making them amenable to construction in large quantities. For example, the WR-2.8X3 broadband tripler, used for ALMA band 7 (LO range 282-366 GHz), covers the entire band 265-400 GHz with typical efficiency of about 3.5%. A quantity of 139 WR-2.8X3 triplers, as well as an additional 139 WR-3.4X3 Band 6 triplers, were built and fully tested in the course of about 4 months. The multipliers were found to be extremely consistent, in terms of both conversion efficiency and input return loss. With the Band 6 and 7 triplers completed, work is now underway on the development of multipliers for other bands, which will be discussed further at the conference.

A range of broadband room temperature receivers have been developed with RF bands from WR-8 (90-140 GHz) to WR-1.2 (600-900 GHz). These receivers use subharmonic mixers, which allow for the use of an LO at half the RF, and also provide LO noise suppression. Measurements at 600 GHz on a WR-1.7 subharmonic mixer have yielded a mixer noise temperature of 1550 K (DSB) and a conversion loss of 8 dB (DSB) using only 4 mW of LO power at 300 GHz. The development of a WR-1.2 mixer, covering the range from 600-900 GHz, will be discussed at the conference. Because of the need for compact receivers, particular emphasis will be given to the size and DC power requirements of these receivers.

The terahertz circuit designs discussed here represent a novel and innovative solution for terahertz source and receiver applications. Their inherent simplicity is a primary benefit and their proven THz performance is extremely encouraging. Additionally, our GaAs-on-dielectric fabrication process is well established and has been shown to be quite robust. This technology is ideal for a variety of science applications such as airborne atmospheric sensing and long duration flights to study the atmospheres of other planets, as well as a range of military and commercial applications, including imaging systems and potentially bioagent and chemical scanners.

Planar Diode Multiplier Chains for THz Spectroscopy

Frank Maiwald, Brian J. Drouin, John C. Pearson, Imran Mehdi
Frank Lewen[a], Christian Endres[a], Gisbert Winnewisser[a]

Abstract— **Broadband frequency multiplier chains based on planar GaAs Schottky diodes [1], developed for the Herschel Space Observatory (Herschel) [2] and ALMA [3], have been applied to high-resolution laboratory spectroscopy covering most frequencies from 0.2 to 2.5 THz. These chains are driven by commercially available frequency synthesizers and millimeter wave multipliers (6x), which provided a broadband RF source with several mW from 70 to 120 GHz. The millimeter wave signal is amplified with recently developed power amplifiers [4] to more than 100 mW with 15% bandwidth to drive cascaded multipliers [5] - [8]. These multipliers are cascaded with up to 4 successive doublers or triplers with a multiplication factor of 2 to 36. By selecting well-matched multiplication stages, sufficient power over 10% bandwidth is generated.**

High-resolution laboratory spectroscopy is utilized as a diagnostic tool to determine noise and harmonic content of balanced [9]-[11] and unbalanced [12]-[14] multiplier designs. Balanced multiplier designs suppress unintended harmonics more than -20dB. Much smaller values were measured on unbalanced multipliers.

Index Terms—**high-resolution spectroscopy, THz, cascaded frequency multipliers, planar GaAs Schottky diode, noise level and harmonic content**

I. Introduction

The development of all-solid-state frequency sources for HIFI (**H**eterodyne **I**nstrument for the **F**ar-**I**nfrared) and ALMA (**A**ttacama **L**arge **M**illimeter **A**rray) has provided broadband RF sources without mechanical tuners in the THz regime. Frequency coverage is central in all remote sensing experiments. Historically atmospheric chemistry instruments like MLS [15] have relied on wide band IF mixers to achieve coverage, while astrophysics missions like SOFIA [16] and [17], ALMA [3], and Herschel use both wide band mixers and multiple local oscillator sources. In all cases, precise frequency knowledge and spectral purity must be maintained in order to obtain accurate observations of molecular and atomic transitions. Laboratory high-resolution spectroscopy provides atomic and molecular data that enables interpretation of atmospheric chemistry observations, remote and local planetary observations, and spectroscopic astrophysical observations.

The challenges in laboratory spectroscopy are similar to the remote sensing one in terms of the need for bandwidth and spectral purity, but there is a difference in that the spectrometer can be re-adjusted by the operator as needed. Unfortunately, such re-adjustment is time-consuming and complicates the collection of comprehensive data. A primary limitation in traditional millimeter and submillimeter spectrometers is the tuning range of the phase lock loop. To avoid this limitation a commercially available frequency synthesizer with a high quality internal lock loop was utilized. If the spectral purity of the synthesizer is sufficient, direct multiplication with planar multipliers and MMIC amplifiers, described herein, allows nearly autonomous operation for rapid collection of data at sub-millimeter wavelengths [18]. As a demonstration, we conducted a series of high-resolution spectra of rotational transitions of isotopomers of H_2O (water), HOCl (hypochlorous acid), and CH_3OH (methanol). The results will be published.

In addition, the spectroscopic techniques provide information on the harmonic content and the noise level of the signal source. In local oscillator applications, it is very important to suppress the harmonics, especially the higher frequency ones which cannot be cut-off by the output waveguide. Balanced multipliers, which can be designed in a symmetric or anti-symmetric configuration, suppress the higher harmonics per design. The symmetry of the diodes arrangement prevents unwanted odd or even harmonics to the order of -20dB to –30dB. It has been observed that the bias conditions strongly impact the generation of harmonics in all tested multipliers. Higher harmonics are spurious signals [20], which can introduce ghost-lines making interpretation of the data more difficult or impossible. This is especially true in unbalanced designs where unwanted harmonics could be higher than the desired ones. The suppression of unwanted harmonics is very important when high spectral purity of the LO [19] is required, as it is the case for laboratory spectroscopy and in heterodyne systems using wideband Hot Electron Bolometers (HEB). Since HEBs are sensitive to amplitude modulation (AM) of incident RF power, AM noise at the modulation frequency impacts the signal to noise ratio. Additionally, in heterodyne systems the system stability is reduced by AM noise because the receiver gain is modulated which prevents efficient integration of the signal. In order to characterize the local oscillators two different spectrometers,

Manuscript received May 30, 2005. This Work has been made possible by the Jet Propulsion Laboratory, California Institute of Technology, under contract to the US National Air and Space Administration.

F. Maiwald is with the Jet Propulsion Laboratory, California Institute of Technology, M/S 168-314, 4800 Oak Grove Drive, Pasadena CA 91109, phone: +1-818-354-0214, E-mail: Frank.Maiwald@jpl.nasa.gov.

a) I.Physikalische Institut der Universität zu Köln, Zülpicher Strasse 77, Köln, Germany, phone +49 221 470 2757

described in the next sections, were utilized.

II. Spectrometer

A. General Description

One of the important components in a spectrometer or a receiver system is a frequency locked source with knowledge of the precise frequency (figure 1).

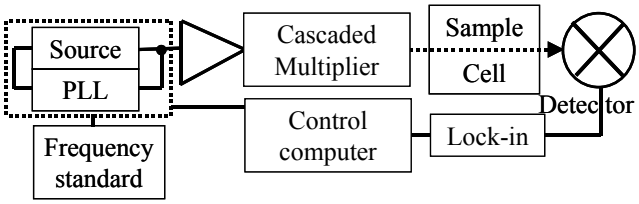

Fig. 1: Block diagram of a spectrometer.

A frequency standard with an accuracy of at least a factor 10x higher than the targeted resolution of the spectrometer is required. In the laboratory this translates to at least a part in 10^9, while remote sensing applications used for investigating wide lines require only a part in 10^6. Further, the close-in spectral purity of the reference source is multiplied to higher harmonics and impacts the noise floor when the reference has high noise levels. When using a highly pure fundamental oscillator at higher frequency, the requirements on the noise in the lock loop of a multiplier chain can be minimized. This approach is used in the Cologne spectrometer. In the JPL spectrometer a fundamental oscillator at X-band frequencies is used, while most radio observatories lock the local oscillator with millimeter wave Gunn oscillators. Since amplification and multiplication can degrade spectral purity and introduce spurs, the fundamental oscillator ultimately limits the spectral purity that the spectrometer or local oscillator can achieve.

In the laboratory the generated RF signal propagates through a gas cell before the signal reaches a sensitive detector. A variety of modulation techniques, AM, FM, and combinations thereof, can be combined with lock-in amplifiers to minimize instrumental effects. Two different implementations of submillimeter spectrometers are described in the following sections.

B. Cologne THz spectrometer

The Cologne THz spectrometer uses a series of Backward Wave Oscillators (BWO) made in Russia as fundamental oscillators operating in the range of 53 to 1200 GHz. Each BWO has an electronic tuning range of 30 to 50 % without any mechanical tuning element. The BWOs are used as a high power monochromatic source in fundamental mode required for sensitive detection of weak transient molecules or they serve to pump quasi-optical THz frequency multipliers. Figure 2 shows the Cologne spectrometer setup including its phase-lock loop circuit, the quasioptical multiplier setup, and the absorption cell with the liquid helium cooled InSB detector. The backbone of the PLL circuit is the subharmonic mixer that combines a multiple of a millimeter wave

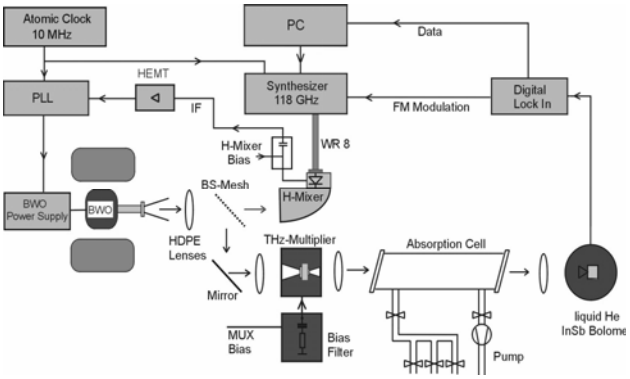

Fig. 2. Block diagram of the Cologne THz Multiplier spectrometer.

synthesizer (78 – 118 GHz) signal quasioptically with a fraction of the BWO power. The resulting intermediate frequency at 350 MHz is amplified with a low noise HEMT and then fed to the phase discriminator, which provides the control signal after being processed by the loop filter to phase- and frequency-lock the BWO [21]. The typical loop bandwidth is about 2 MHz.

BWOs typically generate several 10 mW power up to at least 810 GHz, and deliver the power into an overmoded waveguide which requires a good quasioptical matching between BWO and single mode horn antenna of the THz-tripler. The phase locked BWO system has a limited frequency control provided by the lock loop which allows for approximately 1 GHz of instantaneous tuning at the output frequency before the high voltage power supply and the lock loop parameters require re-adjustment.

The Cologne spectrometer takes advantage of the spectral purity of the BWO. This feature plus a subharmonic mixer which generates negligible harmonics and sideband frequencies at the main optical beam, assure that the spectrometer system is free of spurious signals except a weak (<-40dB) amount of 2nd harmonic from the BWO. A disadvantage of this approach is the need for two lock loops; one in the millimeter synthesizer and the other for the BWO. It also requires a high voltage supply (up to several kV) and 1.2 Tesla magnets for focusing the electron beam of the BWO. The BWO spatial mode quality is generally not an issue for fundamental mode spectroscopy, since most detectors in the submillimeter wavelength couple well to multiple modes.

The BWOs have been successfully used with planar diode multipliers in the past [13]. Several multipliers developed for HIFI have been tested using BWOs, because solid-state pump multiplier chains at frequencies from 800 to 900 GHz were still under development. The spectrometer in Cologne was utilized to characterize 1.9 THz triplers and 2.7 THz triplers. With this spectrometer, transition frequencies up to 2.3 THz were observed on molecular species, like D_2O,HDO, NH_2D and ND_2H. To our knowledge, this setup was the first THz multiplier spectrometer to open the frequency range above 2 THz to broadband high resolution spectroscopy.

C. JPL Frequency Multiplier Submillimeter Spectrometer

The spectrometer at JPL utilizes a fundamentally different approach from the one in Cologne. The spectrometer is built around a commercial core of microwave and millimeter components and relies on direct multiplication and amplification to the submillimeter and THz frequencies. In this approach, it is not possible to use the intrinsic spectral purity of a millimeter or submillimeter fundamental oscillator and PLL to clean-up the signal. As a result, the main requirement is that the input signal is spectrally pure and as free of spurs as possible. The advantage to the approach is that the spectrometer requires only one lock loop under full computer control. This allows tuning anywhere in the desired frequency band with a minimal stabilization time determined by the synthesizer and bias voltages. Only the frequency chains have to be changed to cover different frequency ranges, but the source unit remains the same. This allows the spectrometer to utilize any multiplier source built for HIFI, ALMA or other application that can be driven in the 70-120 GHz range. No quasioptical coupling of the fundamental source is required because all components have input and output waveguides.

Several modifications are required to achieve the desired spectral purity. First, a tracking YIG filter is used at the output of the synthesizers to reduce the harmonic content and spurious content. Second, the W-band MMIC amplifiers [4] are operated in compression. Lastly, the limited ~15% bandwidth of the higher power amplifiers prevent the 5th and 7th harmonics of the millimeter wave sixtupler from being transmitted to the multiplier chain. A WR-10 waveguide filter could be used as well, but this has been so far proven unnecessary. The generated RF signal is quasioptically guided through the sample cell and detected by a sensitive detector such as a 4 K cooled InSb or 2 K cooled Si bolometer. For the measurement of absorption lines, the entire frequency band of frequency multiplier chain can be covered by increasing or decreasing the synthesizer in small frequency steps. The smallest increment is limited by the synthesizer's resolution. Different modulation modes can be selected to acquire the spectroscopic data. A more detailed description of the spectrometer is provided in [18].

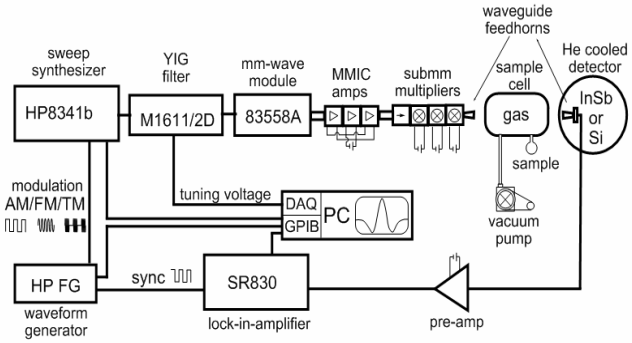

Fig. 3. Block diagram of the JPL Direct Synthesis Spectrometer.

III. Cascaded Frequency Chains

Many of the solid-state frequency chains used in the JPL spectrometer were developed for the HIFI instrument of Herschel. Each chain contains a cascade of three or four frequency doublers or triplers starting from W-band. These modules [6] were designed for wide band operation at 120 K and high efficient power conversion without mechanical tuners. Only electrical tuning with the bias supply is required, which simplifies the operation and enables computer control. Nearly 80% of frequency coverage between 0.15 to 2 THz and partial coverage from 2.4 to 2.7 THz were achieved by cascading a x8 or x12 chain with a single diode doubler/tripler. The input power of the x12 multiplier was provided by a 100-250 mW 71-82 GHz amplifier and the x8 by a 100-200 mW 100-108 GHz amplifier. This signal was multiplied by frequency doublers or triplers up to the THz range. Several fraction of one microwatt at THz frequencies were sufficient to perform sensitive spectroscopy. Coverage of 400-720 GHz was achieved with two Virginia Diodes multipliers. The x8 JPL chain can be used to cover 720-840 [11], a x10 VDI chain covers 770-860 GHz, the JPL x12 covers 840-960 GHz, a JPL x12 covers 1060-1220 GHz [22] and a JPL x18 covers 1575-1700 GHz [23].

IV. Spectroscopy

Ultimately most submillimeter frequency multipliers are used to perform spectroscopy. Laboratory spectroscopy can provide a wealth of detailed information on the source performance. The next section discusses a number of multiplier measurements that can be achieved spectroscopically.

A. Power bandwidth

The important characteristics of any submillimeter source are the output power and bandwidth, which are determined when the RF output in CW mode is maximized at nominal bias parameters. For this characterization, the bias conditions on the frequency multipliers are adjusted to be in the safe range [24] over the entire frequency scan. Safe bias conditions are defined that no excessive forward currents or any reverse currents are induced in the multiplier diodes while the frequency is incrementally changed at constant RF input level. To determine the total power content in a spectrometer setup, the RF signal is AM modulated. If the dynamic range of the detector is exceeded, the power may be attenuated. In most of the cases several sheets of paper are sufficient to prevent saturation of the detector. The total power measurement gives the shape of the output power convolved with the frequency dependent throughput and the characteristic of the optics, sensitivity of the detector, and atmospheric absorption. Once care has been taken to minimize the frequency dependent effects, the multiplier pass band can be determined. For quantitative measurements the detector's responsivity has to be known.

In Figure 4 a total power sweep of a 1600 GHz frequency chain is displayed. The measurement was performed through

a 1.6 meter long gas cell with 150 mTorr of methanol. The step size was 2.5 MHz or about 20 times higher resolution than the one available for the Fourier transform infrared spectrometer system. The red stick spectra present the predicted methanol ground state lines and relative intensity. The frequency coverage can be extracted from the data once the effects of the atmosphere's absorption are accounted for. In this case the dip in the middle is due to a strong water absorption line located at 1.604 GHz and the RF characteristic of the last stage multiplier. When the optical path is purged with dry Nitrogen, the absorption will be reduced.

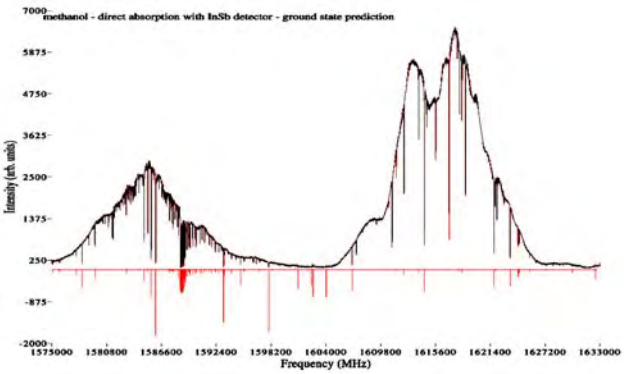

Fig. 4: Total power sweep from 1575 GHz to 1633 GHz with a 1600 GHz frequency chain used in Band 6 for the HIFI instrument in HSO

B. Extraction of noise level and harmonic content

One important consideration for multipliers is to investigate whether the total amount of power is generated in the desired harmonic. For this matter, spectroscopy on well known molecular transitions has to be performed.

The line strength of molecular transitions can be determined with high accuracy by measuring the electric dipole moment and applying the selection rules [25] for the transition. The JPL spectral line catalog [26] and the CDMS [27] provide the line strength for many molecules in Log(I(T)) format where the temperature (T) is 300 Kelvin. The peak absorption for pressure broadened lines is

$$\alpha_{\max} = \frac{I(T)}{\Delta v}\left(\frac{T_0}{T}\right) \times 102.458 cm^{-1}. \qquad (1)$$

Here Δν is the half width at half height of the line at 1 Torr in MHz. The attenuation (A) in a cell of length (L) in cm is given by:

$$A = \alpha_{\max} L \times 4.3429 dB. \qquad (2)$$

Since the catalogs generally do not include the contribution for excited vibrational states the line strength should be divided by the vibrational partition function given below:

$$Q_v = \left(\sum_{v_i} e^{-v_1 h\omega_1 / kT}\right)\left(\sum_{v_{2i}} e^{-v_2 h\omega_2 / kT}\right). \qquad (3)$$

where the v_i is the number of quanta in the i-th of the 3N-6 vibrational modes. Vibrational states above 1000 cm^{-1} (wavenumber, 1cm^{-1} is equal to 29.97925 GHz) in energy contribute less than a 1% correction. When this is done for the Q branch feature in figure 5, the absorption is expected to be between 18.9 and 19.7 dB in the band head in good agreement with the observed transmission. A note of caution is that the detector must be sensitive to the other possible harmonics as well. This technique determines only if there is power at other frequencies, but it cannot distinguish between noise and harmonic content.

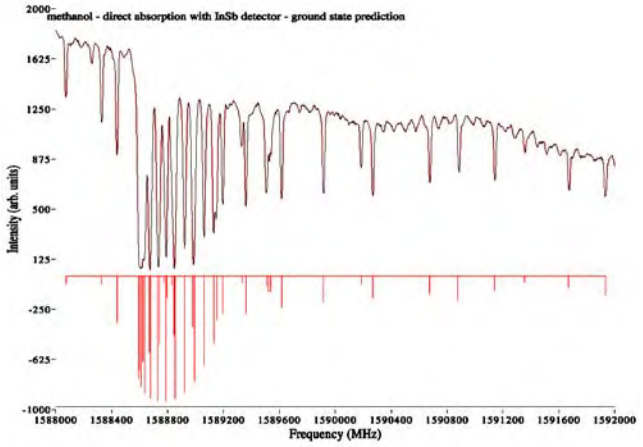

Fig. 5: Determination of noise level and harmonic content. Displayed is only a small section of figure 4 from 1588 to 1593 GHz.

C. Harmonic content

The harmonic content can be directly determined by spectroscopic measurements on known molecules with relatively strong absorption features with known frequencies and intensities in all the possible harmonics. The spectrum is measured at low pressure in the gas cell in FM or tone burst modulation. The harmonic content can be determined by the ratio of the expected line strength in the fundamental harmonic to the other harmonics. The spectrum in Figure 6 is the one for N_2O in natural isotopic abundance in the frequency range from 1.0891 THz to 1.0907 THz. The 18-O has a 0.25% natural abundance and the 15-N isotope of one of the nitrogen atoms has an abundance of 0.36%. Considering the envelope of the total power we determined a content of -27 (+/-2) dB from the fourth harmonic on a balanced 1.2 THz tripler [22]. A rich molecular spectra is required to perform a

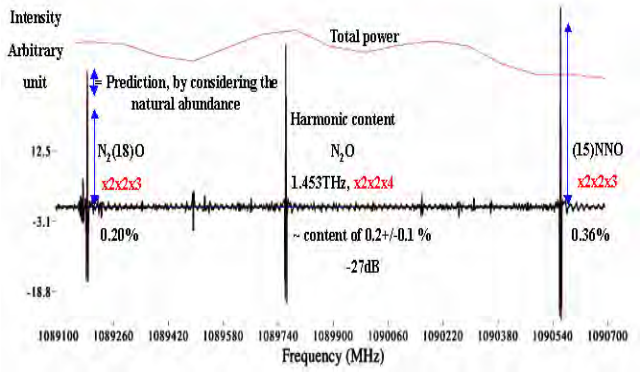

Fig. 6: Harmonic content of a 1200 GHz balanced frequency multiplier operated at 1.09 GHz with fundamental frequency range from 88 to 107 GHz. N_2O was used as molecule.

complete analysis of the pass band. This measurement is an example of how to estimate the harmonic power content. A suppression of at least 20 dB has been measured for every tested balanced multiplier designs including doublers, triplers, and quintuplers. In these designs even or odd harmonics are suppressed internally in the circuit. This suppression is essential to reduce the contribution of the next higher harmonic efficiently. In the unbalanced designs, such as single diode configurations, the next higher harmonic cannot be suppressed by the circuit symmetry. Just about all the multiplier designs with matching waveguide structure possess a common design feature which is the cuts-off of the lower harmonics by the output waveguide, but all the higher contents can propagate to the output. The generation of harmonics is strongly frequency dependent, tunable by the bias point, and impacted by the level of input RF power.

The harmonic content of a single diode circuit a 2.7 THz tripler was measured to be -6dB to the next lower harmonic (second) which was much stronger than the targeted third harmonic. Initially, the low expected power available at 800-900 GHz suggested that a single diode would work more efficiently than a design with several diodes. Further, the difficulty in terminating unwanted harmonics should be appropriately considered in any such trade-off. Currently, power levels on the order of 1 mW at these frequencies suggest that balanced configurations with two diodes at frequencies above 2 THz is now the better design option than the single diode configuration.

D. Noise level

One of the important considerations in designing a receiver is the expected noise level of the local oscillator. In an ideal design it should contribute negligibly to the overall receiver temperature. These receiver utilize SIS or HEB [28] mixers which are the most sensitive detectors up-to-date to test the noise of the LO. However, there are also a number of spectroscopic techniques that can be used to determine if the noise level is significant.

Any source suitable for use as a local oscillator should be noise-limited by the detector in spectrometers. In this case the signal to noise ratio of the detected spectra will improve in proportion to the Noise Equivalent Power (NEP) of the detector used. However, the contribution of the thermal background at 300 Kelvin limits the detectors sensitivity. Without appropriate filters there is no benefit on NEPs better than 10^{-16}, which is substantially worse than narrow banded heterodyne detection. A series of measurements with progressively more sensitive detectors can be made to verify that the signal to noise ratio on weak features improves as expected. The result of this method can't prove that the source will work as a local oscillator, but is will indicate if the source has high noise content.

The other concern is the phase noise generated when frequency multipliers are cascaded. Since the observed spectra are a convolution of the line width of the signal source and the line width of the observed molecule, a quantitative measurement of the signal source line width is possible. Molecular spectra pressure broadens according to the linear relationship:

$$\Delta\nu = 1/2\pi\tau\,. \qquad (4)$$

where τ is the mean time between collisions. Since the Doppler contribution to the line width is directly calculable from the temperature at atomic weight, plotting the pressure broadened line width using AM modulation corrected for Doppler effects will give a slope and a zero intercept. The slope is the pressure broadening constant and the intercept is a measure of source line width [29]. Due to measurement uncertainties the accuracy is generally a few % of the molecular Doppler line width, but this method is sufficient to identify real problems with the phase noise.

E. Molecular Spectroscopy

An advantage of wide frequency range molecular data sets is the ability to apply infrared techniques where all the absorption or emission lines within the frequency range are measured. Once this is performed, computer aided methods can be used to determine the relationship between observed and calculated transitions. This is especially important when very complex spectra of traditional molecular models can not describe the existing quantum mechanic model of the molecule investigated. Measurements performed on molecules of interest allows for extension of existing databases by including more rotational and vibrational states at higher quantum numbers. Since most of the existing molecular constants cannot be used to extrapolate accurate transition frequencies (see figure 7) over the frequency ranges of Herschel, ALMA and SOFIA, it is necessary for exact astronomical interpretation of spectra to perform laboratory measurements in the THz regime of molecules of interest.

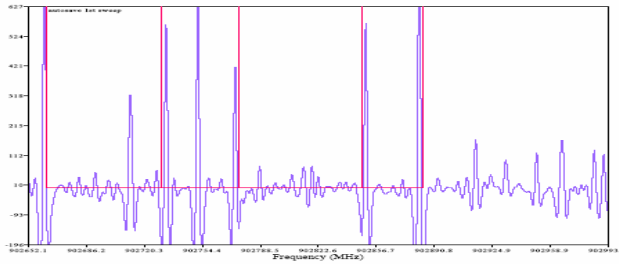

Fig. 7: Comparison of predicted and measured transitions of methanol between 902.6 to 902.9 GHz. The difference in frequency is more than the linewidth of the transitions.

V. Conclusion

The availability of all-solid-state frequency sources enables "IR" spectroscopy techniques to be used in the far-infrared frequency regime. With broadband frequency sweeps at THz frequencies, molecular and atomic transitions can be detected efficiently allowing computer aided processing and identification of more states and energy levels. The outcome is that precise predictions above 2 THz will be achieved, which are essential for interpretation of all radio astronomy data and the planning of future missions like SAFIR [30].

Further, spectroscopy provides a powerful diagnostic tool for characterization of the bandwidth, spectral purity, noise level, and the harmonic content of local oscillator sources. The characterization of a number of LO chains for the HIFI instrument demonstrated that balanced multiplier designs have surprisingly sufficient suppression of higher harmonics for example 2^{nd}, 3^{rd}, 4^{th} etc., while those with unbalanced designs can be remarkable poor. A conclusion of this study is that extreme care should be taken to limit the harmonic content of local oscillators in HEB applications, where ghosts of strong lines could be observed with harmonic content which are more than 60 dB below the carrier. This will be a great challenge for any multiplier to overcome and should be considered in the design of a receiver system.

ACKNOWLEDGMENT

The authors thank Dr. P.H. Siegel for the technical discussions. Further, we like to express our gratitude for the support of the Band 6 Local Oscillator team under the lead of J. Ward: A. Maestrini, E. Schlecht, G. Chattopadhyay, J. Gill, R. Ferber, R. Tsang, R. Lin, A. Peralta, B. Finamore, W. Chun, J. Baker, R. Dengler, and H. Javadi for loaning the Band 6 frequency multiplier chains.

REFERENCES

[1] S. Martin, B. Nakamura, A. Fung, P. Smith, J. Bruston, A. Maestrini, F. Maiwald, P. Siegel, E. Schlecht, I. Mehdi, "Fabrication of 200 to 2700GHz Multiplier Devices using GaAs and Metal Membranes," *IEEE MTT-S Int. Microwave Symp.*, Phoenix, Arizona, May 20-25, 2001.

[2] M.W. de Graauw, N.D. Whyborn, E. Caux, T.G. Phillips, J. Stutzki, K. Wafelbakker, "The Herschel HIFI instrument," Proc. SPIE vol. 5498, 2004.

[3] ALMA web-side: http://www.alma.nrao.edu/.

[4] R.R. Ferber, J.C. Pearson, T.C. Gaier, L.A. Samoska, F.W. Maiwald, M. Wells, A. Campbell, and G. Swift, P. Yocom, K.T. Liao, "W-Band MMIC Power Amplifiers for the Herschel HIFI Instrument," *Proc. 14th Int. Symp. on Space THz Tech.,* Tucson, 22 April 2003.

[5] N.R. Erickson, G. Narayanan, R.P. Smith, S.C. Martin, I. Mehdi, T.W. Crowe, W.L. Bishop, "Planar Frequency Doublers and Triplers for FIRST," *Proc. 11th Int. Symp. on Space THz Tech*., pp 543-551, 2000.

[6] J.S. Ward, E. Schlecht, G. Chattopadhyay, A. Maestrini, J. Gill, F. Maiwald, H. Javadi, I. Mehdi, "Capability of THz Sources Based on Schottky Diode Frequency Multiplier Chain," *IEEE MTT-S Int. Microwave Symp. Digest*, Fort Worth, TX, pp. 1587-1590, June 2004.

[7] F. Maiwald, E. Schlecht, A. Maestrini, G. Chattopadhyaya, J. Pearson, D. Pukala, I. Mehdi, "THz frequency multiplier chains based on planar Schottky diodes," *Proc. of SPIE,* vol. 4855, pp. 447-458, Waikoloa, Hawaii, 22-28 August 2002.

[8] J. Ward, F. Maiwald, A. Maestrini, G. Chattopadhyay, E. Schlecht, J. Gill, I. Mehdi, "1400–1900 GHz Local Oscillators for the Herschel Space Observatory," *Proc. 14th Int. Symp. on Space THz Tech.,* Tucson, AZ, 22-24 April 2003.

[9] D. Porterfield, T. Crowe, R. Bradley and N. Erickson, "A High-Power, Fixed-Tuned, Millimeter-Wave Balanced Frequency Doubler," *IEEE Trans. Microwave Theory Tech.*, vol. 47, p419, 1999.

[10] E. Schlecht, G. Chattopadhyay, A. Maestrini, D. Pukala, J. Gill, S. Martin, F. Maiwald, I. Mehdi, "A High-Power Wideband Cryogenic 200 GHz Schottky "Substrateless" Multiplier: Modeling, Design and Results," *Proc. of the 9th Int. Conf. on THz Tech.*, Charlottesville, VA, October 14-16, 2001.

[11] G. Chattopadhyay, E. Schlecht, J. Gill, S. Martin, A. Maestrini, D. Pukala, F. Maiwald, I. Mehdi, "A Broadband 800 GHz Schottky Balanced Doubler," *IEEE Microwave and Wireless Components Letters*, Vol. 12, No. 4, pp. 117-118, April 2002.

[12] P. Zimmermann, "Multipliers for THz Local Oscillators," *Proc. SPIE* vol. 3357, pp. 152-158, 1998.

[13] F. Maiwald, F. Lewen, B. Vowinkel, W. Jabs, D.G. Paveljev, M. Winnewisser, G. Winnewisser, "Planar Schottky Diode Frequency Multiplier for Molecular Spectroscopy up to 1.3 THz," *IEEE Microwave and Guided Wave Letters*, Vol. 9, No. 5, May 1999.

[14] F. Maiwald, S. Martin, J. Bruston, A. Maestrini, T. Crawford, I. Mehdi, P.H. Siegel, "2.7 THz Waveguide Tripler using Monolithic Membrane Diodes (MOMED)," *IEEE MTT-S Int. Microwave Symp*., Feb. 2001.

[15] J.W. Waters, W.G. Read, L. Froidevaux, R.F. Jarnot, R.E. Cofield, D.A. Flower, G.K. Lau, H.M. Pickett, M.L. Santee, D.L. Wu, M.A. Boyles, J.R. Burke, R.R. Lay, M.S. Loo, N.J. Livesey, T.A. Lungu, G.L. Manney, L.L. Nakamura, V.S. Perun, B.P. Ridenoure, Z. Shippony, P.H. Siegel, R.P. Thurstans, R.S. Harwood, H.C. Pumphrey, M.J. Filipiak, "The UARS and EOS Microwave Limb Sounder Experiments," *J. Atmos. Sci.* 56 , 194 -218, 1999.

[16] R. Guesten, et al., "GREAT: the first-generation German heterodyne receiver for SOFIA," *SPIE In. Symp. on Astronomical Telescopes and Instrumentation*, Conf. 4014, Munich, Germany, 27-31 March, 2000.

[17] M.L. Edgar, J. Zmuidzinas, "CASIMIR: submillimeter heterodyne spectrometer for SOFIA," *SPIE Int. Symp. on Astronomical Telescopes and Instrumentation, Vol. 4014,* Munich, Germany, 27-31 March, 2000.

[18] B. Drouin, F. Maiwald, J. Pearson, "Application of cascaded frequency multiplication to molecular spectroscopy", to be published 2005.

[19] J.C. Pearson, R. Guesten, T. Klein, N.D. Whyborn, "The Local Oscillator System for the Heterodyne Instrument for FIRST (HIFI)," *UV, Optical and IR Space Telescopes and Instruments*, *Proc. of SPIE,* Vol. 4013, 2000.

[20] G. Chattopadhyay, F. Maiwald, E. Schlecht, R.J. Dengler, J.C. Pearson, I. Mehdi, "Spurious Signal Response of Broadband Solid-State Frequency Multipliers at Millimeter and Submillimeter Wavelengths," *Int. Journal of Infrared and Millimeter Waves*, Vol. 24, No. 9, pp. 1485-1498, September 2003.

[21] F. Lewen, R. Gendriesch, I. Pak, D, Paveliev, M. Hepp, R. Schieder, G. Winnewisser, "Phase locked backward wave oscillator pulsed beam spectrometer in the submillimeter wave range," *Rev. Sci. Instrum.* 69 (1), January 1998.

[22] J. Bruston, A. Maestrini, D. Pukala, S. Martin, B. Nakamura, I. Mehdi, "A 1.2 THz planar tripler using GaAs membrane based chips," *Proc. 12th Int. Symp. Space THz Tech*., pp. 310-319, 2001.

[23] A. Maestrini, J. Ward, H. Javadi, C. Tripon-Canseliet, J. Gill, G. Chattopadhyay, E. Schlecht, I. Mehdi, "Local Oscillator Chain for 1.55 to 1.75 THz with 100 mW Peak Power," Submitted to IEEE MWCL.

[24] F. Maiwald, E. Schlecht, R. Lin, J. Ward, J. Pearson, P. Siegel, I. Mehdi, "Reliability of cascaded THz frequency chains with planar GaAs circuits," *Proc. 15th Int. Symp. on Space THz Tech.,* Amherst, MA, 27-29, April 2004.

[25] W. Gordy, R.L. Cook, 1984, Microwave Molecular Spectra, John Wiley & Sons, New York.

[26] H.M. Pickett, R.L. Poynter, E.A. Cohen, M.L. Delitsky, J.C. Pearson, H.S.P. Müller, "Submillimeter, Millimeter, and Microwave Spectral Line Catalog, " *J. Quant. Spectrosc. & Rad. Transfer* 60, 883-890 (1998). http://spec.jpl.nasa.gov/.

[27] H.S.P. Müller, F. Schlöder, J. Stutzki, G. Winnewisser, "The Cologne Database for Molecular Spectroscopy, CDMS: A Useful Tool for Astronomers and Spectroscopists," *J. Mol. Struct*. 742, 215–227 (2005). http://www.ph1.uni-koeln.de/vorhersagen/catalog/main_catalog.html.

[28] J. Zmuidzinas, P. Richards, "Superconducting Detectors and Mixers for Millimeter and Submillimeter Astrophysics," *Proc. of IEEE*, Vol. 92, No. 10, Oct. 2004.

[29] B.J. Drouin, J. Fischer, R.R. Gamache, "Temperature dependent pressure induced lineshape of O3 rotational transitions in air," *Journal of Quantitative Spectroscopy & Radiative Transfer* 83 (2004) 63–81.

[30] D.J. Benford, J.W. Kooi, "Heterodyne Receiver Requirements for the Single Aperture Far-Infrared (SAFIR) Observatory," *Proc. 14th Int. Symp. on Space THz Tech.,* Tucson, AZ, 22 April 2003.

Local Oscillators from 1.4 to 1.9 THz

John Ward, Erich Schlecht, Goutam Chattopadhyay, Hamid Javadi,
John Gill and Imran Mehdi
Jet Propulsion Laboratory, California Institute of Technology,
M/S 168-314, 4800 Oak Grove Drive, Pasadena CA 91109

Alain Maestrini and Charlotte Tripon-Canseliet
LISIF - Université Paris VI, 4, place Jussieu, 75252 Paris, France

***Abstract*—Local oscillators have been produced for band 6 of the Heterodyne Instrument for the Far Infrared (HIFI) on the Herschel Space Observatory and for the Harvard-Smithsonian Center for Astrophysics Receiver Lab Telescope (RLT) in northern Chile. These local oscillators pump hot-electron bolometer (HEB) mixer front-ends to perform high resolution spectroscopy of the interstellar medium. Local oscillator assemblies amplify 1 mW input signals in the 86 to 107 GHz band before multiplying the frequency by 16 or 18 with cascaded chains of Schottky diode frequency doublers and triplers, ultimately covering nearly the entire 1.4 to 1.9 THz band with 3 µW or more at the nominal operating temperature of 120 K. Peak output power at the nominal operating temperature is typically 30 µW or higher. Room temperature performance is sufficient to pump HEB mixers with moderately reduced bandwidth compared to cryogenic operation, with room temperature output power typically in the 1 to 10 µW range. The chain outputs are Gaussian beams produced by diagonal horns integrated into the final stage multiplier blocks. Beam pattern measurements at 1.8 THz confirm the predicted performance of the horns.**

***Index Terms*—local oscillator, varactor, Schottky diode, frequency multiplier, submillimeter wavelength.**

I. Introduction

The results presented here are for planar Schottky diode multipliers electronically tunable with about 10% bandwidth. Power amplifiers driven by commercial synthesizers produce 100 mW in the 86 to 107 GHz band [1,2]. Three or four frequency doublers and/or triplers are cascaded after the W band source. All multipliers are balanced designs implemented with monolithic circuits mounted in split-waveguide blocks. The frequency doublers each have two parallel branches of diodes, while the triplers each have two anti-parallel branches. The low frequency multipliers (below 1 THz) use "substrateless" technology implemented with 1 to $2{\cdot}10^{17}$ cm^{-3} doped GaAs, while the multipliers above 1 THz are fabricated on 3 µm thick GaAs membranes with $5{\cdot}10^{17}$ cm^{-3} doped active layers [3-6]. The first stage multipliers have 3 anodes in series in each branch (for 6 anodes total), and the second stages have 2 series anodes in each branch (for 4 anodes total). All multipliers above 700 GHz have only 1 anode per branch, or 2 anodes per multiplier. Multipliers with output frequencies above 1 THz have di-

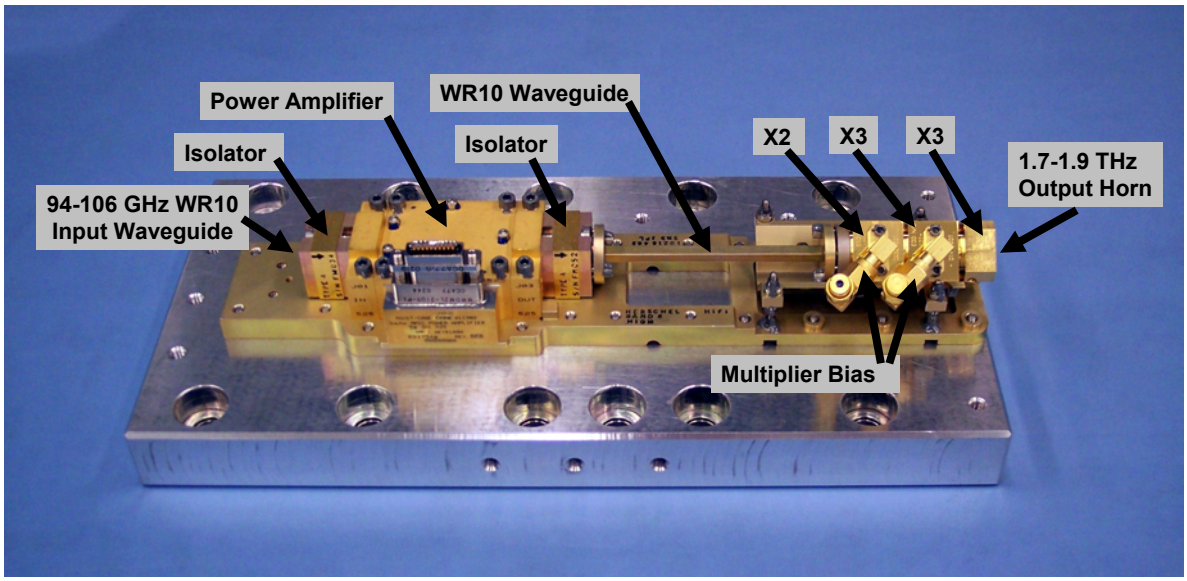

Figure 1. A 1.7 to 1.9 THz local oscillator chain. The signal flows from left to right, with the output at the 18th harmonic of the W band input. The first two frequency multipliers are biased through SMA connectors, and the last stage is unbiased. The maximum envelope of the chain including the gold-colored mounting plate and space for a Ka to W band tripler at the input is less than 250x60x40 mm^3.

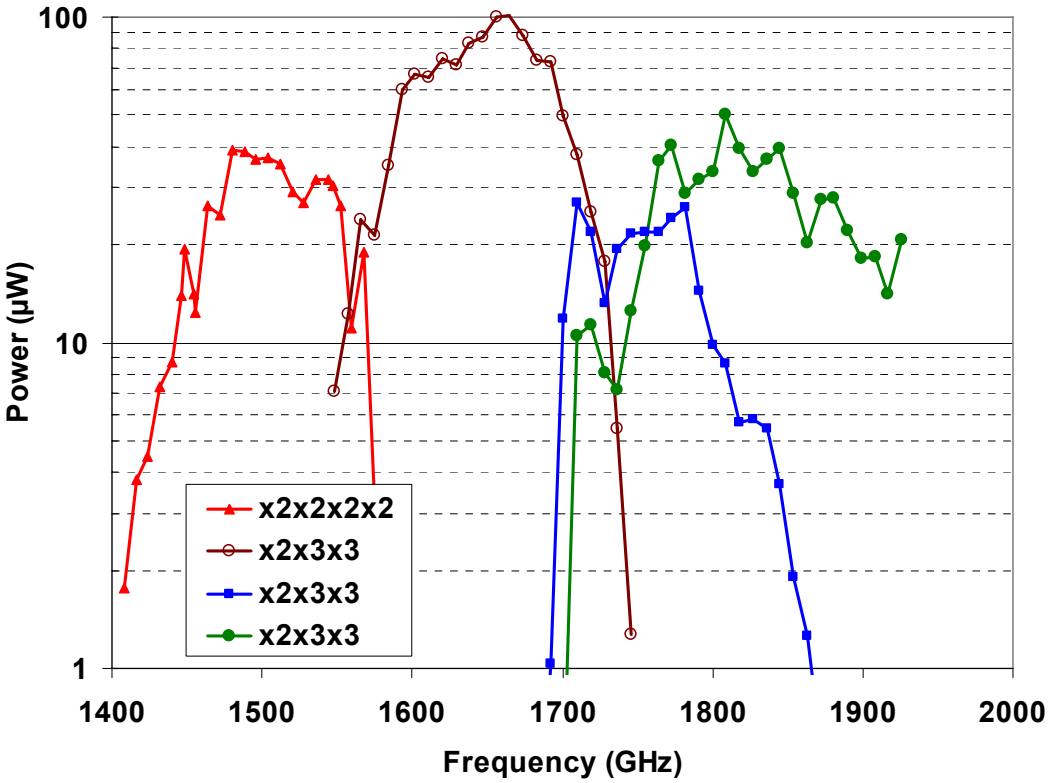

Figure 2. Output power of four local oscillator chains measured at 120 K. For comparison, reported measurements of the optimum LO power incident on the HEB mixer lens at these frequencies ranges from about 0.2 to 1.0 μW [15]. The chain inputs were around 1 mW in the 86-107 GHz range, and the power driving the multiplier chain after the W band power amplifier was 100 mW.

agonal horns integrated into the waveguide split blocks. Further information about the multipliers is given in [7]-[12]. A complete chain is shown in Figure 1.

II. Measured Results

1. Output Power: Chain output power at room temperature was measured with a waveguide calorimeter [13] calibrated with a DC load. The measurements were not corrected for the loss of the connecting waveguides between the device under test and the meter. Chain output power at cryogenic temperatures was measured with a Golay cell calibrated against a Keating meter [14]. All optical measurements were corrected for the losses in the Mylar windows, but were not corrected for other optical losses including non-ideal mirror reflectivity and water vapor absorption. Figure 2 shows the output power measured at 120 K. Four sources cover the entire 1.45 to 1.92 THz band with 10 μW or higher output power, with a useable bandwidth of 150 to 200 GHz per chain. The peak measured power was 100 μW at 1.665 THz. Figure 3 gives an indication of the capability of these sources at room temperature. Although the output power is reduced by roughly a factor of five relative to the cryogenic measurements, the peak output power of 20 μW with broad bandwidth over 4 μW shows that these sources are well suited as local oscillators for HEB mixers even at room temperature.

2. Output Beam: Figure 4 shows the measured beam pattern from the diagonal horn of a x2x3x3 chain at 1.818 THz. The source was rotated about the calculated center of the radius of curvature of the beam with the detector held stationary. The power passed through a small iris approximately 700 mm away from the horn before being measured with a bolometer. The beam is well described by a Gaussian beam with 380 μm beam waist, plus side lobes in the diagonal plane caused by the cross-polar component that is expected for all diagonal horns [16].

3. General purpose lab sources: For the maximum possible output power, the DC biases for the local oscillator chains are adjusted as a function of frequency. Biasing two amplifier gates, two amplifier drains, and up to four multipliers as a function of frequency is further complicated by safety issues, since incorrect bias settings can easily damage the Schottky diodes. For routine laboratory use, we have set up several terahertz sources with reduced bias requirements and simplified operation, with built-in protection to minimize the potential for operator error to damage the multipliers. To achieve this, we have constructed simple passive circuits to bias the multipliers with their own rectified current. A large resistor in series with each multiplier limits the maximum current, and a suitable low-leakage Zener diode in parallel limits the maximum reverse-bias voltage. A potentiometer for each multiplier allows the bias to be optimized over a limited range if needed, and analog current meters are used for diagnostics. Two to four such bias circuits (depending on the number of multipliers to be biased) are mounted in a single small project box. The chains are driven with commercial SMA to WR10 active sextuplers, to provide a total multiple of 96 (x6x2x2x2x2) or 108 (x6x2x3x3). Power amplifier gates are either grounded or set with voltage dividers on the amplifier drain bias line. Thus, the total equipment required to operate the terahertz source is the

chain with passive bias box, two or three power supplies for the active sextupler and power amplifier, and a 10 mW 14-18 GHz SMA source. The output power of the chain may be smoothly varied either electronically by adjusting the drain voltage of the final power amplifier stage or by adjusting a mechanical WR10 waveguide attenuator between the power amplifier and first frequency doubler. The output is a Gaussian beam in the 1.4-1.9 THz range. These general-purpose chains were assembled from "seconds," i.e. hardware unsuitable for other purposes due to issues such as amplifiers with low output power and multipliers with low efficiency or mistuned frequency response. Furthermore, passive bias reduces the bandwidth, especially if the only tuning is changing the frequency of the 14-18 GHz source. Nonetheless, a x96 laboratory chain produced 11 µW at 1.46 THz with 50 GHz of bandwidth above 2 µW, and a x108 chain produced 10 µW at 1.62 THz with 30 GHz of bandwidth above 2 µW.

4. Gas cell and heterodyne mixing tests: Results such as those shown in Figures 2 and 3 were measured with incoherent power meters that provide little useful information regarding the frequency, spectral purity, and noise properties of the output signal. Therefore, additional tests were necessary to confirm the suitability of these sources for use as local oscillators in heterodyne receivers. Gas cell measurements of methanol with a 1.6 THz general-purpose laboratory source described above confirmed that at least 99.8% of the power was in the desired harmonic of the input signal, in this case the 108th harmonic [17]. Two of these x108 chains were used at SRON in the Netherlands to measure HEB mixer beams, with one chain acting as the local oscillator and the other acting as a source with a fixed frequency offset. Mixer beam scans with 80 dB signal-to-noise ratio confirmed the performance of these sources [18]. The ultimate test came from a x96 chain (x6x2x2x2x2) that was lent to the Harvard-Smithsonian Center for Astrophysics. This chain was used at the Receiver Lab Telescope (RLT) in northern Chile to detect the ^{12}CO J=13→12 transition at 1.497 THz in Orion KL [19]. Experience from these tests show that the chain output power is clean and low-noise as long as the source driving the chain is clean and the amplifier is operated in saturation with adequate bias.

III. Conclusion

Compact solid-state electronically tunable broadband sources have been demonstrated to provide complete coverage from 1.45 to 1.92 THz with 10 µW or higher output power. Each frequency multiplier chain has a useable bandwidth of approximately 150 to 200 GHz. The peak measured power was 100 µW continuous at 1.665 THz operating at 120 K. Spectral purity has been confirmed at the 99.8% level or better with gas cell measurements, and mixer tests confirm the suitability of these sources for use as local oscillators in highly sensitive heterodyne receivers. General-purpose multiplier chains have been demonstrated that trade off optimized performance in favor of simplified room temperature operation, requiring only two power supplies and a low power 14-18 GHz source for operation.

The results presented in this paper reflect the current state of the art, and do not yet reflect inherent limits in the capabilities

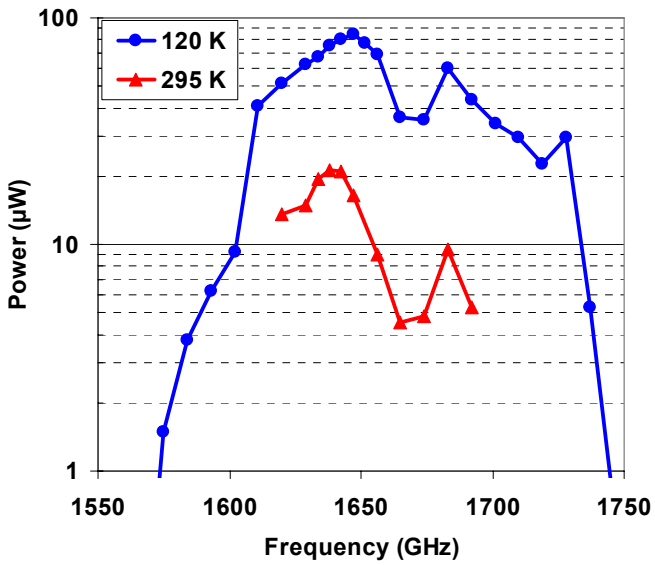

Figure 3. Room temperature and 120 K measurements of a single x18 chain. Although the increase in output power with cooling is dramatic, there is still sufficient power at room temperature to comfortably pump an HEB mixer over a wide band.

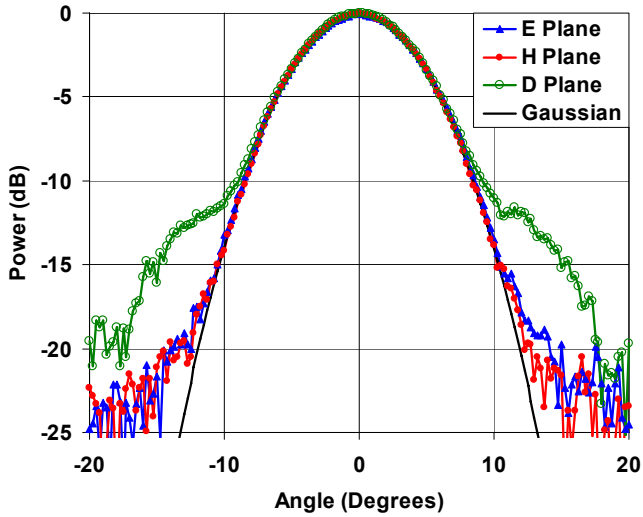

Figure 4. Measured beam pattern from the diagonal horn at 1.818 THz. The source was rotated about the calculated center of the radius of curvature of the beam while the power passing through an iris was measured with a bolometer.

of this technology. The power amplifiers used are typically operated with output power reduced by 3 to 6 dB from the maximum available power. Increasing total anode area and reducing doping may increase the power that can be safely handled by the driver-stage frequency multipliers to enable the full capability of the power amplifiers to be utilized without reducing multiplier lifetime. Power combining could also increase available drive power. Higher drive power would enable higher total multiples to reach higher frequencies. Multiplier designs are not yet fully optimized, leaving room for new designs with increased efficiency and bandwidth as well as simplified fabrication and assembly. New micromachining techniques will enable the manufacture of more complex waveguide circuits at higher frequencies than currently demonstrated. Operation at 77 K (liquid nitrogen)

instead of 120 K can further improve efficiency and increase output power. Continued advances in power amplifier technology may also drive the capability of frequency multiplied sources.

ACKNOWLEDGEMENTS

The authors wish to acknowledge the significant contributions of Frank Maiwald, Ray Tsang, Robert Lin, William Chun, Alex Peralta, Ed Luong, and Jim Velebir. We also thank Peter Bruneau, James Crosby, and Hal Janzen for the superb fabrication of the many high frequency waveguide blocks needed for this project. This work would not have been possible without the continued support of John Pearson and Peter Siegel. The research described in this publication was performed at the Jet Propulsion Laboratory, California Institute of Technology, under a contract with the National Aeronautics and Space Administration.

REFERENCES

[1] H. Wang, et al., "Power-Amplifier Modules Covering 70-113 GHz using MMICs," IEEE Trans. Microwave Theory and Techniques, vol. 49, pp. 9-16, 2001.

[2] Robert R. Ferber, John C. Pearson, Todd C. Gaier, Lorene A. Samoska, Frank W. Maiwald, Mary Wells, April Campbell, Gerald Swift, Paul Yocom, and K. T. Liao, "W-Band MMIC Power Amplifiers for the Herschel HIFI Instrument," Proceedings of the Fourteenth International Symposium on Space Terahertz Technology, Tucson, 22 April 2003.

[3] S. Martin, B. Nakamura, A. Fung, P. Smith, J. Bruston, A. Maestrini, F. Maiwald, P. Siegel, E. Schlecht and I. Mehdi, "Fabrication of 200 GHz to 2700 GHz Multiplier Devices Using GaAs and Metal Membranes," IEEE MTT-S International Microwave Symposium, Phoenix, Arizona, May 20-25, 2001.

[4] A. Maestrini, J. Bruston, D. Pukala, S. Martin and I. Mehdi, "Performance of a 1.2 THz Frequency Tripler Using a GaAs Frameless Membrane Monolithic Circuit", Proceedings of the IEEE MTT-S, Vol. 3, pp. 1657-1660, Phoenix, Arizona, May 20-25, 2001.

[5] E. Schlecht, J. Bruston, A. Maestrini, S. Martin, D. Pukala, R. Tsang, A. Fung, R. P. Smith, I. Mehdi, "200 and 400 GHz Schottky Diode Multipliers Fabricated with Integrated Air-Dielectric 'Substrateless' Circuitry," Proceedings of the Eleventh International Symposium on Space Terahertz Technology, Ann Arbor, Michigan, May 2000.

[6] J. Bruston, S. Martin, A. Maestrini, E. Schlecht, P. Smith, and I. Mehdi, "The Frameless Membrane: a Novel Technology for THz Circuits," Proceedings of the Eleventh International Symposium on Space Terahertz Technology, Ann Arbor, Michigan, May 2000.

[7] G. Chattopadhyay, E. Schlecht, J. Gill, S. Martin, A. Maestrini, D. Pukala, F. Maiwald, and I. Mehdi, "A Broadband 800 GHz Schottky Balanced Doubler," IEEE Microwave and Wireless Components Letters, vol. 12 no. 4, pp. 117-118, April 2002.

[8] E. Schlecht, G. Chattopadhyay, A. Maestrini, A. Fung, S. Martin, D. Pukala, J. Bruston and I. Mehdi, "200, 400 and 800 GHz Schottky Diode 'Substrateless' Multipliers: Design and Results," IEEE Int. Microwave Symp. Digest, pp. 1649-1652, Phoenix, Arizona, May 2001.

[9] A. Maestrini, J. Ward, John Gill, G. Chattopadhyay, F. Maiwald, K. Ellis, H. Javadi, and I. Mehdi, "A Planar-Diode Frequency Tripler at 1.9 THz," Proceedings of the IEEE MTT-S, Philadelphia, Pennsylvania, June 8-13, 2003.

[10] G. Chattopadhyay, E. Schlecht, J. Ward, J. Gill, H. Javadi, F. Maiwald, and I. Mehdi, "An All Solid-State Broadband Frequency Multiplier Chain at 1500 GHz," IEEE Transactions on Microwave Theory and Techniques, vol. 52, no. 5, pp. 1538-1547, May 2004.

[11] A. Maestrini, J. Ward, J. Gill, H. Javadi, E. Schlecht, G. Chattopadhyay, F. Maiwald, N. Erickson, and I. Mehdi, "A 1.7 to 1.9 THz local oscillator source," IEEE Microwave and Wireless Components Letters, vol. 14 no. 6, June 2004.

[12] A. Maestrini, J. Ward, J. Gill, H. Javadi, E. Schlecht, C. Tripon-Canseliet, G. Chattopadhyay, and I. Mehdi, "A 540-640 GHz High Efficiency Four Anode Frequency Tripler," manuscript accepted and to be published in IEEE Transactions on Microwave Theory and Techniques.

[13] N. Erickson, "A Fast and Sensitive Submillimeter Waveguide Power Sensor," Tenth International Symposium on Space Terahertz Technology, pp. 501-507, Charlottesville, VA, 1999.

[14] Thomas Keating Ltd., http://www.terahertz.co.uk.

[15] J. Baselmans, M. Hajenius, J. Gao, P. de Korte, T. Klapwijk, B. Voronov, and G. Gol'tsman, "NbN phonon cooled hot electron bolometer mixers with improved interfaces: noise temperature and LO power requirement," Proceedings of the Fifteenth International Symposium on Space Terahertz Technology, Northampton, MA, April 2004.

[16] J. Johansson and N. Whyborn, "The diagonal horn as a sub-millimeter wave antenna," IEEE Transactions on Microwave Theory and Techniques, vol. 40, no. 5, May 1992.

[17] F. Maiwald, B. Drouin, J. Pearson, I. Mehdi, F. Lewen, C. Endres, G. Winnewisser, "Planar Diode Multiplier Chains for THz Spectroscopy," Proceedings, Sixteenth International Symposium on Space Terahertz Technology, Göteborg, Sweden, May 2005.

[18] W. Jellema, T. Finn, A. Baryshev, M. van der Vorst, S. Withington, A. Murphy, W. Wild, "Phase-sensitive near-field measurements and electromagnetic simulations of a double-slot HEB integrated lens-antenna mixer at 1.1, 1.2, and 1.6 THz," Proceedings, Sixteenth International Symposium on Space Terahertz Technology, Göteborg, Sweden, May 2005.

[19] D. Marrone, R. Blundell, E. Tong, S. Paine, D. Loudkov, J. Kawamura, D. Luhr, C. Barrientos, "Observations in the 1.3 and 1.5 THz atmospheric windows with the Receiver Lab Telescope," Proceedings, Sixteenth International Symposium on Space Terahertz Technology, Göteborg, Sweden, May 2005.

Development and Characterization of an Easy-to-Use THz Source

Jeffrey Hesler, David Porterfield, William Bishop, Thomas Crowe, Andrey Baryshev, Ronald Hesper and Jochem Baselmans

***Abstract*— A primary challenge in creating the next generation of submillimeter-wave receiver systems for space science is generating the required local oscillator power. Full waveguide band performance and power levels suitable for array receivers are desired. Also, the sources must be suitable for use at remote installations. This means they should be compact, reliable and electronically tunable. This papers presents the recent development and testing of a terahertz LO source that meets these requirements. This source uses GaAs Schottky barrier diodes to frequency multiply the power from a millimeter wave amplifier. The final element in the multiplier chain is a frequency tripler to the WR-0.65 waveguide band, spanning from 1.1 – 1.7 THz. This tripler generates of order ten microwatts of power when pumped with 3mW. The complete x72 active multiplier chain is about six-inches in length and requires only milliwatt power level input. It has been tested to demonstrate excellent spectral purity, frequency and power stability and low noise. The construction of the multiplier chain and the test results are reviewed.**

***Index Terms*—Terahertz sources, HEB mixers, frequency multipliers.**

I. The Active Multiplier Chain

Virginia Diodes has developed a series of broadband frequency multipliers based on integrated diode circuits. A tripler to the WR-0.65 waveguide band has recently been demonstrated. It requires only milliwatts of input power anywhere in the 367 – 567 GHz band to generate roughly ten microwatts in the 1.1 – 1.7 THz output band. A complete source based on an input signal from a standard low frequency (<25GHz) synthesizer and generating 5-20 microwatts across a 100 GHz electronic tuning band has been demonstrated. This active multiplier chain (X72) is shown in Figs. 1. It consists of an input doubler/amp with cooling fan (Spacek Labs [1]), an integrated (x2x2) frequency quadrupler and a cascade of two frequency triplers. The entire chain is only six-inches in length and it has no mechanical tuners. The terahertz signal is radiated by an integrated diagonal horn antenna.

Manuscript received June 21, 2005. The development of the terahertz tripler was supported by NASA/JPL through an SBIR contract (NAS5-02126). The development of the driver source was supported by SBIR contracts from the Army Research Office (DAAD19-02-C-0013) and NASA Goddard Space Flight Center (NAS5-02107). The SRON effort was partially financed by the European FP6 program, under the AMSTAR joint research activity.

Hesler, Porterfield, Bishop and Crowe are employed by Virginia Diodes, Inc., Charlottesville, VA 22902, USA. Hesler and Crowe are additionally employed by the University of Virginia Department of Electrical Engineering, Charlottesville, VA 22903, USA

Baryshev, Hesper and Baselmans are employed by the Space Research Organization, Netherlands, 9700 AV GRONINGEN, NL

Fig. 1: A THz source consisting of a low frequency coaxial input, an integrated doubler/amplifier, a quadrupler and two triplers. It has generated up to 25 microwatts in the WR-0.65 waveguide band. Total length is six-inches. No mechanical tuners are used.

A primary aspect of the VDI frequency multipliers is the integrated diode circuit technology, depicted in Fig. 2. This image shows an integrated GaAs-on-quartz diode circuit/mounted into a waveguide housing. The quartz circuit incorporates two waveguide probes, frequency filters, impedance matching elements, other passive circuit elements and the GaAs diode mesas. The GaAs material is only several microns thick and is present only in the areas required to define the Schottky and ohmic contacts. The GaAs epitaxial material is bonded to the quartz at the wafer level. The critical diode regions are then defined photolithographically and all other GaAs material is removed. The integration process minimizes shunt capacitance, achieves alignment precision at the micron level and completely eliminates the need for handling, aligning and soldering microscopic diode chips. The circuit shown in Fig. 2 is actually a 220 GHz phase shifter [2] where the diode bias is used to modulate the diode capacitance, thereby achieving up to 180 degrees of phase shift.

The output power of the frequency quadrupler is shown in Fig. 3. This component is a cascade of two varactor doublers mounted into a single housing. The bias voltage on each doubler can be adjusted to achieve maximum tuning band. The total efficiency of the quadrupler peaks at about 10%.

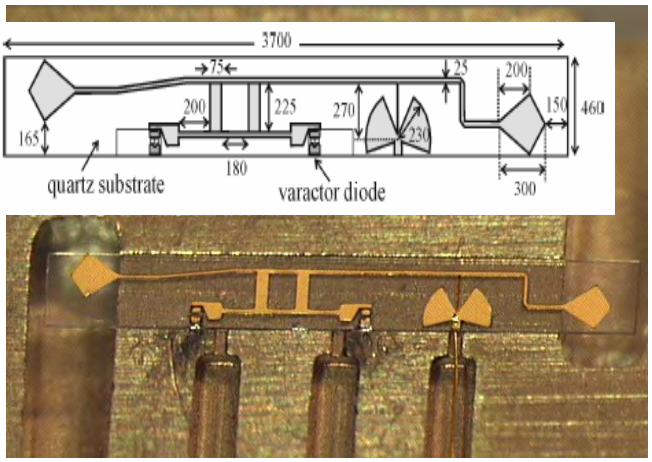

Fig. 2: An integrated GaAs-on-quartz diode circuit mounted in a waveguide housing. The diode bias is used to control the diode capacitance, thereby achieving control of the phase of the transmitted signal. 180 degrees of phase shift is achieved at 220 GHz [2].

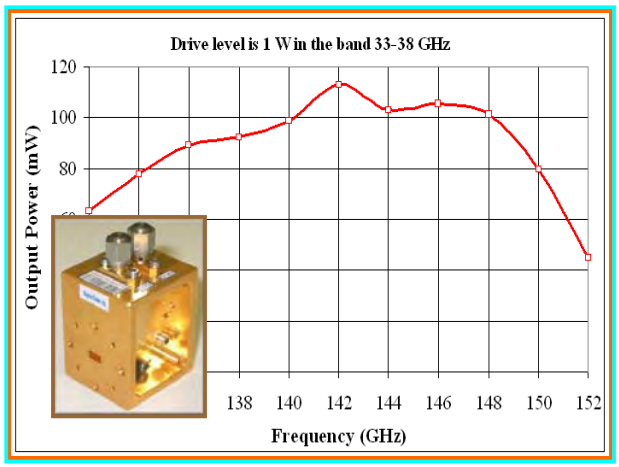

Fig. 3: The output power from the Q145 frequency quadrupler. The bias of the two doubler stages can be adjusted to achieve maximum bandwidth, as shown in the graph. However, similar performance is achieved with fixed voltage bias over most of the frequency range.

The output power of the first frequency tripler is shown in Fig. 4. This component operates across the entire WR-2.2 waveguide band. It has a typical efficiency of 3-5%, depending on the input power level and frequency. Significant ripple is seen in the graph, particularly at the lower edge of the band. This is unfortunately fairly common in cascaded multiplier chains and is generally caused by standing waves between the non-linear components. Good impedance matching can reduce this effect to negligible levels. However, this is often difficult to achieve across the entire waveguide band, particularly since the input impedance of each component will change with the input power level.

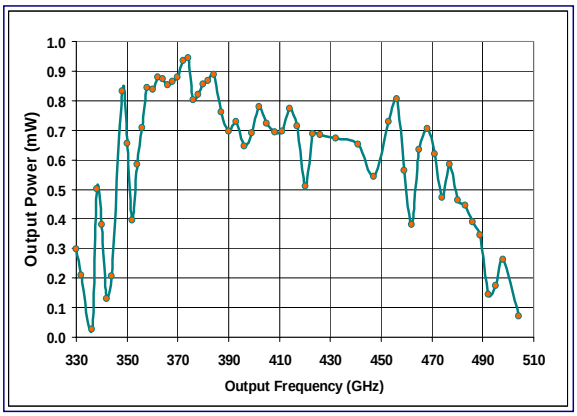

Fig. 4: The measured output power of the WR2.2x3 frequency tripler when driven with about 25mW. The ripple pattern is caused by standing wave effect, as described in the text. When driven with greater power levels, several milliwatts of output power are achieved.

The output power of the complete active multiplier chain is shown in Fig. 5. The input power to the final tripler is also shown. Two separate drivers, consisting of the input doubler/amp and quadrupler were used to achieve this data. The first generated about 2-3mW input to the tripler and produced an 8-12 microwatt output from 1250 – 1320 GHz. The second driver had lower power 0.5-2 mW, but greater bandwidth. It generated about 2-4 microwatts from 1350 – 1535 GHz. Other driver modules can be used to achieve coverage over the frequency band from 1.1 – 1.7 THz and we have achieved as much as 20 microwatts near 1.3 THz using a higher power driver. An important future goal is to achieve individual drivers that cover the entire frequency band with sufficient power.

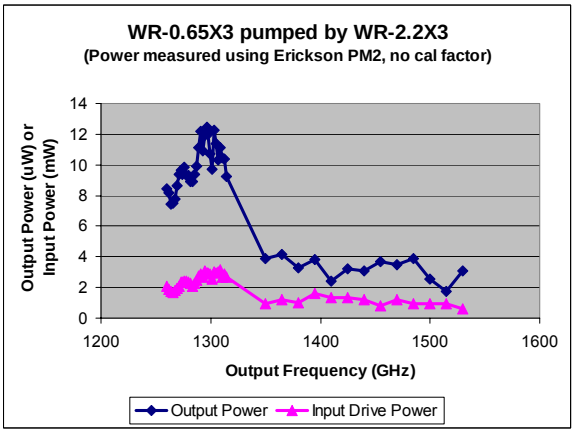

Fig. 5: The measured output power from the active multiplier chain. Two different driver modules, consisting of the input doubler/amp and the quadrupler, were required to achieve this data.

II. Terahertz Source Evaluation

One of the active multiplier chains was tested extensively at SRON with the goal of demonstrating its suitability for use as a local oscillator for HEB mixers in astronomical receivers [3,4]. Although the power level has already been shown to be sufficient by direct measurements, other requirements include narrow linewidth, lack of

spurious signals, stability and low noise. In these measurements the active multiplier chain was driven with a standard Rohde & Schwarz synthesizer (SMP). The terahertz power was coupled to the bolometer with a mylar beam splitter and the LO coupling loss was about 13dB. The coupled power was adjusted with a rotating polarizer.

Spectral analysis by Fourier Transform Spectroscopy indicates that the output signal is very pure, with unwanted harmonics and other signals at least 20 dB below the main signal. Figure 6 shows a spectral measurement of ethanol gas (with a small amount of water). This result indicatess the narrow linewidth of the source and the lack of significant spurious signals.

The source was then used to pump an HEB mixer. Figure 7 shows the IV of the mixer at various LO pumping levels. This result shows that the source had sufficient power to fully saturate the mixer. Figure 8 is a graph of the receiver noise temperature (uncorrected) as a function of bias voltage and LO power. The measurements were made with standard hot/cold (300/78K) load techniques and a 1.5 GHz IF amplifier with 80 MHz bandwidth. Regions of excellent performance (Trec ~ 1,300K, DSB) were measured. This result is comparable to the best results achieved to date [5,6,7,8] and equivalent to those achieved with the same receiver and other LO sources including a molecular gas laser. This indicates that the solid-state LO is not adding any significant additional noise to the receiver.

Finally, the IF power was measured for a period of minutes with hot and cold sources. It is well known that the IF power is a sensitive function of the LO power coupled to the junction, so a stable IF power level indicates good amplitude stability of the source. Figure 9 shows the result of these measurements; which indicates that the source is indeed stabile enough for astronomical measurements.

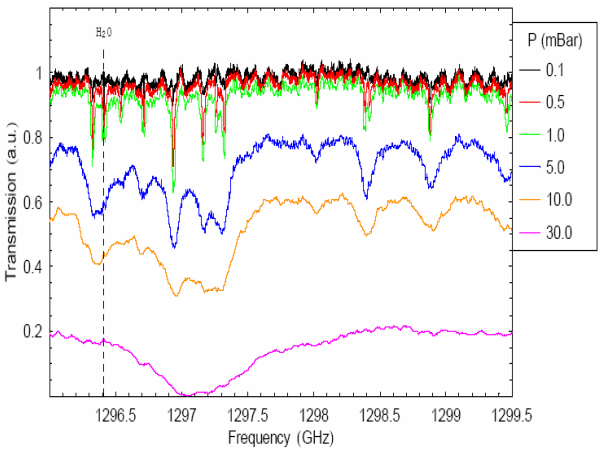

Fig. 6: A measurement of the absorption lines of ethanol and water at various pressures in a one meter long gas cell. These results indicate the narrow linewidth of the terahertz source and the lack of spurious signals.

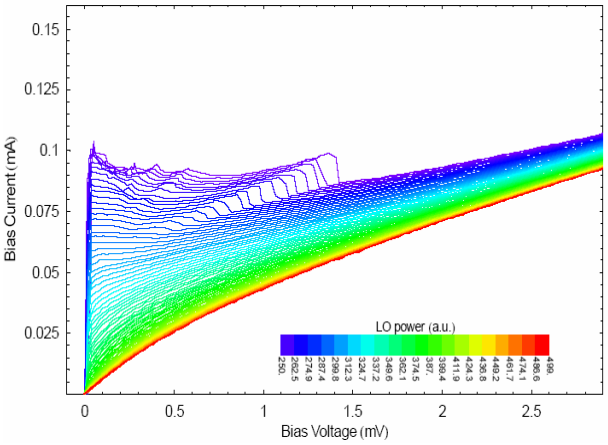

Fig. 7: The pumped IV curve of the HEB junction, showing that the source fully saturates the device.

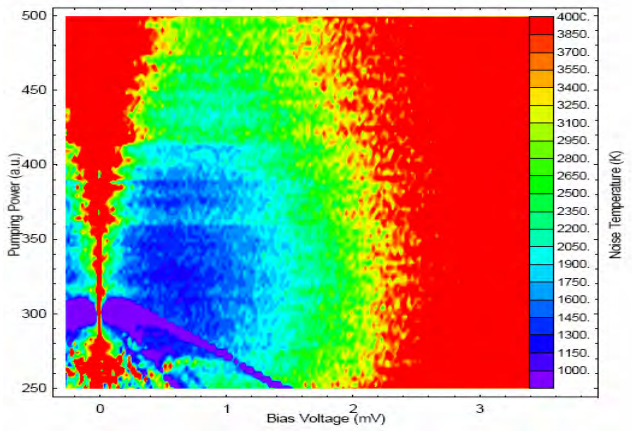

Fig. 8: The mixer noise temperature of the HEB as a function of Bias and LO Power at about 1.3 THz. The mixer is fully pumped and achieves excellent noise temperature. Best performance is achieved in the dark blue regions (1,300K); the narrow purple strip is a spurious response of the mixer.

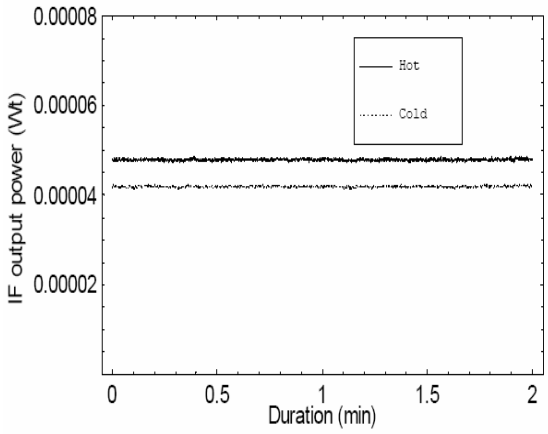

Fig. 9: The IF output power from the mixer as a function of time for hot and cold load conditions. Since the IF power is very sensitive to LO power level, this result indicates that the source has excellent amplitude stability, as is required for astronomical measurements.

III. Conclusion

This paper has reviewed the construction and evaluation of an active frequency multiplier chain for use as a terahertz local oscillator for HEB mixers in radioastronomical observations. The active multiplier uses a commercially available millimeter-wave amplifier and a chain of planar and integrated frequency multipliers to increase the frequency to the WR-0.65 waveguide band (1.1 – 1.7 THz). The chain has been designed to be driven by a standard commercial sweeper or synthesizer below 20 GHz with less than 100mW required to saturate the amplifier. The complete multiplier chain has a length of less than six inches and has no mechanical tuners of any type. The multiplier chain generates power levels in the 5-20 microwatt range and can be rapidly swept across a wide frequency band. The final two triplers in the chain achieve full waveguide band performance. However the driver amplifier and the integrated quadrupler have more limited bandwidth. Typically this limits the tuning band of the final source to of order 100 200 GHz, depending on the power level required and the specific frequency region desired. This drawback can be overcome either by developing better drivers, or reducing the power required by the triplers. Both paths will be pursued in future research.

The analysis of the source was performed at SRON. These measurements included analysis of the spectral purity and linewidth, demonstration that the source readily saturates an HEB mixer, the measurement of low noise mixer performance and evaluation of the amplitude stability via a measurement of the IF power over time. In all regards the source performed very well, indicating that it is well suited for use as an LO for HEB mixers.

REFERENCES

[1] Spacek Labs, Inc., 212 Gutierrez Street, Santa Barbara, CA 93101, www.spaceklabs.com.

[2] Z. Liu, J.C. Midkiff, H. Xu, T.W. Crowe, R.M. Weikle, II, “Broadband 180 Phase-Shifters using Integrated Submillimeter-Wave Schottky Diodes,” In press; IEEE Trans. Microwave Theory Techniques, 2005.

[3] E.M. Gershenzon, G.N. Goltsman, I.G. Gogidze, A.I. Eliantev, B.S. Karasik and A.D. Semenov, Sov. Phys. Superconductivity 3, 1582 (1990).

[4] D.E. Prober, “Superconducting terahertz mixer using a transition-edge microbolometer,” Appl. Phys. Lett. 62, 2119 (1993).

[5] J.J.A. Baselmans, J M. Hajenius, R. Gao, T.M. Klapwijk, P.A.J. de Korte, B. Voronov, G. Goltsman, “Doubling of sensitivity and bandwidth in phonon cooled hot electron bolometer mixers,’ Appl. Phys. Lett. 84, 1958 (2004).

[6] A.D. Semenov, H.-W. Huebers, J. Schubert, G. N. Goltsman, A. I. Elantiev, B. M. Voronov, E. M. Gershenzon, “Design and performance of the lattice-cooled hot-electron terahertz mixer,” J. Appl. Phys. 88, 6758 (2000).

[7] S. Cherednichenko, P. Khosropanah, E. Kollberg, M. Kroug, H. Merkel, “Terahertz superconducting hot-electron bolometer mixers,” Physica C, Vol. 372-376, p. 407 (2002).

[8] J. J. A. Baselmans, A. Baryshev, S. F. Reker, M. Hajenius, J. R. Gao, T. M. Klapwijk, Yu. Vachtomin, S. Maslennikov, S. Antipov, B. Voronov,and G. Goltsman, “Direct detection effect in small volume hot electron bolometer mixers,” Appl. Phys. Lett. 86, 163503 (2005).

AlGaN/GaN Heterostructure Transit-Time Devices: A Novel Device Concept for Submillimeter-Wave Sources

H. Eisele
Institute of Microwaves and Photonics
School of Electronic and Electrical Engineering
University of Leeds, Leeds LS2 9JT, United Kingdom

M. Singh
Research Laboratory of Electronics
Massachusetts Institute of Technology
Cambridge, MA 02139-4307, USA

Y.-R. Wu, J. Singh, and G. I. Haddad
Solid-State Electronics Laboratory
Department of Electrical Engineering and Computer Science
University of Michigan, Ann Arbor, MI 48109-2122, USA

***Abstract*— A novel transit-time device structure for low-noise RF power generation at high millimeter-wave and submillimeter-wave frequencies is proposed. It takes advantage of the unique tunneling properties in strained AlGaN/GaN heterojunctions. The device simulations take realistic heat management for continuous-wave operation on diamond heat sinks into account and, as initial results, predict tunability over a large frequency range and RF power levels (and corresponding dc-to-RF conversion efficiencies) of $>$ 240 mW ($>$ 5%) around 160 GHz and $>$ 15 mW ($>$ 2%) around 320 GHz.**

I. Introduction

A rapidly increasing number of emerging systems applications at submillimeter-wave frequencies, such as imaging, chemical or biological sensing, and wide-bandwidth communications, depends on the availability of compact, reliable, and efficient oscillators [1]. High spectral purity is also a prerequisite when these sources are employed as transmitters or local oscillators (LO) in such applications. Tunneling was recognized as a fast and quiet carrier injection mechanism for transit-time devices in 1958 and the tunnel injection transit-time (TUNNETT) diode was proposed as a millimeter- and submillimeter-wave source [2]. Its operation at submillimeter-wave frequencies was demonstrated first in a pulsed mode [3] and GaAs has been the most commonly used material sytem. Substantial advances in epitaxial growth techniques and refined diode fabrication technologies yielded much improved GaAs TUNNETT diodes whose operation in the continuous-wave (CW) mode was first achieved at V-band (50–75 GHz) and W-band (75–110 GHz) frequencies [4], [5] and, with further improvements in thermal management and oscillator circuits, up to 400 GHz [6]–[9].

Immaterial of the high-frequency properties of the carrier injection mechanism, the carrier drift velocities v_s, dielectric constant ϵ_s, and maximum electric field E_c of the employed semiconductor material system are responsible for the ultimate performance limits of all transit-time devices at high submillimeter-wave frequencies [10]. GaAs as a semiconductor material with direct interband tunneling offers excellent tunneling properties, but its carrier drift velocities, dielectric constant, and breakdown electric field are not so favorable as can be seen from the comparison of relevant semiconductor material properties in Table I.

TABLE I
Properties of Important Semiconductors for RF Power Generation

Property at 300 K	Si	GaAs	InP	6H-SiC (4H-SiC)	GaN	Diamond
Bandgap [eV]	1.12	1.42	1.34	3.06 (3.26)	3.39	5.5
Electron mobility [cm^2/V•s] $\perp$ c-axis $\parallel$ c-axis	1400	8500	4600	400 (850) 80 (1020)	900	2200
Hole mobility [cm^2/V•s]	450	400	140	90 (115)	150	1600
Breakdown field at $N_D \approx 10^{17}$ cm^{-3} [MV/cm]	0.61	0.65	0.75	2.5 (2.2)	2	10
Thermal conductivity [W/cm•K]	1.25	0.46	0.68	4.9	1.3	20
Saturated electron drift velocity at $E > 0.5$ MV/cm [$\times 10^7$ cm/s]	1	0.6	0.75	2	1.6	2.7
Dielectric constant	11.8	12.8	12.6	9.7	9	5.5
Electronic P_{RF} figure of merit, relative to Si $(E_c v_s)^2$	1	0.4	0.9	70	25	2000

This table also shows that the relevant material parameters of GaN, including a higher thermal conductivity, are more favorable than those of GaAs. In addition, the wide bandgap of GaN allows higher safe operating temperatures. Current epitaxial growth techniques, however, are unable to produce the p- and n-type doping levels that are sufficiently high for significant interband tunneling.

II. Physics and Properties of GaN/AlGaN Heterojunctions

Different electronegativities of the group III atoms (Ga, Al, etc.) and N atoms cause III-V nitrides to be strongly

polar semiconductor materials. The wurtzite crystal structure is common in the epitaxial growth of nitrides like GaN and AlGaN and Table I lists some of the properties of GaN in this crystal structure. III-V nitride heterostructures show the presence of piezoelectric and spontaneous polarization charges at the interface of two different materials [11] (for [0001] growth). This feature is commonly not seen in III-V arsenides grown along the [100] direction and offers a novel method of introducing charges at the interface region of the heterojunction [12]. Such an approach frees device designers from some of the limitations involved in doping wide bandgap semiconductors. Tunneling transport across III-V heterojunction diodes has been studied before [13] and these studies revealed good agreement with experimentally observed contact resistance values [14].

The case of an $Al_xGa_{1-x}N$ epitaxial layer grown on a GaN substrate is considered here. The total polarization charge $P(x)$ depends on the Al composition x and has the value [15]

$$\begin{aligned} P(x) &= P_{pz} + P_{sp} \\ &= (-3.2 \times x - 1.9x^2) \times 10^{-6}\ \mathrm{C/cm^2} \\ &\quad -5.2 \times 10^{-6} x\ \mathrm{C/cm^2} \end{aligned} \tag{1}$$

In this system, the effects arising from the piezoelectric effect P_{pz} and the spontaneous polarization mismatch P_{sp} are comparable. However, these two effects may have opposite directions depending on the surface termination conditions and the lattice mismatch between the epitaxial layer and the effective substrate. Because of better crystal morphology, Ga-faced growth is preferred to N-faced growth in most cases and results in the same directions of both effects.

The tunneling transport across the barrier is very sensitive to the composition of the $Al_xGa_{1-x}N$ barrier layer as well as its thickness. For small thicknesses, the probability of tunneling through the barrier is high, but the charge control model shows that there is very little carrier population in the two-dimensional electron gas (2DEG). In this case, there are no allowed 2DEG states for electrons to tunnel to from the metal and, as a result, the tunnel current is supported by a final three-dimensional density of states. For large thicknesses, the number of available states is increased, but the Wenzel-Kramers-Brillouin (WKB) tunneling probability is suppressed. This corresponds to a trade-off situation where the tunneling current needs to be optimized. In the intermediate range, the barrier thickness is large enough to allow the existence of a sizable 2DEG and small enough to allow tunneling through the barrier.

III. Device Simulations

A. Device structure and simulation method

Figure 1 shows the schematic structure of the proposed device. This structure consists of a Schottky contact and the AlGaN/GaN heterojunction as the tunnel injection region. The subsequent n-type doping spike reduces the electric field from values of more than 3 MV/cm at the heterojunction to values of 100–500 KV/cm for electrons (and holes) in the drift region to travel at the highest possible drift velocities. The wide bandgap of GaN makes the formation of excellent ohmic contacts rather difficult. Ohmic contacts with very low contact resistances have been reported [14]–[18], but they are not considered as fully compatible with the envisaged device fabrication technologies. Therefore, a second Schottky contact on the n-type contact region is used instead [19], [20]. Its voltage drop is small compared to the applied bias voltages of more than 12 V and its equivalent contact resistance drops well below $1 \times 10^{-6}\ \Omega\mathrm{cm}^2$ for the applied current densities of more than 50 $\mathrm{kA/cm}^2$.

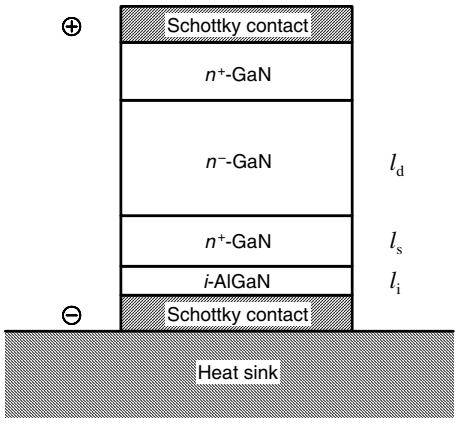

Fig. 1. Schematic structure of the AlGaN/GaN heterojunction transit-time device.

Solving the time-dependent Schrödinger equation for the complete device structure is too computing intensive. Tunneling is much faster when compared with the RF cycles that are considered in this paper. Therefore, the simulation runs for the RF performance predictions are split into two parts. One program considers the tunneling process and determines the quasi-static current-voltage characteristics of the AlGaN/GaN heterojunction. These characteristics are then converted to field-dependent current densities at the location of the heterojunction interface. The subsequent runs of the other program with the hydrodynamic device model [21] use these injection current densities as a variable boundary condition and take the complete doping profile of the device into account. This program determines the device impedance, RF output power, dc-to-RF conversion efficiency, and operating junction temperature as a function of the operating frequency.

B. Band-structure and tunneling calculations

Details of the model have been published earlier [12], [13], [22]. Essentially it involves the following two steps:

- Self-consistent solution of the Schrödinger and Poisson equations to obtain the wavefunctions and energies for the carriers in the heterostructure as well as the shape of the conduction band;

- Use of the quantities obtained above to calculate the Wenzel-Kramers-Brillouin tunneling probability at each energy.

The tunneling current can then be calculated [13]. The results for a device structure with an $Al_{0.3}Ga_{0.7}N$/GaN heterojunction are shown in Fig. 2(a), while the results for an $Al_{0.15}Ga_{0.85}N$/GaN heterojunction are shown in Fig. 2(b), both assuming an active-layer temperature of 600 K. The higher Al composition of 30% is used in the device because better band alignment yields a higher reverse bias current.

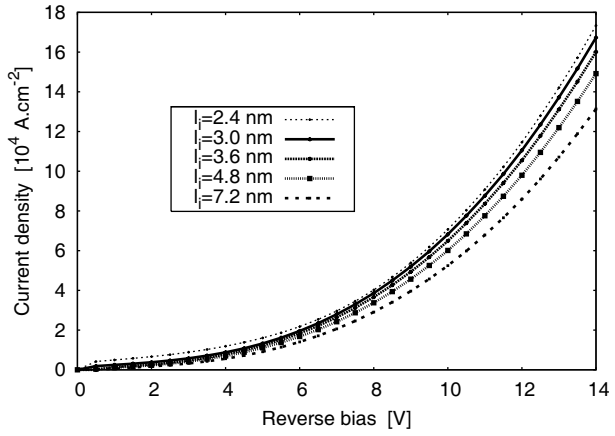

(a) $Al_{0.3}Ga_{0.7}N$/GaN, T = 600 K

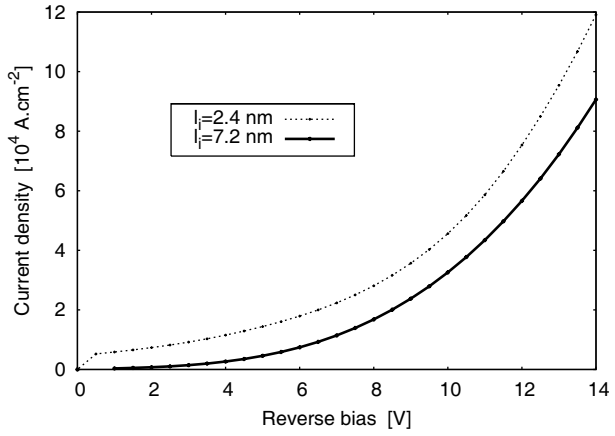

(b) $Al_{0.15}Ga_{0.85}N$/GaN, T = 600 K

Fig. 2. Reverse-bias tunnel current for two Al compositions x and different thicknesses l_i of the $Al_xGa_{1-x}N$ layer.

C. RF simulations

The hydrodynamic model uses material parameters of GaN which were taken from published results of Monte Carlo simulations [23], [24] and experiments [25]. Impact ionization was found to play an insignificant role in this device. However, it is taken into account in the simulation program with appropriate rates for GaN [26].

Thermal management with proper heat sinks critically affects the performance of all fundamental solid-state sources at millimeter- and submillimeter-wave frequencies. Diamond is the material with best thermal properties above 200 K and is the first choice for such a heat sink. Realistic device simulations need to take the influence of the heat sink, that is, the substantial temperature rise inside the heat sink, properly into account. The importance of this can be seen with the IMPATT diode of [27], which actually operates in the CW mode at much higher junction temperatures than 600 K as assumed in that paper. The spreading approximation [28] predicts the thermal resistance of mesa-type two-terminal devices and has yielded excellent agreement with measurements on Si and GaAs IMPATT diodes as well as GaAs and InP Gunn devices since its inception more than two decades ago. This approximation method predicts that the junction temperature of the diode with the area of 1×10^{-6} cm^2 exceeds 2000 K at the bias voltage and current of 50 V and 300 mA [27], respectively, when a diamond heat sink with a typical metalization scheme and a thermal conductivity at 500 K of 11 W/cmK are assumed.

Table II lists the device parameters and bias conditions that have resulted in the best performance so far around the two center frequencies considered in this paper. The thickness of the $Al_{0.3}Ga_{0.7}N$ layer was kept at 4.8 nm. As can be seen from Fig. 2(a), this thickness meets the requirements for efficient device operation: the injected tunneling current is very small at reverse bias voltages below 3 V and rapidly reaches current densities of more than 50 kA/cm^2 at reverse bias voltages of more than 5 V, thus ensuring a sharp turn-on of the carrier injection during the RF cycle.

During the RF simulation runs, the bias current densities were adjusted such that the operating junction temperatures of devices in the CW mode on diamond heat sinks remained below 600 K. To maintain the same load conditions for comparison purposes, the real part of the load impedance, $\underline{Z}_L = R_L + jX_L$, was kept fixed at 1 Ω and the device area at different frequencies adjusted accordingly.

Fig. 3 compares the predicted heat flow resistances of the AlGaN/GaN heterostructure transit-time devices with those of the aforementioned GaAs TUNNETT diodes [6], [29]. The GaN-based devices show much lower heat flow resistances, in particular for device diameters below 25 μm as used in the simulations. Lower heat flow resistances and higher permissible active-layer operating temperatures allow the devices to be operated at dc input power levels higher than those of GaAs TUNNETT diodes. Therefore, much higher RF output power levels are generated.

IV. Results

Fig. 4 shows the RF power levels and corresponding dc-to-RF conversion efficiencies for device structure 1 designed for a center operating frequency of 160 GHz and for a specific contact resistance of 1×10^{-6} Ωcm^2. The device generates more than 240 mW around the design frequency and more than 150 mW over a wide frequency range of 135–200 GHz, which makes the devices well suited for tunable sources in an oscillator circuit with a wide tuning range. The dc input power consumption is less

TABLE II
DEVICE PARAMETERS

Parameter	Structure 1	Structure 2
f_{design} [GHz]	160	320
l_{i} [nm]	4.8	4.8
l_{s} [nm]	54	54
l_{d} [nm]	545	245
N_{s} [$\times 10^{16}$/cm^2]	130	160
N_{d} [$\times 10^{16}$/cm^2]	3	4.5
J_{DC} [kA/cm^2]	55	80
V_{DC} [V]	24	14

than 5 W, which allows the device to be used in portable systems applications.

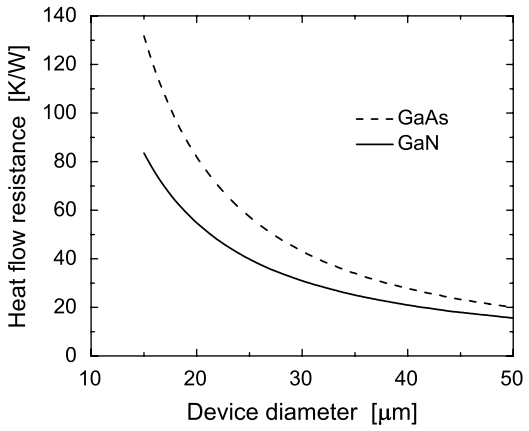

Fig. 3. Predicted heat flow resistances of GaAs and GaN devices on diamond heat sinks

Device structure 2 operates at a higher current density and, therefore, the simulation results of Fig. 5 are based on a lower specific contact resistance of 5×10^{-7} Ωcm^2. Similar to structure 1, the device operates over a wide frequency range with more than 12 mW at 280–380 GHz. The device generates more than 15 mW around the design frequency of 320 GHz. With a bias voltage of less than 14 V and a total dc input power consumption of less than 0.9 W, this device is well suited for battery-operated systems applications.

V. CONCLUSIONS

A novel device structure for low-noise power generation at millimeter- and submillimeter-wave frequencies was proposed and simulated in two frequency ranges around 160 GHz and 320 GHz. The predictions take realistic contact resistances and heat sink properties into account. The predicted RF power levels compare favorably with those from other two-terminal devices in the same frequency range. More importantly, the proposed device structure offers much higher dc-to-RF conversion efficiencies than

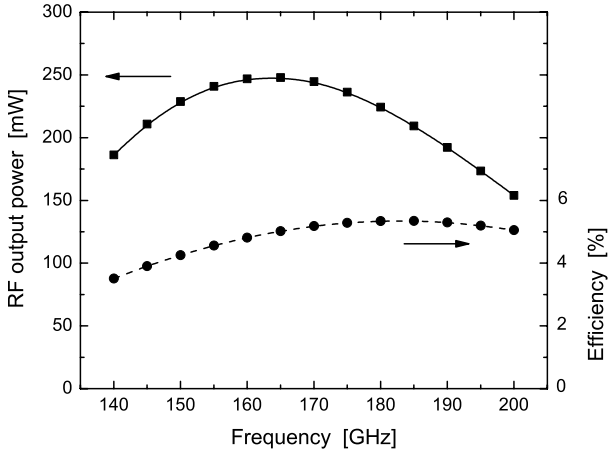

Fig. 4. Predicted RF performance of structure 1

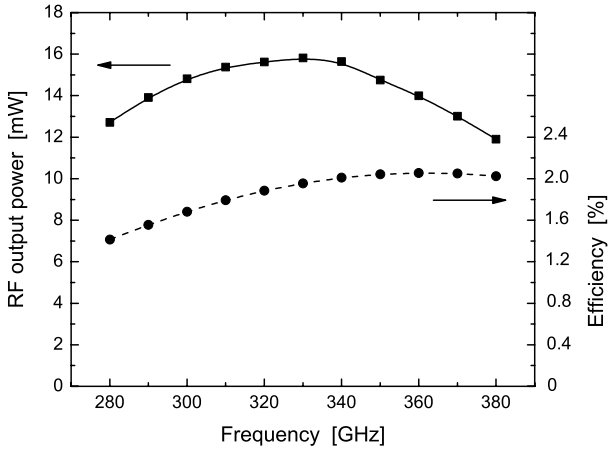

Fig. 5. Predicted RF performance of structure 2

those predicted for other two-terminal devices in the same frequency range.

Additional fine-tuning of the doping profiles and heterojunction parameters is expected to improve the RF performance even further. However, significant advances in device fabrication technologies for GaN-based devices similar to those established for GaAs- and InP-based devices are prerequisites before the potential of these novel devices can be harnessed.

This type of device is also expected to generate signficant amounts of RF power at much higher submillimeter-wave frequencies, but additional relaxation time constants need to be taken into account in the simulation model to obtain realistic performance predictions and optimum device designs.

REFERENCES

[1] P. Siegel, "Terahertz technology," *IEEE Trans. Microwave Theory Tech.*, vol. 50, pp. 910–928, 2002.
[2] J. Nishizawa and Y. Watanabe, "High frequency properties of the avalanching negative resistance diode," Research Institute Tohoku University, Tech. Rep., 1958.

[3] J. Nishizawa, K. Motoya, and Y. Okuno, "Submillimeter-wave oscillation from GaAs TUNNETT diode," in *Proc. 9^{th} European Microwave Conf.*, Sept. 17–20, 1979, pp. 464–467, Brighton, UK.

[4] M. Pöbl, C. Dalle, and W. Harth, "CW mm-wave GaAs TUNNETT diode," *Electron. Lett.*, vol. 26, pp. 1540–1542, 1990.

[5] C. Kidner, H. Eisele, and G. I. Haddad, "Tunnel injection transit-time diodes for W-band power generation," *Electron. Lett.*, vol. 28, no. 5, pp. 511–513, 1998.

[6] H. Eisele, A. Rydberg, and G. I. Haddad, "Recent advances in the performance of InP Gunn devices and GaAs TUNNETT diodes for the 100–300 GHz frequency range and above," *IEEE Trans. Microwave Theory Techniques*, vol. 48, no. 4, pp. 626–631, April 2000.

[7] P. Płotka, J-i. Nishizawa, T. Kurabayashi, and H. Makabe, "240-325-GHz GaAs CW Fundamental-Mode TUNNETT Diodes Fabricated With Molecular Layer Epitaxy," *IEEE Trans. Electron Devices*, vol. 50, no. 4, pp. 867–873, April 2003.

[8] H. Eisele, "355 GHz oscillator with GaAs TUNNETT diode," *Electron. Lett.*, vol. 41, no. 6, pp. 329–331, March 2005.

[9] J-i. Nishizawa, P. Płotka, H. Makabe, and T. Kurabayashi, "290-393-GHz CW fundamental-mode oscillation from GaAs TUNNETT diode," *Electron. Lett.*, vol. 41, no. 7, pp. 80–81, March 2005.

[10] G. I. Haddad, J. East, and H. Eisele, "Two-terminal active devices for terahertz sources," in *Vol I: Electronic Devices and Advanced Systems Technology*, ser. Terahertz Sensing Technology, D. Woolard, M. S. Shur, and W. Leorop, Eds. Singapore: World Scientific Publishing, 2003, pp. 45–77.

[11] O. Ambacher, J. Smart, J. R. Shealy, N. G. Weimann, K. Chu, M. Murphy, W. J. Schaff, L. F. Eastman, R. Dimitrov, L. Wittmer, M. Stutzmann, W. Rieger, and J. Hilsenbeck, "Two-dimensional electron gases induced by spontaneous and piezoelectric polarization charges in N- and Ga-face AlGaN/GaN heterostructures," *J. Appl. Phys.*, vol. 85, pp. 3222–3233, 1999.

[12] M. Singh, Y. Zhang, J. Singh, and U. Mishra, "Examination of tunnel junctions in the AlGaN/GaN system: consequences of polarization charge," *Appl. Phys. Lett.*, vol. 77, no. 12, pp. 1867–1869, 2000.

[13] M. Singh, J. Singh, and U. Mishra, "Current-voltage characteristics of polar heterostructure junctions," *J. Appl. Phys.*, vol. 91, no. 5, pp. 2989–2993, March 2002.

[14] D. Qiao, L. Jia, L. S. Yu, P. M. Asbeck, S. S. Lau, S. H. Lim, Z. Liliental-Weber, T. E. Haynes, and J. B. Barner, "Ta-based interface ohmic contacts to AlGaN/GaN heterostructures," *J. Appl. Phys.*, vol. 89, no. 10, pp. 5543–5546, 2001.

[15] I. P. Smorchkova, C. R. Elsass, J. P. Ibbetson, R. Ventury, B. Heying, P. Fini, E. Haus, S. P. DenBaars, J. S. Speck, and U. K. Mishra, "Polarization-induced charge and electron mobility in AlGaN/GaN heterostructures grown by plasma-assisted molecular-beam epitaxy," *J. Appl. Phys.*, vol. 86, no. 8, pp. 4520–4526, 1999.

[16] Z. Fan, S. N. Mohammad, W. Kim, O. Aktas, A. E. Botchkarev, and H. Morko, "Very low resistance ohmic contacts to n-GaN," *Appl. Phys. Lett.*, vol. 68, no. 12, pp. 1672–1674, 1996.

[17] J. Burm, K. Chu, W. A. Davis, W. J. Schaff, L. F. Eastmann, and T. J. Eustis, "Ultra-low resistive ohmic contacts on n-GaN using Si implantation," *Appl. Phys. Lett.*, vol. 70, no. 4, pp. 464–466, Jan. 1997.

[18] S. J. Cai, R. Li, Y. L. Chen, L. Wong, W. G. Wu, S. G. Thomas, and K. L. Wang, "High performance AlGaN/GaN HEMT with improved ohmic contacts," *Electron. Lett.*, vol. 34, no. 24, pp. 2354–2356, Nov. 1998.

[19] Y. Konishi, S. T. Allen, M. Reddy, and M. J. W. Rodwell, "AlAs/GaAs Schottky-Collector Resonant-Tunnel-Diodes," *Solid-State Electron.*, vol. 36, no. 12, pp. 1673–1676, 1993.

[20] M. Tschernitz and J. Freyer, "140 GHz GaAs double-Read IMPATT diodes," *Electron. Lett.*, vol. 31, no. 7, pp. 582–583, 1995.

[21] C.-C. Chen, R. K. Mains, G. I. Haddad, and H. Eisele, "Numerical simulation of TUNNETT and MITATT devices in the millimeter and submillimeter range," in *Proc. 4^{th} Int. Symp. Space Terahertz Technology*, Los Angeles, CA, March 30 - April 1, 1993, pp. 362–376.

[22] Y.-R. Wu, M. Singh, and J. Singh, "Gate leakage suppression and contact engineering in nitride heterostructures," *J. Appl. Phys.*, vol. 94, no. 9, pp. 5826–5831, 2003.

[23] J. Kolník, Í. H. Oğuzman, K. F. Brennan, R. Wang, P. P. Ruden, and Y. Wang, "Electronic transport studies of bulk zincblende and wurtzite phases of GaN based on an ensemble Monte Carlo calculation including a full zone band structure," *J. Appl. Phys.*, vol. 78, no. 2, pp. 1033–1038, July 1995.

[24] J. D. Albrecht, R. P. Wang, P. P. Ruden, M. Farahmand, and K. F. Brennan, "Electron transport characteristics of GaN for high temperature device modeling," *J. Appl. Phys.*, vol. 83, no. 9, pp. 4777–4781, May 1998.

[25] M. Wraback, H. Shen, J. C. Carrano, T. Li, J. C. Campbell, M. J. Schurman, and I. T. Ferguson, "Time-resolved electroabsorption measurement of the electron velocity-field characteristic in GaN," *Appl. Phys. Lett.*, vol. 76, no. 9, pp. 1155–1157, Feb. 2000.

[26] J. Kolník, Í. H. Oğuzman, K. F. Brennan, R. Wang, and P. P. Ruden, "Monte Carlo calculation of electron initiated impact ionization in bulk zinc-blende and wurtzite GaN," *J. Appl. Phys.*, vol. 81, no. 2, pp. 726–733, Jan. 1997.

[27] A. Reklaitis and L. Reggiani, "Monte-Carlo study of hot-carrier transport in bulk wurtzite GaN and modeling of a near-terahertz impact avalanche transit-time diode," *J. Appl. Phys.*, vol. 95, no. 12, pp. 7925–7935, 2004.

[28] L. H. Holway and M. G. Adlerstein, "Approximate formulas for the thermal resistance of IMPATT diodes compared with computer calculations," *IEEE Trans. Electron Devices*, vol. 24, pp. 156–159, 1977.

[29] H. Eisele and G. I. Haddad, "Enhanced performance in GaAs TUNNETT diode oscillators above 100 GHz through diamond heat sinking and power combining," *IEEE Trans. Microwave Theory Tech.*, vol. 42, no. 12, pp. 2498–2503, Dec. 1994.

HBV Frequency Quintuplers

Arne Øistein Olsen, Tomas Bryllert, Josip Vukusic, Tahereh Arezoo Emadi, Peter Sobis, and Jan Stake

***Abstract*— A 500 GHz heterostructure-barrier-varactor quintupler has been designed and fabricated. The design consists of a mixture of waveguide and microstrip components for impedance matching. A InP based HBV diode is flip-chip mounted onto the quartz circuit, where beam-leads are used for ground connections to the waveguide block. Extensive back-side processing has been carried out in order to create these beam-leads. The multiplier is a frequency scaled version of a successful 100 GHz quintupler with a conversion efficiency of 11.4%.**

***Index Terms*— Harmonic generation, heterostructure barrier varactor (HBV), sub-millimeter wave, multiplier, quintupler.**

I. Introduction

Frequency multipliers are commonly used in sub-millimetre wave frequency region, due to lack of fundamental frequency sources. The heterostructure-barrier-varactor (HBV) diode [1], which only generates odd harmonics, is particularly suitable for frequency multipliers. So far the HBV has mostly been used in frequency triplers ($\times$ 3) [2]. However, recent work has been targeted onto quintupler circuits ($\times$ 5) [3], [4], that enables higher output frequency without cascading a number of multipliers.

The 500 GHz quintupler circuit is based on a previously built 100 GHz quintupler. This frequency scaled multiplier was tested with both a GaAs based [4] and a InP based 4-barrier HBV diode [5]. Measured frequency sweeps for these diodes are shown in Fig. 1.

The multiplier is tuned for optimum performance at each measurement point, and the input power is 15 dBm. A conversion efficiency of 4.7% was obtained at an output frequency of 102.5 GHz using a GaAs HBV. The quintupler performance was later improved by using a InP HBV to 11.4%, at an output frequency of 98.5 GHz with the same input power.

II. Circuit operation

A mixture of waveguide and microstrip elements is used to provide the optimum diode embedding impedance. Two input waveguide tuners are used to match the impedance for the fundamental frequency. The required embedding impedances for the third harmonic (idler) and the output frequency are provided on the quartz substrate with circuit elements. However, a output waveguide back-short is added for flexibility. A picture of the waveguide block is shown in Fig. 2.

A. Ø. Olsen, T. A. Emadi, P. Sobis and J. Stake are with the Department of Microtechnology and Nanoscience, Microwave Electronics Laboratory, Chalmers University of Technology, SE-412 96 Göteborg, Sweden (e-mail: oistein.olsen@mc2.chalmers.se).

T. Bryllert is with the Department of Solid State Physics, Lund University, P. O. Box 118, SE-221 00 Lund, Sweden.

J. Vukusic is with the Institut d'Electronique de Microélectronique et de Nanotechnologies, Université des Sciences et Technologies de Lille, Avenue Pointcaré BP 69, 59652 Villeneuve d'Ascq Cedex, France

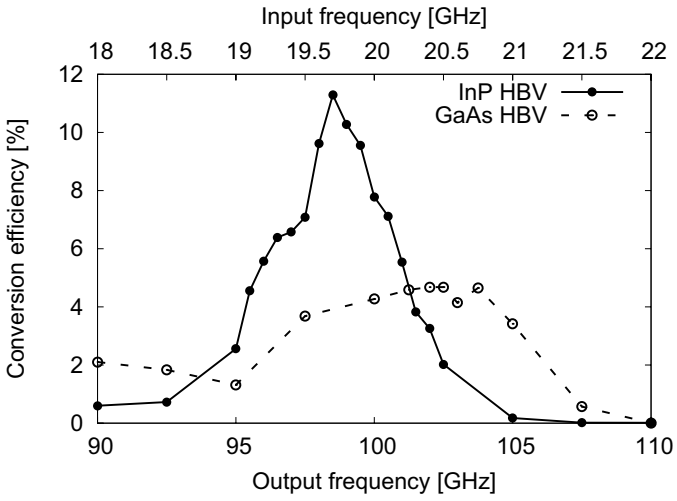

Fig. 1. 100 GHz quintupler measurement where the circuit is tuned for optimum performance at each measurement point. The input power is 15 dBm and measurements for GaAs and InP based HBV are shown.

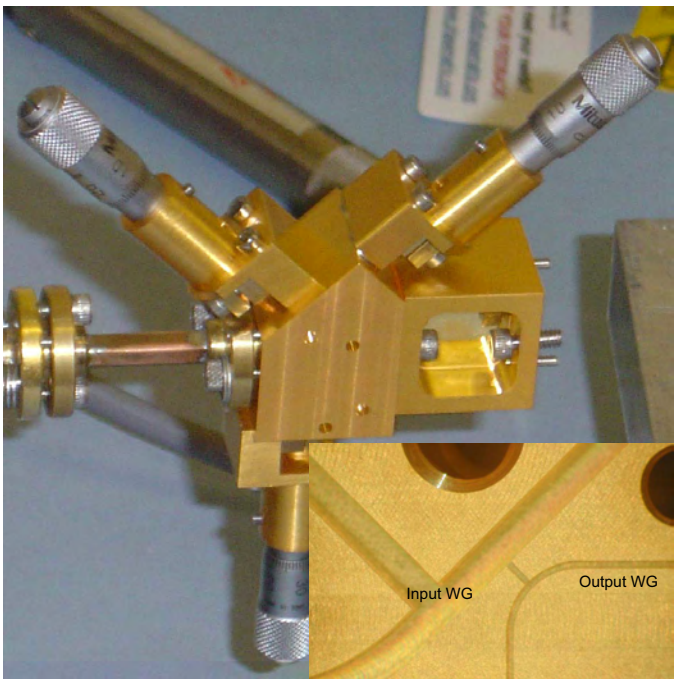

Fig. 2. Waveguide block used for the 500 GHz quintupler, and an internal view over the waveguide channels.

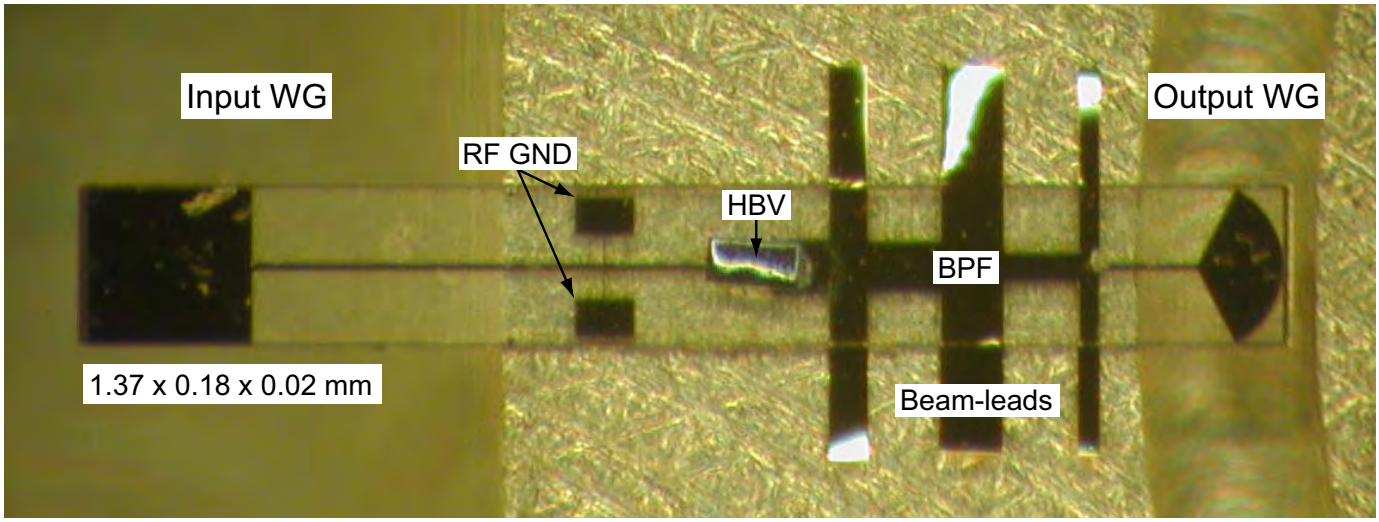

Fig. 3. Quartz circuit with the HBV, microstrip probes and microstrip circuit components.

A short rectangular waveguide section connected to the WR-8 input waveguide, and a transition block from the output WR-1.6 to WR-10 waveguide mounted at the output are also shown in the picture. The multiplier block can be spilt into two halves and an internal view of the waveguide channels is shown at the bottom of Fig. 2. Both the input and the output waveguide are bended to accommodate the waveguide tuners. A narrow channel where the circuit is placed connects the input and the output waveguides. A close-up picture of quartz circuit placed in the circuit waveguide channel is shown in Fig. 3.

The circuit substrate is 1.4 mm long, 180 μm wide and 20 μm thick. It consists of among input and output waveguide to microstrip probes. Two shunt connected hammerhead stubs and a band-pass filter provide the RF ground for the fundamental and the fifth harmonic respectively. This band-pass filter [6], which consists of a ladder-network of quarterwave shorted stubs at the fifth harmonic, also provides the real part of the embedding impedance for the output frequency. Beam-leads are used to ground the quarterwave stubs to the multiplier block, and a small amount of super-glue is used to keep the circuit in position. The HBV diode is flip-chip soldered onto the circuit, and the short inductive impedance lines connecting the diode completes the matching. Both the embedding impedances for the output frequency and the inductive idler impedance are accounted for by use of microstrip components.

III. Circuit fabrication and initial testing

Conventional photo-lithography is used to create the circuit pattern. A thin seed-layer consisting of a 70 Å thick chrome layer and gold is patterned with photoresist. The circuit pattern is plated up to an overall thickness of 1 μm. Chrome was used for the adhesive layer because of its resistance towards HF acid which is used later for the back-side processing. The 100 μm thick quartz substrate is attached upside-down onto a Si-carrier-wafer after the patterning process. A dicing saw is then used to produce the beam-leads. First is the quartz substrate lapped down to an overall thickness of 25 μm as shown in Fig. 4.

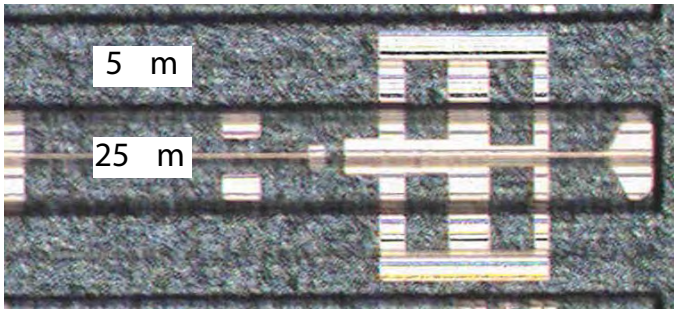

Fig. 4. Backside lapping of the quartz wafer to produce the beam-leads.

5 μm thick streets are then cut across the area above the beam-leads. The wafer is after dicing wet-etched, where 5 μm quartz is removed and the beam-leads emerge. The Cr layer is removed from the beam-leads and the circuits are separated from the carrier wafer.

An initial test has been carried out using a Gunn at 85 GHz. A couple of nano-watts was measured and the test set-up is shown in Fig. 5.

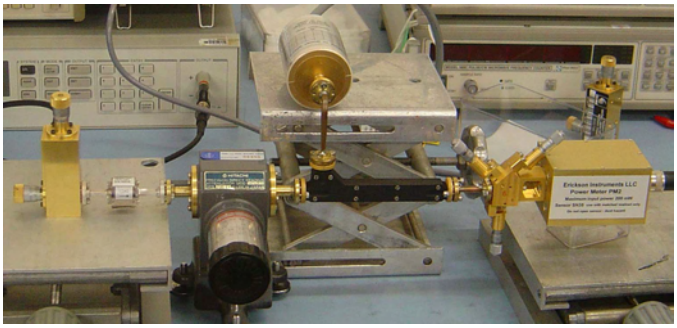

Fig. 5. Measurement set-up for the initial test consisting of a gunn oscillator, isolator, attenuator, coupler, waveguide transition and power meters.

The gunn oscillator provides 40 mW and it is connected to the multiplier through an isolator, attenuator and a coupler. The directional coupler is used to measure the reflected power.

The reflected power is used to set an initial tuning position for the input tuners. A Neil Ericksoon power meter coupled to a waveguide transition is used to measure the output frequency.

IV. Conclusion

A 500 GHz quintupler has been fabricated. It consists of backshort tuners for matching at the fundamental frequency, and conventional microstrip elements for matching at the idler and the output frequency. This quintupler is a frequency scaled version of a very successful 100 GHz quintupler. The 100 GHz quintupler obtained a conversion efficiency of 11.4% with use of a InP HBV. Extensive backside fabrication processing has been performed to create the beam-leads. Initial testing has been carried out at 85 GHz with a gunn oscillator, and an encouraging result was obtained. However, proper testing at 100 GHz input frequency with sufficient input power has to be performed to measure at the proper operation conditions.

V. Acknowledgement

Rutherford Appleton Laboratory, UK, has fabricated the multiplier waveguide block and IEMN, Université des Sciences et Technologies de Lille, France, has supplied the HBV semiconductor material. This work was supported by the ESA HBV multipler project, the EU in the form of the INTERACTION program, and FOI (Swedish Nano Technology Programme).

References

[1] E. Kollberg and A. Rydberg, "Quantum-barrier-varactor diodes for high-efficiency millimetre-wave multipliers," *Electron. Lett.*, vol. 25, no. 25, pp. 1696–1698, Dec. 1989.

[2] T. David, S. Arscott, J. M. Munier, T. Akalin, P. Mounaix, G. Beaudin, and D. Lippens, "Monolithic integrated circuits incorporating InP-based heterostructure barrier varactors," *IEEE Microwave Wireless Compon. Lett.*, vol. 12, no. 8, pp. 281–283, Aug. 2002.

[3] Q. Xiao, Y. Duan, J. L. Hesler, T. Crowe, and R. M. Weikle, "A 5-mW and 5% efficiency 210 GHz InP-based heterostructure barrier varactor quintupler," *IEEE Microwave Wireless Compon. Lett.*, vol. 14, no. 4, pp. 159–61, Apr. 2004.

[4] A. Ø. Olsen, M. Ingvarson, B. Alderman, and J. Stake, "A 100-GHz HBV frequency quintupler using microstrip elements," *IEEE Microwave Wireless Compon. Lett.*, vol. 14, no. 10, pp. 493–495, Oct. 2004.

[5] T. Bryllert, A. Ø. Olsen, J. Vukusic, T. A. Emadi, M. Ingvarson, J. Stake, and D. Lippens, "11% efficiency 100 GHz InP-based heterostructure barrier varactor quintupler," *Electron. Lett.*, vol. 41, no. 3, pp. 30–31, Feb. 2005.

[6] G. L. Matthaei, L. Young, and E. M. T. Jones, *Microwave filters, impedance-matching networks, and coupling structures*. McGraw-Hill, 1964.

Semiconductor-superlattice oscillator for generation of millimeter waves

K. F. Renk, A. Meier, B. I. Stahl, M. Jain, and W. Wegscheider
Institut für Angewandte Physik, Universität Regensburg, 93040 Regensburg, Germany

We report on a GaAs/AlAs superlattice oscillator for generation of millimeter waves. The oscillator operated at a frequency around 60 GHz. It was mechanically tuneable by about 10 %. Driven with a dc-power of about 10 mW, we reached a power of about 0.4 mW corresponding to a conversion efficiency of about 4 %. Possibilities to reach higher frequencies will be discussed.

Session 7:

HEB I

Tuesday May 3, 11:00-12:30
Chairman: Sigfrid Yngvesson

Hot electron bolometer mixer for 20 - 40 THz frequency range

M.I. Finkel, S.N. Maslennikov, Yu.B. Vachtomin, S.I. Svechnikov
K.V. Smirnov, V.A. Seleznev, Yu.P. Korotetskaya, N.S. Kaurova, B.M. Voronov, and G.N. Gol'tsman
Moscow State Pedagogical University, Moscow, 119992, Russia, Email: goltsman@mspu-phys.ru

***Abstract*— The developed HEB mixer was based on a 5 nm thick NbN film deposited on a GaAs substrate. The active area of the film was patterned as a 30×20 μm^2 strip and coupled with a 50 Ohm coplanar line deposited *in situ*. An extended hemispherical germanium lens was used to focus the LO radiation on the mixer. The responsivity of the mixer was measured in a direct detection mode in the 25÷64 THz frequency range. The noise performance of the mixer and the directivity of the receiver were investigated in a heterodyne mode. A 10.6 μm wavelength CW CO_2 laser was utilized as a local oscillator.**

***Index Terms*—Superconducting radiation detectors, Hot carriers, Bollometers, Mixers.**

I. Introduction

The fact that the use of superconducting NbN hot electron bolometer (HEB) mixers has been planned for several widely known ground–based, stratosphere, and space–based platforms proves that their further improvement is the most promising for quantum limited terahertz heterodyne receivers at the frequencies above 1.3 THz. Indeed, it can be seen from fig. 1 that at these frequencies the most admissible noise performance is demonstrated by quasioptical or waveguide coupled NbN HEB mixers which show the values of the noise temperature close to $8\frac{hf_{LO}}{k}$, where f_{LO} is the local oscillator (LO) frequency. The use of a planar antenna or a waveguide in the mixer, on the one hand, enables us to decrease the volume and, consequently, to decrease the required LO power (to $\sim$ 1 μW) at the LO frequencies of several THz. On the other hand, it causes well known imperfections from which the most noticeable is the parasitic resistance of the contacts between the antenna and the sensitive NbN bridge (some improvement of the contacts has been achieved and reported in [1] recently), that becomes more essential when f_{LO} is increased. However, this imperfection can be eliminated by exclusion a separate antenna and, consequently, mentioned contacts from the mixer chip at all and making the sensitive bridge to be directly lens coupled. The reasonable dimensions for such a bridge are diffraction limited for certain value of f_{LO}. Although in most cases it means significant increase in the volume and, consequently, optimal LO power of the mixer, such a solution looks justified if we take into account that the requirements for the optimal LO power can be covered by recently developed quantum cascade lasers which can provide the power of $\sim$ 1 mW.

It should be noted that further experiments with NbN HEB mixers can provide an additional information and, consequently, can lead to a better understanding of the hot electrons and the heterodyne detection phenomena if the operating frequency significantly differs from conventional one for the antenna coupled mixers. The frequency range of 20÷40 THz looks the most reasonable for the first step experiments although at lower frequencies the performance of NbN HEB mixers may be better. In this frequency range, the NbN HEB mixers can be applied in space based planetary, solar and Earth science [28].

The first results on characterization of the directly coupled NbN HEB mixers at the frequencies of 25÷60 THz are given below in sections "Fabrication process", "Characterization", and "Conclusions".

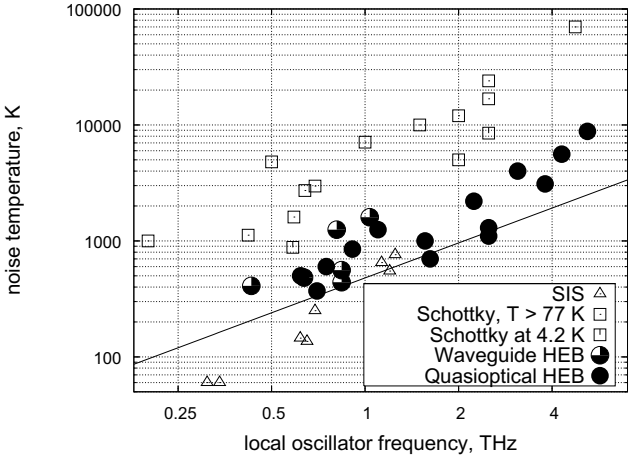

Fig. 1. Noise temperature (T_n) versus LO frequency (f_{LO}) and mixer type. Solid line corresponds to $T_n = 10\frac{hf_{LO}}{k}$. All the references for given graph are formated and shown below. The format is {<LO frequency, THz>, <noise temperature, K>, <reference>}. SIS: {0.31, 60, [2]}, {0.34, 60, [2]}, {0.618, 145, [3]}, {0.65, 136, [4]}, {0.69, 250, [5]}, {1.13, 650, [6]}, {1.2, 550, [7]}, {1.25, 760, [8]}. Schottky, $T \geqslant 77\ K$: {0.2, 1000, [9]}, {0.42, 1120, [10]}, {0.5, 4800, [11]}, {0.59, 1608, [12]}, {0.64, 2720, [12]}, {0.69, 2970, [12]}, {1, 7100, [13]}, {1.5, 10000, [13]}, {2, 12000, [13]}, {2.5, 24000, [14]}, {2.5, 16800, [15]}, {4.750, 70000, [13]}. Schottky, $T \sim 4.2\ K$: {0.585, 880, [16]}, {2.000, 5000, [17]}, {2.500, 8500, [13]}. Waveguide HEB: {0.430, 410, [18]}, {0.636, 483, [18]}, {0.810, 1250, [19]}, {0.840, 560, [19]}, {0.840, 440, [20]}, {1.035, 1600, [19]}. Quasioptical HEB: {0.620, 500, [21]}, {0.700, 370, [22]}, {0.750, 600, [23]}, {0.910, 850, [23]}, {1.100, 1250, [23]}, {1.560, 1000, [24]}, {1.620, 700, [25]}, {2.240, 2200, [24]}, {2.500, 1100, [25]}, {2.500, 1300, [26]}, {3.100, 4000, [27]}, {3.800, 3100, [26]}, {4.300, 5600, [27]}, {5.200, 8800, [27]}. .

II. Fabrication process

The key steps of the fabrication process are schematically shown in fig. 2.

A NbN/Au double–layer system is deposited on the epi–polished side of a semi–insulating GaAs substrate. Before the deposition the substrate is precleaned in acetone and isopropyl alcohol.

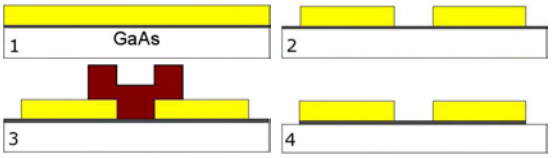

Fig. 2. The route of the structure processing. 1. NbN/Au double–layer system deposition on epi–polished side GaAs substrate. 2. Patterning of contact pads. 3. Patterning of sensitive bridge. 4. Chemical removal the NbN film outside of the bridge.

Ultrathin (5 nm) superconducting NbN film is deposited by dc reactive magnetron sputtering of Nb target in Ar and N_2 mixture in a Leybold Heraus Z–400 sputtering unit [29]. Residual pressure is $5{\cdot}10^{-7}$ mbar. During the NbN film deposition, the substrate is heated to 350 °C. The Ar partial pressure is $5{\cdot}10^{-3}$ mbar, and N_2 partial pressure is 10^{-4} mbar. The sputtering is carried out at a discharge current of 300 mA and a voltage of 400 V. A 100 nm thick Au film is then deposited *in situ* on the NbN film by dc magnetron sputtering at 100 °C. The parameters of the superconducting film are the following: the critical transition temperature is 9.4 K; superconducting transition width is 0.6 K; sheet resistance is 570 $\frac{\Omega}{\square}$ and ratio $R_{300}/R_{20} \sim 0.7$.

The layout is patterned by photolithography using a Karl Suss MA 56 mask aligner. At first the contact pads are formed, and then the topology of the sensitive bridge (30×20 μm^2) is patterned.

At the last stage the GaAs substrate is scribed into the chips (3×3 mm^2) that are cleaned in acetone to strip the photoresist. One of the chips prepared is shown in fig. 3. Although the NbN film thickness is no more than 5 nm, the sensitive element appears as a mesa–structure caused by high etching rate of GaAs during the NbN film removal process.

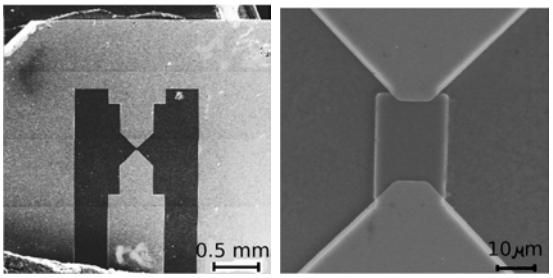

Fig. 3. SEM photos of directly lens coupled NbN HEB mixer.

III. Characterization

A. Noise performance

The experimental setup for the noise performance characterization of directly lens coupled NbN HEB mixers is shown in fig. 4. As a local oscillator (LO) a 10.6 μm wavelength CW

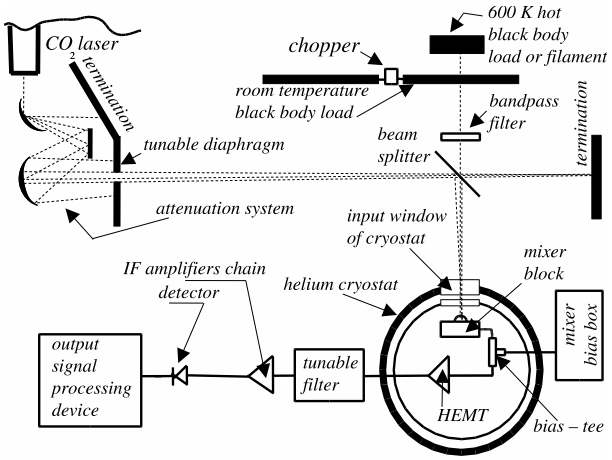

Fig. 4. Experimental setup.

CO_2 discharge laser is used. Its radiation power is attenuated and focused by a system consisting of two off–axis mirrors, several black body terminations and a handled diaphragm. In order to superimpose the radiations of LO and a signal source a beam splitter is used. Signal source (600 K black body or 1200 K filament, T_h) radiation is chopped with a room temperature T_{cold} black body load. A liquid helium cryostat equiped by a Ge input window is utilized to cool the mixer to its operating temperature (4.2 K). The mixer block includes Ge extended hemispherical lens (diameter $D \sim 12$ mm, extension lenght $\sim \frac{1}{6}D$) with a mixing device positioned on the flat surface side. The intermediate frequency signal is guided out of the chip via a 50 Ohm coplanar line which is soldered to an SMA connector. A bias tee is used to feed the bias to the mixer and to transmit the intermediate frequency signal to low noise (noise temperature of $\sim$ 6 K) HEMT amplifier (1.3÷1.9 GHz). The output signal is detected by a broadband microwave detector and processed for Y–factor calculation.

It should be noted that for the noise temperatures close to the quantum limit the term correspondent to the zero fluctuations (quantum) noise is not negligible in the expression for Y–factor:

$$Y = \frac{\frac{1}{k}D(f_{LO}, T_h) + \frac{hf_{LO}}{2k} + T_n^{CW}}{\frac{1}{k}D(f_{LO}, T_{cold}) + \frac{hf_{LO}}{2k} + T_n^{CW}} \qquad (1)$$

where T_n^{CW} is the receiver's equivalent noise power per unit bandwidth divided by k given at the input (*receiver's Callen & Welton noise temperature* [30]), and

$$D(\nu, T) = \frac{h\nu}{e^{\frac{h\nu}{kT}} - 1} \qquad (2)$$

is the radiation spectral density of the black body load at a frequency of ν and a temperature of T.

In the experiments, the values of the Y–factor were measured at the setup described above using both a $\sim$ 1200 K filament and 600 K black body loads, and then the values of T_n^{CW} were calculated for several operating points (fig. 5). For the optimal operating point the values of T_n^{CW} are shown

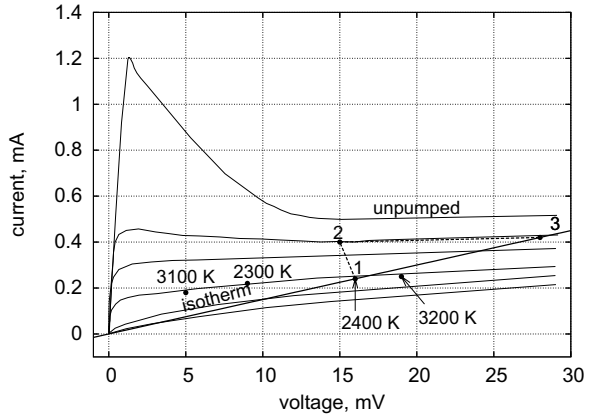

Fig. 5. IV–curves and several values of the noise temperature given at the points near the optimal IV–curve.

TABLE I
DEPENDENCE OF Y–FACTOR AND NOISE TEMPERATURE VERSUS TEMPERATURE OF HOT LOAD T_h.

T_h, K	Y	T_n^{CW}, K
600	1.06	2300
1200	1.2	2400

in table I.

It should be noted that, due to significant increase in the device volume, the contribution of the effect of direct detection to the value of the output signal [26], [31] was negligibly small and, consequently, could not appreciably distort the values of T_n^{CW}.

B. Optimal LO power

So called *isothermal method* was applied to estimate the value of the optimal LO power absorbed. In particular, for the point 1 (close to optimal one, fig. 5), LO power absorbed was deduced from the equations (3) and (4). As the resistances at the points 1 and 3 (fig. 5) are equal, for the electron temperatures at these points it should be true that $T_1^e = T_3^e$, and consequently, for LO powers absorbed P_1^{LO}, P_3^{LO}, bias voltages U_1, U_3 and currents I_1, I_3 it can be written:

$$P_1^{LO} + U_1 I_1 = P_3^{LO} + U_3 I_3 \tag{3}$$

The transition from point 1 to point 2 is done by 3 dB attenuation of the LO power, that gives another equation:

$$P_1^{LO} \simeq 2P_2^{LO} \simeq 2P_3^{LO} \tag{4}$$

From (3) and (4) the estimated value of the absorbed LO power at the operating point close to the optimal one is $P_1^{LO} \simeq 16$ μW.

C. Receiver's beam pattern

The beam pattern of the mixer+lens system was measured in the heterodyne mode with a chopped 1200 K filament as a signal radiation source. The result is shown in fig. 6. It can be seen that beam pattern obtained is essentially narrower than that of mixer—log-spiral—lens antenna system at 2.5 THz [32] (dotted line in fig. 6).

D. Receiver's responsivity versus frequency

The responsivity of the receiver was investigated in the detection mode using a chopped filament and a room temperature black body as the signal loads which radiated a power $\mathrm{d}P$ per solid angle $\mathrm{d}\Omega$, area $\mathrm{d}S_{bb}$, and bandwith $\mathrm{d}\nu$ of

$$\frac{\mathrm{d}P}{\mathrm{d}S_{bb}\mathrm{d}\Omega\mathrm{d}\nu} \simeq \left(\frac{2h\nu^3}{c^2}\right)\frac{1}{e^{\frac{h\nu}{kT}}-1} \equiv \mathcal{D}_{S\Omega\nu}(\nu,T) \tag{5}$$

(here T was the temperature of correspondent load). In the case when both the angle α and solid angle Ω (fig. 7) are small ($S_l \ll l^2$, $S_{bb} \ll l^2$, where S_l is the area of the input diaphragm mounted in the cryostat in front of Ge lens) the expression for the incident power per unit bandwidth can be written as

$$\frac{\mathrm{d}P}{\mathrm{d}\nu} \simeq \mathcal{D}_{S\Omega\nu}(\nu,T)\cdot S_{bb}\cdot\Omega = \\ = \left(\frac{\alpha^2 S_l \pi h\nu^3}{2c^2}\right)\frac{1}{e^{\frac{h\nu}{kT}}-1} \equiv \mathcal{D}_{\nu}(\nu,T) \tag{6}$$

In order to obtain a rough dependence of the receiver's responsivity versus frequency a set of bandpass dispersion filters was used (fig. 4, 8). For certain filter the responsivity can be deduced using (6) and expressed as:

$$s \simeq \frac{U_r}{\int_0^\infty \mathcal{T}(\nu)\left(\mathcal{D}_\nu(\nu,T_{bb}) - \mathcal{D}_\nu(\nu,T_r)\right)\mathrm{d}\nu} \tag{7}$$

where $\mathcal{T}(\nu)$ is the dependence of the filter transmission versus frequency, $T_r \simeq 296$ K and $T_{bb} \simeq 1200$ K are the room and filament temperatures, respectively, and U_r is the response voltage.

In the experiments, U_r was measured by a lock–in amplifier for each filter of the set, and then the responsivity was calculated using (7) (fig. 8). It can be concluded that at the frequencies $\lesssim 30$ THz the device responsivity is cut by Ge input window of the cryostat and the lens, while at the frequencies $\gtrsim 30$ THz the responsivity is almost flat and close to 70 $\frac{V}{W}$.

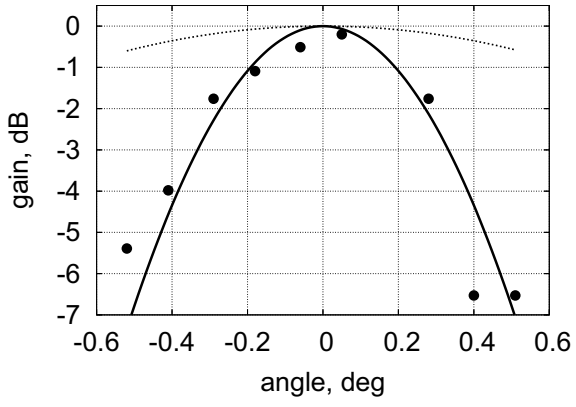

Fig. 6. Receiver's beam pattern. Dotted line corresponds to the beam pattern of the system consisting of Si lens, spiral antenna and mixer at 2.5 THz [32].

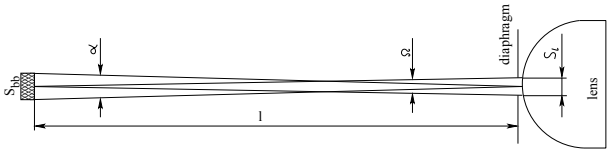

Fig. 7. Denotations for a black body load and the input diaphragm mounted in the cryostat in front of Ge lens.

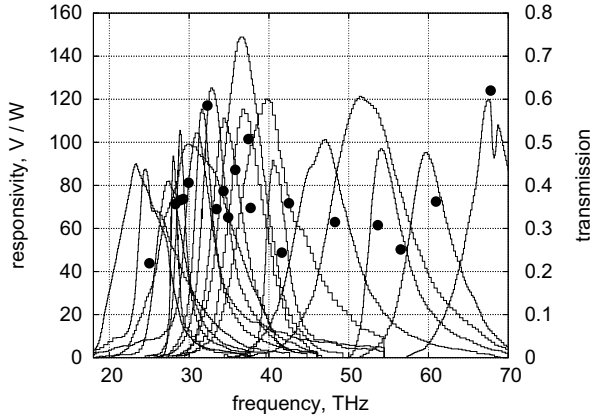

Fig. 8. The dependence of the receiver's responsivity versus frequency (filled circles) and the transmissions of the bandpass filters used in the experiment (lines).

IV. Conclusions

At high frequencies directly lens coupled NbN HEB mixer shows lower noise temperature than antenna coupled one. First experiment with NbN HEB at 30 THz gives the noise temperature about 2300 K that is close to 3 times of the quantum limit. For the 30×20 μm^2 device the optimal absorbed LO power is about 16 μW that is relatively easy to get from solid state sources in the middle IR. The responsivity of the device versus frequncy is almost flat and is about 70 $\frac{V}{W}$ in the frequency range of $25\div60$ THz.

References

[1] J. Baselmans, M. Hajenius, J. Gao, T. Klapwijk, P. de Korte, B. Voronov, and G. Gol'tsman, "Doubling of sensitivity and bandwidth in phonon cooled hot electron bolometer mixers," *Appl. Phys. Lett.*, no. 84, p. 1958, 2004.

[2] S. Claude, "Sideband–Separating SIS Mixer For ALMA Band 7, 275–370 GHz," in *Proc. 14th international symphosium on space terahertz technology*, Tucson, USA, Mar. 2003, p. 41.

[3] S. Shi, C. Chin, M. Wang, W. Shan, W. Zhang, and T. Noguchi, "Development of a 600–720 GHz SIS Mixer for the SMART," in *Proc. 12th international symphosium on space terahertz technology*. San Diego, CA, USA: Jet Propulsion Laboratory, California Institute of Technology, Feb. 2001, p. 215.

[4] A. Baryshev, E. Lauria, R. Hesper, T. Zijlstra, and W. Wild, "Fixed–tuned waveguide 0.6 THz SIS mixer with Wide band IF," in *Proc. 13th international symphosium on space terahertz technology*. Cambridge, MA, USA: Harward University, Mar. 2002.

[5] P. Grimes, P. Kittara, G. Yassin, S. Withington, and K. Jacobs, "Investigation of the performance of a 700 GHz nline mixer," in *Proc. 14th international symphosium on space terahertz technology*, Tucson, USA, Mar. 2003, p. 247.

[6] A. Karpov, D. Miller, F. Rice, J. Zmuidzinas, J. Stern, B. Bumble, and H. LeDuc, "Low noise 1.2 THz SIS receiver," in *Proc. 12th international symphosium on space terahertz technology*. San Diego, CA, USA: Jet Propulsion Laboratory, California Institute of Technology, Feb. 2001, pp. 21–22.

[7] A. Karpov, D. Miller, F. R. Rice, J. A. Stern, B. Bumble, H. G. LeDuc, and J. Zmuidzinas, "Low–noise SIS mixer for far–infrared radio astronomy," in *Proc. SPIE*, vol. 5498, Glasgow, Scotland, UK, June 2004, pp. 616–621.

[8] A. Karpov, D. Miller, J. A. Stern, B. Bumble, H. G. LeDuc, and J. Zmuidzinas, "Low noise NbTiN 1.25 THz SIS mixer for Herschel Space Observatory," in *Abstract Book – ISSTT 2005*, Göteborg, Sweden, May 2005, p. 159.

[9] I. Galin, C. Schnitzer, R. Dengler, and O. Quintero, "177–207 GHz Radiometer Front End, Single–Side–Band Measurements," in *Proc. 10th international symphosium on space terahertz technology*, Charlotte Sville, Virginia, Mar. 1999, p. 70.

[10] J. L. Hesler, K. Hui, and T. W. Crowe, "A Fixed–tuned 400 GHz Subharmonic Mixer Using Planar Schottky Diods," in *Proc. 10th international symphosium on space terahertz technology*, Charlotte Sville, Virginia, Mar. 1999, p. 95.

[11] B. Maddison, R. Martin, M. Oldfield, C. Mann, D. Matheson, B. Ellison, J. Thornton, W. Hall, and D. Lamarre, "A Compact 500 GHz Planar Schottky Diode Receiver with a Wide Instantaneous Bandwidth," in *Proc. 9th international symphosium on space terahertz technology*, 1998, p. 367.

[12] S. M. Marazita, K. Hui, J. L. Hesler, W. L. Bishop, and T. W. Crowe, "Progress in submillimeter wavelength integrated mixer technology," in *Proc. 10th international symphosium on space terahertz technology*, Charlotte Sville, Virginia, Mar. 1999, p. 74.

[13] A. Betz and R. Borejko, "A practical Schottky mixer for 5 THz," in *Proc. 7th international symphosium on space terahertz technology*, 1996, p. 503.

[14] T. Suzuki, C. Mann, T. Yasui, H. Fujishima, and K. Mizuno, "Quasi–integrated planar Schottky barrier diodes for 2.5 THz receivers," in *Proc. 9th international symphosium on space terahertz technology*, 1998, p. 187.

[15] C. Mann, D. Matheson, B. Ellison, M. Oldfield, B. Moyna, J. Spencer, D. Wilsher, and B. Maddison, "On the design and measurement of a 2.5 THz waveguide mixer," in *Proc. 9th international symphosium on space terahertz technology*, 1998, p. 161.

[16] J. Hesler, W. Hall, T. Crowe, R. Weikle, R. Bradley, and Shing–Kuo Pan, "Submm wavelenght waveguide mixers using planar Schottky barier diods," in *Proc. 7th international symphosium on space terahertz technology*, 1996, p. 462.

[17] *Millimeter and Submillimeter Techniques*, , W. Ross Stonel ed., ser. Review of radio science 1993–1996. New York: Oxford University Press Inc, 1996.

[18] J. Kawamura, R. Blundell, C–Y.E. Tong, G. Gol'tsman, E. Gershenzon, B. Voronov, and S. Cherednichenko, "Phonon–cooled NbN HEB Mixers for Submillimeter Wavelengths," in *Proc. 8th international symposium on space terahertz technology*, Mar. 1997, p. 23.

[19] C.-Y. Edward Tong, J. Kawamura, T. R. Hunter, D. C. Papa, R. Blundell, M. Smith, F. Patt, G. Gol'tsman, and E. Gershenzon, "Successful operation of a 1 THz NbN hot–electron bolometer receiver," in *Proc. 11th international symphosium on space terahertz technology*, May 2000, pp. 49–59.

[20] D. Loudkov, C.-Y. Tong, R. Blundell, N. Kaurova, E. Grishina, B. Voronov, and G. Gol'tsman, "An investigation of the performance of the superconducting HEB mixer as a function of its RF embedding impedance," T, lo be published in ASC 2004 proc.

[21] P. Yagoubov, M. Kroug, H. Merkel, E. Kollberg, J. Shubert, H. Hübers, S. Svechnikov, B. Voronov, G. Gol'tsman, and Z. Wang, *Supercond. Sci. Technol.*, no. 12, 1999.

[22] K. Smirnov, Y. Vachtomin, S. Antipov, S. Maslennikov, N. Kaurova, V. Drakinsky, B. Voronov, G. Gol'tsman, A. Semenov, H.-W.Hübers, and H. Richter, "Noise performance of spiral antenna coupled HEB mixers at 0.7 THz and 2.5 THz," in *Proc. 14th international symphosium on space terahertz technology*, Tucson, USA, Mar. 2003.

[23] R. Wyss, B. Karasik, W. McGrath, B. Bamble, and H. LeDuc, "Noise and bandwidth measurements of diffusion–cooled Nb hot–electron bolometer mixers at frequencies above the superconductive energy gap," in *Proc. 10th international symphosium on space terahertz technology*, Charlotte Sville, Virginia, Mar. 1999, pp. 215–229.

[24] E. Gerecht, C. Musante, H. Jian, Y. Zhuang, K. Yngvesson, J. Dickinson, T. Goyette, J. Waldman, P. Yagoubov, G. Gol'tsman, B. Voronov, and E. Gershenzon, "Improved characteristics of NbN HEB mixers integrated with log–periodic antennas," in *Proc. 10^{th} international symphosium on space terahertz technology*, Charlotte Sville, Virginia, Mar. 1999, pp. 200–207.

[25] M. Kroug, S. Cherednichenko, H. Merkel, E. Kollberg, B. Voronov, G. Gol'tsman, H.-W. Hübers, and H. Richter, Presented at the Applied Superconductivity Conference, Virginia Beach, USA (to be published in the IEEE Transactions on Applied Superconductivity), 2000.

[26] Y. Vachtomin, S. Antipov, S. Maslennikov, K. Smirnov, S. Polyakov, N. Kaurova, E. Grishina, B. Voronov, and G. Gol'tsman, "Noise temperature measurements of NbN phonon–cooled hot electron bolometer mixer at 2.5 and 3.8 THz," in *Proc. 15^{th} international symphosium on space terahertz technology*, Northampton, Massachusetts, USA, Apr. 2004.

[27] J. Schubert, A. Semenov, G. Gol'tsman, H.-W. Hübers, G. Schwaab, B. Voronov, and E. Gershenzon, *Supercond. Sci. Technol.*, no. 12, p. 748, 1999.

[28] T. Kostiuk, "Heterodyne spectroscopy in the thermal infrared region: a window on physics and chemistry," in *Proc. International Thermal Detectors Workshop (TDW'03), session 7 (Heterodyne detectors)*. 3501 University Boulevar East Adelphi, MD 20783: University of Maryland Inn and Conference Center, June 2003.

[29] P. Yagubov, G. Gol'tsman, B. Voronov, L. Seidman, V. Siomash, S. Cherednichenko, and E. Gershenzon, "The bandwidth of HEB mixers employing ultrathin NbN films on sapphire substrate," in *Proc. 7^{th} international symposium on space terahertz technology*, Charlottesville, Virginia, USA, Mar. 1996, pp. 290–302.

[30] A. Kerr, M. Feldman, and S.–K. Pan, "Receiver noise temperature, the quantum noise limit, and zero–point fluctuations," in *Proc. 8^{th} international symposium on space terahertz technology*, Mar. 1997, pp. 101–111.

[31] J. Baselmans, A. Baryshev, S. Reker, M. Hajenius, J. Gao, T. Klapwijk, Y. Vahtomin, S. Maslennikov, S. Antipov, B. Voronov, and G. Gol'tsman, "Direct detection effect in small volume hot electron bolometer mixers," *Appl. Phys. Lett.*, no. 86, p. 163503, 2005.

[32] A. Semenov, Heinz.–Wilhelm Hübers, H. Richter, M. Birk, M. Krocka, U. Mair, K. Smirnov, G. Gol'tsman, and B. Voronov, "Performance of terahertz heterodyne receiver with a superconducting hot–electron mixer," in *Proc. 13^{th} international symphosium on space terahertz technology*. Cambridge, MA, USA: Harward University, Mar. 2002, pp. 229–234.

Phase-Sensitive Near-Field Measurements and Electromagnetic Simulations of a Double-Slot HEB Integrated Lens-Antenna Mixer at 1.1, 1.2 and 1.6 THz

Willem Jellema, Timothy J. Finn, Andrey Baryshev, Maarten van der Vorst, Stafford Withington, *Member, IEEE*, J. Anthony Murphy, *Member, IEEE* and Wolfgang Wild

***Abstract*—The application of integrated lens-antennas becomes increasingly important as submillimetre-wave mixer and detector research moves towards frequencies well above 1 THz. Although classical waveguide receivers seem feasible up to 2.5 THz, planar integrated-antenna technology offers clear advantages when losses, manufacturing, integration, and the fabrication of large-format imaging arrays are considered. Modeling of planar antennas in combination with dielectric lenses has been reported by Filipovic and van der Vorst [1, 2]. Their simulations are based on a hybrid geometrical/physical optics (GO/PO) model, which predicts, mainly, far-field radiation patterns. This approach, as implemented in the software package PILRAP, has, for example, been used to design the lens antennas of the quasi-optical mixers used in the Heterodyne Instrument for the Far-Infrared (HIFI). In this paper we present measurements and simulations of a HEB double-slot lens-antenna mixer as present in Band 6L of HIFI. Amplitude and phase measurements were taken at 1.1, 1.2 and 1.6 THz respectively. We provide a detailed description of the experimental technique, which offers phase-sensitive measurements up to 1.6 THz with a dynamic range as high as 80 dB. We also describe comparisons between PILRAP simulations and experimental data. Understanding the precise radiation patterns of these devices is essential because once they are coupled to optical systems, their near-field behavior can influence the performance of the overall instrument considerably. We furthermore discuss to what extent the theory and experiment agree, and identify the key difficulties when modeling fast lens-antennas, particularly the problems associated with modeling the near-field. We conclude by outlining a few ideas as to how it might be possible to model these systems through the use of commercial planar antenna simulators, and new electromagnetic propagation techniques.**

***Index Terms*—Integrated lens-antenna, phase-sensitive, near-field, THz beam measurements.**

Manuscript received May 31, 2005. This work was supported in part by Enterprise Ireland (Prodex), the Science Foundation Ireland (SFI), and in part by the National University of Ireland, Maynooth.

Willem Jellema is with the National Institute for Space Research of the Netherlands (SRON) and the Kapteyn Astronomical Institute, University of Groningen, P.O. Box 800, 9700 AV Groningen, the Netherlands (phone: +31-50-363-4058; fax: +31-50-363-4033; e-mail: W.Jellema@sron.nl).

Timothy J. Finn and J. Anthony Murphy are with the National University of Ireland, Maynooth, Co. Kildare, Ireland.

Andrey Baryshev and Wolfgang Wild are with the National Institute for Space Research of the Netherlands (SRON) and the Kapteyn Astronomical Institute, University of Groningen, P.O. Box 800, 9700 AV Groningen.

Maarten van der Vorst is with the European Space Agency, ESTEC, P.O. Box 229, 2200 AG Noordwijk, the Netherlands.

Stafford Withington is with the Cavendish Laboratory, Madingley Road, Cambridge CB3 0HE, United Kingdom.

I. Introduction

THE use of waveguide feedhorns in submillimeter-wave optical systems is widely established and the electromagnetic properties of these systems are well validated [3, 4]. The application of waveguide feedhorns seems feasible up to 2.5 THz but is mechanically becoming difficult beyond 1.5 THz. At these frequencies planar integrated lens-antennas start to offer manufacturing advantages. Pioneering work in the area of modeling the radiation patterns of planar-integrated lens-antenna systems was carried out by Filipovic and van der Vorst [1, 2]. Their hybrid geometrical/physical optics model (GO/PO) has been verified experimentally mainly in far-field amplitude at frequencies below 1 THz. The implementation of this modeling technique in the software package PILRAP was used for the quasi-optical design of the lens-antenna mixers in band 5, 6L and 6H of the Heterodyne Instrument for the Far-Infrared (HIFI) [5, 6]. Due to mass and volume constraints in HIFI the optical layout around the lens-antenna system is relatively compact. Consequently the mirrors are located in the propagating near-field of the lens-antenna. In [3] and [4] it is shown that the near-field characteristics of such systems can be very important for the overall optical performance of the instrument.

In this paper we report experimental results obtained for a number of lens-antenna geometries at 1.1, 1.2 and 1.6 THz. In addition to the measurement of field amplitudes the presented experimental system is capable of measuring the phase distributions directly. This opens up the possibility to verify the near-field properties of lens-antenna systems and to validate the predicted phase-centers by PILRAP at frequencies beyond 1 THz. Our primary objective in this work is to verify the predicted first-order beam properties: the waist size of the fundamental Gauss-Laguerre mode and the position of its

phase-center relative to the lens geometry. As a secondary objective we will address the question to what extent electromagnetic simulations based on PILRAP and GRASP and phase-sensitive beam measurements of optical systems employing lens-antenna systems agree.

II. Experimental Setup

A. Receiver and Scanner System

The experimental system is based on using an HEB mixer device in the heterodyne detection mode. The HEB mixer device is coupled via a double-slot antenna on a silicon lens to free-space or the optical system. The Local Oscillator (LO) as well as the RF test source are based on a solid-state multiplier chain driven by W-band power amplifiers. The input W-band synthesizers are based on high spectral purity low phase noise X-band synthesizers and Spacek active multiplier chains (sextuplers). The overall diagram for the 1.6 THz configuration is shown in Fig. 1. Two synthesizers S_1 and S_2 drive the RF resp. LO chain. The RF test source is mounted on a mechanical scanner that can move in x, y and z. By scanning the RF test source on a plane in front of the lens-antenna system with HEB mixer, the spatial coupling between the small RF test source probe and the lens-antenna system under test can be mapped. The measured complex coupling coefficient is proportional to the radiated field of the lens-antenna system if it would have been used as a transmitter. The total LO and RF multiplication factor is 108 in this case. To construct a reference signal against which the relative amplitude and phase of the HEB mixer signal can be measured, a fraction of the signal of the two synthesizers is mixed to low frequency (<100 MHz) and multiplied by the same amount as in the LO and RF chain. The obtained reference signal is fully correlated in phase to that of the HEB mixer but has fixed amplitude as a saturated reference multiplier system is used. In Fig. 1. the reference signal is denoted by R and the detected signal (modulated by spatial movement of the scanner) is denoted by S.

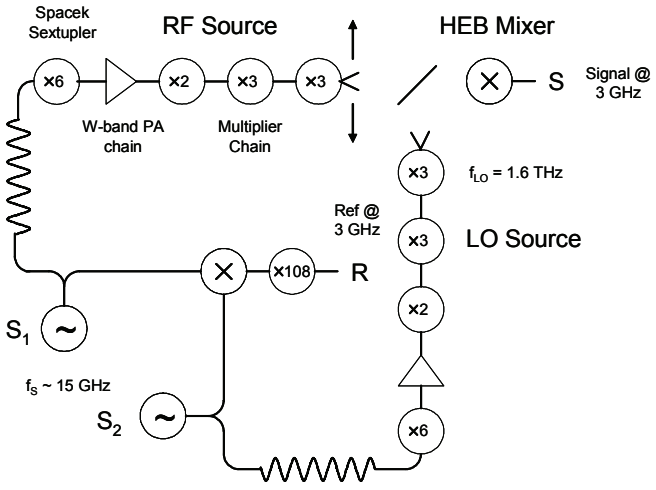

Fig. 1. Diagram of phase-sensitive measurement system at 1.6 THz.

B. Compensation of Correlated Phase Variations

Because of the high multiplication factor the phase variations of the two synthesizers are multiplied by a significant amount. In order to allow for narrow-band detection we first compensate the correlated variations in R and S by the system shown in Fig. 2. The system is based on a standard network S_{21} network parameter measurement using a Vector Network Analyzer (VNA) in CW mode. The test signal transmitted on port 1 of the VNA is first mixed with R to low frequency. This intermediate signal is filtered, amplified and finally drives a second mixer in which the correlated variations of R and S are added in anti-phase. In this process the phase information, i.e. the phase difference between R and S, is conserved whereas the signal power is no longer scattered over a relatively large bandwidth. In practice it is possible to measure in a bandwidth as narrow as 10 Hz yielding a very high signal-to-noise ratio up to 90 dB at 1.6 THz.

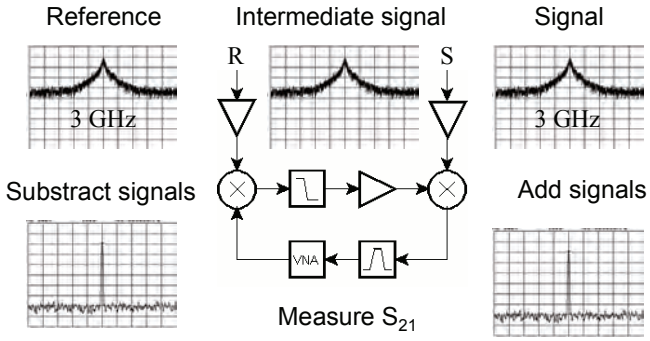

Fig. 2. Compensation of correlated phase variations in the reference and detected signal R resp. S.

C. Sensitivity and Dynamic Range

The noise temperature T_N of the HEB mixer in our experiment at 1.6 THz is typically 2000 K. We estimate an available RF test signal power P_s of order of 10 nW. The coupling efficiency η between test signal probe and lens antenna system under test in this particular case is of order of -20 dB. When an IF bandwidth B of 100 Hz is taken and an integration time τ of 0.26 s the signal-to-noise ratio SNR can be calculated using the radiometer equation[7]:

$$SNR \sim \frac{\eta P_s}{kT_N}\sqrt{\frac{\tau}{B}} \qquad (1)$$

At 1.6 THz the expected SNR is of order of 80 dB which is in very good agreement with the actual measured value.

D. First-order Standing Wave Correction

Another important feature of our experimental setup is the correction of standing waves between RF test probe and lens-antenna system under test. Because phase is directly measured

with high signal to noise a first-order standing wave correction can easily be made. If we denote the complex coupling coefficient between probe and antenna by c the measured signal s can be expressed as follows:

$$s \propto c\left(1+\sum_{n=1}^{\infty} R^n |c|^{2n} e^{-i\frac{4\pi nL}{\lambda}}\right) \qquad (2)$$

In deriving (2) it is assumed that the dominant reflections occur at the multiplier and mixer device. We furthermore assume that the reflected fields have the same first-order Gaussian beam characteristics and couple with equal efficiency for each roundtrip order. The roundtrip reflection coefficient is denoted by R. Each next roundtrip contribution to the measured signal s drops in amplitude by the product of the roundtrip reflection and squared magnitude of the coupling. Each subsequent roundtrip contribution is however modulated in phase by a plane-wave phase shift corresponding to the roundtrip pathlength 2L between the devices.

The first-order standing wave correction that can be made is based on measuring the signals s_1 and s_2 in two planes separated by λ/4. From (2) it can be seen that the phase of the first roundtrip term therefore changes by π. If the beam is reasonably well collimated the first-order effect on the measured coupling is only a plane-wave phase shift of π/2. Ignoring roundtrip terms beyond n = 1 the following relation for the compensated signal s_c can be found which provides a first-order correction for standing waves:

$$s_c = \frac{s_1 + s_2 e^{i\frac{\pi}{2}}}{2} \approx c \qquad (3)$$

In our system we use the z-stage of the xyz-scanner to measure a two-dimensional grid of pairs of points separated in z by λ/4. An on-axis scan in z has shown that when using (3) the standing wave ripple can be reduced by almost an order of magnitude and the residual standing wave ripple can be as low as 0.05 dB in the main beam.

E. Alignment between Scanner and Lens-Antenna System

The absolute alignment between the scanner system and the lens-antenna system under test is established by using two pairs of alignment devices. Two reflecting mirrors are mounted left and right of the optical axis of the lens-antenna system (see Fig. 3). The normal vectors of the mirror surfaces are parallel to the optical axis within a few arcmin. On the mirror surfaces we have machined crosshairs by using a 20 µm diamond dicing saw. The centers of the crosshairs are measured with respect to the optical axis by means of an optical traveling microscope. On the scanner system two plan-parallel alignment windows are mounted left and right of the test signal probe. Again the normal vectors of the windows are nearly normal to the scan plane and the centers of the crosshairs are accurately known with respect to the horn aperture. The orientation of the scan plane is first aligned with respect to the optical axis by auto-collimating on an alignment mirror and window pair using an optical theodolite. When the scan plane is normal to the optical axis the x- and y-stages of the scanner are used to align the crosshairs on the alignment mirror and window. The rotation of the x- and y-axis of the scanner in the plane of measurement is finally determined by measuring the x- and y-offsets between the crosshair centers on the other pair of alignment devices. The alignment accuracy is typically 0.1 mm in lateral position and within a few arcmin for tilt. Rotation in the measurement plane is known as accurate as 0.1 deg and the axial location of the scan plane is determined within 1 or 2 mm. The absolute coordinates of the measured field data is therefore known within fractions of a wavelength.

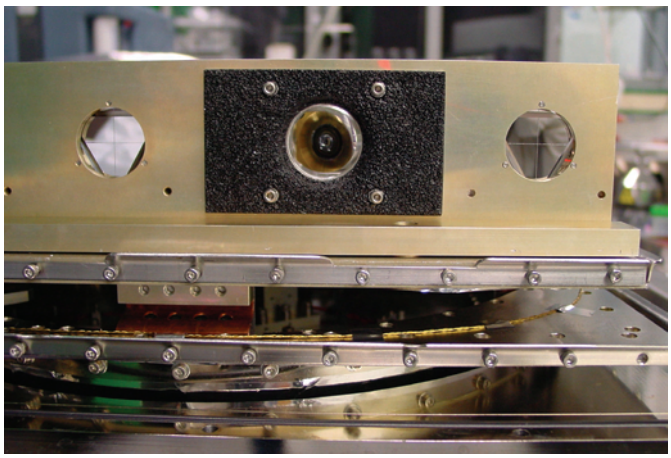

Fig. 3. Alignment mirrors left and right of the optical axis. The silicon lens of the lens-antenna system is visible in the optical port surrounded by a SiC absorber panel.

F. Phase Stability and Drift Correction

Direct measurement of phase at 1.6 THz requires very good mechanical and thermal stability to reduce phase errors as far as possible. We therefore use special phase-stable cables from Reynolds. The differential thermal expansion coefficient of the dielectric material used in this cable is nearly zero at room temperature. By using identical cables between S_1 and S_2 and the RF and LO sources in Fig. 1. the thermal drift problem is furthermore reduced to differential thermal drift. When mapping the 2-dimensional field we take a calibration measurement at a fixed point in space after each line scan. As all data is time-stamped the final data can be corrected for drift by linear interpolation of the calibration trace [8]. The typical drift is 20 to 30º per hour, but the residual error after correction is smaller than 5º. The phase error due to the flexing cable of the RF test source is characterized by measuring the roundtrip phase delay along the cable over the scan plane with a VNA. The maximum phase excursion over the scan plane is kept within 10º by fixing the cable in a constant bending radius.

G. Summary Measurement Accuracy and Performance

In the previous sections we have outlined the key characteristics and unique features of the experimental setup. Novel is the capability of measuring phase at 1.1, 1.2 and 1.6 THz with demonstrated dynamic range of 70, 70 resp. 80 dB in a 100 Hz IF bandwidth. We have presented a system that compensates correlated phase variations allowing for unlimited narrow-band measurements. Furthermore standing wave errors are corrected for to first-order by taking measurements in two planes separated by λ/4. The measurement geometry is mechanically controlled within fractions of a wavelength and the phase stability of the system is excellent because of the symmetric arrangement of special phase-stable cables.

The overall measurement accuracy is better than 20º in phase and 0.5 dB in amplitude in the main beam (above the -20 dB level). For a detailed example of performance characterization and error analysis and demonstration of measurement capability at 480 GHz we refer the reader to [4] and [8].

III. Test Cases

In this paper we consider the lens-antenna design depicted in Fig. 4. The lens-antenna system consists of an elliptical lens of 5 mm diameter. The major axis, along the optical axis, is denoted by a and the minor axis, the lens radius, is denoted by b. In a number of cases a Parylene anti-reflection coating of 28 μm is applied. The lens body is extended by a Silicon cylinder. The total Silicon extension length is denoted by L and is composed of the substrate thickness of the HEB chip and the cylindrical lens extension.

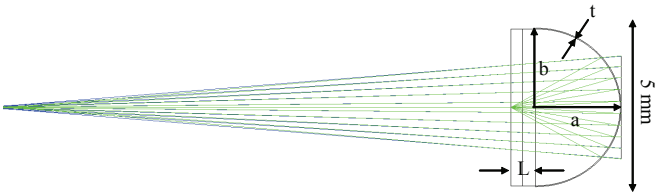

Fig. 4. Optimized elliptical lens design for HIFI Band 6L.

The design values for a and b are 2.548 resp. 2.500 mm and the extension length is designed to be 0.756 mm. The double-slot antenna for Band 6L of HIFI has a slot width of 4 μm, a slot length of 56 μm and a slot separation of 32 μm. For these parameters PILRAP predicts a waist size for the fundamental Gauss-Laguerre mode of 0.57 mm @ 1.6 THz which is located at 18.6 mm behind the lens vertex. The lens design is relatively sensitive to manufacturing tolerances. A change of 10 μm in the extension length changes the waist size roughly by 10% whereas the phase center moves by about 1 mm. Therefore the actual lens-geometry measured should be known within a few μm. For that purpose we designed a special mechanical bracket for the Silicon lens as shown in Fig. 5. At an external mechanical calibration facility the lens surface and flange planes were mechanically sampled in one run using a 0.3 mm radius diamond probe with a contact force of 5 mN applied normal to the surface. The total number of about 50 points was then fitted to an elliptical surface in a three-dimensional coordinate system.

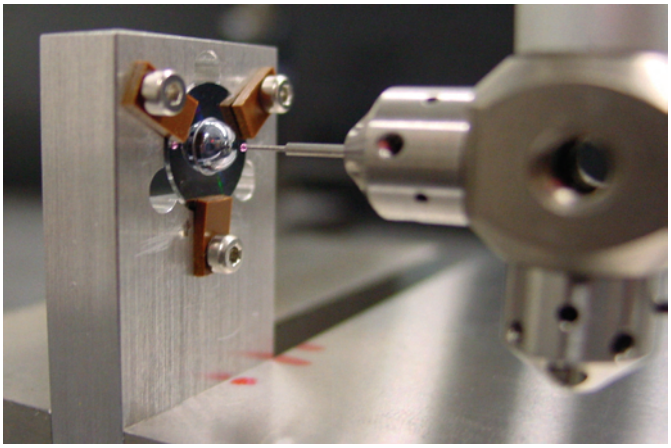

Fig. 5. Mechanical characterization of lens-antenna geometry.

The measurement accuracy of this method is about 2 μm. Although the lenses were ordered from the same company on the basis of the same drawing a large spread in lens geometry was found. As a result the expected spread in F/D ratio ranges from 3.2 to 4.8. Not only deviations in extension length were found but also deviations in ellipticity. The four test cases that are considered in this paper are summarized in Table I.

TABLE I
SUMMARY TEST CASE CHARACTERISTICS

Case	AR coating	a (mm)	b (mm)	ellipticity	L (mm)
SRON[a]	no	2.546	2.499	1.0191	0.758
FM01[b]	yes	2.516	2.501	1.0060	0.771
FM04[b]	yes	2.529	2.496	1.0134	0.726
DM3[b]	no	2.537	2.499	1.0147	0.767

[a]Lens-antenna system and HEB device from SRON-DIMES
[b]Lens-antenna system and HEB devices from CTH

IV. Measurement and Modelling Results

A. SRON lens-antenna system at 1.1 and 1.3 THz

The first measurements are taken at 1.1 and 1.3 THz for the SRON lens (first case in Table I). This lens geometry was very close to the designed case. No AR coating was used for this experiment. In Fig. 6. the measured phase distribution is plotted clearly demonstrating our capability of measuring phase at THz frequencies. Note that at the right of Fig. 6. the frame of the beamsplitter can be recognized although the intensity has dropped already by 45 dB. By Fourier-transforming the near-field data to the far-field a direct comparison between PILRAP and the measurement can be made. The predicted and measured far-field H-plane distribution is shown in Fig. 7 together with the fundamental Gaussian beam providing highest coupling efficiency [9].

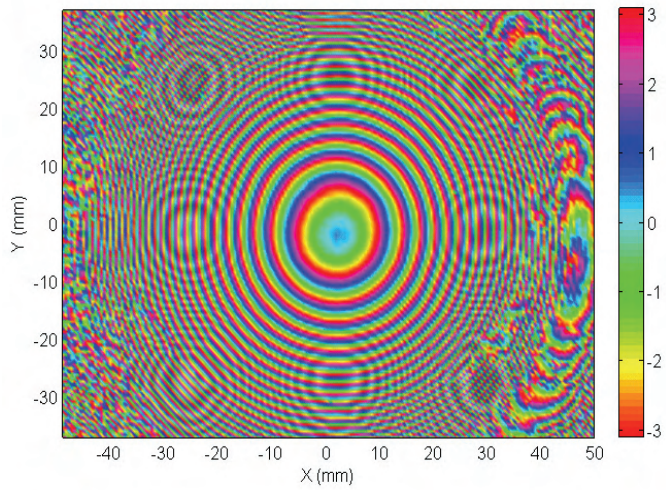

Fig. 6. Measured phase distribution for SRON lens at 1.1 THz.

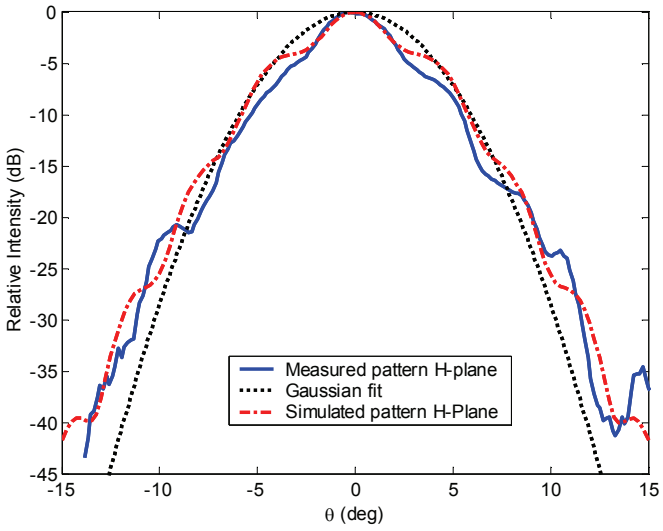

Fig. 7. Predicted and measured H-plane far-field distribution and fundamental Gaussian beam yielding highest coupling for the SRON lens at 1.1 THz

The predicted waist size at 1.1 THz is 0.66 mm whereas we measure 0.67 mm. For the phase center location we measure a value of -(15±2) mm whereas PILRAP predicts -15.7. The measured gaussicity is 92% whereas PILRAP predicts 95%. Within the measurement uncertainties this is all in very good agreement regarding first-order beam properties. Similar agreement is found at 1.2 THz. When looking to the sidelobe structure in Fig. 7. it can be seen that the main beam agrees reasonably well in the upper 5 dB. Below that, the sidelobe structure is different. In the E-plane we find even larger deviations, but also significant asymmetry in the sidelobe structure. The E-plane asymmetry could be chip- or antenna-related as PILRAP only simulates two isolated slots and does not take into account the asymmetrically coupled IF line and RF choke. We conclude that although the first-order properties are reasonably well predicted the measured and predicted sidelobe structure at lower intensity levels is not quite the same.

B. CTH lens-antenna systems at 1.6 THz

In order to achieve more measurement resolution for the phase center position the lenses FM01, FM04 and DM3 listed in Table I are integrated into the Mixer-Sub Assembly (MSA) optics for band 6L. This system images the front of the lens via a three-mirror system to a pupil plane of the Focal Plane Unit (FPU) of HIFI [3-6]. At the output of the MSA the Gaussian beam width is about 3.55 mm and relatively collimated. A measurement accuracy in the axial position of 2 mm at the output corresponds to an accuracy of about 0.1 mm at the input near the lens-antenna system. Assuming the optics are perfectly shaped and well-aligned, the Gaussian beam parameters found at the output plane can be back-traced to the input using the ABCD matrix method for the complex beam parameter [9]. In that way the position of the phase center of the lens-antenna system can be accurately determined by making use of the optical magnification of the MSA optics.

In Fig. 8. the measured and simulated phase distribution for lens DM3 at 1.6 THz at the output of the MSA optics is shown. The simulation is done by using a GRASP model of the MSA optics and the input field predicted by PILRAP.

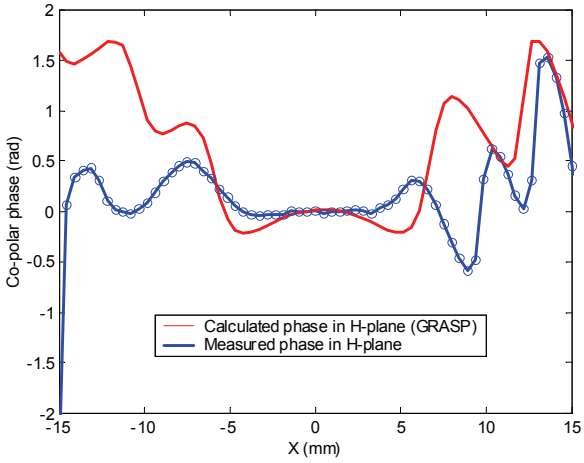

Fig. 8. GRASP8 simulation of MSA optics including lens DM3 at 1.6 THz.

Clearly visible is the difference in phase curvature. Note that the field is only significant in the range between -7 and +7 mm where more than 99% of the power is concentrated. In this particular case the defocus between measured and predicted waist location is 75 mm. The measured and predicted waist sizes are however in good agreement at about 3.6 mm. Using the ABCD matrix method for the complex beam parameter the Gaussian beam parameters at the lens-antenna are retrieved. The results for the retrieved lens-antenna waist size and phase center are summarized in Fig. 9. for lenses DM3, FM01 and FM04 together with the predicted values by PILRAP. The lens-geometry for DM3 is reasonably close to the designed case. The PILRAP simulation for this case is taken as the reference, hence a defocus of 0 mm by definition. Comparing the measured and simulated parameters one can see that in all cases the waist size is in good agreement but the phase center is systematically closer to the lens vertex. The offset

furthermore scales with waist size and is +1.5 mm for DM3, +0.7 mm for FM01 and +0.3 for FM04. The observed offsets in phase center are significant, about 20 to 30% of the confocal distance, and significantly larger than the measurement error of about 0.1 mm. We conclude therefore that PILRAP does not correctly predict the phase-center for this particular lens-antenna design.

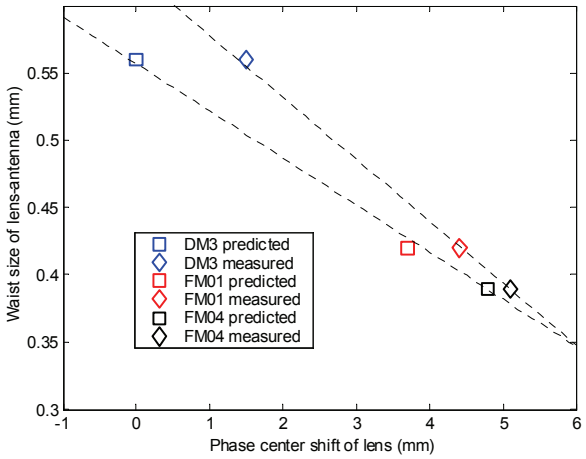

Fig. 9. Measured and predicted lens-antenna waist size and location.

V. Summary And Conclusions

In this paper we have demonstrated phase-sensitive beam pattern measurements of twin-slot HEB lens-antenna mixers at 1.1, 1.2 and 1.6 THz with signal-to-noise ratios ranging from 70 to 80 dB in a 100 Hz bandwidth. We used this system to measure a number of well-known lens-antenna geometries and compared measured beam parameters with those predicted by PILRAP. We found that the measured first-order Gaussian beam widths agree within a few percent with predicted values from PILRAP. The predicted beam patterns agree in general fairly well in the main beam. The H-plane cuts show best agreement, but sidelobe structure is not correctly predicted. In the E-plane we see in general asymmetry which might be chip- or antenna-related. For this particular lens-antenna design our main conclusion is however that the measured phase center appears systematically closer to the lens vertex than predicted by PILRAP. The offset scales furthermore with waist size.

We believe that this experimental investigation addresses for the first time the validation of the predicted phase-center location by PILRAP at frequencies beyond 1 THz. These results invite for independent verification and progress in lens-antenna modeling. Key difficulties for this design might be the relatively short radius of curvature of the lens surface, the position of the lens surface at about 6 confocal distances of the feed pattern, feedback of internal reflections and reflected back-radiation on the current distribution of the double-slot antenna and chip details not considered in PILRAP, e.g. the finite size of the substrate, presence IF line and RF choke and glue layer between chip and lens. We first propose to independently verify the first-order and large-scale effects by a hybrid model combining the strengths of commercial planar antenna simulation packages and a near-field propagation technique scattering a set of incoming polarized plane waves from the antenna through the lens surface by using a Singular Value Decomposition (SVD) technique. As a second step the remaining difficulties, that most likely show up in details of the sidelobe structure, might be addressed through the use of Finite Difference Time Domain (FDTD) techniques.

Acknowledgment

The authors would like to thank Sergey Cherednichenko and Therese Berg from Chalmers University of Technology (CTH), Göteborg, Sweden for providing the lens-antenna HEB mixers used at 1.6 THz. We are furthermore grateful to Merlijn Hajenius and Jianrong Gao from the Kavli Institute of NanoScience Delft, Delft University of Technology, the Netherlands for their work on the HEB lens-antenna mixer used at 1.1 and 1.2 THz. At the National Institute of Space Research of the Netherlands we acknowledge Jochem Baselmans, Pieter Dieleman, Marinus Jochemsen, Martin Eggens and Geert Keizer for their help in taking measurements. We also acknowledge Tully Peacocke and John Lavelle at the National University of Ireland, Maynooth for running PILRAP and GRASP simulations. Finally special thanks to John Ward and John Pearson from Jet Propulsion Laboratory, Pasadena, USA for loaning us the 1.6 THz LO and RF test source as well as test hardware for the 1.1 and 1.2 THz RF test source without which we would not have been able to do these measurements.

References

[1] D. F. Filipovic, S. S. Gearhart and G. M. Rebeiz, "Double-slot Antennas on Extended Hemispherical and Elliptical Silicon Dielectric Lenses", *IEEE Trans. Microwave Theory Tech.*, Vol. 41, 1993, pp. 1738-1749.

[2] M .J. M. van der Vorst, "Integrated Lens Antennas for Submillimetre-wave Applications", Ph.D. dissertation, Eindhoven University of Technology, the Netherlands, 1999.

[3] W. Jellema et al , "Experimental Verification of Electromagnetic Simulations of a HIFI Mixer Sub-Assembly", *Proc. 14th Int. Symp. on Space Terahertz Technology*, Tucson, USA, April 22-24, 2003.

[4] W. Jellema, R. Huisman, N. Trappe, T. J. Finn, S. Withington and J. A. Murphy, "Comparison of Near-Field Measurements and Electromagnetic Simulations of the Focal Plane Unit of the Heterodyne Instrument for the Far-Infrared" et al, *Proceedings of the 5th Int. Conf. on Space Optics*, Toulouse, France, March 30 – April 2, 2004.

[5] B. D. Jackson, "NbTiN-Based THz SIS Mixers for the Herschel Space Observatory", Ph.D. dissertation, University of Groningen, National Institute for Space Research of the Netherlands and the Delft University of Technology, all in the Netherlands, 2005, Chapter 7, pp. 147-176.

[6] B. D. Jackson, K. J. Wildeman and N. D. Whyborn on behalf of the HIFI consortium, "The HIFI Focal Plane Unit", *Proc. 13th Int. Symp. on Space Terahertz Technology*, Cambridge, USA, 26-28 March 2002, pp. 339-348.

[7] J. Lesurf, *Millimeter-wave Optics, Devices & Systems*, Adam Hilger: Bristol and New York, 1990, pp. 113.

[8] W. Jellema et al, "Performance Characterisation and Measurement Results of a Submillimeter-Wave Near-Field Facility for the Heterodyne Instrument for the Far-Infrared", *Proc. 3rd ESA Workshop on Millimeter Wave Technology and Applications*, Espoo, Finland, May 21-23, 2003.

[9] P. F. Goldsmith, *Quasioptical Systems: Gaussian Beam Quasioptical Propagation and Applications*, IEEE Press:New York, 1997, Chapter 3 and 7.

A Hot Spot Model for HEB Mixers Including Andreev Reflection

Harald Merkel
Chalmers University of Technology , SE 412 96 Göteborg , Sweden

Abstract

A device model for HEB mixers is described that takes two additional effects into account: Andreev reflection at the hot spot boundaries and critical current variations on the bridge. This model is capable to predict IV curves even in the unstable areas with acceptable accuracy. Based on these large signal results a more accurate small signal expansion has been developed: In the framework of this model heating due to a small signal current change acts differently from a small signal voltage change at IF.The small signal model allows accurate predictions of the conversion gain and the mixer noise including thermal fluctuation, Johnson and quantum noise.

Introduction

Hot spot models for HEB mixers have been proposed in recent years resulting in a substantial improvement in HEB modelling and understanding of the device physics. Such models require the solution of an one-dimensional heat balance. The occurrence of a DC resistance and the device's mixing capabilities are explained by the formation of a hot spot, i.e. a normal conducting zone wherever the quasiparticles exceed the critical temperature. Depending on the applied heating powers a certain temperature profile is obtained on the HEB bridge resulting in a certain hot spot length. Applying a superposition of a strong LO source and a weak RF signal results in a time-averaged RF heating and in a small beating term oscillating at the difference frequency (IF). The latter causes a tiny change of the hot spot length. This yields a small resistance change at IF which creates small signal currents and voltages through the bridge and finally gives rise to conversion gain of the HEB. Unfortunately none of these hot spot models is capable to predict gain and noise simultaneously with acceptable accuracy without introducing additional empirical parameters or by requiring parameter values being in conflict with experimental results. A popular empirical parameter is the local resistive transition width [1] assuming that the film smoothly turns normal around Tc. This reduction of the resistance slope "helps" to fit the conversion gain but still too much heating power is predicted. Required values for this transition are about 800mK whereas experiments reveal some 50mK. For Nb the case is even worse [2]. There are strong indications that some physical effects are not covered by a simple hot spot based device model. In this paper two additional effects are discussed in order to explain at least part of the discrepancies. These additional effects are due to critical currents and due to Andreev reflection. Throughout this model, **strong localization** is assumed. This applies to quasiparticle and phonon temperatures, the critical current and the quasiparticle bandgap.

Critical current effects on the HEB bridge

In previous models a normal zone is formed wherever the quasiparticle temperature exceeds the critical temperature. This holds only for zero bias current. Otherwise the

normal zone is created wherever the bias current density exceeds the critical current density which is the case at a lower temperature. In the framework of this model, a reduced critical temperature is defined which corresponds to a critical current density equal to the current density caused by the bias current.

Andreev reflection

In simple hot spot models the HEB bridge is assigned a temperature-depending lateral thermal conductivity of exponential or polynomial form [1],[2]. Due to Andreev reflection at the boundary between the hot spot and the superconducting rest of the HEB bridge, only electrons which energy is large enough the overcome the quasiparticle bandgap participate in heat transport. Andreev reflection provides good thermal insulation of the hot spot. As a direct consequence the electron temperature within the hot spot is now more or less constant. The electron temperature profile and the resulting bandgap distribution is summarized in Figure 1:

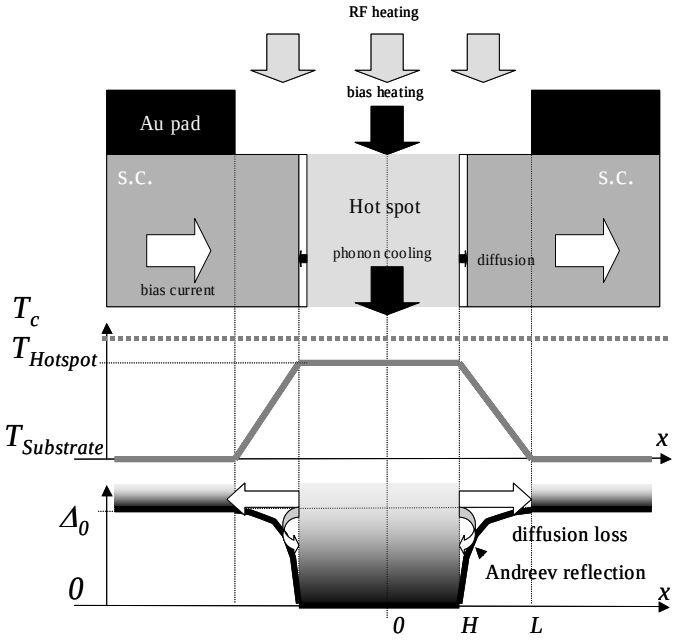

Figure 1: Schematic of a HEB bridge. The whole bridge is heated by RF, the bias heating acts only on the hot spot where superconductivity is suppressed. The electrons are cooled by phonon escape to the substrate and by outdiffusion to the pads. Outdiffusion is reduced by Andreev reflection at the hot spot boundary.

Model assumptions

The HEB device model presented here is based on a set of assumptions. All parameters used here are summarized in Table 1 at the end of the paper including typical values for the calculations presented here:

1: Localization and immediate thermalization

The correlation length is of the order of the film thickness. All superconducting parameters are localized. The film properties in vertical direction are homogenous. Besides that one assumes instantaneous thermalization of the heating powers by electron-electron interaction. Then electrons and phonons are described by effective electron and phonon temperatures.

2: Heating by superposition

The HEB is heated by LO power being the linear superposition of a local oscillator (LO) signal and a weak RF source. This superposition results in a power deposited in the HEB bridge at the intermediate frequency (IF) of the form:

$$p_{IF} \propto 2\sqrt{P_{LO} P_S}$$

In time average the HEB bridge is heated by the mean value of the LO power and DC power.

3: A model for the critical current density on the HEB bridge

Operating a HEB as a mixer requires a substantial bias current to be carried by the HEB bridge. Therefore the superconductivity on the HEB bridge is suppressed wherever the local critical current is exceeded. The theoretical temperature dependence of the local critical current density $j_c(T,x)$ is given by Ginzburg-Landau theory [3]. Performing a nonlinear best fit a simplified and more convenient relation is obtained (the parameters are explained in Table 1):

$$j_c(T,x) = j_c(0) \cdot \left[1 - \frac{T(x)}{T_c}\right]^{\gamma} \qquad (1)$$

Here γ denotes a best fit coefficient set to 0.408. For T_c ranging from 8.5K to 11.5K this yields a more accurate model than the "usual" setting [3] of γ=1.5 for low temperatures and 0.5 for large temperatures. Solving (1) for the quasiparticle temperature, a "reduced" critical temperature is obtained for voltage bias:

$$T_{c,eff,V}(V_0, x_0) = T_c \cdot \left[\left(\frac{V_0}{j_c(0) \cdot A \cdot R_N \cdot \frac{x_0}{L}}\right)^{\frac{1}{\gamma}} - 1\right] \le T_c \qquad (2)$$

The results for the reduced critical temperature for voltage bias for a voltage of V_0=0.8mV (1.0mV and 1.2mV) are summarized in Figure 2.

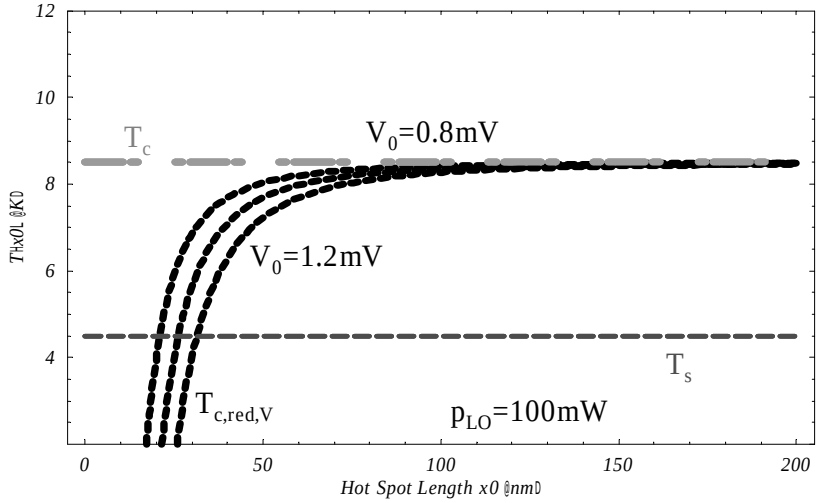

Figure 2: Reduced critical temperature for a bias voltage of V_0=0.8mV (1.0mV and 1.2mV , the black dotted curves) with a substrate temperature of 4.2K and a critical temperature of 8.5K.

4: Almost perfect Andreev reflection at the hot-spot boundaries

A hot spot is formed wherever the bias current exceeds the critical current. The remaining parts of the bridge are in perfect Meissner state. The hot spot is heated by the absorbed bias power and the uniformly absorbed LO power. The quasiparticles in the hot spot are cooled by electron-phonon interaction and the heat is removed from the film by phonon escape. At the NS interfaces Andreev reflection [4] determines the amount of heat being able to leave the hot spot by diffusion. In the ideal case (perfect Andreev reflection) no heat transfer will occur across the interface and the whole cooling power is carried by the phonon path. In reality only the fraction of "normal" electrons with the energy of the quasiparticle levels in the superconductor will be able to carry heat across the NS interface. As a first order approximation we neglect the fact that the quasiparticle bandgap opens slowly on a length given by the thermal healing length and assume the bandgap to be its coldest value reached at substrate temperature immediately. This is an acceptable assumption since we are only interested in the net heat loss of the hot spot to the antenna pads – at some point in the superconductor all electrons with energies smaller than the local bandgap will be reflected and only those being able to overcome the highest bandgap will remove heat laterally from the hot spot. The fraction of electrons transporting heat α across the hot spot boundary is estimated using a Fermi-Dirac distribution function for the electron density $n_E(E)$ [5]:

$$\alpha = \frac{\int_{\Delta}^{\infty} n_E(E)dE}{\int_{0}^{\infty} n_E(E)dE} = \frac{kT\ln\left(1+e^{\frac{\Delta(T)}{kT}}\right)-\Delta(T)}{kT\ln 2},\ \Delta(T)=\Delta_0\left[1-\frac{T}{T_c}\right]^{\gamma} \qquad (3)$$

Calculations show that typical values of the Andreev transmission for critical temperatures around 10K and pad temperatures of the order 5K are in the range 1% to 10% providing good thermal isolation of the hot spot. It is important to note, that this model assumes the antenna pads of the HEB to be in perfect Meissner state. Using this model for HEB configurations with normal conducting antenna pads, the maximum value of the quasiparticle bandgap needs to be changed appropriately. In the next section, the hot spot size is calculated based on the previous model assumption by approximating the solution of an one-dimensional heat transport equation.

Solving for the temperature and the size of the hot spot

The quasiparticle temperature on a hot spot of given (but yet unknown) length $2x_0$ is determined by an equilibrium between electron-phonon cooling P_P, RF and bias heating and cooling due to net outdiffusion through the NS interfaces P_D. One obtains then [6]:

$$P_P + P_D = \frac{P_{LO} + \frac{V_0^2}{R_N \frac{x_0}{L}}}{2 \cdot x_0 \cdot D \cdot W} \qquad (4)$$

The net heat loss due to heat conduction from a hot spot with temperature $T_{c,eff,V}$ is determined by the gradient of the quasiparticle temperature between the hot spot and the antenna pads:

$$P_D = 2\alpha \cdot \lambda \cdot \frac{A}{V} \cdot \frac{T_s + T_{c,eff,V}}{(x_0 - L)} = 2\alpha \cdot \lambda \cdot \frac{T_s + T_c\left[\left(\frac{L \cdot V_0}{j_c A R_N x_0}\right)^{\frac{1}{\gamma}} - 1\right]}{x_0 \cdot (x_0 - L)} \quad (5)$$

For the electron-phonon interaction one is left with the "usual" expression [6]:

$$P_P = \sigma_E\left(T^n - T_p^n\right) \quad (6)$$

The power being transferred to the phonons heats the film phonons that is cooled by phonon escape to the substrate. The heat transport by phonons in direction of the film is neglected. Then a heat balance for the phonons becomes:

$$\sigma_E\left(T^n - T_p^n\right) = \sigma_P\left(T_p^m - T_S^m\right) \approx \delta \cdot \sigma_E\left(T_p^n - T_S^n\right) \quad (7)$$

Inserting (7) in (6) and subsequently in (5) and (4) the temperature of a hot spot T for a given length x_0 is obtained by:

$$\frac{\delta \cdot \sigma_E}{1+\delta}\left(T^n - T_s^n\right) + 2\alpha \cdot \frac{T_s + T_c\left[\left(\frac{L \cdot V_0}{j_c A R_N x_0}\right)^{\frac{1}{\gamma}} - 1\right]}{x_0 \cdot (x_0 - L)} = \frac{P_{LO} + \frac{V_0^2}{R_N \frac{x_0}{L}}}{2 \cdot x_0 \cdot D \cdot W} \quad (8)$$

For (8) a closed form analytical solution is available. A typical result for the quasiparticle temperature is shown in Figure 3. Note that with perfect Andreev reflection (i.e. no diffusion losses) the hot spot will violate the boundary condition under the antenna pads.

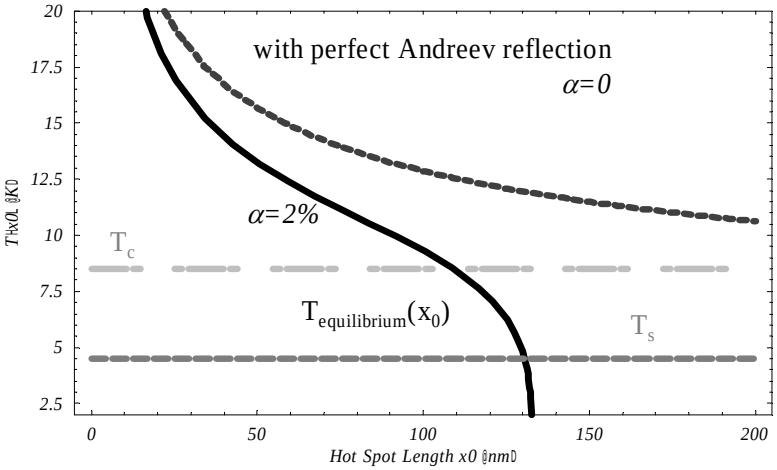

Figure 3: Equilibrium temperature of a hotspot with variable length (for a device length of 2 x 200nm) with 2% Andreev transmission (solid black line) and perfect Andreev reflection (dotted dark gray line) together with the substrate temperature T_s and the critical temperature T_c.

Obviously the temperature in the hot spot (and therefore also at the end of the hot spot) must be equal to the quasiparticle temperature required to break superconductivity for the given bias current. From this the hot spot length is calculated. A graphical solution for a single operating point is shown in the following Figure:

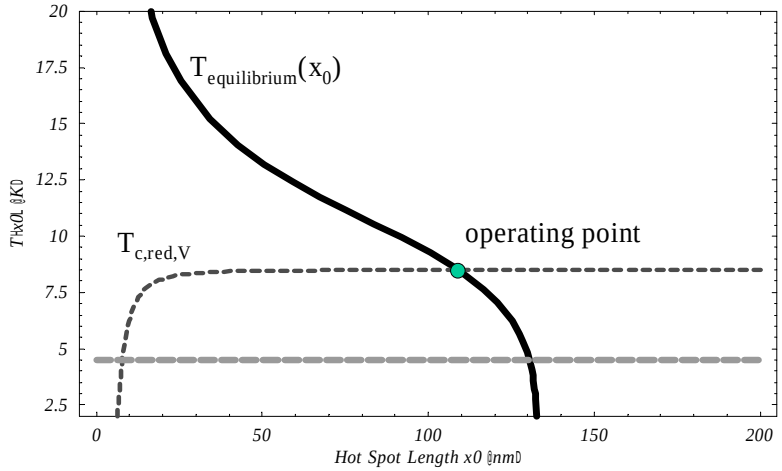

Figure 4: Solving for a hot spot length at 0.3mV bias voltage and 100nW LO power. T_c is 8.5K and the substrate is at 4.2K. The device length is 400nm, its width is 4μm and the thickness is 50Å.

Figure 5 shows a comparison between theory (thin and partially dotted curves) and experiment (thick curves) for various LO powers. The topmost curve is obtained for no RF heating at all and the lowest one for 300nW. The curves in between are obtained in steps of 25nW. For the measured curves, the topmost is obtained at about 25nW LO power and the lowest at about 300nW.

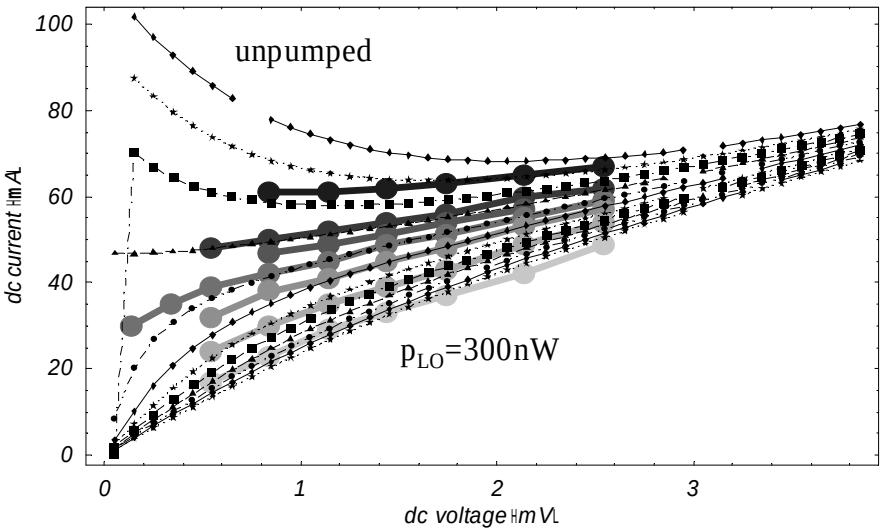

Figure 5: Measurement and theoretical results for the IV curve for a NbN HEB on MgO with the dimensions 400nm x 4μm x 55Å measured at 2.5THz. The measured points are connected by thick gray lines. The black curve is an unpumped curve, the light gray is pumped with about 300nW LO power according to a standard isothermal method applied far away from the optimum point for large bias voltages. The calculated values are obtained for 0nW up to 300nW LO power with a step size of 25nW.

Small signal model

The HEB mixer topology is shown in Fig. 6. It is similar to the topology from [7] where the biasing resistor has been replaced by a large inductance serving as RF coil:

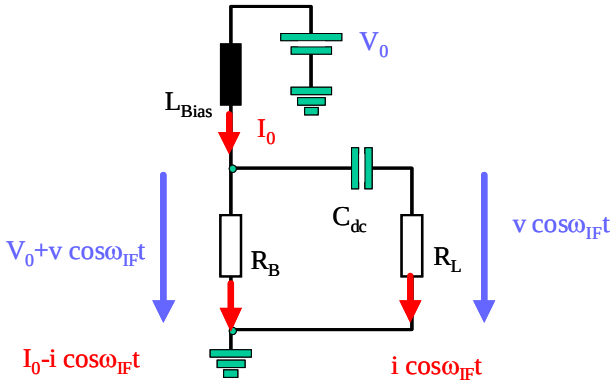

Figure 6: Mixer topology for a typical HEB application – the inductance ensures proper voltage biasing for choosing a proper DC operating point. For IF signals, the inductance poses an open circuit and the IF signal is coupled to the load resistance by a DC block capacitor. ω_{IF} denotes the intermediate frequency i.e. the difference frequency between the LO and the RF signal.

In this model, the large signal relations are behave differently in current and voltage. This is contrasted by older models [1],[7],[8] where only heating powers are considered. Let us assume that the bolometer resistance given by the hot spot length depends on LO heating power, bias current and bias voltage. Then the small signal resistance change in the bolometer r_B is modelled by:

$$r_B = C_{rf}\sqrt{P_{LO}\cdot P_S} + C_V v\cdot I_0 - C_I i\cdot V_0 \qquad (9)$$

From this, the power in the load resistance can be calculated and one obtains for the conversion gain:

$$G = \frac{P_L}{P_S} = \frac{2\cdot I_0^2}{(R_B+R_L)^2}\cdot\frac{C_{rf}^2\cdot P_{LO}}{\left[1-I_0^2\cdot\dfrac{C_I R_B - C_V R_L}{R_B+R_L}\right]^2} \qquad (10)$$

Values for the conversion loss of a HEB and comparison with measurements are indicated in Figure 7.

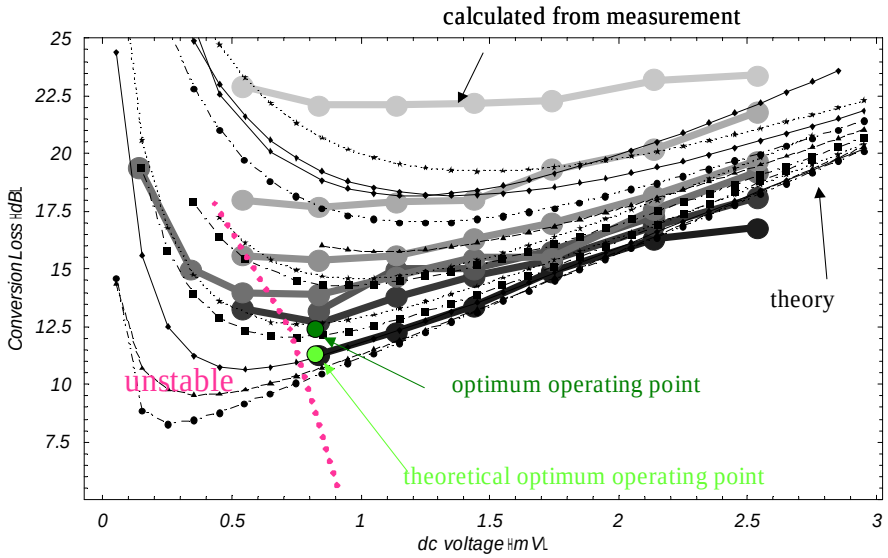

Figure 7: Calculated intrinsic conversion gain based on measurements (thick gray curves) and theoretical results (dashed and dotted curves) for the intrinsic conversion loss for a NbN HEB on MgO with the dimensions 400nm x 4µm x 55Å measured at 0.6THz. The measurement data have been obtained at an IF frequency of 1.5GHz.

HEB Noise

Noise in the HEB is caused by Johnson noise since the hot spot forms a resistor with a certain temperature $T_{Hotspot}$. The noise contribution at the mixer output T_J^{out} is given by [9],[10]:

$$T_J^{out} = \frac{4 \cdot R_L \cdot R_B \cdot T_{Hotspot}}{(R_B + R_L)^2} \cdot \frac{1}{1 - I_0^2 \dfrac{C_V R_L - C_I R_B}{R_B + R_L}} \tag{11}$$

Any system of a given temperature with a given thermal coupling to a cold reservoir and a certain volume exhibits thermal fluctuations [9] resulting in noise. For a hot spot this results in [10]:

$$T_{TF}^{out} = \frac{I_0^2 R_L}{(R_B + R_L)^2} \cdot \frac{1}{1 - I_0^2 \dfrac{C_V R_L - C_I R_B}{R_B + R_L}} \cdot \left[\left. \frac{\partial R}{\partial T} \right|_{T=T_{hotspot}} \right]^2 \cdot \frac{4 T_{hotspot}^2 \tau_{e,relax}}{C_e \cdot V \cdot \dfrac{x_0}{L}} \tag{12}$$

A third noise contribution is caused by quantum noise [11],[12]:

$$T_Q^{out} = 2G \cdot \left(L_{optics} L_{optics\,4K} \left[\frac{R_B}{R_S} + 1 \right] - 1 \right) \cdot \frac{h\nu}{2k} \tag{13}$$

Adding up all the contributions and transferring them to the mixer input, the DSB input noise temperature T_{in} is obtained [11]:

$$T_{in} = L_{optics} \frac{T_{TF}^{out} + T_J^{out} + T_{IF} + T_Q^{out}}{2G} + (L_{optics} - 1) \frac{h\nu \cdot B}{e^{\frac{h\nu}{kT_{optics}}} - 1} \tag{14}$$

Results for the DSB receiver noise temperature are summarized below:

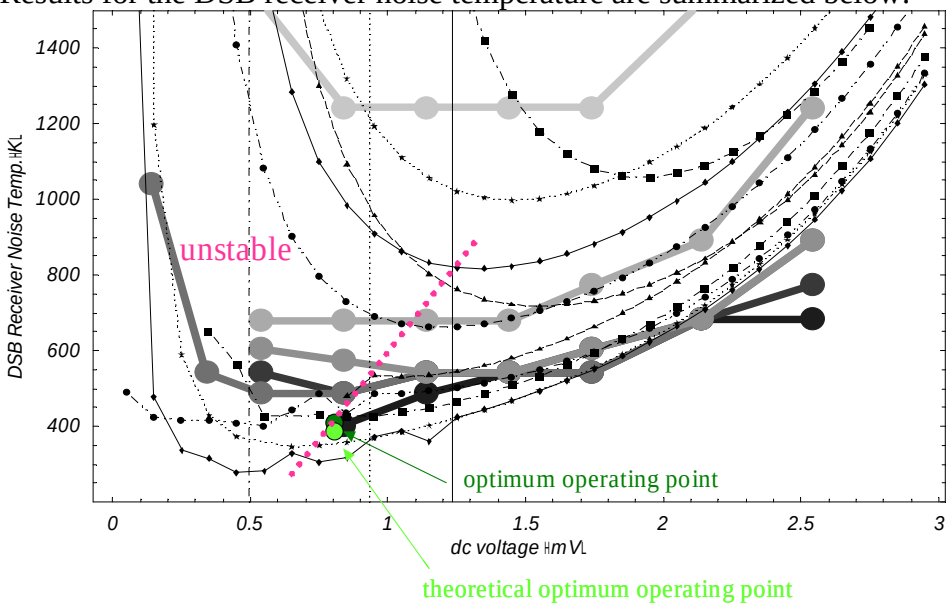

Figure 8: Measured receiver noise (thick gray curves) and theoretical results (dashed and dotted lines) for the DSB receiver noise temperature for a NbN HEB on MgO with the dimensions 400nm x 4µm x 55Å measured at 0.6THz.

The noise measured at the IF output of the HEB is a collection of the warm load at the input T_{lab} of the HEB collected in both sidebands, the fluctuation, Johnson and quantum

noise contributions and the contribution of the optics losses at a given temperature of the optics:

$$T_{out} = T_{lab} \cdot 2G + T_{TF}^{out} + T_J^{out} + T_Q^{out} + \left(L_{optics} - 1\right)\frac{h\nu \cdot B}{e^{\frac{h\nu}{kT_{optics}}} - 1} \cdot 2G \qquad (15)$$

Results for the output noise temperature is summarized below for the same device as in Fig. 5.

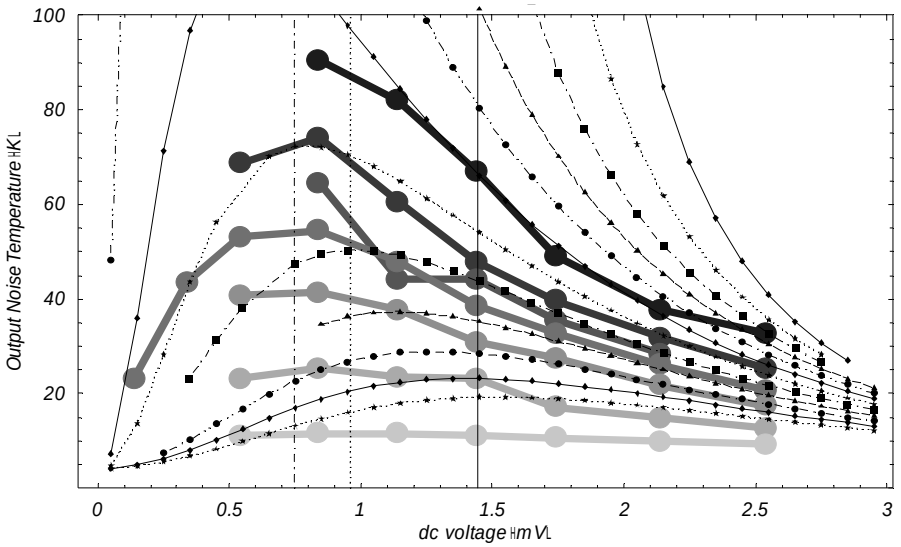

Figure 9: Measurement (thick, gray curves) and theoretical results (dashed and dotted lines) for the output noise temperature for a NbN HEB on MgO with the dimensions 400nm x 4μm x 55Å measured at 0.6THz.

Conclusion

A HEB model including critical current effects and Andreev reflection at the hot spot ends together with a small signal model where heating due to RF, IF currents and voltages is treated differently improves the quality of performance predictions by HEB device models substantially. In addition complete relations for the quantum noise in HEB receivers are now available (c.f. the contribution of K.S.Yngvesson and E.L.Kollberg in this issue) and have already been introduced in the model presented here. The model describes IV curves with satisfying accuracy and yields reasonable conversion gain and noise figures within the accuracy of the measurements. The device model has been successfully tested on various NbN HEBs with different geometries ranging from 120nm x 1μm to 400nm x 4μm. More tests on NbN on a larger geometry range and HEBs based on other materials have to be done to yield conclusive results about the overall model quality.

Model Parameters

Parameter	Description	Value used for model calculation
A	Film cross section	$A = D \cdot W$
α	Transmissivity of the s-n interface due to leaky Andreev reflection	$\alpha \approx 0.02$ typical
B	RF antenna bandwidth	$B = 500GHz$
C_E	Electron thermal capacity	$C_E = 1600\frac{Ws}{m^3 K}$ at T_c

C_I	HEB resistance change due to a small current change at IF	$C_I = \frac{R_N}{2L \cdot V_0} \cdot \frac{\partial x_0}{\partial i}\Big\|_{P_{LO}=const, v=const}$
C_{rf}	HEB resistance change due to a small change of the RF heating power at IF	$C_{rf} = \frac{R_N}{2L} \cdot \frac{\partial x_0}{\partial P_{LO}}\Big\|_{v=const, i=const}$
C_V	HEB resistance change due to a small voltage change at IF	$C_V = \frac{R_N}{2L \cdot I_0} \cdot \frac{\partial x_0}{\partial v}\Big\|_{P_{LO}=const, i=const}$
D	Film thickness	$D = 35\mathring{A}$
δ	Phonon to electron efficiency ratio	$\delta \approx 0.2$
$\Delta(T)$	Quasiparticle bandgap as a function of quasiparticle temperature	
Δ_0	Quasiparticle bandgap extrapolated to 0K	$\Delta_0 = 800GHz$
G	Conversion gain of the HEB	
γ	Exponent in the temperature dependence of the critical current , obtained by best fit to Ginzburg-Landau expression	$\gamma = 0.408$
h	Planck's constant	
I_0	Bias current (DC) across the HEB bridge	$I_0 = \frac{V_0}{R_B}$
i	Small signal current (IF) across the HEB bridge	
$j_c(T,x)$	Local critical current density , function of quasiparticle temperature	
$j_c(0)$	Maximum critical current density at 0K, related to maximum critical current by division by bridge cross section	$j_c = \frac{I_c}{D \cdot W}\ I_c = 160\ \mu A$
k	Boltzmann's constant	
λ	Lateral thermal conductivity	$\lambda = 1\frac{W}{Km}$
λ_{eff}	Lateral effective thermal conductivity across the s-n boundary	
$2 \cdot L$	HEB bridge length (Length between the pads , contact zone under the pads not taken into account)	$L = 200nm$
L_{optics}	Loss of the optics at room temperature	$L_{optics} = 1.3$
$L_{optics4K}$	Loss of the optics at cryogenic (substrate) temperature	$L_{optics4K} = 1.7$
m	Exponent for the temperature dependence of phonon escape	$m = 4.0$
n	Exponent for the temperature dependence of electron-phonon interaction	$n = 3.6$
ν	RF frequency	$\nu = 1600GHz$
P_D	Power leaving the hot spot by electron diffusion	
p_{IF}	Power absorbed by the HEB at the intermediate frequency	
P_L	Power delivered to the load at IF	
P_{LO}	Local oscillator power absorbed by the HEB	variable
P_P	Power leaving the hot spot by phonon cooling	
P_S	RF signal power absorbed by the HEB	

r_B	Small signal HEB resistance change due to IF beating	
R_B	Resistance of the HEB in the operating point	
R_L	Load resistance	$R_L = 50\Omega$
R_N	Normal resistance of the HEB bridge (at 20K)	$R_N = 65\Omega$
R_S	Antenna impedance (Real part)	$R_S = 100\Omega$
σ_E	Electron-phonon cooling efficiency	$\sigma_E = \frac{C_e}{3.6T^{2.6}\tau_{e\to p}}$
σ_P	Phonon escape efficiency	$\sigma_P \approx \delta\sigma_E$
$\tau_{e\to p}$	Electron- phonon interaction time constant	$\frac{1}{\tau_{e\to p}} = 8GHz$
$\tau_{e,relax}$	Electron energy relaxation time constant	$\frac{1}{\tau_{e,relax}} = 5GHz$
$T(x),\quad T$	Local quasiparticle temperature	
$T_{equilibrium}$	Hypothetic hot spot temperature, where heating and cooling powers are equal	
T_c	Critical temperature of the HEB bridge	$T_c = 8.5K$
$T_{c,effI}$	Reduced critical temperature due to critical current effects under current bias conditions	
$T_{c,effV}$	Reduced critical temperature due to critical current effects under voltage bias conditions	
$T_{hotspot}$	Hot spot temperature in a given operating point	
T_{IF}	Noise temperature constribution of the IF amplifier	$T_{IF} = 7K$
T_{in}	Noise temperature at the input of the receiver, DSB receiver noise temperature	
T_J^{out}	Noise temperature at the output of the mixer due to thermal (Johnson/ Nyquist) noise	
T_{lab}	Room temperature in the surrounding laboratory	$T_{lab} = 292K$
T_p	Temperature of the phonons in the hot spot	
T_Q^{out}	Noise temperature at the output of the mixer due to Quantum noise	
T_s	Substrate temperature under the HEB bridge	$T_s = 4.5K$
T_{TF}^{out}	Noise temperature at the output of the mixer due to Thermal Fluctuation noise	
V	HEB bridge volume	$V = D \cdot W \cdot L$
v	Small signal voltage (IF) across the HEB bridge	
V_0	Bias voltage (DC) across the HEB bridge	variable
$2 \cdot x_0$	Length of the hot spot	
W	Film width	$W = 4\mu m$

Table 1: List of used parameters with their abbreviations and model values for the calclation presented in the paper

References

[1] H.F. Merkel, P. Khosropanah, D. Wilms Floet, P. Yagoubov, E.L. Kollberg, "Conversion Gain and Fluctuation Noise of Phonon Cooled Hot Electron Bolometers in Hot Spot Regime", IEEE-Trans. MTT, 14 Apr. 2000, **48**(4), pp.690-699

[2] D. Wilms Floet, J. J. A. Baselmans, T. M. Klapwijk, J. R. Gao " Resistive transition of niobium superconducting hot-electron bolometer mixers", APL, **73**(19), pp. 2826-2828, November 9, 1998

[3] C.P. Poole, H.A. Farach, R.J. Creswick "Superconductivity", Academic Press 1995

[4] A.F. Andreev, Zh. Eksp. Teor. Fiz. **46**, 1823 (1964), Sov. Phys. JETP **19**, 1228 (1964).

[5] N.W. Ashcroft, N.D. Mermin "Solid State Physics", Saunders College Publishing 1976

[6] E.M. Gershenzon, G.N. Gol'tsman, A.M. Lyulkin, A.D. Semenov, A.V. Sergeev," Electron-
phonon interaction in ultrathin Nb films", Sov. Phys JETP. **70**(3). pp 505-511 (1991)

[7] F. Arams, C. Allen, B. Peyton, E. Sard, Proceedings of the IEEE **54**(3) 308-318 (1966)

[8] H.F. Merkel, P. Khosropanah, K. S. Yngvesson, S. Cherednichenko, M. Kroug, A. Adam, E.L. Kollberg, "An Active Zone Small Signal Model for Hot Electron Bolometric Mixers", Proc. 12 ISSTT, San Diego, March 2001

[9] B.S. Karasik, A.I. Elantev, "Noise Temperature Limit of a Superconducting Hot-Electron Bolometer Mixer", Appl. Phys. Lett. **68**, pp. 853-855, 1996

[10] P. Khosropanah, H.F. Merkel, K.S. Yngvesson, A. Adam,
S. Cherednichenko, E.L. Kollberg, "A Distributed Device Model for Phonon-cooled HEB Mixers Predicting IV Characteristics, Gain, Noise and IF Bandwidth", Proc. 11.th ISSTT U.Mich. Ann Arbor MI, May 2000

[11] E.L. Kollberg, K.S. Yngvesson "Quantum Noise Contribution to the Receiver Noise Temperature of HEB THz Heterodyne Receivers", this issue

[12] A.R. Kerr, "Suggestion fo Revised Definition of Noise Quantities Including Quantum Noise", IEEE Trans. MTT **47**(3) pp.325-329, March 1999

Direct correspondence between HEB current-voltage characteristics and the current-dependent resistive transition

R. Barends[1], M. Hajenius[1,2], J.R. Gao[1,2], and T.M. Klapwijk[1]

[1]Kavli Institute of NanoScience, Faculty of Applied Physics, Delft University of Technology, Lorentzweg 1, 2628 CJ Delft, The Netherlands.
[2]SRON National Institute for Space Research, Sorbonnelaan 2, 3584 CA Utrecht, The Netherlands.

***Abstract*— Currently, superconducting hot electron bolometer mixers are the most promising candidates for heterodyne detection above 1 THz. The core of its bolometric operation is the resistive transition of the superconductor. In the past device transitions, parameterised by sigmoidal transitions, entered modelling equations, and proved insufficient to adequately predict current voltage characteristics. Recently we have experimentally observed the intrinsic film transition to be different from the device transition. We analyse the role of the current dependent intrinsic transition and qualify device response, focussing on operating conditions, using a distributed numerical model based on the electron and phonon temperature and the local resistivity. Including the current dependence results in an excellent agreement between predicted and measured pumped $I(V)$, and a modification of the local resistivity, leading to a new view on the device response.**

I. Introduction

Hot electron bolometer mixers have evolved to a valuable addition to the astronomical community, being ideally suited for low noise heterodyne detection above 1 THz. Under operation, due to radiation and bias, the electrons are heated and induce local resistance. The exact shape of temperature and resistivity profiles results from a delicate interplay between thermal mechanisms, contact issues and local resistivity.

In this interplay the response of the superconductor to the electron temperature, the resistive transition, plays a pivotal role. Earlier, sigmoidal transitions, approximating the device transition, have been shown to be valuable for qualifying the device response to radiation and bias [5], and to provide insight in its mixing mechanism [1].

Still, the intrinsic resistive mechanisms remained underexposed, being veiled by contact effects. Recently, we have shown that the intrinsic film transition, measured on a film without usual contact structure, has a much sharper onset [2].

For analysing the influence of the resistive transition in order to describe more correctly recent device results we have performed a comprehensive numerical analysis, using a distributed heat balance. Qualitatively it is found that a current-dependent local oscillator power induced bell-shaped curve rises with increasing bias, which forms the framework from which the device current-voltage characteristics can be derived.

II. Heat Balance

Under operating conditions, primarily LO power and secondarily DC power induce a temperature profile, which in turn leads to a resistivity profile. As such, we are interested in time-independent processes. The specific shape of these profiles is determined using a one-dimensional distributed heat balance, which takes the form of a coupled differential equation for the electron temperature T_e and phonon temperature T_p,

$$\begin{aligned} \frac{d}{dx}(\lambda_e \frac{d}{dx} T_e) + p - p_{ep} &= 0, \\ \frac{d}{dx}(\lambda_p \frac{d}{dx} T_p) + p_{ep} - p_{ps} &= 0, \end{aligned} \tag{1}$$

in which $\lambda = cD$ denotes a thermal conductance, with D the diffusivity; and p the DC and RF power absorbed per unit volume, $p = p_{DC} + p_{RF}$, with the DC power absorption depending on the local resistivity ρ, $p_{DC} = J^2\rho$. The power transfers between electron and phonon subsystems, and subsequently the substrate are denoted by p_{ep} and p_{ps},

$$\begin{aligned} p_{ep} &= \frac{c_e}{n\tau_{ep} T_e^{n-1}} (T_e^n - T_p^n) \\ p_{ps} &= \frac{c_p}{m\tau_{esc} T_p^{m-1}} (T_p^m - T_b^m) \end{aligned} \tag{2}$$

with the powers $n = 4$ and $m = 4$ for our case [8]. The electron temperature dominates over the phonon temperature in determining device response.

The one-dimensional approach is motivated by the skin depth and the magnetic penetration depth being larger than or of the same magnitude as the device width. Since also $hf \gg 2\Delta$ the LO power absorption is assumed uniform. The assumption of full thermalisation, and thus describing the thermal properties in terms of an electron temperature is allowed, since the inelastic electron-electron interaction length, typically around 10 nm, is smaller than the device length. The electron-phonon interaction time being smaller than the phonon escape time, $\tau_{ep} < \tau_{esc}$, and the wavelength of a thermal phonon $\lambda_T = \frac{hu}{k_B T_p}$, typically around 20 nm, being smaller than the device length motivates the usage of the phonon temperature.

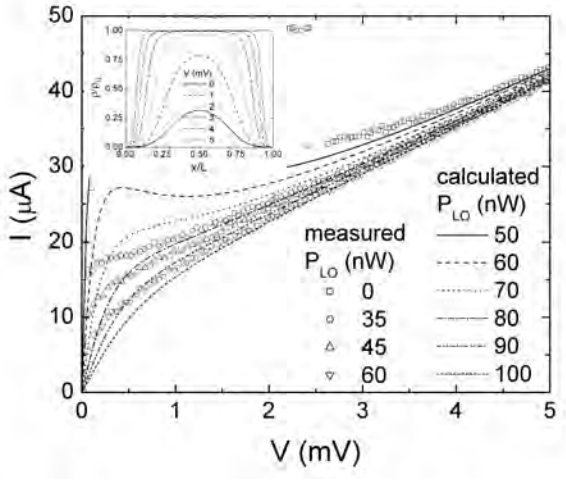

Fig. 1. Using a sigmoidal resistive transition. Results are compared to the $I(V)$ of a small (1x0.15 μm) device measured at 1.6 THz, with $T_b = 4.2K$; pumping power is determined using isothermal technique. At lower bias, near the optimal operating point a structural difference is apparent. The calculated curve with $P_{LO} = 80$ nW is closest to an optimally pumped one. The inset shows the resistivity profiles for this pumping level.

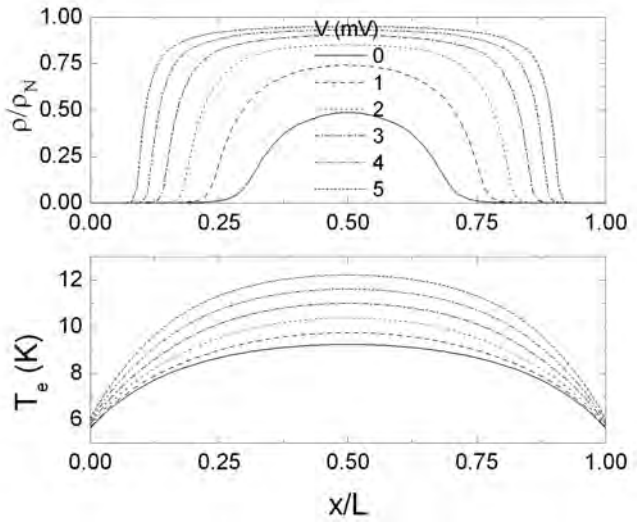

Fig. 2. Electron temperature and local resistivity profiles using the intrinsic resistive transition.

Recently, optimising the contacts between the antenna and the NbN film, by cleaning and inserting a NbTiN interlayer, has virtually doubled sensitivity [3]. This clearly shows the importance of contacts and argues for their involvement in modelling efforts. The phonon temperature at the boundaries equals the bath temperature, following previous modelling [5]. For the electron temperature however, an exponential decay under the contacts is assumed. This conserves the heat flow of the electrons diffusing into the NbTiN and Au, yet involves the contact transparency qualitatively. The boundary condition reads $\frac{d}{dx}T_e(x=0) = \frac{T_e(x=0)-T_b}{l}$. We approximate the decay length with $l = \sqrt{\frac{R_c}{R_\square}} \propto \frac{1}{\sqrt{Tr}}$. For a transparency previously found to be $Tr \approx 0.05$ [4], the thermal decay length is in the order of 5 nm.

Due to the mixed nature of the HEB, with spatial dependent superconductivity, the electronic heat capacity is highly position dependent. Since our interest primarily goes to the role of the resistive transition we take out this complicating factor by assuming a normal state heat capacity and thermal conductance [11]. The phonon heat capacity is assumed close to the Debye model. Experimentally obtained parameters for the NbN film are used for numerical evaluation [6], [7].

III. Resistive Transition

The last step in characterising the HEB's response is translating the knowledge of temperature profiles into the resistance and subsequent $I(V)$ curves. This last step is perhaps the most delicate, and yet essential for validating assumptions used, analysing the response and understanding the physical mechanisms. Therefore, in analysing the HEB, we choose this resistive transition to be a starting point.

From a microscopic view, the resistive transition is a result of many processes, such as flux flow, vortex-antivortex unbinding and material inhomogeneities. Introducing these various processes in a macroscopic heat balance equation is impractical.

In recent modelling a sigmoidal transition has been used, which was fitted to approximate the device transition [2],

$$\frac{\rho(T)}{\rho_N} = \frac{1}{1 + e^{-(T-T_c)/\Delta T_c}} \tag{3}$$

and hence these dynamic microscopics and material properties have been reduced to a T_c, ΔT_c set. This simplification proved to be valuable and gave insight in the formation of resistance, and the subsequent characterisation of $I(V)$ curves and the mixing mechanism [1], [5].

Qualitatively the picture is of a LO power induced bell-shaped resistivity profile, rising fastest in the middle of the bridge, see inset of Fig. 1. Subsequently mixing was found to be most effective in the middle of the bridge.

The downside of models using a sigmoidal transition is that they structurally underestimate the current, thus failing to predict pumped $I(V)$ at low bias, near the optimal operating point, see Fig. 1. The first step in tackling these problems and gain a deeper understanding of the device physics is to choose a better resistive transition. Secondly the LO power needed to pump the device differs significantly between model prediction and experiment, which is partly attributed to simplifications and input parameter accuracy.

Recently, we have learned that the resistive transition of a NbN film without contacts, i.e. the intrinsic film transition, is not sigmoidal, and shows a much sharper onset, see the inset in Fig. 3. The device transition is dominated by contact effects, which do not play a role under operation, since the contacts remain superconducting. The intrinsic transition seems to be a proper choice for describing the local $\rho(T(x))$.

The results of using the intrinsic transition are shown in Fig. 2 and Fig. 3. First of all the electron temperature profiles do not deviate largely from the results previously found, as expected [2]. Note that the electron temperature being higher than the bath temperature at the edges is the result of our choice of the boundary conditions.

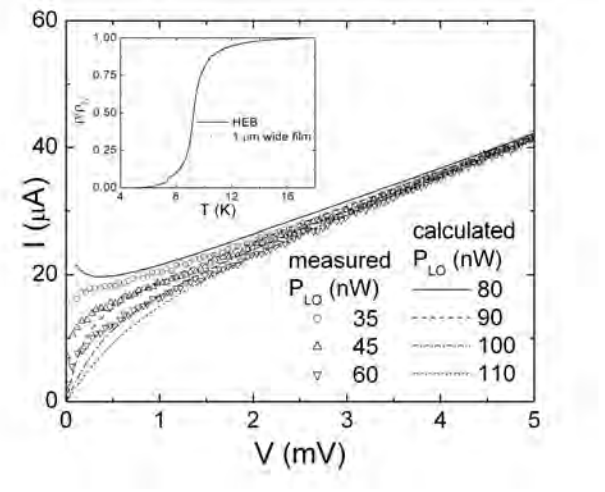

Fig. 3. Modelled and experimental pumped $I(V)$ using the intrinsic resistive transition. The inset shows the difference between the device and film transition.

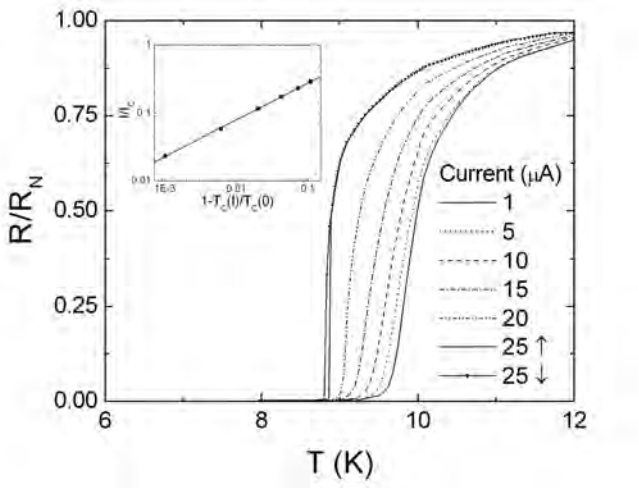

Fig. 4. The intrinsic resistive transition as a function of applied DC bias current of a 1 μm wide processed NbN film. Effectively the critical temperature shifts with increasing bias, and the steepness changes little. The influence of the current on the resistive transition is indicated in the inset, giving $\gamma = 0.54$.

The sharper onset of the intrinsic transition affects the resistivity profiles in the sense that local resistivity is more pronounced at comparable pumping power. Qualitatively the view put forward previously [1], [2] remains valid.

The intrinsic transition shows only marginal improvement for the current-voltage characteristic, and does not capture the device behaviour qualitatively at low bias, where the response is known to be optimal.

IV. Current Dependence

Resistance at the onset of the $\rho(T)$ curve is largely dominated by vortex related behaviour. With increasing electron temperature resistance appears due to vortex-antivortex pair creation, flux flow and phase slip events. These processes depend on the current density [10], hence the local resistivity is an intrinsic current-dependent quantity. Since these processes also depend on material properties, including pinning sites and inhomogeneities, an empirical determination of the resistive transition in the presence of a current is needed.

The intrinsic transition is measured for different DC current bias and shown in Fig. 4. Firstly, the $R(T, I)$ curve shifts, and the apparent downshift of T_c follows the empirical relation

$$\frac{I}{I_c} = (1 - \frac{T_c(I)}{T_c(0)})^{\gamma} \tag{4}$$

for $\gamma = 0.54$, see the inset in Fig. 4. We ignore the small change in the steepness of the resistive transition for different current bias. The shift due to current was first put forward in modelling [9]. Later on the sigmoidal transition, based on the device transition, was extended using a current-dependent critical temperature [5]. Yet the role of current in the intrinsic transition remained underexposed.

The local resistivity profile, calculated using the intrinsic, current dependent resistive transition, is shown in Fig. 5. Again bell-shaped resistivity profiles arise, and the previous conclusions concerning the mixing mechanism remain valid. Yet the resistivity profile is now not only primarily LO-power (and secondarily DC power) induced but also strongly affected by current.

In Fig. 6, we see that the predicted $I(V)$ curves almost fully correspond to the measured curves. For high bias as well as for low bias the model closely follows the measured curves. We achieve a similar result for larger devices.

This unequivocally illustrates that a proper choice of $\rho(T, I)$ is the most pivotal decision in modelling the HEB. We have seen the choice of resistive transition evolve from a sigmoidal transition, approximating the device transition, to the usage of the intrinsic film transition. Yet this change did not have strong effect on the current-voltage characteristics. Only when properly using the current dependence a good agreement is found. This shows that the $I(V)$ is dominated by a good choice of $\rho(T, I)$, not $\rho(T)$, which is in agreement with recent experimental results [12]. Hence device resistance is the result of the interplay between pumping as well as DC power, current, material parameters and the resistive transition: $R = \frac{1}{A}\int_0^L \rho(x, T_e(P_{LO}, P_{DC}), I)dx$.

The current dependence being identified as the dominant choice in modelling the HEB signals a new framework for analysing the device response. The physical behaviour at and around the optimal operating point is much more current oriented than previously assumed. This sheds a new light at our notion of mixing mechanisms, time-dependent processes, related to the thermal time constants, and noise mechanisms, analogous to the excess noise in transition edge sensors [13].

Practically, we might be using the current-dependence twice. In Eq. 1, we use p_{DC}, the local heating due to the transport current, while in $\rho(T, I)$ the current leads to a shift and change of $R(T)$, which may partially be due to heating. We find strong disagreement between measured curves and model calculations for $p_{DC} = 0$. Hence, we believe that the physics contained in Fig. 4 is much more subtle. The thin

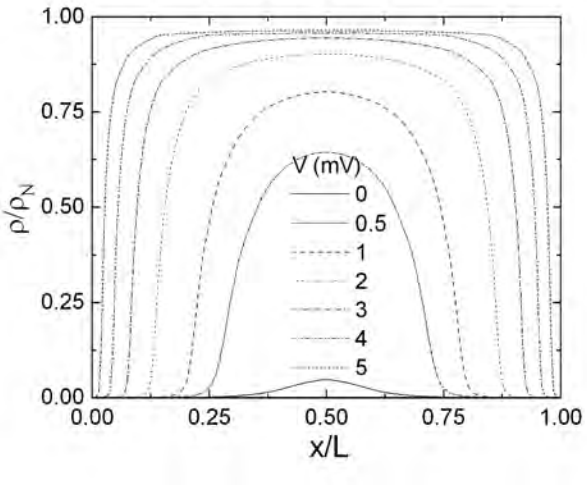

Fig. 5. Local resistivity profiles using the current dependent intrinsic resistive transition. Mixing occurs predominantly in the middle.

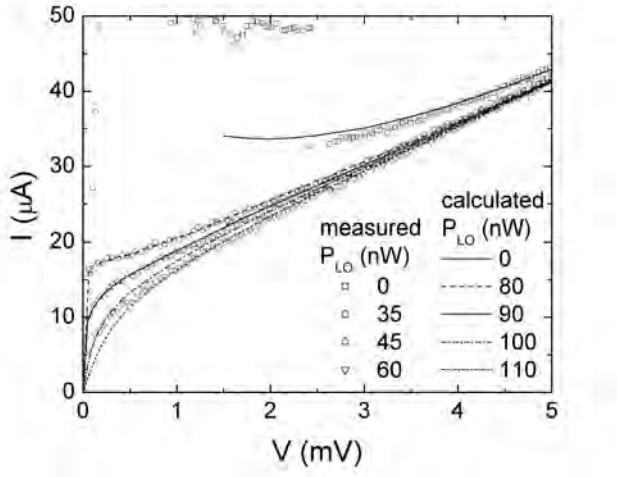

Fig. 6. Using the current dependent intrinsic resistive transition, the model correctly predicts $I(V)$, for high as well as low bias.

NbN films are at the borderline of a superconductor-insulator transition [14], which is known to involve both quasiparticles as well as vortices, topological excitations [15]. Such a two-fluid description will also influence the noise properties [16].

V. Conclusion

Motivated by the inability of present-day HEB models to adequately predict behaviour at low bias, near the optimal operating point, we have analysed different choices for the resistive transition, extending on previous modelling efforts. Using measurements on NbN films, we have replaced sigmoidal transitions, approximating the device transition, with the measured intrinsic film transition. Although this last transition has a significantly different shape, only a marginal improvement was found in predicting current-voltage characteristics. Therefore we have identified the role of current in the intrinsic transition, and, using a $\rho(T, I)$ criterion, our model now correctly predicts the complete $I(V)$ behaviour. Current being identified as a dominant factor in the resistive transition leads to a new view on device response.

Acknowledgements

We thank J. Baselmans for providing the measured $I(V)$ data and A. Baryshev for stimulating discussions. The work is supported partly by RadioNet and partly by INTAS.

References

[1] T.M. Klapwijk, R. Barends, J.R. Gao, M. Hajenius and J.J.A. Baselmans, *Improved superconducting hot electron bolometer devices for the THz range*, Proc. SPIE Vol. 5498, p. 129 (2004).

[2] M. Hajenius, R. Barends, J.R. Gao, T.M. Klapwijk, J.J.A. Baselmans, A. Baryshev, B. Voronov and G. Gol'tsman, *Local resistivity and the current-voltage characteristics of hot electron bolometer mixers*, IEEE Trans. Appl. Sup., in press.

[3] J.J.A. Baselmans, M. Hajenius, J.R. Gao, T.M. Klapwijk, P.A.J. de Korte, B. Voronov and G. Gol'tsman, *Doubling of sensitivity and bandwidth in phonon cooled hot electron bolometer mixers*, Applied. Phys. Letters, **84**, 1958 (2004).

[4] M. Hajenius, J. J. A. Baselmans, J. R. Gao, T. M. Klapwijk, P. A. J. de Korte, B. Voronov and G. Gol'tsman, *Low Noise NbN superconducting Hot Electron Bolometer mixers at 1.9 and 2.5 THz*, Supercond. Sci. Technol. **17**, S224 (2004).

[5] P. Khosropanah, H. Merkel, S. Yngvesson, A. Adam, S. Cherednichenko and E. Kollberg, *A distributed device model for phonon-cooled HEB mixers predicting IV characteristics, gain, noise and IF bandwidth*, Proc. 11^{th} Int. Symp. Space Thz Technology, p 474 (2000); P. Khosropanah, *NbN and NbTiN Hot Electron Bolometer THz Mixers*, Ph. D. Thesis, Chalmers University of Technology (2003).

[6] A.D. Semenov, R.S. Nebosis, Yu.P. Gousev, M.A. Heusinger and K.F. Renk, *Analysis of the nonequilibrium photoresponse of superconducting films to pulsed radiation by use of a two-temperature model*, Phys. Rev. B **52**, 581 (1995).

[7] A.D. Semenov, G.N. Gol'tsman, A. A. Korneev, *Quantum detection by current carrying superconducting film*, Physica C **351**, 349 (2001).

[8] Y. Pellan, G. Dousselin and J. Pinel, *Temperature and Magnetic Field Dependence of NbN Film Resistivity: 3D Weak Localization Effects*, J. Low Temp. Phys. **78**, 63 (1990).

[9] R.S. Nebosis, A.D. Semenov, Yu.P. Gousev and K.F. Renk, *Rigorous Analysis of Superconducting Hot-Electron Bolometer Mixer: Theory and Comparison with Experiment*, Proc. 7^{th} Int. Symp. Space THz Technology, p. 601 (1996).

[10] A.M. Kadin, K. Epstein and A.M. Goldman, *Renormalization and the Kosterlitz-Thouless transition in a two-dimensional superconductor*, Phys. Rev. B **27**, 6691 (1983).

[11] D. Wilms Floet *Hotspot Mixing in THz Niobium Superconducting Hot Electron Bolometer Mixers*, Ph. D. Thesis, Delft University of Technology (2001). Calculations using a powerlaw approximating the superconducting thermal conductance indicate qualitatively equal outcome for a somewhat smaller pumping power.

[12] Z.Q. Yang, M. Hajenius, J.J.A. Baselmans, J.R. Gao , T.M. Klapwijk, B. Voronov, G. Gol'tsman, *Improved sensitivity of NbN hot electron bolometer mixers by vacuum baking*, this conference proceedings.

[13] G.W. Fraser, *On the nature of the superconducting-to-normal transition in transition edge sensors*, Nuclear Inst. and Methods in Physics Research A, **523**, 234 (2004).

[14] H. Su, N. Yoshikawa and M. Sugahara, *Study of electrical conduction properties of NbN thin films using NbN/MgO/NbN double-tunnel junctions*, Supercond. Sci. Technol. **9**, A152 (1996).

[15] V.M. Galitski, G. Refael, M.P.A. Fisher and T. Senthil, *Vortices and quasiparticles near the superconductor-insulator transition in thin films*, cond-mat/0504745.

[16] R.F. Voss, C.M. Knoedler and P.M. Horn, *Phase-slip shot noise at the two-dimensional superconducting transition: evidence for vortices?*, Phys. Rev. B **45**, 1523 (1980).

Hot-Electron Bolometer Mixers on Silicon-On-Insulator Substrates for Terahertz Frequencies

Anders Skalare, Jeffrey Stern, Bruce Bumble and Frank Maiwald

***Abstract*— A terahertz Hot-Electron Bolometer (HEB) mixer design using device substrates based on Silicon-On-Insulator (SOI) technology is described. This substrate technology allows very thin chips (6 μm) with almost arbitrary shape to be manufactured, so that they can be tightly fitted into a waveguide structure and operated at very high frequencies with only low risk for power leakages and resonance modes. The NbTiN-based bolometers are contacted by gold beam-leads, while other beam-leads are used to hold the chip in place in the waveguide test fixture. The initial tests yielded an equivalent receiver noise temperature of 3460 K double-sideband at a local oscillator frequency of 1.462 THz and an intermediate frequency of 1.4 GHz.**

***Index Terms*— Hot–Electron Bolometer, HEB, Superconductor, Heterodyne, Mixer, Terahertz, Submillimeter, Spectrometer**

I. Introduction

The terahertz regime is of significant interest for the study of the interstellar medium and the life cycle of stars due to a large number of spectroscopic lines from species such as ionized carbon and nitrogen, carbon monoxide and water. The low atmospheric transmission requires that such studies be made from space, balloons, aircraft or one of a few high-altitude ground sites. The best concept for high-sensitivity, high-resolution spectrometers from about 1.4 THz up to several THz is the Hot-Electron Bolometer (HEB) Mixer, [1-4] which can provide low-noise operation with local oscillator (LO) power requirements below 1 μW. In order to increase the data gathering speed, future terahertz heterodyne spectrometers will likely use some form of multi-pixel focal plane array. This is especially important for space-borne applications, where the cost of observational platforms is very high.

We are investigating the use of waveguide-based mixers for such arrays, using brass mixer blocks for the prototyping and HEB's on very thin (6 μm) silicon chips that are fabricated from commercial Silicon-On-Insulator (SOI) wafers. The thin silicon chips should allow operation to many THz without the occurrence of substrate modes and resonances that could be expected from thicker substrates. One existing technique uses lapped-down quartz substrates [5], but due to the fragility of these the method is unlikely to work well over about 2 THz. With the SOI approach, the device chips can be shaped almost arbitrarily so that they fit into the waveguide circuit, so that it is not necessary to use larger membranes supported by a frame, which would complicate the microwave design.

The use of a waveguide circuit instead of an open structure (quasioptical) antenna, such as a twin-slot antenna has some advantages. For example, waveguide horn antennas are used, which have better antenna patterns and (in the case of corrugated horns) have better polarization properties than most planar antennas, and which eliminate the risk of cross-talk on the intermediate-frequency side of the mixer. Another advantage, and a main reason for our interest, is that more complex circuits can be constructed to for example allow the LO power to be injected separately from the signal into the mixer block. One of the simplest such configurations is the cross-bar balanced mixer, where a probe on the same chip as the mixer would couple the LO power from a separate waveguide. Since the Signal/LO separation is achieved by use of symmetry and antisymmetry, it should be possible to achieve a broadband mixer circuit that will not require interferometers or beamsplitters in the signal path. Also, a cross-bar mixer does not require moving parts when the local oscillator frequency is tuned, which is an advantage compared to for example a Martin-Puplett interferometer. The mentioned properties would be significant for future space-borne single-pixel mixers, but even more so for a multi-pixel array instrument. We are currently investigating such cross-bar mixers, and will report on produced results in future publications.

Other issues with the SOI chip / waveguide approach that need to be resolved include the difficulties in machining the very small waveguide structures that will be needed at several THz. It is likely that silicon micromachining in some form will be required, for example using laser etching [6] or the Bosch-process Deep Reactive-Ion Etching (DRIE) technique [7]. The purpose of this paper is to report experiments with a 1.5 THz mixer based on the SOI chip / HEB concept, using NbTiN bolometer devices and a diagonal horn waveguide block machined from brass.

Manuscript received Oct 28, 2005. The authors are with the Jet Propulsion Laboratory, California Institute of Technology, Pasadena, CA 91109, United States. The corresponding author is A. Skalare, phone +1-818-3549383, email anders.skalare@jpl.nasa.gov. This research was carried out at the Jet Propulsion Laboratory, California Institute of Technology, and was sponsored by a JPL Research and Technology Development award and by the National Aeronautics and Space Administration. Reference herein to any specific commercial product, process, or service by trade name, trademark, manufacturer, or otherwise, does not constitute or imply its endorsement by the United States Government, or the Jet Propulsion Laboratory, California Institute of Technology.

II. Devices

The mixer chips are produced in-house at JPL and the fabrication has been described in detail in a previous publication [8]. The SOI technology applied is also similar to that described in [9,10]. Commercial Silicon-On-Insulator (SOI) wafers are used, which have a 6 μm thick Si layer bonded to a 400 μm thick oxidized "handle" wafer. In our wafer "front side" process the NbTiN HEB devices and circuits, including gold beam leads, are fabricated on this SOI wafer. In the "back side" process the wafer is attached with wax to a separate thick Si wafer, and the handle wafer is removed from the Si membrane by Deep Reactive-Ion Etching (DRIE). The bared oxide layer is wet-etched, after which the 6 μm thick silicon is patterned and etched by DRIE to define the outline of the silicon chip. The DRIE does not affect the gold beam leads significantly, so that these can extend outside the edges of the silicon. The finished chips are released from the wax using a solvent and then strained out with a filter paper. Fig.1 shows a finished device chip for 1.5 THz. The NbTiN device films produced have a superconducting transition temperature (Tc) of about 9.5 K and a film resistance of about 1250 ohms/square, with slightly lower Tc (8.5 to 9 K) for fully processed devices. The -3dB intermediate frequency bandwidth achieved at a signal frequency of 19 GHz is about 1.4 GHz (Fig. 2), see [8] for more details.

III. Waveguide Circuit

The general approach is to fabricate superconducting HEB's on shaped thin silicon substrates and to install these into a waveguide mixer block, taking advantage of the low losses and the high beam-quality of waveguide horn antennas as well as giving scalability to higher frequencies (waveguide blocks with horns have already been successfully machined at JPL for other applications up to 2.8 THz). The SOI substrate is shaped in such way that it can be installed into a reduced-height waveguide mixer block, and be held in place by clamping the protruding gold beam-leads between different parts of the machined mixer block. The device is mounted with the flat side of the chip against the end of the waveguide, rather in the waveguide E-plane. The primary reason is that the design serves as a prototype for a future cross-bar balanced mixer, where this configuration will allow local oscillator power to be coupled to the devices

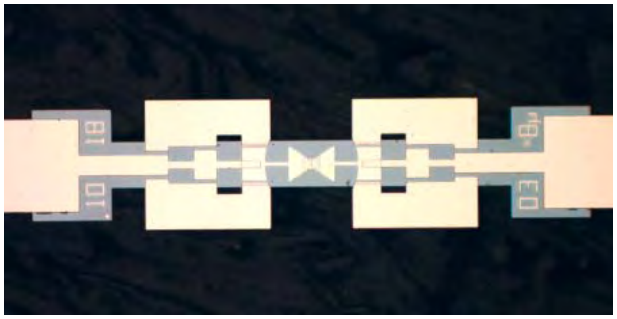

Fig. 1. An HEB/SOI chip. The I-shaped silicon substrate has a thickness of 6 μm, and a width at the bow-tie shaped waveguide probe of 50 μm. Gold beam leads are used to contact the chip and to hold in place in the waveguide circuit. The HEB is at the geometric center.

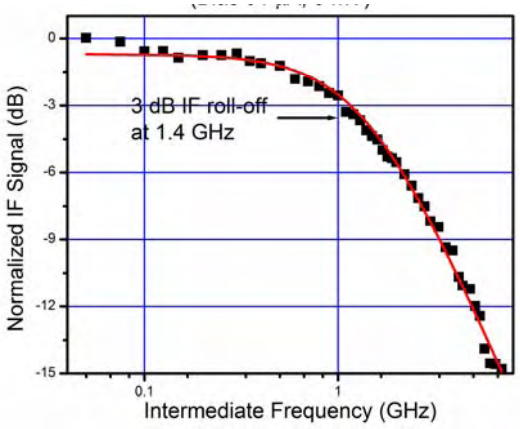

Fig. 2. Bandwidth measurement with a NbTiN HEB, made as an upper sideband measurement by sweeping the LO frequency while keeping the signal fixed at 19 GHz. The LO power level was adjusted to maintain a constant LO pump level.

from a separate waveguide with high coupling efficiencies for both the detection signal and local oscillator without use of an external interferometer. The present (non-balanced) mixer uses a bow-tie shaped capacitively coupled waveguide probe, which is RF-decoupled from the DC/IF lines by a quarter-wavelength section filter. Practically all of the circuit design was made using Ansoft's High-Frequency Structure Simulator (HFSS) software. The goal was to find a prototype design with reasonable coupling in the 1-2 THz band without significant dropouts at any frequency. Initially such dropouts did occur, apparently due to differences between the field generated by the probe and the desired TE10 waveguide mode that lead to excitation of evanescent modes. It was found that this could be overcome by introducing notches in the waveguide probe close to the HEB device, as shown in Fig.3. The notches in that figure are 2.1 μm long 0.8 μm wide. As further seen in the figure, the near edge of the quarter-lambda section bandstop filter was given a curved shape to agree better with the field that was spreading radially into the substrate channel. The substrate channel had a depth of 10 μm on the chip side (towards the horn antenna) and 8 μm on the other side (towards the waveguide backshort). The waveguide backshort distance was 65 μm. Figure 4 shows the reflection coefficient vs. frequency for a 25 ohm device from the HFSS simulations, which included the entire waveguide circuit except for the horn antenna but which neglected conductor losses. As can be seen, the simulated reflection at 1.5 THz is about -5 dB, with optimal coupling occurring at 1.9 THz. A simulation shows that the location of the optimum can be shifted to 1.5 THz by slightly widening the part of the substrate that is inside the waveguide, but this was not implemented in the mask set used for devices in these experiments. Figure 5 shows a device chip such as the one in Fig. 1 installed into the substrate channel of the mixer block. The waveguide is the dark rectangular hole behind the bow-tie shaped waveguide probe at the center of the picture.

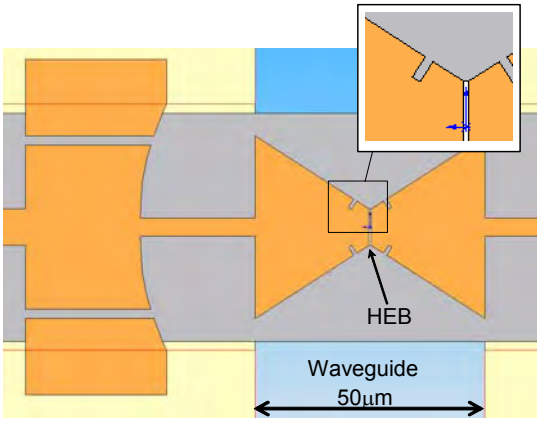

Fig. 3. Close-up schematic of the probe (true to scale).

The quality of the machining of the mixer block (Fig.6) is a crucial factor to the feasibility the waveguide approach at this frequency (1.5 THz) and higher. There are several difficulties that must be overcome: 1) Tool breakage and "wobbling" sets a practical lower limit for the end-mill tool diameter of about 10-15 μm (a 15 μm tool has been successfully used at JPL for cutting a narrow channel in brass). 2) The cutting depths for these small tools are limited to just a couple to a few times the tool diameter. 3) Mating surfaces need to polished to very high flatness and finish to prevent power leakages and resonances in the circuit. 4) Alignment of different component parts in the block is critical, and is usually achieved either by machining the components together in the same run on the numerically controlled milling machine, or by visual inspection and alignment under a stereo microscope. The parts are usually pinned together with cylindrical steel pins. 5) Some structures cannot be implemented with just two pieces, but require several parts that need to be machined separately and then be aligned to each other, which increases complexity. 6) Installation of the HEB device into the block, which is done with micromanipulators, is difficult but doable. In the circuit described in this paper, the block is split in 3 pieces (2 parts that allow the diagonal horn antenna to be cut and a third part that holds the waveguide

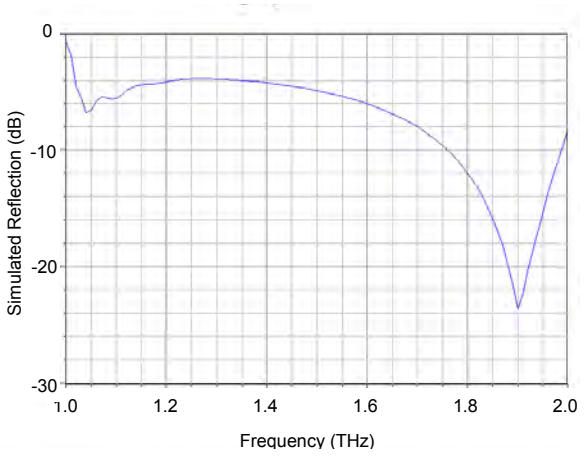

Fig. 4. Simulated reflection coefficient (mismatch) between the waveguide and a 25 ohm detector in the 1-2 THz band. The waveguide cut-off frequency (TE10) is 1 THz. HFSS was used for the calculation.

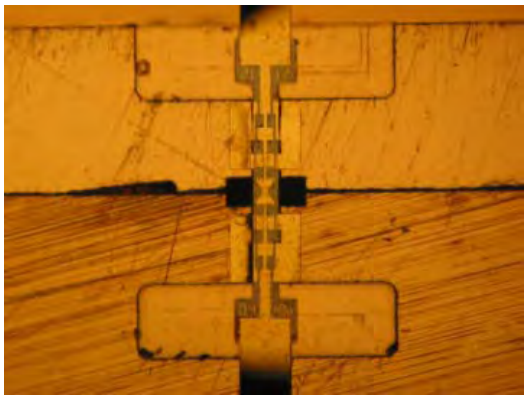

Fig. 5. A 1.5 THz HEB/SOI chip aligned to the waveguide. The waveguide cross-section is 150 by 50 μm.

backshort and that allows the beam-leads on the chip to be clamped). In our case the most difficult issue above is number 4, the alignment of parts. The described mixer block required a visual alignment step where the backshort component was lined up and pinned using microscope observations through the horn antenna, eventually resulting in an alignment error of less than 2 μm. The conclusion from the successful production of this 1.5 THz block was that the techniques involved can likely be extended in frequency up to about 3 THz, but probably not much higher. It is clear that a different technique such as silicon micromachining will eventually be required.

IV. Experiments

The mixer testing was done in a setup using a 4.2 K vacuum cryostat with two different solid-state Schottky diode multipliers as local oscillator sources. The purpose was to show that the coupling efficiency of the structure is high enough to pump the HEB device with such sources, and to do a receiver noise calibration measurement. The device used was a 0.3 μm long and 6 μm wide NbTiN HEB with a room temperature resistance of 58 ohms. A pumping experiment was made with a Gunn diode / power amplifier driven multiplier chain at 1.52 THz. The source output was

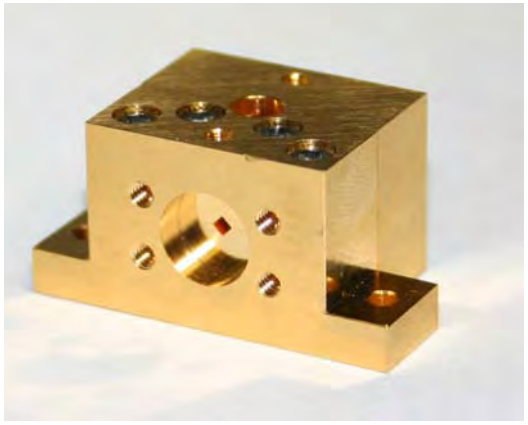

Fig. 6. 1.5 THz mixer test block. The aperture of the diagonal horn antenna is the diamond-shaped hole in the cylindrical cutout on the front side. The entire block is about 1 inch wide.

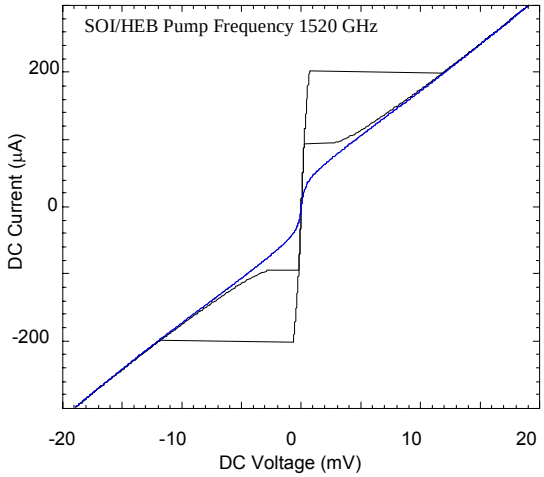

Fig. 7. An unpumped DC IV curve at together with one pumped at 1.5 THz by a JPL solid-state multiplier source. The temperature is 4.2 K.

measured to be about 2-3 μW with a calorimeter. The divergent beam from the source was collimated and refocused onto the mixer horn by two 1-inch diameter off-axis paraboloid mirrors. As can be seen in Fig.7, the device could clearly be pumped by this source, although in this case the power was coupled directly to the mixer block without a beamsplitter or interferometer, which is required for a mixer measurement in the present un-balanced configuration. A different, more powerful multiplier [11] source that produced 11μW (by calorimeter) was used in a subsequent measurement to allow the use of a 50 μm thick Mylar beamsplitter (at 45 degrees angle to the beams with the polarization perpendicular to the plane of reflection). The measurement was made at an LO frequency of 1.462 THz, and with an L-band HEMT amplifier at 1.4 GHz that had an equivalent input noise temperature of 2.3 K.

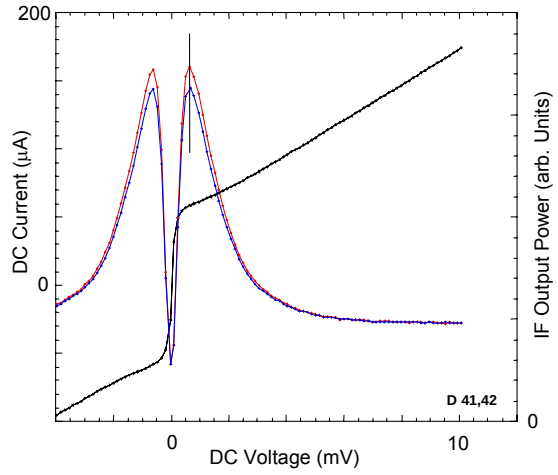

Fig. 8. An LO-pumped IV curve (1.462 THz) together with the detected IF output power at 1.4 GHz. The two power curves were measured with calibration loads at 293 K and 77 K, respectively. The vertical line marks the largest Y-factor response, corresponding to an equivalent noise temperature of 3460 K DSB.

A separate Anritsu bias tee was used to DC bias the device. The highest Y-factor that was measured was 1.061 with calibration target temperatures of 77 K and 293 K, which gives an equivalent noise temperature of 3460 K double-sideband (DSB), see Fig.8 . We believe that this initial number can be improved by modifications of the optical setup such as using an interferometer in place of the beamsplitter, and by using lower-impedance devices that are better matched to the circuit. Also, a modest redesign of the circuit to shift the frequency of best (theoretical) coupling from 1.9 THz to 1.5 THz should contribute to lower input noise.

ACKNOWLEDGMENT

We would like to acknowledge Pete Bruneau at JPL for developing the new procedures needed to machine and align parts for the terahertz waveguide mixer blocks, as well as for skillfully machining these components. We also thank Imran Mehdi, Peter Siegel, Goutam Chattopadhyay, Erich Schlecht and Chris Walker for useful advice. The following people have also provided help and/or advice at various times: Jonathan Kawamura, Raymond Tsang, Dave Pukala, Henry LeDuc, Anupama Kaul, Karen Lee, John Gill, John Ward, Neil Erickson and Edward Tong.

REFERENCES

[1] K. Yngvesson, *et al.*, "Terahertz receiver with NbN HEB device (TREND) – a low noise receiver user instrument for AST/RO at the south pole." Proc. of the 12th International Symposium on Space THz Technology, San Diego, CA, p.26

[2] D. Loudkov, E. Tong, R. Blundell, K. Megerian, J. Stern "Characterization of NbTiN hot electron bolometer mixers with different lengths", 15th International Symposium on Space Terahertz Techonology, Northhampton, MA, 2004

[3] S. Cherednichenko *et al.*, "1.6 THz heterodyne receiver for the far infrared space telescope," Physica C, vol. 372, pp. 427-431, Aug. 2002.

[4] J.J.A. Baselmans, *et al.*, "Noise performance of NbN hot elctron bolometer mixers at 2.5 THz and its dependence on contact resistance," Proceedings of the 14th International Symposium on Space THz Technology, Tucson, Arizona, USA, April 22-24 2003.

[5] C.-Y. Tong, D. Meledin, S. Loudkov, R. Blundell, N. Erickson, J. Kawamura, I. Mehdi, G. Gol'tsman, "A 1.5 THz Hot-Electron Bolometer Mixer Operated by a Planar Diode Based Local Oscillator" , 2003 MTT-S Digest

[6] C.K. Walker, A.L. Hungerford, G. Naranyan, C. Groppi, T.M. Bloomstein, S.T. Palmacci, M.B. Stern, J.E. Curtin, "Laser Micromachining of Silicon : a new technique for fabricating terahertz imaging arrays," in SPIE Proceedings Vol..3357, "Advanced Technology MMW, Radio, and Terahertz Telescopes, T.G. Phillips (Ed.), pp.45-52, ISBN 0-8194-2804-3, 1998

[7] A. A. Ayon, R. Braff, C. C. Lin, H. H. Sawin, and M. A. Schmidt, J. Electrochem. Soc. vol. 146, 339 (1999).

[8] Jeffrey A. Stern, Bruce Bumble, Jonathan Kawamura, Anders Skalare, "Fabrication of Terahertz Frequency Phonon Cooled HEB Mixers," *IEEE Trans. Applied Superconductivity, Vol.15, No.2, June 2005*.

[9] R.B. Bass, *et al.*, Ultra-thin SOI beam lead chips for superconducting terahertz circuits, 6th European Conference on Applied Superconductivity, September 14, 2003

[10] Anupama B. Kaul, Bruce Bumble, Karen A. Lee, Henry G. LeDuc, Frank Rice, Jonas Zmuidzinas, "Fabrication of wide-IF 200-300 GHz superconductor-insulator-superconductor mixers with suspended metal beam leads formed on silicon-on-insulator," J. Vac. Sci. Technol. B 22(5), Sep/Oct 2004.

[11] G. Chattopadhyay, E. Schlecht, J. Ward, J. Gill, H. Javadi, F. Maiwald, and I. Mehdi, "An All Solid-State Broadband Frequency Multiplier Chain at 1500 GHz," IEEE Transactions on Microwave Theory and Techniques, Vol. 52, no. 5, pp. 1538-1547, May 2004.

Superconducting HEB for large direct detector arrays.

S. Cherednichenko, V. Drakinskiy, T. Berg
Microwave Electronic Laboratory, MC2
Chalmers University of Technology, SE-412 96, Gothenburg, Sweden

We present a new detection scheme for Superconducting Transition Edge Detectors. Microwave noise generated by a TED is a function of the electron temperature and therefore can be used to monitor the absorbed RF power instead of traditionally used DC bias current (or voltage) as has been discussed in [1]. We expect a significant improvement of the sensitivity comparing to the DC monitoring, since the thermal fluctuation noise and Johnson noise do not contribute to the detector noise anymore. A perspective for large array applications is possible due to a proposed simplified frequency (wavelength) multiplexing technique.

In the paper, we discuss noise response to both broadband noise signals as well as monochromatic signals from 0.6 THz to 2.6 THz. We present an experimental investigation of this detector performance for two thermal situations: when the detector is heated to the superconducting transition temperature by a heater; and when the bath temperature (4.2K) is well below Tc (about 9 K) and the detector is "heated" with a local oscillator source. For the last regime, both MM and THz heating sources are considered.

[1] A.Semenov, " Superconducting submillimeter direct detector using high-frequency current noise", PhysicaC 416 (2004) pp.85–89.

Session 8:

SIS II

Tuesday May 3, 13:30-15:25
Chairman: Netty Honingh

SuperCam: A 64 pixel superheterodyne camera

Christopher Walker[1], Christopher Groppi[1,2], Craig Kulesa[1], Dathon Golish[1], Paul Gensheimer[1], Abby Hedden[1], Shane Bussmann[1], Sander Weinreb[3,4], Niklas Wadefalk[3], Tom Kuiper[4], Jacob Kooi[3], Art Lichtenberger[5], Gopal Narayanan[6]

1: University of Arizona, 2: National Radio Astronomy Observatory, 3: NASA Jet Propulsion Laboratory, 4: California Institute of Technology, 5: University of Virginia, 6: University of Massachussetts

We report on the development of *SuperCam*, a 64 pixel, superheterodyne camera designed for operation in the astrophysically important 870 μm atmospheric window. *SuperCam* will be used to answer fundamental questions about the physics and chemistry of molecular clouds in the Galaxy and their direct relation to star and planet formation. The advent of such a system will provide an order of magnitude increase in mapping speed over what is now available and revolutionize how observational astronomy is performed in this important wavelength regime.

Unlike the situation with bolometric detectors, heterodyne receiver systems are coherent, retaining information about both the amplitude and phase of the incident photon stream. From this information a high resolution spectrum of the incident light can be obtained without multiplexing. Indeed, each *SuperCam* pixel will provide 1,024 simultaneous spectral measurements. In terms of raw power, each observation made with *SuperCam* will provide ***65,536*** independent measurements of the properties of the object under study. High resolution spectroscopy can, in principle, be performed in this same wavelength regime using incoherent detectors together with frequency dispersive quasi-optical devices such as gratings and Fabry-Perot interferometers. However, the size requirement of quasi-optical devices and/or the need to scan in order to construct a spectrum make them too cumbersome or insensitive for the scientific objectives of the proposed study.

SuperCam will be constructed by stacking eight, 1x8 rows of fixed tuned, SIS mixers. The IF output of each mixer will be connected to a low-noise, broadband MMIC amplifier integrated into the mixer block. The instantaneous IF bandwidth of each pixel will be ~2 GHz, with a center frequency of 5 GHz. A spectrum of the central 500 MHz of each IF band will be provided by the array spectrometer. The spectrometer may be either an array of sixty-four, 500 MHz, 1024 lag correlator chips or sixteen, subdivided, 1 GHz wide A/D converters feeding real-time FFT digital signal processors. Each mixer will have its own electromagnet to suppress unwanted Josephson noise. Mixer, magnet, and MMIC bias of each mixer will be optimized under computer control. Local oscillator power is provided by a frequency multiplier whose output is divided between the pixels by using either a phase grating or a matrix of waveguide power dividers. The mixer array will be cooled to 4K by a closed-cycle refrigeration system. *SuperCam* will reside at the Cassegrain focus of the 10m Heinrich Hertz telescope (HHT) with a dedicated secondary and re-imaging optics. Each pixel will have a 22” diffraction limited beam on the sky.

A prototype single row of the array will be tested on the HHT in early 2006, with the first engineering run of the full array in late 2007. The array is designed and constructed so that it may be readily scaled to higher frequencies.

The ALMA band 7 mixer

D. Maier, A. Barbier, B. Lazareff, and K. F. Schuster

***Abstract*—A sideband separating SIS mixer with a 4–8 GHz IF band and covering the RF frequency range of 275 to 373 GHz has been developed and characterized for integration into the ALMA band 7 cartridge. The obtained results regarding noise as well as image rejection are well within the ALMA specifications. SSB noise temperatures as low as 55 K could be achieved for the lowest frequencies and over 98% of the frequency range the noise is less than 100 K. Image rejection is better than 10 dB.**

***Index Terms*—sideband separating mixer, SIS mixer**

I. Introduction

THE MIXER intended for integration into the ALMA band 7 cartridge has to fulfill a multitude of specifications. First of all the RF band has to cover frequencies between 275 and 373 GHz. For a 2SB mixer as chosen for band 7 the IF bandwidth has to be 4 GHz per sideband. The SSB noise limit has been set to 133 K for 80% of the RF band and 198 K for the rest of the band. Finally, the image rejection has to be at least 10 dB.

With the prospect of producing all 128 mixer units for the 64 antennas and thus bearing reproducibility and reliability in mind, a modular approach has been chosen based on single-ended double sideband mixers and waveguide and IF hybrids. This allows testing of the different parts prior to integration and in particular choosing two similar DSB mixers to achieve an optimum result for the 2SB mixer.

II. 2SB mixer assembly

A schematic view of a sideband separating mixer is shown in Fig. 1. The two DSB mixer units are connected at their inputs and outputs to quadrature hybrids. The LO signal is split and applied in-phase to the two mixers through –16 dB injection couplers. Since upper and lower sideband signals undergo different phase shifts, they appear separately at the two outputs of the IF quadrature hybrid [1].

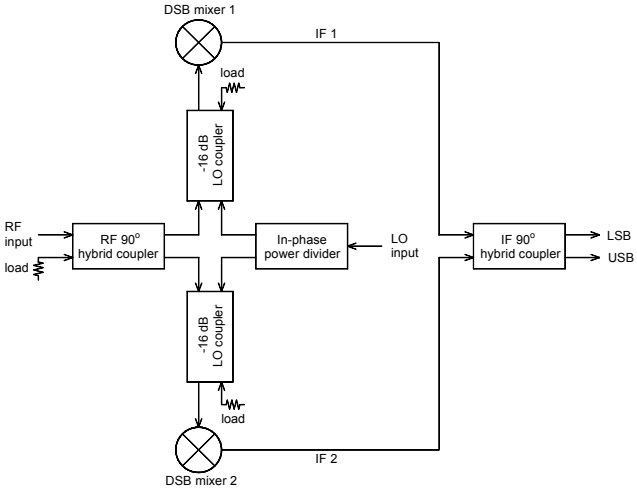

Fig. 1. Schematic view of a sideband separating mixer.

In order to allow testing of the different parts prior to integration, we have chosen a modular approach for our 2SB mixer. Each 2SB mixer assembly consists of a waveguide coupler combining the RF 90° hybrid coupler, the two –16 dB LO couplers and the in-phase power divider in one E-plane split-block [2], two separate DSB mixer units, and a commercially available IF 90° hybrid coupler. A photo of such a 2SB mixer assembly is shown in Fig. 2. The two DSB mixer units as well as the feedhorn are mounted onto the waveguide coupler. In order to allow the suppression of Josephson currents, each mixer has a magnetic yoke assembly attached to it (only one is shown in the photo). The IF outputs of the mixers are connected via semirigid cables to the inputs of the IF quadrature coupler.

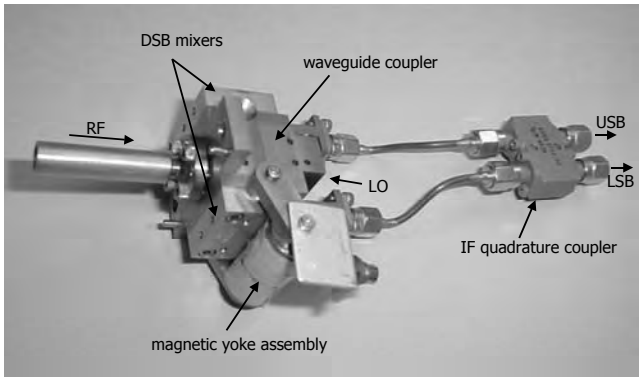

Fig. 2. 2SB mixer assembly with feedhorn, waveguide coupler, two DSB mixer units, and IF quadrature hybrid.

D. Maier, A. Barbier, B. Lazareff, and K. F. Schuster are with the Institut de RadioAstronomie Millimétrique, 300, rue de la piscine, 38406 St. Martin d'Hères, France (phone: +33476824900; fax: +33476515938; e-mail: maier@iram.fr).

III. DSB MIXER

A. RF design

The essential part of the mixer is a superconductor-insulator-superconductor (SIS) tunnel junction, which is deposited together with a superconducting circuit onto a quartz substrate. This circuit comprises the antenna providing a full-height waveguide to suspended microstrip transition, the RF choke and the actual tuning circuit whose role is compensation of the junction capacitance and matching to the antenna impedance. Fig. 3 shows the layout of one individual mixer chip with a size of $0.25 \times 2 \times 0.08$ mm^3. These devices are fabricated by IRAM's SIS group. The Nb-Al/AlO_x-Nb tunnel junction has an area of 1 μm^2 and is made by e-beam lithography [3].

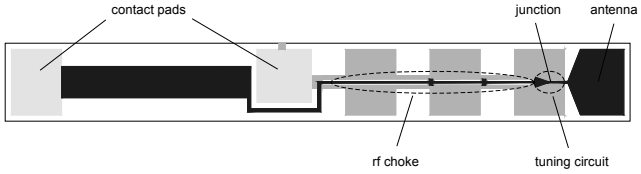

Fig. 3. Layout of the mixer chip.

The mixer chip is placed in a channel perpendicular to the waveguide axis and stretches only partly across the waveguide as can be seen in Fig. 4. The full-height waveguide to microstrip transition is provided by an antenna structure that has been optimized using CST Microwave Studio [4]. The resulting antenna impedance is almost constant over the operating frequency range (see Fig. 5).

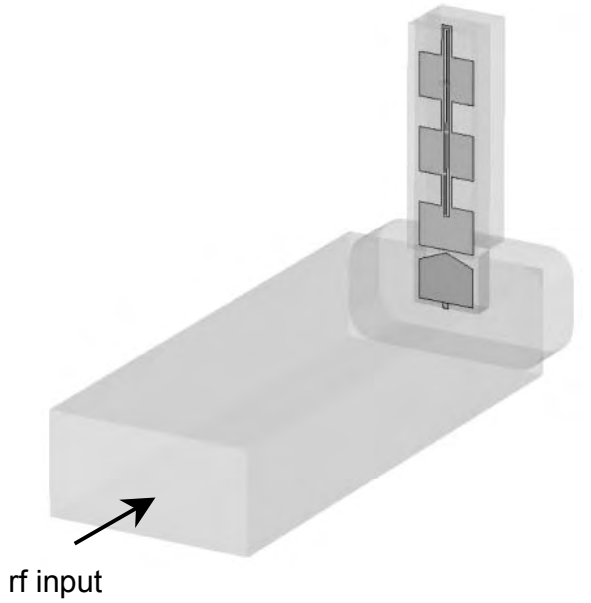

Fig. 4. Full-height waveguide to mircostrip transition.

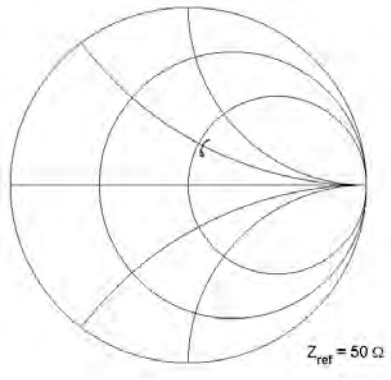

Fig. 5. Antenna driving point impedances for frequencies between 275 and 370 GHz.

A superconducting tuning circuit has been developed and optimized using Sonnet [5] and ADS [6]. Fig. 6 shows a photo of a fabricated mixer chip with a close-up of the tuning structure. The equivalent circuit is shown in Fig. 7.

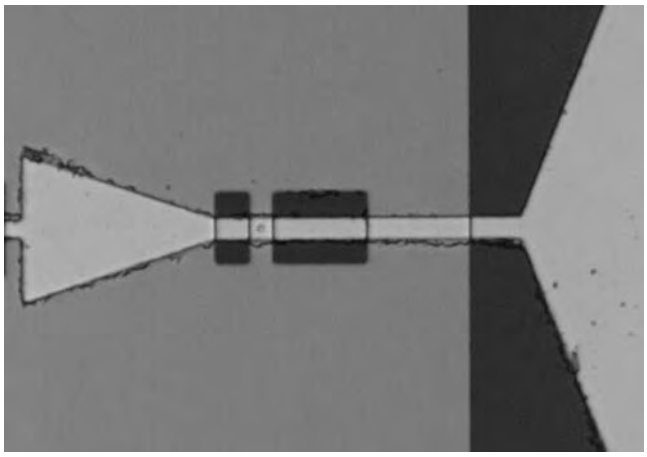

Fig. 6. Photo of the tuning circuit.

The junction capacitance is compensated by a parallel inductance consisting of a coplanar waveguide. In order to limit the parasitic capacitances and thus ensure a large IF bandwidth, the virtual ground has been realized using a delta-stub instead of the commonly used radial stub. Matching to the antenna impedance is achieved with a structure that can be viewed either as a CLCPW λ/4-transformer or as a discrete L-C transformer.

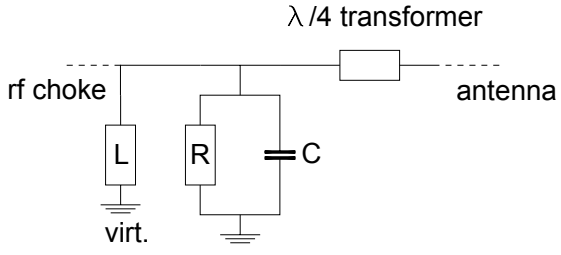

Fig. 7. Equivalent circuit of the tuning structure.

The achieved matching to the junction is quite homogenous over the whole frequency range as can be seen by the junction's embedding impedance plotted in the Smith chart in Fig. 8. The power coupled to the junction lies

between 85 and 97% (see Fig. 9).

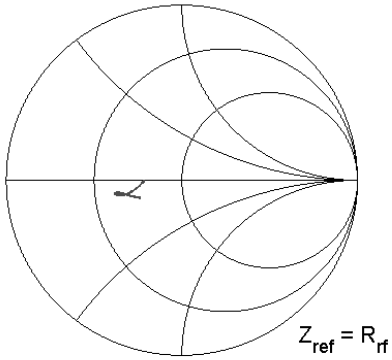

Fig. 8. Embedding impedance of the junction. Smith chart is normalized to the junction's RF impedance.

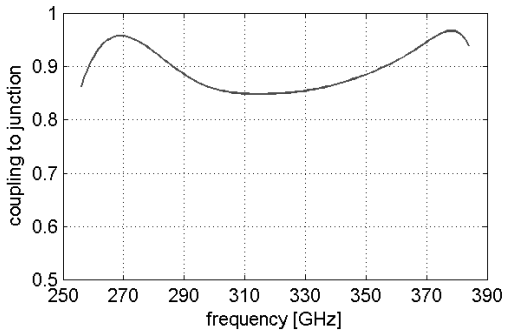

Fig. 9. Fraction of power coupled to the junction.

B. Mixer block and magnetic yoke assembly

The actual mixer block is a simple device. It only features a waveguide cavity and a substrate channel which allows to place the mixer chip just above the cavity (see Fig. 10, above). For DSB mixer testing the block is directly mounted onto a –16 dB LO coupler providing the input waveguide. In the 2SB mixer assembly the input waveguide is part of the waveguide coupler (see Fig. 2). The IF circuit consisting of a 50 Ω line realized as microstrip with a Rodgers 4003 substrate is mounted into a substrate holder which is fixed on top of the mixer block. The mixer chip is contacted via bonding wires to the block and the Rodgers microstrip (see Fig. 10, below). For the band 7 frequency range it is necessary to apply a local magnetic field to the junction in order to suppress Josephson currents which are a source of mixer noise and instability. Therefore a custom-made superconducting magnet and yoke assembly is attached to the mixer block (see Fig. 2).

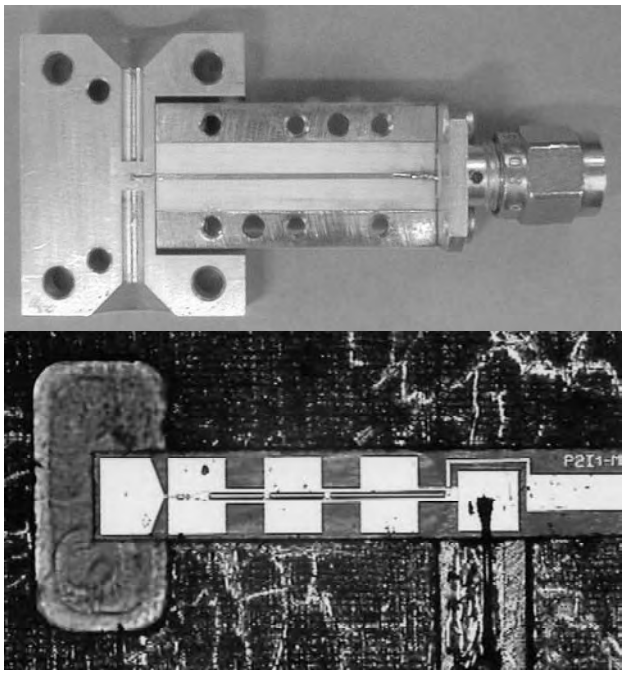

Fig. 10. Junction mounted into the mixer block. Above: Mixer block with holes for the magnetic yoke assembly and attached IF circuit. Below: Close-up of the mixer chip with the antenna mounted above the waveguide cavity.

C. Noise measurements

Several junctions from different wafers have been tested as DSB mixers. The best results so far were obtained with junctions from wafer 43. These junctions have a normal state resistance and area close to the design values. The best obtained DSB noise temperatures integrated over the 4 to 8 GHz IF band are presented in Fig. 11. The achieved values are better than 30 K over 85% of the RF band and increase up to 34 K for the highest frequency.

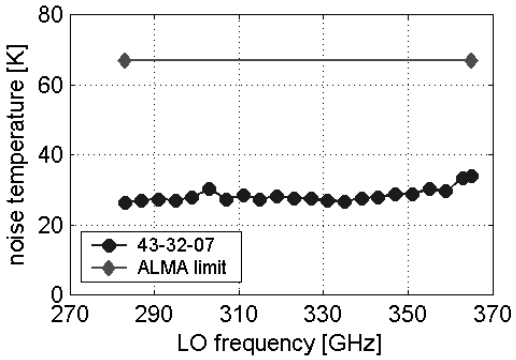

Fig. 11. Result of DSB noise measurements integrated over 4 to 8 GHz IF band.

IV. 2SB RESULTS

Two junctions from wafer 43 have been mounted together and tested as sideband separating mixer. The obtained noise temperatures for the two IF bands integrated respectively over the whole 4 GHz bandwidth are shown in Fig. 12. For the lowest frequencies the achieved noise temperatures are below 60 K rising with increasing

frequency up to 95 K for the highest frequency. These results are well below the ALMA specification represented by the red line.

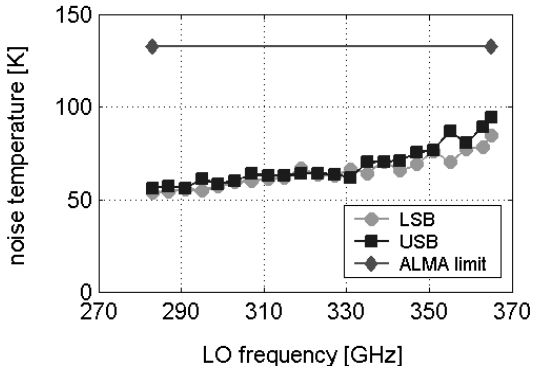

Fig. 12. Noise temperatures of sideband separating mixer with junctions 43-12-01 and 43-12-02. Measurements have been integrated respectively over each IF band of 4 to 8 GHz. The red line represents the ALMA limit.

ALMA mixers are submitted to a complete set of testing before they can be integrated into the cartridge. Apart from measuring the noise temperature integrated over the IF band for different LO frequencies (as shown in Fig. 12) IF sweeps with steps of 100 MHz are carried out for each of these LO frequencies and noise temperature and image rejection are measured.

Fig. 13 shows the results of such measurements for the image rejection over the RF frequency band. In general, values around –13 dB are achieved. Only a few points measured at the IF band edges are slightly above –10 dB.

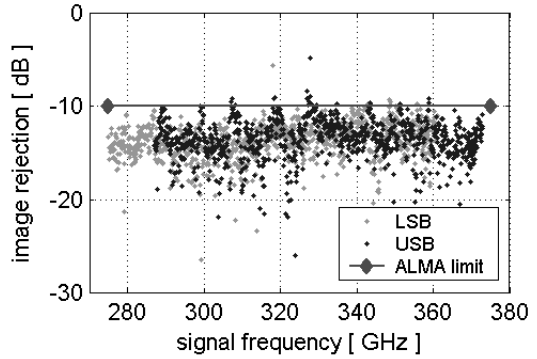

Fig. 13. Image rejection over the whole RF band resulting from the IF sweeps. Measurements obtained in the lower sideband are plotted in grey, those achieved in the upper sideband are represented by the black dots. The red line indicates the ALMA limit.

Fig. 14 shows the noise temperatures resulting from the IF sweeps as a function of the signal frequency. These are true SSB noise temperatures, corrected for the residual response in the image band. The achieved results are well below the ALMA specification indicated by the red line.

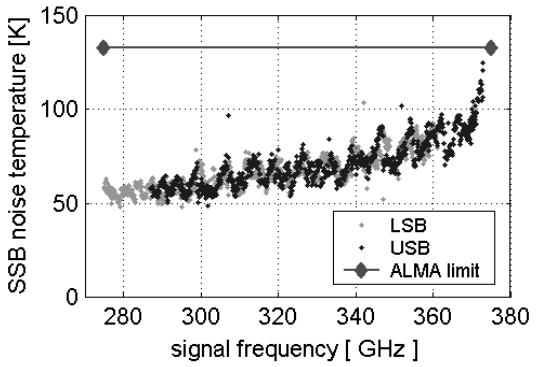

Fig. 14. SSB noise temperatures resulting from the IF sweeps. Measurements obtained in the lower sideband are plotted in grey, those achieved in the upper sideband are represented by the black dots. The red line indicates the ALMA limit.

V. Conclusions

A sideband separating mixer fulfilling the ALMA specifications for band 7 has been successfully developed, fabricated and characterized. Currently IRAM is working on the fabrication of 16 2SB mixer units for the production of a pre-series of 8 cartridges. The first cartridge has been equipped with two 2SB mixers and will be delivered this year.

References

[1] S. A. Maas, *Microwave mixers*. Artech House, Inc., 1986

[2] S. Claude "Sideband-Separating SIS Mixer For ALMA band 7, 275-370 GHz*," Proc. of the 14th International Symposium on Space Terahertz Technology*, pp. 41-51, 2003

[3] I. Péron, P. Pasturel, and K.F. Schuster, "Fabrication of SIS junctions for space borne submillimeter wave mixers using negative resist e-beam lithography," IEEE Trans. Applied Superconductivity, Vol. 11, pp. 377-380, March 2001

[4] CST Microwave Studio, Bad Nauheimer Str. 19, D-64289 Darmstadt, Germany

[5] Sonnet Software, 100 Elwood Davis Road, North Syracuse, NY 13212

[6] Advanced Design System, Agilent EEsof EDA

A 279-381 GHz SIS Receiver For the new APEX Telescope

C. Risacher, V. Belitsky, I. Lapkin*, R. R. Monje, M . Pantaleev, V. Vassilev, E. Sundin, A. Pavolotsky, D. Meledin, K-Å. Johansson, L-G. Gunnarsson, M. Svensson, M. Fredrixon, S-E. Ferm, V. P. Robles, M.. Hagström, R. Booth

***Abstract*—We present a 279-381 GHz fixed-tuned double sideband (DSB) receiver based on superconductor-insulator-superconductor (SIS) junction mixer. This receiver has been installed and is under commissioning at the new Atacama Pathfinder EXperiment (APEX) 12 m submillimetre telescope located on Chajnator, at an altitude of 5100 m on the Atacama Desert, in Northern Chile. The cryostat is equipped with two channels; one is currently installed and is the one described here. The second channel is for a 210-280 GHz sideband separating SIS mixer that will be installed fall of 2005. A full characterization of the receiver performance was done, the measured system noise temperature (uncorrected) is 30-50 K corresponding to about 2-3 quantum noises across the full frequency band with the IF from 3.8 to 7.6 GHz. Measurements of the mixer saturation and receiver stability are presented. Finally, we will describe the control system that allows operating the receiver remotely and automatically tuning any given frequency in less than 5 minutes.**

***Index Terms*—Superconductor-Insulator-Superconductor (SIS) junction, radial E-probe, bias-T.**

I. INTRODUCTION

The Atacama Pathfinder EXperiment (APEX) submillimeter telescope [1] is a collaboration between the Max Planck Institute for Radioastronomy (MPIfR) (in collaboration with Astronomisches Institute Ruhr Universitet Bochum (RAIUB)), Onsala Space Observatory (OSO) and the European Southern Observatory (ESO) to construct a single dish antenna on the high altitude site of Llano Chajnantor at an altitude of 5100 m on the Atacama Desert on the Atacama Large Millimeter Array (ALMA) site, in Northern Chile. This site is believed to be one of the best for sub-millimeter wave observations. The antenna is a prototype antenna of the ALMA, but with improved surface accuracy (down to 14 μm rms) to allow higher frequency operation. Another difference with the ALMA antennas is the presence of 2 Nasmyth cabins to accommodate more instruments. APEX is planned to have both heterodyne and continuum instruments, covering the frequency range (230 GHz–1.5 THz).

The authors are with the Onsala Space Observatory with Chalmers University of Technology, Gothenburg, Sweden.

* I. Lapkin is also with the Institute of Applied Physics, Russian Academy of Sciences, 46 Ulyanov str.,603950, Nizhny Novgorod, Russia.

The cassegrain cabin will contain the bolometer arrays, the cabin A will contain single pixel heterodyne receivers and the cabin B will accommodate the heterodyne arrays. The telescope is in the final installation phase (Fig. 1).

The work presented here is done for APEX band 2, covering the frequency range 275-370 GHz with the center frequency at approximately 345 GHz. The receiver described in this paper is double sideband (DSB) and will be used as a first light facility receiver for the APEX telescope and will be the first instrument available to the astronomical community. This development aims also as a base for a future sideband-separating mixer (2SB) that will be installed in the final facility receiver together with 3 other channels (230 GHz, 450 GHz and 1.3 THz).

Fig. 1. View of the Apex telescope.

II. RECEIVER OVERVIEW

A. Cryostat

The receiver is equipped with 2 channels (Fig. 2 and Fig. 3). The first is for the APEX band 2, 275-370 GHz, which is double sideband (DSB), and is currently being installed and tested. The second channel is for APEX band 1, 210-280 GHz sideband separation (2SB). That mixer will be installed end of 2005 while all optics is in the Dewar already.

The mixer uses superconductor-insulator-superconductor

(SIS) junctions using Niobium technology. The mixer chip is mounted in a full-height waveguide mixer block. The cryostat window is a 5 mm HDPE window with linear corrugations. The infrared material is 10 mm of PPA30 material [2]. The optics inside the receiver consists of a flat and an ellipsoidal mirrors (Fig. 4). The input is a corrugated horn [3]. The IF output of the mixer is connected to a 4-8 GHz isolator followed by a 2-stage 4-8 GHz LNA sitting on the 4 K plate; the second 2-stage LNA with its respective isolator is placed on the 12 K plate. The cold amplification is about of 45 dB.

The receiver RF operating range actually is 279 - 381 GHz limited by the Gunn oscillator tuning range (95-125 GHz). The mixer itself has a broader bandwidth 260-385 GHz.

The cryostat is a hybrid closed-cycle system using 2 independent helium systems, a Gifford Mac-Mahon 2-stage refrigerator, together with a Joule-Thomson refrigerator previously used in the SEST telescope. The 2-stage gives a temperature of about 70 K and 15 K for the outer shields. The Joule-Thomson circuitry cools the helium gas further where it condensates with a slight overpressure (about 4.5 K). The cooling takes usually about 12-15 hours.

Fig. 2. View of the receiver after installation in the Apex telescope.

B. *Receiver optics*

The optics of the telescope consists of 11 mirrors, the main dish, the sub-reflector, 4 mirrors in the cassegrain cabin and 5 mirrors in the cabin A. The first mirror after the Nasmyth flange is rotating along the elevation axis in order to select different instruments placed in the Cabin A. The second mirror is also rotating (Fig. 2) and it allows selecting the channel of the receiver. At present, we have 2 channels in the receiver, and for the final facility receiver, a 6-channel system will be built. The last 2 cold mirrors are inside the cryostat. Figure 3 shows the inner part of the receiver with the optics for the 2 channels.

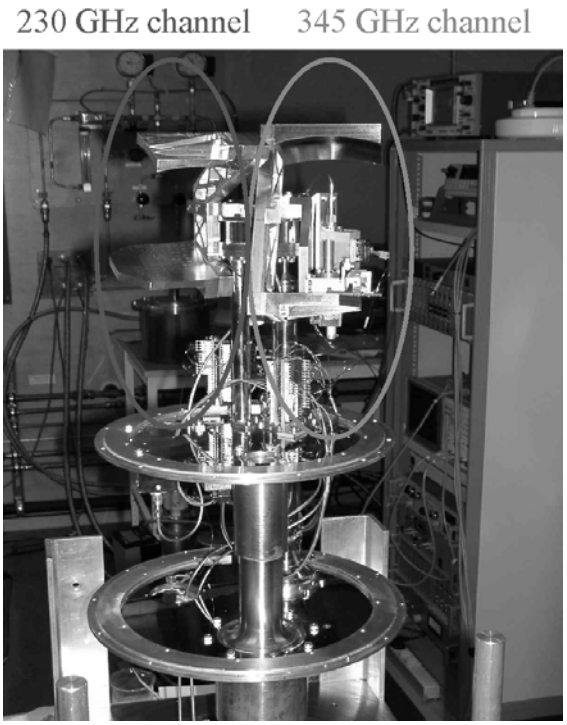

Fig. 3. View of the inner part of the cryostat.

Fig. 4 shows the Gaussian beam propagation inside the receiver cold optics. The 4 K cold plate can be seen together with the mixer bracket with the mixer block, the 4-8 GHz isolator and the LNA.

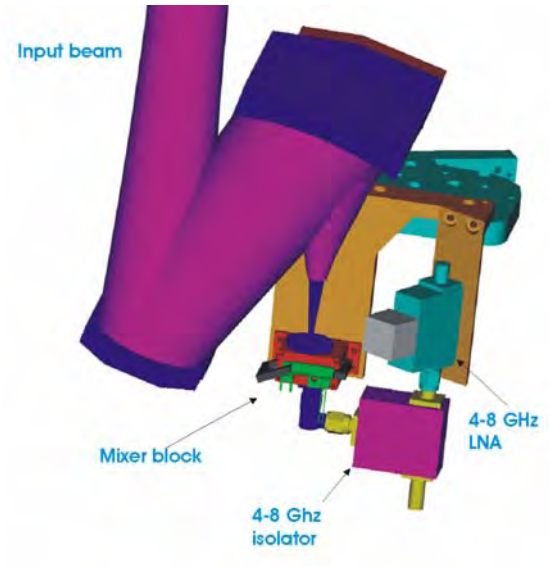

Fig. 4. Receiver optics inside the cryostat for the 345 GHz channel.

C. Mixer Design

1) Mixer layout

The mixer design is based on a novel waveguide-to-microstrip transition with an integrated wideband bias-T [4]. The novelty of this probe comes from the fact that it couples the input waveguide signal to the SIS junction via a radial probe [5] (see Fig. 5) while having an isolated port at the opposite side of the substrate where the IF signal can be extracted and DC current can be injected to bias SIS junctions or suppress Josephson current. This design is optimized for a full-height waveguide, therefore with reduced RF losses and easier machining, which are important advantages becoming especially crucial for mm and sub-mm frequency waveguide components with extremely small dimensions and high losses. The waveguide dimensions chosen for the mixer are 380 x 760 μm^2. The mixer chip uses a 65 μm thick crystalline quartz substrate. The microstrip RF chokes 1 and 2 in the Fig. 5 are of a hammer type to minimize space. The thin-film superconducting microstrip lines used for the SIS integrated tuning circuitry are placed on 400 nm layer of SiO_2 sputtered on top of the RF choke 2, which acts as the ground for the tuning circuitry

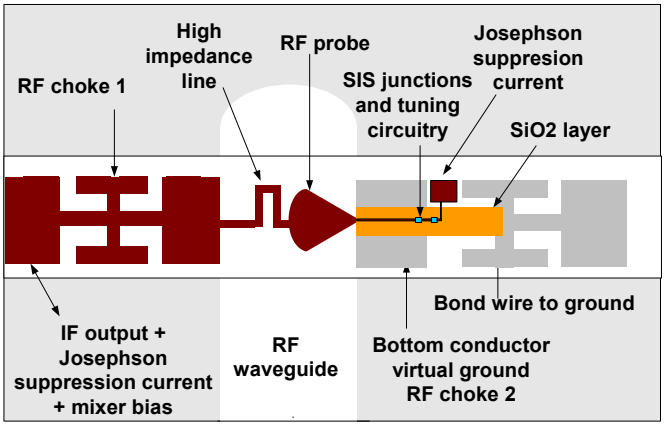

Fig. 5. Mixer chip layout.

2) Josephson effect suppression

One of the main motivation to use this novel layout for the mixer chip was to have an additional port available to apply a DC current through the wiring superconducting lines as demonstrated in [6]. This current creates a localized magnetic field parallel to the plane of the SIS junction and therefore suppresses the Josephson effect. The standard solution to suppress the Josephson effect in SIS junctions is to use external solenoids, usually employing a superconducting wire. For the sideband separating [7] or balanced mixers, that we intend to have for the final version of the APEX telescope heterodyne receiver, the SIS junctions will be at a very close distance (typically about 1 mm spacing). Thus, using exclusively superconducting coils to suppress the Josephson effect would not provide an independent suppression of the Josephson current in adjucent SIS junctions simultaneously. The main advantage of the used type of Josephson suppression circuit is its compactness as it uses the existing superconducting lines from the SIS integrated tuning circuitry. Unfortunately, first results on the suppression of the Josephson effect using the control line indicated that we couldn't reach the first null in the sin(x)/x dependence of the Josephson current. A field higher than 60 Gauss is required to reach that null, or according to our measurements a current over 50 mA is required. The highest current that we could apply before a part of the superconducting circuitry switched to the normal state was between 20 and 40 mA depending on the chip. This limit is due to weak points in the design where a very narrow line (4 μm) goes through different steps in height, where its thickness is probably very little; therefore the critical current at those points is reduced. Our future designs will take into account this fact so the control line can work as expected.

One solution was to use a pair of permanent magnets that create a magnetic field strong enough to get closer to a minimum and then to use the control line to fine-tune the magnetic field. However, for the installation of the receiver we used an external solenoid (from a commercial relay), thermally decoupled from the mixer block, with iron-made magnetic concentrators. The required current to get to the first null was about 3-4 mA only. The solenoid resistance is about 200 Ohms; therefore power dissipation was not an issue.

3) Mixer chip design

Three different chip designs were fabricated differing in the probe RF impedance (either 30 Ohm or 60 Ohm). The calculations of the probe impedance were done using High Frequency Structure Simulator (HFSS) [8]. To tune out the junction capacitance, the first design uses a single junction with a parallel inductive line whereas the other designs use twin junctions scheme where two SIS junctions are connected through a short inductive line [9, 10]. The remaining resistive part is matched to the RF probe by a λ/4 transformer. Mixer design parameters are described in more details in [11].

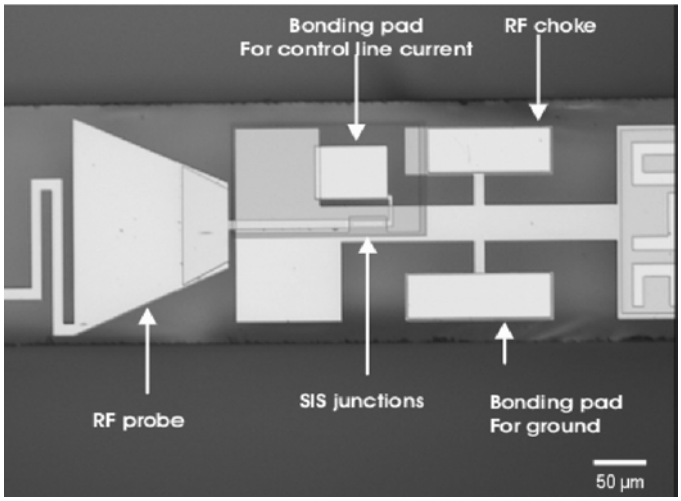

Fig. 6. Optical microscope view of a chip using an RF probe of 30 Ohm impedance

4) SIS fabrication

The SIS junctions were fabricated by in-house process using Chalmers MC2 clean room facility and dedicated cluster sputter tool. The Nb-AlOx-Nb SIS junctions are designed to have an area of 3 μm^2 and with a normal state resistance Rn = 7 Ω. The chips were fabricated on a 65 μm thick crystalline quartz substrates glued on a 250 μm 1" square substrate. The process flow for the SIS chips was based on Nb/Al-AlOx/Nb trilayer technique [12], which proved to provide the most reproducible properties of the SIS junctions. The yield is higher than 85 %, with Rn having the specified value and with deviations of less than 10 %. The actual area of the junctions was somewhat smaller (2.4 μm^2) implying a critical current density Jc of 9 kA/cm^2. The sub-gap to normal resistance ratio is typically of 20-25 at 4.2 K.

5) Mixer block

The mixer block was fabricated using Copper-Tellurium alloy and the split-block technique to facilitate machining. The mixer chip is placed in a 130 μm-deep channel milled in one half of the mixer block. The probe was designed to be slightly offset so that the mixer sits in the bottom of that channel and there is 65 μm air-gap above the quartz substrate. Therefore the other half of the mixer block doesn't need to have a channel and this eases the fabrication. The chip size is 1 mm x 200 μm x 65 μm. A very thin layer of gold (2 μm) is plated onto the mixer block to allow wire-bonding. The IF circuit integrated in the mixer block comprises a bias-T and 20 Ohm-to-50 Ohm IF transformer on an alumina substrate, which is placed on the same half of the mixer block. Three bond wires connect the mixer chip to the circuitry on the alumina substrate. The DC circuitry for the SIS biasing is placed on the backside of the mixer block half. The mixer block also includes a transition from rectangular to circular waveguide.

D. The 4-8 GHz cryogenic LNA

Nowadays, radio telescope receivers typically employ IF amplifiers with 1 GHz bandwidth. But with the increasing interest for sub-mm observations, larger bandwidths are required for broader spectral line and continuum observations of extragalactic sources. The selected IF band was 4-8 GHz and a 4-8 GHz LNA was developed in GARD group [13]. This LNA uses commercial GaAs HEMTs and when measured at a cryogenic temperature of 12 K, gives gain of 26 dB and a noise temperature of 5 K with a total power consumption of 12 mW (optimized for the best noise performance). With the power consumption minimized to 4 mW, the amplifier has 24 dB gain and the noise temperature degrades only to 6 K. Figure 7 shows measurements for 12 pieces of this LNA showing consistency of the performance. raise

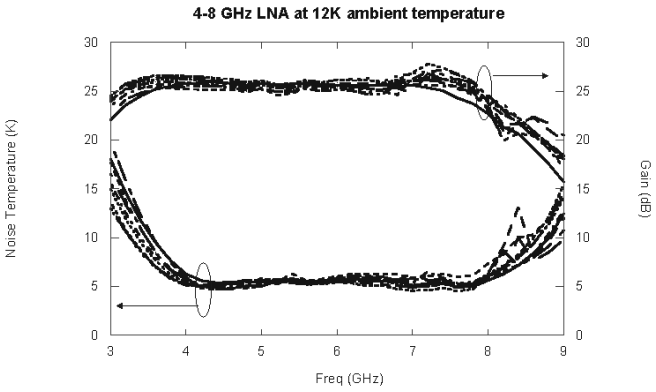

Fig. 7. Performance of series of 12 LNA, 4-8 GHz.

E. The local oscillator

Figure 8 shows the LO chain. The local oscillator incorporates mechanically tunable Carlstrom Gunn oscillator for 96 to 125 GHz. It can be tuned down to 95 GHz if necessary. The output power is typically above 30 mW. The Gunn is Phased-Locked with a reference signal of 400 MHz. The self-biased tripler is from Virginia Diodes, giving a typical output power of 0.5-2 mW. The LO uses a conical feed-horn with refocusing lens and a flat mirror; LO signal is injected through a 12 μm Mylar beam splitter giving about 1-2 % coupling.

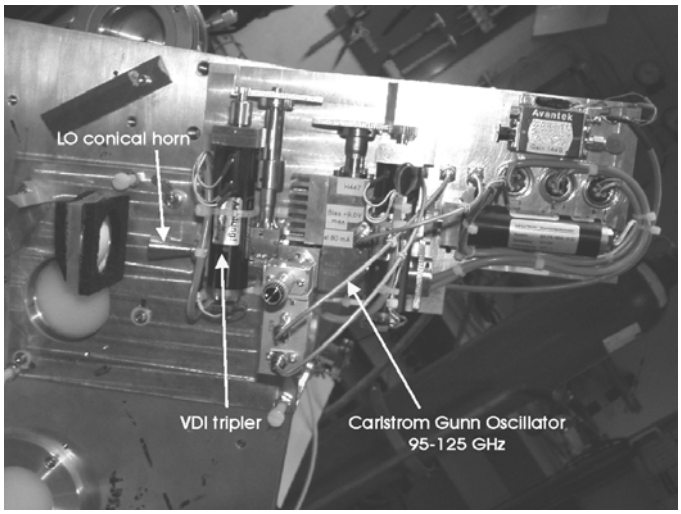

Fig. 8. LO source comprising a Gunn oscillator and a tripler.

III. Receiver Performance

A. Noise temperature measurement in lab

Noise temperature measurements were performed with the Y factor technique using a hot (293 K) and cold load (77 K) in front of the input window. Fig. 9 shows the uncorrected noise temperature achieved for different mixer blocks with different junctions when measured in a laboratory test Dewar. We used a BWO LO for frequencies between 220–380 GHz. Results show a noise temperature of 30-50 K across almost all of the frequency range, increasing to 60 K at the high frequency end for 2 mixers. Two different wafers were produced and the

junctions selected were completely randomly chosen within these wafers. Having so repeatable results ensures that the design is remarkably insensitive to small differences in the mixer blocks dimensions and to the junction's parameters.

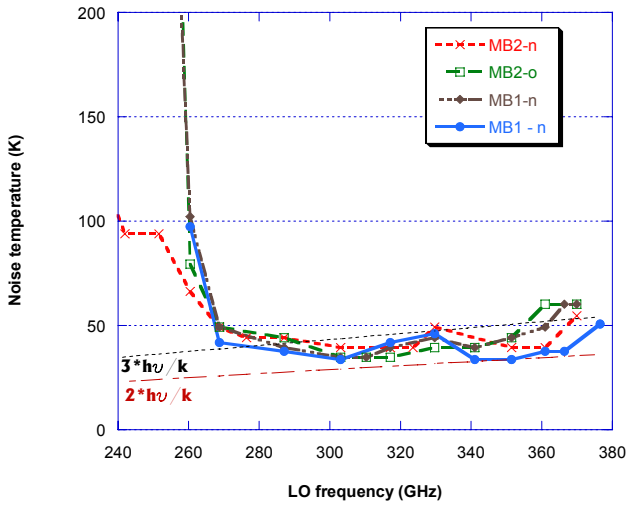

Fig. 9. Uncorrected receiver noise temperature for 4 mixer blocks with twin junctions measured in a lab test cryostat.

The mixer block MB1-n, the lowest curve in the Fig. 9, was selected to be installed in the First Light receiver.

B. IF noise temperature

Fig. 10 shows an example of noise temperature measurement across the IF band at an LO frequency of 351 GHz corresponding to a signal frequency centered at 345 GHz, which is the rest frequency of the rotational transition 3-2 of CO, one of the most important lines in our frequency range. The noise temperature is reasonably flat for an IF band of 3.8-7.6 GHz, not far from the designed IF band of 4-8 GHz.

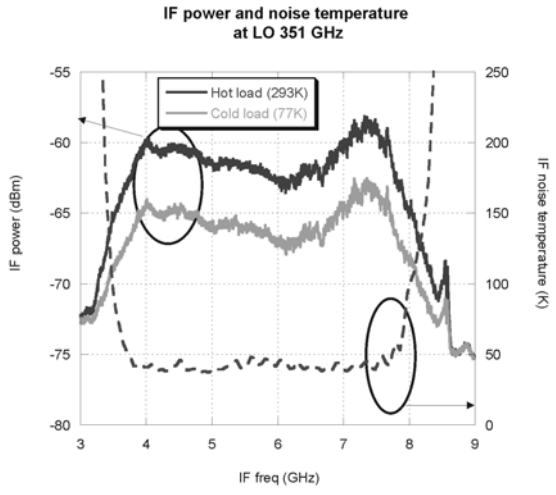

Fig. 10. Measured uncorrected noise temperature for the receiver across the IF band at 351 GHz.

C. Receiver saturation

The saturation was measured using two different techniques. The first one uses a variable temperature load. The temperature of the load can be varied from –30 C to +100 C and the IF output power is recorded for various input load temperatures. At the lower frequency end (LO of 290 GHz) where the saturation is expected to be highest, it appears to be no noticeable saturation; there is about 1.5 % saturation. The accuracy of this method is mainly set by the accuracy of the load temperature measurements. Multiple temperature sensors are used across the load. Apart from the temperature sensors accuracy (± 0.3 K), gradients of temperature are limiting the accuracy. Very roughly the saturation error is given by ΔT*2 %, so an error of 1 K in the hot load physical temperature measurement translates into 2 % added error.

The second method uses a scheme described by A. R. Kerr et al. [14] using a weak CW test signal introduced through a beam splitter while the receiver input is switched between liquid nitrogen and room temperature loads. The CW signal incremental gain compression can then be measured and through the calculations the large signal gain compression is estimated. A summary of the results using the CW signal method is given in the following table:

LO freq	Incremental gain compression	Large signal gain compression
291 GHz	5.4 %	3 % ± 2 %
300 GHz	4.7 %	2.8 % ± 2 %
318 GHz	3.3 %	1.7 % ± 2 %
351 GHz	3 %	1.5 % ± 2 %

Here the accuracy is limited by how well we can resolve the peak value, which is ± 0.1 dB, corresponding to an error of ± 2 %. Therefore, both methods are consistent in that the saturation values are lower than 5 % and are within the measurement error, which is of about ± 2 %.

D. Receiver stability

The total power receiver stability was measured, using a set up with 600 MHz filter centered at 6 GHz. Depending on the measurement data, the Allan time [15] varies from 30-100 seconds. Fig. 11 shows example of the measured data.

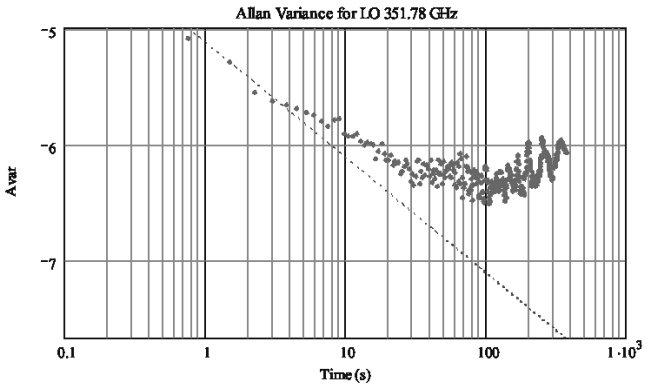

Fig. 11. Example of Allan stability measurements.

IV. Control system

The receiver was designed to be entirely remotely operated, and thus the tuning procedure to be fully automated. with the entire tuning procedure to be done remotely through a computer. The tuning is based on the use of tuning tables. First the local oscillator is set using rough values in tuning tables, the PLL is locked and then the tuning motor is adjusted to have the Gunn bias to the optimum value. After that the SIS is biased to its optimum value. The mixer performance is quite insensitive to small variations of tuning values. The magnetic coil current is set to a value close to 15 mA, which is about the 4th minima in the Josephson current versus coil current relation. We need to go that high because the twin junctions behave SQUID-like and therefore it is much more sensitive to the applied magnetic field. Possible small differences between the two junctions make the use of the first minima more difficult.

Fig. 12. View of the receiver control system, together with a test notebook.

A newly developed SIS bias supply provides bias to the mixer within the requited -10 to +10 mV range with accuracy of setting better than 5 μV. To decrease interferences and the effect of grounding loops the mixer is biased by a floating power supply. Setting to a given voltage is done via digital output module in the control rack that sends a pulse TTL signal. This signal goes through an opto-coupler to three cascaded 4 bits counters, which are forming 12-bit word. This word is then fed to a 12-bit DAC set in bipolar mode (-5 to +5 V). Each successive pulse increases (or decreases) the DAC output with 2.4 mV. A 3 K and 10 Ohm resistors circuitry inside the mixer block forms a voltage divider, which provides the -10 to +10 mV DC voltage bias range on the SIS junction.

V. Conclusion

A 279-381 GHz SIS receiver was designed, built, tested and installed on the APEX Telescope in Northern Chile. The receiver noise temperature as measured in the labs is between 30-50 K across the entire frequency range. The IF band is from 3.8-7.6 GHz. The receiver saturation was measured to be less than 5 %, and the receiver total power Allan variance time was measured to be between 30 and 100 seconds for a BW of 600 MHz. Installation on the APEX telescope in Atacama Desert, Chile, was made in April 2005, with the planned technical and scientific commissioning in May-June 2005. The receiver should be available to the astronomical community from September 2005. Future development is to combine two of these DSB mixers to produce a sideband separation mixer. Acknowledgment

The authors would like to thank the APEX staff for their help during the installation and successful completion of this work. This work was supported by the Swedish Research Council and by the Alice and Knut Wallenberg Foundation via their respective grants.

References

[1] APEX homepage at Onsala: http://www.oso.chalmers.se/oso/apex/index.html
[2] PROPOZOTE® PPA30 material, Zotefoams plc, Croydon, Surrey, England.
[3] RPG Radiometer Physics GmbH, Birkenmaarstrasse 10, 53340 Meckenheim, Germany.
[4] C. Risacher, V. Vassilev, V. Belitsky, A. Pavolotsky, "Waveguide-to-Microstrip Transition with Integrated Bias - T", *IEEE Microwave and Wireless Components Letters*, Vol. 13, Issue 7, July 2003.
[5] G. Yassin, S. Withington, "Analytical expression for the input impedance of a microstrip probe in waveguide", International Journal of Infrared and Millimeter Waves, Vol. 17, No. 10, 1996.
[6] V. P. Koshelets et al., "Integrated sub-mm receivers", IEEE Transactions on Applied Superconductivity, pp. 3057-3060, June 1995.
[7] V. Vassilev, V. Belitsky, C. Risacher, I. Lapkin, A. Pavolotsky, E. Sundin, "A Sideband Separating Mixer for 85-115 GHz", IEEE Microwave and Wireless Components Letters, Vol. 14, Issue 6, June 2004.
[8] High Frequency Structure Simulator v. 5.6, Agilent Technologies, 395 Page Mill Road, Palo Alto, CA 94304, U.S.A.
[9] V. Belitsky, M. Tarasov, "SIS Junction Reactance Complete Compensation", IEEE Trans. on Magnetic, 1991, MAG- 27, v. 2, pt. 4, pp. 2638-2641.
[10] V. Belitsky, S.W. Jacobsson, L.V. Filippenko, S.A Kovtonjuk, V.P. Koshelets, E.L. Kollberg, "0.5 THz SIS Receiver with Twin Junctions Tuning Circuit", Proc. 4th Space Terahertz Technology Conference, pp. 538, March 30 - April 1, 1993, Los Angeles, USA.
[11] C. Risacher, V. Belitsky, V. Vassilev, A. Pavolotsky, "A 275-370 GHz DSB SIS mixer for the Apex Telescope", SPIE conference on Astronomical instrumentation, Glasgow, Scotland, 21-23 May 2004.
[12] M. Gurvitch, M.A. Washington and H.A. Huggins, "High quality refractory Josephson tunnel junctions utilizing thin aluminium layers", Applied Physics Letters, 1983, v.42, No 5, p.472.
[13] C. Risacher and V. Belitsky, "GaAs HEMT low-noise cryogenic amplifiers from C-band to X-band with 0.7 K/GHz noise temperature", IEEE Microwave and Wireless Components Letters, Vol. 13, Issue 3, March 2003.
[14] A. R. Kerr, J. Effland, S.K. Pan, G. Lauria, A. W. Lichtenberger and R. Groves, "Measurement of Gain Compression in SIS Mixer receivers" ALMA memo 401.
[15] D W. Allan, "Statistics of Atomic Frequency Standards", Proc. IEEE, Vol. 54, No. 2, pp 221-230, 1969

550-650 GHz spectrometer development for TELIS

P.A. Yagoubov, W.-J. Vreeling, H. van de Stadt, R.W.M. Hoogeveen, O.V. Koryukin, V. P. Koshelets, O.M. Pylypenko, A. Murk

***Abstract*—In this paper we present design and first experimental results of the 550 - 650 GHz channel for the Terahertz Limb Sounder (TELIS), a three-channel balloon-borne heterodyne spectrometer for atmospheric research. This frequency channel is based on a phase-locked Superconducting Integrated Receiver (SIR). SIR is an on-chip combination of a low-noise SIS mixer with quasioptical antenna, a superconducting Flux Flow Oscillator (FFO) acting as Local Oscillator (LO) and SIS harmonic mixer (HM) for FFO phase locking. The microcircuit is designed as a quasioptical mixer. Amplification of the mixer IF signal and first stage PLL circuitry is done by InP based low noise HEMT amplifiers. Optical design analysis and first experimental results, which include FTS and noise temperature measurements, are reported.**

***Index Terms* — Josephson mixers, integrated receiver, superconducting devices**

I. Introduction

TELIS (Terahertz Limb Sounder) is a cooperation between DLR (Institute for Remote Sensing Technology, Germany), RAL (Rutherford Appleton Laboratories, UK) and SRON (National Institute for Space Research, the Netherlands), to build a three-channel balloon-borne heterodyne spectrometer for atmospheric research. The three receivers utilize state-of-the-art superconducting heterodyne technology and will operate simultaneously at 500 GHz (channel developed by RAL), at 550-650 GHz (SRON in collaboration with IREE), and at 1.8 THz (DLR). TELIS is designed to be a compact, lightweight instrument capable of providing broad spectral coverage, high spectral resolution and long flight duration (~24 hours duration in a flight campaign). The combination of high sensitivity and extensive flight duration will allow evaluation of the diurnal variation of key atmospheric constituents such as OH, HO_2, ClO, BrO together will longer lived ones such as O_3, HCL and N_2O. The balloon platform on which TELIS will fly also contains a Fourier transform spectrometer MIPAS-B developed by the IMK (Institute of Meteorology and Climate research of the University of Karlsruhe, Germany). MIPAS-B will simultaneously measure within the range 680 to 2400 cm^{-1}. The combination of the TELIS and MIPAS instruments will provide an unprecedented wealth of scientific data and will also be used to validate other instruments and atmospheric chemistry models. First flight is foreseen in 2006.

Manuscript received May 2, 2005

The work was supported in parts by the RFBR projects 03-02-16748, INTAS project 01-0367, ISTC projects # 2445, 3174, the President Grant for the Scientific School 1344.2003.2, and SNF grant 200020-100167.

P.A. Yagoubov, W.-J. Vreeling, H. van de Stadt, and R.W.M. Hoogeveen, are with the National Institute for Space Research SRON, P.O. Box 800, 9700 AV Groningen, the Netherlands, (telephone: 31-50-3634074, e-mail: p.a.yagoubov@sron.rug.nl)

O.V. Koryukin and V.P. Koshelets are with the Institute of Radio Engineering and Electronics, Russian Academy of Science, Moscow, Russia; they are also partially with the National Institute for Space Research SRON, the Netherlands, (e-mail: valery@hitech.cplire.ru)

O.M. Pylypenko is with the State Research Center of Superconductive Electronics "Iceberg", Ukraine (e-mail: o_pylypenko@online.com.ua)

A. Murk is with the Institute of Applied Physics, University of Bern, Switzerland, (e-mail: axel.murk@mw.iap.unibe.ch)

II. TELIS Configuration

The optical front-end of TELIS consists of a pointing telescope, calibration blackbody and relay optics, common for the three channels: 500 GHz, 550-650 GHz and 1.8 THz [1]. The telescope is a dual offset Cassegrain antenna. Primary, secondary and tertiary mirrors of the telescope are mounted on a common frame. The unit is rotated as a whole around the axis coinciding with the direction of the output beam to scan the beam through the required limb sequence on the sky. Primary parabola has an elliptical cross-section of 260x140 mm. 2:1 anamorphicity is introduced by the cylindrical tertiary mirror, which is flat in the vertical direction and spherical in horizontal. An anamorphic design was selected to improve telescope compactness, mass, and moment of inertia. A vertical (elevation) resolution at the tangent point is about 2 km at 500 GHz (FWHM), inversely proportional to the frequency. The limb scans range from upper troposphere (10 km) to stratosphere (30-40 km). Horizontal (azimuth) resolution is about a factor of 2 worse but not of prime importance for this mission as the atmospheric properties within the beam depend only on the altitude.

Calibration of the radiometric gain of the spectrometers is done with two blackbody reference sources at submillimeter wavelengths: the hot-load, which is a conical black-body at the ambient temperature, and the cold sky. The two references are measured in every antenna scan. The cold sky reference is measured with the telescope set at 40 degree upwards with respect to the limb position. For the hot load calibration, a

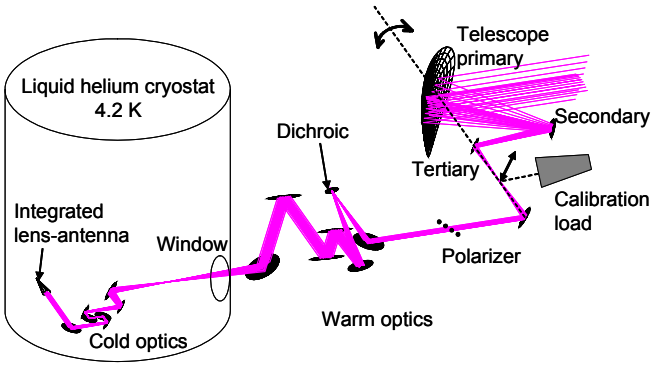

Fig. 1. Schematics of the 550-650 GHz channel optics. The telescope is rotated around the axis coinciding with the direction of the output beam. Wire grid polarizer and dichroic plate are used to separate this receiver from the two other frequency channels (not shown). The cold optics and mixer element are located inside the cryostat at the ambient temperature 4.2 K.

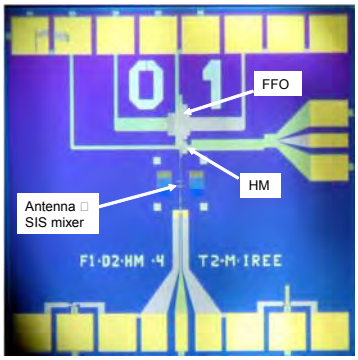

Fig. 2. Photo of the SIR chip. Antenna coupled SIS mixer, FFO and HM for FFO phase locking are located on a 4x4 mm^2 chip. FFO, SIS, and HM are connected with microstrip transmission lines, which contain a number of RF-coupling and dc-blocking elements. The SIS mixer and FFO are provided with local magnetic fields via integrated control lines.

switching mirror is inserted between the telescope and the warm optics for the TELIS receivers to view the reference.

Frequency separation between the channels is performed quasioptically, allowing simultaneous observations by all receivers. First, one linear polarization of the incoming signal is selected by a wire grid and is reflected into the 500 GHz channel. The other linear polarization, which is transmitted by the grid, is then split between two other frequency channels by a dichroic filter. After the splitting, the three beams enter a custom designed liquid helium cooled cryostat. A number of off-set reflectors are used to interface the optics from the telescope to the cryogenic channels. Fig. 1 shows schematics of the optics directly related to the 550-650 GHz channel. The optical beams of the two other frequency channels after the splitting as well as their dedicated optical elements are not shown here.

Inside the cryostat the receivers have dedicated cold optics, mixing element and IF amplifiers. Three amplified output IF signals are fed to an IF processor which converts the IF to the input range of the digital autocorrelator of 2 x 2 GHz bandwidth. An on-board microcontroller controls the instrument and interfaces with the ground station.

III. SIR Design

A key element of the 550-650 GHz channel is Superconducting Integrated Receiver (SIR) [2], which comprises in one 4 x 4 x 0.5 mm^3 chip a low-noise SIS mixer with quasioptical antenna, superconducting Flux Flow Oscillator (FFO) acting as Local Oscillator (LO) and SIS Harmonic Mixer (HM) for FFO phase locking, Fig. 2. The FFO is a long Josephson tunnel junction in which an applied dc magnetic field and a bias current drive a unidirectional flow of fluxons, each containing one magnetic flux quantum. The velocity and density of the fluxons and thus the power and frequency of the emitted mm-wave signal may be adjusted independently by joint action of bias current and magnetic field. The SIR microcircuits are fabricated on a Si substrate using high quality Nb-AlOx-Nb tri-layer. The technological procedure does not require any additional equipment compared to conventional SIS junction technology. The receiver chip is placed on the flat back surface of the Si lens, forming an integrated lens-antenna. One of the constraints implied by SIR is a requirement to place the receiver chip inside cylindrical magnetic shield, as FFO is very sensitive for the external interferences. The magnetic shield consists of two coaxial cans. The external layer is made from cryo-perm and the internal one is copper covered with 100 μm of superconducting led. The SIR chip is positioned far enough from the opening of the shielding cans, which is the only aperture for entering the signal beam and all electrical connections. The magnetic shield is 90 mm long and has an inner clear aperture of 25 mm. Thus the integrated lens-antenna configuration should be compatible with large f-number optics. This is realized by using an elliptical lens and locating the feed antenna at the more distant focus of the ellipse. The lens diameter of 10 mm is selected by optimizing for the minimum beam size at 100 mm from the integrated lens-antenna at 550-650 GHz, so that the shielding cylinder does not truncate the beam. To minimize the reflection loss at the lens-air interface, the curved surface of the lens is coated with a 74 micron thick Stycast antireflection coating, optimized for the center frequency 600 GHz.

IV. FFO Phase Locking

SIR shall detect atmospheric lines with a spectral resolution of the order 5 MHz. To achieve this resolution, FFO is locked to an external reference oscillator using Phase Lock Loop (PLL) system. Schematically the FFO stabilization circuit and characteristic frequencies of its subsystems are shown in Fig. 3. The required references are provided by the Local oscillator Source Unit (LSU), all phase locked to the internal 10 MHz Master Oscillator.

FFO is used as a 550-650 GHz LO for the SIS mixer. A small fraction of the FFO is also directed towards the integrated on the same chip HM. The latter mixes the FFO with the n-th harmonic of the 19-21 GHz reference. The

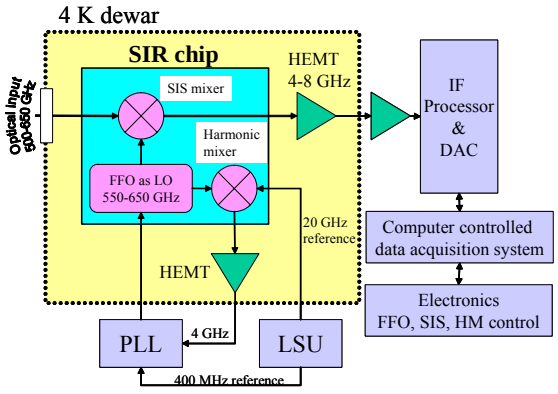

Fig. 3. Schematics of the FFO stabilization circuit. FFO frequency is mixed in HM with the 19-21 GHz reference. The mixing product is amplified, downconverted and compared with the 400 MHz reference in the PLL. The phase difference signal generated by PLL is used to feedback the FFO control line.

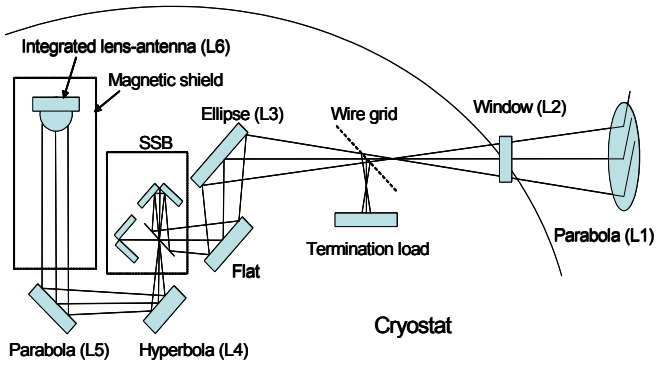

Fig. 4. Layout of the cold channel optics. Lines show the optical beam trajectories.

mixing product at 4 GHz is amplified by a cryogenic HEMT amplifier. In the PLL the mixing product is downconverted to 400 MHz, and its frequency and phase are compared with the reference 400 MHz. Finally, the phase difference signal generated by the PLL is used as a feedback to the FFO control line current to compensate for the phase error. To obtain wideband operation of the PLL (15 MHz full width), it resides right outside the cryostat to minimize the total loop length. Dedicated software (IRTECON) controls SIR electronics and PLL settings, allowing automatic optimization and remote operation of the phase locked SIR.

V. SIR Channel Cold Optics

The SIR cold channel optics consists of the integrated lens-antenna, Martin-Puplett polarizing interferometer used as a SSB (Single Side Band) filter and a number of curved and fold mirrors, all located in the liquid helium cryostat at the ambient temperature 4.2 K. The layout of the optics is shown in the Fig. 4. The interface of the SIR channel optics to the telescope & warm optics system is defined at the position of an image of the pupil which is located outside the cryostat window 160 mm in front of the warm parabolic mirror (L1). The interface accepts a "parallel" and frequency independent beam. The input beam waist has a radius of 11.0 mm for all frequencies. An off-axis parabolic mirror (L1) focuses the beam into an image of the sky located about 70 mm behind the cryostat window (L2). Between the cryostat window and the first cold mirror (L3), infrared radiation filter (not shown in the Fig. 4) and a grid for injecting the cold image load are located. The ellipse L3 serves as an optical relay. Just in front of the magnetic shielding cylinder is a combination of 2 curved mirrors (L4 and L5). With suitable focal lengths they image the system-pupil in the front surface of the integrated lens antenna. Thus we have frequency independent imaging. A de-magnified image of the sky is projected on the chip on the back surface of the elliptical lens (L6). All optical components have a minimum diameter of 4 beam radii (1/e field level), corresponding to an edge taper of -35 dB. Only the integrated lens is smaller than 4 beam radii. (L3), (L4) and (L5) mirrors are $\sqrt{2}$ larger in horizontal direction than in vertical direction, because of the 45 degrees angle of incidence.

VI. Verification of the Optical Design

The quasioptical performance of the reflective optics of the TELIS instrument has been calculated using the GRASP8 package [3] (from TICRA in Denmark). To simulate the 550-650 GHz cold (located at 4.2 K) channel we used configuration illustrated by Fig. 4. The center frequency is 625 GHz. As an input feed, the calculated by PILRAP (Program for Integrated Lens and Reflector Antenna Parameters [4]) integrated lens-antenna system field distribution is used. The SSB filter is replaced by a set of two plane mirrors to maintain the optical path length, as we could not find a way to model accurately roof top mirrors in GRASP.

Fig. 5 shows the far field beam profile simulated by GRASP. Solid lines are the power patterns in the vertical

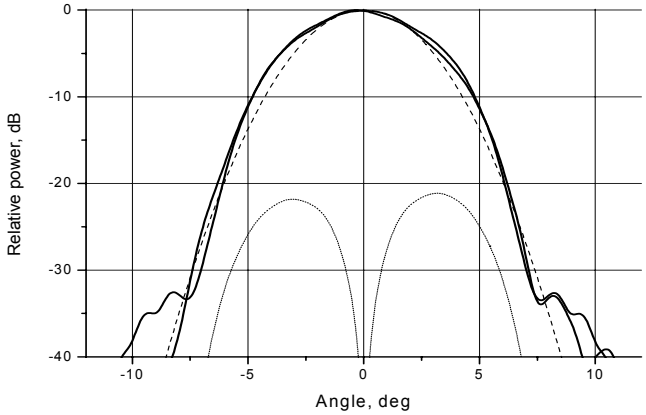

Fig. 5. Calculated far field beam pattern of the 550-650 GHz cold channel. Frequency is 625 GHz. Solid lines show beam pattern in two orthogonal planes. Dotted line is a cross-polarization component. An ideal Gaussian profile is indicated by the dashed line.

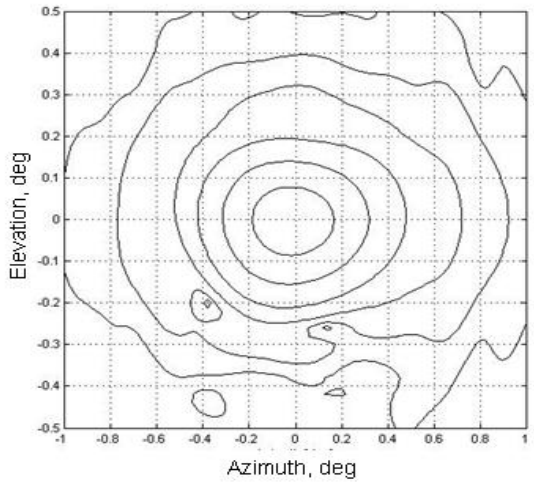

Fig. 6. Calculated far field 2-D beam profile of the 550-650 GHz instrument, including the warm optics and telescope, at 625 GHz. Solid lines represent the -3 dB and the -10 dB to -50 dB contours.

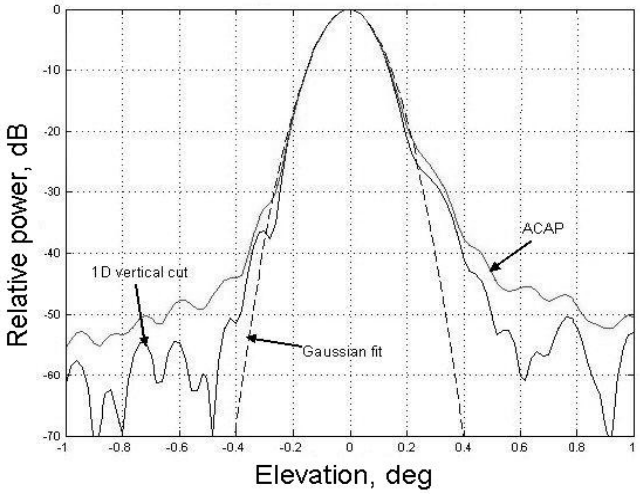

Fig. 7. Calculated far field 1-D vertical (elevation) cut and ACAP at 625 GHz.

(perpendicular to the optics base plate) and horizontal planes. One can see that in one plane (vertical) the beam is absolutely symmetric. A 13% asymmetry (expressed as a difference of integrated powers in positive and negative angles) in the horizontal plane is caused by non-axissymmetric optics in this plane. The dotted line indicates a cross- polarization component which appears at <-20 dB level. Just for a reference purpose, an ideal Gaussian beam profile is indicated by dashed line.

Complete optics of the 550-650 GHz receiver, including the cold channel, warm optics and the telescope (as drawn in Fig. 1), was also simulated by GRASP. Fig. 6 shows calculated 2-D far field pattern of the receiver at 625 GHz. The pattern exhibits an elliptical form (note different scale in azimuth and elevation) determined by the anamorphicity of the telescope. Strongly asymmetric pattern in the azimuth plane is mainly caused by the fast off-axis optics of the telescope. However, for the atmospheric limb scans, only the vertical (elevation) profile of the receiver beam is of interest for the retrieval, while the atmosphere is uniform in the horizontal plane within the field of view.

The 2-D results were used to calculate the Azimuthally Collapsed Antenna Pattern (ACAP) by summing over the co- and cross-polarization amplitudes at each elevation, Fig. 7. FWHM of the ACAP at 625 GHz is 0.17 deg, corresponding to a 1.65 km FWHM beam at the tangent point in 550 km distance. The ACAP is symmetric and has an almost Gaussian shape for amplitudes larger than -20 dB. An asymmetric sidelobe starts at the -25 dB level. This beam shape will be relevant for the retrieval of atmospheric data and has to be considered in the retrieval model. The calculated total spillover loss of the optics (not including the integrated lens-antenna) is <10%.

VII. Alignment and Tolerance Analysis

An optical configuration of the TELIS SIR channel consists of about 20 optical elements, located within three major sub-assemblies: telescope, warm optics and cold channel. Fabrication and positioning errors of each element and sub-assemblies as a whole cause deviation of the optical performance from the ideal design. Therefore, comprehensive study of mechanical tolerances and their impact on the system performance has been performed using commercial programs ZEMAX for Geometrical Optics analysis and GRASP for Physical Optics analysis. There are other factors as well which cause deterioration of the system performance during the maintenance. These are thermal effects, position non-reproducibility of the sub-assemblies or potential deformations caused by 5g acceleration during instrument landing. These all made it absolutely necessary to envisage visible light alignment and/or verification. For this reason, all reflective optical elements, including the telescope, are required to have an optical surface quality.

A. Geometrical optics analysis

As a first step, an inverse sensitivity analysis of mechanical tolerances was performed using ZEMAX. Both linear and angular misalignments of each optical element were considered. Shapes of reflecting surfaces were assumed to be ideal. In the inverse sensitivity mode ZEMAX computes the value of each tolerance that will result in the decrease in performance specified by Max Criteria. Only one optical element is perturbed at once, other elements remain unperturbed. For the Max Criteria we selected a maximum offset of 1/3 beam radius (1/e field level) at each mirror. This criterion keeps under control the aperture efficiency and spillover loss as the size of all optical elements is 4 beam radii. This analysis identifies optical elements most critical to the misalignments and their individual tolerances.

As a next step, statistical (Monte Carlo) analysis of the tolerances was performed. This method analyses the effect of all perturbations simultaneously. For each Monte Carlo cycle, all parameters which have specified tolerances are randomly set using the defined range of the parameter (found by the

inverse sensitivity analysis) and a statistical model of the distribution of that parameter over the specified range. More than 200 Monte Carlo cycles were run to get statistics on performance degradation.

As a last step, all tolerances, and especially those of most critical mirrors, have been tightened until the performance degradation is in 90% of the runs within the Max Criteria mentioned above. Similar analysis was performed for the groups of elements. This covers the cases of global misalignment of the cold channel and the telescope with respect to the warm optics. The geometrical optics tolerance analysis allowed us to draw the following conclusions:

- Typical angular tolerance within the cold channel is 0.06-0.08 deg. This can be translated to a linear tolerance of about 20 micrometers. All elements can be mounted on the common baseplate using dead-reckoning, if the above mentioned mechanical accuracy is maintained for all mirrors and the baseplate. Visible light alignment verification should be performed to check for fabrication errors.
- Within the warm optics, the typical angular tolerances are 0.1-0.2 deg, translated to about 30 micrometers requirements for the production.
- The telescope should be aligned with visible light.
- The tolerances on position and rotation of groups of elements can not be met. Therefore, two first (after the telescope) and last mirrors in the warm optics should have alignment possibility to (co)align the warm optics with the telescope and cold channel, respectively.

B. Physical Optics analysis

The physical optics simulations are time consuming and allow only a limited number of cases to be analyzed. We have selected the cases of global misalignments between the sub-assemblies.

The simulations of the telescope to warm optics misalignments showed that ±1 mm lateral and ±0.5 deg misalignments do not degrade substantially the quality of the beam, and keep it within the requirements. The FWHM of the ACAP changes are within 3%, spillover loss is not increased by more than 0.5%, the difference in sidelobes is only noticeable at <-25 dB level. A maximum pointing error of ±0.04 deg will cause a beam shift of ±0.4 km at the tangent point, close to the requirement on ±0.5 km beams co-alignment on the sky of the three frequency channels of TELIS instrument.

A case of warm optics to cold channel misalignments is particularly interesting as the reproducibility of the cold channel mount in the cryostat is not yet known and could be poor because of thermal cycling. In this case, the effects of lateral misalignments of ±1 mm and angular misalignments of ±0.3 deg were investigated. Here, the results are in general very similar to the previous case. Note only that here the angular tolerances are almost a factor of two tighter. In conclusion, we have shown that the main requirements on the maximum performance degradation due to sub-assemblies misalignments could be met if the tolerances are within ±1 mm and ±0.5 deg for the telescope-warm optics interface and ±1 mm and ±0.3 deg for the cold channel-warm optics interface.

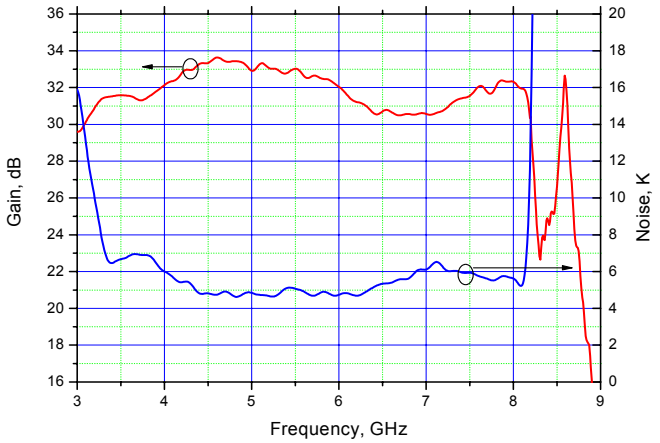

Fig. 8. Gain and noise temperature of the LNA based on InP transistors.

VIII. IF Chain

Intermediate Frequency (IF) signal of the SIR is amplified by 4-8 GHz. cryogenic HEMT Low Noise Amplifier (LNA). LNA has two stages and is based on InP transistors. The amplifier is integrated with Pamtech isolator. Gain and noise temperature of the amplifier were measured at 4.2 K ambient temperature, results are shown in Fig. 8. Noise performance was determined using Y-factor technique with a 50 Ω load at the amplifier input. Temperature of the load was varied in a range from 6.5 to 15 K. An output was further amplified by a room temperature amplifier (total gain 67 dB, noise temperature <150 K) and registered by a spectrum analyzer. Both gain and noise of the LNA were measured during one cooling cycle using a cryogenic switch to connect LNA to either external signal for gain measurements or internal heatable 50 Ohm load for noise measurements. Gain is corrected for the loss in the dewar cables; noise temperature is corrected only for the 0.2 dB cable loss. The total power dissipation of the LNA is 5 mW.

IX. Experimental Results

The experimental results discussed here have been obtained with the SIR device (T3-031#6) of the most recent design [5]. Optimization of the FFO-SIS and FFO-HM matching circuits and implementation of submicron junctions for both mixers improved pumping of SIS and HM by FFO. As seen from the Fig. 9, both mixers have enough FFO power for the optimum operation in the frequency range 500-640 GHz. The data are normalized to the Ig (current just above the gap voltage) of each mixer. Dashed lines indicate the operation level of corresponding mixer, 0.25 is optimum for the SIS, while 0.05 is enough for the HM. The latter mixer needs less power due to highly non-linear regime of operation [6]. Note that the curves show the envelope (maximum) of a set of data taken at

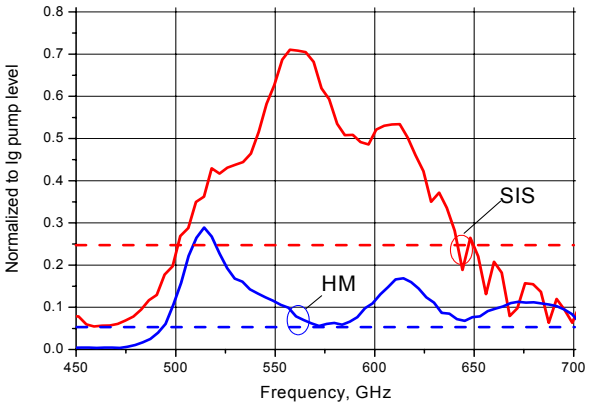

Fig. 9. Pumping of SIS and HM by FFO, normalized to their individual Ig. The dashed lines indicate optimum levels, 0.25 for the SIS, and 0.05 for the HM. Note that the curves show the envelope (maximum) of a set of data taken at different control line currents of the FFO.

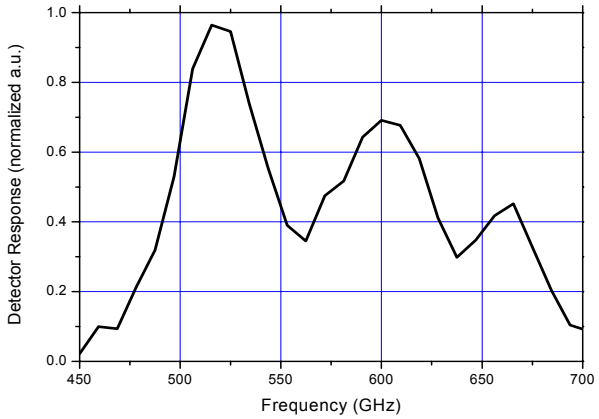

Fig. 10. FTS response of the SIR measured in direct detector mode.

different magnetic fields applied to the FFO by control line. SIS mixer is based on twin submicron (0.8 μm^2) Nb-AlOx-Nb tunnel junctions with J_c>7 kA/cm^2. SIR chip is mounted in a "flight" mixer block surrounded by magnetic shield. No other optical elements of the cold channel were installed yet for these very first measurements. All tests reported here were done in a liquid helium cooled cryostat at 4.2 K ambient temperature. Noise temperature measurements are done using Y-factor technique by chopping between hot (295 K) and cold (80 K) loads in the signal path of the receiver. IF response of the mixer is amplified by a "flight" IF chain configuration. It consists of a cryogenic InP based 4-8 GHz LNA amplifier followed by a RT amplifier. The signal is detected by fast power meter in 40 MHz bandwidth, selected by tunable YIG filter. We have also used "flight" configuration of the PLL system and could lock the FFO practically at any frequency in the 550-650 GHz range.

Fig. 10 and Fig. 11 show the FTS response of this device measured in direct detector mode and results of Noise Temperature (NT) measurements, which are not corrected for any loss. The minimum DSB NT of 250 K is measured at 520 GHz, slightly outside the designed frequency range. From these graphs one can see that NT data correspond well to that of FTS. Frequency dependence of the mixer response is in general determined by combination of few factors: design of the antenna-mixer and matching circuits, SIS junction area and its current density. It is obviously a challenge to optimize performance of three interdependent superconducting elements on one chip in such wide frequency range. Further experimental tests of different chip configurations and development of SIR microstrip coupling circuitry are needed.

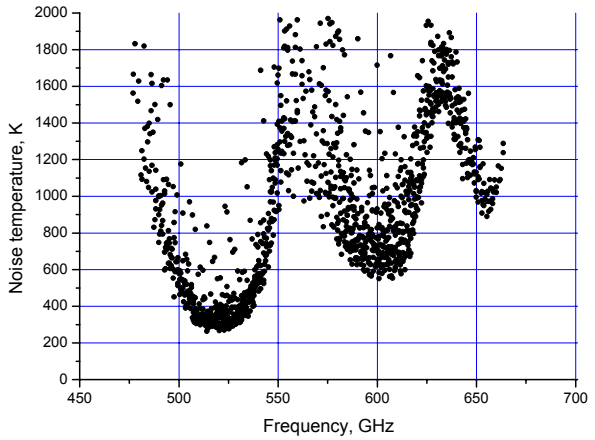

Fig. 11. Noise temperature of the SIR. At each frequency different values of magnetic field was applied to the FFO. Magnetic field controls power of the FFO and thus pumping level of the SIS, resulting in a set of data points.

ACKNOWLEDGMENT

The authors thank M. van der Vorst for supplying PILRAP, Microwave Electronics group of Swiss Federal Institute of Technology in Zurich (ETHZ) for supplying InP transistors. T. de Graauw and W. Wild are acknowledged for their support in this work, L. Filippenko for SIR microcircuit fabrication.

REFERENCES

[1] Hoogeveen, R.W.M., Yagoubov, P.A., Maurellis, A.N., Koshelets, V.P., Shitov, S.V., Mair, U., Krocka, M., Wagner, G., Birk, M., Hübers, H.-W., Richter, H., Semenov, A., Gol`tsman, G., Voronov, B., Ellison, B., Kerridge, B., Matheson, D., Alderman, B., Harman, M., Siddans, R., Reburn, J., eds. Strojnik, M., "New cryogenic heterodyne techniques applied in TELIS: the balloon borne THz and submm limb sounder for atmospheric research", Proc. of SPIE, Infrared Spaceborne Remote Sensing XI, 5152, p. 347-355, 2004.

[2] V. P. Koshelets *et al*, "Towards a Phase-Locked Superconducting Integrated Receiver: Prospects and Limitations," *Physica C*, vol. 367, pp. 249-255, 2002.

[3] Knud Pontoppidan, editor. "*Technical Description of GRASP8"*. TICRA Engineering Consultants, Copenhagen, Denmark, 2003. ISBN 87-989218-0-0.

[4] M. J. M. van der Vorst. Integrated Lens Antennas for Submillimeter-wave Applications. PhD thesis, Elect. Eng. Dept., Eindhoven Univ. Technol., Eindhoven, The Netherlands, 1999.

[5] Valery. P. Koshelets, Pavel N. Dmitriev, Andrey B. Ermakov, Lyudmila V. Filippenko, Oleg V. Koryukin, Andrey V. Khudchenko, Mikhail Yu. Torgashin, Pavel A. Yagoubov, Ruud W.M Hoogeveen, and Wolfgang Wild, "Superconducting Submm Integrated Receiver with Phase-Locked Flux-Flow Oscillator for TELIS", this Proceedings

[6] V. P. Koshelets *et al.*, "Optimization of the Phase-Locked Flux-Flow Oscillator for the Submm Integrated Receiver", *IEEE Trans. on Appl. Supercond.y*, vol. 15, no. 2, June 2005.

Space-qualified SIS mixers for Herschel Space Observatory's HIFI Band 1 instrument

Y. Delorme[1], M. Salez[1] , B. Lecomte[1], I. Péron[1,2], F. Dauplay[1],
A.Féret[1], J.Spatazza[3], J.-M. Krieg[1], K. Schuster[2]

Abstract **We have developed a wideband SIS mixer for the heterodyne instrument (HIFI Band 1) of ESA's Herschel Space Observatory. This double-sideband mixer uses twin Nb/AlOx/Nb junctions and, without any mechanical tuner, covers a relative bandwidth greater than 30%, optimized in the Band 1 frequency range from 480 to 640 GHz . Two identical mixers will be used in orthogonal polarizations to make up the HIFI Band 1 receiver, which, with Bands 2 to 5, will be the first SIS receivers to ever fly in space. Therefore our mixers design and fabrication process include several innovations to meet the specifications requested by a space environment, such as high operation reliability, robustness to vibration, thermal variation and cosmic irradiation. This paper presents the characteristics of the flight model and the space qualification tests performed on the qualification model. The mixer's performance analysis confirms that it has a very low noise (less than 3 times the quantum limit) over the entire bandwidth, as expected from early simulations.**

Key words: heterodyne, SIS, submillimeter, space qualification

I. INTRODUCTION

The Herschel Space Observatory is a cornerstone astronomical satellite of the European Space Agency (ESA), with a 3.5 m dish. Herschel is scheduled for launch in 2007 by an Ariane V rocket, and should operate during more than 3 years. Located at 1.5 million kilometres from the Earth (Lagrangian point L2), it will observe the universe at wavelengths so far rarely studied: far-infrared and submillimetre wavelengths for which the strong atmospheric absorption prevents ground-based observations.

HIFI is one of the three detection instruments of Herschel. It is a very high resolution spectrometer and the first space instrument using superconductive heterodyne receivers [1]. Covering a frequency range from 480GHz to 1900GHz and with a receiver sensitivity and spatial resolution higher than the previous submillimeter satellites SWAS and ODIN, HIFI will probe a large number of astrophysical sources via their rotational molecular lines.

[1]LERMA, Observatoire de Paris, 77 avenue Denfert-Rochereau, 75014 Paris, France
[2]IRAM, 300 rue de la piscine, 38406 Saint-Martin d'Hères, France
[3]CNRS-INSU, Division Technique, 1 place Aristide Briand, 92195 Meudon, France

HIFI has 6 channels, 5 of which (band 1 to 5) use SIS technology covering continuous frequencies from 480 GHz to 1250 GHz and the last one (band 6) uses HEB technology for frequencies from 1250 GHz to 1900 GHz. Each channel contains 2 identical mixers intended to simultaneously detect two orthogonal polarizations.

LERMA has been responsible for the developement and realization of the HIFI band 1 mixers covering the frequency range from 480 to 640 GHz, in collaboration with IRAM which was in charge of the SIS (Nb/Al-AlOx/Nb) junctions' fabrication and the corrugated feedhorn's beam pattern measurements.

II. MIXER'S DEVELOPEMENT

II.1 Specifications

The key of the HIFI channel 1 receiver consists of a SIS mixer in waveguide technology, without any mechanical tuner, with a frequency bandwidth around 30% and a noise temperature near 3 times the quantum limit. In addition to the constraints imposed by the space environment, such as high operation reliability, robustness to vibration, thermal variation and cosmic irradiation, achieving both these bandwidth and sensitivity represented a technological challenge in the field of heterodyne detection.

The specifications for HIFI band 1 include:

- the noise temperature (DSB) is limited at 70K for 480 GHz and 110K for 640 GHz,
- the ripple over the whole IF 4-8GHz should be less than 2dB/GHz,
- the mixer block should weigh less than 75g and be enclosed in a volume of 32x32x40mm with all predefined connection interfaces,
- the electromagnet with a superconductor coil should be capable of suppressing the Josephson effects with a current lower than 10mA,
- the mixer block must pass the qualification tests concerning the resistance to launch vibrations, the reliability and stability in space environment.

II.2 Mixer's design

To design such device, we have developed special programs combining the theoretical physics of superconductor, of quantum mixing and of electromagnetic propagation in microstrips [2]-[5]. Using these programs and with the help of the commercial and public field simulation tools as HP-Libra, ADS, Microwave Studio, HFSS and Supermix, we have simulated the device's performance, optimized the mixer's configuration (the geometries of the feedhorn, the waveguide and the circuit's substrate)[6]-[7]. We have also predicted the effects of fabrication tolerances on the performance. A model of the mixer on 100:1 scale has been built and tested to confirm some simulation results.

The key element of this mixer, containing two SIS junctions and an integrated tuning circuit with a planar antenna, is deposited using thin film technology on a 50µm thick x 115µm wide quartz substrate. This substrate is placed in a 135µm wide channel which is orthogonal to a 100µm × 400µm reduced-height rectangular waveguide. The substrate channel and the waveguide are both closed by the same flat metal piece (Fig. 1).

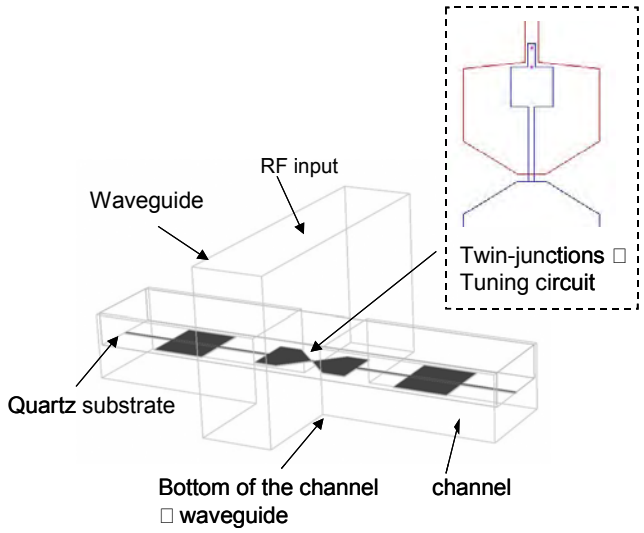

Fig. 1. mixer's configuration with no backshort waveguide and the SIS junctions' tuning circuit.

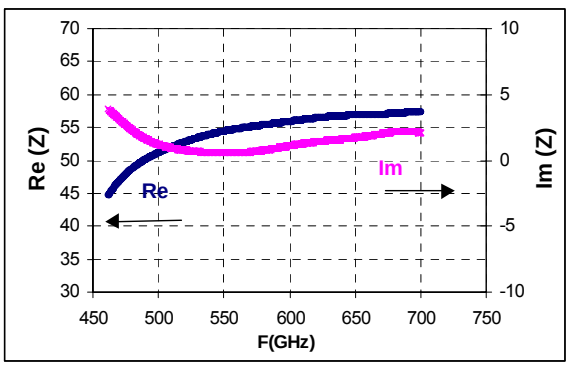

Fig. 2. embedding impedance at the bowtie antenna.

This innovative configuration has not only provided at the bowtie antenna an embedding impedance almost purely real over the whole frequency range (Fig. 2), but also allowed to skip a very critical step of waveguide alignment as in most fix-tuned waveguide SIS mixer's design. Therefore it makes the design more reliable.

The SIS junction's tuning circuit was made by using superconductive Nb stripline technology. A two-section Tchebychev transformer was designed to connect the planar bowtie antenna to twin-parallel junctions spaced by a narrow (5µm) stripline (see the box of Fig.1). The embedding impedance described above was used as an input parameter to design this matching circuit. According to the experience acquired at IRAM, the junction's area is defined as 1µm² with a current density of 10kA/cm².

During the design of the tuning circuit, the effects of parameters' uncertainties or fabrication tolerances were investigated. The circuits the least sensitive to these effects were selected .

In order to minimize the Josephson effects which cause extra noise in an SIS mixer[8], we have designed an electromagnet (Fig.3) using a high permeability cryogenic alloy "Cryoperm" (µ=30000 at 4.2 K) coiled with a superconductive wire (NbTi). This special shaped integrated electro-magnet is designed to produce, with a current lower than 10mA, enough magnetic field (about 250 Gauss in our case) to set the junction's Josephson current at the second global minimum.

Another item intended to suppress the trapped magnetic flux was designed and integrated in the mixer block : the deflux heater, a specially designed 1 kohms thin film resistor located near the junctions, able to drive them quickly from the superconducting to the normal state..

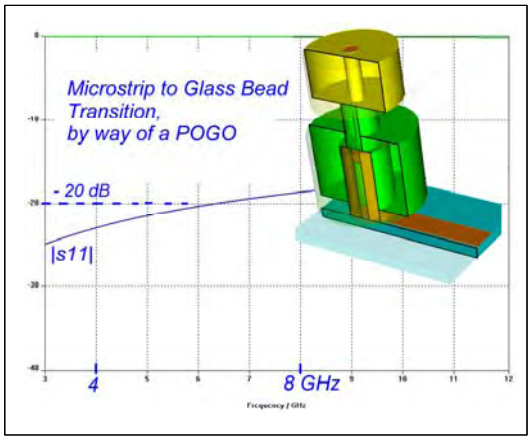

Fig. 4. spring-loaded POGO contact and the simulated S_{11} parameter for IF band.

To meet the specified connection interfaces of HIFI, an orthogonal transition was needed between the mixer's IF output SMA connector and our IF board. In order to minimize this transition's return loss and have a flexible but resistant (to thermal cycles and vibrations) contact, we have chosen a SMA-pogo connector. This is a BeCu spring bellow fixed to

the SMA's glass bead and pressed on the IF board via a spring allowing the right amount of pressure (Fig.4). The simulation has shown that the return loss is about -20 dB over the 4-8GHz IF band. And the qualification tests have confirmed the connector's robustness to thermal and mechanical shocks.

II.3 Mixer's fabrication

The junction was fabricated with the Nb/Al-AlOx/Nb SNEP (selective niobium etch) process using electron beam lithography, and the tuning circuits in Nb/SiO_2/Nb microstrip with the following parameters[9]: 150nm of ground-plane Nb, 200nm of SiO2, 450nm of contacting electrode Nb. The junctions have a current density between 7-9 kA/cm² and a quality factor (R_{subgap}/R_n) around 13.

The mixer blocks (containing demonstration model DM, qualification model QM and flight model FM), the high-quality corrugated mandrels and waveguides have been made by *Société Audoise de Précision* [10]. The electrodeposition and the mandrel dissolution processes have been optimized and performed in collaboration with *Protection des méteaux* [11].

This 67g mixer block's outside and inside view are illustrated in the Fig.5. It contains the corrugated feedhorn, the integrated superconductor electromagnet, the IF circuit board on alumina, the bias and filter circuits on kapton. The alumina and kapton circuit boards were fabricated by the companies *Hymec* and *Reihnart.*

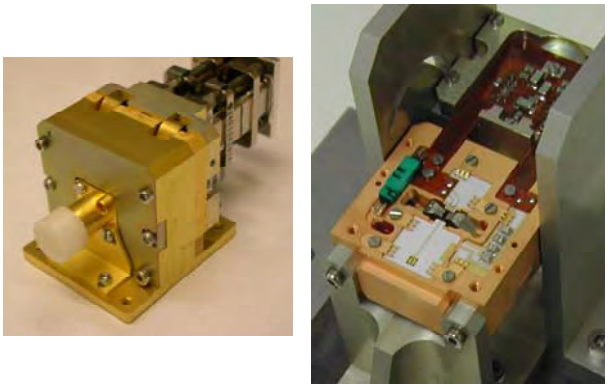

Fig. 5. Mixer block's outside and inside view.

III. MIXER'S PERFORMANCE

III.1 Space qualifications

The qualification programs are intended to submit the mixers (qualification model) to extensive tests corresponding to the constraints caused by the launch and the space environment. These programs include: thermal cycling (20-30 cycles) between 300K and 4,2K, 144 hours bake-out at 380K, vibrations at room temperature and liquid nitrogen temperature. The cold vibration tests have been performed at NLR (Holland) for each of 3 axis between 5 and 2000 Hz with a vibration level from 0,5g to 20g, levels specified by ESA and corresponding to the Ariane V rocket launch. At the end of these tests, no functional anomaly was present on the QM [12].

According to the function and the sensitivity of mixer's different elements, the specified tests determined by a pre-qualification program have been carried out separately.

Since Herschel will be exposed to cosmic radiations during more than 3 years, the effect of ionizing radiation on the junction has been studied. We performed the 10 MeV proton irradiation tests using the cyclotron at CERI-CNRS, Orléans[13]. More than 100 junctions have been irradiated with doses between 10^9 and 10^{13} protons/cm². According to the analysis, a 2.10^{10} protons/cm² dose would correspond to the 2007's launch and 4 years mission with an 1 mm thick Al shielding. After the tests, only small and not significant changes (about 1%) were observed on the junctions I-V curves.

The SIS junctions have also been submitted to the electrostatic discharge tests (performed at KOSMA, Germany). Among the 19 tested junctions, 18 junctions have resisted to 1000 pulses of 75V.

III.2 Measured performance

1. FTS measurement

The FTS measurement is performed systematically on every mounted mixer block. The mixer is mounted in an Infrared Lab liquid helium cryostat, with a 25-µm mylar vacuum window and a 180 µm zitex infrared filter.

Figure 6 shows the frequency response of the flight model FM03. The test was done under atmospheric pressure which causes the water absorption line near 557GHz. The bandwidth is larger than 480-640 GHz indicating a good performance of the RF coupling and junction's tuning circuit.

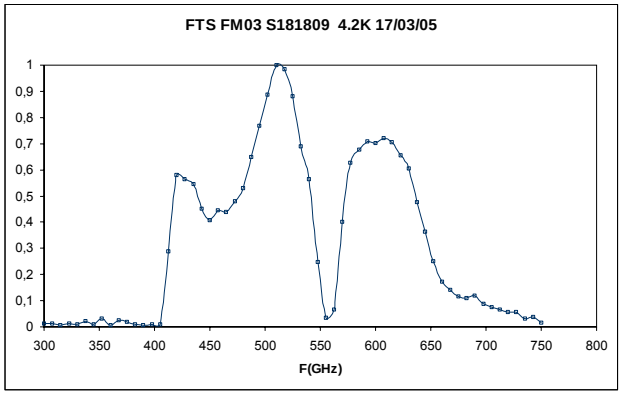

Fig. 6. FTS response of the mixer FM03.

2. *Josephson effect suppression*

The efficiency of the integrated electromagnet of the FM01 was checked and illustrated in Fig. 7. Less than 8mA coil's current was needed to produce necessary magnetic field to set the junctions to the second global minimum of Josephson current.

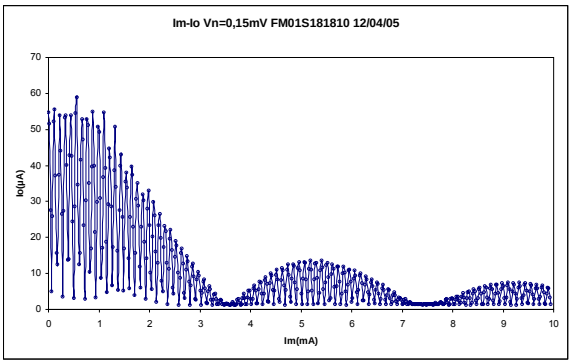

Fig.7. Josephson current of the twin-parallel junction in FM01 vs the current of the integrated electromagnet.

Figure 8 plots the two parallel junctions' IV curve of the mixer FM03 before and after applying a 14mA and 5 seconds current pulse on the integrated heater. The junctions characteristics have transited to that of a normal resistance after the pulse and returned to their initial state in about 5 seconds.

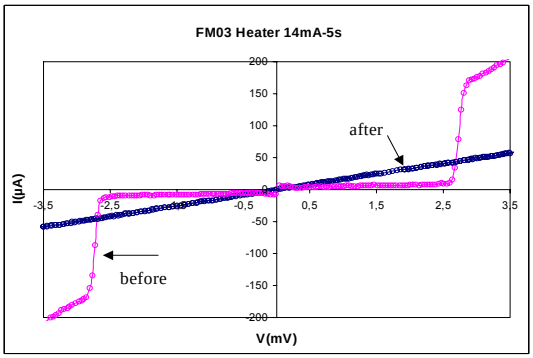

Fig. 8. Junction's IV curve of the FM03 before and after applying the 14mA and 5 seconds heating current pulse

3. *Heterodyne measurement*

Heterodyne tests were performed on two flight models for the whole band 1 frequency range using a liquid helium cryostat pumped to 2K and three RPG[14] solid state LO sources. The IF output of the mixer was connected to a 4 to 8GHz cryogenic isolator followed by a Yebes[15] low noise cryogenic HEMT amplifier with a noise temperature around 3K at a working temperature of 2K. This IF chain was calibrated using a variable thermal load at its input, as well as by the shot noise produced by the SIS junction, biased in the linear part of the IV curve above the gap voltage.

The double sideband (DSB) receiver noise temperature was obtained by the well-known "Y-factor" method, placing

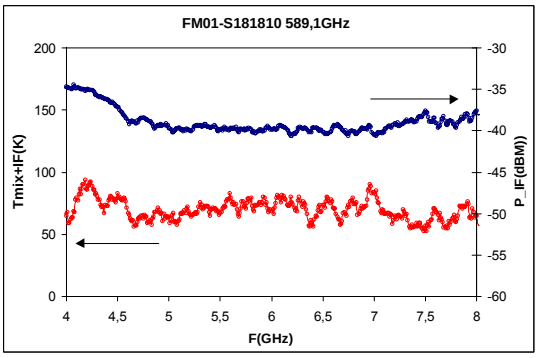

Fig. 9. IF power spectrum and receiver noise versus 4-8 GHz IF bandwidth of the FM01 at 589GHz.

alternatively two blackbodies of different temperatures at the receiver input and measuring the corresponding IF output powers. From their ratio, called Y factor, one derives the receiver's noise temperature and gain. In our case, a chopping wheel switched the receiver input between a room-temperature absorber and a Thomas Keating load cooled to about 100 K, and permanently monitored in a liquid nitrogen dewar. The whole calibration setup is under vacuum, to avoid the strong attenuation of the 557 GHz water line, i.e. in the center of HIFI Band 1. The IF power was measured in the full 4-8 GHz bandwidth and in narrower bandwidths using a spectrum analyzer : Figure 9 shows the mixer's IF output power and noise temperature vs IF frequency of FM01 at 580 GHz. Across the whole 4-8 GHz IF band, the response is flat within the HIFI specifications.

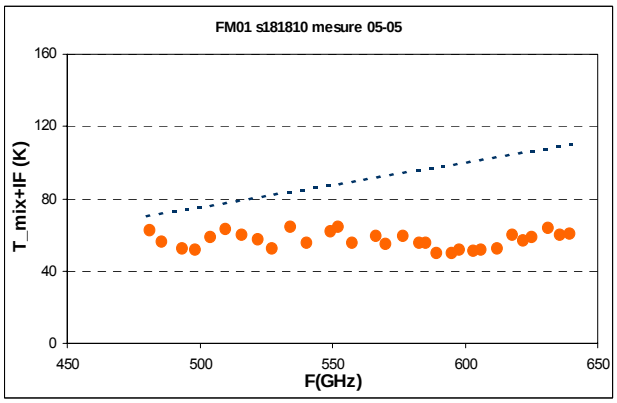

Fig. 10. Noise temperature of the mixer FM01 for the whole HIFI band 1

Figure 10 summarizes the DSB noise temperature of the mixer FM01. The noise was corrected for the optical losses, due to the various windows. These windows include those of the cryostat, of the vacuum box between the cryostat and input signal sources, and of the 10 µm mylar beamsplitter coupling the LO and load signals. The transmission of each optical component was determined experimentally by measuring its effect on the Y factor. Additional work is under way to refine this correction. We can notice that the mixer noise temperature is well under the HIFI specifications over the

whole band, and therefore, smaller than three times the quantum limit. More details on the mixer behaviour (temperature vs. DC bias, LO power, magnetic field and receiver stability) will be published elsewhere.

IV. CONCLUSION

We have developed successively the demonstration, qualification and flight models of the SIS mixers for Herschel-HIFI band 1, covering the frequency range 480 to 640 GHz. These mixers include several innovative features such as a new block mechanical structure, a high-efficiency integrated electromagnet, a 4-8GHz right-angle transition using a POGO connector, and a new corrugated feedhorn process. We have fully passed the pre-qualification and qualification tests simulating the extreme conditions to which space flight hardware is subjected. The flight models have demonstrated excellent performances and satisfied all the required instrument specifications.

ACKNOWLEDGMENT

This work has been funded by the Centre National d'Etudes Spatiales (CNES) and the Centre National de Recherche Scientifique (CNRS) – Institut National des Sciences de l'Univers (INSU). We thank N. Honnigh, J. Kooi, G. De Lange, A. Kowacz, H. Golstein, P. Dieleman, J. Evers, H. Goulouze and W. Hatch for fruitful discussions, and T. De Graauw, P.J. Encrenaz, Y. Viala, G. Beaudin and J.-M. Lamarre for their supportive spirit.

REFERENCES

[1] H.van de Stadt, "Detectors for the Heterodyne Spectrometer of FIRST", Proceedings of the ESA Symposium 'The Far Infrared and Submm Universe', 1997, p.457.

[2] R. M. Fano, "Theoretical limitations on the broadband matching of arbitrary impedances", J. of the Franklin Institute, 49, 57, 139, 1950

[3] J.R. Tucker, "Quantum limited detection in tunnel junction mixers", IEEE J. of Quantum Electronics, QE-15(11), pp.1234-1258, 1979; J.R. Tucker and M.J. Feldman, "Quantum detection at millimeter wavelengths", Rev. Mod. Phys., vol. 57, no. 4, pp. 1055-1113. 1985.

[4] J.C. Swihart, "Field sulution for thin-film superconducting strip transmission line", J.appl. Phys. 32 (3). pp. 461-469, 1961.

[5] H. A. Wheeler, "Transmission-line properties of a strip on a dielectric sheet on a plane", IEEE Microwave Theory Tech., vol 25, pp.631-647, 1977.

[6] M.Salez, Y. Delorme, I. Peron, F. Dauplay, B. Lecomte, M.H. Chung, I. Spatazza. M. Guillon, K. Schuster, J.M. Krieg et A. Deschamps, "Development of a 480-640 GHz tunerless SIS mixer for FIRST HIFI/Band 1", Proc. 12th International Symposium on Space Terahertz Technology, March 23, San Diego, 2001.

[7] M.Salez, Y. Delorme, I. Peron, B. Lecomte, F. Dauplay, "A 30% bandwidth tunerless SIS mixer of quantum-limited sensitivity for Herschel / HIFI Band 1", SPIE Proc. "Millimeter and Submillimeter Detectors for Astronomy", Août 2002, 22-28.

[8] S. Shapiro, "Josephson currents in superconducting tunneling : the effect of microwaves and other observations," *Phys. Rev. Lett., vol. 11, pp. 80-82, 1963.*

[9] I. Peron, P. Pasturel, and K.F. Schuster, "Fabrication of SIS junctions for space borne submillimeter wave mixers using negative resist e-beam lithography", Proc. of the Applied Superconductivity Conference, ASC'00, Virginia Beach, Sep. 17-23, 2000.

[10] *Société Audoise de Précision*, Z.A du Pont 81500 Ambres, France

[11] *Protection des Métaux*, 57-59 Rue de St-Mandé, BP.117, 93511 Montreuil, France

[12] Internal report for HIFI-band 1 qualification tests.

[13] I. Peron, G. Faury, Y. Delorme, F. Dauplay, B. Lecomte, M. Salez, K.F. Schuster, "Investigation of radiation hardness of SIS junctions for space borne radioastronomy", to appear in Proc. 5th European Workshop on Low Temperature Electronics, WOLTE 5, Grenoble, 2002.

[14] *Radiometer Physics* GmbH, Birkenmaartr. 10, 53340 Meckenheim, Germany.

[15] *Centro Astronomico de Yebes*, Apartado 148, 19080 Guadalajara, Spain.

The band 3 and 4 Flight Model mixer units for HIFI

G. de Lange, B.D. Jackson, M. Jochemsen, M. Eggens, H. Golstein, W.M. Laauwen, L. de Jong, S. Kikken, C. Pieters, H. Smit, and D. Van Nguyen
SRON National Institute for Space Research
Postbus 800, 9700 AV Groningen, The Netherlands

T. Zijlstra, M. Kroug, and T.M. Klapwijk
Department of Applied Physics,Delft University of Technology
Lorentzweg 1, 2628 CJ Delft, The Netherlands

The Heterodyne Instrument for the Far-Infrared (HIFI) will cover the 0.48-1.9 THz frequency range. This frequency range is divided into 7 bands. SRON is developing the band 3 and 4 SIS waveguide mixer units. Band 3 and 4 cover the 800-960 GHz and 960-1120 GHz frequency range, respectively. Each of these bands contains two mixers for dual polarization measurements. Delivery of the Flight model mixer units is due spring 2005.
The mixers have a corrugated horn antenna and operate with a 4-8 GHz IF bandwidth. Nb/AlOx/Nb SIS tunnel junctions with NbTiN/Al wiring layers are used as mixing element. Besides the heterodyne functionality, the units also incorporate a superconducting magnet, an internal ESD/EMC protection circuit, a 4-8 GHz bias T, and a de-flux heater.
The mechanical and optical design is to a large extent driven by the specific environmental requirements for a space mission, the mass and thermal budget, and the electrical and optical interfaces with the rest of the instrument.
In the paper we discuss the design and performance of the Flight Model mixer units. The current best laboratory receiver noise temperatures are 250-280 K DSB across the band 3 frequency range and 400-600 K across the band 4 frequency range. The performance within HIFI is expected to be significantly lower, because of the absence of warm optics. Results of the characterization of the Flight Model mixer units will be presented. Furthermore we will show some of the specific design solutions necessary for building reliable space instrumentation and the problems encountered in implementing these. .

Low noise NbTiN 1.25 THz SIS mixer for Herschel Space Observatory

A. Karpov, D. Miller, F. Rice, J. A. Stern*, B. Bumble*, H. G. LeDuc*, J. Zmuidzinas

California Institute of Technology, Pasadena, CA 91125, USA
* Jet Propulsion Laboratory, Pasadena, CA 91109, USA

We summarize the development of a SIS mixer for the 1.1-1.25 THz band of the heterodyne spectrometer of Herschel Space Observatory (HSO). The quasi-optical SIS mixer has two Nb/AlN/NbTiN junctions with the area of 0.25 μm^2. The Josephson critical current density in the junction is 30-50 kA/cm^2. The tuning circuit integrated with SIS junction has the base electrode of Nb and a gold wire layer.
With the new SIS mixer the test receiver maximum Y factor is 1.41. The Y factor is measured with detection of IF power in entire 4-8 GHz IF band. The minimum receiver uncorrected DSB noise temperature is 450 K. The SIS receiver noise corrected for the loss in the optics is 350 – 450 K across the 1100 – 1250 GHz band (Fig. 1). The receiver has a uniform sensitivity in the full IF range of 4 – 8 GHz (fig. 2). The sub-micron sized SIS junction design is optimized to ease the suppression of the Josephson current (fig. 3), and the receiver operation is stable. The measured mixer beam pattern is symmetrical and, in a good agreement with the design requirements, has the f/d =4.25 at the central frequency of the operation band (fig. 4). The developed mixer satisfies the requirements for the use at the HSO.
The minimum DSB SIS receiver noise is close to 6 hν/k, apparently for the first time in the far infrared band. The Local Oscillator power used for frequency mixing is only 100 nW. The combination of a low noise and a low LO power requirement makes the SIS receiver a prospective instrument for exploration in 1-2 THz band.

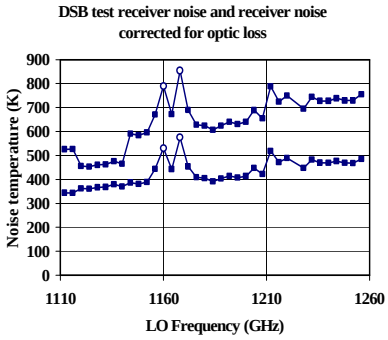

Fig. 1.

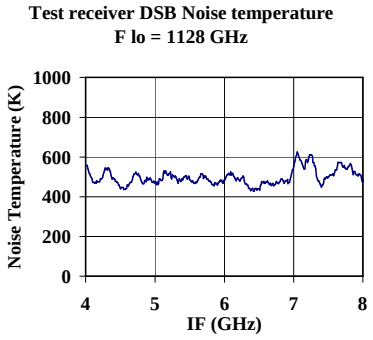

Fig.2

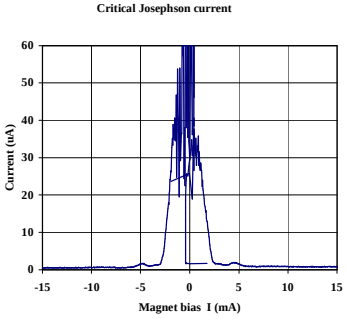

Fig. 3

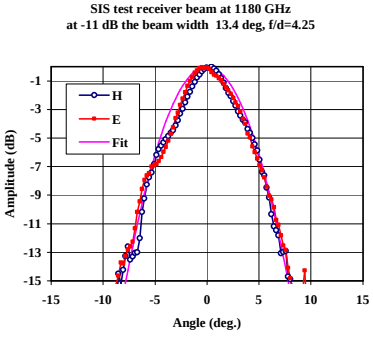

Fig. 4

Session 9:

HEB II

Tuesday May 3, 15:45-17:15
Chairman: Heinz-Wilhelm Hübers

Vector Measurement of the Beam Pattern of a 1.5 THz Superconducting HEB Receiver

C.-Y. Edward Tong, Denis N. Loudkov, Scott N. Paine, Dan P. Marrone, and Raymond Blundell

***Abstract*— Near-field vector beam pattern of the 1.5 THz superconducting Hot Electron Bolometer (HEB) receiver currently in operation in Northern Chile has been performed in our laboratory. Using an open waveguide probe, we have mapped both the amplitude and phase of the beam emerging from our 1.5 THz HEB receiver package, across a number of planes along the line of propagation of the radio-beam. With an integration time of about 100 ms per point, a signal-to-noise ratio of about 25 dB was achieved for a beam waist of 3.5 mm. These measurements have proved to be invaluable in achieving good alignment between the cryostat housing the HEB mixer and the remainder of the receiver and telescope optics. The accuracy of our beam measurement is estimated to be ±0.2 mm in position and ±5 arc minutes in angular displacement.**

***Index Terms*—Near-field antenna measurements, vector measurements, submillimeter waves.**

I. Introduction

THE VECTOR BEAM MEASUREMENT TECHNIQUE DEVELOPED for the longer submillimeter wavelengths [1,2] is an extremely useful tool in the alignment of high performance superconducting receivers [3]. This method has been demonstrated to work up to a frequency of 1 THz [4]. Recently, we have further extended the frequency range of our Terahertz near-field measurement capability to 1.5 THz.

In this paper, we report the laboratory measurement of the beam pattern of the 1.5 THz superconducting Hot Electron Bolometer (HEB) receiver [5] currently installed in the Receiver Lab Telescope on Cerro Sairecabur, in Northern Chile [6,7]. This receiver employs an HEB mixer based on an NbTiN film. The Local Oscillator (LO) is a cascaded doubler cascade pumped by a 90 GHz power amplifier chain [8]. Our approach is to pre-align the receiver package in our laboratory in Cambridge using the near-field measurement range. These measurements have proved invaluable in achieving good alignment between the cryostat housing the HEB mixer and the remainder of the receiver and telescope optics which include a Martin Puplett diplexer various plane mirrors and focusing elements. This ensures good pointing at telescope and minimizes the amount of operation performed at 5500 meter altitude.

Manuscript received May 2, 2005.

C.-Y. E. Tong (e-mail: etong@cfa.harvard.edu), S.N. Paine, D.P. Marrone and R. Blundell are with the Harvard-Smithsonian Center for Astrophysics, 60 Garden St., Cambridge, MA 02138 USA.

Denis N. Loudkov was with the Harvard-Smithsonian Center for Astrophysics. He is currently with the Physics Department, Moscow State Pedagogical University, Moscow, Russia.

II. The Transmitter

Following standard near-field measurement techniques, we employ an open waveguide probe in the measurement. This ensures that we are accurately sampling the near field profile, with minimal disturbance on the beam to be measured. The open waveguide probe measures 0.5 x 0.25 mm. It is significantly over-moded at 1.5 THz but since the aperture is much smaller than the size of the beam to be measured, the fundamental waveguide mode should be most efficiently coupled to the receiver beam.

Given that the HEB mixer is quite sensitive, the required transmitter power should be quite small. The following formula gives a reasonable estimate of the required transmitter power, P_t, for a given signal-to-noise ratio, SNR, at the beam center:

$$P_t \sim 2n\, k\, T_n\, B\, R_{\text{area}} * \text{SNR}, \qquad (1)$$

where n is the number of double-side-band mixers in the down conversion from 1.5 THz to the final frequency of amplitude and phase measurement; k is the Boltzmann constant; T_n equals the receiver noise temperature plus 300 K (background temperature); B is the noise equivalent bandwidth of the vector measuring instrument; and R_{area} is the ratio of areas between the mean beam size and the probe size. In our measurement set-up n = 2 and B ~ 10 Hz for an integration time of 100 ms. The double-side-band receiver noise temperature is about 1500 K. The size of the beam is taken to be πw^2, where w is the beam waist radius at the measurement plane. Depending on the plane of measurement, the area ratio ranges from 80 to 400. For an SNR of 25 dB, the required transmitter power is of the order of 0.1 pW.

A harmonic generator is sufficient to generate such small power. A point contact Schottky barrier multiplier is most suited for this application. We have chosen a multiplier chain consisting of a doubler – tripler cascade originally intended for 650 GHz operation. A high-pass filtering section was inserted between the output of the multiplier and the probe to allow only frequency components higher than 1 THz to be radiated. The multiplier was pumped by a Gunn oscillator operating at around 122 GHz. The measurement frequency of 1.464 THz was the 12th harmonic of the multiplier.

III. Measurement Setup

One key issue in THz vector measurement is that the frequencies of the transmitted signal and the Local Oscillator (LO) have to be perfectly synchronized. Our strategy was to employ a single synthesizer to operate both the transmitter and the THz LO in a homodyne set-up. A block diagram of the measurement set-up is given in Fig. 1. To maintain phase coherency, the secondary LO in the second down converter unit and the reference to the phase-lock unit were derived from direct multiplication from the 10 MHz reference output of the synthesizer.

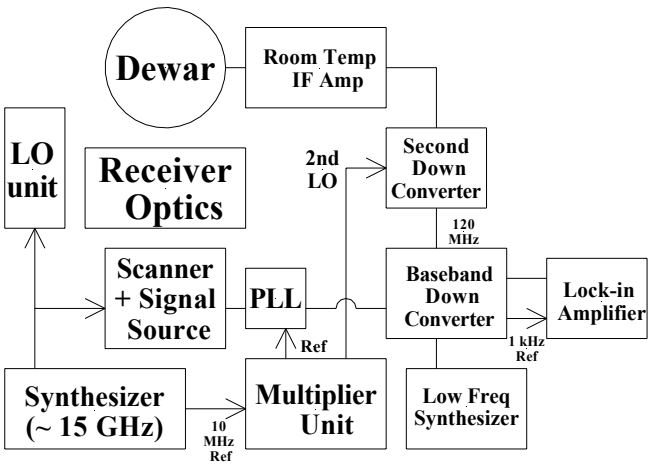

Fig. 1 Block diagram of the Set-up of vector beam measurement at 1.464 THz of HEB receiver.

The THz LO unit consists of a cascade of multipliers and 90 GHz power amplifier modules [8]. The net multiplication factor from the driving synthesizer is 96. Because of this high multiplication ratio, there is considerable amount of phase noise at the output frequency of 1.5 THz, even if we start with a very clean source at 15 GHz. This is especially true for frequency components close to the carrier. Consequently, we have chosen to use a lock-in amplifier instead of the vector voltmeter as the final vector measurement instrument. One advantage of the lock-in amplifier is that it affords very narrow and adjustable noise equivalent detection bandwidth. In contrast, the vector voltmeter offers a noise equivalent bandwidth in excess of 1 kHz. A low frequency synthesizer was used to down convert both the reference and the signal channels to 1 kHz for measurement by the lock-in amplifier. An integration time of 10 ms was used, yielding an equivalent bandwidth of around 100 Hz.

IV. Results of Measurements

A number of scans have been performed along the line of propagation of the THz beam. Depending on the beam size in the plane of scan, the beam pattern was sampled with a step size of 0.25 – 0.5 mm. The amplitude and phase stability of the measurement was monitored by returning the probe to the center of the scan in the middle of every row of the raster scan. In Fig. 2, we plot the variation of the measured amplitude and phase with time over a typical scan of 20 minutes (over a 35 x 35 grid).

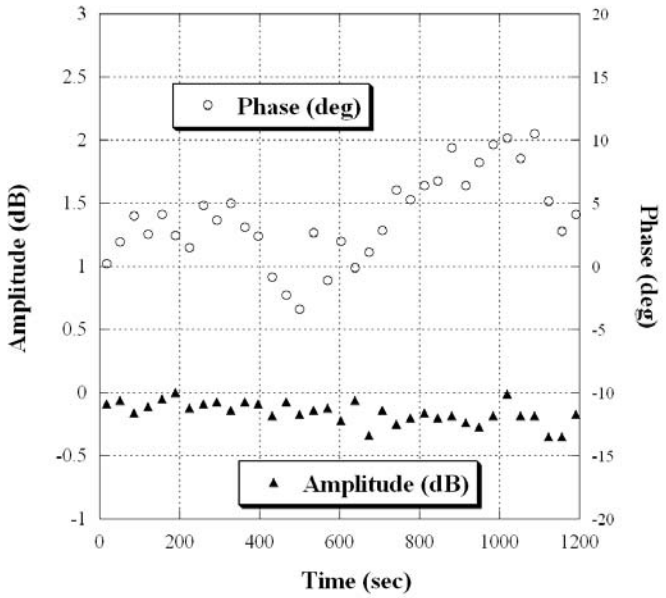

Fig. 2 Measured amplitude and phase fluctuations at 1.464 THz over a 20 minute scan. These values were registered as the probe was returned to the center of the scan area at each row of the raster scan.

Fig. 2 shows that the maximum amplitude fluctuation is better than 0.3 dB and the peak-to-peak phase fluctuation is only 15 degrees over a 20 minute scan. This amazing good performance is attributed to the stability of NbTiN based HEB mixer [9]. It should be noted that in the course of our scan the mixer bias current, which reflects the amount of absorbed LO power hardly moved.

Fig. 3 gives a two-dimension amplitude pattern. A dynamic range of 25 dB was generally attained. This dynamic range could be increased by increasing the integration time. With an integration time of 10 ms, the scan time was dominated by the motion of the stepper motor, plus the time needed to return the probe to origin for calibration at the middle of each row. Therefore, small increase in integration time would not need to excessive increase in scan time. Note that a settling time equal to 10 times the integration time was built in at each measurement point to allow the lock-in amplifier to settle. Our dynamic range is, however, limited by cross-talk between the reference and measurement channels, generated in the base-band down converter. A more sophisticated circuit is needed.

V. Extraction of Beam Parameters

The position of the beam and its tilt angles with respect to the normal of the plane of scanning are extracted by fitting to the fundamental Gaussian beam:

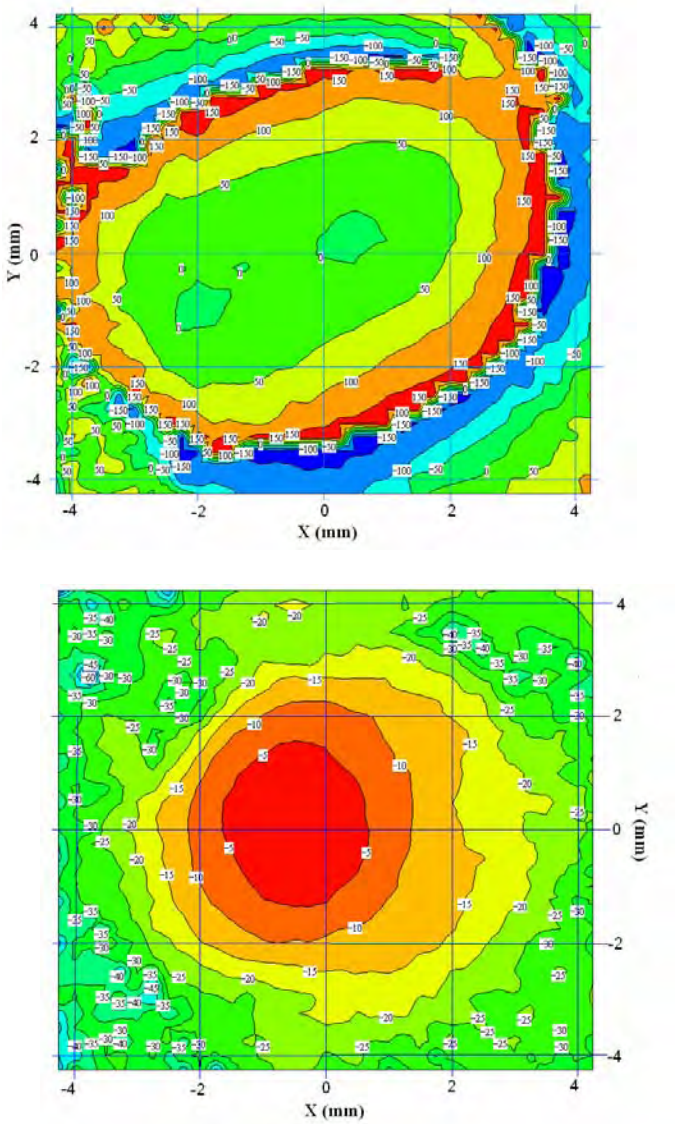

Fig. 3 Two dimensional phase (top) and amplitude (bottom) beam map of the 1.5 THz HEB receiver. The phase contours are labeled in degrees and the amplitude contours are labeled in dB. The asymmetry of the beam pattern is caused by the presence of two 90-degree off-axis parabolic mirrors in the optics train.

$$\Psi(x',y') = \sqrt{\frac{2}{\pi}}\frac{1}{w}\exp\left(-\frac{x'^2+y'^2}{w^2}\right)\exp\left[j\beta_0\left(\frac{x'^2+y'^2}{2R}+\delta_x x'+\delta_y y'\right)\right] \quad (2)$$

where $x' = x - x_c$ and $y' = y - y_c$. x, y are scan coordinates. x_c and y_c are the coordinates of the amplitude center of the beam, w is the beam waist radius, R is the radius of curvature of the phase front, and δ_x and δ_y are the angles (in radians) of tilt of the beam with respect to the normal to the scan plane. The beam parameter set of (x_c , y_c , w, R, δ_x , δ_y) is obtained by optimizing the power coupling coefficient:

$$O(x_c, y_c, w, R, \delta_x, \delta_y) = \frac{\iint E_{meas}(x,y)\,\Psi_{00}^*(x,y)\,dx\,dy}{\iint E_{meas}(x,y)\,E_{meas}^*(x,y)\,dx\,dy} \quad (3)$$

For the beam pattern given in Fig. 3, the optimal power coupling coefficient is 88.6%. The coordinates of the beam center are (-0.32, 0.05), with a beam waist radius of 1.9 mm and a radius of phase curvature of 75 mm. The beam tilt angles are 5.2 arc minutes and 3 arc minutes along the x and y axes respectively.

VI. Reliability of Phase Measurement

The challenge of vector near-field measurement at THz frequencies is the reliability of phase measurement. Since there are considerable amount of cabling in the measurement system, any temperature change can alter the measured phase. At 1.5 THz, a 0.4 μm change in cable length would introduce a 1 degree measurement error in phase. Furthermore, the transmitter is linked to the synthesizer through a flexible cable which moves with the scanner. This cable is likely to introduce phase distortion into the measured phase map.

In order to counteract these effects, we have adopted a few counter-measures. First, the synthesizer was first connected to a power splitter and then linked to the transmitter by a 0.9 m phase stable cable. Next, an identical cable was employed to link the second port of the above splitter to the LO unit. Any phase change caused by temperature changes would, therefore, be canceled out. Finally, the cable was bent into a U-shape. Because of our small area of scan (5 x 5 mm), the radius of curvature of our cable does not change appreciably. For larger scan areas, a longer cable may be necessary.

In order to check the reliability of our measurements, we have performed a series of scans in a number of planes along the direction of propagation of the THz beam (Z-axis) emerging from the receiver package. For each of these data sets, we extract the beam centers. Beam tilt angles are derived by fitting a pair of straight lines to the x- and y- coordinates of the beam centers. The results are summarized in Fig. 4.

From the plot, we can deduce that we can determine the position of the beam center to an accuracy of about 0.2 mm. for a beam waist radius of a few mm. The slopes of the fitted lines give us an added measure of the beam tilt angle. This method does not depend so much on the phase measurement. It can. Therefore, be used to check the extracted beam tilt angles which depend critically on the measured phase front of the beam. Table 1 gives the comparison between the extracted beam tilt angles (in radians) in each plane, their average values and the values derived from the slopes of the fitted lines in Fig. 4.

From these data, we can conclude that the standard deviation of the extracted beam tilt angles about their mean is better than 2 milli-radians (~7 arc minutes) and they agree with the amplitude-based method to about 1 milli-radian (~3.5 arc minutes). This confirms the reliability of our phase measurements.

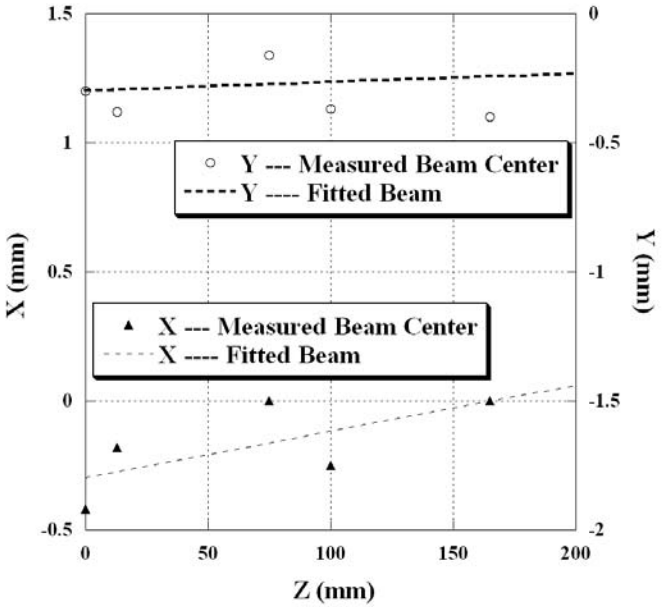

Fig. 4 Propagation of the beam along the Z-axis. The markers give the *x*- and *y*- coordinates of the fitted beam centers from the measured data. The 2 sets of data are fitted by 2 straight lines. The slopes of these lines, +0.0018 and +0.00035 for the *x*- and *y*- data set respectively, give the beam tilt angles in radians.

Z (mm)	0	13	75	100	165	Aver-age	From Fig. 4
1000*δx	-0.90	0.35	-0.70	3.10	3.10	1.00	1.80
1000*δy	-0.60	-1.20	0.70	0.10	0.10	-0.20	0.35

Table 1 Extracted beam tilt angles (given in milli-radians) in different scan planes along the *Z*-axis. These values are compared to their average values and the beam tilt derived from the slopes of the fitted lines in Fig. 4.

VII. Conclusion

Near-field vector beam measurements have been performed successfully at 1.464 THz. A dynamic range of 25 dB has been achieved and the measured data demonstrates good stability, with very low amplitude and phase drifts. By fitting to the fundamental Gaussian beam, we were able to extract the beam center coordinates, beam waist radius and the beam tilt angles. These measurements allow us to determine beam displacement to an accuracy of 0.2 mm and beam tilt angles of 5 arc minutes. We have also established that near-field phase measurements are highly reliable even at 1.5 THz. Finally, this technique is a key step in the alignment and operation of the 1.5 THz HEB receiver currently installed in Northern Chile.

Acknowledgment

The authors would like to thank Imran Mehdi and his group at Jet Propulsion Lab for making the 1.5 THz LO source available for use with our 1.5 THz HEB receiver.

References

[1] C-Y..E. Tong, S. Paine, and R. Blundell, "Near-field characterization of 2-D beam patterns of submillimeter superconducting receivers," in *Proc. 5th Int. Symp. Space THz Tech., Ann Arbor, MI,* pp. 660-672, May 1994.

[2] M.T. Chen, C.E. Tong, D.C. Papa, and R. Blundell, "A near-field alignment technique at millimeter and sub-millimeter wavelengths," *IEEE MWSYM,, Boston, MA,* vol. 3 pp. 1631-1633, June 2000.

[3] M.T. Chen, C.-Y.E. Tong, R. Blundell, D.C. Papa, and S. Paine, "Receiver beam characterization for the SMA," in *Proc. SPIE Conference on Advanced Tech. MMW, Radio, and THz Telescopes*, (vol. P-3357), pp. 106-113, Kona, Hawaii, Mar. 1998.

[4] C.-Y.E. Tong, D.V. Meledin, D.P. Marrone, S.N. Paine, H. Gibson, and R. Blundell, "Near field vector beam measurements at 1 THz," *IEEE Microwave & Wireless Components Lett*., vol. 13(6), pp. 235-237, Jun. 2003.

[5] C.-Y.E. Tong, D. Meledin, D. Loudkov, R. Blundell, N. Erickson, J. Kawamura, I. Mehdi, and G. Gol'tsman, "A 1.5 THz hot-electron bolometer mixer operated by a planar diode based local oscillator," in *2003 IEEE MTT-S Digest,* pp. 751-754, Philadelphia, PA, Jun. 2003.

[6] R. Blundell *et al*, "Prospects for Terahertz Radio Astronomy from Northern Chile," in *Proc. 13th Intl. Symp. Space THz Tech*., pp. 159-166, (Ed. E. Tong), Harvard Univ., Cambridge, MA, Mar 2002.

[7] D. Marrone, E. Tong, S.N. Paine, J.H. Kawamura, and R. Blundell, "Observations in the 1.3 and 1.5 THz atmospheric windows with the Receiver Lab Telescope*," These proceedings*, 2005. R. Blundell *et al*,

[8] G. Chattopadhyay, E. Schlecht, J.S. Ward, J.J. Gill, H.H.S. Javadi, F. Maiwald, and I. Mehdi, "An all-solid-state broad-band frequency multiplier chain at 1500 GHz," *IEEE Trans. Microwave Theory Tech.,* vol. 52, pp. 1538-1547, May 2004.

[9] D. Loudkov, E. Tong, R. Blundell, K. Megerian, and J. Stern, "Characterization of NbTiN hot electron bolometer mixers at 0.8 THz," presented at the *15th Int. Symp. Space THz Tech.,* University of Massachusetts, Amherst, MA, April 2002.

Full characterization of small volume NbN HEB mixers for Space Applications

J. Baselmans, J. Kooi, A. Baryshev, Z.Q. Yang, M. Hajenius, J.R. Gao, T.M. Klapwijk, B. Voronov, and G. Gol'tsman

***Abstract*— NbN phonon cooled HEB's are one of the most promising bolometer mixer technologies for (near) future (space) applications. Their performance is usually quantified by measuring the receiver noise temperature at a given IF frequency, usually around 1 - 2 GHz. However, for any real applications it is vital that one fully knows all the relevant properties of the mixer, including LO power, stability, direct detection, gain bandwidth and noise bandwidth, not only the noise temperature at low IF frequencies. To this aim we have measured all these parameters at the optimal operating point of one single, small volume quasioptical NbN HEB mixer. We find a minimum noise temperature of 900 K at 1.46 THz. We observe a direct detection effect indicated by a change in bias current when changing from a 300 K hot load to a 77 K cold load. Due to this effect we overestimate the noise temperature by about 22% using a 300 K hot load and a 77 K cold load. The LO power needed to reach the optimal operating point is 80 nW at the receiver lens front, 59 nW inside the NbN bridge. However, using the isothermal technique we find a power absorbed in the NbN bridge of 25 nW, a difference of about a factor 2. We obtain a gain bandwidth of 2.3 GHz and a noise bandwidth of 4 GHz. The system Allan time is about 1 sec. in a 50 MHz spectral bandwidth and a deviation from white noise integration (governed by the radiometer equation) occurs at 0.2 sec., which implies a maximum integration time of a few seconds in a 1 MHz bandwidth spectrometer.**

***Index Terms*— HEB mixers, sensitivity, bandwidth, stability, LO power**

I. Introduction

NBN phonon cooled hot electron bolometer (HEB) mixers are currently the most sensitive heterodyne detectors at frequencies above 1.2 THz [1], [2]. Their performance is usually specified by means of double sideband receiver noise temperature and the mixer IF Gain bandwidth. The present day state-of-the-art mixers combine a good sensitivity (8-15 times the quantum limit), an IF bandwidth of the order of 4-6 GHz [3], [4], [5], [6] and a wide RF bandwidth from 0.7-5.2 THz. However, if these mixers are to be used as central elements in real heterodyne receiver systems, either ground based or space based, it is not enough to know the sensitivity and bandwidth alone. A complete evaluation of a HEB mixer needs to include the following device properties: The noise temperature over the entire IF band, the Gain bandwidth, the RF bandwidth of the antenna, the beam pattern, the direct detection effect, the LO power requirement and the stability of the mixer. In this paper we discuss a complete set of measurements of all these parameters performed on one single small volume HEB mixer. The device under consideration is one of many similar devices, which have all comparable DC and RF properties [7].

J. Baselmans, A. Baryshev, Z.Q. Yang, M. Hajenius and J.R. Gao are with the SRON National Institute for Space Research, Sorbonnelaan 2, 3584 CA Utrecht, The Netherlands.

J. Kooi is with the California Institute of Technology, MS 320-47 Pasadena, California 91125, USA.

M. Hajenius, j.R. Gao and T.M. Klapwijk are with the Kavli Institute of NanoScience Delft, Faculty of Applied Sciences, Delft University of Technology, Lorentzweg 1, 2628 CJ Delft, The Netherlands.

B. Voronov, and G. Gol'tsman are with the Moscow State Pedagogical University, Moscow 119435, Russia.

II. Device layout and experimental setup

The device is fabricated on a double side polished high purity Si wafer with a measured thickness of 0.335 mm that is covered at MSPU, Moscow with a NbN film with a critical temperature $T_c = 9.3$ K and a thickness of about 4 nm. The

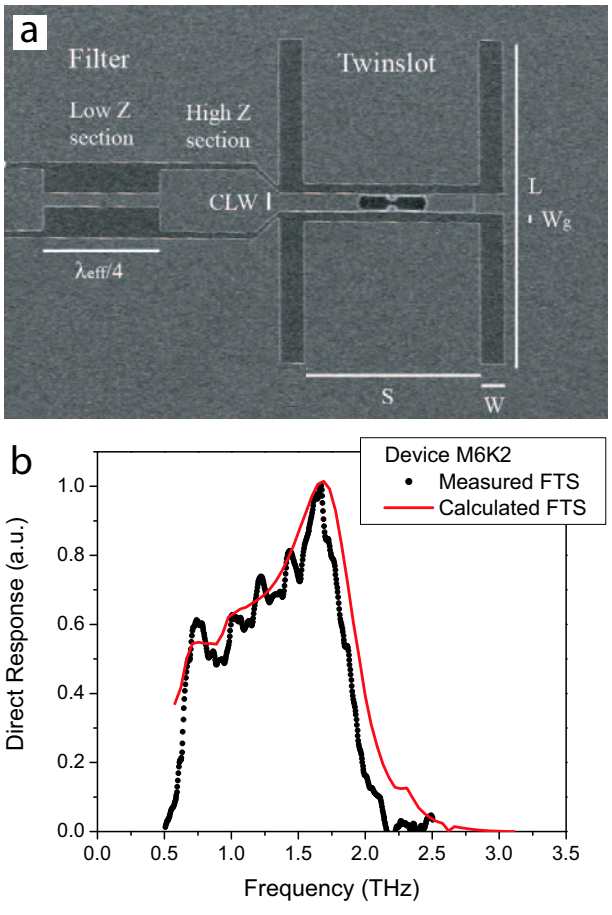

Fig. 1. **a** SEM picture of the antenna structure of the device showing all relevant dimensions: $S = 32\ \mu m$, $L = 56\ \mu m$, $W = 4\ \mu m$, $Wg = 1.4\ \mu m$, $CLW = 2.8\ \mu m$, $\lambda_{eff}/4 = 187.5/4\ \mu m$. **b** Calculated and measured direct response of the antenna using a Fourier Transform Spectrometer.

bolometer length is 0.15 μm, the width 1 μm, the critical current Ic = 51 μA at 4.2 K, The transition temperature of the bridge is 8.9 K, the normal state resistance is 175 Ω at 11 K. The contact pads between the NbN bridge and the antenna are made by cleaning the NbN layer *in-situ* prior to the deposition of 10 nm NbTiN and 40 nm of Au, for details we refer to Refs. [3], [7]. To couple the RF radiation to the HEB we use a twin slot antenna [8] designed to give an optimum response at 1.6 THz. A SEM picture of the antenna including all relevant dimensions is given in Fig 1a. The calculated direct response of the antenna as well as the measured response using a Fourier Transform Spectrometer (FTS) is shown in Fig. 1b. Model calculation and experiment overlap nicely. The direct response peaks at 1.6 THz as expected and has an effective bandwidth of 0.9 THz, obtained by integrating the normalized measured curve.

In the experiment we use a quasi-optical coupling scheme in which the HEB mixer chip is glued to the center of an elliptical Si lens with a design identical to the HIFI band 6 lens design. It has a diameter of 4.995 mm, an ellipticity of 1.0193, a flange diameter of 12 mm and an extension length of 0.421 mm, which results in a total extension length from the ellipse center to the HEB antenna structure of 0.756 mm. The beam from the antenna-lens combination has been evaluated at 1.1 THz using an uncoated lens. The beam is within a few % of the expected f-number at that frequency and also shows a good agreemenet with a PILRAP simulation (for details see Ref. [9]). For the experiments discussed hereafter the lens is coated with a 29 μm thick layer of Parylene-C as a anti-reflection coating with a center frequency of 1.6 THz. The lens is placed in a mixerblock with internal bias-T, identical to the HIFI band 6 design and thermally anchored to the 4.2 K plate of a liquid Helium cryostat. We use one layer Zytex G104 at 77 K and 2 layers at 4.2 K as infrared filter and 0.9 mm HDPE sheet as vacuum window. A focusing mirror is used to convert the fast beam form the lens into a f/D=23.7 beam with a 3 mm waist located at the cryostat window.

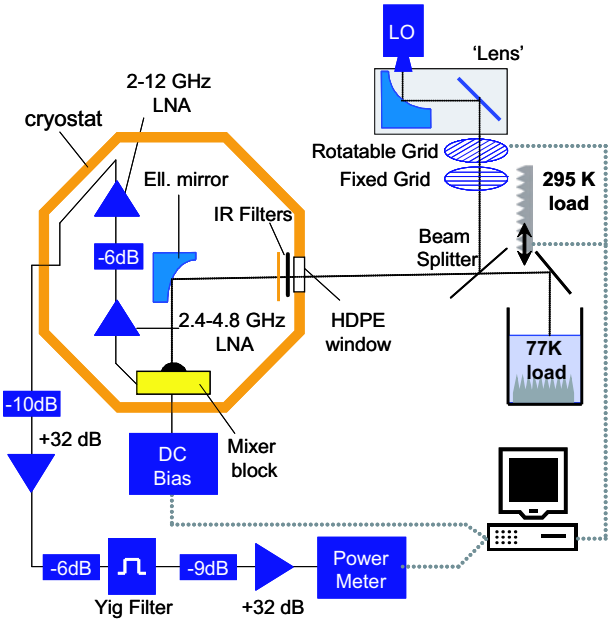

Fig. 2. Schematical picture of the experimental setup.

The setup is designed to measure all relevant mixer parameters as discussed above. A schematic picture is given in Fig. 2. As LO source we use a JPL 1.45-1.55 THz LO Chain, SN 2 [10]. The chain is used at 1462.4 GHz where it has a peak output power 11 μW. This value has been evaluated using a calibrated Thomas-Keating power meter and a Neil-Erickson power meter. Directly in front of the LO is a 2 mirror system, consisting of a focusing ellipse and a flat mounted on a XYZ stage on a second optical parallel rail. This element behaves as a single lens, with 3 degrees of freedom less than a mirror, enabling an easier alignment. A two grid system, consisting of a computer controlled wire grid and a fixed wire grid with a vertical polarization follows which is used to attenuate the signal from the LO. Because the LO is vertically polarized each grid attenuates the power by a factor of $\cos(\phi)^2$ (with ϕ the rotation angle of the rotatable grid), giving an expected attenuation of $\cos(\phi)^4$ for the full system, which has been verified using a measurement with a Golay cell (See the inset of Fig. 5). After the grids the signal is coupled into the Cryostat reflectively by a 3.5 μm Mylar beam splitter. The total transmitted power from the LO horn output to the front of the HEB mixer lens is given by 1.66%. We measure the Y facor using a 300 K hot load and a 77 K cold load by means of a chopper wheel with absorber and 2 large holes allowing optical acces to a small dewar filled with liquid nitrogen. This signal is transmitted through the beam splitter. The loss from the callibration load to the HEB lens front is estimated to be -1.52 dB at the LO frequency, the total loss from the hot/cold load to the HEB itself is -2.82 dB, which includes -1.3 dB loss from the lens surface to the HEB itself, caused by lens absorption and the theoretical antenna efficiency. The effective temperature of the hot and cold load at the mixer chip are calculated in the Callan and Wellton limit to be 204 K and 92 K respectiveley and the total power difference between the hot and cold load evaluated at the mixer chip is about 1.4 nW at the mixer, calculated from the antenna bandwidth (Fig. 1) and the effective temperatures from the hot and cold loads. The IF output of the mixer unit is connected with a 10 cm semi-rigid Al SMA cable to the input of Low Noise Amplifier (LNA), a SRON/Kuo-Liang SN 2, with a bandwidth from 2.4-2.8 GHz with 25-26 dB of Gain and a noise tempersature of 5 K. Because of its low gain this amplifier is connected to a second cryogenic LNA, the Sandy Weinreb 2-14 GHz SN 20B MMIC with 35-36 dB of Gain and 5 K of noise. In between is a 6 dB attenuator to prevent standing waves. The signal is further amplified at room temperature, routed to a Yig filter with a 50 MHz bandwidth and detected using a HP power meter. Note that the entire setup, and in particular the grid transmission, DC bias Voltage and Hot-Cold chopper position, is computer controlled

III. EXPERIMENTS

A. Noise performance and direct detection

In the first experiment we measure the uncorrected double sideband receiver noise temperature T_N at each bias point at the IF frequency that yields the lowest noise temperature, experimentally found to be $F_{IF} = 2.78$ GHz. This is done by measuring the Y factor $Y = P_{hot}/P_{cold}$. $P_{hot/cold}$ is the output power of the receiver at a hot/cold load evaluated at a single bias point, i.e. at one single value of V and P_{LO}. We use the Callen and Welton definition to calculate T_N from the measured Y factor [11]. Simultaneously we measure $I_{hot/cold}$, the mixer bias current at a hot/cold load at each bias point. In Fig. 3a we present the measured values of T_N. We observe a relatively broad region of optimal response with a maximum sensitivity of $T_N = 900$ K. Interestingly we observe also that the mixer bias current is not stable when we switch from hot load to cold load. This current change is the telltale sign of the direct detection effect. In Fig. 3b we show the measured direct detection current, I_{DD} defined as $I_{DD} = I_{hot} - I_{cold}$. We observe that I_{DD} is always negative, in agreement with results reported in [12], [13], [14], [15]. This indicates that the difference in RF power P_{RF} between the 77 K and 300 K load changes the bias current of the mixer in the same way as an increase in P_{LO}. The magnitude of the direct detection current ranges from virtually 0 μA at high bias voltages to more than -1 μA at very low bias voltages. Imagine now that we observe, with the receiver discussed in this paper, an astronomical source which represents itself as a small input power change on top of a background with an identical power input as our 77 K load. A small input power change is in this context defined as a power change that results in a negligible value of I_{DD}. To obtain the receiver noise temperature in this case we need to evaluate the small signal Y factor, defined as the Y factor obtained at an identical value of the bias current for both hot and cold load. This implies that we have to reduce P_{LO} at hot load to make sure that the bias current remains constant, thus compensating for the bias current shift caused by P_{RF} at hot load. We realized this *after* the measurement by constructing a 2 dimensional graph of the receiver output power at hot load and at cold load as a function of bias voltage and current. From these two maps we evaluate the small signal Y factor from which we obtain the noise temperature in the small signal limit, $T_{N,S}$ as shown in Fig. 4. We find a minimum value of $T_{N,S} = 700$ K, which is 22% lower than the minimum value of $T_N = 900$ K. We also observe that the location of the minimum in the noise temperature is shifted to lower bias voltages. For a more detailed analysis we refer to Ref. [15]. Note that this result is strongly dependent on the transparency of the receiever optics and that it implies a complication in any instrument calibration. The only way out of this for the present mixer design is to reduce the 1.4 nW power difference between the hot and cold load within the full RF bandwidth of the mixer. This can be achieved by either using a narrow band metal mesh filter in the signal path or by reducing the tempersature difference between the calibration loads.

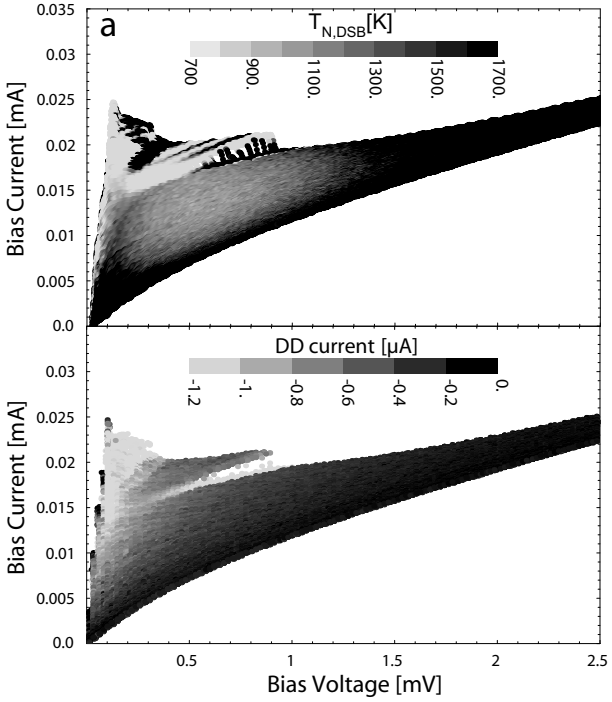

Fig. 3. **a**$T_{N,DSB}$ uncorrected for any optics losses over the entire IV plane of the mixer, the minimum value is $T_N = 1400$ K. **b**: The direct detection current $I_{DD} = I_{hot} - I_{cold}$

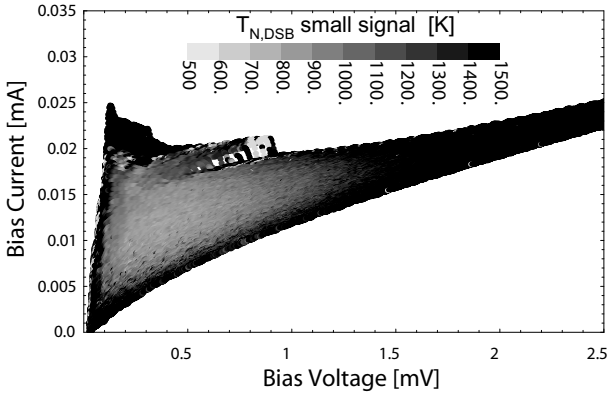

Fig. 4. The double sideband receiver noise temperature in the small signal limit, $T_{N,S}$, around a background corresponding to the 77 K load. The minimum value is $T_{N,S} = 900$ K. A background corresponding to the 300 K load gives an identical result.

B. LO power requirement

Since we know the total optics loss from the LO horn output to the mixer lens front and because the optics is designed to give a perfect beam coupling we can replot the data from Fig. 3 as to give the noise temperature as a function of the LO power available at the receiver lens front. This is shown in Fig. 5. It is obvious that 80 nW of LO power is needed in front of the mixer unit ens to bring the mixer to its optimal operating point. This corresponds to 56 nW of power inside the NbN bridge itself, calculated from the power at the lens front by adding -1.3 dB losses, consisting of the theoretical antenna efficiency and Si lens loss. However, using the isothermal technique [16] on the unpumped an optimally pumped IV

curve we obtain an LO power absorbed in the NbN bridge at the optimal operating point of only 25 nW. Hence there is a factor of 2.3 difference between LO power inferred from the isothermal technique and the one inferred from the LO source output power and known optics losses. Using the grid to evaluate the LO power difference between more closely spaced pumping levels gives a similar result. This discrepancy can be investigated further by using the direct detection effect around the optimal operating point: Around the optimal pumping level we see a clear direct detection current, resulting in a difference between the IV curves at hot load and at cold load. Using the isothermal technique we find a difference in absorbed power in the NbN bridge between hot and cold load IV curves at the optimal pumping level of 1.45 nW. This value is in good agreement with the calculated power difference between hot and cold load available at the mixer (1.4 nW). Hence we must conclude that the isothermal technique correctly addresses the power absorption in the mixer. The 1 to 1 correspondence between isothermal technique and real LO power has also been reported for waveguide HEB mixers [17] and a calculation based upon a distributed temperature model also gives a 1 to correspondence between the calculated IV curve for a given LO power and the isothermal technique LO power obtained from the calculated IV curves [18]. The factor two in our quasioptical experiment can therefore only be attributed to either imperfect beam matching between the diagonal LO horn and the twin slot antenna beam or a misalignment in the optics, despite the great care that was taken to optimize the latter.

C. Bandwidth

The measured noise bandwidth is shown by the gray line in Fig. 6. Obviously we have severe problems in the IF circuit which make a correct evaluation of the mixer properties all but impossible at higher IF frequencies. We therefore re-measure the noise- and gain bandwidth using an identical HEB mixer in a different mixer block. We use a basic IF board of TMM that only forms the transition between a CPW at the HEB chip and a SMA launcher at the other end. An external Miteq bias-T is used to enable mixer biasing. After the bias T we use a Pamtech 3-10 GHz isolator followed by the Sandy Weinreb LNA described before. The rest of the setup remains identical. In the experiment we measure, at the optimum bias operating point of the mixer, the hot and cold load output power as a function of the YIG filter center frequency. Since the noise of the amplifier is very low this measurement enables a direct measurement of both the noise temperature from the Y factor using the Callan and Wellton definition together with the single sideband mixer gain $G^{CW}_{mix,SSB}$ using:

$$G^{CW}_{mix,SSB} = \frac{\Delta P_{out}}{2 \cdot BW_{IF} \cdot k_B G_{IF}(T^{CW}_{in,hot} - T^{CW}_{in,cold})} \quad (1)$$

with $\Delta P_{out} = P_{hot} - P_{cold}$, $T^{CW}_{in,Hot/Cold}$ the effective temperature of the hot and cold load at the input of the receiver, G_{IF}

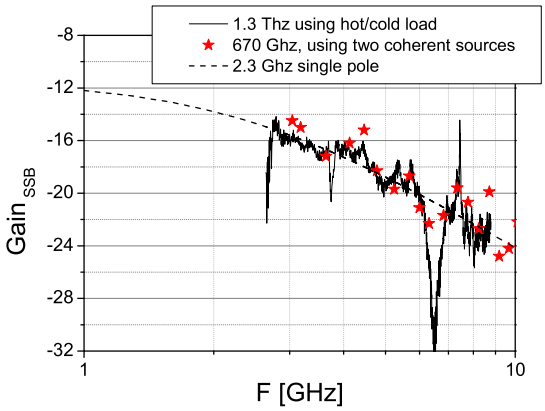

Fig. 6. SSB Gain bandwidth obtained form the measured hot and cold load output power using the Sandy Weinreb MMIC LNA, Pamtech isolator at 1462.4 THz. Stars: SSB Gain bandwidth using the same setup but obtained at 670 GHz using two coherent sources. The dotted line represents a single pole Roll-Off at 2.3 GHz.

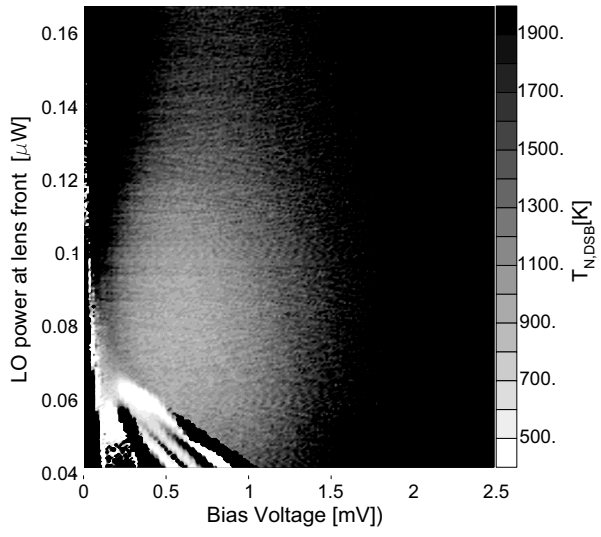

Fig. 5. Uncorrected DSB receiver noise temperature as a function of the LO power available at the mixer unit lens front.

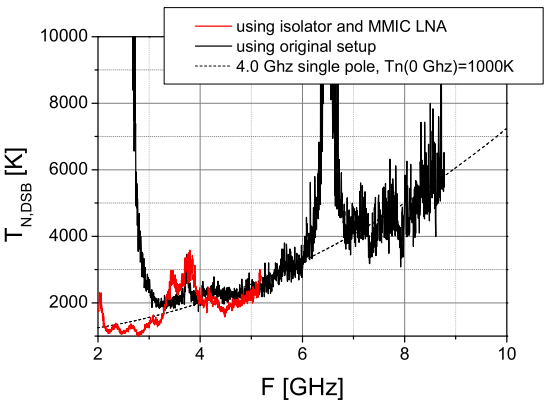

Fig. 7. DSB receiver noise temperature as a function of IF frequency at 1.4624 THz at the optimal operating point of the mixer. Black line: using the Sandy Weinreb MMIC LNA and isolator. Grey line: Using the original setup as shown in Fig. 2. The dotted line represents a single pole roll off at 4 GHz.

the gain of the IF chain, k_B Boltzmann's constant and BW_{IF} the Yig filter bandwidth. A correct evaluation of $G^{CW}_{mix,SSB}$ is thus only possible if all the parameters of the above equation are known, especially the (frequency dependence of) the gain of the IF chain. To obtain this we calibrate the If chain after the measurement by using the HEB mixer as a thermal load with known temperature and impedance. To be able to do this we mount a resistive heater and a thermometer on the mixer block and reduce the thermal anchoring of the mixer block by placing a thin Stainless Steel plate in between the copper block and the 4.2 K plate of the cryostat and by adding a thin copper thermal strap. In addition we use 5 cm of stainless steel SMA between the mixer block and the bias-T. We now measure the IF output power as a function of frequency for different temperatures of the mixer. Since the HEB mixer is, in this temperature range, just a thermal radiator with a resistance of $175\ \Omega$ we know the exact input (noise) power of the IF chain and can therefore use this measurement to calibrate the IF chain gain and noise. We find an IF chain noise temperature of about 10 K, which is higher than the amplifier noise due to the impedance mismatch between the HEB and the isolator and the isolator noise, and a gain of approximately 90 dB at 2 GHz which slowly decreases to 80 dB at 9 GHz. As a control measurement we also measure the total gain of the warm part of the chain using a Vector Network Analyzer. Adding to this measurement the known gain of the cryogenic LNA gives a IF circuit gain virtually identical to the one obtained from the the calibration measurement using the HEB mixer as a thermal load. The measured gain- and noise bandwidth are shown in Figs. 7 and 6 respectively. In Fig. 7 we show also, by the stars, a direct measurement of the (relative) SSB conversion Gain at 670 GHz using 2 coherent sources, one as LO signal and the other as the RF signal. Within the error bars both datasets overlap nicely. Also shown is a first order fit to a single pole, yielding a 3 dB Gain bandwidth of 2.3 GHz. Note that this experimental result agrees very well with totally independent results obtained in Ref. [20] elsewhere in these proceedings. There it is shown that the experimental single pole in the gain bandwidth is in reality a synthesized pole consisting of 4 time constant. Note that the frequency dependence of the noise temperature (Fig. 6) obtained with the new setup Bblack line) does not show the If circuit problems of the original measurement (grey line) and that both datasets can be fitted to first order by a 4 GHz single pole roll-off. The measured ratio of the noise bandwidth with the gain bandwidth, $f_N/f_G = 1.7$, can be compared to a theoretical estimation based upon the analysis used in Ref. [21] and [22], where it is found that $f_N/f_G = \sqrt{\frac{T_{out}(0)+T_{IF}}{T_J(0)+T_{IF}}}$. Here $T_{out}(0)$ is the single sideband mixer output noise at low IF frequencies, 45 K in our case, $T_J(0)$ the mixer Johnson Noise, which is approximately equal to $T_c = 9$ K [22], [21] and $T_{IF} = 10$ K the IF chain noise temperature. Thus we find $f_N/f_G = 1.7$ in good agreement with the measurements.

D. Stability

In the last experiment we have measured the stability of the mixer at the optimal bias point by means of a measurement of the Allan Variance [19]. In practice the noise from a receiver such as a HEB mixer appears to be a combination of three terms: 1/f noise, low frequency drift and uncorrelated (white) noise. To first order, only white noise can be integrated down, with the result that there is an optimum integration time, known as the "Allan" time (t_A), after which the observing efficiency is lost. Experimentally a measurement of the "Allan Variance", defined as $\sigma^2_A(t) = \frac{1}{2}\sigma^2(t)$ is a powerful tool to discriminate between the various noise terms in a real receiver. Plotting $\sigma^2_A(t)$ on a log-log plot demonstrates the usefulness of this approach in analyzing the noise statistics. The minimum in the plot gives the "Allan" time. For the sake of optimum integration efficiency, one is advised to keep the integration time well below the system's Allan time at a level where the noise still closely follows the white noise behavior. In the experiment we have changed the IF chain of the setup as depicted in Fig. 2 slightly. We have added, after the first room temperature amplifier, a 3 dB splitter. After the splitter we use in each channel a Yig filter with a 50 MHz bandwidth, a room temperature amplifier and, in one of the channels, a tunable attenuator. A dual frequency power head is then used to measure the power output as a function of time $P(t')$ for two IF channels simultaneously at a rate of 40 times per second. This has been done for IF frequencies very close to each other at the low end of the IF band (2.5 GHz and 2.7 GHz), and for two frequencies near the IF band edges (2.5 GHz and 4.7 GHz). The attenuator allows us to keep the powers in each channel about identical which is important to maintain an equal effective bandwidth in both channels. The reason for this is that the power meter is a wideband detector with the result that the ratio of in band signal power to the total power as seen by the detector will change the effective measurement bandwidth. For the same reason it is vital to use signal powers of the order of 0 dBm within the YIG filter bandwidth to ensure a measurement of the mixer properties in stead of a measurement of the noise statistics out of the YIG filter band. We show, In Fig. 8, the single

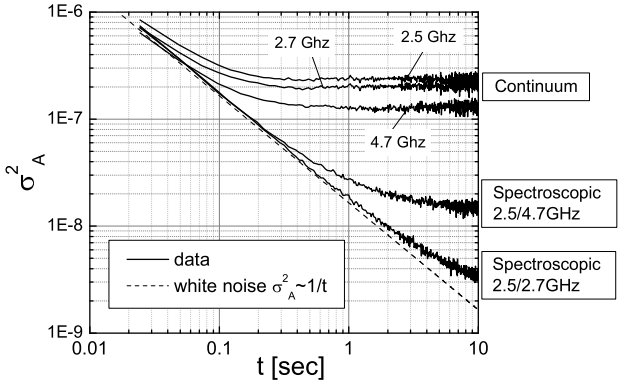

Fig. 8. Single channel Allan Variance at 1.4624 THz, obtained in a 50 MHz bandwidth around 2.5, 2.7 and 4.7 GHz together with the spectroscopic Allan Variance at 1.4624 THz as defined by Eqn. 2, between closely spaced (2.5-2.7 GHz) and far spaced (2.5-4.7 GHz) IF channels. The theoretical white noise behavior is included for comparison.

channel Allan Variance taken at the optimal bias point at 3 different IF frequencies, 2.5 GHz, 2.7 GHz and 4.5 GHz. In these measurements the mixer stability curves deviate from the white noise integration time at already 0.2 seconds. We also show in Fig. 8 the spectroscopic Allan Variance. This is the Allan variance of the quantity $s(t')$ given by

$$s(t') = \frac{x(t')}{< x(t') >} + \frac{y(t')}{< y(t') >} \quad (2)$$

with $x(t')$ and $y(t')$ the original measurements of the powers in each IF channel as a function of time t'. Note that the spectroscopic HEB receiver stability is considerably better than the one observed for a single channel observation, this implies that observing the spectral response of an astronomical source is less limited by the HEB stability than a single channel continuum observation. Note that the spectroscopic data between 2.6 and 4.5 GHz represents the stability within the full spectroscopic IF band of HIFI band 6. The spectroscopic Allan variance between the closer spaced 2.5 and 2.7 GHz is even better. Given that the mechanics of the measurement setup was very rigid, and the loss in air small (0.1 dB), it is likely that we are observing the effect of a frequency dependent hot electron bolometer mixer gain.

IV. CONCLUSIONS

The small volume twin slot antenna coupled HEB mixer is the detector of choice for a heterodyne observatory at frequencies above 1.3 THz. The low LO power need of 80 nW at the lens front makes it easily compatible with present day THz LO sources with an output power in the μW range up to frequencies of 2 THz. The sensitivity is comparable to the one of large volume devices, we measure 900 K at 1.4 THz and have obtained 700 K [23] for another device at 1.6 THz using an optimised optical coupling in the signal path. However, the bandwidth of the devices is limited to 2.3 GHz for the Gain and 4 GHz for the noise, limiting the IF band edge to about 4-5 GHz. Increasing the bandwidth with a similar performance would greatly enhance the practical usability of these mixers. The stability is also limited allowing integration times of the order of a few seconds, which is enough for a line survey in chopped mode, however, continues observations are likely impossible. As a last point we found that there is a direct detection effect due to the low LO power requirements and the large direct bandwidth of these devices. As a result the mixer sensitivity is underestimated by about 20%-30%, dependent on the optics transmission when evaluated using a 300 K hot load and 77 K cold load, furthermore, the optimal operating point is shifted to higher bias voltages due to this effect.

REFERENCES

[1] E.M. Gershenzon, G.N. Goltsman, I.G. Gogidze, A.I. Eliantev, B.S. Karasik and A.D. Semenov, *Millimeter and submillimeter range mixer based on electronic heating of superconducting films in the resistive state*, Sov. Phys. Supercondcutivity **3**, 1582 (1990).

[2] D.E. Prober, *Superconducting terahertz mixer using a transition edge microbolometer*, Appl. Phys. Lett. **62**, 2119 (1993).

[3] J.J.A. Baselmans, J.M. Hajenius, J.R. Gao, T.M. Klapwijk, P.A.J. de Korte, B. Voronov, G. Gol'tsman. *Doubling of sensitivity and bandwidth in phonon cooled hot electron bolometer mixers*, Appl. Phys. Lett. **84**, 1958 (2004).

[4] A.D. Semenov, H.-W. Hübers, J. Schubert, G. N. Gol′tsman, A.I. Elantiev, B.M. Voronov, E.M. Gershenzon, *Design and Performance of the lattice-cooled hot-electron terahertz mixer*, J. Appl. Phys. **88**, 6758 (2000).

[5] S. Cherednichenko, P. Khosropanah, E. Kollberg, M. Kroug, H. Merkel, *Terahertz superconducting hot-electron bolometer mixers*, Physica C **372-376**, 407 (2002).

[6] P. Yagoubov, M. Kroug, H. Merkel, E. Kollberg, G. Gol'tsman, S.Svechnikov and E. Gershenzon, *Noise temperature and local oscillator power requirement of NbN phonon cooled hot electron bolometric mixers at terahertz frequencies*, Appl. Phys. Lett. **73**, 2814 (1998).

[7] M. Hajenius, J. J. A. Baselmans, J. R. Gao, T. M. Klapwijk, P. A. J. de Korte, B. Voronov and G. Goltsman, *Low noise NbN superconducting hot electron bolometer mixers at 1.9 and 2.5 THz*, Supercond. Sci. Technol. **17**, S224S228 (2004)

[8] W.F.M., Ganzevles, L.R. Swart, J.R. Gao, PA.J. de Korte, and T.M. Klapwijk, *Direct response of twin-slot antenna-coupled hot-electron bolometer mixers designed for 2.5 THz radiation detection*, Appl. Phys. Lett., **76**, 3304 (2000).

[9] W. Jellema, T. Finn, A. Baryshev, M. van der Vorst, S. Withington, A. Murphy and W. Wild, *Phase-Sensitive Near-Field Measurements and Electromagnetic Simulations of a Double-Slot HEB Integrated Lens-Antenna Mixer at 1.1, 1.2 and 1.6 THz*, these proceedings (2005).

[10] G. Chattopadhyay, E. Schlecht, J. Ward, J. Gill, H. Javadi, F. Maiwald, and I. Mehdi, *An All Solid-State Broadband Frequency Multiplier Chain at 1500 GHz*, IEEE Transactions on Microwave Theory and Techniques, **52**, 5, 1538, (2004).

[11] A.R. Kerr, *Receiver noise temperature, the quantum noise limit, and the role of the zero-point fluctuations*, IEEE Trans on Microwave Theory and Techn. **47-3**, 325 (1999).

[12] Yu. B. Vachtomin. S.V. Antipov, S.N. Maslennikov, K.V. Smirnov, S.L Polyakov, N.S. Kaurova, E.V. Grishina, B.M. Voronov, G.N. Gol'tsman, *Noise temperature measurements of NbN phonon-cooled Hot Electron Bolometer mixer at 2.5 and 3.8 THz*, 15th Int. Symp. On Space THz. Techn., Northampton, Ma,(2004).

[13] S. Svechnokov, A. Verevkin, B. Voronov, E. Menschikov. E. Gershenzon, G. Gol'tsman, *Quasioptical phonon-cooled NbN hot-electron bolometer mixer at 0.5-1.1 THz*, 9th Int. Symp. On Space THz. Techn., 44, (1999).

[14] J. Kawamura, C.-Y. Edward Tong, R. Blundell, D. Cosmo Papa, T. R. Hunter, F, patt, G. Gol'tsman, E. Gershenzon, *Terahertz-frequency waveguide NbN hot-electron bolometer mixer*, IEEE trans. on Appl. Supercond. **11**, 952 (2001).

[15] J.J.A. Baselmans, A. Baryshev, S.F. Reker, M.Hajenius, J.R. Gao, T.M. Klapwijk, Yu. Vachtomin, S. Maslennikov, S. Antipov, B. Voronov, G. Gol'tsman. *Direct detection effect in small volume hot electron bolometer mixers*, Appl. Phys. Lett. **86**, 163503 (2005).

[16] H. Ekstrom, B.S, Karasik, E.L. Kollberg, K.S. Yngvesson, *Conversion Gain and Noise of Niobium Superconducting Hot-Electron-Mixers*, IEEE trans on Microwave Theory and Techn., **43**, (1995).

[17] D. Loudkov, C.-Y.E. Tong, K.G. Megerian, J.A. Stern, *Performance of the NbTiN Hot Electron Bolometer Mixer with AlN buffer layer at Terahertz Frequency Range*, IEEE trans. on Appl. Supercond. In press (2005).

[18] R. Barends, M. Hajenius, J.R. Gao, and T.M. Klapwijk, *Analysing the intrinsic resistive transition for modelling hot electron bolometer mixers*, these proceedings (2005).

[19] J.W. Kooi, G. Chattopadhyay, M. Thielman, T.G. Phillips, and R. Schieder, *Noise Stability of SIS receivers*, Int J. IR and MM Waves, **21 (5)**, (2000).

[20] J. W. Kooi, J. J. A. Baselmans, J. R. Gao, P. Dieleman, Z. Q. Yang, A. Baryshev, M. Hajenius, G. de Lange, and T. M. Klapwijk, *IF Impedance and Mixer Gain of Phonon Cooled Hot-Electron Bolometers and the Perrin-Vanneste/Nebosis Two Temperature Model*, these proceedings (2005).

[21] S. Cherednichenko, M. Kroug, P. Khosropanah, A. Adam, H. Merkel, E. Kollberg, D. Loudkov, B. Voronov, G. Gol'tsman, H. Richter, H.-W Hübers, *A beroadband terahertz heterodyne receiever with an NbN HEB mixer*, 13th Int. Symp. On Space THz. Techn., Harvard University, (2002).

[22] B.S. Karasik, A.I. Elantiev, *Noise temperature limit of a superconducting hot-electron bolometer mixer* , Appl. Phys. Lett **68**, 853 (1996).

[23] Z.Q. Yang, M. Hajenius, J. J. A. Baselmans, J.R. Gao, T.M. Klapwijk, B. Voronov, and G. Gol'tsman, *Improved sensitivity of NbN hot electron bolometer mixers by vacuum baking*, these proceedings (2005).

Direct Detection Effect in Hot Electron Bolometer Mixers

A. Baryshev, J.J.A. Baselmans, S.F. Reker
SRON National Institute for Space Research, Landleven 12, Postbus 800, 9700 AV Groningen, The Netherlands

M. Hajenius, J.R. Gao
SRON National Institute for Space Research, Sorbonnelaan 2, 3584 CA Utrecht, The Netherlands and *Kavli Institute of Nanoscience, Delft University of Technology, Lorentzweg 1, 2628 CJ Delft, The Netherlands*

T.M. Klapwijk
Kavli Institute of Nanoscience, Delft University of Technology, Lorentzweg 1, 2628 CJ Delft, The Netherlands

Yu. Vachtomin, S. Maslennikov, S. Antipov, B. Voronov, and G. Gol'tsman
Moscow State Pedagogical University, Moscow 1199992, Russia

Abstract

NbN phonon cooled hot electron bolometer (HEB) mixers are currently the most sensitive heterodyne detectors at frequencies above 1.2 THz. They combine a good sensitivity (8-15 times the quantum limit), an IF bandwidth of the order of 4-6 GHz and a wide RF bandwidth from 0.7-5.2 THz. However, for use in a space based observatory, such as Herschel, it is of vital importance that the Local Oscillator (LO) power requirement of the mixer is compatible with the low output power of present day THz LO sources. This can be achieved by reducing the mixer volume and critical current. However, the large RF bandwidth and low LO power requirement of such a mixer result in a direct detection effect, characterized by a change in the bias current of the HEB when changing the RF signal from a black body load at 300 K to one at 77 K. As a result the measured sensitivity using a 300 K and 77 K calibration load differs significantly from the small signal sensitivity relevant for astronomical observations. In this article we describe a set of dedicated experiments to characterize the direct detection effect for a small volume quasi-optical NbN phonon cooled HEB mixer.

We measure the direct detection effect in a small volume (0.15 μm · 1 μm · 3.5 nm) quasi-optical NbN phonon cooled HEB mixer at 1.6 THz. We found that the small signal sensitivity of the receiver is underestimated by approximately 35% due to the direct detection effect and that the optimal operating point is shifted to higher bias voltages when using calibration loads of 300 K and 77 K. Using a 200 GHz wide band-pass filter at the 4.2 K the direct detection effect virtually disappears. Heterodyne response measurements using water vapor absorption line in a gas cell confirms the existence and a magnitude of a direct detection effect. We also propose a theoretical explanation using uniform electron heating model.

This direct detection effect has important implications for the calibration procedure of these receivers in real telescope systems.

HEB Device Development for a Submillimeter Heterodyne Array Camera

M.O. Reese[*], D.F. Santavicca[*], A. Hedden[**], L. Frunzio[*],
D.E. Prober[*] and C. Walker[**]

We are developing Nb HEBs for a large-format, diffusion-cooled hot electron bolometer (HEB) array submillimeter camera. The goal is to produce a 64 pixel array together with the University of Arizona to be used on the HHT on Mt Graham. It is designed to detect in the 850 GHz atmospheric window. We have fabricated Nb HEBs using a new angle-deposition process, which had previously produced high quality Nb-Au bilayer HEB devices at Yale. [1] We have characterized these devices using heterodyne mixing at ~30 GHz to compare to 345 GHz tests at the University of Arizona. We can also directly compare our Nb HEB mixers to SIS mixers in this same 345 GHz system. This allows us to rigorously calibrate the system's losses and extract the mixer noise temperature in a well characterized mixer block, before undertaking the 850 GHz system. Here we give a report on the initial devices we have fabricated and characterized.

* Department of Applied Physics, Yale University
** Department of Astronomy, University of Arizona
[1] Applied Physics Letters 84, Number 8; p.1404-7, Feb 23 (2004)

IF Impedance and Mixer Gain of Phonon Cooled Hot-Electron Bolometers and the Perrin-Vanneste Two Temperature Model

J. W. Kooi[1], J. J. A. Baselmans[2], J. R. Gao[3], P. Dieleman[4], Z. Q. Yang[4], A. Baryshev[4], M. Hajenius[3], G. de Lange[4], and T. M. Klapwijk[3]

[1]California Institute of Technology,
MS 320-47 Pasadena, California 91125, USA.

[2]SRON National Institute for Space Research,
Sorbonnelaan 2, 3584 CA Utrecht, The Netherlands.

[3]Department of Nanoscience, Faculty of Applied Sciences, Delft University of Technology,
Lorentzweg 1, 2628 CJ Delft, The Netherlands.

[4]SRON National Institute for Space Research,
Landleven 12, 9747 AD Groningen The Netherlands.

Abstract—
We have measured the IF impedance and mixer gain bandwidth of a small area phonon cooled hot-electron bolometer in the 0.05-10 GHz range under a variety of bias and LO pumping level conditions. The device used is a twin slot antenna coupled NbN HEB mixer, with a bridge area of 1 μm x 0.15 μm, and a critical temperature of 8.3 K.

We model the HEB IF impedance following the work of Nebosis, Semenov, Gousev, and Renk, from now on refered to as the "NSGR" model. This model is based on the two-temperature model of Perrin-Vanneste, and is found to accurately describe the measured data at different bias and LO pump levels. Three fitting parameters are used in the NSGR model to describe the frequency dependent modulation of the electron temperature; the electron-phonon interaction time τ_{eph}, the phonon escape time (into the substrate) τ_{es}, and the ratio of the electron and phonon specific heat capacity c_e/c_{ph}. The described time constants and temperature dependent heat capacity ratio obtained from fitting the model to the measured data agrees well with those reported on for thin NbN films in literature.

Using an expression for mixer gain from the NSGR model, but modified to take additional parasitic loss and the complex voltage reflection between mixer and IF load impedance into account, we find when we use the impedance fit parameters τ_{eph}, τ_{es}, c_e/c_{ph}, an excellent agreement between measured and modeled HEB conversion gain.

Keywords— **IF Impedance, phonon cooled hot electron bolometer (pHEB), two-temperature model, "hot" electrons, Perrin-Vanneste, NSGR model, electron temperature modulation, electron-phonon interaction time, phonon escape time, electro-thermal feedback, complex impedance, HEB mixer conversion gain.**

I. Introduction

In the context of history, traditional InSb hot electron bolometers[1] mixers suffer from a small (<100 MHz) IF bandwidth, due to a relatively long electron relaxation time in the film. To enhance the science that may be done with these devices, there has in recent years been a strong push to expand the gain and noise bandwidth of hot electron bolometers. To a large extend success has been achieved with the use of ultra thin ($\approx$ 4-6nm) NbN films with very short phonon escape times. The majority of such films have been supplied by the Moscow Pedagogical State University [2][3]. In fact the band 6 mixers on the HIFI instrument of ESA's Herschel's FIR satellite are all comprised of phonon cooled HEB's with a specified IF bandwidth of 2.4 - 4.8 GHz [4][5]. As the IF bandwidth exceeds several GHz however, a proper knowledge of the IF behavior of thin film hot electron bolometers, and the effect of electrothermal feedback on the mixer gain is required. Some work on understanding the IF impedance and gain bandwidth has been done by Morales *et.al* [6], however this work is based on large area phonon-cooled hot electron bolometers (1μm x 4μm), and uses a theory developed for diffusion HEB's [7] to fit the IF impedance mixer conversion gain data. Recent trends however have been to reduce the phonon cooled HEB active area by factors of 16 or more, in an effort to accommodate terahertz solid state multipliers (reducing the HEB area reduces the required LO pump power level). These sub-micron area NbN devices are considerably different than those studied by Morales *et.al*, and hence the renewed interest.

In this paper we use a two temperature model introduced by Perrin-Vanneste[8] and expanded upon by Nebosis, Semenov, Gousev, and Renk [9], to describe the phonon cooled HEB IF impedance and mixer gain. The NSGR impedance model includes an electro-thermal feedback mechanism which effects the mixer's non-linear hot spot region by means of complex voltage reflections at the mixer output port. This feedback mechanism is seen to modulate the mixer conversion gain as a function of IF frequency, resulting in some of the observed wiggles and fluctuations in the receiver noise temperature. The inhomogeneous "hot spot", hypothesized to govern the mixing process in hot electron bolometers, is located in the superconducting film that is in contact with the normal metal (Au) contacts pads. This hot spot region is created by the

application of bias, LO power, and modulated in a nonlinear fashion by incident (RF) radiation. In practice HEB mixers are thus operated at elevated and time dependent electron temperatures, near the critical temperature of the material. We use this information to constrain the fit parameters τ_{eph}, τ_{esc} and c_e/c_{ph} in the NSGR impedance model, as there appears to be not one single unique solution. With the obtained fit values we proceed to calculate the complex IF impedance and mixer gain, inclusive of the discussed electro-thermal feedback, and are able to successfully compared it to actual measurement.

II. Theory

If a hot electron bolometer is exposed to incoming RF radiation (or dc bias) in the form: $P_o[1 + cos(\omega t)]$, then this energy is absorbed by raising electrons in the superconducting film to a higher temperature. The primary cooling mechanism of these "hot" electrons occurs via phonon interaction, with a time constant equal to τ_{eph}. In turn the phonons escape into the substrate with an escape time τ_{esc} , though some may diffuse out of the metal contact pads. In general it has been found that the heat capacities of the electrons and phonons is quite temperature dependent. Following the two temperature analyses of Perrin-Vanneste[8] and the NSGR model[9], where the electron and phonon cooling rates and their respective heat capacities in a superconducting HEB mixer are treated as arbitrary, we find the following heat balanced equations for a linearized ($|T_e - T_0| \ll T_0$) system:

$$c_e \frac{\partial T_e}{\partial t} = P_{dc} + \alpha P_{lo} e^{i\omega t} - \frac{c_e}{\tau_{eph}}(T_e - T_{ph}) \qquad (1)$$

$$c_{ph} \frac{\partial T_{ph}}{\partial t} = \frac{c_e}{\tau_{eph}}(T_e - T_p h) - \frac{c_p}{\tau_{esc}}(T_{ph} - T_0) \qquad (2)$$

c_e and c_{ph} are the electron and phonon heat capacity, α the LO coupling coefficient which is typically 5-10%, and T_e, T_{ph}, T_0 the respective electron, phonon and bath temperatures. Diffusion thru the contact pads is neglected. Following the NSGR analyses, the frequency dependent IF mixer impedance may be solved as:

$$Z = \frac{d}{dI}[I \cdot R(I, T_e)] = R(I, T_e) + I\frac{\partial R}{\partial I} + I\frac{\partial R}{\partial T_e}\frac{\partial T_e}{\partial I} \ , \quad (3)$$

with the film resistance $R(I, T_e)$ obtained from work by Elant'ev [10], and T_c the critical temperature of the superconductor. Here

$$R(I, T_e) \approx \frac{Rn(T_e)}{2}\left(1 + \zeta(T_e) - \frac{[1 - \zeta(T_e)]^3}{[1 + I/I_o - \zeta(T_e)]^2}\right) , \qquad (4)$$

with

$$\zeta(T_e) = \frac{1}{1 + e^{\frac{4(T_c - T_e)}{\Delta T_c}}} \ . \qquad (5)$$

$Z(\omega)$, the frequency dependent HEB output impedance, may be found by assuming that a small perturbation in the current, $dI = \delta I e^{i\omega t}$, causes a change in the electron temperature $dT_e = \delta T_e e^{(i\omega t + \varphi 1)}$, and phonon temperature $dT_{ph} = \delta T_{ph} e^{(i\omega t + \varphi 2)}$. These partials may then substituted in the linear heat balance Eqn's 1, 2 to give:

$$Z(\omega) = R_o \cdot \frac{\Psi(\omega) + C}{\Psi(\omega) - C} \ , \qquad (6)$$

where $\Psi(\omega)$ represents a frequency dependent modulation of the electron temperature, ω the IF frequency, R_o the DC resistance at the bias point of the mixer, and C the self heating parameter[13][14]. The latter is important as it forces the complex part of the impedance (Eqn. 6) to be zero at very low and very high IF frequencies. $\Psi(\omega)$ is defined as

$$\Psi(\omega) = \frac{(1 + i\omega\tau_1)(1 + i\omega\tau_2)}{(1 + i\omega\tau_3)}, \qquad (7)$$

and the self heating parameter

$$C = \frac{I^2}{V}\frac{\partial R}{\partial T_e}\left(\frac{\tau_{eph}}{c_e} + \frac{\tau_{esc}}{c_{ph}}\right) \ = \ \frac{dV/dI \ - \ R_o}{dV/dI \ + \ R_o} \ . \qquad (8)$$

In the transfer function $\Psi(\omega)$; τ_1, τ_2, τ_3 maybe solved as:

$$\tau_1^{-1}, \tau_2^{-1} = \frac{\Omega}{2}\left(1 \mp \sqrt{1 - \frac{4{\tau_{eph}}^{-1}{\tau_{esc}}^{-1}}{\Omega^2}}\right) \ , \qquad (9)$$

with

$$\Omega = \left(1 + \frac{c_e}{c_{ph}}\right)\tau_{eph}^{-1} + \tau_{esc}^{-1} \ , \qquad (10)$$

and

$$\tau_3^{-1} = \frac{c_e}{c_{ph}}{\tau_{eph}}^{-1} + {\tau_{esc}}^{-1} \ . \qquad (11)$$

To derive an expression for the conversion gain of the mixer, we use standard formalism to obtain the (frequency selective) responsivity[11][12] of a bolometer. Included in the responsivity is a complex load impedance Z_l, which in any real system is connected across the output port of the bolometer, and the HEB output reflection coefficient Γ_{if}. In this manner electro-thermal feedback, due to (complex) voltage reflections between mixer and IF circuitry, may be taken into the account.

$$S(\omega) = \frac{dV_l}{dP} = \frac{\alpha}{I}\frac{Z_l}{R_o + Z_l}\ \frac{C}{(\Psi + \Gamma_{if}\ C)} \ , \quad \Gamma_{if} = \frac{R_o - Z_l}{R_o + Z_l}. \qquad (12)$$

Here α presents the (RF) coupling factor, and I the signal current thru the load (and device). Because the IF load impedance connected to the mixer is in general complex, it is important to use the complex responsivity, and not the absolute responsivity, $|S(\omega)|$, to reflect the true nature of the electro-thermal feedback on the conversion gain, $\eta(\omega)$. To find the (complex) conversion gain of the mixer, we use the standard expression;

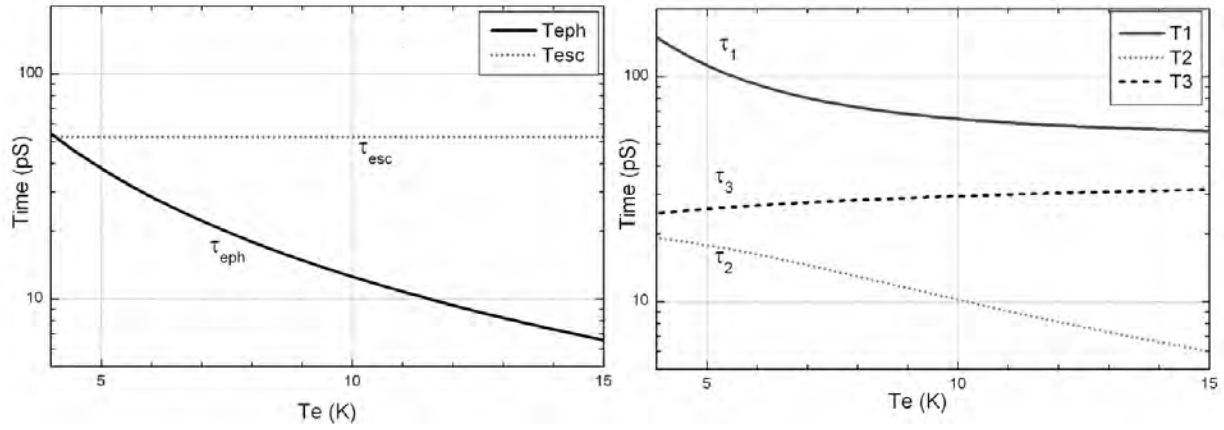

Fig. 1. Time constants and their temperature relationship as described it the text. Values for τ_{eph}, τ_{esc}, and the heat capacity ratio c_e/c_{ph} (not shown) have been obtained from literature. In the plot a 5nm thick NbN film is assumed. Values for τ_1, τ_2, τ_3 are derived from Eqn's [9-11], and serve to constrain the impedance model (Secion VI). Fit values obtained for τ_{eph}, τ_{esc}, and c_e/c_{ph}, for different HEB bias and LO pump conditions, are presented in Table I.

$$\eta(\omega) = \frac{2S(\omega)^2}{Z_l} P_{lo} \ . \tag{13}$$

After substitution of Eqn. 12, and making the assumption that most of the signal current thru the device is in fact DC bias current, i.e. P_{dc}=$I^2 \cdot R_o$ we find after some algebraic manipulation the magnitude of the conversion gain as

$$\eta(\omega) = \frac{2\alpha^2 P_{lo}}{P_{dc}} \left| \frac{R_o Z_l}{(R_o + Z_L)^2} \frac{C^2}{[\Psi(\omega) + \Gamma_{if}\ C]^2} \right| . \tag{14}$$

To obtain a better understanding of the range of plausible values for τ_{eph}, τ_{esc}, and c_e/c_{ph}, and to constrain the fit parameters to our data set, we resort to values used in literature. For the electron-phonon interaction time, we used an empirical relation $\tau_{eph} \approx 500T^{-1.6}$ [12]. Similarly, the phonon-escape time has been noted [19] [20] [5] to follow the relationship $\tau_{esc} \approx 10.5\ d$ (ps/nm), where d equals the NbN film thickness. Finally, taken from [20] [5], the ratio of the electron to phonon heat capacity is seen to be approximately 18.77 T_e/T_{ph} [3]. When the electron temperature is similar to the phonon temperature, i.e. $T_e \sim T_{ph}$, as is ordinarily the case under optimal bias conditions, then the ratio of c_e/c_{ph} follows a T^{-2} dependence. These quantities are plotted in Fig. 1 for a 5 nm NbN superconducting film.

III. experiment and Calibration

In Fig. 2 we describe the setup and calibration of the experiment. A twin-slot NbN HEB mixer chip (M12T-F2) with a bridge area of 1 μm x 0.15 μm is glued to the back of a silicon lens. The twin-slot antenna is positioned at the second foci of the ellipse, and produces an essentially diffraction limited beam with an f/D ratio of $\approx$ 20. The co-planar wave HEB IF output connects, via a number of parallel wire bonds, to a broad bandwidth (Baryshev, Kooi *et.al*) grounded CPW-to-microstrip transition and then via a 50 Ohm transmission line to a SMA bulkhead output connector. Details on the device's noise temperature, mixer gain as a function of bias, and R-T curve maybe found in a separate paper by Yang *et.al* [21].

To calculate the LO pumped HEB IF impedance we use the following procedure: First we measure the reflection coefficient at the mixer block SMA connector reference plane with a vector network analyzer. Included in this measurement is the bias Tee (not shown in Fig. 2. Next we use HFSS[26], a full 3D finite element electromagnetic field simulator, to obtain a 2 port S-parameter model of the IF circuitry, including wire bonds, via holes, and air space. And finally we use a linear circuit simulator [27] to de-embed the IF circuit from the measured complex input reflection coefficient, and use it to fit the two-electron temperature NSGR IF impedance model (Eqn. 6). This procedure provides the fit parameters that determine the HEB frequency selective IF impedance and mixer gain: τ_{eph}, τ_{es}, and c_e/c_{ph}.

Actual network analyzer calibration was done at room temperature. To correct for thermal contraction and increased conductivity of the coax cable intern to the cryostat upon cooling, we did a reflection measurement at 77K and at LHe temperature with the HEB biased at 20mV. At this bias voltage the device impedance maybe expected to be purely real. We did attempt to bias, and calibrate at 0mV, however instability in the HEB prevented a proper measurement. The resultant calibrations at room temperature, 77K and 4.5 Kelvin are shown in Fig.'s 3 and 4. Modeled vs. measured calibration is very good up to about 8 GHz, after which some discrepancy develops. This is most likely due to the way the SMA connector is mounted to the pc board/mixer unit. In the fits, the frequency range below 8 GHz has been weighted extra heavily for this reason.

IV. IF Impedance

In Fig.'s 5-9 we present the de-embedded and modeled IF impedance of the HEB. The IF impedance of the device has been obtained at a number of carefully chosen bias and LO pumping levels, as demonstrated in Fig. 5a.

To model the IF impedance we use equations 6-11. Parameters used to fit the impedance model are the electron-

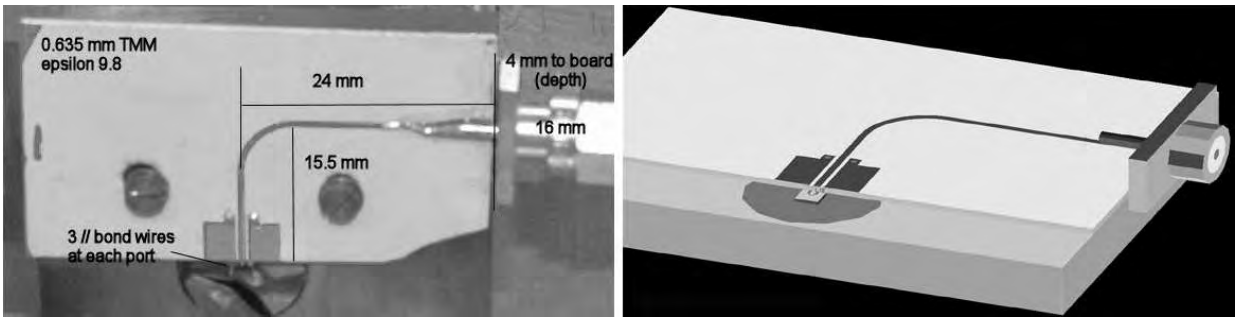

Fig. 2. Left: Quasi optical mixer block with a broad bandwidth grounded cpw to microstrip transition. The mixer block was designed to measure HEB gain and noise bandwidth to $\sim$ 10 GHz. Right: HFSS 3D model. Dielectric material was Rogers, Tmm 10i (Er=9.8) with a board thickness of 635 μm. Wire bond, air space, via holes, electrical conductivity have all been taken into account.

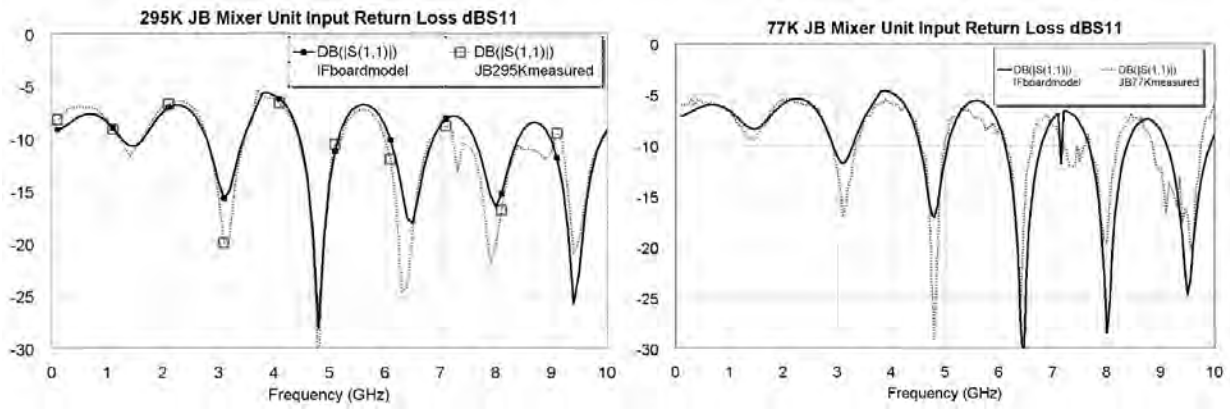

Fig. 3. Left: Calibration at room temperature. Shown is the measured (dotted), and modeled (black) input return loss at the SMA mixer block output flange. Data in all cases was taken at a power level of -65 dBm, with no effect on the pumped I/V curve. 64 averaged traces were obtained to integrate down the noise. Right: Quality of the calibration correction at 77K. Here we used the measured DC impedance (R_o) of the HEB to calibrate for thermal contraction (4.37mm) and reduction in (frequency dependent) loss of the coaxial cable connected to the mixer unit. At 77K the HEB impedance was reduced by $\approx$ 3-4% from room temperature which is attributed to the reduction in Ohmic loss in the Au wiring of the HEB mixing chip. Vertical scale is in units of dB.

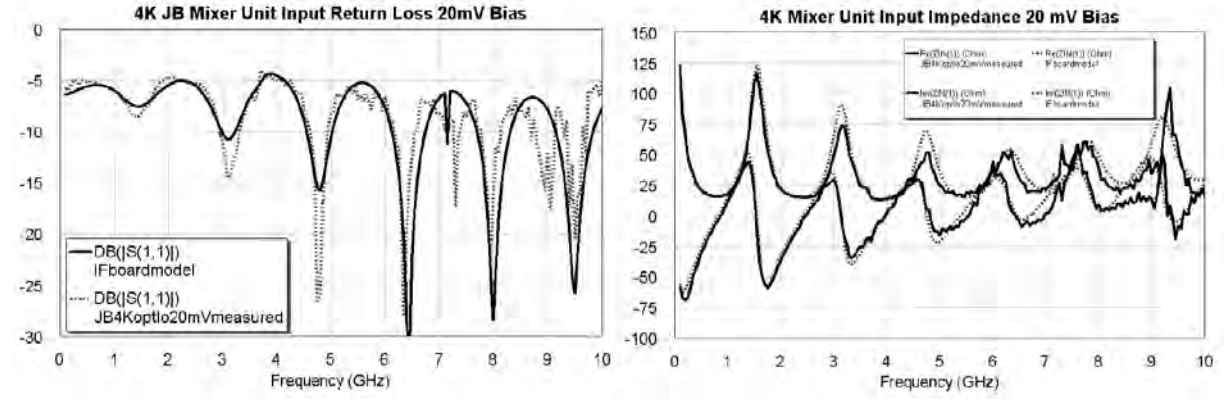

Fig. 4. Left: Measured (dotted) vs modeled (black) input return loss at the SMA flange. Right: Measured (black) vs modeled (dotted) input impedance at the SMA flange. In both cases, the mixer unit was at 4.5 Kelvin, with the HEB biased at 20 mV. Vertical scale is in units of dB.

phonon interaction time τ_{eph}, the phonon escape time τ_{es}, and the ratio of the electron and phonon specific heat capacity c_e/c_{ph}. Particularly in the underpumped LO case, the HEB IF impedance demonstrates quite a large real and reactive component. For bias voltages $>$ 2mV, the situation reverses and the reactive part $\rightarrow$ zero.

Because there is no uniqe solution to the best fit values of τ_{eph}, τ_{esc}, and c_e/c_{ph}, we use literature to provide appropriate boundary conditions (Fig. 1, Section II). The results in Table I provide for some interesting statistics on the material properties of the NbN film, and assumptions of the temperature dependence of τ_{eph}, and c_e/c_{ph} used in literature. For example, the mean escape time for the phonon's into the substrate is 62.2 $\pm$ 4.8 pS. Using the empirical re-

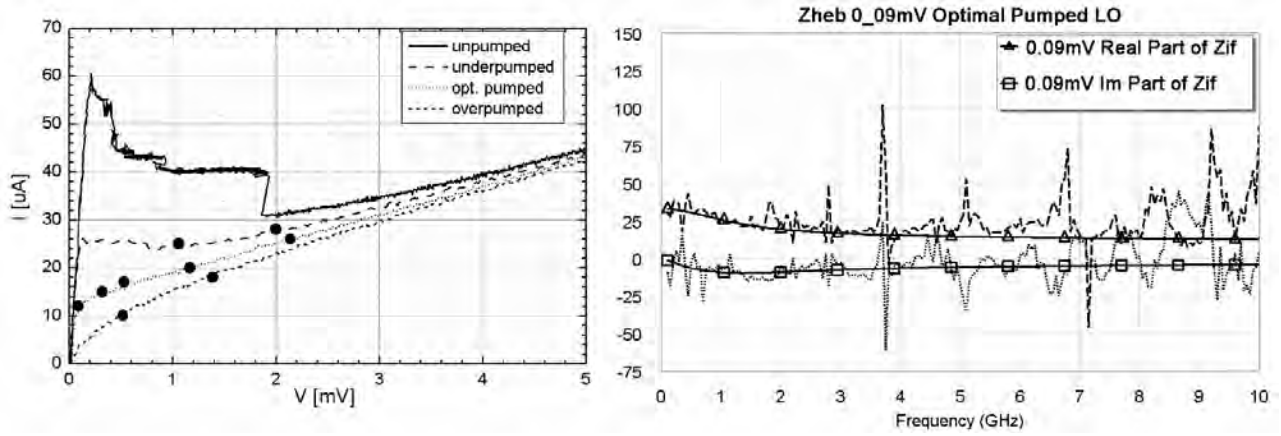

Fig. 5. Left: Unpumped, Under, Optimal, and Over pumped I/V curves. Circles indicate HEB reflection measurements bias points. Right: 0.09 mV (de-embed and modeled) HEB IF impedance at optimal pumped LO. τ_{eph}=12.1 pS, c_e/c_{ph}=0.166, and $< T_e >$= 10.45 K. Vertical scale is in Ohm.

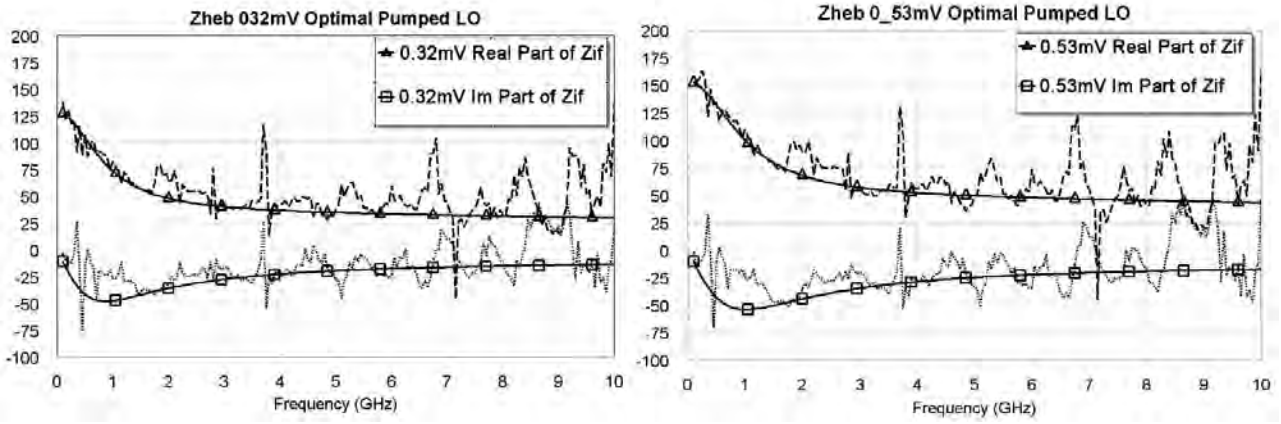

Fig. 6. Left: 0.32 mV (de-embed and modeled) HEB IF impedance, optimal pumped LO. τ_{eph}=11.4 pS, c_e/c_{ph}=0.161, and $< T_e >$= 10.73 K. Right: 0.53 mV HEB IF impedance, optimal pumped LO, τ_{eph}=10.4 pS, c_e/c_{ph}=0.167, and $< T_e >$= 10.95 K.

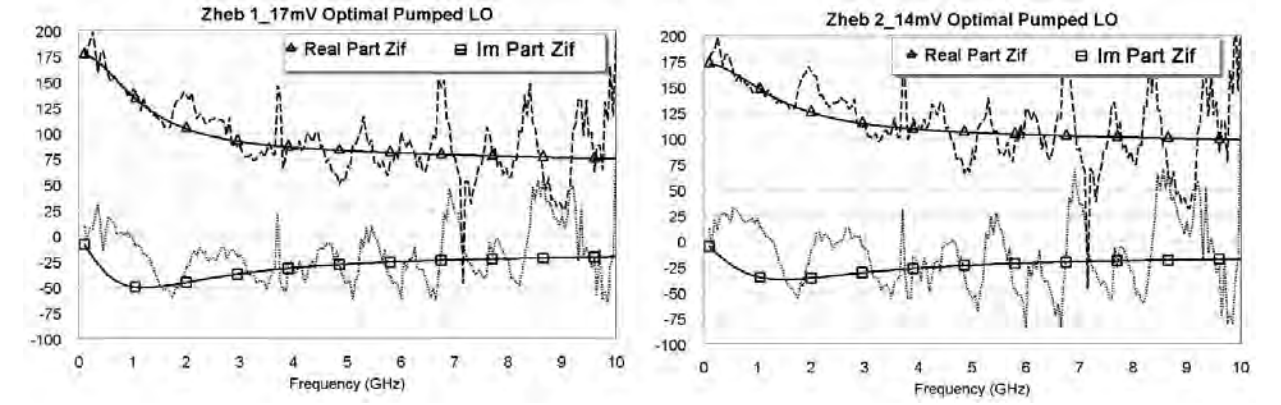

Fig. 7. Left: 1.17 mV HEB IF impedance, optimal pumped LO. τ_{eph}=10.0 pS, c_e/c_{ph}=0.163, and $< T_e >$= 11.15 K. Right: 2.14 mV HEB IF impedance, optimal pumped LO. τ_{eph}=8.82 pS, c_e/c_{ph}=0.167, and $< T_e >$= 11.55 K.

lationship that $\tau_{esc} \approx 10.5\ d$ (pS/nm), we find a suggestive NbN film thickness of 5.9 ± 0.44 nm. This is supported by a recent study of the film by Transmission Electron Microscopy (TEM), in which the thickness seems to be around 5 nm instead of the intended thickness of 3.5 nm [22]. Secondly, the temperature relationship of the electron-phonon interaction time, and the ratio of the electron-phonon heat capacities may, to a first order, be verified. Using the empirical relationships (Section II) that for thin NbN films, $\tau_{eph} \approx 500\ T^{-1.6}$ (pS·K) and $c_e/c_{ph} \approx 18.77\ T^{-2}$, we obtain an estimate for the mean (or effective) electron temperature in the NbN bridge. The last two colums in Table I show the calculated results. The mean electron temperature, $< T_e > \ = \ < T_e(eph) + T_e(c_e/c_{ph}) >$ is reported

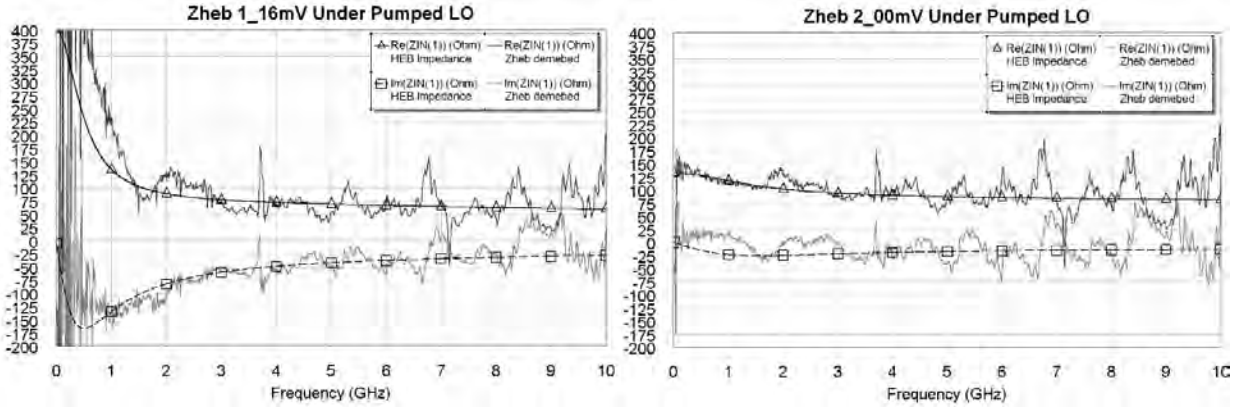

Fig. 8. Left: 1.06 mV HEB IF impedance, under pumped LO. τ_{eph}=14.9 pS, c_e/c_{ph}=0.213, and $< T_e >$= 9.21 K. Right: 2.00 mV HEB IF impedance, under pumped LO. τ_{eph}=12.9 pS, c_e/c_{ph}=0.210, and $< T_e >$= 9.67 K.

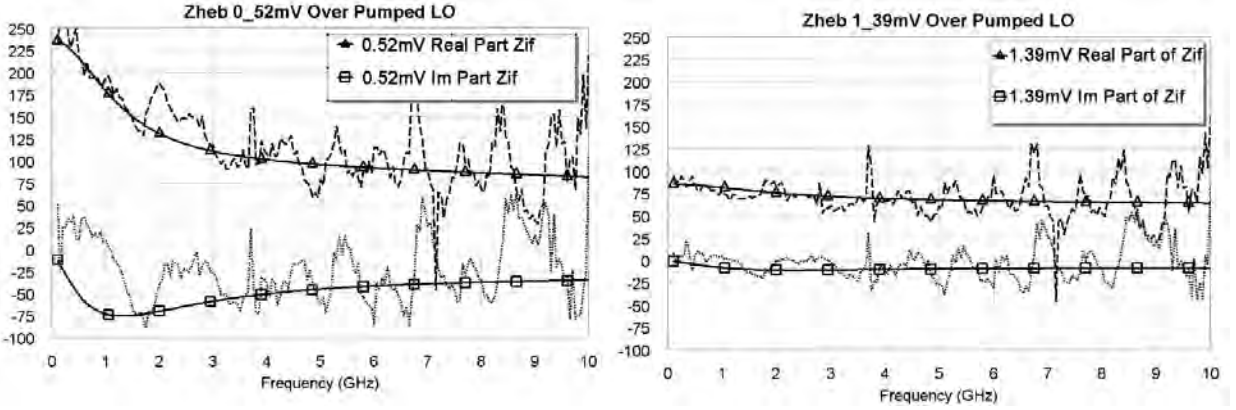

Fig. 9. Left: 0.52 mV HEB IF impedance, over pumped LO. τ_{eph}=7.99 pS, c_e/c_{ph}=0.094, and $< T_e >$= 13.7 K. Right: 1.29 mV HEB IF impedance, over pumped LO. τ_{eph}=7.04 pS, c_e/c_{ph}=0.088, and $< T_e >$= 14.46 K. Details on Fig.'s 5 - 9 may be found in Table I below. Vertical scales are in Ohm.

TABLE I

HEB Parameters for different bias Conditions.

Units of dV/dI, R_o, $R_o{}^*$ are in Ω, τ_{esc} and τ_{eph} in pS, $T_e(eph)$ and $T_e(c_e/c_{ph})$ in Kelvin, and ν_{-3dB} in GHz.

Vbias	dV/dI	R_o	$R_o{}^*$	C	C^*	τ_{esc}	τ_{eph}	c_e/c_{ph}	$T_e(eph)$	$T_e(c_e/c_{ph})$	ν_{-3dB}
0.09mV Opt	42	7.5	9.5	0.697	0.551	56.5	12.1	0.166	10.24	10.67	1.842
0.32mV Opt	110	21.3	21.3	0.675	0.715	58.8	11.4	0.161	10.62	10.84	2.122
0.53mV Opt	167	31.2	31.2	0.685	0.662	57.5	10.4	0.167	11.25	10.65	2.551
1.17mV Opt	168	58.5	58.5	0.483	0.504	67.6	10.0	0.163	11.53	10.77	2.981
2.14mV Opt	169	82.3	82.3	0.345	0.355	67.6	8.82	0.167	12.47	10.64	3.020
20.0mV Opt	150	140	140	0.034	0.033	—	—	—	—	—	—-
1.06mV Under	600	42.4	47.4	0.868	0.788	68.2	14.9	0.213	8.99	9.42	2.426
2.00mV Under	230	71.4	71.4	0.526	0.300	65.2	12.9	0.210	9.83	9.51	2.797
0.52mV Over	80	52.0	52.0	0.212	0.639	58.2	7.99	0.094	13.27	14.18	4.081
1.39mV Over	127	77.2	52.2	0.243	0.240	60.4	7.04	0.088	14.36	14.66	3.727

$T_e(eph)$ is the effective electron temperature based on the fitted electron-phonon interaction time, τ_{eph}, and temperature relationship obtained from literature. $T_e(c_e/c_{ph})$ is electron temperature based on the, from literature obtained temperature, relationship of electron and phonon heat capacity. $R_o{}^*$ and C^* area actual values used in the model fit. Note that for the Under and Over pumped I/V curves there appears some discrepancy between model and measurement. ν_{-3dB} is the calculated -3dB HEB mixer gain roll-off frequency based on $\Psi(\omega)$ and τ_p.

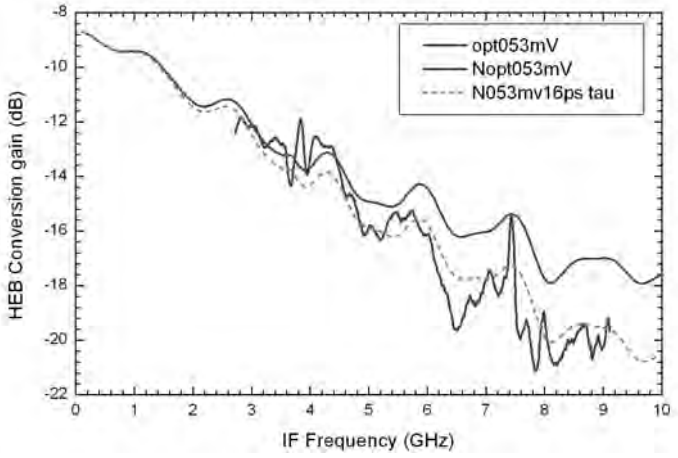

Fig. 10. Measured and modeled HEB mixer conversion gain as a function of IF frequency for optimal LO, and 0.53 mV bias. Input parameters to the model are: τ_{eph}=10.4 pS, τ_{esc}=57.5 pS, c_e/c_{ph}=0.167, and T_e = 10.95 K. The effect of electro-thermal feedback is taken into account by means of the (modeled) complex IF load impedance. The dotted curve indicates the mixer gain when Eqn. 14 is modified with an additional at 10 GHz pole ($\tau = 15.8\ pS$), see text for details.

in figures 5-9, and shows a consistent trend with bias and LO pump level [23].

V. Mixer Conversion Gain and the Effect of Electro-thermal Feedback

To properly model the HEB mixer conversion gain, the effect of voltage reflection modulations of the hot electron temperature, and subsequent mixing efficiency ($\partial R/\partial T$) needs to be taken into account. Because, as part of the de-embedding exercise, an accurate 3D EM model[26] of the IF embedding circuitry was developed (Fig. 2),

we can use this model to accurately predict the IF impedance presented to the HEB mixer IF output port. The model includes discontinuities such as the wire bonds that typically connect the IF board to the HEB output port. With this information we are able to calculate Γ_{if} and $[R_o \cdot Z_l/(R_o + R_l)^2]$ in Eqn. 14. It has been observed that the addition of a 10 GHz ($\tau = 15.8\ pS$) pole to Eqn. 14 helps to improve the accuracy of the modeled conversion gain. At low IF frequencies where the vast majority, if not all, of the HEB's operate the addition of an added pole to $\eta(\omega)$ is of little consequence. As to the cause of the additional high frequency pole, it is most likely the result of unaccounted for parasitic reactances in the HEB mixer stripline circuitry, Ohmic contact pads, and wirebonds that contact the HEB chip. Since parasitic reactances have not been taken into account in the "idealized" responsivity formulism of Eqn. 12, it may be advisable to include them. The HEB mixer gain modified for device parasitics may thus be rewritten as

$$\eta(\omega) = \frac{2\alpha^2 P_{lo}}{P_{dc}} \left| \frac{R_o Z_l}{(1+i\omega\tau_p)^2(R_o+Z_L)^2} \frac{C^2}{[\Psi(\omega)+\Gamma_{if}\ C]^2} \right|, \quad (15)$$

where $\tau_p \approx 15.8$ pS. Note that τ_p will be device and application dependent.

Several additional observations may be made. First, to minimize receiver noise temperature modulation across the IF operating bandwidth, one has to carefully consider ways to 1) minimize the complex part of Z_l such that Γ_{if} is frequency independent and 2) have $Z_l \approx R_o$ such that $\Gamma_{if} \rightarrow 0$. Secondly, to extend the HEB mixer IF bandwidth, the time dependent response of the electron temperature, $\Psi(\omega)$, needs to be increased. As discussed by Gao *et.al* [24], the most effective way to do so is to use films with higher T_c. The physical reason for the increase in IF bandwidth with higher T_c films is that at a higher T_c, or higher electron and phonon temperature, the phonon specific heat (c_{ph}) increases much faster than the electron cpecific heat (c_e). In this way the phonons can act as an important intermediate heat bath between the electron gas and the substrate. Of course, if we can reduce the thickness and thereby τ_{esc}, it too will enlarge the IF bandwidth.

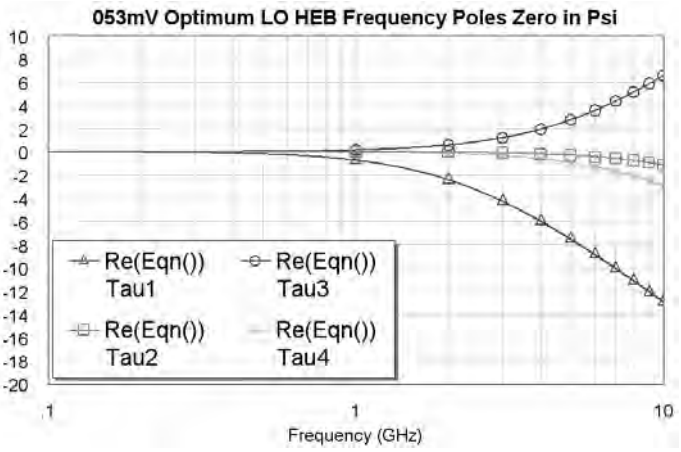

Fig. 11. $\Psi(\omega)$, the frequency dependent transfer function of the electron temperature at 0.53mV bias and optimal LO pumping level. τ_1 = 68.79 pS, which results in a pole at 2.313 GHz. τ_2 = 8.69 pS with a pole at 18.3 GHz, and τ_3 = 29.9 pS with a zero at 5.32 GHz. Included in the plot is τ_p due to unaccounted for device parasitics (see text). The three poles and zero effectively synthesize a "single pole" with ν_{-3dB} listed in Table I. To increase the frequency response of the system ν_{-3dB} will need to be increased. Refer to text for details.

This concept is illustrated in Fig. 11, where we plot the time dependent transfer function, $\Psi(\omega)$, of the electron temperature at 0.53mV bias and optimal LO pump level. τ_3 (5.32 GHz) is seen to slightly compensate τ_1 (2.31 GHz), whereas τ_2 (18.3 GHz) enhances the effect of τ_1, though to a very small extend. Adding a third pole (τ_p) to take into account residual device parasitics, we effectively synthesize a "single pole" mixer gain transfer function governed by $\Psi(\omega)$ and tau_p. This is depicted by ν_{-3db} in Table I. At 0.53 mV the synthesized "single pole" corresponds to a -3 dB roll-off frequency of 2.551 GHz, in a good agreement with measurements by Baselmans *et.al* [25].

VI. Conclusion

A novel de-embedding technique has been demonstrated to obtain the IF impedance of a small area (0.15 μm^2) phonon cooled HEB under a variety of bias and LO pump level conditions. In the same setup the HEB mixer conversion gain has, at an LO frequency of 1.3 THz, been measured in a 2.5-9 GHz IF bandwidth. To understand the observations, we have successfully modeled the HEB IF impedance and conversion gain based on a two-temperature electron cooling model first introduced by Perrin-Vanneste, and expanded upon by Nebosis, Semenov, Gousev, and Renk *et.al*. Good agreement between model and theory is obtained, and we are able to extract from the NSGR model (using published temperature and thickness relationships) values for the electron-phonon interaction time τ_{eph}, the phonon escape time τ_{esc}, the ratio of the electron and phonon specific heat capacity c_e/c_{ph}, and effective electron temperature of the NbN bridge as a function of bias and LO pump level. From these relationships, the NbN film thickness may be infered to be 5.9 $\pm$ 0.44 nm.

The mean electron temperature is indirectly calculated to vary, in the case of an optimal LO pumped HEB from 10.5-11.6 K, in the case of an under pumped HEB from 9.2-9.6 K, and in the case of an over pumped HEB mixer from 13.7-14.5 K. In addition, the presented analyses allows us to calculate the effective -3 dB mixer gain as a function of bias and LO pumping level. As an example, at 0.53 mV the -3dB mixer roll-off is observed to be 2.551 GHz, in good agreement with measurement. To extend the HEB IF response to higher frequencies, it can be seen from Eqn. 9-11 that either τ_{eph} and/or τ_{esc} ought to be reduced. This may in practice be accomplished with the use of a higher T_c superconducting material, thinner film, or both.
By using the complex IF impedance presented to the HEB chip we are able to demonstrate, for the first time, the effect of electro-thermal feedback on the mixer gain. Flat mixer gain (receiver noise temperature) within IF band may only be achieved if the variance of the complex load impedance presented to the HEB is small compared to the HEB DC resistance at it's operating point. Finally, using the NSGR model with the presented values for τ_{eph}, τ_{esc}, c_e/c_{ph} and a measured (LO pumped) I/V curve, expressions for $Z(\omega)$ and $\eta(\omega)$ for thin NbN films may now be derived.

VII. Acknowledgements

We wish to thank Willem Jellema, Wolfgang Wild, Thijs de Graauw, and Tom Phillips for their support. This work was supported in part by NSF Grant# AST-0229008

References

[1] T.G. Phillips and K.B. Jefferts, "A Cryogenic Bolometer Heterodyne Receiver for Millimeter Wave Astronomy", "*Review of Sci. Instrumentation,* Vol 44, 1009, 1973.

[2] P. Yagoubov, G. Gol'tsman, B. Voronov, L. Seidman, V. Siomash, S. Cherednichenko, and E. Gershenzon, " " "*Proceedings 7th International Symposium on Space Terahertz technology, Charlottesville, VA, 1996, pp290-302.*

[3] H. Ekström and E. Kollberg "Gain and noise bandwidth of NbN hot-electron bolometric mixers" *Appl. Phys Letters,* 70 (24), 16 June 1997.

[4] J.J.A. Baselmans, J M.Hajenius, R. Gao, T.M. Klapwijk, P.A.J. de Korte,B. Voronov, G. Gol'tsman "Doubling of sensitivity and bandwidth in phonon cooled hot electron bolometer mixers" *Appl. Phys. Lett,* 84, 1958, 2004.

[5] S. Cherednichenko, P. Yagoubov, K. Il'in, G. Gol'tsman and E. Gershenzon, "Large bandwidth of NbN phonon cooled hot-electron bolometer mixers on sapphire substrates", *Proc. 8th Int. Symp. on Space Terahertz Technology,* Cambridge, MA, 245, 1997.

[6] F. Rodriques-Morales and K.S. Yngvesson, "Impedance and Bandwidth Characterization of NbN Hot Electron Bolometric Mixers", *14th International Symposium on Space Terahertz Technology,* UAz, 2003.

[7] B. Karasik and W. McGrath "Microwave transmission technique for accurate impedance characterization of superconducting bolometer mixers" IEEE Transactions on Applied Superconductivity, March 1998.

[8] N. Perrin and C. Vanneste, "Dynamic behavior of a superconductor under time dependent external excitation", *J. Physique.* 48, 1311 (1987).

[9] R. S. Nebosis, A. D. Semenov, Yu. P. Gousev, and K. F. Renk, "Rigorous Analyses of a Superconducting Hot-Electron Bolometer Mixer: Theory and Comparison with Experiment", *7th International Symposium on Space Terahertz Technology,* Charlottesville, March 1996.

[10] A. I. Elant'ev, and B. S. Karasik, *Sov. J. Low Temp. Physics,* Vol 15, pp 379, 1989.

[11] D. F. Fillipovic, S. S. Gearhart, and G. M. Rebeiz, *IEEE Transactions on Microwave Theory and Techniques,* Vol. 41, pp. 1738, 1993

[12] Yu. P. Gousev, G. N. Gol'tsman, A. D. Semenov, E. M. Gershenzon, R. S. Nebosis, M. A. Heusinger, and K. F. Renk, "Broadband ultra fast superconducting NbN detector for electromagnetic radiation", *J. Appl. Phys.* 75, 3695 (1994).

[13] H. Ekström, B. Karasik, E. Kollberg, and K. Yngvesson Conversion gain and noise of niobium superconducting hot-electron mixers, *IEEE trans Microwave Theory and Techniques,* Vol.43, pp. 938, 1995

[14] P. J. Burke, R. J. Schoelkopf, and D. E. Prober Mixing and Noise in diffusion and phonon cooled superconducting hot-electron bolometers *Journal of Applied Physics,* Vol 85, No. 3, Feb. 1999

[15] J.J.A. Baselmans, A. Baryshev, S.F. Reker, M. Hajenius, J.R. Gao, T.M. Klapwijk, Yu. Vachtomin, S. Maslennikov, S. Antipov, B. Voronov, and G. Gol'tsman Direct detection effect in small volume hot electron bolometer mixers, *submitted to Applied Physics Letters (2005).*

[16] A. Sergeev and V. Mitin, "Electron-phonon interaction in disordered conductors: Static and vibrating scattering potentials", *Phys. Rev B,* Vol 61, 6041 (2000).

[17] J. Rammer and A. Schmid, "Destruction of phase coherence by electron-phonon interactions in disordered conductors", *Phys. Rev. B,* Vol 34, 1352(1986).

[18] Y. Pellan, G. Dousselin, J. Pinel, and Y.U. Sohn, "Temperature and Magnetic Field Dependence of NbN Film Resistivity: 3D Weak Localization Effects", *J. Low Temp. Phys.,* Vol. 78, 63(1990).

[19] S.B. Kaplan, *J. Low Temp. Phys.* Vol. 37, 343(1979)

[20] A. D. Semenov, R. S. Nebosis, Yu. P. Gousev, M. A. Heusinger, and K. F. Renk, "Analysis of the nonequilibrium photoresponse of superconducting films to pulsed radiation by use of a two-temperature model", *Phys. Rev. B* Vol. 52, 581 (1995).

[21] Z. Q. Yang, J. J. A. Baselmans, J. R. Gao, T. M. Klapwijk, B. Voronov, and G. Gol'tsman, Improved sensitivity of NbN hot electron bolometer mixers by vacuum baking", "*Proceedings 16th International Symposium on Space Terahertz technology,* Chalmers University, Göteborg, Sweden, 2005.

[22] J.R. Gao, B. Voronov, and F.D. Tichelaar (unpublished)

[23] T. M. Klapwijk, R. Barends, J. R. Gao, M. Hajenius, and J. J. A. Baselmans, "Proc. of the SPIE, 5498: Millimeter and Submillimeter Detectors for Astronomy II," by J. Zmuidzinas, W. S. Holland, S. Withington, Editors, 23-25 June 2004, Glasgow, Scotland, UK, p. 129.

[24] J. R. Gao, J. J. A. Baselmans, M. Hajenius, T. M. Klapwijk, and P. A. J. de Korte, "Expected bandwidth-increase of superconducting hot electron bolometer mixers by operation at high electron temperatures", in preparation.

[25] J. J. A. Baselmans, J. W. Kooi, A. Baryshev, Z. Q. Yang, M. Ha-

jenius, J. R. Gao, T. M. Klapwijk, B. Voronov, and G. Gol'tsman, "Full characterization of small volume NbN HEB mixers for space applications", in preperation.
[26] Ansoft Corporation,Pittsburgh, PA 15219, USA
[27] Microwave office, Applied Wave Research Inc. El Segundo, CA 90245

IF Impedance Optimization of HEB's for Band 6 at the Herschel Space Observatory

Therese Berg, Sergey Cherednichenko, Jacob Kooi[1], Vladimir Drakinskiy, Erik Kollberg.

Chalmers University of Technology
Dept of Microtechnology and Nanoscience (MC2)
SE-412 96 Göteborg, Sweden
Telephone: +46 (0)31 772 5035
E-mail: therese.berg@mc2.chalmers.se

[1]California Institute of Technology
MS 320-47 Pasadena
California 91125, USA

The Herschel band 6 mixers have recently been assembled and tested together with the SRON prototype LNA IF amplifier. Experimentally we found that the circuit between the HEB mixer and the amplifier resulted in high peaks in the noise at certain IF frequencies and significant ripples in the noise over the entire IF band. Due to design constraints in the HIFI instrument, the IF signal is brought from the mixer unit to the LNA via an approximately 24 cm long semi-rigid coaxial cable without an isolator in between. It is therefore of great importance that the impedance match between the HEB chip and low noise amplifier is good.

In this paper we investigate influences of the HEB device impedance. Devices with different room temperature resistance and dV/dI at the bias point were tried. Also a new IF board was developed. It is designed to better match the HEB IF output impedance to the 50 Ω load at the mixer unit output connector. We will show noise temperature results using HEB's with different impedances operated at different bias points, measured with different LNA's and IF boards, see fig. 1. The results will be discussed in detail.

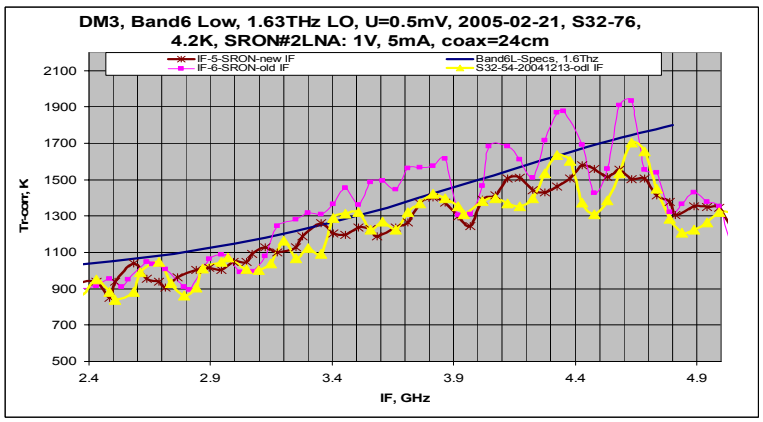

Figure 1 Noise temperature as a function of IF frequency for HEB device S32-76 with the old (squares) and the newly proposed IF board (stars). S32-54 with the old IF board is also shown (triangles).

The result from our investigation show that a well chosen bias point can improve the IF properties since it influences the impedance of the HEB. The IF board acts like a band pass limited transformer between the HEB and LNA, and as such also influences the IF performance of the mixer. For optimimal IF mixer performance, it is therefore important that the entire HEB - IF circuitry - LNA chain are considered in the design.

Session 10:

Schottky receivers

Wednesday May 4, 8:30-9:45
Chairman: Tony Kerr

A CAD Tool for the Design and Optimization of Schottky Diode Mixers up to Terahertz Frequencies

José V. Siles and Jesús Grajal
Dept. Señales, Sistemas y Radiocomunicaciones
E.T.S.I.T., Universidad Politécnica de Madrid
Ciudad Universitaria s/n, E-28040 Madrid, Spain
Email: {jovi, jesus}@gmr.ssr.upm.es
Telephone: +34 913367358
Fax: +34 913367362

Viktor Krozer
Orsted-DTU
Technical University of Denmark
Orsted Plads, building 348
DK-2800 Kgs. Lyngby, Denmark

Bruno Leone
European Space Agency
ESA/ESTEC
Keplerlaan, Noordwijk
The Netherlands

***Abstract*— Emerging applications at millimeter and submillimeter-wave spectral bands demand reliable CAD tools to be employed in the design of receivers up to Terahertz frequencies. In this paper we present a CAD tool for the design and optimization of Schottky diode frequency mixers at millimeter and submillimeter-wave spectral bands. This tool couples a diode physical numerical model with the circuit simulator using a multi-tone harmonic balance technique based on the *Almost Periodic Fourier Transform* (APFT). Contrary to approximate approaches, as matrix conversion techniques, no restrictions are considered regarding LO and RF pump powers. The mixer CAD tool allows a complete analysis of mixer circuits up to Thz frequencies taking into account both the external circuit and the Schottky diode structure.**

I. Introduction

Terahertz spectral bands are one of the least explored regions of the electromagnetic spectrum with applications in radio-astronomy, planetary science, security, medicine, etc. The necessity for Terahertz circuit development makes essential to have accurate simulation tools to be employed in the design and optimization of these circuits as a previous step to the fabrication process [1].

In this paper we present a novel CAD tool that couples a Schottky diode physical numerical model with a circuit simulator using appropriate harmonic-balance techniques (Fig. 1). This allows the concurrent design of circuits (mixers, detectors and multipliers) taking into account both the device structure (doping and length of the epitaxial layer, and area of the device) and the embedding circuit (bias, available power, and loads at different harmonics and intermodulation frequencies). A similar CAD for Schottky multipliers design was already presented in [2], [3], [4].

The Schottky diode model consists of a physics-based numerical device simulator which incorporates accurate boundary and interface conditions for self-consistent treatment of tunnelling transport, image-force effects, impact ionization, and non-constant recombination velocity. This physics-based simulator accounts for limiting mechanisms such as avalanche breakdown, velocity saturation, and increase in the series resistance with the input power.

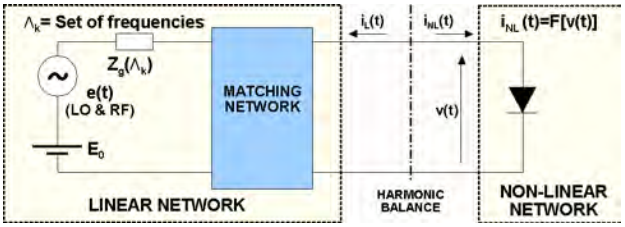

Fig. 1. Schematic of the analyzed circuit for mixers simulation.

Commercial programmes are based on approximate approaches, as conversion matrix techniques. Our general-purpose mixer CAD tool takes into account not only LO and RF harmonics but also their intermodulation products, with no restrictions regarding LO and RF pump powers. Thus, a complete mixer design and full optimization task can be performed with this tool up to Terahertz frequencies. All mixer parameters can be taken into account during the optimization (LO and RF power, impedances at every frequency, etc.).

Mixer analysis requires a proper selection of the time-frequency conversion technique if a general-purpose mixer simulator is required. Several techniques have been studied: Discrete Fourier Transform (DFT), Multidimensional Discrete Fourier Transform (MDFT) and Almost Periodic Fourier Transform (APFT). As a conclusion, APFT has been finally selected. It supports non-commensurable frequencies and can be applied to numerical models non-defined by algebraic equations (in contrast to MDFT).

II. Techniques for Multi-tone Harmonic Balance

There are different methods available for transforming signals between time and frequency domains that are suitable for use with multi-tone signals. The most important are:

- **FFT (*Fast Fourier Transform*):** Only applicable to mixer analysis when LO and RF frequencies are commensurable. In this case, a base frequency for the FFT can be selected as the great common divider of LO and RF.

- **MFFT (*Multidimensional Fast Fourier Transform*):** A generalization of the FFT to analyze circuits whose base frequencies are incommensurable. It is the most general algorithm with no additional assumptions to the ones assumed for the traditional harmonic balance for periodic signals, but it requires models described by algrebraic equations [5].
- **APFT *(Almost Periodic Fourier Transform):*** APFT is based on a generalization of the matrix form of the Fourier transform without any restriction regarding the frequencies to be analyzed and the sampling instants. These approaches are slower than MFFT and mapping techniques because APFTs do not employ the FFT. However, APFTs support incommensurable frequencies and are easy to implement and very flexible.
- **Mapping Techniques:** Actual base frequencies are replaced by artificially selected base frequencies, so that the original spectrum is mapped onto an equivalent periodic and dense spectrum. Waveforms transformed through the mapping become periodic and its Fourier coefficients can be efficiently calculated by the one-dimensional FFT.

Aspects such as underlying assumptions, limitations, flexibility, dynamic range and time consumption in the calculations have been considered before selecting the algorithms to be implemented in the simulator. After an in-depth study of the different approaches, the most appropriate algorithm are the APFTs. This is because *MFFT* and *Mapping Techniques* are only valid for non-linear systems described by algebraic relationships, i.e., memoryless systems. FFT does not support incommensurable frequencies and the computational cost highly depends on $gcd(f_{LO}, f_{RF})$.

A. Introduction to the APFT

APFT is based on a generalization of the matrix form of the Fourier transform without any restriction regarding the frequencies to be analyzed and the sampling instants.

By considering only a finite number of frequencies $\Delta_K = \{w_0,\ w_2,\ ...,\ w_{K-1}\}$, it is possible to sample a waveform at a finite number of time points and calculate its Fourier coefficients.

If $X(k) = X_k^C + j \cdot X_k^S$ represents the Fourier coefficients at frequencies w_k of a certain waveform $x(t)$, and assuming a certain truncation error, $x(t)$ can be expressed as:

$$x(t) = \sum_{w_k \in \Lambda_k} \left(X_k^C \cdot \cos(w_k \cdot t) + X_k^S \cdot \sin(w_k \cdot t) \right) \quad (1)$$

By sampling $x(t)$ at S time points, Eq. 1 can be rewritten as a matrix product,

$$x = A \cdot X \quad (2)$$

where,

$$x = [x(t_1)\ x(t_2)\ x(t_3)\ ...\ x(t_S)]^T \quad (3)$$

$$X = \left[X_0\ X_1^C\ X_1^S\ ...\ X_{K-1}^C\ X_{K-1}^C \right]^T \quad (4)$$

$$A = \begin{bmatrix} 1 & \cos(w_1 t_1) & \sin(w_1 t_1) & ... & \cos(w_{K-1} t_1) & \sin(w_{K-1} t_1) \\ 1 & \cos(w_1 t_2) & \sin(w_1 t_2) & ... & \cos(w_{K-1} t_2) & \sin(w_{K-1} t_2) \\ 1 & \cos(w_1 t_3) & \sin(w_1 t_3) & ... & \cos(w_{K-1} t_3) & \sin(w_{K-1} t_3) \\ . & . & . & . & . & . \\ . & . & . & . & . & . \\ . & . & . & . & . & . \\ 1 & \cos(w_1 t_s) & \sin(w_1 t_s) & ... & \cos(w_{K-1} t_s) & \sin(w_{K-1} t_s) \end{bmatrix} \quad (5)$$

Fig. 2 shows a general flowchart for APFT methods, including the three steps mentioned above.

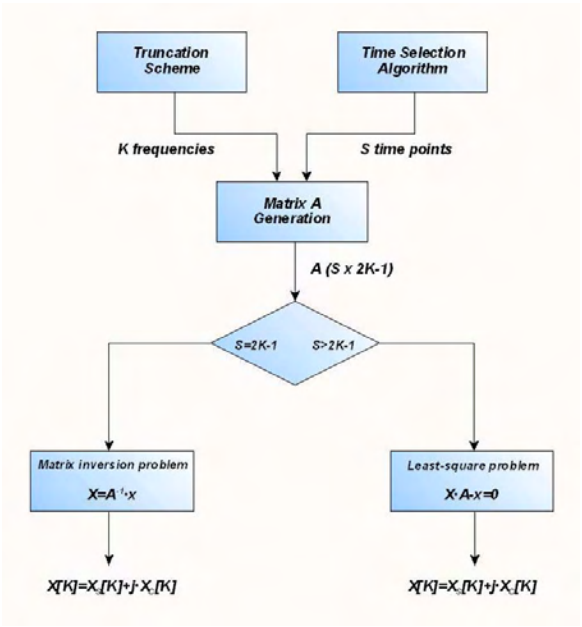

Fig. 2. General flowchart of APFT techniques.

The accuracy on the estimation of Fourier coefficients with the APFT is determined by two factors. On the one hand, the aliasing error due to omitting frequencies in the transform is reduced by increasing the number of components in the frequency set Λ_k (truncation scheme in Fig. 2). On the other hand, assuming a certain discretization error in the time domain waveforms, a numerical error will be present in the Fourier coefficients, which will be given by,

$$\frac{\|\Delta X\|}{\|X\|} \leq \kappa(A) \cdot \frac{\|\Delta x\|}{\|x\|} \quad (6)$$

where $\kappa(A) = \|A\| \cdot \|A^{-1}\|$ is the condition number of matrix A and $\|\cdot\|$ represents the norm of a matrix in a certain metric space. Usually 2-norm, $\infty - norm$ and Frobenius norm are employed.

To reduce the error, the condition number must be minimized, and this occurs when columns in matrix A becomes near-orthogonal.

Initial approaches to the APFT consisted of an uniform or random selection of the minimum necessary time points ($S = 2K - 1$) to form an square matrix A, which was in general extremely ill-conditioned leading to bad APFT results. Kundert and Sorkin [6]

proposed in 1988 a time-selection algorithm to choose an adequate set of time points in order to guarantee a well-conditioned square matrix A. In this case, the time-selection algorithm can be seen as an orthogonalization process. The vector X of Fourier coefficients can be directly calculated just by computing the ordinary inverse of A, and yields Eq. 7.

$$X = A^{-1} \cdot x \tag{7}$$

If A is not an square matrix, that is $S > 2K - 1$, the problem of computing Fourier coefficients consists of finding the shortest vector X that minimizes the distance $\rho(X)$ (Eq. 8). This is a typical least-square problem that can be solved by methods published in literature: [7] - [10]. This APFT scheme was firstly suggested by Zhang and Hong in 1990 [11]. Another time-selection algorithm, different from the one employed in [6] was applied to obtain S time points 2 or 3 times the $2K-1$ points required. By combining the orthogonalization in the time-selection algorithm with the solving of the overdetermined system by least-squares accuracy is improved with respect to previous methods.

$$\rho(X) = \|x - A \cdot X\| \tag{8}$$

Other implementations of the APFT have been published since [11]. The orthogonal APFT by Rodrigues [12] achieves the best possible conditioning for matrix A by making it exactly orthogonal. Unfortunately, this method has a big inconvenient when applied to device models that are not described by analytical equations. This inconvenient is related to the highest time instant t_{max} where the time domain waveform must be evaluated, which in Rodrigues' APFT depends on the desired significant digits to be taken into account for representing the frequency values in the analysis. As the numerical model of the Schottky diode is described by partial differential equations, and considering that a high sampling frequency (low time steps) is mandatory to reduce the error in the time domain resolution of such a system, then a high number of points would be necessary to reach the mentioned t_{max}.

B. APFT implementation in the mixers CAD tool

To summarize, a good APFT method should solve two important problems. First, the need for accuracy in the estimation of Fourier coefficients, which is directly proportional to the condition number of matrix A. Second, the computation time that is required, which depends not only on the number of frequencies and the number of time points to be considered but also on the time-selection algorithm. Thus, for the mixers CAD tool we have implemented an APFT method, conceptually similar to the one by Zhang and Hong but with the following simplifications and considerations:

- The time-selection algorithm is simplified to a random selection of S time-points. As a consequence, a poor-conditioned matrix A is generated .
- Fourier coefficients vector X is estimated by $X = A^I x$, where A^I is the Moore-Penrose pseudo-inverse of matrix A (also known as generalized inverse) [9]. The motivation for employing pseudo-inverse lies on the fact that this method proportionates the solution that minimizes the distance given by Eq. 6. In [7] it is discussed the strategy of using the Moore-Penrose generalized inverse to solve poorly-conditioned systems.

Table I shows a comparison between several APFTs and the one we have proposed and employed in the multi-tone harmonic balance tool for mixer analysis. The test has been performed by applying the APFT to the time domain current signal obtained by pumping a Schottky diode with a 2-tone (P_{LO}=2 mW @ 100 GHz and P_{RF}=0.1 mW @ 105 GHz) voltage waveform. A *box* truncation scheme (box H_1XH_2) has been employed, where H_1 and H_2 indicate that only those frequency components corresponding to H_1 LO harmonics, H_2 RF harmonics and their intermodulation products have been taking into account. M is the number of points employed in the time-selection algorithms to choose the S points that will be used to form matrix A

The random component inherent to the time points selection in APFT techniques makes necessary to perform a Monte Carlo analysis in order to evaluate the statistical goodness of the results. An unbiased estimation of conversion loss (taking as reference the results obtained by the FFT) together with a low standard deviation are desired. Results are shown in table I), where $E[L]$ represents the mean conversion loss and σ_L is the standard deviation.

Computation times correspond to a single execution of the APFT. The Monte Carlo analysis has been done using *Mathworks MATLAB 7.0* running on a Pentium IV platform with a 2.8 GHz clock frequency and 1 GB of available RAM.

TABLE I
COMPUTATION TIME AND ACCURACY OF APFT TECHNIOUES

				Kundert-Sorkin's APFT			Zhang-Hong's APFT			Proposed APFT		
Truncation	k	N=2k-1	M	E[L] (dB)	σ_L (dB)	Time (s)	E[L] (dB)	σ_L (dB)	Time (s)	E[L] (dB)	σ_L (dB)	Time (sec)
Box 2X2	13	25	2·N	5.82	5.18	**0.890**	6.86	4.60	**0.735**	7.60	4.63	**0.890**
			5·N	8.20	4.31	**1.880**	6.91	2.89	**1.080**	7.52	3.30	**1.285**
			8·N	7.42	4.64	**1.516**	7.11	1.69	**1.719**	6.88	1.80	**1.625**
Box 4X4	41	81	2·N	6.98	2.57	**3.109**	6.92	0.97	**6.110**	6.63	0.81	**3.172**
			5·N	6.75	0.43	**6.954**	6.71	0.24	**43.703**	6.72	0.27	**7.203**
			8·N	6.77	0.36	**10.781**	6.68	0.15	**124.390**	6.69	0.18	**11.203**
Box 6X6	85	169	5·N	6.68	0.16	**31.578**	6.70	0.03	**1002.125**	6.70	0.03	**32.422**

Fig. 3 shows the influence of the truncation on the accuracy of APFT methods. Results have been compared with those obtained by FFT that is the technique that proportionates the best accuracy because it is the best conditioned and consequently it is much less influenced by the aliasing error. Notice that APFT results tend to FFT results with an accuracy better than 0.2 dB when a *Box 4X4* truncation or higher is selected. It is also important to have in mind that the computation of the pseudo-inverse of A is only performed once at the beginning of the simulation process, and there is no need to recalculate it during the analysis.

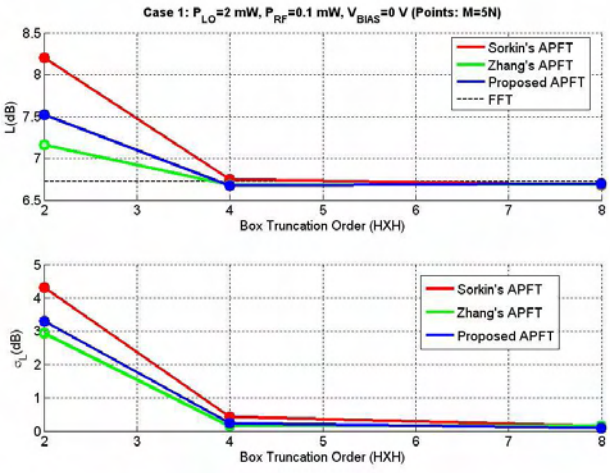

Fig. 3. Influence of truncation on APFT performance

III. Mixers Design and Optimization

It has been already commented that our CAD tool allows the concurrent analysis and optimization of the external circuit and the Schottky diode. In this section we present how the different design parameters affect to the performance of the mixer circuit.

A. External circuit parameters

In contrast to multiplier design, mixers are limited less by the properties of the Schottky diode than by those of the circuit, especially the practical impossibility of achieving optimum terminations at a large number of mixing frequencies. Some ways to optimize the external circuit are the use of DC bias, optimization of LO power, image enhancement, and the use of matched source and load impedances [13]. Of course, IF impedance must be also optimized to minimize conversion loss. In the CAD tool, this task is done by an optimization algorithm based on the gradient descent method.

As can be seen in Fig. 4, there is a trade-off between LO power and bias [13]. Furthermore, conversion loss is minimized and gets constant beyond a certain LO power, consequently, there is a linear relationship between IF and LO powers. Fig. 5 shows the variation in the real part of the conjugate-matched LO impedance as a function of LO power. As in multipliers [3], $Re[Z(f_{LO})]$ increases with bias as a consequence of the higher electric fields inside the Schottky diode that reduce the electron mobility.
The sensitivity of conversion loss with IF impedance is analyzed in Fig 6. It can be depicted that the IF impedance is not a limiting factor due to the wide range of values where minimum loss are achieved.

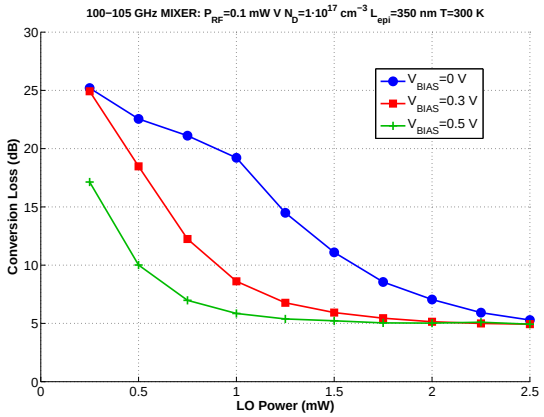

Fig. 4. 100-105 GHz Mixer. Influence of DC bias on conversion loss

One of the best known methods of reducing the conversion loss of a mixer is to terminate the diode in a reactance at the image frequency. Thus, power that would be dissipated in the image termination is converted to the IF [13]. It can be noticed in Fig 7 the reduction of the conversion loss through a correct choice of the image terminating reactance in the 100-105 GHz mixer circuit. Although the minimum conversion loss occurs for a 50Ω reactance, it is convenient to choose a higher value for it in order to avoid the high sensitivity region.

Another well-known characteristic of mixers performance is illustrated in Fig. 8. When the RF power is much lower than the LO power, which is the general regime in space applications receivers, conversion loss are determined by LO power and the influence of RF power can be neglected. This is the fundamental assumption of

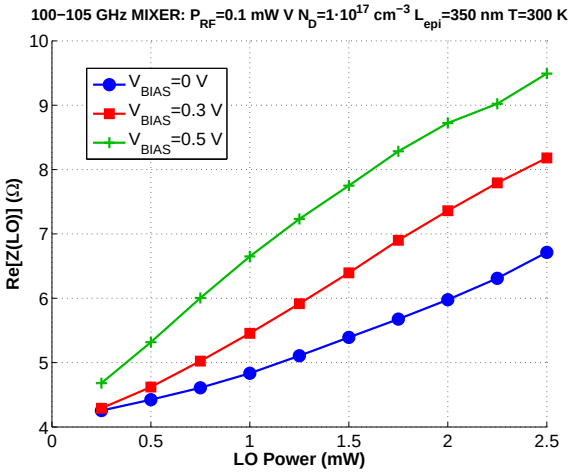

Fig. 5. 100-105 GHz Mixer. Influence of DC bias on matched $Re[Z(f_{LO})]$

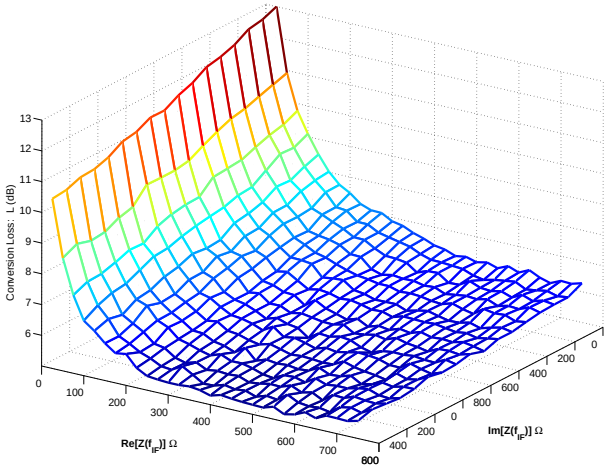

Fig. 6. 100-105 GHz Mixer. Influence of IF impedance on conversion loss. $P_{LO} = 2$ mW

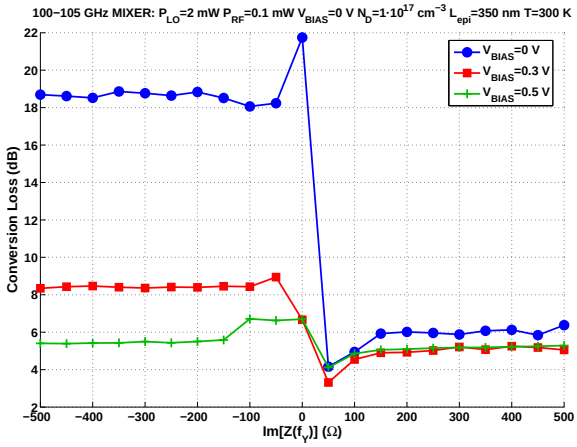

Fig. 7. 100-105 GHz Mixer. Image Enhancement

those simulators based on approximate approaches as the impedance matrix conversion techniques. Fig. 8 also demonstrates that our mixer CAD tool allows the analysis of mixers when they are operating well into the non-linear region for RF.

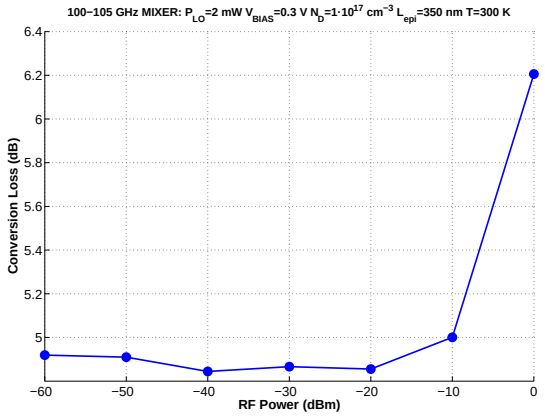

Fig. 8. 100-105 GHz Mixer. Influence of RF power on conversion loss. P_{LO}=3 dBm

B. Schottky diode parameters

The influence on performance of the Schottky diode parameters (anode are, epilayer length and doping, temperature, ...) is analogous to the multipliers performance (see [2]). For instance, as it occurs in multipliers, dividing by 2 the anode area of the Schottky diode, the curve of conversion loss shifts 3 dBm to the left so minimum losses can be achieved with half LO power (Fig. 9). Fig. 10 shows the reduction in conversion loss when the length of the epitaxial layer is reduced, as a consequence of a lower series resistance.

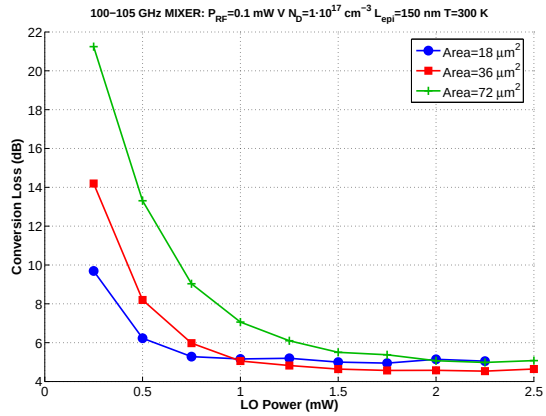

Fig. 9. 100-105 GHz Mixer. Influence of anode area on conversion loss

Influence of ambient temperature (self-heating has not been considered) in the mixer performance is also presented in Fig. 12. Conversion loss is reduced as a consequence of higher electron mobilities at low temperatures.

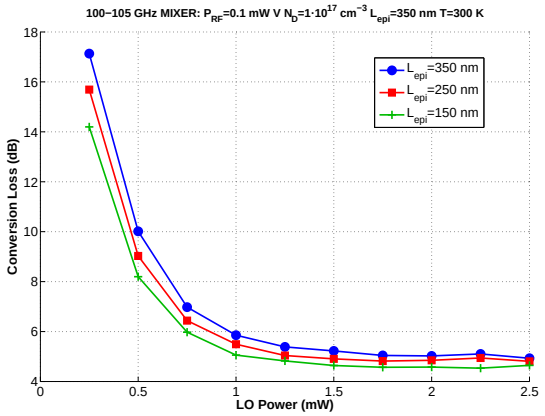

Fig. 10. 100-105 GHz Mixer. Influence of epilayer length on conversion loss

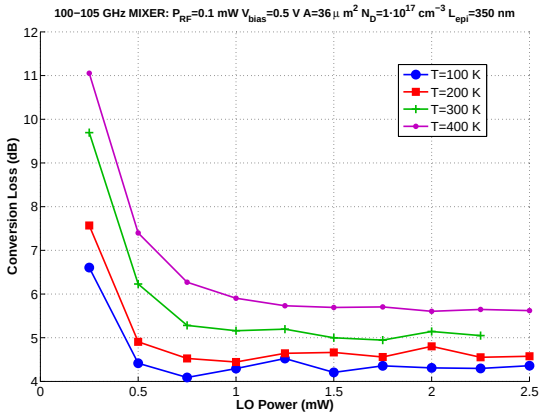

Fig. 11. 100-105 GHz Mixer. Influence of temperature on conversion loss

IV. Validation

The validation of the numerical simulator for mixers design, as for multipliers, requires a great quantity of data from Schottky mixer measurements. Unfortunately, only a few data have been published in literature [14] - [20], which is not enough to afford a complete validation of the simulation tool. Anyway, the numerical simulator was already validated for multipliers design and this can be extended to the mixer design just by taking into account that the only change in the simulator lies on the time-frequency conversion techniques that are employed.

Fig 12 shows simulation results for the 585 GHz mixer described in [18]. A conversion loss of 8 dB, achieved in the range of 0.2 to 1 mW LO power is reported for this mixer. According to harmonic balance simulations, the 8 dB conversion loss is obtained at around 0.6 mW of LO power. Since no information is given in [18] regarding the termination impedances at the image frequency, three cases have been simulated: $Z_Y = 50\Omega$, $Z_Y = Z_{LO,matched}$ and $Z_Y = 0+j300$ Ω (image enhancement).

A 100 GHz mixer has been also simulated with similar parameters to those corresponding to the mixer circuit reported in [14]. The conversion loss (5.3 dB) is analogous to the obtained by the numeric mixer CAD tool.

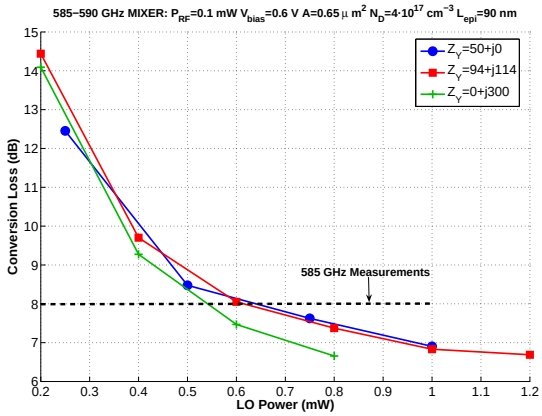

Fig. 12. Simulated conversion loss for the 585 GHz mixer described in [18]

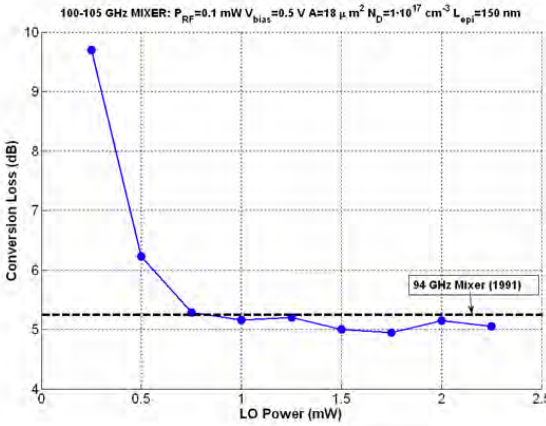

Fig. 13. Simulated conversion loss for the 94GHz mixer described in [14]

V. Conclusion

A novel CAD tool has been presented for the design and optimization of mixer circuits at millimeter and submillimeter-wave bands. One of the advantages of this tool is that no assumptions are made regarding LO and RF powers and frequencies. The mixer CAD tool represents a complement to a previous existent simulation tool for multipliers. As a result, a complete simulation tool is available for the design of receivers up to Terahertz frequencies.

The degree of freedom that arises as a consequence of the coupling of a numerical model for Schottky diodes with the harmonic balance circuit simulator has enabled us to study the different operation regimes and the physical limitations of mixers from the circuit point of view: bias, input power, loads at different frequency components, etc.

Mixer design and optimization aspects have been presented, which show the potential of the CAD tool to perform different analysis of mixer circuits taking into account all possible design parameters. Some comparisons between simulations and measurements have been presented. Further efforts to validate the mixer CAD tool are in progress.

Acknowledgment

The authors would like to thank the partial financial support of the European Space Agency to this work, under contract GSTP-3 ref. RIDER1 15293/01/NL/NF.

References

[1] P. H. Siegel, "Terahertz technology," *IEEE Transactions on microwave theory and techniques*, vol. 50, pp. 910–928, March 2002.

[2] J. Grajal, V. Krozer, E. Gonzalez, F. Maldonado, and J. Gismero, "Modelling and design aspects of millimeter-wave and submillimeter-wave Schottky diode varactor frequency multipliers," *IEEE Transactions on microwave theory and techniques*, vol. 48, pp. 910–928, April 2000.

[3] J. Grajal, J. Siles, V. Krozer, E. Sbarra, and B. Leone, "Analysis and design of schottky diode multiplier chains up to Terahertz frequencies," *In Proc. ESA Microwave Technology Techniques Workshop: Preparing for Future Space Systems*, May 2004.

[4] J. Grajal, J. Siles, V. Krozer, E. Sbarra, and B. Leone, "Performance evaluation of multiplication chains up to THz frequencies," *In Proc. 29th International Conference on Infrarred and Millimeter Waves 12th International Conference on Terahertz Electronics*, September 2004.

[5] P. Heron and M. Steer, "Jacobian calculation using the Multidimensional Fast Fourier Transform in the harmonic balance analysis of nonlinear circuits," *IEEE Transactions on Microwave Theory and Techniques*, vol. 38, no. 4, pp. 429–431, 1990.

[6] K.S.Kundert, G. Sorkin, and A. Sangiovanni-Vincentelli, "Applying harmonic balance to almost-periodic circuits," *IEEE Transactions on Microwave Theory and Techniques*, vol. 36, no. 2, pp. 366–378, 1988.

[7] G. Golub and C. Loan, *Matrix Computations (2nd Edition)*. John Hopkins University Press, 1989.

[8] A. Bjorck, *Least squares methods: Handbook of numerical analysis Vol. 1. Solution of equations in N*. Elsevier North Holland, 1988.

[9] R. Penrose, "A generalized inverse of matrices," *Proc. Cambridge Philos. Soc. 51*, 1954.

[10] B. Rust, W. Burrus, and C.Schneeberger, "A simple algorithm for computing the generalized inverse of a matrix," *Communications of the ACM*, vol. 9, pp. 381–387, 1966.

[11] X.-D. Zhang, X.-N. Hong, and B.-X. Gao, "An accurate fourier transform method for nonlinear circuits analysis with multi-tone driven," *IEEE Transactions on Circuits and Systems*, vol. 37, no. 5, pp. 668–669, 1990.

[12] P. J. Rodrigues, *Computer-aided analysis of nonlinear microwave circuits*. Artech-House, Inc. Boston-London, 1997.

[13] S. Maas, *Microwave Mixers (Second edition)*. Artech-House, Inc. Boston-London, 1986.

[14] D. Garfield, R. Mattauch, and S. Weinreb, "RF performance of a novel planar millimeter-wave diode incorporating an etched surface channel," *IEEE Transactions on Microwave Theory and Techniques*, vol. 39, pp. 1–5, January 1991.

[15] A. Kerr, R. Mattauch, and J. Grange, "A new mixer design for 140-220 GHz," *IEEE Transactions on Microwave Theory and Techniques*, pp. 399–401, May 1977.

[16] P. Siegel and A. Kerr, "The measured and computed performance of a 140-220 GHz schottky diode mixer," *IEEE Transactions on Microwave Theory and Techniques*, vol. 32, pp. 1579–1590, December 1984.

[17] T. Newman and K. Ng, "A submillimeter-wave planar diode mixer design and evaluation," *IEEE MTT-S Digest*, pp. 1293–1296, 1991.

[18] K. Hui, J. Hesler, D. Kurtz, W. Bishop, and T. Crowe, "A micromachined 585 GHz Schottky mixer," *IEEE Microwave and Guided Wave Letters*, vol. 10, pp. 374–376, September 2000.

[19] P. Siegel, I. Mehdi, R. Dengler, T. Lee, D. Humphrey, and A. Pease, "A 640 GHz planar-diode fundamental mixer/receiver," *IEEE MTT-S Digest*, pp. 407–410, 1998.

[20] S. Gearhart, J. Hesler, W. Bishop, T. Crowe, and G. Rebeiz, "A wide-band 760 GHz planar integrated schottky receiver," *IEEE Microwave and Guided Wave Letters*, vol. 3, pp. 205–207, July 1993.

Semiclassical description of Schottky diode mixer properties at THz frequencies

Joerg Heiermann
Institute of Space Systems, Universität Stuttgart
Pfaffenwaldring 31, 70550 Stuttgart, Germany
Email: heierman@irs.uni-stuttgart.de

Hans–Peter Roeser
Institute of Space Systems, Universität Stuttgart
Pfaffenwaldring 31, 70550 Stuttgart, Germany
Email: roeser@irs.uni-stuttgart.de

***Abstract*— For nanostructured Schottky diode mixers being used for airborne far–infrared spectrocopy a simple semiclassical description is presented to describe their properties. Applying the Heisenberg uncertainty principle reveals the limits of this semiclassical approach.**

I. Introduction

Schottky diodes can be used as coherent detectors in high–resolution spectrometers in the THz frequency range. The Schottky diodes serve as low–noise mixers and permit the detection of weak signals, for example from cold interstellar clouds, with a high spectral resolution of $10^6 - 10^7$ with a bandwidth of several GHz [1].
An important feature of Schottky diodes is that they need not necessarily be cooled down to cryogenic temperatures when being used as coherent detectors and that they perform with high sensitivity even at room temperature.
Requiring no cryogenic cooling leads to enormous advantages with regard to energy consumption and system weight. Hence, using Schottky diodes as heterodyne detectors is of great interest for air– and spaceborne astronomical and Earth observation missions.
Schottky diode mixers based on gallium arsenide have been employed successfully for airborne FIR astronomy for many years. The quasi–optical setup of a detector block is shown in the figures 1 and 2.

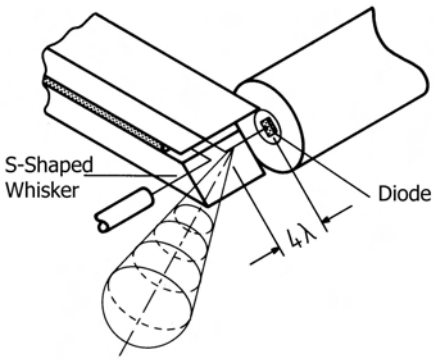

Fig. 1. Schematic drawing of the quasi–optical mixer block with signal beam, 90°–reflector, whisker antenna and diode chip

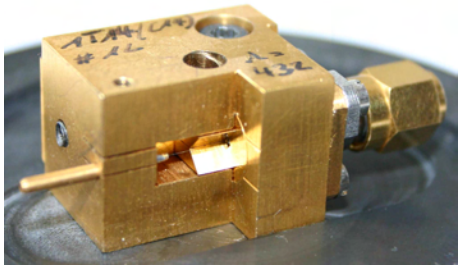

Fig. 2. Photo of a quasi–optical detector block

During the preparing, optimizing and qualifying for flight experiments, many measurement data were taken. The re–investigation of these data revealed the following relationships under room temperature conditions without external magnetic fields, with only the local oscillator illuminating the detector antenna, and for optimum mixing and best signal–to–noise ratio [2], [3]:

1. The net current through the depletion layer of the Schottky contact is proportional to the frequency of the local oscillator. The proportionality constant can be interpreted as the number of electrons being transported through the depletion layer per local oscillator cycle times the electric elementary charge e:

$$I = N_e \, e \, \nu \tag{1}$$

2. The square of the depletion layer thickness is proportional to the electron mobility in the semiconductor material. The proportionality constant is the magnetic flux quantum $h/2e$:

$$D_{depl}^2 = \frac{h}{2\,e}\,\mu \tag{2}$$

3. The resistivity is proportional to the number of electrons being transported through the depletion layer per local oscillator cycle. The proportionality constant is the quantum hall resistivity h/e^2:

$$R = \frac{h}{e^2}\,\frac{1}{N_e} \tag{3}$$

4. The current density in the depletion layer reaches up to $10^6 A/cm^2$.

II. Semiclassical model

One can describe the functioning of the Schottky diode mixer via a modified Millikan–type experiment: A laser beam ($h\nu$) is incident on a cathode which is acting as a photon detector, see figure 3. The electrons travel from the cathode to the anode, whereby the cathode and the anode are acting like a capacitor. The geometry of this capacitor is given by its thickness, which is defined by the depletion layer thickness D_{depl}, and by its diameter, which is defined by the whisker contact diameter $\varnothing_A$. The capacitor is filled with semiconducting material.

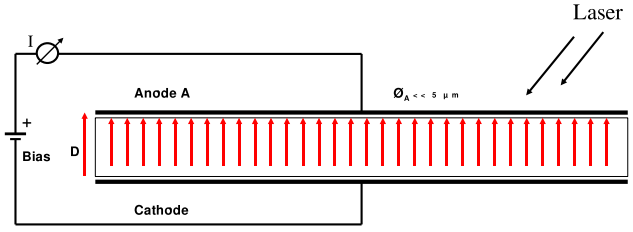

Fig. 3. A Millikan–type experiment with a semiconductor between anode and cathode

A semiclassical description can be achieved through an equation describing the photoelectric effect for one electron

$$e\,V_0 = h\,\nu - \frac{e^2}{2\,C}\ , \tag{4}$$

where $\frac{e^2}{2C}$ replaces the work function in Millikan's experiment with the energy change that the electron undergoes when traveling from the cathode to the anode.

Assuming that $h\,\nu >> \frac{e^2}{2\,C}$ (which is valid for the diode operating envelopes), and with $V_0 = R\,I$, one gets

$$R = \frac{h}{e^2} \tag{5}$$

for one electron. Assuming that all N_e electrons are travelling in parallel, the resistance finally becomes

$$R = \frac{h}{e^2}\,\frac{1}{N_e}\ . \tag{6}$$

If one assumes that the diode acts like a velocity filter such that

$$v = \mu\,E = \mu\frac{V_0}{D_{depl}} = 2\,D_{depl}\,\nu\ , \tag{7}$$

the result

$$D_{depl}^2 = \frac{h}{2\,e}\mu \tag{8}$$

is evident. Equation 7 requires that the transport of charge takes place during half the laser cycle time $\frac{1}{\nu}$.

In table I, the contact diameter $\varnothing_A$, the depletion layer thickness D_{depl}, the mean free path of the electrons λ_e, the number of electrons being transported per laser cycle N_e, the electron mobility μ and the doping level N_D for diodes with different geometries are listed.

TABLE I
Data for different diodes I

Diode	J118	1I17	1I12	1T15
$\varnothing_A$ [nm]	1000	800	450	250
D_{depl} [nm]	32	27	26	21
λ_e [nm]	84	64	52	35
N_e [-]	2800	4500	2200	1300
μ [cm^2/(V s)]	5000	3600	3100	2100
N_D [10^{23}/m^3]	1.0	3.0	4.5	10.0

Obviously, the electron transport through the depletion layer is ballistic because the mean free path is roughly twice as large as the depletion layer thickness for all diodes.

III. Limits of the semiclassical model

1. From the data given in table I it is possible to calculate the number

$$N_{cc} = \varnothing^2\,\frac{\pi}{4}\,N_D^{2/3} \tag{9}$$

which is an estimation of the number of doping atoms in a plane layer perpendicular to the direction of the current transport. Comparing N_{cc} (see table II) with N_e, one can say roughly that

$$N_e \approx 2\,N_{cc}\ , \tag{10}$$

so that one could speculate that the number N_{cc} denotes the number of current channels defined by the crystal structure where 2 electrons travel through during each laser cycle time $1/\nu$. It is an open question whether the electrons behave like Cooper pairs interacting with the laser photons.

It is also interesting to calculate the number

$$N_{dd} = D_{depl}\,N_D^{1/3} \tag{11}$$

which is also tabulated in table II. This reveals that $N_{dd} + 1 \approx 3$ doping atoms apparently make up one current channel in the direction of the current transport. This raises the question if and how the crystal (and hence, charge) structure influences the electron transport.

The de Broglie wavelength for an individual electron is defined by

$$\lambda_{dB} = \frac{h}{m_e^*\,v}\ . \tag{12}$$

The velocity v shall be estimated here by

$$v = D_{depl}\cdot 1\,THz \tag{13}$$

because $1\,THz$ is the typical laser frequency. The values (table II) show that $\lambda_{dB} >> D_{depl}$. Hence, the wave–like behaviour of the electrons and a confinement effect certainly play an important, role which has to be explained. In addition, once one starts regarding the wave–like behaviour of the electrons, the question is raised if all electrons N_e behave in a coherent manner.

Appplying Heisenberg's uncertainty principle in the current direction

$$\Delta x \, \Delta p_x \geq \frac{\hbar}{2} \ , \tag{14}$$

with $\Delta x = D_{depl}$ and $p_x = m_e^* \, v$, one gets the uncertainty of the velocity

$$\Delta v_x \geq \frac{\hbar}{2} \, \frac{1}{D_{depl}} \, \frac{1}{m_e^*} \tag{15}$$

which is listed in table II. The uncertainty of the velocity is of the same order like the estimated velocity v which raises the question how correct it is in the semiclassical description to talk about a velocity filter mechanism of the diodes.

Applying Heisenberg's uncertainty principle in the direction perpendicular to the current direction and assuming that the initial uncertainty is $N_D^{1/3}$, the uncertainty is calculated as

$$\Delta y \geq \frac{\hbar}{2} \, \frac{1}{m_e^*} \, N_D^{1/3} \, \frac{1}{\nu} \tag{16}$$

which is also tabulated in table II. The values for Δy are of the same order like D_{depl}.
With $N_D^{-1/3}$ representing the distance between the above mentioned current channels, it becomes clear that it is not possible to assign one electron (or an additional one due to equation 10) to one current channel, because its uncertainty Δy due to the Heisenberg principle is bigger than $N_D^{-1/3}$.

Hence, the processes involved in the electron transport through the nanoscale Schottky barrier have to investigated further by using the more fundamental principles of quantum electrodynamics. This is also highlighted by the fact that the wavelength of the laser photons is way bigger than the device structure so that it also remains an open question where and how photons and electrons interact.

TABLE II
DATA FOR DIFFERENT DIODES II

Diode	J118	1I17	1I12	1T15
N_{cc} [-]	1692	2253	933	490
N_{dd} [-]	1.5	1.8	2.0	2.1
v [km/s] (1 THz)	32	27	26	21
λ_{dB} [nm] (1 THz)	361	428	444	550
Δv_x [km/s]	29	34	35	44
Δy [nm] (1 THz)	43	62	70	92
$N_D^{-1/3}$ [nm]	22	15	13	10

IV. CONCLUSION

A Millikan–type photoelectric effect equation and the concept of a velocity filter allow a semiclassical description of the properties of Schottky diodes being used as heterodyne mixers for FIR astronomy. Some simple calculations of the crystal lattice structure and the application of Heisenberg's uncertainty principle reveal some astonishing new questions that need to be answered in the future. We have decided to attack these questions via a direct simulation on the basis of quantum electrodynamics.

REFERENCES

[1] H.–P. R¨oser, H.–W. H¨ubers, "Schottky barrier devices for THz applications," *in: J.M. Chamberlain, R.E. Miles (eds.): New Directions in Terahertz Technology, NATO ASI Series E: Applied Sciences, Vol. 334, Kluwer Academic Publishers*, 1997.

[2] H.–P. R¨oser, H.–W. H¨ubers, E. Br¨undermann, M.F. Kimmitt, "Observation of mesoscopic effects in Schottky diodes at 300 K when used as mixers at THz frequencies," *Semicond. Sci. Technol. 11, pp. 1328—1332*, 1996.

[3] H.–P. R¨oser, H.–W. H¨ubers, "Mesoscopic effects in nanostructured GaAs Schottky detectors," *IRMMW 2001, pp. 2-46–2-49, ISBN 2-87649-035-8*, 2001.

Modelling of THz power generation based on ultra-fast PIN photodiodes

Carsten Fritsche and Viktor Krozer
Technical University of Denmark, Oersted•DTU, Department of Electromagnetic Systems,
Oersteds Plads 348, 2800 Kgs. Lyngby, Denmark, Phone:+45-45253769, E-mail:vk@oersted.dtu.dk
and Center for Applied Technology and Electronics ATHENE e.V., Darmstadt, Germany

***Abstract*— A large-signal model for PIN photodetector is presented, which can be applied to ultra-fast photodetection and THz signal generation. The model takes into account the tunnelling and avalanche breakdown, which is important for avalanche photodiodes. The model is applied to ultra/fast superlattice photodiodes for THz signal generation. Results show that the output power at THz frequencies is in the order of tens of μW. The embedding impedances are found to be as low as 13Ω.**

I. Introduction

A large amount of literature exists on the performance and circuit modelling of PIN diodes both for electrical and optical applications. A number of models exist for the PIN photodiode, which are in general small-signal models, including the models for travelling-wave structures [1], [2], [3], [4]. Most models do net lend themselves to implementation in a circuit simulator, because they are either based on numerical techniques [5] or are based on black-box models extracted from small-signal measurements. Parasitics modelling of fast PIN photodiodes has been presented by Wang et al .

A PIN photodiode model suitable for circuit simulations has been presented in [6] for avalanche photodiodes and for reverse bias only. This model has been used as a basis for the development of the large-signal model for standard PIN and superlattice PIN photodiodes and has been employed for the implementation into the circuit simulator.

This paper gives details on the model and compares results from measurements with simulations. Both avalanche InGaAs photodiodes as well as GaAs PIN THz photodiodes are considered in the discussion. To our knowledge we demonstrate for the first time a PIN device large-signal model suitable up to THz frequencies implemented into a commercial CAD tool. The model is then used for the prediction of the signal output from the photodetector up to THz frequencies and the determination of the embedding impedances.

II. PIN photodiode large-signal model

The PIN model is based on the drift-diffusion model with a modified velocity versus field characteristic and takes into account the rate equations. The following assumptions are made, which are generally valid for high speed devices:

1) The depletion width in the n^+ and p^+ regions is negligible compared to that in the I-region.
2) The electric field is uniform in the I-region.
3) The electric field is negligible in the n^+ and p^+ regions.
4) In real devices the I-region contains residual doping, which is used as a parameter in the model.

The model equations can be divided into those describing the optical performance and those determining the electrical performance of the device, respectively. Illumination is currently assumed from the n^+ side, but can be changed to illumination from the p^+ side by interchanging the parameters of the n^+-region with those of the p^+-region. A diffusion current conduction is assumed for the highly doped regions and drift conduction in the I-region. The rate equations can be given in the following form for the n^+-region:
n-region:

$$\frac{\mathrm{d}P_n}{\mathrm{d}t} = P_G - \frac{P_n}{\tau_p} - \frac{I_p}{q} \tag{1}$$

i-region: for electrons

$$\frac{\mathrm{d}N_i}{\mathrm{d}t} = N_{Gi} + v_n\zeta_n N_i + v_p\zeta_p P_i - \frac{N_i}{\tau_{nr}} - \frac{N_i}{\tau_{nt}} + \frac{I_n}{q} \tag{2}$$

p-region:

$$\frac{\mathrm{d}N_p}{\mathrm{d}t} = N_G - \frac{N_p}{\tau_n} - \frac{I_n}{q} \tag{3}$$

where the P_n and N_p are the total excess holes and electrons in the n- and p-regions, N_i are the total excess electrons in the i-region, q the electron charge, P_G and N_G are electron-hole pair generation rates in the n- and p-regions by incident light, N_{Gi}(=P_{Gi}) is the generation rate in the i-region, τ_p and τ_n are the hole and electron life-time in the n- and p-regions, τ_{nr} and τ_{pr} are the recombination life-time of electron and hole in the i-region, τ_{nt} and τ_{pt} are the electron and hole transit-time through the i-region, I_p and I_n are the hole and electron diffusion current in the n- and p-regions, v_n and v_p are the electron and hole drift velocities in the i-region, and ζ_n and ζ_p are the electron and hole impact ionization rates in the i-region. The schematic structure of a PIN is shown in fig. 1. The solution of the above equations determines the charge flow in the device and its frequency and voltage dependent performance. The solution is found by applying the according boundary conditions as outlined in [6]. The electron-hole pair generation rate is given

$$G(x) = \Phi_0\alpha\exp\left(-\alpha x\right) \tag{4}$$

where Φ_0 is the incident photon flux per unit area given by $P_{in}(1-R)/Ah\nu$, where R is the facet reflectivity of

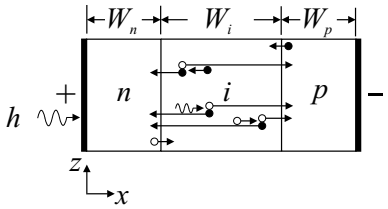

Fig. 1. Schematic illustration of carrier fbw in a PIN diode.

the n-region, $h\nu$ is the photon energy and A is the device area, and α is the absorption coefficient for the individual semiconductor layer.

The proposed equivalent circuit has the structure as shown in Fig. 2. It contains an optical part and an electronic part. These two are coupled via controlled current and voltage sources. In the case of multi-section devices the equivalent circuit is being connected is series on both the electrical and optical ports. The resistor R_{uu} is then employed only once in the circuit, because it represents the optical power delivered to the substrate. Adding mirrors can be taken into account by appropriate manipulation of additional absorption terms. Therefore, it is believed that the equivalent circuit is rather complete including the dominant physical phenomena. The optical

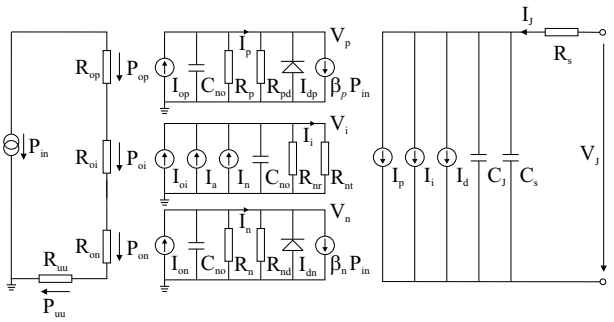

Fig. 2. Electrical and optical equivalent circuit for the PIN photodetector.

input power P_{in} is represented by the equivalent voltage source. The power P_{op} represents the amount of the power P_{in} that will be dissipated on the resistance R_{op} due to generation of electron-hole pairs in the n-layer. The power P_{oi} is that part of the total power P_{in} that will be dissipated on the resistance R_{oi}. Photons that will be absorbed in the i-layer and generate electron-hole pairs are represented by the power P_{on} and its resistance R_{on}. The photons that will not be absorbed in the APD can be represented by the amount of power P_{uu} that is dissipated on the resistance R_{uu}.

The rate equations can be transformed to current equations by multiplying each equation with the electron charge q. In order to improve numerical accuracy, a constant C_{no} is introduced, which can be thought as a capacitance. Defining the following equivalent voltages

$$V_p = \frac{qP_n}{C_{no}} \qquad V_n = \frac{qN_p}{C_{no}} \qquad V_i = \frac{qN_i}{C_{no}} \quad (5)$$

the rate equations (1),(3) and (**??**) can be written as

$$\frac{P_{op}}{V_{opt}} = C_{no}\frac{\mathrm{d}V_p}{\mathrm{d}t} + \frac{V_p}{R_p} + I_p \quad (6)$$

$$\frac{P_{on}}{V_{opt}} = C_{no}\frac{\mathrm{d}V_n}{\mathrm{d}t} + \frac{V_n}{R_n} + I_n \quad (7)$$

$$\frac{P_{oi}}{V_{opt}} = C_{no}\frac{\mathrm{d}V_i}{\mathrm{d}t} + \frac{V_i}{R_{nr}} + \frac{V_i}{R_{nt}} - I_a - I_n \quad (8)$$

where

$$R_p = \frac{\tau_p}{C_{no}}; \quad R_n = \frac{\tau_n}{C_{no}}; \quad R_{nt} = \frac{\tau_{nt}}{C_{no}}; R_{nr} = \frac{\tau_{nr}}{C_{no}};$$
$$I_i = \frac{V_i}{R_{nt}}; \quad I_a = C_{no}V_i(v_n\zeta_n + v_p\zeta_p) \quad (9)$$

The diffusion currents can be found solving the continuity equations for the steady state and applying the appropriate boundary conditions [6]. The steady-state diffusion currents then are given by

$$I_n = \frac{V_n}{R_{nd}} + \beta_n P_{in} - I_{dn} \quad (10)$$

$$I_p = \frac{V_p}{R_{pd}} + \beta_p P_{in} - I_{dp} \quad (11)$$

The current through the photodetector is the sum of the hole diffusion current in the n-region, the current through the i-region, that includes the electron diffusion current in the p-region, the displacement current and tunnelling and parasitic currents

$$I_J = I_p + I_i + C_T\frac{\mathrm{d}V_J}{\mathrm{d}t} + I_{par} \quad (12)$$

where V_J is the junction voltage, $C_T = C_s + C_J$, C_s is the parasitic capacitance and C_J is the junction capacitance and I_{par} represents the tunnelling and parasitic current contributions.

III. Implementation of the large-signal PIN model

The implementation of the above model has been pursued with the help of the so called symbolic defined device (SDD), which is able to model linear and nonlinear devices and can be used in harmonic-balance simulations. The SDD model is defined through relations for the terminal currents and voltages. The major task here is the appropriate formulation of the individual elements of the equivalent circuits in order to achieve convergence. The implemented SDD in Agilent ADS2003C is provided in fig.3.

IV. Results

This circuit has been verified with data available for an APD and an ultra-fast photodetector. The results for the DC characteristics for both diodes is provided in fig. 4. The results demonstrate very good agreement with measured values over all bias points up to avalanche breakdown. Large-signal harmonic-balance analysis can then be used for the determination of the embedding impedances for ultra-fast photodiodes. The photodetector has been simulated in a setup with two laser colors,

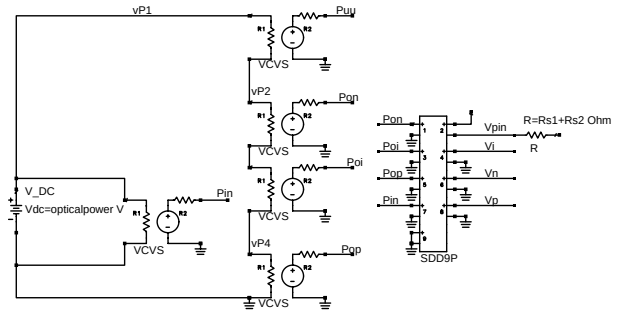

Fig. 3. Equivalent circuit for light input

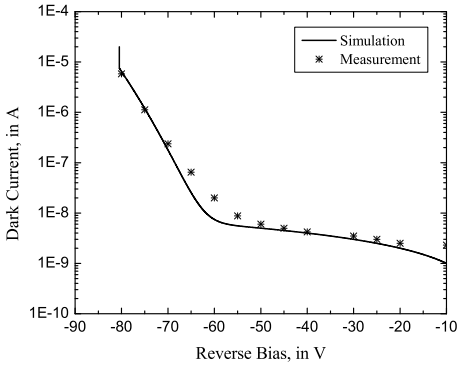

a)

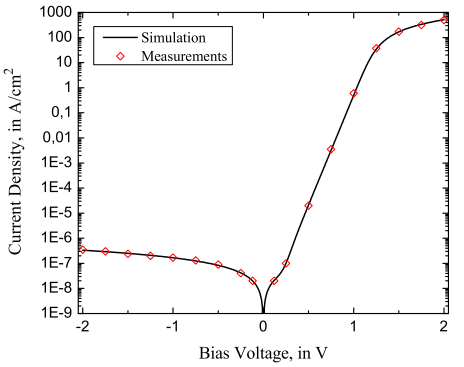

b)

Fig. 4. Comparison of simulated and measured I/V characteristics of an APD diode [6] and an ultra-fast PIN diode fabricated by the Univ. of Erlangen [**?**].

resulting in a beat frequency, which has been varied from 100 GHz up to 1000 GHz. The output power versus the beat frequency for the ultra-fast PIN diode from fig. 4 is provided in fig. 5 together with the embedding impedances. It can be verified that the output power drops with frequency according to $1/f^4$ which indicates that the diode suffers from transit time and RC time constant limitations.

The real part of the impedance is relatively low and equal to $R_{PIN} \approx 13\Omega$. This indicates that relatively low impedance embedding circuits or antennas have to be used in order to match the diode.

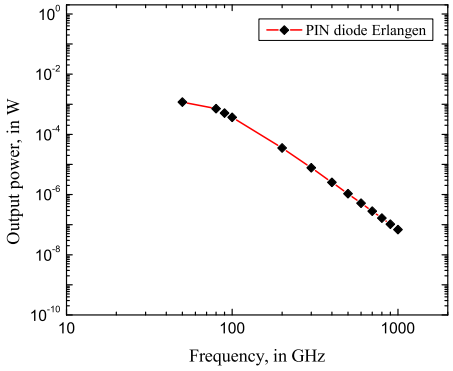

a)

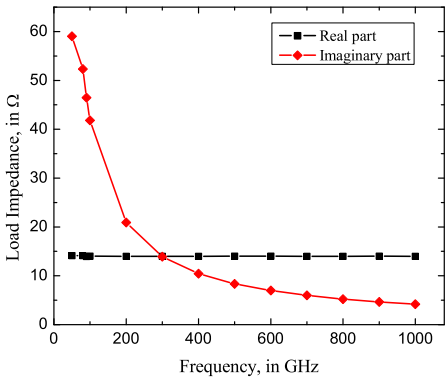

b)

Fig. 5. Comparison of simulated and measured I/V characteristics of an APD diode [6] and an ultra-fast PIN diode fabricated by the Univ. of Erlangen [**?**].

V. Conclusions

The paper presents a large-signal model for PIN diodes applicable up to THz frequencies. Comparison between measured and simulated DC and AC characteristics show excellent agreement. The model can also be used for travelling-wave photodiodes and the implementation of the travelling-wave structure into the CAD environment is currently under way and will be shown during the conference.

References

[1] A. Malcoci, A. Stöhr, R. Heinzelmann, K. Hagedorn, R. Güsten, F. Schäfer, H. Stüer, F. Siebe, P. van der Wal, V. Krozer, M. Feiginov, and D. Jäger, "Photonic (sub)millimeterwave local oscillators," in *Microwaves, Radar and Wireless Communications, 2002. MIKON-2002. 14th International Conference on*. 2002, vol. 3, pp. 722–734 vol.3, Telecommun. Res. Inst.

[2] M. Dentan and B. de Cremoux, "Numerical Simulation of the Nonlinear Response of a p-i-n Photodiode Under High Illumination," *Journal of Lightwave Technology*, vol. 8, no. 8, pp. 1137–1144, 1990.

[3] J. J. Jou, C.-K. Liu, C.-M. Hsiao, H.-H. Lin, and H.-C. Lee, "Time-Delay Circuit Model of High-Speed p-i-n Photodiodes," *IEEE Photonics Technology Letters*, vol. 14, no. 22, pp. 525–5274, 2002.

[4] G. Torrese, I. Huynen, M. Serres, D. Gallagher, M. Banham, and A. Vander Vorst, "An Analytical Small-Signal Bias-Dependent Nonuniform Model for p-i-n Traveling-Wave Photodetectors," *IEEE Trans. Microwave Theory & Techniques*, vol. MTT-50, no. 11, pp. 2553–2557, 2002.

[5] G. George and J. P. Krusius, "Transient Response of High-Speed p-i-n Photodiodes Including Diffusion Effects," *Solid-State Electronics*, vol. 37, no. 11, pp. 1841–1847, 1994.
[6] W. Chen and S. Liu, "PIN Avalanche Photodiodes Model for Circuit Simulation," vol. QE-32, no. 8, pp. 2105–2111, 1996.

Schottky-Structures for THz-Applications based on Quasi-Vertical Design-Concept

O. Cojocari[(1)], C. Sydlo[(1)], H.-L. Hartnagel[(1)] , S. Biber[(2)], J. Schür[(2)] and L.-P. Schmidt[(2)]

[(1)] *Advanced Technologies Group (ATech)*, Institute of Microwave Engineering, Technical University of Darmstadt, GERMANY. E-mail: cojocari@hf.tu-darmstadt.de

[(2)] Institute for Microwave Technology, University of Erlangen-Nuremberg, GERMANY.

***Abstract*—This work presents results of systematically performed optimizations of a quasi-vertical Schottky-structure for THz-applications. Three versions of structure-design based on a quasi-vertical concept were successfully fabricated and characterized. The first-developed anti-parallel mixer-diode pair demonstrated a high performance at frequencies below 200GHz. Measurement results show a conversion efficiency (DSB) of 5.1dB, 5.8dB, 6.3dB and a system noise-temperature (DSB) of 940K, 950K and 1450K at frequencies of 140GHz, 150GHz and 183GHz respectively. A room-temperature power-sensitivity of about 3000V/W has been attained at frequencies between 75GHz and 95GHz of a single-diode structure fabricated with the second design-version in combination with a broadband planar logarithmic-periodic antenna. Measurements at frequencies about 600GHz of a similar structure mounted in a heterodyne mixer revealed a voltage responsivity of about 1500V/W and conversion loss (SSB) of about 10dB. Microwave-noise measurements of such a structure revealed typical values of the junction noise-temperature to be lower than 300K at frequencies between 2.1GHz and 4.8GHz and at a bias current up to 3mA. Low-frequency noise of these diodes is normally about $4\mu V/Hz^{1/2}$ at 1Hz. Typical DC-characteristics of the third design-version of a single-diode-structure are as follows: series resistance $Rs<7\Omega$, ideality factor $\eta<1.2$ and junction capacitance at 0V $C_{0j}<2.3fF$. The total capacitance of this structure is $C_0<7fF$. These data result in a calculated cut-off-frequency of well above 3THz.**

***Index Terms*—Schottky diodes, quasi-vertical structure, THz-applications.**

I. Introduction

Schottky diodes based on n-GaAs have been shown to be the best-performing devices at room temperature up to several Terahertz for both mixing and multiplying applications [1-3]. In recent decades GaAs Whisker-contacted structures were found to be an optimal solution for THz-frequency operation due to their small parasitic capacitance and series resistance, with a vertical current flow providing an uniform field and current density distribution over the whole anode area[2,3]. Because whisker contacted diodes are very sensitive to mechanical influences and the contacting procedure is very difficult and time consuming, ever-widening application fields and the potential commercial market push the development of planar devices suitable for monolithic integration.

But planar technology is usually related to certain limitations which mainly consist of an additional parasitic capacitance, series resistance and thermal difficulties. Due to the fact that Schottky and Ohmic contacts are situated on the same plane, a current overloading of the anode region closest to the Ohmic contact may occur. High local current density may heat electrons considerably above their thermal energy, causing excess noise in the device.

An alternative to a planar structure is a quasi-vertical structure, whose relevant features can diminish some of these problems.

First quasi-vertical structures are developed and fabricated at TUD a few years ago [4]. They demonstrated good mixing performance at millimetre waves [5]. However measurements of a similar structures at 650GHz revealed deficient results [6]. The most significant frequency-limiting factor of these structures is suggested to be the parasitic capacitance [7]. In order to make a quasi-vertical structure suitable for applications in a high-THz-frequency region further structure optimisations are required.

In this work we present and discuss some results of systematically performed optimisations of quasi-vertical structures in order to improve their high-frequency performance.

II. Design Considerations

One of main advantages of a quasi-vertical structure is a vertical current flow, as in the case of whisker-contacted [3] or substrate-less[2,8] structures, namely, from the anode on the top of the epitaxial layer to the back-side Ohmic-contact (see Fig. 1). In this case, the field distribution is kept uniform across the entire anode area excluding current overloading of the anode region closest to the Ohmic contact, which may generate additional noise in traditional planar structures due to high current density.

Secondly, since the GaAs mesa, as thin as 1.5µm, is enclosed between the Ohmic-contact and Schottky-contact, a very good heat sink from the Schottky contact to the back-side

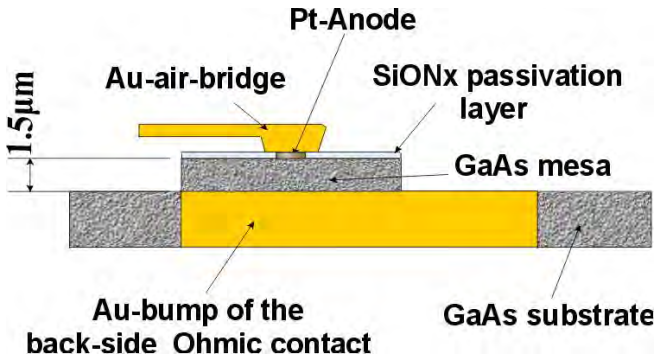

Fig. 1. Sketch of single planar quasi-vertical diode.

Au-bump and other massive metallic elements of the circuitry is organised. This considerably increases the power capability of the quasi-vertical structure.

Gold-bumps deposited on back-side Ohmic-contacts (which are specific to these kind of structures) may be used as contact pads for mounting on corresponding filter structures. That means that in contrast to the traditional flip-chip mounting approach, where the structure is mounted up-side-down, a quasi-vertical structure may be mounted also in a up-side-up position. In such a position anode fingers are automatically taken away from the filter-substrate which may reduce the influence of the substrate to the structure performance. This represents an alternative mounting approach and represents an potential advantage of the quasi-vertical concept.

Additionally this kind of structures enables the use of the anode formation technology as-optimised on relatively simple and easy-to-fabricate whisker-contacted structures, as described in [9] and in more details in [10].

Fig. 2 illustrates top view of all three versions of fabricated structures with a proportional magnitude. At this stage chips are just separated from the carrier wafer but are not cleaned yet. Nevertheless, overall changes in dimensions and design are obvious.

All three structures have similar geometrical features, which are as follows:

- The active device is fabricated on a 1.5 µm thick GaAs mesa placed on a few µm thick gold cathode;
- Pt-Au anodes have a circular geometry with the diameter of about 1µm (0.8µm for first structure);
- Anodes are defined in a $SiON_x$-passivation layer and are situated in the centre of mesas;
- Anodes are connected to an anode contact-pad through an air bridge running 4 µm above the substrate;
- Contact-pads are plated to a height of 6 – 8 µm above the top of the GaAs-substrate, offering significant mechanical protection for air bridges;
- The backside gold cathode is embedded in a few µm thick GaAs/AlGaAs substrate and offers a direct connection to a cathode contact-pad on the top of the chip.

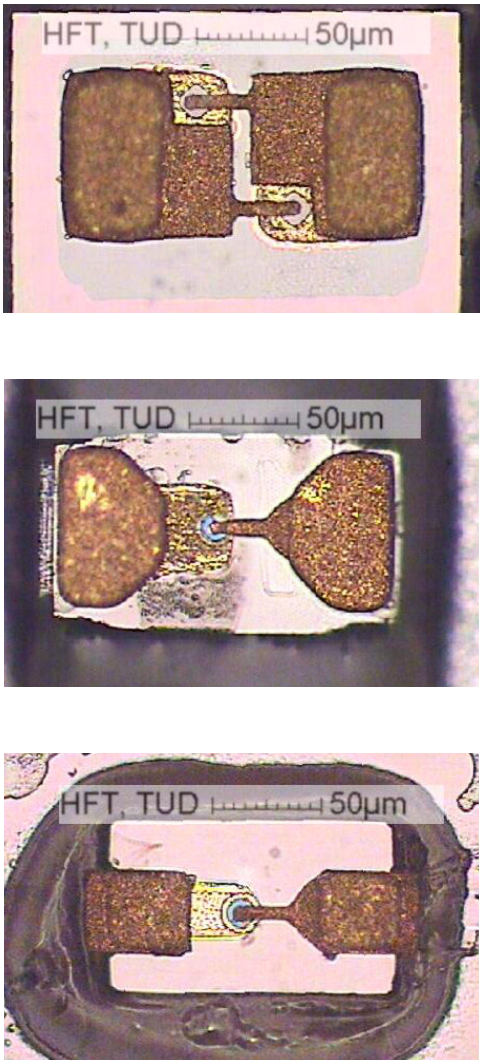

Fig. 2. Optical pictures of structures fabricated by first (a), second (b) and third (c) design versions.

III. Results and Discussions

A. First Design-Version.

The first-developed design of quasi-vertical structures includes both single diode (SD) and anti-parallel diode-pair (APD). However only an APD for frequency mixing application is considered in this work (Fig. 2a.). This structure was designed to be mounted in a subharmonically-pumped waveguide mixer operating at frequencies around 200GHz. For a minimum loss, the structure is carried out on a 8µm to 10µm thick semi-insulating GaAs-membrane. For a comparison to the sketch of a quasi-vertical structure illustrated in Fig. 1 a SEM picture of a mesa-region prepared by Focused Ion Beam (FIB) is shown in Fig. 3. Here one can distinguish a thin GaAs-mesa encapsulated between Au-air-bridge and a massive Au-bump of a back-side Ohmic-contact.

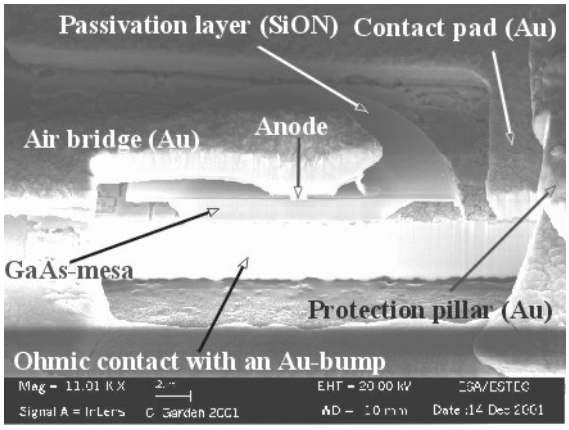

Fig. 3. SEM picture of an APD prepared by Focused Ion Beam (FIB).

Electrical parameters of this structure with an anode diameter of d=0.8µm are as follows: junction capacitance at 0V C_{j0}=1.6fF to 2.1fF (for two anodes switched in parallel), series resistance R_s<15Ω, ideality factor η<1.18, pad-to-pad capacitance C_{tot}=16fF to 18fF. These values resulted from various on-waver DC- and S-parameters-measurements and simulations.

In order to determine a complete S-Parameter matrix of the structure mounted in a waveguide, detailed simulations are performed in Electro-Magnetic Field-Solving software (HFSS). The structure is modelled entirely, including air bridges, mesas, embedded back-side Ohmic-contacts, oxide layers and GaAs substrate. In such a way an accurate analysis, including all parasitics is obtained. A non-linear diode simulation is performed in a Harmonic Balance analysis package (Microwave Office), where the S parameter file is imported from the HFSS-model. Diode-parameters such as C_{j0}, R_s η are varied to ensure the tolerance of the design to small changes of diode-parameters. For our simulations starting values as follows are chosen: C_{j0}=2.5fF, R_s=14Ω and η=1.2. Real diode-parameters can vary somewhat, however the chosen starting values are deliberately pessimistic.

The mixer is designed in such a way that the RF bandwidth is kept as large as possible and it typically achieves 25% at frequencies bellow 200GHz. For mixer fabrication, split-block technology was used with suspended substrate micro-strip technology for couplers and filters. This design allows easy assembly with minimal handling of the substrate and diode. Mixer blocks are lapped flat, the waveguide polished and electrochemically plated with gold for a minimum loss.
Just before mounting all diodes are tested on a Gel-Pack for good I-V-characteristics.

Several Mixers were made and measured at three frequencies, namely 140GHz, 150GHz and 183GHz. Measurements revealed broadly repeatable results of different mixers and their typical values are shown in Table I. Measurement results at 150GHz are rating along-side with the best achieved.

All mixers exhibit extremely flat sensitivity with IF frequency and a good IF match up to high IF frequencies (typically 16GHz).

TABLE I
TYPICAL VALUES OF THE MEASURED RESULTS

Frequency (GHz)	Conversion efficiency (dB)	Tsys (K)	Tmix (K)	LO Level (mW)
140	5.1(DSB)	940(DSB)	650(DSB)	3.5
150	5.8(DSB)	950(DSB)	650(DSB)	3.0
183	6.3(DSB)	1450(DSB)	870(DSB)	4.0
215 [5]	9.2 (SSB)	3500(SSB)	_	3.5

Our results compare well to those reported in [5] which are evaluated by another group and by different measurement set-up (also summarized in the Table I). This just confirms a very good diode performance at frequencies up to around 200GHz. However, the HFSS computer model pointed to parasitic capacitance of the structure being a significant limiting factor at higher frequencies, where additional inductive tuning devices have to be employed (reducing bandwidth). An increase in the required LO power for optimal pumping in our measurements and increasing conversion loss and noise temperature at 183GHz and 215GHz also suggest capacitance effects. Measurements of a similar structure in a 650GHz-mixer revealed poor results [6], which just confirms our assessments.

B. Second Design-Version.

The second quasi-vertical structure is designed for mixer and multiplier applications in the frequency range from 200GHz to 400GHz. In order to improve operational capability of the structure at higher frequency some changes in the design are implemented. The most significant of them in respect to the previous version are listed below:

- Pad-to pad capacitance is reduced in two ways: on the one hand pad area is reduced from 5 x 10^{-3} mm^2 to 3 x 10^{-3} mm^2; on the other hand the pads are chamfered;
- The GaAs-substrate is reduced down to 6µm...8µm
- The parasitic inductance of the bridge is considerably reduced since the bridge is shortened;
- Chip dimensions are also reduced (see Fig. 2 b).

S-parameter-measurements using a network analyser exhibited following electrical parameters: C_{j0}=1.3fF to 1.6fF, R_s<10Ω, η<1.18, C_{tot}=10fF to 12fF. Since a similar wafer is used for the diode fabrication, the ideality factor did not significantly change in comparison to previous structures, whereas R_s and C_{tot} are smaller and compare well to our simulation-results.

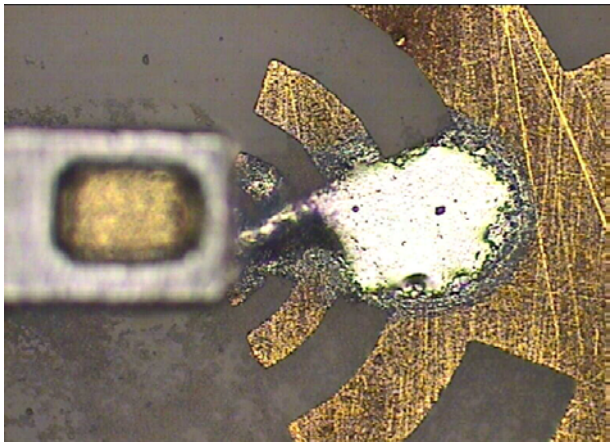

Fig. 4. Optical microscope picture of the soldered diode chip on an antenna arm.

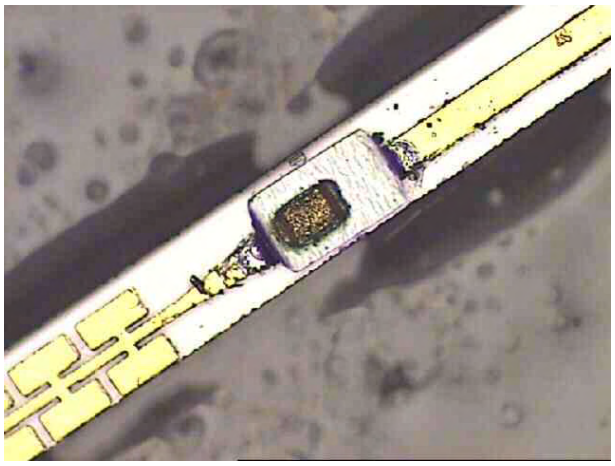

Fig. 5. Optical microscope picture of the soldered diode chip on filter-structure. The filter-substrate is glued with wax on a glass-carrier.

In order to check the quality of the Schottky-contact the low-frequency noise is measured by means of a HP 3562A Dynamic Signal Analyzer. The results show a 1/f-noise of these diodes of about $4\mu V/Hz^{1/2}$ at 1Hz under current bias of 1mA. The 1/f-noise value is bellow $100nV/Hz^{1/2}$ at frequencies above 500Hz.

For the evaluation of DC-performance of fabricated diodes a similar structure was centrally flip-chip-soldered with indium into waist of a circularly-toothed planar logarithmic-periodic antenna fabricated on a 50µm-thick fused-silica substrate, as shown in Fig. 4. The height of about 12µm moves the diode out of the microscope focus but the diode chip and the Au-bump of the back-side Ohmic-contact are still observable.

In such a way we fabricated a millimetre-wave power-detector. With this approach room-temperature sensitivities of more than 3000V/W are attained at frequencies between 75GHz and 95GHz [11]. These tests and attained results assume a very good quality of fabricated Schottky-contacts. The structure appears to be stable and withstood to handling and mounting procedures.

As a next step, being convinced in the Schottky-contact quality and the structure robustness, we proceeded to a high frequency test. For that we soldered a similar structure with indium on 40µm-thick quartz substrate with a previously defined filter structure as illustrated in Fig. 5. The filter-structure was embedded in a 600GHz heterodyne mixer. The mixer characterization included measurements of DC-performance and conversion loss. These measurements revealed a best value of voltage responsivity of 1690V/W at frequencies between 592GHz and 602GHz for a signal-power of 40µW [12]. To measure single sideband (SSB) conversion loss of the mixer we used an LO-power of 2.2mW at 600.5GHz and a RF signal-power of 40µW at frequencies between 592.0GHz and 601.5GHz. Best results showed an IF signal with a dynamic range of about 60dB and a conversion loss (SSB) of 9.4dB [12].

Unfortunately, noise characteristics of this mixer are not investigated yet. However, we performed microwave-noise measurements of several similar structures using a set-up described in [13]. Results showed typical values of the junction noise-temperature significantly lower than 300K at frequencies between 2.1GHz and 4.8GHz and at a bias current up to 3mA. A remarkable low microwave noise at high current-bias is suggested to be a benefit of quasi-vertical design [14].

C. Third Design-Version.

The third quasi-vertical structure is dedicated to operate in a 600GHz heterodyne mixer. For an irreproachable operation at this frequency requirements to the structure-parameters considerably increase. In order to minimise the total parasitic capacitance and the series resistance following changes in the design are made:

- The backside gold cathode and contact pads dimensions are further reduced.
- GaAs-substrate is replaced by AlGaAs-layer and the substrate thickness is reduced down to 4µm.
- The R_s of the Schottky contact is reduced by reducing the thickness of the active n-GaAs epi-layer.
- Chip dimensions are reduced as well (see Fig. 2c).

The structure was firstly simulated and the total capacitance was calculated using a 3D electromagnetic solver from CST (Computer Simulation Technologies). Accordingly to our simulations a total capacitance of the structure with an anode diameter of 1µm is C_{tot}=6.35fF. Then few structures were fabricated and the capacitance was measured using an network analyzer at 1GHz. An accurate measurement of such a small capacitance is not trivial. Nevertheless, it resulted in a C_{tot}<7fF, which well agrees with simulation results. On-wafer measurements and calculations exhibited structure-parameters shown in Table II under structure signed as 3/SD.

Comparing parameters of the third structure with those of the other two also summarised in Table II, one can observe a higher junction capacitance of the structure 3 in respect to that of the structure 2 whereas the anode diameters are the same.

TABLE II
TYPICAL PARAMETERS OF CONSIDERED STRUCTURES.

Structure version/typ	Series resistance Rs (Ω)	Ideality factor η	Anode diameter (µm)	Junction capacitance Cj0 at 0V (fF)	total capacitance Ctot (fF)
1/APD	< 15	< 1.20	0.8	1.6-2.1	16-18
2/SD	< 10	< 1.20	1.0	1.3-1.6	10-12
3/SD	< 7	< 1.25	1.0	1.8-2.3	< 7

Most probably this is due to a thinner n-GaAs active layer of the structure 3. The last is even thinner as depletion layer of the Schottky contact at 0V which probably result in a slightly higher ideality factor of the structure 3 in comparison to other two structures. A slight increase of the ideality factor does not significantly affect the mixer performance [15]. Instead, a significant decrease of the series resistance of the structure 2 is obvious. According to our computer model of a 600GHz mixer block, modelled by a 3D field solver Microwave Studio from CST, a variation of R_s with 2Ω may influence the mixer performance at 600GHz with approximately the same magnitude as the variation of the C_{tot} with 1fF does. A simple calculation reveals a gain of a thinner active layer as in the case of structure 3.

D. Monolithically-Integrated Structure.

According to our computer models any substrate is able to considerably increase the pad-to-pad capacitance of the structure. As is described bellow, even the 4µm-thick AlGaAs-membrane increases a total capacitance of our structure with up to 1fF which is already a significant value at THz-frequency. In order to exclude an additional capacitance and losses in an AlGaAs-membrane we proceeded to develop a monolithically-integrated diode with a transition-line and filter-structures on a quartz-substrate. An optical microscope picture of such a structure is shown in Fig. 5. Due to the structure height, the top details of the structure are out of the focus, however one can still distinguish the Au-cathode, mesa, air-bridge and protection pillars. Unfortunately, this structure is not characterized yet but since the anode fabrication technology does not significantly differ from that of the structure 3 we believe that their DC-characteristics are also comparable (see Table II). Our computer model (CST EM-Studio) of such a structure revealed a capacitance of C_{tot}=5.45fF for a structure with an anode diameter of 1µm (substrate and filters are not included). Reduction of the anode diameter considerably reduces C_{tot}.

IV. CONCLUSIONS AND OUTLOOK

The main conclusions on this work can be drawn as follows:

- Devices designed for operation at frequencies up to 200GHz were successfully fabricated and characterized at several frequencies. They demonstrated good mixer-performance at frequencies up to around 200GHz. However, at higher frequencies parasitic pad-to-pad capacitance becomes a significant limiting factor affecting structure performance.
- A second structure-version designed for operation at frequencies between 200GHz and 400GHz is successfully fabricated and characterized. A test in a 600GHz-mixer demonstrated good performance. Although the substrate is thinner these structures appear to be stable and withstood to various handling and mounting procedures. Various measurements revealed excellent quality of Schottky contact.
- A third version of quasi-vertical structure designed for operation in a 600GHz-mixer is also fabricated and partially characterized. Measured and calculated values of electrical parameters of this structure result in a calculated cut-off frequency of well above 3THz.
- A technology is developed for the fabrication of a monolithically integrated diode with transmission-line and filter structures on a quartz-substrate.

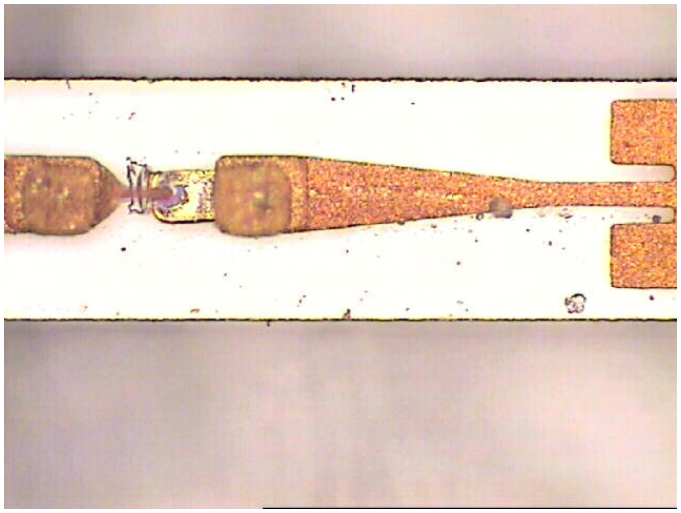

Fig. 5. A single monolithically-integrated diode with filter-structures and transition-line (not shown) on a quartz-substrate. The quartz-substrate dimensions are 40X120X2000µm.

Due to an apparent relatively high capacitance of back-side cathodes and the absence of a surface channel, quasi-vertical structures seemed to be not suitable for operation in a high-THz frequency-region side-along with surface-channel structures, described for instance in [16]. However, recently obtained measurement results at frequencies up to 600GHz are encouraging. Various computer models of a quasi-vertical structure suggest a possible reduction of the parasitic capacitance (junction capacity not included) to bellow 1.5fF for an APD and bellow 1fF for a SD. Monolithically-integrated structures (i.e. substrateless) can have even less capacitance without a significant increase of the inductance. Such a structure would have a cut-off frequency of above

7THz. However in order to demonstrate a full potential of this kind of structures additional investigations and technology developments are needed.

ACKNOWLEDGMENT

The authors want to acknowledge Mr. R. Zimmerman, A. Walber and H. Gibson Radiometer Physics GmbH (RPG) for qualitative mixer measurements and fruitful discussions.

The authors would like also to thank the company CST for providing the MST Microwave Studio and EMS electromagnetic Studio software packages.

This work was partly supported by European Space Agency (ESA) and Deutsche Forschungsgemeinschaft (DFG).

REFERENCES

[1] P.H.Siegel, R.P.Smith, M.C.Gaidis and S.C.Martin: *"2.5-THz GaAs Monolithic Membrane-Diode Mixer",* IEEE Transactions on Microwave Theory and Techniques, Vol.47, No.5, May 1999. pp. 596-604.

[2] K.Huber, R.Hillermeier, H.Brand, C.I.Lin, A.Simon, M.Rodriguez-Girones and H.L.Hartnagel: *"2.5THz Corner Cube Mixer with Substrateless Schottky Diodes"*, in Proc. of the 5th Int. Workshop on Terahertz Electronics, (Grenoble, France), 1997.

[3] D.S.Kurtz, J.L.Hesler, W.Growe and R.M.Weikle: *"Submillimeter-Wave Sideband Generation Using Varactor Schottky diodes"*, IEEE Trans. on Microwave Theory and Techniques, Vol.50, No.11, November 2002. pp. 2610-2617.

[4] Simon A, Grüb A, Krozer V, Beilenhoff K, and Hartnagel H L Proc. 4th Int. Symp. Space Terahertz Tech., Los Angeles, CA, USA,1993, pp. 392-403.

[5] V. S. Möttönen, P. Piironen, J. Zhang, A. V. Räisänen, C.-I. Lin, A. Simon and H. L. Hartnagel: "Subharmonic Waveguide mixer at 215 GHz utilizing quasivertical Schottky diodes", Microwave and Opt. Technol. Lett. Vol. 27, No.2, Oct. 2000.

[6] Progress reports #29and #30. ESTEC Contract N°11806/96/NL/CN.

[7] Final Report. ESTEC Contract N°11806/96/NL/CN.

[8] C. I.Lin et al., *"Substrateless Schottky diodes for THz applications"*, Proc. Eighth Int. Symp. on Space Terahertz Technology. Cambridge, MA: Harvard Univ., Mar. 1997.

[9] Cojocari O, Mottet B, Rodriguez-Girones M, Biber S, Schmidt L -P, Hartnagel H -L *"Whisker-device-based optimisation of fabrication process for planar THz Schottky diodes"*, Proc. 3rd ESA Workshop on Millimetre Wave Technology and Applications, 21-23 May 2003, Millilab, Espoo, Finland, pp. 255-260.

[10] O.Cojocari, B.Mottet, M.Rodriguez-Girones, S. Biber, L.Marchand, L.-P. Schmidt and H.L. Hartnagel *„A New Structural Approach for Uniform Sub-Micrometer Anode Metallisation of Planar THz Schottky Components",* Semocond. Sci. Technol. 19 (2004), 237-242.

[11] Cezary Sydlo, Benjamin Kögel, Oleg Cojocari, Hans L. Hartnagel and Peter Meissner: "Characterisation of a circularly-toothed planar logarithmic-periodic antenna for broadband power detection", Frequenz. 9-10/2004, pp. 207-210.

[12] J. Schür, S. Biber, O. Cojocari, B. Mottet, L.-P. Schmidt, H.-L. Hartnagel: "600 GHz Heterodyne Mixer in Waveguide Technology using a GaAs Schottky Diode", to be published in Proc. 16th Int. Symp. Space THz Technol. ISSTT-2005.

[13] Biber S, Cojocari O, Rehm G, Mottet B, Schmidt L -P, Hartnagel H L "A Novel System for Systematic Microwave Noise and DC Characterization of THz Schottky Diodes". IEEE Transactions on Instrumentation and Measurement, Vol.53, No.2, April 2004, pp. 581-587;

[14] O. Cojocari, S. Biber, B. Mottet, C. Sydlo, H.-L. Hartnagel and L.-P. Schmidt: "IF-noise improvement of the GaAs Schottky diodes for THz-frequency mixer applications", Proc. European Microwave Week 2004, pp. 211-214, RAI, Amsterdam, The Netherlands, 11-15 October 2004.

[15] Hugh. Gibson, Radiometer Physics GmbH (RPG), private communication.

[16] Imran Mehdi, Steven M. Marazita, Dexter A. Humphrey, Trong-Huang Lee, Robert J. Dengler, John E. Oswald, Andrew J. Pease, Suzanne C. Martin, William L. Bishop, Thomas W. Crowe, and Peter H. Siegel: "Improved 240-GHz Subharmonically Pumped Planar Schottky Diode Mixer for Space-Borne Applications", IEEE Trans. on Microwave Theory and Techniques, Vol. 46 No. 12, Dec. 1998, pp. 2036-2042.

600 GHz Heterodyne Mixer in Waveguide Technology using a GaAs Schottky Diode

J. Schür[1], S. Biber[1], O. Cojocari[2], B. Mottet[2], L.-P. Schmidt[1], H.-L. Hartnagel[2]

[1] Institute for Microwave Technology (LHFT), University of Erlangen-Nuremberg, Cauerstr. 9, 91058 Erlangen, Germany, and
[2] Institut für Hochfrequenztechnik, Technische Universität Darmstadt, Germany

e-mail: jan@lhft.eei.uni-erlangen.de

In this paper we will present first measurement results for a 600 GHz heterodyne mixer in split-block waveguide technology. In this mixer design we use a planar GaAs Schottky diode which is flip-chip mounted on a quartz substrate. The split-block structure includes an octagonal horn antenna to feed the signal and local oscillator into the split-block mixer, a waveguide to microstrip transition and coaxial IF output. In addition to the GaAs diode the quartz substrate also includes the required filter structures and DC bias supply. Figure 1 shows the split-block mixer with the mounted octagonal horn antenna.
We will present the field simulations for the designed mixer and compare the results to scaled model measurement at 11 GHz.
The main focus of this paper will be the characterization of the device in both detector and mixer operating mode. First measurements have been carried out in a quasioptical setup using a backward wave oscillator (BWO) to determine the detector characteristics. These measurements show voltage responsivities of over 350 V/W at 625 GHz.
Using a Gunn oscillator based multiplier chain (75 GHz x2 x4) as a signal source and a BWO at 600 GHz as local oscillator we measured an IF signal at 5 GHz with a signal-noise ratio of about 50 dB. A preliminary estimation of the conversion loss of the mixer is less than 22 dB.
Figure 2 shows the IF output spectrum of a 605 GHz signal. In this experiment the signal power was less than -10 dBm.
For further optimization of the mixer we will implement an enhanced diode layout with reduced diode parasitics. For this reason the GaAs diode will be directly integrated on the quartz substrate which carries the waveguide to microstrip transition and the filter structures. We expect a noticeable reduction of the diode parasitic capacitance and a reduction of the series resistance.
Detailed noise characterizations and conversion loss measurements will be presented.

Figure 1: 600 GHz split-block mixer

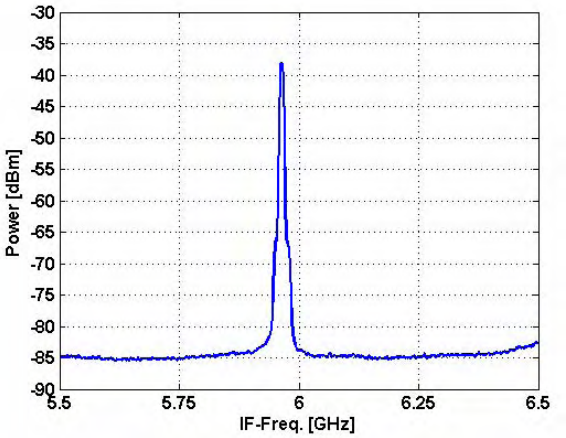

Figure 2: IF spectrum of a 600 GHz signal

Session 11:

Components

Wednesday May 4, 10:15-12:00
Chairman: Alexandre Karpov

A TES Finline Detector for Bolometric Interferometry

Louisa Dunlop*, David Goldie*, Stafford Withington*, Dorota Glowacka* and Ghassan Yassin†
*Detector Physics Group, Cavendish Laboratory,
University of Cambridge,
Madingley Road, CB3 0HE, UK
† Department of Physics, University of Oxford, Denys Wilkinson Building,
Keble Road, Oxford, OX1 3RH, UK

***Abstract*— We present work on a highly unusual single-chip antenna-coupled bolometric interferometer for high performance applications at 150 GHz. The design of the detector is suitable for many areas of astronomical research ranging from Sunyaev–Zeldovich (SZ) mapping through to B-mode polarisation measurements of the CMB. The design employs corrugated feedhorns for coupling the astronomical signal to the detectors. This arrangement provides a well–collimated beam with low side lobes and low cross polarization. Two back-to-back finline tapers couple the incoming waveguide modes to a single chip, where a miniature microstrip hybrid coupler and pair of Mo/Cu microstrip coupled TES detectors are located. The scheme overcomes mechanical restrictions associated with the geometry of the waveguide. Numerous extensions to the basic technique are now possible.**

I. Introduction

Low temperature TES detectors are widely used for ground, balloon and satellite based millimetre and sub millimeter wave astronomy. The current state of the art technology is to develop microstrip coupled TES detectors [1]. Here at Cambridge we offer the next stage polarisation detector that employs these detectors in an interferometric arrangement. This will be be useful for high performance applications in many different areas of research including: SZ mapping, where for the thermal SZ one sees a significant decrement in Intensity, interferometric mapping of dust at wavelengths between 3mm and 300μm and CMB B-mode polarisation measurements.

With our design we demonstrate how it is possible to construct a single chip interferometer based on known SQUID and TES technology. The detector chip and block designs are based on our finline mixer work that has been reported in several publications [2]. Our scheme will produce cos and sin fringes directly and with a slight modification could be used for single chip polarimetry. This is an extremely versatile design that will benefit many areas of astronomy in the future.

II. The single chip Interferometer

In the first phase of the project, the two element interferometer comprises of two identical broadband corrugated horn antennas machined into an aluminium spilt-block. The chip sits in a recess in the chip block. A schematic view of the chip is shown in Fig.1. The signals from the two horns are fed to a back-to-back finline taper that transforms the waveguides into niobium superconducting microstrip. The two inputs from the opposite microstrips are then combined by a 4-port 180° hybrid that provides the sum ($E_1 + E_2$) and the difference ($E_1 - E_2$) at either output [3]. Each output is transferred via microstrip to a matched resistor that lies on the TES membrane. The RF power is converted into heat, which causes a sharp increase in the Voltage Biased TES resistance. This reduces the bias current which is read by a Superconducting Quantum Interference Device (SQUID). Transferring the signal from waveguide to microstrip allows the circuitry to become independent of the waveguide geometry, therefore the substrates size and shape between the tapers are now restricted only by the TES and miniature microstrip hybrid coupler.

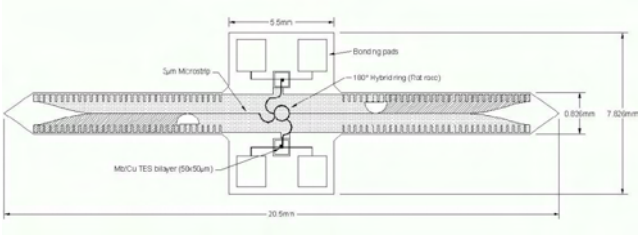

Fig. 1. The Design for the chip as created on AutoCAD. This shows the layout of all the components that will be processed using lithography techniques.

A. Feed horns

The corrugated feed horn selects the HE_{11} mode which provide a symmetric main beam with a low side lobe response. The Gaussian beam mode diffraction method is suitable for sub mm beam characterisation. This method of analysis provides a reasonable understanding of the profile of the beam throughout the system and allows the element sizes and beam pattern to be calculated using simple formulae [4]. Corrugated feed horns have been designed using the software CORRUG. They possess a 12 degree pitch angle and have a return loss of -22.9 dB at 150GHz. There is excellent matching between the E and H Plane in this design shown in Fig.2. A disadvantage of the Gaussian Beam assumption is that the beam is not of infinite extent, therefore the effect of the aperture on the beam must be considered and this is discussed in [5].

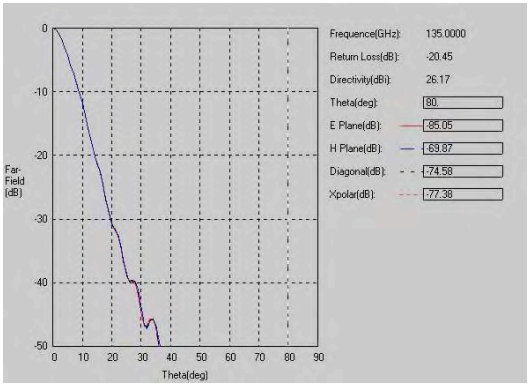

Fig. 2. A diagram to show the beam pattern of our corrugated horn feed.

B. Finline Taper

The antipodal finline taper allows the merger of two desirable techniques for our detector. Transforming the waveguide into microstrip not only allows the implementation of high performance horns but also enables the electromagnetic design from finline to detector to be fabricated using planar circuit technology. This creates a highly reproducible technique that will be required to allow compact packaging of detectors with increasing and variable baselines which will, as a consequence, increase the sensitivity of the device. The finline taper is constructed from two superconducting niobium films that are deposited on one side of a silicon substrate and are isolated by a $400\,\mathrm{nm}$ SiO_2 layer. Before the fins overlap the SiO_2 is significantly thinner than the Si wafer, therefore the transmission line behaves as a unilateral finline on a Silicon substrate. At this stage the impedance is several hundred ohms [2] assuming a dielectric constant of Si and SiO_2 are 11.7 and 3.8 respectively. As the fins overlap the structure behaves like a parallel plate waveguide with an effective width equal to the overlap region. As soon as the overlap is significant, fringing can be ignored and the fins can be tapered to form microstrip. At this stage it is the SiO_2 that determines the electrical properties of the microstrip. For a microstrip width $w \approx 3\mu$m and a thickness $t \approx 400$nm we obtain an impedance value $Z_0 \approx 20\Omega$. A circular arc transforms the antipodal finline to microstrip by extending the base fin to form the ground plane at the same time as tapering the top fin inwards until a width of 3μm is achieved. The finline design, a combination of the unilateral, antipodal and circular arc sections, is displayed in Fig.3. It should be noted that even with the use of the optimum

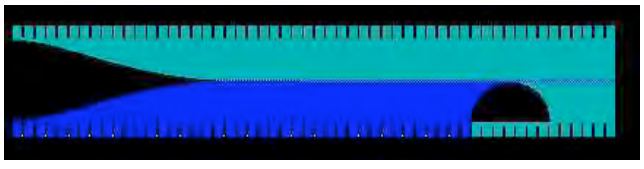

Fig. 3. The completed finline constructed with the use of 4 programs in total, 3 existing Fortran 77 programs and one written in the C programming language.

taper method, where the coupling coefficient is minimised between the incident and reflected waves in the z-direction, there may be reflections from the front surface of the chip. This may be minimised with the use of a quarter wave transformer. In our design a 0.5 *mm* high triangular section was designed and was successfully fabricated.

C. The 180° Hybrid Ring and the matched resistor

The Rat Race hybrid ring was chosen over the Wilkinson combiner for its ease of processing (i.e. no resistors) and because it is ideal for our geometry that employs two TES detectors. The hybrid produces the required output with a low return loss, although over a relatively narrow bandwidth. It consists of a 4-port network made of microstrip that has a 180° phase shift between the two output ports [3].

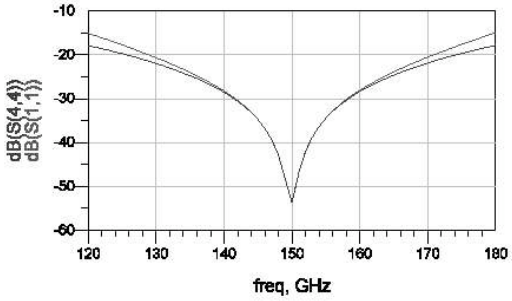

Fig. 4. The Reflection parameter (S11) of the rat race as simulated using ADS.

The ring has impedance $\sqrt{Z_0}$ where Z_0 has a value of 20 Ω. This requires a microstrip of width, $W \approx 2\mu$m, in the ring. When ports 2 and 3 are used as the inputs of the rat race then the outputs provide a combined signal. The sums and differences of the inputs are taken at ports 1 and 4 respectively. The rat race was modelled using Automated Design System (ADS) and was found to provide a bandwidth of around 30GHz, shown in Fig.4. The bandwidth could be extended further if required with the addition of extra rings. The two outputs from the combiner are taken to opposite sides of the chip by two superconducting microstrips that reach the TES membranes where each is terminated by a matched resistor close to a TES. Optimising the space available on the TES island, ensuring minimal reflection and the feasibility of processing were important considerations when designing the resistor termination. The resistor was modelled using Sonnet em software. For z=24.5Ω and a 3 μm wide Gold/Copper resistor with a resistivity of $1.02\pm0.18\times10^{-7}$ and a thickness of 42nm, a length of 30.5mm is required.. The simulation confirmed that good termination is possible providing a return loss of around -20dB at 150GHz.

D. Cryostat

A Janis Liquid Helium Dewar hosts a 3 stage Sub-kelvin Helium 3 cooler developed by Chase Research Cryogenics Ltd. The Dewar has a nitrogen and helium reservoir both

of which are surrounded by a vacuum in order to isolate the reservoirs from room temperature. The interior of the Dewar is constructed from Stainless steel which has a low thermal conductivity and is extremely robust, therefore it can withstand many cycles between room temperature and helium temperature. The Chase fridge contains a sealed ^{3}He system. The ^{4}He is transferred to the ultrahead and cools it to 4K then the charcoal pump is cooled to below 20K and absorbs the ^{4}He. This decreases the pressure and cools the fridge to its condensation point.It is important that all the ^{4}He is depleted otherwise the ^{4}He will form a super-fluid and will have a negative effect on the performance of the system. Next the ^{3}He is released into the inner chamber of the ultrahead. The charcoal is used in the same way until the desired temperature is reached at which time the charcoal temperature is once again increased. The hold time before all of the liquid ^{3}He has boiled off is 7 hours. Thermal straps are required as a thermal link to the chase fridge which will reduce and sustain the temperature of the chip block at around 250mK. The metal surfaces of the table and the chip block are gold plated to ensure good thermal contact and low emissivity. Low Pass filters are placed on the radiation shields and on the table to prevent the transmission of the Blackbody radiation at high T. This is achieved by controlling the wavelengths of the radiation that pass. The window is constructed from a 1.3mm thickness of high density polyethene that has a 100% transmission at 150GHz [5]. The magnetic shielding is an important feature

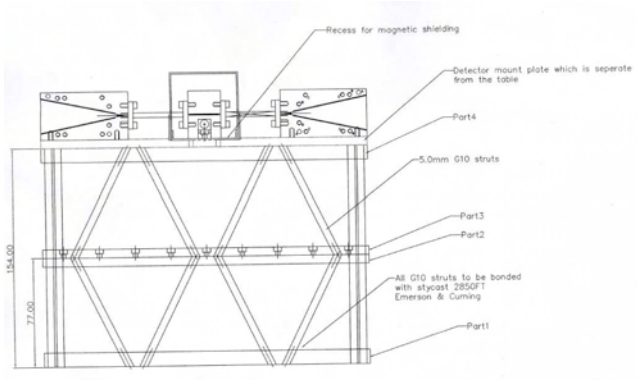

Fig. 5. A CAD drawing of the cryostat interior.

of the design because it prevents external magnetic fields from penetrating the TES bilayer. The attenuation of a magnetic field can be accomplished by inserting a screen made from a magnetic material with a high permeability ($\mu \gg 1$) between the source and the sensitive component. The inner field is reduced because the external magnetic field tends to remain in the magnetic layer of the shield because it offers a low-reluctance path. The shielding factor of the magnetic shield is defined as,

$$S = \frac{H_a}{H_i}, \tag{1}$$

where H_a is the external field strength and H_i is the residual internal field strength. It is typical to calculate a shielding factor for a sphere or a cylinder however these shapes are not always the most practical. It was decided that a cuboid structure was best suited to our design, however it was noted that magnetic flux lines prefer not to turn by 90 degrees and a cylindrical or spherical shape would have been more efficient at restricting the magnetic field. The shielding effect of a cube with edge length a is,

$$S_c = \frac{4}{5}.\frac{\mu_r.d}{a} + 1, \tag{2}$$

This is an average shielding factor, with the value of S less in the centre compared to at the edges; therefore the smaller the value a, the better. The geometry of the shield is kept simple in order to ensure magnetic continuity i.e the flux can continue along the low reluctance path. Our design incorporates a base tray that will hold the cuboid shield. This then allows the structure to be secured on the bottom edge. The design aims to minimise the number of openings and only contains unavoidable openings where necessary, for example the waveguide and thermal straps must pass through to the rest of the system. The cuboid structure can be slid over the waveguide by cutting two slits in opposite sides of the box. An external cover will be fixed to cover any unnecessary gaps. For our shield we have chosen to use Cryoperm 10. This is an ideal material for our application because its permeability increases with decreasing temperature. The influence of openings has been studied closely for common magnetic shield shapes like the cylinder. We have calculated an approximate value for the cuboid structure that follows the previous work by Vacuumchmetlz. The exponential relationship between the field and the distance travelled past the gap is also an important consideration. It is generally accepted that a 3/1 ratio of gap diameter and length of shield is the best for this application. Our Shielding factor has been calculated to be 1217.39 ignoring holes, but a more realistic worse case scenario is of the order 577. This gives an internal field of 0.097 $\frac{A}{m}$. inserting multiple magnetic shields would increase the shielding factor and as a consequence decrease the internal magnetic field. The shield is mounted on a copper strip of width 48mm and depth 6mm which is itself mounted on a custom built table. The copper strip will also be cooled to the required temperature by two straps that are linked to the chase fridge.

III. Detector Readout

A. Introduction

The TES is a $50 \times 50\mu\text{m}^2$ superconducting molybdenum/copper film of thickness 40nm and 30 nm respectively, deposited on a 1μm membrane of silicon nitride. A constant voltage source is used to bias the device in the middle of the transition between the normal and the superconducting states. Incident RF power creates a small increase in the device temperature which causes a large change in resistance allowing the detection of very weak signals.

$$\alpha = \frac{d(logR)}{d(logT)}. \tag{3}$$

Figure 6 shows how we model the TES as a variable resistor

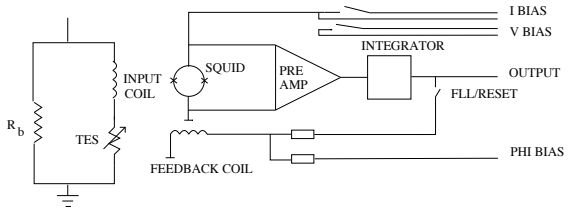

Fig. 6. A diagram to show the set up of a TES with ETF.

in a voltage bias circuit. The constant bias voltage leads to an Electro-Thermal Feedback signal (ETF) that keeps the device biased in the middle of the transition. This occurs because increasing the resistance of the TES decreases the bias current and therefore the bias power, keeping the detector at a constant temperature. The signal is then detected as a reduction in the bias current which is read by a SQUID. We are in the process

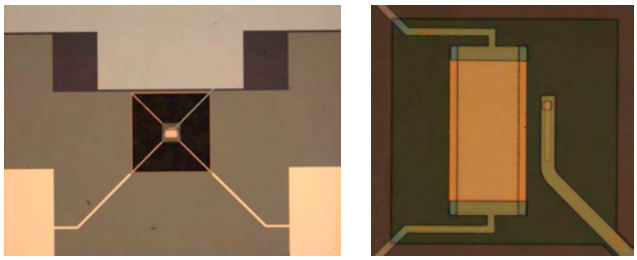

Fig. 7. (Left) The TES membrane is the central region on the plot. The length of the thermal links are 350 μm each. We have experienced signifi cant success with the processing of the membrane using our wet etching tecnique which utilises 20% KOH at 80°C. (Right) The TES detectors have been successfully fabricated in our laboratory. The Au/Cu termination resistor, the niobium bias lines and the copper banks can be seen clearly.

of fully characterising the noise associated with our system. We expect our results to match noise theory [6]:

$$\begin{aligned} NEP^2 &= NEP_{ph}^2 + NEP_{jn}^2 + NEP_{sq}^2 + {NEP_{\text{excess}}}^2; \\ NEP_{ph}^2 &= \gamma 4kT_c^2 G, \\ NEP_{jn}^2 &= \frac{4kT}{\mid Si \mid^2 R}\left(\frac{\tau}{\tau_0}\right)^2\left(\frac{1+\omega^2\tau_0^2}{1+\omega^2\tau^2}\right), \\ NEP_{sq}^2 &= \frac{i_{squid}^2}{\mid Si \mid^2}, \end{aligned} \tag{4}$$

where γ is a factor that takes into account the temperature gradient along the thermal link, G is the thermal conductance and Si is the responsivity of the TES. The terms in the above equation represent the phonon noise, a consequence of thermal fluctuations between the the TES and the heat sink, Johnson noise, SQUID noise and excess noise associated with the system. The SQUID noise is a measure of the noise associated with the readout including the SQUID and the pre-amplifier. Assuming that the detector is phonon noise limited reduces equation (4) to,

$$NEP^2 = \gamma 4k_b T_c^2 G(T_c). \tag{5}$$

Since γ remains constant, The NEP_{phonon} depends strongly on G and T_c . This implies that G must have an optimum value to obtain the best NEP of the device. If the value for G is too low the TES heats up increasing the undesired phonon noise. The temperature dependence of the conductance is given as,

$$G = nKT^{(n-1)}, \tag{6}$$

and the power flow equation is given as

$$P = K(T_c^n - T_b^n). \tag{7}$$

The minimum NEP can be obtained when $T_c \approx 2T_b$ where T_b is the temperature of the heat bath. An expression for the optimum $G(T_c)$ is given as,

$$G_{opt}(T_c) = \frac{n}{1-\left(\frac{T_b}{T_c}\right)^n}\frac{\beta P_{opt}}{T_c}, \tag{8}$$

where,

$$\beta - 1 = \frac{\frac{V_b^2}{R}}{P_{opt}}, \tag{9}$$

which depends on the ratio of Joule heating to background power heating. This value is predicted to be $250\frac{pW}{K}$ where P_{opt} =10pW, $T_c = 440mK$, n≈3 and β =3. The SQUID is a flux to voltage converter and will be used to read out the minute changes in current from the TES. A SQUID consists of two resistively shunted josephson junctions on a loop of superconducting inductance, L. In a closed loop made of superconducting material, the flux is quantised. The periodicity of the quantization is known as the flux quantum and is given as $2.07\times10^{-15}Wb$. When there is zero flux present a constant bias current, I_b is applied to the SQUID that divides equally between the junctions. When a current passes through the input coil, see Fig.6, magnetic flux is induced through itself and the SQUID, Φ_0. This generates a current in the loop of the SQUID that adds to the bias current in one junction and subtracts it in the other. The resulting flux in the SQUID is converted into a signal voltage, $V_s = \Phi\frac{dV}{d\Phi}$. This voltage is amplified and then passed through a feedback resistor and the resulting current flows though a feedback coil and causes a feedback flux, $-\Phi_F = -MI_F$ in the SQUID, where M is the mutual inductance between the feedback coil and the SQUID. The feedback flux cancels the external flux allowing the SQUID to act as a null detector [7].

IV. Preliminary noise and Dark NEP measurements

Initial measurements of our TES detectors have been carried out in an Oxford Instrument Heliox that has a base temperature of 250mK and multiple superconducting and Cryoperm shielding to reduce the incident magnetic field. We are using SuperSQUID designed by Polushkin et al [7] and fabricated by ourselves in the Detector Physics groups clean room facility at the Cavendish Laboratory. The input coil is coupled to the SuperSQUID with a mutual inductance of 25pH and the feedback coil has a mutual inductance of 0.75pH. The large V$-\phi$ and low noise pre–amp give a current noise $< 1\frac{pA}{\sqrt{Hz}}$

and a bandwidth in excess of 1MHz in the Flux Locked Loop mode. The circuit in Fig.6 was constructed and a

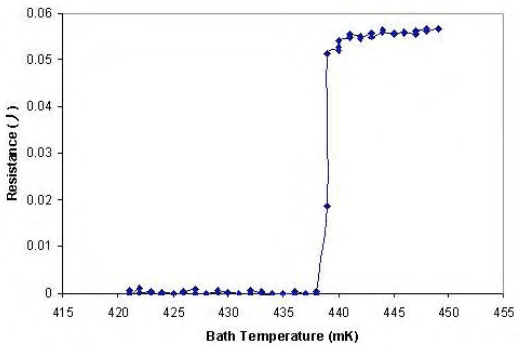

Fig. 8. A plot of the Resistance against Temperature for our 176_2 TES detector.

set of IV curves of varying input bias voltages were taken to provide the relationship between power and temperature. Plotting power against the bath temperature, Fig.9, allowed us to determine the key parameters associated with the power flow (7). From the results K and n were calculated to be 490 $\frac{pW}{K^n}$ and 2.95 respectively. A transition temperature of 440mK is displayed on our resistance against temperature plot in Fig.8. The thermal conductance for our Mo/Cu TES detectors, that are positioned on a 1μm of silicon nitride, is given by (6) [8] and using the variables above is calculated to be 291pW/K for a transition temperature of 440 mK. These measurements have been obtained for a membrane with thermal bridges of width 14μm and length 350μm. Work on the time constant for this device will be presented shortly. Noise characteristics of the

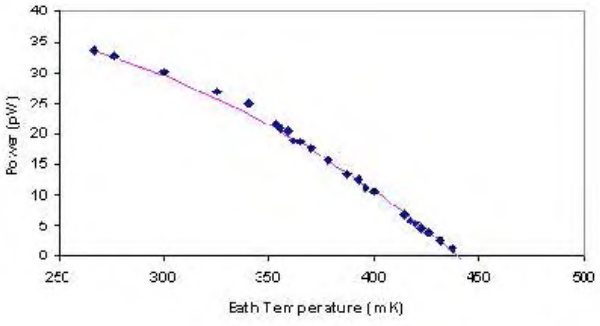

Fig. 9. A plot of the power flow against bath temperature.The points are the measured data and the line is the predicted values using equation (eq:power).

device, Fig.10 allow us to independently determine the NEP of the TES to be $4.5 \times 10^{-17} \frac{W}{\sqrt{Hz}}$ which agrees well with the value calculated substituting our value of G into (5). We are currently developing theoretical models that will complement a variety of our results.

V. Discussion

We have presented the design of a two element bolometric Interferometer that employs antenna coupled TES detectors

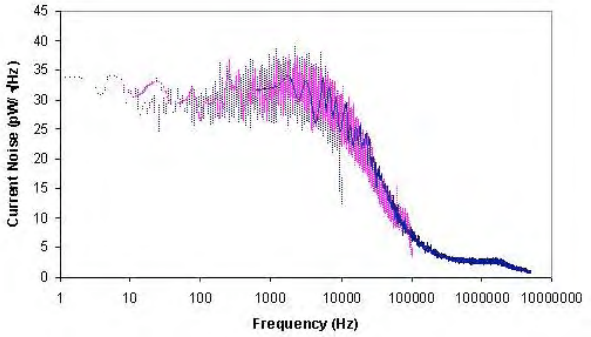

Fig. 10. Dark Current noise measurements of our 176_2 Mo/Cu TES detector for varying filter cutoffs of 10k, 100k and fout which had zero artificial frequency cutoff. Data is taken for a bias voltage of 1.2 μV at 251mK.

and corrugated horn feeds for good beam circularity and low cross polarisation. Development of the device and the test system is well advanced and we have a reproducible technique for the processing of sensitive TES detectors.

Future work will include the development of microstrip filters that will be inserted between the antenna and the TES. This will replace optical filters that are mounted on the cryostat.

References

[1] M. Yun *et al.*, "Fabrication of antenna-coupled transition edge polarization-sensitive bolometer arrays," *Nuclear Instruments and Methods in Physics Research A*, vol. 520, pp. 487–489, 2004.

[2] G.Yassin *et al.*, "A 350- ghz antipodal finline mixer," in *Proc. IEEE Transactions on Microwave Theory and Techniques*, vol. 48, April 2000.

[3] D. M. Pozar, *Microwave Engineering*, 2nd ed. New York: John Wiley & Sons inc, 1998.

[4] T. Edwards and M. Steer, *Foundations of Interconnect and Microstrip Design*, 3rd ed. John Wiley & Sons Ltd, 2000.

[5] P. F. Goldsmith, *Quasioptical Systems*. IEEE Press/ Chapman & Hall Publishers Series on Microwave Technology and RF, 1998.

[6] S.Lee *et al.*, "Voltage-biased superconducting transition-edge bolometer with strong electrothermal feedback operated at 370mk," *Applied Optics*, vol. 37(16), June 1998.

[7] V. Polushkin *et al.*, "A tightly coupled dc squid with an intermediary transformer," *Physica C*, vol. 72, 1998.

[8] M. Leivo and J. Pekola, "Thermal characteristics of silicon nitride membranes at sub-kelvin temperatures," *Applied Physics Letters*, vol. 367, 2002.

Quantum Dot detector for a Passive Terahertz Imager

P Kleinschmidt[1] , H Hashiba[2], S Giblin[1], A Tzalenchuk[1], S Komiyama[3,*], V Antonov[2]

[1] *National Physical Laboratory, Hampton Road, Teddington, Middlesex TW11 0LW, England*
[2] *Physics Department, Royal Holloway University of London, Egham, Surrey TW20 0EX, UK*
[3] *Department of Basic Science, University of Tokyo, Komaba 3-8-1, Meguro-ku,Tokyo 153-8902, Japan*
** CREST. Japan Science and Technology Corporation (JST), Kawaguchi-shi, Saitama 332-0012, Japan*

To implement a Passive Terahertz Imager probing natural terahertz radiation of an object at room temperature, one need a low temperature detector of high sensitivity, with NEP better than ~ 10^{-19} $Watt/\sqrt{Hz}$. We have designed and tested such a detector. It is based on a lateral semiconductor Quantum Dot (QD) capacitively coupled to a metallic Single Electron Transistor (SET), Fig 1. The QD is an efficient trap for terahertz radiation due to Koch mode plasma resonance. If the potential barriers forming the QD are tuned to a few meV, the plasma oscillations, caused by the photon absorption, quickly decay by the excitation of a small number of electrons out of the QD. These charge excitations of the QD is capacitively coupled to the SET, and detected as telegraph-type switches in its conductance, Fig. 2. We have studied detector at different parameters of the QD and at different temperatures, ranging from 30 to 300 mK. An estimated NEP is ~ 10^{-20} $Watt/\sqrt{Hz}$ at 30mK, which does not change substantially with the temperature elevated to 300 mK. A simple handling and a moderate demands on the fabrication process, combined with flexibility in the design make this detector a good candidate for a Passive Terahertz Imager.

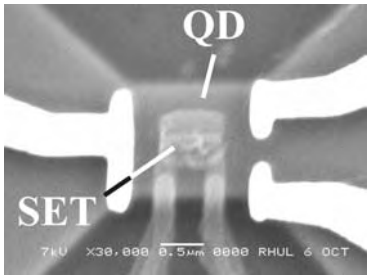

Fig.1 SEM picture of the QD detector. QD is formed by pinch-off of a mesa channel.

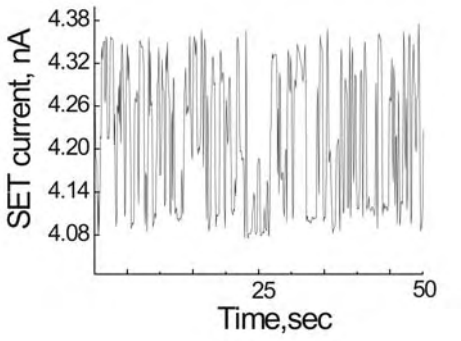

Fig. 2 Telegraph type switches of SET current under radiation.

Noise Bolometer for Terahertz Waves

Alexei Semenov, Heiko Richter, Heinz-Wilhelm Hübers, Konstantin Il'in, Michael Siegel,

Andreas Engel

***Abstract*—An advantage of superconducting detectors is a much lower noise in comparison to their semiconductor counterparts. We have studied the magnitude and spectrum of electric noise in thin superconducting NbN nanostrips carrying a subcritical current. Analysis of the experimental data suggests that the noise appears due to fluctuations in the two-dimensional vortex gas below the Kosterlitz-Thouless phase transition. Implementing this approach to the noise mechanism, we proposed a novel detector. The novelty is the use of the noise, which generally hampers the performance of conventional detectors, as the physical quantity that itself senses radiation. Our detector patterned from a thin NbN superconducting film and integrated in a planar log-periodic antenna. The detector operates at 4.2 K in the current-carrying superconducting state. Optically measured noise-equivalent power amounted at 10^{-13} W / Hz$^{1/2}$ and is likely to improve at lower temperatures.**

***Index Terms*—Noise in superconductors, nonequilibrium superconductivity, Superconducting terahertz and submillimeter wave detectors.**

I. Introduction

THERE have been several superconductor detector technologies for THz-frequency range successively developed during the last decade. Transition edge microbolometers [1] working at millikelvin temperatures provide a lowest noise equivalent power (NEP) of 10^{-18} W/Hz$^{1/2}$ along with the 100-millisecond time constant. Hot-electron detectors [2], although less sensitive, are much faster since their response is controlled by electron-phonon interaction. The strength of this interaction and, consequently, the response time, can be varied [3] via controllable disorder. Superconducting kinetic inductance detectors [4] are supposed to achieve background limited NEP if they would operate at a very low temperature with a low-noise SQUID pre-amplifier. Superconductor-Insulator-Superconductor (SIS) and Normal (metal)-Insulator-Superconductor (NIS) direct detectors have been also proposed. A noise equivalent power of 10^{-15} W/Hz$^{1/2}$ at 4 K [5] and 10^{-17}-10^{-18} W/Hz$^{-1/2}$ at 100 mK [6] was estimated for SIS and NIS direct detectors, respectively. For all these sensors, an electrical noise of any type hampers the ability of a sensor to detect radiation. In an ideal detector, fluctuations of the background radiation dominate over other noise sources. In practice, the detector itself and a pre-amplifier generate at least a part of the noise. A concept of the noise bolometer has been recently proposed [7] in that a detector senses radiation via radiation induced changes of its own electrical noise. Somewhat analogous, a temperature dependence of the fundamental Johnson noise has been used [8] for thermometry.

In this paper we present experimental evaluation of a noise bolometer and estimate its ultimate performance.

A. Semenov, H. Richter and H.-W. Hübers are with the DLR Institute of Planetary Research, 12489 Berlin, Germany (Corresponding author A. Semenov, e-mail: Alexei.Semenov@dlr.de).

K. Il'in and M. Siegel are with the Institute of Micro- and Nanosystems, University of Karlsruhe, 76187 Karlsruhe, Germany.

A. Engel is with the Physics Institute, University of Zürich, 8057 Zürich, Switzerland

II. Detector Design and Experiment

The detector is a 80 nm wide meander line made from a 5 nm thin superconducting NbN film (as shown in Fig. 1). It operates deep in the superconducting state and carries a supercurrent slightly less than the critical current. Radiation couples with the detector via an immersion lens and a planar log-periodic antenna, which jointly define the useful spectral range from 1 to 5 THz. The current RF noise was recorded at a frequency of 3 GHz in a hundred megahertz band. The noise equivalent power was evaluated for the signal produced by alternating thermal loads (300 & 77 K) at the detector input. At an ambient temperature of 4.2 K measured noise-equivalent power amounted at ≈ 10^{-13} W/Hz$^{1/2}$ while a time-constant of approximately 250 ps was anticipated.

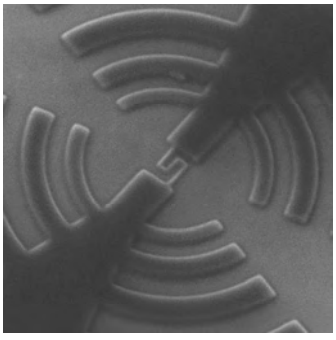

Fig. 1. Microphotograph of the NbN meander line incorporated into the planar log-periodic antenna.

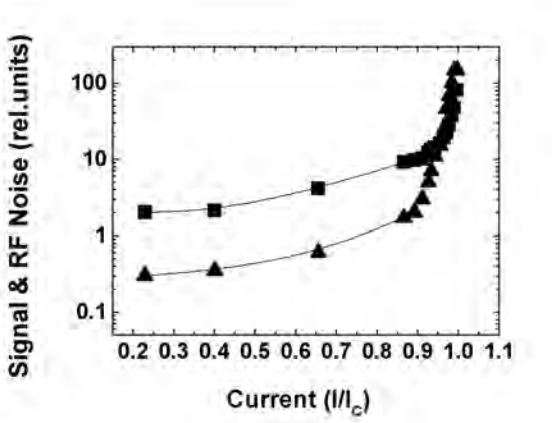

Fig. 2. RF noise (squares) and the signal (triangles) as function of the bias current. Both measured at 4 K.

The sensitivity of the detector is limited by statistical variations of the noise power. Assuming that the time variations of the spectral power density are totally uncorrelated, the dispersion of the noise power can be found with the radiometric equation as $\delta P_\omega \approx P_\omega (B\, t_0)^{-1/2}$ where P_ω is the mean value, t_0 is the integration time and B the bandwidth. The noise equivalent power for the detector is then $NEP = \delta P_\omega / (\mathrm{d}P_\omega / \mathrm{d}W)$ where W denotes the radiation power at the detector input. Fig 2 shows the signal due to alternating hot/cold load and the mean RF noise power as function of the bias current. Both the signal and the noise demonstrate similar variation resulting in a practically frequency independent noise equivalent power.

III. Noise Appearance & Mechanisms

Noise of a superconducting current-biased meander appears as a sequence of random voltage pulses. When measured with a broad-band microwave amplifiers in series with a band-pass filter, it causes additional microwave power. If measured with an integrating low frequency voltmeter, the noise causes a non-zero dc voltage over the nominally superconducting structure. The shape of the superconducting transition and the current and temperature dependence of the noise pulse rate in our meanders are best understood when fluctuations in the gas of magnetic vortices are taken into account [9]. Below the two-dimensional Kosterlitz-Thouless transition, almost all vortices are bundled into vortex-antivortex pairs. The binding energy of a pair depends on its orientation with respect to the current and has a current dependent minimum value E_{VP}. The process of unbinding can be seen as a thermal excitation across this energy. Free partners of a vortex-antivortex pair are driven apart by the Lorentz force F_L exerted by the bias current (Fig. 3). Vortex motion (even over a distance smaller than the strip width) produces a change in the superconducting phase difference between the strip ends and, consequently, a voltage pulse. The rate of these events is proportional to the thermodynamic probability of pair

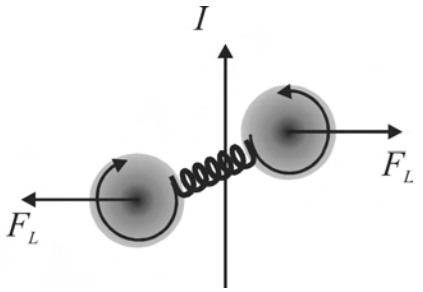

Fig. 3. Schematics of the current-induced unbinding of a vortex-antivortex pair. Unbinding force peaks when the pair is oriented normal to the current.

unbinding and depends on the fractional bias current I/I_C and material parameters A as

$$N \propto \exp\left(-\frac{E_{VP}}{k_B T}\right) \propto \left(\frac{I}{I_C}\right)^A; \quad E_{VP} \approx A \ln\left(\frac{I_C}{I}\right)$$

It has been shown in [7] that, due to an exponential temperature dependence of the recombination time, NEP of the detector using this noise mechanism should scale as $T \exp(\Delta / k_B T)$. Estimates for our NbN detector show that NEP can reach 10^{-18} W·Hz$^{-1/2}$ at 0.3 K. Preliminary data on the temperature dependence of the noise support the expectations.

IV. Conclusion

In comparison to relatively slow low temperature detectors, an obvious benefit of our detector approach is that the $1/f$ noise is not present in the high-frequency readout. Another practical advantage of the use of the current noise is that it dramatically increases with the bias current making it possible to substitute a complicated SQUID readout with less sensitive and cheaper microwave amplifiers.

References

[1] P.L. Richards, "Bolometers for infrared and millimeter waves," *J Appl. Phys.*, vol. 76, 1 (1994).

[2] A.D. Semenov, G.N. Gol'tsman, and R. Sobolewski, "Hot-electron effect in superconductors and its application for radiation sensors," *Supercond. Sci. Technol*, vol. 15, R1 (2002).

[3] B.S. Karasik, W.R. McGrath, M.E. Gershenson, and A.V. Sergeev, "Photon-noise-limited direct detector based on disorder-controlled electron heating," *J. Appl. Phys.*, vol. 87, 7586 (2000).

[4] E.N. Grossman, D.C. McDonald, and J.E. Sauvageau, "Far-infrared kinetic-inductance detectors," *IEEE Transactions on Magnetics*, vol. 27, 2677 (1991); A.V. Sergeev, V.V. Mitin, and B.S. Karasik, "Ultrasensitive hot-electron kinetic-inductance detector operating well below the superconducting transition," *Appl. Phys. Lett.*, vol. 80, 817 (2002).

[5] H.J. Hartfuss and K.H. Gundlach, "Video detection of MM-waves via photon-assisted tunneling between two superconductors," *Int. J. Infrared and Millimeter Waves*, vol. 2, 809 (1981).

[6] M. Nahum and J.M. Martinis, "Ultrasensitive-hot-electron microbolometer," *Appl. Phys. Lett.*, vol. 63, 3075 (1993); L. Kuzmin, D. Chouvaev, M. Tarasov, P. Sundquist, M. Willander, and T. Claeson, *IEEE Transactions on Applied Superconductivity*, vol. 9, 3186 (1999).

[7] A. Semenov, "Superconducting submillimeter direct detector using high-frequency current noise," *Physica C*, vol. 416/3-4, 85 (2004).

[8] G. Schuster, D. Hechtfischer, and B. Fellmuth, "Thermometry below 1 K," *Rep. Prog. Phys.* vol. 57, 187 (1994).

Design and Measurement of a 600 GHz Micromachined Horn Antenna Manufactured by Combined DRIE and KOH-Etching of Silicon

Stephan Biber[1], Axel Murk[2], Lorenz-Peter Schmidt[1], Niklaus Kämpfer[2]

***Abstract*— We present a detailed discussion of a manufacturing process used for silicon-micromachining of horn antennas for submillimeter wave applications. The developed process was applied to the machining of an octagonal horn antenna for 600 GHz and can be scaled for frequencies up to 3 THz. The antenna geometry was optimized for maximum coupling to a Gaussian beam using the commercial simulation tool "Microwave Studio". It was found that maximum Gaussian coupling can be up to 86%. Measurement results for an E-plane and an H-plane scan of the antenna pattern show good agreement with simulation results. The process involves a deep reactive ion etching process (DRIE) creating rectangular trenches which form the waveguide (overall size of 420x210 μm) and open the antenna in the E-plane. A KOH-etching process is applied on the bottom of the trenches formed in the preceding DRIE process. This wet etching process with a depth of 320 μm allowed to open the antenna aperture in the H-plane.**

***Index Terms*— antenna-design, THz-technology, micromachining, silicon-technology, quasi-optics**

I. Introduction

Antennas are an integral part of quasi-optical systems at THz-frequencies. Many applications require antennas with high coupling efficiency to a Gaussian beam. Horn-antennas as well as lens antennas are mostly used for this purpose. As the dimensions of the antennas become very small at submillimeter wave frequencies, conventional manufacturing processes such as milling and drilling etc. hardly enable to manufacture the complex structures with the desired tolerances.

The application of micromachining techniques for the manufacturing of antennas is a new challenge for the available micromachining technologies, because antennas usually have complex geometries. It is difficult to achieve an antenna aperture similar to a pyramidal or conical horn using a micromaching process because this requires a rectangular waveguide to be opened in three directions. Antennas for THz-mixers are usually optimized for maximum coupling between a fundamental mode Gaussian beam and the antenna. Therefore the geometry of the antenna has to be adapted to the circular pattern of the Gaussian beam.

Best coupling coefficients can be obtained by circular corrugated feed horns with an integrated circular to rectangular waveguide transition [1], [2], but these structures require high geometrical flexibility during the manufacturing process. Rectangular horn antennas [3], diagonal horn antennas [4] as well as hexagonal horn antennas are widely used because of their simple geometry and comparatively large coupling efficiencies of up to 88%. Another approach to integrate both rectangular structures for waveguides and antennas in the same micro-machining process is the application of different etching techniques in silicon. Hesler et al. have demonstrated an octagonal horn antenna based on SU-8 for the waveguide layer and wet etching of 100-oriented silicon [5] for widening the antenna aperture. We propose the machining of an antenna, purely based on silicon machining techniques, replacing the SU-8 process with a dry-etching technique. The antenna can be assembled from two symmetrical split-block halves, cutting the waveguide in the E-plane.

One major advantage of silicon micromaching technology compared to conventional techniques is its capability to manufacture many components in one production process. With the antenna design described below, more than 40 antennas can be machined on one single silicon wafer (with 100 mm diameter). The silicon micromachining technology allows not only the production of many isolated components. Various different components can be machined quasi-monolithically for an advanced production of THz-circuits and systems such as receiver arrays for imaging applications.

This paper will discuss the special issues related to the manufacturing process and the combination of DRIE and KOH-etching. We will present a detailed examination of the coupling efficiency and its dependence on the geometry of the antenna. A comparison between simulation and measurement results for the antenna pattern at 600 GHz will conclude the paper.

II. The Micromachining Process

The manufacturing process described in Fig. 1 shows the major steps for the production of the antenna and the necessary masking of the silicon structures. In step 1, a DRIE-process ("Bosch-process" [6]) is used to form one half of the waveguide and to form the antenna by opening the waveguide in the E-plane. The waveguides used for 600 GHz have dimensions of a =420 μm and b =210 μm. Therefore an etching depth of $t_{DRIE} = a/2$ =210 μm is required. As such an antenna would be an E-sectoral horn antenna with a rather poor Gaussian coupling efficiency, an enhanced opening of the antenna aperture in the H-plane is required. This is accomplished in step 2 by using a KOH-etching process. The KOH-etching process is a wet etching process which allows

[1]Institute for Microwave Technology, University of Erlangen-Nuremberg, Germany
[2]University of Bern, Institute of Applied Physics, Switzerland

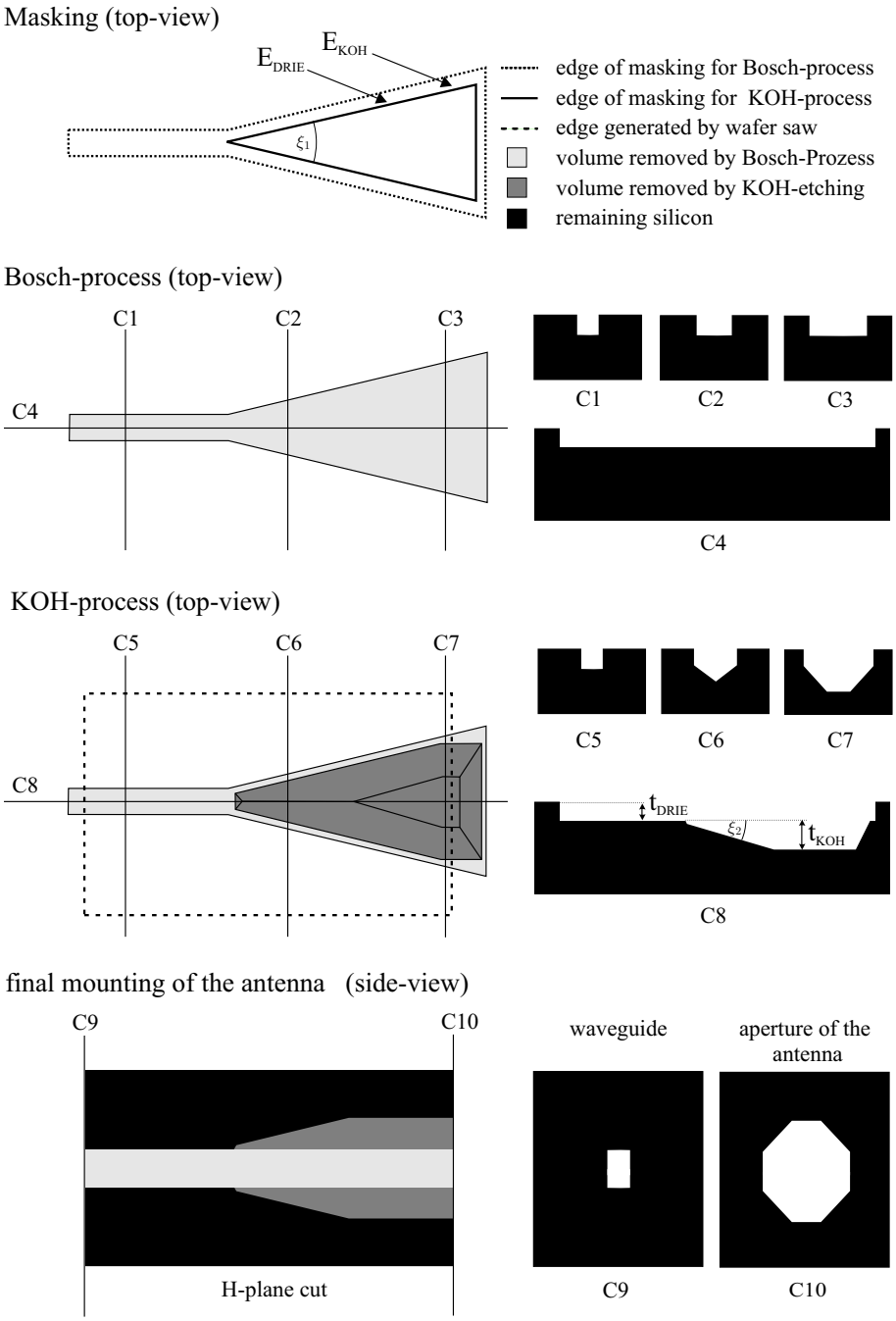

Fig. 1. Overview on the process. Left: top-view on the structures, right: respective cut-views (C1-C3, C5-C7, C9-C10) and (C4, C8).

strongly anisotropic etching of silicon crystals [7], [8]. With the 100-wafers used for this process, it is possible to use the 111-planes of the silicon crystal as etch-stop layers, because the etching rate in 111-direction is 400 times slower than it is in the 100 -direction.

Several difficulties have to be overcome in order to successfully complete the micromachining process: The necessary dry etching depth has to be achieved in one etching step, which requires the deposition and structuring of a thick, chemically robust masking layer. In order to combine the structures generated by the DRIE process with the KOH-etching process, two technological problems have to be solved: First the complex topology generated by the DRIE process has to be completely masked to ensure that the KOH-etching process can only etch the silicon in the desired, triangular region shown in Fig. 1a. Second, photolithographic mask transfer with a large distance t_{DRIE} between the mask and the substrate has to be accomplished successfully.

The wafers used for the process have a thickness of 1325 μm and a diameter of 100 mm. Comparatively thick wafers are necessary to ensure mechanical stability of the device even after the completion of the etching process, which is generating deep trenches in the silicon. Before starting the ”Bosch-process” for the etching of the waveguide and the opening of

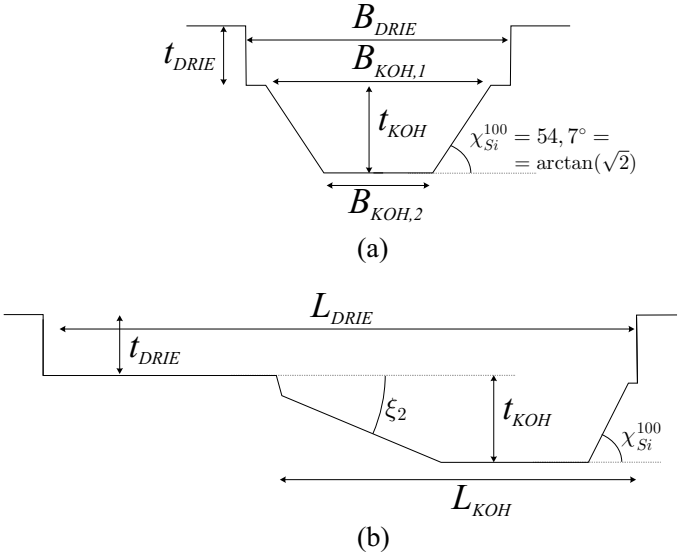

Fig. 2. Dimensions: (a) one split-block half of the antenna, front-view on the aperture, (b) cut through the side-view of the antenna

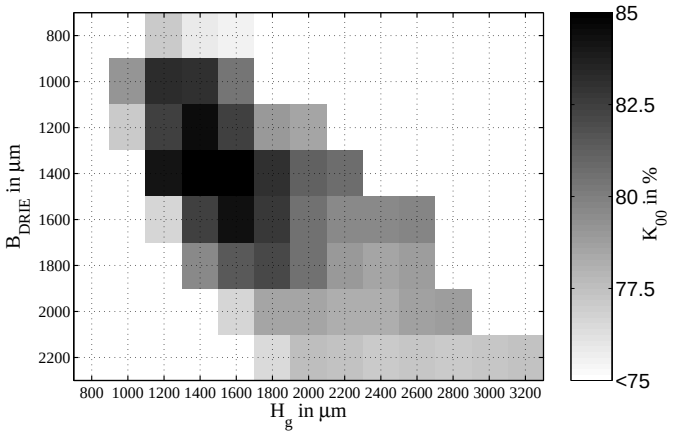

Fig. 3. Coupling efficiency K_{00} of the antenna with a fundamental mode Gaussian beam as a function of the antenna geometry. B_{DRIE} is the aperture width in the E-plane, H_g the width in the H-plane.

the antenna in the E-plane, the mask for this process has to be deposited and structured on the wafer. As this mask has to be very thick in order to withstand an etching depth of 210 μm it was deposited in three steps. The first SiO_2 layer was grown thermally, the second SiO_2 layer was deposited using a chemical vapour deposition process and finally the third layer consisting of photoresist was spun on top. This gives an overall thickness of the mask of 3 μm.

After the completion of step 1 (Fig. 1b), the whole structure was coated with an SiO_2 layer using a thermal oxidation process and then coated with photoresist. In order to have a complete coating of the topology - also on the vertical sidewalls generated by the DRIE process - the photoresist was not spun but sprayed on the wafer. The difficulty to illuminate the photoresist on the bottom of the 210μm deep trenches could be overcome by using a projection aligner. The projection aligner allows a mask transfer with a large distance between the mask and the wafer.

After the completion of the etching processes, the antennas are diced using a wafer-saw (Fig. 1c) and then coated with a 2 μm thick gold layer providing high electrical conductivity. In the final step 3 (Fig. 1d), the two split-block halves are assembled in a conventionally machined brass mount.

III. Design and Optimization of the Antenna

The available etching technologies and the limitations given by the principal planes of the silicon crystal limit the possible geometries available for this antenna design. Figure 2 shows the most important dimensions of the antenna.

The opening angle of the antenna ξ_1 is given by the parameters B_{KOH} and L_{KOH} due to:

$$\xi_1 = \arctan(\frac{B_{KOH}}{2L_{KOH}}) \quad . \tag{1}$$

Together with the geometry of the silicon crystal, this yields:

$$\xi_2 = \arctan(\tan(\frac{\xi_1}{2}) \cdot \tan(\chi_{Si}^{100})) \quad , \tag{2}$$

with the angle χ_{Si}^{100} between the 100- and the 111-plane of the silicon crystal:

$$\chi_{Si}^{100} = 54.74° \quad . \tag{3}$$

The depth of the KOH-etching process t_{KOH} is limited by the width $B_{KOH,1}$ of the structures on the wafer surface:

$$t_{KOH} < t_{KOH}^{max} = \frac{B_{KOH,1}}{2} \tan(\chi_{Si}^{100}) \quad . \tag{4}$$

If the etching process is stopped before reaching the maximum depth t_{KOH}^{max}, the width $B_{KOH,2}$ is given by:

$$B_{KOH,2} = B_{KOH,1} - \frac{2t_{KOH}}{\tan(\chi_{Si}^{100})} \quad . \tag{5}$$

Equations 1 - 5 define the mutual dependencies of the geometry of the antenna after the completion of the etching process.

In order to maximize the Gaussian coupling to this antenna, a model of the antenna was implemented in "Microwave Studio" (MWS). The electric fields calculated by MWS were exported to MATLAB where the maximum coupling coefficient K_{00} between the antenna and a fundamental mode Gaussian beam was calculated for each antenna design. The major antenna parameters examined in a comprehensive parameter study are the diameter of the aperture in the E- and in the H-plane. The diameter of the aperture in the E-plane is defined by B_{DRIE} while it is defined in the H-plane by:

$$H_g = 2 \cdot (t_{DRIE} + t_{KOH}) \quad , \tag{6}$$

$$t_{DRIE} = 210\ \mu\text{m} \quad . \tag{7}$$

The results of this parameter study, including an analysis of over 60 different antenna designs, are summarized in Fig. 3. This Figure shows that the maximum coupling to a Gaussian beam with a beam radius of $w_0 = \lambda_0 = 500$ μm can be achieved for a horn aperture with $B_{DRIE} = 1200$ μm and $H_g = 1600$ μm. The simulated coupling efficiency for this antenna yields $K_{00}^{max} = 86\%$. As the length of the antenna L_{KOH} does not have a significant influence on the coupling efficiency for L_{KOH}= 8000-14000 μm, the simulations presented here are based on L_{KOH}= 10000 μm.

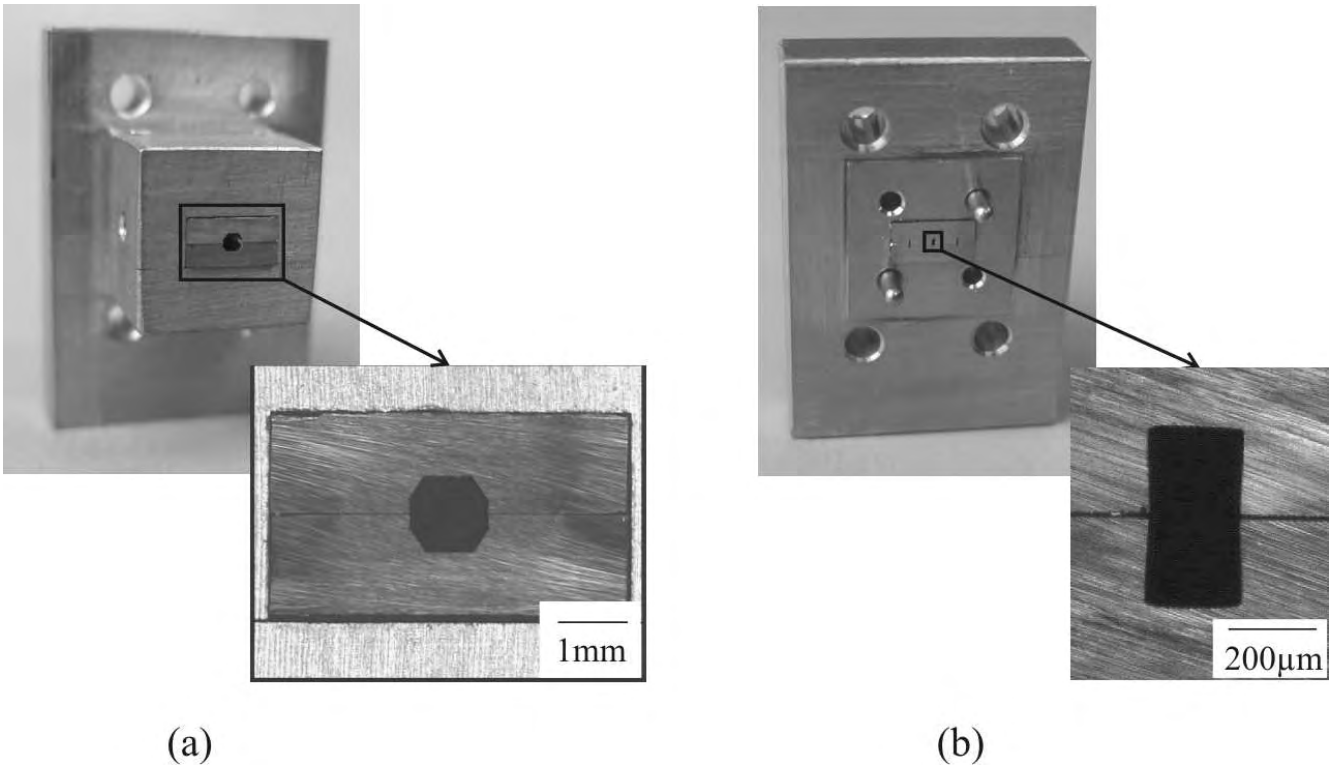

Fig. 4. Antenna assembled in brass-mount; (a) front-view on antenna aperture (b) waveguide input with flange and dowel pins

As the optimum antenna geometry with an H-plane diameter of $H_g = 1600$ μm requires a rather large KOH-etching depth of $t_{KOH} = 590$ μm, we decided to produce a slightly smaller aperture with $H_g = 1300$ μm and $B_{DRIE} = 1100$ μm. This design only requires an etching depth of $t_{KOH} = 450$ μm and still provides a coupling efficiency of $K_{00} = 85\%$ which is just 1% less than the maximum achievable efficiency.

IV. Results of the Micromaching Process

The desired etching depth for the DRIE-process of $t_{DRIE} = 210$ μm could be achieved with negligible variations of less than 4 μm. Larger variations from the original goal had to be accepted for the KOH-etching depth t_{KOH}. A critical parameter in the described process is the underetching of the edges E_{KOH} (see Fig. 1a) which are not parallel to the principal planes of the silicon crystal. If the underetching proceeds beyond the point, where the edges E_{KOH} and E_{DRIE} coincide, the structure would be destroyed because the new crystal planes which would be opened are etched at a very high rate by the KOH-solution.

Although the underetching rate can be calculated from the etching rate along the principal planes [9], in the actual process it can only be controlled by measuring the distance between the edges E_{KOH} and E_{DRIE} using a microscope. The etching process was stopped, as soon as both edges could not be distinguished anymore. As both edges are separated vertically by $t_{DRIE} = 210$ μm it is very difficult to precisely determine the moment when both edges coincide. Therefore the etching process was stopped slightly earlier than desired in order to prevent the destruction of the structure. This led to an overall KOH-etching depth of $t_{KOH} = 330$ μm. Although this is significantly less than the desired etching depth of 450 μm it has only minor impact on the coupling efficiency K_{00}. From Fig. 3 it can be seen that the machined antenna still provides a coupling efficiency of $K_{00} = 81\%$. The readily assembled antenna has an octagonal aperture with 1080 μm width in the E-plane and 1074 μm in the H-plane and is shown in Fig. 4.

V. Measurement Results

For the characterization of the antenna, the far-field antenna pattern C_s was measured in the E- and in the H-plane at a frequency of 600 GHz. For the two different orientations, the antenna under test was mounted on a rotation stage with its aperture close to the rotational axis. The antenna was connected to a harmonic Schottky diode mixer which was pumped at 100 GHz by a Gunn diode local oscillator. A similar Gunn oscillator followed by a $\times 6$ multiplier and a 550 GHz high-pass filter was used as signal source mounted in a distance of about 300 mm from the rotation stage. Both oscillators were phase-locked to the same reference signal. The down-converted signal at an intermediate frequency of 59 MHz was analyzed in amplitude and phase with an ABmm vector network analyzer. The available dynamic range in this configuration is more than 50 dB. In order to reduce the effect of standing waves between the two horn antennas the measurements in each plane were repeated four times after an axial $\lambda/4$ shift of the signal source. The surrounding areas in the field of view of the antenna were covered with microwave

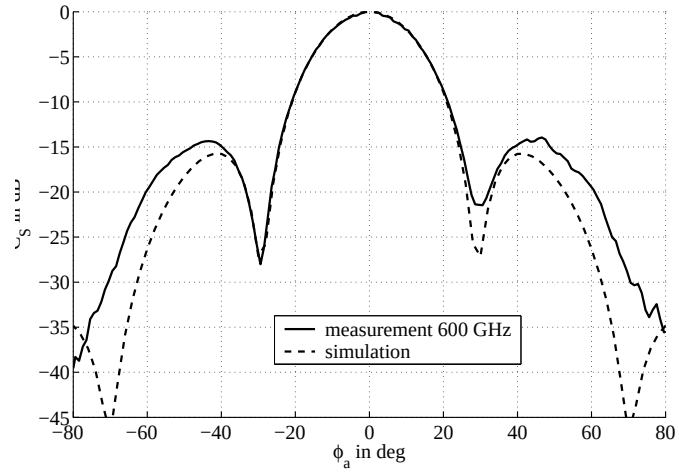

Fig. 5. Antenna pattern in the E-plane: Comparison of measurement results at 600 GHz with simulation results based on "Microwave Studio".

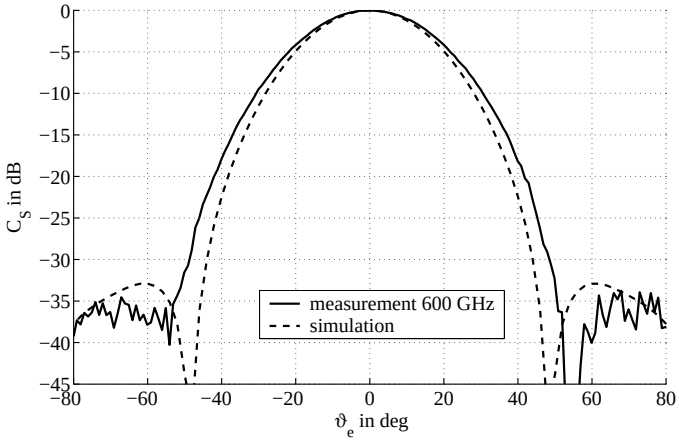

Fig. 6. Antenna pattern in the H-plane: Comparison of measurement results at 600 GHz with simulation results based on "Microwave Studio".

absorbing materials (TK-RAM and Eccorsob) to prevent other multi-path signals which could not be corrected with the phase-shifting technique.

The E-plane scan was accomplished by scanning the azimuth angle Φ_a, while the H-plane scan was accomplished by scanning the elevation angle ϑ_e with the main lobe of the antenna oriented in the direction of $\vartheta_e = 90°$.

Fig. 5 and 6 show the comparison between the simulated and measured antenna pattern. The antenna parameters used in the simulations are based on the geometry of the antennas after the completion of the micromachining process and the assembly of both split-block halves ($B_{DRIE} = 1080$ μm, $H_g = 1074$ μm).

A very good agreement between the simulated and the measured results can be observed for the E-plane. The maximum measured side lobe level in the E-plane is with -14.5 dB only about 1 dB higher than predicted by the simulation. The location of the minima in the antenna pattern at $\Phi_a = \pm\, 29.5°$ could also be verified very precisely. The 3-dB-beamwidth of the main lobe of the antenna equals 24.5°.

A comparison of simulated and measured data in the H-plane shows that the measured beamwidth is larger than the beamwidth given by the simulation. As the difference between the measured 3-dB-beamwidth of 33.6° and the simulated beamwidth of 31.6° is only 2°, this effect is only of minor importance for the overall performance of the antenna. The sidelobe level in the H-plane is -34 dB. This is still significantly above the noise floor of the measurement system.

A precise calculation of the coupling efficiency K_{00} from measurement data requires a complete hemispherical scan of the antenna, which would be very time-consuming. As a good agreement between simulation and measurement could be observed in the principal planes of the antenna, a complete hemispherical scan would not significantly add new information. The good agreement allows to conclude that the coupling efficiency $K_{00} \approx 80\%$ calculated for the antenna model in MWS also holds for the real antenna.

VI. Discussion and Outlook

A micromachining technology for the manufacturing of an octagonal horn antenna with high coupling to a Gaussian beam has been presented. Coupling coefficients for more than 60 antenna geometries have been calculated using the field simulator MicrowaveStudio. The maximum coupling coefficient found was $K_{00}^{max} = 86\%$. Special questions concerning the combination of the DRIE- and the KOH-etching process such as underetching effects and masking of complex topologies have been addressed. With the measurement results at 600 GHz being in good agreement with the simulation, a coupling efficiency of $K_{00} \approx 80\%$ could be verified. The antenna has been successfully used as an input of a conventionally machined GaAs Schottky-diode mixer with a conversion loss as low as 9.5 dB [10].

Acknowledgment

We are very grateful to the German Research Foundation ("Deutsche Forschungsgemeinschaft") for partially funding this project. The work at IAP in Bern was supported by the Swiss National Science Foundation under the grant 200020-100167. Special thanks to Gudrun Rattmann and Sven Berberich from "Fraunhofer Institute for Integrated Systems and Device Technology" (IISB) and to Theo Hartmann from Nanoworld GmbH. Micromachining of the antennas would not have been possible without their help and the availability of the machining technologies in the clean-room facility of IISB on the campus of the University of Erlangen-Nuremberg.

References

[1] P. F. Goldsmith, "Quasi-optical techniques," *Proceedings of the IEEE*, vol. 80, pp. 1729–1747, November 1992.

[2] P. H. Siegel, R. P. Smith, M. C. Gaidis, and S. C. Martin, "2.5 THz GaAs monolithic membrane-diode mixer," *IEEE Transactions on Microwave Theory and Techniques*, vol. 47, pp. 596–604, May 1999.

[3] F. Maiwald, J. C. Pearson, J. S. Ward, E. Schlecht, G. Chattopadhyay, J. Gill, R. Ferber, R. Tsang, R. Lin, A. Peralta, B. Finamore, W. Chun, J. J. Baker, R. J. Dengler, H. Javadi, P. Siegel, and I. Mehdi, "Solid-state sources for space applications," in *Conference Digest of the 29th Int. Conf. On Infrared and Millimeter Waves, Karlsruhe, Deutschland* (T. M. and W. W., eds.), 2004.

[4] J. F. Johansson and N. D. Whyborn, “The diagonal horn as a submillimeter wave antenna,” *IEEE Trans. Microwave Theory and Techniques*, vol. 40, no. 5, pp. 795–800, 1992.
[5] J. L. Hesler, K. Hui, and T. Crowe, “Analysis of an octagonal micromachined horn antenna for submillimeter-wave applications,” *IEEE Transactions on Antennas and Propagation*, vol. 49, pp. 997–1001, June 2001.
[6] F. Laermer and A. Schlip, “Method of anisotropically etching silicon,” in *US Patent No. 5501893*.
[7] E. Bassous, “Fabrication of novel three-dimensional microstuctures by the anisotropic etching of (100) and (110) silicon,” *IEEE Transactions on electron devices*, vol. 25, pp. 1178–1193, Oct. 1978.
[8] M. Madou, *Fundamentals of Microfabrication - The Science of Miniaturization*, vol. ISBN 0-8493-0826-7. CRC Press, 2002.
[9] T. J. Hubbard, *MEMS Design: The Geometry of Silicon Micromachining*. Ph.d. thesis, California Intsitute of Technology, Pasadena, CA, USA, 1994.
[10] J. Schür, S. Biber, O. Cojocari, B. Mottet, L.-P. Schmidt, and H. L. Hartnagel, “600 ghz heterodyne mixer in waveguide technology using a gaas schottky diode,” in *International Symposium on Space Terahertz Technology, Göteborg, Schweden*, 2005.

Broadband Finline Ortho-Mode Transducer for the 750-1150 GHz Band

Christopher E. Groppi, Christian Y. Drouet d'Aubigny, Arthur W. Lichtenberger, Christine M. Lyons, Christopher K. Walker

***Abstract*—We present the design and fabrication of a novel full waveguide band ortho-mode transducer (OMT) for operation from 750-1150 GHz, and scalable to frequencies as high as 5 THz. At submillimeter and THz frequencies, quasioptical techniques are generally used to implement dual polarization receiver systems. OMTs offer significantly increased simplicity, eliminating polarization diplexing optics. Since both linear polarizations use the same feedhorn and optics, alignment issues between polarizations are also eliminated. Advances in micromachining technology, semiconductor processing techniques and electromagnetic simulation now allow the design and fabrication of OMTs at frequencies where quasioptical approaches were the only viable option. While most OMTs used for radio astronomy are derivatives of the Bøifot design, the proposed design uses a finline circuit to separate orthogonal linear polarizations. Unlike Bøifot type designs, the Robinson OMT is fully planar, allowing easy fabrication as a single split block waveguide structure with all ports in one plane. The finline circuit is also planar, and can be fabricated using photolithographic techniques on a thin dielectric substrate. This design uses micromachining technology to fabricate the waveguide split-block by laser etching a silicon substrate that is later metallized. At lower frequencies, direct micromilling can be used to fabricate the split block directly. The finline chips are fabricated on a thin (1 μm) SOI substrate with thick (5 μm) gold finline metallization, and gold beam leads for chip grounding. This chip construction technique compatible with both direct and laser machined waveguide blocks. Both the waveguide and the finline structures can be scaled to frequencies as high as 5 THz using these fabrication techniques. Feedhorns are integrated with the structure at all three ports to allow testing with a Fourier transform spectrometer and ^{4}He bolometer system. This technique can measure the throughput, cross-polarization and isolation of the OMT through comparison with a back to back feedhorn. Later, this OMT design could be a part of a fully integrated dual polarization mixer block, with the input horn, OMT and both mixers fabricated in a single flangeless split block. Integrated dual polarization mixers of this type can dramatically decrease the complexity of dual polarization imaging arrays as well as traditional single beam receiver systems at submillimeter and THz frequencies.**

***Index Terms*—Radio Astronomy, Ortho-mode Transducer, Micromachining**

C.E. Groppi is with the National Radio Astronomy Observatory, Tucson, AZ 85721 USA (ph: 520-882-8250; fax: 520-882-7955; e-mail: cgroppi@nrao.edu).

C.Y. Drouet d'Aubigny & C.K. Walker are with the University of Arizona, Tucson, AZ 85721 USA.

A.W. Lichtenberger & C.M. Lyons are with the University of Virginia, Charlottesville, VA 22904 USA.

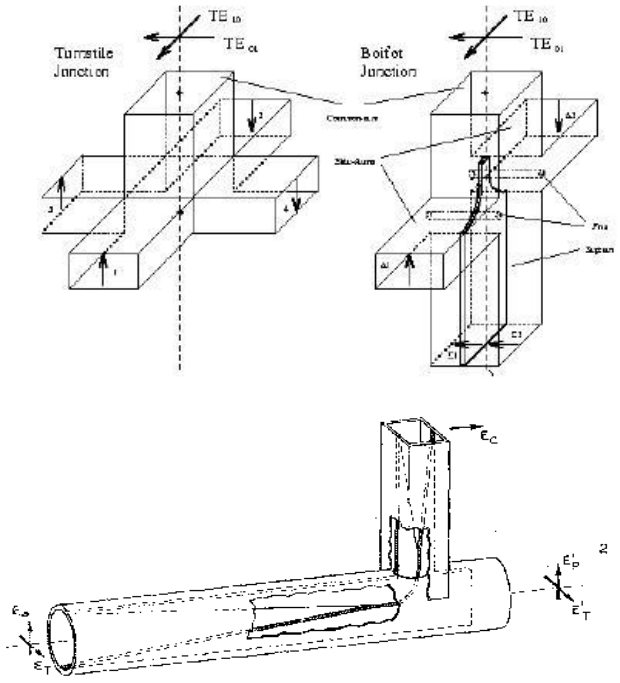

Fig. 1- Finline coupler.

Fig. 1: The Bøifot OMT [1], [2] (top) and Robinson finline OMT [1] (bottom) designs.

I. Introduction

The design of symmetric ortho-mode transducers at mm-wave frequencies has been discussed extensively by Wollack [1], [2]. This design, referred to as the Bøifot OMT, is based on the 5 port turnstyle junction [3], folded into a more compact shape (Figure 1). Recently, Narayanan and Erickson [4], [5], have developed a Bøifot type design replacing the capacitive pins used in previous designs with a capacitive step. This and other refinements make the design far easier to fabricate and make it suitable for scaling to frequencies as high as 1 THz. These waveguide designs offer very low loss, good crosspolarization performance and excellent isolation, but are fundamentally three dimensional. Another design exists, using finline to extract one polarization from the square or round input guide. This design was originally proposed by Robinson [6] and was recently pursued by Chattopadhyay and Carlstrom, Skinner and James and this group [7],[8],[9] (Figure 1). This design is planar, and could be easily fabricated at THz frequencies using micromachining techniques for the waveguide, and

photolithographic techniques on a silicon substrate for the finline. This structure does suffer from somewhat higher loss than the Bøifot design due to ohmic losses in the fin. For operation at frequencies below the bandgap of NbTiN (1.4 THz), the fin could be fabricated from this superconducting material if the losses in a normal metal fin prove to be too high. With a fin of zero resistivity (PEC) the losses in the device are significantly reduced.

In the past, the ability to fabricate waveguide structures at high frequency was limited by available machining technology. Electroforming techniques allow construction of high frequency waveguide components, but this technique is extremely costly and time consuming. Today, classical CNC micromachining equipment is available commercially, and micromachining techniques have been pioneered by the JPL Sub-mm Wave Advanced Technology group and the University of Massachusetts [10]. In addition, the Steward Observatory Radio Astronomy Lab has developed a laser micromachining system that uses a He-Ar laser to machine structures in silicon. This technique is a non-contact process, with no debris field. The silicon vaporized by the laser is reacted with chlorine gas in the milling chamber producing silicon tetrachloride gas. Additionally, silicon melted at the etching site re-grows epitaxially as it cools, producing high surface quality [11]. The current system has the potential for fabricating waveguide structures at frequencies beyond 5 THz. A Veeco optical profiling system is used to measure structure depth and surface roughness to accuracies better than 100 nm. In addition to their laser micromachining and metrology capabilities, SORAL is equipped with a Coherent/DEOS far infrared laser system. This THz source is complimented by a Fourier Transform Spectrometer (FTS) system and an Infrared Laboratories ^{4}He bolometer.

II. OMT Design

Two design features have prevented scaling successful Bøifot type OMT designs to higher frequencies: the septum and the capacitive pins used to compensate the septum. As shown in Figure 1, the septum is a thin metallic plate that acts like a splitting junction for one polarization of the input guide, directing that mode into the two side arms. The presence of the septum requires capacitive compensation for broadband performance in the side arms. In the newest NRAO design for use in ALMA, these pins are realized as thin gold wire run through holes in the guide walls. At high frequencies, these pins are nearly impossible to fabricate. The design by Narayanan and Erickson has eliminated these pins in favor of capacitive steps in the waveguide walls. The capacitive steps could be too small to reliably etch at frequencies above 1 THz.

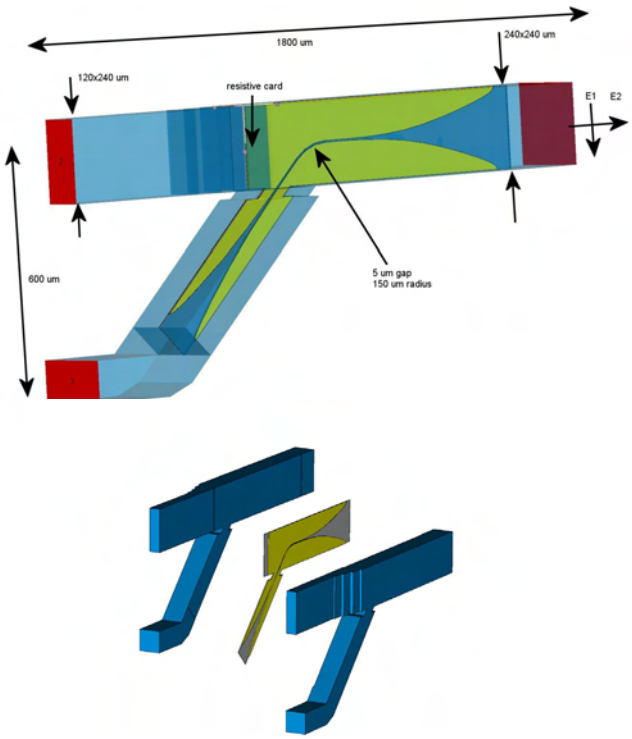

Fig. 2: CST Microwave Studio model of the Robinson OMT design for THz applications. The design consists of a laser machined silicon split-block structure, with a gold on SOI finline chip grounded via beam leads.

An OMT design proposed by Robinson in 1956 (Figure 1) has the potential to be the superior approach for THz applications. We have chosen to optimize this design for terahertz applications, and fabrication with silicon processing technology. This device is planar, unlike the Bøifot type designs. A single split block structure contains all the necessary waveguide components, and will allow integration of horns and mixers. In the Chattopadhyay and Carlstrom scale model design, the fins were realized as two separate metallic plates, held at the proper separation with alignment pins. Scaling their design to 1 THz, the fin gap is ~5 μm. Since construction of freestanding fins would be exceptionally difficult, the finline structure for our design is fabricated on a thin silicon membrane with photolithographically defined gold fins. A thick substrate requires a transition from waveguide to dielectric loaded waveguide, then a transition from dielectric loaded waveguide to finline [12]. Since silicon has a very high dielectric constant (ε_r~11.66), even relatively thin membranes can require a vacuum to dielectric loaded waveguide transition. Simulations with CST microwave studio show that a 1 μm thick substrate requires no transition at 1 THz, producing S11 less than -25 dB from 800-1200 GHz. The match degrades as the substrate thickness is increased.

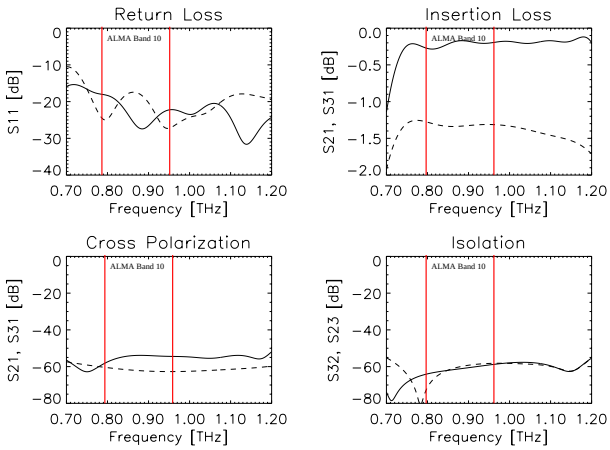

Fig. 3: OMT simulation results. Frequency range is 700-1200 GHz for all plots. Return loss, insertion loss, crosspolarization and isolation are shown for horizontal (solid) and vertical (dotted) polarizations. These CST Microwave Studio simulations include conductor, dielectric and surface roughness losses, assuming 30% increase in the conductivity of gold for operation at 4K.

When the thickness exceeds ~5 μm, a transition becomes needed. The finline tapers are of a simple exponential form $a_0 e^{z/l}$, where a_0 is half the b dimension of the waveguide, and l is the taper length. The taper length was chosen to be 550 μm, as the best compromise between matching and loss. The 5 μm fin gap at 1 THz should allow scaling of this design to ~5 THz. In addition, the use of silicon as a substrate material allows easy realization of the resistive card at the end of the finline. A palladium-gold film with a surface resistivity of 12.5 Ω/❑ was deposited on the thin silicon substrate to realize the resistive card.

The Robinson OMT design has been simulated using CST microwave studio, including conductor losses for both the waveguide and the fin, dielectric losses for the silicon substrate and losses due to waveguide roughness. We assume that the conductivity of gold is increased by 30% at 4K, and assume 25 nm RMS surface roughness in the waveguide (typical of Si micromachined waveguide after an isotropic polishing etch). The design consists of two waveguide to finline transitions connected via a 45 degree, 1/2 wave radius finline bend. Chattopadhyay and Carlstrom found that a 45 degree finline bend minimized mode conversion, improving crosspolarization performance. The through-arm transitions from square to full height rectangular waveguide via a three section matching transformer, while the full height rectangular side arm uses a mitered 45 degree bend to bring both output guides to the same plane. The test structure has been fabricated with the mitered bend reversed to make the two arms perpendicular to facilitate the addition of output horns. A 40% height waveguide iris is used at the junction between the side and main arms to minimize the effect of the side arm on the horizontal polarization, while not disturbing the finline guide mode. The waveguide structure is fabricated as a split-block, with the finline chip sandwiched between the block halves (See Figure 2). As shown in Figure 3, the device offers good performance from 750-1150 GHz, fully including ALMA band 10 (787-950 GHz). The input match is approximately -20 dB across the band for both polarizations. Insertion loss for the horizontal (through) polarization is ~0.5 dB, while the loss for the vertical (side) polarization is ~1.3 dB. Crosspolarization performance of the design is good, with crosspolarization levels of less than -50 dB. Because the current density in the fin near the narrow gap is relatively high, conductor losses in the fin increase the loss in the side arm. These losses could be eliminated by fabricating the fin using NbTiN rather than gold. Losses would be dramatically reduced. This is a straightforward application of NbTiN, since exceptional film quality is not vital as in SIS junction fabrication. For the prototype, we plan to fabricate and test only gold fins. If the measured losses prove to be too high, a design with superconducting fins can be developed in the future, with losses of less than 0.5 dB (Figure 4).

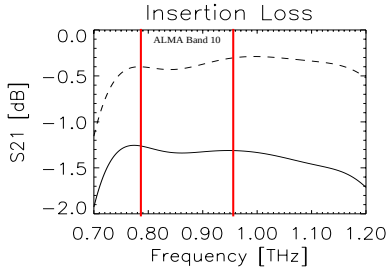

Fig. 4: Comparison of insertion loss for the side arm of the Robinson OMT with NbTiN superconducting fins (dotted) and gold fins (solid).

The design will also allow easier integration of mixer chips for future development as an integrated dual polarization mixer. Since both output ports are in the same plane and very close to one another (600 μm), two mixing devices and their associated waveguide probes and tuning structures can be fabricated on a single chip for integration with the OMT/feedhorn assembly. The small separation between ports, with all output ports in the same plane and axially aligned with the input port allow this design to be used in large, two dimensional focal plane array applications. An example of a compatible mixer design is shown in Figure 5. This design was developed to be compatible with both HEB and SIS devices, and is scalable to frequencies as high as 5 THz. The mixer is entirely fabricated from laser machined and photolithographically processed silicon [13].

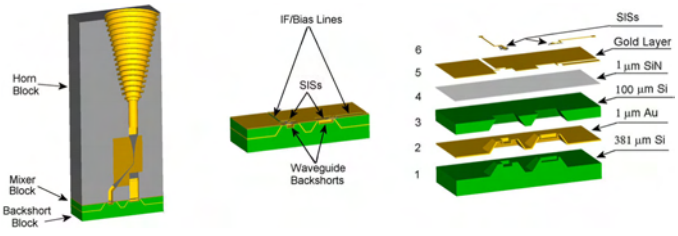

Fig. 5: A laser micromachined, SiN membrane mixer mount (Designs for beamlead/SOI devices also exist). This device, consisting of 4 blocks, has 33% bandwidth at 1 THz, and is made entirely of micromachined and photolithographically processed silicon.

III. OMT Fabrication

We are fabricating the OMT waveguide circuit using a standard split-block approach and laser micromachining technology. The finline chip has been fabricated using photolithography on a 1 μm thick SOI substrate (Figure 6).

Beamleads are used to ground the device to the block. Beamleads are thin, freestanding metallic tabs fabricated on a substrate that is later etched away [14]. They are thick enough to act as handles for manipulating the structure, and offer very good RF grounding performance. During assembly, a beam lead device is placed in a split-block waveguide structure, suspended by the beam leads. When the split-block is assembled, the gold beam leads are crushed between the block halves providing grounding. Beam lead devices are used extensively in the multipliers used in the Hershel HIFI LO system, as well as in many modern SIS and HEB detector designs. The SOI (Silicon-On-Insulator) technique allows silicon membranes thinner than 1 μm to be produced. The thin membrane is attached to a carrier wafer. After fabrication of the structure, the back side carrier wafer is released from the thin membrane. Silicon membranes are fairly flexible, and are much easier to handle than quartz wafers of the same thickness. The finline chip is a straightforward fabrication task compared to a SIS junction; only a single gold metallization layer needs to be deposited on the substrate. The finline has been defined using standard photolithographic processes on the SOI wafer, using thick photoresist techniques. A 1:1 aspect ratio of finline gap width to metallization thickness realizable with these techniques. SEM and interferometric microscope imaging show that the finline chips fabricated conform to all design dimensions to better than 5% (Figures 6,7).

Because there is no out of plane guide, milling the waveguide split block for the Robinson OMT is relatively straightforward. There are no small, tuned structures (i.e. capacitive steps) in the design, relaxing fabrication tolerances. In addition, the entire device can be made from a single split block, including input and output horns. The design of the waveguide block, including the side arm iris, is compatible with fabrication using the SORAL laser micromachining system. Prototype devices will be fabricated with a feedhorn at each port for quasi optical testing with a FTS and a ^{4}He bolometer. Alignment crosses are machined into the silicon away from the waveguide structure during the milling process to facilitate alignment. After laser machining, the waveguide split block halves are gold plated with an e-beam evaporator (the alignment crosses are masked off during plating). The planar beamlead structure is dropped (by hand) into a pocket milled into the bottom of the split-block. The precision milled pocked registers the chip (Figure 8). No electrical contacts need be made, since the beam leads will contact when the split block is closed. Alignment of the top split block with the bottom is achieved with an infrared semiconductor alignment tool or flip-chip bonder. This tool holds both the top and bottom halves of the chip in air chucks on precision motion stages. An IR microscope looks through the (transparent) silicon at the location of the alignment crosses to allow registration of the top and bottom of the structure. The air chucks then clamp the halves together. The Van der Waals forces between the gold metallization layers bond the split block together. The silicon block is then glued into a copper fixture for use. This design is also well suited for fabrication via direct micromilling in a metal block, for frequencies as high as 1.5 THz. Only small modifications to the design are necessary to compensate for finite sized tools.

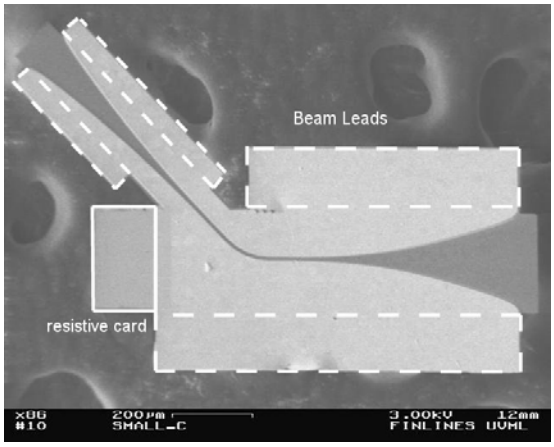

Fig. 6: SEM image of a finline chip fabricated at the University of Virginia. The finline gap is 5 μm, with a 1 μm thick SOI substrate and 5 μm thick gold metallization. The resistive card is realized as a palladium gold film, with a surface resistivity of 12.5 Ω/❑.

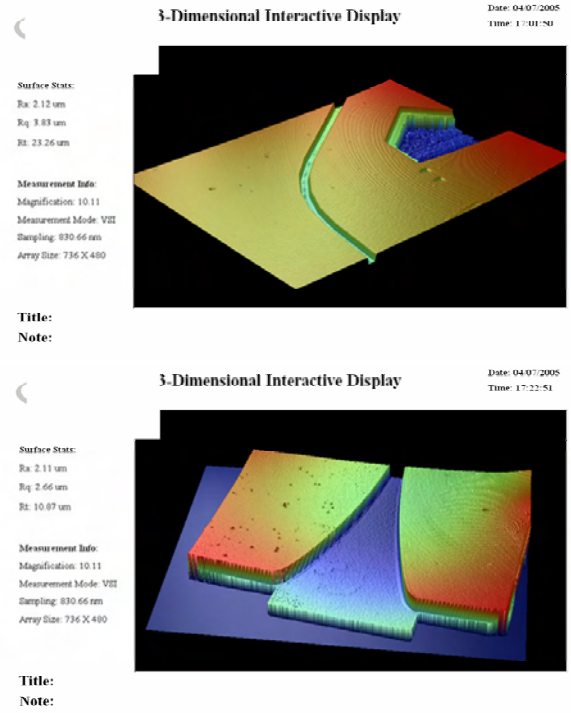

Fig.7: Veeco interferometric microscope images of a SOI finline chip. Metallization thickness is controlled to better than 100nm (the vertical resolution of the microscope). The width of the fin gap is within 5% of the design value.

IV. OMT Testing

For testing, horns will be laser machined at both the input and output ports, integrated with the OMT. In addition, a back to back feedhorn structure will be fabricated to allow measurement of the loss of the feedhorn structures. The FTS in the SORAL lab has a broadband FIR source. Combined with a IR Laboratories ^{4}He bolometer system, measurements can be made throughout the sub-mm and FIR. The system has been measured to respond from below 200 GHz to several THz, with peak sensitivity at ~ 1 THz (Figure 9). We can measure insertion loss, crosspolarization and

isolation of the OMT structure through comparison with the back-to-back feedhorn structure. With some additional optics, it is also possible to measure return loss from the device as well. Measurement with a FTS does not provide the same accuracy expected from a scalar network analyzer at lower frequencies, but should be able to verify the performance of the device. A block diagram of the proposed test set is shown in Figure 10. If the dynamic range of this test set proves to be too small to measure the crosspolarization and isolation signals, the FIR laser can be used in place of the FTS to measure these properties at discrete frequencies.

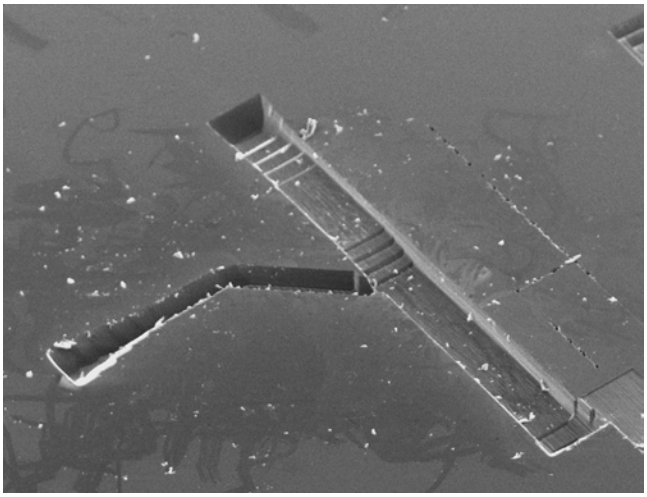

Fig. 8: SEM image of a laser micromachined prototype mixer block. Final blocks will have three integrated, corrugated feedhorns, and will be gold plated before assembly.

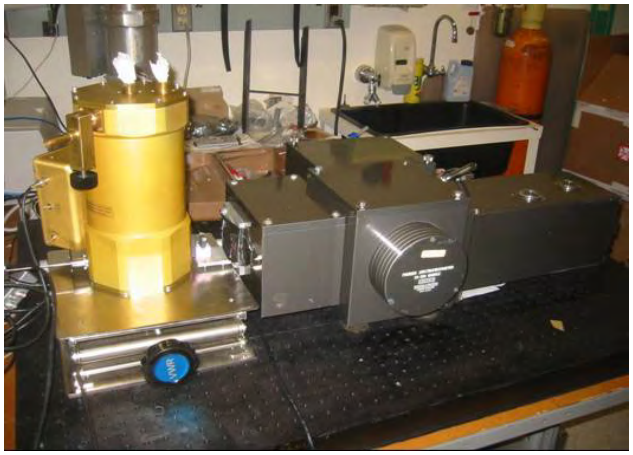

Fig 9: The University of Arizona 4He FTS system. This system has been verified to work from 200 GHz to 2 THz, and provides peak sensitivity at ~1 THz.

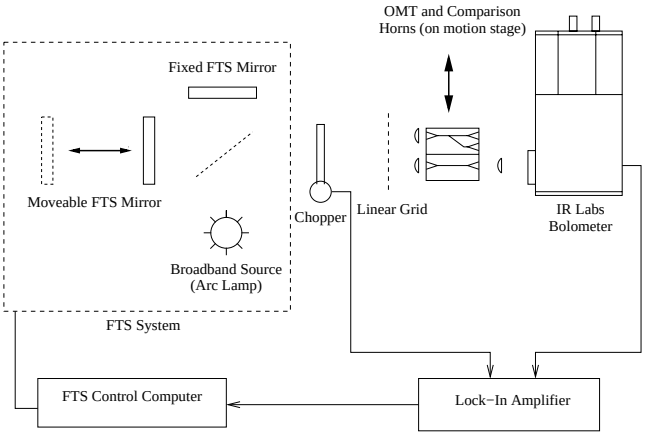

Fig 10: A block diagram of the OMT measurement system. This test set can measure throughput, crosspolarization and isolation of the OMT by comparison to a back-to-back feedhorn structure.

V. Conclusion

We have designed and have began fabrication of a 40% bandwidth orthomode transducer capable of operation from 750-1150 GHz. This design is scalable to frequencies as high as 5 THz. Recent advances in micromachining and electromagnetic simulation allow the realization of such a structure. A laser micromachining system at the University of Arizona will allow low cost and high precision waveguide structures to be milled directly in silicon. A finline OMT design first proposed by Robinson in 1956 is planar and relatively easy to fabricate. Simulations of an OMT based on this design demonstrate good performance from 750-1150 GHz. This design uses laser machined silicon waveguide components with a photolithographically defined finline circuit on a thin SOI substrate with beamlead grounding. Waveguide structures fabricated at SORAL will be combined with planar structures fabricated at the University of Virginia, and assembled at either UVa or SORAL. Testing will be done using a Fourier transform spectrometer and ^{4}He bolometer system, allowing measurements of throughput, isolation and crosspolarization. Eventually, the OMT could become part of a dual polarization mixer, with the feedhorn, OMT and mixers integrated into a single, flangeless block.

References

[1] E.J. Wollack, W. Grammer, & J. Kingsley, “The Bøifot orthomode junction,” ALMA memo #425, 2002.

[2] E.J. Wollack & W. Grammer, “Symmetric waveguide orthomode junctions,” 14th International Symposium on Space Terahertz Technology, University of Arizona, 2003, pp. 169.

[3] M.A. Meyer & H.B. Goldberg, “Applications of the turnstile junction,” IRE Trans. MTT, vol. 3, no. 6, 1955, pp 40.

[4] G. Narayanan & N.R. Erickson, “A novel full waveguide band orthomode transducer,” 13th International Symposium on Space Terahertz Technoogy, Harvard University, 2002.

[5] G. Narayanan & N.R. Erickson, “Full-waveguide band orthomode transducer for the 3mm and 1mm bands,” 14th International Symposium on Space Terahertz Technology, University of Arizona, 2003, pp. 508.

[6] S.D. Robinson, “Recent advances in finline circuits,” IRE Trans, MTT, vol. MTT-4, 1956, pp. 263.

[7] G. Chattopadhyay & J.E. Carlstrom, “Finline ortho-mode transducer for millimeter waves, IEEE Microwave and Guided Wave Let., vol. 9, no. 9, 1999, pp. 339.

[8] S.J. Skinner & G.L. James, Wide-band orthomode transducers, IEEE MTT, vol. 39, no.2, 1991, pp. 294.

[9] C.E. Groppi, C.Y. Drouet d’Aubigny, A.W. Lichtenberger & C.K. Walker, “A broadband finline ortho-mode transducer for THz applications,” 15th International Symposium on Space Terahertz Technology, University of Massachusetts, 2004, pp. 314.

[10] G. Narayanan, N.R. Erickson & R.M. Grosslein, “Low cost direct machining of terahertz waveguide structures,” 10th International Symposium on Space Terahertz Technology, 1999, pp. 518.

[11] C.Y. Drouet d’Aubigny, C.K. Walker, D. Golish, M.R. Swain, P.J. Dumont & P.R. Lawson, “Laser micro-machining of waveguide

devices for sub-mm and far IR interferometry and detector arrays," Proc. SPIE., vol. 4852, 2003, pp.568.

[12] K. Uhde & R. Eimertenbrink, "Design and applications of optically controllable finline structures," IEEE MTT, vol. 38, no. 5, 1990, pp. 679.

[13] C.K. Walker, C.E. Groppi, C.Y. Drouet d'Aubigny, C. Kulesa, A.S. Hedden, D.E. Prober, I. Siddiqi, J.W. Kooi. G. Chen, & A.W. Lichtenberger, "Integrated heterodyne array receivers for submillimeter astronomy," Proc. SPIE, vol. 4855, 2003, pp. 349.

[14] R.B. Bass, A.W. Lichtenberger, R.M. Weikle, S.-K. Pan, E. Bryerton, C.K. Walker, "Ultra-thin silicon chips for submillimeter-wave applications," 15th International Symposium on Space THz Technology, University of Massachusetts, 2004, pp. 392.

A Turnstile Junction Waveguide Orthomode Transducer for the 1 mm Band

Alessandro Navarrini, Richard L. Plambeck, and Daning Chow

***Abstract*—We describe the design and construction of a waveguide orthomode transducer (OMT) for the 200-270 GHz frequency band. The OMT provides a circular waveguide input (diameter 1.12 mm) and two WR3.7 rectangular waveguide outputs. It utilizes a turnstile junction and two E-plane power combiners. A tuning stub located at the base of the circular waveguide matches the input over the full frequency band.**

We have machined two such OMTs, but their performance has not yet been measured. Electromagnetic simulations predict a reflection coefficient at the circular input port below -20 dB for both polarizations and a transmission loss of ~0.6 dB at room temperature. When cooled to 4 K, the transmission loss is expected to be ~0.2 dB. In previous tests of a K-band scale model of the OMT, the measured performance matched the theoretical results closely.

***Index Terms*— Radio astronomy, Turnstile junction, Power combiner, Polarimetry, Waveguide transitions**

I. Introduction

We are constructing orthomode transducers for dual polarization 200-270 GHz radio astronomy receivers on the CARMA array. In order to fit into the existing dewars, the OMTs must be compact; hence we strongly prefer to use waveguide-based designs rather than wire grid polarizers.

Wollack amd Grammer [1] constructed a waveguide OMT based on a Bøifot junction that gave excellent performance over the 211-275 GHz band. We felt that this OMT would be challenging for us to mass produce because it requires careful alignment of a 0.036 mm thick septum and four 0.061 mm diameter capacitive compensation pins inside the waveguides. Other designs using a thicker septum have been proposed; here the pins are eliminated in favor of short capacitive steps [2] or standard multi-step transitions on the side arms [3]. Although in these cases the construction of the blocks is simplified, the alignment of the septum inside the waveguide is still critical.

In [4] we described an alternative to the Bøifot OMT that is based on a turnstile junction. An advantage of this design is that neither the pins nor the septum of the Bøifot junction are required to achieve polarization separation and low VSWR over a wide bandwidth; in addition, all rectangular waveguides can be split along their midplanes. As reported in [4], we constructed and tested a K-band version of the turnstile OMT. From 18-26 GHz we measured an input reflection coefficient of less than -16 dB, a cross-polarization of less than -47 dB, and a transmission loss of ~0.1 dB. We also used electromagnetic simulations to estimate the degradation in performance that machining errors of ± 0.13 mm would cause in the 18-26 GHz band, with the expectation that the fabrication tolerances could be held to ± 13 μm for a 200-270 GHz OMT.

Here we describe the design and construction of a 1mm version of the turnstile OMT. Two have been machined so far, but have not yet been tested.

The authors are with the Radio Astronomy Laboratory, University of California, Berkeley, CA 94720 (e-mail: navarrin@astro.berkeley.edu).

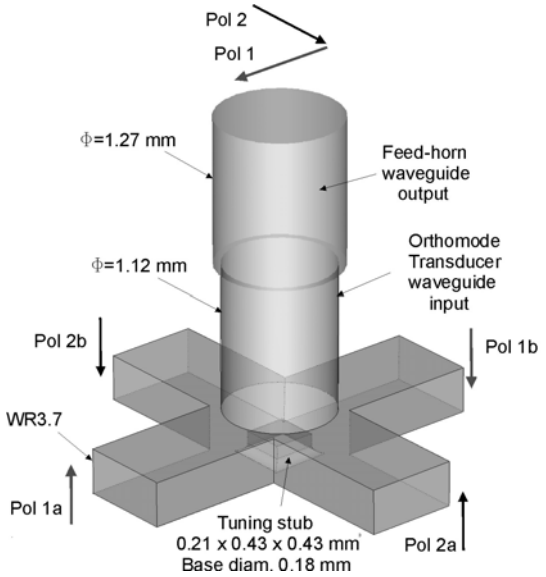

Fig. 1. Internal view of the turnstile junction with a circular waveguide input and four full-height waveguide outputs. The tuning stub is optimized for broadband performance. The circular waveguide on top represents the output of the 1 mm feed horn to which the OMT will attach.

II. Design and Optimization

As shown in Fig. 1, the turnstile junction uses a round input waveguide and four rectangular output waveguides. We note that a Bøifot junction is essentially a turnstile in which two of the arms have been folded around a septum. After emerging from the turnstile, signals in opposite pairs of waveguides are combined in power combiners before they are directed to two output waveguides.

The input circular waveguide on the turnstile junction has a diameter D = 1.12 mm, but attaches to the D = 1.27 mm circular waveguide at the output of the existing feed horns. The reflection coefficient caused by this step in the waveguide diameter is below –30 dB over most of the band. The

rectangular waveguides are full height WR3.7 (0.94 mm x 0.47 mm).

In addition to the fundamental TE_{11} modes associated with the orthogonal polarizations, the circular waveguide can propagate higher-order modes in the 200-270 GHz frequency band. These are the TM_{01} mode, with λ_c~1.306 D (ν_c=205.0 GHz), and the TE_{21} mode with λ_c~1.028 D (ν_c=260.5 GHz). In theory, these modes can be excited by the discontinuity created by the sidearm junctions. However, their excitation can be avoided as long as the four-fold symmetry of the structure is maintained.

The metallic tuning stub located at the base of the circular waveguide enables broadband operation with low reflection coefficient. The stub is a square prism with dimensions 0.43 mm x 0.43 mm x 0.21 mm, centered on the circular waveguide axis. The base is filleted with radius 0.09 mm so the stub can be machined from the side. The structure was optimized using the electromagnetic simulator CST Microwave Studio [5] based on the finite integration technique. Fig. 2 shows the simulation result for the reflected amplitude of the TE_{11} mode at the 1.27 mm diameter circular waveguide input, with all four rectangular ports terminated with matched loads. The reflection coefficient is below -28 dB over the frequency range of interest.

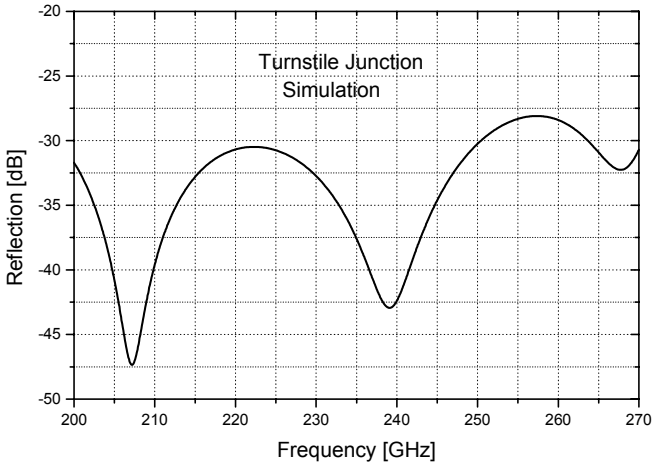

Fig. 2. Simulated reflected amplitude for a TE_{11} mode at the circular waveguide port of the five-port device illustrated in Fig. 1.

Figure 3 shows the complete OMT. Signals split by the turnstile junction exit opposite waveguides 180^0 out of phase. These signals are recombined in a power combiner that also is 180^0 out of phase, implemented using the E-plane Y-junction shown in Fig. 4. The electrical lengths of the waveguides from the turnstile to the power combiner are kept equal to maintain the 180^0 phase shift. The combiner was based on a W-band design by Kerr [6] and was further optimized using CST Microwave Studio. The steps of the three-section transformer are filleted so they can be machined with an 0.45 mm diameter end-mill. The cusp at the junction of the curved arms is truncated at a width of 0.05 mm. Fig. 5 shows the simulated reflection coefficient at the WR3.7 common port when the two curved arms are terminated with matched loads. It is below –30 dB from 200-270 GHz.

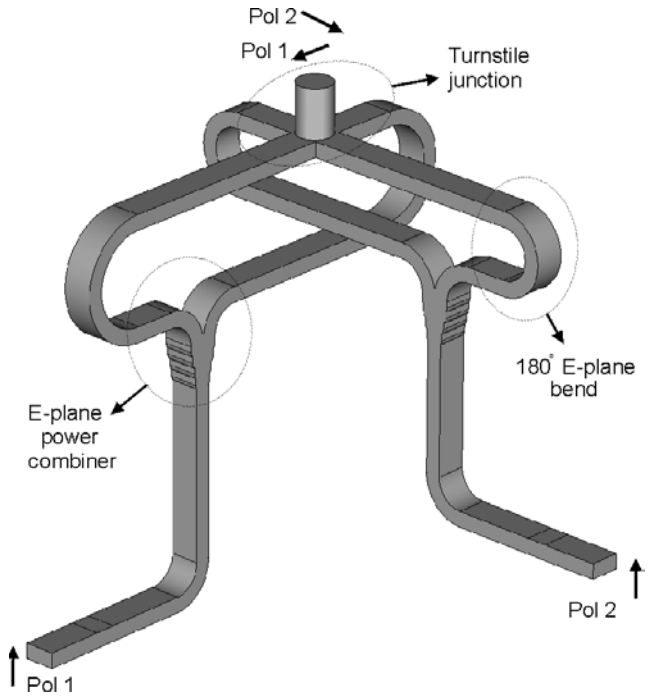

Fig. 3. Internal view of the full OMT. Opposite ports of the turnstile junction are brought together with E-plane bends and power combiners.

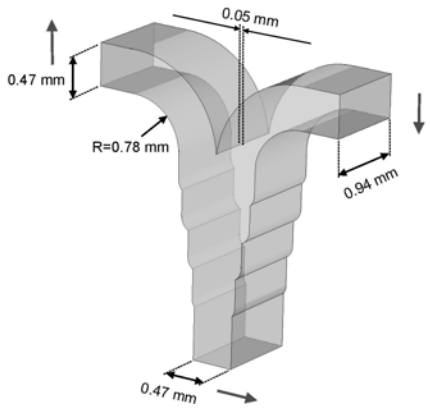

Fig. 4. Internal view of the E-plane Y-junction used to recombine the 180^0 out of phase signals at the output of the turnstile junction.

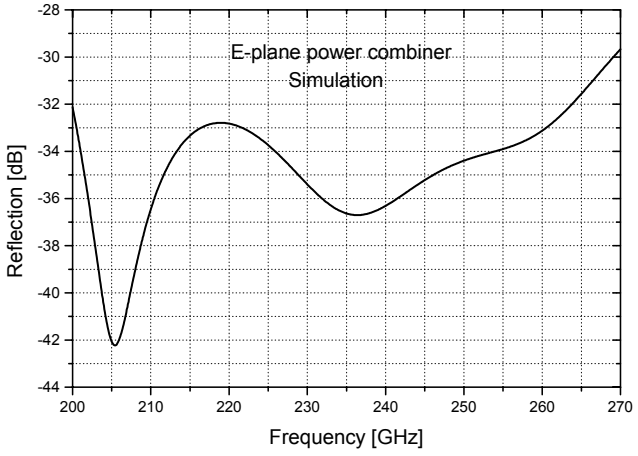

Fig. 5. Simulated reflection coefficient at the common waveguide port of the three-port device illustrated in Fig. 4.

The inside radius of the waveguide bends is 1.41 mm for Pol 1 and 0.78 mm for Pol 2. Electromagnetic simulation shows that even the tighter bend has reflection coefficient below –38 dB across the full waveguide band.

After recombination in the Y-junction, each signal is directed to its output flange through a 90^0 E-plane bend with inner radius 0.78 mm.

Figs. 6 and 7 show the simulated reflection coefficient and transmission losses for both polarization channels of the full OMT. The simulation was performed with the three-port model shown in Fig. 3, including the turnstile junction, power combiners, and all connecting waveguides. The model included the short section of 1.27 mm diameter circular waveguide at the input port to take into account the discontinuity at the feed-horn/OMT interface. A Cartesian mesh was automatically generated and the time domain solver calculated the broadband response of the device in one simulation run. We set the parameter "lines per wavelength" to 12; this is the minimum number of mesh lines per wavelength in each coordinate direction for the shortest wavelength in the simulation.

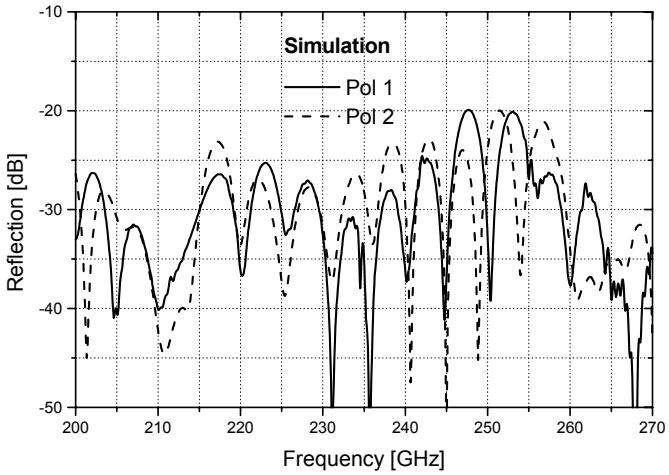

Fig. 6. Simulated Pol 1 (solid line) and Pol 2 (dotted line) amplitude reflection of TE_{11} mode at the circular waveguide output of the feed-horn when looking into the OMT input. The simulation refers to the 3-port device illustrated in Fig. 3 modified to include the abrupt transition between circular waveguides shown in Fig. 1.

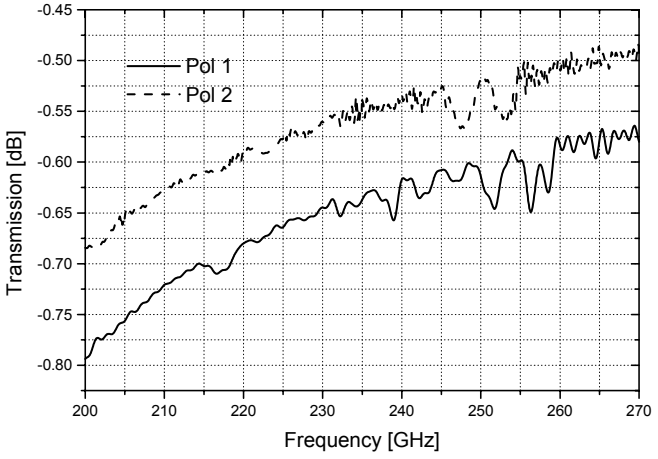

Fig. 7. Simulated room temperature transmission losses for Pol 1 (solid line) and Pol 2 (dotted line) of the OMT. We assumed a conductivity of half the dc value of gold $\sigma_{Au}=(4.26\cdot10^7)/2\ \Omega^{-1}m^{-1}$.

The predicted reflected amplitude at the circular waveguide port is below –20 dB for both polarizations between 200 GHz and 270 GHz. The room temperature transmission loss is below 0.8 dB for both polarizations. For this calculation we assumed the blocks are plated with pure gold and used a gold conductivity of half its dc value. For comparison, we estimate the theoretical room temperature loss [7] of a straight section of WR3.7 waveguide with perfectly smooth surfaces and a conductivity $\sigma_{Au}=(4.26\cdot10^7)/2\ \Omega^{-1}m^{-1}$ to be in the range 0.18-0.26 dB/cm between 200-270 GHz.

The electrical path length from the circular waveguide at the input of the OMT to the WR3.7 waveguide outputs is 30 mm for Pol 1 and 26 mm for Pol 2. The 0.1 dB higher insertion loss predicted for Pol 1 compared to Pol 2 is consistent with its 4 mm extra length.

The insertion loss of the OMT is expected to decrease by a factor of ~3 when it is cooled to cryogenic temperatures [8]. Therefore, we expect insertion losses in the range 0.16-0.27 dB when the OMT is operated at 4 K in front of SIS mixers.

III. Mechanical Design

The OMT is constructed by dividing the structure of Fig. 3 into four blocks that intersect along the circular waveguide axis. This allows all rectangular waveguides to be split along their midplanes. The power combiner for Pol 1 could be located along the central axis of the structure, but it is deliberately offset so that the sharp cusp of the Y-junction does not coincide with the plane where two blocks join. The tuning stub at the center of the turnstile junction is split into four identical sections that are machined at the same time as the rectangular waveguides.

The top of the OMT accepts a standard UG387 flange so it can mate with our existing feed horns. Although the locating pins for this flange are on the normal 14.29 mm diameter bolt circle, it was not possible to locate the waveguide screws in their normal positions, so a special clamp will be made to attach the flange. Custom mini-flanges, rather than standard UG387 flanges, are used for the output waveguides. Reducing the flange diameter allows the OMT to be smaller, hence reduces the waveguide lengths and insertion losses. The alignment pins and screw holes in the mini-flanges are on a 7.11 mm diameter bolt circle.

Thus far we have machined two OMTs on our numerically controlled milling machine. To minimize setup time, we machine all four blocks at one time as part of a single 12.7 x 12.7 x 165 mm metal bar. The bar is mounted to a tool steel fixture on the milling machine table with five 10-32 screws. A light cut is taken off one surface of the bar, then the fixture is rotated to expose the second surface of the bar and a light cut is taken off this surface as well. The waveguide circuitry, screw holes, and alignment pin holes are cut into this face of the four blocks in one pass, then the fixture is rotated back to the original position and the waveguide circuitry and holes are cut into the first face of the four blocks, again in one pass. Figure 8 shows the bar after it is removed from the fixture. To complete the OMT, the bar is cut into four sections; these are

aligned with 2.38 mm diameter dowel pins and bolted together. Finally, the outer surfaces are faced off and the round input waveguide and associated mounting holes are machined into the top face of the OMT.

Figs. 9-12 show photos of, respectively, one of the blocks in detail, all four unassembled blocks, the mated block pairs, and the fully assembled OMT. The final OMT, after finish of the surfaces, is a cube 23 mm on a side.

From the electromagnetic simulations described in [4] we estimate that machining tolerances must be ±10 μm to avoid degrading the OMT performance. Four types of mechanical imperfections were considered in these simulations: a difference in lengths of the opposite waveguide arms between the turnstile junction and the power combiner; a tuning stub that was too high; a circular waveguide offset from the intersection of the four blocks; and a difference in the height of the four quadrants of the tuning stub. Among the fabrication and alignment errors considered, differences in the lengths of the waveguide sidearms, between the turnstile junction and the power combiner, are the most harmful. These cause the appearance of a series of narrow resonances regularly spaced in frequency.

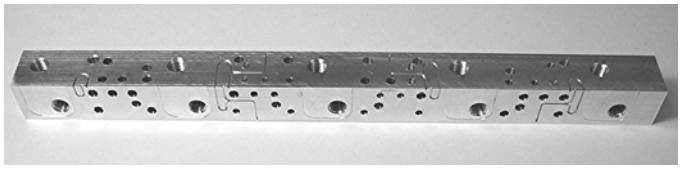

Fig. 8. View of the aluminum bar showing the machined waveguide circuitry of the two internal faces of the OMT. The bar is later cut in four parts which are assembled to form the OMT.

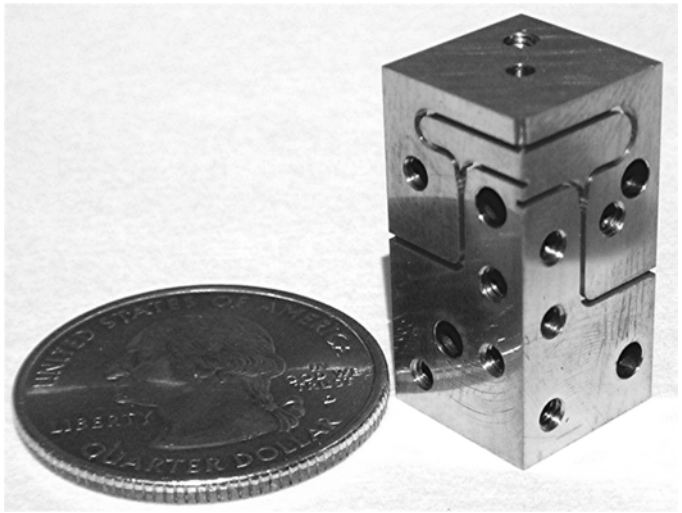

Fig. 9. View of one of the four TeCu blocks of the OMT showing the internal waveguide circuitry of turnstile junction, bends, and power combiners.

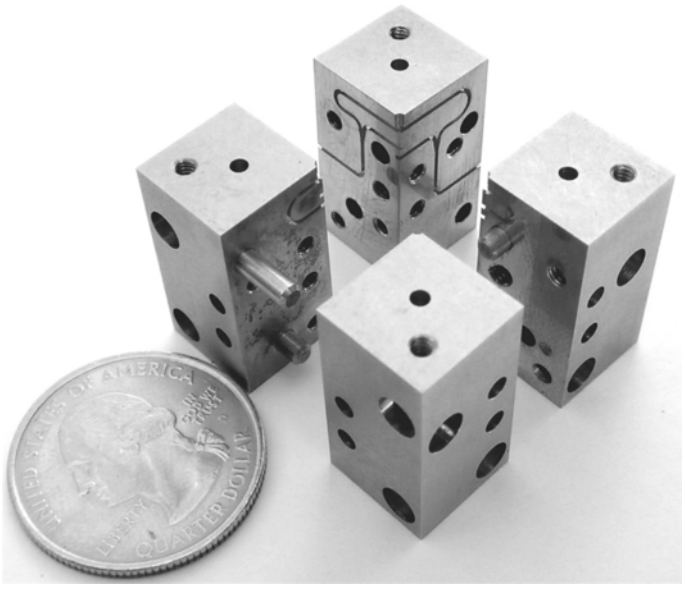

Fig. 10. View of the four blocks of the OMT.

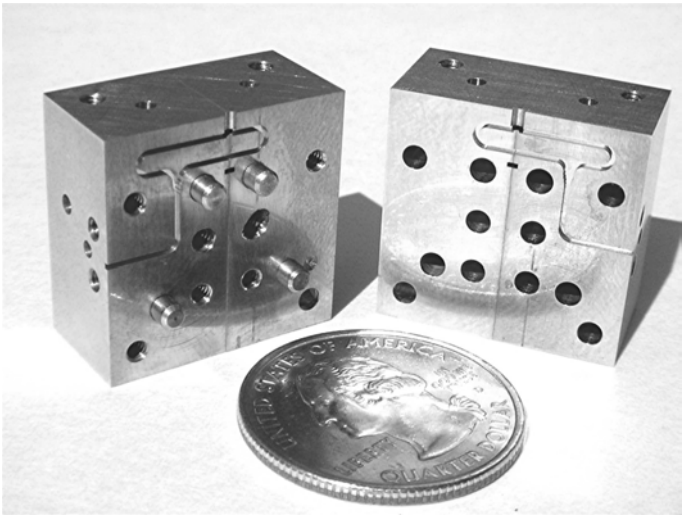

Fig. 11. View of assembled mating pairs of blocks showing the waveguide circuitry for Pol 2.

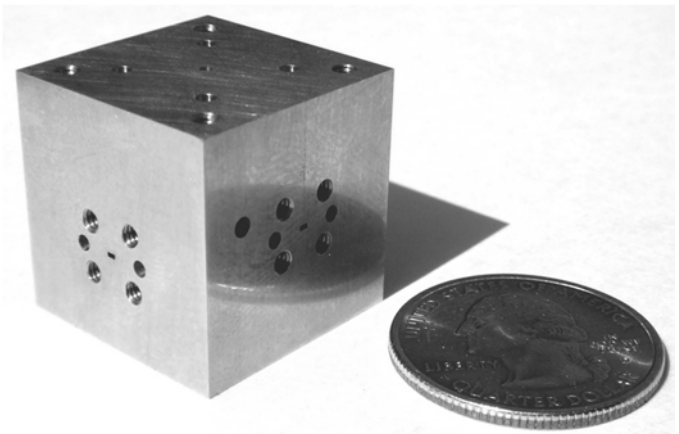

Fig. 12. View of assembled OMT with the circular waveguide input on top and the two WR3.7 waveguide outputs with custom mini-flanges. The external dimensions are 23 mm x 23 mm x 23 mm.

IV. Conclusion

We presented the design of an OMT with a circular waveguide input (diameter 1.12 mm) and two WR3.7 waveguide outputs for the 200-270 GHz band. The OMT utilizes a turnstile junction and two E-plane power combiners. A tuning stub located at the base of the circular waveguide matches the input over a broad frequency band.

The predicted amplitude of the reflection coefficient at the circular input port is below -20 dB for both polarization channels from 200-270 GHz.

The OMT is constructed from four blocks that intersect along the circular waveguide axis. Room temperature insertion losses below 0.8 dB are predicted. From simulation we estimate that machining tolerances must be within ±10 μm to avoid degraded performance.

References

[1] E. J. Wollack and W. Grammer, "Symmetric Waveguide Orthomode Junctions," *Proceedings of the 14th. International Symposium on Space Terahertz Technology*, Tucson, Arizona, Apr. 2003, pp 169-176.

[2] G. Narayanan and N. Erickson, "Full-Waveguide Band Orthomode Transducer for the 3 mm and 1mm Bands," *Proceedings of the 14th International Symposium on Space Terahertz Technology*, Tucson, Arizona, Apr. 2003, pp 508-512.

[3] A. Navarrini, and M. Carter, "Design of a Dual Polarization SIS Sideband Separating Receiver Based on Waveguide OMT for the 275-370 GHz Frequency Band," *Proceedings of the 14th International Symposium on Space Terahertz Technology*, Tucson, Arizona, Apr. 2003, pp 159-168.

[4] A. Navarrini and R. L. Plambeck, "A Turnstile Junction Waveguide Orthomode Transducer," *IEEE Trans. Microwave Theory Tech.* submitted.

[5] CST Microwave Studio. Büdinger Str. 2 a, D-64289 Darmstadt, Germany.

[6] A. R. Kerr, "Elements for E-plane Split-Blocks Waveguide Circuits," National Radio Astronomy Observatory, ALMA Memo No. 381, Jul. 2001.

[7] A. F. Harvey "Microwave Engineering," Academic Press Inc. London, 1963, pp. 15.

[8] E. J. Wollack, W. Grammer, J. Kingsley, "The Bøifot Orthomode Junction," ALMA Memo No. 425, May 2002.

A. Navarrini (S.M. '96-Ph.D '02) received an S. M. degree in physics from the University of Florence, Italy, in '96. After one year of graduate research in optoelectronics at University of College London he started to work on heterodyne instrumentation at IRAM, France, where he completed his Ph. D. in '02.

He is currently a postdoctoral fellow at the Radio Astronomy Lab at the University of California, Berkeley. His research interests include superconducting devices, low noise heterodyne instrumentation, submillimeter and quasioptical techniques, analysis of 3-D electromagnetic problems, and star formation.

R. L. Plambeck (S.B. '71-Ph.D '79) received an S.B. from M.I.T. and a Ph.D. from the University of California, both in Physics. Since 1979 he has worked at the University of California Radio Astronomy Lab, currently as Research Astronomer. His interests are in observational millimeter astronomy, particularly star formation, and in low-noise instrumentation.

D. Chow (S.B. '81) received an S.B. from College of South China. He is a Principle Laboratory Machinist for the Radio Astronomy Lab, University of California, Berkeley since 1990. He has worked extensively on precision machining of microwave and millimeter-wave components. His work includes manufacturing prototype mixer blocks, filters, feeds and orthomode transducers.

Micro-machined quasi-optical Elements for THz Applications

K.-F. Schuster, N. Krebs, Y. Guillaud, F. Mattiocco, M. Kornberg and A. Poglitsch

***Abstract*—We review the possibilities of micro-machined quasi-optical elements for THz radiation and report on the development of such elements at IRAM. Micro-machining of dielectrics permits us to create effective media for the THz frequency range. These media can be used to fabricate novel types of efficient quasi-optical elements. We discuss the technical challenges and compare the results of various modeling approaches with preliminary measurements.**

***Index Terms*—THz quasi-optics, Silicon micro-machining, artificial dielectrics**

I. Introduction

Micro-machining techniques and, in particular, Si micro-machining, has been recognized as an essential tool for THz technology. Most applications so far try to use micro-machining to extend existing concepts like waveguide elements and planar circuits from the millimeter into the THz range. However these techniques also allow us to create new and un-conventional quasi-optical elements. Due to its excellent properties as a low-loss dielectric, Silicon is of high interest. A key question remains the creation and modeling of artificial dielectrics. The term "artificial dielectrics" is normally used for heterogeneous dielectric material with structuresof sub-wavelength size or smaller, and for which the assumption of an effective dielectric response is a good approximation. Here we consider waves propagating nearly perpendicular to the translation-invariant direction of 1D or 2D structures. Other cases are often described as photonic band-gap materials, a class of materials which is not the subject ofthis work.

II. Silicon and possible Applications

Silicon is a unique material for THz technology for many reasons. (1) It has outstanding dielectric properties with very low loss up to 10 THz. (2) Due to its importance for semiconductor technology, it can be obtained in excellent quality. (3) There is a large variety of technologies to structure silicon and to combine it with structured metal layers or dielectric membranes, and, (4) Silicon is well suited for cryogenic applications due to its small coefficient of thermal expansion and its high thermal conductivity.

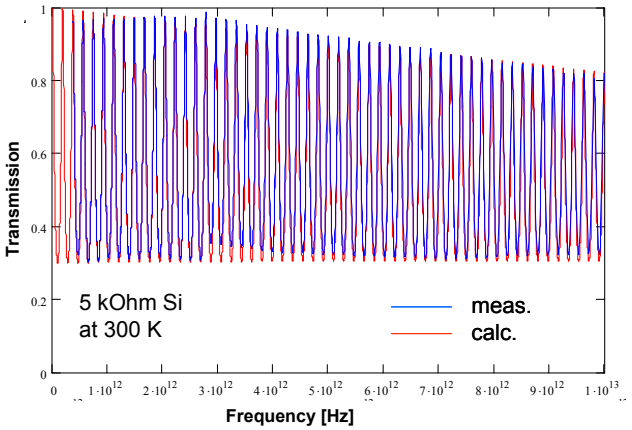

Figure 1: Transmission through a plane silicon wafer (240µm) at room temperature as measured by Fourier transform spectroscopy (FTS). The measurements can be fit up to 10 THz with good precision with a single dielectric constant and loss tangent (11.7, $\leq 7 \cdot 10^{-4}$).

Artificial dielectrics have a rapidly increasing impact on optical science, but also have long been used in the microwave and in the mm/submm ranges in their simplest forms like linear rectangular grooves. Silicon micro-machining has opened up the way to create artificial dielectrics in the THz range [1][2]. The relatively high dielectric constant of Si (11.7) allows tailoring of the dielectric constant of a micro-machined sample on a very broad range when using vacuum as a second medium. An example of the Si material used by us is given in Fig. 1.

The possibility to freely modulate the effective dielectric constant leads to a series of new devices in the THz range. If stacked in flat layers, high performance antireflection coatings [3][4] and dielectric filters or dichroics are possible (see Fig. 2). These devices will be well suited for cryogenic application, because layers of different dielectric constant will have the same thermal contraction and effective cooling. If the

Manuscript received May 28, 2005.

K.-F. Schuster, N. Krebs, Y. Guillaud, F. Mattiocco are with the Institute Radio Astronomy in the Millimetrerange IRAM, St Martin d'Heres, 38406, 300 Route de la Piscine, France (phone: 0033-476824921; fax: 0033-476515938; e-mail: schuster@ iram.fr).

M. Kornberg and A. Poglitsch are with the Max-Planck-Institute for extraterrestrial Physics, Giessenbachstraße, 85748 Garching, Germany.

effective dielectric constant is modulated laterally, diffractive elements can be created like flat lenses and lens arrays.

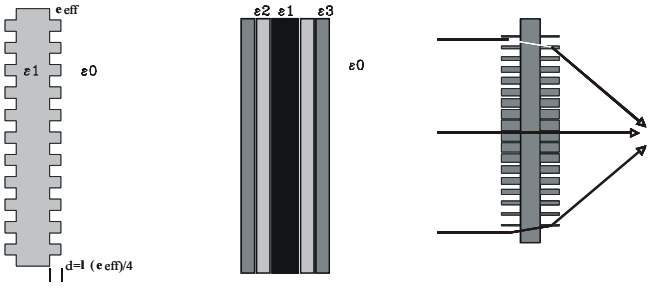

Figure 2: Planar quasi-optical elements made by micro-machining of dielectrics (matched window, dielectric filter and planar lens).

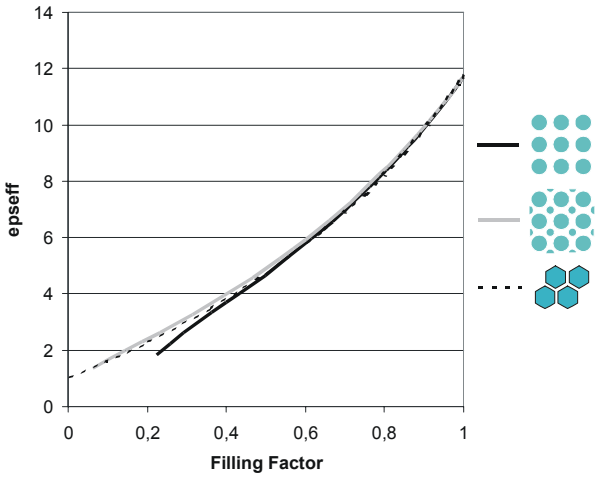

Figure 3: Low frequency effective dielectric constant versus filling factor for different isotropic patterns etched into Silicon.

III. The Problem of Isotropy

While linear grooves are employed frequently for materials with relatively low dielectric constant (plastics, quartz, etc), silicon shows very strong polarization effects for such grooves. In fact the difference in ε_{eff} between co-polarized and cross-polarized waves can be as large as 200% for filling factors between 0.5 and 0.7. For most applications, this behavior is undesirable, and it is therefore of great importance to develop patterns that are polarization independent Symmetry considerations lead to the conclusion that for perpendicular incidence, only regular lattices are fulfilling these requirements, e.g. the square and the hexagonal lattice. The pattern of the individual cells can be of any shape that offers rotational symmetry of order 2 or higher (e.g. holes, polygons >4 and combinations). In optics, such materials are called uniaxial. Oblique incidence destroys the rotational symmetry of the two-dimensional patterns and will therefore generate polarization effects. As long as the incidence angles are smaller than 30 degrees, however, these effects tend to be small.

IV. Modelling

Although special cases were treated several decades ago, the general problem of modeling artificial dielectrics is a matter of current research. It is common to develop the effective refractive index n_{eff} in a power series of the structure period to wavelength ratio Λ/λ :

$$n_{eff} = n^{(0)} + n^{(2)}(\Lambda/\lambda)^2 + n^{(4)}(\Lambda/\lambda)^4 + \mathrm{K}$$

For the 0th order or low-frequency solutions linear grooves can be calculated analytically (Born & Wolf). Low-frequency solutions for more complex artificial dielectrics can be easily obtained by numerical simulations of the electrostatic case. These calculations are also useful to calculate the maximum range of effective dielectric tuning for a given pattern. In particular, hole patterns have minimum filling factors which limit the minimum achievable effective dielectric constant (see Fig. 3). Other patterns might not be used close to a zero filling factor simply because of machining tolerances and/or mechanical stability considerations.

Second-order analytical solutions exist for linear grooves and have been used to derive a practical approximation for 2nd order solutions to a square pattern [4][5]. Beyond this only numerical solutions can be found. Numerical methods include finite-element methods, conformal mapping, shoot-back methods and Fourier expansion techniques (see references in [3], [6]).

We have implemented 0th-order finite element codes for a quick check of the general behavior of different patterns and filling factors (Fig. 3). To derive higher-order solutions we have used commercial software (CST Microwave-Studio) in the time domain mode to calculate dispersion for different geometries (Fig. 4).

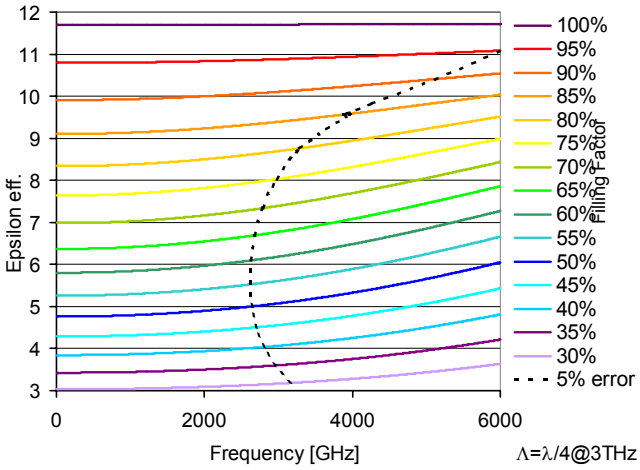

Figure 4: Effective dielectric constant of hexagonal pattern with different filling factors in Silicon as calculated with a time-domain FEM. The structure size is λ/4 at 3 THz. The area to the left of the dashed line can be approximated by the low frequency solution to within an error of less than 5%.

A question of practical importance is how large the period of any mixing pattern can be made. This will determine the machining effort required for a desired electrical behavior. In fact, two questions have to be distinguished in this respect. Firstly, one may ask how large the pattern can be made before the effective dielectric constant differs noticeably from the 0^{th}-order solution. Secondly, it is important to know at which pattern size the concept of an effective, although possibly frequency-dependent dielectric constant breaks down, because of higher-order mode propagation or diffraction effects. The answers to both questions depends on the material parameters, the detailed form of the pattern and the filling factor. Concerning the dispersion a typical result can be seen in Fig. 4 for a hexagonal pattern. For this particular case of silicon, the relative difference between the long-wavelength limit and the actual value of ε_{eff} stays below 5% for all filling factors as long as the structure period is smaller than $\lambda/4$.

The question about the validity of an effective-medium approach is more complex to answer, as several conditions have to be fulfilled independently. A necessary, but not sufficient condition, is the exclusive propagation of 0^{th}-diffraction order in the far field of the element. For perpendicular incidence it follows from the diffraction grating equation that $\Lambda/\lambda < 1/\max(n_1,n_2)$, where n_1 and n_2 are the refractive indices of the media in the front and in the back of the artificial dielectric, respectively. For silicon this condition requires $\Lambda/\lambda < 3.5$, fairly close to the requirements for relative dispersion < 5% as described above. Other conditions must be fulfilled to exclude higher-order mode propagation within the artificial dielectric, and are leading to constraints of the material index and the particular shape of the pattern [7][8].

V. First Results and Technical Challenges

As a first step in our development program, we have used 0^{th}-order calculations to design a hexagonal pattern with a filling factor 0.35. This corresponds to an effective low-frequency dielectric constant of 3.42, the geometrical mean of Si and vacuum/air and as required for matching between these medias. The distance of two cells was 51µm (See Fig. 5). The hexagonal pattern offers the advantage of being mechanically very rigid and well suited for low filling factors.

A Si-wafer of 240µm thickness was etched from both sides with the designed pattern to a nominal depth of 22µm and the transmission was measured at room temperature in an intermediate waist of the optics of a commercial FTS spectrometer (see Fig. 6). The result shows a matching very close to 2 THz with a matched bandwidth of greater than 30% for transmission above 90%. The measurements can be described well with a simple transmission line model up to 2 THz. Above this frequency, the model fails due to diffraction and excitation of higher-order modes.

New ways of measuring planar devices are under development at IRAM. These include setups with mm-wave network analyzers and resonant cavity measurements which will give complete amplitude and phase information as well as antenna range measurements to characterize polarization-dependent off-axis scattering.

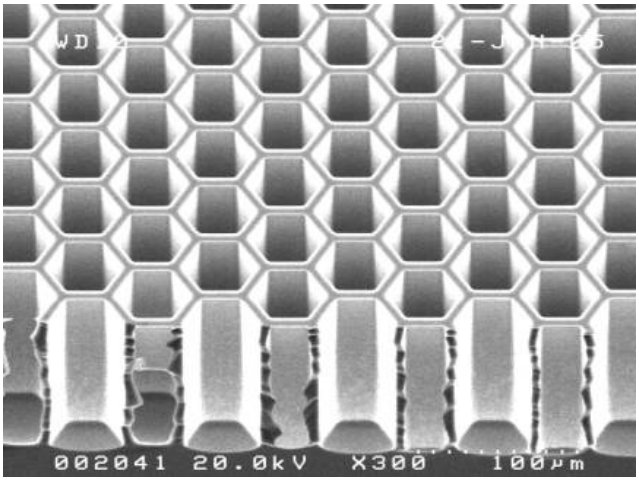

Figure 5: Micrograph of a hexagonal pattern as machined with deep Silicon etching and an effective dielectric constant close to 3.42, as required to match air and silicon.

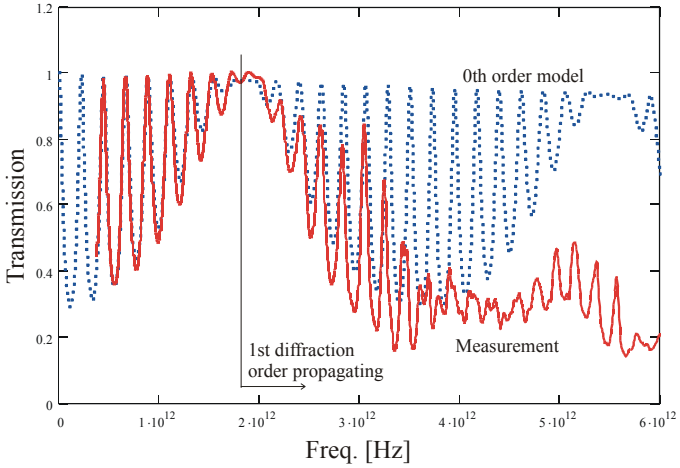

Figure 6: Transmission of a silicon wafer at room temperature with micro-machined matching layer for 2 THz (FTS measurement). Above 2 THz, the simple transmission line model using the 0^{th}-order solution breaks down.

Future technical challenges include improving the control of etch depth as well as aspect ratio dependent etching effects (ARDE). Further on, it will be necessary to study etch-induced surface damage or pollution and its consequences for the THz properties of the samples.

Future modeling must include finite angles of incidence and propagation of higher-order modes.

VI. Conclusion

Silicon micro machining allows tailoring of artificial dielectrics for the THz range with a widely adjustable dielectric constant. First simple examples of polarization independent quasi-optical elements have been successfully designed and fabricated. Next steps will include improved modeling and the design of planar diffractive elements.

ACKNOWLEDGMENT

This work has been supported by ADIXEN Alcatel Vacuum Technology.

REFERENCES

[1] Wagner-Gentner, Poster P6-12 , this conference.
[2] S. Biber, D, Schneiderbanger, L.-P. Schmidt, M. Walter, B. Fischer, M. Schwarzer, P.U. Jepsen, 2004, Proceedings of Int Conf. on Infrared and Millimeter Waves, Karlsruhe.
[3] E.B. Grann, M.G. Morharam and D.A. Pommet, 1994, J. Opt. Soc. Am. A. Vol. 11, No. 10 p. 2695.
[4] R. Bräuer and O. Bryngdahl, 1994, App. Optics, Vol. 33, No. 34, p. 7875.
[5] S.M. Rytov, 1956, Soviet Physics JETP **2**, 466-475.
[6] Ph. Lalanne, 1998, Phys. Rev **B58**, 9801-07.
[7] H. Kikuta, Y. Ohira, H. Kubo and K. Ywata, 1998, J. Opt. Soc. Am. A **15**, 1577-1585.
[8] Ph. Lalanne, S. Astilean, P. Chavel, E. Chabril and H. Lanois, 1998, Opt. Let. **23**, 1081-1083.

Session 12:

New detectors

Wednesday May 4, 13:20-15:00
Chairman: Eyal Gerecht

A New Hot Electron Bolometer Heterodyne Detector Based On Single-Walled Carbon Nanotubes

Sigfrid Yngvesson

***Abstract*— A new type of hot electron bolometer heterodyne detector is proposed that has the potential for achieving intermediate frequency bandwidths of several hundred GHz. The concept relies on experimentally measured ballistic/quasi-ballistic transport properties of single wall carbon nanotubes and the measured temperature dependence of the resistance of such tubes. The concept is related to that of Lee et al. [1] that utilized the ballistic transport in short 2DEG structures to achieve a bandwidth of 40 GHz. Receiver noise temperatures of a few thousand Kelvin, and local oscillator powers of 1 microwatt or less are estimated. This paper will explain the principle of the new detector, and give quantitative estimates of its performance.**

***Index Terms*—Carbon nanotubes, hot electron bolometers, terahertz heterodyne detectors, mixers.**

I. Introduction

HOT Electron Bolometer (HEB) heterodyne detectors have a history that goes back to the InSb mixers of the 1960s [2]. Since that time, HEB heterodyne detectors (mixers) have steadily progressed in terms of desirable system properties such as noise temperature and IF bandwidth.

HEBs are two-terminal devices with a heat-able bolometer medium between ohmic contacts. It is characteristic of HEBs that the electrons in the bolometer increase their electron temperature (θ) above the lattice temperature, in response to electromagnetic radiation absorbed in the bolometer. It is also required that the bolometer resistance be a function of the electron temperature. As the bolometer is heated, it will then change its resistance, and the change in resistance is detected by DC biasing the HEB. If the radiative input is turned off, the electron temperature will relax back to the lattice temperature due to heat conduction to the thermal bath, with a characteristic time-constant, τ_{TH}. The HEB can also be operated in the heterodyne mode. Two frequencies, the signal or RF frequency (f_{RF}) and the local oscillator frequency (f_{LO}), are then applied to and absorbed by the bolometer. Such a detector can sense the difference (or intermediate) frequency ($f_{IF} = |f_{RF}-f_{LO}|$), for which the intermediate frequency (IF) bandwidth will be given by

$$B = 1/2\pi\tau_{TH} \quad (1)$$

Table 1 reviews the main characteristics of different types of HEB mixers that have been developed.

Table 1. Characteristics of different types of HEB mixers

#	Type of HEB	Max. IF Bandwidth	Bandwidth determined by	Ref.
1	InSb	1 MHz	Carrier excitation	[2]
2	2DEG	3 GHz	Optical phonon emission	[3]
3	DHEB Superc.	10 GHz	Electron diffusion	[4,5]
4	PHEB Superc.	5 GHz	Acoustic phonon emission	[6,7]
5	2DEG	20 GHz	Electron diffusion to contacts	[8,9]
6	2DEG	40 GHz	Ballistic electron transport	[1]

HEBs have gone from being bulk type (3-D, #1) to different 2-D configurations (#2-6). The diffusion-cooled type (DHEB) has a bandwidth given by

$$BW \sim \pi D/(2L^2) \quad (2)$$

where D is the diffusivity of the electrons and L the bolometer length [4]. Superconducting DHEBs can achieve wide bandwidth if they are made very short [5] (0.1 μm for Nb devices). In all DHEBs, the heat is transferred preferentially through diffusion of the heated electrons to the contacts. Longer (10 μm) 2DEG devices have bandwidth limited by optical phonon emission [3], but shorter 2DEG devices act as DHEBs and can achieve even wider bandwidth (20 GHz), since the diffusivity is very high (~ 2,000 cm^2/s; compare Eq. (2)) [8,9]. For very high mobility 2DEG material (>10^6 cm^2/Vs) one can reach ballistic transport conditions in short

S. Yngvesson is with the Department of Electrical and Computer Engineering, University of Massachusetts, Amherst, MA 01003, USA; email: yngvesson@ecs.umass.edu

bolometers, and the bandwidth then varies as 1/L, instead of as $1/L^2$ (compare Eq. (2)). Lee et al. [1] measured close to 40 GHz bandwidth in such a 2DEG device that was 1.5 μm long. The electron transit velocity which can be inferred from the measurements is

$$v_t = 2\pi BL = v_F \qquad (3)$$

where v_F = 2.3 x 10^7 cm/s is the Fermi velocity of the 2D electron gas in the channel. Lee et al. [1] quote a measured temperature dependence of the device resistance, dR/dT, of 2 Ω/K. Based on HEB theory [10] one can show that the measured conversion gain of about -20 dB is consistent with this value of dR/dT. The factors that influence the conversion gain are discussed in detail in Sec. III. This gain is about 10 dB lower than for superconducting HEBs, but there are practical situations where the lower conversion gain of the 2DEG mixer is quite acceptable. The origin of the temperature-dependence of the resistance of this *fully ballistic* electron waveguide between two low-loss ohmic contacts is so far not understood. Based on the above papers, especially ref. [1,8,9], one may ask: are there other HEB bolometer media that are capable of reaching even wider bandwidths? This paper explores one such type of medium, that is known to be capable of ballistic and near-ballistic transport, that of single-wall carbon nanotubes (SWNTs). Wider bandwidths in the hundreds of GHz are indeed predicted, as the further discussion will show.

II. REVIEW OF THE TRANSPORT PROPERTIES OF SWNTs

The fabrication of SWNTs has made major advances in the last few years, and it is now possible to reproducibly fabricate and contact SWNTs which exhibit ballistic transport over fairly long lengths [11,12,13]. CNTs can be visualized as 2-D graphene (as in graphite) sheets rolled up at a number of allowed angles (different "chiralities"), see Figure 1 for an example. The energy bands in a SWNT are the result of quantization of the electrons in the *circumferential* dimension; different types of energy bands result depending on the chirality of the particular tube. Given these energy bands, we can then regard the SWNT as a one-dimensional conductor that is either metallic or semiconducting, depending on whether there are electron states near the Fermi energy or not [14]. Metallic contacts can be made to the SWNT (e.g. Pd or Ti). Close to ideal contacts, allowing a transmission probability for electrons of close to 100 %, have recently been produced [12,13]. There is also convincing evidence for ballistic transport in many cases. In general, we can find the conductance of a ballistic 1-D conductor such as a SWNT based on the Landauer model [15]. In this model, the conductance of a ballistic channel, including the effect of the contacts, is

$$G = \frac{2e^2}{h} MT \qquad (4)$$

or a maximum conductance of G_0 =1/(12.9 kΩ) per mode (for T=1). Here, we regard the channel as an electron waveguide, carrying M modes, with an average transmission probability of T between the waveguide channel(s) and the contacts. Metallic SWNTs have two degenerate bands near the Fermi level [14], i.e. M=2, leading to G(max) = 1/(6.45 kΩ).

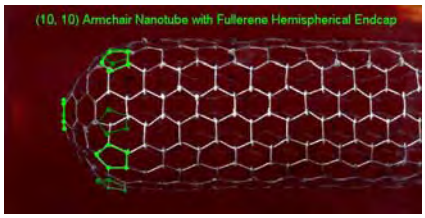

Figure 1. Structure of a so-called "arm-chair" SWNT with chirality designation (10,10).

As metioned above, SWNTs can be either metallic or semiconducting, but we concentrate our discussion on the metallic version. A typical SWNT has a diameter of 1.5 nm. The Fermi velocity is known to be considerably higher than for the 2DEG case, 8.1 x 10^7 cm/s [14]. If we insert this value in (3), and assume L = 200nm, we estimate a bandwidth of 650 GHz, more than an order of magnitude larger than for the 2DEG device. There are several different situations which may occur. For purely ballistic transport, we have already quoted the bandwidth in Eq. (3). In the case of quasi-ballistic transport, we set τ_{TH} equal to the effective transit time, t_{tr}, and calculate the bandwidth by inserting t_{tr} in (1). In surveying some of the available experimental evidence on transport in SWNTs, we will be interested in these questions:

(i) is the resistance temperature dependent;
(ii) what type of scattering occurs;

The fully ballistic regime. Kong et al. showed that the conductance of a SWNT with a length of about 200 nm depends on the temperature [12], most strongly below 100 K. For the shortest tubes, G approaches 2 G_0, consistent with M = 2 in Eq. (4). The conductance and its temperature dependence could be changed by adjusting the gate voltage and thus the Fermi energy in the SWNT. Some SWNTs showed Fabry-Perot like oscillations in their resistance, as the gate voltage was changed [12,13,16]. This and other experiments confirm that ballistic transport applies in the shortest samples. The conductance for the shortest SWNTs [12,13] measured with low voltages shows no temperature dependence.

The acoustic phonon cooling regime. A lower limit of the MFP for acoustic phonon scattering in SWNTs of 300 nm was inferred from measured I-V curves by fitting these to Monte Carlo simulations [13]. This MFP determines a minimum scattering time τ_{ap} = 370 fs.

The optical phonon cooling regime. Optical phonon emission occurs primarily at higher voltages > 0.1 V. Based on the Fermi velocity and MFP = 15 nm obtained by fitting simulations to measured I-V curves [13], we find that the scattering time is as short as 19 fs.

Effects due to defect scattering. The measured temperature dependence of the conductance for a 200nm long SWNT was explained as being due to scattering by a localized defect [12]. The assumption was that localized states within the SWNT create energy-dependent scattering, and that this effect combined with that of the temperature-dependence of the phonon populations. Defect scattering in SWNTs was also investigated in [17].

Semiconducting SWNTs. Without going into this topic in any depth, we may note that experiments again indicate the possibility of MFP's as large as 1 μm [11,17,18].

Based on the experimental evidence available so far, we can now attempt to identify ranges of parameters for which SWNT operation as HEBs would be optimized in terms of conversion gain and bandwidth. *Is it possible to obtain electron temperature-dependent resistance for a fully ballistic SWNT device?* The parallel case of the ballistic 2DEG device [1] clearly obtained such conditions. In the absence of theoretical understanding of the mechanism operating in the 2DEG device [19], we have no guidance as to whether the same mechanism may occur in a SWNT. Until such time as the theoretical situation has been cleared up, we instead propose that *the optimum condition may be one where the device has a length of only a few times the MFP*, so that even a small change in temperature may trigger the onset of a few additional collisions which may alter the current significantly and so the resistance of the nanotube. The bandwidth can be predicted by finding the transit time, and using Eq. (1). In the above regime, the bandwidth will be less than that maximally possible with purely ballistic transport, but only by a small factor. The operating temperature and the device length would be traded off to satisfy the condition of L ~ MFP. We identify three potentially useful parameter ranges below:

1) The data of Kong et al. [12] indicate a 20 % change in resistance for a change in temperature of 20 K, or 1%/K. For a certain gate voltage, a positive dR/dT was measured, and at other gate voltage values a negative dR/dT. The 2DEG device of Lee et al. [1] had dR/dT= + 2 Ω/K, or 2%/K, given that the resistance was about 100 Ω. It thus appears feasible, after optimization, to find a comparable value of dR/dT (in %/K) in SWNTs. The bias voltage at this point [12] was about 10 mV, and the main scattering mechanism invoked is defect/phonon scattering. Based on the bias voltage, the phonons involved would be acoustic phonons.

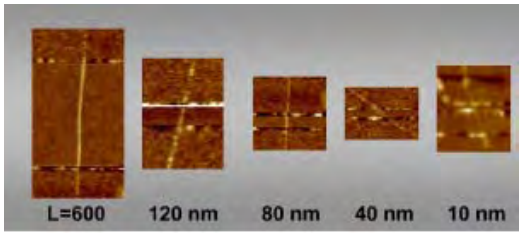

Figure 2. SWNTs of different length placed across gaps between metallic contacts. Reproduced from Javey et al. [13]

The transit time would depend on the type and location of the defect, as well as the MFP for acoustic phonon scattering. Assuming a transit time of 750 fs the bandwidth would be about 210 GHz, and the temperature of operation up to about 50 K.

2) Javey et al. [13] mention a similar temperature dependence of the resistance, up to 150 K, but with little quantitative data. Photographs of their contacted SWNTs are reproduced in Figure 2. McEuen et al. [20] review work in which a temperature dependent resistance is measured for a 1 μm long SWNT up to 290 K, but with a smaller derivative of about 0.2 %/K. Bandwidths similar to case 1) are likely.

3) If we assume optical phonon scattering, McEuen et al. [20] describe a sharply decreased conductance above 100 mV, which must be due to optical phonon emission setting in. The temperature dependence is similar to that in case 2). The optimum length for a SWNT HEB utilizing optical phonon emission would be much shorter, however (the above results [20] are for L= 1 μm).

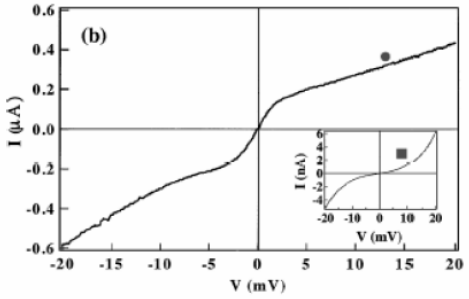

Figure 3a. IV-curve for SWNT of 300 nm length at a specific gate voltage. Reproduced from Kong et al. [12].

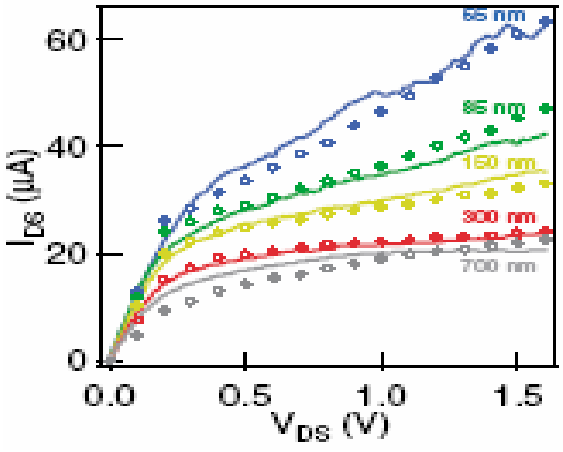

Figure 3b. IV-curves for SWNTs of different lengths in a higher voltage range than for Figure 3a. The knee in the curves is a result of optical phonon emission by the electrons. The measurements were taken at room temperature. Reproduced from Javey et al. [13].

If one were to use the principle described above of choosing L as a small number times the MFP, for example L ≈ 50 nm, one would anticipate a much steeper temperature dependence. We note that tubes down to L=10 nm have been fabricated and measured [13]. The IF bandwidth based on the transit time would theoretically be of the order of 2.5 THz, but kinetic inductance phenomena to be discussed below are predicted to limit the response to much lower frequencies.

The conversion gain can be estimated from measured I-V-curves [10]. A parameter C_0 is defined as follows

$$C_0 \equiv \frac{dR_0}{dP} = \frac{dR_0}{d\theta} \times \frac{d\theta}{dP_{DC}} \qquad (5)$$

Here, R_0 is the bolometer DC resistance = V_0/I_0 and P_{DC} the DC power dissipated in the bolometer. The AC resistance at a specific operating point (V_0,I_0) is given by $(dV/dI)_{DC}$, which can be read from an IV-curve. One can show [10] that

$$C_0 = \frac{R_0}{P_{DC}} \frac{(dV/dI)_{DC} - R_0}{(dV/dI)_{DC} + R_0} \qquad (6)$$

The most important factor in determining the conversion gain of an HEB mixer is $C_0 I_0^2$. This factor is typically about 0.5 for a good superconducting PHEB mixer [7], and 0.1 to 0.2 for the 2DEG mixer [3]. It then is clear why in order to identify a promising candidate for a HEB mixer, we have been emphasizing the desirability of large values for dR/dθ. The second factor in Eq. (5) is the inverse of the thermal conductance (G) of the bolometer. We can also write G as $C_e * V/\tau_{TH}$, where C_e is the heat capacity (per unit volume) of the electron medium in the bolometer, and V the bolometer volume. We are striving to achieve a very small value for τ_{TH} in this paper, which tends to make G large. However, the effective bolometer volume of a SWNT HEB is also extremely small, which makes it feasible to still achieve the desired value of C_0, such that $C_0 I_0^2$ is not much less than 1.0. The usefulness of the IV-curves[1] is that they directly tell us (through Eq. (6)) the value of the parameter C_0: a good bolometer has an IV-curve with a slope at the operating point that differs as much as possible from $1/R_0$. Such curves measured for SWNTs in [12,13] compare favorably with those of 2DEG devices which have about -18 dB to -20 dB conversion gain [1,8,9], see Figure 3 (previous page) for examples of such curves. The conclusion from evaluating cases 1) through 3) is that quasi-ballistic SWNTs could provide at least a similar conversion gain as 2DEG ballistic HEBs, with a much wider bandwidth. The optimum device length, bias voltage, LO power and temperature range must first be empirically determined through DC measurements, at different temperatures. In some cases, a gate voltage may be required for optimum operation. We should finally note that our discussion of the conversion gain assumes that the bolometer impedance is close to being matched at all three frequencies involved, the LO, RF and IF frequencies, respectively. How this may be accomplished is the topic of the next section.

[1] Strictly speaking, we should use an IV-curve under LO pumping for this evaluation. In the case of 2-DEG HEB mixers, it was shown that using the unpumped IV-curves yields close to a correct result [3].

III. CHARGE-CARRIER INERTIA AND OPTICAL AND MICROWAVE COUPLING TO SWNTs.

We would anticipate coupling electromagnetic waves to a SWNT in a manner similar to what is already a very popular method for other HEB mixers – quasi-optical coupling using a silicon lens and an antenna photo-lithographically etched on a silicon substrate, as shown in Figure 4. A typical antenna impedance is 100 Ω. We next need to estimate the equivalent circuit at terahertz frequencies for the SWNT. One-dimensional conductors have an unexpectedly large inductance, basically due to quantum-mechanical effects, the kinetic inductance, L_K. As shown in [21] and other papers referred to therein, the kinetic inductance $L_K = \hbar\pi/4e^2v_F$ or about 4nH/μm, a kinetic inductance of roughly 1 nH for a 200 nm long SWNT. At 1 THz, the inductive reactance would be 7.4 kΩ, about equal to the minimum resistance of the tube.

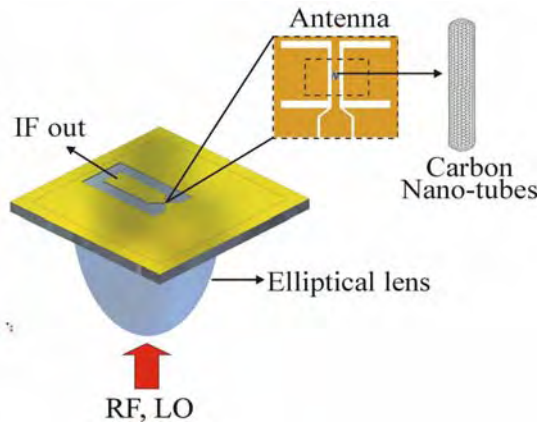

Figure 4. Quasi-Optical Coupling of a SWNT, using a twin-slot antenna and an elliptical silicon lens.

Measurements of SWNTs at GHz and THz frequencies are needed to confirm this kinetic inductance. Microwave measurements on metallic SWNTs [18] indicate that *the microwave resistance can be considerably smaller than that measured at DC*, however, and actually much smaller than the quantum resistance predicted from (4). As explained in [18], this is possible if the contacts have a large capacitance, which shorts out the contact resistance at high frequencies. This will considerably simplify the problem of impedance matching at to the bolometer.

In order to tackle the problem of coupling to the bolometer resistance, which may still be larger than the range of 50 – 100 Ω typical for antennas or microwave circuits, we can use a matching circuit such as shown in Figure 5, tuned to about 500 GHz. For the sake of illustration, we assume a bolometer resistance of 6.5 kΩ, that should be matched to a 50 Ω circuit. The frequency response is given in Figure 6. This example shows that a good match can be obtained, at the expense of a narrower bandwidth, in this case about 15 % bandwidth at the – 3dB level. It would also be very useful to measure SWNTs at lower microwave frequencies (a few GHz) in microstrip or CPW circuits. The matching circuit would in general need to take into account the kinetic inductance. Similar techniques could be used for matching at the IF frequency. In order to decrease the device resistance it is also possible to place several SWNTs parallel across the gap between the contact pads. The experimental techniques for accomplishing this are not yet well developed, however.

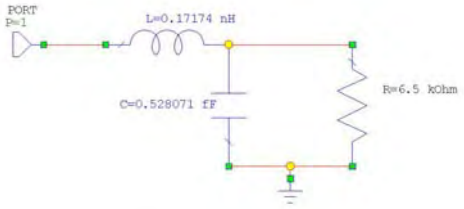

Figure 5. Matching circuit for a SWNT. Port 1 is a 50 Ω port.

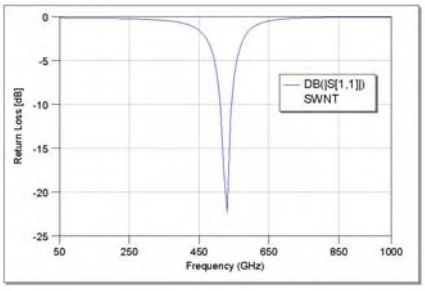

Figure 6. Frequency response of the circuit in Figure 5.

IV. PREDICTION OF THE PERFORMANCE OF A SWNT MIXER RECEIVER

In Section III we very roughly estimated a conversion loss of 20 dB (or better) for a SWNT mixer. There is again only sparse guidance available for predicting the output noise of such a mixer. However, Lee et al. [1] noted that in the ballistic regime the output noise decreased by about an order-of-magnitude, compared with the diffusion-cooled regime. A possible explanation for this observation may be that the thermal fluctuation noise (the dominant source of noise in all other HEB mixers) decreases drastically in ballistic HEBs. The remaining output noise can then be estimated as the Johnson noise at the operating temperature. The Johnson noise contribution in other HEB mixers is somewhat less than the operating (thermal bath) temperature. The actual double-sideband (DSB) mixer noise temperature will be the device output noise temperature multiplied by one half times the conversion loss. With a conversion loss of about 20 dB we estimate a DSB receiver noise temperature of < 50 x 77 K or < 4,000 K for a device operating at 77 K, and lower for lower operating temperatures. There will also be a small contribution from the IF amplifier. The receiver noise temperature may thus be somewhat higher than that of a Schottky barrier mixer. We predict a much smaller LO power for the SWNT compared with the Schottky mixer, however; at least three orders of magnitude less. This estimate is based on the fact that only the contact regions need to be heated, and these are very small (i.e. low heat capacity, as noted in Sec. III). A very rough estimate yielding a value less than $P_{LO} \leq 1$ μW can be obtained by comparison with the 2DEG HEB, which required 10 μW of LO power when operated at 77 K. We note that the contact regions in a SWNT are much smaller than those of the 2DEG HEB, so the estimate of 1 μW is likely to be on the high side. The low LO power will be advantageous in focal plane array applications, for example. We can estimate the system performance of an SWNT mixer element used for broadband imaging of a thermal object at, say, 700 GHz, by using the standard radiometer formula

$$\Delta T_{RMS} = \frac{T_{SYS}}{\sqrt{B * \tau}} = 0.5K \qquad (7)$$

We inserted T_{SYS} = 5,000 K, B = 100 GHz and an integration time τ = 1 ms in (7) to arrive at this estimate of the RMS equivalent temperature fluctuations at the system input. The system can detect a temperature difference in the object comparable to a few times ΔT_{RMS}. *The above estimate would represent a state-of-the-art performance that can presently only be achieved by THz detectors cooled to liquid helium temperature* [22], if one also stipulates that the LO power (per pixel) be low enough to allow feeding a focal plane array with many elements, while employing presently available compact LO sources. Such a focal plane array would be able to perform passive thermal imaging at video rates of objects of interest for security applications as well as for medical/biological purposes.

V. CONCLUSION

We summarize the conclusions reached in this paper in Table 2 below (next page). The left column gives different potential regimes of operation, as discussed above.

There are several major challenges that must be overcome in order to realize the potential performance estimated in this paper; the primary ones have to do with finding conditions that yield a sufficiently steep temperature-dependence of the SWNT resistance, and thus a high conversion gain; impedance matching; and fabrication/placement of SWNTs. Any of the

versions of SWNT HEB mixers we have discussed is likely to work over a record bandwidth for HEBs. This also creates a challenge for the IF amplifier design that must match the bandwidth of the HEB. If these challenges can be overcome, the SWNT HEB mixer has the potential for being employed in many system applications, such as THz focal plane array imagers, and broadband detectors for THz spectroscopy investigations.

Table 2. Summary of results discussed in this paper

Ballistic transport	May not show dR/dθ	BW ~600 GHz	
Acoustic phonon/defect scattering	Experim. evidence for dR/dθ	BW 100-200 GHz	Lowest LO power, lowest operating temperature
Optical phonon scattering	Experim. evidence for dR/dθ	BW < 300 GHz	Higher LO power/ operating temperature

ACKNOWLEDGMENT

I acknowledge stimulating and useful discussions related to ballistic/quasi-ballistic transport with Massimo Fischetti. I also thank Fernando Rodriguez-Morales who drew Figures 4 - 6, and performed the circuit calculations described in Sec. III.

REFERENCES

[1] M. Lee, L.N. Pfeiffer, and K.W. West, "Ballistic cooling in a wideband two-dimensional electron gas bolometric mixer", *Appl. Phys. Lett*. vol. 81, pp. 1243-1245, 2002.

[2] F. Arams et al.,"Millimeter wave mixing and detection in InSb," *Proc. IEEE*, vol. 54, pp. 672-676, 1966.

[3] J.-X. Yang et al., "Wide bandwidth electron bolometeric mixers: A 2DEG prototype and potential for low-noise THz receivers", *IEEE Trans. Microw. Theory Tech.* vol. MTT-41, pp. 581-589, 1993.

[4] D. Prober, "Superconducting terahertz mixer using a transition-edge bolometer," *Appl. Phys. Lett.* , vol. 62, pp. 2119-2121 (1993).

[5] R. Wyss et al., *Proc. 10th Intern. Symp. Space THz Technol*., Charlottesville, VA, 1999, p.214.

[6] E.M. Gershenzon et al., "Millimeter and submillimeter range mixer based on electronic heating of superconducting films in the resistive state," *Sov. Phys. Superconductivity, vol.3, pp. 1582-1597, 1990.*

[7] S. Cherednichenko et al., *Physica C* v ol. 372, p. 427, 2002.

[8] K.S. Yngvesson, "Ultrafast two-dimensional electron gas detector and mixer for terahertz radiation," *Appl. Phys. Lett*. vol. 76, pp. 777-780, 2000.

[9] M. Lee, L.N. Pfeiffer, K.W. West, and K.W. Baldwin, *Appl. Phys. Lett.* vol. 78, pp. 2888-2890, 2001.

[10] H. Ekstroem et al., *IEEE Trans. Microw. Theory Techniques*, vol. 43, pp. 938-947, 1995.

[11] S.J. Wind, M. Radosavljevic', J. Appenzeller, and Ph. Avouris, "Transistor structures for the study of scaling in carbon nanotubes", *J. Vac. Sci. Technol. B,* vol. **21(6),** p. 2856, 2003.

[12] J. Kong, E. Yenilmez, T.W. Wombler, W. Kim, H. Dai, R.B. Laughlin, L. Liu, C.S. Jayanthi, and S.Y. Wu, "Quantum Interference and Ballistic Transmission in Nanotube ElectronWaveguides", *Phys. Rev. Lett*., vol. 87, p.106801-1, 2001.

[13] A. Javey, J. Guo, M. Paulsson, Q. Wang, D. Mann, M. Lundstrom, and H. Dai, "High-Field Quasiballistic Transport in Short Carbon Nanotubes", *Phys. Rev. Lett*., vol. **92,** p.106804-1, 2004.

[14] R. Saito, G. Dresselhaus, and M.S. Dresselhaus, *Physical Properties of Carbon Nanotubes,* Imperial College Press, London, UK, 1998.

[15] S. Datta, *Electronic Transport in Mesoscopic Systems* Cambridge University Press, Cambridge, UK, 1995.

[16] Liang et al., " Current saturation in multiwalled carbon nanotubes by large bias," *Nature*, vol. 411, pp. 665-669, 2001.

[17] M. Bockrath et al., "Resonant Electron Scattering by Defects in Single-Walled Carbon Nanotubes", *Science*, vol. 291, p. 283, 2001.

[18] S. Li, Z. Yu, S.-F. Yen, W.C. Tang, and P.J. Burke, "Carbon Nanotube Transistor Operation at 2.6 GHz," *Nano Letters,* vol. 4, p. 753-756, 2004.

[19] As noted above, theoretical evaluations of dR/dT relevant to our case, assuming ballistic or quasi-ballistic transport, do not appear to have been published, so far. Unpublished work by M.Fischetti indicates a (small) negative dR/dT for the case of ballistic transport, when the current is dominated by the source function. Further theoretical work is required to clarify the features exhibited in the experimental data of [1].

[20] P.L. McEuen, M.S. Fuhrer, and H. Park, "Single-Walled Carbon Nanotube Electronics," *IEEE Trans. Nanotechn*., vol. 1, p. 79, 2002.

[21] P.J. Burke, "AC performance of nanoelectronics: towards a ballistic THz nanotube transistor," *Solid State Electronics,* vol. 48, p. 1981, 2004.

[22] R. Zannoni K.S. Yngvesson, F. Rodriguez-Morales, J. Nicholson, D. Gu, and E. Gerecht," A Prototype Terrestrial Terahertz Imaging System", this symposium; also references therein.

Study of Superconducting Transition in a Mo/Cu Thin Film Structure and Estimation of Sensitivity of SUBMM Waveband Region TES Bolometers on the Basis of such a Structure

Alexander N. Vystavkin, *Member*, *IEEE*, Alla G. Kovalenko, Sergey A. Kovtonyuk

Abstract — Transition edge sensor (TES) bolometers are using now in more than ten projects of imaging radiometers for ground based and balloon SUBMM telescopes. In this work the temperature dependences of the resistance of bi-layer Mo/Cu structures destined for TES bolometers were measured in the range of 0.05–1.0 K. Using these dependences and the electron energy balance equation the current–voltage and power–voltage characteristics of bolometers on the basis of such structures for the case of a fixed d.c. bias voltage are calculated. The expression for the current increment produced by such a bolometer in response to absorbed radiation power is derived. The noise equivalent power of a realizable bolometers is calculated from the current response in the case when detected signals are amplified by a highly sensitive SQUID.

Keywords—*Radio astronomy, millimeter- and submillimeter-wave detectors, superconducting devices, superconducting radiation detectors, transition edge sensor bolometers.*

I. Introduction

During last three-four years the developments of imaging radiometers based on TES bolometer arrays for more than ten short millimeter – long submillimeter waveband region ground based and balloon telescopes take place in the world (see for example [1-8]. Such developments has been started in Russia too. In this situation further study of different aspects of such radiometers, in particular, TES bolometer arrays for optimization of bolometers themselves, biasing and signal multiplexing systems, optical (quasioptical) cameras etc. is necessary. In this paper we report some investigation results of superconducting transition in a Mo/Cu thin film structure. Results of other said above aspects are given in three more our papers at this Symposium.

Manuscript received May 2, 2005. This work was supported in part by the Russian Council on Leading Scientific Schools under Grant No. SSCH-1548.2003.2 and by the Department of Physical Sciences of Russian Academy of Sciences in frames of the Program "Problems of Radiophysics" – section "The Development of Terahertz Frequency Band".

A. N. Vystavkin (corresponding author: phone: 7-095-203-25-05; fax: 7-095-203-84-14; e-mail: vyst@hitech.cplire.ru) , A. G. Kovalenko and S. A. Kovtonyuk are with the Institute of Radioengineering and Electronics of Russian Academy of Sciences, 11 Mokhovaya Street, 125009 Moscow, Russian Federation.

II. Superconducting transition in Mo/Cu thin film bi-layer structure

It is well known that the use of transition edge sensor bolometers with low transition temperatures (~ 0.3 - 0.1 K) is one of the most promising ways to achieve appropriate sensitvity of radiometers for submillimeter astronomy [9-11, 8]. Since it is important to have temperature of superconducting transition in the range of stable operation of used refrigerator it has been proposed [12] to use the "superconductor-normal metal" bi-layers showing a proximity phenomenon. Changing the thickness of layers the temperature of the superconducting transition of the whole bi-layer structure can be adjusted to the desired value. Toward this end the Mo/Cu bi-layers with different layers thickness showing the superconducting transition in the temperature range 0.05 - 1.0 K have been fabricated and experimentally tested in this work. We have fabricated them in high vacuum magnetron sputtering machine. Mo and Cu layers were deposited on a polished Si wafer in one vacuum cycle from two magnetrons successively by DC magnetron sputtering in argon atmosphere.

The Mo and Cu layers sputtering rate was measured using test samples and profiler; working sample layer thicknesses were determined through sputtering time measurement. Layer thicknesses (nm) of fabricated Mo/Cu samples were:

8/0, 8/30, 8/50, 8/100; 15/50, 25/50, 35/50, 50/50;
12/0, 12/30,12/50,12/100; 10/40, 15/35, 20/30, 30/20.

The investigation of film and bi-layer structures surfaces quality on the electron and atomic forces microscopes were fulfilled. Results are shown on Fig. 1 and Fig. 2. Results of investigations on both microscopes show that surfaces are continuous and sufficiently smooth.

The dependences $R(T)$ of 13×1.3 sq. mm size samples have been measured in the ^{3}He/^{4}He dilution cryostat using four- point method [13]. It occurred that 12-15 nm Mo samples are most sensitive for influence of Cu. Samples with Mo thickness < 12 nm have not transition. Samples with Mo thickness > 15 nm have transition edge temperature > 0.4 – 0.5 K. At these temperatures the Andreev electron reflection phenomenon [14] enhancing the heating of electrons becomes negligible [15].

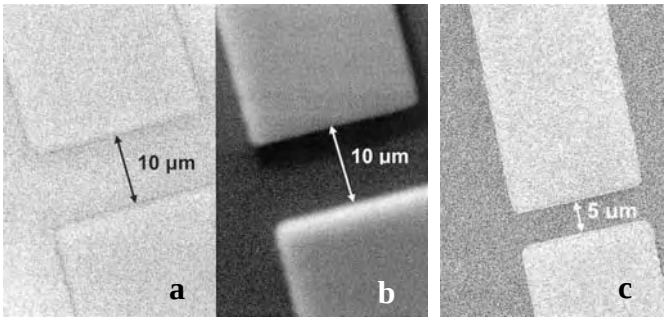

Fig. 1. Investigation results on electron microscope. Mo film in secondary electrons (a) and in reflected electrons (b); Mo/Cu structure in secondary electrons (c).

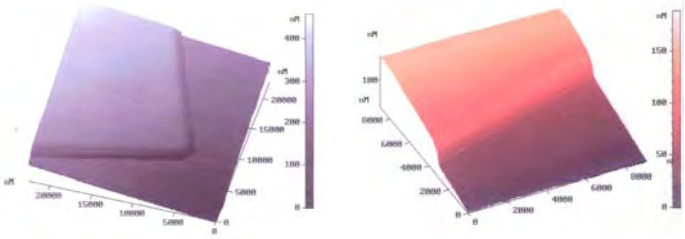

Fig. 2. Investigation results on atomic forces microscope. The surface roughness of 15 nm Mo layer is δ_{Mo} = 0.25 nm (a); the surface roughness of 15/35 nm Mo/Cu bi-layer is δ_{Cu} = 0.41 nm (b).

The thickness 12 – 15 nm is close to Cooper pairs coherent distance. The proximity phenomenon is clearly seen from the shown dependences moving from (a) to (d) at Fig. 3 and Table. $R(T)$ dependence for pure Mo film of 12 nm thickness is given for comparison. It has shown transition temperature of 0.93 K, which is expected value for Mo. The transition temperature decreases with the increasing of the Cu layer thickness. Simultaneously the resistance of bi-layer structure getting smaller. It is seen as well a possibility of the transition edge temperature fitting by means of layers choice. Low resistance is the reason that functions of absorber and thermometer are shared by most of authors to optimize a receiver scheme in case of antenna-coupled bolometer [5]. We have proposed the way how to avoid this circumstance using the planar antenna-microstrip transformer (see paper of S. V. Shitov & A. N. Vystavkin at this Symposium). The parameter $\alpha = (T/R)\cdot dR/dT$ which characterizes the sharpness of the superconducting transition has been derived in the vicinity of the superconducting transition edge temperature (T_c) for three measured samples. These parameters are given in the Table. Comparing thicknesses of Mo layers of samples b and c and their transition edge temperatures one may find that 5 Å of Mo layer thickness accuracy correspond to approximately 5% of temperature accuracy.

III. Estimation of Sensitivity of Bolometers Based on Mo/Cu Structures

With the purpose to estimate a noise equivalent power of

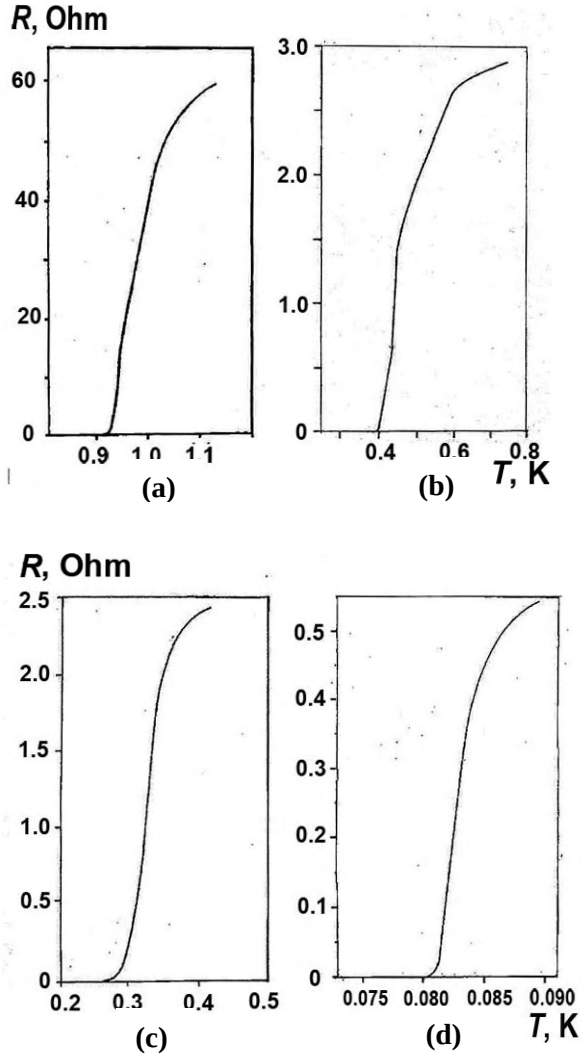

Fig. 3. Results of measurements $R(T)$ dependences of Mo/Cu samples which main parameters are given in the Table.

TABLE
Main Parameters of Measured Samlles

Sample	Layer hickness, nm		T_c, K	R_N, Ohm	$\alpha = \frac{T}{R}\cdot\frac{dR}{dT}$
	Mo	Cu			
a	12	0	0.93	67	1070
b	15	35	0.4	2.9	150
c	12	35	0.27	2.6	320
d	12	100	0.08	0.6	510

TES bolometers on the basis of the studied structures we have calculated IV-curves of possible bolometer microstructures using the assumptions:

(i) The shape of $R(T)$ and the critical temperatures of Mo/Cu bi-layer structures are functions of layers thickness and practically do not depend on transverse dimensions, i.e. length and width, as long as they are much greater than the coherence

distance for Cooper pairs in normal metal and superconductor: ξ_n, $\xi_s \approx 100 - 10$ nm [16].

(ii) The dependences $R(T)$ corresponding to the measurements described above taken at small bias currents and $R(T_e)$ when electrons are heated by current of comparatively large value are close each to other at least in the vicinity of transition edge.

(iii) The absorber of bolometer is voltage-biased to provide stable mode of operation and negative electro-thermal feedback [17]. The absorber is connected to the bias circuit through superconducting electrodes with high enough critical temperature to assure Andreev electron reflection [15] at bolometer absorber-electrodes boundaries.

(iv) The IV-characteristic of the TES bolometer connected to the voltage-biasing circuit as well as the negative electro-thermal feedback are controlled by the electron energy balance equation [17, 12]:

$$P_J = U^2 / R(T_e) = \Sigma v (T_e^5 - T_{ph}^5), \qquad (1)$$

where the left side term $P_J = U^2 / R(T_e)$ is the Joule power incoming to the electron system from the bias circuit and heating electrons and the right side term is the hot-electron power flowing from the electron system to the thin metal film lattice and the substrate, U is the fixed bias voltage, T_e is the hot-electron temperature, $R(T_e)$ is the resistance of the bolometer depending on electron temperature. The right side of (1) is written in analogy to the electron energy balance equation for the normal metal hot-electron bolometer [18,19], T_{ph} is the temperature of phonons, i.e. of the film lattice and substrate, $\Sigma \cong 3$ nW·K^{-5}·μm^{-3} is the material parameter taken from [19] where the electron energy balance equation for thin normal metal film bolometer on Si substrate at the same temperatures has been studied, v is volume of the bolometer absorber.

In our calculations of IV-curves we assume the temperature T corresponding right to the beginning of the increase of resistance from zero (see Fig. 3) as T_{ph} in equation (1). The stable values of $R(T_e)$ together with T_e and consequently current I through the bolometer bi-layer structure are established at given bias voltage U in accordance with the equation (1) what means that the equation (1) controls the IV-curve of strongly nonlinear bi-layer structure. This gives the possibility to calculate IV-curves using the measured dependences $R(T)$ and equation (1) keeping in mind the assumption (II). The length[1)] and width of structures were reduced from 13×1.5 mm^2 proportionally to 8×0.8 μm^2 keeping in mind the assumption (I). Since the length-to-width ratio of the absorber remained the same like in case of measured samples – the absolute values of their resistances and temperature dependences remain the same as well. For IV-curves calculations we approximate the total bi-layer structure thickness of samples b, c and d by their Cu layers thickness values equal to 35 nm and 100 nm respectively because these

layers determine structure resistances. The results of current-voltage curves calculation are shown in Fig. 4. In the same figure the dependences of dissipated d.c. power in absorber as a function of bias voltage are given as well. The common shape and order of magnitude of values of these dependences are like for dependences measured directly for similar bi-layer structure [12]. The difference of results in [12] in comparison with Fig. 2 is that the positive slope portions of IV-curves at very small bias voltages are absent in our case. The reason is that we don't take into account critical current and besides a non-controlled small resistance connected in series with bi-layer structure occurring in [12] is absent in our case for three structures. Nevertheless we suppose that the obtained IV-curves can be used for estimation of the sensitivity of possible bolometers based on the studied Mo/Cu bi-layer structures.

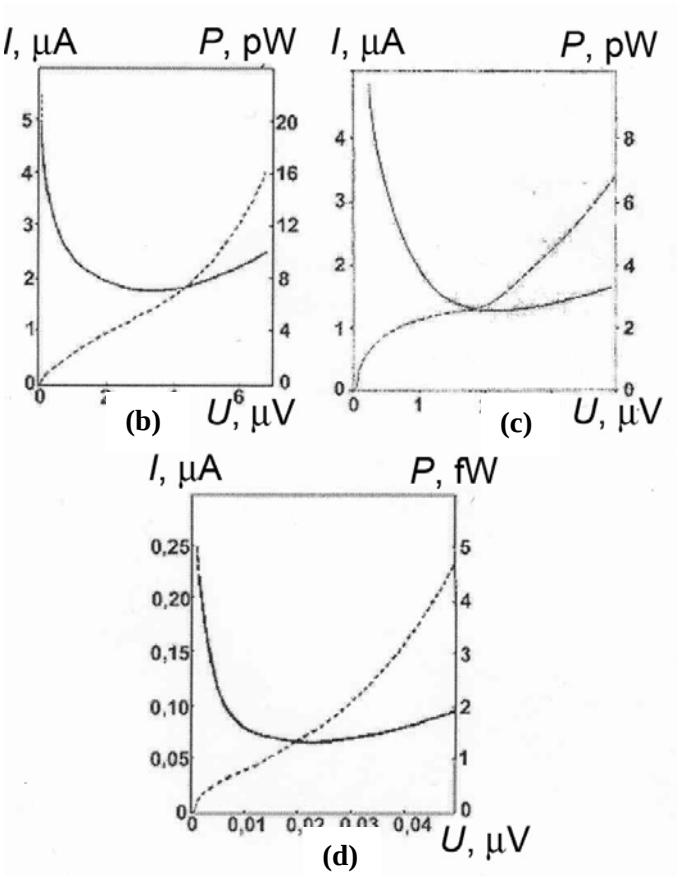

Fig. 4. Calculated current-voltage (solid lines) and power-voltage (dashed lines) characteristics of constructed TES bolometers based on data of three measured Mo/Cu bi-layer structures at T = 0.4 K, T = 0.27 K and T = 0.08 K respectively.

When small submillimeter radiation power P_{rad} is absorbed by TES bolometer at fixed bias voltage $U = const$ the equation (1) has to be modified to

$$U^2 / [R(T_e) + \Delta R] + P_{rad} = \Sigma v [(T_e + \Delta T_e)^5 - T_{ph}^5], \qquad (2)$$

where P_{rad} is added to the Joule power and small increments ΔR and ΔT_e are added to the resistance $R(T_e)$ and

1) 13 mm – distance between potential probes.

the temperature T_e. The equation for small values can be extracted from (2):

$$-\frac{U^2\Delta R}{R^2(T_e)}+P_{rad}\cong\Sigma v5T_e^4\cdot\Delta T_e. \qquad (3)$$

After simple transformations using expressions $I+\Delta I = U/(R+\Delta R)$ and $\alpha\cong(T_e/R)\cdot(\Delta R/\Delta T_e)$ one obtains the expression for the current responsivity of TES bolometer

$$S_I=\frac{-\Delta I}{P_{rad}}=\frac{1}{U}/[1+(5/\alpha)/(\Sigma vT_e^5/P_J)]. \qquad (4)$$

From (1) we have $\Sigma vT_e^5/P_J\le 1$ and from results of measurements we also have $\alpha>100$. So

$$S_I=\frac{-\Delta I}{P_{rad}}\cong\frac{1}{U}, \qquad (5)$$

what practically coincides with analogous expression in [4] with the difference that in our case radiation energy is absorbed directly by TES. Besides.given here derivation of the expression for the current responsivity S_I of TES bolometer reflects clearly the mechanism of negative electrothermal feedback.

Minimal values of the voltage bias U take place in the vicinity of the transition edge. From Fig. 4 $U_{0.4}\cong 10^{-7}$ μV, $U_{0.27}\cong 10^{-8}$ μV and $U_{0.08}\cong 10^{-9}$ μV for structures at T = 0.4 K, T = 0.27 K and T = 0.081 K respectively. The noise equivalent power of TES bolometers $NEP=\sqrt{\overline{i_{noise}^2}}/S_I$ [3] where $\sqrt{\overline{i_{noise}^2}}$ is root-mean-square noise current of a readout-amplifier next to the bolometer. We have SQUID readout-amplifier with $\sqrt{\overline{i_{noise}^2}}\cong 4\cdot 10^{-12}$ A/Hz$^{1/2}$. With this readout-amplifier we have $NEP_{0.4}\cong 4\cdot 10^{-19}$ W/Hz$^{1/2}$, $NEP_{0.27}\cong 4\cdot 10^{-20}$ W/Hz$^{1/2}$ and $NEP_{0.08}\cong 4\cdot 10^{-21}$ W/Hz$^{1/2}$. Of course these are just estimation values and measurements of real bi-layer structures IV-curves and bolometer *NEP*'s are needed. The preparations for such measurements are now in progress.

The obtained results give a possibility of the better understanding of the TES bolometer operation mechanism as well as show the way of the adjustment of its layer thickness values to a stable temperature of the used refrigerators and permit the preliminary estimation of the noise equivalent power of bolometers during their fabrication and bolometer sample selection for the mounting of receivers with bolometers.

ACKNOWLEDGMENT

Authors thank V. V. Dmitriev and V. V. Zavialov for the participation in measurements.

REFERENCES

[1] J. G. Staguhn, D. J. Benford, F. Pajot, T, A. Ames, J. A. Chervenak, E. N. Grossman, et al., "Astronomical demonstration of superconductiong bolometer arrays", *Proc. SPIE, Millimeter Submillimeter Detectors Astronomy*,2003, v. 4855, pp. 100-107.

[2] D. J. Benford, M. J. Devlin, S. R. Dicker, K .D. Irwin, P. R. Jewell, J. Klein, et al., "A 90 GHz array for Green Bank Telescope", *Nuclear Instruments and Methods in Physics Research,* A 520, 2004 (Proc. of the 10th Intern. Workshop on Low Temperature Detectors – LTD-10, Genoa, Italy, July 7-11, 2003), pp. 387-389.

[3] R. F. Silverberg, S. Ali, A. Bier, B. Campano, T. C. Chen, F. S. Cheng, et al., "A bolometer array for the spectral energy distribution (SPEED) camera", ibid, pp. 421-423.

[4] T. C. Chen, A. Bier, B. A. Campano, D. A. Cottingham,,F. M. Finkbeiner, C. O'Dell, E. Sharp, R. F. Silverberg, G. Wilson, "Development of molybdenum-gold proximity bilayers as transition edge sensors for the SPEED camera", ibid, pp. 446-448.

[5] M. J. Myers, W. Holzapfel, A. T. Lee, R. O'Brient, P. L. Richards, D. Schwan, A. D. Smith, H. Spieler, H. Tran, "Arrays of antenna-coupled bolometers using transition edge sensors", ibid, pp. 424-426.

[6] W. Duncan, D. Audley, W. Holland, D. Atkinson, T. Baillie, M. Cliffe, et al., "SCUBA-2 arrays to system interfaces", ibid, pp. 427-430.

[7] M.D. Audley, W.S. Holland, W.D. Duncan, D. Atkinson, M. Cliffe, M. Ellis, et al., SCUBA-2: A large format TES array for submillimeter astronomy, ibid, pp. 479-482.

[8] J. E. Ruhl, P. A. R. Ade, J. E. Carlstrom, H. M. Cho, T. Crawford, M. Dobbs, et al., "The South Pole Telescope", *Proc. SPIE (Intern. Symp. on Astronomical Telescopes)*, 2004.
www.spt.uchicago.edu/extweb/spt_spie_2004.pdf.

[9] P. L. Richards, C .R. McCreight, "Infrared detectors for astrophysics", *Physics Today*, February 2005, pp. 41-47..

[10] J. Zmuidzinas, P. L. Richards, "Superconducting detectors and mixers for millimeter and submillimeter astrophysics", *Proc. IEEE*, 2004, v. 92, # 10, pp. 1597-1616.

[11] "Detector needs for long wavelength astrophysics", *A report by the infrared, submillimeter and millimeter detector working group* (June 2002), Young E. – the Chair of working group, after the Far-infrared, sub-mm & mm detector technology workshop, NASA, Monterey, California, 1 - 3 April, 2002,

[12] K. D. Irwin, G. C. Hilton, J. M. Martinis, B. Cabrera, "A hot-electron microbolometer for X-ray detection using a superconducting transition edge sensor with electrothermal feedback", *Nucl. Instr. and Meth*., 1996, A370, pp.177-179.

[13] A. N. Vystavkin, V. V. Dmitriev, V. V, Zavialov, A. G. Kovalenko, S. A. Kovtonyuk, A. A. Cnebotarev, "Investigation of superconducting transition in bi-layer molybdenum-copper structure showing proximity phenomenon", *Radiotekhnika i Elektronika* (in Russian), 2003, v. 48, # 7, pp. 874-876.

[14] A. F. Andreev, "Thermal conductivity of superconductors intermediate state", *Soviet Phys. ZhETP*, 1964, v. 46, # 5, pp. 1823-1828.

[15] A. N. Vystavkin, "Supersensiting hot-electron microbolometer with Andreev electron reflection phenomenon for submillimeter radio astronomy", *Radiotekhnika i Elektronika* (in Russian), 2001, v. 46, # 7, pp. 806-815.

[16] N. R. Werthamer, "Theory of the superconducting transition temperature and energy gap function of superposed metal films", *Phys. Rev*., 1963, v. 132, # 6, pp. 2440-2445.

[17] K D. Irwin, "An application of electrothermal feedback for high resolution cryogenic particle detection", *Appl. Phys. Lett.,* 1995, 10 April, 66 (15), pp. 1998-2000.

[18] M. Nahum, J. M. Martinis, "Ultrasensitive hot-electron microbolometer", Appl. Phys. Lett. ,1993, 63(22), pp. 3075-3077.

[19] A. N. Vystavkin, D. V. Shuvaev, L. S. Kuzmin, M. A. Tarasov, E. Andersted, M. Willander, T. Claeson, "Normal metal hot-electron bolometer with Andreev reflection in superconducting electrodes", J. of Exp. and Theor. Phys., 1999, 88 (3), pp. 598-602.

[20] S. Lee, J. Gildemeister, W. Holmes, A. Lee, and P. Richards, "Voltage-biased superconducting transition-edge bolometer with strong electrothermal feedback operated at 370 mK," *Appl. Opt.*, 1998, v. 37, #.16, pp. 3391–3397.

Implanted Silicon Resistor Layers for Efficient Terahertz Absorption

James Chervenak

Broadband absorption structures are an essential component of large format bolometer arrays for imaging GHz and THz radiation. We have measured electrical and optical properties of implanted silicon resistor layers designed to be suitable for these absorbers. Implanted resistors offer a low-film-stress, buried absorber that is robust to longterm aging, temperature, and subsequent metals processing. Such an absorber layer is readily integrated with superconducting integrated circuits and standard micromachining as demonstrated by the SCUBA II array built by ROE/NIST (1). We present a complete characterization of these layers, demonstrating frequency regimes in which different recipes will be suitable for absorbers.

Single layer thin film coatings have been demonstrated as effective absorbers at certain wavelengths including semimetal (2,3), thin metal (4), and patterned metal films (5,6). Astronomical instrument examples include the SHARC II instrument is imaging the submillimeter band using passivated Bi semimetal films and the HAWC instrument for SOFIA, which employs ultrathin metal films to span 1-3 THz. Patterned metal films on spiderweb bolometers have also been proposed for broadband detection. In each case, the absorber structure matches the impedance of free space for optimal absorption in the detector configuration (typically 157 Ohms per square for high absorption with a single or 377 Ohms per square in a resonant cavity or quarter wave backshort). Resonant structures with ~20% bandwidth coupled to bolometers are also under development; stacks of such structures may take advantage of instruments imaging over a wide band.

Each technique may enable effective absorbers in imagers. However, thin films tend to age, degrade or change during further processing, can be difficult to reproduce, and often exhibit an intrinsic granularity that creates complicated frequency dependence at THz frequencies. Thick metal films are more robust but the requirement for patterning can limit their absorption at THz frequencies and their heat capacity can be high.

We describe implanted silicon resistor layers suitable for absorber coating and patterned absorber structures that offer low heat capacity, absence of aging, and uniform, predictable behavior at THz frequencies. We have correlated DC electrical and THz optical measurements of a series of implanted layers and studied their frequency dependence of optical absorption from .3 to 10 THz at cryogenic temperatures. We have modeled the optical response to determine the suitablity of the implanted silicon resistor as a function of resistance in the range 10 Ohms/Sq to 300 Ohms/sq.

References:

1) W. Duncan, W. Holland, E. Robson, K. Irwin, G. Hilton, A. Watson, "SCUBA 2 – a wide field camera for the James Clerk Maxwell Telescope" Proc. Low. Temp. Det. 9 (2000)

2) J. Clarke, G. Hoffer, P. L. Richards, N.-H. Yeh "Superconductive Bolomerters for Submillimeter Wavelengths, J. Appl. Phys 48, 4865 (1977)

3) C.A. Allen, S. Babu, M. Jhabvala, S.H. Moseley, G. M. Voellmer "The 12x32 Pop-Up Bolometer Array for the SHARC II Camera", Far_IR, Sub-mm, and mm Detector Technology Workshop, NASA/CP 211408 (2002)

4) C. A. Allen and E. Wollack, private communication (2003)

5) J. Gildemeister, A. T. Lee, P. L. Richards, "A Fully lithographed Voltage-Biased Superconducting Spiderweb Bolometer" Appl. Phys. Lett.(1999)

6) Wilson, in preparation (2005)

Electron-Drift and Plasmon Response in Millimeter- to -Submillimeter-wave Mixers Based on High Electron Mobility GaAs-AlGaAs Heterostructures

Mark Lee, Michael C. Wanke, Eric A. Shaner, Albert Grine, John L. Reno
Sandia National Laboratories, Albuquerque, New Mexico, USA

Millimeter-to-submillimeter-wave radiation can couple to a very high mobility (10^6 to 10^7 cm^2/V·s at 4 K) electron gas in a III-V semiconductor heterostructure interface or quantum well in two distinct manners that are both useful in detection and mixing applications. The first and more conventional response is based simply on electron drift, while the second response is for the radiation to resonantly excite coherent charge density oscillations, or plasmon modes, of the electron gas. We will show examples and contrast the fundamental limitations on frequency response and mixing characteristics resulting from the different physics of the two responses.

We have shown[1] that hot-electron bolometer (HEB) mixers made from a high-mobility two-dimensional electron gas (2DEG) can enter a regime where neither energy nor momentum relaxes in a channel between source and drain electrodes, leading to ballistic electron drift. For a source-drain channel of length L, this minimizes the charge transit time τ_{tr} and hence maximizes the intermediate frequency (IF) bandwidth to $f_{3dB} = v_F/2\pi L$, where v_F, the Fermi velocity, is typically ~ 10^7 cm/s in a 2DEG. Even for $L > 1$ μm, IF bandwidths approaching 40 GHz have been observed. The IF spectrum of such an HEB mixer has very low harmonic distortion, as expected for the square-law non-linearity of a bolometer, while the responsivity and conversion gain are generally low, owing to the small temperature coefficient of resistance of the high-mobility 2DEG. In addition, in the ballistic electron drift regime the 2DEG has kinetic inductance that will degrade coupling to the electromagnetic field as local oscillator (LO) frequency increases. We estimate that, for practical antenna/mixer geometries and electron densities, the inductive reactance will set an upper limit on LO frequency coupling of roughly 500 GHz.

By contrast, the plasmon response we have observed is resonant and not limited by kinetic inductance. Using a grating-gated field-effect transistor geometry, resonant plasmon response has been observed from 135 to nearly 700 GHz in various devices.[2] In a single device, the resonant frequency of the response can be tuned continuously over a ~ 200 GHz range by an applied gate voltage bias. Heterodyne experiments show that, unlike an electron-drift device, the IF bandwidth of this detector operated as a mixer is not limited by the plasmon transit time, but more likely by the plasmon lifetime. The measured IF bandwidth of approximately 8 GHz is in rough agreement with the half-width of the observed plasmon resonance peak. The IF spectrum of the plasmon mixer also shows significant harmonic content, indicating that the non-linear mechanism generating the IF is significantly more complicated than a simple square-law.[3] We are also investigating plasmon detector configurations that could significantly improve responsivity and conversion gain.

---

[1] Mark Lee, L. N. Pfeiffer, and K. W. West, Appl. Phys. Lett. **81**, 1243 (2002)
[2] X. G. Peralta, *et al*., Appl. Phys. Lett. **81**, 1627 (2002)
[3] Mark Lee, M. C. Wanke, and J. L. Reno, Appl. Phys. Lett **86**, 033501 (2005)

A Photon Counting Hot-Electron Bolometer for Space THz Spectroscopy

Boris S. Karasik, Andrei V. Sergeyev, David Olaya, Jian Wei, Michael E. Gershenson, Jonathan H. Kawamura, and William R. McGrath

***Abstract*—We discuss a concept of the hot-electron transition-edge sensor (TES) capable of counting THz photons. The main need for such a THz calorimeter is spectroscopy on future space telescopes with a background limited *NEP* ~ 10^{-20} W/Hz$^{1/2}$. The micromachined bolometers will unlikely reach such sensitivity at temperatures above 10 mK. The hot-electron TES with sufficient sensitivity will still have a time constant ~ 0.1-1.0 ms that is too short for integrating a flux of THz background photons arriving at a rate of < 100 s^{-1}. The Hot-Electron Photon Counter based on a submicron-size superconducting *Ti* bridge with *Nb* Andreev contacts will be able to detect individual photons above 170 GHz due to its very low heat capacity. A discrimination of the low energy fluctuations with a threshold device would allow for realization of an *NEP* ~ 10^{-20} W/Hz$^{1/2}$ at ≥ 1 THz while operating at 300 mK. With the sensor time constant of a few microseconds, the dynamic range is ~ 30-40 dB. A compact array of the antenna-coupled counters can be fabricated on a silicon wafer without membranes. The initial fabricaiton effort has been successful yielding nanodevices with desired characteristics, which are currently are being tested.**

***Index Terms*—radiation detectors, submillimeter wave detectors, bolometers, superconducting devices.**

I. Introduction

Several new advanced space submillimeter (SMM) astronomy missions (Single-Aperture FIR Observatory – SAFIR [1,2], Submillimeter Probe of the Evolution of Cosmic Structure – SPECS [3], Space Infrared Telescope for Cosmology and Astrophysics – SPICA [4]) have been recently proposed. They are expected to make a dramatic impact on the attainable sensitivity in the moderate resolution mode ($\nu/\Delta\nu \sim 1000$) where direct detectors are typically used. This will be achieved by active cooling of telescope mirrors to 4-5 K. For all existing platforms, the radiation of the atmosphere and/or the temperature of the telescope set the sensitivity limit. Deep cooling of a telescope mirror to ~4K would almost completely eliminate the effect of the telescope emissivity. Then the limiting noise equivalent power (*NEP*) would be set by the background fluctuation at the level of ~ 10^{-19}-10^{-20} W/Hz$^{1/2}$ in the most of the SMM range (see Fig. 1).

The required *NEP* is two-three orders of magnitude lower then that currently achieved by the state-of-the-art (SOA) micromachined bolometers. Although it has been speculated that more than an order of magnitude improvement of the performance could be achieved for SOA detectors [2,5], we show in Section II that the improvement of the bolometer sensitivity is restricted by the quantum limitations imposed on the phonon conductance in 1-D channels below 1 K.

Alternative approaches for achieving the *NEP* ~ 10^{-20} W/Hz$^{1/2}$ include a number of concepts, namely, a superconducting [6] or normal metal [7] hot-electron bolometer, a kinetic inductance detector [8,9], a superconducting tunnel-junction device with a single-electron transistor readout [10], a hot-spot superconducting detector [11], and quantum-dot devices [12]. Data of Fig. 1 show that the low *NEP* above 1 THz corresponds to a very low photon arrival rate N_{ph} < 100 s^{-1}. This makes integration of weak signals impossible for all perspective detector concepts. Indeed, the time constant cannot be easily engineered and is determined by either the electron-phonon relaxation time [6,7,11] or by the quasiparticle recombination time [8-10] which both are of the order of a few milliseconds at 100 mK where the low *NEP* can only be achieved (see Section III). This circumstance makes photon counting a preferable mode of operation, at least for

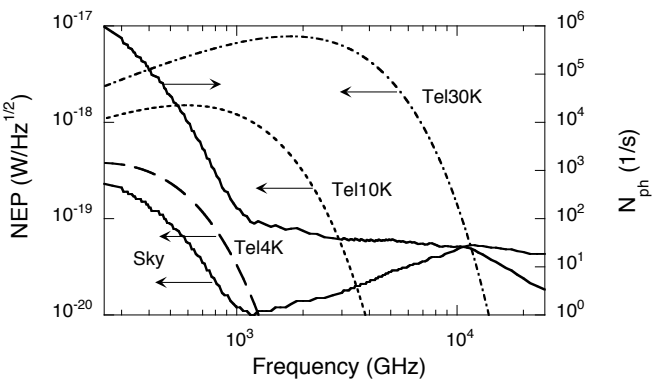

Fig. 1. The *NEP* limited by the background and by the telescope emission (5% emissivity, mirror temperature 4K, 10K, and 30K) for a moderate resolution spectrometer ($\nu/\Delta\nu$ = 1000, single mode) and the rate of photon arrival from the background. The latter is less than 100 s^{-1} above 1 THz. Below 1 THz, the radiation originates from the Cosmic Microwave Background. At higher frequencies, the radiation from the galactic core and from the dust clouds dominates.

Boris S. Karasik (phone: +1-818-393-4438; fax: +1-818-393-4683; e-mail: boris.s.karasik@jpl.nasa.gov), Johathan H. Kawamura, and William R. McGrath are with the Jet Propulsion Laboratory, California Institute of Technology, Pasadena, CA 91109, USA.

Andrei V. Sergeyev is with the SUNY at Buffalo, Buffalo, NY 14260, USA.

David Olaya, Jian Wei and Michael E. Gershenson are with the Department of Physics and Astronomy of Rutgers University, 136 Frelinghuysen Rd., Piscataway, NJ 08854, USA.

The work of B.S.K., J.H.K. and W.R.M. was carried out at the Jet Propulsion Laboratory, California Institute of Technology, under a contract with the National Aeronautics and Space Administration and funded through the internal Research and Technology Development program.

The work of A.V.S. was supported by a NASA grant.

The work of D.O., J.W. and M.E.G. at Rutgers University was supported in part by the NASA grants NNG04GD55G and NAG5-10357 and the Rutgers Academic Excellence Fund.

detection of weak signals. The photon counting mode at SMM has been considered in [10] and [11]. The only experimental demonstration of the detection of single SMM photons has been done using quantum-dot devices [12]. However, the potential difficulties associated with coupling of radiation and with detector array readout make alternative approaches worth of pursuing.

In Section IV, we analyze the photon counting regime for a Hot-Electron Direct Detector (HEDD) [6], which is a transition-edge sensor (TES) operated in the hot-electron mode and whose sensitivity is enhanced due to the disorder-suppressed electron-phonon coupling [13]. The main advantage of the photon counting is that the *NEP* ~ 10^{-20} W/Hz$^{1/2}$ can be actually achieved at 300 mK instead of 100 mK that tremendously relieves the cryocooling problem for space applications.

In Seciton V, we present the current status of the device nanofabrication and testing.

II. Sensitivity Limit in Micromachnied Bolometers

Bolometers are currently detectors of choice for SMM astronomical instruments. The SOA design of a SMM bolometer represents a very fine mesh ("spider-web") etched from a 1-μm thick Si_3N_4 membrane that suspends a sensitive Neutron-Transmutation-Doped *Ge* (NTD-*Ge*) thermometer. The mesh plays simultaneously the role of the thermal conductance to the bath and of the radiation absorber. One of the most important applications of these bolometers will be the High-Frequency Instrument on the NASA/ESA Planck Surveyor Mission where a typical background-limited *NEP* ~ 10^{-17}-10^{-16} W/Hz$^{1/2}$ will be utilized in several frequency bands between 100 GHz and 857 GHz [14].

The fundamental *NEP* of a bolometer is set by the minimum possible thermal conductance between the absorber of radiation and the thermal sink. "Spider-web" bolometers use several (~10) 500 μm long, 1 μm thick and 3 μm wide Si_3N_4 legs, each of which contributes ~ 1 pW/K into the thermal conductance at 100 mK. The further decrease of the thermal conductance might be seen via change of the leg geometry and decrease of the number of legs assuming that the "classical" T^3-dependence of the thermal conductivity holds down to the lowest temperatures. There is, however, new data on the thermal conductance of dielectric nanowires setting some doubt about a realism of this approach. Theory [15], which takes into account the quantization of phonon modes in thin wires, gives the following low temperature ballistic transport limit for the thermal conductance:

$$G_Q = 4\pi^2 k_B^2 T / 3h = 3.8 \cdot T \quad [pW/K]. \tag{1}$$

Remarkably, this quantity does not depend on the length of the wire and on its material. The experiments with Si_3N_4 [16], *GaAs* wires [17] and nanotubes [18] confirm the theory demonstrating the crossover of the conductance from the T^3-dependence to the linear dependence of (1). Although the crossover temperature depends on the material purity, the lowest possible conductance is still given by (1). If we assume a hypothetical 4-leg isolated bolometer then the quantum conductance limited NEP_Q will be given by:

$$NEP_Q = \sqrt{4k_B T^2 \cdot 4G_Q} \tag{2}$$

At 100 mK, (2) yields an *NEP* which is slightly less than 10^{-18} W/Hz$^{1/2}$. It approaches the 10^{-20} W/Hz$^{1/2}$ only below 10 mK, which is an impractically low temperature for space instruments. Unless an efficient way for a drastic increase of the reflectivity for phonons entering the bolometer leg is figured out, the sensitivity of micromachined bolometers will be fundamentally limited by expression (2).

III. Relaxation Time and Operating Modes in Non-Equilibrium Sensors

Two actively pursued approaches to sensitive integrating SMM detectors are the HEDD [6] and the Kinetic Inductance Detector (KID) [9]. The time constant in those detectors cannot be engineered as readily as in micromachined bolometers and requires a special consideration.

The low background *NEP* corresponds to a low photon arrival rate:

$$N_{ph} = \frac{1}{2}\left(\eta \frac{NEP}{h\nu}\right)^2, \tag{3}$$

where η is the quantum efficiency. Above 1 THz, $N_{ph} < 100$ s^{-1} (see Fig. 1). A detector with a time constant τ will integrate photon flux if $N_{ph}\tau >> 1$. Therefore, a background limited integrating detector must have a time constant of 100 ms or greater. Such a long time constant is problematic for both KID and HEDD approaches.

The KID senses a number of Cooper pairs broken by photons. This causes a decrease of the kinetic inductance of a superconducting film that can be detected either by an inductive bridge with a SQUID [8] or via a shift of the resonance frequency in a strongly coupled microstrip resonator [9]. The fundamental sensitivity limit is set by the quasiparticle generation-recombination noise [8]:

$$NEP_{GR} = 2\Delta\sqrt{N_{qp}/\tau_{qp}}\,. \tag{4}$$

Here N_{qp} is the number of quasiparticles, τ_{qp} is the quasiparticle lifetime due to the recombination modified by phonon trapping effects in the film. In an *Al* sample [19], $N_{qp} \approx 10^4$ and $\tau_{qp} \approx 0.1$ ms have been realized at 0.2 K, thus yielding $NEP_{GR} \sim 10^{-19}$ W/Hz$^{1/2}$. Although, theoretically, τ_{qp} has strong exponential temperature dependence and could be very long at low temperatures, no value greater than 0.1 ms has been reported to date. Sometimes, a saturation of τ_{qp} is seen below some certain temperature [9].

The HEDD relies on a weak electron-phonon coupling in disordered *Hf* or *Ti* superconducting films. The fundamental noise limit is set by the thermal energy fluctuations (TEF):

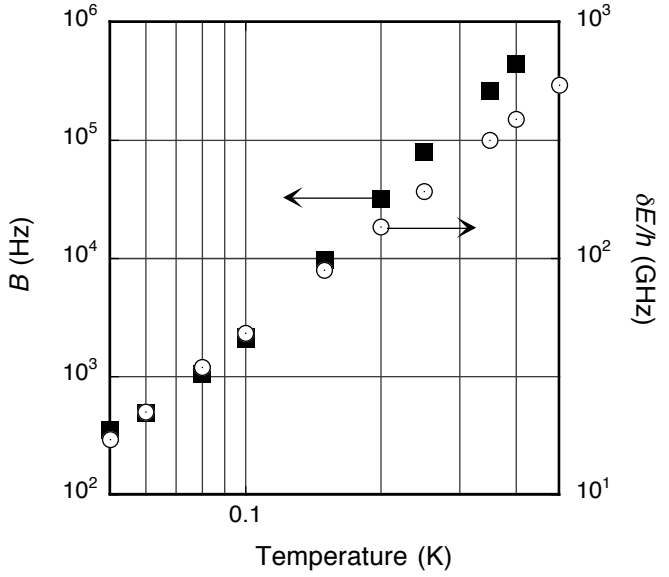

Fig. 2. The expected minimum detectable frequency (red boundary) and the detector system output bandwidth as functions of temperature. At ~ 0.3 K where T_C in *Ti* HEPC is, the red boundary is ~ 170 GHz and the output bandwidth is ~ 100 kHz.

$$NEP_{TEF} = \sqrt{2k_B T_C^2 C_e / \tau_{e-ph}} \qquad (5)$$

Here C_e is the electron heat capacity, $\tau_{e\text{-}ph}$ is the electron-phonon energy relaxation time. NEP_{TEF} can reach 10^{-20} W/Hz$^{1/2}$ for small sensor size at $T \approx 100$ mK [6]. The relaxation time increases with the film disorder and also has a stronger temperature dependence than in a pure metal:

$$\tau_{e-ph} = AT^{-(n-2)} [\mu \text{sec}]. \qquad (6)$$

where $A = 0.4$ for *Hf* and 0.2 for *Ti*, $n = 6$ [13] (in a pure metal, $n = 5$). A record long $\tau_{e\text{-}ph} = 25$ ms has been measured in *Hf* at 40 mK [13] but this is still insufficient for integrating of photons with $N_{ph} \sim 100$ s^{-1}.

IV. Hot-electron TES photon counter

As follows from the above, it will be very difficult if possible at all to realize a combination of the *NEP* $\sim 10^{-20}$ W/Hz$^{1/2}$ and the time constant >> 100 ms. Thus, the photon counting mode for THz radiation becomes unavoidable. Superconducting TES based bolometric photon counters/calorimeters achieving a high energy resolution without using external wavelength dispersing elements have been successfully developed from X-ray to near-IR wavelengths. Their advantages are robust thin-film technology, compatibility with low-noise SQUID readout and the negative electro-thermal feedback improving the energy resolution.

The energy resolution of a calorimeter scales as a square root of the heat capacity of the absorber, therefore very small devices and low temperatures are needed for THz calorimetry. On the other hand, $T \geq 0.3$ K is quite desirable for space applications since this significantly simplifies the cryocooling.

Submicron-size (0.45 μm × 0.17 μm × 0.025 μm) planar antenna-coupled *Ti* HEDD devices have already become available for our work (see Section V). The devices are fabricated on silicon substrates between *Nb* contacts, which will block the diffusion of hot electrons out of the bridge due to Andreev reflection. Further minimization of the device length is limited by the proximity effect: for shorter nanobridges, the superconducting order parameter will propagate from *Nb* contacts in the *Ti* nanobridge and raise its critical temperature. The lower limit on the nanobridge length corresponds to the coherence length in normal metal $L_C = \sqrt{hD/\left(4\pi^2 k_B T\right)} \approx 30$ nm ($D = 2.4$ cm^2/s is the electron diffusivity in *Ti* films). Since L_C is an order of magnitude less then the device length, $L \sim 0.5$ μm, the proximity effect can be neglected.

Here we evaluate the performance of a Hot-Electron Photon Counter (HEPC) in the THz regime. The *Ti* nanobridge will operate in the voltage-biased TES mode with the negative electro-thermal feedback (ETF), that is, its operating temperature will be somewhat lower than the critical temperature, $T_C \approx 300$ mK, and the resistance at the operating point will be much smaller than the normal resistance. An absorbed photon causes a fast increase of the electron temperature in the device, $\delta T_e = h\nu/C_e$, within the characteristic time $\tau_D \approx L^2/\pi^2 D \approx 0.1$ ns. Then the relaxation of electron temperature occurs with the time constant $\tau \approx \tau_{e\text{-}ph} n/\alpha$ ($\alpha \approx 2T_C/\delta T_C$, δT_C is the superconducting transition width). In our previous work [20] with thin–film micron-size *Ti* bridges, $\delta T_C \approx 10$ mK was routinely observed. So $\alpha \sim$ 60-70 is expected to be realized in HEPC devices. The ability of the device to detect single photons depends on the magnitude of the intrinsic thermal fluctuations. The rms energy fluctuation for a TES with strong ETF is given by [21]:

$$\delta E \approx \sqrt{4\sqrt{n/2} k_B T_C^2 C_e / \alpha}\,. \qquad (7)$$

A frequency $\nu_R = \delta E/h = 170$ GHz can be treated as the "red boundary" or the low frequency limit for the detection mechanism. Equation (7) presumes that an optimized filter with the bandwidth $B \approx (2\pi\tau^*)^{-1}$, where $\tau^* = \tau(2/n)^{1/2}$, is used to cut the out-of-band Johnson noise [22].

Both δE and B strongly depend on temperature. In Fig. 2, both temperature dependencies are shown for a *Ti* nanodevice with aforementioned dimensions using experimenatal $\tau_{e\text{-}ph}$ data [13]. Adjusting (reducing) the critical temperature in *Ti* devices, for example, by means of magnetic ion implantation [23] may significantly reduce δE and make detection of THz photons easier. At the same time, the detector bandwidth and its dynamic range will also decrease. The actual trade-off is a matter of several practical cosiderations among which the possibility to operation a detector system in space at 0.3 K instead of 0.1 K stands out as a very important engineering and cost saving factor.

In order to realize the photon-noise limited *NEP*, the dark count rate imposed by the energy fluctuations in the electron subsystem should be below the count rate due to the background radiation. This is achieved by adjusting the discrimination threshold, $E_T < h\nu$, in the photon counter or/and in the readout electronics. Then only the energy

fluctuations, exceeding the discriminator threshold are counted. The corresponding dark count rate is approximately given by [24]:

$$\gamma = \frac{B}{\sqrt{2\pi}} \cdot \int_{E_T/\delta E}^{\infty} \exp\left(-x^2/2\right) dx. \quad (8)$$

The quantum efficiency of the HEPC can be presented as $\eta = \eta_{opt}\eta_{int}$. η_{opt} is the optical coupling efficiency that can be engineered to be close to 100% for a good antenna design. η_{int} is the intrinsic quantum efficiency, that is, a probability of detection after a photon is actually absorbed. This statistical quantity depends on the threshold energy [24]:

$$\eta_{\text{int}} = \frac{1}{\sqrt{2\pi}} \cdot \int_{(E_T - h\nu)/\delta E}^{\infty} \exp\left(-x^2/2\right) dx \quad (9)$$

The result of a numerical modeling of the $NEP = h\nu\sqrt{2\gamma}$ and the quantum efficiency as functions of frequency is shown in Fig. 3. For a higher frequency (1 THz), both low *NEP* (10^{-20} W/Hz$^{1/2}$) and high η_{int} can be readily obtained by adjusting the threshold to $(3\div4)\delta E$. For lower frequencies, the same *NEP* can be obtained only at the expense of the quantum efficiency. Eventually, when $h\nu$ gets close to δE, the optimal E_T approaches zero and the *NEP* approaches that in the integrating mode (~10^{-19} W/Hz$^{1/2}$). Since γ depends very strongly on the lower integration limit (8) it can be varied broadly by choosing E_T or by adjusting the device volume. The latter may be necessary in order to increase the range of frequencies where the counter would operate ($\nu_{max} = C_e\delta T_C/h$).

The value of B determines the maximum count rate and the dynamic range of a counter $10\cdot\log(B/N_{ph}) = 30$-$40$ dB. It is important to understand that the limited device speed is a key condition for keeping the dark count rate low. In another version of the hot-electron bolometric photon counter [25], a normal metal absorber with a normal metal-insulator-superconductor (NIS) thermometer is capacitively coupled to an antenna. In that concept, the thermal relaxation would be governed by the electron diffusion with the characteristic time τ_D ~ ns rather than by the electron-phonon relaxation as in our case. This would result in a very high rate of dark counts exceeding the background photon arrival rate.

Dc SQUIDs with the bandwidth ~ 1 MHz are broadly used for TES readout and are suitable for the HEPC. In future, microwave multiplexed SQUIDs [26] or fully digital RSFQ readouts could be ultimate solutions for the HEPC arrays.

V. Fabrication Procedure and DC Characterization

Currently, we have succeded in fabrication of *Ti* nanodevices with desired dimensions and T_C using *in-situ* e-beam evaporation of *Ti* and *Nb* through a lift-off mask and perfomed some dc tests of the device superconducting properties.

The fabrication process starts with the coating of the substrate (p-type silicon covered with 400 nm of silicon

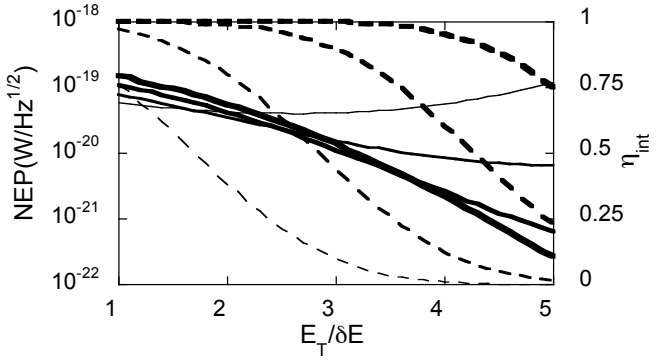

Fig. 3. *NEP* (solid lines) and η_{int} (dashes) as functions of the threshold energy E_T. The optical frequencies are 300 GHz, 500 GHz, 750 GHz, and 1 THz. The line width incrementally increases with the frequency.

oxide) with a double layer of PMGI and PMMA e-beam resist. We have tested several types of the organic shadow masks that can withstand the process of e-gun deposition of *Nb* in the process of multi-angle deposition of the nanoscale HEPCs. These lift-off masks include the top thin PMMA layer, used as a high-resolution electron resist, and the bottom thicker layer that provides a large undercut required for multi-angle deposition through a suspended lift-off mask (see Fig. 4). Our tests showed that the standard PMMA/copolymer masks are incompatible with the e-gun deposition of *Nb* films because of a strong heat-induced outgassing from the mask. The PMGI-based masks compare favorably with the copolymer-based masks because of a higher glass-transition temperature of PMGI (~190^0C).

The device patterning is made using a FEI Sirion SEM and J. C. Nabity's nanometer pattern generation system. After the developing process the samples are mounted in the rotatable stage and in the evaporation chamber.

Our electron-gun evaporation system enables the multi-angle deposition of several (up to four) metals in the same vacuum cycle through the suspended sub-micron mask. The oil-free deposition system is equipped with a cryopump and sorption pumps to avoid possible hydrocarbon contamination. Because of the high melting point of *Nb* ($T = 2468$ C), the electron-gun deposition of superconducting *Nb* films for multi-angle nanopatterning is a non-trivial task: strong radiation from the e-gun source

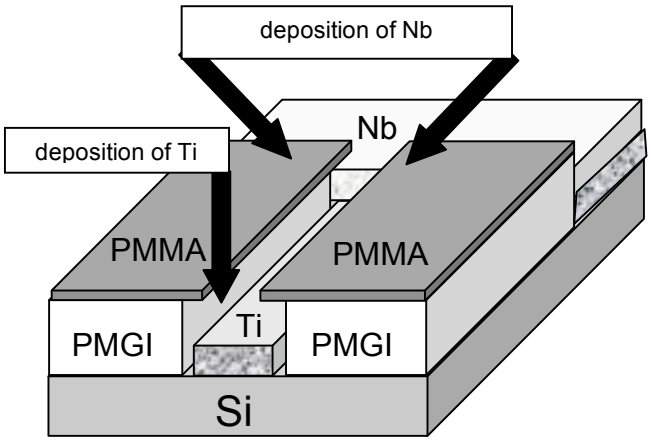

Fig. 4. Illustration of the multi-angle deposition technique. Two layers of resist form a lift-off mask with an overhang protecting *Ti* deposited at 90 deg. into a submicron channel from the following deposition of *Nb* at 45 deg. In the areas much wider than the channel width both layers overlap.

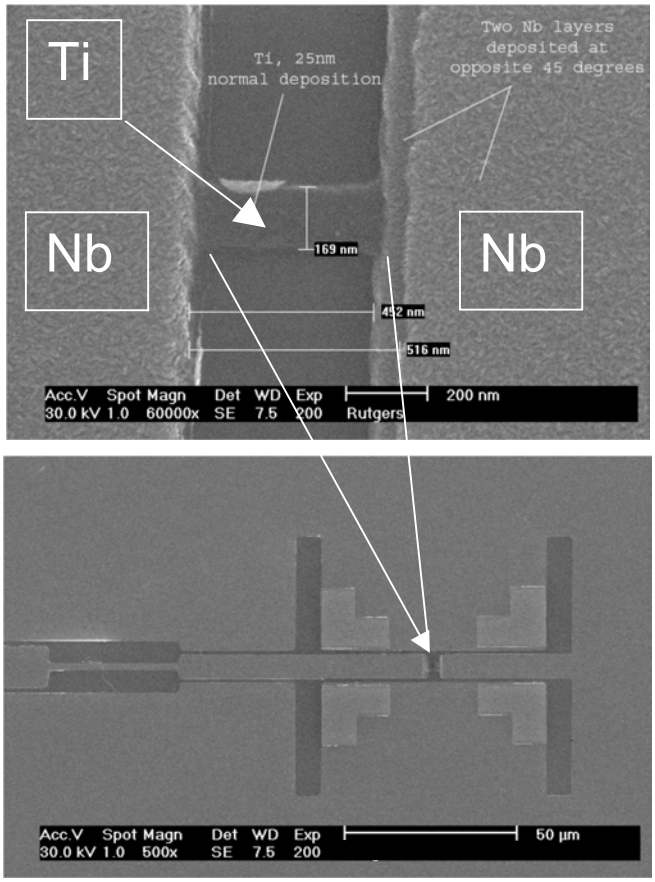

Fig. 5. Upper panel: a 0.45 µm × 0.17 µm *Ti* HEPC device with *Nb* Andreev contacts. Lower panel: an HEPC device integrated into a twin-slot planar antenna centered at 650 GHz.

usually results in compromising the mechanical stability of the PMMA lift-off mask, contamination of the growing *Nb* film with organics, and suppression of superconductivity. To reduce substrate/resist heating, we deposited *Nb* films at an unusually large substrate-to-source distance (~ 37cm). For such a large distance and, hence, a relatively low deposition rate (~ 0.5 nm/sec), the oxidation of growing film becomes a critical issue

To achieve the low pressures needed to obtain clean metal films the chamber is continuously pumped while it is baked for fifteen hours at a temperature of 100 C. At higher temperatures, significant "rounding" of sharp features in the lift-off masks was observed.

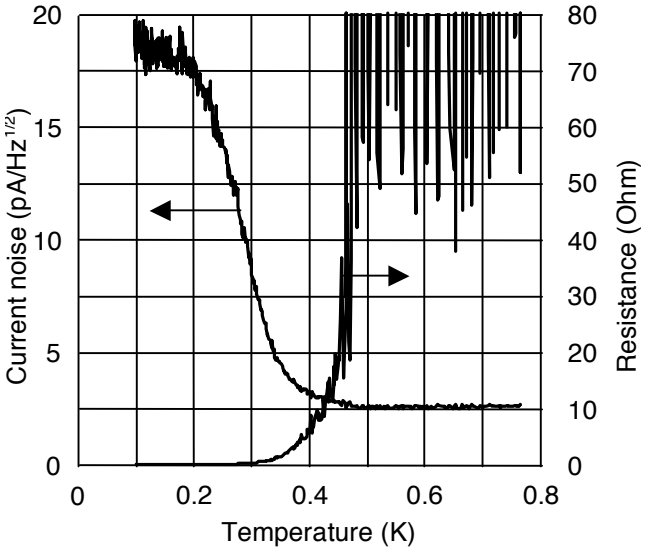

Fig. 6. The temepature dependence of the current noise measured by a SQUID and the corresponding *R(T)* dependence derived from (10). The noise floor above 0.5 K is due to the internal SQUID noise.

During cool down of the chamber the metal sources are outgassed in repeated cycles until small changes in pressure are observed in the process or heating the sources up to the point where we achieve adequate evaporation rates. After cool down, regeneration of the cryopump, and a last outgassing cycle of the sources the base pressure is in the mid 10^{-9} Torr range.

The evaporation of *Ti* and *Nb* is done in a single vacuum cycle to be able to obtain a clean (oxide-free) interface between a *Ti* nanosensor and *Nb* current leads for efficient Andreev confinement of "hot" electrons.

Ti is first deposited at normal incidence to the substrate; the deposition rate is around 0.6 nm per second. During evaporation the pressure in the chamber rises to around 3×10^{-8} Torr. Next, the stage is rotated and *Nb* is deposited at 45 degrees to the substrate and perpendicular to the thin channel. In this way, the thin *Ti* bridge is left uncovered but capped at both ends by *Nb*. A last deposition of *Nb* is done at the opposite 45-degree position to ensure complete covering of the leads. During evaporation of *Nb* the pressure in the chamber will go from about 7×10^{-8} to 3×10^{-7} Torr due to the intense heat radiated from the source. The evaporation rate is 0.5 – 0.6 nm per second. Lift off is done in N-Methyl Pyrrolidione at 95 C followed by rinsing in DI water. An example of the resulting structure is seen in Fig. 5.

Electrical testing of completed HEPC devices represents a significant problem because of the very low power needed to saturate the device, that is, to wash out the superconductivity. This amount can be estimated as $\delta T_C C_e/\tau_{e\text{-}ph} \sim 0.1$ fW. Besides the full enclose of the device into a 0.3 K radiation shield, a properly design low-pass electical filter with cold stages is needed (see, for example, [27]). Such a filter must suppress both low-frequency interferences and rf noise in the range from kHz to several GHz which may overheat the device.

The desing and construction of the filtering system are in progress and, meanwhile, we applied a rather simple SQUID based technique for determining the presence of the superconducting transition in the devices. In this technique, the device is directly connected to the input coil of the dc SQUID without any bias lines. The SQUID senses the device Johnson noise I_{nJ} in the registration bandwidth Δf following the behavior of the device ohmic resistance R:

$$I_{nJ}(T) = \sqrt{4k_B T \Delta f / R(T)}\,. \qquad (10)$$

The available to us SQUID system apparently has strong enough built-in filtering to prevent the HEPC device from overheating by the external noise. An example of the superconducting transition trace for a device similar to that shown in Fig. 5 is demonstrated in Fig. 6. This measurement was done in a dilution refrigerator Kelvinox[25] (Oxford Instruments). The SQUID was situated at a 1.5 K platform so its noise did not depend on the device temperature and remained constant at a level of ≈ 2.5 pA/Hz$^{1/2}$. This sets the limit of sensitivity for this technique and the maximum detectable device resistance was about 50 Ohm. The data clearly demonstrate a superconducting transition above 0.3

K which is similar to what has been observed in larger *Ti* thin-film samples [13,20].

VI. Conclusion

The photon counting detector is important for low-background applications in space THz astronomy where this kind of technology is currently absent. A proposed superconducting HEPC approach is promising for meeting the sensitivity needs while operating at 0.3 K. Beside the astronomical applications, such sensors might be of interest for laboratory molecule spectroscopy, quantum information applications, and nanoscale physics of thermal processes.

References

[1] http://safir.jpl.nasa.gov/technologies/index.asp.

[2] D.J. Benford and S.H. Moseley, "Cryogenic detectors for infrared astronomy: the Single Aperture Far-InfraRed (SAFIR) Observatory," *Nucl. Instr. Meth. Phys. Res. A*, vol. 520, no. 1-3, pp. 379-383, Mar. 2004.

[3] D. Leisawitz, "NASA's far-IR/submillimeter roadmap missions: SAFIR and SPECS," *Adv. Space Res.*, vol. 34, no. 3, pp. 631-636, 2004.

[4] T. Nakagawa, "SPICA: space infrared telescope for cosmology and astrophysics," *Adv. Space Res.*, vol. 34, no. 3, pp. 645-650, 2004.

[5] J.J. Bock, P. Day, A. Goldin, H.G. LeDuc, C. Hunt, A. Lange et al., "Antenna-coupled bolometer array for astrophysics," *Proc. Far-IR, SubMM & MM Detector Technology Workshop, April 1-3, 2002, Monterey, CA*, pp. 224-229.

[6] B.S. Karasik, W.R. McGrath, H.G. LeDuc, and M.E. Gershenson, "A hot-electron direct detector for radioastronomy," *Supercond. Sci. Technol.*, vol. 12, no. 11, pp. 745-747, Nov. 1999; B.S. Karasik, W.R. McGrath, M.E. Gershenson, and A.V. Sergeev, "Photon-noise-limited direct detector based on disorder-controlled electron heating," *J. Appl. Phys.*, vol. 87, no. 10, pp. 7586-7588, May 2000.

[7] A. Vystavkin, D. Chouvaev, L. Kuzmin, M. Tarasov, E. Aderstedt, M. Willander, and T. Claeson, "Andreev reflection based normal metal hot-electron bolometer for space applications", *Proc. SPIE*, vol. 3465, pp. 441-448 (1998).

[8] A.V. Sergeev, V.V. Mitin, and B.S. Karasik, "Ultrasensitive hot-electron kinetic-inductance detectors operating well below superconducting transition", *Appl. Phys. Lett.,* vol. 80, no. 5, pp. 817-819, Feb. 2002.

[9] P.K. Day, H.G. LeDuc, B.A. Mazin, A. Vayonakis, and J. Zmuidzinas, "A broadband superconducting detector suitable for use in large arrays," *Nature*, vol. 425, pp. 817-821, Oct. 2003.

[10] R.J. Schoelkopf S.H. Moseley, C.M. Stahle, P. Wahlgren, and P. Delsing, "A concept for a submillimeter-wave single-photon counter," *IEEE Trans. Appl. Supercond.*, vol. 9, no. 2, Pt. 3, pp. 2935-2939, June 1999.

[11] A. Semenov, A. Engel, K. Il'in, G. Gol'tsman, M. Siegel and H.W. Hubers, "Ultimate performance of a superconducting quantum detector", *Eur. Phys. J. Appl. Phys.*, vol. 21, no. 3, pp. 171-178, Mar. 2003.

[12] S. Komiyama, O. Astafiev, V. Antonov, T. Kutsuwa, and H. Hirai, "A single-photon detector in the far-infrared range," *Nature*, vol. 403, pp. 405-407, Jan. 2000; O. Astafiev, S. Komiyama, T. Kutsuwa, V. Antonov, Y. Kawaguchi, and K. Hirakawa, "Single-photon detector in the microwave range," *Appl. Phys. Lett*, vol. 80, no. 22, pp. 4250-4252, June 2002; H. Hashiba, V. Antonov, L. Kulik, S. Komiyama, and C. Stanley, "Highly sensitive detector for submillimeter wavelength range," *Appl. Phys. Lett.,* vol. 85, no. 24, pp. 6036-6038, Dec. 2004.

[13] M.E. Gershenson, D. Gong, T. Sato, B.S. Karasik, and A.V. Sergeev, "Millisecond Electron-Phonon Relaxation in Ultrathin Disordered Metal Films at Millikelvin Temperatures," *Appl. Phys. Lett.,* vol. 79, no. 13, pp. 2049-2051, Sep. 2001.

[14] M. Yun, J. Beeman, R. Bhatia, J. Bock, W. Holmes, L. Husted et al., "Bolometric Detectors for the Planck Surveyor," *Proc. SPIE,* vol. 4855, pp. 136-147 (2002); W. Holmes, J. Bock, K. Ganga, V.V. Hristov, L. Histead, T. Koch et al., "Preliminary Performance Measurements of Bolometers for the Planck High Frequency Instrument," *Proc. SPIE,* vol. 4855, pp. 208-216 (2002).

[15] L.G.C. Rego and G.Kirczenow, "Quantized thermal conductance of dielectric quantum wires," *Phys. Rev. Lett*., vol. 81, no. 1, pp. 232-235, July 1998.

[16] K. Schwab, E.A. Henriksen, J.M. Worlock, and M.L. Roukes, "Measurement of the quantum of thermal conductance," *Nature,* vol. 404, pp. 974-977, Apr. 2000.

[17] C.S. Yung, D.R. Schmidt, and A.N. Cleland, "Thermal conductance and electron-phonon coupling in mechanically suspended nanostructures," *Appl. Phys. Lett.*, vol. 81, no. 1, pp. 31-33, July 2002.

[18] T. Yamamoto, S. Watanabe, and K. Watanabe, "Universal features of quantized thermal conductance of carbon nanotubes," *Phys. Rev. Lett.*, vol. 92, no. 7, art. no. 075502, Feb. 2004.

[19] C.M. Wilson, L. Frunzio, and D.E. Prober, "Time-Resolving Measurements of Thermodynamic Fluctuations of the Particle Number in a Nondegenerate Fermi Gas," *Phys. Rev. Lett.*, vol. 87, no. 6, art. 067004, Aug. 2001.

[20] B.S. Karasik, B. Delaet, W.R. McGrath, J. Wei, M.E. Gershenson, and A.V. Sergeev, "Experimental Study of Superconducting Hot-Electron Sensors for Submm Astronomy," *IEEE Trans. Appl. Supercond.*, vol. 13, no. 2, Part 1, pp. 188-191, June 2003.

[21] K.D. Irwin, "An application of electrothermal feedback for high resolution cryogenic particle detection," *Appl. Phys. Lett.*, vol. 66, no. 15, pp. 1998-2000, April 1995.

[22] D. McCammon, "Physics of low-temperature microcalorimeters," *Nucl. Instr. Meth. Phys. Res. A*, vol. 520, no. 1-3, pp. 11-15, Mar. 2004.

[23] B.A. Young, J.R. Williams, S.W. Deiker, S.T. Ruggerio, and B. Cabrera, "Using ion implantation to adjust the transition temperature of superconducting films," *Nucl. Instr. & Methods A,* vol. 520, no. 1-3, pp. 307-310, Mar. 2004.

[24] R.H. Kingston, "Detection of Optical and Infrared Radiation," Springer Ser. in Opt. Sci., Ed. D.L. MacAdam, Springer-Verlag, 1978, Ch. 10.

[25] D.V. Anghel and L. Kuzmin, "Capacitively coupled hot-electron nanobolometers as far-infrared photon counter," *Appl. Phys. Lett.*, vol. 82, no. 2, pp. 293-295, Jan. 2003.

[26] K.D. Irwin and K.W. Lehnert, "Microwave SQUID multiplexer," *Appl. Phys. Lett.*, vol. 85, no. 11, pp. 2107-2109, Sep. 2004.

[27] K. Bladh, D. Gunnarson, E. Hürtfled, S. Devi, C. Krisotffersson, B. Smålander, S. Pehrson, T. Claeson, P. Delsing, and M. Taslakov, "Comparison of cryogenic filters for use in single electonics experiments," *Rev. Sci. Instr.,* vol. 74, no. 3, pp. 1323-1327, Mar. 2003.

Superconducting Cold-Electron Bolometers with JFET readout for OLIMPO balloon telescope

Leonid Kuzmin[1)], and Phillip Mauskopf[2)]
[1)] Chalmers University of Technology, S-41296 Gothenburg, Sweden,
[2)] Cardiff University, United Kingdom

***Abstract*— The OLIMPO experiment is a large balloon-borne telescope, aimed at measuring the Sunyaev-Zeldovich effect in many clusters of Galaxies. OLIMPO will carry out its surveys in four frequency bands centered at 140, 220, 410 and 540 GHz. The detector system is made of four bolometer arrays. In order to achieve low dispersion in the characteristics of the detectors, a fully photo-lithographic process producing sensors on silicon nitride islands or plane Si substrate should be developed. Filters and antennas can be integrated on the detectors wafer by means of micro-strip technology.**

Attractive variant is to use Capacitively Coupled Cold-Electron Bolometers (CEB) with JFET readout. The JFET readout has been developed already for the BOOMERanG and Planck-HFI. The problem is to match relatively low-ohmic dynamic resistance of CEB (1kOhm) and high noise equivalent resistance of JFET (1 MOhm).

The goal is to achieve level of noise-equivalen power (NEP) of CEB less than photon noise. Analysis of a single CEB with JFET readout has not given positive results in both current-biased and voltage-biased modes. Current fluctuations of JFET and feedback resistor are rather low. The main reason of fail is strong influence of voltage noise. The voltage is divided by small dynamic resistance of the junctions in cooling region (voltage-biased mode) and gives strong current noise. Any attempts to increase dynamic resistance moving to smaller voltages led to strong decrease of cooling and degradation of responsivity.

To achieve noise matching with JFET, a Cold-Electron Bolometer with a weak Superconducting Absorber (SCEB) has been proposed. In this case we can operate in voltage-biased mode with voltage in the range between (Delta 1-Delta 2) and (Delta1 + Delta 2). In this region the IV of SIS´ junctions is rather flat with considerably increased dynamic resistance up to the level of Rj=1000*Rn (typical level of leakage). Electron cooling will be still very effective for incoming power. Simulations show that we can achieve photon noise level for structure with Ti absorber and Al/Ti tunnel junctions (Al antenna electrode) for all frequency ranges with estimated power load.

***Index Terms*— Cold-Electron Bolometer, SIS´tunnel junction, superconducting absorber, Noise Equivalent Power**

Manuscript received May 31, 2005. This work was supported in part by Swedish Research Council, SNSB, and .

L. Kuzmin is with the Chalmers University of Technology, S-41296 Gothenburg, Sweden, on leave from the SINF of Moscow University (phone: 46 31 772 3608; fax: 46 31 772 3471; e-mail: leonid.kuzmin@mc2.chalmers.se).

P. Mauskopf is with the Cardiff University, United Kingdom (e-mail: Philip.Mauskopf@astro.cf.ac.uk).

I. INTRODUCTION

The OLIMPO experiment is a large balloon-borne telescope, aimed at measuring the Sunyaev-Zeldovich effect in many clusters of Galaxies, during long-duration balloon flights.The high Galactic latitude sky at far infrared and millimetric frequencies has three main sources of diffuse emission: the Cosmic Microwave Background (CMB) with its primary anisotropy and with the Sunyaev-Zeldovich effect from Clusters of Galaxies, and the Far Infrared Background (FIRB) from early galaxies. The "cosmological window" extends roughly from 90 to 600 GHz: at lower frequencies interstellar emission of spinning dust grains, free-free and synchrotron emission from the interstellar medium dominate over the cosmological background; at higher frequencies the clumpy foreground from "cirrus clouds" of interstellar dust dominates the sky brightness even at high Galactic latitudes. The only way to separate these different emissions and to extract cosmological information is using multi-band experiments. OLIMPO will carry out its surveys in four frequency bands centered at 140, 220, 410 and 540 GHz. CMB primary anisotropy can be detected in the lower frequency bands of OLIMPO. Taking advantage of its high angular resolution, and concentrating on a limited area of the sky, OLIMPO will be able to measure the angular power spectrum of the CMB up to multipoles around 3000, significantly higher than BOOMERanG, WMAP and Planck. The measurement of the damping tail of the power spectrum will provide estimates of the dark matter density and of the spectral index of the primordial perturbations. We will present the angular power spectrum which can be obtained with OLIMPO from 4 days of deep integration over 0.3% of the sky, and how the cosmic parameters can be inferred from such power spectrum.The OLIMPO bands are chosen to optimally sample the Sunyaev-Zeldovich effect in clusters of galaxies and distinguish it from CMB primary anisotropies and competing foregrounds. Moreover, the simultaneous observation of the positive effect at 410 and 540 GHz, in addition to the "zero effect" measurement at 220 GHz will allow us to measure the relativistic corrections and the temperature of the gas even in the absence of X-ray data. We have carried out extensive simulations of the OLIMPO

observations of clusters in the presence of Galactic Dust, CMB anisotropy, and instrumental noise. We plan to map about 40 known clusters for each long duration flight of the payload. Reasonable integration time for each target can thus easily be several hours, spread on a sky patch of about 1 square degree centered on the cluster. The OLIMPO payload is implementing a number of advanced technical solutions. The inner frame, with the attached telescope and the cryostat housing the detector system, can be tilted to set the observing elevation from 0^o to 60^o. The low elevations achievable allow accurate ground-based calibrations of the system and the observation of planets for calibration during polar flights. The telescope, developed in Rome, is an on-axis Cassegrain configuration with a 2.6m aluminum primary. The secondary mirror is suspended by means of thin stainless steel blades to minimize the background from local structures and to avoid beam vignetting. Sky scans are performed by slowly scanning the primary mirror in the cross-elevation direction. Up to 3o wide, 1o cross-elevation scans are possible with this system. The full payload can also perform azimuthal scans, to cover wider regions. The detector system is made of four bolometer arrays. These detectors are an evolution of the highly successful devices used in the BOOMERanG and Planck-HFIinstruments. In order to achieve low dispersion in the characteristics of the detectors, a fully photo-lithographic process producing TES (transition edge superconductor) sensors on silicon nitride islands on a Si wafer has been developed. In this way the entire bolometric array is fabricated with a single process. Filters and antennas can be integrated on the detectors wafer by means of micro-strip technology. The four arrays at 140, 220, 410 and 540 GHz will be composed of 19, 37, 37, 37 detectors respectively. Each array will fill the optically correct area of the focal plane (about 0.25 o in diameter projected in the sky). The bolometer arrays and the reimaging optics will be arranged into a modified version of the long duration cryostat developed for BOOMERanG. The main difference here is the use of fiberglass cylinders to replace the kevlar cords suspending the LN and LHe tanks. Fiberglass cylinders provide higher stiffness to the system.

II. Power load

We estimate the expected optical loading on the OLIMPO detectors assuming an emissivity of the OLIMPO telescope of 5%, an effective temperature of 250 K and an optical efficiency of the receiver of 30%. The power on each detector at 140, 220, 410 and 540 GHz is 4, 6, 14 and 28 pW respectively. Estimated detector parameters are given in Table 1.

Frequency (GHz)	150	220	410	540
Bandwidth (GHz)	35	45	50	50
Telescope loading (pW)	4	6	14	28
RJ sensitivity (μK/ÖHz)	90	100	80	65
CMB sensitivity (μK/ÖHz)	160	300	2100	10000

Table 1: Optical loading and sensitivities of OLIMPO detectors

III. SCEB – JFET

The main question is could we match the photon noise level with CEB-JFET?

Single CEB

Analysis of a single CEB bolometer [2] with JFET readout has not given any positive results in both current-biased and voltage-biased modes. The main reason for voltage-biased mode is strong influence of voltage noise. The voltage is divided by small dynamic resistance of the junctions in cooling region and gives strong noise current. Any attempts to increase dynamic resistance moving bias point to smaller voltages led to strong decrease of cooling and degradation of current responsivity.

A new idea: **to use a single SCEB (CEB with a weak superconducting absorber, SIS´IS) in voltage-biased mode.**

The exciting chance to achieve photon noise level with single CEB has been proposed. For this purpose we should use a single CEB with superconducting absorber, SCEB [2]. In this case we can use v.-b. mode with V in the range between (Delta 1-Delta 2) and (Delta1 + Delta 2). In this region the IV of SIS´junctions is flat or even with negative slope with considerably increased dynamic resistanse. Formally, it could be increased to infinity, in reality it will be limited by fluctuations or leakage resistance at the level of 1000*Rn-2000*Rn (typical level of leakage in our technology). Electron cooling will be still very effective for incoming power. The theoretical model of a cold-electron bolometer based on Superconductor-Insulator- weaker Superconductor-Insulator-Superconductor (SIS'IS) structure. has been developed with certain simplifying assumptions. First, complete relaxation of the quasiparticle distribution function in the absorber has been assumed and described by a single parameter – effective temperature. Second, Josephson current is ignored since the the structure is biased close to the gap voltage, in which case the Josephson current gives relatively weak contribution. Besides that Josephson effect can be suppressed by relatively weak magnetic field.

Within the framework of this model we can evaluate the responsivity and Noise Equivalent Power of the device and make the comparison with the corresponding values for CEB

bolometer. This comparison shows that for JFET readout only a single SCEB can satisfy to noise requirements.

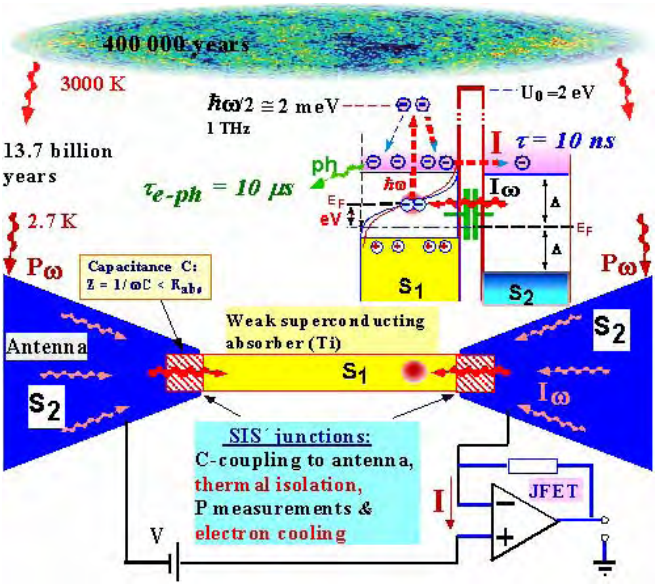

Fig 1. Schematic of a **Superconducting Cold-Electron Bolometer (SCEB) with capacitive coupling to the antenna**. The schematic covers different scales of time from **13.7 billion years** to **10 nanoseconds.**

Drawback of the SCEB is increase of shot noise due increased level of energy quantization, Delta 1, instead of kT_e for normal metal absorber [2]. Total noise will be determined by shot noise in this case but this increase does not still achieve the level of photon noise. Gain due to suppression of large voltage noise of JFET is larger than increase of shot noise.

Current fluctuations of JFET could be rather low and would be determined by feedback resistor.

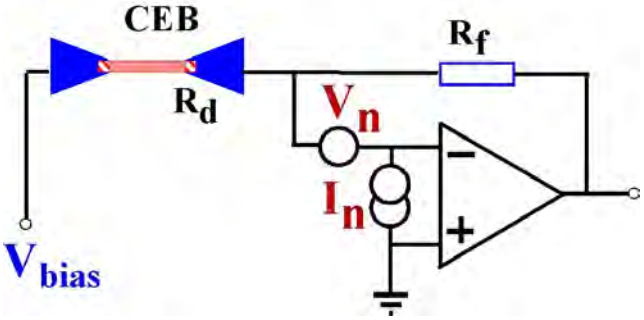

Fig 2. Schematic and noise sources of a JFET readout for superconducting cold-electron bolometer (SCEB).

For example, current noise of silicon JFET "TIA" produced by Infrared Lab, is dominated by Johnson noise for feedback resistors up to $1x10^{11}$ Ohm. For 100 MOhm (acceptable for all range of our currents) at 4K the current noise will be at the level of 5 $fA/Hz^{1/2}$. The voltage fluctuations will be suppressed by high dynamic resistance of the junctions to this level or lower.
Simulations of the SCEB have been made with total noise current of 10 $fA/Hz^{1/2}$.

First estimations give optimistic figures of NEP better than photon noise for all channels for possible typical parameters of Al-Ti tunnel junctions.

1. Channel I: "2.1 mm" (140 GHz)

Power load is relatively high: $P_0 = 2 – 3$ pW.
Let's accept minimum value for NEP estimations: $P_0 = 2$ pW.

Photon noise: $NEP_{phot} = \sqrt{2P_0 * hf}$

For channel I, 140 GHz:

$$NEP_{phot} = 2*10^{-17} W/Hz^{1/2} .$$

Total NEP of CEB should be less than photon noise: $NEP_{tot} < NEP_{phot}$.

Single CEB doesn't give proper results.
Only SCEB could give the proper NEP.

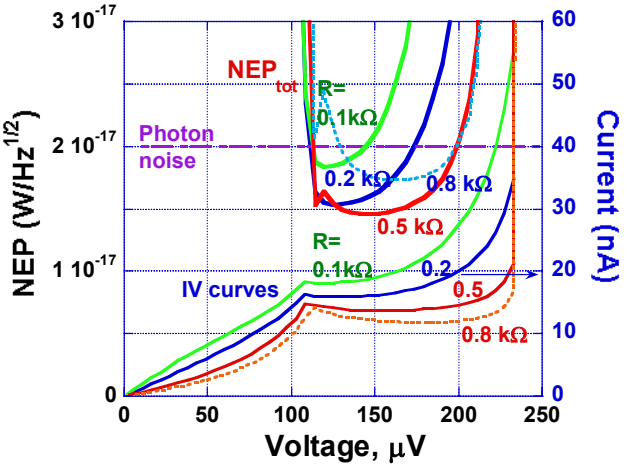

Fig. 3. Total NEP is less than NEPphot for SCEB, total i_{JFET}=10 $fA/Hz^{1/2}$, R=0.5 kOhm and 0.1 kOhm (one junction), Vol=0.05um^3, power load – 2 pW. IV curves are shown for estimation of high dynamic resistance of the junctions. Smearing of the gap (imaginery part of Delta = 0.01) is included in simulations. Leakage resistance is not included.

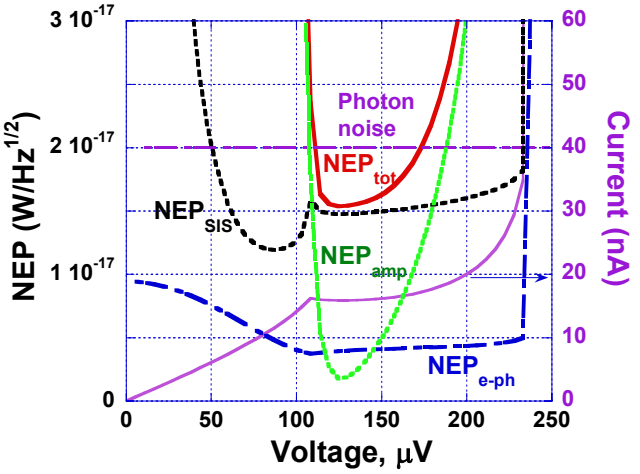

Fig. 4. NEP components for SCEB with JFET readout for i_{JFET}=10 fA/Hz$^{1/2}$, R=0.2 kOhm (one junction), Vol=0.1um^3, power load – 2 pW. IV curve is shown for estimation of high dynamic resistance of the junctions. Smearing of the gap (imaginery part of Delta = 0.01) is included in simulations. Leakage resistance is not included

The NEPtot of SCEB is mainly determined by shot noise (NEPsis) related with power load removed from Delta1 level by tunnel junctions (in contrast to the CEB with clear domination of JFET noise (NEPamp)).

Channel IV: "0.5 mm" (600 GHz)

Power load is rather high: P_0 = 10 – 20 pW.
Let's accept highest value for NEP estimations : P_0 = 20 pW.

Photon noise: $NEP_{phot} = \sqrt{2P_0 * hf}$

For channel IV – 600 GHz:

$NEP_{phot} = 1.2*10^{-16} W/Hz^{1/2}$.

Total NEP of CEB should be less than photon noise: NEPtot < NEPphot.
Single CEB doesn't give proper results.
Only SCEB gives proper NEP.

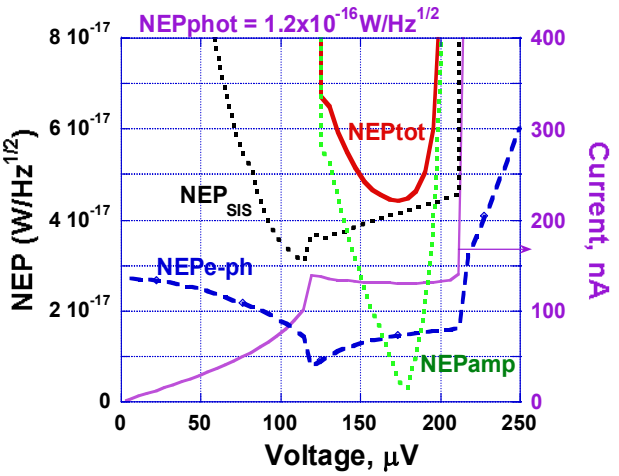

Fig. 5. Total NEP is less than NEPphot for SCEB, total i_{JFET}=10 fA/Hz$^{1/2}$, R=0.5 kOhm, 0.2 and 0.1 kOhm (one junction), Vol=0.05um^3, power load – 20 pW. IV curves are shown for estimation of high dynamic resistance of the junctions. Smearing of the gap (imaginery part of Delta = 0.01) is included in simulations. Leakage resistance is not included in this simulation.

Ideology of the SCEB - JFET matching:
For typical values of JFET noise: 5 nV/Hz$^{1/2}$ and 5 fA/Hz$^{1/2}$, we have an effective noise impedance around 1 MOhm. Typical resistance of CEB in operating point (near gap for strong electron cooling) is around 1 kOhm. We have clear mismatch at three orders of magnitude.
Replacing CEB by SCEB (with weak superconducting absorber) we choose a flat region of IV curve with very high dynamic resistance. Increase of resistance will be possibly limited by leakage resistance (or gap smearing) and is just around 3 orders of magnitude needed for noise-matching conditions.
Thus, the SCEB can bring remarkable progress in implementation of bolometers with JFET readout for all channels of OLIMPO.
The proper technology of Al/Aloxide/Ti junctions should be developed for this purpose. Possibly it should be a three-layer technology due to rather large areas of the junctions for lower frequencies (difficult for shadow evaporation technique). In principle, all steps in this technology, including etching the tunnel junctions area (say 2x2 um^2) could be done by photolithography..

IV. Series array of CEBs in current-biased mode

Analysis of lumped bolometer with one absorber and JFET readout has not given any positive results in both current-biased and voltage-biased modes. Typical results for current-biased mode can be seen in Fig. 3 for N=1 (single bolometer). The main reason is degradation of responsivity under high power load.
The only chance to achieve photon noise level is to use array of the bolometers. In this case each bolometer is not overload and show high responsivity. The resulting signal is collected from all bolometers. In the case of lumped antenna coupled

bolometer it could be realized as parallel connection of bolometers for HF and series connection of them for DC.
In the case of distributed antenna or array of slot antennas for one pixel, it could be realized rather natural as series connection of bolometers for dc signal.
First estimations give optimistic figures of NEP for array of bolometers even for existing level of technology. The gain of array is especially effective for 600 GHz channel with higher power load.

Channel IV: "0.5 mm" (600 GHz)

Power load is rather high: P_0 = 10 – 20 pW.
Let's accept highest value for NEP estimations : P_0 = 20 pW.

Photon noise: $NEP_{phot} = \sqrt{2P_0 * hf}$

$$NEP_{phot} = 1.2*10^{-16} W/Hz^{1/2} .$$

Total NEP of CEB should be less than photon noise: NEPtot < NEPphot.
Single CEB doesn't give proper results.
Only array gives proper NEP

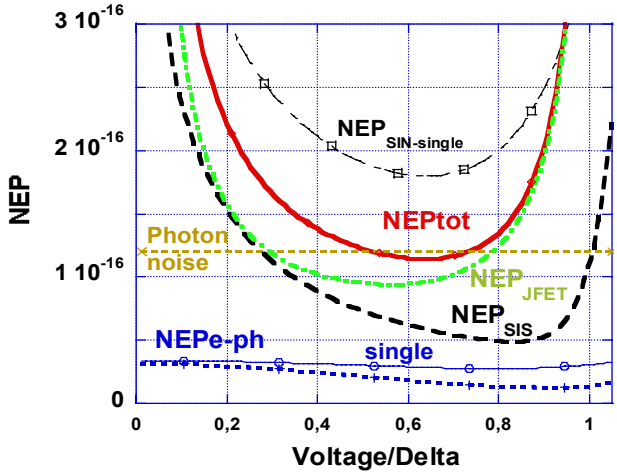

Fig. 1. Total NEP for array of 10 CEB, v_{JFET}=3 nV/Hz$^{1/2}$, R=0.5 kOhm (one junction), Vol=0.05um^3, power load – 20 pW. Junction noise and e-ph noise for single junction are shown for comparison. The power is split between bolometers and responsivity is considerably improved. For larger number of CEBs, the relation between NEPtot and NEPphot is even better (see fig. 3).

The NEPtot is still mainly determined by JFET noise (NEPamp)..

2. Channel I: "2.1 mm" (140 GHz)

Power load is relatively high: P_0 = 2 – 3 pW.
Let's accept minimum value for NEP estimations : P_0 = 2 pW.

Photon noise: $NEP_{phot} = \sqrt{2P_0 * hf}$

$$NEP_{phot} = 2*10^{-17} W/Hz^{1/2} .$$

Total NEP of CEB should be less than photon noise: NEP_{tot} < NEP_{phot}.
Single CEB doesn't give proper results.
Only array gives proper NEP

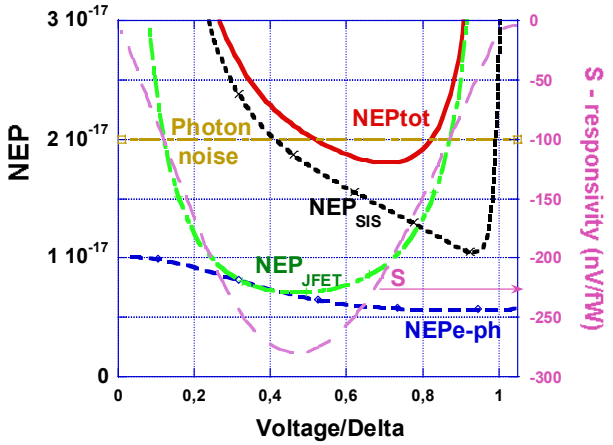

Fig. 2. Total NEP is less than NEPphot for array of 10 CEB, v_{JFET}=2 nV/Hz$^{1/2}$, R=0.5 kOhm (one junction), Vol=0.02um^3, power load – 2 pW. The power is split between bolometers and responsivity is considerably improved. The resistance is typical minimum resistance for our structures. Technological parameters are tougher than for previous case of array for 600 GHz.

Optimal number of CEBs in series array

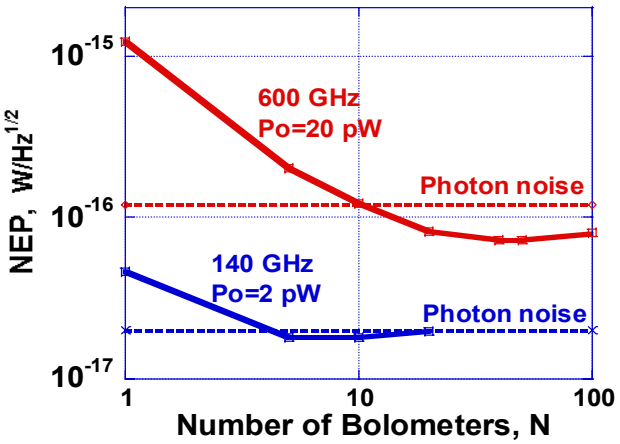

Fig. 3. Total NEP of CEB and NEPphot for series array of CEBs in dependence on number of CEBs a) ***600 GHz, power load P_0 = 20 pW***, v_{JFET}=3 nV/Hz$^{1/2}$, R=0.5 kOhm (one junction), Vol=0.05um^3. The power is split between bolometers and responsivity is considerably improved. The resistance is typical minimum resistance for our structures. Optimal number of bolometers is 40-50.
b) ***140 GHz, power load P_0 = 2 pW***, v_{JFET}=2 nV/Hz$^{1/2}$, R=0.5 kOhm (one junction), Vol=0.02um^3. The power is split between bolometers and responsivity is considerably improved. Optimal number of bolometers is 5-10.

The general rule of array design is the following:
Number of bolometers, N, should be increased to split Po between bolometers but up to the moment when $P_0/N = P_{ph}$, , where $P_{ph} = T_{ph}^5 \Sigma V$, V- volume.

There is no sense to increase number of bolometers more than this figure because power load in each bolometer becomes less than power from phonons. The phonon power is determined by only one parameter, volume of absorber. The volume should be decreased as much as possible to decrease this figure (in contrast to SQUID readout where resistance of the junctions is the most important).

Thus, the progress in improvement of NEP for series array of bolometers is determined by technological limit of absorber volume. For higher power limit, the use of array is more effective than for lower power limit.
Channel IV, 600 GHz, looks more preferable for use of array of CEBs with JFET than channel I, 140 GHz.

V. Conclusions

For typical values of JFET noise: 5 nV/Hz$^{1/2}$ and 5 fA/Hz$^{1/2}$, we have an effective noise impedance around 1 MOhm. Typical resistance of CEB in operating point (near gap for strong electron cooling) is around 1 kOhm. We have clear mismatch at three orders of magnitude.
Replacing CEB on SCEB (with weak superconducting absorber) we choose flat region of IV curve with very high dynamic resistance. Increase of resistance will be possibly limited by leakage resistance and is just around 3 orders of magnitude that is enough for noise-matching conditions.

Thus, the SCEB can bring remarkable progress in implementation of bolometers with JFET readout for all channels of OLIMPO.
The proper technology of Al/Aloxide/Ti junctions should be developed for this purpose. Possibly it should be a three-layer technology due to rather large areas of the junctions for lower frequencies (difficult for shadow evaporation technique). In principle, all steps in this technology, including etching the tunnel junctions area (say 2x2 um^2) could be done by photolithography.

1. S. Masi, P. Ade, A. Boscaleri, P. de Bernardis, M. De Petris, G. De Troia, M. Fabrini, A. Iacoangeli, L. Lamagna, A. Lange, P. Lubin, P. Mauskopf, A. Melchiorri, F. Melchiorri, L. Nati, F. Nati, A. Orlando, F. Piacentini, M. Pierre, G. Pisano, G. Polenta, Y. Rephaeli, G. Romeo, L. Salvaterra, G. Savini, E. Valiante, D. Yvon, *OLIMPO: a balloon-borne, arcminute-resolution survey of the sky at mm and sub-mm wavelengths* , in 16th ESA Symposium on European Rocket and Balloon Programmes and Related Research, June 2-5, 2003, St.Gallen (2003), ESA-SP-530, 557-560.
2. Leonid Kuzmin, "Ultimate Cold-Electron Bolometer with Strong Electrothermal Feedback", Proc. of SPIE conference "Millimeters and Submillimeter Detectors", Vol. 5498, pp 349-361, Glasgow, June 21-25, 2004.
3. Leonid Kuzmin, "Superconducting Cold-Electron Bolometer with Proximity Traps", Microelectronic Engineering, 69, 309-316 (2003).
4. Dmitri Golubev and Leonid Kuzmin "Cold-electron bolometer with superconducting absorber", Proceedings of the 9th International Workshop "From Andreev Reflection to the Earliest Universe", Bjorkliden, Sweden, April 2005.

Superconducting nanostructured detectors capable of single-photon counting in the THz range

G. Gol'tsman, A. Korneev, O. Minaeva, I. Rubtsova, I. Milostnaya, G. Chulkova, B. Voronov, K. Smirnov, V. Seleznev, W. Słysz, J. Kitaygorsky, A. Cross, A. Pearlman, and Roman Sobolewski

***Abstract*—We present the results of the NbN superconducting single-photon detector sensitivity measurement in the visible to mid-IR range. For visible and near IR light (0.56 — 1.3μm wavelengths) the detector exhibits 30% quantum efficiency saturation value limited by the NbN film absorption and extremely low level of dark counts ($2x10^{-4}$ s^{-1}). The detector manifested single-photon counting up to 6 μm wavelength with the quantum efficiency reaching 10^{-2}% at 5.6 μm and 3 K temperature.**

***Index Terms*—Infrared optical detectors, single-photon counters, superconducting devices, NbN superconducting films**

I. Introduction

At present the expansion of the traditional single-photon counting detectors such as avalanche photodiodes (APD) and photomultiplier tubes (PMT) to the middle IR and far-IR (THz) ranges is significantly hampered. The main reason of this is in fact that the typical bandgap of semiconductors and electronic work function of a metal (in case of PMT) become higher than the energy of the IR photon at the THz frequency. Superconducting devices, on the other hand, seem to be very prospective for these purposes. As the typical energy gap of superconductors 2Δ is several orders of magnitude smaller than the bandgap of semiconductors (2Δ~2meV for NbN at 4.2 K). For example, an absorbed 1-μm wavelength photon is able to produce an avalanche of ~100-1000 excited electrons in the NbN superconductor detector vs only one electron-hole pair in the APD. Picosecond energy relaxation time in superconductors allows one to create a photon counter with GHz counting rate. Cryogenic operation environment significantly reduces thermal fluctuations and as the consequence provides very low dark counts rate eliminating complicated biasing circuits common for APDs.

We have already reported on the successful development and fabrication of the superconducting single-photon detector (SSPD) for IR radiation [1]-[3]. The SSPD is made of 4-nm-thick NbN film deposited on the double-side polished sapphire substrate. The film was patterned by the electron beam lithography into a meander-shaped 100-nm-wide strip, covering the square area of 10x10 μm^2. The fabrication process did not affected the superconducting properties of the NbN film, i.e. the critical temperature T_c, the transition width ΔT_c and the critical current density j_c remain as high as they were for the unpatterned film (T_c=10-11 K, ΔT_c~0.3 K, j_c=6-7×10^6 A/cm^2 at 4.2 K). The detector exploits a combined detection mechanism, in which avalanche quasiparticle multiplication and the bias supercurrent jointly produce a transient voltage response to a single absorbed photon, via formation of a normal hotspot and phase-slip-centers in a quasi-two-dimensional superconducting strip [1],[4]. Being operated at 2 K, the SSPDs are capable of GHz-rate IR single photon counting with a record low dark counts rate. In this paper we present the result of our research on the SSPD spectral sensitivity up to 6μm wavelength.

II. Exprimental Setup

The SSPD is placed inside the optical liquid helium cryostat and maintained at the constant temperature in 2-5 K range. The SSPD is wire-bonded to a coplanar transmission line and then connected to the cryogenic bias-T. The bias-T, in turn, is connected to the very stable, constant-voltage bias source and the output RF circuitry. Constant voltage operation regime assured a rapid return to the superconducting state after the photon detection by the SSPD and prevented self-heating of the device. The SSPD photoresponse was amplified by the chain of the room temperature amplifiers (total gain is 70 dB, and 0.05 to 2 GHz-bandwidth) and then fed to the oscilloscope and the pulse counter for statistical analysis.

Manuscript received June 8, 2005.
This work was funded by RFBR grant 03-02-17697 (Moscow), CRDF grants RE2-2529-MO-03 (Moscow and Rochester) and RE2-2531-MO-03 (Moscow), INTAS grant INTAS 03-51-4145 (Moscow) and US AFOSR grant FA9550-04-1-0123 (Rochester).
G. Gol'tsman (phone: +7(095)2461202; fax: +7(095)2466321; e-mail: goltsman00@mail.ru), A. Korneev, O. Minaeva, I Rubtsova, I. Milostnaya, , G. Chulkova, V. Voronov, K. Smirnov, V. Seleznev are with the Moscow State Pedagogical University, Moscow 119345, Russia.
W. Slysz, J. Kitaygorsky, A. Cross, A. Pearlman and R. Sobolewski are with the University of Rochester, Rochester, NY 14627, USA; W. Slysz is also with the Institute of Electron Technology, PL-02668 Warszawa, Poland. R. Sobolewski is also with the Institute of Physics, Polish Academy of Sciences, PL-02668 Warszawa, Poland.

To study the SSPD spectral sensitivity in 1-6 μm wavelength range we used the infrared grating spectrometer as the light source. The mirrors of the spectrometer focused the radiation in a rather uniform light spot with the diameter of about 1 cm. We used silicon input windows of the cryostat and also placed cold silicon filters inside to cut the parasitic visible and near IR (below 1 μm) radiation. We used a Gollay cell detector and a lock-in amplifier to calibrate the output power of the spectrometer in the whole range of 1-6 μm.

For better accuracy of the QE measurement we also calibrated the SSPD sensitivity at 1.26 and 1.55 μm wavelengths. In this case the SSPD was installed in a dipstick and maintained in the storage dewar. The light was delivered to the SSPD by the multi-mode optical fiber and fell on the SSPD through its sapphire substrate. As the light sources we used cw laser diodes. We used the InGaAs powermeter operating in the 800-1600 nm range to determine the number of the incident photons delivered by the fiber to the SSPD. We used calibrated optical attenuators and always measured separately the power of our light sources. For this purpose we mounted a small piece of the sapphire substrate (the same as we use for the SSPD fabrication) on the device holder instead of the SSPD and collected the light passing through the sapphire on the fiber coupled to the optical powermeter. From the power measurement we obtained the average density of the photon flux; considering that the light was rather uniformly distributed on the SSPD active area, we calculated an average number of incident photons. We define quantum efficiency QE as the ratio of the detection events registered by the counter N_{reg} to the number of incident photons N_{inc} for a given time interval per the device area:

$$QE = N_{reg} / N_{inc} \qquad (1)$$

The measured QE at 1.26 μm together with the relative measurements with the spectrometer could be used for the SSPD QE calculation in the whole studied wavelength range.

The dark counts rate was studied in the dipstick setup. The SSPD was completely shielded. The cold metal shield prevented the illumination of the SSPD by the parasitic 300 K background radiation, which might manifest itself as extrinsic dark counts.

The temperatures below 4.2 K were achieved by the helium vapor pumping.

III. Experimental results

From the application point of view the telecommunication 1.3 μm and 1.55 μm wavelengths are very interesting. Fig. 1 presents the results of QE measurements performed with cw lasers at 0.56, 1.26 and 1.55 μm wavelengths and at the temperatures of 4.2 and 2 K. The QE was measured as a function of the normalized bias current I_b/I_c (i.e. the ratio of the SSPD bias current I_b to its critical current I_c at the given temperature). One can see that at 1.26 μm, the QE reaches 30% value, while at 1.55 μm, the maximum QE is 17%. At 4.2 K, the QE for IR light is much smaller. For example, the maximum QE at 1.55 μm at 4.2 K is only 3.7% and only for I_b approaching I_c (Fig. 1).

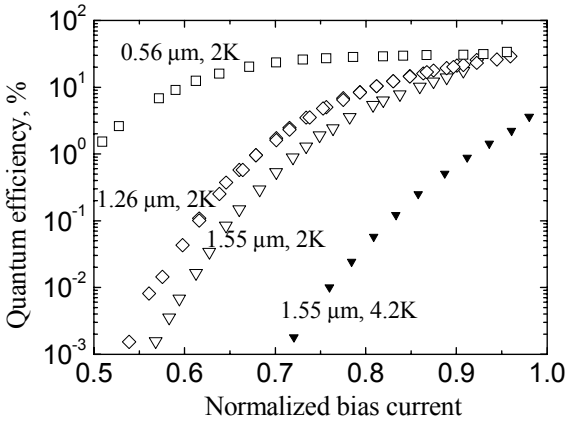

Fig. 1. SSPD QE measured using cw laser diodes at 4.2 K (solid symbols) and 2 K (open symbols) temperatures.

For comparison, we also present the QE vs. I_b/I_c measured with 0.56 μm cw laser at 2.0 K. One can note an obvious saturation-like behavior, which we explain as the achievement of the limit determined by the film absorption. For visible-light photons this limit reaches a ~30% value.

The results of our investigation of the SSPD spectral sensitivity are presented in Fig. 2. Our most recently fabricated devices exhibited single-photon counting up to 5.6-μm wavelength. The QE vs. wavelength was measured at 2 K temperature and four different bias currents. The spectral sensitivity strongly depends on the ratio of I_b/I_c. The highest detection probabilities are measured for I_b values very close to I_c. The decrease of the operating temperature for a given I_b/I_c improves QE, as well as extends the SSPD's single photon counting capabilities further into the IR wavelength range providing the QE of 10^{-2}% at 5.6 μm wavelength.

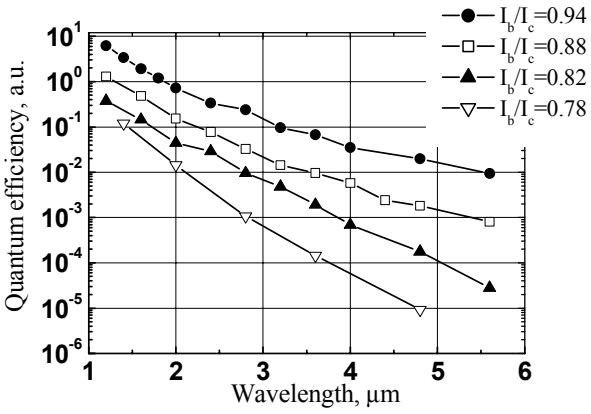

Fig. 2. QE (in arbitrary units) vs. wavelength measured at different I_b/I_c values and 2 K temperature.

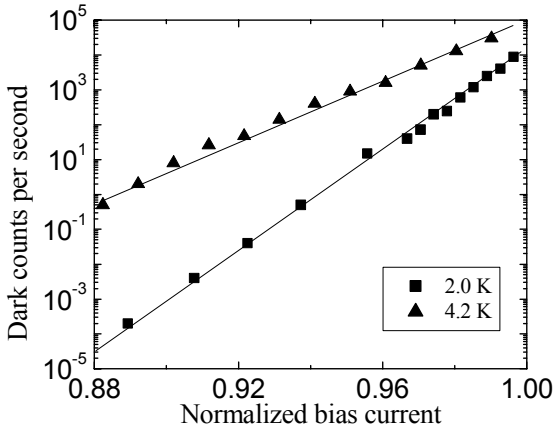

Fig. 3. Dark counts rate vs normalized bias current measured at 4.2 K (triangles) and 2 K (squares) temperatures.

Fig. 3 presents the dark count rate R vs. I_b/I_c. measured at 4.2 K and 2 K temperatures. The $R(I_b/I_c)$ dependence demonstrates the activation law in the whole biasing range used in our experiments ($0.87<I_b/I_c<0.99$):

$$R = a \cdot \exp(b\frac{I_b}{I_c}), \qquad (2)$$

where a and b are constants. The activation-type behavior of $R(I_b)$ at 2 K extends up to over seven orders of magnitude. The minimum measured R was as low as 2×10^{-4} s^{-1} and was limited by the duration of the experiment, i.e., accumulating several dark counts took about 8 hours. Lowering of the operation temperature also drastically reduces the dark counts rate.

An optimal operation regime of the SSPD is a trade-off between QE and R. The maximum value of QE corresponds to rather high (~1000 s^{-1} or above) R. Quantitatively this interplay between QE and R can be presented in terms of the Noise Equivalent Power (NEP), which can be defined for quantum detectors as:

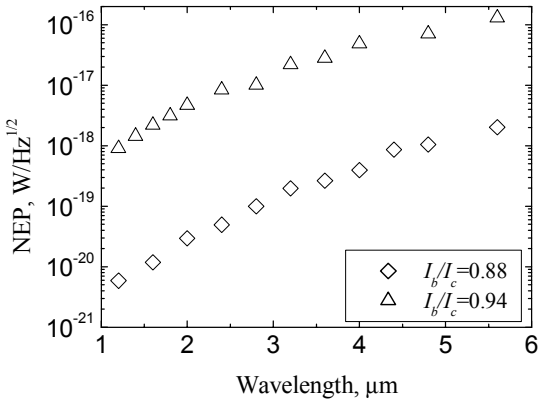

Fig. 4. Noise equivalent power (NEP) vs wavelength calculated from the measured QE and dark counts rate at 2 K temperature.

$$NEP = \frac{h\nu}{QE}\sqrt{2R} \qquad (3)$$

where $h\nu$ is photon energy. We used the experimentally measured QE values presented in Fig. 1 and the result of the SSPD spectral sensitivity measurement presented in Fig. 2 to calculate the QE in the whole studied wavelength range. Then these data together with the dark counts rate at 2 K temperature (Fig. 3) allowed us to calculate NEP. The result of our calculation for I_b/I_c values of 0.94 and 0.88 is presented in Fig. 4. The NEP values for I_b/I_c=0.88 were calculated using the extrapolated value of dark counts rate. One can see, that the NEP level as low as $5\cdot10^{-21}$ W/Hz$^{1/2}$ can be achieved for photon at the telecommunication wavelengths at 2.0 K, whereas at 5 – 6 μm the NEP is about 10^{-18} W/Hz$^{1/2}$.

IV. Conclusion

In conclusion we would like to underline that our SSPD is the only practical quantum detector that exhibits single-photon sensitivity at 5 – 6 μm wavelength. Being operated at 3 K temperature it exhibits 10^{-2}% QE at 5.6 μm wavelength. On the other hand, in the visible range QE has already achieved its saturation value of 30% limited by the film absorption.

Further significant improvement of the SSPD performance in the mid-IR range is expected with currently undertaken implementation of superconductors with a narrow energy gap and low quasiparticle diffusivity. The use of a material with the low transition temperature will shift the sensitivity cutoff towards longer wavelengths. Depending on the material and operation conditions, such a detector should obtain a background-limited NEP below 10^{-21} WHz$^{-1/2}$ and a high dynamic range in THz frequencies, when exposed to 4-K background radiation.

References

[1] G. N. Gol'tsman, O. Okunev, G. Chulkova, A. Lipatov, A. Semenov, K. Smirnov, B. Voronov, A. Dzardanov, C. Williams, and Roman Sobolewski, Appl. Phys. Lett., vol. 79, no. 6, pp. 705-707, 2001.

[2] A.Verevkin, J.Zhang, R.Sobolewski, A.Lipatov, O.Okunev, G.Chulkova, A.Korneev, K.Smirnov, G.Gol'tsman, A. Semenov, Appl. Phys. Lett., vol.80, no. 25, pp.4687-4689, 2002

[3] A. Korneev, P. Kouminov, V. Matvienko, G. Chulkova, K. Smirnov,B. Voronov, and G. N. Gol'tsman, M. Currie, W. Lo and K. Wilsher, J. Zhang, W. Slysz, A. Pearlman, A. Verevkin, and Roman Sobolewski, Appl. Phys. Lett. vol. 84, no. 26, 28, pp 5338-5340, 2004

[4] A. Semenov, G. Gol'tsman, A. Korneev, Physica C, 352 (2001) pp. 349-356P

Heterojunction GaAs/AlGaAs Terahertz Detectors

A. G. U. Perera, M. I. Stockman, G. Hastings,
M. B. M. Rinzan, and S. G. Matsik
Dept. of Physics and Astronomy
Georgia State University
Atlanta, GA 30303

H. C. Liu, Z. R. Wasilewski,
and M. Buchanan
Institute for Microstructural Sciences
National Research Council
Ottawa K1A 0R6, Canada

***Abstract*— The THz region is of considerable interest for many applications, in particular for applications in astrophysics and biophysics. The limits on Al growth fraction have restricted previous devices to a 3.1 THz (96.8 μm, 103 cm^{-1}) threshold. A new approach, replacing doped GaAs emitters with doped Al$_x$Ga$_{1-x}$As, overcomes this limit, extending the threshold to lower frequencies. Here, results are reported on a p-Al$_x$Ga$_{1-x}$As/GaAs heterojunction interfacial workfunction internal photoemission (HEIWIP) detector operating in the 30-2.3 THz (10-128 μm)range. The spectra for a detector using this approach have a strong response for frequencies lower than 150 THz with a threshold of 2.3 THz. The peak frequency at 9.6 THz ($\lambda = 31$ μm) gave a response of 7.3 A/W and $D^* = 5.3 \times 10^{11}$ Jones. A BLIP temperature of 20 K was obtained. As future developments, possible response enhancing mechanisms such as surface plasmon (SP) effects, alternate material systems, and a possible dual band detector are considered.**

I. Introduction

Astrophysics has traditionally been an important area for THz applications. The large number of spectral lines associated with molecules and the ability of THz radiation to travel through dust clouds have made this range increasingly important for the study of numerous astronomical objects. Also recently, extension of FTIR difference spectroscopy techniques down to $\sim$ 6 THz (200 cm^{-1}) have been used for studies of biological systems.[1], [2], [3] In these biophysical measurements silicon bolometers were used. Silicon bolometers have a very long time constant, which makes these biophysical FTIR measurements problematic because considerable signal averaging is required in these experiments. Given the bolometer time constant, the low frequency biophysical FTIR measurements can take many hours to days to complete. This is quite impractical and the development of new and "fast" THz detector technologies should positively impact the feasibility of these biophysical FTIR measurements. In addition to these applications, the recent developments in THz sources and imaging systems have led to renewed interest in detectors. The work presented here is aimed at developing fast broadband THz detectors with multiple applications. The quantum well photodetectors (QWIPs) have recently extended the f_0 to $\sim$ 5 THz.[4] However, it is still below the response region of HEIWIPs. In QWIPs, decreasing the frequency further requires the doping density to be decreased to reduce dark current, but this lowers the absorption and therefore the sensitivity. The work presented here involves a different approach using free-carrier absorption and an interfacial workfunction to operate in the THz regime.

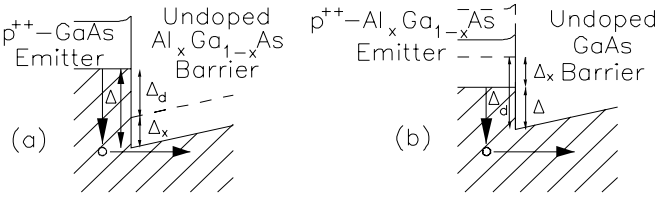

Fig. 1. A partial band diagram showing the detection mechanism in HEIWIP detectors. (a) In the standard design Doped GaAs was used as the emitter and undoped AlGaAs was used for the barrier. (b) To extend the threshold doped AlGaAs was used as the emitters while undoped GaAs forms the barriers. The dashed lines indicate the location of the fermi level and band edge if the AlGaAs layer were GaAs.

A. Basic Detector Design

The basic design of an Interfacial Workfunction Internal Photoemission (IWIP) detector consists of a sequence of alternating heavily doped emitter layers and undoped barrier layers.[5] Depending on whether the layers have the same or different compositions, the detectors are classified as Homojunction (HIWIP)[6] or HEterojunction (HEIWIP) Interfacial Workfunction Internal Photoemission detectors[7]. The detection mechanism is the same in both the HIWIP and HEIWIP detectors. The radiation is absorbed in the highly doped emitter layers producing photoexcited carriers. The carriers then undergo internal photoemission across the interface between the layers, and are swept out of the active region by the applied field, and collected at the contact. There are two contributions to the workfunction: i) the bandgap narrowing due to the doping in the emitters which occurs for both HIWIPs and HEIWIPs, and ii) the bandgap offset due to composition difference which occurs only in the HEIWIPs. The zero response threshold frequency is given by $f_0 = 0.242\Delta$ with f_0 in THz and the workfunction Δ in meV.

If GaAs emitters and AlGaAs barriers were used as is typically done in QWIPs or HEIWIPs designed with a higher frequency threshold, the two contributions to the workfunction would add together as shown in Fig. 1(a). The Al fraction x can be reduced to any value in theory. However, a practical lower limit will be around $x \geq 0.005$ with $f_0 \geq 2.7$ THz. (Although x = 0 is practical, then the device will no longer be a HEIWIP, and will have a $\sim$ 9 meV offset for $N_A = 3 \times 10^{18}$

cm^{-3} giving $f_0 = 2.17$ THz.) Although Δ_d can be reduced by increasing the doping, difficulties in controlling the doping and potential limits due to light-heavy hole transitions[8] make this approach unappealing. Further decrease in f_0 below 2.7 THz (i.e. beyond ~ 110 μm) requires a change in the design due to the minimum $\Delta = \Delta_d$ imposed by the bandgap narrowing.

One possible approach to avoid this limit is to use AlGaAs as the emitter and GaAs as the barrier. A partial band diagram of a THz HEIWIP detector is shown in Fig. 1(b). A key feature of this structure is the use of AlGaAs in the emitters and GaAs in the barriers. This is done in order to reduce the workfunction and obtain THz response. In such a device, the bandgap narrowing in the doped AlGaAs will be partially offset by the increased bandgap of the AlGaAs material relative to the GaAs as seen in Fig. 1, giving $\Delta = \Delta_d - \Delta_x$. For example, a $f_0 = 0.9$ THz (335 μm) detector would have an Al fraction of ~ 0.012. Based on calculations and measurements on doped AlGaAs films,[9] the FIR absorption in AlGaAs is expected to be very similar to GaAs, due to the very low Al content giving performances similar to the current devices with AlGaAs barriers.

One possible method of increasing the response is through the use of resonant cavity effects[10], [11]. The idea of the cavity architecture is to use the reflection from the top and bottom surfaces to create a standing wave in the device. Placing the emitters at the antinodes in the resulting resonant cavity structure will increase absorption and enhance the response at the resonant wavelengths. Resonant cavity effects have already been demonstrated in the reflection, transmission and absorption of structures even with semi-insulating substrates[12] and in detectors grown on doped substrates.[13] A complete model detailing the calculation of response including the cavity effect is given elsewhere.[14]

II. Experiment

A. Detector Design and Fabrication

The detector structure consisted of 10 periods of 3×10^{18} cm^{-3} Be-doped 500 Å thick $Al_{0.005}Ga_{0.995}As$ emitter and 2000 Å thick GaAs barrier sandwiched between two contacts. The top and bottom contacts are 1×10^{19} cm^{-3} Be-doped 500 Å and 7000 Å thick $Al_{0.005}Ga_{0.995}As$ layers, respectively. The detectors were fabricated by using wet etching techniques to isolate 400×400 to 1000×1000 μm^2 mesas and depositing Ti/Pt/Au ring contacts to allow for frontside illumination. As the devices use free-carrier absorption, normal incidence illumination can be used.

B. Dark Current

The devices were first characterized by measuring the dark current at 4.2 K, which showed good uniformity between devices with less than 5% variation in dark current density between mesas. Both the dark current and the photocurrent when exposed to a 300 K background were measured for various temperatures, and a BLIP temperature of 20 K was obtained. The dark current at different temperatures was also used to obtain the workfunction from an Arrhenious plot. The workfunction decreased with bias as shown in Fig. 2, which is believed to be due to band bending. The sharp jumps in Δ with bias were observed in multiple samples but their origin is unexplained at this time.

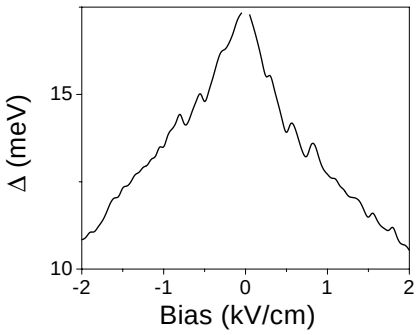

Fig. 2. The variation of the workfunction Δ with the applied bias. The effect is believed to be related to band bending from space charge in the barriers.

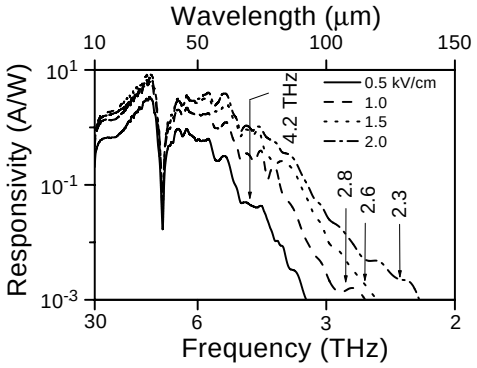

Fig. 3. The observed response for the THz detector. The peak response was at 9.6 THz with a responsivity of 7.3 A/W and $D^* = 5.3 \times 10^{11}$ Jones at 4.8 K and 2.0 kV/cm bias. The variation of f_0 with bias shown by the arrows is in good agreement with the values predicted from the arrhenious plots.

C. Spectra

The spectral response was measured at 4.2 K using a Fourier Transform Infrared (FTIR) spectrometer calibrated using a silicon composite bolometer. The results are shown in Fig. 3. Response was recorded from 30 THz to the threshold which varied with bias. The spectral threshold was in good agreement with the values predicted from the Arrhenious plot. This indicates that the electrical and optical barriers are the same. The predicted f_0 for this design was ~ 1.5 THz (200 μm) while the observed value was only 2.3 THz. This difference is believed to be related to the variation in Δ observed from the arrhenious plot caused by band bending. For detectors with thresholds below 3 THz the bending has become more important and future designs will consider methods of offsetting its effects, possibly by increasing the Al fraction.

The detectors were designed (for a total device thickness near 3 μm) with the first order cavity peak at ~ 7.5 THz which is near the decrease in absorption due to the reststrahlen band. Increasing the device thickness would increase the response

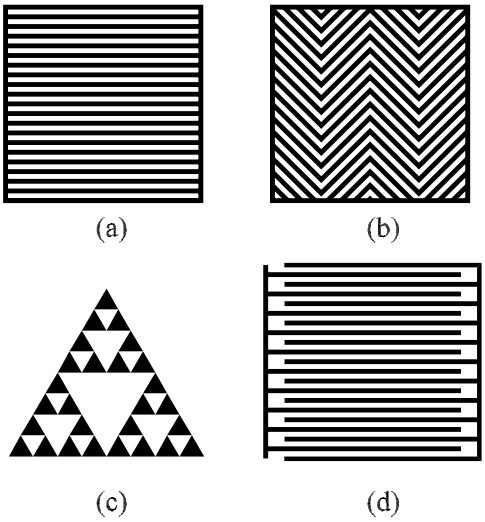

Fig. 4. Examples of the metal film patterns planned for testing. (a) A uniform grid to look for a polarized response. (b) A series of line segments to obtain a polarization independent response. (c) A Sierpinski gasket to test fractal patterns for a broad response. (d) An interdigitated contact to test the effects of a modulated lateral field on the plasmon resonances.

at longer wavelengths but would also be impractical for MBE growth. For example, a device optimized for $f_0 = 1$ THz with a cavity peak at 1.5 THz would require a total device thickness near 15 μm.

III. Plasmon Enhanced Detectors

Electromagnetic waves at metal-dielectric or metal-semiconductor interfaces, such as surface plasmon polaritons (SPPs), and SPs, have remarkable properties of generating highly enhanced local fields. These local fields in nanostructured systems can exceed excitation fields by orders of magnitude and undergo giant fluctuations in space and in time. These giant local fields are responsible for a multitude of enhanced optical phenomena and their applications. One of the most important and frequently used for applications, in physics, chemistry, molecular biology, medicine, and homeland security and national defense, is the Surface Enhanced Raman Scattering (SERS), gigantically enhanced Raman scattering from molecules adsorbed at metal nanosystems or in a vicinity of a metal system. The SERS is approximately proportional to $|E|^4$, where E is the local optical electric field in the units of the excitation field (i.e., E is the local field-enhancement factor). Typically, $E \sim Q = -\Re(\epsilon)/\Im(\epsilon) \sim 10$ - 100 for noble metals in the visible to IR region. Correspondingly, SERS is expected to be enhanced by factor of $G_{SERS} \sim 10^4$ - 10^8. This is the case for most of the experimental observations. However, under certain conditions, namely for molecules adsorbed on fractal clusters of colloidal silver, the enhancement is so large that SERS by single molecules can be seen. In this case the SERS enhancement is much larger, $G_{SERS} \sim 10^{12}$ - 10^{14}.

Enhancing detector performance by placing metal or semiconductor nanostructures in the vicinity of the electron-gas region of the detectors could lead to enhanced detector performance. The metal nanostructures will act as enhanced couplers, which will allow more efficient absorption of light as it is converted into surface plasmons (SPs). In the near field region, the electric field of the SPs will be enhanced over the incident radiation field. The near field of SPs will affect the electron gas in the photodetectors the same way as the far-field does. Thus the local field enhancement known for other phenomena and devices could be achieved. Surface plasmon enhanced absorption has been shown in the visible with "gold-blacks" and "silver-blacks" having absorption over 95%.[15] The idea is to employ this enhancement in the THz range. The near-field enhancement can be further increased by the use of self-similar patterns or tapered waveguides to concentrate the electric field in localized spatial regions. A simple self-similar nanosphere nanolens (known as a "snowman" nanolens) consists of a self-similar sequence of nanospheres with progressively decreasing radii and separations. For a symmetric six-nanosphere nanolens, the electric field enhancement is $\sim 10^3$.[16] A tapered waveguide also showed enhancement.[17] An alternate approach considered is the use of a periodic grating structure to produce plasmonic enhancements. Decreasing the grating spacing would increase the resonance frequency. This approach has already been applied with a grating on a double quantum well transistor detector for GHz radiation.[18] Such a grid could be used as a polarization-sensitive detector. By using a chevron-shaped grid or a fractal pattern, a non-polarization sensitive detector could be obtained. Some potential grid patterns are shown in Fig. 4.

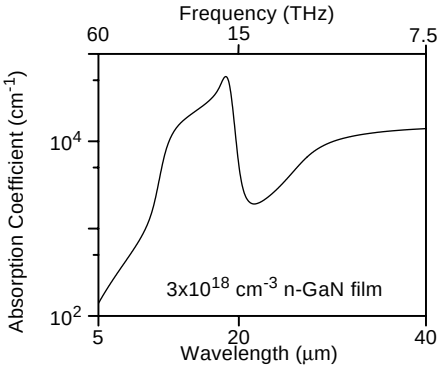

Fig. 5. Absorption coefficient for n-doped GaN film calculated from the reflection measurements.

IV. Other Materials

The use of materials other than GaAs can offer specific advantages to compensate for their disadvantage in material development. The well developed technology and ability to vary the Al fraction over a wide range due to the lattice matched nature of GaAs and AlAs have made the GaAs/AlGaAs material system a good choice during the development of these detectors. Other systems however, can provide advantages in certain ranges. Going to wider bandgap systems such as the

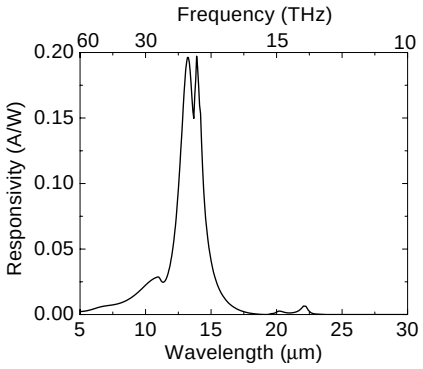

Fig. 6. The calculated response for a GaN/$Al_{0.02}Ga_{0.98}N$ detector with 10 layers calculated for a field of 1 kV/cm with the gain taken as 1. The device should have a BLIP temperature near 40 K.

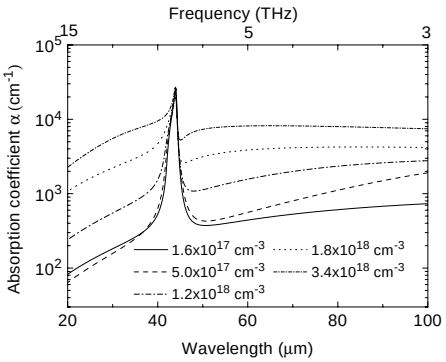

Fig. 7. Absorption coefficient for a GaSb film obtained from the reflection measurements.

nitrides and phosphides would improve radiation hardness. The increased bandgap would also mean that dual band detectors which would operate at higher frequencies could be designed. In particular, AlGaN would allow operation in the UV without responding to the visible.

1) GaN/AlGaN: The absorption of doped GaN films were obtained by measuring the reflection of GaN films grown on a sapphire substrate. The material parameters of the film were obtained by fitting the reflection to a model, and the resulting parameters were used to calculate the absorption coefficient shown in Fig. 5. This approach was used as the sapphire substrate does not transmit radiation above 6 μm, making a direct measurement of the absorption impossible. This could be used to design detectors for frequencies above 7.5 THz. While the response from the highest absorption value near 17 THz will be reduced due to reflection associated with the reststrahlen band, there will still be strong response in the range of 20-24 THz. The response of a GaN/AlGaN detector with Al fraction $x = 0.02$ is shown in Fig. 6 with a peak value of 0.2 A/W for a bias field of 1 kV/cm. This detector should operate up to $\sim$ 70 K with a BLIP temperature near 40 K. Due to the change in material the reststrahlen band has been moved to just near 17 THz making this a good alternative to GaAs/AlGaAs near 7.5 THz. A GaN based detector also would be likely to be more radiation hard due to the larger bandgap.

2) GaSb/InGaSb: The use of GaSb/GaInSb is of interest specifically for frequencies below 3 THz as better control of the workfunction is possible due to the much lower value of Δ_x in this system. In a GaAs/AlGaAs detector, $\Delta_x = 530$ meV while for GaSb/InGaSb $\Delta_x \sim 40$ meV. This much lower value means that unlike the GaAs/AlGaAs system in which the Al fraction is $< 1.7\%$ and must be controlled to 0.1% to obtain the desired thresholds, a GaSb/InGaSb detector would have In fractions near 15% allowing easier control. The disadvantage of this system is that the lattice mismatch will introduce defects which can reduce the detector efficiency. The absorption coefficient of doped GaSb films has been obtained using reflection measurements and are shown in Fig. 7.

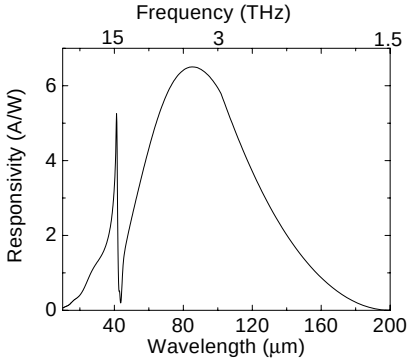

Fig. 8. The calculated response for a GaSb/$In_{0.2}Ga_{0.8}Sb$ detector with 30 layers calculated for a field of 1 kV/cm with the gain taken as 1.

Based on these results a detector with 30 periods using $In_{0.2}Ga_{0.8}Sb$ emitters and GaSb barriers has been modeled and the response is shown in Fig. 8. The peak response was 6 A/W at 3.1 THz for a bias field of 1 kV/cm. This detector is designed to operate at 4.2 K. The major advantage in this design is the large In fraction possible. For a similar threshold AlGaAs/GaAs design, an Al fraction of 0.010 would be needed with a corresponding high level of control.

V. Dual Band Response

One interesting possibility for these detectors is a dual band design in which both interband and intraband transitions are used.[19] By using two different transitions response is possible in very different spectral ranges. The basic design of a dual band detector using a single emitter and a barrier is shown in Fig. 9. The long wavelength operation is the same as for the standard IWIP detector, while the short wavelength response is via an interband transition. This mode of operation allows a device to operate in the THz range, and by choosing a material with the correct band gap, in the UV-NIR range. Preliminary measurements have been done using a GaAs HIWIP detector for which the interband transition is in the NIR range. The structure consists of a bottom contact (p^{++}) layer with 1.0 μm thickness, a barrier layer with 1.0 μm thickness, an emitter (p^{+}) layer with 0.2 μm thickness, and a top contact layer. During processing, the top contact and a part of the emitter

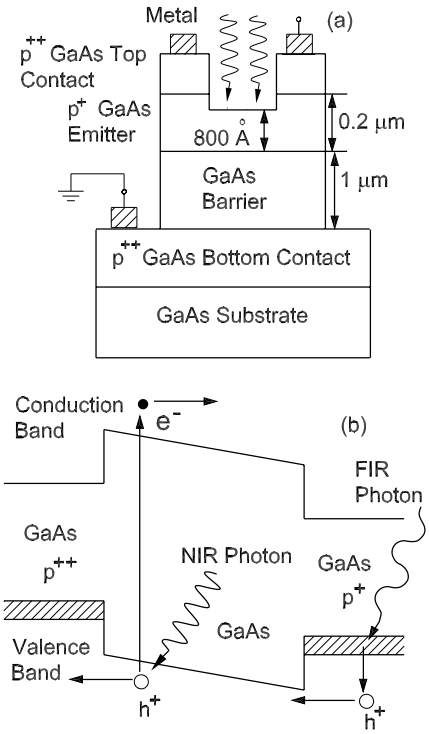

Fig. 9. (a) The detector structure as processed for use in the dualband measurements. Part of the top contact and emitter have been etched out to improve IR transmission into the detector. (b) The band diagram of the detector showing the two detection mechanisms. The THz detection occurs by an intraband transition in the bottom emitter, while the NIR detection occurs by an interband process in the barrier.

layer were etched out in the region inside the ring contact, leaving about 800 Å thick emitter region (out of 0.2 μm). The response obtained from the HIWIP detector is shown in Fig. 10. The response due to intraband transition is observed to 4.3 THz (70 μm) and it has a responsivity of $\sim$ 1.8 A/W and a detectivity of $\sim 5.6\times10^{10}$ Jones at 5.1 THz (57 μm) under 100 mV reverse bias. The peaks at 57 and 63 μm are due to transitions in the hydrogenic states of the impurity atoms present in the barrier. The interband response was observed at wavelengths below 0.8 μm. An optimum responsivity of $\sim$ 8 A/W and a detectivity of $\sim 6\times10^{9}$ Jones were obtained at 0.8 μm. By changing the material, the short wavelength response could be tailored to the desired range. One possibility for a dual band detector would be to use GaN/AlGaN with an interband transition in the UV giving a device which responds in both the UV and THz while ignoring the visible.

VI. Conclusion

The extension of HEIWIP response to $f_0 = 2.3$ THz has been demonstrated with a response of 7.3 A/W and $D^* = 5.3 \times 10^{11}$ Jones by the use of AlGaAs emitters and GaAs barriers. The response could be increased by the use of metal nanostructures to create plasmon effects. A dual band detector responding in the NIR and THz range was demonstrated based on using both interband and intraband transitions. As future developments, the use of alternate materials, GaN/AlGaN in a

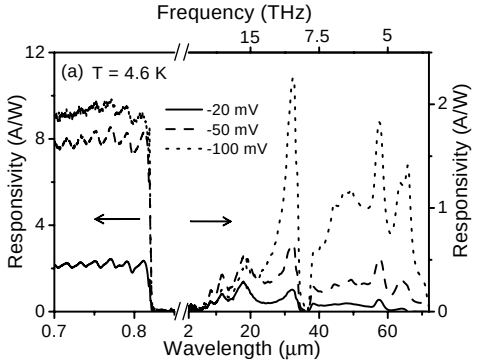

Fig. 10. Measured responsitivy for the dual band GaAs detector.

dual band structure to allow UV detection and GaSb/InGaSb for better control of the workfunction in THz designs were suggested. The absorption of both these materials was obtained and is similar to that of GaAs indicating their suitability.

Acknowledgment

This work was supported in part by the NSF under grants #ECS-0140434 and DBI: 0352324.

References

[1] H. A. Chu, M. T. Gardner, W. Hillier, and G. T. Babcock, Photosyn. Res. **66**, 57 (2000).
[2] H. A. Chu, H. Sackett, and G. T. Babcock, Biochem. **39**, 14371 (2000).
[3] J. Breton, E. Nabedryk, and A. Clerici, Vibrational Spectroscopy **19**, 71 (1999).
[4] H.C. Liu, C.Y. Song, A.J. Spring Thorpe, and J.C. Cao, Appl. Phys. Lett. **84**, 4068 (2004).
[5] A. G. U. Perera, H. X. Yuan and M. H. Francombe, J. Appl. Phys. **77**, 915 (1995).
[6] D. G. Esaev, M. B. M. Rinzan, S. G. Matsik, A. G. U. Perera, H. C. Liu, B. N. Zhonkov, V. I . Gavrilenko, and A. A. Belyanin, J. Appl. Phys. **95**, 512 (2003).
[7] A. G. U. Perera, S. G. Matsik, B. Yaldiz, H. C. Liu, A. Shen, M. Gao, Z. R. Wasilewski and M. Buchanan, Appl. Phys. Lett **78**, 2241 (2001).
[8] A. G. U. Perera, S. G. Matsik, M. B. M. Rinzan, A. Weerasekara, M. Alevli, H. C. Liu, M. Buchanan, B. Zvonkov, and V. Gavrilenko, Infrared Phys. Technol. **44**, 347 (2003).
[9] M. B. M. Rinzan, D. G. Esaev, A. G. U. Perera, S. G. Matsik, G. Von Winckel, A. Stintz, and S. Krishna, Appl. Phys. Lett. **85**, 5236 (2004).
[10] A. L. Korotkov, A. G. U. Perera, W. Z. Shen, H. C. Liu, M. Buchanan, Solid State Electronics **45**, 87 (2001).
[11] D. G. Esaev, S. G. Matsik, M. B. M. Rinzan, A. G. U. Perera, H. C. Liu, and M. Buchanan, J. Appl. Phys. **93**, 1879 (2003).
[12] A. L. Korotkov, A. G. U. Perera, W. Z. Shen, J. Herfort, K. H. Ploog, W. J. Schaff, and H. C. Liu, J. Appl. Phys **89**, 3295 (2001).
[13] S. G. Matsik, M. B. M. Rinzan, D. G. Esaev, A. G. U. Perera, G. von Winckel, A. Stintz, S. Krishna, H. C. Liu, M. D. Byloos, T. Oogarah, G. I. Sproule, K. Liu, and M. Buchanan, IEEE Transanctions Electron Devices **52**, 413 (2005).
[14] D. G. Esaev, M. B. M. Rinzan, S. G. Matsik, and A. G. U. Perera, J. Appl. Phys. **96**, 4588 (2004).
[15] C.-M. Wang, Y.-C. Chen, M.-S. Lee, and K.-J. Chen, Jpn. J. Appl. Phys. **39**, 551 (2000).
[16] K. Li, M. I. Stockman, and D. J. Bergman, Phys. Rev. Lett. **91**, 227402-1-4 (2003).
[17] M. I. Stockman, Phys. Rev. Lett. **93**, 137404 (2004).
[18] V. V. Popov, T. V. Teperik, O. V. Polischuk, X. G. Peralta, S. J. Allen, N. J. M. Horing, and M. C. Wanke, Phys. Solid State **46**, 153 (2004).
[19] G. Ariyawansa M. B. M. Rinzan D. G. Esaev S. G. Matsik A. G. U. Perera H. C. Liu B. N. Zvonkov V. I. Gavrilenko, Appl. Phys. Lett. **86**, 143510-3 (2005).

PARTICIPANTS

First name	Surname	Email	Country	Affiliation
Aurelé	Adam	a.j.l.adam@tnw.tudelft.nl	The Netherlands	Delft University of Technology
Ian Jasper	Agulo	ian.agulo@mc2.chalmers.se	Sweden	Chalmers University of Technology
Féret	Alexandre	alexandre.feret@obspm.fr	France	Observatoire de paris
Vladimir	Antonov	v.antonov@rhul.ac.uk	UK	University of London
Ian	Bacchus	ian.bacchus@astro.cf.ac.uk	UK	Cardiff University
Rami	Barends	r.barends@tnw.tudelft.nl	The Netherlands	Delft University of Technology
Andrey	Baryshev	andrey@sron.rug.nl	The Netherlands	SRON National Institue for Space Research
Jochem	Baselmans	J.Baselmans@sron.nl	The Netherlands	SRON National Institue for Space Research
Jean	Baubert	jbbaubert@yahoo.fr	Sweden	Chalmers University of Technology
Lukasz	Bednarz	bednarz@emic.ucl.ac.be	Belgium	Microwave Laboratory UniversitÈ catholique de Louvain (UCL)
Sven	Bedorf	bedorf@ph1.uni-koeln.de	Germany	Universität zu Köln
Victor	Belitsky	belitsky@oso.chalmers.se	Sweden	Chalmers University of Technology
Therese	Berg	therese.berg@mc2.chalmers.se	Sweden	Chalmers University of Technology
Xiaochuan	Bi	xbz@umich.edu	USA	University of Michigan
Stephan	Biber	stephan@lhft.de	Germany	University of Erlangen-Nuremberg
Roy	Booth	roy@oso.chalmers.se	Sweden	Chalmers University of Technology
Kjell	Brantervik	kbr@chl.chalmers.se	Sweden	Chalmers University of Technology
Tomas	Bryllert	Tomas.Bryllert@ftf.lth.se	Sweden	Lund University
Ivan	Cámara Mayorga	imayorga@mpifr-bonn.mpg.de	Germany	Max Planck Institut für Radioastronomie
Massimo	Candotti	massimo.candotti@may.ie	Ireland	NUIM, National University of Ireland
Lars-Erik	Ceicer	lars-erik.ceicer@ericsson.com	Sweden	Ericsson Microwave Systems AB
Sergey	Cherednichenko	serguei.cherednichenko@mc2.chalmers.se	Sweden	Chalmers University of Technology
James	Chervenak	James.A.Chervenak@nasa.gov	USA	NASA Goddard Space Flght Center
Moon-Hee	Chung	mhchung@trao.re.kr	South Korea	Taeduk Radio Astronomy Observatory
Thomas	Crowe	twc8u@virginia.edu	USA	University of Virginia / Virginia Diodes, Inc.
Gert	de Lange	gert@sron.rug.nl	The Netherlands	SRON National Institute for Space Research
Simon	Doyle	Simon.Doyle@astro.cf.ac.uk	UK	Cardiff University
Vladimir	Drakinskiy	drakinsk@mc2.chalmers.se	Sweden	Chalmers University of Technology
Louisa	Dunlop	ld273@mrao.cam.ac.uk	UK	Cavendish Laboratory
Jack	East	jeast@eecs.umich.edu	USA	University of Michigan
Heribert	Eisele	h.eisele@leeds.ac.uk	UK	University of Leeds
Arezoo	Emadi	arezoo.emadi@mc2.chalmers.se	Sweden	Chalmers University of Technology
Anders	Emrich	ae@omnisys.se	Sweden	Omnisys Instruments AB
Kamran	Ezdi	kezdi@wave.ihf.ing.tu-bs.de	Germany	Technische Universität Braunschweig
Jianrong	Gao	j.r.gao@tnw.tudelft.nl	The Netherlands	SRON/TU Delft
Gregory	Gol'tsman	goltsman@mspu-phys.ru	Russia	Moscow State Pedagogical University
Jan	Grahn	jan.grahn@mc2.chalmers.se	Sweden	Chalmers University of Technology
Paul	Grimes	pxg@astro.ox.ac.uk	UK	University of Oxford
Christopher	Groppi	cgroppi@nrao.edu	USA	National Radio Astronomy Observatory
Merlijn	Hajenius	M.Hajenius@tnw.tudelft.nl	The Netherlands	SRON/TU Delft
Abby	Hedden	ahedden@as.arizona.edu	USA	SORAL, University of Arizona
Joerg	Heiermann	heierman@irs.uni-stuttgart.de	Germany	Universität Stuttgart
Doug	Henke	doug.henke@nrc.ca	Canada	Herzberg Institute of Astrophysics
Jeffrey	Hesler	hesler@vadiodes.com	USA	Virginia Diodes Inc.
Ronald	Hesper	R.Hesper@sron.rug.nl	The Netherlands	SRON National Institute for Space Research
Netty	Honingh	honingh@ph1.uni-koeln.de	Germany	Universität zu Köln
Qing	Hu	qhu@mit.edu	USA	MIT
Peter	Huggard	p.g.huggard@rl.ac.uk	UK	Rutherford Appleton Laboratory
Todd	Hunter	thunter@cfa.harvard.edu	USA	Harvard-Smithsonian Center for Astrophysics
Heinz-Wilhelm	Hübers	heinz-wilhelm.huebers@dlr.de	Germany	DLR Institute of Planetary Reserach
Junji	Inatani	inatani.junji@jaxa.jp	Japan	Japan Aerospace Exploration Agency
Willem	Jellema	W.Jellema@sron.nl	The Netherlands	SRON National Institute for Space Research
Boris	Karasik	boris.s.karasik@jpl.nasa.gov	USA	Jet Propulsion Laboratory, California Institute of Technology
Schuster	Karl-Friedrich	schuster@iram.fr	France	IRAM Institut de Radio Astronomie MillimÈtrique
Alexandre	Karpov	karpov@submm.caltech.edu	USA	California Institute of Technology
Irmantas	Kasalynas	irmantak@tnw.tudelft.nl	The Netherlands	TU Delft
Shigeo	Kazama	shigeo-kazama@sogoel.co.jp	Japan	Sogo Electronics, Inc.
Anthony	Kerr	akerr@nrao.edu	USA	National Radio Astronomy Observatory
Pourya	Khosropanah	p.kh@mac.com	Sweden	Chalmers University of Technology
Kenichi	Kikuchi	kikuchi.kenichi@jaxa.jp	Japan	Japan Aerospce Exploration Agency (JAXA)
Erik	Kollberg	erik.kollberg@mc2.chalmers.se	Sweden	Chalmers University of Technology
Jacob	Kooi	kooi@caltech.edu	USA	California Institute of Technology
Valery	Koshelets	valery@hitech.cplire.ru	Russia	Institute of Radio Engineering and Electronics
Viktor	Krozer	vk@oersted.dtu.dk	Denmark	Tech. Univ. Denmark (DTU)
Leonid	Kuzmin	leonid.kuzmin@mc2.chalmers.se	Sweden	Chalmers University of Technology
Igor	Lapkin	lapkin@oso.chalmers.se	Sweden	Chalmers University of Technology
Bernard	Lazareff	lazareff@iram.fr	France	IRAM Institut de Radio Astronomie MillimÈtrique
Mark	Lee	mlee1@sandia.gov	USA	Sandia National Laboratories
Chris	Lodewijk	C.F.J.Lodewijk@TNW.TUDelft.nl	The Netherlands	Delft University of Technology
Denis	Loudkov	denisnl@mail.ru	Russia	Moscow State Pedagogical University
Thomas	Lüthi	luethi@ph1.uni-koeln.de	Germany	Universität zu Köln
Alain	Maestrini	amaestrini@noos.fr	France	Université Pierre et Marie Curie
Sylvain	Mahieu	mahieu@iram.fr	France	IRAM Institut de Radio Astronomie MillimÈtrique
Doris	Maier	maier@iram.fr	France	Institut de RadioAstronomie
Ulrich	Mair	Ulrich.Mair@dlr.de	Germany	DLR German Aerospace Center
Frank	Maiwald	Frank.Maiwald@jpl.nasa.gov	USA	Jet Propulsion Laboratory, California Institute of Technology
Dan	Marrone	dmarrone@cfa.harvard.edu	USA	Harvard-Smithsonian Center for Astrophysics
Imran	Mehdi	Imran.Mehdi@jpl.nasa.gov	USA	Jet Propulsion Laboratory, California Institute of Technology
Denis	Meledin	meledin@oso.chalmers.se	Sweden	Chalmers University of Technology
Patricio	Mena	mena@sron.rug.nl	The Netherlands	SRON National Institue for Space Research
Harald	Merkel	harald.merkel@mc2.chalmers.se	Sweden	Chalmers University of Technology
Foulon	Michel-Francois	michel.foulon@iemn.univ-lille1.fr	France	IEMN
Raquel	Monje	raquel@oso.chalmers.se	Sweden	Chalmers University of Technology
Tetsuo	Mori	mori@infrared.co.jp	Japan	Infrared Limited
Axel	Murk	murk@mw.iap.unibe.ch	Switzerland	University of Bern
Alessandro	Navarrini	navarrin@astro.berkeley.edu	USA	University of California
Cojocari	Oleg	cojocari@hf.tu-darmstadt.de	Germany	Darmstadt Technical University.
Arne Øistein	Olsen	oistein.olsen@mc2.chalmers.se	Sweden	Chalmers University of Technology
Scott	Paine	spaine@cfa.harvard.edu	USA	Smithsonian Astrophysical Observatory
Miroslav	Pantaleev	pantaleev@oso.chalmers.se	Sweden	Chalmers University of Technology
Ferdinand	Patt	fpatt@eso.org	Germany	European Southern Observatory
Dimitry	Paveliev	pavelev@rf.unn.ru	Russia	Novgorod State University
Sergey	Pavlov	sergeij.pavlov@dlr.de	Germany	DLR Institute of Planetary Research
Unil	Perera	uperera@gsu.edu	USA	Georgia State University
Radoslaw	Piesiewicz	piesiewicz@ifn.ing.tu-bs.de	Germany	Technische Universität Braunschweig

Daniel	Prober	daniel.prober@yale.edu	USA	Yale University
Patrick	Puetz	ppuetz@as.arizona.edu	USA	SORAL, University of Arizona
Farshid	Raissi	raissi@kntu.ac.ir	Iran	K. N. Toosi University of Technology
Karl F.	Renk	karl.renk@physik.uni-regensburg.de	Germany	University of Regensburg Institute of Applied Physics
Heiko	Richter	Heiko.Richter@dlr.de	Germany	German Aerospace Center Berlin
Christophe	Risacher	risacher@oso.chalmers.se	Sweden	Chalmers University of Technology
Fernando	Rodriguez-Morales	rodrigu@ecs.umass.edu	USA	University of Massachusetts Amherst
Josef	Rosenzweig	Josef.Rosenzweig@iaf.fraunhofer.de	Germany	Fraunhofer-Institut für Angewandte Festkörperphysik
Staffan	Rudner	starud@foi.se	Sweden	FOI
Hans	Rudolf	hrudolf@eso.org	Germany	European Southern Observatory
Pär	Rundqvist	par.rundqvist@mc2.chalmers.se	Sweden	Chalmers University of Technology
Antti	Räisänen	antti.raisanen@tkk.fi	Finland	Helsinki University of Technology Radio Laboratory
Morvan	Salez	morvan.salez@obspm.fr	France	LERMA Observatoire de Paris
Theo	Scherer	scherer@iram.fr	France	IRAM Institut de Radio Astronomie MillimÈtrique
Matthias	Schicke	schicke@iram.fr	France	IRAM Institut de Radio Astronomie MillimÈtrique
Jan	Schuer	jan@lhft.eei.uni-erlangen.de	Germany	University of Erlangen-Nuremberg
Alexei	Semenov	alexei.semenov@dlr.de	Germany	DLR Institute of Planetary Reserach
Masumichi	Seta	seta@nict.go.jp	Japan	National Institute of Information and Communications Tech.
Wenlei	Shan	shawn@nro.nao.ac.jp	Japan	National Astronomical Obervatory of Japan
Shi	Sheng-Cai	scshi@mail.pmo.ac.cn	China	Purple Mountain Observatory
Sergey	Shitov	s.shitov@nao.ac.jp	Japan	National Astronomical Observatory of Japan (NAOJ)
Peter	Siegel	phs@caltech.edu	USA	California Institute of Technology
José Vicente	Siles	jovi@gmr.ssr.upm.es	Spain	Universidad Politecnica de Madrid
Anders	Skalare	anders.skalare@jpl.nasa.gov	USA	California Institute of Technology
Peter	Sobis	peter.sobis@mc2.chalmers.se	Sweden	Chalmers University of Technology
Benjamin	Stahl	Benjamin.Stahl@physik.uni-regensburg.de	Germany	University of Regensburg
Jan	Stake	jan.stake@chalmers.se	Sweden	Chalmers University of Technology
Piotr	Starski	starski@chalmers.se	Sweden	Chalmers University of Technology
Erik	Sundin	sundin@oso.chalmers.se	Sweden	Chalmers University of Technology
Stig Busk	Sørensen	sbs@ticra.com	Denmark	TICRA
Gie Han	Tan	ghtan@eso.org	Germany	European Southern Observatory
Rafael	Teipen	rteipen@ph1.uni-koeln.de	Germany	Universität zu Köln
Roman	Tesar	roman.tesar@aist.go.jp	Japan	National Institute of Advanced Industrial Science and Tech.
Thomas	Tils	tils@ph1.uni-koeln.de	Germany	Universität zu Köln
Edward	Tong	etong@cfa.harvard.edu	USA	Harvard-Smithsonian Center for Astrophysics,
Mattias	Torstensson	mattias.torstensson@mc2.chalmers.se	Sweden	Chalmers University of Technology
Armin	Wagner-Gentner	wagner@ph1.uni-koeln.de	Germany	Universität zu Köln
Christopher	Walker	cwalker@as.arizona.edu	USA	University of Arizona
John	Ward	john.ward@jpl.nasa.gov	USA	Jet Propulsion Laboratory, California Institute of Technology
Vessen	Vassilev	vevas@oso.chalmers.se	Sweden	Chalmers University of Technology
Robert	Weikle	rmw5w@virginia.edu	USA	University of Virginia
Hans-Olof	Vickes	hans-olof.vickes@ericsson.com	Sweden	Ericsson Microwave Systems AB
Wolfgang	Wild	W.Wild@sron.rug.nl	The Netherlands	SRON National Institue for Space Research
Dag	Winkler	dag.winkler@mc2.chalmers.se	Sweden	Chalmers University of Technology
Josip	Vukusic	vukusic@mc2.chalmers.se	Sweden	Chalmers University of Technology
Richard	Wylde	r.wylde@terahertz.co.uk	UK	Thomas Keating Ltd QMC Instruments Ltd
Alexander	Vystavkin	vyst@hitech.cplire.ru	Russia	IRE
Pavel	Yagoubov	p.a.yagoubov@sron.rug.nl	The Netherlands	SRON National Institue for Space Research
Ghassan	Yassin	ghassan@astro.ox.ac.uk	UK	University of Oxford
Sigfrid	Yngvesson	yngvesson@ecs.umass.edu	USA	University of Massachusetts Amherst
Ric	Zannoni	thezs@att.net	USA	University of Massachusetts Amherst
Cunlin	Zhang	cunlin_zhang@mail.cnu.edu.cn	China	Capital Normal University

AUTHOR'S INDEX

CHALMERS

MC2 ACCESS

To research groups in
EU, associate and candidate countries:

We offer free access to advanced processing for microwave electronics, photonics and nanotechnology.

Through an EU-financed programme we offer free access to advanced micro- and nanotechnology device processing environments for microwave and photonic devices, MEMS structures and for nanotechnology at the Department of Microtechnology and Nanoscience (MC2), Chalmers University of Technology, in Göteborg, Sweden. This offer is open for visiting researchers as well as remote users, both from universities and SMEs (small and medium size enterprises).

The facility provides means to develop process steps, process sequences, and components in small/medium quantities. In 1240 m² of clean-room area, more than 150 tools are available, including two e-beam lithography systems, silicon processing on up to 150 mm wafers, III-V and wide bandgap processing, molecular beam epitaxy, CVD and dry etching systems.

Only research groups that are entitled to disseminate the knowledge they have generated under the project are eligible to benefit from access to the infrastructure under the contract. **NOTE!** The sole exception to this rule are user groups from an SME that wish to use the infrastructure for the first time.

Contract No: 026029
Contract Period: 2006-2009

Project Manager:
Associate Professor
Ulf Södervall
access@mc2.chalmers.se

MC2
Microtechnology and Nanoscience

www.mc2.chalmers.se/MC2ACCESS